GSI

GSI Report 2017-1
September 2017

SCIENTIFIC REPORT 2016

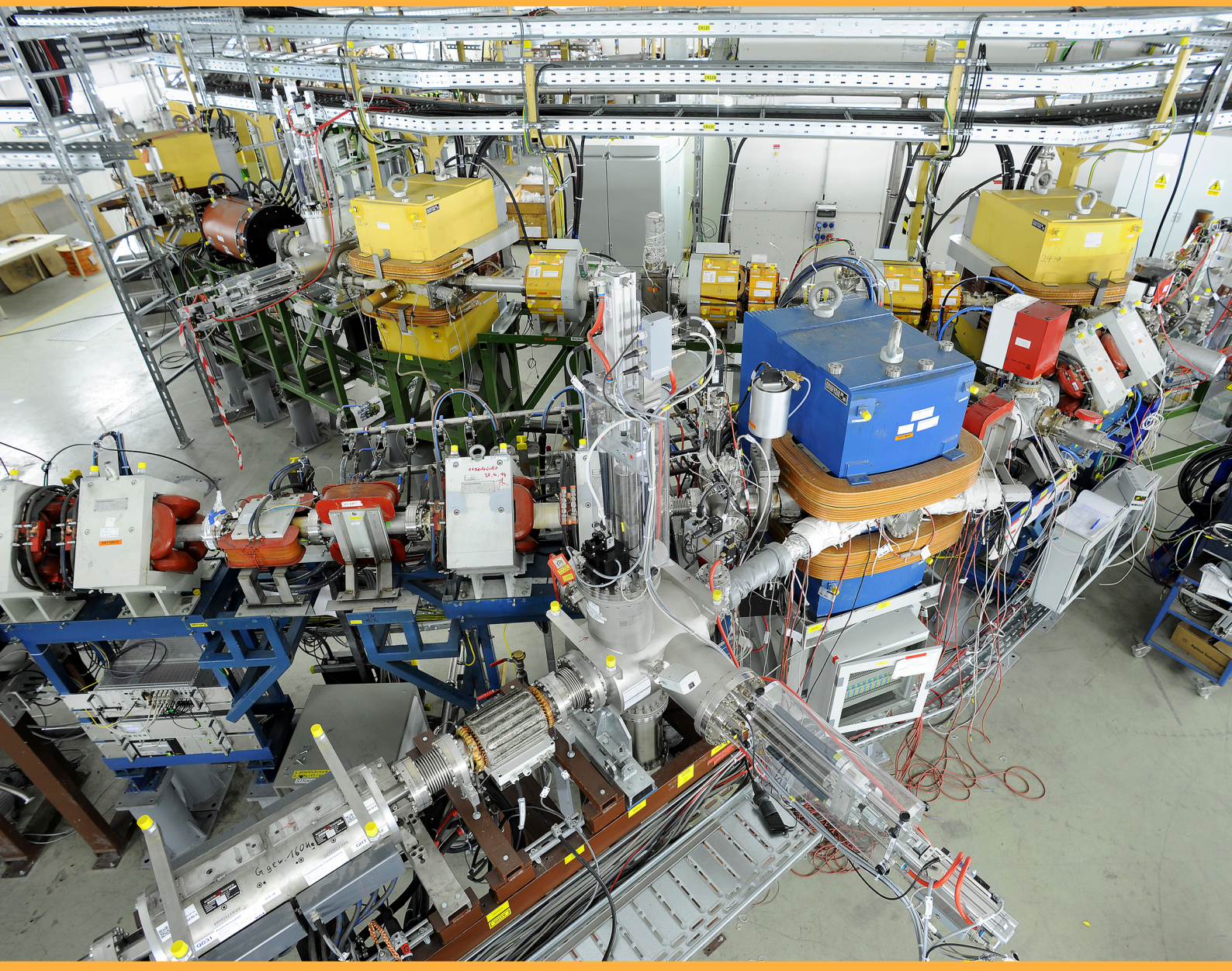

GSI Helmholtzzentrum für Schwerionenforschung GmbH
Member of the Helmholtz Association

The cover's photograph shows parts of the newly installed low enery storage ring CRYRING at the GSI, which was formerly located at the Manne Siegbahn Laboratory at Stockholm university. The storage ring has a diameter of 17m, and a maximum rigidity of 1.4 Tm. In the foreground the merging section of the beam from the local ion source coming the left and of the beam out of the storage ring ESR (coming from the lower left) is visible. In the background the ring magnets can be seen.
The storage ring is part of the international project CRYRING@ESR to support the FAIR research programmes SPARC, Biomat, FLAIR, and NUSTAR. For more information see the section ACCELERATOROPERATIONS-CRYRING (403pp.) in this report.

Photograph: detail of a photograph by G. Otto/GSI.

GSI Scientific Report 2016

GSI Report 2017-1

DOI:10.15120/GR-2017-1

ISSN: 0174-0814
and GSI Report 2017-1

Publisher: GSI Helmholtzzentrum für Schwerionenforschung GmbH,
Planckstr. 1, 64291 Darmstadt, Germany, <http://www.gsi.de>
GSI is a member of the Helmholtz association of national research centres <http://www.helmholtz.de>.
E-only-edition: DOI:10.15120/GR-2017-1

Editor: Katrin Große,
Contact: gsilibrary@gsi.de, phone: +496159 712610, fax: +496159 713049.
Photograph related to the cover: G. Otto/GSI
Publication date: September 2017

For the production of this report templates and scripts of the JACoW collaboration (Joint Accelerator Conferences on Web <http://www.jacow.org>) were used.

Contents

Thermal dilepton radiation at FAIR energies as probes of the fireball *

F. Seck[†1], *T. Galatyuk*[1,2], *R. Rapp*[4], *and J. Stroth*[2,3]

[1]Technische Universität Darmstadt, Darmstadt, Germany; [2]GSI, Darmstadt, Germany; [3]Goethe-Universiät, Frankfurt, Germany; [4]Texas A&M University, College Station (TX), USA

One of the main goals of the CBM experiment is the exploration of the states of matter created in heavy-ion collisions. Under conditions of extreme temperature and baryon density, the restoration of chiral symmetry and the transition to deconfinement might (partially) take place and lead to exotic phases of strongly interacting matter. The experimental detection of the resulting modifications to the properties of matter is, however, challenging since the traces of these signals can get convoluted or washed-out by several other effects, e.g. final-state interactions.

A prime tool in this search are, therefore, electromagnetic probes. Once they are produced, dileptons decouple from the collision region and retain the valuable information about the medium at the time of their creation.

Dileptons are emitted during all stages of a heavy-ion collision. Of particular interest in this respect is the thermal excess radiation above the hadronic cocktail, i.e. after the subtraction of the decays of long-lived mesons. The yield of thermal low-mass dileptons is sensitive to the fireball lifetime, while the slope in the intermediate-mass region of the dilepton invariant-mass spectrum can serve as a thermometer which is unaffected by blue-shift effects caused by the collective expansion of the medium [1].

For a proper description of the dilepton invariant-mass spectrum realistic thermal rates have to be convoluted with a model of the fireball's space-time evolution. As a compromise between the microscopic transport and macroscopic hydrodynamics at FAIR energies a coarse-graining procedure was developed and successfully applied to the SIS energy regime [2-4]. The local matter properties extracted with this approach are fed into a parametrization of the Rapp-Wambach spectral function [5] for in-medium ρ emission and lQCD-inspired QGP rates [6] (if high enough temperatures are reached). The pertinent dilepton spectra are then obtained by integrating these rates over the whole space-time evolution. An example of an invariant-mass spectrum of thermal dileptons in Ar+KCl collisions at 1.76A GeV is shown in Fig. 1 together with the data from the HADES experiment.

The thermal rates of e^+e^- and $\mu^+\mu^-$ pairs for Au+Au collisions at top SIS-100 energies of 11A GeV are now available to the CBM collaboration. With the implementation into the fast Monte-Carlo generator Pluto, it is possible to create a large statistics sample of dileptons that can be passed into the usual simulation and reconstruction chain.

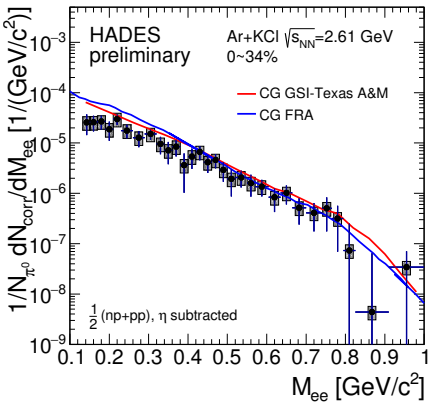

Figure 1: Comparison of dilepton excess spectra from two independent coarse-graining approaches [2-4] and the experimentally extracted yield above the hadronic cocktail in Ar+KCl collisions at 1.76A GeV from HADES [7,8].

The provided thermal spectra can serve as a basis for comprehensive experimental investigations. A significant deviation from this baseline in terms of extra yield in the low-mass range or a change in the emitting source temperature, extracted from the intermediate-mass range, could indicate a possible 1^{st} order phase transition [9]. Such scenarios and their observable consequences are currently subject to further investigations.

In the context of FAIR Phase-0 roughly 10% of the CBM time-of-flight detector modules will be installed as an endcap TOF in the STAR experiment during the upcoming RHIC beam energy scan II [10]. To fill the gap in the excitation function of dilepton production, our framework for the calculation of thermal dilepton spectra will also be applied to the proposed beam energies and be used for detector studies in the preparation of this scan in the years 2019-2020.

References

[1] R. Rapp and H. van Hees, PLB **753** (2016) 586

[2] S. Endres *et al.*, PRC **92** (2015) 014911

[3] T. Galatyuk *et al.*, EPJ A **52** (2016) 131

[4] F. Seck *et al.*, CPOD 2016 proceedings to appear in Acta Phys. Polon. Supp.

[5] R. Rapp and J. Wambach, EPJ A **6** (1999) 415

[6] R. Rapp, Adv. High Energy Phys. **2013** (2013) 148253

[7] HADES coll., G. Agakishiev *et al.*, PRC **84** (2011) 014902

[8] HADES coll., G. Agakishiev *et al.*, PLB **690** (2010) 118

[9] CBM coll., T. Alyazimov *et al.*, EPJ A **53** (2017) 60

[10] STAR coll. & CBM TOF group,`arXiv:1609.05102` (2016)

* This work was supported by the U.S. National Science Foundation under grant PHY-1306359, by the Humboldt foundation (Germany), by the Helmholtz-YIG grant VH-NG-823 at GSI and TU Darmstadt (Germany), and by the Hessian Initiative for Excellence (LOEWE) through the Helmholtz International Center for FAIR (HIC for FAIR).

† f.seck@gsi.de

Design of a control and monitoring system for the mirror alignment of the CBM RICH detector*

J. Bendarouach† [1] *and C. Höhne*[1]
[1]Justus Liebig University, Giessen

The alignment of the RICH mirrors is a decisive aspect for a reliable and high quality operation of the detector. A correction cycle, consisting of three stages, has been developed to address this problem [1, 2].

First a qualitative check of the mirrors using the CLAM (Continuous Line Alignment Monitoring [3]) method has been successfully implemented in the RICH prototype and validated during a beamtime at CERN. A correlation between mirror misalignments, inducing distorted rings and broken reflected stripes has been shown [4].

An additional quantification method for detected misalignments, inspired from the HERA-B experiment [5], has been adapted and tested in the simulation framework of the CBM-RICH detector. The method uses data to extract the rotation angles of a particular tile, provided a sufficient number of accumulated events are fully hitting the considered tile [6].

The last step combines the misalignment information from the two previous techniques, to correct for track projections.

The second step of the correction cycle, namely the quantification method, has been further developed and optimized. It can now detect misalignments on different mirror tiles simultaneously misaligned.

Subsequently, the performances of the correction routine have been investigated. The accuracy of the misalignment correction was calculated for different mirror tile locations in the mirror wall. For this study misalignments have been artificially induced around the horizontal and vertical axes and reconstructed using the quantification method. Two cases have been reviewed: for mirror tiles close to the beam pipe (later called inner tiles) and for tiles located in the outer region of the mirror wall (outer tiles).

Fig. 1 shows the reconstructed rotation angle, β, depending on the applied one, α, for both an inner tile (left plot) and an outer tile (right plot). In this case the tiles were artificially rotated around their horizontal axis, with misalignments ranging with various steps from 0.1 to 5 mrad. In the case of an inner tile, the reconstructed rotation angle of the rotated axis is very close to the applied one (orange line, left plot), while the reconstructed rotation angle of the unrotated axis is not influenced (green line, left plot). In case of the outer tile, the reconstructed rotation angle of the rotated axis increasingly diverges from the applied angle (orange line, right plot) and the unrotated axis picks up misalignment angles (green line, right plot).

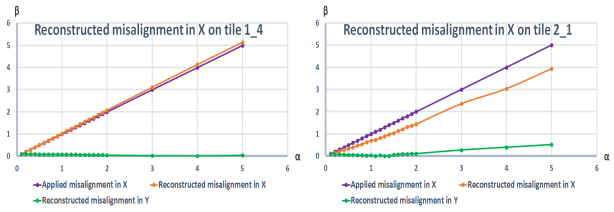

Figure 1: Reconstructed misalignment, β, depending on the applied one, α, for inner tiles (left plot) and outer tiles (right plot). The reconstructed misalignment angles, β, on the horizontal axis (orange lines) and on the vertical axis (green lines) are represented. Ideal reconstruction is shown by the purple line.

A similar behaviour, even more pronounced, has been observed in case of a rotation around the tile's vertical axis [2]. This effect is believed to be due to the detector geometry. Indeed for outer tiles, a rotation around a single axis causes a shift of the fitted ring center in both directions, which is then reconstructed as misalignment on both axes.

In the next step, the impact of misalignment and corrections on the full RICH performances will be studied. An automated correction routine, run with Urqmd events and for a fully misaligned mirror wall will be tested. The CLAM method will be further investigated in the lab.

References

[1] J. Bendarouach (CBM Collab.) J. Phys.: Conf. Ser. 742 2016 012007 http://dx.doi.org/10.1088/1742-6596/742/1/012007

[2] J. Adamczewski-Musch et al., "Design of a control and monitoring system for the mirror alignment of the CBM RICH detector", Nucl. Instr. Meth. Phys. Res. (2017), http://dx.doi.org/10.1016/j.nima.2017.02.033

[3] L. Steiger et al., Nucl. Instr. Meth. Phys. Res. A 639 (2011) 219

[4] J. Bendarouach et al., CBM Progress Report 2014, p.56

[5] M. Staric et al., Nucl. Instr. Meth. Phys. Res. A 586 (2008) 174

[6] J. Bendarouach et al., CBM Progress Report 2015, p.62

*Work supported by HIC for FAIR, HGS-HIRe, the GSI F&E-Cooperation with Giessen and BMBF grants 05P15RGFCA and 05P12RGFCG.

† jordan.bendarouach@exp2.physik.uni-giessen.de

DOI:10.15120/GR-2017-1

Procedure for charged hadrons identification in the CBM experiment

V. Klochkov[1,2] *and I. Selyuzhenkov*[1]
[1]GSI, Darmstadt, Germany; [2]Goethe-University Frankfurt, Germany

The goal of the CBM experiment at FAIR is to investigate the properties of dense baryonic matter. Important observables are the yields, spectra, collective flow, and correlations of identified particles. Particle Identification (PID) is required for a study of the mass and flavour composition of particle production in high-energy physics experiments. We present the procedure for identification of charged pions, kaons and protons tested with simulated Au+Au collisions at SIS100 energies. Particle identification via time-of-flight is based on simultaneous measurement of momentum p, time t and track lenght l of a particle using the relation to its mass m: $m^2 = p^2((t/l(p))^2 - 1)$. The CBM experiment allows identification of hadrons (pions, kaons and protons) in the angular range $2.5° < \Theta < 25°$.

To develop an automated procedure for PID a sample of 1.5M Au+Au collisions with beam energy of 10 AGeV simulated with UrQMD [2] event generator were used. CBM setup is simulated with CBMRoot version Nov16 and includes the beam pipe, magnet, MVD, STS, RICH, TRD, PSD and TOF [1]. For this analysis we used reconstructed tracks with at least 4 hits in STS and MVD, fit quality $\chi^2/NDF < 3$ and distance to primary vertex normalized to its error $\chi^2_{prim} < 3$.

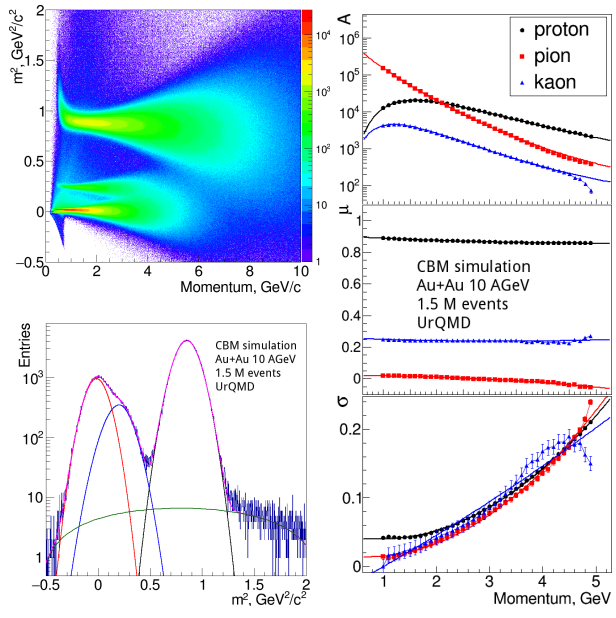

Figure 1: Distribution of m^2 versus p (top left) and for p = 4.0-4.1 GeV/c (bottom left) for positively charged hadrons. Magenta line shows the combined fit, green line shows background, others colors show contributions from different particles (π, K, p). (right) Parametrization of m^2 spectra in different momentum bins.

PID procedure is similar to that developed in ALICE [4]:

1. Fill m^2 vs p distribution for a pure sample of π, K and p (denoted below as 2D-(π,K,p)) and for all particles (2D-all). Pure sample of pions, kaons and protons can be obtained from decay daughters of K^0_s, Λ and ϕ using KF Particle Finder [3].
2. Parameterize m^2 distribution in slices of momentum:
   (a) Fit each slice of 2D-(π,K,p) using generalized Gaussian function $G(m^2) = Ae^{-(\frac{|m^2-\mu|}{\sigma})^k}(1 + Erf(s\frac{m^2-\mu}{\sqrt{2}\sigma}))$ with 5 paramemters abundance (A), mean (μ), sigma (σ), s and k are connected with skewness and kurtosis.
   (b) Fit each slice of 2D-all with a sum of generalized Gaussians $G(m^2, p)$ and polynomial function for background $BG(m^2, p)$.
3. Parametrize momentum dependence of the fit parameters. Repeat until parameters are stabilized.
4. Save fit parameters to the ROOT file for further use in the analysis.
5. Calculate a bayesian probability P_j for a given m^2 and p for a particle to be of type j:

$$P_j(m^2, p) = \frac{G_j(m^2, p)}{\sum_{i=\pi,p,K} G_i(m^2, p) + BG(m^2, p)}.$$

This procedure should be applied in different centrality classes [5]. In Fig. 1 an illustration of PID determination procedure using Gaussian fit function ($k = 2$ and $s = 0$ in $G(m^2)$) is shown. A pure sample of particles is obtained using MC-true information.

In summary, procedure for particle identification was developed for CBM. Bayesian approach allows to select sample of high-purity charged hadrons as a function of centrality and momentum and to unfold the measured observables based on parametrization of abundances of each particle. In future the efficiency, purity and misidentification of the PID method will be investigated.

References

[1] N. Herrmann et al. [CBM Collaboration], TDR for the CBM TOF, http://repository.gsi.de/record/54798.

[2] M. Bleicher et al., J.Phys. G25, 1859 (1999).

[3] M. Zyzak, PhD Thesis, http://publikationen.ub.uni-frankfurt.de/frontdoor/index/index/docId/41428

[4] J. Adam *et al.* [ALICE Collaboration], Eur. Phys. J. Plus **131**, no. 5, 168 (2016)

[5] V. Klochkov and I. Selyuzhenkov, GSI Scientific Report 2015 p.23 (2016) http://repository.gsi.de/record/189686

DOI:10.15120/GR-2017-1

Neutron shielding for PSD readout by SiPM*

O. Svoboda†[1], *F. Guber*[3], *A. Kugler*[1], *and A. Senger*[2]
[1]NPI CAS, Rez, Czech Republic; [2]GSI, Darmstadt, Germany; [3]INR RAS, Moscow, Russia

Radiation damage of the components of the CBM Projectile Spectator Detector (PSD) is an important issue. High intensity beams at the FAIR SIS100 will cause fast degradation of currently available types of SiPM planned for the detector readout. Parallel to the search for more radiation hard SiPM also the ways to reduce the neutron doses were investigated and polyethylene based neutron shielding was developed.

Radiation sensitive SiPM readout

The PSD is a compensating lead-scintillator calorimeter designed to measure the energy distribution of the projectile nuclei fragments (spectators) and forward going particles produced close to the beam rapidity [1]. Beams at FAIR SIS100 of up to 1E7 interactions/s will lead to a high radiation emission to the PSD producing a high neutron fluence of up to 4E12 n/cm^2 accumulated during one year of the experiment operation. Silicon photomultipliers (SiPM, sometimes marked also as avalanche photodiodes (APD)) are planned to be used for light readout from the wavelength shifting fibers (WLSF) connected to the plastic scintillators.

Although there is a relatively large number of SiPM manufacturers today, all types of SiPM suffer from low radiation hardness. In PSD, the SiPMs are the weakest component from the radiation hardness point of view. Intensive studies of SiPM radiation hardness are being performed at NPI Rez, see e.g. [2]. Currently available SiPMs from different vendors are irradiated with different neutron doses and their properties are studied in detail. Parallel to this, also the ways to reduce neutron dose are tested.

PSD as spallation target

Taking into account the composition of the PSD detector, namely lead and plastic, the PSD may be seen as a massive spallation target with neutron moderator. To see the "spallation" spectra at the end of the PSD setup, where the SiPMs are placed, a MCNPX 2.7 simulation was run [3]. One PSD module represented by an alternating lead-plastic structure of real dimensions was irradiated in the center with a white beam of 100 MeV - 10 GeV protons in the simulation. Neutron spectra were scored at the end of PSD and it was checked, that similar result will be obtained for the white spectra neutron beam of the same energy span. Gained neutron spectra were later used to fast simulate the efficiency of the proposed shielding.

MCNPX simulation

Several dimensions and boron enrichment of polyethylene neutron shielding were consequently tested in the MCNPX simulation. Neutron and proton spectra were calculated in the volume representing the SiPM diode, for results please see Figure 1. It was shown that even only 5 cm of 3 percent borated polyethylene can significantly lower the thermal neutron flux. Number of secondary protons created in this shielding is negligible. However, the MCNPX simulation was only an approximation due to unknown particle spectra hitting the PSD in real experiment.

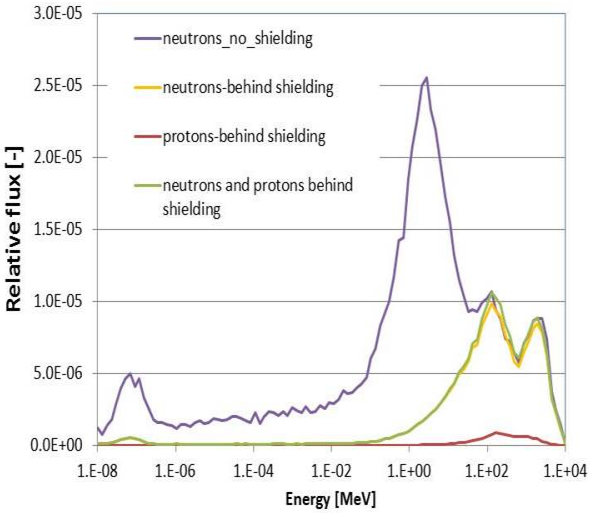

Figure 1: MCNPX 2.7 simulation of single PSD module with neutron shielding.

Fluka simulation

The proposed neutron shielding was tested also in the Fluka code [4], taking into account complex CBM setup and conditions. Fluka simulation proved significant decrease in neutron equivalent fluence at the position of PSD SiPM readout, especially for the most central modules, please see Figure 2. Differences in the neutron fluence with and without the polyethylene shielding are almost one order of magnitude. This might be the difference between slightly damaged SiPM, which can still read-out the light

*Work supported by Czech MEYS - LM2015049 , OP VVV - CZ.02.1.01/0.0/0.0/16_013/0001677
† svoboda@ujf.cas.cz

DOI:10.15120/GR-2017-1

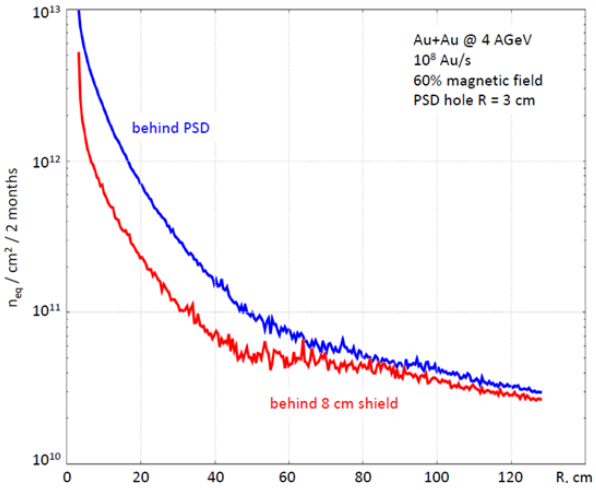

Figure 2: Fluka simulation of neutron shielding for PSD.

pulses from WLSF, and completely damaged SiPM with unacceptable high noise.

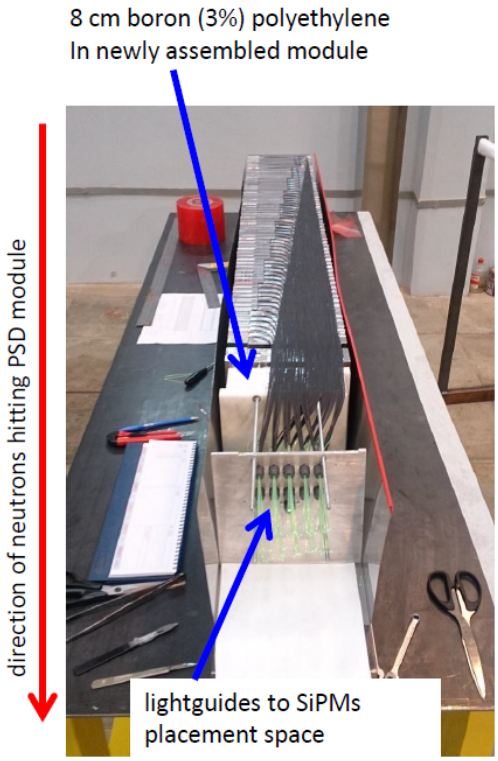

Figure 3: Assembly of PSD module including neutron shielding.

PSD module construction

Taking into account the results of MCNPX and Fluka simulations, it was decided to use neutron shielding of SiPM in PSD in the form of 8 cm thick polyethylene blocks, with three percent of boron. Shielding blocks are being mounted in the currently build PSD modules, see Figure 3. This shielding should provide additional safety reserve and lower the SiPM degradation in normal operation conditions.

Conclusion

Simple idea on significant reduction of neutron flux at the end of PSD was verified in MCNPX and Fluka simulations and successfully adopted in the construction of PSD modules. Lowering of especially thermal neutron flux can help together with the search on more radiation hard SiPM to build the PSD ready for SIS100 experiments and their high beam intensities.

References

[1] CBM collaboration, Technical Design Report for the CBM Projectile Spectator Detector (PSD), GSI Darmstadt 2015

[2] V. Kushpil et al., Neutron irradiation study of silicon photomultipliers from different vendors, NIM A (2016), http://dx.doi.org/10.1016/j.nima.2016.06.101

[3] MCNPX (Monte Carlo N-Particle eXtended), Los Alamos National Laboratory LA-CP-11-0438

[4] T.T. Bohlen et al., The FLUKA Code: Developments and Challenges for High Energy and Medical Applications, Nuclear Data Sheets 120, 211-214 (2014)

DOI:10.15120/GR-2017-1

Status of micro-strip sensor development for the CBM Silicon Tracking System

J. M. Heuser[1], C. J. Schmidt[1], C. Sturm[1], A. Lymanets[1,5], O. Bertini[1], M. Teklyshin[2,5], Ie. Momot[3,1,5], H. Malygina[3,1,5], P. Larionov[3,4], and Y. Murin[6]

[1]GSI, Darmstadt, Germany; [2]FAIR, Darmstadt, Germany; [3]Goethe Universität, Frankfurt, Germany; [4]now at INFN-LNF, Frascati, Italy; [5]KINR, Kiev, Ukraine; [6]JINR, Dubna, Russia

Double-sided silicon microstrip sensor technology will be employed in CBM's Silicon Tracking System as one of the measures to achieve two-coordinate track-point determination with high spatial resolution and high momentum resolution through a minimized material budget [1]. Depending on their positions within the eight tracking stations, the sensors have been designed in four geometrical shapes. They have the same total width and numbers of strips but differ in the lengths of the strip-shaped electrodes, matched to the particle densities in the respective detector region. The main sensor parameters have been listed e.g. in reference [2]. Here shall be emphasized only: a) the thickness (285/320 $\pm$15 μm, vendor dependent), b) the outer dimensions (6.2 cm width; 2.2, 4.2, 6.2 and 12.4 cm height) and c) the strip lengths (2, 4, 6 and 12 cm), yielding 1024 strips of 58 μm pitch per sensor side. Front-and back-side strips are arranged under a 7.5 degree stereo angle. The short angled corner strips of the p-side are interconnected via routing lines on a second metal layer to allow read-out of the entire sensor from one sensor edge.

The production masks, established together with the two vendors, have been further advanced with respect to several important details. Small series of sensors have been realized through GSI and JINR purchase orders incorporating those improvements. They include e.g. multiple guard rings on the sensors' n-sides, with the intention to further increase operaration voltage limits, and perimeter lines being compatible with "stealth" laser dicing also at CiS to yield high-precision mechanical dimensions. Processing on 6" wafers, pre-requisite for fabricating the largest sensor, is standard at Hamamatsu and being put into operation at CiS next to the established 4" production line.

The assessment of the sensors has been advanced further. Quality assurance procedures, equipment and work sharing have been nearly finalized and documented. A test with non-irradiated sensors under anticipated thermal operating conditions (T=-5 °C) was carried out at COSY, Research Center Jülich, using a proton beam at close to minimum ionizing energy. Sensor samples have been altered with protons to beyond the end-of-life neutron equivalent fluence at the irradiation facility of the Karlsruhe Institute of Technology (KIT). The performance of the sensors with respect to ionizing radiation was addressed in a comprehensive CBM workshop at KIT bringing together silicon detector experts from different experiments and vendors. A STS project-internal workshop took place at GSI in March 2017 to define the roadmap for sensor production readiness. [1]

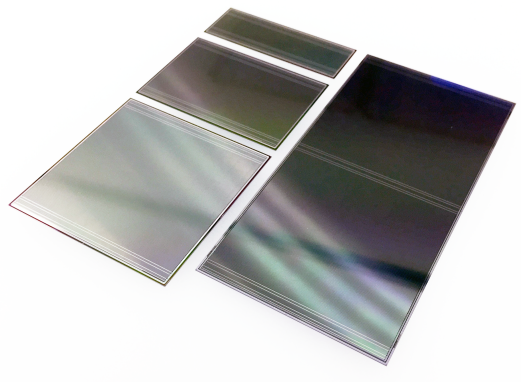

Figure 1: Microstrip sensors for the CBM Silicon Tracking System produced in the four major shapes (6.2 by 2.2, 4.2, 6.2 and 12.4 cm outer dimensions).

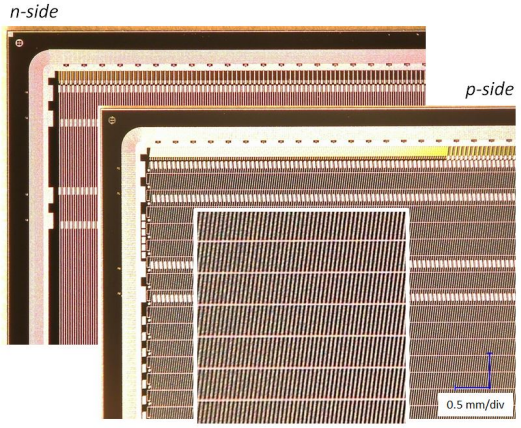

Figure 2: Close-up views of the most recent microstrip sensors, showing the strip segmentation on two sensor sides, the double-metal routing lines (magnified in the inlet) and sensor edge structures including multiple guard rings.

References

[1] GSI Report 2013-4 (2013), chapter 2.3

[2] CBM Progress Report 2015 (2016), p. 22

[3] http://www.cismst.org

[4] http://www.hamamatsu.com

[1]supported by HICforFAIR and EU-H2020 Project CREMLIN

DOI:10.15120/GR-2017-1

Test performance of the basic architecture for the inner zone of the CBM-TOF wall using heavy-ion beam at SPS-CERN *

M. Petriş[1], D. Bartoş[1], M. Petrovici[1], L. Rădulescu[1], V. Simion[1], J. Frühauf[2], M. Kiš[2], P-A. Loizeau[2], I. Deppner[3], N. Herrmann[3], and C. Simon[3]

[1]NIPNE, Bucharest, Romania; [2]GSI, Darmstadt, Germany; [3]PI, Heidelberg University, Germany

The Time Of Flight (TOF) subsystem is one of the core detectors of the CBM experiment. The TOF wall in conjunction with Silicon Tracking System (STS) is foreseen to identify charged hadrons, i.e. pions, kaons and protons, in the full acceptance of the system (the angular range covered by the STS detector of 2.5^0-25^0). It covers an active area of about 120 m^2 approximately rectangular in shape. A system time resolution of at least 80 ps including all possible contributions, such as electronics jitter and the resolution of the time reference system is needed. This requires a single channel time resolution better than 60 ps with an efficiency of at least 95%. Such a performance should be maintained up to a counting rate which, very close to the beam pipe, exceeds 30 kHz/cm^2 [1].

Our R&D activity has been focused on the development of a Multi-Gap RPC with Multi-Strip readout (MSMGRPC) for high counting rate and multiplicity environment, as it is anticipated to be in the inner zone of the CBM-TOF. Based on the good results obtained with the narrow strip pitch (2.54 mm) double stack counter (2 x 5 gas gaps of 140 μm), in terms of efficiency, time and two-dimensional position resolutions [2], a new prototype with the strip pitch equal with 7.4 mm (5.6 mm strip width) and a strip length of 96 mm was designed and built. Construction details of this prototype, called RPC2012, and its performance in the in-beam tests performed at CERN-PS accelerator together with the concept of the modular configuration of the CBM-TOF inner wall based on this RPC architecture were reported in [3].

The prototype was tested at H4 beam line of CERN SPS-facility, using reaction products produced by an Ar beam of $13A$ GeV energy incident on a Pb target. The average obtained cluster size was 1.6 strips per hit and the time resolution, including the electronics contribution, was of $\sim$60 ps [4]. For all these tests mentioned above a front-end electronics based on 8 channel NINO chip [5] was used for signal processing.

Here we report the performance, in close to real conditions, of this architecture operated with a FEE based on a 32 channel motherboard [1] containing 4 PADI chips[7], the front-end electronics anticipated to be used for the CBM-TOF wall. The signals were digitized by 32-channel FPGA-TDCs [8] and readout via TRB3 [9] data hubs. The in-beam test were performed at CERN-SPS with a $30A$ GeV Pb ions incident on a Pb target.

The CBM-TOF experimental setup was divided in "low rate" and "high rate" branches, the last one being positioned at a polar angle of about 3^0 relative to the beam axis. A comprehensive description of the whole setup is given in [6]. Our prototypes were positioned in the high rate setup, the RPC2012 prototype being 'sandwiched' between RPC2015 [11] and RPCref prototypes. A diamond detector positioned in front of the target together with RPCref positioned at the end of the set-up, delivered the information for particle velocity measurement. A photo of the "high rate" branch is shown in Fig. 1. The spatial position along the

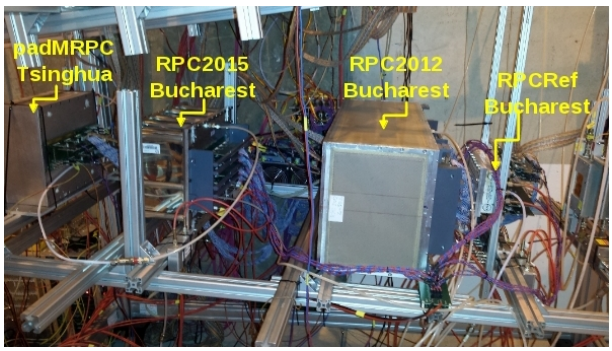

Figure 1: Photo of the high rate experimental set-up based on MGRPC prototypes used in the in-beam test.

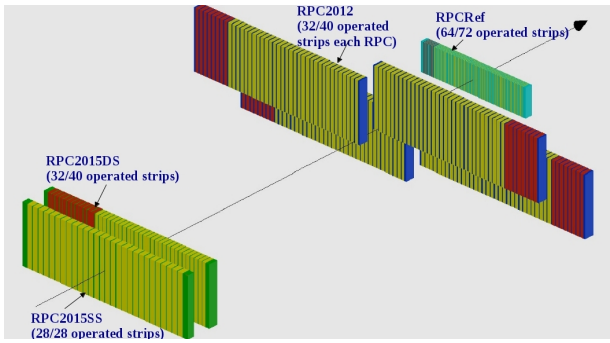

Figure 2: Sketch of the spatial position of the seven RPCs tested in the high rate setup at CERN-SPS.

*Romanian NASR/contract RO-FAIR F04 and NASR/NUCLEU Project PN16420104

beam line of the seven prototypes tested by our group and their operated area (green color) are presented in Fig. 2.

The principles of the data analysis starting from unpacking to calibration and corrections for slewing effect, position and reaction product velocity spread are described in [12]. In the left side of Fig. 3 is presented the time difference spectrum between one of the four counters positioned in the upper part of the text box (called RPC2012_3) and RPC2015DS (see reference [11]), with the same inner geometry and the same strip pitch. The 63 ps standard de-

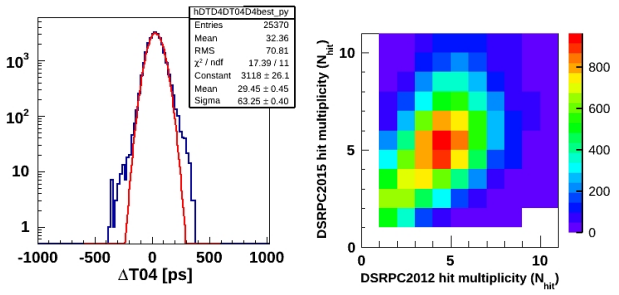

Figure 3: Time difference spectrum - left. Hit multiplicitiy correlation - right.

viation of the Gauss fit demonstrates the very good system time resolution. A single counter time resolution of 44 ps, including the electronic contribution is obtained supposing equal contributions of the two detectors. The comparison of the 63 ps standard deviation with the 71 ps RMS of the spectrum shows a non-significant contribution of the non-Gaussian tails. The correlation of the hit multiplicities in the two counters shows that in the most part of the events, almost the same multiple hits are incident on both detectors. The detectors were operated at 2 x 5.5 kV voltage. Due to their staggered positions, position cuts on both x and y directions were applied in the RPC2015DS, considered as reference counter, for efficiency estimation. However, due to a partial overlap of the active area of each of the four counters relative to the RPC2015DS, the obtained values are still affected by the hits lost at the edges of the overlaped area.

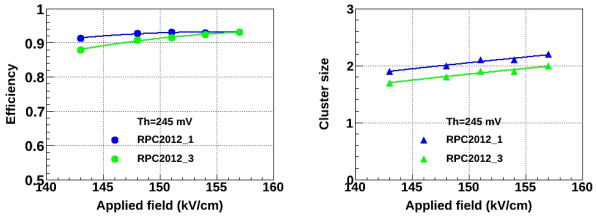

Figure 4: Efficiency - left and cluster size - right as a function of high voltage for RPC2012_1 and RPC2012_3.

In Fig. 4 is shown an expected behaviour of the efficiency and cluster size as a function of high voltage, for RPC2012_3 and RPC2012_1 (right mirrored relative to the axe shown in Fig. 2) for a PADI threshold of 245 mV. In the mentioned geometry of the experiment, a 93% efficiency for both counters was obtained. If we take into consideration the inner geometry of the RPC2012 counters of 2 x 5 gaps of 140 μm, the same as for RPC2015DS [10, 11], we could consider that at a nominal voltage of 2 x 5.5 kV the efficiency is in fact at the same value as for RPC2015DS (97%). The cluster size is of 2.2 strips for RPC2012_1 and of 2.0 strips for RPC2012_3 in the region of efficiency plateau. Average system time resolution of 73 ps for RPC2012_1 and of 67 ps for RPC2012_3 remain almost unchanged over the investigated high voltage range, as is shown in Fig. 5.

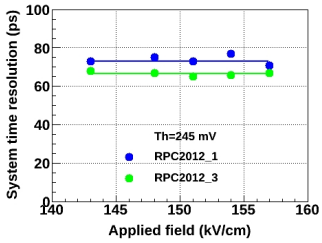

Figure 5: Time resolution as a function of high voltage for RPC2012_1 and RPC2012_3.

The single counter time resolution of 52 - 47 ps fullfils the single counter performance required for the inner zone of the CBM-TOF wall.

The results presented in the contributions to this Progress Report (present one and [11]), show that the MSMGRPC prototypes and the proposed basic architecture fulfill the requirements for the inner zone of the CBM-TOF wall.

References

[1] CBM-TOF Collaboration, CBM-TOF TDR, October 2014

[2] M. Petrovici et al, 2012 Journal Of Instrumentation, Volume 7, 2012 (2012 JINST 7 P11003).

[3] M. Petris et al., CBM Progress Report 2012 (2013), p.68

[4] M. Petriş et al., Journal of Physics: Conference Series 724 (2016) 012037

[5] F. Anghinolfi et al., Nucl.Instr.and Meth. A533(2004)183

[6] C. Simon et al., CBM Progress Report 2015, (2016), p.90

[7] M. Ciobanu et al., CBM Progress Report 2013, (2014), p.84

[8] C. Ugur et al., GSI Scientific Report 2014 (2015), p.212

[9] M. Traxler et al., GSI Scientific Report 2014 (2015), p.514

[10] V. Aprodu et al., CBM Progress Report 2015 (2016), p.98

[11] M. Petriş et al., this GSI Scientific Report

[12] M. Petriş et al., Journal of Instrumentation, Volume 11, September 2016 (2016 JINST 11 C09009)

DOI:10.15120/GR-2017-1

Prototype carbon fiber ladders for the CBM-STS made in industry

W. Niebur, M. Faul, and J. M. Heuser
GSI, Darmstadt, Germany

Carbon fiber support structures for the detector ladders of the CBM Silicon Tracking System are a central element for achieving a mechanically stable and, at the same time, low-mass detector [1].

Recently, prototype carbon fiber supports have been produced using an industrial process. That is based on winding high-modulus carbon fibers [2] around three support tubes. During this process, the tubes are installed on a hub that has been custom-designed at GSI and produced from Aluminum in precision mechanics industry [3]. The winding itself has been carried out in aerospace industry [4]. The hub is shown in Fig. 1. It consists of a core piece that can be installed on a rotating fixture, and three side pieces receiving the longitudinal support tubes. After winding and drying of the epoxy-clad fibers, the side pieces can be retracted and the hub removed from the produced structure. With a length of 130 cm, the hub allows producing carbon ladders of 110-120 cm length, matching the largest STS tracking stations. The base of the ladders is 6.1 cm wide, the height is 2.0 cm. The cell spacing realized by winding is ca. 4.0 cm. The tube support structure was chosen as it is best suited for overlaying it with the wound fibers, not risking sharp bends. With an outer/inner diameter of 1.5/0.5 mm, the tubes offer a low material cross section at essentially all particle crossing angles. Table 1 shows technical specifications of the three types of prototype ladders produced so far; they are depicted side by side in Fig. 2. The ladders differ in the carbon fiber used, both type and filaments contained, as well as the number of rovings per strud. A further, fourth prototype is being processed using fiber type M60J/3K with roving 4 or 5.

As the weight of the objects differ only slightly, the decision on which prototype to consider for further pre-series manufacturing will be based on the forthcoming analysis of the mechanical strength obtained, in terms of bending, twisting and squeezing. Sections of the carbon fiber ladders produced are already being employed in the ladder assembly tool that is currently under development [5].

Table 1: Specifications of the prototype ladders.

	prototype 1	prototype 2	prototype 3
support	CFK pipe	CFK pipe	CFK pipe
	0.5/1.5 mm ∅	0.5/1.5 mm ∅	0.5/1.5 mm ∅
matrix	L20/EPH960	L20/EPH960	L20/EPH960
fiber	M55J/6K	M55J/6K	M60J/3K
roving	1	2	3
weight	11.2 g	14.8 g	11.2 g

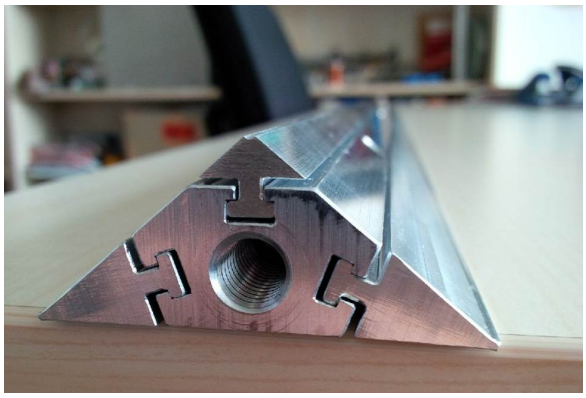

Figure 1: Hub made from Aluminum for the winding of carbon fibers around suport structures of different shapes.

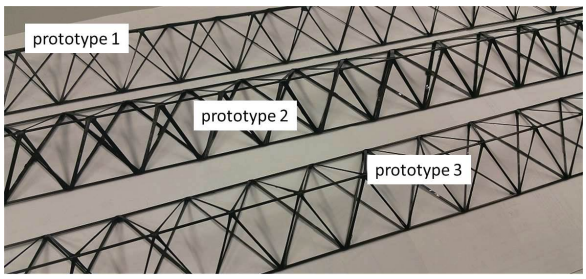

Figure 2: Prototype carbon fiber ladders produced according to the specifications shown in Table 1.

References

[1] Technical Design Report for the CBM Silicon Tracking System, GSI Report 2013-4 (2013), chapter 5.4

[2] Toray Industries Inc., www.toray.com

[3] Frühwein Mechanik GmbH & Co. KG, 64839 Münster/ Dieburg, Germany; www.mechanik-fruehwein.de

[4] xperion GmbH & Co. KG, Performance Polymer Composites, 88677 Markdorf, Germany; www.xperion-ppc.de

[5] U. Frankenfeld et al., Ladder assembly concept and tool, this report

DOI:10.15120/GR-2017-1

A data model for time slices and events in cbmroot

V. Friese
GSI Helmholtzzentrum für Schwerionenforschung GmbH, Darmstadt, Germany

The data interface of experiment and reconstruction software in CBM is the so-called time slice, a container comprising the complete detector raw data within a given time interval. These data are not associated to "events" (beam-target interactions) by a hardware trigger. It is the task of the reconstruction software to establish events out of this data stream. Thus, reconstruction starts from time slices and ends with events, which are either used for online data selection or given offline to the high-level physics analysis. The simulation faces the reverse challenge: Starting from modeling physical events by some suitable event generator, the detector response has to generate a data stream equivalent to that in the real experiment. The `cbmroot` framework thus has to provide an environment which allows to handle time slices and events at the same time.

Historically, `cbmroot` evolved along the lines of a classical, event-based framework, using the `FairRoot` layer on top of `ROOT` as a platform. Events were naturally represented by entries of a `ROOT TTree`, with event data in TClonesArrays as branches of the tree. Tasks operated on these data arrays event by event, triggered by each new entry of the `TTree`. Meanwhile, a complete reconstruction chain is available for this event-based mode.

The necessity to go beyond the event-by-event data processing towards the real, free-streaming data flow was clear from the beginning, and developments in this direction started many years ago by extensions of the framework [1, 2]. This was accompanied by the development of the DAQ software and the time slice data format [3] and by corresponding developments of the `FairRoot` software layer supporting the treatment of free-streaming data [4]. However, the necessity to define a data format suitable to the specific CBM needs remained. Such a data model was developed, tested and implemented in the year 2016.

The new data model closely resembles the old one on a formal level. It continues relying on the `ROOT TTree`, but one tree entry now represents one entire time slice, containing data from many physics events. Data are again arranged in TClonesArrays as branches of the tree, one array per data type (e.g, digi, cluster, hit, track). Events are represented by the dedicated data class `CbmEvent` in their own TClonesArray. The event class does not contain the data themselves, but a collection of indices of the associated data objects in their respective array (Fig. 1). Based on this scheme, the reconstruction can be divided into three parts:

1. Tasks before event building ("time-based tasks") operate on the entire time slice without information on events. Such time-based reconstruction was already developed for cluster-, hit- and track-finding in the STS.
2. The event-building task associates data to events by the method `CbmEvent::AddData(Cbm::DataType, UInt_t)`, with the type and index of the data object as argument. Event-building can be done on any data level, e.g., based on digis (raw data) or on already reconstructed tracks.
3. Tasks after event building ("event-based tasks") operate on data previously associated to events by the event-building task. They thus involve at each call a loop over all events within the current time slice. All already developed event-based tasks can be used here with only minor modifications in the data interfaces.

The chosen approach fulfills the requirements outlined above. Besides being simple and requiring minimal intervention to the existing code base, its advantages are manifold. First, no data copy is required when associating a data object to an event. Second, the scheme provides the flexibility to define events based on any data level, e.g., with digis before any reconstruction or with reconstructed tracks. Both time-based and event-based algorithms can easily be integrated. The old, event-based simulation and reconstruction can be used within the same framework for reference; formally, this merely constitutes a special case with exactly one event per time slice. The price to pay are one additional integer (for the index) per data object and an additional (event) loop for event-based tasks. Performance checks up to now did not show a significant impact on the computing speed.

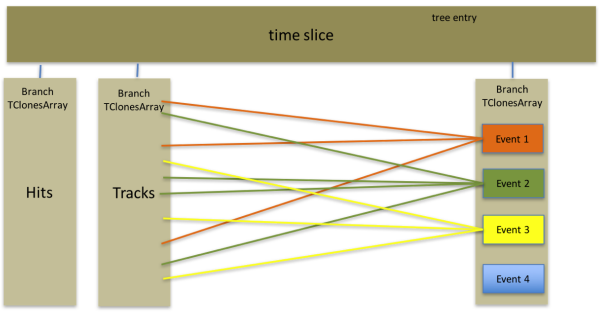

Figure 1: Event representation in the new data model. In this example, events are defined from reconstructed tracks.

References

[1] V. Friese, J. Phys. Conf. Ser. **331** (2011) 032008
[2] V. Friese, Springer Lect. Notes Comp. Sci. **7125** (2012) 17
[3] J. de Cuveland and V. Lindenstruth, subm. to J. Phys. Conf. Ser. (proceedings CHEP 2016)
[4] M. Al-Turany *et al.*, J. Phys. Conf. Ser. **396** (2012) 022001

DOI:10.15120/GR-2017-1

Time-based selection of $J/\psi \rightarrow \mu^+\mu^-$ decays with the CBM-MUCH

T. Ablyazimov[1,2]*, V. Friese*[1]*, and V. Ivanov*[2,3]

[1]GSI Helmholtzzentrum für Schwerionenforschung GmbH, Darmstadt, Germany; [2]LIT JINR, Dubna, Russia;
[3]National Research Nuclear University "MEPhI", Moscow, Russia

The detection principle of the CBM muon system (MUCH) suggests to derive a software trigger on high-mass muon pairs using data from the MUCH alone, without a prior, compute-expensive reconstruction of tracks in the main tracking system (STS). A library of algorithms suitable for standalone track reconstruction in MUCH is being developed by the authors starting from 2013 [1]. It also comprises an approach suitable for the selection of J/$\psi \rightarrow \mu^+\mu^-$ decays based on reconstructed MUCH tracks with good efficiency and a suppression ratio exceeding 10^3 [2–4].

The results described in the referenced articles were obtained with simulated data which were separated into distinctive portions corresponding to collision events. For application in the real experiment, the triggering software must be able to work with bunches of measured data ("time slices") containing measurements from many different events.

The introduction of this paradigm entailed two aspects. First, the time attribute of the measurements had to be taken into account for the association of hits to tracks. This could be realised in a straightforward way by an upgrade of the data structures with the new attribute and its use in the determination of the measurement vicinity. The second consequence of the time-based approach is that the algorithms have to deal with severely increased combinatorics when the input data chunks contain many events instead of just one. Coping with this situation required to completely revise the search data structures and the corresponding algorithms.

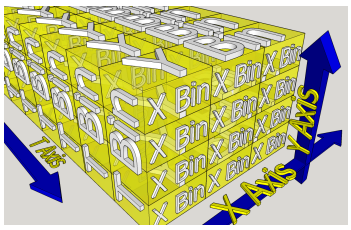

Figure 1: Bin hierarchy in the x, y and time space

All measured hits were placed into 3-dimensional binned structures, where "bins" are cuboids in the 3-dimensional space of the x-, y- and time coordinates. Each "bin" contains only a very limited number of hits or is even empty. The procedure of finding the corresponding bin for a given point in the x-, y- and time space is simple and straightforward. Each MUCH station is represented as a 3-dimensional, hierarchically organized array of bins (Fig. 1).

Although the main goal of the library is to trigger on J/$\psi \rightarrow \mu^+\mu^-$ decays, it is also considered to use it for the selection of the decays of lighter vector mesons. In previous versions, the track reconstruction started from the last MUCH station, to reduce combinatorics as much as possible. This approach excluded the reconstruction of low-mass vector meson decays, the daughter muons of which do not pass the last absorber. Thus, the approach was changed for the current library version: reconstruction now starts from the station before the last absorber. This enables the reconstruction of a sufficient share of low mass vector meson decays into the di-muon channel.

The tracks reconstructed in this way are later checked for the possibility to prolong them up to the last station. In the SIS-100 CBM muon setup, the last MUCH station is a TRD station with 4 detecting layers. The reconstructed tracks are checked for matching with hits in TRD as schematically shown in Fig. 2. Only tracks fulfilling this criterion are used for triggering on J/$\psi \rightarrow \mu^+\mu^-$.

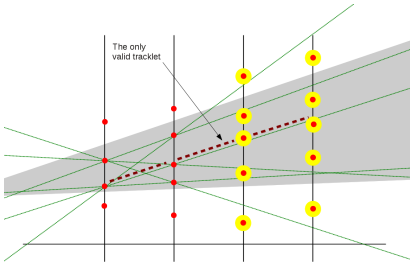

Figure 2: Matching a MUCH track with TRD hits

The performance of the algorithm was assessed by simulations for Au+Au collisions at 10A GeV from UrQMD. The reconstruction efficiency for J/ψ embedded into central events is 83%. The average reconstruction time for minimum-bias events is 4 μs on an Intel Xeon 3.1 GHz processor. The event number is reduced by a factor of 3,800; the data suppression factor is 1,700.

References

[1] T. O. Ablyazimov and V. V. Ivanov, CBM Progress Report 2014, GSI-2015-01521, p. 117

[2] T. O. Ablyazimov and V. V. Ivanov, CBM Progress Report 2014, GSI-2015-01521, p. 119

[3] T. O. Ablyazimov and V. V. Ivanov, Phys. Part. Nucl. Lett. **12** (2015) 559

[4] T. O. Ablyazimov and V. V. Ivanov, Eur. Phys. J. Web Conf. **108** (2016) 02001

DOI:10.15120/GR-2017-1

Time-based MUCH digitizer

V. Singhal[1], *S. Chattopadhyay*[1], *and V. Friese*[2]
[1]Variable Energy Cyclotron Centre, Kolkata, India; [2]GSI, Darmstadt, Germany

The task of the MUCH digitization is to calculate the detector response to a track traversing an active detector element. Inside `cbmroot`, this means creating `CbmMuchDigi` objects (representing the smallest unit of raw data) from `CbmMuchPoint` objects, which store the geometrical information of the track intersection with the detector obtained from transport simulation. MUCH digitization was developed previously for event-by-event simulations. This report describes the modifications to the MUCH digitization software in order to describe the self-triggered, free-streaming readout of the detector.

The task class for MUCH digitization is `CbmMuchDigitizeGem`. This task class and related data classes were re-written to cope with the requirements to a) work both in event mode and time-based (free-streaming) mode; b) be compatible with the framework scheme of `CbmReadoutBuffer`; c) properly treat interference of tracks in a given readout channel both in the event mode (interference within one event) and in the time-based mode (interference within the dead time of the electronics, within or across events).

The modified Much Digitizer iterates over each MuchPoint and correspondingly calculates the charge deposition in terms of the number of primary and secondary electrons. The number of primary electrons is simulated based on the energy, track length, particle type information and specification of the gas mixture. Then for each primary electron, the number of secondary electrons is determined based on the gas gain setting. The charge in each channel/pad is determined based on the segmentation of each layer and a spot radius of the electron avalanche. Noise and electronics effects are added afterwards [1].

For each channel/pad a `CbmMuchSignal` is generated, which describes the analogue response. It contains the unique detector address, the signal time, the time until the signal is active and can be influenced by subsequent signals (stop time), and the signal time shape represented by a `TArrayD` in steps of nanoseconds. The time of the signal, which is crucial for the correct description of the free-streaming behaviour, is calculated from the event start time (obtained from `FairRunAna`), the time of the `CbmMuchPoint` (time-of-flight from event start to detector) and the drift time in the GEM. A random factor for the time resolution of the detector is added.

The created signals are buffered in the `CbmMuchReadoutBuffer` singleton object, deriving from the `CbmReadoutBuffer` template. This buffer is responsible for dealing with pile-up. In case a second signal arrives in a given readout channel (pad) within its dead time, the `Modify()` function is called. This method merges the two signals into one. The start time of the resulting signal is the minimum of the start times of the merged signals, the stop time the maximum of the two stop times. The new signal shape is obtained by bin-by-bin addition of the two merging signal shapes.

After processing all `CbmMuchPoint` objects of one event in this manner, the readout buffer releases all buffered signals with stop time before the current event time, since they cannot be influenced by following signals any more. In case of event-by-event simulation, the entire buffer is read out irrespective of time, which excludes interference of tracks from different events.

`CbmMuchSignal` objects released by the readout buffer are converted into digital information (`CbmMuchDigi`) taking into account the properties of the readout ASIC like number of ADC bins, dynamic range and threshold. The digis are delivered to the `CbmDaq` software instance, which aggregates digis from all detector systems, builds time slices and stores then in the output tree. In case of event-by-event simulation, the digis are directly written into the output tree. The work flow for digitization in MUCH is schematically shown in Fig. 1.

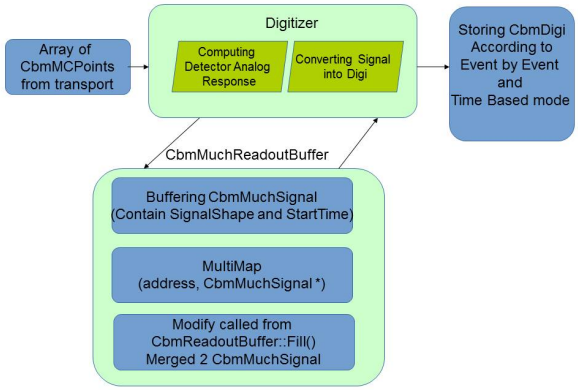

Figure 1: Scheme for time-based digitization in MUCH

All newly developed and modified classes are available in the trunk version of `cbmroot`. A detailed study is in process to test the performance of this newly developed scheme. Future plans include the reconstruction of dimuon signals in the time-based mode, the inclusion of detector inefficiencies, and others.

References

[1] V. Friese and E. Kryshen, CBM Progress Report 2010, GSI-2013-04801, p. 74

DOI:10.15120/GR-2017-1

An estimate of the required data bandwidth for the sensors of the CBM-MVD*

P. Sitzmann[1,2] and the CBM-MVD collaboration[2]
[1]GSI, Darmstadt, Germany; [2]Goethe Universität, Frankfurt am Main, Germany

The Micro Vertex Detector (MVD) of CBM is designed to operate at rates of up to 100 kHz Au-Au collisions and up to 10 MHz p-Au collisions. The CBM experiment will run with a free streaming triggerless readout. The limited time resolution of the CMOS Monolithic Active Pixel Sensors (MAPS) foreseen for this detector creates a pile-up in the detector. This will lead to a maxium of processeable hits per readout and complicates the track reconstruction, especially in the first station.

Recent progresses in CMOS industry allow for integrating discriminators into the pixel cell of MAPS. Therefore one may replace the previously considered rolling shutter readout by a priority encoder. This modification accelerates the time resolution of the sensors by about one order of magnitude, which has the potential to alleviate the pile-up problem substantially. It was decided to derive the CBM sensor MIMOSIS from a first related sensor design, which was developed for the ALICE ITS upgrade [1]. The radiation tolerance and rate capability of the ALICE sensor has to be improved by about one order of magnitude to match the more demanding requirements of CBM. The necessary modifications are carried out by the IPHC Strasbourg, which include adapting the sensor to the mechanical integration concept of the MVD.

To do so, a new internal readout structure is being designed for MIMOSIS (see Fig. 1). It foresees three stages of data buffering. The 64, so-called, region buffers receive each discriminated digital data from 16 columns of 504 pixels. Four neighbouring region buffers concentrate their data toward one super region buffer, which forwards it to one central elastic buffer. This solution balances the inhomogeneous occupancy of the sensors. Moreover, the elastic buffer flattens peaks in the data rate as caused by fast beam fluctuations are averaged out. Both steps reduce the required external bandwidth of the sensors to a maximum of eight parallel 320 Mbps data links. Some of the links may be deactivated in order to reduce the power dissipation of sensors with low occupancy.

The validity of the concept was confirmed with CBM-Root simulations for collision rates of 100 kHz (10 AGeV Au+Au) and 10 MHz (30 GeV p+Au). A security margin of a factor of three was considered in order to account for beam fluctuations. The delta electrons kicked out by the beam from the target was found to dominate the sensor occupancy. The required buffer memory was computed assuming a 5 µs readout time. The bandwidth of the data links (except for the external link) was assumed to allow for evacuating the full buffer during one frame time. The overhead caused by headers and trailers has been accounted for.

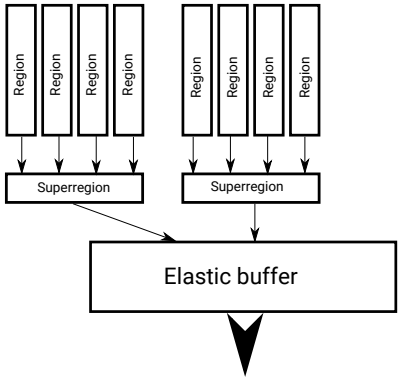

Figure 1: Sketch of the new readout layout in MimoSIS sensors

Component	average	3x av.	available
Region	10	30	100
Superregion	37	111	400
El. buffer input	345	1035	3200
Ext. links	345	–	800

Table 1: Required and available buffer memory and bandwidth in units of 16 bit words.

The results of the study are listed in Tab. 1. The results hold for the most exposed sensor of the first MVD station. The entries labelled "3x av." represent avarage peaks in the data rate as caused by beam intensity fluctuations. The memory and bandwidth foreseen is found sufficient for a reliable operation at the anticipated collision rates.

However, this promising result holds so far only for a detector operation with full magnetic field. Some physics cases call for reducing this field. This turns into a reduced deflection of delta electrons and thus to a higher occupancy. The consequences of this is currently being studied. First and preliminary results suggest that the occupancy increases by a factor of 2 reaching the limits of the capabilities of the sensor.

References

[1] D. Kim et al., 2016 JINST 11 C02042 and references therein

* Work supported by GSI(SIS)/HIC4FAIR/HGS-HIRE and Strategic Cooperation Contract GSI-Frankfurt

Online data preprocessing for the CBM Mirco Vertex Detector *

Qiyan Li[1], *M. Deveaux*[1], *J. Michel*[1], *C. Müntz*[1], *J. Stroth*[1,2], *and the CBM-MVD Collaboration*
[1]Institut für Kernphysik, Goethe-Universität Frankfurt, Germany; [2]GSI, Darmstadt, Germany

The CBM Micro Vertex Detector (MVD) is being designed to handle 10^5 Au+Au or 10^7 p+Au collisions/s. Weakly decaying particles like Hyperons or D Mesons will be identified in real time by means of a free streaming DAQ system, the FLES, which includes stages for event reconstruction and decay topology identification. To fulfill this task with the available computing resources, each processing step has to be optimized for low CPU load and bandwidth consumption. This does also hold for the cluster finding of the MVD. The current CBMRoot/C++ code was estimated to consume up to 80% of the CPU-power of the FLES once being confronted with a realistic data rate. To reduce this load, we tested strategies to perform preprocessing of the data before sending it to the computing farm.

A first stage of the proposed preprocessing is already integrated in the CMOS Monolithic Active Pixel Sensors used in the MVD. The MIMOSA-26 pixel sensor used for our test includes circuits for signal discrimination, on-chip zero suppression and one-dimensional cluster finding. The second stage as discussed in this work comprises full cluster finding and encoding on free resources of the FPGAs controlling the sensors. The related algorithm was required to match the available FPGA resources and to keep all information on cluster shapes without increasing the data volume and bandwidth.

In a first step, we found a way to encode reconstructed clusters into one 32 bit word per cluster. Tests showed that the protocol encodes 99.99% of the clusters recorded during beam test data of the MVD-prototype with MIMOSA-26 without loss of information [1, 2]. A VHDL module doing cluster finding and encoding was designed and tested successfully with the TRB2 board [3]. Real time cluster finding was demonstrated by operating it with a MIMOSA-26 sensor, which was illuminated with a β-source. To test the accuracy of this cluster finding, the output was stored together with its raw data, which was processed with the C++ reference code in a next step. The clusters recorded with both chains were compared for 260k frames. They were found to agree for physics data while some pathological signatures, as e.g. caused by a broken line, were rejected by the FPGA code. The output of the FPGA showed a mild compression of 14% w.r.t. the raw data (see Figure 1), which matches our requirements. The CPU time for the remaining steps to be done with C++ at the FLES (C++ cluster finding vs. unpacking of the encoded cluster information) was compared. Note that in both cases the first processing stage was carried out by the sensor . The low occupancy reached with the β-source causes a bias in favor of the offline processing. Nevertheless, the FPGA-processing reduces the remaining CPU load by a factor of four (see Figure 2).

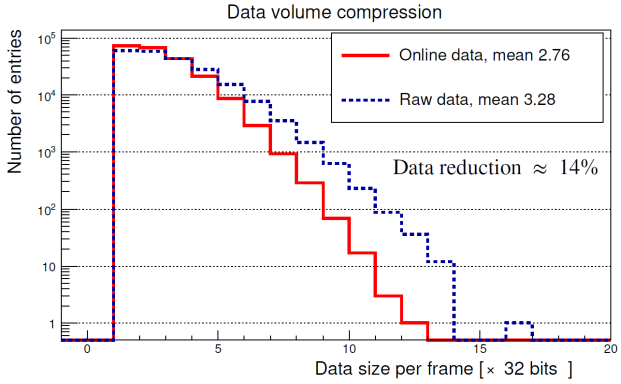

Figure 1: Data size per frame for a MIMOSA-26 exposed to β-rays (raw data vs. FPGA-encoded clusters).

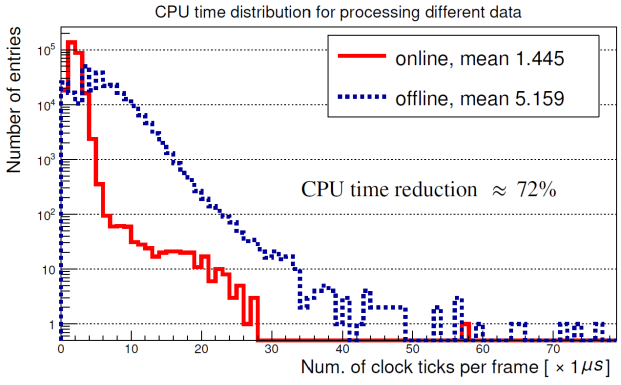

Figure 2: The CPU time per frame (decoding of FPGA-encoded clusters vs. C++ cluster finding).

The explorative study presented here demonstrates that the proposed strategy is suited to reduce the load of the FLES. It remains to be adapted to the internal data processing of the final MVD sensor, which is currently under design.

References

[1] Qiyan Li et al., GSI Scientific Report 2012 (2013) 56
[2] Qiyan Li et al., J. Phys.: Conf. Ser. 513 (2014) 022021 (Proceedings of CHEP-2013)
[3] Qiyan Li et al., GSI Scientific Report 2014

* supported by BMBF (05P15RFFC1), HIC for FAIR and GSI.

DOI:10.15120/GR-2017-1

Radiation damage caused by neutron capture in boron doped silicon sensors*

B. Linnik, T. Bus, M. Deveaux†, D. Doering, A. Yazgili, and J. Stroth
Goethe University, Frankfurt, for the CBM-MVD Collaboration

The active medium of CMOS Monolithic Active Pixel Sensors (MAPS), as foreseen for the CBM Micro Vertex Detector (MVD), is formed from p-doped silicon. Besides being affected by fast hadrons, this medium might subject to damage from thermal neutrons, which dissociate the boron dopands via the reaction n + ^{10}B $\rightarrow$^{7}Li + ^{4}He + 2.8 MeV. The consequences of this effect was tested experimentally and found being incompatible with the Non Ionizing Energy Loss (NIEL) hypothesis, which is commonly used for dosimetry.

The tolerance of MAPS to non-ionizing radiation damage has been extensively studied with fast ~ 1 MeV reactor neutrons in accordance with the NIEL (Non-Ionizing-Energy-Loss) model [1]. This model assumes that radiation damage, which is caused by the neutrons removing atoms from their location in the silicon crystal, scales with the radiation energy. Despite the validity of the model is known to be limited by its ignorance to defect chemistry, it is commonly used for doing dosimetry for silicon sensors. Tables [2] are used to normalize the damage caused by different sources of radiation with respect to the one of 1 MeV neutrons, the so-called neutron equivalence.

The large cross sections of neutron induced fission of ^{10}B is not considered in those tables. We studied, if potential additional radiation damage may occur, which might e.g. endanger the operation of the CBM-MVD. The study was performed with MIMOSA-19 sensors provided by the PICSEL group of IPHC Strasbourg. The sensors were manufactured in the 0.35 μm AMS OPTO process and feature a 14 μm thick epitaxial layer with an anticipated P-doping of few $10^{15}/\mathrm{cm}^3$. The 196×196 3T-pixels with 12x12 $\mu\mathrm{m}^2$ pitch have L-shaped diodes with 39.6 $\mu\mathrm{m}^2$ surface. The doping of the substrate of the P-Well is likely $\sim 10^{19}/\mathrm{cm}^3$. Fission products created in the P-well can travel into and damage the epitaxial layer as our simulations showed.

The sensors were irradiated with neutrons at the FRM II research reactor in Garching. The irradiation was done at room temperature. Either a direct fission spectrum (MEDAPP beam line, $E_{\mathrm{peak}} = 2$ MeV) or cold neutrons (PGAA beam line, $E_{\mathrm{peak}} = 1.8 \times 10^{-3}$ eV) were used for irradiation, the sensors were bonded hereafter for testing. During our tests, they were illuminated with X-ray sources (^{55}Fe$\rightarrow$ 5.9 keV, ^{109}Cd$\rightarrow$ 22.1 keV) and the amplitude spectrum was obtained. This amplitude is typically reduced with increasing radiation dose as the radiation damage reduces the charge collection efficiency (CCE) of MAPS. The CCE is deduced from the Amplitude spectrum [3]. In accordance with the NIEL hypothesis, we assumed that this would be observed also for the sensors exposed to cold neutrons.

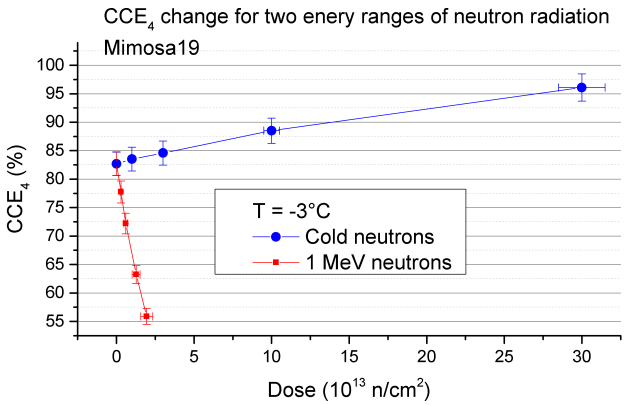

Figure 1: The charge collection efficiency for the four most significant pixel in a 5x5 cluster.

The results are displayed in Figure 1. The sensors irradiated at MEDAPP (1 MeV n) display the expected *decrease* of the the average CCE with increasing radiation dose. The the sensors irradiated at PGAA (cold n) show an unexpected *increase* of the CCE, which cannot be explained within the NIEL model. A more detailed study of out experimental data revealed that the sensors irradiated with cold neutrons show signatures of a strong acceptor removal. This reduces the doping of the sensing volume, which is known to increase the CCE [3]. This is not observed for the fission neutrons up to the highest doses applied.

The results prove that cold and thermal neutrons do not endanger the operation of the CBM-MVD. More importantly, they suggest that the response of sensors with p-doped sensing volume to neutron radiation changes in a qualitative way depending on the neutron energy. This creates a so far unknown exception for the NIEL model, which is likely of general interest in silicon detector physics.

References

[1] A. Vasilescu, ROSE/TN/97-2, CERN (1997)

[2] A. Vasilescu, G. Lindstroem, http://rd50.web.cern.ch/RD50/NIEL/default.html

[3] M. Deveaux et al., JINST 6.02 (2011): C02004.

* Work supported by BMBF (05P15RFFC1), GSI and HIC for FAIR.
† deveaux@physik.uni-frankfurt.de

Geometry database development for the CBM experiment

E. P. Akishina[1], *E. I. Alexandrov*[1], *I. N. Alexandrov*[1], *I. A. Filozova*[1], *V. Friese*[2], *and V. V. Ivanov*[1,3]
[1]LIT JINR, Dubna; [2]GSI, Darmstadt, Germany; [3]National Research Nuclear University "MEPhI", Moscow, Russia

The geometry of the CBM detector systems ("modules") is described in the ROOT TGeo format, with one separate file for each system. An entire CBM geometry is defined by a set of such geometry files with given versions.

Currently, the geometry files are stored and distributed through the CBM software repository. Setups as combinations of geometry files are defined on the ROOT macro level. This situation is rather complicated and error-prone.

The CBM Geometry Database (DB) is designed and implemented as a part of the CBM Databases project [1] according to the User Requirements Document [2]. A simplified object model of the CBM Geometry DB is shown in Fig. 1.

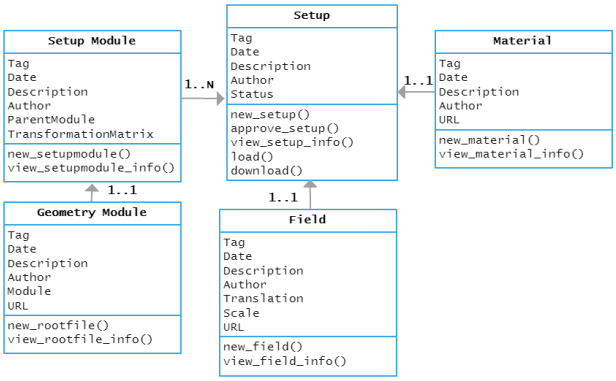

Figure 1: Object model of the CBM Geometry DB

Each object has a unique tag that can be used as a key for searching. Any object has the parameters: Description, Author and Date. Description is a short description of the object, Author is the user who created the object and Date is the time of object creation. The parameter URL is a string with the full path to the data file. This file is accessible from the Geometry DB. It should store geometry data in ROOT format if there is a link to the Geometry Module object, materials if there is a link to the Material object, and magnetic field if there is a link to the Field object.

The CBM geometry database is realized as a tree structure. The top-level object is the Setup. It has relations with one Material object, one Field object and several Setup Module objects. A Setup Module object has relation with one Geometry Module object. The Geometry Module object contains information about the sub-detector and its geometry data. The Setup Module object has a link to the mother Setup Module. Its Transformation Matrix parameter describes the placement of the module in the mother module.

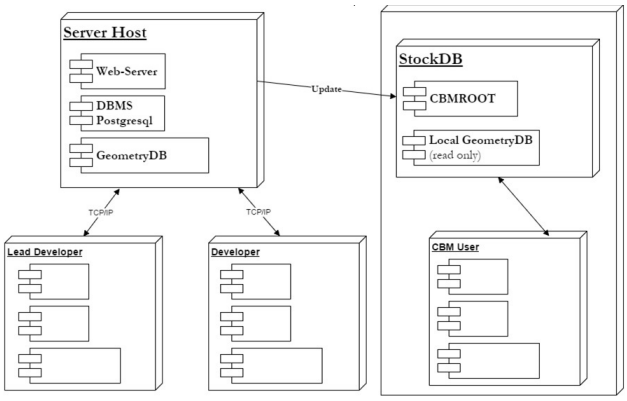

Figure 2: General architecture of the CBM Geometry DB

The Geometry DB has three type of users: Lead Developer, Developer and CBM User. The Lead Developer is a coordinator and the responsible person for the Setups. He/she can upload new versions of Setup and materials file. The Developer is a person responsible for a Setup Module and its Geometry Module. The CBM User has only read access.

The General architecture of the CBM Geometry DB is shown in Fig. 2. The Geometry DB consists of a Central DB and Local DB components. The Central DB keeps primary data and is unique within the entire CBM environment. Lead Developers and Developers use the Central DB in order to update Setups and corresponding data. Updates can be done through both web server and API modules. A Local Geometry DB is a copy or several copies of the Central DB. Local copies are implemented in SQLite. Any Local Geometry DB is updated after a change to the Central DB. It is available for CBM users via their local file system.

The API and GUI accesses are designed and implemented. The API is implemented as macros in the `cbmroot` environment.

References

[1] E. P. Akishina *et al.*, *Conceptual Considerations for CBM Databases*, JINR Communications E10-2014-103, JINR, Dubna

[2] E. P. Akishina *et al.*, *User Requirements Document of the Geometry DB for the CBM experiment*, http://lt-jds.jinr.ru/record/69336?ln=e

DOI:10.15120/GR-2017-1

CERN-SPS in-beam performance test of the new strip readout MRPC prototypes for the inner zone of the CBM-TOF wall *

M. Petriş[1], D. Bartoş[1], M. Petrovici[1], L. Rădulescu[1], V. Simion[1], J. Frühauf[2], M. Kiš[2], P-A. Loizeau[2], I. Deppner[3], N. Herrmann[3], and C. Simon[3]

[1]NIPNE, Bucharest, Romania; [2]GSI, Darmstadt, Germany; [3]PI, Heidelberg University, Germany

Due to the high interaction rates of 10^7 interaction/s at which the CBM experiment is anticipated to run the readout will be based on a free streaming concept. This imposes to the MSMGRPCs (Multi-Strip, Multi-Gap RPCs), a perfect matching of the characteristic impedance of the signal transmission line to the input impedance of the front-end electronics, in order to reduce fake signals produced by reflections [1].

Two new MSMGRPC prototypes, based on low resistivity glass ($\sim 10^{10}$ Ωcm) from China, match the characteristic impedance of the RPC signal transmission line to the input impedance of the front-end electronics ([2, 3]). They have also the granularity required by the inner zone of the CBM-TOF wall through a proper adjusting of their strip length. The transmission line impedance of a single readout channel of each prototype was estimated using APLAC Software. The first prototype has a classical single stack architecture (RPC2015SS) with 8 gas gaps of 140 μm. The pitch size (10.16 mm) and strip width (8.63 mm) are the same for both high voltage and readout electrodes. The second prototype has a double stack configuration (RPC2015DS) of 2 x 5 gas gaps of 140 μm, with the same pitch size (7.2 mm) for both high voltage and readout electrodes, but with different values of the strip widths: 1.3 mm for readout electrodes and of 5.6 mm for high voltage ones. This gives the possibility to exploit in an innovative way the advantage of having a strip structure for both readout and high voltage electrodes. Thus the tuning of the characteristic impedance of the signal transmission line to the value of the input impedance of the front-end electronics can be decoupled by the granularity adjustments. With the described geometrical parameters both counters have a characteristic impedance of the transmission line of 100 Ω.

The prototypes were tested in-beam at SPS-CERN with a 30A GeV Pb ions incident on a Pb target in conditions similar with those expected at SIS100, or even closer to those anticipated for SIS300. Our prototypes were positioned in the "high rate" branch of the CBM-TOF experimental setup, a comprehensive description of the whole set-up being given in [4]. The two described prototypes are positioned one behind the other (see Fig.1), in the same housing box, identified as RPC2015 Bucharest [5]. They were followed by four MSMGRPCs mounted in the same gas tight box, called RPC2012 and a narrow strip pitch (2.54 mm) MSMGRPC called RPCRef, the last one in the experimental set-up. A 16 strip polycrystalline diamond detector and a 4-pad single crystal diamond detector were positioned in front of the target, providing a start time for particle velocity measurements between the diamond detector and the RPCRef counter. The signals delivered by the RPCs were fed to PADI fast amplifiers [6] and processed by the same electronics chain described in [5].

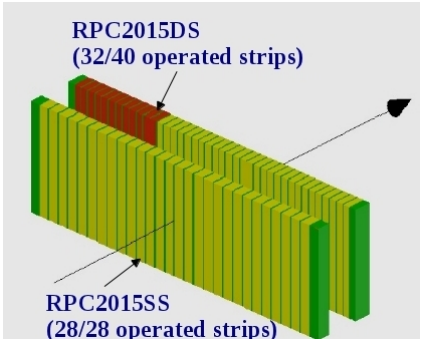

Figure 1: Overlap of the active area of the two RPC2015 prototypes.

We report here the performance of the RPC2015 prototypes, the results obtained with RPC2012 prototype being reported in detail in [5]. The principles of the data analysis starting from unpacking to calibration and corrections are presented in [7].

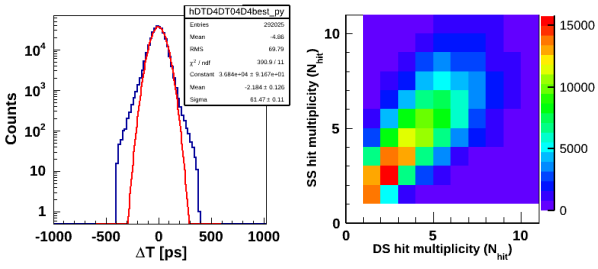

Figure 2: Time difference spectrum - left. Hit multiplicity correlation - right.

The time difference spectrum between RPC2015DS and RPC2015SS, for operation of RPC2015DS at 2 x 5.5 kV (157 kV/cm) and of RPC2015SS at 2 x 9 kV (161 kV/cm), with the PADI threshold set to 245 mV is presented in Fig.2, left side. A very good system time resolution of

* Romanian NASR/contract RO-FAIR F04 and NASR/NUCLEU Project PN16420104

61 ps, including the contribution of the electronics, was obtained. The correlation plot from the right side of Fig.2 shows that the two counters were exposed to almost the same hit multiplicities. If we consider equal contributions of the two counters, a single counter resolution of 43 ps is obtained. The observed tails in the time spectrum are negligible, if we compare the obtained 61 ps σ of the Gaussian fit with 69 ps RMS value of the spectrum. The obtained efficiency for this run, was of 97% for the RPC2015DS and of 98.5% for the RPC2015SS. The slight difference could be due to the difference in the applied potentials and also in the overlapped operated area, as is shown in Fig.1. The

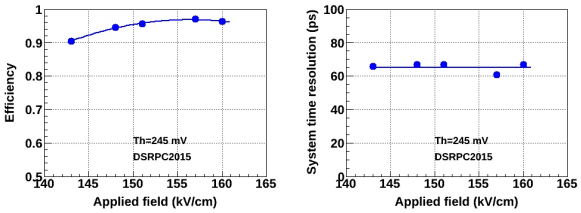

Figure 3: Efficiency - left and time resolution - right as a function of high voltage for RPC2015DS.

obtained detection efficiency and time resolution as a function of applied high voltage for RPC2015DS are shown in Fig. 3. An average system time resolution of 65 ps corresponds to the efficiency plateau, reached at applied electric fields in the gas gap larger than 157 kV/cm. The efficiency

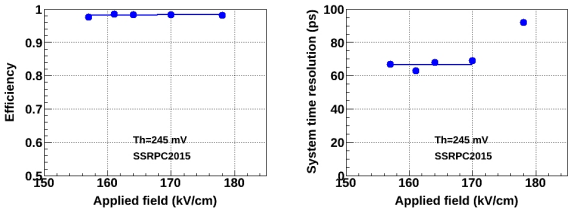

Figure 4: Efficiency - left and time resolution - right as a function of high voltage for RPC2015SS.

and system time resolution obtained for RPC2015SS are presented in Fig. 4. As can be observed, the counter was operated at the efficiency plateau of ∼98%, with an average system time resolution of 66 ps. The larger value of the time resolution observed for operation at 178 kV/cm is due, most probable, to the operation at a too high electric field which pushes the counter in a streamer regime. The

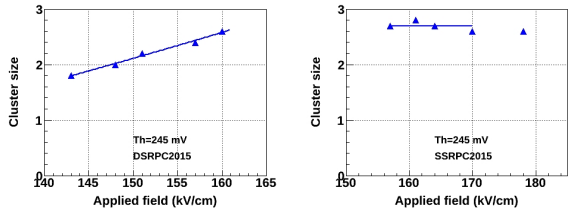

Figure 5: Cluster size for RPC2015DS - left and RPC2015SS - right as a function of high voltage.

obtained cluster size (number of strips with signal in a single hit) for the two counters is presented in Fig. 5. The cluster size is increasing for RPC2015DS as a function of applied potential while for RPC2015SS in the same high voltage range is almost constant. It slightly decreases at the largest applied fields due to possible distortions of the electric field produced by the space charge inside the gas gaps. The obtained values of the cluster size are larger than the one expected from the values of pitch sizes for the two counters. Previous obtained results for RPC2012 with a pitch size of 7.4 mm and the same inner geometry, showed a cluster size of the order of 1.4 - 1.5 strips [8] for single hit. These larger values can be due to large ionization created by heavy reaction products crossing the detector.

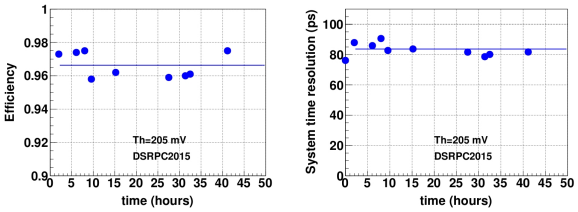

Figure 6: Aging effect for RPC2015DS for 40 hours operation with the same high voltage and threshold settings.

The detector performance stability was checked for a period of operation of about 40 hours with the same settings (RPC2015 at 157 kV/cm, RPC2015SS at 178 kV/cm). The efficiency and system time resolution were evaluated for the runs acquired over this period at similar counting rates. The stability of the detectors is demonstrated by the plots shown in Fig. 6. The obtained ∼80 ps system time resolution is affected by the operation of the RPC2015SS at a too high electric field, (178 kV/cm), in a region of the working curve where its time resolution started to deteriorate (see Fig. 3). The operation of the detectors at a PADI threshold of 205 mV does not not influence the time resolution performance, as it is shown in [7, 9].

The performance of the RPC2015DS with the innovative adjustable characteristic transmission line impedance was demonstrated. The obtained results show that the two new prototypes with characteristic transmission line impedance matched to the input impedance of the front-end electronics, fulfill the challenging requirements of the inner zone of the CBM-TOF wall.

References

[1] CBM-TOF Collaboration, CBM-TOF TDR, October 2014

[2] V. Aprodu et al., CBM Progress Report 2015 (2016), p.97

[3] V. Aprodu et al., CBM Progress Report 2015 (2016), p.98

[4] C. Simon et al., CBM Progress Report 2015, (2016), p.90

[5] M. Petriş et al., this GSI Scientific Report

[6] M. Ciobanu et al., CBM Progress Report 2013, (2014), p.84

[7] M. Petriş et al., Journal of Instrumentation, Volume 11, September 2016 (2016 JINST 11 C09009)

[8] M. Petriş et al., Journal of Physics: Conference Series 724 (2016) 012037

[9] M. Petriş et al., GSI Scientific Report 2015 (2016), 32

DOI:10.15120/GR-2017-1

4-dimensional reconstruction of time-slices

V. Akishina[1,2,3], *I. Vassiliev*[1], *I. Kisel*[1,2,4], *and M. Zyzak*[1]

[1]GSI, Darmstadt, Germany; [2]Goethe-Universität, Frankfurt am Main, Germany; [3]JINR, Dubna, Russia; [4]Frankfurt Institute for Advanced Studies, Frankfurt am Main, Germany

Traditional latency-limited trigger architectures, typical for conventional experiments with a hardware trigger, are inapplicable for CBM. Instead, the experiment will ship and collect time-stamped data into a readout buffer in a form of a time-slice of a certain length with no isolated collisions, and deliver it to a large computer farm, where online event reconstruction and selection will be performed. Grouping of measurements into physical collisions must be performed in software and requires reconstruction not only in space, but also in time, the so-called 4-dimensional track reconstruction and event building.

Table 1: Track reconstruction efficiency in mbias Au+Au collisions at 10 AGeV in case of event-by-event reconstruction and 4-D reconstruction at different interaction rates.

Efficiency, %	3-D	0.1 MHz	1 MHz	10 MHz
All tracks	92.5	93.8	93.5	91.7
Prim. high-p	98.3	98.1	97.9	96.2
Prim. low-p	93.9	95.4	95.5	94.3
Sec. high-p	90.8	94.6	93.5	90.2
Sec. low-p	62.2	68.5	67.6	64.3
Clone level	0.6	0.6	0.6	0.6
Ghost level	1.8	0.6	0.6	0.6

The core of reconstruction in CBM is the Cellular Automaton (CA) based track reconstruction in the Silicon Tracking System (STS). This algorithm was modified to enable time-based reconstruction. It takes as input hits produced with the time-based cluster and hit finding algorithms from the time-slices, simulated in the `cbmroot` framework. Time-based detector response simulations in CBM take into account the anticipated timing behavior of detectors and readout electronics like e.g. time resolutions and strip dead times. Due to the self-triggered digitization and readout scheme, simulation has to take into account that signals of particles from different collisions can interfere in a detector volume. Thus, it puts the reconstruction chain in a more challenging condition.

Since the triplets are to be built of three hits potentially produced by the same particle, these hits should correlate in time. All combinations of hits with difference in time measurements exceeding the expected STS time resolution are rejected. The resulting reconstruction efficiencies of the 4-D CA track finder for various interaction rates are given in Table 1. For comparison, the corresponding values for the event-by-event analysis ("3-D") are included. Only a slight deterioration w.r.t. event-by-event is observed at the highest interaction rate of 10 MHz.

After the stage of the CA track finder is finished, all

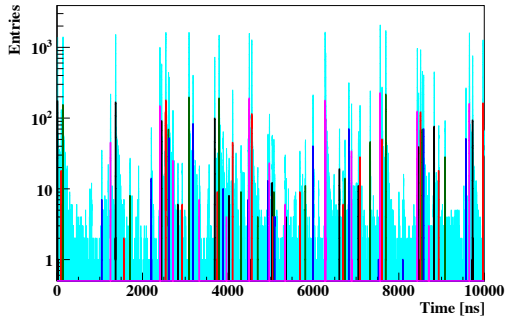

Figure 1: Distribution of reconstructed track time in a part of time-slice at 10 MHz interaction rate: hits (light blue) and tracks (different event-corresponding colors).

tracks found in the time-slice are fitted in 4-D space. Time was added as a parameter to the track state vector with the covariance matrix modified accordingly. Thus, both spacial and time track parameters are treated equally by the reconstruction chain. An event-building algorithm based on the reconstructed tracks was developed. The time distribution of hits is shown in Fig. 1 with light blue colour, illustrating the complexity of defining event borders in a time-slice. The time distribution of reconstructed tracks is shown in the same plot with different colours. The tracks clearly form groups corresponding to events. Tracks are combined into event-corresponding clusters according to the estimated time at the target position and its errors.

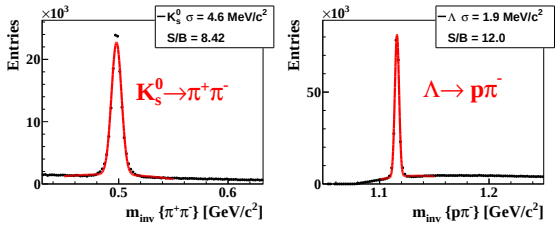

Figure 2: Performance of short-lived particle reconstruction on the example of K^0_s and Λ for time-slices with 0.5M mbias Au+Au events at 10 MHz interaction rate.

The obtained events were given as an input to the KF Particle Finder package for reconstruction of short-lived particles. A primary vertex is constructed in each event. Since TOF is not yet included into the time-based reconstruction, Monte-Carlo information for the identification of charged particles was used. The obtained K^0_s and Λ mass spectra are shown in Fig. 2. The combinatorial background for short-lived particles is similar to the event-based analysis, showing high values for the signal to background ratio.

DOI:10.15120/GR-2017-1

J/ψ interaction in nuclear matter at FAIR SIS100

P. P. Bhaduri[1], *M. Deveaux*[2], *and A. Toia*[3]

[1]Variable Energy Cyclotron Centre, 1/AF Bidhan Nagar, Kolkata-700 064, India; [2]Goethe-Universität Frankfurt, 60438 Frankfurt am Main, Germany.; [3]GSI, 64291 Darmstadt, Germany

J/ψ suppression in relativistic heavy-ion collisions is considered as an indicator for the formation of quark-gluon plasma (QGP). This is as the formation of the $c\bar{c}$ bound states is hampered by Debye screening in a deconfined medium. However, some J/ψ suppression was also observed in proton induced ($p + A$) collisions, which are not considered to form a deconfined medium. Isolating the genuine effects of the hot and dense medium of heavy-ion collisions requires a precise knowledge on the J/ψ dissociation in cold hadronic matter as produced in $p + A$ collisions.

J/ψ production in hadronic collisions is generally believed to be a factorizable two step process. The first step is the production of a color octet $c\bar{c}$ pair, which requires $\tau_0 \simeq 0.25$ fm in the rest frame of the pair and can be described by perturbative QCD (pQCD). This is followed by the non-perturbative formation of the color singlet resonance from the initially compact $c\bar{c}$ pairs, which is considered to require $\tau_R \simeq 0.35$ fm in the case of the J/ψ. In the nucleus and laboratory frame, the formation times are extended by Lorentz dilation. A conclusive experiment requires to chose a beam energy, which allows to create J/ψ particles without giving them a too high velocity. Otherwise, the $c\bar{c}$ pair will scatter or leave the nuclear core before the formation is completed. In both cases, the results will reflect the properties of the $c\bar{c}$ instead of providing the wanted information on the properties of the fully formed J/ψ. This consideration hampered a measurement of the hadronic dissociation of J/ψ e.g. with a 160 GeV/c proton beam the CERN-SPS [1].

CBM will be able to produce and detect J/ψ mesons in $p + A$ collision systems with unprecented rates at very low beam energies of $15 - 30$ GeV. We checked if those kinematic conditions would be suited to measure the interactions between fully formed J/ψ - mesons and cold nuclear matter. We consider this fulfilled if i) the formation path of the J/ψ in the rest frame of the nucleus remains below the ~ 2 fm distance between two nuclei and ii) the survival probability of the J/ψ is significantly modified by the medium. As shown in Fig. 1, the first condition is fulfilled for a beam energy of 15 GeV.

The J/ψ survival probability was calculated for three assumptions on the absorption cross section inside the nuclear medium. An estimate of the geometric cross-section (σ_{abs}^{Geo}), an estimate relying on perturbative QCD [2] (σ_{abs}^{QCD}), and a prediction of hadronic models based on meson exchange [3] (σ_{abs}^{Had}) were considered. The results of the calculations are displayed in Fig. 2. They suggest that

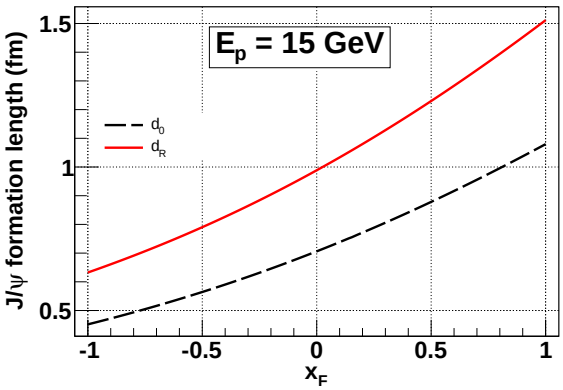

Figure 1: x_F dependence of the formation length of J/ψ mesons, in the laboratory frame, in 15 GeV p+A collisions.

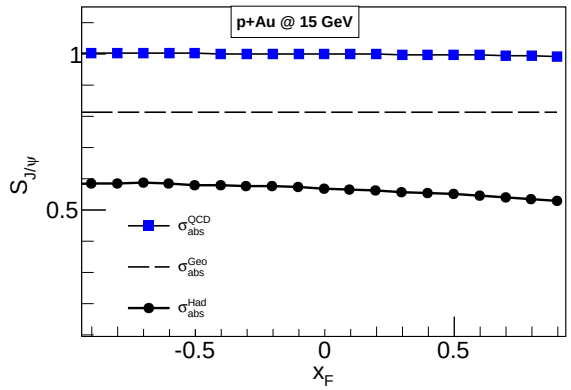

Figure 2: x_F dependence of the J/ψ survival probability in 15 GeV $p + Au$ collisions at FAIR.

the J/ψ yields will depend strongly on the anticipated scenario, which will allow to separate them by experiment. Measuring charmonium at CBM would thus be highly rewarding in terms of performing pioneering studies on the interaction of the physical resonances in the baryonic matter.

References

[1] D. Kharzeev and H. Satz, Phys. Lett. B **356** (1995) 365.

[2] D. Kharzeev and H. Satz, Phys. Lett. B **334** (1994) 155.

[3] R. Molina, C. W. Xiao and E. Oset, Phys. Rev. C **86** (2012) 014604; nucl-th/12030979

DOI:10.15120/GR-2017-1

Systematic study of sensor properties

O. Bertini[1] *and A. Lymanets*[1]
[1]GSI, Darmstadt, Germany

The Silicon Tracking System (STS) is main tracking detector of the Compressed Baryonic Matter (CBM) experiment providing tracking information of charged particles trajectories. The STS will consist of about 900 double-sided silicon microstrip sensors in four different sizes. Complicated fabrication technology of double-sided silicon sensors and large-scale production requires a solid and efficient quality assurance procedure of every sensor before connecting it to readout electronics [1].

The vendors of the present prototype sensors, CiS and Hamamatsu, provide results of bulk electrical tests. Since the leakage current value strongly depends on the temperature during the measurement, a calibration procedure has been developed in order to compare the results. As it is shown in Fig. 1 leakage current measurements after being scaled to 20°C are in good agreement with vendor's data.

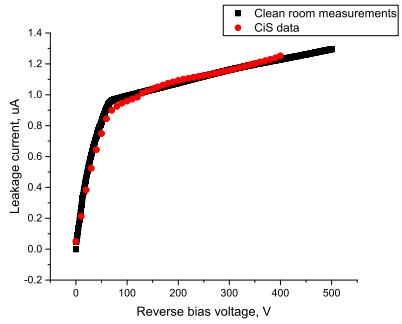

Figure 1: Comparison of leakage current measurements provided by a vendor (CiS) with tests performed at GSI, here for sensor type CBM06C2, batch 350714, wafer 18.

Another parameter which demonstrates functionality of the sensors is called slope and is defined as the ratio of the leakage current at 150 V to the current at 100 V. It provides information about how the leakage current changes between the depletion voltage (max. $\sim$ 100 V) and the expected operation voltage ($\sim$ 150 V). If the slope is steep, the sensor is already in a hard breakdown. The comparison of the slope between vendor's data and measurements at GSI is presented in Fig. 2. Compared to the direct leakage current measurements, the slope demonstrates the health of the sensors independently of the temperature measurement.

The strip quality tests are particularly important for identifikation of strip defects that can develop during fabrication, transportation or handling of sensors. The results of pinhole test of coupling capacitors are provided by the vendors as well. An automated strip test procedure has been developed and the test stand assembled in the clean room environment at GSI [2]. Newest prototype sensors of type

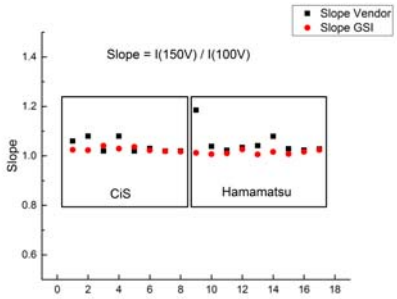

Figure 2: Measured slope compared with vendors' data.

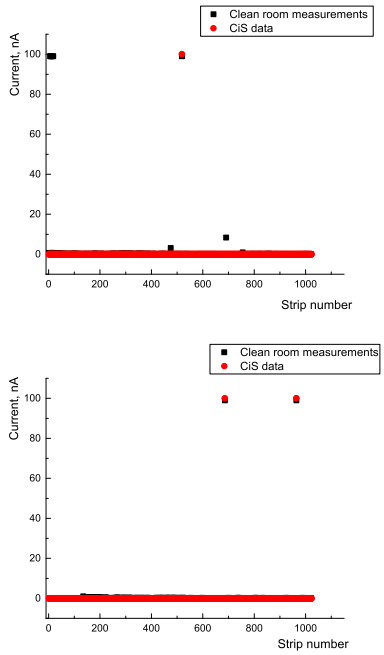

Figure 3: Comparison of the pinhole tests with vendor information for the latest prototype sensor CBM06. Top: N-side; bottom: P-side.

CBM06 have been tested there; the results for one sensor are shown in Fig. 3. New pinholes have been detected on the N-side of the sensor (Fig. 3, top) which demonstrates the necessity of sensor parameters verification shortly before sensor will be connected to readout electronics.

References

[1] P. Larionov and P. Ghosh, GSI Scientific Report 2012, p.47

[2] P. Larionov, CBM Progress Report 2015, p.24

DOI:10.15120/GR-2017-1

Investigation on low mass copper flex micro-cables for the STS detector

T. Blank[1], *M. Caselle*[1], *C. J. Schmidt*[2], *and M. Weber*[1]
[1]KIT, Karlsruhe, Germany; [2]GSI, Darmstadt, Germany

The silicon sensors of the Silicon Tracking System (STS) will be connected to the read-out chips (ROC) by means of up to 0.5 m long high-density and low-capacitance flex cables. Two flex micro-cable designs are currently under investigation. The first one is based on a stack of two single layer flex cables with aluminium traces, the second is a double-sided flex cable with copper traces on the top and bottom side. First 18 cm long samples of the copper flex cables have been delivered and electrically characterized. The measured capacitance of the copper cable surrounded by air was found to be 0.44 pF/cm. Finite Element (FE) simulation yields a capacitance value of 0.41 pF/cm. A parametric sweep of the geometric design parameters reveals the relationship between the capacitance and the design parameters of the cable.

Copper Micro Cable Design and Production

The copper flex micro-cable is produced utilizing advanced PCB production technologies. Thus, the signals can be routed over two planes resulting in a reduction of the amount of micro-cables by a factor of two compared to single layer aluminum cables. Figure 1 schematically shows a proposed high-density interconnection scheme between the micro-cable and die.

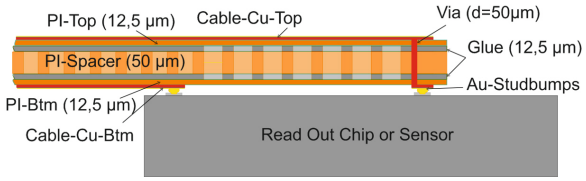

Figure 1: Cross section through the copper cable mounted on the ROC or sensor.

Owing to the PCB-processes, many cables can be manufactured in parallel on a panel. In a first test run, all cables for three sensors were produced on one panel. Figure 2 shows a set of cables with a length of 186 mm and 200 mm. They can be used to contact the top or bottom side of the sensor and the front-end electronics. The cables are delivered on a release tape (Fig. 2 – right), which eases the handling of the micro-cables.

The assembly process of the cables to the ROC chips includes a gold stud bump process on the ROC chips. The gold stud bumps are formed by means of an automated gold wire bonding machine (Fig. 3). The process is fast and reliable. More than 15 bumps can be deposited per second. The gold stud bumping process is an alternative to galvanic metallization processes to provide a solderable pad metallization on the ROC and sensor chips.

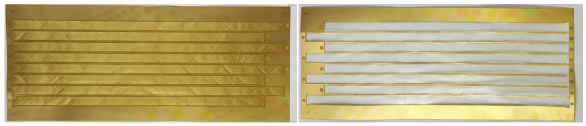

Figure 2: Eight copper micro cables (left) are required to connect the top or bottom side of the sensor to the ROC chips. The cables are delivered on a release tape (right).

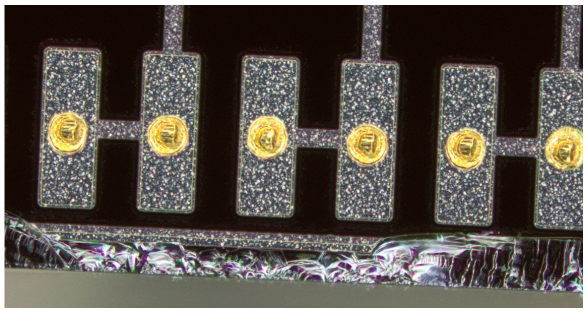

Figure 3: Gold stud bumps placed on a test ROC chip.

The stud bump process is followed by dispensing or printing anisotropic conducting epoxy glue onto the cable. The ROC is picked up from a tray or wafer and placed with a flip-chip machine on the contact pads of the cable. The glue on the cables is snap cured at a temperature of 150 °C for 10 seconds inside the flip-chip machine by means of a heated pick head. Figure 4 shows a ROC-dummy mounted onto a cable (left) and an X-ray image, revealing the placement accuracy of the process.

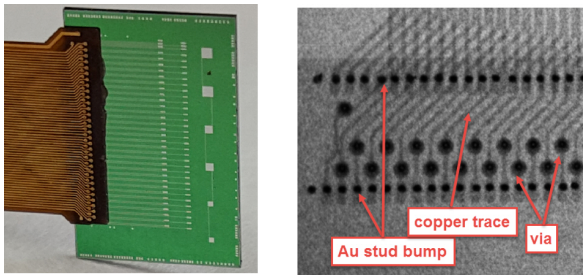

Figure 4: A dummy ROC is mounted to the cable (left), X-ray of the cable glued on the ROC (right).

DOI:10.15120/GR-2017-1

Electrical Characterization and Simulation

The total electronic noise in a detector channel strongly depends on the capacitance of the cable. Thus, the capacitance of the cable has been measured on a SUESS probe station. One copper trace on the top side was set to HIGH voltage. Both neighbouring lines on the top layer and four lines located directly underneath the "HIGH-line" on the bottom layer were connected to ground. The capacitance measured was 8.8 pF for a 20 cm long copper cable (0.44 pF/cm). In order to minimize the cable capacitance an FE simulation was performed. Geometric design parameters of the micro-cable like the copper trace width and the height of the meshed polyimide interposer were varied. The trace width changed from 18 μm to 36 μm, the height of the meshed interposer from 25 μm to 100 μm.

The FE-simulation results for the capacitance in dependence of the "Meshed Polyimide Layer" (MPL) are summarized in Fig. 5. The simulated capacitance for the real cable with a 50 μm thick meshed polyimide layer and 36 μm wide copper traces results in a capacitance of approximately 0.41 pF/cm. This value is in good agreement with the simulation results given in [1, 2], and the measured results of 0.44 pF/cm. The next generation of micro-cables will be realized with a 75 μm meshed interposer and 24 μm wide traces. Thus, a capacitance reduction of 18% down to 0.34 pF/cm might be possible.

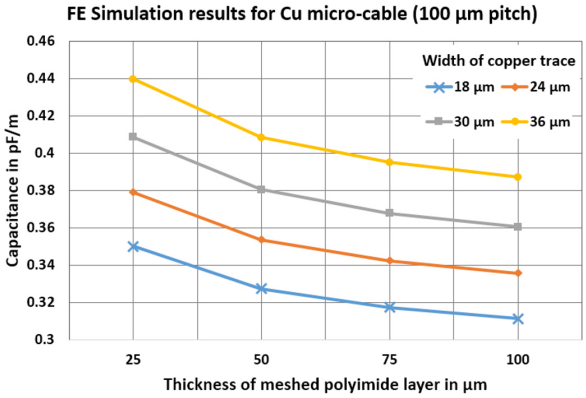

Figure 5: Simulation results of the capacitance over the thickness of the MPL and for varying copper traces width.

Figure 6 shows the electrical potential of a one cm long piece of cable within air. Additional grounded shielding layers were not considered for these simulation runs.

Status and outlook

From the first production run of the copper cable promising conclusions could be derived:

- High production yields can be reached with up to 20 cm long cables.
- The capacity of the copper cable is comparable to the cables comprising aluminium traces.

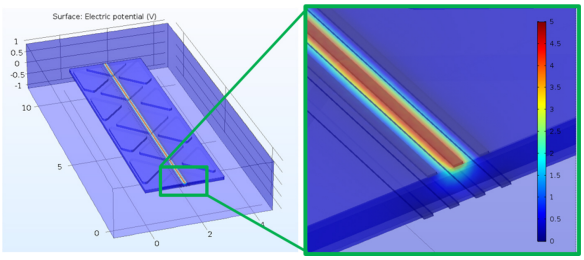

Figure 6: Simulation results of the capacitance over the mesh thickness and a varying copper traces width.

- The amount of production processes for the sensor-cable-ROC sub-system can be reduced by at least a factor of two due to the doubled number of signal layers in the copper cable.

However, the mounting processes for the cable needs further research. The glue process on the sensor side might be tricky, hence, alternative technologies based on small solder ball interconnects will be evaluated.

References

[1] T. Blank et al., Investigation on low-mass copper flex cables for the STS detector, CBM Progress Report 2015, ISBN 978-3-9815227-3-0

[2] D. Soyk et al., Capacity studies of CBM STS micro-cable stack-up, this report

DOI:10.15120/GR-2017-1

Assembly of dummy modules for a STS test unit

C. Simons[1], *R. Visinka*[1], *O. Vasylyev*[1], *and I. Tymchuk*[2]
[1]GSI, Darmstadt, Germany; [2]LTU Ltd, Kharkov, Ukraine

With the construction of a demonstrator for the CBM Silicon Tracking System a lot of questions in matters of assembly techniques, cooling and cabling can be answered. Dummy-modules for this unit are assembled to gain experience with the longest microcables, the biggest sensors (62 mm by 124 mm), the ladder assembly, and to be able to fix the total cable lengths.

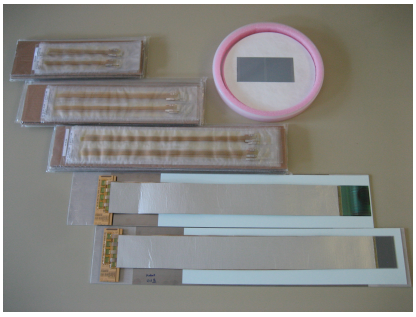

Figure 1: Dummy-modules for quarter unit 7.

The longest sensor modules

Unit 7, as the biggest unit, needs the longest microcables. For the n-side of the inner 42 mm silicon sensor, microcables of about 495 mm length are necessary. Until now the longest microcables delivered had a length of 250 mm and therefore important experience could be gained during the module-assembly with cables of up to such length. The storage plates and storage systems had to be adapted.

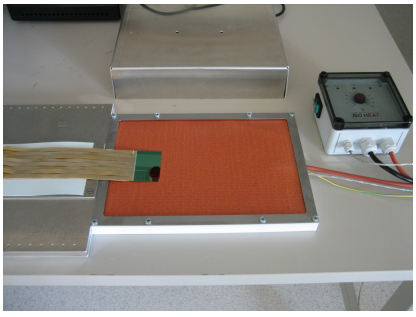

Figure 2: Dummy-module on the heating mat.

Since these longest modules do not fit in the oven for the curing process, a heating mat has been acquired. The mat can be placed next to the assembly tables, helps to avoid longer transport ways for the module and offers heating only in the glued area (sensor, ASIC or FEB).

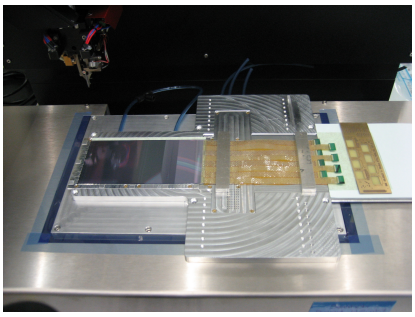

Figure 3: TAB-bonding on a 124 mm sensor.

The vacuum plates were adapted for the 124 mm sensors and the handling procedures were optimized (see Fig. 3).

The total cable lengths

The microcable lengths measured in the CATIA-model result from different factors: sensor position on the ladder, position of the sensor bonding rows, position of the ASIC bonding rows, overlap of the sensors, bending radius of the microcable, etc..
On one hand the aim is to pack the microcable stacks of the five modules closely and to avoid cable loops. On the other hand the mounting of the front-end-boards in the electronic boxes has to be considered (Fig. 4). The p-side-FEB is fixed on the bottom side of the cooling plate, the n-side-FEB on the top side.
Based on the microcables lengths measured in the CATIA-model the length for the module-cables have been increased in little steps to gain experience during the assembly-procedures and to find the optimal lengths.

Figure 4: Microcables in electronic box.

The dummy-modules for unit 7 will be used to test the ladder assembly tool with regard to functionality and accuracy.

DOI:10.15120/GR-2017-1

Capacitance studies of the CBM STS microcable stack-up

D. Soyk, H. Faber, and C. J. Schmidt
GSI, Darmstadt, Germany

Several studies with FEM tools have been made to find a thin microcable stack-up with a reduced capacitance and good assembly properties.

Discussion of parameters

The capacitance of a simple flat capacitor is calculated as follows:

$$C = \epsilon_r \epsilon_0 \frac{Lb}{d} \quad (1)$$

The vacuum permittivity ϵ_0 is a natural constant. If we assume that the capacity is directly proportional to the length L three parameters are left to optimize:

1. the relative permittivity ϵ_r depends upon the material.
2. the distance d between two layers of metal strands or the ground layer of the microcable. (N.B.: the pitch between two strands must be kept to avoid mismatch between sensor and microcable or between microcable and chip.)
3. the width b of the metal strands.

Choice of simulation tool

Two software tools were available to generate this study. The first was Ansys and the second was the Transmission Line Electromagnetic Modeling Tool - called TNT. Ansys employs the finite element method (FEM), TNT the near element boundary method (NEBEM). Some comparision studies were done to avoid errors due to systematical errors in the calculation method or simple software errors. For theses studies a defined layer stack was used and the permittivity ϵ_r of the spacer was varied. The stack consisted of the following materials above a metallic plane: 100 μm spacer, 10 μm polyimid, 14 μm aluminium outer signal layer; 50 μm spacer, 10 μm polyimid, 14 μm aluminium inner signal layer and 100 μm spacer. In the table below the results obtained with TNT and Ansys are displayed in comparison.

ϵ_r	TNT outer layer [pF/cm]	Ansys outer layer [pF/cm]	TNT inner layer [pF/cm]	Ansys inner layer [pF/cm]
3.5	0.91	0.99	0.89	0.94
2.25	0.68	0.72	0.66	0.69
1.5	0.53	0.55	0.51	0.52

Both simulation tools show the same trends: higher ϵ_r effects higher capacitance and the outer layer has a higher capacitance than the inner layer. Both trends are expected from equation (1). The results differ less than 1/10. Therefore both tools seems to be sufficent for our needs, and we chose the TNT tool for further studies.

Stack and material variations

In [1] a cable stack for the CBM STS readout was proposed. Further investigation especially concerning the produceability and the handling of the different layers of the micro-cable required some modifications. First the central spacer had to be split in two halfs to result in a symmetrical stack of the micro-cable for the p- and n-side of the sensor. Additionally the polyimid layer between the grounds and the outside spacer was suppressed to avoid the lamination of 2 flimsy, 10 μm thick polyimid layers during the production process. It turned out that at least the spacer under each signal layer should be the same to make the laboratory assembly procedures easier. The modified cable stack is shown in Fig. 1.

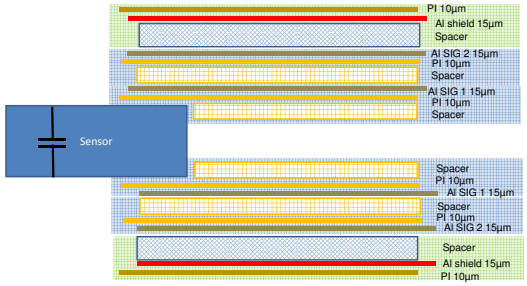

Figure 1: Modified CBM STS microcable stack-up

Variation of the spacer material and thickness give possibilities to influence the capacity of the cable. There were 6 material options to investigate:

material	ϵ_r	thickness [μm]
polyimid 5/10 filled	2.25	50
polyimid 5/10 filled	2.25	100
polyimid 3/10 filled	1.8	50
polyimid 3/10 filled	1.8	75
polyimid 3/10 filled	1.8	100
Foamtak II	1.5	165

DOI:10.15120/GR-2017-1

Possible stack-ups were chosen. In the following table one half of the symmetric stack-ups are described (from the outer layer to the plane of symmetry where the sensor is located):

No.	Layers
1	10μm polyimid,14μm aluminium,100μm polyimid 5/10, 14μm aluminium,10μm polyimid,50μm polyimid 5/10, 14μm aluminium,10μm polyimid,50μm polyimid 5/10
2	10μm polyimid,14μm aluminium,100μm polyimid 3/10, 14μm aluminium,10μm polyimid,50μm polyimid 3/10, 14μm aluminium,10μm polyimid,50μm polyimid 3/10
3	10μm polyimid,14μm aluminium,165μm Foamtak II, 14μm aluminium,10μm polyimid,50μm polyimid 5/10, 14μm aluminium,10μm polyimid,50μm polyimid 5/10
4	10μm polyimid,14μm aluminium,165μm Foamtak II, 14μm aluminium,10μm polyimid,50μm polyimid 3/10, 14μm aluminium,10μm polyimid,50μm polyimid 3/10
5	10μm polyimid,14μm aluminium,165μm Foamtak II, 14μm aluminium,10μm polyimid,75μm polyimid 3/10, 14μm aluminium,10μm polyimid,75μm polyimid 3/10
6	10μm polyimid,14μm aluminium,165μm Foamtak II, 14μm aluminium,10μm polyimid,100μm polyimid 3/10, 14μm aluminium,10μm polyimid,100μm polyimid 3/10
7	10μm polyimid,14μm aluminium,165μm Foamtak II, 14μm aluminium,10μm polyimid,165μm Foamtak II, 14μm aluminium,10μm polyimid,165μm Foamtak II

These 7 stack-ups were simulated for a strand width of 46 μm. The results for the inner and outer signal layer were calculated.

No.	inner layer [pF/cm]	outer layer [pF/cm]	thickness [μm]
1	0.715	0.724	544
2	0.615	0.620	544
3	0.715	0.613	674
4	0.615	0.566	674
5	0.569	0.534	774
6	0.548	0.518	874
7	0.468	0.476	1134

Stack no. 1 and no. 2 differ only by the polyimid material for the spacer used. No. 2 uses the polyimid 3/10 filled mesh with a mean ϵ_r of 1.8 instead of 2.25. An improvement of the strand capacitance for both layers is observable. No. 3 and 4 have the same structure as No. 1 and 2 between the signal layers, but the spacer between shielding and outer signal layer is thicker and with lower ϵ_r. This has mainly an influence on the capacitance of the outer signal layer, not on the inner signal layer. If the capacitance of both layers is to be improved the structure between the signal layers also needs improvement. No. 5 and 6 has the same stack of materials as no. 4, but the thickness of the polyimid 3/10 filled spacer is increased to 75 and 100 μm. The capacitance consequently decreases with the increasing thickness of the spacer as anticipated. No. 7 contains only 165 μm thick Foamtak II spacers. The low ϵ_r and the high thickness of the material results in a low capacitance of the signal layers.

Due to mechanical space restrictions in the CBM STS detector the "best" micro cable stack-up is not the one with the lowest capacitance, but the one with the lowest capacitance fitting in the foreseen space. In the final detector 5 microcable stack-ups will be adjacent and the overall thickness of these 5 stacks should be less than 5 mm (with some safety margin). Therefore the stack no. 5 was chosen. Now 2 of 3 parameters are optimized, namely the relative permittivity ϵ_r and the distance d between the signal layers (in other words the thickness of the spacer). To reach the design goal of a capacitance of less than 0.5 pF/cm, the last parameter must be modified: the width b of the metal strands of the signal cable. The strand width is reduced to a width of 30 μm and the calculation for the stack no. 5 is done. The following values are obtained for 30 μm strands:

inner layer [pF/cm]	outer layer [pF/cm]
0.387	0.367

For comparison, these are similar to the values obtained from the measurements of a realistic stack-up, where the width of the strands was 35 μm. The simulation is something like 1/10 off the measurement.

Conclusion

As shown above it is possible to obtain a thin microcable stack for the CBM STS detector with a relative capacitance lower than 0.5 pF/cm. In the real world the measured values for the capacitance should be well under the simulations, because the stack-up is in general not tightly laminated so that the average distance between the layers is generally larger. Also the layers of glue are assumed to be equal to zero and are neglected in the simulation.

References

[1] D. Soyk et al., "Modification of the CBM-STS micro-cable stack-up", CBM Progress Report 2014

DOI:10.15120/GR-2017-1

Optimization of multi-strange hyperons cuts in KF Particle Finder

H. Cherif[1,2], *A. Toia*[1,2], *and I. Vassiliev*[2]
[1]Goethe University Frankfurt am Main, Germany; [2]GSI, 64291 Darmstadt, Germany

One of the main goals of the CBM experiment is the measurement of very rare probes and the investigation of possible signatures of the phase transition from nuclear matter to deconfined phase and formation of the Quark Gluon Plasma (QGP). The enhanced production of multi-strange (anti)particles is one among those signatures, thus we investigate the performance of multi-strange hyperons measurement in the CBM experiment. Multi-strange (anti) hyperons are reconstructed via their weak decay into charged hadrons ($\Lambda \rightarrow p\pi, \Xi \rightarrow \Lambda\pi, \Omega \rightarrow \Lambda K$) measured by the Silicon Tracking System (STS) detector installed in a large acceptance dipole magnet. Identification of the decay products is performed by a time-of-flight measurement with TOF detector located at a distance of 6 to 10m behind the target. The analysis is performed by the KF Particle Finder (KFPF) package [1].. In order to reduce the combinatorial background, three selection criterias are applied in the reconstruction of multi-strange (anti)hyperons:

- χ^2_{geo} : To ensure that the trajectories of the daughter particles intersect within their errors.
- χ^2_{topo}: To ensure that the particle is produced in the primary vertex region.
- $l/\Delta l$: Distance from the decay point of the candidate to the primary vertex normalized on the error.

The values of these cuts are optimized by a scan over the whole set of selection criteria with a requirement to maximize the signal-to-background ratio with a minimal loss of efficiency. Specifically we studied the efficiency and significance of the signal in central Au+Au collisions at 10 AGeV simulated with the UrQMD event generator, coupled to a Geant3-based description of the CBM detector. The significance is defined as $S/\sqrt{S+B}$, where S and B are total numbers of signal and background of the candidate from Monte Carlo. We distinguish two types of efficiency, which are defined as:

- The efficiency of KF Particle Finder package which is the efficiency of the method followed in the reconstruction of particles, including the topological cuts and the Particle Identification in the ToF.
- The total efficiency in the 4π solid angle which, in addition to the previous, take into account the acceptance of the detector and the inefficiencies of track reconstruction and PID algorithms.

Fig. 1 shows the variation of the significance and the 4π efficiency as function of the cut values for the different cuts mentioned above. Then the default value is optimized for

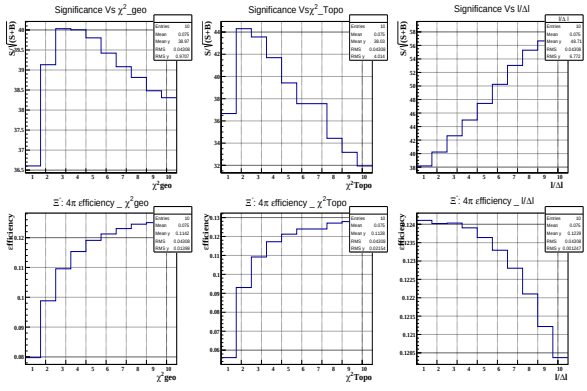

Figure 1: Significance and 4π efficiency as a function of cuts for the reconstruction of Ξ^-

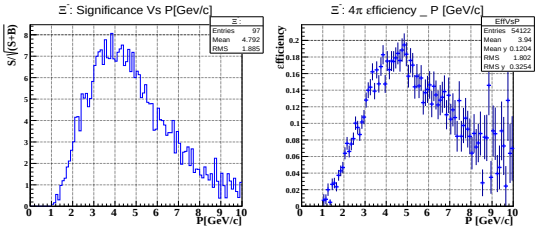

Figure 2: Significance and efficiency vs p for Ξ^-

each cut, taking into account the best arrangement between the significance and the efficiency. Table 1 shows the mean efficiency calculated with the default optimal cut values for all hyperons. Since the background as well as the selections

Hyperons	Λ	$\bar{\Lambda}$	Ξ^-	$\bar{\Xi}^+$	Ω^-	$\bar{\Omega}^+$
KFPF efficiency(%)	70.7	43.6	47.6	30.6	15.9	12.9
4π efficiency (%)	26.6	16.5	10.2	6.8	4.6	3.9

Table 1: Efficiency of reconstruction of multi-strange hyperons in the CBM experiment:

used for the reconstruction, depend on the average particle momenta, efficiency and significance are studied as a function of the particle momentum. The significance and the efficiency as function of momentum for Ξ^- is shown in Fig. 2. The high quality of these parameters demostrate the capability of CBM to reconstruct strange particles both with a high signal to background ratio and efficiency.

References

[1] M. Zyzak (2016), PhD thesis, Goethe University Frankfurt.

DOI:10.15120/GR-2017-1

Reconstruction of π^0 via double conversion method *

I. Kres[1], *C. Pauly*[1], *and K.-H. Kampert*[1]
[1]Department of Physics, University of Wuppertal, Germany

The CBM experiment is designed to study heavy ion collisions at high net-baryon densities and moderate temperature, at high interaction rates. Under these conditions, heavy particles containing charm quarks, like J/ψ, are produced, but also vector mesons ω, ρ, ϕ will be created, and detected via their rare dileptonic channel $\omega/\rho/\phi \rightarrow e^+e^-$. As leptons are not affected by hadronic interaction with the dense medium, the dileptonic decay channel offers the possibility to look into the early, dense phase of the fireball evolution. Due to their comparatively small production cross section, together with small branching ratio (BR) into e^+e^- a precise understanding of background is needed. A major source of this background are π^0, which have two main decay channels: $\pi^0 \rightarrow \gamma + \gamma$ with BR of 98.8% and $\pi^0 \rightarrow e^+ + e^- + \gamma$ (Dalitz decay) with BR of 1.1%.

Instead of measuring directly photons, using an electromagnetic calorimeter, the CBM-RICH detector is able to measure photons indirectly by detecting e^+e^--pairs stemming from conversion $\gamma \rightarrow e^+e^-$ in the target or in the material of the detectors. Two such reconstructed photons are then further combined to form a π^0.

In previous work this study was done for cases, when both photons from π^0 underwent conversion only in the target [1]. Using the secondary vertex finder included in the KFParticle package [2], one can reconstruct conversion vertices also outside the target, which will increase statistics by about a factor of 5, because the probability for conversion outside the target compared to conversion inside the target is roughly 50:50, as shown in figure 1.

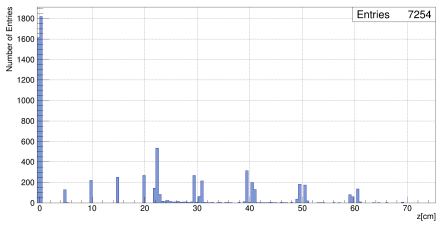

Figure 1: Distribution of z-position of reconstructed $\gamma \rightarrow e^+e^-$ vertices. The spikes correspond to the target (0 cm), MVD stations (5, 10, 15, and 20 cm), and STS (22, 30, 40, 50, and 60 cm) positions.

This previous study is now extended, including reconstruction of conversion vertices outside the target. The results shown here are based on 5×10^6 simulated UrQMD events of central Au+Au collisions at beam energy of 8 AGeV. The detector simulation includes the Micro Vertex Detector (MVD), Silicon Tracking System (STS), and Ring Imaging Cherenkov detector (RICH). The magnetic field has its nominal value 100%. The RICH geometry was used with the new cylindrical shaped photon detection plane.

In the first analysis step, all charged tracks are reconstructed in STS, and only lepton tracks are selected based on particle identification (PID) in the RICH. Since the leptons from $\pi^0 - e^+e^-e^+e^-$ signal events have in most of cases small momenta, half of them are outside of acceptance of the RICH detector, which makes the probability to register all four leptons from π^0 very low. A less restrictive requirement of at least two (one from each pair) out of four are identified in the RICH as leptons, helps to increase statistics by about factor of 10, compared to full identification in RICH.

When only one lepton of a potential e^+e^- pair is identified in the RICH, then the second candidate must not necessarily be a lepton as well. Applying additional cuts on the invariant mass of γ (< 10 MeV) and opening angle between charged particles ($< 1°$), one can exclude most of situations, where the second particle is not an electron. For all γ candidate events surviving these cuts, the invariant mass spectrum of π^0 is calculated and shown in figure 2.

The background was estimated with Event Mixing Technique (EMT) and was substracted from the spectrum. The subtracted spectrum was fitted using a Gaussian and the number of reconstructed π^0 is determined to be 4404±82.

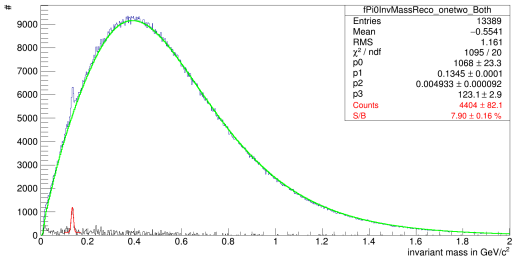

Figure 2: Invariant mass spectrum of reconstructed π^0 with double conversion method (blue), estimated background from EMT (green), background-substracted spectrum (black), Gaussian fit (red).

References

[1] Dissertation of Sascha Reinecke, Wuppertal, 2016.

[2] Dissertation of Maksym Zyzak, Frankfurt am Main, 2015.

* Work supported by BMBF 05P15PXFCA, and GSI

DOI:10.15120/GR-2017-1

CBM operation at low SIS100 beam energies

A. Senger[1]
[1]GSI, Darmstadt, Germany

Motivation

The CBM physics program covers the full beam energy range of SIS100. The operation of the CBM experiment at low beam energies has to be optimized with respect to the setting of the magnetic dipole field which deflects the beam. One condition for save operation is that the beam has to hit the beam dump which is located about 20 m downstream the target. Moreover, the beam should stay within the beam pipe, and should not directly hit the detectors. In order to fulfil these requirements, the magnetic field of the CBM dipole has to be reduced for operation at low beam energies. However, a reduced dipole field might have severe consequences for the tracking performance of the experiment. This report presents a study of a CBM operation scenario at low beam energies together with the resulting tracking performance. Simulations have been performed with the FLUKA package ([1], [2]), and with the FLAIR interface ([3]) for visualization of the results. Multi-scattering of the Au beam in in the Au target (1% interaction length) is included in the FLUKA calculations. A typical beam divergence is also taken into account, however, the width of the beam profile is dominated by multiple scattering.

Beam position in the beam dump

The beam profile for different Au beam energies at the entrance of the CBM iron beam dump (25.75 m downstream the target) is shown on figure 1. At the full magnetic field and a beam energy of 2 AGeV the maximum of the beam intensity is deflected by more than 1 m which is already outside the iron core of the beam dump (total width 2 m). Moreover, the width of the beam at 2 AGeV increases up to factor of 2 in comparison to 8 AGeV. The beam positions in the region of beam dump for different energies and scaled magnetic field are shown on figure 2. The symbols indicate the position of the maximum of the beam intensity, whereas the circles describe the width of the beam containing 99% of the intensity. In order to catch the beam for both polarities of the dipole magnetic field, the horizontal size of the beam dump was chosen to $\pm$100 cm (red dashed line in figure 2). Nevertheless, the magnetic dipole field has to be reduced to about 70% of the nominal value in order to dump 99% of the beam particles with an energy of 2 AGeV into the iron beam stopper.

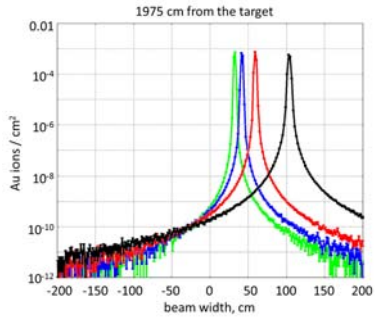

Figure 1: Beam profile at the region of the CBM beam dump for different Au beam energies: black - 2 AGeV, red - 4 AGeV, blue - 6 AGeV, green - 8 AGeV.

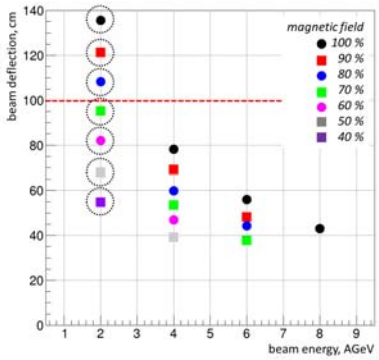

Figure 2: The beam positions at the iron beam dump for different energies and scaled magnetic field: black symbols - 100% magnetic field, red - 90%, blue - 80%, green - 70%, magenta - 60%, gray - 50%, and violet - 40% magnetic field. The circles indicate the beam width corresponding to 99% of the beam intensity for an energy of 2 AGeV. The red dashed line shows the horizontal width of the beam dump.

Beam position at the detector stations

As examples, we study the beam positions in the STS region (20-120 cm downstream the target) and the horizontal beam profile at the position of the TRD (5 m downstream the target) for an Au beam with an energy of 2 AGeV. Figure 3 illustrates the beam deflection in the region of the STS for different magnetic fields. The black dashed line depicts the radius of the beam pipe. At 60% of the nominal field value the beam still is very close to the beam pipe edge, and, hence, it seems preferable to reduce the magnetic field

DOI:10.15120/GR-2017-1

to 50% of the nominal value. In figure 4 the horizontal beam profile is shown at the position of the TRD. The red histogram in figure 4 corresponds to the beam profile for 100% magnetic field. The dashed black lines illustrate the central hole in the detector required for the beam pipe. As shown in figure 4, in case of 100% magnetic field the beam fully hits the detector area. In order to reduce the number of beam particles hitting the detector to 10^{-6} of the full beam intensity, the magnetic field has to be reduced to 50% of the nominal value. The resulting beam profile is shown in figure 4 as a light blue line.

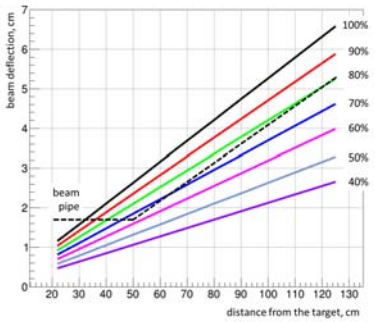

Figure 3: Beam position in the region of the STS (20-120 cm downstream the target) for Au beam at 2 AGeV for different magnetic field scaling (see explanation on picture). The black dashed line illustrates the radius of the beam pipe.

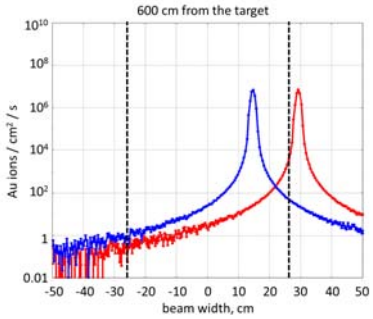

Figure 4: Horizontal beam profile at the position of the TRD (5 m downstream the target) for Au beam at 2 AGeV for 100% magnetic field (red line) and for 50% magnetic field (blue line). The black dashed lines illustrate the size of the detector hole for the beam pipe.

Particle reconstruction performance with reduced magnetic dipole field

The effect of a reduced magnetic dipole field on the particle reconstruction performance was studied using the cbmroot software and the KFParticle package. The simulated setup consists of STS and ToF. The particle reconstruction efficiency for Au beam energy of 2 AGeV with full and reduced magnetic field is shown in figure 5 (left panel). For the reduced magnetic field, the reconstruction efficiency for low momentum particles increases due to the increased acceptance. The momentum resolution for the same beam energy with full and reduced magnetic field is shown in figure 5 (right panel). At an Au beam energy of 2 AGeV and a magnetic field of 40% nominal value, the momentum resolution decreases by a factor of 2.

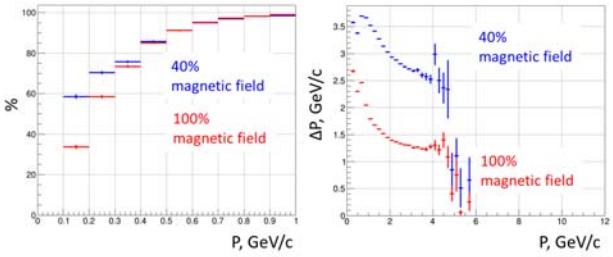

Figure 5: The particle reconstruction efficiency as function of particle momentum (left) and the momentum resolution versus momentum (right) for Au beam energy of 2 AGeV with full (red) and scaled (blue) magnetic field.

In order to study the effect of a reduced magnetic field on particle mass resolution and signal-to-background ratio, simulations have been performed for Λ and K_S mesons. The results on reconstruction efficiency, mass resolution and signal-to-background ratio for Λ and K_S are presented in figure 6.

Magnetic field	100%	40%	100%	40%	100%	40%
	Reconstruction efficiency		Mass resolution		Signal-to-background ratio	
Λ	6.0%	9.0%	1.7 MeV	3.4 MeV	4.7	2.0
K_s^0	2.8%	3.6%	4.0 MeV	9.0 MeV	25.0	20.7

Figure 6: The reconstruction efficiency of Λ and K_S, mass resolution and signal-to-background ration for reconstruction for Au beam energies of 2 AGeV with full and reduced magnetic field.

References

[1] "The FLUKA code: Description and benchmarking" G. Battistoni, S. Muraro, P.R. Sala, F. Cerutti, A. Ferrari, S. Roesler, A. Fasso', J. Ranft, Proceedings of the Hadronic Shower Simulation Workshop 2006, Fermilab 6–8 September 2006, M. Albrow, R. Raja eds., AIP Conference Proceeding 896, 31-49, (2007)

[2] "FLUKA: a multi-particle transport code" A. Fasso', A. Ferrari, J. Ranft, and P.R. Sala, CERN-2005-10 (2005), INFN/TC_05/11, SLAC-R-773

[3] "FLAIR: A Powerful But User Friendly Graphical Interface For FLUKA" V. Vlachoudis, Proc. Int. Conf. on Mathematics, Computational Methods & Reactor Physics (M&C 2009), Saratoga Springs, New York, 2009

DOI:10.15120/GR-2017-1

Hypernuclei reconstruction at the CBM experiment *

I. Vassiliev[1], *I. Kisel*[1,2,3], *and M. Zyzak*[1]

[1]GSI, Darmstadt, Germany; [2]Goethe-Universitaet Frankfurt, Frankfurt am Main, Germany; [3]Frankfurt Institute for Advanced Studies, Frankfurt am Main, Germany

In the CBM experiment at FAIR high net-baryon densities and moderate temperatures will be reached in heavy-ion collisions. Model calculations predict structures in the QCD phase diagram at large baryon chemical potentials, like the critical endpoint followed by a first order phase transition. Moreover, new phases are predicted, such as quarkyonic matter. Experimental discovery of these landmarks and regions in the QCD phase diagram would be a major breakthrough in our understanding of properties of strongly interacting matter at extreme conditions, with fundamental consequences for our knowledge on the structure of neutron stars, chiral symmetry restoration, and the origin of hadron masses. The aim of the CBM experiment is the measurement of very rare probes including multi-strange hyperons and hypernuclei at interaction rates of up to 10 MHz.

Theoretical models predict that single and double hypernuclei can be produced via coalescence in heavy-ion collisions with the maximum yield in the region of SIS100 energies [1, 2]. This is due to the superposition of two effects: the increase of light nuclei production with decreasing beam energy, and the increase of hyperon production with increasing beam energy. The CBM experiment at SIS100 will measure hydrogen and helium hypernuclei in huge amounts. To study the performance of multi-strange hyperon and hypernuclei reconstruction, several sets of $5 \cdot 10^6$ central Au+Au UrQMD events (Fig. 1) at the FAIR energy range 2-10 AGeV have been simulated.

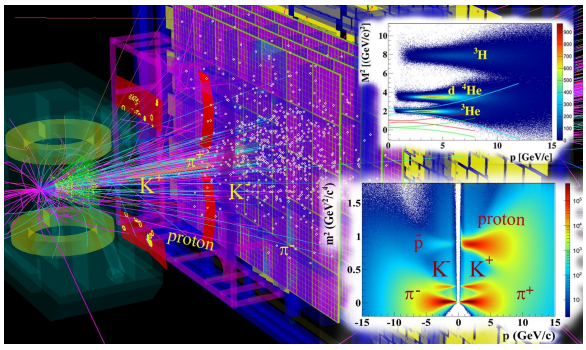

Figure 1: A simulated CBM event of a Au+Au collision. Reconstructed in the STS tracks propagated via RICH and TRD to the TOF detector. The TOF detector identifies hadrons i. e. pions, kaons, protons and fragments.

The combination of Micro Vertex Detector (MVD) and fast segmented strip detectors of the Silicon Tracker System (STS) with cables and support frames was used for event simulation and reconstruction. The TOF detector identifies hadrons i.e. pions, kaons, protons, and fragments, i. e. d, t, ^{3}He and ^{4}He in the angular range covered by the STS detector.

The current KF Particle Finder package includes search of Lambda hypernuclei: the bound state $\{\Lambda n\}_b$, ${}^3_\Lambda$H, ${}^4_\Lambda$H, ${}^4_\Lambda$He, ${}^5_\Lambda$He and corresponding anti-particles and double Lambda hypernuclei: ${}^4_{\Lambda\Lambda}$H, ${}^5_{\Lambda\Lambda}$H and ${}^6_{\Lambda\Lambda}$He. Hypernuclei will be reconstructed in the CBM experiment by their decays into charged hadrons and fragments, like d, t, ^{3}He and ^{4}He, which are detached from the primary vertex. As an example reconstructed ${}^4_\Lambda$He$\rightarrow{}^3$He$p\pi^-$ decay is shown in Fig. 2.

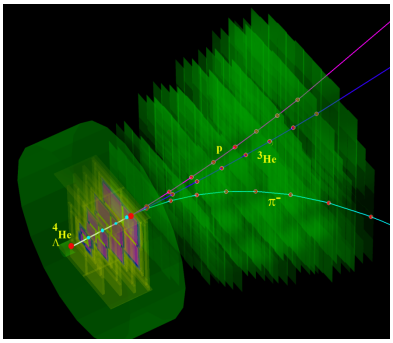

Figure 2: A reconstructed ${}^4_\Lambda$He$\rightarrow{}^3$He$p\pi^-$ decay topology.

${}^4_\Lambda$He hypernuclei are created at the primary vertex and decay to ^{3}He$p\pi^-$ several centimeters downstream of the target. Presence of the ^{3}He fragment in a 3-prong vertex is a unique signature of such decay. The reconstructed invariant-mass spectrum of ^{3}He$p\pi^-$ is shown in Fig. 3.

Small amount of background events in the high-mass region is due to misidentified high-momentum hadrons in the sample of ^{3}He selected particles.

Assuming the ${}^4_\Lambda$He production multiplicity for minimum bias Au+Au events at 10 AGeV about $5 \cdot 10^{-4}$ [1, 2], the branching ratio of 20% to ^{3}He$p\pi^-$ decay [3], taking into account the 14.7% ${}^4_\Lambda$He detection efficiency, one would expect the ${}^4_\Lambda$He extremely high collection rate of up to $5.4{\cdot}10^5$ per hour.

Moreover, the experiment has a substantial discovery potential for light double Lambda hypernuclei. The topology of double-Lambda hypernuclei decay is complicated. For example ${}^6_{\Lambda\Lambda}$He first decays to ${}^5_\Lambda$He$p\pi^-$ several centimeters downstream of the target, then single-Lambda hypernuclei ${}^5_\Lambda$He weekly decays to ^{4}He$p\pi^-$. In order to reconstruct

* Work supported by HICforFAIR, FIAS and HGS-HIRe for FAIR.

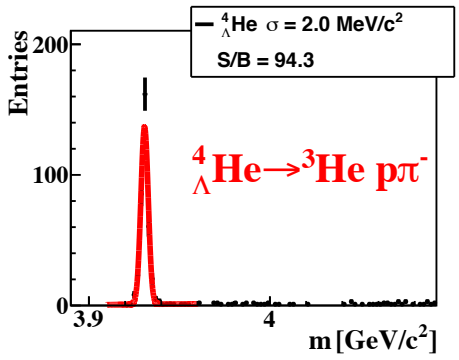

Figure 3: The reconstructed invariant-mass spectrum of ^{3}He$p\pi^-$ in $5 \cdot 10^6$ central Au+Au collisions at 10 AGeV. The red line indicates the signal plus background fit by a polynomial plus Gaussian function.

such a complicated topology KF Particle Finder first reconstructs detached 3-prong decay of $^5_\Lambda$He combining secondary ^{4}He, p and π^-, then a mass constraint is applied to selected $^5_\Lambda$He candidates, and $^6_{\Lambda\Lambda}$He particles are constructed as combination of secondary $^5_\Lambda$He, p and π^-. Finally the reconstructed $^6_{\Lambda\Lambda}$He candidates checked to be primary.

In the Table 1 the multiplicities, branching ratios, decay modes, efficiencies and collection rate per week at 10 MHz interaction rate of selected single- and double Lambda hypernuclei for the CBM experiment are shown.

particle	multiplicity	decay	BR	$\varepsilon_{4\pi}$%	yield/week
$^3_\Lambda$H	$0.9 \cdot 10^{-2}$	^{3}Heπ^-	0.25	19.2	$2.6 \cdot 10^9$
$^4_\Lambda$He	$0.4 \cdot 10^{-3}$	^{3}He$p\pi^-$	0.32	8.9	$6.9 \cdot 10^7$
$^5_\Lambda$He	$1.0 \cdot 10^{-5}$	^{4}He$p\pi^-$	0.4	7.9	$1.9 \cdot 10^6$
$^4_{\Lambda\Lambda}$H	$3.7 \cdot 10^{-5}$	$^4_\Lambda$Heπ^-	0.06	2.6	$3.8 \cdot 10^5$
$^5_{\Lambda\Lambda}$H	$5.0 \cdot 10^{-7}$	$^5_\Lambda$Heπ^-	0.08	2.0	$4.9 \cdot 10^3$
$^6_{\Lambda\Lambda}$He	$2.5 \cdot 10^{-8}$	$^5_\Lambda$He$p\pi^-$	0.08	1.3	160

Table 1: Multiplicities, branching ratios, decay modes, efficiencies and collection rate per week at 10 MHz interaction rate of single- and double Lambda hypernuclei for the CBM experiment.

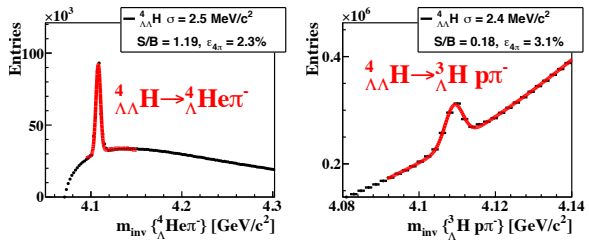

Figure 4: The reconstructed invariant-mass spectra of $^4_\Lambda$Heπ^- (left) and $^3_\Lambda$He$p\pi^-$ (right) in 10^{12} central Au+Au collisions at 10 AGeV. The red lines indicate the signal plus background fit by a polynomial plus Gaussian function.

The invariant-mass spectra of $^4_\Lambda$Heπ^- and $^3_\Lambda$He$p\pi^-$ are shown in Fig. 4. Left plot is obtain by combination of secondary $^4_\Lambda$He and π^-. Three particle invariant-mass spectrum of $^3_\Lambda$He$p\pi^-$ is shown in the right plot. The simulated amount of $5 \cdot 10^6$ central Au+Au collisions at 10 AGeV is not enough for determination of the background shape, so we use typical shapes of two or three particle background for hypernuclei scaled to simulated number of entries in the corresponding histogram. Assuming a reaction rate of 10^7 Au+Au minimum bias events/s (MVD will be removed from the setup), production multiplicity about $3.7 \cdot 10^{-5}$ and $2.5 \cdot 10^{-8}$ [1, 2], the branching ratios of 6.4% and 2.3% [3], one would expect to measure within one week about $3.8 \cdot 10^5$ and $1.8 \cdot 10^5$ $^4_{\Lambda\Lambda}$H, respectively.

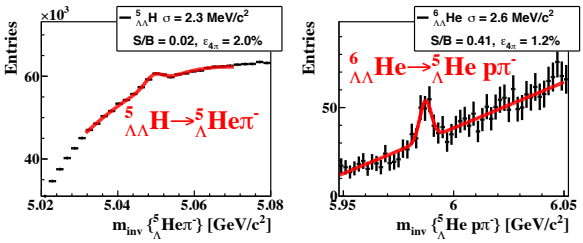

Figure 5: The reconstructed invariant-mass spectra of $^5_{\Lambda\Lambda}$He (left) and $^6_{\Lambda\Lambda}$He (right) in 10^{12} central Au+Au collisions at 10 AGeV. The red lines indicate the signal plus background fit by a polynomial plus Gaussian function.

With extremely low production multiplicity $2.5 \cdot 10^{-8}$ of $^6_{\Lambda\Lambda}$He and small branching ratio of 8% [3], one would expect to measure within one week about 160 $^6_{\Lambda\Lambda}$He (see Fig. 5). Such measurements would represent a breakthrough in hypernucleus physics, as up to now only very few double-Lambda hypernuclei events have been found [4]. The discovery of double lambda hypernuclei and the determination of their life-times will provide information on the hyperon-nucleon and hyperon-hyperon interactions, which are essential ingredients for the understanding of the nuclear matter equation-of-state at high densities, and, hence, of the structure of neutron stars [5].

Discovery and investigation of new hypernuclei and of hypermatter will shed light on the hyperon-nucleon and hyperon-hyperon interactions, which are essential ingredients for the nuclear equation-of-state at high densities and moderate temperatures. The CBM experiment will provide a unique machinary for their study.

References

[1] A. Andronic et al., Phys. Lett. **B697** (2011) 203.

[2] H. Stoecker et al., Nucl. Phys. **A827** (2009).

[3] H. Kamada et al., Phys. Rev., Ser. C **57** (1998) 1595.

[4] J. K. Ahn et al., Phys. Rev. C**88** (2013) 014003

[5] A. S. Botvina et al., Phys. Lett. B**742** (2014) 7

DOI:10.15120/GR-2017-1

Towards full event topology reconstruction with KF Particle Finder *

M. Zyzak† [1], *I. Kisel*[1,2,3], *and I. Vassiliev*[1]

[1]GSI, Darmstadt, Germany; [2]Goethe-Universitaet Frankfurt, Frankfurt am Main, Germany; [3]Frankfurt Institute for Advanced Studies, Frankfurt am Main, Germany

Physics analysis requires the cleanest possible samples of reconstructed particles. Therefore background for them should be suppressed. An independent analysis of each decay separately cannot guarantee this, since abundant particles can contribute to the background generation for all other particles. Thus, to solve the problem full event topology reconstruction is required.

We started the development of full event topology reconstruction at the example of $K^0_s \to \pi^+\pi^-$ and $\Lambda \to p\pi^-$. At first, all possible particle candidates are constructed in a usual manner (see Fig. 1, blue line). We would like to notice, that charged particles without PID are participating in reconstruction of both decays with the corresponding mass hypothesis.

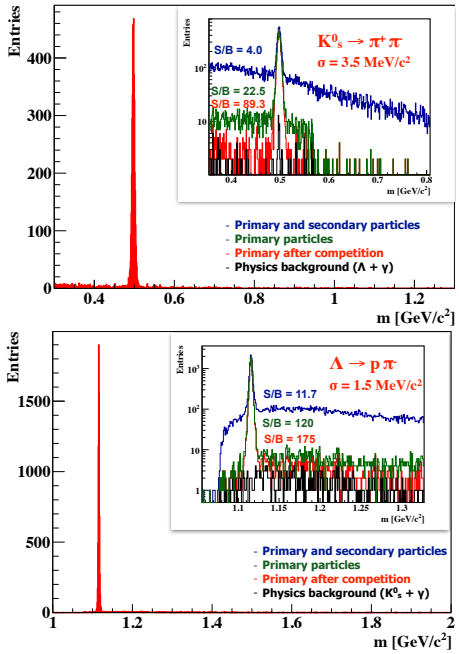

Figure 1: Full event topology reconstruction at an example of $K^0_s \to \pi^+\pi^-$ and $\Lambda \to p\pi^-$ decays reconstruction in 10k mbias UrQMD AuAu events at 10 AGeV with ToF PID

Only primary particles, which are produced directly in the collision, should be selected for physics analysis, since secondary particles produced as a result of a decay or interaction with the material of the detector do not carry information of the collision. The obtained spectra of the primary candidates are shown with a green line. We would like to notice, that the signal to background (S/B) ratio improved by about one order at this step, because the most of the background is due to the random combinatorial intersections of charged particles, that do not point to the primary vertex.

Candidates constructed with the incorrect mass hypothesis of the charged daughters but corresponding to the real primary particles (K^0_s, γ) cannot be rejected at this step. Since the mass of the daughters is assigned incorrectly, such candidates do not form a peak, but a broad structure at the mass spectrum (see Fig. 1, green line). However, candidate from the same daughter particles but with the correct mass hypothesis should be constructed, and it will contribute to the signal peak at the corresponding spectrum. Thus, from the particle candidates with the same set of daughters but different mass hypothesis only one can be selected. Currently, if at least one candidate lies within 3σ from the corresponding mass peak, the distances to the peaks normalised to the peak width are calculated for all candidates, and only the closest candidate is stored. As a result, background formed by the real short-lived particles can be suppressed, that additionally increases the S/B ratio (see Fig. 1, red line). The residual physics background is formed by γ and candidates with the incorrect mass hypothesis that are accidentally closer to the incorrect peak, it is shown with the black line in Fig. 1.

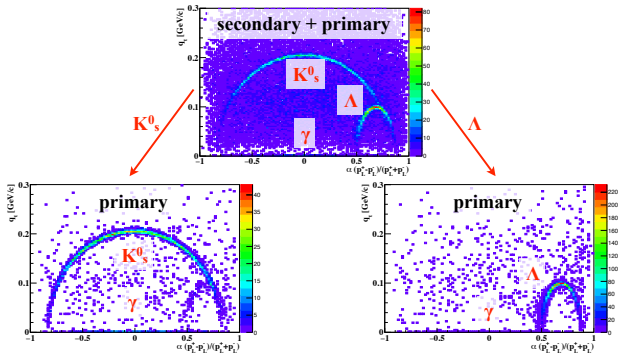

Figure 2: Illustration of the full event topology reconstruction with the Armenteros-Podolanski plots.

The procedure is illustrated by the Armenteros-Podolanski plots in Fig. 2. It is clearly seen, that initial spectra can be significantly cleaned up by the topology reconstruction.

Providing clean particle samples, full event topology reconstruction is a powerful tool for the physics analysis.

* Work supported by HICforFAIR, FIAS and BMBF.

† m.zyzak@gsi.de

DOI:10.15120/GR-2017-1

Reconstruction of resonances with KF Particle Finder *

M. Zyzak[†1], *I. Kisel*[1,2,3], *and I. Vassiliev*[1]

[1]GSI, Darmstadt, Germany; [2]Goethe-Universitaet Frankfurt, Frankfurt am Main, Germany; [3]Frankfurt Institute for Advanced Studies, Frankfurt am Main, Germany

The main task of the CBM experiment is investigation of hot and dense matter created in the collision of heavy ions. One of the possible observables for such study are resonances. Comparison of the line shape of resonances together with their yields in pp and AA collisions are of the physics interest of CBM.

Resonances decay in the vicinity of the collision point. The main part of particles created in a heavy ion collision are originated there as well. Thus, fake particle-candidates produced as a result of random combination of primary tracks can not be separated from the real particles, for instance, by the decay topology. Thus, such random combinations create a huge background for resonances.

One of the possible ways to describe the background shape is fitting the spectrum with a smooth function, that is widely used to study, for example, ρ, K^*, ϕ, and Λ^* resonances [1]. Other methods, like mixed-event and like-signed techniques, will be studied further. We would like to notice, that the function should not have a peak-like structures not to distort the physics signal. In our studies we found an empirical function that satisfies our requirements:

$$f(x) = Ae^{(a_1x^2+b_1x)}(B - e^{(a_2x^2+b_2x)})^p, \qquad (1)$$

which reasonably describes the shape of the background. Here the first exponential term stands for description of the decreasing right part of the spectrum, the second term — for the left edge. Since the rice of the left edge and fall of the right edge are faster than exponential, the second order polynomials are used in the power of the exponents. The Function 1 is empirical and can be further improved.

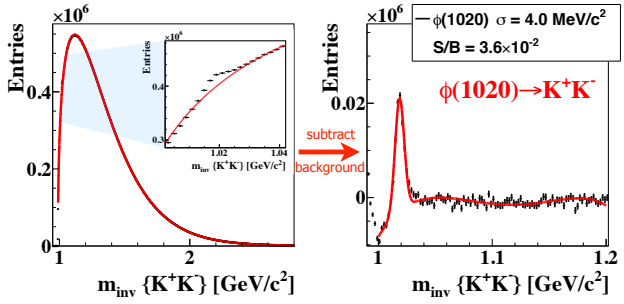

Figure 1: Illustration of the background fit procedure on the example of the ϕ meson spectrum reconstructed in 5M central AuAu UrQMD events at 10 AGeV with ToF PID.

The procedure for extraction of the resonance signal is illustrated on the example of $\phi \to K^+K^-$ spectrum obtained for 5M central AuAu UrQMD events in Fig. 1. At first, the spectrum is fitted with the Function 1. Then the background function is extracted from the total spectrum and the residual spectrum is fitted with a sum of Gauss and polynomial functions. The signal to background ratio is calculated in the region of $\pm 2\sigma$ of the Gauss fit tacking into account the total background.

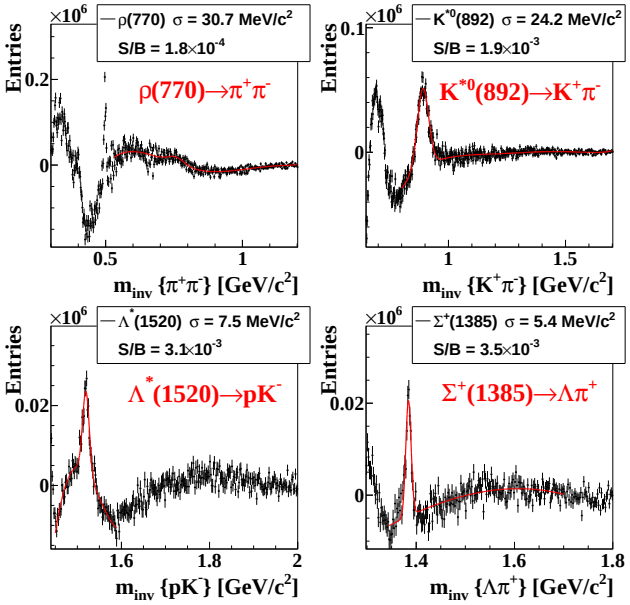

Figure 2: Spectra of resonances with the fitted background subtracted and a signal peak with a residual background shown.

The same procedure can be applied for background fit of other resonances. In Fig. 2 spectra of light vector mesons are shown at the example of $\rho(770) \to \pi^+\pi^-$, excited states of strange mesons — at the example of $K^0(892) \to K^+\pi^-$, excited states of hyperons — at the example of $\Lambda(1520) \to pK^-$ and $\Sigma^+(1385) \to \Lambda\pi^+$.

Summarising, the particles with a very low signal to background ratios down to 10^{-4} can be analysed even in central AuAu events in CBM.

References

[1] M. Aguilar-Benitez *et al.*, "Inclusive particle production in 400 GeV/c pp-interactions," Z. Phys. C — Particles and Fields 50, 405 426 (1991)

* Work supported by HICforFAIR, FIAS and BMBF.

† m.zyzak@gsi.de

DOI:10.15120/GR-2017-1

Σ^+ and Σ^- reconstruction by the missing mass method*

I. Kisel[1,2,3], *P. Kisel*[† 1,2,4], *P. Senger*[1], *I. Vassiliev*[1], *and M. Zyzak*[1]

[1]GSI, Darmstadt, Germany; [2]Goethe-Universität Frankfurt, Frankfurt am Main, Germany; [3]Frankfurt Institute for Advanced Studies, Frankfurt am Main, Germany; [4]Joint Institute for Nuclear Research, Dubna, Russian Federation

Properties of the quark-gluon plasma (QGP) can be studied using the idea of strangeness enhancement, since strange quarks are not brought into the reaction by the colliding nuclei. Any strange quarks or antiquarks observed in experiments are produced in the collision of heavy ions. Therefore, the abundance of strange quarks is sensitive to the conditions and dynamics of the deconfined matter phase, and strangeness enhancement can be indicating that deconfinement conditions were reached. Being abundant particles, Σ^+ and Σ^- carry out large fraction of produced strange quarks. Reconstruction of Σ together with other strange particles completes the picture of strangeness production and allows to compare yields of Σ and Σ^*. Reconstruction of Σ-particles will open a possibility to investigate H-dybarion objects, if such exist, by the decay channel $\Sigma^- p$, which is expected to be the dominant one.

All strange mesons and hyperons, except Σ-particles, can be either registered directly by the tracking system and identified by the PID detectors or have decay modes with all charged particles and, as a result, can be reconstructed through their daughters. Σ^+ and Σ^- have all decay modes with at least one neutral daughter, which can not be registered by the CBM detector at all (decay modes with n or ν) or can be registered with an efficiency on the 10^{-7} level (decay modes with π^0).

Having a lifetime sufficient to be registered by the tracking system ($c\tau_{\Sigma^+} = 2.4$ cm and $c\tau_{\Sigma^-} = 4.4$ cm), these particles can not be identified by the PID detectors. The missing mass method can be applied for their identification. Let us consider it at an example of $\Sigma^- \to n\pi^-$. Tracks of the mother (Σ^-) and the charged daughter (π^-) particles are reconstructed in the tracking system; the neutral daughter particle (n) is reconstructed from these tracks; a mass constraint is set on the reconstructed neutral daughter, that modifies also its momentum; the mother particle is constructed out of the charged and reconstructed neutral daughter particles and the mass spectrum is obtained, by which the particle can be identified.

Investigation of the Σ decays has shown that a large fraction of the background comes from misinterpretation of the tracks, which were reconstructed in two parts (clones). The problem is illustrated in Fig. 1 at an example of π^0 reconstruction from the $\Sigma^+ \to p\pi^0$ decay. Since the reconstructed momentum of both parts is the same, the resulting values of rapidity and momentum for π^0-candidate are close to zero and are nicely separated from the signal

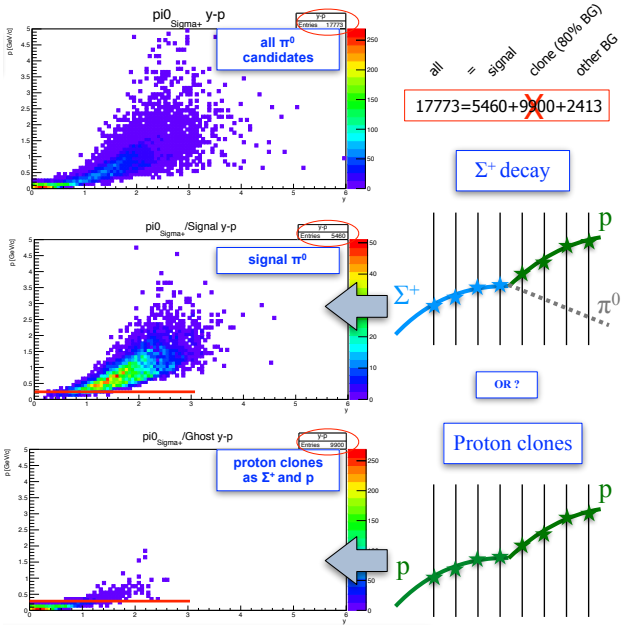

Figure 1: Momentum-rapidity distribution of reconstructed π^0 candidate in $\Sigma^+ \to p\pi^0$ decay.

region. Thus, such fake candidates can be strongly suppressed by cutting on the low momentum of the neutral candidate.

The topology of decays alows to require the decay point to be positioned after the last hit of a mother track and before the first hit of a daughter track. A cut on z-position of the reconstructed decay point reduces a significant part of the combinatorial background.

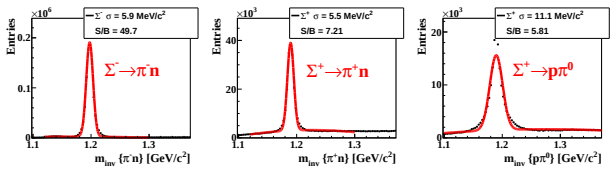

Figure 2: Mass distributions of reconstructed $\Sigma^- \to n\pi^-$, $\Sigma^+ \to n\pi^+$ and $\Sigma^+ \to p\pi^0$.

These cuts have been added to the KF Particle Finder package. Corresponding mass distributions of Σ decays with TOF PID are shown in Fig. 2. As a result of the study the signal to background ratios have been significantly improved, keeping the efficiencies at the same level.

* Work supported by BMBF, HICforFAIR and HGS-HIRe for FAIR.

† P.Kisel@gsi.de

Development of a CO_2 - based cooling demonstrator for the CBM STS

K. Agarwal, E. Lavrik, and H. R. Schmidt
Universität Tübingen, Tübingen, Germany

As the core detector of the CBM experiment, the Silicon Tracking System (STS) located in the dipole magnet provides track reconstruction and momentum determination of charged particles from beam-target interactions. Due to the expected irradiation damage, the sensors will dissipate some power and have to be kept at or below -5°C by complete removal of the heat dissipated by the front-end electronics (FEE) boards (total power load $\sim$ 40 kW). The heat must be removed to avoid thermal runaway and reverse annealing of the irradiated silicon sensors. Therefore, the STS will be operated in a thermal insulation box and will use bi-phase CO_2 cooling system for the FEE to maintain the desired environment for optimal detector operation at all times [1]. The effort presented in this report is aimed towards building a cooling demonstrator for two STS half-stations to show that the CBM-STS cooling concept is viable.

This work is an extension of the previous R&D conducted on bi-phase CO_2-cooling for CBM-STS aimed at FEE box design optimization where up to 200 W/FEE box heat was removed by keeping it at -15 °C for -40 °C coolant temperature [2]. Additionally, a 1 kW bi-phase CO_2 test cooling system, TRACI-XL [3] will be used for completing the demonstrator.

Thermal Interface Material (TIM) Studies

The CO_2 cooling system for the FEE primarily removes heat via conduction from FEE boxes mounted tightly on to the cooling plate. Since the mating surfaces are not absolutely flat and have micro-level imperfections, there is a presence of air-filled gaps with very low thermal conductivity (0.026 W/m·K at room temperature) acting as a thermal barrier. Hence temperature measurements are conducted by using different thermal-interface materials to replace all the space that otherwise would be occupied by air. Since heat transfer measurements are relative in nature, water will be used as the coolant for initial studies as it is easier to handle and has simpler experimental setup than CO_2 cooling. Later these results will be verified by using bi-phase CO_2.

Finite Element Method (FEM) Simulations

In order to understand the process, a series of FEM studies was performed using Solidworks Flow Simulations by keeping the component geometries as realistic as possible. The water inlet temperature was kept at 15 °C with a mass flow rate of 40 l/hr. Ceramic surface resistors are used as heat producing FEE components (2 W/resistor; 160 W/FEE box) glued on Aluminium Nitride (AlN180) plates attached to the FEE box fins. Table 1 describes all the TIMs that were used to fabricate the FEE boxes previously and the same are used for simulations for consistency. The annotations used are:

Interface 1: FEE Box - Cooling Plate
Interface 2: FEE Box Fin - AlN Plate
Interface 3: Resistor - AlN Plate
k: Thermal Conductivity of TIM
d: Thickness of TIM
RΘ: Distributed Thermal Resistance

Interface	TIM	k W/m·K	d μm	RΘ m^2·K/W
1 & 2	KP97	5.0	30	6.0×10^{-6}
	QGF-G03	16.0	125	7.8×10^{-6}
3	WLK 10	0.836	30	3.6×10^{-5}
	Arctic Silver	7.5	30	4.0×10^{-6}
	WLK DK 10	1.0	30	3.0×10^{-5}

Table 1: TIM Properties used for FEM Simulations.

Please note that the layer thickness of glue and grease is variable in reality, but it is taken as 30 μm for simulation purpose only which is consistent with the results presented in [2]. Additionally, since the specific heat capacity of none of the Interface 3 materials is available, it has been taken as 1000 J/kg·K which is of the same order as rest of the TIMs. Also note that QGF-G03 exhibits biaxial thermal conductivity with in-plane k = 470W/m·K and its effect is a subject of further simulations.

Interface 1	Interface 2	Interface 3	Max. Setup Temp ^{0}C
KP97	KP97	WLK 10	52.74
		Arctic Silver	52.16
		WLK DK 10	52.56
	QGF-G03	WLK 10	51.99
		Arctic Silver	51.33
		WLK DK 10	51.86
QGF-G03	KP97	WLK 10	52.80
		Arctic Silver	52.16
		WLK DK 10	52.70
	QGF-G03	WLK 10	52.14
		Arctic Silver	51.52
		WLK DK 10	52.03

Table 2: FEM simulation results.

Table 2 presents the simulation results for different interface combinations already fabricated. It shows that KP97,

DOI:10.15120/GR-2017-1

QGF-G03 and Arctic Silver as Interface 1, 2 and 3 respectively cools the FEE box to the lowest temperatures. It is evident, however, that the differences between the various interface materials are relatively small.

Experimental Readout Development

The experimental setup shown in Fig. 1 is adopted from the setup in [2]. PT100 temperature sensors will be installed on the cooling plate, on the aluminum fins of the FEE box and on the heat producing resistors to monitor the heat transfer, hence indicating the setup performance. Since the temperature sensors give an absolute value at a particular location rather than giving a temperature gradient, an overhead IR Camera has been installed to obtain a complete picture, thus verifying the results from the sensors. Since it is difficult to remove all the reflections in the camera's field of view, differential measurements of two images at different setup conditions is a proposed solution to analyze temperature change across the whole setup.

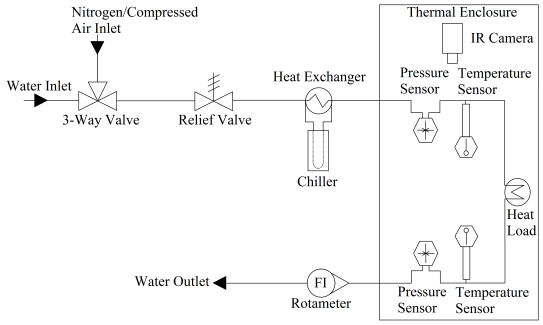

Figure 1: Experimental setup for TIM studies.

STS Thermal Insulation Box Development

The requirements for the STS thermal enclosure are:

- Large volume of ∼4m ^{3} with highly thermal insulating walls (maximum thickness 20 mm).
- Mechanically stable to hold the STS weight (maximum allowed deformation of 100 μm for ∼2 t).
- Electrical and light shielding.
- Feedthroughs for cables and pipes such that the vapor barrier is maintained (∼0.5% RH at room temperature to avoid condensation).
- Easy to assemble and disassemble for detector maintainence tasks.

As the first step, a smaller insulation box (0.75 × 0.50 × 1.50 m^3) will be fabricated from *Carbon Faserverstärkter Kunststoff* (CFK) sandwiches. Rohacell-51 (Polymethacrylimide) has been chosen as the foam because of its superior mechanical properties (compressive strength = 0.9 N/mm^2) and low thermal conductivity (0.036 W/m.K). Given the space constraints, calculations for thickness optimization were done keeping in mind that the outer wall temperature must be higher than the dew point of the surrounding environment. The following calculations have been done by taking [4] as a reference.

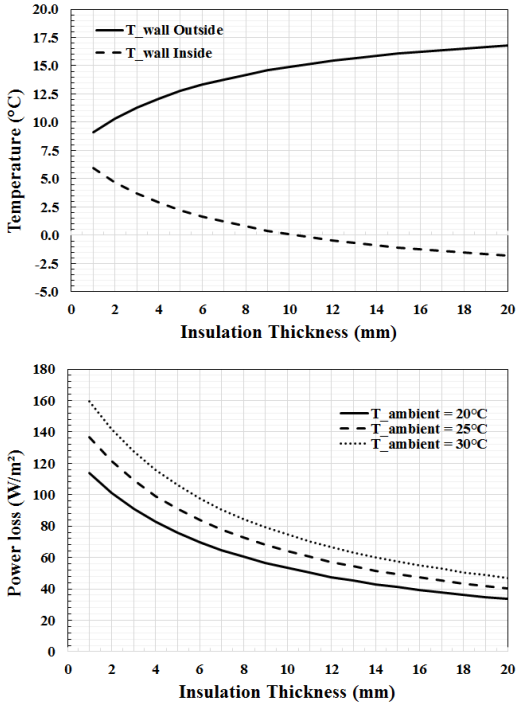

Figure 2: Insulation thickness optimisation

For the upper panel in Fig. 2, T$_{ambient}$ = 20 °C and RH = 50% which corresponds to T$_{dewpoint}$ = 9.27 °C. So 16 mm insulation thickness is safe as the temperature of outside wall is 16 °C which is fairly above the dew point.

The lower panel in Fig. 2 tells the additional power that has to be removed because of heat transfer from the outside environment to the box. The temperature inside the box has been taken as -5 °C and the power transferred per unit area has been studied for different ambient temperatures. At 16 mm insulation thickness, 40 W/m^2 of power has to be removed for T$_{ambient}$ = 20 °C, which increases to 47 W/m^2 for T$_{ambient}$ = 25 °C and 55 W/m^2 for T$_{ambient}$ = 30 °C. So the ambient temperature should also be considered with the heat dissipated from the sensors and FEE for determining the cooling efficiency of the setup.

Eventually 16 mm Rohacell-51 sheets are sandwiched from all sides with CFK of 2 mm thickness for adding mechanical strength.

References

[1] J. Heuser *et al.*, Technical Design Report for the CBM Silicon Tracking System, GSI Report 2013-4

[2] E. Lavrik *et al.*, CBM Progress Report, 2014 (2015) 52

[3] J. Sanchez *et al.*, CBM Progress Report, 2012 (2013) 21

[4] F. Lehner *et al.*, LHCb Silicon Tracker 2002-066

Pre-series production of ultra-light microcables for STS detector modules at LTU Ltd

V. M. Borshchov[1], C. J. Schmidt[2], Yu. A. Murin[3], M. A. Protsenko[1], I. T. Tymchuk[1], R. A. Kushniruk[1], M. S. Tykhomirova[1], C. Simons[2], K. M. Liholitova[1], L. V. Klimova[1], and J. M. Heuser[2]

[1]LED Technologies of Ukraine (LTU) Ltd, Kharkov, Ukraine; [2]GSI, Darmstadt, Germany; [3]JINR, Dubna, Russia

More than 1000 microcables for CBM-STS detector modules and demonstrators have been developed, manufactured and delivered to date. They are being used for verification of the work flow and tooling for STS detector module assembly and for investigations of possible read-out schemes at GSI and JINR. The work was carried out partly within the STCU project P635 by the partners GSI and LTU, partly within the contracts between LTU and GSI and also JINR.

Ultra-light microcables for STS detector modules

Ultra-light micro-cables are a key component for the CBM-STS. They are employed to realize the analog signal interconnection between silicon sensors and readout electronics, providing minimized material budget. Few different microcable types are foreseen to be used for STS detector modules [1]. They are composed of a stack of analog signal cables, meshed spacers and shield layers. The required total amount of microcables and meshed spacers for the STS is more than 75 thousands. Basically, the ultra-light analog cables are realized using aluminium-polyimide adhesiveless dielectric with 14 μm thick aluminum, and include 64 signal lines. The length of the cables ranges from about 100 mm up to about 500 mm. Within the performed works we have developed, manufactured and delivered pre-series batches of microcables for two purposes:

- pre-series microcables – for verification of work flows and tooling for STS detector module and ladder assembly;
- test microcables – for investigations of possible read-out schemes.

Pre-series microcables

Taking into account the different designs of the detector modules, the different lengths of the microcables involved, and further complications due to ladder assembly we have developed, manufactured and delivered 27 batches of microcables (about 900 pcs) for the verification of work flows and tooling used during STS detector module and ladder assembly. Batches of microcables were realized in the whole range of cable lengths from 100 mm up to 500 mm. A photo of a typical analog microcable is depicted in Fig. 1.

Also a new type of microcable has been developed, manufactured and delivered in several batches. It is intended

Figure 1: Analog connecting cable with meshed spacer.

for shielding of STS-XYTER ASICs which are covered by analog microcables.

The delivered cables allow to gain practical experience with module and ladder assembly and to apply further modifications to their design if required. The manufactured and delivered microcables allow to identify the production yield and define ways for increasing the yield at forthcoming pre-production and production stages. This includes studies of the reproducibility of the lithographic process, also involving new high-resolution masks, from where specifications towards the final production could be deduced.

Test microcables

For investigations of different possible read-out schemes (Fig. 2) we have developed, manufactured and delivered batches of microcables for demonstrators, as well as several assembled demonstrators with different length of cables and different types of microstrip sensors. The total amount of delivered and tested microcables, like the one shown in Fig. 3, is about 100 pcs.

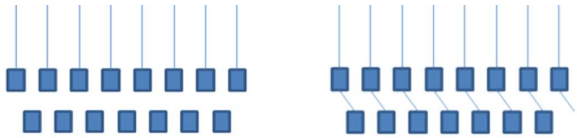

Figure 2: Read-out schemes: Every second strip (left) and two neighboring strips in parallel (right).

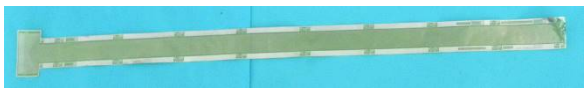

Figure 3: Test microcable for investigations of different readout schemes.

References

[1] V. M. Borshchov et al., CBM Progress Report 2015, p. 36

DOI:10.15120/GR-2017-1

Misalignment effects on track reconstruction for CBM-STS

S. Das and H. R. Schmidt
Universität Tübingen, Tübingen, Germany

The alignment uncertainties of the CBM-STS detector, made from silicon strip sensors with excellent position resolution, affect the performance of the track reconstruction. The basic sources of these uncertainties are the limited mechanical mounting precision ($\sim$ 100 μm) during the assembly of the detector, deformations of the detector elements due to temperature effects, and (or) influence of the magnetic field; so, during the experiment, we cannot rely on the mechanical mounting or the detector geometry alone to yield the required spatial resolution of the STS. Therefore, our approach is to use track based alignment methods (relying on tracks only) to determine the exact positions of the silicon sensors ($\sim$ 10 μm). In this report, we will address the effects of misalignment on the track reconstruction along with the discussion of the possibility to recover the alignment.

Misalignment Scenarios

For this report three misalignment scenarios have been introduced in the STS geometry on hierarchial basis (i.e., to the sensors, ladders, and then to the stations). A Virtual technique has been used for misalignment, i.e., according to the misalignment scenarios, the transformations have been applied on the STS hits at the time of track reconstruction without modifying the ideal geometry (Scenario_0). We have used the STS geometry (version 15b) to apply the misalignment scenarios. But in future the same implementation can be done easily on the updated geometry. The applied misalignment scenarios are detailed in the following table.

Element	Sensor	Ladder	Station
X	10 μm	50 μm	200 μm
Y	10 μm	50 μm	200 μm
α	50 μrad	250 μrad	1000 μrad
β	50 μrad	250 μrad	1000 μrad
γ	50 μrad	250 μrad	1000 μrad

Table 1: Summary of applied misalignment.

All the data (standard deviation to the distribution) have been diced using Gaussian distribution to make the transformations random. All the transformations (translations and rotations) have been applied to the detector elements as per the above data table.

- On the first scenario (Scenario_1), transformed data have been applied at the local sensor level to the ideal geometry (Scenario_0).
- On the second scenario (Scenario_2), in addition to the sensor level modifications, transformed data have been applied to the local ladder level.
- On the third scenario (Scenario_3), in addition to the last two scenarios, transformed data have been applied to the local station level.
- Important assumption: The Z-value has been kept constant throughout, as the projection has always been taken to the X-Y plane.

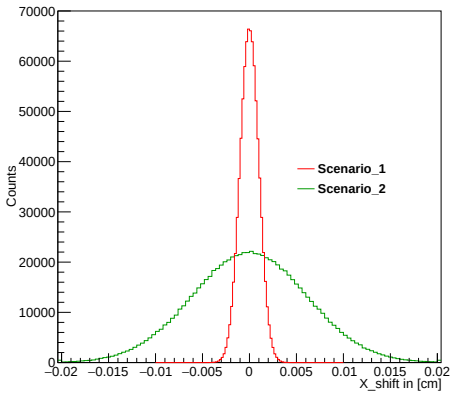

Figure 1: Resulting misalignment shifts on STS hits in X direction (example) for Scenario_1 and Scenario_2.

Effect of misalignment on track reconstruction

The investigation of the effect of the misalignment of the STS on primary track properties is performed using 200 UqQMD events under SIS100 energy. The track reconstruction is performed in several steps: Track seeding from the STS hits, trajectory building using combinatorial Cellular Automaton, track fitting and smoothing using Kalman Filter. The error on the hit position in the track fit is obtained by combining the spatial resolution of the detector with the applied misalignment uncertainty. The effect of the STS misalignment results in deterioration of the momentum resolution (Fig. 2).

Standard rules for matching a reconstructed track with the MC track have been performed. The effect of misalignment can also be seen for the primary track efficiency (quality of matching reconstructed tracks with MC tracks) plotted against momentum (Fig. 3).

DOI:10.15120/GR-2017-1

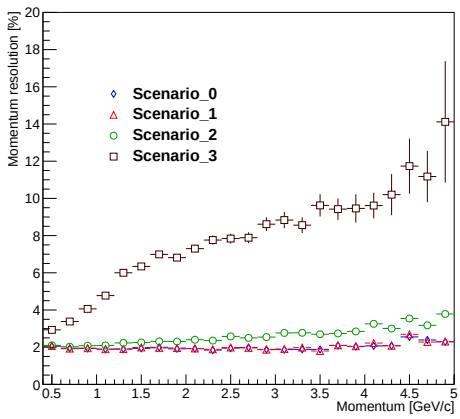

Figure 2: Momentum resolution for UrQMD events.

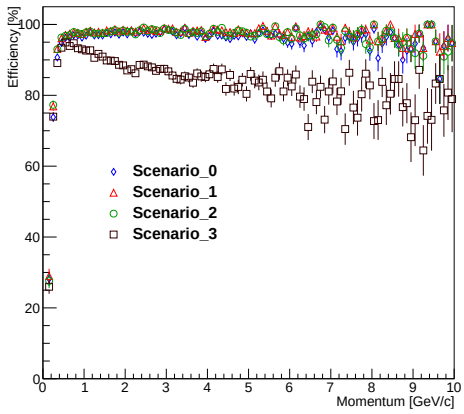

Figure 3: Primary track efficiency for UrQMD events.

Comparisions of track fit quality in terms of χ^2/NDF have also been plotted for ideal and misaligned cases for UrQMD events (Fig. 4). A clear deterioration of track fit quality can be seen with higher level misalignment.

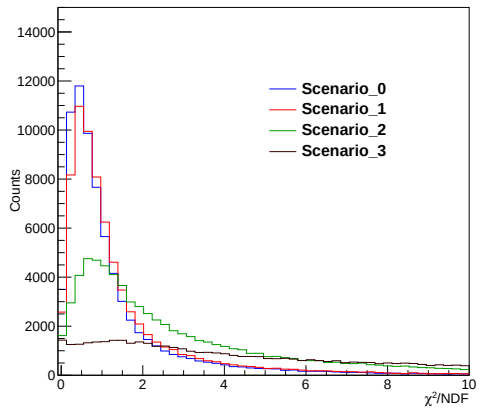

Figure 4: Track fit quality for UrQMD events.

Effect of misalignment on invariant mass

Figure 5 depicts the impact of misalignment on reconstructed invariant mass of the particle, based on decay topology (from the reconstructed secondary vertex).

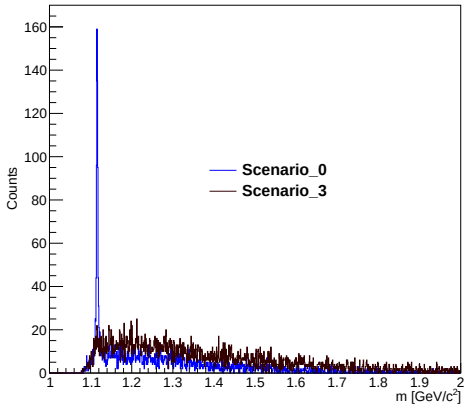

Figure 5: Invarint mass of Lambda (example) reconstructed from for UrQMD events.

Conclusion

This study has been the first attempt to misalign the STS components in order to check the effects on tracking and the physics observables. The obtained results are clearly indicating the direct influence on track and vertex reconstruction and emphasize the necessity of precise alignment of STS detector to achieve high spatial resolution. As a next step, the MILLEPEDE software package will be used to recover the alignment from the applied misalignment scenarios by computation. This will allow us to determine the limits of the required mechanical precision, during the assembly, as well as the overall precision required of the whole mechanical setup, to apply MILLEPEDE successfully [1, 2, 3, 4, 5].

References

[1] V. Blobel and C. Kleinwort, A New Method for the High-Precision Alignment of Track Detectors (2002), arXiv:hep-ex/0208021

[2] V. Blobel, Millepede II. Institut für Experimentalpyhsik, Universität Hamburg (2007), http://www.desy.de/ blobel/mptalks.html

[3] R. Frühwirth, Nucl. Instr. and Meth. A 262 (1987) 444

[4] Impact of CMS silicon tracker misalignment on track and vertex reconstruction, Nucl. Instr. and Meth. A 566 (2006) 45–49

[5] http://aliceinfo.cern.ch/Offline/Activities/Alignment.html

DOI:10.15120/GR-2017-1

Construction of a neutron source for radiation hardness tests of silicon strip detectors

E. Friske and H. R. Schmidt
Universität Tübingen, Tübingen, Germany

Radiation tolerance requirements

The microstrip detectors to be used in the Silicon Tracking System (STS) of CBM are expected to experience a non-ionizing radiation dose of up to 10^{14} n_{eq}/cm^2 [1] over the projected lifetime of $\approx$ 6 years, mainly causing lattice defects in the detector material. The detectors are read out as self triggering sensors, which sets high demands on their performance, particularly on the charge collection efficiency. Since this figure of merit will decrease over the course of the irradiation, subsequent properties like the signal-to-noise ratio will also be affected. To anticipate these changes and to give a realistic lifetime estimation of the sensors several irratiation campaigns have been, and are being, performed [2].

Long term irradiation

Non-ionizing radiation damage is caused by high energy particles expelling atoms from their lattice spaces, creating both lattice vacancies and interstitial atoms, which act as additional dopants and scattering centers, thus changing the electrical properties of the bulk material. Since neutrons are not charged and interact mostly with the nucleus by collisions they are a prime tool to study this phenomenon separately.
In addition to the actual damage, there are both annealing and reverse annealing effects present. These contribute on a timescale of days and depend on temperature, so an ideal simulation should recreate these conditions as closely as possible and reasonable.

Neutron source

As described in the preceding Progress Report [3], a Van-de-Graaf ion accelarator is used to generate a deuteron beam which is targeted at a deuterium gas cell. The neutrons generated from this deuterion fusion are used to irradiate the sensor material as sketched out in Fig. 1. The cell itself is shown in Fig. 2.

Since the accelerator used is limited in beam energy (2.4 MeV deuteron energy is the maximum we have been able to achieve) and beam current (a few μA), the setup needs to be as efficiently as possible in creating neutrons and irradiating the sensors. As the deuterium fusion cross section peaks at around 2 MeV and drops sharply toward lower energies, energy losses passing the gas cell entrance foil have to be minimized while maintaining a high gas density within the cell.

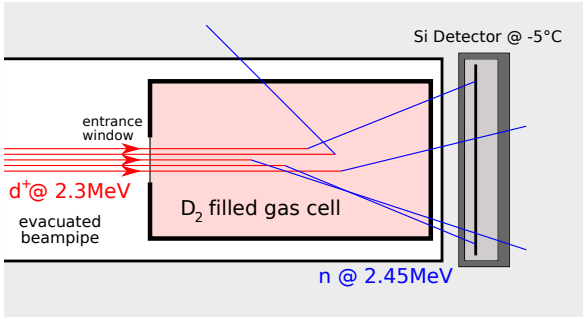

Figure 1: Schematic view of the cryogenic source.

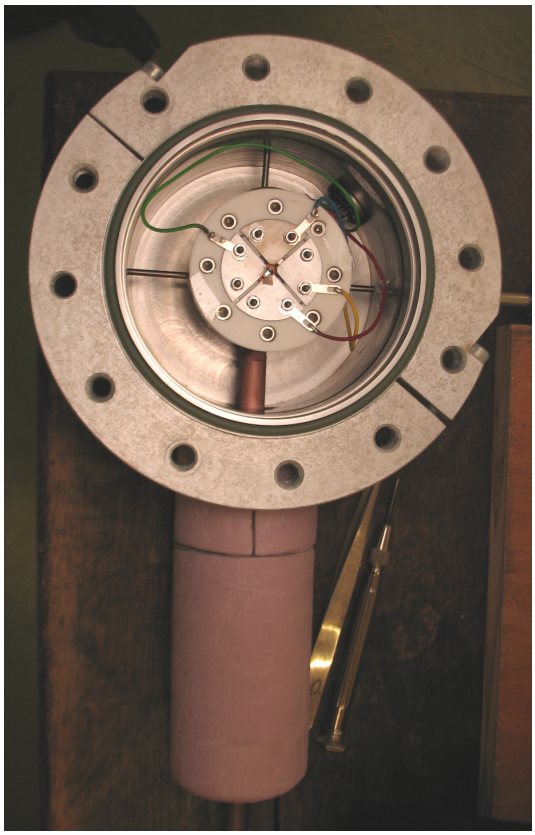

Figure 2: Photo of the manufactured cell with beam monitoring metal plates arranged around the titanium window.

Therefore, the entrance window has to be mechanically durable at a thickness of less than 5 μm, and consist of light elements to minimize scattering of the incident deuteron beam. Several materials were considered, including Havar®, aluminum, titanium and mica. TRIM simula-

DOI:10.15120/GR-2017-1

tions of the energy losses (Fig. 3) show that Havar, consisting mostly of heavier elements, has the strongest restrictions regarding material thickness, and has turned out to be unusable as a result. Aluminum alloy cannot be reasonably manufactured to the desired dimensions, and pure aluminum cannot withstand the 2-3 bars of pressure difference required. Tests with Mica were abandoned as it is a rather brittle material and very difficult to work with. In the end, a titanium foil with a thickness of 2.5 μm was successfully tested against a 3 μm beam while maintaining a pressure difference of 4 bar. Figure 2 shows the cell after a beamtime; one can see the burn traces from a badly aligned beam on the lower metal plate. The simulated average energy loss of this window for a 2.4 MeV beam is 0.14 MeV.

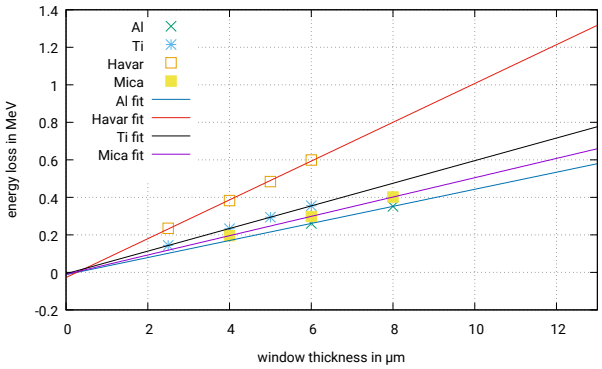

Figure 3: TRIM simulations showing the average energy losses of a 2.4 MeV deuteron beam.

Detector holder

To closely match the environment with the later in the experiment, in particular the operating temperature of -5 °C, a steel enclosure has been manufactured to house the sensor itself, the Alibava readout board and the trigger system. Although the Alibava system also provides self-triggering readout boards, an external trigger consisting of a plastic scintillator and a small photomultiplier tube has been chosen as the more reliable solution. Figure 4 shows the arrangement; the frame housing the actual sensor has been removed to allow a view onto the internal components.

Since the neutrons themselves do not generate signal in the silicon detector, a collimated beta source is currently being commissioned to provide both the signal in the detector and a trigger signal in the scintillator.

Next steps

The readout chains for the sensors, environment and enutron flux monitoring have to be established, tested and calibrated before the actual sensor irradiation can commence.

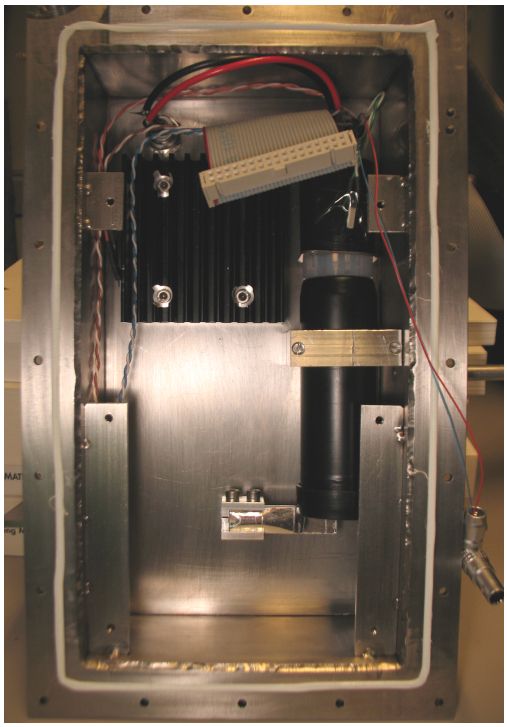

Figure 4: Photo of the sensor box with cooling fins, electrical feedthroughs and the photo multiplier tube with attached scintillator encased in reflective foil.

References

[1] I. Sorokin, Characterization of silicon microstrip sensors, front-end electronics, and prototype tracking detectors for the CBM experiment at FAIR, PhD thesis, Univ. Frankfurt, April 2014

[2] J. Heuser et al., Performance of neutron irradiated prototype sensors for the CBM Silicon Tracking System, CBM Progress Report 2013, p. 25

[3] E. Friske and H. R. Schmidt, A scalable neutron source for STS detector radiation hardness tests, CBM Progress Report 2015, p. 25

[4] W. von Witsch and J. G. Willaschek, High-pressure gas target for the production of intense fast-neutron beams, Nuclear Instruments and Methods Vol. 138 (1976) p. 13-17

DOI:10.15120/GR-2017-1

Optical quality assurance procedures for the STS detector

E. Lavrik[1], *I. Panasenko*[1,2], *and H. R. Schmidt*[1]
[1]Universität Tübingen, Tübingen, Germany; [2]KINR, Kiev, Ukraine

The CBM Silicon Tracking System (STS) is a compact detector built from about 900 double sided silicon microstrip sensors. The sensors will be delivered in 4 different form factors [1]. Current prototypes are from Hamamatsu, Japan, and CiS, Germany. In order to assure the quality of these sensors, highly efficient and automated optical quality assurance methods and procedures should be developed. For this purpose a metrology and quality assurance test station has been built at the University of Tübingen, which allows to measure various QA parameters for the sensors such as surface conditions (scratches, durst grains, photoresist residues, etc.) and geometry (wafer thickness and warp, edge (non-)parallelity and profile etc.) [2]. Having the sensor quality assured at a very early stage allows tp reject the faulty sensors as well as providing input data for further control stages such as electrical control.

The test station consists of an XY-inspection table with a replaceable vacuum chuck mount. Currently a custom-built three-zone chuck for sensor and a porous aluminum chuck for cable inspection are used. On the Z-stage a microscope camera and an optical assembly with motorized zoom and focus are mounted. The XY-stage allows to inspect sensors up to a size of 12.4 $\times$ 6.2 cm^2. A highly customizable software solution, which allows the adaptation to other hardware as well as other inspection objects like sensor micro-cables and detector modules, has been developed as a part of the project.

Sensor warp inspection

The methods for a non-destructable contactless way of sensor warp measurements based on focus adjustment developed in [3] were further improved and optimized. The accuracy of the method has been characterized by a calibration against a certified gauge block set from Mitutoyo Corp. (Fig. 1). The extracted height measurement accuracy is estimated to be 1 μm. Especially important was, given the fact of the upcoming mass inspection of sensors arriving from vendors, to reduce the measurement times without negatively impacting the measurement precision. With the development of new methods we were able to reduce the measurement times by a factor of up to 30.

Figure 2 shows the warp of both sides of a prototype CBM06C6 sensor. The warp of all available (25) prototype sensors has been measured; it ranges from 6 to 78 μm.

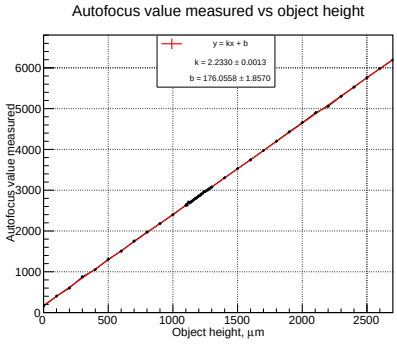

Figure 1: Fitted calibration curve for the height measurements.

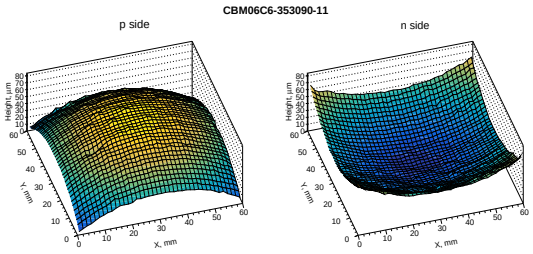

Figure 2: Warp of a prototype CBM06C6 sensor.

Edge parallelity inspection

The sensor's cutting edge profile inspections presented previously have been improved and extended with edge parallelity inspection. In this type of analysis, the distances between the sensor's features and the cutting edges are measured. The alignment marks being the outermost features on the sensor's surface are taken as reference. Figure 3 shows the measurement principle. First the center of the alignment mark (denoted with a red square on the figure) is located with pattern matching algorithms, then it is perpendicularly projected to both fitted edges of the sensor and the distances are measured. By comparing the distances measured at one corner with others, one extracts the information of the sensor's edge parallelity.

The distribution of the values extracted for the available sensors' edge parallelity is shown in the Fig. 4. The precision of the method is estimated to be better than 1 μm. This measurement shows that the sensor edge could be used for the sensor alignment during assembly yielding a precision better than 10 μm.

DOI:10.15120/GR-2017-1

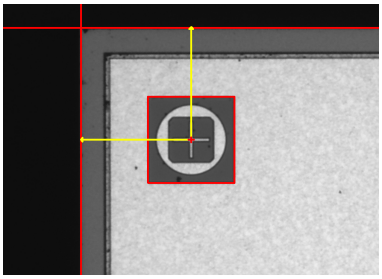

Figure 3: Detection principle for edge parallelity analysis.

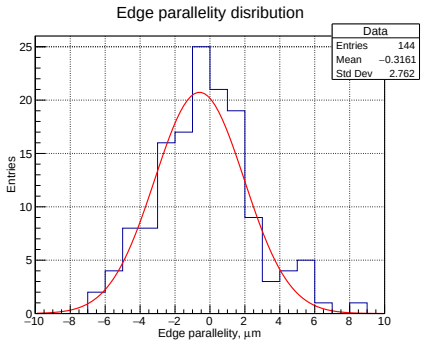

Figure 4: Edge parallelity distribution from the prototype sensors.

Micro-cable inspection

Figure 5 shows the schematics of the micro-cable stack as a part of the module, in which individual signal micro-cables are separated by meshed spacers and enclosed within an aluminum shield and polyimide coat. The optical inspection of micro-cables is only possible before their assembly into a stack, thus it should be best done at the production site.

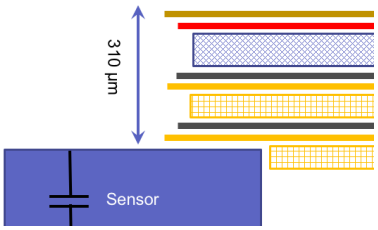

Figure 5: A schematic view of a micro-cable stack with signal cables in dark gray color.

We already reported on the micro-cable inspection R&D in [3]. These automated QA methods and procedures were developed for a certain type of illumination - ring light source. Since then, the setup was upgraded to use a direct light source, which has changed the approach to the cable inspection - aluminum traces reflect much more direct light, which "blinds" the camera. For this reason an alternative approach has been developed to perform two pass measurements with higher and lower camera sensors light exposure values. The first pass allows to detect the "silhouette"-type defects such as trace breaks, cut-offs, thinnings and lift-offs. The second pass allows to look at the aluminum surface defects such as foreign objects etc. This method change required the adaptation of the detection procedures and software algorithms.

Figure 6 shows the same region of interest under different exposure settings of the camera. What appears to be a trace break at low exposure (left panel) is identified as a dust grain at high exposure (right panel).

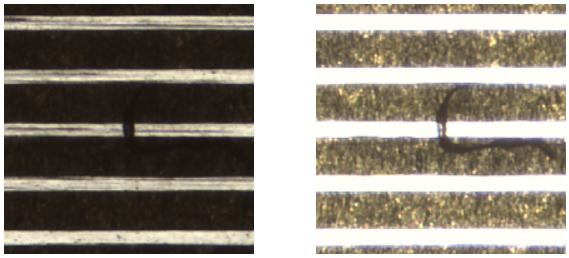

Figure 6: Images of the same region of interest taken with different exposure values allow to detect the defect.

A batch of 10 prototype micro-cables provided to GSI from LTU for tab-bonding tests were inspected. The defects listed in Table 1 had been successfully detected together with a small number of others (possibly introduced by handling or misidentification) in a fully automated scan mode.

Eventual reintroduction of the ring light source and replacement of the vacuum chuck with a back-lit pair of transparent glass sheets to clamp the cables between should further improve the performance of the inspection.

Cable number	Defects on the cable
40-2	1 break, 2 traces cut-off, 2 thinned traces
186-2	2 breaks, 2 traces cut-off, 1 thinned trace
163-3	1 break, 2 traces cut-off, 1 trace lift-off
181-1	Hole in Pi, deformation in the bond area
116-3	2 breaks, 1 trace cut-off, 1 trace lift-off
176-2	1 trace cut-off, 2 thinned traces
192-2	2 trace cut-off
194-2	1 thinned trace, deformation in bond area
168-1	5 traces cut-off
169-2	1 break, 3 traces lift-off

Table 1: Cable defects information from manual inspection enclosed in the package.

References

[1] Technical Design Report for the CBM Silicon Tracking System, GSI Report 2013-4, p. 23

[2] E. Lavrik et al., CBM Progress Report 2014, p.30

[3] E. Lavrik et al., CBM Progress Report 2015, p.23

DOI:10.15120/GR-2017-1

Microcable quality assurance: capacitance measurements

I. Panasenko[1,2], *H. R. Schmidt*[1], *E. Lavrik*[1], *C. Simons*[3], *and C. J. Schmidt*[3]
[1]Universität Tübingen, Tübingen, Germany; [2]KINR, Kiev, Ukraine; [3]GSI, Darmstadt, Germany

Ultra-light micro-cables are the key component for the CBM Silicon Tracking System. However, in addition to the total strip capacitance, microcables also contribute to the load capacitance seen by the FEE. Therefore it is important to know the total parasitic capacitance of the single trace (C_{tot}). For the module assembly a micro-cable stack which consists of 4 signal and 2 shield layers will be used. A schematic view of such a stack is depicted in Fig. 1. Here we report on the measurements of C_{tot} for an aluminum microcable stack # 2-11 (N-Top layer is 28.1 cm long, P-Top layer is 27.1 cm long) manufactured by LTU Ltd (Kharkov, Ukraine) [1].

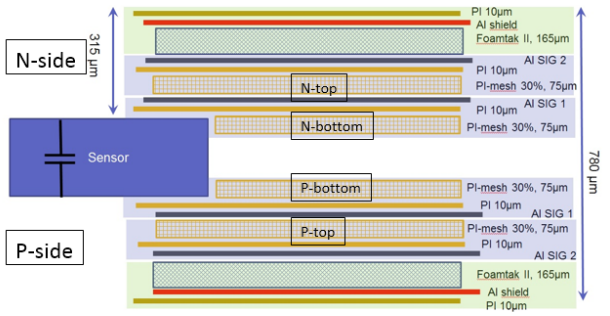

Figure 1: Schematic side view of the micro-cable stack for one CBM module.

Measurements were carried out on a custom, fully automated probe station developed at University Tübingen [2]. A 3-needle configuration was used to measure the capacitance of a single trace to two neighbors and a small extra fraction. The network simulator SPICE [3] was used to estimate the contribution of all other traces to the measured value in a 3-needle configuration and thus to derive C_{tot} of a single trace, and also to extract other capacitances (like trace-to-trace) which are impossible to measure directly. Because the microcable stack can be considered as an array of capacitors , without resistors, the measured capacitance does not depend on the frequency of the applied test signal.

Fig. 2 shows the results of measurements for all 64 traces of one layer of the microcable stack. Such measurements were performed for all 4 layers. Then the total trace capacitance was derived and the results are plotted in Fig. 3.
The capacitance measurements are summarized as follows:

$$C_{tot} = 0.382 \pm 0.020 \text{ pF/cm},$$
$$C_{TT} = 0.094 \pm 0.008 \text{ pF/cm},$$
$$C_{LL} = 0.083 \pm 0.010 \text{ pF/cm},$$
$$C_{TS} = 0.090 \pm 0.009 \text{ pF/cm},$$

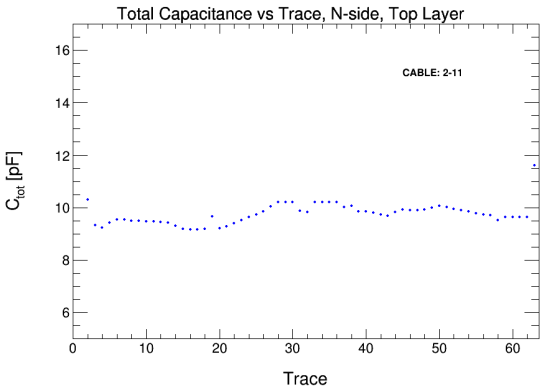

Figure 2: Measurements of C_{tot} for every trace of the 28,1 cm long microcable.

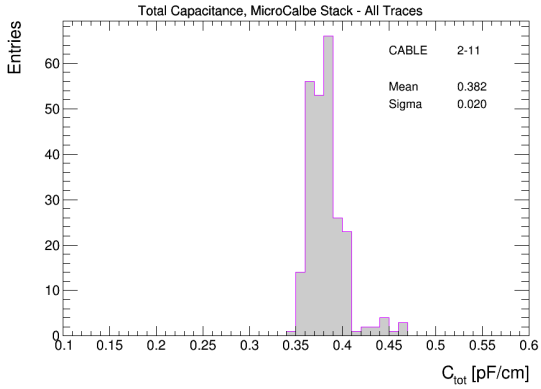

Figure 3: Measured total trace capacitance of the microcable stack.

where C_{TT} is the capacitance between two adjacent traces of a single layer, C_{LL} – the capacitance between two nearest traces of adjacent layers, C_{TS} – the capacitance between single trace and shield layer.

References

[1] V. M. Borshchov et al., Pre-series production of microcables for STS detector modules at LTU Ltd, CBM Progress Report 2015 (2015) 36

[2] I. Panasenko et al., Equipment and procedures for electrical quality assurance of CBM-STS silicon microstrip sensors, CBM Progress Report 2015 (2015) 25

[3] http://www.linear.com/designtools/software/#LTspice

DOI:10.15120/GR-2017-1

Sensor quality assurance: capacitance measurements

I. Panasenko[1,2], *H. R. Schmidt*[1], *E. Lavrik*[1], *and J. M. Heuser*[3]
[1]Universität Tübingen, Tübingen, Germany; [2]KINR, Kiev, Ukraine; [3]GSI, Darmstadt, Germany

We already reported [1] on the development of a custom-built automatic probe station for the microstrip sensors quality assurance (QA) of the CBM experiment. It was used to perform in-depth measurements of the capacitances which are important for the operation of double-sided microstrip sensors. Sensors of the CBM06 type from CiS [2] and Hamamatsu [3] were under investigation.

Experimental set-up

We have measured interstrip, coupling and backplane capacitances as a function of strip number, frequency and bias voltage using the experimental set-up and techniques described in [4]. In total 7 sensors were tested and 9 more sensors are currrently being measured.

Results

Backplane capacitance

The capacitance between a single implant strip and the backplane of the sensor can be obtained from CV measurements. Also, this measurement was used to determine full depletion voltage (V_{FD}). The results are summarized in the table below where H and C in the sensor type correspond to Hamamatsu and CiS, respectively.

Sensor ID	Type	V_{FD}, V	C_b, pF/cm
10938-1609-5	H04DM	70.2	0.18
10938-2695-2	H06SM	67.0	0.17
10938-4440-58	H06DM	74.3	0.18
10938-4440-60	H06DM	67.4	0.18
331827-3	C06SM	78.1	0.21
350714-06-1	C02DM	70.2	0.22
351139-23	C04DM	70.2	0.21

Coupling capacitance

The coupling capacitance C_c is the capacitance between the strip implant and the read-out aluminum strip. Measurements have shown that coupling capacitance has a strong frequency dependence. It can be explained considering the sensor as an extended network of capacitors and resistors [5, 6]. The network simulator SPICE [7] was used to reproduce and understand frequency dependence of the measured capacitance and to extract frequency independent values. The experimental and simulated results are plotted in Fig. 1.

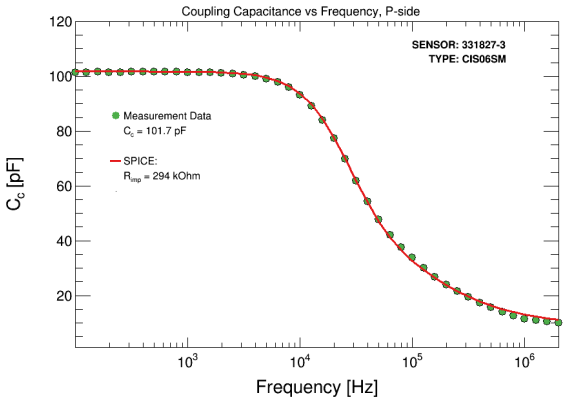

Figure 1: Coupling capacitance for p-side strips of a CiS 6x6 cm^2 sensor as function of frequency (measurements and SPICE simulation).

The strip implant resistance was also extracted from the simulation and is 92 kOhm/cm and 49 kOhm/cm for Hamamatsu and CiS sensors, respectively. A bias voltage scan of the coupling capacitance showed that it is practically independent of the biasing conditions for p-side strips and saturates after full depletion for n-side strips. The coupling capacitance was measured for all 1024 strips on each side of every sensor (14336 strips in total) and the experimental results are summarized in Fig. 2.

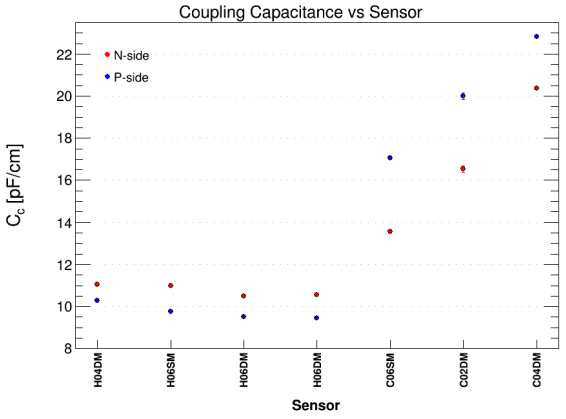

Figure 2: Experimental values of the coupling capacitance for all tested sensors.

DOI:10.15120/GR-2017-1

Interstrip capacitance

The interstrip capacitance C_{is} is the main contribution to the input capacitance of the FEE, therefore it determines the noise performance of the FEE. Figure 3 shows the experimental and simulated results for frequency dependence of the interstrip capacitance (between two adjacent strips including metal and implant contributions, the other strips are grounded).

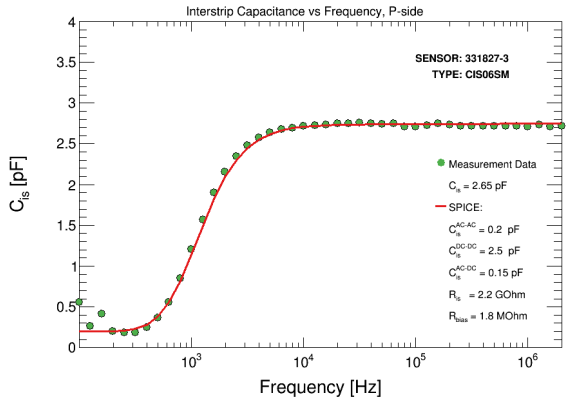

Figure 3: Interstrip capacitance for p-side strips of a CiS 6x6 cm^2 sensor as function of frequency (measurements and SPICE simulation).

The bias voltage scan of the interstrip capacitance showed that C_{is} becomes constant beyond full depletion for all tested sensors but an overdepletion of +40 V is suggested.

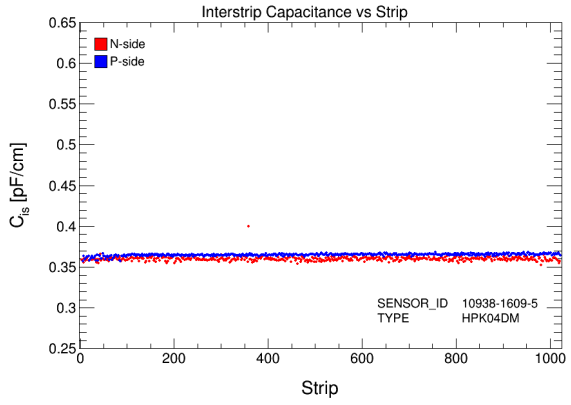

Figure 4: Automated strip scan: the interstrip capacitance for p- and n-sides of a Hamamatsu 6x4 cm^2 sensor.

An example of the interstrip capacitance measurements across the entire sensor is given in Fig. 4. The measured C_{is} for the tested Hamamatsu sensors is uniform over all strips, for CiS sensors small deviations were observed [6]. The average value of C_{is} is 0.36 pF/cm for Hamamatsu sensors and it is slightly higher for CiS sensors: 0.43 pF/cm and 0.57 pF/cm for p- and n-sides, respectively.

Total strip capacitance

The total strip capacitance C_{tot} is defined as the sum of the capacitance of the strip to the backplane and the interstrip capacitance to adjacent strips [4]:

$$C_{tot} = C_b + 2C_{is} + C_{rs}, \quad (1)$$

where C_{rs} is a contribution to interstrip capacitance due to remaining strips. C_{rs} was estimated experimentally and is about 10% of C_{is}. The total strip capacitance is dominated by the interstrip capacitance and the backplane capacitance contributes only 15–25% to the total one. Figure 5 show the total strip capacitance of p- and n-side strips for all tested sensors. The avarage value of C_{tot} for Hamamatsu sensors is 1 pF/cm for both sensor sides. We observed a higher C_{tot} for CiS sensors especially from n-side in comparison with Hamamatsu sensors. For both vendors total strip capacitance is significantly smaller than coupling capacitance which insures a good charge collection:

$$C_c/C_{tot} > 10. \quad (2)$$

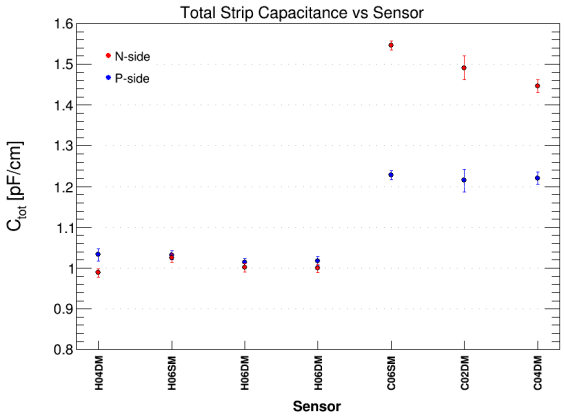

Figure 5: Total strip capacitance for all tested sensors.

References

[1] I. Panasenko et al., Equipment and procedures for electrical quality assurance of CBM-STS silicon microstrip sensors, CBM Progress Report 2015 (2015) 25

[2] http://www.cismst.org

[3] http://www.hamamatsu.com

[4] STS Note 2016-1, Specifications for Quality Assurance of Microstrip Sensors in the CBM Silicon Tracking System (2017) 22

[5] E. Barberis, Nucl. Instr. Meth. A342 90-95 (1994)

[6] I. Panasenko, Capacitance Measurements of Microstrip Sensors, Workshop on radiation induced surface effects in double-sided silicon microstrip sensors, Karlsruhe, 3 Nov. 2016

[7] http://www.linear.com/designtools/software/#LTspice

Ladder assembly concept and tool

U. Frankenfeld[1], *H. R. Schmidt*[2], *C. Simons*[1], *O. Vasylyev*[1], *and R. Visinka*[1]
[1]GSI, Darmstadt, Germany; [2]Universität Tübingen,Tübingen, Germany

Ladder assembly

The sensors of the Silicon Tracking System (STS) are mounted onto a carbon fibre structure (CF-ladder). Before the mounting, the sensors are assembled with read-out cables and the front-end electronic (module assembly [1, 2]). The task of the ladder assembly is to mount the modules with a sensor position precision better than 100 μm.

Concept and tool

The CF-ladder is mounted into a supporting fixture. In order to be able to reproduce the positioning the fixture has to be kept at a constant temperature in a controlled environment. In a first step the holding structure (L-leg [3]) is positioned with a tool (Fig. 1) and glued onto the CF-ladder.

The concept is based on positioning the sensor with a vacuum holder (Fig. 3). The position of the sensor is defined by the surface of the vacuum-holder and the two ledges (Fig. 2). This implies that corners of the sensors have to be cut precisely since the edges define the position of the sensor. The vacuum holder is positioned onto the jig with dowel pins.

A concept tool has been designed and produced to study the feasibility of the assembly procedure. The size of the tool has been chosen to mount two 6.2 $\times$ 6.2 cm^2 sensors on a CF-ladder. The surface of the sensor holder has been lapped to avoid scratches to the surface of the sensor. An alternative approach is the usages of a protecting layer (e.g. paper) between the sensor and the vacuum holder. The positioning tool for the L-legs is made from plastic in 3D-printing; for a final tool the precision can be enhanced.

Feasibility tests

Several gluing test of the L-legs have been performed to ensure the mechanical properties of the structure. The first ladder will be assembled with two non-functional sensors to measure the precision of the mounting. Finally a ladder with functional sensors will be assembled and tested to ensure that the handling and gluing of the sensors has no influence of the performance of the detector.

Further developments

Further developments will be the optimization of the shape of the L-leg to avoid glue spreading onto the edges of the sensor. After proving the concept of the ladder assembly a full-scale prototype tool will be designed and build to assemble a large ladder with ten modules. A transfer tools to take the ladder out of the mounting jig is under development. It will also be used to store the ladders before installing them into the STS. For the quality assurance and to measure the sensor positions after assembly an optical inspection system has to be established.

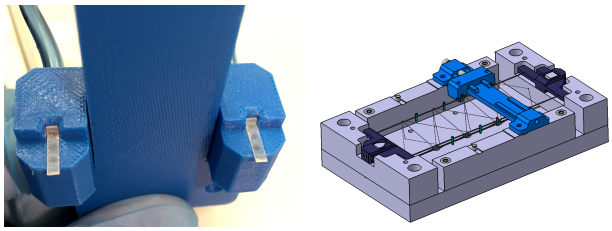

Figure 1: Positioning tool to holde two L-legs with vacuum (left). The mounting height of the L-leg is defined by the tool, in lateral direction they are moved onto the CF-ladder structure (right).

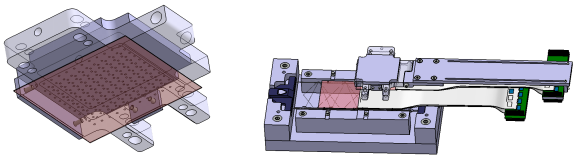

Figure 2: The vacuum tool to position the sensor; the position is defined by the ledges and dowel pins (left). A module is positioned onto the ladder (right).

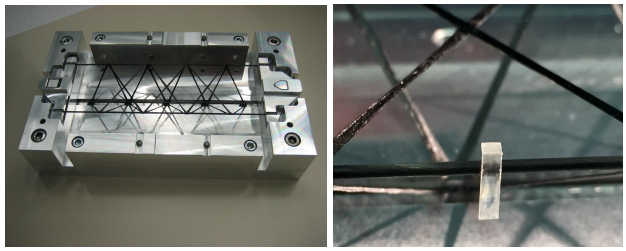

Figure 3: The CF-ladder is placed into the mounting fixture (left). One L-Leg is glued with the tool onto the CF-ladder (right).

References

[1] C. Simons et al., CBM Progress Report 2015, p. 38
[2] A. Sheremetev et al., CBM Progress Report 2015, p. 40
[3] A. Voronin et al., this report

DOI:10.15120/GR-2017-1

3D calculation for the CBM magnet quench protection system.

P. Kurilkin[1], P. Szwangruber[2], E. Floch[2], F. Toral[3], A. Bychkov[1], Yu. Gusakov[1], V. Ladygin[1], A. Malakhov[1], and A. Shabunov[1]

[1]LHEP-JINR, Dubna, Russian Federation; [2]GSI, Darmstadt, Germany; [3]CIEMAT, Madrid, Spain

CBM dipole magnet

The H-type superconducting magnet [1] of the CBM experiment is designed to provide a vertical magnetic field with bending power of 1 Tm over a length of 1 m from the target. The maximum energy storage is evaluated as 5.15 MJ when the operating current of the CBM magnet is rated at 686 A. A 3D model of the magnet with the support is presented in figure 1. Calculations have been performed to design the coil case, the coil vessel, the support links and the quench protection scheme for the CBM superconducting dipole magnet [2]- [8]. The code TOSCA [9] was used for calculating electromagnetic forces exerted on the coil, while the structural analysis was made using the code ANSYS [10].

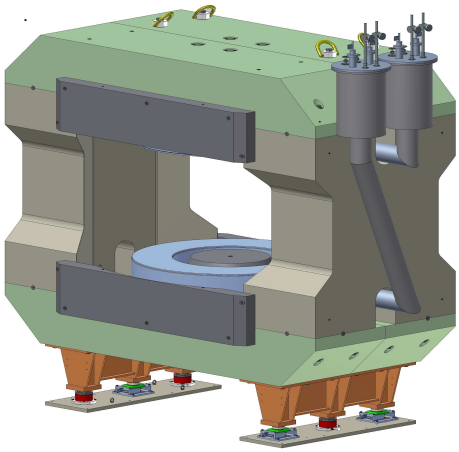

Figure 1: 3D view of CBM dipole magnet with the support.

3D Quench simulation for CBM magnet

The 3D quench calculations for the CBM magnet coil have been carried out by two numerical programs based on the finite-difference method. One of them is used currently at GSI and its detailed description can be found in [11].The other (SQUID) based on CIEMAT numerical code [12] was adapted to perform the quench simulation for the CBM magnet. The magnet coil is represented as a straight slab with a length equal to the average turn length. A regular mesh is applied to the slab so that the cross section of the one mesh element equal to the cross-section of the insulated conductor. Longitudinally, the coil is divided into a number of slices which define a mesh element size. The material properties are homogeneous within each mesh element.

The calculations take into account the inductance function $L_d(I)$[1]. The 3D SQUID program takes into account the real field map distribution in the coil and two layer of conductor insulation (0.1 mm Kapton, 0.2 mm G10).

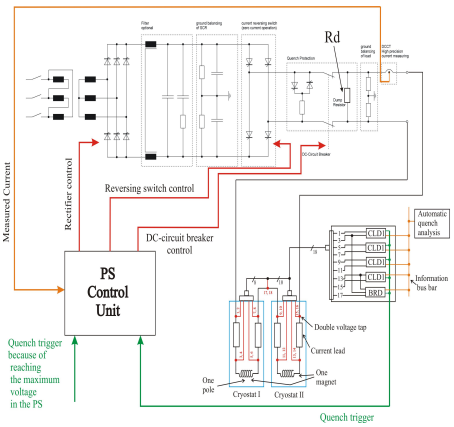

Figure 2: Quench detection and protection scheme (including power supply and voltage taps.

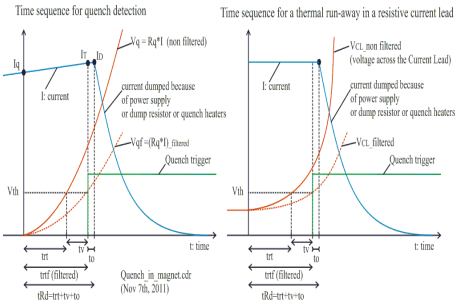

Figure 3: Quench detection time sequence.

Quench protection system

Earlier, the 3D quench calculations [6]- [8] have been performed to optimize the behavior of the winding of the magnet during the quench. The quench protection system for the CMB magnet will be based on the extraction of the energy stored in the magnet via a dump resistor Rd (see figure 2). The details can be found in [1]. The dump resistor is connected in parallel to the magnet and it is always on.

In case of the quench the magnet will be disconnected from the power supply and the magnet current will be

DOI:10.15120/GR-2017-1

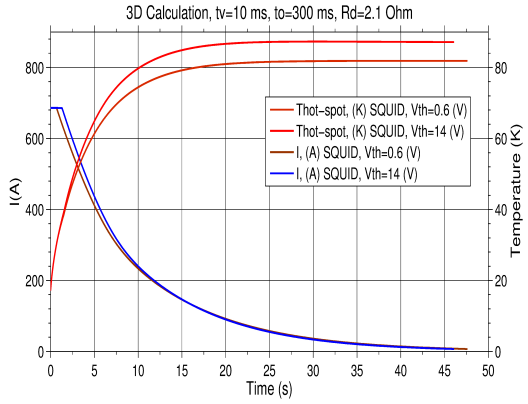

Figure 4: 3D quench calculation of the CBM dipole magnet – the magnet current and the hot-spot temperature.

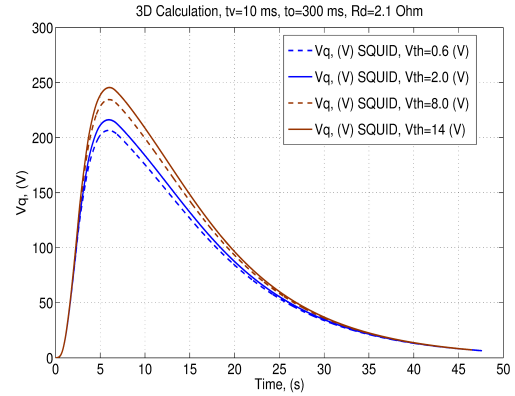

Figure 5: 3D quench calculation of the CBM dipole magnet – the quench voltage.

dumped via the dump resistor. The quench detection time sequence is presented schematically in figure 2. A few calculations were performed for the power supply team, which works on the power converter specification. The detection voltage threshold (Vth) was varied from 0.6 V to 14 V. The favored mechanical switch has an opening time (to) of 300 ms. Validation time (tv) is equal to 10 ms. Figure 4 presents the time dependence of the magnet current and hot-spot temperature with the use $Vth = 0.6V$ and $Vth = 14V$. The 2.1 Ohm dump resistor is also taken into account in the calculations. The maximal "hot-spot" temperature in the coil is about 87 K, when $Vth = 14V$. The time dependence of quench voltage is shown in figure 5. The quench voltage does not exceed the 250 V using the $Vth = 14V$. The maximum voltage across the magnet (1441 V) occurs when the dump resistor turns on.

Conclusion

The designed superconducting dipole magnet will be a unique component of CBM detector setup due to a large pole gap and wide horizontal opening.

The quench protection system will be based on the energy evacuation from the 2.1 Ω dump resistor. The 3D calculations were made for the several values of the detection voltage threshold to estimate the behavior of the magnet coil during the quench.

References

[1] P. Akishin et al., The CBM collaboration, *Technical Design Report for the CBM Superconducting Dipole Magnet* (2014).

[2] A. Bychkov et al., *CBM Progress Report 2014*, (Darmstadt, 2015) 12.

[3] Yu. Gusakov et al., *CBM Progress Report 2015*, (Darmstadt, 2016) 4.

[4] Yu. Gusakov et al., *CBM Progress Report 2015*, (Darmstadt, 2016) 5.

[5] P. Akishin et al., *CBM Progress Report 2013*, (Darmstadt, 2014) 5.

[6] P. Kurilkin et al., *CBM Progress Report 2015*, (Darmstadt, 2016) 7.

[7] P. Kurilkin et al., *CBM Progress Report 2013*, (Darmstadt, 2014) 8.

[8] P. Kurilkin et al., J. Phys.: Conf. Ser. **742**, 012017 (2016).

[9] Vector Fields Ltd., *Tosca. 3d electromagnetics code*, Kidlington (1984).

[10] http://www.ansys.com/

[11] P. Szwangruber et al., IEEE Trans. Appl. Supercond., **23** 4701704 (2013).

[12] F. Toral, *Design and Calculation Procedure for Particle AcceleratorSuperconducting Magnets: Application to an LHC Superconducting Quadrupole*, Ph. D. Thesis. (Madrid) (2001).

DOI:10.15120/GR-2017-1

Tests of the STS-XYTER v2 ASIC for the CBM STS readout

A. Rodriguez Rodriguez[1], *J. Lehnert*[2], *V. Kleipa*[2], *C. Simons*[2], *R. Visinka*[2], *and C. J. Schmidt*[2]
[1]Goethe Universität, Frankfurt, Germany; [2]GSI, Darmstadt, Germany

The STS-XYTER frontend ASIC for the readout of the CBM silicon tracking system (STS) provides self-triggered hits for 128 channels with 5-bit flash ADC charge information and 14-bit timing information with a resolution of < 5 ns. Version 2 of the ASIC from AGH Cracow[1] is available since fall 2016 and implements a large number of optimizations in the analog frontend such as lower noise, larger signal range and improved radiation hardness. The digital backend for control and data readout is completely revised [2], now implementing a custom protocol optimized for readout via the CERN GBTX data aggregation ASIC.

The test setup at GSI

A test system has been set up at GSI for initial ASIC characterization and tests of operation. The setup (Fig. 1) features a frontend board (FEB) with a single STS-XYTER v2 ASIC, the common CBM data processing board (DPB) prototype (AFCK) [3] and a gDPB FMC card from the CBM TOF as connector interface. The AFCK firmware reuses the functionality of the STS protocol tester [4] backend implementation, which allows a quick transition from an ASIC emulation to the real hardware device. Up to three FEBs can be connected to a single gDPB FMC, allowing to test multi-ASIC operation as well as parallel tests on multiple devices.

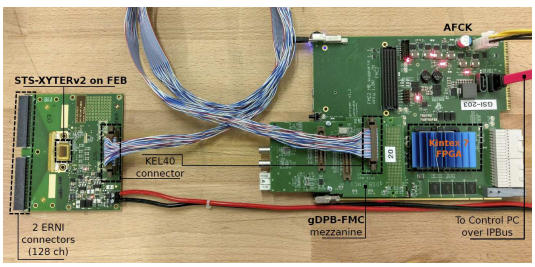

Figure 1: STS-XYTER version2 test setup

Operational tests

The STS-XYTER was brought into operation, the synchronization procedure used to initiate communication with the ASIC was successfully tested and basic control access established. Multiple test modes which produce hits at different stages of the analog and digital processing chain were used and data generation, processing and readout of hit data and control information over a configurable set of AC coupled SLVS links were tested. Using internally generated analog calibration pulses, the full internal processing chain was operated and basic settings for hit generation were exercised.

ADC trim procedure

A reliable ADC calibration procedure is a prerequisite for reading real sensor data. The 5-bit ADC implements a set of 31 discriminators for the ADC values with a subsequent thermometric encoding. Discriminator reference thresholds are provided by a resistor chain; the individual thresholds can be adjusted by trim voltages provided by 8-bit DACs. Trim values can modify discriminator thresholds over a large range, allowing also to set up non-linear responses of desired. A procedure was developed to determine the individual trim values required to achieve a predefined ADC response characteristics. Figure 2 shows the result of a trim procedure. The uncorrected discriminator thresholds which exhibit even a non-monotonous behavior are corrected to a linear response over a predefined signal range.

ASIC characterization in various lab setups and in beam tests will continue in 2017.

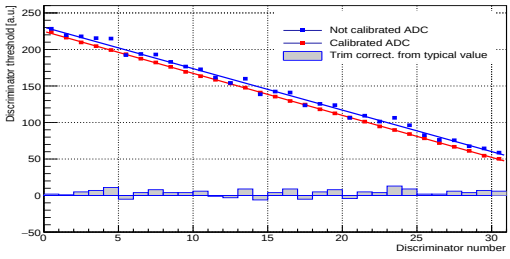

Figure 2: Single 5-bit ADC channel before and after threshold trim.

References

[1] K. Kasinski, R. Kleczek, R. Szczygiel, Front-end readout electronics considerations for Silicon Tracking System and Muon Chamber, JINST 11 (2016) C02024, doi:10.1088/1748-0221/11/02/C02024

[2] K. Kasinski, R. Szczygiel, W. Zabolotny, Back-end and interface implementation of the STS/MUCH-XYTER2 prototype ASIC for CBM experiment, JINST 11 (2016) C11018

[3] W. Zabolotny et al., Versatile prototyping platform for Data Processing Boards for CBM experiment, JINST 11 (2016) C02031 (Proceedings of TWEPP-2015)

[4] W. Zabolotny et al., Design of Versatile ASIC and Protocol Tester for CBM Readout System, JINST (2017) (Proceedings of TWEPP-2016)

DOI:10.15120/GR-2017-1

Charge collection studies of silicon microstrip sensors with different read-out bonding configurations using perpendicular β-particles

Ie. Momot[1,3,4]*, M. Teklishyn*[2,4]*, C. Simons*[3]*, and J. M. Heuser*[3]

[1]Goethe Universität, Frankfurt, Germany; [2]FAIR, Darmstadt, Germany; [3]GSI, Darmstadt, Germany; [4]KINR, Kiev, Ukraine

The STS design aperture covers the polar angles 2.5° to 25°. A read-out strip pitch of 58 μm was chosen to match the design requirement of spatial resolution. About 900 sensors will be installed in the 8 stations of the STS, which translates into $\sim 1.8 \times 10^6$ of read-out channels [1].

To increase signal from charged particles in the outer aperture, where tracks are inclined with respect to the sensor surfaces, different read-out configurations between the sensor strips and electronics are considered. Three types of connections were realized on a test board with a double-sided Si sensor: when each strip is read out by one electronics channel, when only every second strip is read out, and when two strips are bonded to one read-out channel. On the board, 384 sensor strips were divided in 7 groups and bonded to 256 read-out channels applying those three patterns.

For the study, a dedicated setup was built in the STS laboratory. The sensor with the acquisition system was mounted inside a light tight aluminum box, which has a movable support for a radioactive source on the top and a trigger on the bottom. A scintillator connected to a photomultiplier tube is used as a trigger system. The scintillator, sensor and collimated source are aligned in such way that mostly perpendicular particles can penetrate. The source and the scintillator are mechanically interconnected and can move simultaneously in X and Y direction. The height of the source above the sensor can be adjusted independently. For sensor readout the Alibava system [2] was used. It employs the Beetle chip which was developed for the tracker system of the LHCb experiment [3].

Electrons with energies between 1 and 2.28 MeV (^{90}Y β-decay energy) can be considered as minimum ionizing particles. In order to avoid triggering on the also occuring soft component < 1 MeV, a threshold was applied for the signals from the photo multiplier. During analysis a time cut was applied, edge channels of each connection were considered as noisy and removed. After obtaining reliable data, a simple clustering was applied. The resulting spectrum was fitted with a Landau-Gaussian convolution and the most probable value interpreted as collected charge. Noise was calculated as an average fluctuation of the signal baseline. An example of the obtained spectra is depicted in Fig. 1 (top). The dependence of the charge collection on the applied reverse bias in steps of 20 V is shown in Fig. 1 (bottom). The signal-to-noise ratio (S/N) for one-strip clusters was calculated for all connections: (1) for one to one connection: S/N $\backsim$ 26; (2) every second r/o: S/N $\backsim$ 25; (3) two to one: S/N $\backsim$ 22.

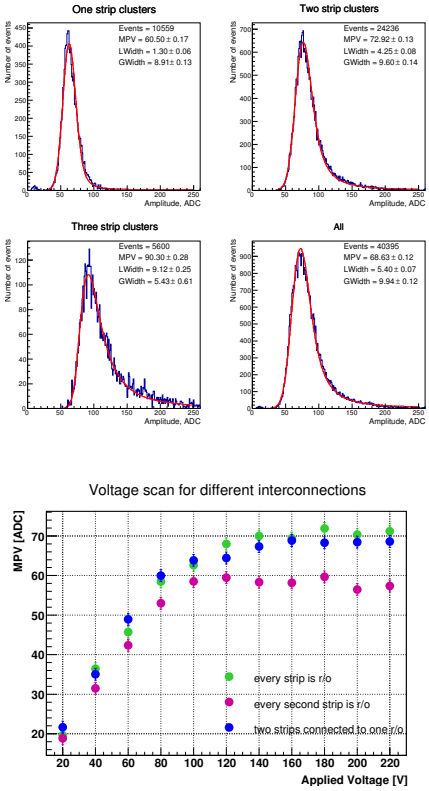

Figure 1: ^{90}Sr spectra fitted with Landau-Gauss convolution for one-to-one connection (top). Charge collection dependence from applied voltage for three configuration schemes (bottom).

Three types of connection schemes have been studied with perpendicular penetrating particles. For each of them, the analysis yields S/N > 20. A further study with inclined beam to mimic the real experiment was made at the COSY facility, Jülich, in August 2016 with 1.6 GeV/c proton beam. Results are forthcoming.

References

[1] J. Heuser et al., Technical Design Report for the CBM Silicon Tracking System, GSI Report 2013-4, http://repository.gsi.de/record/54798

[2] http://www.alibavasystems.com

[3] S. Löchner and M. Schmelling, *The Beetle reference manual for Beetle version 1.3/1.4/1.5*, LHCb note 2005-105, August 22, 2006.

DOI:10.15120/GR-2017-1

Studies of the charge collection efficiency of the prototypes of the silicon microstrip sensors for the STS with 1.7 GeV/c protons

M. Teklishyn[1,2], *O. Bertini*[3], *J. M. Heuser*[3], *A. Lymanets*[3], *H. Malygina*[4,3,2], *and I. Momot*[4,3,2]
[1]FAIR, Darmstadt, Germany; [2]KINR, Kiev, Ukraine; [3]GSI, Darmstadt, Germany;
[4]Goethe Universität, Frankfurt, Germany

Motivation for the proton beam tests

There is a large variety of prototype silicon microstrip sensors for the CBM Silicon Tracking System (STS). The key quantity to be tested is the ratio of the signal over the noise, which makes a direct impact on the detection efficiency of the whole system. The amplitude of the signal itself is directly linked to the ability of the sensor to collect an electrical charge, produced by an interaction with a charged particle. We study the charge collection efficiency by irradiating our sensors with the beam of monochromatic relativistic protons: in this way we expect an equal amount of energy being deposited in the sensor sensitive volume per interaction. It allows us to study systematically what fraction of the deposited energy is transformed to the electrical charge which is then later being collected by the read-out electronics.

The charge in the sensitive volume of the silicon microstrip sensor can be induced by different sources, including an infrared laser, cosmic muons and relativistic electrons from β isotopes. However, the beam of the high momentum protons allows us to perform ultimate tests with the conditions that approach to those in the CBM experiment. Meanwhile, due to the very low momentum spread of the proton beam at COSY accelerator in Jülich, Germany [1], one can perform precise studies of the angular dependence of the sensor response.

The proton kinetic energy is known within 0.1% precision. It allows us to calculate a correction factor of the deposited energy comparing to the minimum ionizing particle (MIP):

$$\Delta E(1.7\,\mathrm{GeV}/c)/\Delta E_{\mathrm{MIP}} = 1.08(4) \qquad (1)$$

The dependency of the energy losses on the incident particle energy is shown in Fig. 1. Values of the mean energy losses in silicon are taken from the NIST Standard Reference Database [2].

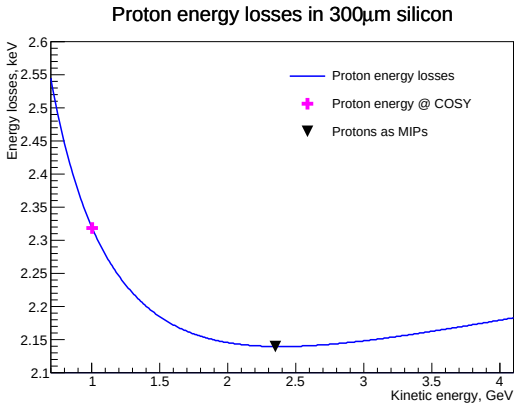

Figure 1: Mean energy losses of protons penetrating a 300 μm thick silicon sensor.

Setup description

We selected 7 sensors to be tested at the COSY accelerator during one week from August 24 till September 4, 2016. Two sensors with the double metallization, two single-metal sensors and two single-metal with oxygenation for better radiation tolerance were fixed in sandwich PCBs and then attached to the read-out electronics via 68-pin ERNI connectors. One single-metal non-oxygenated sensor was directly wire bonded to the read-out electronics. For the latter one we had an access to the 256 read-out channels, merged in 5 groups representing different connection schemes. For the PCB-mounted sensors we used two kinds of interconnectors, which also allowed us to test various connection schemes.

The main cryostation was placed on the movable platform, which allowed a manual vertical adjustment. The platform was equipped with two step motors in a way that one could remotely control the transverse position and the azimuth angle of the cryostation. The latter feature was used for the angular scan procedure.

Two rectangular ($5 \times 20 \times 100\,\mathrm{mm}^3$) plastic scintillators with the photomultiplier tubes were involved in the trigger chain. They were mounted on two aluminium frames upstream and downstream the cryostation. The scintillators were positioned cross-like in plastic holders; in that way they constrained a square cross-section of $5 \times 5\,\mathrm{mm}^2$ for the incident particles.

During the preparation phase in the first two days several configurations of the sensors and stations were tried. Initially, it was foreseen to measure two PCB mounted sensors in the cryostation at once. However, it was observed, that two sensors, being close in one aluminium box together with corresponding electronics, suffered from severe noise.

Thus it was decided to operate only one sensor in the cryostation per run during the first phase of tests. Meanwhile, we put a warm aluminium box mounting a direct-bonded single-metal sensor to the upstream aluminium frame just behind (few millimeters) the plastic holder of the

DOI:10.15120/GR-2017-1

scintillator. In this configuration a series of measurements were performed during the next three days. The sensors in the cryostation were mainly operated at the temperature $T = -10\,^{\circ}\mathrm{C}$ to reduce noise and approach to the final conditions of the future experiment.

In the second phase of measurements we decided to dismount the warm aluminium box, to remove it from its cover and to place it inside the cryostation. The latter was then operated at $T \simeq 10\,^{\circ}\mathrm{C}$ due to the limited thermal coupling through the thick aluminium walls of the partially disassembled warm station. In such a configuration a set of angular scans was performed with the direct-bonded sensor.

Read-out electronics

Due to significant technical issues that occurred with the `nXYTER v.1` based read-out chain [3], we had to find an alternative option for reading out signals from the silicon microstrip sensors during the proton beam tests. We stopped at the `Alibava` system [4], based on the *Beetle* chip [5], initially developed for the tracking system of the LHCb experiment. The read-out chain of the Alibava system consists of two PCBs: the Daughter Board, attached directly to the sensor under the test, and the Mother Board, which performs the digitization and communication with the PC via the USB protocol.

The chosen electronics showed a good performance during the test in the STS laboratory. Since it could be only operated in the external trigger mode only, we designed a trigger chain based on the pair of plastic scintillation detectors. The requirement of the coincidence of two signals within a window of $40\,\mathrm{ns}$ was performed with a NIM crate electronics. Then the logical signal was feed to the two Alibava Mother Boards, thus we triggered a signal read-out from two sensors at once.

The time to digital converter of the Alibava system provides us a relative time between the trigger occurrence and the snap shot of all read-out channels within the $25\,\mathrm{ns}$ time window. Thus before the main measurements we had to make a latency scan, studying the signal amplitude with respect to the time delay.

Data analysis status

Considering complicated structure of the beam time profile, mainly its significant non-uniformity, the main task of the current stage of the data analysis is selection of the events that can be further analyzed. We develop algorithms which should allow us to reject noisy events and events with multiple interactions (thus one can not associate a time-stamp to a given interaction) without significant suppression of the acquired statistics.

Particularly, one procedure has been developed for effective off-line noise reduction. We implement a median correction for every 64 channels for a given event. It allows us to reduce a noise level almost by $1/3$ for some data sets. Typical histograms before and after median correction

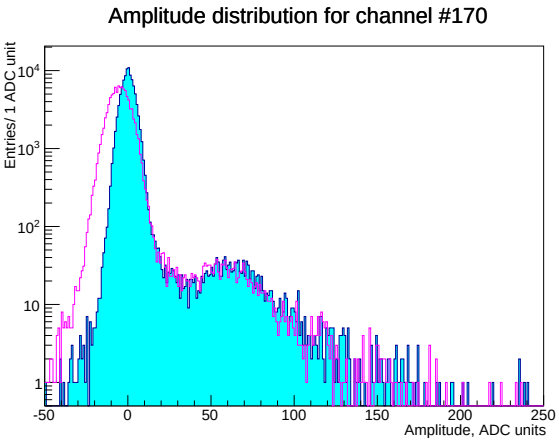

Figure 2: An example of the amplitude distribution in a single channel before (magenta histogram) and after (filled cyan histogram) correction to the common mode.

are shown in Fig. 2.

Further investigations will touch a cluster finding algorithm. This task becomes nontrivial due to complex read-out scheme implemented differently in different set of data taking. A set of the transitional matrices M_{ij} may be implemented to transform data from the channel basis to strip basis:

$$M_{ij} \times C_i = S_j,\ i = 0..255,\ j = 0..1023 \qquad (2)$$

With the properly reconstructed cluster we will be able to proceed to the comparison of signal strength in different conditions which will link us to the charge collection efficiency and the signal over noise ratio.

References

[1] R. Maier, Cooler synchrotron COSY — Performance and perspectives, Nuclear Instruments and Methods in Physics Research Section A: Accelerators, Spectrometers, Detectors and Associated Equipment, Volume 390, Issues 1—2, 1 May 1997, Pages 1-8, ISSN 0168-9002

[2] M.J. Berger, J.S. Coursey, M.A. Zucker and J. Chang (2005), ESTAR, PSTAR, and ASTAR: Computer Programs for Calculating Stopping-Power and Range Tables for Electrons, Protons, and Helium Ions (version 1.2.3). [Online] Available: http://physics.nist.gov/Star [2017, February 10]. National Institute of Standards and Technology, Gaithersburg, MD.

[3] A.S. Brogna et al. 2006. N-XYTER a CMOS read-out ASIC for high resolution time and amplitude measurements on high rate multi-channel counting mode neutron detectors, Nucl. Instrum. Meth. Phys. Res. A568 301

[4] Alibava Systems, http://www.alibavasystems.com

[5] S. Löchner and M. Schmelling, The Beetle reference manual for Beetle version 1.3/1.4/1.5, LHCb note 2005-105, August 22, 2006.

DOI:10.15120/GR-2017-1

A thermal enclosure for microstrip sensor tests in laboratory and beam

A. Lymanets[1,4], *M Teklishyn*[2,4], *O. Bertini*[1], *H. Malygina*[3,1,4], *I. Momot*[3,1,4], *and J. M. Heuser*[1]
[1]GSI, Darmstadt, Germany; [2]FAIR, Darmstadt, Germany; [3]Goethe Universität, Frankfurt, Germany;
[4]KINR, Kiev, Ukraine

A shielded thermal enclosure has been developed that allows for testing silicon microstrip sensors of different sizes from different vendors under temperature conditions as later in the CBM experiment. The enclosure can be operated in the laboratory as well as in the beam and provides integrated cooling infrastructure that is required to operate irradiated sensors at below room temperature. It has been successfully used during the August 2016 beam time at COSY (Reserach Center Jülich) [1] where sensors with different strip readout schemes have been operated and parameter scans, such as beam incidence angle and temperature scan, have been performed. A key design requirement addressed in the thermal enclosure is the minimal cool-down time that would facilitate the measurements of irradiated sensors.

Experimental setup

The enclosure consists of a shielding *Al* box that is nested in a plastic box with styrofoam isolated walls and windows for the beam. It has separate cooling circuits for front-end electronics and dry nitrogen that is blown into the box in order to reduce humidity and prevents possible water vapor condensation. In order to speed up cooling of nitrogen gas, a forced convection is provided by the built-in fans that are switched on during the cooling time only. The setup provides simultaneous operation of two sensor boards read out by two ALIBAVA [2] daughter boards equipped with BEETLE [3] front-end chips (see Fig. 1).

In order to control the experimental conditions, temperature and humidity has been measured inside and outside the enclosure using a custom microcable resistive temperature detector (RTD) as well as combined temperature and humidity sensors (Honeywell HIH-3602-C). Environment parameters outside the box have been used to calculate the dew point. The sensor data have been acquired and stored using custom LabVIEW-based software. Figure 2 shows the temperature and relative humidity trend recorded over a time period of above 11 hours. A cool-down time from room to operation temperature of -5.7° is below 2 hours. The nitrogen flow during the measurements was 150 l_n/min which kept the relative humidity in the enclosure well below 30%.

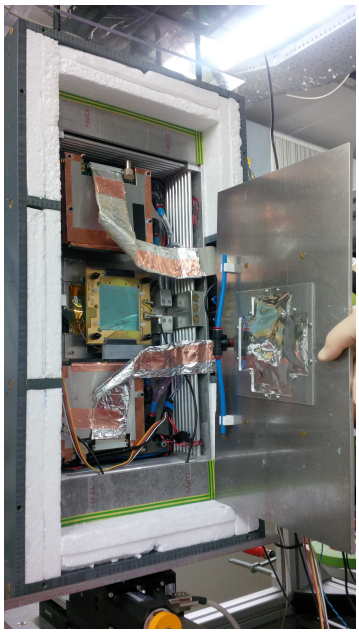

Figure 1: Thermal enclosure with cooling lines at the perimeter of the core part and two ALIBAVA daughter boards.

Conclusions

The constructed enclosure has provided stable and low-noise operation conditions during the beam test at COSY (Jülich) in 2016. Fast cool-down time allowed to test many microstrip sensors in various configurations and to study the effect of operation conditions on the system performance.

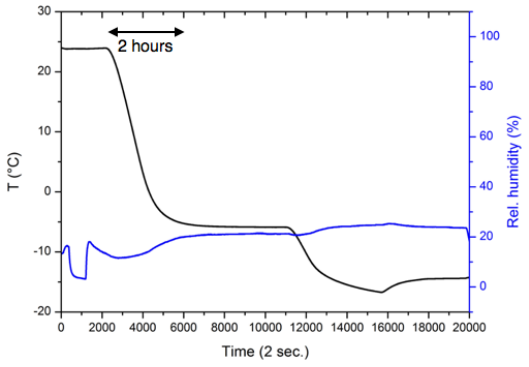

Figure 2: Temperature and humidity trend during the cool-down cycle.

References

[1] R. Maier, NIM A 390 (1997) 1-8

[2] http://www.alibavasystems.com, Feb. 10, 2017

[3] S. Löchner and M. Schmelling, LHCb note 2005-105, Aug. 22, 2006

DOI:10.15120/GR-2017-1

Control software for the DPB based readout chains and related beamtime activities

P.-A. Loizeau[1]*, D. Emschermann*[1]*, and the CBM DAQ working group*
[1]GSI, Darmstadt, Germany

Since 2015, several of the CBM sub-detectors groups are starting to use new readout chains based on the AFCK FPGA board, on the IPbus system for slow-control communication and on the FLES system for data acquisition. For the configuration and control of these new chains, a set of libraries and binaries based on IPbus was developed. The first step in 2015 was the conversion of tools from the previous chains to support the readout of a single nXYTER front-end board through the control path (Control DAQ or CDAQ) [1]. This set of tools is now expanded for multi-boards operations and synchronized data taking with different CBM sub-detectors (TOF, MUCH, STS).

The *dpbcontrols* software is available to all CBM members [2] with support for the following firmware modules: (i) FEB-F: nXYTER v2 ASIC front-end board, (ii) PADI-GET4: PADI 6 or X board associated with GET4 v1.23, v1.3 or v2.0 board, (iii) CDAQ: data readout through the IPbus control path, (iv) FLIM: data readout in Micro-Slice containers (μS) through the 10 Gb FLES link [3], (v) TS slave: receiver part of the Time Synchronization (TS) system used for multi-boards systems in the CBM 2016 beamtimes with Data Processing Boards (DPBs) [4].
AFCK boards loaded with a CBM firmware are tagged *xDPB*, with *x* a letter corresponding to the firmware type. Two DPB firmware systems are currently in use: nDPB for STS and MUCH with FEB-F + CDAQ + FLIM + TS slave modules and gDPB for TOF with PADI-GET4 + CDAQ + FLIM + TS slave modules. For each of these systems, a Command-Line-Interface binary (CLI) is provided to the users, with access to low level commands (e.g. registers setting) but also higher level operations such as the automatic calibration of front-end parameters using data samples acquired through the CDAQ. The two CLI programs also support the execution of configuration scripts to simplify the operation of systems with hundreds of channels.

For quick monitoring and debugging, the CDAQ data can be either sampled and directly printed out in the CLI tools as text or integrated in simple ROOT monitoring macros for continuous readout. One limitation of this CDAQ is that in most operating conditions data are lost between two readout cycles. It is therefore mostly a tool for setup tuning and not for detector characterization.

In order to operate experimental setups with multiple DPBs or multiple DPB types, all boards need to use a common clock and some commands need to be executed synchronously on all targets. The TS system provides to all DPBs a 40 MHz clock and a synchronization pulse locked to it with a period of $1024 * 2^{15}$ cycles or 0.8388608 s. Before sending a command needing synchronous execution, the time elapsed since the last synchronization pulse is readout to ensure that all targets can receive the command before the next pulse. Three programs are used with this method to perform the synchronization procedure of the current prototype systems: 1) one to reset all DPBs in the setup in a synchronized way and prepare them for configuration, 2) one to reset and synchronize the clock counters of all DPBs and reset the μS counter of their FLIM module (timing synchronization) 3) one to enable data emission in a synchronized way (data synchronization: all DPBs start sending their data at the same μS).

All these tools were used during a beamtime in the H4 cave at CERN SPS in November 2016 [5]. Two prototypes from the MUCH sub-detector were readout with the FEB + nDPB system (7 nDPBs with up to 4 FEBs per board) and multiple RPC prototypes from the TOF sub-detector were readout with the PADI-X + GET4 + gDPB system (6 gDPBs with up to 3 front-end boards each).
During this beamtime, an online monitor was developed based on CBMROOT [6]. It allowed the shift crew to check on a web page with interactive histograms and in real time the status of all front-end boards and of the DAQ system.

Another test setup was installed for the TOF sub-detector group in the STAR experiment at BNL [7], with a single gDPB. No CBM expert will be on-site when beam will be available during the STAR 2017 run. Therefore, the integration of the tools and configuration files in simple scripts was pushed further, to the point where a reboot of the DAQ computer triggers a full automatic reconfiguration, followed by the execution of the FLES DAQ and the CBMROOT online monitor.

References

[1] P.-A. Loizeau *et al.*, "Configuration, monitoring and data acquisition with the IPbus-AFCK readout chains", CBM Progress Report 2015 (2016) 106

[2] "CBM GitLab repository", https://cbmgsi.githost.io/p.-a.loizeau/dpbcontrols

[3] D. Hutter *et al.*, "CBM FLES input interface developments", CBM Progress Report 2015 (2016) 112

[4] L. Meder *et al.*, "Timing synchronizer system developments for pre-production beam test setups", CBM Progress Report 2015 (2016) 109

[5] D. Emschermann *et al.*, "Common CBM beam test at CERN SPS 2016", this report

[6] F. Uhlig *et al.*, "Online monitoring with CbmRoot", this report

[7] I. Deppner *et al.*, "TOF Status Report", this report

DOI:10.15120/GR-2017-1

Design and development of the nDPB FPGA mezzanine card

C. de J. García Chávez[1], *D. Emschermann*[2], *and U. Kebschull*[1]
[1]Infrastructure and Computer Systems for Data Processing (IRI), Frankfurt University, Frankfurt/Main, Germany;
[2]GSI, Darmstadt, Germany

Introduction

With the introduction of the AFCK [1] as a Data Processing Board DPB, several CBM subsystems such as the Silicon Tracking System STS and the Muon Chamber MUCH require the integration of nXYTER-based front-end boards into the current CBM-DAQ. For this reason, an FPGA mezzanine card was developed in order to allow the interconnection of the front-end boards to the AFCK.

Design considerations

In order to achieve a correct time-stamping in a free-running data acquisition chain, a global synchronization system is necessary. Therefore a connection to an external synchronization system [2] is made through a RJ45 connector, which receives the synchronization signals from a tDPB. Given the fact that the nDPB is floating at the high-voltage bias level of the STS module, which is around +/- 150V, an isolation between the FPGA fabric and the RJ45 is mandatory. The isolation is made by a magnetic Ethernet isolator.

A Small Form Factor SFP optical transceiver module is also included on the nDPB-FMC to allow a 10 Gbps FLIM or 1Gpbs IPBUS communication between the AFCK and the DAQ-PC. Moreover, two KEL-68 connectors have been included on the nDPB-FMC to connect to the nXYTER front-end boards. Finally, in order to facilitate prototyping, three LVDS General Purpose Input/Output GPIO pins were also included on the FMC.

Because of the high speed signals and high pin-out density of the FMC design, an 8-layer PCB stack-up was selected. Five layers were used for high speed transmission lines while three layers where used as power planes. In order to reduce the high-frequency losses caused by the PCB dielectric material, a MEGTRON-6 material was selected for the *cores* and the *prepegs*. The final nDPB-FMC is shown in the Fig.1.

Closing notes

The nDPB-FMC was successfully used and tested during the CERN SPS 2016 beamtest [3]. The FLIM optical connection as well as the external synchronization by the RJ45 were also successfully tested. Moreover, the nDPB-FMC was shown to be also useful for the SPADIC 2.0 readout, as presented in [4]. Fig.2 shows the experimental nDPB setup used during the CERN SPS 2016 beamtest where multiple nDPB-FMC were used.

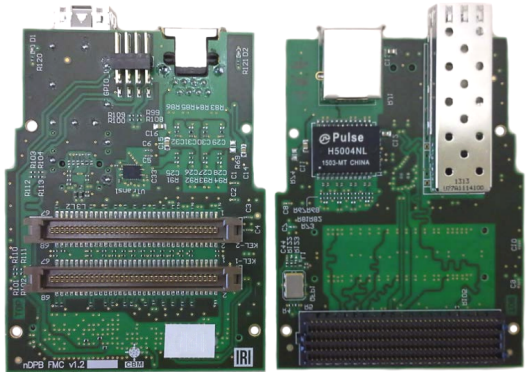

Figure 1: Left: Top side of the nDPB-FMC, two KEL-68 connectors are shown as well as the GPIO connector. Right: Bottom side of the nDPB-FMC, RJ45, magnetic isolator, FMC-HPC connector and the SFP with a cage are shown.

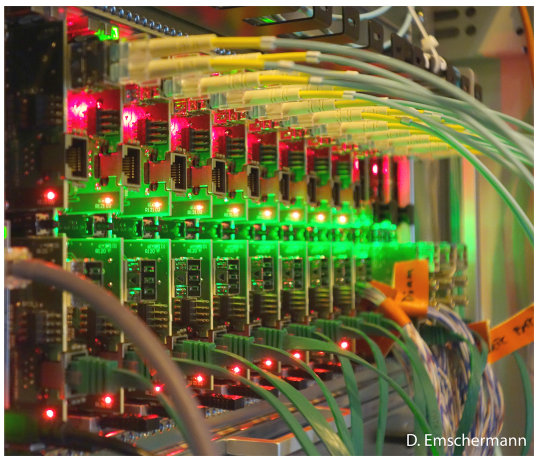

Figure 2: nDPB setup at CERN SPS 2016 beamtest

References

[1] W. Zabołotny et al., "The AFCK Board as the Data Processing Board prototype for the CBM experiment". CBM Progress Report 2015.

[2] L. Meder et al., "A timing synchronizer system for beam test setups requiring galvanic isolation". Real Time Conference (RT), 2016 IEEE-NPSS Conference Record, doi:10.1109/RTC.2016.7543119.

[3] D. Emschermann et al., "Common CBM beam test at CERN SPS 2016", this report.

[4] C. de J. García Chávez et al., "Development of the SPADIC v2.0 read-out chain at CERN SPS 2016". This report.

DOI:10.15120/GR-2017-1

Simplification of the TRD readout chain and related modification of the pad plane layout

D. Emschermann[1]
[1]GSI, Darmstadt, Germany

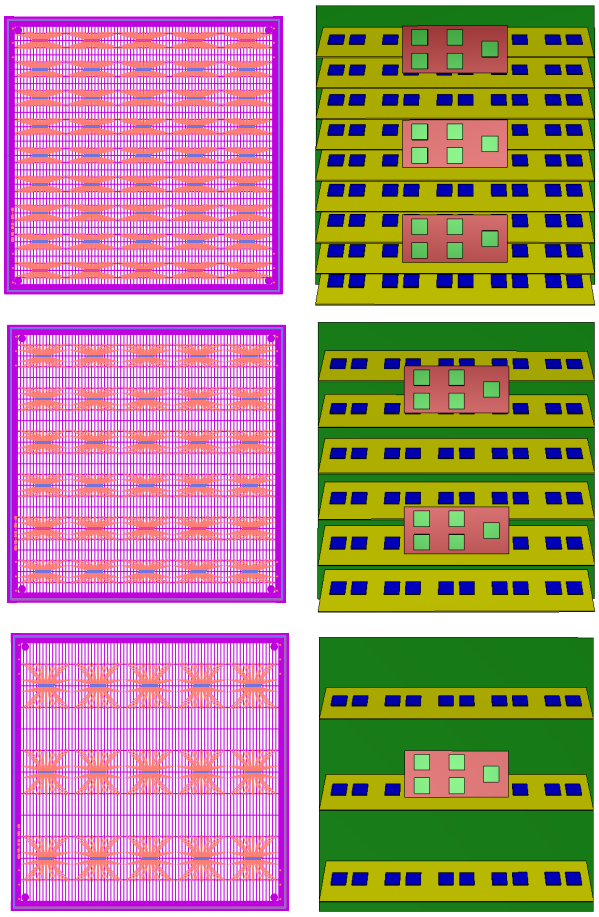

Figure 1: Pad plane layout of the small TRD module types 1, 2 and 3 (from top to bottom), with a respective pad length of 15.0 mm, 22.5 mm and 45.0 mm. The pad plane is interfaced with 9x, 6x or 3x FEB-5x2 and readout with 3x, 2x or 1x ROB-5.

The TRD v16a uses four different FEB types (FEB-5x3, FEB-5x2, FEB-5x1, FEB-8x1) and 3 ROB types (ROB-7, ROB-5, ROB-3). The detector layout was further optimised in TRD v17a, aiming at a reduction of the amount of different components in the readout chain. A modification of the pad plane layout for the three small 57×57 cm^2 TRD module types (1, 2, and 3), see Fig. 1, allows to equip all of them with a single FEB-5x2 type.

The modification consists in using the same 64-pin connector on all 3 module types. With increasing pad size the 64-pin footprint needs to be adapted to the related pad length. That is possible until the increase in pad capacitance deteriorates the signal-to-noise ratio below a given threshold value. As a result of this optimisation the FEB-5x3, FEB-5x1 and ROB-7 are no longer required.

module type	1	2	3	6	7	8
# of modules	32	24	40	24	32	48
ASICs / FEB	10	10	10	8	8	8
FEBs / module	9	6	3	8	4	3
# of FEBs	288	144	120	192	128	144
# of ROB-5	96	48	40	48	32	0
# of ROB-3	0	0	0	0	0	48

Table 1: Key numbers of the SIS100 TRD v17a detector, summarising to 9232 SPADIC and 1464 GBTx ASICs.

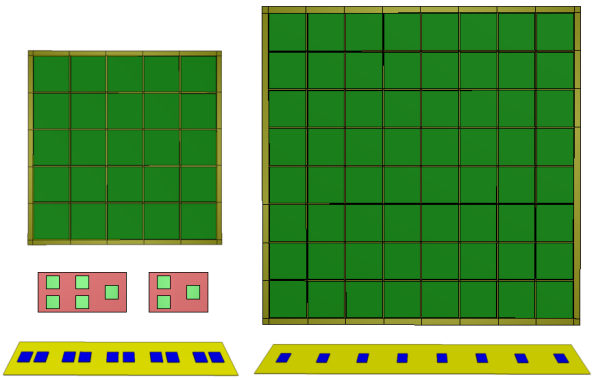

Figure 2: The building blocks of the TRD detector system: (green) modules of 2 different sizes, (yellow) 2 FEB types, 5x2 and 8x1, and (red) 2 ROB types, ROB-5 and ROB-3.

All 3 small module types are now based on an identical readout tree: a group of 30 SPADIC ASICs with 60 e-links is interfaced to a ROB-5 providing 70 e-link inputs. The module types 1, 2 and 3 consist of 3, 2 and 1 such readout trees, as detailed in Tab.1. The total number of ASICs sums up to 9232 SPADIC and 1464 GBTx.

Thanks to this simplification the TRD detector is built from only 2 FEB types (FEB-5x2, FEB-8x1) and 2 ROB types (ROB-5, ROB-3), see Fig. 2. Further benefits of a readout chain employing only the ROB-3 and no ROB-5 are currently under study.

References

[1] The CBM Collaboration, *Technical Design Report for the CBM Transition Radiation Detector (TRD)*, to be published

DOI:10.15120/GR-2017-1

Development of the SPADIC v2.0 readout chain at the CERN-SPS in 2016 *

C. de J. García Chávez[1], *C. Bergmann*[2], *D. Emschermann*[4], *P. Kähler*[2], *M. Kohn*[2], *P. Munkes*[2], *F. Roether*[3], *and U. Kebschull*[1]

[1]Infrastructure and Computer Systems for Data Processing (IRI), Frankfurt University, Frankfurt/Main, Germany; [2]Institut für Kernphysik, Münster, Germany; [3]Institut für Kernphysik, Frankfurt, Germany; [4]GSI, Darmstadt, Germany

Overview

By November 2016, front end boards equipped with the new SPADIC v2.0 chip have become available [1]. Together with the introduction of a new readout architecture based on the *AFCK*, the *FLIM* [2] data transmission protocol and the *IPBUS* protocol for slow-control and system configuration, a set of firmware and software designs were developed to enable the readout of the SPADIC v2.0 chips during the test beam at the CERN-SPS in 2016.

Experimental Setup

Two SPADIC v2.0 front end boards were installed on a 95×95 cm^2 MWPC of the CBM-TRD type-8 [3][4][5] at the CERN-SPS [6]. The location of components are shown in Fig. 1. On the left side of the image, the red squares denotes the location of the SPADIC v2.0 front end boards on the MWPC while on the right side, denoted by a yellow square, an *AFCK* installed in a *mTCA* is shown.

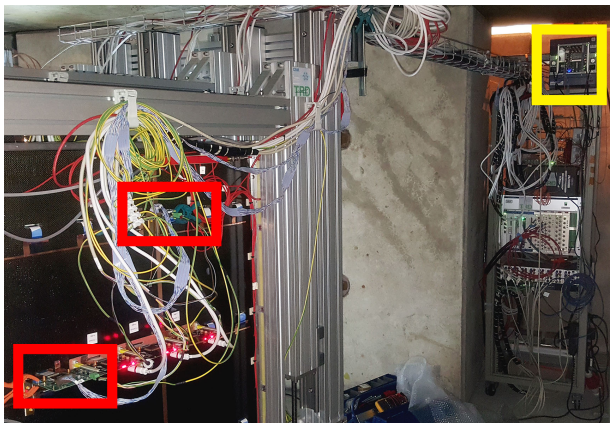

Figure 1: Experimental setup at the CERN-SPS in 2016.

Firmware Development

The readout architecture used during the CERN-SPS beam time in 2016 is represented by a diagram as shown in Fig. 2. The SPADIC v2.0 front end boards are connected to the *AFCK* by means of a *gDPB-FMC* mezzanine card. The SPADIC v2.0 uses the *STS-HCTSP* protocol [7] for data transmission and configuration. After the front end data is readout and processed by the *AFCK*, it is transmitted towards the *FLIB* installed in a *DAQ-PC* by an optical connection available at the *nDPB-FMC* [8] using the *FLIM* protocol. For future reference, this firmware architecture will be named *eDPB*, where *"e"* comes from the *e-link* transmission protocol used by the front-end and *DPB* as acronym for *Data Processing Board*.

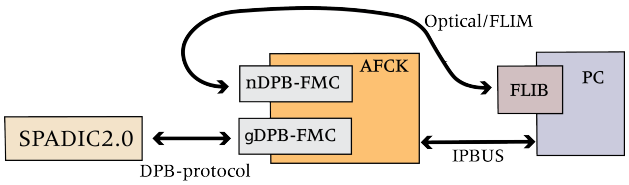

Figure 2: SPADIC v2.0 readout architecture.

An overview of the AFCK firmware design is shown in Fig. 3. Data coming from multiple SPADIC v2.0 front end boards is buffered and then pre-processed by a *Feature Extraction* core [9]. Finally, a simple timeslice building is performed before the data is sent to the *FLIB*.

Feature Extraction

Feature Extraction is required to process and extract as much valuable information as possible from the SPADIC chips with a minimum of data bandwidth. In the presented *eDPB* design, it is possible to either process data from SPADIC v2.0 front end boards or from a *StreamSim* device. A *StreamSim* device is basically an AFCK board working as a front end emulator, where SPADIC data recordings can be downloaded and then transmitted by a 3 Gbps optical line, built on top of a Xilinx Aurora protocol [10], towards the *eDPB*. Scenarios where testing and developing of feature extraction algorithms are required, can benefit from this configuration. For data integrity tests, two independent data streams are sent to the *FLIB*. An optical line would only transmit the original SPADIC messages without any pre-processing, while the second optical line would only transmit the data resulting after SPADIC messages are processed by the feature extraction core. The *eDPB* design has used the *nDPB* firmware design as basis, given its similarities, but differing in the front end and the configuration requirements.

Software Development

The *IPBUS* protocol has been used to transmit the configuration commands from the *DAQ-PC* towards the front end boards. For this purpose a software library was built to provide a feasible way to initialize the data transmission

* Work supported by BMBF No. 05P15RFFC1.

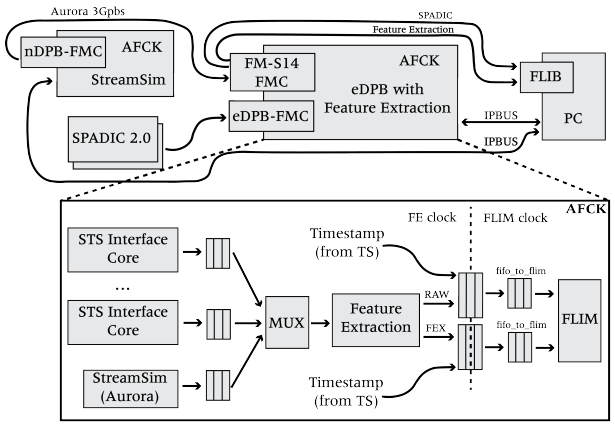

Figure 3: Up: DAQ diagram with SPADIC v2.0 as front end and a StreamSim device. Down: AFCK firmware design diagram.

from the SPADIC v2.0. Initialization and configuration scripts facilitates both the analog and digital configuration of the SPADIC v2.0 such as baseline adjustment and neighbour forced trigger matrix. A considerable contribution for the software stack has been developed by the *CBM-DAQ* group.

Current Status

The design and evaluation of the *eDPB* firmware design was successfully performed during the CERN-SPS test beam in 2016. Communication tests between the *eDPB* and the SPADIC v2.0 were as well successful. Configuration scripts that were developed during previous beam tests for the SPADIC v1.0 and SPADIC v1.1 were successfully ported to the SPADIC v2.0 in order to work with the new *eDPB* design by using the *IPBUS* protocol.

References

[1] M. Krieger et al., *Development of new SPADIC versions 1.1 and 2.0*, this report.

[2] D. Hutter et al., *CBM FLES input interface developments*, CBM Progress Report 2015.

[3] P. Kähler et al., *Operation and measurement programme of a SPADIC readout chain on type-8 CBM-TRD prototypes at the CERN-SPS 2016*, this report.

[4] F. Roether et al., *Construction of type-8 MWPCs for the CBM-TRD*, this report.

[5] *Technical Design Report for the CBM Transition Radiation Detector*, The CBM Collaboration, 2017 (to be published).

[6] D. Emschermann et al., *Common CBM beam test at CERN-SPS 2016*, this report.

[7] K. Kasinski et al., *A protocol for hit and control synchronous transfer for the front-end electronics at the CBM experiment*, NIM A835(2016)66 or doi:10.1016/j.nima.2016.08.005.

[8] C. de J. García Chávez et al., *Design and development of the nDPB FPGA mezzanine card*, this report.

[9] C. de J. García Chávez et al., *Status Update of the Feature Extraction Framework for Automatic FPGA Firmware Generation*, CBM Progress Report 2015.

[10] "Xilinx", http://www.xilinx.com.

DOI:10.15120/GR-2017-1

Status of the CBM-MVD station precursor PRESTO *

M. Koziel[1], *P. Klaus*[1], *C. Müntz*[1], *J. Stroth*[1,2], *and the CBM-MVD Collaboration*
[1]Institut für Kernphysik, Goethe-Universität Frankfurt, Germany; [2]GSI Darmstadt, Germany

Sensor Integration When integrating touchy sensors on carriers, the yield represents a vital assembly parameter and drives the optimization of quality assessment (QA). In 2015, the first side of the PRESTO module (comprising six 50 μm thin MIMOSA-26 AHR sensors) was assembled [1]. After assembly, five out of six sensors were functional. Note, all sensors have been subject to probe testing with dedicated needle cards and test procedures prior to integration. One half of the sixth sensor worked well while the remaining half did not produce any data. With time, an additional sensor started to exhibit malfunctioning. Despite visual inspection did not reveal problems with the sensors or wire bonding, we extensively examined our wire-bonding hardware and procedures. The latter pointed to a possible weakness originating from edging of bond wedges and Al-wire. After replacing the hardware components, wire-bonds from the two mentioned sensors were taken off and replaced. As a result, one of the two malfunctioning sensors was recovered. The other one, where output data were not produced, did not change its behavior.

We therefore associate the malfunction of this particular sensor to be caused by improper handling during the assembly process. After considering all tests related to the first side of PRESTO to be accomplished, we have focused meanwhile on the assembly of the second side. It hosts three rows of sensors, each populated with three 50 μm thin MIMOSA-26. For this side, sensors based on low- and high-resistivity substrates were chosen. The use of low-resistivity is motivated by reserving the high-resistivity based devices for other projects. Some sensors with minor malfunctions, revealed during the probe test campaign, were also placed on purpose. We hope to trace the possible development of these malfunctions during each of the integration steps. Figure 1 shows the newly equipped front side of PRESTO.

Continuous Operation and Control System The long-term operation of PRESTO was assessed in our vacuum vessel during summer 2016. A 24/7 readout was achieved for several weeks. This campaign helped us decide which metrics to monitor and which software and hardware interlock systems to employ to prevent system failure. During the run, a custom software solution was used to gather relevant metrics such as electrical sensor currents, module temperature, vacuum pressure, cooling system status. Some further metrics from the data stream that should be monitored include e.g. cluster multiplicities, local hit rates and occupied bandwidth. To do so, an EPICS based control and monitoring system is currently under planning and will soon put into operation in a pilot system to be evaluated when operating the then fully equipped PRESTO. Later, it shall serve the full CBM-MVD as control and monitoring solution.

Cooling System and Planning Systematic cooling studies are now under way for PRESTO and for the later full MVD. New equipment was put into operation to increase the performance and fully characterize the cooling system. This includes a water cooling pump for pressure boost, temperature sensors for the cooling medium, flow meters, and pressure gauges in the next expansion stage. Some of those systems might be excluded from the final MVD to make the cooling system less prone to malfunction. For now, they are required to fully characterize the properties of our system.

Figure 1: Configuration of sensors assembled on the front side of the PRESTO module. First side assembled with sensors and flex cables.

Conclusion Extensive tests of the first-side assembly of PRESTO were conducted in 2016. They triggered many activities, e.g. optimization of QA, development of the monitoring and control system for the MVD, and evaluations of the cooling system. The latest progress on PRESTO – the integration of the second side – is under way.

References

[1] M. Koziel et al., "Vacuum-compatible, ultra-low material budget Micro-Vertex Detector of the compressed baryonic matter experiment at FAIR", NIM-A 845 (2017) 110 (dx.doi.org/10.1016/j.nima.2016.05.093)

* supported by BMBF (05P15RFFC1), HIC for FAIR and GSI.

Online data preprocessing for the CBM Mirco Vertex Detector *

Qiyan Li[1], *M. Deveaux*[1], *J. Michel*[1], *C. Müntz*[1], *J. Stroth*[1,2], *and the CBM-MVD Collaboration*
[1]Institut für Kernphysik, Goethe-Universität Frankfurt, Germany; [2]GSI, Darmstadt, Germany

The CBM Micro Vertex Detector (MVD) is being designed to handle 10^5 Au+Au or 10^7 p+Au collisions/s. Weakly decaying particles like Hyperons or D Mesons will be identified in real time by means of a free streaming DAQ system, the FLES, which includes stages for event reconstruction and decay topology identification. To fulfill this task with the available computing resources, each processing step has to be optimized for low CPU load and bandwidth consumption. This does also hold for the cluster finding of the MVD. The current CBMRoot/C++ code was estimated to consume up to 80% of the CPU-power of the FLES once being confronted with a realistic data rate. To reduce this load, we tested strategies to perform preprocessing of the data before sending it to the computing farm.

A first stage of the proposed preprocessing is already integrated in the CMOS Monolithic Active Pixel Sensors used in the MVD. The MIMOSA-26 pixel sensor used for our test includes circuits for signal discrimination, on-chip zero suppression and one-dimensional cluster finding. The second stage as discussed in this work comprises full cluster finding and encoding on free resources of the FPGAs controlling the sensors. The related algorithm was required to match the available FPGA resources and to keep all information on cluster shapes without increasing the data volume and bandwidth.

In a first step, we found a way to encode reconstructed clusters into one 32 bit word per cluster. Tests showed that the protocol encodes 99.99% of the clusters recorded during beam test data of the MVD-prototype with MIMOSA-26 without loss of information [1, 2]. A VHDL module doing cluster finding and encoding was designed and tested successfully with the TRB2 board [3]. Real time cluster finding was demonstrated by operating it with a MIMOSA-26 sensor, which was illuminated with a β-source. To test the accuracy of this cluster finding, the output was stored together with its raw data, which was processed with the C++ reference code in a next step. The clusters recorded with both chains were compared for 260k frames. They were found to agree for physics data while some pathological signatures, as e.g. caused by a broken line, were rejected by the FPGA code. The output of the FPGA showed a mild compression of 14% w.r.t. the raw data (see Figure 1), which matches our requirements. The CPU time for the remaining steps to be done with C++ at the FLES (C++ cluster finding vs. unpacking of the encoded cluster information) was compared. Note that in both cases the first processing stage was carried out by the sensor . The low occupancy reached with the β-source causes a bias in favor of the offline processing. Nevertheless, the FPGA-processing reduces the remaining CPU load by a factor of four (see Figure 2).

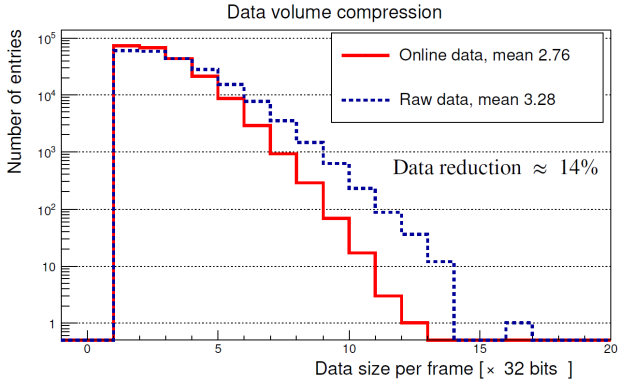

Figure 1: Data size per frame for a MIMOSA-26 exposed to β-rays (raw data vs. FPGA-encoded clusters).

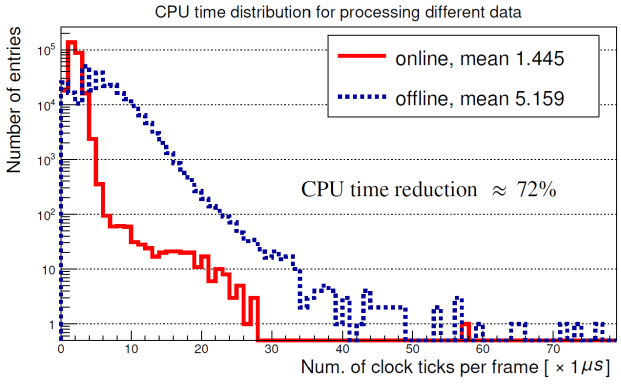

Figure 2: The CPU time per frame (decoding of FPGA-encoded clusters vs. C++ cluster finding).

The explorative study presented here demonstrates that the proposed strategy is suited to reduce the load of the FLES. It remains to be adapted to the internal data processing of the final MVD sensor, which is currently under design.

References

[1] Qiyan Li et al., GSI Scientific Report 2012 (2013) 56
[2] Qiyan Li et al., J. Phys.: Conf. Ser. 513 (2014) 022021 (Proceedings of CHEP-2013)
[3] Qiyan Li et al., GSI Scientific Report 2014

* supported by BMBF (05P15RFFC1), HIC for FAIR and GSI.

DOI:10.15120/GR-2017-1

Cooling studies with thermal pyrolytic graphite for the CBM-MVD *

D. Mijatovic[1], M. Koziel[1], P. Klaus[1], C. Müntz[1], J. Stroth[1,2], and the CBM-MVD Collaboration
[1]Institut für Kernphysik, Goethe-Universität Frankfurt, Germany; [2]GSI Darmstadt, Germany

The CBM Micro Vertex Detector (MVD) comprises four planar detector stations, each divided in quadrants, and equipped with dedicated pixel sensors. Their operation results in about 300 W of total heat input. The challenging material budget of the stations ($< 0.5\%$ X_0) in combination with the operation in vacuum asks for an elaborated cooling concept. It is based on conductive cooling inside the geometrical acceptance employing thin sheets of high-performance materials as sensors carriers, featuring heat conductivities in the order of four times the one of copper, like poly-crystalline CVD-Diamond and Thermal Pyrolytic Graphite (TPG) [1]. These carriers guide the heat to actively cooled heat sinks outside the acceptance. This report presents systematic studies on the in situ cooling performance of MVD quadrants, with a focus on assessing TPG carriers of different thicknesses. Note, the in-plane heat conductivity of TPG is about 1600 W/mK at room temperature, and less than 20 W/mK perpendicular to the surface. Figure 1 (left) depicts the setup geometry by showing the temperature distribution on a TPG sensor carrier of the 3rd station attached to a actively cooled Aluminum heat sink, measured by the IR camera (Vario Cam). The heat load (in the order of 700 mW/cm^2) was mimicked by sheets of Kapton heaters, operated in a standardized vacuum test stand. The thermal performance was

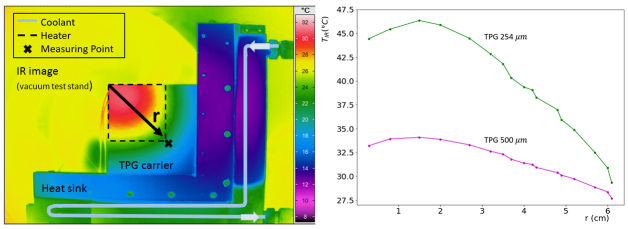

Figure 1: Left: IR image of a 500 µm thin 8×8 cm^2 TPG carrier attached to the heat sink, heat load of 15 W applied 180 s, $T_{cooling\ fluid} = 15$ °C, the heat sink was not corrected for emissivity. Right: Temperature along diagonal coordinate, both TPG thicknesses, $T_{cooling\ fluid} = 25$ °C, after 10 s of heating.

quantitatively characterized by analyzing temperature differences and heating curves of TPG sheets with different thicknesses (254 and 500 µm), shown in figures 1 (right) and 2, respectively. Fitting the temperature rise during the first 10 s ("fast") with $\propto (1 - \exp(-t/\tau))$ results in τ_{fast} of 3-4.5 s, almost independent of the TPG thickness. This

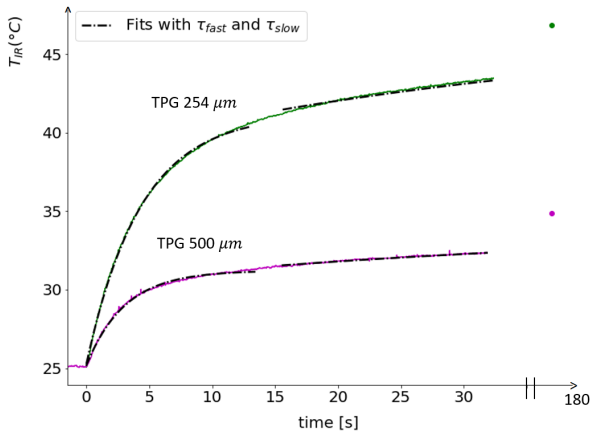

Figure 2: Heat-up curves of TPG carriers of two different thicknesses in vacuum, measured in the point depicted fig. 1, $T_{cooling\ fluid} = 25$ °C, relative adjustment of curves at $t = 0$ s. Broken lines: Exponential fits to initial and saturating time range, see text.

fast time constant is in agreement with the above mentioned outstanding in-plane heat conductivity of TPG, a result derived from solving the equation of heat conductivity [2]. A second common time constant of $\tau_{slow} \approx 45$ s characterizes the saturation phase.

In summary, a standardized test stand was set into operation to characterize the cooling performance of CBM-MVD quadrants. First results on the cooling performance, given by both, the material properties of TPG (τ_{fast}) and the power to evacuate the heat from the carrier (τ_{slow}), have been derived by measuring characteristic time constants of heating curves. The measured time constant τ_{fast} underlines the excellent thermal performance of this material. Temperature differences and τ_{slow} offer a quantitative assessment to further improve the heat evacuation and selecting the optimum TPG thickness. Next campaigns will focus on characterizing Parylen-coated TPG, even thinner pyrolytic graphite foils (PGS) and pCVD-Diamond. They will be complemented by and compared to thermal CAD simulations aiming at optimizing the contact to the heat sink and its design.

References

[1] Diamond Materials www.diamond-materials.com; Momentive momentive.com, Optigraph www.optigraph.eu

[2] P. Klaus, priv. communication

* supported by BMBF (05P15RFFC1), HGS-HIRe and GSI.

The TOF FAIR phase 0 project *

I. Deppner[1], *N. Herrmann*[1], *and the CBM-STAR eTOF working group*[1]
[1]Ruprecht-Karls-Universität Heidelberg, Heidelberg, Germany

The FAIR phase 0 project of TOF comprises the installation and operation of CBM TOF MRPCs (MRPC3a/b [1]) in the STAR experiment at BNL and the analysis of the data taken during the Beam Energy Scan (BESII) in 2019/20.

For BESII the STAR collaboration aims to increase the acceptance of their detector in the pseudorapidity range between $1.0 \leq \eta \leq 1.5$. Therefore an upgrade of the inner TPC (iTPC) is foreseen. The upgrade improves the momentum resolution for particle tracks pointing in forward direction. In order to improved also the particle identification (PID) capability in the same acceptance range an additional upgrade on the TOF system (eTOF) is intended. The impact of these upgrades are clearly visible in Figure 1 [2] showing the acceptance region and PID limitations for electrons (upper left), pions (upper right), kaons (lower left) and protons (lower right). The eTOF upgrade

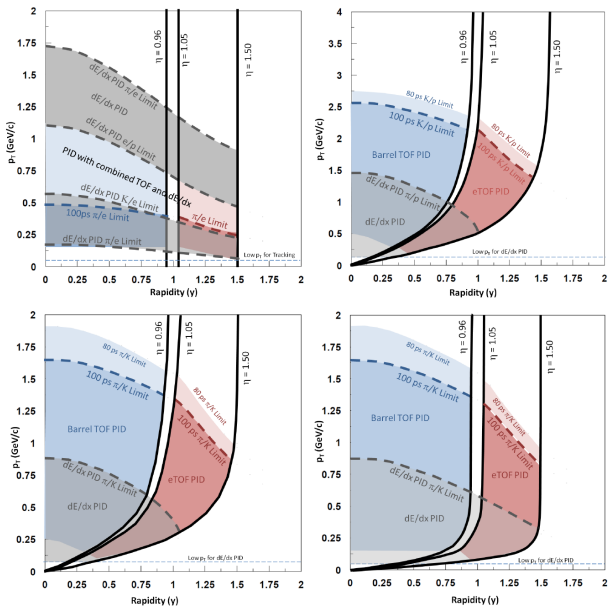

Figure 1: The $p_T - y$ acceptance region for electrons (upper left), pions (upper right), kaons (lower left) and protons (lower right) showing the limits due to tracking and PID.

requires the installation of a new TOF system in the abovementioned pseudorapidity range. This system will be provided by CBM TOF subgroups from China and Germany in the context of the CBM FAIR phase 0 program. It includes about 6 % of the CBM TOF MRPCs with the complete front end and readout electronics and the necessary software packages. The operation of this CBM TOF subsystem opens the opportunity to gain experience with the handling of the system, with the calibration procedures and data preprocessing leading to a reduced commissioning time within CBM later on. In addition the CBM members have access to the entire data set produced by STAR during BESII. After the BESII campaign in 2021 the full system will be dismantled and shipped to back FAIR where the componets will be used as part of the final CBM-TOF wall.

The conceptional design of the eTOF is depicted in Figure 2. Each STAR CBM TOF module contains 3 MRPC3a/b counters. The modules will be mounted on a frame sitting at the east side magnet pole tip of the STAR experiment forming a wheel. The modules are arranged in three layers grouped in 12 sectors which have full overlap with the TPC sectors. The eTOF wheel has in total an active area of about 9.3 m^2 and comprises 6912 readout channels. This geometry was implemented in CBM ROOT. Simulations show that in the fixed target mode which is also anticipated by the STAR collaboration a maximal particle flux of about 45 $\mathrm{Hz/cm}^2$ and a multi hit probability of 7.5 % is reached.

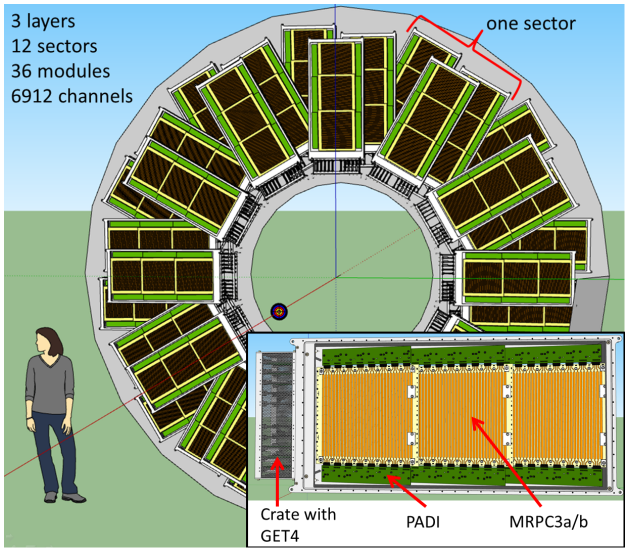

Figure 2: Illustration of the STAR eTOF wheel. The modules are arranged in 12 sectors and contain 3 MRPC3a/b each.

In order to make a first DAQ integration test a mod-

*This project was partially funded by BMBF 05P12VHFC7 and by EU/FP7-HadronPhysic3/WP19 and has received funding from the European Union's Horizon 2020 research and innovation program under grant agreement No 654168.

DOI:10.15120/GR-2017-1

ule (conf. Fig. 3) housing two MRPC3b counters produced at USTC was shipped to BNL and mounted at the 6 a clock position at the magnet pole tip in October 2016 (see Fig. 4). The goal is to participate in the physics run (Run17) starting in Feb. 2017 and test all components under real beam conditions. The counters were positioned behind each other in the module in order to find coincidences among themselves. The data readout is based on an AFCK

Figure 3: View inside the open STAR CBM TOF module.

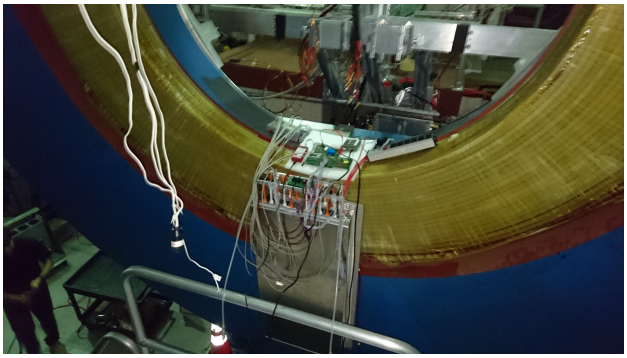

Figure 4: STAR CBM TOF module mounted on the east pole tip of the STAR experiment.

board and the FLES system as indicated in Fig. 5 which is in contrast to the triggered STAR DAQ free running. Since the AFCK is not magnetic field resistant it is placed in a region with very low field 6 m away from the module. The data are transmitted via 100 m long optical fibers to the FLIB of the DAQ-PC which is sitting in the STAR DAQ-room. A synchronization scheme has been developed for the clocking systems by locking our CLOSY system to the STAR TDC clock and the AFCK firmware was extended to interpret the trigger token sent by the STAR trigger system and inserting it into the data stream. If such a token word is detected in the data by the CBM monitoring system based on CBMROOT a window with a proper time shift is extracted from the data stream and the data are sent to the STAR event builder. The system can be inspected and monitored via the CBMROOT web-interface and in general is setup such that no CBM manpower is required to be present on site during data taking.

That the DAQ system and the interface to STAR indeed works can be seen in Figure 6. It shows the time difference between the MRPC hits and the STAR trigger. At a time difference of about 1.75 μs a correlation between trigger and MRPC hits is visible.

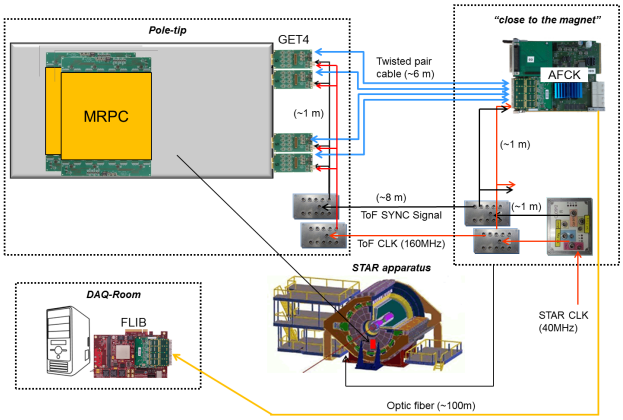

Figure 5: Overview of the CBM components used during the STAR physics run in 2017.

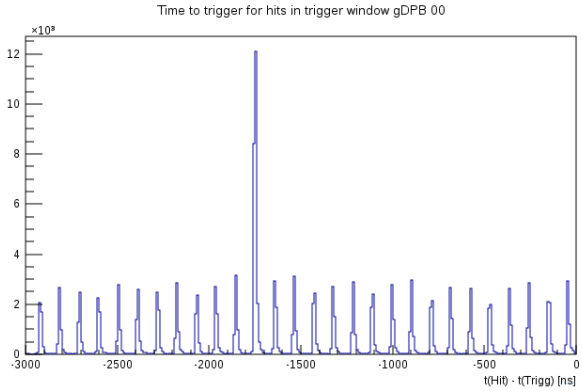

Figure 6: Time difference between the MRPC hits and the trigger token. At about 1.75 μs a correlation between trigger and MRPC hits is visible.

The time line for the next major steps are the following:

- Installation of a full sector (3 modules) in summer 2017,
- 2^{nd} system integration test with one full sector by participating in the physics run (Run18) in February 2018,
- shipping 36 modules including infrastructure to BNL in summer 2018,
- installation and commissioning in fall 2018,
- start of BESII campaign in February 2019,
- decommission and shipping all modules including infrastructure to FAIR in 2021.

DOI:10.15120/GR-2017-1

References

[1] N. Herrmann et al. “CBM-TOF Technical Design Report”, http://repository.gsi.de/record/109024/files/, October 2014

[2] “Physics Program for the STAR/CBM eTOF Upgrade”, arXiv:1609.05102

DOI:10.15120/GR-2017-1

Common CBM beam test at the CERN SPS 2016

D. Emschermann and the CBM collaboration
GSI, Darmstadt, Germany

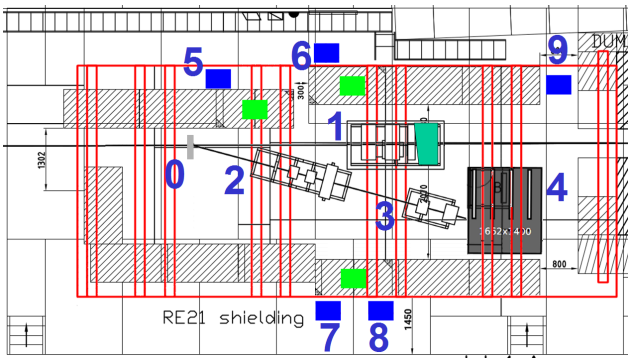

Figure 1: Layout of the RE21 experimental area. 0: Pb-foil target, 1: mainframe with TOF MRPC and MUCH GEM detectors, 2: Bucharest TRD setup, 3: Bucharest TOF MRPC setup, 4: Münster/Frankfurt TRD setup, 5: service rack for TOF/MUCH mainframe, 6: free-streaming DAQ rack, 7: service and readout rack for Bucharest detectors, 8: TRD gas analysis rack, 9: service and readout rack for Münster/Frankfurt detectors

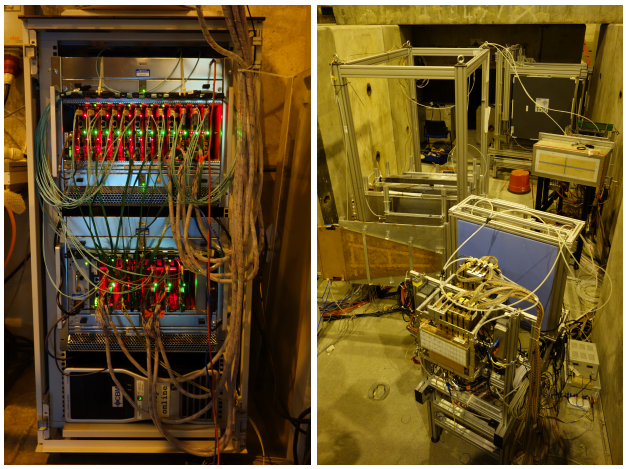

Figure 2: (left) The free-streaming DAQ system (6) for MUCH and TOF consisting of 18 AFCK boards operated in 2 microTCA crates in a common rack. (right) A downstream view of the RE21 detectors during the setup phase.

In November and December 2016 the CBM DAQ, MUCH, TOF and TRD subgroups gathered at the CERN SPS for the annual heavy ion run [1, 2, 3, 4, 5, 6]. A dedicated radiation bunker, see Fig. 1, was prepared along the H4 beamline in the North Area. A large number of full-size detector prototypes (MWPCs, GEMs, MRPCs, Bakelite RPCs and diamond counters) from pre-series production were installed in the zone, see Fig. 2 (right). The SPS accelerator delivered a primary Pb-beam at momenta of 13 AGeV/c, 30 AGeV/c and 150 AGeV/c which was impinging on a 1 mm thick Pb-foil as target. The CBM detectors were installed at small angles to the primary beam to measure the spray of secondary particles at hit rates of up to few kHz/cm^2.

A highlight of this beam test was the new, free-streaming DAQ system, see Fig. 2 (left). It was used to readout the TOF MRPCs equipped with GET4 electronics (using AFCKs with gDPB firmware), MUCH GEM detectors readout with NXYTER v2.0 ASICs (employing AFCKs with nDPB firmware). These two DAQ branches were kept in phase by the timing and synchronisation system [7] (made of AFCKs with tDPB firmware). In a separate TRD DAQ setup, the new SPADIC v2.0 was readout with an AFCK board connected to a FLIB node [8]. New hardware [9] and software tools for configuration and online monitoring for the DAQ system were developed for this beamtest [10, 11, 12]. The operation of CBM subsystems with a common DAQ system is a first step towards the future miniCBM@SIS18 setup [13].

References

[1] F. Fidorra et al., *Development and construction of a gas system for the CBM-TRD*, this report

[2] P. Kähler et al., *Operation and measurement programme of a SPADIC readout chain on type-8 CBM-TRD prototypes at the CERN-SPS in 2016*, this report

[3] F. Roether et al., *Construction of type-8 MWPCs for the CBM-TRD*, this report

[4] A. Kumar et al., *Beamtest of triple GEM prototypes with Pb+Pb collisions at CERN SPS*, this report

[5] A. Bercuci et al., *Bucharest RPC and TRD prototypes at the CERN-SPS test beam in 2016*, this report

[6] M. Petriş et al., *CERN-SPS in-beam performance test of the new strip readout MRPC prototypes for the inner zone of the CBM-TOF wall*, this report

[7] L. Meder et al., *Integration of the Timing Synchronizer System into the Readout System for the Beamtime at CERN SPS in 2016*, this report

[8] C. de J. García Chávez et al., *Development of the SPADIC v2.0 readout chain at the CERN-SPS in 2016*, this report

[9] C. de J. García Chávez et al., *Design and development of the nDPB FPGA mezzanine card*, this report

[10] P.-A. Loizeau et al., *Control software for the DPB based readout chains and related beamtime activities*, this report

[11] F. Uhlig, *Online monitoring with* `cbmroot`, this report

[12] M. Mitkov et al., *Prototype of EPICS based detector control system for the ToF test stand at CERN 2016*, this report

[13] C. Sturm et al., *mCBM@SIS18 - a CBM full system test in high-rate nucleus-nucleus collisions at GSI / FAIR*, this report

DOI:10.15120/GR-2017-1

DiRICH readout electronics - status and first measurements

V. Patel[1], *C. Pauly*[1], *J. Michel*[2], *P. Skott*[3], *M. Traxler*[3], *C. Ugur*[3], *and K.-H. Kampert*[1]
[1]Wuppertal university; [2]Frankfurt university; [3]GSI Darmstadt

The realization of the new DiRICH electronic readout chain for Hamamatsu H12700 MAPMTs (CBM- and HADES RICH detectors), as well as for Photonis MCP sensors (PANDA DIRC), has seen major progress over the last year. Since mid 2016, first prototype modules of all components are available for detailed testing and evaluation. Figure 1 shows photographs of a partly equipped 3x2 MAPMT module, and of the individual DiRICH, DiRICH-Combiner, and DiRICH-Power cards. All these modules seem to work as expected, no critical design flaws have been encountered yet.

The only major item still missing is a working FPGA design for the full 32ch TDC. The TDC base design (even with 64 channels) for the Lattice ECP3 platform of the HADES TRB3 "Trigger and Readout board" is in use since many years, and has to be adapted now to the Lattice ECP5 platform of the DiRICH module. Here, the loss of the main FPGA-TDC developer is causing a critical delay. So far, only a first 4 channel version of the TDC is available for the DiRICH, proving the principal feasibility of the project. However, all tests of the DiRICH readout chain so far look very promising, some first results are summarized below.

Testing of the full readout chain is carried out at two places: At GSI, in the HADES cave, a large test chamber has been installed, already carrying the new HADES RICH MAPMT photon detector flange (see Figure 2). This setup will later allow for a full size system test, when larger numbers of modules become available. After successful commissioning of the new photon detector, the whole detector flange will be craned to the HADES frame and mounted to the HADES RICH. At the moment, blind flanges cover all open module ports, allowing for tests with single MAPMTs and few modules. A pulsed laser system (Picoquant 630nm, 50ps pulse length, kindly provided by the GSI PANDA group) is installed in the tank, allowing for precise timing measurements based on single photons. An additional LED light source in the tank, connected to an adjustable DC current source, allows for high rate tests with uncorrelated photon rates (in addition to the triggered light source) of up to several 100 kHz per channel, comparable to the maximum photon rates expected for CBM SIS 100 high rate experiments.

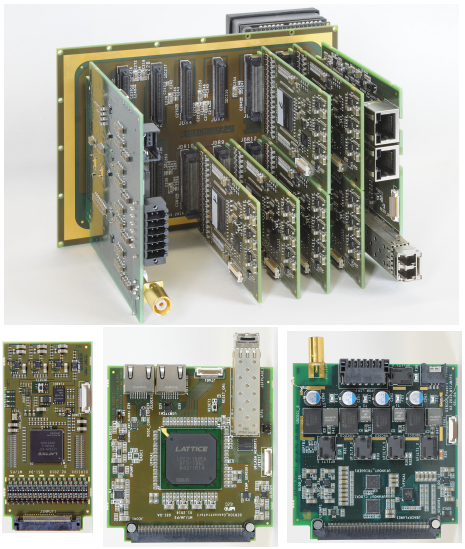

Figure 1: A 3x2 MAPMT readout module (top), with one out of 6 MAPMTs on front side, and few 32ch DIRICH FPGA-TDC frontend modules (lower left), a DiRICH-Power supply module (lower right), and a DiRICH-Combiner module (lower center).

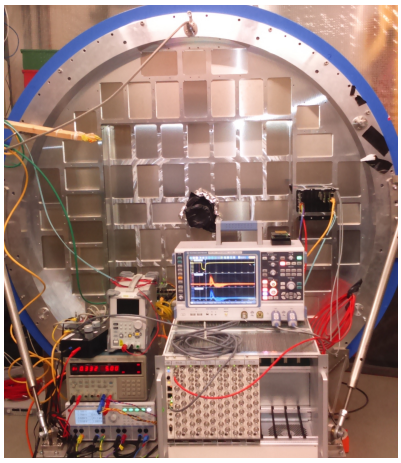

Figure 2: Test setup in the HADES cave, showing the new HADES RICH photon detector flange mounted to the test chamber, with one 3x2 readout module installed for testing.

The new CBM RICH prototype box for COSY beam tests is used for smaller scale tests of up to 2 fully equipped readout modules at Wuppertal university (see [1]).

The most critical part in the DiRICH design is the analog input stage. The input signals of the MAPMTs (few mV average amplitude for single photons) are galvanically decoupled using transformers, and then amplified ($\simeq \times 30$) in a single stage transistor amplifier operating at very low Vcc of only 1.1V to minimize power consumtion. The amplified signal is then discriminated and time stamped inside the FPGA.

DOI:10.15120/GR-2017-1

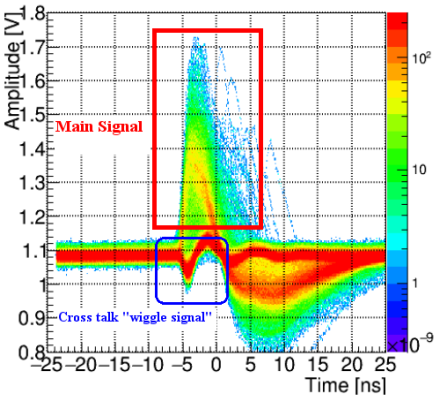

Figure 3: Typical MAPMT single photon signals from DIRICH after preamplification.

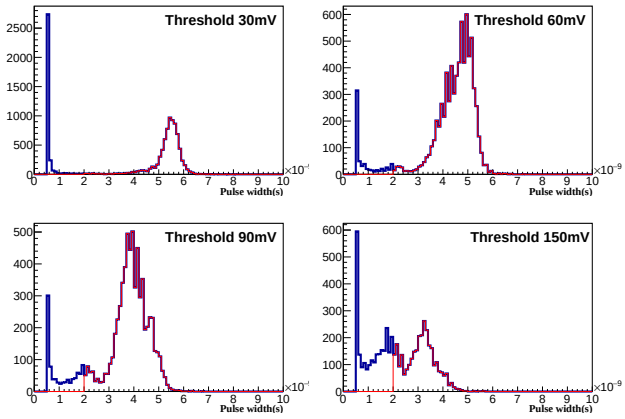

Figure 4: Time over threshold information for various software threshold settings

In order to test the analog part, we have equipped a single DiRICH module with two active, 4 GHz oscilloscope probes (input impedance 0.8 pF), read out by a fast digital oscilloscope. The probes are connected to the preamp output of two different channels. This setup serves to visualize the amplified input signals directly before entering the FPGA for discrimination and digitization. Moreover, the digital scope allows us to save the full signal traces of both channels for later offline analysis (with up to 100 events/second). Analyzing these data offline allows us to simulate the FPGA functionality (TDC and discrimination) in software, and to study the leading- and trailing edge timing precision, Time-over-Threshold measurement, threshold behaviour, efficiency, or noise, independant of the FPGA-TDC itself. In addition, one can also correlate these time-based measurements with signal amplitude or charge extracted from the scope traces (which are not available from the TDC measurement), for performance evaluation. This approach turned out to be extremely helpful not only for characterizing the analog input stage, but also for debugging of the FPGA-TDC design, since we know exactly what data to expect from the TDC measurement.

Figure 3 shows the preamplifier output signal for single photon pulses, directly before discrimination in the FPGA. After shaping, the photon signals have a mean positive amplitude of 250 mV (gain $\simeq \times$ 30), with a FWHM of 4-5 ns. A pronounced undershoot of the shaped signal is intentional in order to achieve a fast threshold crossing for trailing edge time measurement.

The laser intensity in these measurements was adjusted such, that only in 10% of pulses a single photon is detected in a given channel. In triggered events with no photon hitting the particular channel, a different signal shape can be observed, attributed to a capacitive coupling in the MAPMT anode plate. This "wiggle" signal is of opposite polarity, and comparatively small. The amplitude of this signal scales with the number of simultaneous photon hits on the full MAPMT surface, which is here in the order of 6-10, a realistic upper value for later detector operation. For low discriminator threshold settings, this cross talk signal could produce additional "ghost" hits, causing smearing of the Cherenkov ring pattern. This effect of strongly increased cross talk hits at lower thresholds has been already observed (though not fully understood at that time) in the last CERN test beam 2014, where the amplitude sensitive PADIWA readout chain was used, triggering on the leading edge of the signal only. In previous measurements using the charge-sensitive nXYter readout chain, this cross talk signal was much suppressed due to its bipolar shape in combination with the large integration time of the slow shaping amplifier input stage.

A powerful tool to effectively suppress these cross talk "wiggle" pulses in the DiRICH readout is provided by the simultaneous measurement of leading- and trailing edge time, i.e. by the Time-over-Threshold (ToT) of the signal. For relatively low thresholds (30-90 mV after preamp), the ToT of the wiggle signal is rather small (below 1-2 ns), where the single-photon pulses have a ToT in the order of 4-5 ns. The observed ToT distribution for various threshold settings (based on the offline analysis of the scope trace data) is shown in Figure 4. Applying a cut of ToT $>$2 ns (red graph), the pulses induced by crosstalk can be easily suppressed, as long as the threshold is reasonably low ($<$100 mV).

The effectiveness of the ToT cut can be clearly observed in the leading/rising edge arrival time distribution with respect to the trigger signal of the laser pulser, shown in Figure 5. Without ToT cut, two peaks are observed: The early peak around T=0 ns stems from real photon hits, where the hits induced by crosstalk cause a delayed signal around T=4 ns due to their opposite polarity. Applying the cut on ToT $>$ 2 ns completely suppresses this delayed peak without loss of real photon events, even at very low thresholds (red graph). The width of the photon peak (RMS $\simeq$ 480 ps) corresponds well to the expected PMT timing precision (MAPMT Transit-Time-Spread TTS $\simeq$ 300 – 400 ps), in particular if keeping in mind that no walk correction is applied.

DOI:10.15120/GR-2017-1

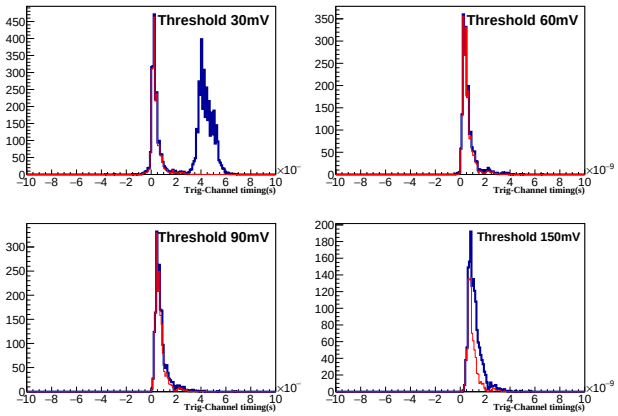

Figure 5: Leading edge timing difference between laser trigger and one of the channels

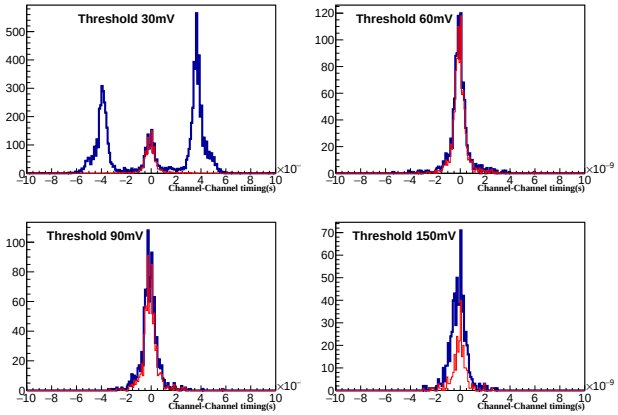

Figure 6: Leading edge timing difference between two channels

Figure 6 shows the leading edge time difference between the two channels equipped with the scope probes. This distribution, with its three distinct peaks in the time difference observed at low threshold, is well reproduced also in the first measurements with the full FPGA-TDC, but caused some confusion at first observation. It can now be fully understood based on the signal characteristics discussed above: The center peak, around ΔT=0, is caused by events, where both channels either detected one simultaneous photon each (laser pulse length 50 ps), or both channels only detected a cross talk signal (the latter is suppressed here by the scope acquisition trigger). The side peaks at +/- 4 ns correspond to events with a photon in one channel, and a cross talk signal in the other (blue distribution). Applying the ToT cut on both individual channels fully suppresses the side peaks (red distribution), and gives a nice single correlation peak close to $\Delta T \simeq 0$. The width of this peak (RMS $\simeq$ 650 ps) is again a good measure for the overall system timing precision, and is in fair agreement with the expected value of $\sqrt{2} \times TTS$=430–550 ps.

The DiRICH-Power module allows two different operation modes to provide LV power to all modules: Either

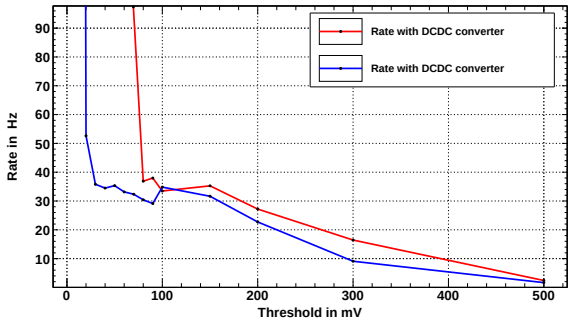

Figure 7: Rate using DCDC and without DCDC converter.

using on-board DCDC converters to generate the required 1.1 V / 1.2 V / 2.5 V and 3.5 V supply voltages out of a single low-current input at 20-30 V, or by external supply via 4 different input lines, providing only filtering and monitoring on the module itself. The second method avoids operation of noisy DCDC converters close to the sensitive analog input electronics of the DIRICH modules, but requires substantial cabling effort, in particular in view of the large required current (up to 15 A) on the 1.1 V supply line, where the voltage drop on the supply cables becomes substantial. A comparison of both operation modes is given in Figure 7, showing the detected hit rate of a single MAPMT channel as function of threshold. The observed plateau around 35 Hz corresponds to the MAPMT single photon dark rate in the given pixel. Without using the DCDC supply mode, threshold settings down to 20 mV can be achieved (after preamplification, corresponding to $<$1 mV MAPMT signal). In DCDC powering mode, the system noise kicks in at thresholds around 75 mV. However, additional cuts on the ToT will allow to partly suppress this noise in the offline analysis. Additional copper shielding enclosing the DCDC converters is already foreseen and will be tested.

The first tests of the new DiRICH readout concept look very promising, and seem to qualify the overall concept. In particular, the importance of the ToT-measurement for background suppression in comparison to simple leading edge measurement already became evident. A few minor design issues have already been found, and will be fixed in a second iteration of the DiRICH module, which is under production now.

For further validation of the concept a test beam at COSY/Jülich is scheduled for end of May, where two fully equipped 2x3 MAPMT modules will be put into operation. We hope, that a first 32ch FPGA-TDC design will become available until then. If everything goes well, we plan to start mass production of all modules end of 2017, in order to equip the full HADES RICH detector in time for the next HADES beamtime at SIS18 earliest mid 2018.

References

[1] C. Pauly et al., ”A small RICH prototype for beam tests at COSY”, this report.

DOI:10.15120/GR-2017-1

mCBM@SIS18 – a CBM full system test-setup for high-rate nucleus-nucleus collisions at GSI / FAIR

C. Sturm[1], J. de Cuveland[3], D. Emschermann[1], V. Friese[1], N. Herrmann[2], P.-A. Loizeau[1], W. Niebur[1], A. Senger[1], F. Uhlig[1] for the CBM collaboration

[1]GSI, Darmstadt, Germany; [2]Ruprecht-Karls-Universität Heidelberg, Germany; [3]Frankfurt Institute of Advanced Studies (FIAS), Frankfurt am Main, Germany

The Compressed Baryonic Matter experiment (CBM) is one of the major experimental projects at the upcoming FAIR facility. It will explore strongly interacting matter at highest net-baryon densities by investigating nucleus-nucleus collisions in fixed-target mode with extracted beams from the SIS100. The unique feature of CBM is its high-rate capability of up to 10^7 interactions per second, which will make it sensitive to extremely rare probes and, consequently, will give it a high discovery potential. In order to achieve these ambitious goals, CBM will employ fast and radiation-hard detectors and readout electronics. Moreover, a novel, free-streaming data acquisition system will be used, which aggregates the data sent by the self-triggered front-end electronics and push them to an online compute farm for data reconstruction and selection in real time.

By today, the design of the detector and electronics components for CBM is largely completed, and series production is going to start. The components were tested in the laboratory and in beam. However, it is highly desirable to test and optimize the operation of the full system of complex hard- and software components – from the detectors over the readout ASICs and the DAQ to on- and offline data processing and analysis – under realistic experiment conditions before the installation and commissioning of the full CBM detector setup.

We thus are going to install a full-system test-setup for CBM at the GSI/FAIR host lab site under the name *mCBM@SIS18* ("mini-CBM", later shortened to mCBM). The test setup shall include detector modules from all CBM detector subsystems (MVD, STS, RICH, MUCH, TRD, TOF, ECAL, see [1] - [5]) using (pre-)series production specimen. Hence, mCBM will allow to test and optimize

- the operation of the detector prototypes in a high-rate nucleus-nucleus collision environment,
- the free-streaming data acquisition system including the data transport to a high-performance computer farm located in the Green IT Cube,
- the online track and event reconstruction as well as event selection algorithms,
- the offline data analysis and
- the detector control system.

Commissioning and running mCBM in the first two years (2018 and 2019) will complete our knowledge on proper functioning as well as on the performance of the CBM detector systems and their associated Front-End Electronics (FEE) before the final series production starts. The experiences gained during the complete mCBM campaign will significantly shorten the commissioning period for the full CBM experiment at SIS100.

The mCBM test-setup will be positioned downstream a solid target under a polar angle of about 25° with respect to the primary beam (see Fig. 3 and 3). mCBM does not comprise a magnetic field, and, therefore, will measure charged particles produced in nucleus-nucleus collisions traversing the detector stations following straight trajectories. The tracking system comprises 2x STS (mSTS), 3x MUCH (mMUCH) and 4x TRD stations (mTRD) in total 9x track-

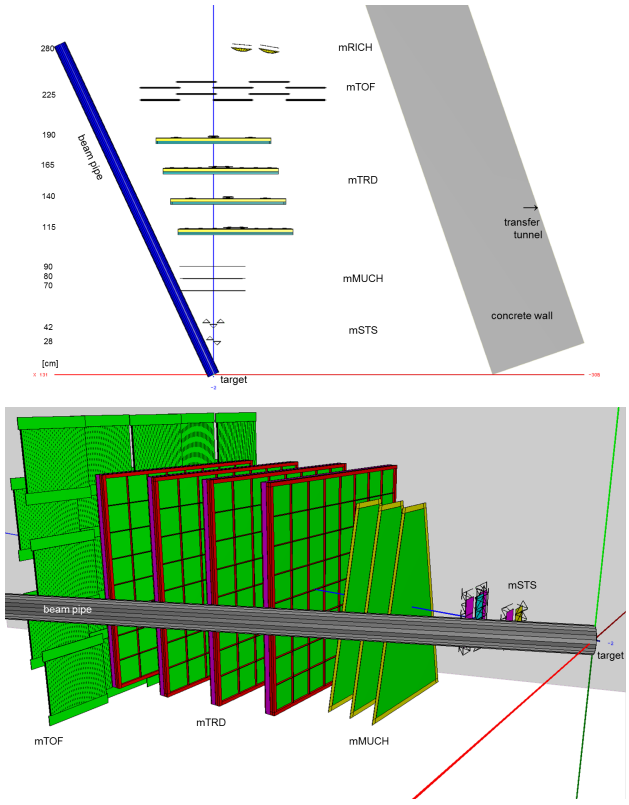

Figure 1: Top view (top panel) and side view (bottom panel) of the mCBM test setup at the HTD cave. The detector stations are aligned at an emission angle of about $\Theta_{lab} = 13°$ (beam pipe side, y = 0). Note, the GEM counters of the mMUCH subsystem are trapezoidal shaped (see lower panel), which is not visible in the top-view projection.

DOI:10.15120/GR-2017-1

ing layers which provide redundant position information and allow to perform tracklet searches. The setup will possess a high-resolution time-of-flight system consisting of a fast and segmented diamond counter for time-zero (T_0) determination in front of the target as well as a TOF stop wall (mTOF). Four RICH solid-state-modules forming the mRICH subsystem will be placed behind the mTOF detector and deliver a second measurement of the particle velocity in a selected acceptance window. A small calorimeter (mECAL) will also be mounted behind the mTOF covering a reduced acceptance. Additionally, 8x PSD prototype-modules (mPSD) will be used to characterize the collision geometry. In a later stage MVD stations (mMVD) will be included into the test-setup enabling a high-precision vertex reconstruction. For tracks passing the active area of the mSTS, mMUCH, mTRD and mTOF subsystems the covered Θ_{lab} range results to $13° - 37°$. According to the needs, the initial configuration of the mCBM test-setup is rather versatile and can be variably adapted.

The mCBM design focuses on the system performance aspect integrating existing (or currently under construction) prototype modules of all CBM detector subsystems into a common, high-performance free-streaming data acquisition (DAQ) system. The detector stations will be equipped with final readout electronics containing ultra-fast and radiation-tolerant ASICs as front-end chips followed by CERN GBTx-based radiation-tolerant data aggregation units. Further down-stream, the data streams are handled by Data Processing Boards (DPB) containing powerful FPGAs and are forwarded via FLES Input Boards (FLIB), a PCIe based FPGA board, to a large-scale computer farm, the First-Level Event Selector (FLES), which performs on-line track and event reconstruction and selection, see Fig. 2.

The installation site for the mCBM test-setup is the detector test area named HTD in the GSI nomenclature (see Fig. 3) situated at the beam entrance of the experimental area cave-C (HTC) hosting the nuclear structure experiment R^{3}B. Although the space is very limited in the HTD area, the compact mCBM setup measuring a full length of about 3 m will fit into the HTD cave.

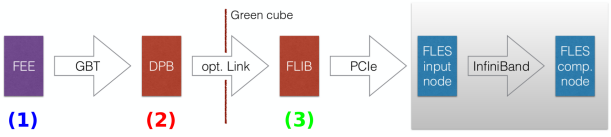

Figure 2: Envisaged mCBM readout chain for the startup phase, based on DPB and FLIB. The mCBM subsystems are equipped with individual front-end electronics FEE (1). These front-ends are interfaced by the GBTx ASIC, which forwards the detector data via optical GBT link. All GBT links are received by the DBP layer located at 50 m distance in the DAQ container (2). The DPB is a FPGA based board which allows for subsystem specific pre-processing of the arriving data stream. A long distance optical link connects the DPB output to the FLIB board installed in the FLES input node in the Green IT Cube (3).

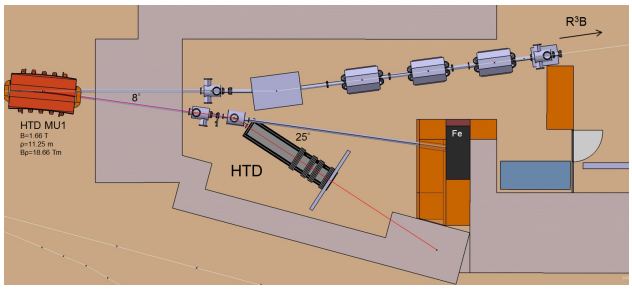

Figure 3: Design of the HTD site modified for the mCBM test-setup.

As illustrated in Fig. 3, the incoming beam will be either transported to the R^{3}B experiment or deflected to the detector test area HTD by a switching magnet (dipole magnet) mounted directly in front of cave-C carrying the name HTD MU1 in the GSI nomenclature. The design of the switching magnet HTD MU1 leads for the (design) track with a bending radius of $\rho = 6.25$ m to an effective deflection angle of 14.5°, corresponding to an magnetic rigidity of $B\rho = 10$ Tm. Using HTD MU1 as currently designed would substantially limit the projectile energy available at the HTD cave. Accordingly the maximum kinetic energy for heavy projectiles like Au would be limited to 0.45 AGeV generating unrealistic conditions due to a large number of low-momentum fragments emitted during the collision.

In order to exploit the full beam energy range of SIS18 we plan to bend the beam projectiles on the expanded track with a significantly larger bending radius ρ through the switching magnet HTD MU1. Choosing the expanded track with a radius of $\rho = 11.25$ m results for the top rigidity of the SIS18 synchrotron of 18.66 Tm in an effective deflection angle of 8.0°. The loss in horizontal aperture of 22 mm [6] is acceptable and will not limit the beam quality.

To verify the performance of the CBM data taking concept the mCBM setup will be used to reconstruct physics observables that can be compared to published data. A feasibility study with the mCBM setup was performed using the Λ production probability in heavy-ion collisions as a benchmark observable. At SIS18 beam energies Λ baryons are produced close to or below the free NN production threshold. Thus their production probability is rather small (see Table 1) posing a CBM-like challenge to the reconstruction and selection task.

	Ni + Ni at 1.93 AGeV	Au + Au at 1.24 AGeV
Λ production probability	$2.3 \cdot 10^{-2}$	$3.2 \cdot 10^{-2}$
signal counts	5645	2011
signal / background	8.4	0.24
significance	71.0	19.8
efficiency · acceptance	$1.7 \cdot 10^{-3}$	$7.0 \cdot 10^{-4}$

Table 1: Results of MC simulation of 10^8 UrQMD minimum-bias events with full mCBM detector response.

DOI:10.15120/GR-2017-1

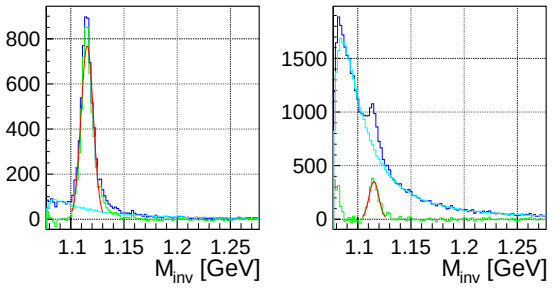

Figure 4: Λ-identification in UrQMD events in Ni + Ni collisions at 1.93 AGeV (left) and in Au + Au at 1.24 AGeV (right). Invariant mass distributions are shown for pair combinations (combinatorics) within events (dark blue), for pair combinations from mixed events (cyan) and for the subtracted distribution (green). Statistics information is obtained from a Gaussian fit to the subtracted distribution (red line) and is summarized in Table 1.

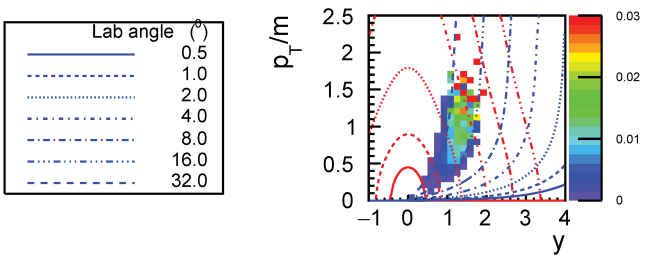

Figure 5: Efficiency of reconstructed Λ - baryons with mCBM produced in Ni + Ni collisions at 1.93 AGeV (input: events generated with UrQMD). Red and blue lines indicate constant laboratory momenta and laboratory polar angles, respectively.

Since mCBM does not include a magnetic field for momentum measurement, the reconstruction has to be done via time-of-flight (TOF) and track topology. That the limited information available is sufficient for Λ reconstruction is demonstrated by a MC simulation, modeling the full data analysis chain. For simplicity, only STS and TOF hits are considered for the reconstruction algorithm.

The result of the procedure for 10^8 minimum bias UrQMD events of the reactions Ni + Ni at an incident energy of 1.93 AGeV and Au + Au at 1.24 AGeV is shown in Fig. 4.

The phase space coverage is shown in Fig. 5 demonstrating that the acceptance of mCBM is limited to a small angular range close to mid-rapidity. In this range published data are available in [7] [1] that the mCBM results can be quantitatively compared to. It is worth noting that the technical goal and challenge is to reconstruct the invariant mass distributions shown in Fig. 4 within a time period of 10 s data taking at SIS18, assuming a beam intensity of 10^8 ions per second bombarded on a 10 % interaction target.

To get even closer to the load anticipated for CBM operation at SIS100 the feasibility of reconstructing Λ baryons in the heavier system Au + Au implying lower beam energies was investigated. Fig. 4 (right) presents the results of the analysis for the reaction Au + Au at an incident beam energy of 1.24 AGeV employing the same selection cuts that were used for the Ni + Ni analysis (see Fig. 4, left panel). After background subtraction a clear peak is visible albeit with a much worse signal to background ratio as compared to the Ni + Ni case (see Table 1). Improvements are certainly possible by tuning the selection cut values. However, at the current state of planning the presented performance obtained on a clean event based reconstruction is considered to be sufficient to demonstrate mCBM's capabilities.

Thus also all the background rejection strategies necessary to reconstruct rare probes with CBM at SIS100 can be prepared and exercised with mCBM. In addition, if the technical goals of mCBM are achieved a measurement of the Λ production excitation function should become feasible. This was not yet measured in the SIS18 beam energy range thus offering a unique opportunity to contribute to world data, although the covered phase space is limited and therefore systematic errors become large when extrapolating to unmeasured regions.

The successful implementation and demonstration of the technical capabilities would also open the road to more relevant physics observables like the measurement of light hypernuclei. The beam time request for more physics oriented observables will be placed in the next beamtime period from 2020 – 2021, once the preliminary results are supporting the high expectations.

[1] HADES results on Λ production in Au + Au collisions at 1.23 AGeV will be published soon.

References

[1] J. Heuser, W. F.J. Müller, V. Pugatch, P. Senger, C. J. Schmidt, C. Sturm and U. Frankenfeld, Technical Design Report for the CBM Silicon Tracking System (STS), GSI-2013-05499, http://repository.gsi.de/record/54798

[2] S. Chattopadhyay, Y. P. Viyogi, P. Senger, W. F.J. Müller and C. J. Schmidt, Technical Design Report for the CBM : Muon Chambers (MuCh), GSI-2015-02580, https://repository.gsi.de/record/161297

[3] C. Höhne, Technical Design Report for the CBM Ring Imaging Cherenkov Detector (RICH), GSI-2014-00528, http://repository.gsi.de/record/65526

[4] N. Herrmann, Technical Design Report for the CBM Time-of-Flight System (TOF), GSI-2015-01999, https://repository.gsi.de/record/109024

[5] F. Guber and I. Selyuzhenkov, Technical Design Report for the CBM Projectile Spectator Detector (PSD), GSI-2015-02020, https://repository.gsi.de/record/109059

[6] C. Mühle (GSI), private communication

[7] M. Merschmeyer et al. (FOPI collaboration), K^0 and Λ production in Ni+Ni collisions near threshold, Phys. Rev. C 76 (2007) 024906

A slow control system for the HADES and CBM RICH detectors *

A. Weber[1], *P. Zumbruch*[2], *and C. Höhne*[1]
[1]Justus-Liebig Universität, Giessen, Germany; [2]GSI, Darmstadt, Germany

An EPICS based slow control system for the HADES RICH700 upgrade and the future CBM RICH is developed. The slow control system is server-client-model based and highly flexible due to variations in the experimental setup. The control software for the ISEG HV power supply (see Fig. 1) is designed in a 3 layer outline. It allows the control of every channel of every module of the crate individually, but also the control of predefined groups of channels from different modules. In addition it is possible to group channels via the GUI, too. The ISEG HV crate (*ECH 44A*) has a *CC24* Master module which includes the EPICS IOC. This allows to run the slow control software of the crate without any additional computer. The HV crate has 6 *EHS F620n-F_SHV* modules with 16 channels each. The modules are limited to 1,5 kV and with single channel floating-GND.

Figure 1: The ISEG crate with 6 modules à 16 channels and a CC24 master.

To cope with low voltage a TDK Lambda Genesis 60-40 is used (see Fig.2). The EPICS IOC runs on an own computer which is connected to the TDK Lambda via LAN. The IOC uses `StreamDevice` with an own protocol for the device. It is possible to control the voltage, set current limits and control different statuses of the LV device.

Figure 2: The TDK Lamda low voltage power supply.

During the experiment the temperature and the humidity will be measured. The temperature is mapped with many DS18B20 1-Wire Sensors from *Maxim Integrated*. To measure the humidity HDC1000 humidity sensors from *Texas Instruments* are used. These sensors support the I^2C protocol and have address pins which allow to use up to 4 of these sensors at one port (see Fig.3). Both sensor types are connected to a HadCon2 Board which controls the pins. The HadCon2 is connected to a raspberry pi 2 model B via USB connection. The EPICS IOC runs on the raspberry pi and sends the HadCon2 the commands for the measurement of temperature and humidity.

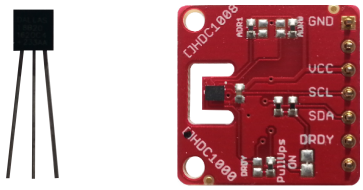

Figure 3: left: One DS18B20 1-wire sensor from Maxim Integrated. right: A HDC1000 sensor on a breakout board.

The HADES RICH upgrade will use many DIRICH boards which have a 1-wire temperature sensor. This temperature can be readout via the TrbNet. Therefore an EPICS IOC is written. It gets the value from many different boards with one call which reduces the traffic on the TrbNet. It is also possible to get more further status values from the TrbNet with the IOC.
The Control System Studio (CSS) is used as the GUI of the HADES RICH experiment and shows the EPICS process variables in a human readable, graphical layout (see Fig.4). It replaced the *Motif Editor and Display Manager* (MEDM) which is known from previous HADES running periods.

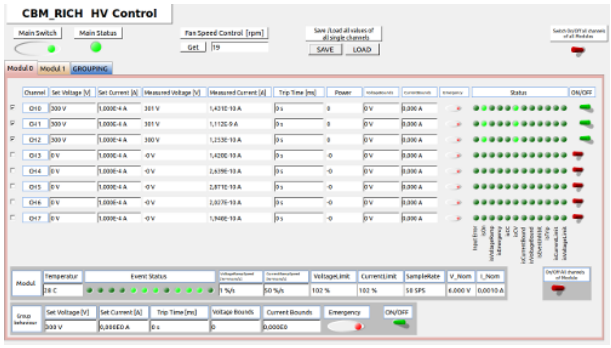

Figure 4: The CSS BOY GUI for the HV power supply.

* supported by BMBF grant 05P15RGFCA

DOI:10.15120/GR-2017-1

Performances of two strip-readout MRPC prototypes towards CBM-TOF *

P. Lyu[1], *Y. Wang*[1], *B. Guo*[1], *D. Han*[1], *Y. Li*[1], *N. Herrmann*[2], *I. Deppner*[2], *C. Simon*[2], *P. Weidenkaff*[2], *J. Frühau*[3], *P. Loizeau*[3], *and M. Kis*[3]

[1]Department of Engineering Physics, Tsinghua University, Beijing, China; [2]PI, Heidelberg University, Heidelberg, Germany; [3]GSI, Darmstadt, Germany

On basis of the strip-readout MRPC prototype produced and tested in 2014 [1], we have developed two new prototypes by improving original design aiming at the CBM-TOF's high rate situation [2]. They both apply double-stack structure, consisting of two mirrored stacks of resistive plates, which fit into the three parallel readout PCBs. In each stack, there are four 0.25 mm gas gaps divided by five resistive plates composed of the low-resistive glass [3]. The gas gaps are defined by nylon monofilaments spacers aiming at a more homogeneous gap width. On each readout PCB, the 32 readout strips are on a 10 mm pitch with 3 mm interval. Signals induced with both polarities are sent in differential fashion to the PADI front-end-electronics. Parameters of these two prototypes are shown in Fig.1. Among the two MRPCs, one is of the seal-sealed structure, which is named THU-DS. The other one is traditional unsealed MRPC, called THU-DU.

MRPC Parameter	Design Value/mm
PCB dimension	360 × 338
Glass dimension	330 × 276
Gas gap number	2 × 4
Gas gap width	0.25
Strip pitch	7 + 3
Strip length	270
Strip number	32
Detection area	317 × 270

Figure 1: Parameters of the strip-readout MRPCs.

The thought of self-sealed MRPC comes from the gas pollution caused by CBM-TOF's extremely high beam intensity. The gas exchange inside a gas box mainly occurs through diffusion which is dominated by several factors including boundary conditions. Less space for gas flowing outside the MRPC means the boundary is closer to the polluted gas area. We can infer that the gradient of impurities concentration is steeper, so the gas should exchange faster. A simulation was done to confirm this assumption [4]. The results are shown in Fig.2. In a horizontal transect inside a 100×100 cm^2 gas box under irradiated flux rate of 25 kHz/cm^2, Fig.2(a) demonstrates the concentration of pollutants produced in MRPC's effective area. In the 50×50 cm^2 MRPC area which is marked by the white dot line, there is a vortex caused by jet entrainment near the gas inlet at the left boundary, which results from pressure dropping around the inlet. The center of pollutants distribution is shifted to the vortex, and the maximum concentration is 20%. Then, the gas box volume is decreased to 60×60 cm^2, and the maximum value in the MRPC region drops by a great amount to 11.8% as shown in Fig.2(b). It is proved that small flow gas volume is propitious to weakening the influence of gas pollution.

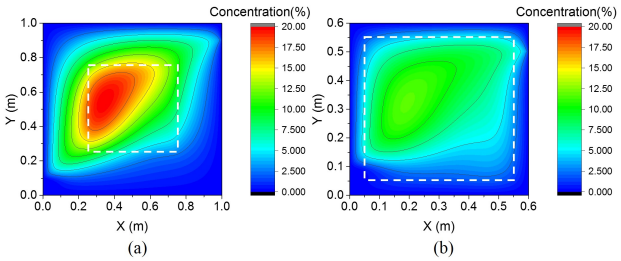

Figure 2: The simulated concentration distribution of gas pollutants produced by a 50×50 cm^2 MRPC (marked by white dot line) under 25 kHz/cm^2 particle flux.(a) The maximum concentraiton is 20% when putting this MRPC in a 100×100 cm^2 gas box. (b) The maximum concentration decreases to 11.8% when putting this MRPC in a 60×60 cm^2 gas box. [4]

To make the THU-DS self-sealed, two rectangular frames made of PMMA are inserted into the three readout PCBs as shown in Fig.3. Gas inlets and outlets are arranged on the two bars vertical to the direction of nylon monofilaments spacers. These frames are 5 mm in width and with the same height of each stack. They are fixed to the PCB surfaces with the silicon glue. When this MRPC is fully assembled, the silicon glue is again potted into outside edges in order to make the chamber gas tight.

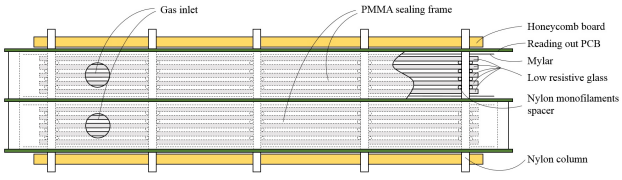

Figure 3: Sectional sketch of the THU-DS MRPC.

In order to further examine the performance of these two prototypes working under higher particle flux rate, they

*This study is supported by National Key Programme for S&T Research and Development under Grant No.2016YFA0400100, the Ministry of Science and Technology under Grant No.2015CB856905 and National Natural Science Foundation of China under Grant No.11420101004, 11461141011, 11275108.

have been tested in the 2015 November SPS beam time using the secondary particles from a 30 AGeV Pb beam hitting on a 1/2/3 mm Pb target. The layout of beamtest is shown in Fig.4 [5]. It contained two parts, the upper setting and lower setting. The THU-DS and THU-DU were installed among the upper setting. Theoretically the THU-DS could work independently, but for consistency with other chambers it was placed inside of the gas box together with THU-DU. The gas was injected first into the THU-DS directly from gas box inlet, and then it flew out from the prototype to the whole box. The gas mixture used was 90% $C_2H_2F_4$, 5% i-C_4H_{10} and 5% SF_6.

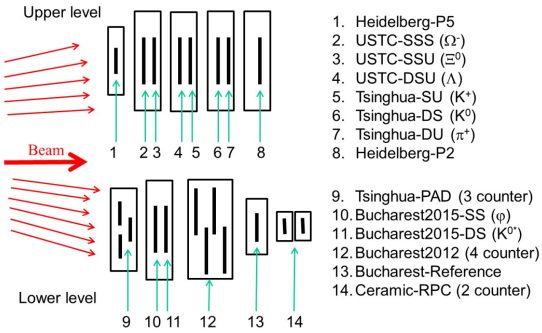

Figure 4: Setup sketch of TOF MRPCs in CERN SPS Nov 2015 beam time. The THU-DS and THU-DU were installed among upper level. [5]

The analysis on raw data from beam time was done with CBM-Root macros developed by TOF groups. In order to obtain the performance of each counter, one among them is taken as the reference of another. A series of calibration types, including strip alignment, velocity correction, gain correction and walk correction, were looped in an iterative way until the time of flight is no longer correlated to any of the interfering factors, and then the MRPCs' performances were obtained. An analysis scan of each 30-minute run throughout the beam time from Nov 28^{th} to Dec 1^{st} 2015 was completed. Data of efficiency scan and FEE threshold scan were selected and made the plots in Fig.5.

As shown in Fig.5(a), the efficiency of THU-DU enters into plateau region at 112 kV/cm and maintains around 98%. The THU-DS's efficiency is slightly lower at 97%. For the time resolution in Fig.5(b), it gets improved with higher applied voltage, and it decreases to 85 ps for both MRPCs when reaching nominal voltage. Assuming that the THU-DS and THU-DU are of the same time resolution, an independent value of $85/\sqrt{2} \approx 60$ ps for both counters is calculated. The cluster size grows with applied field in Fig.5(c) because of the expanded avanlanche. The THU-DS has a smaller value of 1.4.

A FFE threshold scan is demonstrated in Fig.5. Application of higher threshold helps to filter the noise, and thus we observe a better time resolution (Fig.5(f)). Signal loss caused by rising threshold, at the other hand, reduces the efficiency (Fig.5(e)) and cluster size (Fig.5(d)). All properties observed from THU-DS and THU-DU fit our expectation very well. Both of these two strip-readout MRPCs' performances prove that they are capable of requirements from the high-particle-rate TOF system include CBM TOF.

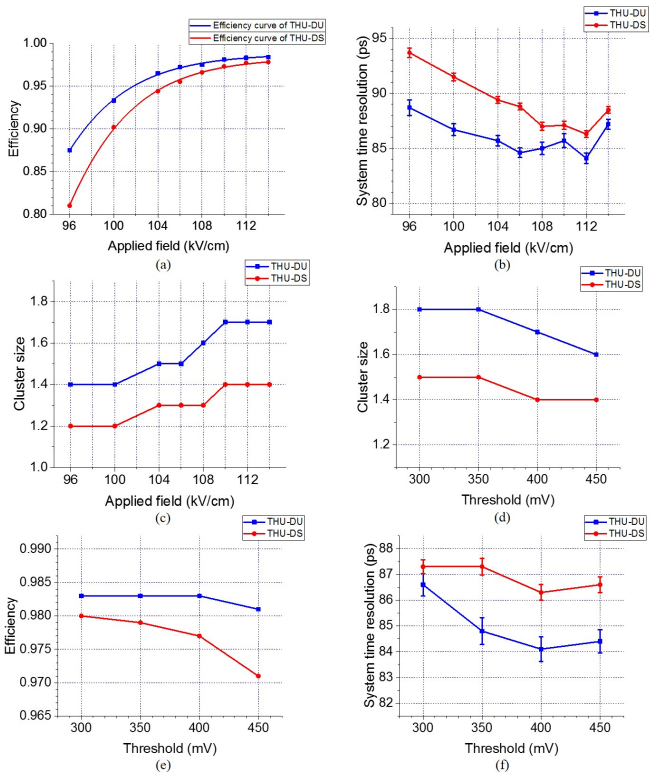

Figure 5: (a) Efficiency of THU-DS and THU-DU in HV scan. (b) System time resolution of THU-DS and THU-DU in HV scan. (c) Cluster size of THU-DS and THU-DU in HV scan. (d) Cluster size of THU-DS and THU-DU in FEE threshold scan. (e) Efficiency of THU-DS and THU-DU in FEE threshold scan. (f) System time resolution of THU-DS and THU-DU in FEE threshold scan.

However, neither obvious differences in the performances between the THU-DS and THU-DU nor the influences of gas aging have been found. At the moment, we are working on optimization of the sealed structure of THU-DS and confirmation on its recovering ability from higher rate condition. Further studies with the help of higher intensity beam is still necessary.

References

[1] Y. Wang, et al. JINST. 11 (2016) C08007.

[2] The CBM collaboration, Technical Design Report for the CBM Time-of-Flight System (TOF). (2014) 13.

[3] J. Wang, et al. Nucl. Instr. and Meth. A713 (2013) 40.

[4] P. Lyu, et al. JINST. 11 (2016) C11041.

[5] C. Simon, et al. CBM Progress Report 2015, 90.

DOI:10.15120/GR-2017-1

Prototype of EPICS based detector control system for the TOF test stand at CERN 2016

M. Mitkov[1], *P. Zumbruch*[1], *J. Frühauf*[1], *and I. Deppner*[2]
[1]GSI, Darmstadt, Germany; [2]Ruprecht-Karls-Universität, Heidelberg, Germany

During the Nov. beamtime 2016 at SPS/CERN, a setup with several ToF prototype detectors were controlled for the first time by an EPICS[1] based prototype **D**etector **C**ontrol **S**ystem (**DCS**). It featured full control, including software based open-loop control, monitoring, and alarming of the ToF Setup's devices operational parameters, which corresponds to a typical SCADA[2] System. In addition all relevant process variables (PVs) were archived for a long-term availability of data, e.g. for analysis.

Based on the open-sourced EPICS framework, i.a. featuring high scalability, modular design, and sustainability, this prototype consists of $\approx 10^3$ PVs and can almost freely be scaled up to larger experimental setups, e.g. in the FAIR phase 0 program at STAR/BNL and miniCBM or even the final CBM TOF wall, of up to 10^5-10^7 PVs. The communication between the different devices and the ToF DCS is based on Ethernet.

The current ToF DCS version supports the following devices:

- CAEN SY1527LC: High voltage power supply
- ISEG CC24: High voltage power supply
- TDK-LAMBDA GEN 90-8: Low voltage power supply
- Bronkhorst EL-Flow Series valve: Three input control valves and one output flow monitor
- ADAM CPWplus 150: Gas bottle scale for laboratory use

The headless CS-Studio[3] RDB[4] archiver application stores selected DCS detector control and monitoring values to a PostgreSQL Database. In our case those values are voltages and currents delivered by the high voltage (HV) and low voltage (LV) power supplies and the gas flow for 3 different gases delivered by the flow regulators of the gas-mixing station. With the CS-Studio Data Browser it is possible to visualize seamlessly historic and live data (see Fig. 1) in order to analyze the detector operation behavior.

The software open-loop control was programmed to protect the detectors from damages caused by e.g. a gas blockage by ramping down the HV but also to trigger an alert in order to inform the experimentalist in case e.g. of a gas leakage or a FEE power consumption mismatch.

All features are graphical visualized with CS-Studio. Figure 2 shows the main ToF DCS view, which contains

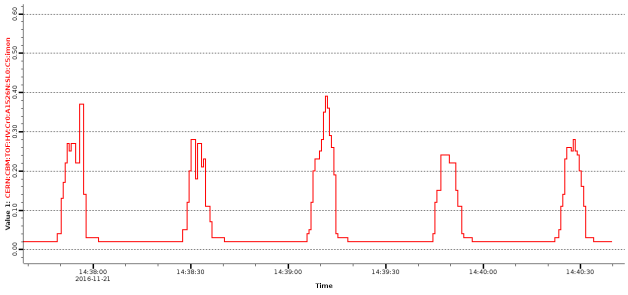

Figure 1: PV monitoring of the current of one high voltage channel af function of time. The spill structure of the beam is clearly reflected in the MRPC current.

a header monitoring the low voltages and the gas flows and a control part. The control part has different sub-menu tabs for getting access to each device or individual sub-detector, by default the high voltage tab is active.

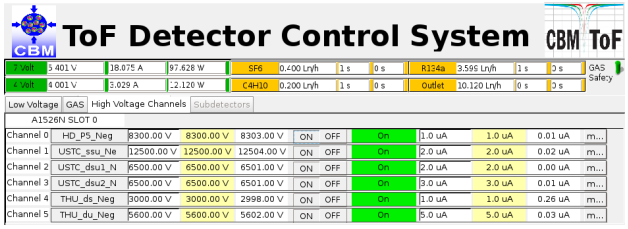

Figure 2: ToF DCS screenshot

We can conclude that the ToF DCS prototype successfully controlled, monitored and archived the ToF detector during the last beamtime 2016 at CERN. It can be extended for a larger setups, e.g. STAR at BNL, or final CBM. This current project of a ToF DCS prototype will be continued as a bachelor thesis' subject.

In the near future additional safety features will be implemented in the ToF DCS. One feature is a sound alarm informing the local operators if a value is not regular. A second feature could be to inform not present users an emergency case by email or sms[5].

References

[1] EPICS, http://www.aps.anl.gov/epics/

[2] K.Kasimir, G. Garcassi, Control System Studio Guide, 2016

[3] Time–of–Flight System(TOF), Technical Design Report for the CBM, 2014, Darmstadt

[1]Experimental Physics and Industrial Control System
[2]Supervisory Control and Data Acquisition
[3]Control System Studio is an Eclipse-based collection of tools to monitor and operate large scale control systems
[4]Relational Database
[5]Short Message Service

DOI:10.15120/GR-2017-1

Test performance of the basic architecture for the inner zone of the CBM-TOF wall using heavy-ion beam at SPS-CERN *

M. Petriş[1], D. Bartoş[1], M. Petrovici[1], L. Rădulescu[1], V. Simion[1], J. Frühauf[2], P-A. Loizeau[2], I. Deppner[3], N. Herrmann[3], and C. Simon[3]

[1]NIPNE, Bucharest, Romania; [2]GSI, Darmstadt, Germany; [3]PI, Heidelberg University, Germany

The Time Of Flight (TOF) subsystem is one of the core detectors of the CBM experiment. The TOF wall in conjuction with Silicon Tracking System (STS) is foreseen to identify charged hadrons, i.e. pions, kaons and protons, in the full acceptance of the system (the angular range covered by the STS detector of 2.5^0-25^0). It covers an active area of about 120 m^2 approximately rectangular in shape. A system time resolution of at least 80 ps including all possible contributions, such as electronics jitter and the resolution of the time reference system is needed. This requires a single channel time resolution better than 60 ps with an efficiency of at least 95%. Such a performance should be maintained up to a counting rate which, very close to the beam pipe, exceeds 30 kHz/cm^2 [1].

Our R&D activity has been focused on the development of a Multi-Gap RPC with Multi-Strip readout (MSM-GRPC) for high counting rate and multiplicity environment, as it is anticipated to be in the inner zone of the CBM-TOF. Based on the good results obtained with the narrow strip pitch (2.54 mm) double stack counter (2 x 5 gas gaps of 140 μm), in terms of efficiency, time and two-dimensional position resolutions [2], a new prototype with the strip pitch equal with 7.4 mm (5.6 mm strip width) and a strip length of 96 mm was designed and built. Construction details of this prototype, called RPC2012, and its performance in the in-beam tests performed at CERN-PS accelerator together with the concept of the modular configuration of the CBM-TOF inner wall based on this RPC architecture were reported in [3].

The prototype was tested at H4 beam line of CERN SPS-facility, using reaction products produced by an Ar beam of $13A$ GeV energy incident on a Pb target. The average obtained cluster size was 1.6 strips per hit and the time resolution, including the electronics contribution, was of $\sim$60 ps [4]. For all these tests mentioned above a front-end electronics based on 8 channel NINO chip [5] was used for signal processing.

Here we report the performance, in close to real conditions, of this architecture operated with a FEE based on a 32 channel motherboard [1] containing 4 PADI chips[7], the front-end electronics anticipated to be used for the CBM-TOF wall. The signals were digitized by 32-channel FPGA-TDCs [8] and readout via TRB3 [9] data hubs. The in-beam test were performed at CERN-SPS with a $30A$ GeV Pb ions incident on a Pb target.

The CBM-TOF experimental setup was divided in "low rate" and "high rate" branches, the last one being positioned at a polar angle of about 3^0 relative to the beam axis. A comprehensive description of the whole setup is given in [6]. Our prototypes were positioned in the high rate setup, the RPC2012 prototype being 'sandwiched' between RPC2015 [11] and RPCref prototypes. A diamond detector positioned in front of the target together with RPCref positioned at the end of the set-up, delivered the information for particle velocity measurement. A photo of the "high rate" branch is shown in Fig. 1. The spatial position along the

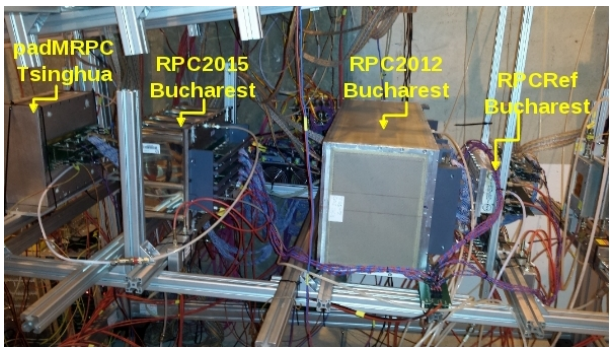

Figure 1: Photo of the high rate experimental set-up based on MGRPC prototypes used in the in-beam test.

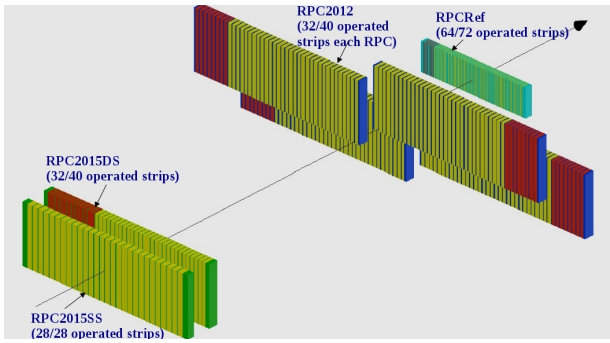

Figure 2: Sketch of the spatial position of the seven RPCs tested in the high rate setup at CERN-SPS.

*Romanian NASR/contract RO-FAIR F02 and NASR/NUCLEU Project PN09370103

DOI:10.15120/GR-2017-1

beam line of the seven prototypes tested by our group and their operated area (green color) are presented in Fig. 2.

The principles of the data analysis starting from unpacking to calibration and corrections for slewing effect, position and reaction product velocity spread are described in [12]. In the left side of Fig. 3 is presented the time difference spectrum between one of the four counters positioned in the upper part of the text box (called RPC2012_3) and RPC2015DS (see reference [11]), with the same inner geometry and the same strip pitch. The 63 ps standard de-

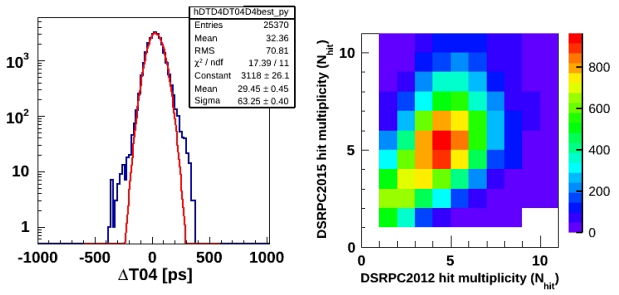

Figure 3: Time difference spectrum - left. Hit multiplicitiy correlation - right.

viation of the Gauss fit demonstrates the very good system time resolution. A single counter time resolution of 44 ps, including the electronic contribution is obtained supposing equal contributions of the two detectors. The comparison of the 63 ps standard deviation with the 71 ps RMS of the spectrum shows a non-significant contribution of the non-Gaussian tails. The correlation of the hit multiplicities in the two counters shows that in the most part of the events, almost the same multiple hits are incident on both detectors. The detectors were operated at 2 x 5.5 kV voltage. Due to their staggered positions, position cuts on both x and y directions were applied in the RPC2015DS, considered as reference counter, for efficiency estimation. However, due to a partial overlap of the active area of each of the four counters relative to the RPC2015DS, the obtained values are still affected by the hits lost at the edges of the overlaped area.

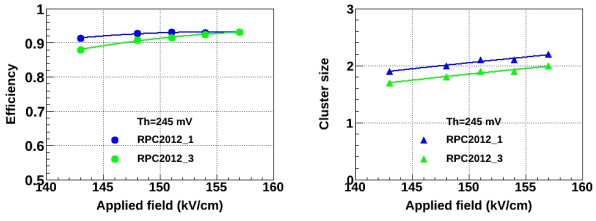

Figure 4: Efficiency - left and cluster size - right as a function of high voltage for RPC2012_1 and RPC2012_3.

In Fig. 4 is shown an expected behaviour of the efficiency and cluster size as a function of high voltage, for RPC2012_3 and RPC2012_1 (right mirrored relative to the axe shown in Fig. 2) for a PADI threshold of 245 mV. In the mentioned geometry of the experiment, a 93% efficiency for both counters was obtained. If we take into consideration the inner geometry of the RPC2012 counters of 2 x 5 gaps of 140 μm, the same as for RPC2015DS [10, 11], we could consider that at a nominal voltage of 2 x 5.5 kV the efficiency is in fact at the same value as for RPC2015DS (97%). The cluster size is of 2.2 strips for RPC2012_1 and of 2.0 strips for RPC2012_3 in the region of efficiency plateau. Average system time resolution of 73 ps for RPC2012_1 and of 67 ps for RPC2012_3 remain almost unchanged over the investigated high voltage range, as is shown in Fig. 5.

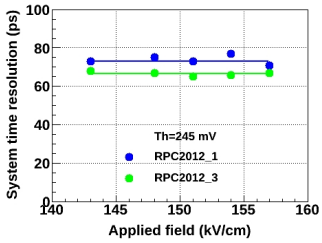

Figure 5: Time resolution as a function of high voltage for RPC2012_1 and RPC2012_3.

The single counter time resolution of 52 - 47 ps fullfils the single counter performance required for the inner zone of the CBM-TOF wall.

The results presented in the contributions to this Progress Report (present one and [11]), show that the MSMGRPC prototypes and the proposed basic architecture fulfill the requirements for the inner zone of the CBM-TOF wall.

References

[1] CBM-TOF Collaboration, CBM-TOF TDR, October 2014

[2] M. Petrovici et al, 2012 Journal Of Instrumentation, Volume 7, 2012 (2012 JINST 7 P11003).

[3] M. Petris et al., CBM Progress Report 2012 (2013), p.68

[4] M. Petriş et al., Journal of Physics: Conference Series 724 (2016) 012037

[5] F. Anghinolfi et al., Nucl.Instr.and Meth. A533(2004)183

[6] C. Simon et al., CBM Progress Report 2015, (2016), p.90

[7] M. Ciobanu et al., CBM Progress Report 2013, (2014), p.84

[8] C. Ugur et al., GSI Scientific Report 2014 (2015), p.212

[9] M. Traxler et al., GSI Scientific Report 2014 (2015), p.514

[10] V. Aprodu et al., CBM Progress Report 2015 (2016), p.98

[11] M. Petriş et al., this CBM Progress Report

[12] M. Petriş et al., Journal of Instrumentation, Volume 11, September 2016 (2016 JINST 11 C09009)

CERN-SPS in-beam performance test of the new strip readout MRPC prototypes for the inner zone of the CBM-TOF wall *

M. Petriş[1], D. Bartoş[1], M. Petrovici[1], L. Rădulescu[1], V. Simion[1], J. Frühauf[2], M. Kiš[2], P-A. Loizeau[2], I. Deppner[3], N. Herrmann[3], and C. Simon[3]

[1]NIPNE, Bucharest, Romania; [2]GSI, Darmstadt, Germany; [3]PI, Heidelberg University, Germany

Due to the high interaction rates of 10^7 interaction/s at which the CBM experiment is anticipated to run the readout will be based on a free streaming concept. This imposes to the MSMGRPCs (Multi-Strip, Multi-Gap RPCs), a perfect matching of the characteristic impedance of the signal transmission line to the input impedance of the front-end electronics, in order to reduce fake signals produced by reflexions [1].

Two new MSMGRPC prototypes, based on low resistivity glass ($\sim 10^{10}$ Ωcm) from China, match the characteristic impedance of the RPC signal transmission line to the input impedance of the front-end electronics ([2, 3]). They have also the granularity required by the inner zone of the CBM-TOF wall through a proper adjusting of their strip lenght. The transmission line impedance of a single readout channel of each prototype was estimated using APLAC Software. The first prototype has a classical single stack architecture (RPC2015SS) with 8 gas gaps of 140 μm. The pitch size (10.16 mm) and strip width (8.63 mm) are the same for both high voltage and readout electrodes. The second prototype has a double stack configuration (RPC2015DS) of 2 x 5 gas gaps of 140 μm, with the same pitch size (7.2 mm) for both high voltage and readout electrodes, but with different values of the strip widths: 1.3 mm for readout electrodes and of 5.6 mm for high voltage ones. This gives the possibility to exploit in an inovative way the advantage of having a strip structure for both readout and high voltage electrodes. Thus the tuning of the characteristic impedance of the signal transmission line to the value of the input impedance of the front-end electronics can be decoupled by the granularity adjustments. With the described geometrical parameters both counters have a characteristic impedance of the transmission line of 100 Ω.

The prototypes were tested in-beam at SPS-CERN with a 30A GeV Pb ions incident on a Pb target in conditions similar with those expected at SIS100, or even closer to those anticipated for SIS300. Our prototypes were positioned in the "high rate" branch of the CBM-TOF experimental setup, a comprehensive description of the whole set-up being given in [4]. The two described prototypes are positioned one behind the other (see Fig.1), in the same housing box, identified as RPC2015 Bucharest [5]. They were followed by four MSMGRPCs mounted in the same gas tight box, called RPC2012 and a narrow strip pitch (2.54 mm) MSMGRPC called RPCRef, the last one in the experimental set-up. A 16 strip polycrystalline diamond detector and a 4-pad single crystal diamond detector were positioned in front of the target, providing a start time for particle velocity measurements between the diamond detector and the RPCRef counter. The signals delivered by the RPCs were fed to PADI fast amplifiers [6] and processed by the same electronics chain described in [5].

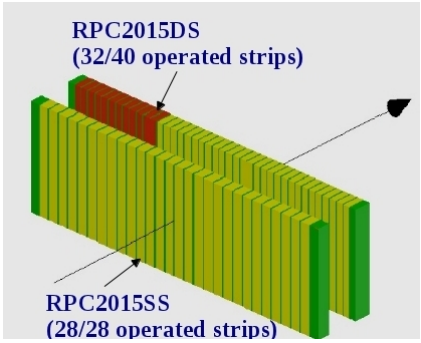

Figure 1: Overlap of the active area of the two RPC2015 prototypes.

We report here the performance of the RPC2015 prototypes, the results obtained with RPC2012 prototype being reported in detail in [5]. The principles of the data analysis starting from unpacking to calibration and corrections are presented in [7].

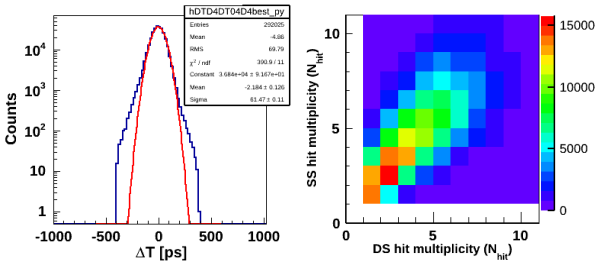

Figure 2: Time difference spectrum - left. Hit multiplicitiy correlation - right.

The time difference spectrum between RPC2015DS and RPC2015SS, for operation of RPC2015DS at 2 x 5.5 kV (157 kV/cm) and of RPC2015SS at 2 x 9 kV (161 kV/cm), with the PADI threshold set to 245 mV is presented in Fig.2, left side. A very good system time resolution of

* Romanian NASR/contract RO-FAIR F02 and NASR/NUCLEU Project PN09370103

DOI:10.15120/GR-2017-1

61 ps, including the contribution of the electronics, was obtained. The correlation plot from the right side of Fig.2 shows that the two counters were exposed to almost the same hit multiplicities. If we consider equal contributions of the two counters, a single counter resolution of 43 ps is obtained. The observed tails in the time spectrum are negligible, if we compare the obtained 61 ps σ of the Gaussian fit with 69 ps RMS value of the spectrum. The obtained efficiency for this run, was of 97% for the RPC2015DS and of 98.5% for the RPC2015SS. The slight difference could be due to the difference in the applied potentials and also in the overlaped operated area, as is shown in Fig.1. The

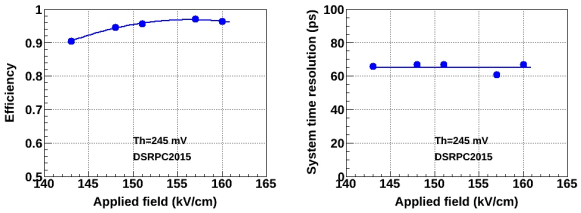

Figure 3: Efficiency - left and time resolution - right as a function of high voltage for RPC2015DS.

obtained detection efficiency and time resolution as a function of applied high voltage for RPC2015DS are shown in Fig. 3. An average system time resolution of 65 ps corresponds to the efficiency plateau, reached at applied electric fields in the gas gap larger than 157 kV/cm. The efficiency

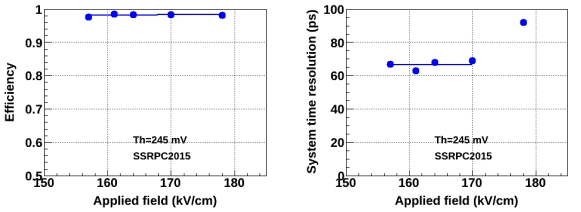

Figure 4: Efficiency - left and time resolution - right as a function of high voltage for RPC2015SS.

and system time resolution obtained for RPC2015SS are presented in Fig. 4. As can be observed, the counter was operated at the efficiency plateau of ∼98%, with an average system time resolution of 66 ps. The larger value of the time resolution observed for operation at 178 kV/cm is due, most probable, to the operation at a too high electric field which pushes the counter in a streamer regime. The

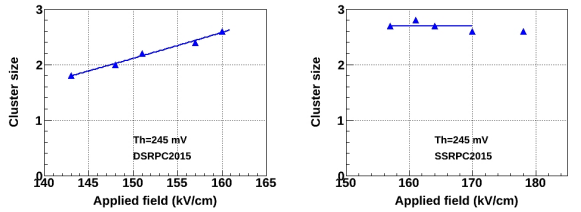

Figure 5: Cluster size for RPC2015DS - left and RPC2015SS - right as a function of high voltage.

obtained cluster size (number of strips with signal in a single hit) for the two counters is presented in Fig. 5. The cluster size is increasing for RPC2015DS as a function of applied potential while for RPC2015SS in the same high voltage range is almost constant. It slightly decreases at the largest applied fields due to possible distorsions of the electric field produced by the space charge inside the gas gaps. The obtained values of the cluster size are larger than the one expected from the values of pitch sizes for the two counters. Previous obtained results for RPC2012 with a pitch size of 7.4 mm and the same inner geometry, showed a cluster size of the order of 1.4 - 1.5 strips [8] for single hit. These larger values can be due to large ionization created by heavy reaction products crossing the detector.

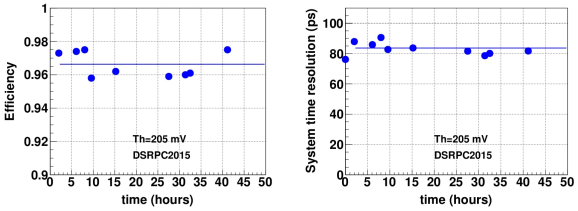

Figure 6: Aging effect for RPC2015DS for 40 hours operation with the same high voltage and threshold settings.

The detector performance stability was checked for a period of operation of about 40 hours with the same settings (RPC2015 at 157 kV/cm, RPC2015SS at 178 kV/cm). The efficiency and system time resolution were evaluated for the runs acquired over this period at similar counting rates. The stability of the detectors is demonstrated by the plots shown in Fig. 6. The obtained ∼80 ps system time resolution is affected by the operation of the RPC2015SS at a too high electric field, (178 kV/cm), in a region of the working curve where its time resolution started to deteriorate (see Fig. 3). The operation of the detectors at a PADI threshold of 205 mV does not not influence the time resolution performance, as it is shown in [7, 9].

The performance of the RPC2015DS whith the inovative adjustable characteristic transmission line impedance was demonstrated. The obtained results show that the two new prototypes with characteristic transmission line impedance matched to the input impedance of the front-end electronics, fullfil the challenging requirements of the inner zone of the CBM-TOF wall.

References

[1] CBM-TOF Collaboration, CBM-TOF TDR, October 2014

[2] V. Aprodu et al., CBM Progress Report 2015 (2016), p.97

[3] V. Aprodu et al., CBM Progress Report 2015 (2016), p.98

[4] C. Simon et al., CBM Progress Report 2015, (2016), p.90

[5] M. Petriş et al., this CBM Progress Report

[6] M. Ciobanu et al., CBM Progress Report 2013, (2014), p.84

[7] M. Petriş et al., Journal of Instrumentation, Volume 11, September 2016 (2016 JINST 11 C09009)

[8] M. Petriş et al., Journal of Physics: Conference Series 724 (2016) 012037

[9] M. Petriş et al., CBM Progress Report 2015 (2016), 95

Simulation of the MRPC response degradation with increasing time in spill *

C. Simon[1], N. Herrmann[1], I. Deppner[1], A. Akram[1], E. Bao[1], P.-A. Loizeau[2], Ph. Weidenkaff[1], and the CBM ToF working group[1]

[1]Ruprecht-Karls-Universität Heidelberg, Heidelberg, Germany; [2]GSI, Darmstadt, Germany

Following avalanche formation in an MRPC gas gap, electrons and positively charged gas ions drift towards opposing glass plates, accumulate on the surfaces and—as a consequence—cause a local reduction of the electric field in the gap. These charges compensate one another by means of bulk and surface currents on relaxation time scales of $\mathcal{O}(ms) \leq \tau \leq \mathcal{O}(s)$, depending on the glass resistivity. The growth of subsequent avalanches in the very location is therefore influenced by the formation time and the charge content of the preceding ones.

The average effect of different recovery times for the electric field between events, i.e. of different incident particle fluxes, on MRPC performance criteria like detection efficiency, time resolution and mean cluster size has been extensively studied by the ToF working group on prototypes equipped with both float and low-resistive glass (cf. e.g. [1], [2] and [3]). In all these cases, detector data were averaged within spills and across spills. These measurements did therefore not address the question of how the degradation of the MRPC response evolves with increasing time in spill. Exposing the detector to a sustained particle flux should—regarding the operation principle—decrease its detection efficiency until local reduction and recovery of the electric field cancel out.

A self-triggered, front-end driven data acquisition with readout channel dead times of a few nanoseconds allows for studying the degradation and saturation of the MRPC response in unprecedented detail. Such a system was realized for the first time on a large scale in the GET4-AFCK-FLIB chain used in the 2016 heavy-ion beam time at CERN/SPS to read out multiple MRPC prototypes. This significant progress on the experimental hard- and software side has been accompanied by the development of a more realistic ToF digitizing scheme which the following parametrization of the MRPC response degradation builds upon.

Be $Q_{\mathrm{ind},0}$ a random variable which describes the total electric charge spectrum induced by avalanches in the readout plane of an unloaded MRPC. Be $q_{\mathrm{max},0}$ the highest possible value of $Q_{\mathrm{ind},0}$ and $q_{\mathrm{ind},i}$ the charge actually induced by the i-th avalanche at position $\mathbf{x}_i$ and time t_i. Be further r_{imp} an impact radius quantifying the spatial extent of an E-field reduction and τ_{MRPC} the relaxation time for field restoration. Then in this approach the induced charge spectrum accessible to the n-th avalanche at coordinates $(\mathbf{x}_n, t_n)$ follows the probability distribution of the random variable

$$Q_{\mathrm{ind},n} = \left[1 - \sum_{i=1}^{n-1} \left\{ \frac{q_{\mathrm{ind},i}}{q_{\mathrm{max},0}} \times \frac{1}{1 + \left(\frac{\mathbf{x}_n - \mathbf{x}_i}{r_{\mathrm{imp}}}\right)^2} \times \exp\left(-\frac{t_n - t_i}{\tau_{\mathrm{MRPC}}}\right) \right\}\right] Q_{\mathrm{ind},0} \quad . \tag{1}$$

In a Monte-Carlo parameter study the detection efficiency of a $1\,\mathrm{cm}^2$ spot in the center of an MRPC prototype with dimensions $32 \times 27\,\mathrm{cm}^2$ was simulated for low-resistive (cf. Fig. 1, left) and float glass electrodes (cf. Fig. 1, right) as a function of time in spill at three different incident particle fluxes. The impact radius r_{imp} of $100\,\mu\mathrm{m}$ is the same in both cases. With low-resistive glass the MRPC degrades efficiency rather slightly and reaches saturation quickly while preserving its operability even at $25\,\mathrm{kHz/cm}^2$. With float glass it shows a decline in efficiency of about $3\,\%$ already at $1\,\mathrm{kHz/cm}^2$ that might actually be observable in the 2016 test beam data.

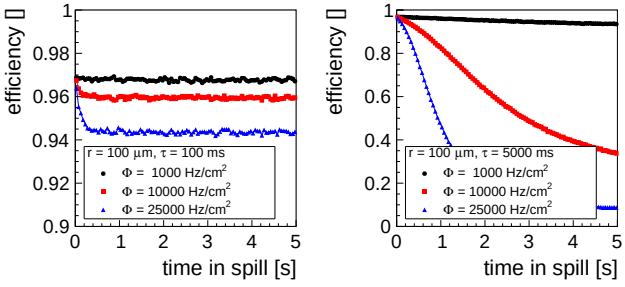

Figure 1: MRPC efficiency degradation (input efficiency: $\varepsilon_0 \approx 0.97$) as a function of time in spill with low-resistive glass (left) and with float glass (right) for different particle fluxes.

As the run time of the summation in Eq. (1) grows quadratically with the number of MRPC hits (about 8.5 hours for 1 million mutually interacting hits in a single-threaded process) possible applications of multi-threading and batch processing are under investigation.

References

[1] I. Deppner *et al.*, 2012 JINST 7 P10008

[2] M. Petriş *et al.*, J. Phys. Conf. 533 (2014) 012009

[3] Y. Wang *et al.*, JINST 9 (2014) C08003

* This project was partially funded by BMBF 05P2015 and by EU/FP7-HadronPhysic3/WP19.

DOI:10.15120/GR-2017-1

Observation of after-pulses in the detector response of MRPC prototypes for CBM-TOF

Ph. Weidenkaff[1], *A. Akram*[1], *I. Deppner*[1], *N. Herrmann*[1], *P.-A. Loizeau*[2], *and C. Simon*[1]
[1]Ruprecht-Karls-Universität, Heidelberg, Germany; [2]GSI, Darmstadt, Germany

First characterizations of CBM-ToF MRPC prototypes have been performed using the free-streaming time-to-digital converter Get4. The high double hit resolution of the Get4-TDC (better than $5\,ns$ [2]) allows to study effects in the detector response immediately after a primary hit. An series of after-pulses has been observed in the first 50 nanoseconds after a primary signal. The probability, multiplicity and temporal distribution of these after-pulses have been compared between six MRPC prototypes in a cosmic radiation test. A short description of all tested prototypes can be found in [1].

The MRPC read out chain consists of PADI as pre-amplifier, the Get4 TDC and the AFCK as data processing board. The slow-control interface IPbus was used as a read-out interface between AFCK and the data acquisition PC since a proper PCI-E based read-out interface was not available in time.

An example of the temporal distribution of after-pulses after a primary signal can be seen in figure 1a. Several common features can be observed on all prototypes:

No after-pulses in the first nanosecond followed by a steep rise of the time distribution. This feature originates from the double hit capability of Get4. In this time window after each hit in a channel, the TDC channel is either fully inactive or not completely efficient.

A rather flat maximum is seen between $5\,ns$ and $10\,ns$ after the primary signal. In this region the prototypes show either a flat distribution or a slight rise of the distribution.

The spectrum continuously decreases over time after the maximum. This decrease can be described reasonably well by an exponential decay. The shape as well as the length of the decline leads to the conclusion that the majority of the observed after-pulses are not caused by electronic reflections.

It is also observed that the time over threshold of the after-pulses is independent of the after-pulse delay with respect to the primary signal.

The likelihood to observe such after-pulses was significantly higher than the expected rate of random coincidences from the measured dark rate on all studied prototypes. A correlation between these after-pulses and the primary signal is therefore evident. The probability to observe any after-pulses after a primary signal is shown in figure 1b for the two prototypes from USTC.

A higher probability for multi-hit events is observed on the unmatched USTC-DSU prototype. However, also the impedance matched USTC-DSM prototype shows multiple hits on the same TDC channel in $10\% - 20\%$ of the events. In mean, such an event contains the primary signal

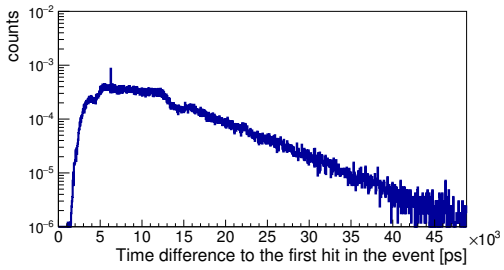

(a) *Temporal distribution of after-pulses after the primary hit on an example channel (Channel 16 of USTC-DSM). The distribution is normalized to the number of Events in which the TDC-channel detected at least one hit. Source: [3]*

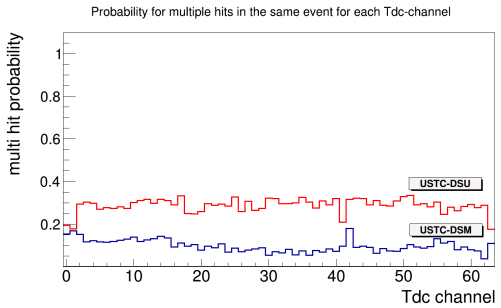

(b) *Probability to find after-pulses in an event in which a primary signal is found for each TDC channel of the prototypes USTC-DSU (red) and USTC-DSM (blue).*

and 1.12 after-pulses on USTC-DSM and 1.47 after-pulses on USTC-DSU. The tails of the after-pulse multiplicity distributions extent to up to 10 after-pulses.

Since the observed after-pulses are correlated with primary signals, it is expected that this problem persists also at high rates. For highest interaction rates, the influence of after-pulses on the physics performance of MRPCs has to be studied.

References

[1] I.Deppner et al, "Narrowing down the MRPC design with heavy ion beams at CERN/SPS", GSI Scientific Report 2015 (2016) p.90

[2] H. Deppe and H. Flemming, "The GSI Event driven TDC with 4 Channels Get4", Technical report, GSI, Darmstadt 2014

[3] Ph. Weidenkaff, "Characterizations of Multi-Gap Resistive Plate Chamber Prototypes in a Freestreaming Read-Out Environment", Master-thesis, Ruprecht-Karls Universität, Heidelberg 2017

DOI:10.15120/GR-2017-1

RICH geometry optimization*

I. Kres[1], *T. Mahmoud*[2], *and C. Höhne*[2]
[1]University of Wuppertal, Germany; [2]II. Physikalisches Institut, JLU-Gießen, Germany

Due to modifications of the CBM dipole magnet the overall RICH geometry has to be re-optimized. In previous reports [1,2] we described the optimization procedure and showed results with two-wing PMT-plane (left part in figure 1). Although the two-wing geometry showed very good performance in simulations, it is not realizable in the real experiment due to overlap of electronics modules in the center as illustrated in the figure. Therefore, in a second step a cylindrical shaped geometry of the MAPMT plane was investigated (right part in figure 1). This geometry not only overcomes the overlap problem, but also brings the PMTs closer to the focal plane of the mirrors.

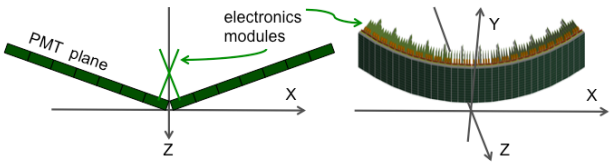

Figure 1: MAPMT plane geometries. Left picture represent two-wing geometry. Right picture represent cylindrical geometry.

The detailed optimization procedure is described in [1]. For the curved geometry the following parameters were optimized: rotation around the x-axis, radius of the cylindrical curvature, and y- and z-position coordinates. As for the two-wing geometry, two main criteria were optimized: the ratio of minor to major axis of an ellipse fit to the ring (B/A) and the RMS of the distribution of the distance between the fit and the individual hits forming the ring (dR). In the study single electrons and positrons were generated isotropically in space with a flat distribution in transverse momentum from 0 to 4 GeV/c.

The best integrated B/A and dR values are 0.93 and 2.8 mm respectively. They are achieved with a rotation angle $\theta = 16°$ around the x-axis, a cylindrical radius $r = 165$ cm, and a position of plane center at $y = 158$ cm and $z = 218.6$ cm from the interaction point. The B/A distribution on the upper half of the PMT plane is shown in the upper panel of figure 2. For a wide area the B/A ratio is larger than 94% indicating a low grade of ellipticity and consequently high ring finding efficiency, which is found to be about 97% for Au-Au collisions at energies of 8 AGeV [3]. Compared to results with the two-wing

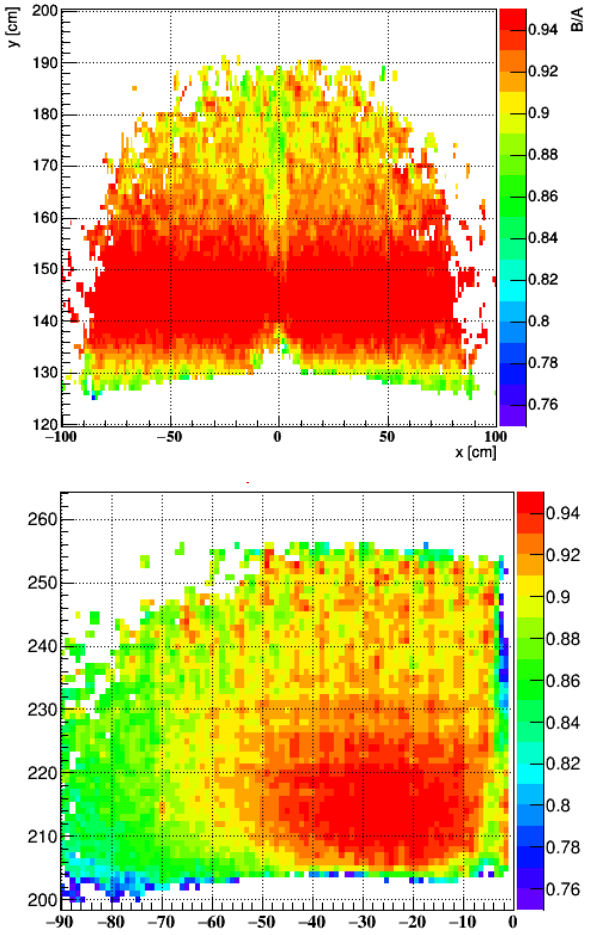

Figure 2: B/A ratio distribution versus position on the cylindrical (up) and the two-wing (low) MAPMT plane. Note that in the lower panel only one half of the plane is shown.

geometry (lower panel in figure 2), the B/A distribution with the cylindrical geometry is much more homogeneous. The dR distribution is shown in figure 3. It is distinctly low and homogeneous within a resolution of 1 mm, which is only 2% of the ring radius.With the two-wing geometry dR lay between 3 mm and 5 mm.

The plane dimensions of 111.3×74.2 cm^2 were adjusted to cover the experiment acceptance and to be integer multiples of modules containing 2×3 PMTs each. The upper plane has 14 strips in the x-direction with 7 modules each

*Work supported by HIC for FAIR, by the GSI F&E- Cooperation with Giessen and Wuppertal, and by BMBF grants 05P12RGFCG and 05P15PXFCA.

DOI:10.15120/GR-2017-1

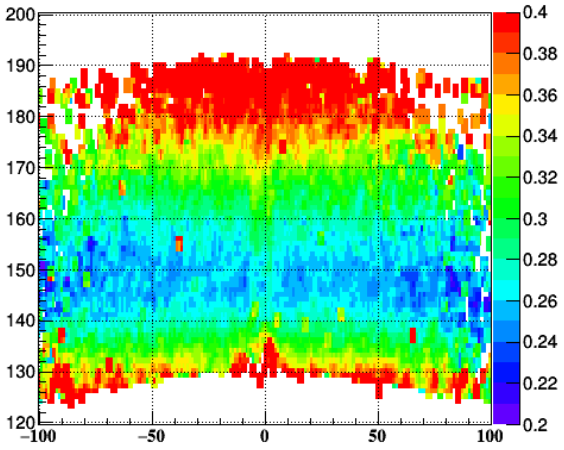

Figure 3: dR distribution versus position on the cylindrical MAPMT plane

(in the y-direction). This module structure was adopted due to electronics development considerations, see [4].

We recall that the RICH detector is designed to detect electrons stemming from vector mesons like ρ, ω, and ϕ. Their small production cross section, together with the small branching ratio into e^+e^-, is challenging in terms of the large (physical) background stemming from Dalitz decays of π^0 and γ-conversions.

To evaluate the optimal detector size of the new geometry, simulations of heavy-ion collisions were carried out aiming at localizing the rings stemming from low mass vector mesons and those from background. 2×10^6 events were simulated with PLUTO at a beam energy of 10 AGeV. We consider the Micro Vertex Detector (MVD), the Silicon Tracking System (STS), and RICH in the simulations. The magnetic field has its nominal value of 100%.

Figure 4 shows the results for electrons from ω decays. The same behaviour is observed for electrons from ρ decays. The corresponding rings are mostly concentrated in the middle of the PMT plane, which is comprehensible as these electrons have momenta of about 2 GeV/c and hence their tracks are less curved by the magnetic field.

The background electrons come to a large extend from conversion photons, which in turn come from π^0 decays: $\pi^0 \to \gamma + \gamma \to (e^+e^-) + (e^+e^-)$. The electrons have momenta of about 0.2 GeV/c and accordingly they populate the full MAPMT plane due to large deflection in the magnetic field. To be able to detect as many of these electrons as possible the PMT plane was enlarged by adding one additional strip (i.e. 7 modules along the y-axis) on each of its outer sides. This measure results in recording 10% of additional electrons originating from π^0 decays. This is particularly important when one considers the RICH contribution to the direct photon signal, where it is essential to understand the background from π^0 decays and to have

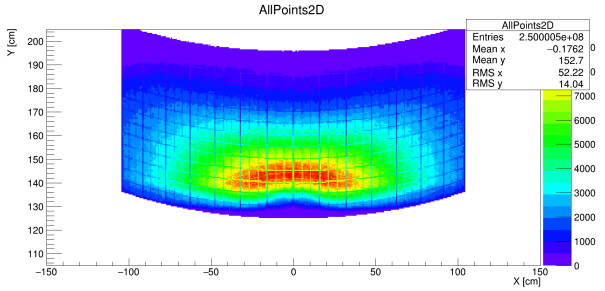

Figure 4: $x - y$ position of RICH hits from Cherenkov light on the upper PMT plane produced by e^+e^- from ω particles. Standard geometry (14 strips).

it under control. Figure 5 shows Cherenkov light on the extended PMT plane with 16 strips coming from from π^0.

Please note that not the whole PMT plane will be equipped with PMTs due to costs consideration (1344 PMTs in total for the 16-strip configuration). However, as clearly seen in the figures 4 and 5, the outer upper parts of the plane are not relevant for any of the signals.

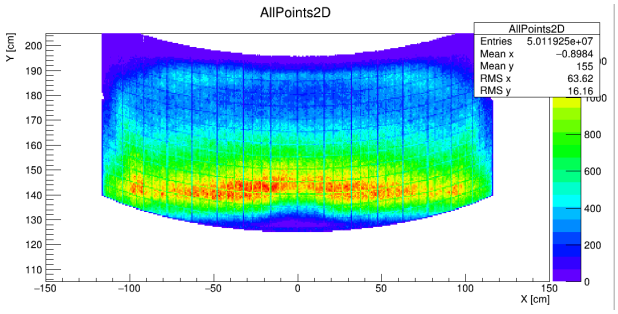

Figure 5: $x - y$ position of RICH hits from Cherenkov light on the upper PMT plane produced by e^+e^- from π^0 particles. Geometry with 16 strips.

For a better understanding of advantages and disadvantages of the 16-strips geometry feasibility studies with dielectrons are required. A detailed analysis shows how the extended geometry improves the π^0-reconstruction and accordingly the background suppression for dilepton analysis.

In summary, we state that the investigated cylindrical geometry not only solves the overlap problem of electronics boards, but also leads to better results in view of ring finding and fitting quality.

References

[1] T. Mahmoud and C. Höhne, CBM Progress Report 2014, Darmstadt 2015, p. 60

[2] T. Mahmoud and C. Höhne, CBM Progress Report 2015, Darmstadt 2016, p. 46

[3] S. Lebedev et al., this report

[4] V. Patel et al., this report

Cooling studies with Thermal Pyrolytic Graphite for the CBM-MVD*

D. Mijatovic[1], *M. Koziel*[1], *P. Klaus*[1], *C. Müntz*[1], *J. Stroth*[1,2], *and the CBM-MVD Collaboration*
[1]Institut für Kernphysik, Goethe-Universität Frankfurt, Germany; [2]GSI Darmstadt, Germany

The CBM Micro Vertex Detector (MVD) comprises four planar detector stations, each divided in quadrants, and equipped with dedicated pixel sensors. Their operation results in about 300 W of total heat input. The challenging material budget of the stations ($< 0.5\%$ X_0) in combination with the operation in vacuum asks for an elaborated cooling concept. It is based on conductive cooling inside the geometrical acceptance employing thin sheets of high-performance materials as sensors carriers, featuring heat conductivities in the order of four times the one of copper, like poly-crystalline CVD-Diamond and Thermal Pyrolytic Graphite (TPG) [1]. These carriers guide the heat to actively cooled heat sinks outside the acceptance. This report presents systematic studies on the in situ cooling performance of MVD quadrants, with a focus on assessing TPG carriers of different thicknesses. Note, the in-plane heat conductivity of TPG is about 1600 W/mK at room temperature, and less than 20 W/mK perpendicular to the surface. Figure 1 (left) depicts the setup geometry by showing the temperature distribution on a TPG sensor carrier of the 3rd station attached to a actively cooled Aluminum heat sink, measured by the IR camera (Vario Cam). The heat load (in the order of 700 mW/cm^2) was mimicked by sheets of Kapton heaters, operated in a standardized vacuum test stand. The thermal performance was

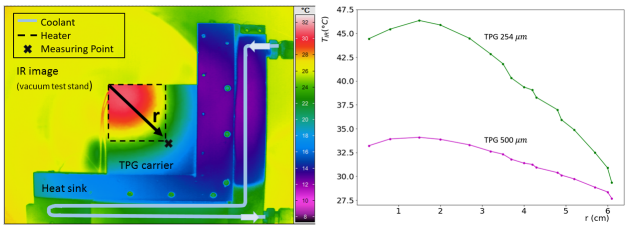

Figure 1: Left: IR image of a 500 µm thin 8×8 cm^2 TPG carrier attached to the heat sink, heat load of 15 W applied 180 s, $T_{cooling\ fluid} = 15$ °C, the heat sink was not corrected for emissivity. Right: Temperature along diagonal coordinate, both TPG thicknesses, $T_{cooling\ fluid} = 25$ °C, after 10 s of heating.

quantitatively characterized by analyzing temperature differences and heating curves of TPG sheets with different thicknesses (254 and 500 µm), shown in figures 1 (right) and 2, respectively. Fitting the temperature rise during the first 10 s ("fast") with $\propto (1 - \exp(-t/\tau))$ results in τ_{fast} of 3-4.5 s, almost independent of the TPG thickness. This fast time constant is in agreement with the above mentioned

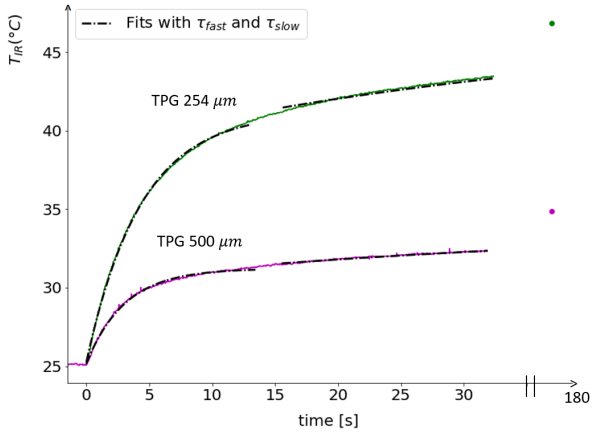

Figure 2: Heat-up curves of TPG carriers of two different thicknesses in vacuum, measured in the point depicted fig. 1, $T_{cooling\ fluid} = 25$ °C, relative adjustment of curves at $t = 0$ s. Broken lines: Exponential fits to initial and saturating time range, see text.

outstanding in-plane heat conductivity of TPG, a result derived from solving the equation of heat conductivity [2]. A second common time constant of $\tau_{slow} \approx 45$ s characterizes the saturation phase.

In summary, a standardized test stand was set into operation to characterize the cooling performance of CBM-MVD quadrants. First results on the cooling performance, given by both, the material properties of TPG (τ_{fast}) and the power to evacuate the heat from the carrier (τ_{slow}), have been derived by measuring characteristic time constants of heating curves. The measured time constant τ_{fast} underlines the excellent thermal performance of this material. Temperature differences and τ_{slow} offer a quantitative assessment to further improve the heat evacuation and selecting the optimum TPG thickness. Next campaigns will focus on characterizing Parylen-coated TPG, even thinner pyrolytic graphite foils (PGS) and pCVD-Diamond. They will be complemented by and compared to thermal CAD simulations aiming at optimizing the contact to the heat sink and its design.

References

[1] Diamond Materials www.diamond-materials.com; Momentive momentive.com, Optigraph www.optigraph.eu

[2] P. Klaus, priv. communication

* supported by BMBF (05P15RFFC1), HGS-HIRe and GSI.

DOI:10.15120/GR-2017-1

DiRICH readout electronics - status and first measurements *

C. Pauly[1], *K.-H. Kampert*[1], *J. Michel*[2], *V. Patel*[1], *P. Skott*[3], *M. Traxler*[3], *and C. Ugur*[3]
[1]Wuppertal university; [2]Frankfurt university; [3]GSI Darmstadt

The realization of the new DiRICH electronic readout chain for Hamamatsu H12700 MAPMTs (CBM- and HADES RICH detectors), as well as for Photonis MCP sensors (PANDA DIRC), has seen major progress over the last year. Since mid 2016, first prototype modules of all components are available for detailed testing and evaluation. Figure 1 shows photographs of a partly equipped 3x2 MAPMT module, and of the individual DiRICH, DiRICH-Combiner, and DiRICH-Power cards. All these modules seem to work as expected, no critical design flaws have been encountered yet.

A particular challenge in the development of the DiRCH readout module is the low signal amplitude of the MAPMT / MCP signals for single photons. With sensor gain in the order of 1×10^6, and a signal width in the order of few ns, a typical single photon pulse has an average amplitude of about 10 - 20 mV. In order to achieve good detection efficiency, this requires operation at thresholds down to the mV level. This poses particular challenges on the noise characteristic of the analog input stage of the DIRICH.

* Work supported by BMBF grants 05P15PXFCA, 05P15RGFCA, and GSI

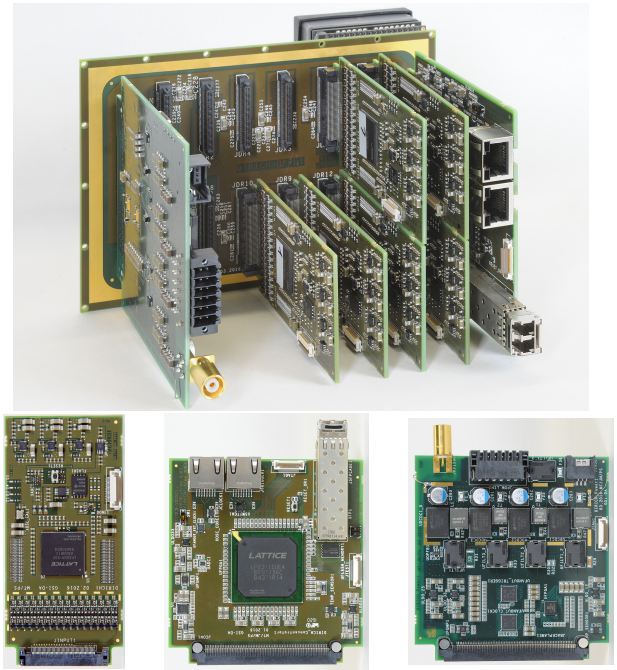

Figure 1: A 3x2 MAPMT readout module (top), with one out of 6 MAPMTs on front side, and few 32ch DIRICH FPGA-TDC frontend modules (lower left), a DiRICH-Power supply module (lower right), and a DiRICH-Combiner module (lower center).

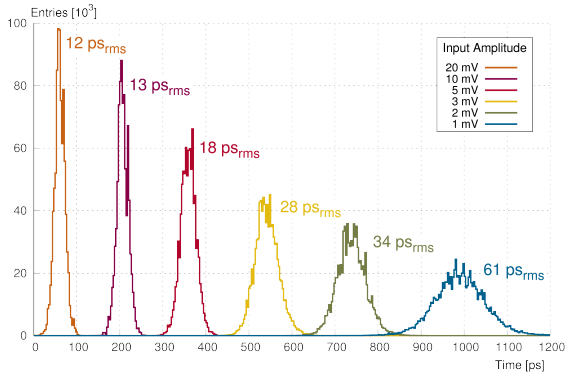

Figure 2: Achieved timing precision measured as time difference (RMS) for analog input pulses of varying amplitude. The absolute peak positions were artificially shifted for better differentiation.

The achieved performance in terms of timing precision for low amplitude signals is demonstrated in Figure 2. Here, a pulser was used to generate PMT like signals of varying amplitude down to 1 mV only. The signal was split into two identical signal paths, and injected into the DiRICH preamplifier. The timing precision was determined as RMS of the measured time difference of the leading edge threshold crossing of both channels. After proper TDC calibration, a timing precision down to 12 ps RMS could be observed, depending on input signal amplitude. Even at very low input amplitude of 2 mV, still a timing precision of 34 ps RMS could be demonstrated. This is fully sufficient given the internal timing accuracy of the photon sensors (PMT: 290 ps Transit time spread, MCP <100 ps).

The first tests of the new DiRICH readout concept look very promising, and seem to qualify the overall concept. A few minor design issues have already been found, and will be fixed in a second iteration of the DiRICH module, which is under production now.
For further validation of the concept a test beam at COSY/Jülich is scheduled for end of May, where two fully equipped 2x3 MAPMT modules will be put into operation. If everything goes well, we plan to start mass production of all modules end of 2017, in order to equip the full HADES RICH detector in time for the next HADES beamtime at SIS18 earliest mid 2018.

DOI:10.15120/GR-2017-1

Update on MAPMT delivery and series testing, interim results*

J. Förtsch †[1], *D. Pfeifer*[1], *C. Pauly*[1], *V. Patel*[1], *and K.-H. Kampert*[1]
[1]Bergische Universität Wuppertal, Germany

To cover the photo-detection plane of the CBM-RICH detector, 1100 HAMAMATSU H12700 MAPMTs were ordered by GSI in Summer 2015. The delivery starting in November 2015 consists of 50 delivered MAPMTs each month and will thus be finished late 2017. To ensure a high quality, all the MAPMTs need to fulfill certain requirements that are discussed in [1]. To measure these requirements and to fully characterize each 64 ch MAPMT, a single photon scanning test bench was built (see [2]).

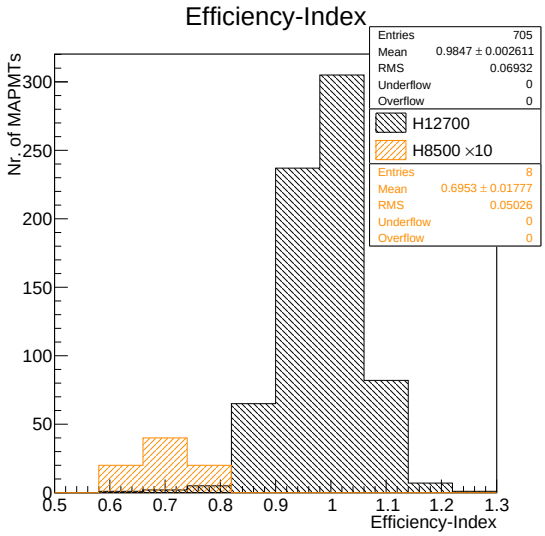

Figure 1: Efficiency-index distributions for the H12700 (black) and its predecessor H8500 (orange). The distribution of the H8500 is scaled by a factor of 10 for visibility. An efficiency-index of 1 states that the measured MAPMT is as efficient as the reference MAPMT averaged over its full surface.

Currently, 705 H12700 MAPMTs have been characterized using the test bench. This allows for a first broader look on the quality of the delivered MAPMTs. Therefore, the distributions of the 705 MAPMTs for parameters such as the efficiency-index, dark rate, gain, and skewness will be discussed in the following.

The efficiency-index uses a continuously measured reference-MAPMT as scale. The distributions of the efficiency-index for the H12700 MAPMTs and its predecessor, the H8500, are shown in figure 1. From the distributions it is clearly visible that the new H12700 has, in average, a 30% higher efficiency for single photons at 405 nm, as compared to the H8500. Furthermore, one can see that the distribution of the H12700's efficiency is rather narrow, featuring a RMS of 0.07.

In the RICH-detector each six MAPMTs will share one HV supply channel, distributed via a common backplane. To effectively group the MAPMTs and to reject MAPMTs not meeting the minimum gain requirements, a precise knowledge of the gain is important. Figure 2 shows the gain of all measured MAPMTs. The gain shows a rather broad distribution ranging from 1×10^6 up to 5×10^6, with all tested MAPMTs meeting the specified minimum gain of 0.8×10^6.

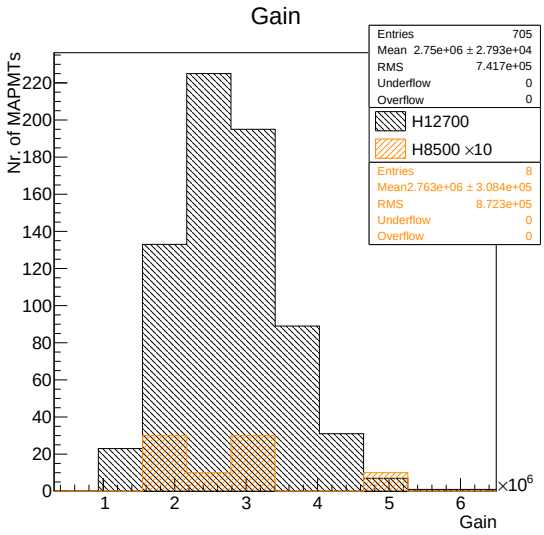

Figure 2: Gain distributions for the H12700 (black) and its predecessor H8500 (orange, scaled by a factor of 10).

As the CBM-RICH will consist of 1000 MAPMTs, being read out by a free streaming and self triggered DAQ, a requirement of less than 100 Hz dark rate per pixel has been set. To show the trend of the dark rate, the total dark rates of the different MAPMTs are shown in figure 3 and sorted by their production number. As the dark rate depends strongly on the temperature during the measurement, the temperature in the test bench was measured from mid of charge 11 onwards. The temperature was then taken into account following the extrapolation procedure described in [3]. Although no temperature measurement exists for the early measurements, one can still compare the measured dark rates to the recalibrated ones, as these measurements were done latest early summer, with a rather constant room temperature at around 25 °C. One can see that from the

* Work supported by GSI and BMBF contract No. 05P15PXFCA
† j.foertsch@uni-wuppertal.de

DOI:10.15120/GR-2017-1

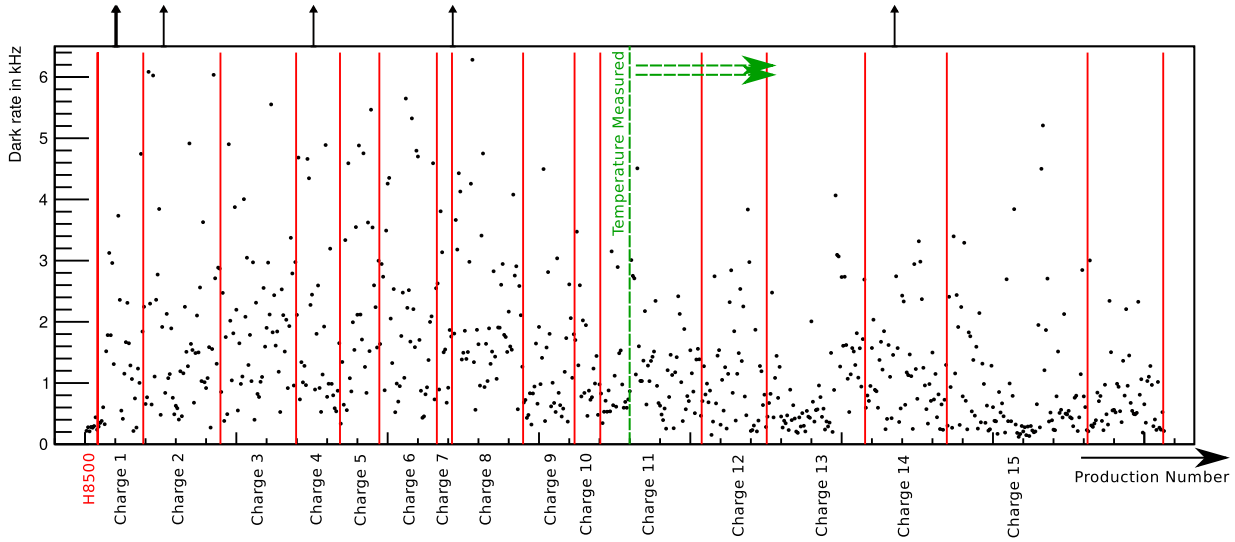

Figure 3: Dark rate in kHz vs. production number. The black arrows indicate MAPMTs having a dark rate higher than 6.4 kHz (specified maximum). The MAPMTs measured after the green dashed line are recalibrated to 25 °C using the measured temperature during the scan and the extrapolation procedure described in [3]. The red vertical lines indicate different delivery charges, with the first division being all the measured H8500 MAPMTs.

measured MAPMTs only very few do not fulfill the requirement of 6.4 kHz dark rate at maximum (black arrows in figure). Those MAPMTs are mainly found in the first few charges in which many MAPMTs show a tendency to higher dark rates. Furthermore one can see that the H8500 (first production numbers of fig. 3) show a much lower dark rate. This might be due to the H8500 MAPMTs being older and thus having a better alkali balance inside of the MAPMT. Still one can assume that the dark rate of the H12700 might remain slightly higher than that of the H8500.

A persistent feature one can observe for nearly all MAPMTs is a gradient in the efficiency from the left to the right side on the MAPMT surface. To better describe this feature the skewness parameter was introduced as the average efficiency of the MAPMT's left side (side of pixel 8) divided by the average efficiency of the MAPMT's right side (side of pixel 1). For the first 12 delivered charges an average skewness of 0.942 ± 0.002 was determined. This gradient was not observed for the H8500 having an average skewness of 1.007 ± 0.012. For newer charges (13-16) the feature seems to be slightly less prominent, as the average skewness for these charges is 0.951 ± 0.002.

From a sub-sample of 550 fully examined MAPMTs 27 MAPMTs were reclaimed. From these 27 MAPMTs, 13 were approved by HAMAMATSU to not meet the given requirements with six more MAPMTs still being analysed, and eight MAPMTs being rejected by HAMAMATSU for the time being. Nine out of these 13 MAPMTs missed the requirement on the dark rate[1]. The second most common failed requirement was the cathode uniformity, with six from 13 MAPMTs being too inhomogeneous. To prove the inhomogeneity of the photo-cathode an additional spatially resolved quantum efficiency-scan was carried out. An example for an accepted reclamation due to extreme inhomogeneity is shown in figure 4, where the spatially resolved quantum efficiency is compared to the spatially resolved efficiency measured by the single photon test bench.

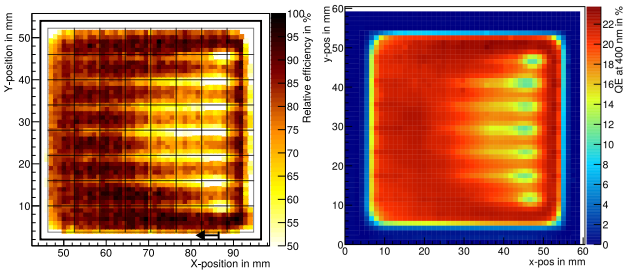

Figure 4: Left: Spatially resolved single photon efficiency. Right: Spatially resolved quantum efficiency.
The similar structure in both measurements suggests that the observed inhomogeneity stems from the photo-cathode.

[1] Maximum average dark rate 100 Hz per pixel with no pixel above 1 kHz maximum.

References

[1] J. Eschke et al., Ordering of 1100 MAPMTs H12700 for the CBM-RICH photon detector, CBM Progress Report 2015, Darmstadt 2016, p.57

[2] J. Förtsch et al., Development of a MAPMT test stand and first results, CBM Progress Report 2015, Darmstadt 2016, p.58

[3] V. Patel et al., Temperature dependence of dark noise for H12700 MAPMTs : A quantitative approach, this report

Radiation hardness tests of SiPMs for CBM PSD readout - in lab and at NA61@CERN beamtime*

V. Mikhaylov† [1,2], *A. Kugler*[1], *V. Kushpil*[1], *S. Morozov*[3], *and O. Svoboda*[1]
[1]NPI of CAS, Řež, Czech Republic; [2]CTU, Prague, Czech Republic; [3]INR RAS, Moscow, Russian Federation

PSD radiation environment

The Projectile Spectator Detector (PSD) of the CBM experiment is a compensating lead-scintillator calorimeter designed to measure the energy distribution of the forward going projectile nucleons and nuclei fragments (spectators) produced close to the beam rapidity [1]. High intensity beams at FAIR SIS100/300 up to 1E6/1E7 interactions/s lead to the high radiation emission to the PSD making it act as a spallation target producing the high neutron fluence up to 4E12 n/cm^2 accumulated during a year of the experiment operation. Studies of passive parts of PSD including the scintillators shown that it can work in this conditions. The radiation hardness of the Silicon Photomultipliers (SiPM, also called multipixel avalanche photodiodes (M-APD)) to be used for the light readout is the main topic to be discussed.

SiPM irradiation conditions

Several SiPM devices produced by different manufacturers were tested as options for the PSD readout: Zecotek MAPD-3A, Zecotek MAPD-3D, Hamamatsu S12572-010P, Sensl uF-C30020, uF-B30020 and Ketek PM-3350 [2]. SiPMs were irradiated at the cyclotron of NPI Řež with a "white" (2-35 MeV) and mono-energetic (22 MeV) neutron spectrum and total fluxes in the range of 2E10-1E13 n/cm2.

Choice of the SiPM device

The drastic change of the dark current was observed for all the SiPM samples after irradiation by total fluence around 4E12 n/cm^2 as shown at Figure 1. For the Ketek and Sensl devices, the change was the most abrupt requiring more than 1 mA of power supply for the operation making them inapplicable for the readout. Another factor to be mentioned is the dynamic range which is directly dependent on the square of SiPM pixel size. The Sensl and Ketek SiPMs are available on the market with the smallest size of 20-50 um, which compared to the Hamamatsu and Zecotek SiPMs available pixel size of 10 um shortens the dynamic range by 1-2 orders. The dark current of Hamamatsu and Zecotek SiPMs was found to be about an order of magnitude less than for Sensl and Ketek samples. However, Zecotek SiPMs available on the market have pixel recovery time about 2-10 us making them too slow for the PSD readout where hundreds or tens of nanoseconds are required for the operation at 1E6/1E7 interactions/s. Consequently, Hamamatsu S12572-010P was chosen as the best available candidate for the PSD readout in the high radiation environment of CBM experiment.

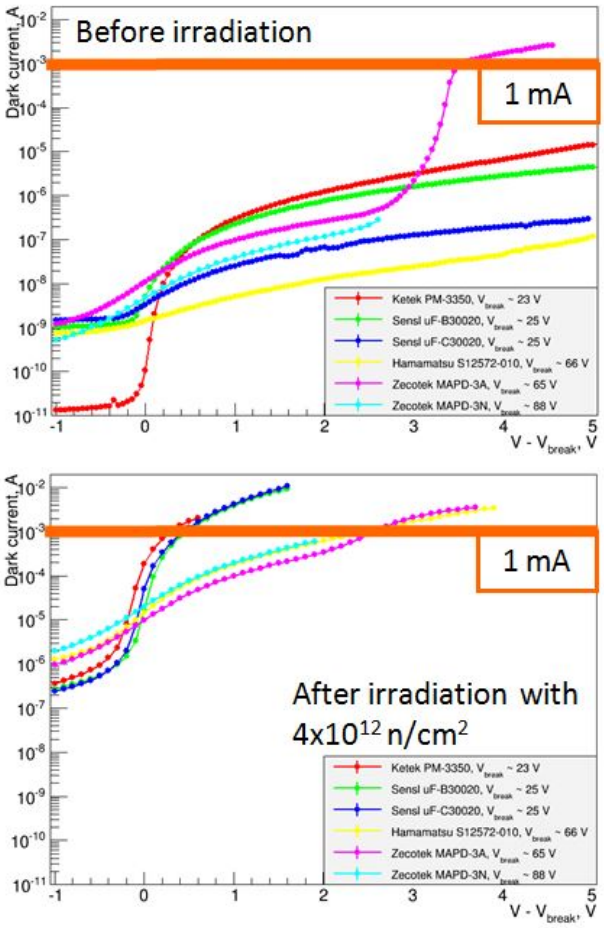

Figure 1: Dark current of SiPMs produced by various manufacturers. Top - before irradiation, bottom - after irradiation.

Investigation of Hamamatsu SiPMs

The change of dark current, breakdown voltage, noise and signal response to LED for Hamamatsu SiPMs was further studied at the lab. Variation of the breakdown voltage due to irradiation was found relatively small to be up to

*Work supported by Czech MEYS - LM2015049 , OP VVV - CZ.02.1.01/0.0/0.0/16_013/0001677
† mikhaylov@ujf.cas.cz

DOI:10.15120/GR-2017-1

0.5 V. This pose no problem for the operation of SiPM itself, but raise requirement of regular module recalibration as section response depends on the SiPM gain which is dependent on the breakdown voltage.

Figure 2 represents the results of SiPMs laboratory tests by the signal to noise ratio (SNR) for the SiPM response to same amplitude LED illumination. One can see the gradual decrease of the SNR with the increase of total absorbed neutron fluence. With neutron fluence up to 7E11 n/cm^2, SNR is dropping to value of 30 which is quite safe for the device operation. However, signals are still visible even for SiPMs irradiated by 1E13 n/cm^2 fluence. Generally speaking, the SNR degradation means the requirement for the regular module recalibration as well as inevitable shortening of the dynamic range.

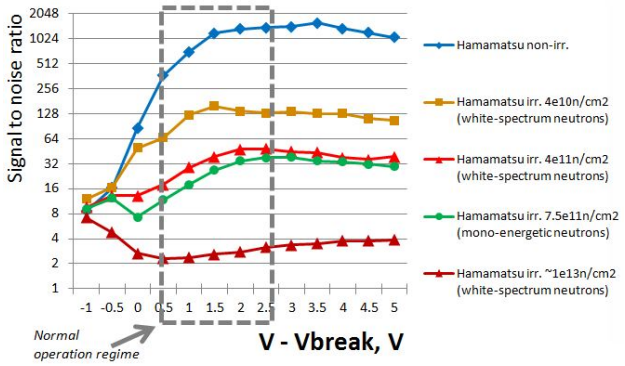

Figure 2: Signal to noise ratio for Hamamatsu SiPMs illuminated by LED.

Further studies were conducted at the NA61 CERN beamtime in summer 2016 with help of NA61 PSD calorimeter similar to CBM PSD with SiPM-based readout [3]. Three packs of 5 Hamamatsu SiPMs - non-irradiated, irradiated with 4E10 and 4E11 n/cm^2 ("white spectrum" of 2-34 MeV) were soldered to NA61 PSD readout boards and mounted to the calorimeter module. With the module equipped with SiPMs irradiated to the same dose, we estimated dependence of the proton energy determination resolution on the neutron fluence applied to SiPMs. First five sections of the module were equipped with the investigated SiPMs, so the achieved energy resolution values are greater than in the case of the full 10-sections operation.

The 80 GeV/c proton beam was utilized to access the calorimeter energy determination performance with irradiated SiPMs. Module energy resolution R_E was calculated from the deposited energy as the sigma of Gauss fit divided by its mean (see Figure 3). For the module equipped with non-irradited SiPMs R_E was equal to 16.5 %. For the SiPMs irradiated by total fluence of 4E10 n/cm^2 it remained the same; even though noise RMS of the module during the simple LED-test shown increase in 1.7 times, it was not visible during the proton beam tests probably due to to increased noise from the other electronic sources during the whole detector operation. Still, signal from muons was not possible to detect, which is not a problem for the detector operation, but makes muon-calibration impossible, so other calibration methods have to be employed. For the SiPMs irradiated by total fluence of 4E11 n/cm^2 R_E was equal to 21.1 %, meaning decrease in the energy resolution by 4.6 %.

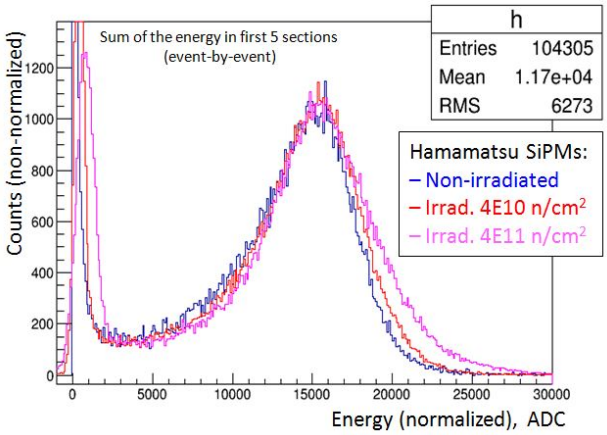

Figure 3: Energy resolution for 80 GeV/c proton beam with half of NA61 PSD module equipped with Hamamatsu SiPMs.

Conclusion

During the SiPM irradiation tests, Hamamatsu S12572-010P was chosen as the best available candidate for the PSD readout. Dark current increase with the absorbed fluence raises the requirement for the corresponding high-current power supply up to 1 mA per SiPM (channel). Gradual degradation of the SiPM signal to noise ratio with the absorbed fluence poses the requirement for the regular PSD module recalibration during the experiment operation. PSD energy resolution R_E studied at NA61 beamtime dropped only slightly - by 4.6 % for the SiPMs irradiated by total fluence of 4E11 n/cm^2.

References

[1] CBM collaboration, Technical Design Report for the CBM Projectile Spectator Detector (PSD), GSI Darmstadt 2015

[2] V. Kushpil et al., Neutron irradiation study of silicon photomultipliers from different vendors, NIM A (2016), http://dx.doi.org/10.1016/j.nima.2016.06.101

[3] V. Mikhaylov et al., Performance of the forward calorimeters for heavy-ion experiments at FAIR, NICA, and CERN SPS, Proceedings of Science, PoS(EPS-HEP2015)281.

A slow control system for the HADES and CBM RICH detectors

A. Weber[1], *P. Zumbruch*[2], *and C. Höhne*[1]
[1]Justus-Liebig Universität, Giessen, Germany; [2]GSI, Darmstadt, Germany

An EPICS based slow control system for the HADES RICH700 upgrade and the future CBM RICH is developed. The slow control system is server-client-model based and highly flexible due to variations in the experimental setup. The control software for the ISEG HV power supply (see Fig. 1) is designed in a 3 layer outline. It allows the control of every channel of every module of the crate individually, but also the control of predefined groups of channels from different modules. In addition it is possible to group channels via the GUI, too. The ISEG HV crate (*ECH 44A*) has a *CC24* Master module which includes the EPICS IOC. This allows to run the slow control software of the crate without any additional computer. The HV crate has 6 *EHS F620n-F_SHV* modules with 16 channels each. The modules are limited to 1,5 kV and with single channel floating-GND.

Figure 1: The ISEG crate with 6 modules à 16 channels and a CC24 master.

To cope with low voltage a TDK Lambda Genesis 60-40 is used (see Fig.2). The EPICS IOC runs on an own computer which is connected to the TDK Lambda via LAN. The IOC uses `StreamDevice` with an own protocol for the device. It is possible to control the voltage, set current limits and control different statuses of the LV device.

Figure 2: The TDK Lamda low voltage power supply.

During the experiment the temperature and the humidity will be measured. The temperature is mapped with many DS18B20 1-Wire Sensors from *Maxim Integrated*. To measure the humidity HDC1000 humidity sensors from *Texas Instruments* are used. These sensors support the I^{2}C protocol and have address pins which allow to use up to 4 of these sensors at one port (see Fig.3). Both sensor types are connected to a HadCon2 Board which controls the pins. The HadCon2 is connected to a raspberry pi 2 model B via USB connection. The EPICS IOC runs on the raspberry pi and sends the HadCon2 the commands for the measurement of temperature and humidity.

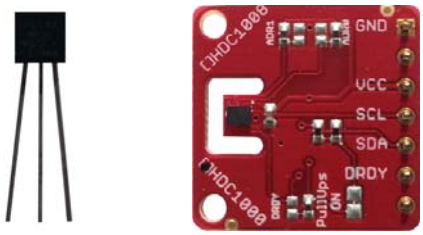

Figure 3: left: One DS18B20 1-wire sensor from Maxim Integrated. right: A HDC1000 sensor on a breakout board.

The HADES RICH upgrade will use many DIRICH boards which have a 1-wire temperature sensor. This temperature can be readout via the TrbNet. Therefore an EPICS IOC is written. It gets the value from many different boards with one call which reduces the traffic on the TrbNet. It is also possible to get more further status values from the TrbNet with the IOC.
The Control System Studio (CSS) is used as the GUI of the HADES RICH experiment and shows the EPICS process variables in a human readable, graphical layout (see Fig.4). It replaced the *Motif Editor and Display Manager* (MEDM) which is known from previous HADES running periods.

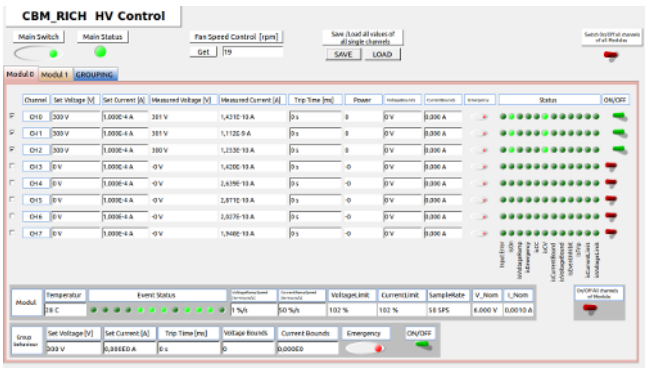

Figure 4: The CSS BOY GUI for the HV power supply.

DOI:10.15120/GR-2017-1

Laboratory tests of the Bucharest TRD prototype performance in High Counting Rate environment*

A. Bercuci[1], *G. Caragheorgheopol*[1], *V. Cătănescu*[1], *M. Petriş*[1], *and M. Petrovici*[1]
[1]National Institute for Physics and Nuclear Engineering (IFIN-HH), Bucharest, Romania

At collision rates of 10^7 $events/sec$ the inner zones of the CBM experiment will be exposed to $\sim 100\ kHz/cm^2$ [1]. This is beyond what was reached so far with current test setups at present irradiation facilities [2], [3]. Although the inverse of time difference between consecutive events, during CERN-SPS bunches, is compatible with or even higher rates [3], since they are not sustained for longer times make all tests done so far incomplete. The TRD prototype developed in Bucharest [4] and the FEE designed to operate it, the FASP [5], [6] and the motherboards housing it, were optimised for high-counting rate environment applications. An alternative to particles bombardment, although less complete, is the use of high flux X-ray tubes.

Experimental set-up

Our experimental setup was aimed to study the alterations of a known signal - in our case the ^{55}Fe detection rate - in the presence of a heavy X-ray detector irradiation. The experimental setup is sketched in Fig. 1 left.

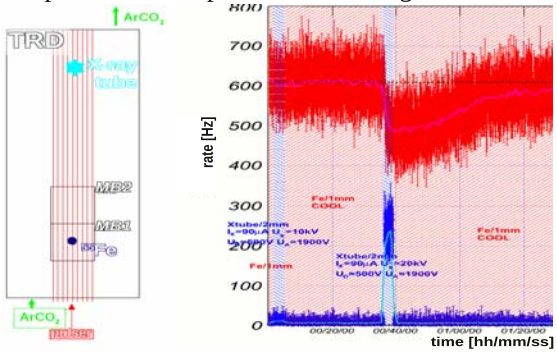

Figure 1: Left : The experimental setup including the position of the X tube and ^{55}Fe wrt TRD, the direction of $ArCO_2$ gas flow and the read-out areas (MB). Right : Monitoring of ^{55}Fe rate (red/magenta) before and after X-ray (blue shaded area) tube irradiation.

The collimated X-ray tube is placed at one end of the detector surface, close to the $ArCO_2$ outlet, while the witness ^{55}Fe source at the other end to assure that the gas flow will not have a detrimental influence. The distance between the center of the two irradiated areas is $\sim\ 20\ cm$.

^{55}Fe rate variation after X-rays irradiation

The measurement was done using 2 areas of $\sim\ 8\ cm^2$ each. The first is used to record ^{55}Fe rate (red in Fig. 1 right) while the other (blue same figure) the background. Blueish areas in the figure mark the X-ray tube irradiation, typical a couple of minutes. It was estimated that a current intensity on the tube (I_X) of 90 μA will produce in the current setup $\approx\ 100\ kHz/cm^2$. For $U_X = 10\ kV$ the X-ray spectrum is smooth and limited at $10\ keV$ while $U_X = 20\ kV$ extends the X-ray spectrum up to $20\ keV$ with pronounced Au L lines at $9.71,\ 11.44$ and $13.38\ keV$. After the irradiation with the harder spectrum a noticeable degradation of efficiency is measured in the witness rate through a drop of more than $15\ \%$ which is recovered after $\sim\ 1\ h$ probably through the gas flow. Less significant effects are produced by the soft spectrum.

Pulser signal monitoring after X-rays irradiation

Squared shaped signals injected on the anode wires are used to induce equal amplitude signals in all FEE channels They are sensitive to parasitic currents which may be produced on HV electrodes by heavy irradiation. In Fig. 2 the monitoring of such signals for all 16 FEE channels used in the setup of Fig. 1 left is shown.

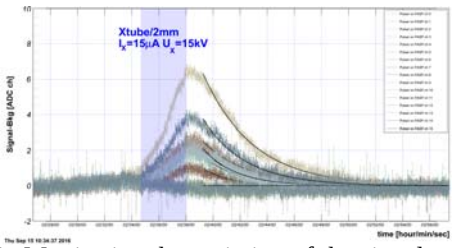

Figure 2: Monitoring the variation of the signal amplitude on different FASP channels before and after X ray (shaded area) tube irradiation.

During irradiation an increase of max. $6\ ADC\ ch$ of the measured signal is recorded on some channels which represent at most $0.4\ \%$ of the standard signal. An exponential time decay of the amplitude excess is recorded with a time constant of $\approx\ 150\ s$ depending on the FEE channel. Such electronic effects, although present in the detector are too low in magnitude to explain the large variations seen in the ^{55}Fe rate.

References

[1] CBM Technical Status Report.
[2] A. Bercuci et al., this report.
[3] A. Bercuci et al., this report.
[4] M. Petrovici et al., Nucl.Instr. and Meth. A579(2007)961.
[5] V. Cătănescu et al., CBM Progress Report (2009) 47.
[6] V. Cătănescu et al., CBM Progress Report (2014) 82.

* Work supported by Romanian ANCSI/CAPACITATI Modul III Contract F04 and NUCLEU Project Contract PN 16420104.

Tracking with the Bucharest TRDs at the CERN-SPS 2015 Testbeam * †

A. Bercuci[1], *D. Bartoş*[1], *G. Caragheorgheopol*[1], *V. Cătănescu*[1], *M. Petriş*[1], *and M. Petrovici*[1]
[1]National Institute for Physics and Nuclear Engineering (IFIN-HH), Bucharest, Romania

A main application of the TRD subsystem within the CBM experiment planned to be build at GSI-FAIR is prolonging tracks defined by the SPS subsystem and improve matching with TOF. The Bucharest TRD prototypes designed for the inner zone of the TRD wall are particular suited for such application as they are optimized for $2D$ position information [1] in high-counting rate environments. A testbeam organized at SPS-CERN was aimed to prove this using a beam of $30\ AGeV/c$ Pb on Pb target.

Experimental setup

A compact setup of 3 TRD prototypes was installed downstream of target at $\sim\ 2\ m$ at an angle of $\sim\ 30^o$. A sketch of the TRD read-out units - the triangular pads - and their relative alignment pointing to the target is shown in Fig. 1 with target position on the left side.

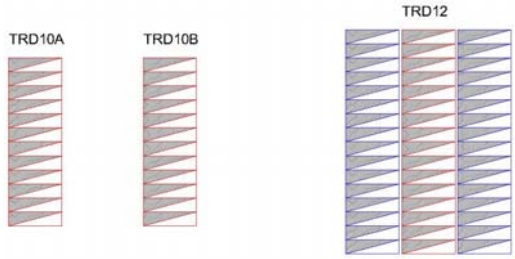

Figure 1: A sketch of the Bucharest TRD setup in which the alignment of pad-rows is emphasised in red for the 3 operated prototypes.

The TRD setup was operated with FASP[2] ASIC for the overlapped area. A MBS-DAQ system was used to record data triggered by a combination of plastic scintillators, a Bucharest RPC_{2013} [3] prototype and a diamond CVD detector mounted in front of the target.

Tracking performance

In order to asses position reconstruction performance of the TRD prototypes a selection on the data was implemented such that cluster quality was defined based on their total charge and shape and events with one such cluster/detector were selected. Due to various reasons pertaining to the triggered setup and read-out an acceptance of less than $0.1\ \%$ off all triggered events was accomplished.

In the left panel of Fig. 2 the residual distribution between clusters position across pads and a track fit is shown.

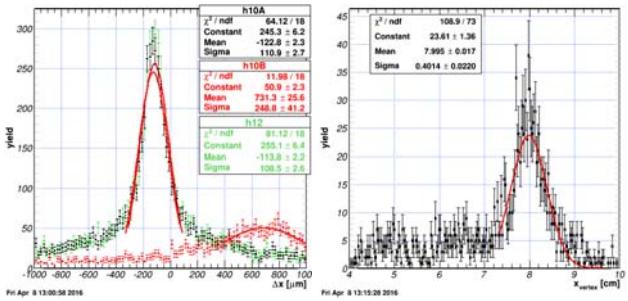

Figure 2: Tracking performances of the TRD prototypes; Left : The residual distribution between clusters position across pads and a linear track model crossing all 3 detectors; Right: Intersection of the track with the target plane. The enhance is clearly visible and it is related to the interaction region on the target.

An alignment procedure was applied based on normalizing[1] simultaneously the three distinct linear position correlations of type $\Delta x_{i-j} : \Delta x_{k-i}$ between the position across pads of each of the 3 cluster/detector. The alignment procedure produced biased results as can be seen by scanning the mean values of the residuals in the figure due to the lack of a reference detector and secondary particle contamination. A further consequence is the under/over estimation of detector resolution reported as the $Sigma$ parameter of the gaussian fit of the residual distribution. Qualitatively, a position resolution across pads better than $200\ \mu m$ seem to be supported by the data.

A further exercise was to extrapolate the track fit in the prompt plane. A further selection was applied at this stage such that tracks having outliers above the $\pm\ \sigma$ level according to Fig. 2 left results were rejected resulting in a $40\ \%$ drop in tracked data statistics. The results for vertex definition are shown in Fig. 2 right where a clear enhancement around a position, shifted with $8\ cm$ wrt. projected vertex defined by the TRD setup, and a resolution of few mm, can be seen. Qualitatively the observed shift is a nice confirmation of the trigger bias used in data acquisition in which only one quadrant of the CVD detector was used in the trigger logic.

References

[1] A. Bercuci et al., CBM Progress Report (2015)81.
[2] V. Cătănescu et al., CBM Progress Report (2009) 47.
[3] M. Petriş et al., CBM Progress Report (2012)68.

* Work supported by Romanian NUCLEU Project Contract PN 09370103.
† Special thanks to CERN-SPS operating crew and to our technicians V.Aprodu, L.Prodan and A.Radu for their highly professional contribution without which all these things would'n have been operational in due time.

[1] Correlation distribution is centered at 0 and has slope 1.

DOI:10.15120/GR-2017-1

Bucharest RPC and TRD prototypes at CERN-SPS 2016 Testbeam *

A. Bercuci[1], *V. Aprodu*[1], *D. Bartoş*[1], *G. Caragheorgheopol*[1], *V. Cătănescu*[1], *F. Constantin*[1], *M. Petriş*[1], *M. Petrovici*[1], *L. Prodan*[1], *A. Radu*[1], *and C. Şchiaua*[1]

[1]National Institute for Physics and Nuclear Engineering (IFIN-HH), Bucharest, Romania

The RPC [1],[2] and TRD [3]-[5] prototypes developed in Bucharest for low polar angles region of CBM experiment were tested at CERN-SPS at the end of 2016. The reaction products produced by colliding the Pb beam of 13 GeV/c ($run1$), 30 GeV/c ($run2$) and 150 GeV/c ($run3$) on a Pb target were used. The RPC signals were processed by fast amplifiers/discriminators NINO chip [6] of which differential outputs were covered by CAEN V1290A TDCs. The information was read-out using the MBS-DAQ system [7]. The frontend electronics used for the three TRD prototypes was based on FASP-01 and FASP-02 [8] ASICs. FASP-01 signals were processed using MADCs and MBS-DAQ operated in a trigger mode. In parallel, other regions of the TRDs were operated using FASP-02 and 2 free running systems, one already presented in previous CBM reports [9],[10] and a new one coined FASPRO [11].

Experimental setup

In Fig. 1 a downstream towards target view of the Bucharest experimental setup is presented. It consists of 2 RPC prototypes and three layers of TRDs. The TRD setup is zoomed in the right panel of Fig. 2 where, from left to right, 2 TRD_{2010} prototypes read-out on a $\sim 94cm^2$ area completed by a TRD_{2012} detector of $60 \times 60cm^2$ partially equipped with electronics. The experimental arm was completed with 2 plastic scintillators for triggering and timing purpose one mounted at $\sim 1m$ from target and a second one in front of the RPC setup.

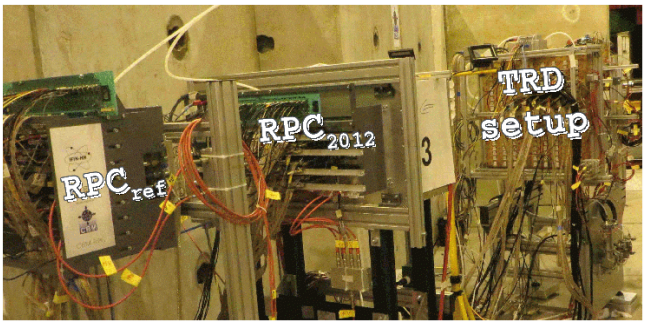

Figure 1: The Bucharest setup, from downstream to the target position RPC_{ref}, RPC_{2012} and the three TRD layers zoomed out in Fig. 2.

For each beam energy/run a different configuration of the TRD read-out was used as follows: tracking optimized in $run1$ with MBS and FASPRO on all 3 TRD detectors on parallel directions, $2D$ position information for the TRD_{2010} prototypes fully equipped with FASPRO and the TRD_{2012} alone operated with MBS on $run2$ and tracking in two divergent directions wrt. beam plane by using TRD_{2010}-TRD_{2012} in the horizontal plane with MBS and the second TRD_{2010} with a different area of TRD_{2012} operated with FASPRO at a small inclination angle wrt. horizontal plane.

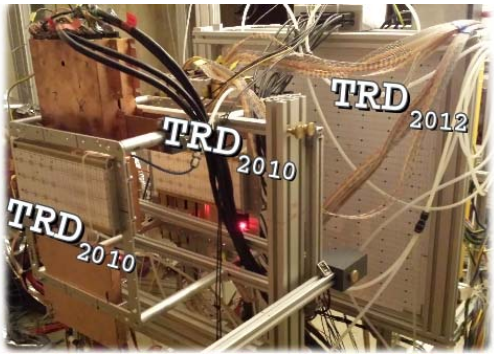

Figure 2: The TRD setup, from left to right, 2 TRD_{2010} and the $60 \times 60\ cm^2$ TRD_{2012}.

For calibration purposes a pulser signal was injected on all TRDs with $0.1\ Hz$ and varying amplitudes during the data taking.

MBS DAQ for the RPCs and TRDs detectors

The information from MBS DAQ is aimed to be used for tracking and $dE/dx - time$ studies. The acquisition of all TRD self trigger signals together with the particle arrival time from plastics were also collected up to 14 channels. Two classes of triggers were used based on the TRDs self trigger topology and plastic correlation.

Using the self trigger TRD signal the interaction rate was monitored as shown in Fig. 3 left. The hit rate per second on a $\sim$ 15.5 cm^2 area operated on the central part of the TRD_{2012} with 2 FASP-02 ASICs was recorded during $run3$. The time of flight of particles between the front plastic and the RPC can be estimated from the information shown in Fig. 3 right. The arrival time at both ends of 16 RPC strips is presented for one of the TDCs, channel wise, in units of 25 ps. In TDC channel 8 the arrival time at the front plastic is registered. Data are un-calibrated and the colour code represent the yield.

* Work supported by Romanian ANCSI/CAPACITATI Modul III Contract F04 and NUCLEU Project Contract PN 16420104.

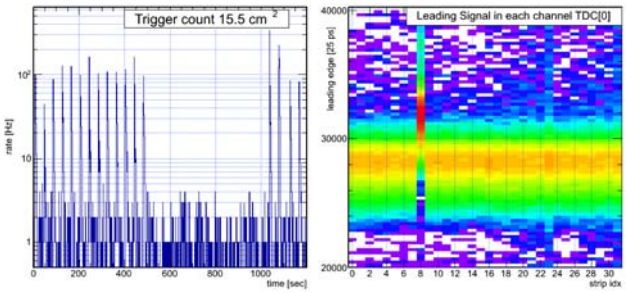

Figure 3: Left: Trigger rate variation on an area of $15.5\ cm^2$ of the TRD_{2012} during and off spill for $20\ min$ acquisition time. Right: The distribution of particle arrival time on RPC_{2012} for 16 strips read-out at both ends and the plastic synchronisation signal on TDC channel 8.

Free Running DAQ based on FASP-02 ASIC for the TRD setup

The capabilities of the FASP-02 were fully exploited for the first time by the FASPRO mother-board. Together with a system of timing and data processing the DAQ is completely driven by the channel wise self triggering option of the ASIC.

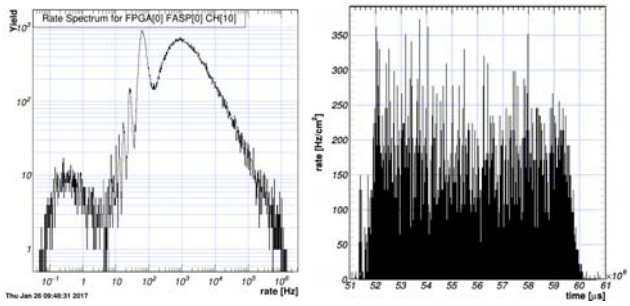

Figure 4: *FASPRO* free-running DAQ results : Left: Disribution of the inverse of time difference between two consecutive events per FASP channel with the pulser ripples up to $100\ Hz$, bunch distribution up to $1\ kHz$ and the intra-bunch interactions up to $1\ MHz$. Right: The frequency profile of a spill of $\approx\ 9\ s$ averaged on $1\ ms$ intervals as seen on $94\ cm^2$ of the forward TRD_{2010} detector.

An example of the inverse of time difference between consecutive events distribution seen by each channel reading-out 2 paired triangular pads spanning $\sim\ 2\ cm^2$ of detector area is shown in Fig. 4 left. The spectrum contains 3 regions as follows pulser ripples on next interaction event up to $100\ Hz$, rates of consecutive events from different bunches up to $1\ kHz$ and consecutive events from the same bunches above this limit. It is worth observing that using a channel wise read-out mode, consecutive hits compatible with rates of up to almost the theoretical limit of $1\ MHz$ of the FASP can be recorded. The proper response time of TRDs, dictated by the drift time, is on the level of $100\ ns$ but secondary effects produced in the detector volume and systematic effects of FEE response to signal can increase it. For the current analysis an event is defined on an interval of $150\ ns$. After building up events based on matching the channel-wise time labels within the predefined time window the event frequency spectrum can be reconstructed. In Fig. 4 right an SPS spill is presented cooresponding to one spike in the left panel of Fig. 3. The average rates are calculated on $1\ ms$ intervals and are integrated on the total area operated of the forward TRD_{2010} detector in $run3$.

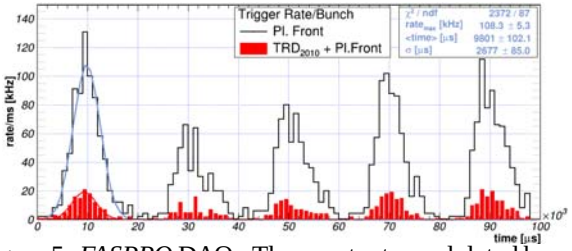

Figure 5: *FASPRO* DAQ : The event rate modulated by machine bunches, during $100\ ms$ acquisition time, as function of time for the forward plastic scintillator w/o condition on the whole TRD_{2010} surface (black) and with (red).

A further zooming of the spill structure can be followed in Fig. 5 as measured with the free-running DAQ based on *FASPRO* [11]. Here the machine bunches interacting with the target are visible simultaneously in two detectors: the forward plastic scintillator and, after calibrating out the delay between the two, in the correlation with the forward TRD_{2010} detector. More details of this operation mode are presented in a separate report [11].

Conclusions

The detector prototypes developed in Bucharest were used in a unique setup during the 2016 CERN-SPS testbeam to scan 3 beam energies with 3 different DAQ systems used in each of the three runs in a different configuration. Such redundant information is of mandatory importance to study systematic effects in the new conditions for which these prototypes were developed.

References

[1] M. Petriş et al., CBM Progress Report (2011)55
[2] M. Petriş et al., CBM Progress Report (2012)68
[3] M. Petriş et al., CBM Progress Report (2011)47
[4] M. Petriş et al., CBM Progress Report (2012)60
[5] A. Bercuci et al., CBM Progress Report (2015)81
[6] F.Anghinolfio et al., Nucl.Instr.Meth. A533(2004)183
[7] H.G.Essel and N.Kurz, GSI Ann. Rep. (1988)188
[8] V. Cătănescu et al., CBM Progress Report (2014) 82
[9] F. Constantin et al., CBM Progress Report (2012)56
[10] F. Constantin et al., CBM Progress Report (2014)83
[11] A. Bercuci et al., this report.

DOI:10.15120/GR-2017-1

Tests of the *FASPRO* free-running DAQ for the Bucharest TRD prototypes at the CERN-SPS 2016 testbeam*

A. Bercuci[1], *G. Caragheorgheopol*[1], *V. Cătănescu*[1], *M. Petriş*[1], *M. Petrovici*[1], *and C. Şchiaua*[1]

[1]National Institute for Physics and Nuclear Engineering (IFIN-HH), Bucharest, Romania

Processing the large amounts of data expected in the central region of the TRD subsystem of the CBM experiment, based on the results obtained with the very first TRD prototypes developed by us [1], an optimal ASIC, Fast Analog Signal Processing (FASP) [2] was developed. The 2^{nd} version of the chip[3] has 16 independent channels, each providing the total charge and its arrival time information collected on the read-out unit - the pad. In order to cope with limitations in the S/N ratio along the TRD triangular pad read-out geometry [4] an analog summing is performed before charge integration. Thus each FASP channel reads-out a detector area of $\approx\ 2\ cm^2$ of two paired pads, alternating rectangular and tilted coupling, for robust estimation of position and PID related measurements.

The FASPRO board and Detector setup

To fully exploit the capabilities of the FASP, a new mother board, FASP-Read-Out (FASPRO), was developed to house the chip, 16 ADCs and the drivers for connection to the outside world. The board is driven by a $40\ MHz$ clock which can also be fed from outside. On each differential output channel the digitized values of the signal amplitude and the corresponding channel-wise self-trigger time signal - the Chip Select (CS) - are delivered. The output is ready for GBTx [5] integration - the solution foreseen for the CBM experiment to ship data from the hot zone to the online/offline processing units.

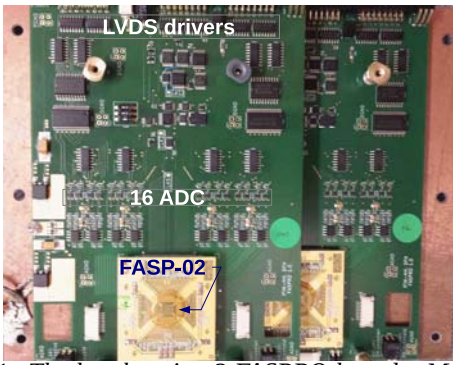

Figure 1: *The box housing 2 FASPRO boards. Major elements of the FASPRO board are emphasized on the picture.*

The free running DAQ based on FASPRO boards was tested during the CERN-SPS 2016 testbeam [6]. The detector setup used for $150\ GeV/c$ Pb beam is shown in Fig. 2. Within this setup an inclined direction, wrt to horizontal beam plane, was used to test the tracking performance of the TRD prototype in free-running operation.

* Work supported by Romanian ANCSI/CAPACITATI Modul III Contract F04 and NUCLEU Project Contract PN 16420104.

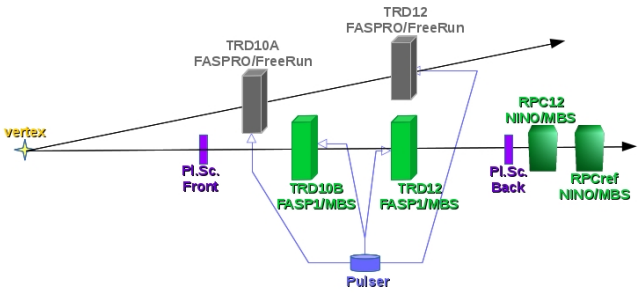

Figure 2: *Schematic view of the experimental setup used for 150 GeV/c Pb testbeam; the horizontal direction was operated with MBS (green) and the tilted one (gray) run with FASPRO in free-running mode for two TRDs and two plastic scintillators.*

The forward $TRD10A$ was operated with 6 FASPRO boards $i.e.$ 96 read-out channels on an area of $8.16 \times 11.52\ cm^2$ organized in 3 pad rows (see Fig. 3 right). A similar read-out geometry was used on the back $TRD12$ situated at a $\approx 60\ cm$ larger distance. A plastic scintillator was installed, in the beam plane, at $\approx\ 1\ m$ from the target and a second scintillator, aligned with the first, at $\approx\ 3\ m$ from the target, shadowed by the TRD setup. For calibration purposes a pulser signal was injected synchronously on the anode plane of all TRD detectors during the measuring time at a main frequency of $0.1\ Hz$ and varying amplitudes. The HV U/I characteristics of all TRDs were read-out and stored with the data as described in the next section.

Overview of the Free-running DAQ

A simple DAQ, schematically shown in Fig. 3, was build to synchronize all FASPRO boards used in acquisition and to ship data to a permanent storage. A FASPRO-box (see Fig. 1) with 2 FASPs can operate 32 read-out channels $i.e.$ one pad-row in our setup. The digitized signals and their CS status are send to the Local Data Concentrators (LDC) phased with a unique $40\ MHz$ clock. The LDCs are implemented on Xilinx Zynq 7000 cores [7] and run an event buffer for each FASP channel. For each valid data (CS status on) the time label is attached to data.

A further extension of the system consists of 16 dual NIM-LVDS / LVDS-NIM translators used to read external signals (see "Ext. Signals" label in Fig. 2) with the proper clock of the DAQ. We have used during the testbeam the following signals: 2 logic ANDs each coming from the two PMs reading one plastic scintillator (see Fig. 2 $Pl.Sc.\ Front/Back$) and the beam start/stop signals provided by the machine. For monitoring the detector itself

DOI:10.15120/GR-2017-1

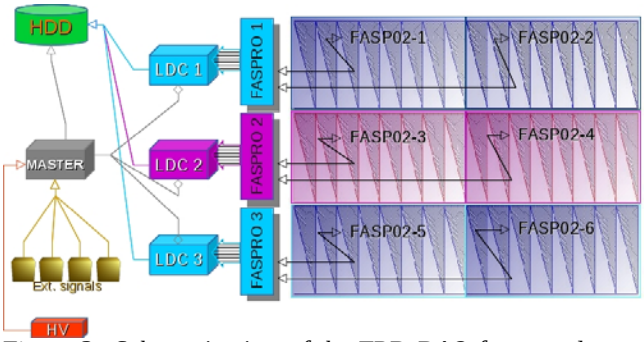

Figure 3: *Schematic view of the TRD DAQ from read-out units (triangular pads) to storage (HDD).*

during irradiation the HV parameters (U, I)[1] were included in the data flow at continuous reading interval of $1.33\ ms$.

Event types and characteristics

The output of the DAQ is defined by the 3-tuple (GEO, $TLAB$, VAL) with GEO the identifier of the "geographical" position of the channel, $TLAB$ the time in $25\ ns$ clocks as registered by the FPGA counters and VAL the data measured per channel (ADC channels for FASPRO, XADC values for HV and the on/off status of the external detectors signals respectively). The channel wise data are packed offline to $EVENT$s based on their $TLAB$. For each signal source the delays are constant such that for $e.g.$ the TRDs, the $EVENT$ is directly reconstructed based only on the $TLAB$ information[2].

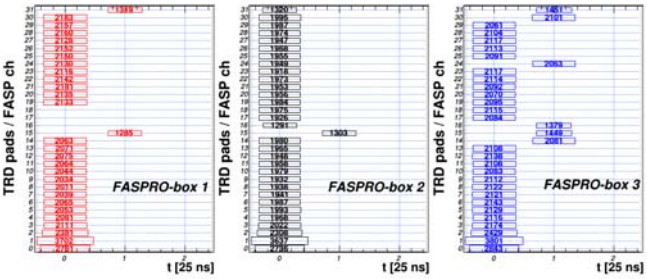

Figure 4: *Pulser event seen on $TRD10A$ (3×32 pads) by 6 FASP-02 ASICs (see Fig. 3). Each channel signal is characterized by its delay in $25\ ns$ clocks wrt. prompt signal and value expressed in ADC channels.*

There were three types of signals which were measured quasi-synchronously during the testbeam: pulser events of constant frequency and amplitude used for FEE calibration, ^{55}Fe X-rays for assessing detector performance during irradiation and the proper beam-target events respectively. In Fig. 4 a detailed view of a pulser event is presented based only on the channel wise information from DAQ. The event is seen in 3 pad-rows/LDCs (each represented as a panel in Fig. 4) of 32 pads/channels (shown on the vertical axis) corresponding the operated area of $TRD10A$. The arrival time of each signal wrt. to prompt is represented on the horizontal axis in DAQ clocks. The response of each FEE channel to the unique signal induced by the pulser can be read in the figure. The result demonstrates the correctness of the principles implemented in our FEE-DAQ approach.

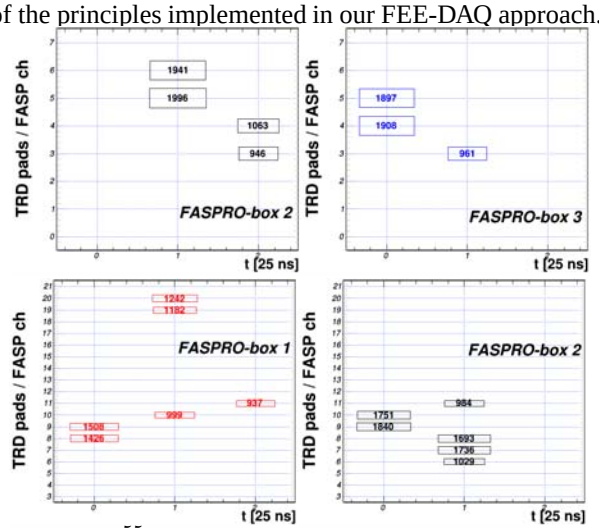

Figure 5: *A ^{55}Fe (top) and a Beam-Target (bottom) event seen on the $TRD10A$ detector in 2 adjacent rows. Data representation and matching with DAQ according Fig. 4.*

Pulser events are used for equalizing the effective gain and delay of each FASP channel but for detector efficiency/gain calibration in high counting rate conditions a $standard\ candle$ is used as $e.g.$ ^{55}Fe. Another application of such events is to provide a basis for understanding more complicated events as those produced by charged particles. A typical event of such type is shown in the top 2 panels of Fig. 5 where the interaction happens close the pad-row boundary and therefore the response is seen in 2 rows/panels. The relative delay pattern of the signals of a cluster carry detailed 2D position information but such correlations will not be discussed here. In the bottom 2 panels of Fig. 5 an event obtained in a beam-target interaction is shown. The event contains 2 distinctive interaction spots: a topological-simple type around pad/channel 20 and one with a complicated topology, spanning 2 pad-rows of TRD and a large time window front around 9. Such examples show that using the correlations induced by the triangular-pad read-out and the time/signal cluster topology accessible with FASP, the TRD can provide information with unprecedented precision both for position and PID.

References

[1] M. Petrovici et al., Nucl.Instr. and Meth. A579(2007)961.

[2] V. Catanescu et al., CBM Progress Report (2009)47

[3] V. Cătănescu et al., CBM Progress Report (2014) 82.

[4] A. Bercuci et al., CBM Progress Report (2014) 81.

[5] P.Moreira, J.Christiansen and K.Wyllie, The GBTx Link Interface Asic, Draft v1.7, October 2011.

[6] A. Bercuci et al., this report.

[7] https://www.xilinx.com/products/silicon-devices/soc/zynq-7000.html.

[1] We used two CAEN NDT 1471H HV units each having 4 channels which provide analogic, channel wise monitoring capabilities for U and I. The monitoring outputs were converted to LVDS signals by a custom made converter and digitized via the build-in XADC of the Zynq platform.

[2] The matching of different sources within an $EVENT$ needs calibration of physical delays and is not covered here

DOI:10.15120/GR-2017-1

Towards the Common Readout Interface boards for STS*

W. Zabolotny[†1], *G. Kasprowicz*[1], *A. Byszuk*[1], *M. Guminski*[1], *K. Pozniak*[1], *and R. Romaniuk*[1]
[1]Institute of Electronic Systems, Warsaw University of Technology, Warszawa, Poland

Version control friendly project management

Development of the firmware for CBM readout requires maintaining of complex HDL designs. To allow efficient management of projects incorporating multiple independently maintained IP blocks, the Tcl scripts proposed in 2015 have been further developed into the VEXTPROJ environment [1]. This environment allows rebuilding Vivado projects from the textual description stored in the version control systems. It supports importing IP blocks from remote repositories (Git, SVN, and others), and allows utilization of the "Out of Context Compilation" (OOC) to speed up rebuilding of the whole design. Figure 1 shows an example of a project consisting of locally and remotely managed sources.

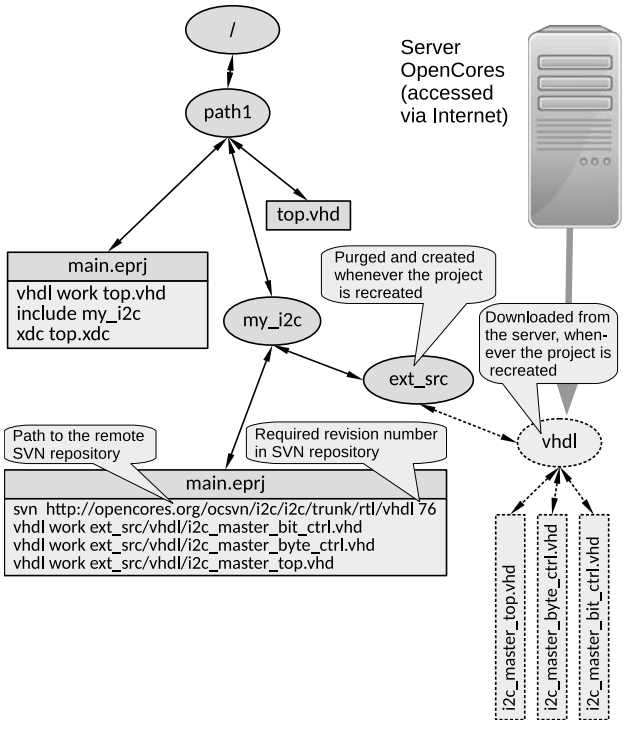

Figure 1: Example of the VEXTPROJ project, that uses the particular version of IP block stored in a remote SVN directory [1].

STS/MUCH-XYTER2 tester

The VEXTPROJ approach has been used in further development of the STS/MUCH-XYTER2 (SMX2) tester [2]. The design has been split between two repositories: "SMX2 tester" and "SMX2 model". The tester design imports the model as an OOC compiled block, which results in faster compilations. In 2016, the exhaustive tests of the SMX2 model have been performed in cooperation with the AGH and GSI teams. The tests covered the operation of the SMX2 model with varying number of uplink connections, recovery from induced and random error conditions and transmission of generated test hit data. The tests resulted in disclosing and fixing of a few subtle bugs, and improvements to the protocol [3] and the design of the SMX2 digital backend [4]. After the STS/MUCH-XYTER2 has been manufactured, the SMX2 tester has been also successfully used for communication and testing of the real ASICs.

Assessment of the new FPGA platform for STS Common Readout Interface

The work on the prototype of the Common Readout Interface (CRI) predecessor - the DPB boards, and the SMX2 tester was started when "Family 7" was the newest FPGA series available from Xilinx. Therefore the AFCK board designed for that purpose was based on Kintex 7 XC7K325T chip [5]. In the meantime, two new families - the "Ultrascale" and the next "Ultrascale+" were offered by Xilinx. As the initial step for selection of the final hardware platform for the CRI boards, the preliminary analysis of the feasibility of CRI implementation in the Ultrascale+ chips was performed. The prices of comparable "Kintex Ultrascale+" and "Zynq Ultrascale+" are similar. Therefore the Zynq Ultrascale+ ZU11EG chip was selected for the analysis. Obtained preliminary results show that it should be possible to use a single ZU11EG FPGA to concentrate data from up to 8 Common ReadOut Boards (CROB) [6] into up to 8 FLES links. The analysis included different architectures for the STS data concentration. The approach based on the heap sorter [7], offers better memory blocks utilization but requires too high clock frequency (896 MHz) to handle the incoming data stream. The approach based on the simple stream merger allows to parallelize data processing in the input stage, and group concentrated data in the longer words at the output to lower the required clock frequency. Of course, those preliminary results may be significantly changed by further progress in technology.

* Work partially supported by GSI
† wzab@ise.pw.edu.pl

DOI:10.15120/GR-2017-1

Forth based AFCK board controller

The AFCK board used as a prototyping platform for STS readout requires initial configuration of various components (clock generators, clock crossbar, connected FMC boards). It is equipped with the separate ARM processor, but it is used as an MTCA MMC controller, and modification of its firmware is inconvenient. Therefore, another approach was proposed. The solution [8] is based on a very simple J1B Forth CPU developed by James Bowman [9]. The Forth language offers very good code density and supports an interactive development of control/diagnostic procedures, without a necessity to use an external compiler. Simultaneously, the developed and tested procedures (Forth "words") may be added to the initial Forth CPU program included in the FPGA configuration bitstream. It is also possible to define a procedure to be executed automatically, after the FPGA is configured or after the reset. Afterward, the interactive operation is possible. The controller may be used for configuration and diagnostics even before the Ethernet-based IPbus control connection is established, or in setups where the IPbus is not available at all. Communication with the controller is provided by the USB connector and the on-board USB/UART bridge. Defined Forth words support control of typical programmable clock generators (Si57x, IDT ICS8N4Q001), control of the internal I2C busses in the AFCK and communication with the user logic in FPGA.

Preparations for the GBT-based readout

The SMX2 tester used the "Black Box" models of the GBT e-Links. It allows direct connection to the SMX2 ASIC. However, the final setup, based on the CROB boards [6] must use the real e-Links implemented by the GBT-FPGA IP core in the tester (future CRI) and by the GBTX ASIC in CROB. Implementation of the GBT-compatible SMX2 tester and CRI required a few introductory steps. The GBT-FPGA IP core is still under development. Therefore to facilitate its replacement with the new version, the VEXTPROJ compatible version of the GBT-FPGA sources has been prepared. To test the communication with the GBTX ASIC, the dedicated test setup has been created consisting of the AFCK board and the Versatile Link Demonstrator Board (VLDB). The AFCK firmware includes the Forth controller, the GBT-FPGA core, and dedicated test cores. First tests have been performed, and the current work is focused on the verification (with the CERN GBTX-SUPPORT team) that the GBTX operation modes required by the SMX2 communication protocol are working correctly.

Controlling of the e-Link data and clock delays in the GBTX requires the GBT IC controller core, which should be delivered by the CERN team. Before it is available, it is necessary to emulate it using the I2C control of the GBTX chip. To make it possible, the original Windows-compatible Python scripts provided by CERN have been modified to ensure Linux compatibility.

The current work is aimed at implementation of the GBT-compatible SMX2 tester. First attempts, based on the 3.1.1 version of the GBT-FPGA core required the special clock-domain-crossing (CDC) blocks in the uplink channel. Fortunately, the new release of the GBT-FPGA (4.1.0 in July 2016) provides the portable CDC blocks in the GBT-FPGA core itself[1]. Further research is desired to check if using the Xilinx-specific blocks for CDC may result in even smaller resources consumption.

References

[1] W.M. Zabolotny, "Version control friendly project management system for FPGA designs", Proc. SPIE 10031 (2016) 1003146, doi:10.1117/12.2247944

[2] W.M. Zabolotny and A.P. Byszuk and D. Emschermann and M. Guminski and B. Juszczyk and K. Kasinski and G. Kasprowicz and J. Lehnert and W.F.J. Müller and K. Poznniak and R. Romaniuk and R. Szczygiel, "Design of Versatile ASIC and Protocol Tester for CBM Readout System", February 2017, JINST, vol. 12, C02060, doi:10.1088/1748-0221/12/02/C02060

[3] K. Kasinski and R. Szczygiel and W. Zabolotny and J. Lehnert and C.J. Schmidt and W.F.J. Müller, "A protocol for hit and control synchronous transfer for the front-end electronics at the CBM experiment", November 2016, NIMA, pp. 66-73, doi:10.1016/j.nima.2016.08.005

[4] K. Kasinski and R. Szczygiel and W. Zabolotny, "Back-end and interface implementation of the STS-XYTER2 prototype ASIC for the CBM experiment", November 2016, JINST, vol.11, C11018, doi:10.1088/1748-0221/11/11/C11018

[5] W.M. Zabołotny and G. Kasprowicz, "Data processing boards design for CBM experiment", Proc. SPIE 9290 (2014) 929023, doi:10.1117/12.2073377

[6] J. Lehnert and A.P. Byszuk and D. Emschermann nad K. Kasinski and W.F.J. Müller and C.J. Schmidt, and R. Szczygiel and W.M. Zabolotny, "GBT based readout in the CBM experiment", 2017, JINST, in press

[7] W.M. Zabolotny, "Dual port memory based Heapsort implementation for FPGA", Proc. SPIE 8008 (2011) 80080E, doi:10.1117/12.905281

[8] W.M. Zabolotny, "AFCK_J1B_FORTH - Forth based system for AFCK board initialization and diagnostics", https://github.com/wzab/AFCK_J1B_FORTH

[9] J. Bowman, "Swapforth is a cross-platform ANS Forth", https://github.com/jamesbowman/swapforth

[1] The newest 5.1.0 version released in January 2017 also offers that functionality.

DOI:10.15120/GR-2017-1

Σ^0 Hyperon Production in p + Nb at E_{kin} = 3.5 GeV*

L. Fabbietti[1,2], J. Friese[1] and T. Kunz[†1,2] for the HADES collaboration
[1]Physik Department E62, Technische Universität München, D-85748 Garching; [2]Excellence Cluster 'Origin and Structure of the Universe', D-85748 Garching

The production of Λ^0 – baryons (M = 1115.7 GeV/c^2) has been investigated by the HADES collaboration in various collision systems ranging from p + p to Au + Au at SIS energies. In this context it is of interest, to which amount feeding from Σ^0 (M = 1192.6 GeV/c^2) decays via the processes $\Sigma^0 \rightarrow \Lambda^0\gamma$ (BR = 100 %) and $\Sigma^0 \rightarrow \Lambda^0 e^+e^-$ (BR = 0.005 %) contributes to the observed Λ yields [1]. While at low collision energies close to the NN threshold the production cross sections $\sigma_\Lambda/\sigma_\Sigma \approx 10$ [2] suggest a feeding of ~ 10% it is expected that at energies around 1 GeV above threshold this contribution increases to ~30% [3]. For even higher energies it may reach up to 50%.

We have therefore started an attempt to identify Σ^0 – decays in the reaction p + Nb at E_{kin} = 3.5 GeV ($\epsilon \approx$ 0.67 GeV). In the collected data sample of 4.21· 10^9 events Λ particles have been reconstructed through their weak decay $\Lambda \rightarrow p\pi^-$ utilizing momentum, dE/dx and track vertex information [4]. Coincident γ detection is achieved through conversion pair $\gamma \rightarrow e^+e^-$ identification in HADES, although the design of the detector is rather optimized for low conversion probability. Furthermore, the momentum measurement for electrons is limited to $p_e \geq 50$ MeV/c because of the strong magnetic field between the two tracking stations MDCI/II and MDCIII/IV. GEANT simulations show that the conversion probability (mostly in the Nb target) for γs (E_γ ~ 80 MeV) from Σ^0 decays is only ~3.0%.

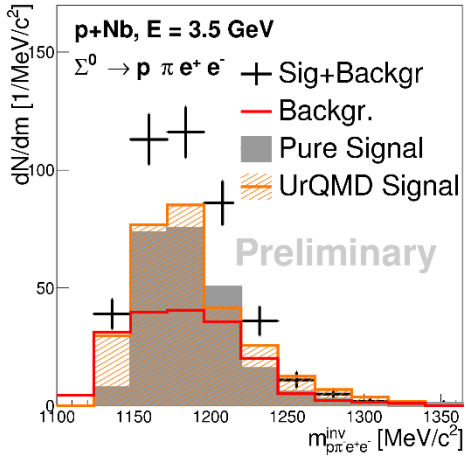

Figure 1: Invariant mass of the proton, pion and one dielectron pair for the selected Σ^0 candidates. The reconstructed events (black) are plotted together with background (red), extracted signal (grey) and UrQMD simulations (orange).

In the present analysis we require for each event with Λ content at least the momentum vector of one fully reconstructed electron or positron with a good quality RICH ring. For the identification of the converted photon we search for a second electron/positron candidate characterized by at least a RICH signal with hits in the inner tracking detectors only. The momentum of the latter is then determined by an event hypothesis method.

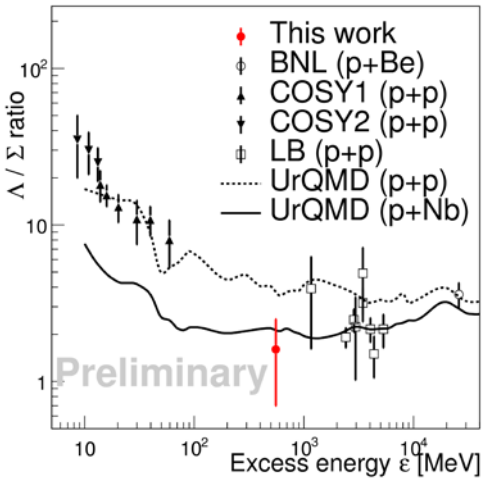

Figure 2: Λ/Σ^0 ratio as a function of the excess energy ε. For the calculation of ε the Fermi motion has not been taken into account. The statistical and systematic errors have been summed up quadratically.

The reconstructed four particle invariant mass spectrum is presented in fig. 1. The background has been determined via a sideband analysis technique. Around 220 Σ^0 candidates are visible and are reasonably reproduced by a full scale simulation using UrQMD events as an input. After acceptance and efficiency correction the signal has been extrapolated to the uncovered p_t region using Boltzmann functions. The differential cross section is extracted to be $\frac{d\sigma}{d\Omega}(\Sigma^0) = 2.3 \pm (0.2)^{stat} \pm (^{+0.6}_{-0.6})^{sys} \pm (0.2)^{norm}$ within the rapidity region of $0.5 < y < 1.1$. An extrapolation based on UrQMD predictions and measured Λ^0 rapidity distributions yields a total cross section of $\sigma^{tot}_{p+Nb}(\Sigma^0) = 5.8 \pm (0.5)^{stat} \pm (^{+1.4}_{-1.4})^{sys} \pm (0.6)^{norm} \pm (1.7)^{expol}$. The ratio $\frac{\Lambda}{\Sigma^0} = 1.6 \pm (0.1)^{stat} \pm (^{+0.5}_{-0.5})^{sys} \pm (0.4)^{expol}$ compares to the world data as shown in fig. 2.

[1] K.A. Olive et al., Chin. Phys. C, 38, 0900001 (2014)
[2] P.Kowina et. al, Eur. Phys. J. A 22, 293-299 (2004)
[3] H.Landolt, R.Börnstein, Landolt-B.12, (1988)
[4] G.Agakishiev et. al, Eur. Phys. J. A 50 (2014) 81

* Work supported by BMBF 05P15WOFCA, GSI TMLFRG 1316
† tobias.kunz@tum.de

Charged kaon and ϕ reconstruction in Au+Au collisions at 1.23A GeV*

H. Schuldes[1†] *for the HADES collaboration*
[1]Goethe-University Frankfurt

The High Acceptance DiElektron Spectrometer HADES took data of Au+Au collisions at a kinetic beam energy of 1.23A GeV. At this energy all hadrons carrying strangeness are produced well below their respective elementary production threshold ($NN \rightarrow N\Lambda K^+$: $\sqrt{s}_{thr}$ = 2.55 GeV, $NN \rightarrow NNK^+K^-$: $\sqrt{s}_{thr}$ = 2.86 GeV, $NN \rightarrow NN\phi$: $\sqrt{s}_{thr}$ = 2.89 GeV). Therefore, the study of these rarely produced particles can reveal information about the high-density phase created and about the production and propagation of strangeness in heavy-ion collisions.

In total 2.1×10^9 Au+Au events were used in the analysis, corresponding to the 40% most central events. Kaons were identified via their momentum, time-of-flight and energy loss information measured with the magnet spectrometer, consisting of Mini-Drift Chambers MDC and a superconducting magnet, and a scintillator hodoscope TOF at high polar angles (44 - 85°) or a Resisitve Plate Chamber RPC at low polar angles (18 - 45°). A detailed description of HADES can be found in [1]. The residual background of proton and pion tracks was subtracted in an iterative fitting procedure using a polynomial function. The neutral ϕ meson was reconstructed via its decay into charged kaons (BR($\phi \rightarrow K^+K^-$) = 49.8%). The uncorrelated background, mainly from mis-identification of the kaon candidates, is described using the mixed-event technique.

For the first time in the SIS18 energy regime, it is possible to perform a multi-differential analysis as a function of transverse mass and rapidity, as well as for different centrality classes, of charged kaons and ϕ mesons in the same data sample. HADES has a large phase space coverage at mid-rapidity down to the lowest m_t. The raw count rates are corrected for acceptance and efficiency losses using a Monte-Carlo simulation. The spectra are extrapolated assuming thermal production according to Boltzmann distributions. For more details see [2, 3].

The resulting ratios of the 4π multiplicities K^-/K^+, as well as ϕ/K^- are found to be independent of the centrality of the collision. The multiplicity ratio ϕ/K^- is shown in Fig. 1 in comparison to measurements at similar energies in lighter systems [4–6], as well as from higher $\sqrt{s_{NN}}$ [7–9]. Whereas this ratio stabilizes at higher energies at a value of about $\sim$ 0.15, it substantially increases towards lower energies. As a consequence, ϕ feed-down decays become a sizeable source ($\sim$ 25%) for K^- production below the NN threshold energy.

This fact is not taken into account in the microscopic transport models which are commonly used to describe the particle production and dynamics of a heavy-ion collision. In these models the sub-threshold K^- production is realized almost exclusively via the so-called strangeness exchange reaction $\Lambda\pi \rightarrow NK^-$ [10]. Therefore our new measurement will help to stimulate progress in transport theoretical descriptions of strangeness production in heavy-ion collisions.

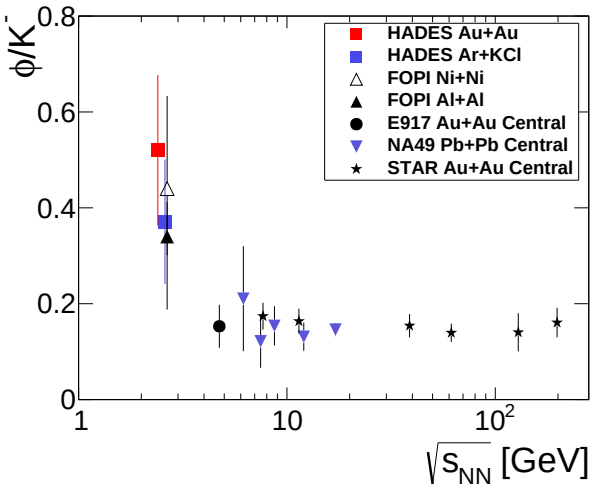

Figure 1: ϕ/K^- multiplicity ratio as a function of $\sqrt{s_{NN}}$ [2, 4–9].

References

[1] G. Agakishiev *et al.* (HADES), Eur. Phys. J. A **41** (2009) 243.

[2] J. Adamczewski-Musch *et al.* (HADES), arXiv 1703.08418 (2017).

[3] H. Schuldes, PhD Thesis Goethe-University Frankfurt (2016).

[4] G. Agakishiev *et al.* (HADES), Phys. Rev. C **80** (2009) 025209.

[5] K. Piasecki *et al.* (FOPI), Phys. Rev. C **91**, (2015) 054904.

[6] P. Gasik *et al.* (FOPI), Eur. Phys. J. A **52** (2016) 177.

[7] B. Holzman *et al.* (E917), Nucl. Phys. A 698 (2002) 643.

[8] S. V. Afanasiev *et al.* (NA49), Phys. Lett. B 491 (2000) 59.

[9] J. Adams *et al.* (STAR), Phys. Lett. B 612 (2005) 181.

[10] C. Hartnack, H. Oeschler, Y. Leifels, E. L. Bratkovskaya, J. Aichelin, Phys. Rept. **510** (2012) 119.

*Work supported by BMBF (05P15RFFCA), GSI, HGS-HIRe and HICforFAIR

†h.schuldes@gsi.de

DOI:10.15120/GR-2017-1

System-size dependence of the integrated dilepton excess yield in heavy-ion collisions*

S. Harabasz[1,2†] *for the HADES collaboration*[1]

[1]Technische Universität Darmstadt, Germany; [2]Jagiellonian University, Kraków, Poland

Electromagnetic probes provide valuable information on the properties of the hot and dense medium produced in heavy-ion collisions. In particular, the yield of dilepton radiation in the invariant-mass region above the π^0 mass and below the vector meson region (around 0.7 GeV$/c^2$) can be related to the lifetime of the fireball [1].

An important ingredient of understanding this relation is the dependence of the integrated dilepton yield on the size of the collision system. This is possible with the data sets collected and analyzed by HADES. Fig. 1 shows the yield as a function of mean number of participating nucleons for the collisions C+C at $E_{\text{beam}} = 2A$ GeV ([2], triangles), Ar+KCl at $E_{\text{beam}} = 1.76A$ GeV ([3], stars) and four 10%-wide classes [4] of Au+Au at $E_{\text{beam}} = 1.23A$ GeV ([5], points with systematic error rectangles). Points in blue are integrals in the range $0.15 < M_{ee} < 0.5$ GeV$/c^2$, studied previously in light systems in [3], red points correspond to an integration range $0.3 < M_{ee} < 0.7$ GeV$/c^2$, which is expected to be sensitive to medium effects also at high beam energies [6].

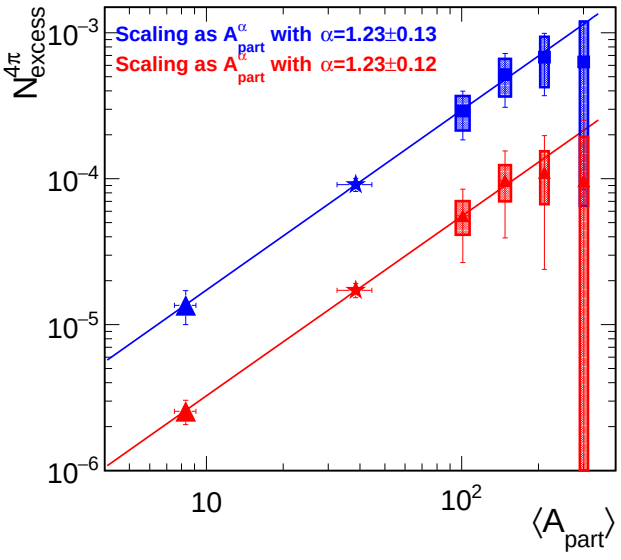

Figure 1: Dilepton excess as function of number of participants integrated in two different invariant mass ranges. Details are given in the text.

The medium radiation was distilled by subtracting contributions before the fireball formation and after its freeze-out. The latter was done by subtracting the η radiation, based on an independent analysis [7]. The former – by subtracting the appropriately normalized yield in p+p and n+p collisions at the same beam energy [8].

In order to take into account different collision energies, an ansatz was made, that for a given system, the dilepton yield scales with energy like π^0 production in the case of the lower integration range and like η in the higher integration range. The E_{beam} dependence, obtained from various measurements [2, 3, 7, 9, 10, 11, 12, 13], is in this low-energy regime stronger for η than for π^0, reflecting the higher mass of the former.

Only after proper energy scaling of the C+C and Ar+KCl points in Fig. 1 down to the values corresponding to $E_{\text{beam}} = 1.23A$ GeV, it was possible to fit power law to the $\langle A_{\text{part}} \rangle$ dependence of the dilepton yield in the two lighter systems and two peripheral classes of Au+Au collisions. The two most central classes are not included in the fit, since they have large systematic and statistical uncertainties. However, within these uncertainties they are compatible with the fitted line. The power law exponent turns out to be the same for both integration ranges. It is larger than unity, which means that scaling with the number of participants is stronger than linear. This points to regeneration of baryonic resonances as the source of the enhanced dilepton radiation, which in turn happens more often, if the fireball lives longer.

References

[1] T. Galatyuk *et al.*, EPJA **52** (2015) 131
[2] HADES Collaboration, PLB **663** (2008) 43
[3] HADES Collaboration, PRC **84** (2011) 014902
[4] B. Kardan, Diploma thesis 2015
[5] S. Harabasz, PhD thesis 2017
[6] P. Huck, NPA **931** (2014) 659
[7] C. Behnke, J. Phys. Conf. Ser. **599** (2015) 012029
[8] HADES Collaboration, PLB **690** (2010) 118
[9] HADES Collaboration, PRL **98** (2007) 052302
[10] DLS Collaboration, PRL **79** (1997) 1229
[11] TAPS Collaboration, Z. Phys. A **359** (1997) 65
[12] TAPS Collaboration, PRC **56** (1997) R2920
[13] E895 Collaboration, PRC **68** (2003) 054905

*Work supported by VH-NG-823, EMMI, GSI, HGS-HIRe and H-QM.

† s.harabasz@gsi.de

Dielectron helicity in Au+Au collisions at 1.23A GeV with HADES *

P. Sellheim[1,2] *and the HADES collaboration*[1]
[1]Goethe-Universität, Frankfurt am Main, Germany

HADES measured Au+Au collisions at 1.23A GeV to extend the studies of QCD matter at high temperatures and densities. This measurement complements the previous measurement of Ar+KCl collisions at 1.76A GeV [1]. The matter produced in heavy-ion collisions can be probed by dielectrons, i.e. virtual photons decaying into an electron positron pair. Electrons and positrons are identified via observables reconstructed with HADES in various detector subsystems (e.g. time-of-flight, energy loss) and used within a neural network. The identified electrons and positrons are then paired with each oppositely charged particle in the same event. After subtraction of the combinatorial background of uncorrelated pairs, the pair distributions are corrected for detector inefficiencies, acceptance effects and extrapolated to the full phase space. Finally, systematic errors are estimated to consider the uncertainties due to the spectra corrections and normalizations and background subtraction. The signal mass spectra are in agreement with the results obtained by two different methods [3, 2]. f The reconstructed invariant mass distribution revealed an excess above a mass of 0.15 GeV/c^2 due to medium radiation. In order to characterize this excess, the helicity of the dielectron signal, probing the polarization of the virtual photon, is reconstructed (see [1] for details of the helicity reconstruction). The latter describes the angle of the virtual photon to the electron (positron) in the rest frame of the virtual photon. The helicity distribution is assumed to be flat in case of thermal emission but differs from a flat distribution for non thermal dielectrons.

The resulting helicity distributions are presented in Fig. 1 for a mass range dominated by π^0-Dalitz decays (upper) and the dielectrons in the excess region (lower). The data is compared to the assumption of a flat helicity distribution. A filtering of the cocktail with the HADES acceptance shows that the helicity distribution shape is strongly modified due to the limited detector acceptance. In order to compare the data to the assumption of a flat helicity, a ratio of data over cocktail filtered by acceptance is evaluated and presented (see Fig. 1 (small boxes)). Since the ratio is closer to one in the lower ratio, the yield in the excess mass range fits better to the cocktail. In conclusion, this observation fits to the assumption that the excess seems of a thermal origin while the yield in the π^0-Dalitz mass range shows the expected anisotropy.

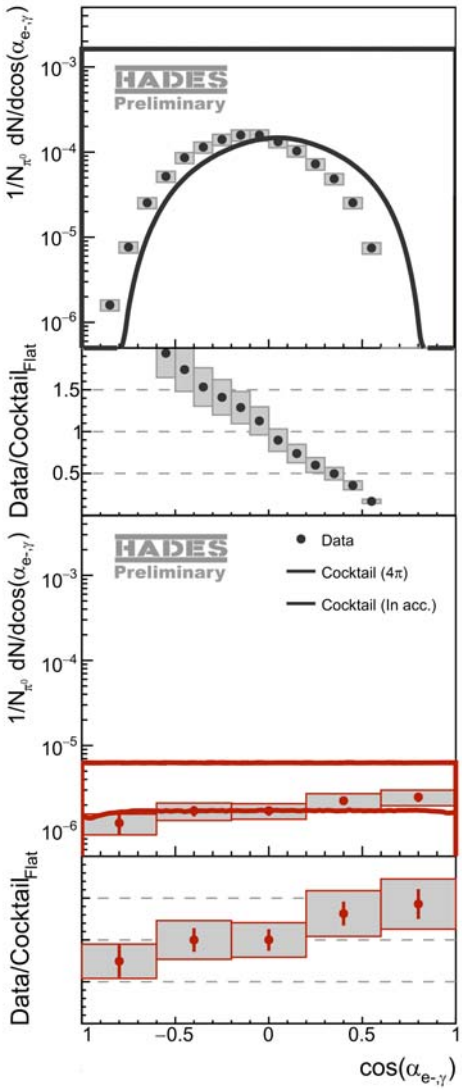

Figure 1: Reconstructed helicity distribution compared to cocktail (large boxes) and ratio of data to cocktail (small boxes). Both are shown for the mass range $0 < M_{ee} < 0.15$ GeV/c^2 (upper) and $0.3 < M_{ee} < 0.7$ GeV/c^2 (lower).

References

[1] G. Agakishiev et al., Dielectron production in Ar+KCl collisions at 1.76A GeV, Phys. Rev., vol. C84, p. 014902, 2011

[2] S.Harabasz, Reconstruction of virtual photons from Au+Au collisions at 1.23 GeV/u, PhD thesis, 2017

[3] P.Sellheim, Reconstruction of the low-mass dielectron signal in 1.23A GeV Au+Au collisions, PhD thesis, 2017

* This work has been supported by BMBF (05P15RFFCA), GSI, HIC for FAIR, HGS-HIRe and H-QM.

DOI:10.15120/GR-2017-1

Multi-differential proton flow measurements with HADES in Au+Au collisions at 1.23A GeV*

Behruz Kardan[1†] *(for the HADES Collaboration)*

[1]Goethe-Universität Frankfurt, Max-von-Laue-Str. 1, 60438 Frankfurt am Main, Germany

Collective flow phenomena are a sensitive probe for the general properties of extreme QCD matter [1], such as its shear viscosity [2]. To achieve a good understanding of these phenomena, flow observables are deduced and compared with model calculations to constrain the nuclear Equation-of-State (EoS) [3, 4]. The understanding of the EoS of dense matter is of great importance for the investigation of supernovae and compact stars [5].

HADES [6] has a large acceptance combined with a good mass-resolution and therefore allows the study of dielectron and hadron production in heavy-ion collisions with unprecedented precision. At the BEVALAC and SIS18 directed and elliptic flow have been measured for pions, charged kaons, protons, neutrons and fragments, but higher-order harmonics have not yet been studied. With the statistics of seven billion Au-Au collisions at 1.23A GeV recorded in 2012, the investigation of higher-order flow harmonics will be possible. Within the 5 weeks of the Au+Au run the SIS18 synchrotron delivered 684 hours of Au^{69+} ion beam to the HADES cave [7] with an intensity of $(1.2-2.2)\times10^6$ ions per sec. A 15-fold segmented gold target with an interaction probability of 1.51% was used. A fraction of around 80% of the total recorded events was triggered by selecting mostly central events with a charged hit multiplicity in the TOF detector $N_{ch} > 20$. According to detailed comparison of the charged track and hit multiplicity distribution with a Glauber Model simulation, this central trigger selects about 47% of the total hadronic cross section of 6.83 ± 0.43 barn, corresponding to a maximum impact parameter of $b_{max} = 10$ fm [8]. In this analysis 4.32×10^7 events were used after event selection.

In high-energy collisions of nuclei a highly excited nuclear medium is created and its collective expansion causes a correlated emission of particles. In perfectly central collisions the expansion should be isotropic, leading to radial flow, observable in the transverse-mass spectra of the produced particles. Less central collisions are characterized by an overlap region which is more anisotropically shaped. This event-shape characteristics is usually studied via the azimuthal anisotropy of the momentum space of identified particles w.r.t a corresponding symmetry plane and it is common to analyze this by a Fourier decomposition yielding the flow coefficients v_1, v_2, v_3 and higher. Due to their correlation to the collision geometry, the directed v_1 and elliptic v_2 are linked to the reaction plane, which itself is also observable via the spectators.

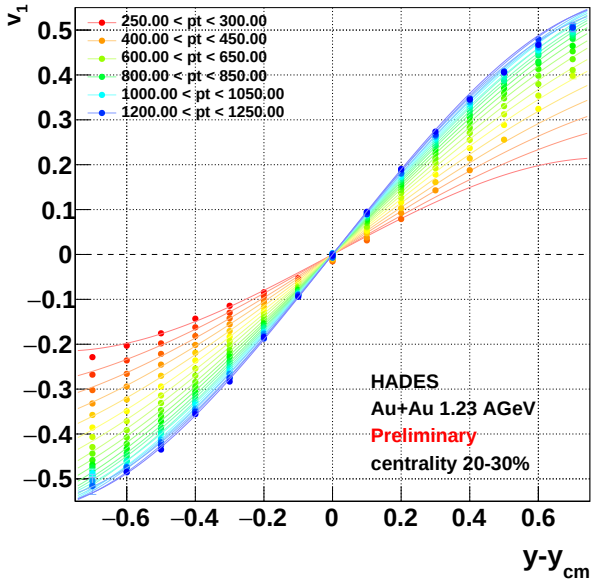

Figure 1: Preliminary data on directed flow (v_1) of protons as measured by HADES in semi-central ($20-30\%$) Au+Au collisions at 1.23A GeV, shown as a function of the center-of-mass rapidity in transverse momentum intervals of 50 MeV$/c$. The lines are to guide the eye.

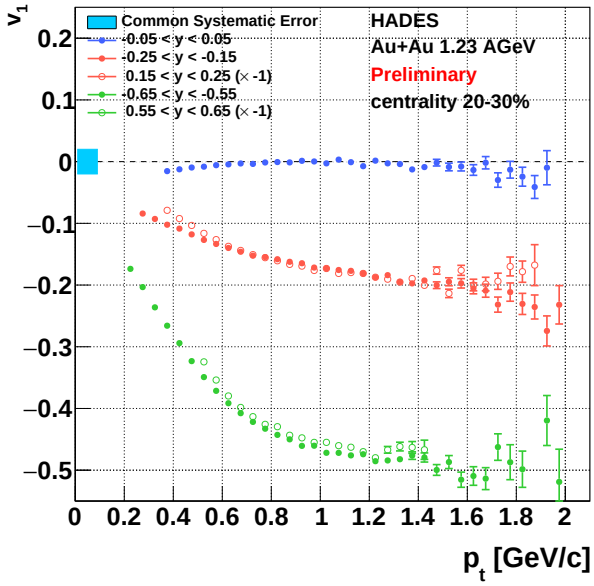

Figure 2: Comparison of the p_t dependence of proton v_1 in five rapidity intervals, symmetric around mid-rapidity.

* Work supported by BMBF (05P15RFFCA), GSI, HGS-HIRe, H-QM and HICforFAIR

† bkardan@ikf.uni-frankdurt.de

We present here a high-statistics, multi-differential measurement of v_1 and v_2 for protons in Au+Au collisions at 1.23A GeV, extracted over a large region of phase space using the standard event plane method. The data have been corrected for the event plane resolution [9, 10]. In addition, an efficiency correction due to the differential detector load has been applied track-by-track, as a function of the polar angle, the relative angle to the event plane and the track multiplicity in a given sector. Figure 1 shows the results on v_1. A good forward-backward symmetry with respect to mid-rapidity is seen, as expected due to the symmetry of the collision system. Remaining discrepancies are well within the systematic error, which has been estimated by embedding simulated protons into real or UrQMD background events. A similar symmetry is seen for v_2, see Fig. 3. A sizeable negative v_2 is measured around mid-rapidity. Its value clearly depends on the centrality of the collision, as illustrated in Fig. 4. The preliminary results indicate a good consistency of the first two flow coefficients of protons with FOPI data [4, 11, 12] and are in the process of being finalized. Due to the large collected events statistics and the large acceptance HADES will also be able to address the measurement of higher-order flow harmonics in the low energy regime. This will allow to extend the existing data into so far unexplored regions and will provide new insights into the properties of strongly interacting matter at extreme densities, as e.g. its viscosity. The employment of multi-particle methods will also enable the disentanglement of the contributions of collective and non-flow processes.

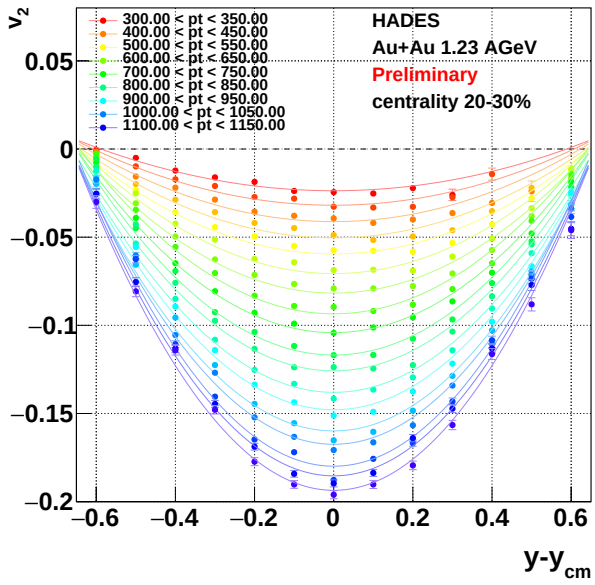

Figure 3: Preliminary data on elliptic flow (v_2) of protons measured with HADES in semi-central ($20-30\%$) Au+Au collisions at 1.23A GeV. Shown is v_2 as a function of the center-of-mass rapidity in transverse momentum intervals of 50 MeV$/c$ (lines are to guide the eye).

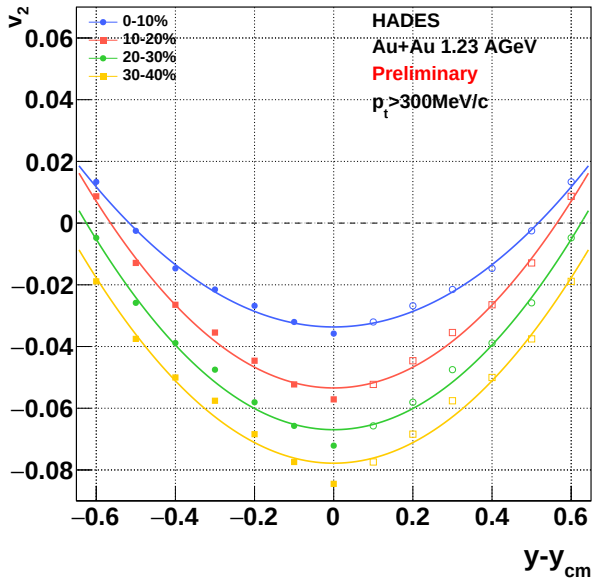

Figure 4: Preliminary data on elliptic flow (v_2) of protons measured with HADES in different centrality intervals of Au+Au collisions at 1.23A GeV. Shown is the p_t integrated v_2 as a function of the center-of-mass rapidity.

References

[1] H. G. Ritter and R. Stock, J. Phys. G **41** (2014) 124002 arXiv:1408.4296.

[2] B. Barker and P. Danielewicz, arXiv:1612.04874.

[3] P. Danielewicz, R. Lacey and W. G. Lynch, Science **298** (2002) 1592 arXiv:nucl-th/0208016.

[4] A. Le Fèvre *et al.* Nucl. Phys. A **945** (2016) 112 arXiv:1501.05246.

[5] M. Oertel, M. Hempel, T. Klähn and S. Typel, Rev. Mod. Phys. **89** (2017) no.1, 015007 arXiv:1610.03361.

[6] G. Agakishiev *et al.* [HADES Collaboration], Eur. Phys. J. A **41** (2009) 243 arXiv:0902.3478.

[7] W. Bayer et al., Accelerator Operation Report, GSI Report 2013-1, pages 255-p.

[8] B. Kardan, Diploma thesis 2015, G. Agakishiev *et al.* [HADES Collaboration], paper in preparation.

[9] A. M. Poskanzer and S. A. Voloshin, Phys. Rev. C **58** (1998) 1671 arXiv:nucl-ex/9805001.

[10] J. Y. Ollitrault, Nucl. Phys. A **638** (1998) 195. arXiv:nucl-ex/9802005.

[11] T. Galatyuk, HADES overview, Nuclear Physics A, Vol 931, November 2014, Pages 41-51.

[12] W. Reisdorf *et al.* [FOPI Collaboration], Nucl. Phys. A **876** (2012) 1 arXiv:1112.3180.

DOI:10.15120/GR-2017-1

Charged pion flow in Au+Au collisions at 1.23AGeV with HADES *

M. Gumberidze[1], *P. Tlusty*[2] *for the HADES Collaboration*
[1]Technische Universität Darmstadt, Germany; [2]Nuclear Physics Institute, (CAS), 25068 Rez, Czech Republic

The properties of a compressed system formed in a heavy-ion collision can be studied looking at the azimuthal momentum distribution of the emitted particles. If the system was in thermal equilibrium, the resulting pressure generates a common velocity in the outgoing particles: *collective flow*. The term *collective flow* includes a common radial expansion, modifying the momentum distribution of outgoing particles, and an anisotropic expansion, affecting the spatial orientation of particle momenta. The first component is called *radial flow*, the second *anisotropic flow*.

The yield of various hadrons with respect to the reaction plane can be characterized by a Fourier expansion where the different coefficients measure different anisotropies present in the system:

$$\frac{dN}{d(\phi-\phi_R)} = [1+2v_1cos(\phi-\phi_R)+2v_2cos(\phi-\phi_R)+...] \quad (1)$$

where ϕ denotes the azimuthal angle of the outgoing particles and ϕ_R is the orientation of the event plane which is determined event-by-event. The first harmonic (v_1) represents an overall shift of the distribution in the transverse plane and is called directed flow. The second harmonic (v_2) represents an elliptical volume and is called elliptic flow.

The study of collective flow in heavy-ion collisions has potential to offer insight into the equation of state of the produced matter. In particular, the shape of v_1 as a function of rapidity in the mid-rapidity region is of interest because it is sensitive to crucial details of the expansion of the participant matter during the early stage of collision. It is generally believed that the directed flow is generated early in the heavy-ion collision. The models indicate that the evolving shape and orientation of the participant zone and its surface play a role in determining anisotropy measured among these particles in the final state.

In this contribution, we focus on the results of the directed flow of positevely charged pions in Au+Au collisions. The charged pions identification in HADES [1] is done via the velocity of particles detected in the time-of-flight detectors as a function of momentum. Directed flow is measured with respect to the reaction plane determined from the spectator flow using the Forward Wall (FW) of HADES. The FW, a plastic scintillator hodoscope array, is placed at a distance of 7m behind the target at small forward angles between 0.3° and 7.3° to detect charged projectile spectators by time-of-flight. The distribution of the FW hits is used to reconstruct the event plane.

The directed flow of charged pions in Au+Au@1.23AGeV has been measured over a large region of phase space. The data have been corrected for the event plane resolution using the so-called Ollitrault method [2]. In addition, efficiency losses due to high particle multiplicities have been taken into account on track-by-track basis. Those corrections were determined from experimental data as a function of the polar θ and azimuthal $\phi-\phi_R$ angles and the local track multiplicity. In Fig. 1, the results on v_1 as a function of center-of-mass rapidity (y) is presented for four 10% centrality bins. All data points in Fig. 1 are antisymmetric around mid-rapidity, as expected due to the symmetric collision system. The most central bin 0-10% shows nearly no directed flow, where for other bins the slope of $v_1(y)$ (dv_1/dy) has negative sign showing so-called anti-flow, on contrary to the proton flow pattern. A systematic study of this effect and its comparison with transport model predictions can disentagle the influence of the reaction geometry, like shadowing of emitted pions by the spectator matter, from the effects coming from the compressed matter produced in an early stage of the collision.

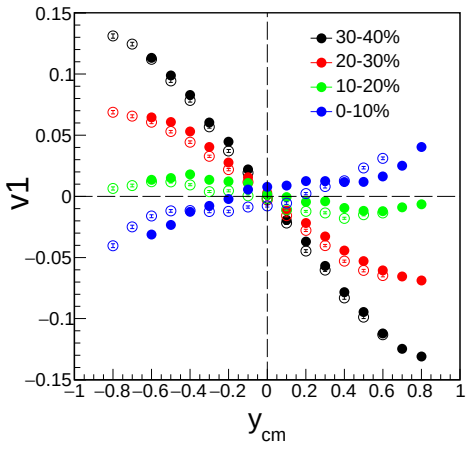

Figure 1: Rapidity dependence of the directed flow, v_1 of positively charged pions (π^+) for Au+Au collision at 1.23 AGeV for four 10% centrality bins. Closed points correspond to measured data, open are mirrored.

References

[1] G. Agakishiev *et al.* (HADES Collaboration), Eur. Phys. J. A 41 (2009) 243

[2] Y. Ollitrault arXiv:nucl-ex/9711003

* Work supported by TU Darmstadt: VH-NG-823, GSI, NPI AS CR, Rez (Czech Republic): MSMT LM2015049, GACR 13-06759S

Efficiency and volume corrections to particle number fluctuations *

M. Szala[1], *R. Holzmann*[2], *and the HADES collaboration*
[1]Goethe Universität, Frankfurt am Main, Germany; [2]GSI, Darmstadt, Germany

By varying the collision system and the beam energy of heavy-ion collisions one can access broad areas of the phase diagram of strongly interacting matter. Higher order moments of conserved quantities (e.g. baryon number, charge, strangeness) are predicted to be sensitive to a first order phase transition and especially to a critical point of the QCD phase diagram. Strong critical fluctuations would indeed modify these moments, resulting in deviations from the baseline Poisson distribution. The HADES experiment can address these signals in heavy-ion collisions at beam energies of a few GeV/u.

In the analysis of Au+Au collisions at $\sqrt{s_{NN}}$ = 2.41 GeV measured with HADES in 2012 the efficiency correction is an important step in obtaining the higher order moments of the proton number distribution.

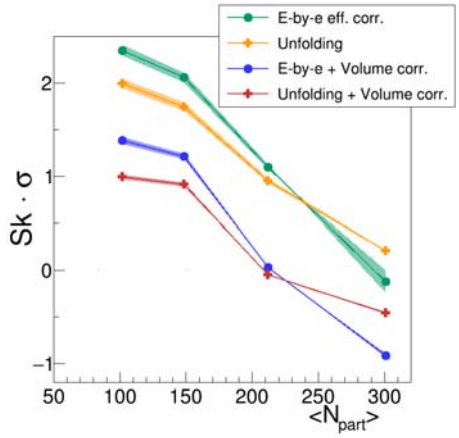

Figure 1: Measured Sk · σ of protons as function of mean number of participants. Two different methods of efficiency correction were tested, correcting the moments (green) and unfolding (yellow). The results are modified further by volume fluctuation corrections (see text).

For this purpose, detailed investigations of efficiency correction methods to the ratios of cumulants $\frac{c_3}{c_2} = Sk \cdot \sigma$ and $\frac{c_4}{c_2} = \kappa \cdot \sigma^2$ were performed with Au + Au UrQMD events and GEANT simulations. Two different approaches were tested: correction of the moments (as proposed in [1, 2]) and unfolding of the distributions [3]. After their successful assessment in the simulation, the two methods were applied to the HADES experimental data and the higher moments of the proton distributions were extracted. We find that the two methods provide plausible and consistent results in the Au + Au data (see Figs. 1, 2).

* Supported by GSI and EMMI.

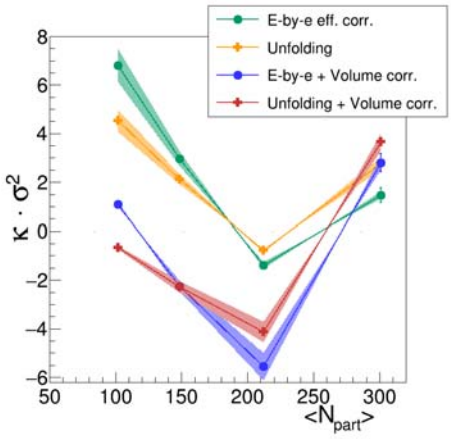

Figure 2: Measured $\kappa \cdot \sigma^2$ of protons. For most central collisions the volume corrected results show contrary behavior.

Experimentally measured dynamical event-by-event fluctuation signals such as cumulants of (net-)particle distributions can also be modified by the fluctuations of the number of participants in a given centrality selection [4, 5]. To correct the data for this effect, we have applied the procedure of Skokov et al. [4] on the higher order moments (see Figs. 1, 2). For the volume correction we assume that the volume scales like the number of participants and the corresponding N_{part} distributions are modeled with a Glauber model [6]. The necessary corrections need to be carefully studied before comparison with other experiments and theory.

As the fully conserved quantity investigated here is the baryon number, further investigations will focus on including protons bound in the fragments produced in Au+Au collisions to the efficiency and volume corrections.

References

[1] A. Bzdak, V. Koch, Phys.Rev. C91 (2015) 027901.

[2] A. Bzdak, V. Koch, Phys.Rev. C86 (2012) 044904.

[3] S. Schmitt, JINST 7 (2012) T10003.

[4] V. Skokov, B. Friman, K. Redlich, Phys. Rev. C 88 (2013) 034911

[5] P. Braun-Munzinger, A. Rustamov, J. Stachel, Nucl.Phys. A960 (2017) 114-130

[6] B. Kardan, Diploma thesis, Goethe University Frankfurt (2015)

DOI:10.15120/GR-2017-1

Collision time reconstruction and particle identification in AuAu collisions at 1.23A GeV with HADES *

G. Kornakov[†1] *for the HADES Collaboration*

[1]Technische Universität Darmstadt, Germany

The time-of-flight technique plays a central role in particle identification in HADES [1]. The time measurement is performed by a diamond START detector [2], placed in front of the target, and two STOP detectors, placed behind the magnet and the tracking detectors. Low polar angles are covered by a Resistive Plate Chamber detector [3], for the rest, a wall of fast timing scintillator bars [4] are used.

The velocity of a detected particle is calculated from the time difference between the STOP and START signals divided by the track length, measured from the collision vertex to the time of flight walls. Although the resolution of the diamond detector is of 60 ps, the collision time can be improved further if enriched with information from tracking. For each reconstructed and identified track is possible to calculate the residual between the measured and the theoretical expected time of flight. The weighted average of all residuals is called T_0. In order to avoid the statistical correlations between the estimated time and the measured time in the STOP detectors, for each individual track the T_0 time is evaluated individually by combining all the other reconstructed traces. Effects like multiple scattering and energy loss are properly incorporated in a dedicated Monte-Carlo simulation with detailed detector response functions. The result of applying such a technique is shown in the Figure 1. Since all the times can be considered to be independent, the characterisation of the difference between the START time and the T_0 as a function of number of used particles x, can be parametrized as follows: $\sigma(T_0 - T_{START}) = \sqrt{a^2 \times x^{2b} + c^2}$, where the constant a is the mean uncertainty of a single track, b is the coefficient that scales the improvement to the T_0 by adding n tracks and c is the constant resolution of the diamond detector. If instead of making the difference between both times, they are combined with weights, the collision time resolution function is obtained, as accurate as 54 ps for peripheral collisions and 31.4 ps for the most central.

Once the velocity is corrected by the new START time, each track is identified with the best mass hypothesis. For that, also the specific energy loss in the tracking detectors is used in order to be sensitive to the intrinsic charge of the produced particles in the collisions and providing separation for example for deuterons and Helium. In the Figure 2 it is shown the reconstructed mass spectrum and the identified particles by shaded areas. More than 90 % of all reconstructed tracks are identified. The rest are random combinations of traces matched to STOP detectors.

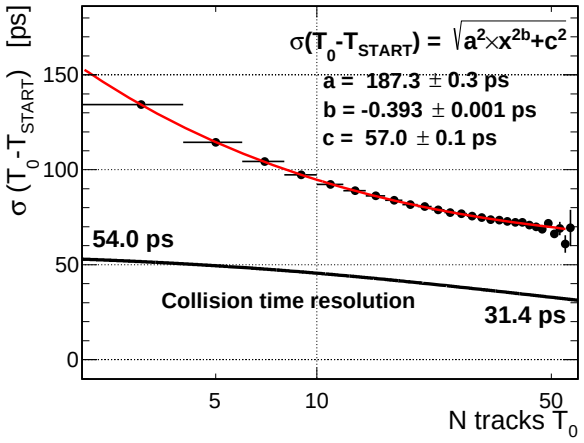

Figure 1: Collision time reconstruction using the T_0 method. The lower line is the combined resolution as a function of the number of tracks that is used in the analysis.

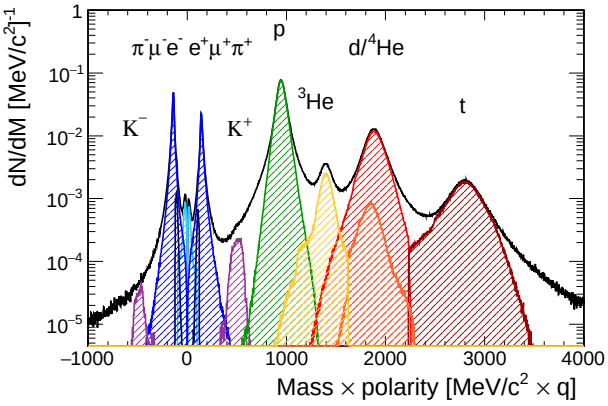

Figure 2: Mass times polarity histogram measured in HADES after applying the T_0 method.

References

[1] G. Agakishiev et al., Eur. Phys. J. A41 February 2009, p. 243-277

[2] J. Pietraszko et al., Nucl. Instrum. Meth. A763, November 2014, p. 1-5

[3] G. Kornakov at al., JINST 9, C11015, November 2014

[4] C. Agodi et al., Nucl. Instrum. Meth. A492, October 2002, p. 14-25

* Work supported by VH-NG-823 and GSI.

† g.kornakov@gsi.de

Azimuthal anisotropy of virtual photons in Au+Au collisions at $\sqrt{s_{NN}} = 2.4\,\mathrm{GeV}$ *

D. Dittert† [1] *and for the HADES collaboration*[1]

[1]Technische Universität Darmstadt, Germany

Virtual photons, that decay into dileptons, are penetrating probes which directly access the entire space-time-evolution of the fireball produced in HIC and they escape from the collision zone without further interactions. Thus they provide unique information about the various stages of the collision. Studying the azimuthal anisotropy of dileptons can accordingly give an insight into the time evolution of collectivity in the system [1].

The collective flow consists of radial flow, which affects the thermal spectra of the outgoing particles, and anisotropic flow, which affects the spatial orientation of the particle momenta. The former one is especially useful to disentangle early and late emission sources, because the effective temperature $T_{eff} \propto T + M \langle\beta_T\rangle^2$ results from the superposition of all fireball stages with decreasing temperature T but increasing flow β_T over time. The azimuthal anisotropies are small as well in the early phases of the fireball evolution, where the flow is not yet fully developed and grow larger for the later phases [2].

The flow coefficients v_1 (directed flow), v_2 (elliptic flow), v_3 (triangular flow), etc., are defined as the Fourier coefficients of the azimuthal angle expansion [3]:

$$\frac{dN}{d\Delta\Phi} \propto 1 + 2\sum_{n=1}^{\infty} v_n cos\,(n\Delta\Phi) \qquad (1)$$

In Figure 1 such a Fourier expansion is fitted to the dilepton $\Delta\Phi$-distribution below 120 MeV/c^2 and additionally the first two Fourier coefficients v_1 and v_2 are plotted separately.

To extract the $\Delta\Phi$ of dileptons, the reaction plane has to be determined, using the spectator hits in the forward wall, placed 7 m behind the detector. Then the azimuthal angle of the dilepton pair is substracted from the angle of the event plane, due to the correlation between the directed and elliptic flow components and the collision geometry. For background determination a like-sign geometric mean is used in the pion region, where correlated background pairs do not allow the use of event mixing. For the higher invariant masses the use of the event mixing method is possible and leads to a slight decrease of statistical fluctuations in the signal to background ratio. The physics background at SIS18 energies is low, with the largest contribution from η Dalitz decays on the 10 % level. Hence for a first analysis the physics background is not taken into account.

The analysis of the azimuthal anisotropy is performed in four bins of invariant mass altogether, to provide information of v_1 and v_2 vs. M_{ee}. The dileptons in the first mass bin up to 120 MeV/c^2 origin mainly from π^0 Dalitz decays, thus it is useful to compare the flow of dileptons of this mass to the one obtained from the pions. This comparison shows a good agreement between the dilepton elliptic flow and the elliptic flow of charged pions. For the higher masses a comparison to the flow of the η or the kaon could be realized. In the pion region, where statistics is high, it is also possible, to perform a multi-differential analysis and analyze the flow in different bins of centrality, rapidity and transverse momentum.

In conclusion the analysis of azimuthal anisotropies of dileptons gives a good insight into the collective behaviour of the fireball and provides additional information to complement the effective temperature, which can be used to validate different theories describing the fireball evolution.

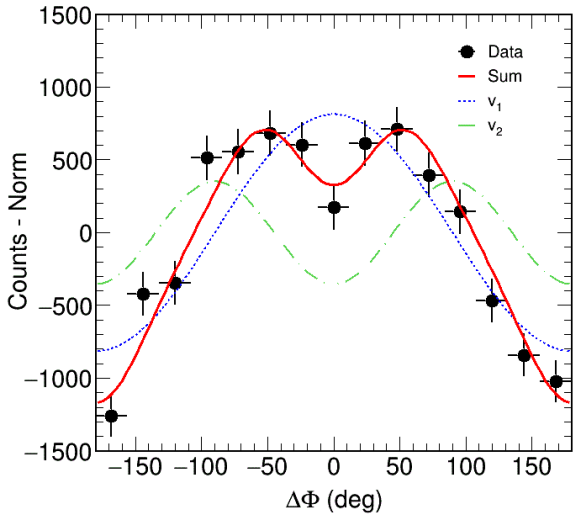

Figure 1: Azimulthal anisotropies of dileptons with $M_{ee} \leq 120\,\mathrm{MeV/c^2}$ measured with HADES in Au+Au.The data are shifted down by the norm of the Fourier expansion. The solid red line shows the sum of this expansion, fitting the data well. The blue dotted line displays the directed flow component v_1 and the green dashed line represents the elliptic flow component v_2.

References

[1] P. Mohanty et al, Phys. Rev. C 85 031903 (R) (2012)

[2] R. Rapp, arXiv:1304.2309 [hep-ph] (2013)

[3] G. Vujanovic, Phys. Rev. C 89, 034904 (2014)

* Work supported by VH-NG-823, EMMI and GSI.

† d.dittert@gsi.de

DOI:10.15120/GR-2017-1

Charge-dependent azimuthal correlations in Au+Au collisions with HADES *

F. Kornas[1], *I. Selyuzhenkov*[2], *T. Galatyuk*[1,2], *and the HADES collaboration*[2]
[1]TU, Darmstadt, Germany; [2]GSI, Darmstadt, Germany

In non-central heavy-ion collisions there could be a manifestation of quantum fluctuations through the coupling of chiral fermions with the magnetic field and the vorticity [1]. This could lead to an electric current among the magnetic field or the total angular momentum, which is measurable by using charge-dependent azimuthal correlations.
The magnetic field (or total angular momentum) is perpendicular to the reaction plane (RP) which is spanned by the beam axis and impact parameter of the collision. A separation of charge would be in this direction perpendicular to the reaction plane, the so called "out-of-plane" direction.
To disentangle the charged particle motion relative to each other, the two-particle correlator γ has been proposed [2]:

$$\gamma_{\alpha\beta} = \langle \cos\left(\phi_\alpha + \phi_\beta - 2\Psi_{\mathrm{RP}}\right)\rangle \,. \qquad (1)$$

ϕ is the azimuthal angle of the charged particle, Ψ_{RP} is the reaction plane angle, α, β account for the different particle charges and the brackets $\langle ... \rangle$ denote the average over particles and events.
The correlator γ is very useful, since all background not related to the reaction plane orientation is removed by construction. It is only sensitive to the difference of "in-plane" and "out-of-plane" background. First investigations of all known background sources indeed show that this difference is much smaller than the observed signal [3].
Yet the correlator γ cannot distinguish for same-charged particles whether they fly together in the out-of-plane or opposite in the in-plane direction. Hence a second correlator is needed to distinguish these two scenarios:

$$\delta_{\alpha\beta} = \langle \cos\left(\phi_\alpha - \phi_\beta\right)\rangle \,. \qquad (2)$$

This correlator has the disadvantage that it has large contribution also from backgrounds unrelated to the reaction plane. Therefore, a proper knowledge of all background sources is required.
Of special interest is the centrality dependence of both correlators, since any effect related to the magnetic field or the total angular momentum should decrease towards more central collisions and even vanish in case of a head-on collision. First measurements of the correlator γ by STAR [4] and ALICE [5] prove the expected centrality dependence. For the correlator δ the situation is more involved which can be attributed to unknown background contributions.

In April 2012, seven billion Au+Au collisions at $\sqrt{s_{NN}} = 2.42\,\mathrm{GeV}$ have been measured with HADES.

* Work supported by VH-NG-823, Helmholtz Alliance HA216/EMMI and GSI.

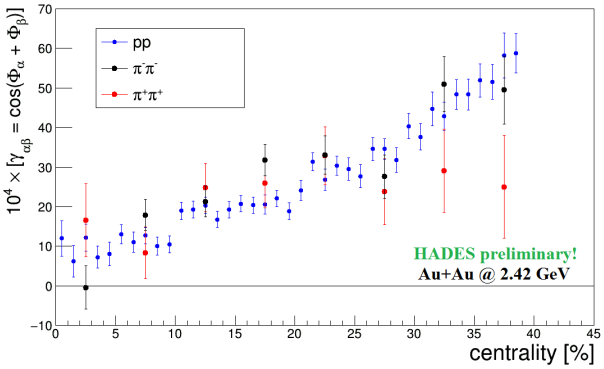

Figure 1: Preliminary results by HADES for the two-particle correlator γ as a function of the collision centrality for Au+Au collisions at $\sqrt{s_{NN}} = 2.42\,\mathrm{GeV}$. The results are shown for same-charged pairs: pp, $\pi^+\pi^+$ and $\pi^-\pi^-$. Only statistical errors are shown.

For the present analysis only $\sim 1/30$ of the total statistics is used. The analysed particles are protons and charged pions which are identified using their measured velocity as a function of momentum. The reaction plane is reconstructed in each event by a Q-vector analysis [6].
The current results for the correlator γ in case of same-charged pairs are shown in figure 1. The results are corrected for efficiency and event plane resolution. To avoid strong flow contributions a transverse momentum cut of $150 < p_t < 600\,\mathrm{MeV/c}$ for pions and $p_t > 600\,\mathrm{MeV/c}$ for protons is applied. For all three particles the correlator γ shows a strong enhancement towards more peripheral collisions. Within statistical errors the magnitudes are comparable.
HADES data provides new information about charge-dependence of correlations with respect to the reaction plane in a few GeV region of $\sqrt{s_{NN}}$ and together with the existing data from STAR and ALICE at much higher energies helps to shed light about a possible chiral magnetic effect (CME) in heavy-ion collisions.

References

[1] D.E.Kharzeev et al., Prog. Part. Nucl. Phys. 88 (2016) 1-28.
[2] S.A.Voloshin, Phys. Rev. C70 (2004) 057901.
[3] A.Bzdak, V.Koch and J.Liao, Phys. Rev. C81 (2010) 031901.
[4] B.Abelev *et al.*, Phys. Rev. Lett. 103 (2009) 251601.
[5] B.Abelev *et al.*, Phys. Rev. Lett. 110 (2013) 1.
[6] J.Barrette et al., Phys. Rev. C55 (1997) 1420.

Kaon and phi production in pion-nucleus reactions at 1.7 GeV/c*

J. Wirth[1,2], *L. Fabbietti*[1,2], *A. Scordo*[3], *and the HADES collaboration*

[1]Excellence Cluster Universe, Technische Universität München, 85746 Garching, Germany; [2]Physik Department, TU München, 85746 Garching, Germany; [3]INFN Laboratori Nazionali di Frascati, 00044 Frascati (Roma), Italy

The production and properties of open and hidden strange mesons (K^+, K^-, ϕ) in cold nuclear matter generated in pion-nucleus reactions ($\pi^- + A, A = C, W$) at $p_{\pi^-} = 1.7$ GeV/c have been studied with the HADES setup.

Of particular interest is the modification of the (anti-)kaon spectral function in nuclear matter which should be already apparent at saturation density [1]. While, for the kaon (K^+, K^0) the repulsive KN-potential has been investigated to some extent and was found to have a moderate strength ($20 - 40$ MeV) [2, 3], the existing data on in-medium effects of the antikaon produced off nuclear targets are very scare [4]. Moreover, the situation of the antikaon is more involved, since the K^- can be absorbed in nuclear matter via strangeness exchange processes on one ($K^-N \rightarrow Y\pi$) or more nucleons ($K^-NN \rightarrow YN\pi$). On the contrary, K^+ does not undergo strong absorption processes and can be treated as a quasi particle within nuclear matter, providing stringent constraints on the production mechanism of strange hadrons. In this context, also the ϕ production and absorption ($\phi \rightarrow K^+K^-$, $BR \sim 48.9\%$) off light and heavy nuclear targets is studied.

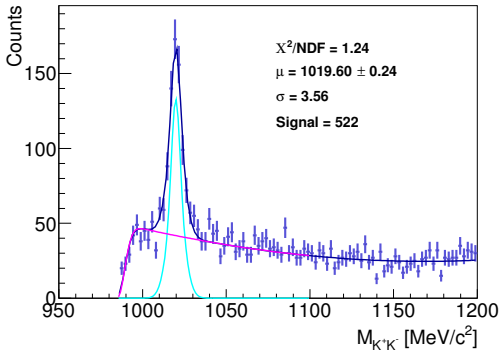

Figure 1: Invariant-mass distribution of K^+K^- pairs in $\pi^- + C$ reactions. The fit consists of two Gaussian for the ϕ signal together with the background described by a polynomial and Gaussian functions

Both charged kaons are identified by means of time-of-flight (START/RPC/TOF) and momentum measurements as well as by the specific energy loss information in the drift chambers to enhance the signal to background ratio. The neutral ϕ is reconstructed employing the invariant mass of charged kaons ($M_{K^+K^-}$) (Fig. 1), which have been selected within a distinct velocity β range. In total about 4×10^5 K^+, 2×10^4 K^- and 500 ϕ ($\pi^- + C$) and 2×10^5 K^+, 1×10^4 K^- and 300 ϕ ($\pi^- + W$) were reconstructed, respectively.

Evidence on the K^- absorption is obtained on the basis of K^-/K^+ ratios in both nuclear environments (C, W) as a function of four different kinematic observables (p, θ, p_T, y). Figure 2 shows the ratios as a function of momentum. Furthermore they are compared the expected ratios without absorption based on existing and extrapolated cross-sections (Fig. 2 gray line). A clear K^- disappearance for a higher nucleon density is observed, which is even more evident for low momenta. Moreover the ratios give a hint for K^- absorption in all four kinetic observables (p, θ, p_T, y).

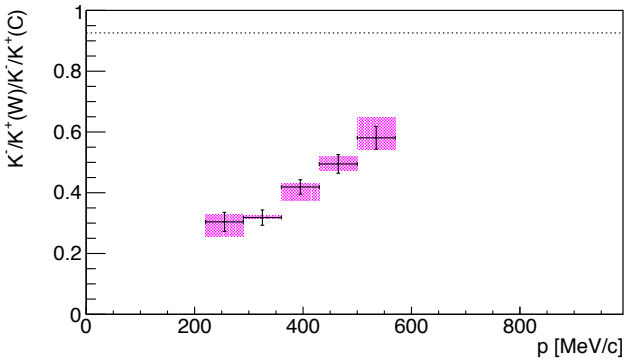

Figure 2: K^-/K^+ double ratio in $\pi^- + W$ collisions compared to $\pi^- + C$ as a function of momentum. The gray line reflects the expected double ratio without absorption.

References

[1] J. Schaffner et al., "In-medium production of kaons at the mean field level", Nucl. Phys. A625: p. 325 – 346 (1997)

[2] M. L. Benabderrahmane et al., "Measurement of the in-medium K0 inclusive cross section in π^--induced reactions at 1.15 GeV/c", Phys. Rev. Lett. 102, 182501 (2009)

[3] G. Agakishiev et al.: "Medium effects in proton-induced K0 production at 3.5 GeV", Phys. Rev. C90: p. 054906 (2014)

[4] W. Scheinast et al., "First observation of in-medium effects on phase space distributions of antikaons measured in proton-nucleus collisions," Phys. Rev. Lett. 96, 072301 (2006)

* Supported by the DFG cluster of excellence "Origin and Structure of the Universe and SFB 1258"

DOI:10.15120/GR-2017-1

$\Lambda - p$ correlation in π^--induced reactions at 1.7 GeV/c *

S. Maurus[1,2], *L. Fabbietti*[1,2], *and the HADES collaboration*[1]

[1]Physik Department, TUM, Garching, Germany; [2]Excellence Cluster "Universe", Garching, Germany

World data for elastic $\Lambda - p$ scattering over a wide range of relative momenta are quite scarce and only available for small beam momenta with a integrated statistic in the order of 200 events [1]. For π^--induced reactions the available data is even more limited [2,3]. In order to improve the theoretical description of $\Lambda - p$ scattering, new constraints are necessary to parametrize the cross sections. In this context a dedicated π^- + A (A = C, W) experimental campaign was performed at $p_\pi = 1.7$ GeV/c with the HADES detector. The recorded data is analyzed in terms of the inclusive Λ yield and Λ-p correlation. For the reconstruction of the Λ in the inclusive spectra the charged decay channel ($\Lambda \rightarrow p\pi^-$, BR = 63.9%) has been examined. Applying topological cuts, an integrated yield of $\sim$11k Λ has been extracted with a purity of 93% ($\pi^- + W$) (Fig. 1). These extracted yields are further corrected for the limited efficiency and acceptance by means of simulations. A Boltzmann distribution has been employed to extrapolated the yield to the full momentum phase space.

After the Λ has been produced it can interact with the nuclear environment and eventually scatter elastically with a nucleon. To isolate this process, events with a matching charge pattern ($\Lambda \rightarrow \pi^- p, K^0 \rightarrow \pi^+\pi^-, p$) are selected. Based on a likelihood-method the particle species has been determined considering the specific energy-loss in the MDCs and velocity β. Since the selected pattern contains two π^- and p in the final state, an event hypothesis has to be applied to assign their corresponding mother particle (Fig. 2, $m_{\pi^+\pi^-} - m_{K^0}$ and $m_{p\pi^-} - m_\Lambda$). The best combination is selected by a simultaneous matching of the invariant mass to the nominal value within the detector resolution. This procedure leads to an extraction of $\sim$6k events in the $\pi^- + W$ system. For a full description of all kinematic properties of the system the Λ before the scattering is reconstructed by applying energy and momentum conservation to the incoming π^- beam and the reconstructed outgoing K^0 from the $\pi^- p \rightarrow \Lambda K^0$ reaction. All of these observables will in principle allow to reconstruct the $\Lambda - p$ scattering process and extract its cross section.

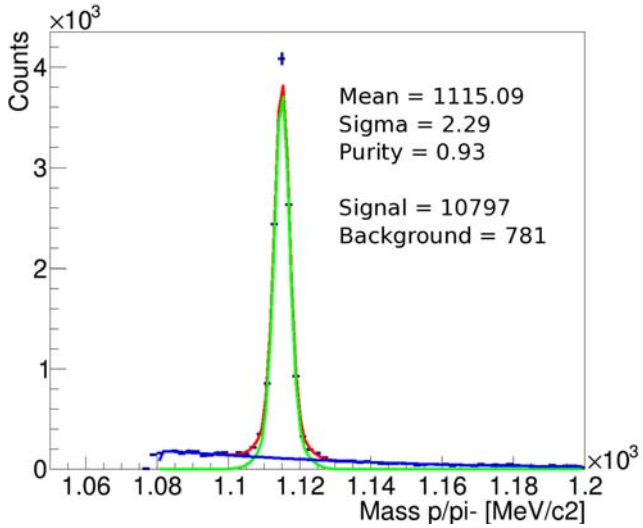

Figure 1: Invariant mass spectra of $\pi^- p$ pairs in $\pi^- W$ reactions after the topological cuts have been applied. The signal is fitted with a double Gaussian and the background is described by a polynomial together with a Gaussian.

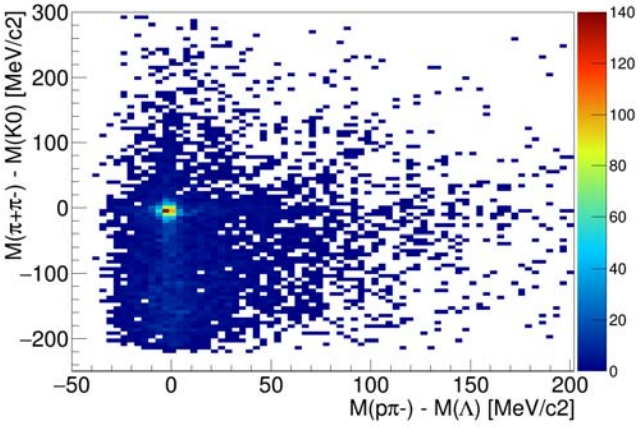

Figure 2: Correlation of the invariant mass spectra of $\pi^+\pi^-$ and $\pi^- p$ for the event pattern $pp\pi^-\pi^-\pi^+$ in $\pi^- W$. The pole mass of Λ and K^0 is subtracted, respectively.

References

[1] Engelmann et al., Phys. Lett. B19, 715 (1966)

[2] Alexander et al., Phys. Rev. Lett. 7, 348 (1961)

[3] Crawford et al., Phys. Rev. Lett. 2, 174 (1959)

* Work supported by BMBF 05P15WOFCA

Status of data acquisition software DABC *

J. Adamczewski-Musch[1], *N. Kurz*[1], *S. Linev*[1]

[1]GSI, Darmstadt, Germany.

The software framework DABC (Data Acquisition Backbone Core) [1] provides a flexible environment for distributed data acquisition with online monitoring and control capabilities. It is used for event building at the HADES experiment since 2014 [2]. Moreover, DABC has been deployed for data taking with detector and readout electronics tests [3]. This article reports the most recent applications and developments for the DABC framework.

DABC framework

Improvements

Version 2.9 of DABC was released in November 2015. A number of improvements have been introduced to the base framework since this time. These were driven by requirements showing up during the developments for the *hadaq* and *saft* plug-ins. The changes concern some internal functionality of data transport and socket classes, with the goal to improve performance, stability, and error handling. Additionally, it is now possible to configure event handler priorities for any active DABC entity, like processing modules and sockets. Moreover, the configuration syntax has also been extended, e.g. to allow more easy treatment of array values in the DABC XML files.

HTTP server

Since 2013 DABC offers monitoring and control features by means of the public *civetweb* HTTP server in combination with a proprietary JavaScript GUI [1].

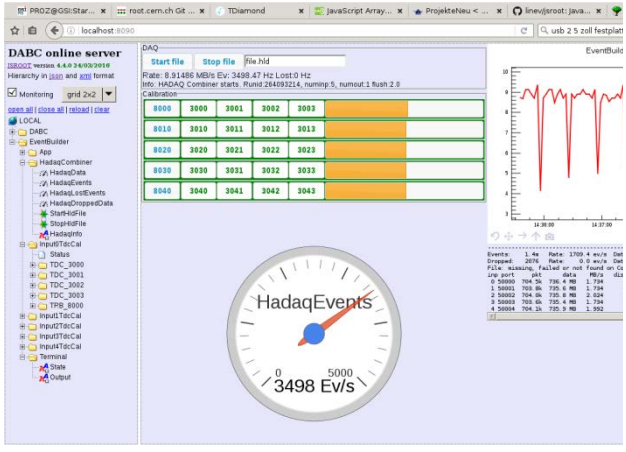

Figure 1: Example of DABC web GUI application for monitoring and control of a trb3 calibration test.

A screenshot of a web browser controlling a DABC application is shown in Fig.1.

These web control features have been implemented in close connection with the JavaScript ROOT project [4]. So the DABC web GUI benefits also from the further developments of JavaScript ROOT in 2016. Currently DABC v 2.9.1 is distributed with JSROOT version 4.4

Linux Device Drivers

PEXOR asynchronous readout

The PCIe optical receiver boards PEXOR and KINPEX are widely used for data acquisition of various front-end boards developed for FAIR. The Linux device driver *pexor* [5] is used for DABC and FESA based read out of such systems. Most recently this kernel module and the user library software have been further improved. One goal was to provide an asynchronous readout of different SFP chains without the need of the common trigger module hardware TRIXOR. This can be useful for large beam position monitoring applications, or for detector set-ups with readout chains that are to be triggered independently.

In such use case the data read out of each SFP chain is synchronized independently by means of the *gosip* protocol [5]: The host software sends a data request for a readout chain to the front-end FPGAs and polls for the data to arrive. If a chain has delivered data, it is further processed by the DAQ software and the next data request is send. If a chain has not yet sent anything, the corresponding subevent is just omitted in the collected data event. So it is possible to handle the readout of systems with different local trigger frequencies into one combined data stream. This technique has been implemented and tested with two different approaches: An explicit polling for each chain data in the DABC readout application, and an implicit polling in the kernel module software. The latter approach will have the advantage that a concurrent access to the front-end by a control system is possible, since the *gosip* operations can be locked in the kernel module. Furthermore, this implementation in the driver software is independent from DABC and may also be applied for future FESA readout.

First tests with independently triggered front-ends look promising. The developments are continued and will be ready for application in 2017.

PEXORNET

The *pexornet* Linux device driver [6] has been developed as novel approach to read out a commonly triggered PEXOR/KINPEX system. Here the kernel module registers the GSI proprietary optical receiver hardware as a

* PSP codes: HADES 1.1.2.4, SD -SEM 2.3.6.5.1.6.30

DOI:10.15120/GR-2017-1

regular Ethernet network device to the operating system. Each hardware trigger at the TRIXOR module will invoke an automatic read out in the interrupt handler of the driver. The collected data will be sent as an UDP packet via any socket that is connected to this pseudo network. So any user application may receive such data from a regular network socket and may process it at will. By means of a special DABC plug-in, however, it is possible to read from such socket and produce the same data format as the alternative DAQ system MBS [7], and apply the same Go4 [8] analysis for checking data integrity.

The *pexornet* readout has been tested in comparison to MBS with POLAND and FEBEX front-end hardware [6]. For two FEBEX devices at one SFP chain, *pexornet* achieved about the same performance as the conventional MBS readout, i.e. 150 MB/s at 7.6 kHz event rate if triggered by 20 kHz pulser [6].

Plug-in developments

HADES event builder

The *hadaq* plug-in is used for production event building at the HADES experiment since 2014 [2]. In the scope of the trb3 TDC developments [3] it has been further tested and improved. A special time sorter module in the event builder has been developed to cope with parallel high speed data streams from a single trb3 via separate UDP connections. Furthermore, the possibility to calibrate the TDC fine time values "on the fly" in the event builder before writing the raw subevents to disk has been optimized for different calibration methods (statistical approach, temperature calibration function, simple linear calibration). Advanced analysis and monitoring techniques in such a DABC code have been helpful to further understand functionalities and limitations of the FPGA TDC

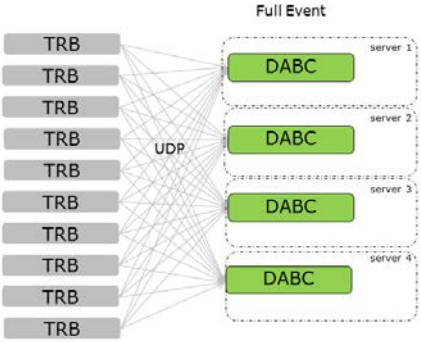

.

Figure 2: Previous HADES event building network topology: Each trb front-end hub sends to all event builders via UDP in an "n x m barrel shifter" scheme

The HADES detector is going to be equipped with numerous additional trb3 readout boards for the expected FAIR-0 beam time. To fully benefit from such an online trb3 TDC calibration, the topology of the event building network is going to be changed (see Fig.2). In the previous set up, each front-end hub was sending data via Gb Ethernet UDP connections to all receiving event builder nodes in a barrel shift mode (Fig.2). Instead, each front-end will send to a dedicated entry server only and the full event combination is done by a second TCP/IP "builder network" BNET (Fig.3) [1].

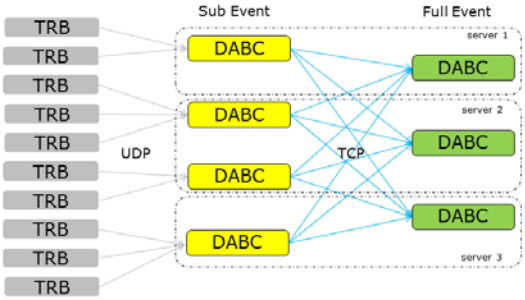

Figure 3: New HADES event building network topology as tested: The trb front-end hubs send via UDP to dedicated "subevent input" processes. Full events are built via TCP in a second stage builder network (BNET).

This allows to configure the TDC calibration modules of each entry server according to the connected front-ends. A first test of such an alternative builder topology has been carried out in December 2016. The *trbnet* hub configuration has been modified and DABC has been started with separate input and builder processes on each server (1 input and 2 builder processes at 4 server machines). Using a pulser trigger, the data taking of full events from 17 active front-end hubs could be verified. Switching between the old and new topologies is handled simply by changing a flag parameter in the HADES DAQ startup scripts.

White Rabbit SAFT library

The FAIR timing and messaging system will be based on the White Rabbit technology [9]. Therefore it can be interesting to read out timestamps and machine events from timing receiver hardware (PEXARIA or EXPLODER5) with DABC. The timing messages may then be processed together with regular event data from the experiment detectors.

A DABC plug-in has been developed based on the official FAIR SAFT library (Simple API for Timing) [10]. Here the timing events to be recorded can be configured in the DABC XML setup file. Whenever an event of the requested type arrives at the timing receiver hardware, the appropriate SAFT "Event Condition Action" (ECA) callback will be caught and evaluated by DABC. The detected timing events are queued, packed into dedicated *lmd*- or *hld*-formatted events, may be stored to a file, or may be send to an online monitoring Go4 [8] application. In future DABC applications such timing events may be simply combined as subevents with other detector data.

Performance tests of such read out have been done at a commodity PC (DELL T3500, 2 cores, Linux kernel 4.1.20) with EXPLODER5 timing receiver hardware at the PCIe slot. Version 1.0.8 of the SAFTlib was used. A

DOI:10.15120/GR-2017-1

TTL pulser of different frequencies was connected to input IO1 of the EXPLODER5 to deliver an input timing event (signal rising edge) to be detected. In this test DABC was configured to produce *hld* data format as it is in use for the HADES experiment. The sequence of timing events was checked and monitored with a Go4 analysis.

Figure 4 shows the relative loss of timing events versus the event pulser frequency (plot above), and the corresponding CPU load for several relevant processes (plot below). The loss of timing events could be detected both by the overflow counter of the SAFTlib FIFO, and by histograming the time difference of subsequently collected messages in the Go4 analysis. The relative loss in Fig.4 is the ratio of detected FIFO overflows by the total number of received timing events. Note that the data points for the lowest frequency 1.2 kHz give just a worst case estimation from the total measurement time without any loss. It turned out that the event rate limit for lossless readout with this setup was at about 2 kHz. For higher frequencies, the dual-CPU host load reached 200% in total, split into the participating processes of DABC, the SAFTlib demons (*saftd* and *dbus*), and the Linux kernel interrupts (*kworker*), see plot below in Fig.3.

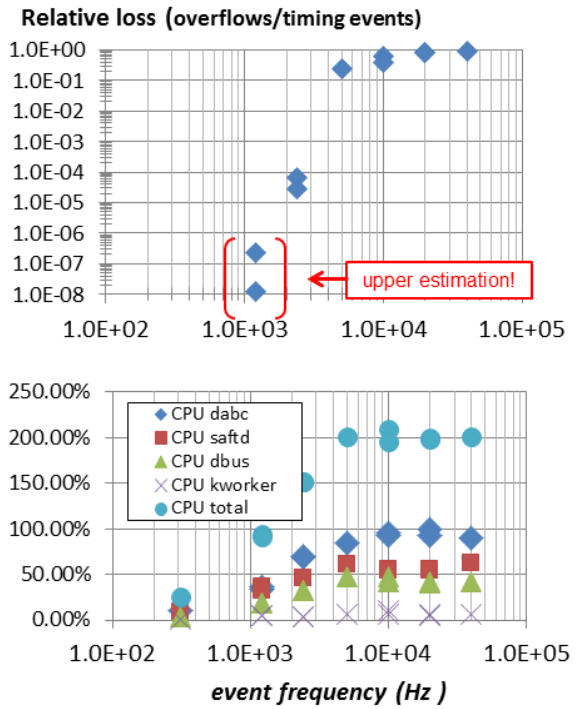

Figure 4: Relative loss of timing events (above) and host CPU consumption (below) versus event frequency for DABC *saft* plug-in tests. See text for details

This limit can probably be extended by using more powerful PC hardware, and by further optimizing of the SAFTlib. However, for the slow control use case a maximum event rate of 1 kHz may already be sufficient. For DAQ applications with trigger rates up to 100 kHz, a trigger time-latch readout with every event seems to be not possible by such SAFTlib approach. But for a downscaled trigger time latch, or to embed occasional accelerator messages into the experiment data stream, the DABC *saft* plug-in could be useful though.

New mass storage interface

Since the old tape storage tool *gstore* has almost reached the end of its life, the new software *ltsm* [11] is proposed as generic storage interface at FAIR. Therefore in November 2016 the project has started to develop a DABC plug-in that utilizes the *ltsm* libraries from the event builder process. The aim is that data acquisition software like DABC and MBS can open new files at a dedicated IBM tape storage server and can write directly data buffers to such file. This will preserve the previous use case [2] that experiment data can be written to the mass storage immediately during data taking, without requiring an intermediate file on a local disk.

First tests of the *ltsm* software looked promising. The DABC plug-in for *ltsm* is currently being developed in close collaboration with the GSI IT storage group. It is expected to be ready for application during 2017.

Outlook

The DABC software for data acquisition and monitoring on Linux X86 PC is mature and has been constantly maintained. Special improvements for the HADES experiment and various trb3 readout systems have been implemented in 2016. GSI proprietary read out hardware, like the PEXOR system, are supported up to the device driver level. Several new software interfaces, such as the FAIR machine timing *saft* plug-in, and the *ltsm* mass storage plug-in, are currently under development.

The DABC framework and the most important user plug-ins are available under GPLv2 via the DABC web site [12].

References

[1] J.Adamczewski-Musch, N.Kurz, S.Linev: “Developments and applications of DAQ framework DABC v2”, J.Phys.Conf.Series 2015, vol.664, http://iopscience.iop.org/article/10.1088/1742-6596/664/8/082027

[2] J. Adamczewski-Musch, S.Linev: “DABC as event builder at HADES experiment”, GSI scientific report 2014, doi:10.15120/GR-2015-1-MU-NQM-HADES-26

[3] http://trb.gsi.de/

[4] B.Bellenot, S.Linev “JavaScript ROOT”, J.Phys.Conf.Series, 2015, vol. 664, http://iopscience.iop.org/article/10.1088/1742-6596/664/6/062033

[5] J. Adamczewski-Musch, H.G.Essel, S. Linev : “The DABC Framework Interface to Readout Hardware”, IEEE TNS Vol.58, No.4, August 2011, pp. 1728-1732

[6] J. Adamczewski-Musch, N. Kurz, S. Linev, “MBSPEX and PEXORNET - Linux device drivers for

DOI:10.15120/GR-2017-1

PCIe Optical Receiver DAQ and control", presented at IEEE RT2016, submitted for publication at IEEE TNS
[7] http://www.gsi.de/mbs
[8] http://go4.gsi.de
[9] D. Beck et al., "Paving the Way for the FAIR General Machine Timing System", GSI scientific report 2013, doi:0.15120/GR-2014-1-FG-CS-08
[10] https://www-acc.gsi.de/wiki/Timing/TimingSystemDocumentsSaftlib
[11] T. Stibor et al., "LTSM - Lightweight TSM API", https:/github.com/tstibor/ltsm
[12] http://dabc.gsi.de

Stabilizing aged Drift Chambers under high rates

C. Wendisch [*1], *O. Fateev* [4], *L. Lopes*[2], *C. Müntz*[3], *and J. Stroth*[1,3] *for the HADES Collaboration*[†]

[1]GSI, Darmstadt, Germany; [2]LIP, Coimbra, Portugal; [3]Goethe-Universität, Frankfurt, Germany; [4]Joint Institute of Nuclear Research, Dubna, Russia

The future physics program of HADES at FAIR demands high detection standards, meanig in precision and also stability of the tracking system comprising four layers of planar drift chambers (MDC-I - IV). Compared to the exposure of 18 beam-times within 15 years, stable operation of the wire chambers has to be ensured now for factors 2-3 higher particle load than the maximum so far.

Progression of drift chambers during 15 years

Built in the end of the 1990s the drift chambers operation started with a gas mixture of helium/isobutane (60/40) to achieve the lowest material budget for the HADES detector. Later the gas was changed to argon/isobutane (84/16) to increase the primary ionization. During the beam-time in 2012 (Au+Au reactions at E_{kin} = 1.23 AGeV) massive wire aging occurred, revealed in the Malter effect, causing self sustained currents [1]. Therefore isobutane, which tends to polymerize, was substituted and now Ar/CO_2 (70/30) is used to prevent further aging in high load experiments. Since 2013, MDC II operates at a high voltage of -1770 V (drift cell size 6 x 5 mm^2) with H_2O additive to recover stability [2]. An overall stable operation was observed with the admixture of 1000-3000 ppm water vapor to the counting gas, tested in beam and in equivalent X-ray irradiation.

During X-ray tests with an intensity corresponding to the highest particle beam load reached, a sense wire broke inside sector 4 of MDCII. The consequent repair offered the opportunity to microscopically investigate the reasons for stability breakdown, expected to be aging of wires since an observed persistent Malter-effect points to wire deposits.

Wire inspection

The visual inspection of the drift chamber interior 13 wire planes, depicted in figure 1, revealed abundant black deposits randomly distributed on all cathode and field wires (aluminum, diameter 80 μm) providing the high voltage.

Investigating the material compounds of the deposits by energy dispersive X-ray spectroscopy (EDX), carbon and oxide in several μm thick layers covering the wire surface were found, shown by the inlay of figure 2. Further, no sign for aging of anode wires (tungsten, diameter 20 μm) was observed.

Cleaning all wires to remove deposits manually and via solvents in an ultrasonic bath was tested to be not successful. But operating with water vapor as gas additive turned out to be the stable solution and should also prevent further polymerization.

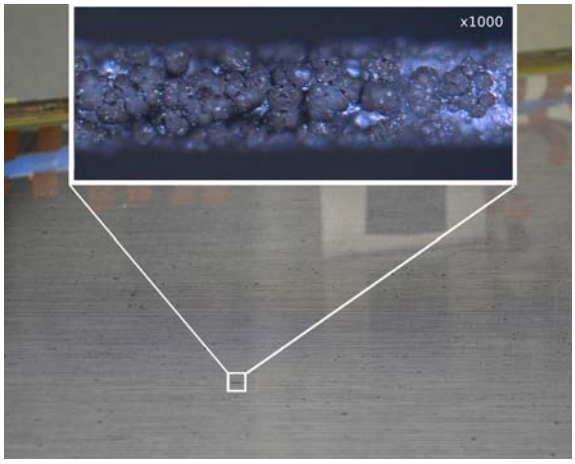

Figure 1: Single wire plane, showing dark deposits on field wires (diameter 80μm, Al) magnification 1000x, optical microscope.

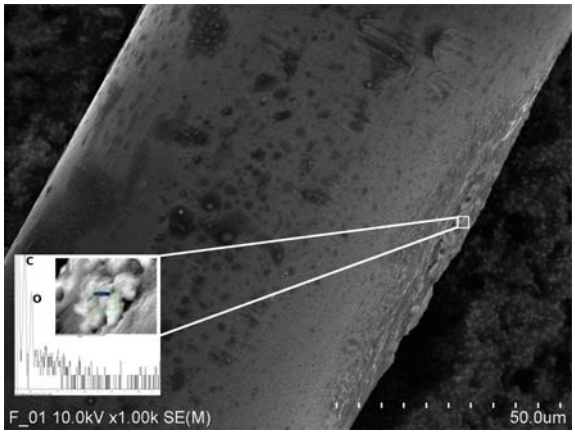

Figure 2: Scanning electron microscope view of field wire surface (diameter 80 μm, Al) magnification 1000x. Inlay shows EDX spectroscopy results: atomic compounds of deposits are carbon 73.2 %, oxygen 26.8 %.

We acknowlage Helmholtz-Zentrum Dresden-Rossendorf for the support with the EDX analysis.

References

[1] L. Malter, Phys. Rev., vol. 50 (1936) 48-58.

[2] A. Boyarski, Nucl.Instrum.Meth.A515 (2003) 190-195.

* c.wendisch@gsi.de

† Work supported by BMBF, HIC for FAIR and GSI.

DOI:10.15120/GR-2017-1

Towards new front-end electronics for the HADES drift chambers*

M. Wiebusch[1], *J. Michel*[1], *C. Müntz*[1], *M. Traxler*[2], *C. Wendisch*[2], *J. Stroth*[1,2], *and the HADES Collaboration*

[1]Goethe-Universität Frankfurt, Germany; [2]GSI, Darmstadt, Germany

Track reconstruction in HADES is realized with 24 planar, low-mass drift chambers (MDC). About 27000 drift cells provide both precise spatial information of track hit points and energy loss information. In order to handle high rates and track densities required at the future SIS100 accellerator at FAIR, an upgrade of the MDC system is necessary. This involves new front-end electronics, as the original analog read-out ASIC (ASD8) is no longer procurable.

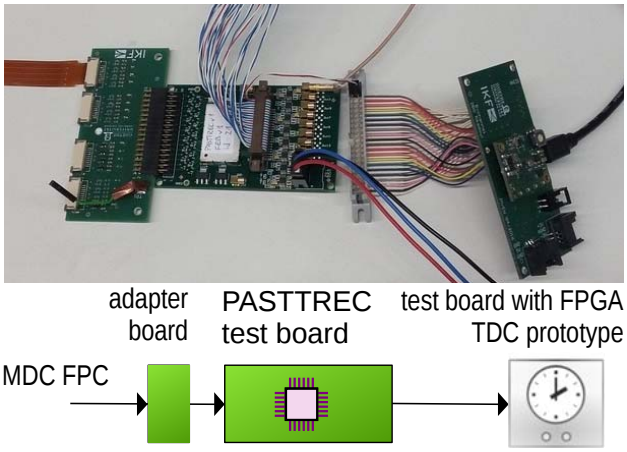

Figure 1: PASTTREC read-out line, here equipped with a stand-alone FPGA-based prototype TDC.

A promising replacement read-out chip candidate is the PASTTREC ASIC [1], developed at Jagiellonian University, Krakow, for reading-out straw tubes e.g. of the PANDA experiment and the future HADES forward tracker. It is supplemented by a high precision FPGA-based TDC [2], implemented on a TRB3 board. In parallel, a cost-efficient and lightweight but coarse binned (500 ps) FPGA-based prototype TDC was successfully tested. It is foreseen to replace the currently used dedicated TDC ASICs.

To arrive at conclusive performance results, the tests are being conducted under realistic conditions in direct comparison to the present ASIC. To do so, a spare drift chamber is employed and both signal-to-noise and dE/dx as well as time measurement precision is systematically characterized with radioactive sources and cosmic rays.

Figure 1 depicts the PASTTREC read-out line, which is attached by means of a dedicated flex cable (MDC FPC) to the detector. One key issue is the compatibility of the PASTTREC ASIC with the present flex-based signal routing which significantly affects the noise immunity together with determining the optimum amplifier and shaper settings for the chip. Due to the unique arrangement of the two innermost sense wire layers (see figure 2) it is possible to assess the time (and spatial) precision by correlating adjacent drift cells. Plotting the difference against the sum of both drift time signals for perpendicular tracks of cosmic muons (triggered by an external scintillator) allows to access the drift time precision. This is done by projecting a selected data sample (small drift time difference) on the axis representing the drift time sum. The width of the resulting peak is closely related to the time precision. This study, together with future beam tests, will help to answer the other key question on the possibility of assigning an ASIC optimized for straw tube signals to read out the mini (cell) drift chambers of HADES. Compared to MDC, the straws (operated at 2 atm gas pressure, avg. 50% longer track path) provide longer drift times and more primary ionization. The decision on the replacement of the existing electronics is foreseen to be taken in the second half of 2017.

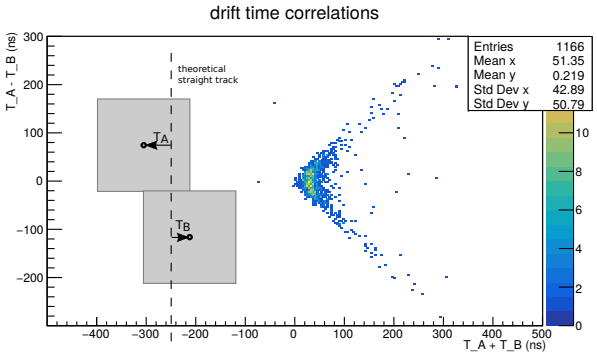

Figure 2: Drift time correlations from two adjacent, shifted cells (see schematic inlay) as function of drift time sum and difference.

References

[1] M. Idzik, G. Korcyl, D. Przyborowski, P. Salabura, J. Smyrski and P. Strzempek, doi:10.1109/RTC.2016.7543165

[2] C. Ugur, et al., 264 Channel TDC Platform applying 65 channel high precision (7.2 ps RMS) FPGA based TDCs, in: IEEE Mediterranean Workshop on Time to Digital Converters, 2013.

* supported by BMBF, HGS-Hire and GSI

Tracking resolution studies of the HADES Forward Detector

A. Blanco[1], *L. Fabbietti*[2,3], *R. Lalik*[2,3], *K. Nowakowski*[4], *P. Salabura*[4], *L. Silva*[1], *and A. Zinchenko*[5]

[1]LIP-Laboratório de Instrumentação e Física Experimental de Partículas , 3004-516 Coimbra, Portugal; [2]Excellence Cluster 'Origin and Structure of the Universe', 85748 Garching, Germany; [3]Physik Department E62, Technische Universität München, 85748 Garching, Germany; [4]Smoluchowski Institute of Physics, Jagiellonian University of Cracow, 30-059 Kraków, Poland; [5]Joint Institute for Nuclear Research, 141980 Dubna, Russia

The forthcoming upgrade of the HADES detector (see Fig. 1) with the newly developed Forward Detector will allow for measurements in the until now inaccessible angular region of the very forward direction ($\theta < 7^\circ$). The new Forward Detector will essentially extend the HADES acceptance in the kinematic region specially important for hyperon spectroscopy in the elementary and light-ion target reactions. The Forward Detector consists of two tracking stations based on straw tubes developed for the PANDA Forward Spectrometer [1] and a time-of-flight wall using RPC detector benefiting from the NeuLAND development [2]. Since the Forward Detector operates in a magnetic field free region of HADES, a precise reconstruction of displaced secondary vertices of Λ, Σ^0 and Ξ requires good spatial resolution and challenging reconstruction procedures, momentum reconstruction using time of flight information from RPC and kinematical refit analysis.

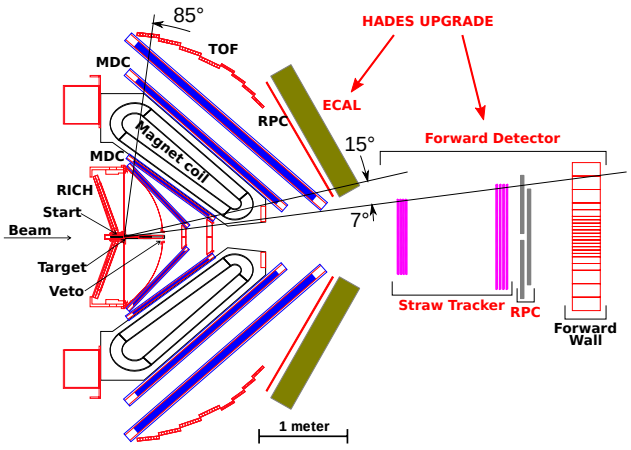

Figure 1: Upgrade of the HADES setup.

The straw tracker comprises eight double straw layers organized in two stations of four layers each, placed 3 m (the first station) and 4.6 m (the second station) downstream from the target. The layers are rotated respectively by 0, 90, 0, 90° and 0, 90, -45 and +45° around the beam axis. Each layer consists of tubular 10.1 width (diameter) straws made of 20 μm thin Mylar foil, filled with Ar:Co_2 (90:10 mixture) at over-pressure of 2 atm, and a 20 μm thick copper sense wire. The first module contains 80 straws (in each plane of a single double plane layer) and the second 112 straws. The stations have a hole for the beam opening, with a width of 8 straws in the first module and 16 in the second module.

The RPC detector is located behind the second straw module at about 5 m distance from the target. It is made of four modules organized in two front and two backward stations, rotated accordingly by 0 and 90° around the beam axis. Each module is made of twelve gas gaps spanning the whole module area with a segmented readout of 30 strips in each module.

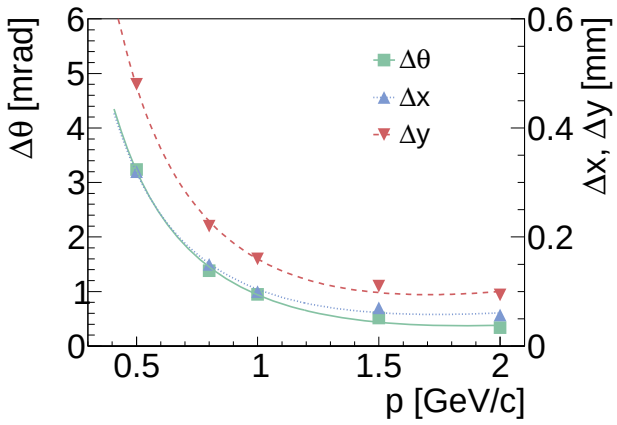

Figure 2: The θ, x and y resolutions in function of momentum. Fitted curves are only parametrizations for the simulated points and cannot be extrapolated.

The complete geometry of the Forward Detector, digitization and tracking algorithms have been implemented and integrated in the HADES simulation framework.

The tracking resolution was investigated by means of mono-energetic protons emitted from the target region into the detector acceptance. Five different proton momenta were studied: 0.5, 0.8, 1.0, 1.5 and 2 GeV/c. The resolution is defined as one standard deviation of a spectrum of differences between simulated and reconstructed values. Three main track parameters were under investigation: θ — track polar angle and x,y — coordinates of intersection between track and the first plane of the first layer. In both cases, a strong momentum dependency was observed resulting from multiple scattering. The resolution results are summarized in Fig. (2).

References

[1] W. Erni et al. *EPJA*, 49(2):25, 2013.

[2] J. Machado et al. *JINST*, 10(01):C01043, 2015.

DOI:10.15120/GR-2017-1

Temperature dependence of dark noise for H12700 MAPMTs : A quantitative approach*

V. Patel[1], *C. Pauly*[1], *J. Förtsch*[1], *and K.-H.Kampert*[1]
[1]Bergische University of Wuppertal

Motivation

The CBM RICH project will use Hamamatsu H12700 MAPMTs for detection of di-leptons. These MAPMTs are specially designed to detect single photons e.g. from Cherenkov radiation. One of the primary tasks at our laboratory in University of Wuppertal is to do QC tests for all the MAPMTs delivered by Hamamatsu. These tests are being done since fall 2015 and are still on going with every delivery. We measure various parameters and compare them with specifications which we agreed upon with Hamamatsu. During these tests we found that the dark rate of same MAPMTs differ depending on whether it was measured in summer or winter due to variation of temperature in our lab. However, without active temperature control in our setup, it was not possible to determine this effect quantitatively. Good understanding of the temperature behaviour of the PMTs is important in view of the required cooling efforts needed later in the experiment. According to the specification, the allowed level of dark rate is 6.4 kHz per MAPMT and, if during QC test this limit is exceeded, we return the MAPMT to manufacturer.

Experimental Setup

To study the temperature dependence of dark rate we used a climate chamber. It has automated temperature control for a variety of settings. The setting of the climate chamber was made such that one particular temperature settles for three hours and then increases to the next step in two minutes. The main reason to do so was to give MAPMT time to get into equillibrium with surrounding temperature. For measuring dark rate n-XYTER cards were used outside the climate chamber. This made sure that the n-XYTER does not contribute to change in noise and we measure noise contribution only from a MAPMT. The n-XYTER was connected to a water cooling system which kept its temperature at 22 °C while the PMT was subjected to varying temperature settings.. At any given temperature the n-XYTER takes data of rates at thresholds from 30 to 100 in steps of ten in every 15 minutes. Thus, we have a dataset of approximately ten observations for each temperature. The complete test required 36 to 40 hours for one MAPMT. We tested three MAPMTs and they all showed similar results. A typical temperature dependence behaviour of a PMT is shown in Figure 2. The results are discussed as follows.

Figure 1 shows that there is an exponential behaviour in

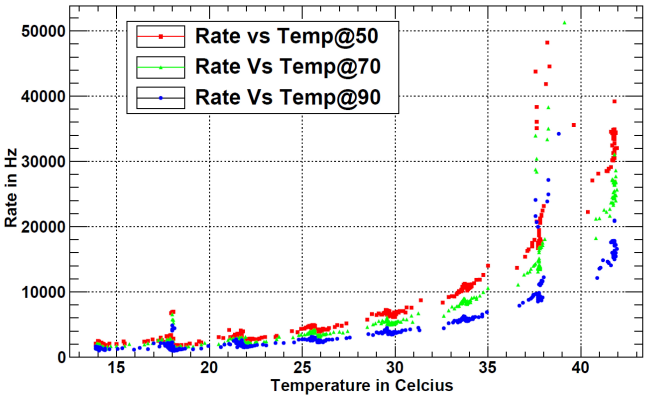

Figure 1: Relation between temperature (°C) and dark rate (Hz) for different thresholds at the ADC.

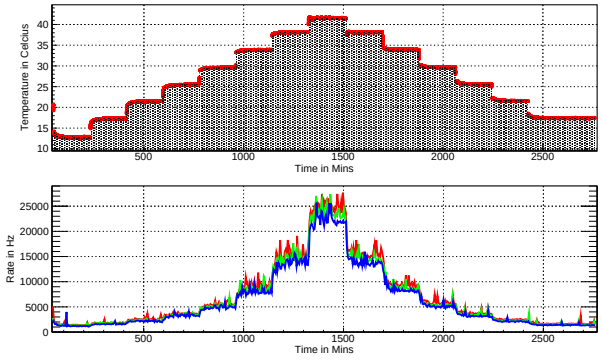

Figure 2: Time evolution of the temperature in the climate chamber and corresponding change of dark rate in the MAPMT at three different ADC thresholds.

increase of dark rate with change in temperature. As temperature increases beyond 30 °C this becomes a serious issue.
Figure 2 shows the evolution of both temperature in the climate chamber and change in dark rate of the PMT as a function of time. We can observe a clear correlation between environmental temperature and dark rate of the MAPMT.

Analytical description of temperature dependence

An important result of this study is the deduction of an analytical description of dark rate for the MAPMTs. This can help us to estimate the dark rate at room temperature

* BMBF grant 05P15PXFCA, and GSI.

Table 1: Comparision of measured and extrapolated rates

PMT Number	Rate(Hz) @ Temp(°C)	Rate(Hz) @ Temp(°C)	Extrapolated Rate(Hz)	Difference(%) bet measured & extrapolated
HA0150	494 @ 22.96	1162 @ 29.10	1033 @ 29.10	-11%
HA0151	353 @ 22.96	637 @ 29.10	736 @ 29.10	13%
HA1089	816 @ 27.06	1213 @ 30.11	1177 @ 30.11	-3%
HA1215	855 @ 27.06	1744 @ 32.69	1680 @ 32.69	-4%
HA1469	1161 @ 20.82	3332 @ 26.05	3112 @ 26.05	-6%

(or to extrapolate to any temperature). Since we check many other parameters of these MAPMTs in an independent setup, this relation is implemented there so that we can claim about dark rate related failures of MAPMTs with proper proofs. The dark rate temperature dependence of the PMT follows an exponetial behaviour, and can be described as:

$$Darkrate(T) = Darkrate(T0) \cdot e^{(\lambda \cdot (T - T0))}$$

where T0 = 20 °C is the reference temperature and (T-T0) is the difference . The exponetial coefficient λ has been verified for three different MAPMT and it is found to be similar for all MAPMTs, while the dark rate at room temperature varies strongly between different MAPMTs.

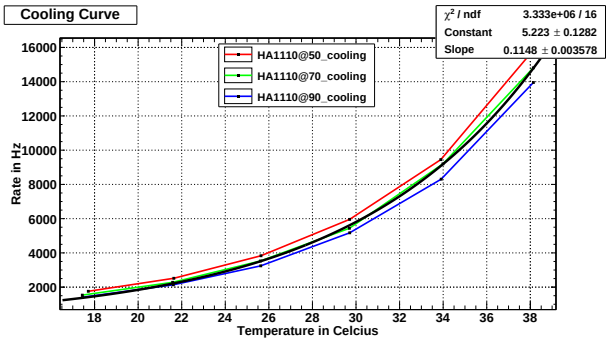

Figure 3: Fits of the rate constant

From our measurements we deduce an average value for $\lambda = 0.12$. Using this value one can extrapolate the rate values to any temperature. This exponential coefficient has been implemented to calculate the dark rate of MAPMTs in our main setup where we study different parameters of MAPMT. In our present Quality Control tests we extrapolate dark rate to 25 degrees which helps us to claim about PMT performance with Hamamatsu. The authenticity of this value has been varified in our main setup which is shown in Table 1.

The Table1 shows the measured dark rate for various PMTs at two different temperatures (column 2+3). Column 4 shows the expected dark rate, extrapolated from the first measurement (column 2) to the temperature of the second measurement (column 3) using exponential extrapolation with $\lambda = 0.12$. The difference between measurement of rate at higher temperatures and extrapolation is shown in column 5, and proves the validity of the analytical description.

Discussion

The studies presented in this article provide a good understanding of the temperature behaviour of H12700 MAPMT, which is necessary to plan the required cooling and temperature control efforts in the final detector design. The main observations can be summarized as follows:

- Strong increase of dark rate with temperature is observed which puts stringent requirements on the operating conditions in the detector. Temperature above 30 °C must be avoided in order to keep dark rate (and thus data rate of the self-triggered acquisition system) in tolerable levels.
- With Hamamatsu we agreed on an upper dark rate value of 6 kHz at room temperature. In order to qualify this criteria for all PMTs, the measured dak rates have to be extrapolated to room temperature using the found correlation law. An exponential coefficient of $\lambda = 0.12$ could be deduced, which allows for rate extrapolation to room temperature in the PMT QC setup.
- The weak threshold dependence of measured dark noise rates confirm the single photon nature of these noise signals, which can not be suppressed by simply increasing the threshold. This can be also infered from Figure [3]
- Our measurements in the climate chamber show no hysteresis effects of dark rate with temperature change. The dark rate is a direct consequence of the actual PMT temperature.

References

[1] M. Calviab *et al.* , Characterization of the Hamamatsu H12700A-03 and R12699-03 multi-anode photomultiplier tubes,LHCb-PUB-2014-043, September 2014

[2] P. Koczon *et al.*, Readout of the Hamamatsu H8500-03 MAPMT with n-XYTER chip, CBM Progress Report 2009, Darmstadt 2010,p.20

[3] J. Förtsch *et al.*, The new H12700 PMT for CBM , CBM Progress Report 2014, Darmstadt 2015 ,p.63

DOI:10.15120/GR-2017-1

Correlation analysis tool using the Schrödinger equation (CATS)*

D. Mihaylov[1] *and L. Fabbietti*[1]

[1]Physics Department E62, TU München, James-Franck-Str., 80805 Garching, Germany

Femtoscopy

The femtoscopy investigates particle correlations using the experimentally accessible two-particle correlation function $C(k)$. Theoretically $C(k)$ can be defined in terms of a source function $S(k,r)$, which describes the relative two-particle spatial distribution at thermal freeze-out, and the two-particle wave function $\Psi(k,r)$, which carries information about the interaction potential $V(r)$ between the particle species of interest (equation 1).

$$C(k) = \int S(k,\vec{r}) \cdot |\Psi(k,\vec{r})|^2 \mathrm{d}\vec{r} \qquad (1)$$

The HADES collaboration has published a femtoscopy analysis of $p\Lambda$ correlations, extracted form the experimental data collected during the 3.5 GeV pNb beam-time, which demonstrated that measuring the correlation function may be used in order to differentiate between different potentials [1]. This is a very nice proof that femtoscopy can be used, among other things, in order to expand our knowledge about hyperon-nucleon interactions. Although the currently available data does not provide enough statistics to achieve those goals, it is expected that once HADES is moved to the FAIR facility high-precision femtoscopy studies will be possible. In addition we are involved in the femtoscopy program of ALICE at LHC, which will give us the opportunity to directly compare and analyze results stemming from different collision systems.

CATS

The femtoscopic data analysis poses many difficulties. This report concentrates on one in particular, namely the theoretical modeling of $C(k)$. From eq. 1 it is evident that both the emission source and the wave-function have an influence on the profile of $C(k)$. Hence it is essential that one is capable to accurately compute $C(k)$ based on any source and potential. Solving eq. 1 analytically is feasible only for larger source-sizes and usually in the absence of Coulomb interaction (e.g. the Lednicky model [2]). Thus it is better to use numerical methods. However the currently openly available tools are either not very flexible and easy to integrate into any analysis framework or evaluate the wave-function by using certain approximations which may lead to inaccuracies when working with smaller sources.

The considerations above motivated the development of the "Correlation Analysis Tool using the Schrödinger equation" (CATS), which relies entirely on numerical methods to evaluate the correlation function. CATS is developed as a stand-alone C++ class and is designed to handle any short-range potential with or without the inclusion of the Coulomb interaction and/or quantum statistics. The wave function is computed by solving the Schrödinger equation fully numerically and thus obtaining an accurate solution event at small radii. The numerical solver has an adaptive grid which optimizes the performance. In addition CATS is capable of working with either an analytical or a data-defined source. This allows to extract the emission source from transport models. CATS is currently in test phase but will be made available to the general public in the future. So far we have confirmed that CATS is in agreement with other theoretical calculations that are optimized to work with larger sources but starts to deviate, as expected, in the case of smaller sources (fig. 1).

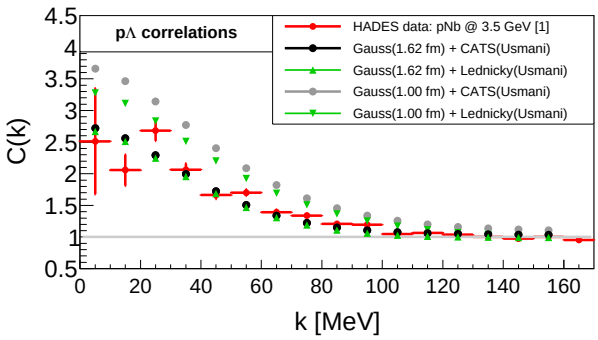

Figure 1: Comparison of the $C(k)$ predictions using different tools. The interaction is modeled by the Usmani potential. The source is assumed to have a Gaussian shape.

Summary

We have used our experience in investigating particle interactions using femtoscopy to develop a numerical tool called CATS, which allows for a fast and accurate computation of the theoretical correlation function for any source and potential. In addition this tool is very flexible which will make it a valuable asset for future femtoscopy studies.

References

[1] J. Adamczewski-Musch et al. (HADES Collaboration), Phys. Rev. C 94, 025201 (2016)

[2] R. Lednicky and V. L. Lyuboshits, Sov. J. Nucl. Phys. 35, 770 (1982)

* Work supported by SFB1258

DOI:10.15120/GR-2017-1

Report from the ALICE group at GSI

R. Averbeck, S. Masciocchi[*]*, and the GSI ALICE group*
GSI, Darmstadt, Germany

ALICE is currently engaged in the Run-2 period of the LHC operation at CERN, which started in 2015. Collisions of lead nuclei (Pb) at the highest energy ever reached in the laboratory (at the center-of-mass energy per nucleon pair of 5.02 TeV) were recorded in 2015, and a second Pb–Pb run will take place in 2018. During the heavy-ion period in Autumn 2016 proton–lead collisions were investigated which do not only provide a reference for the Pb–Pb system but are also interesting in their own right. Data were recorded at two collision energies: a first period was devoted to $\sqrt{s_{\rm NN}} = 5.02$ TeV to match the energy of the Pb–Pb run and to increase the statistics of the p–Pb data sample recorded in 2013 with a new minimum bias data sample. Collisions at the highest reachable energy of 8 TeV were recorded in a second period at high interaction rate, with triggers from the muon system, the calorimeters and the transition radiation detector (TRD). The remaining running time was dedicated to proton–proton collisions at 13 TeV.

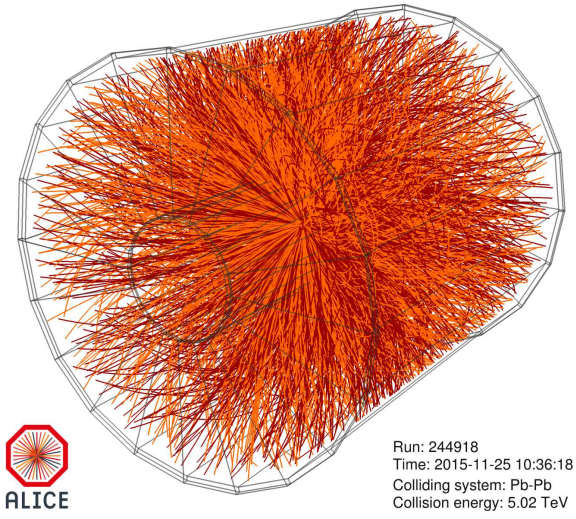

Figure 1: Event display of one of the first lead-lead collisions at the Large Hadron Collider at the top energy of 5.02 TeV per nucleon pair in the center of mass, recorded by the ALICE detector in November 2015.

The GSI ALICE group is deeply involved in Run-2, starting from the responsibility to continuously operate the Time-Projection-Chamber (TPC) and the participation in the obligatory shifts to run the experiment at CERN, up to the analysis of the recorded data and the publication of the results.

[*] s.masciocchi@gsi.de

Since 2015, large field distortions due to space charge effects were observed in the TPC, operated then with an Ar:CO_2 gas mixture. These distortions cause a significant displacement of the electron clusters produced by traversing particles and recorded with the readout chambers. As a consequence, the track reconstruction performance was seriously affected. Detailed investigations and extensive systematic studies (both from the software and the hardware sides) were conducted by the TPC experts to characterize the features of the distortions and to look for possible reasons for the unexpected size of the phenomenon. A full explanation is not yet available, however a strong correlation with the use of the Ar:CO_2 gas is now suspected. In early 2017, the gas in the TPC was changed back to the original Ne:CO_2:N_2 mixture, and the strong distortions in first approximation are no longer present since then. To mitigate the impact of the distortions on the 2015-16 data, a complex calibration procedure has been developed (with leading contributions from the GSI ALICE group), which is based on the computation of time-dependent corrections of the distortions in the TPC, exploiting also the tracking information from the TRD. This development anticipates to some extent the data calibration procedure for data read out in continuous mode from the upgraded TPC in 2021, where Pb nuclei will collide at a rate of 50 kHz, corresponding to an average of five pile-up events in the TPC at any moment. The correction framework allowed a successful re-processing of all high interaction proton–proton, proton–lead and lead–lead data recorded in 2015 and 2016.

In 2017, a high-statistics data sample of proton–proton collisions will be recorded at $\sqrt{s} = 13$ TeV in order to be able to measure reference spectra up to high transverse momenta. The Collaboration will further exploit a high-multiplicity trigger to study features of events with a very high multiplicity of produced particles which, surprisingly, were observed to resemble some aspects typical for heavy-ion collisions.

The GSI ALICE group is engaged in the analysis of data from all collisions systems and, recently, made public several results of high scientific impact. All relevant results are discussed individually in contributions to this GSI Annual Report. Here, a short overview is given.

The production of J/ψ mesons is measured in proton–proton collisions as a function of the charged-particle multiplicity, showing an increase of the J/ψ abundance which is faster than that of the charged-particle multiplicity. In comparison with models, the data support a scenario in which multi-parton interactions play a significant role. J/ψ production in Pb-Pb collisions at 5.02 TeV con-

DOI:10.15120/GR-2017-1

firms the enhanced yields at low transverse momenta in comparison to the expected rates, even considering the energy loss of charm quarks in the quark-gluon plasma. This confirms that J/ψ mesons are produced via statistical (re)combination of charm quarks at the LHC. This novel behaviour is further proven by the observation of non-zero elliptic flow of J/ψ mesons, measured by ALICE at forward rapidity, in the di-muon decay channel. Two charmonium measurements earned contributed talks at the Quark Matter 2017 conference by the leading analyzers, both doctoral students in the ALICE group at GSI.

Fundamental improvements in methodology are being implemented in the analysis of other observables, preparing the path to further publications in the near future, coordinated by scientists from the GSI ALICE group. The measurement of the nuclear modification factor R_{AA} of electrons from open heavy-flavor hadron decays at low transverse momentum allows to probe with unprecedented precision the role of shadowing in Pb–Pb collisions at the LHC and, possibly, will give hints about the hadronization mechanism for charm (via coalescence or via fragmentation in vacuum). A new analysis method was developed to improve the precision of the lifetime measurement of (anti-)hyper-triton. In the future, the GSI ALICE group will strengthen the analysis efforts related to (anti-)(hyper-) nuclei studies in ALICE, exploiting the excellent particle identification capabilities of the apparatus.

Until June 2017, ALICE has published 178 peer reviewed scientific papers, with an average of 85 citations each, including a report from 2017 on the observation of an 'enhanced production of strange particles in high-multiplicity proton–proton collisions'. This phenomenon, which was one of the first proposed signatures of quark-gluon plasma formation, was observed for the first time unambiguously in collisions of protons in which a large number of charged particles was produced. This result is likely to challenge existing theoretical models that do not predict such an increase of strange particles yields in these events [ALICE collaboration, Nature Physics 2017, doi:10.1038/nphys4111].

The GSI ALICE group is centrally involved in the preparation of the experiment upgrades, to be completed until the end of 2020. These upgrades will allow ALICE to fully exploit the improved performance of the LHC in Run-3, when Pb nuclei will collide with a rate of 50 kHz.

The construction of new readout chambers for the ALICE TPC, equipped with Gas Electron Multiplier (GEM) foils (see Fig. 2), is moving from the prototype stage to the final production chambers. The preparations for the building and testing of the Outer Read-Out Chambers (OROC) are completed. Two full-size chambers were completed in November 2016 and extensively tested in the laboratory with an ^{55}Fe source and x-ray tubes. For the x-ray measurements, a dedicated testing facility was set up, which will be used further by colleagues from the PANDA experiment (see Fig. 3).

The test results obtained from the GSI OROC chambers, together with those from the Inner Read-Out Chamber built at Yale University (USA), allowed the TPC upgrade team to successfully pass the Production Readiness Review, a crucial milestone required by CERN in the course of the development of a new detector, in March 2017. This achievement allows the mass production of the final chambers to start. Further tests of the chambers with a test beam and in the ALICE hall at Point-2 of the LHC are planned for May and July 2017, respectively.

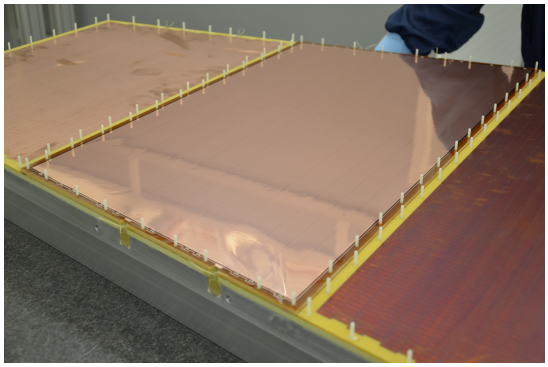

Figure 2: Inner structure of an OROC chamber during its assembly, showing the subdivision of the chamber into three regions which will house three stacks of GEMs. Two stacks on the left are already mounted, while in the third region (on the right) the chamber backplane with the readout pads is visible.

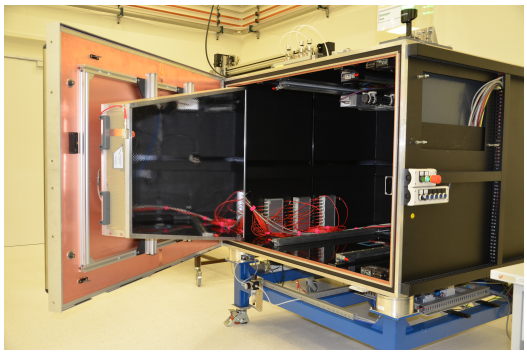

Figure 3: OROC chamber mounted on the door of the so-called Panda box. Inside the box, two high-rate x-ray tubes are mounted for testing chambers under high radiation rates. This testing facility has been prepared to be also used for the test of the PANDA GEM forward tracker.

DOI:10.15120/GR-2017-1

ALICE measurement of the J/ψ nuclear modification factor at mid-rapidity in Pb-Pb collisions at $\sqrt{s_{\rm NN}} = 5.02$ TeV*

A. Andronic[1], *I. Arsene*[2], *R.T. Jimenez Bustamante*[1,3], *S. Masciocchi*[1], *S. Weber*[1,4], *D. Weisser*[3] *for the ALICE Collaboration*

[1]GSI; [2]Oslo University; [3]Heidelberg University; [4]Darmstadt University

Introduction

The suppression of charmonium production induced by color screening of quarks was proposed more than 30 years ago as a probe of the formation of the Quark-Gluon Plasma (QGP) [1]. At LHC energies, the number of produced c$\bar{\rm c}$ pairs per events is one order of magnitude larger than at RHIC, therefore new mechanisms like (re)generation, start playing a role in charmonium production. A charmonium enhancement was predicted for the most central A-A collisions [2, 3]. The nuclear modification factor of the J/ψ mesons ($R_{AA}^{J/\psi}$) measured by ALICE at $\sqrt{s_{\rm NN}} = 2.76$ TeV [4, 5], showed a striking enhancement compared to the one measured at lower energies [6, 7], supporting the models including (re)generation. The transport and comovers models assume the creation of charmonium states through continuous dissociation and regeneration throughout the lifetime of the medium [8, 9, 10]. On the other hand the statistical hadronization model [11] assumes creation of charmonium at the phase boundary.

With the increase of the collision energy at the LHC in Run-2, and the accompanying increase in number of initial c$\bar{\rm c}$ pairs, all models predict a further increase of the J/ψ production by (re)generation. The measurement at $\sqrt{s_{\rm NN}} = 5.02$ TeV and the comparison to lower energies provides important information for the suppression and regeneration picture.

Analysis and results

The ALICE experiment [12] allows to measure J/ψ at mid-rapidity ($|y| < 0.8$) in the decay channel $\rm e^+e^-$https://www.google.com/gmail/. Two main detectors are used for the electron reconstruction. The Inner Tracking System (ITS), consisting of six layers of silicon detectors located around the interaction point, is used for tracking, vertex determination and triggering. The Time Projection Chamber (TPC) is the main tracking detector, and is also used for particle identification via the measurement of the specific energy loss in the detector gas (dE/dx). The electrons are identified using the TPC information, and the invariant mass distribution is constructed using opposite sign pairs.

The analysis presented here is based on 75 million minimum bias events in Pb-Pb collisions at $\sqrt{s_{\rm NN}} = 5.02$ TeV. This corresponds to a similar statistics to the one collected by ALICE during the LHC Run 1 for the most central events, and more than 10 times the statistics collected for peripheral events. This sample allows to measure the J/psi production in 5 different centrality classes: 0-10%, 10-20%, 20-40%, 40-60%, and 60-90%.

The inclusive R_{AA}, containing both prompt and non-prompt contribution at $\sqrt{s_{\rm NN}} = 5.02$ TeV as a function of centrality is shown in the left panel of Fig. 1 compared to the ALICE measurement at $\sqrt{s_{\rm NN}} = 2.76$ TeV at mid-rapidity [5]. The centrality dependence, characterized by a similar suppression with centrality at the two energies, however an increase of 18% is observed in the most central collisions. Within our systematic uncertainties the results at both energies are compatible. The main systematic uncertainty is due to the reference J/ψ cross section in pp collisions and corresponds to 16%. The measurement is also compared to different models in Fig.1.

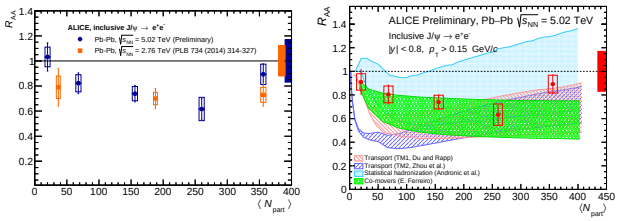

Figure 1: *Left:*R_{AA} at mid-rapidity ($|y|$ <0.8) as a function of centrality. *Right:*R_{AA} compared to different theory models.

References

[1] T.Matsui, H.Satz, Phys Lett B.178 (1986) 416.

[2] P. Braun-Munzinger, J. Stachel, Phys. Lett. B 490, (2000) 196–202 .

[3] R. L. Thews, M. Schroedter, J. Rafelski, Phys. Rev. C 63, (2001) 054905.

[4] ALICE Coll., Phys.Rev.Lett. 109 (2012) 072301.

[5] ALICE Coll., Phys. Lett. B 734 (2014) 314–327.

[6] NA 50 Coll., Eur. Phys. J. C 39, 335 (2005).

[7] PHENIX Coll.Phys. Rev. C 84, 054912 (2011).

[8] X Zhao, R. Rapp, Nucl. Phys. A 859 (2011) 114–125.

[9] K. Zhou et al, Phys. Rev. C 89 5, 459 (2014) 054.

[10] E.G. Ferreiro, Phys. Lett. B 731 (2014) 57–63.

[11] A.Andronic, P. Braun-Munzinger, J. Stachel, Phys. Lett. B 652 (2007) 259-261.

[12] Int. J. Mod. Phys. A 29 (2014) 1430044.

*Work supported by GSI, BMBF, CONACYT, H-QM ,Heidelberg University, and HGS-HIRe

Measurement of J/ψ production as a function of event multiplicity in pp collisions at $\sqrt{s} = 13\,\mathrm{TeV}$ with ALICE *

S. Weber[1,2], *A. Andronic*[1,2], *I. Arsene*[3] *for the ALICE Collaboration*

[1]GSI, Darmstadt, Germany; [2]Technische Universität Darmstadt, Germany; [3]Universitetet i Oslo, Norway

The event multiplicity dependent production of charmonium gives insight on processes on the parton level and on the interplay between the hard and soft mechanisms in particle production. ALICE has performed multiplicity dependent measurements in pp collisions at $\sqrt{s} = 7\,\mathrm{TeV}$ of inclusive J/ψ production at mid- and forward rapidity [1], reaching multiplicities of about 4 times the mean values. The results are consistent with a linear, or stronger than linear increase. Similar observations were also made for J/ψ originating from beauty-hadron decays, and for open-charm hadrons [2].

A new measurement of J/ψ production as a function of event multiplicity in pp collisions at $\sqrt{s} = 13\,\mathrm{TeV}$ was performed with the ALICE detector [7]. J/ψ particles were reconstructed at mid-rapidity ($|y| < 0.9$) in the dielectron decay channel, employing the tracking and PID capabilities of the ALICE Inner Tracking System (ITS) and the Time Projection Chamber (TPC).

In order to have access to high multiplicities the data taking was performed using a trigger on high event multiplicities, based on a large deposited charge in the ALICE V0 scintillator arrays sub-detector, which consists of two scintillator arrays at forward ($2.8 < \eta < 5.1$) and backward ($-3.7 < \eta < -1.7$) rapidity. The charged-particle multiplicity was measured at mid-rapidity ($|\eta| < 1.0$), applying corrections for detector inefficiencies, depending on the offset of the primary interaction vertex in beam direction. Multiplicities of about 7 times the mean value in minimum bias collisions. The signal was extracted in 8 bins of the charged-particle multiplicity from the invariant mass distribution by bin counting in the J/ψ signal region after subtracting the combinatorial background, estimated with the event-mixing technique.

Figure 1 shows the normalized inclusive J/ψ yield (i.e. the yield per event divided by the mean yield per event in minimum bias collisions) as a function of the normalized charged-particle multiplicity. A smooth monotonic increase in the J/ψ yield is observed, which at high multiplicities is clearly stronger than linear. The data are compared to theoretical model predictions. In the PYTHIA8 event generator [3] multiple parton interactions are a key meachanism for particle production. For open-charm hadrons at $\sqrt{s} = 7\,\mathrm{TeV}$, this mechanism was shown to explain the data [2], the current J/ψ data is slightly underestimated from this model.

The EPOS 3 event generator [4] assumes parton ladders as sources of particle production, each composed of a pQCD hard process with initial and final state radiation. This model provides a very good description of the presented measurement.

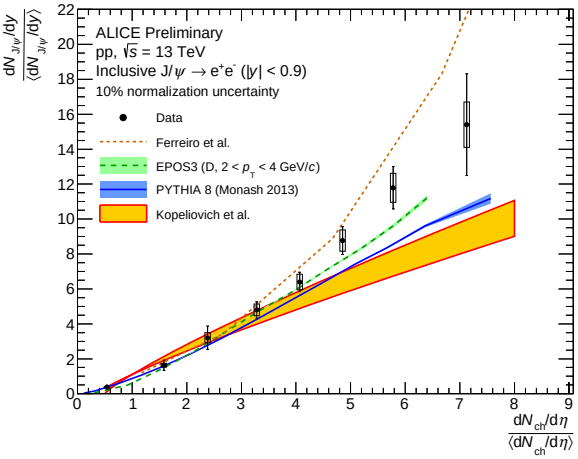

Figure 1: Multiplicity dependence of inclusive J/ψ production at mid-rapidity at $\sqrt{s} = 13\,\mathrm{TeV}$ and comparison to theoretical model predictions.

In the percolation model [5], the screening of color strings leads to a stronger than linear increase at high multiplicities. At very high multiplicities it seems to slightly overestimated the observed increase.

A model by Kopeliovich et al. [6] assumes that high multiplicities are the results of contributions from higher Fock states in the incoming protons, leading to an increase of J/ψ production with the event multiplicity, with a flattening expected at high multiplicities. The current data are underestimated by this model.

References

[1] B. Abelev, et al., Phys. Lett. B712 (2012) 165–175.

[2] J. Adam, et al., JHEP 09 (2015) 148.

[3] T. Sjostrand, S. Mrenna, P. Z. Skands, Comput. Phys. Commun. 178 (2008) 852–867.

[4] K. Werner, B. Guiot, I. Karpenko, T. Pierog, Phys. Rev. C89 (6) (2014) 064903.

[5] E. G. Ferreiro, C. Pajares, Phys. Rev. C86 (2012) 034903.

[6] B. Z. Kopeliovich, H. J. Pirner, I. K. Potashnikova, K. Reygers, I. Schmidt, Phys. Rev. D88 (11) (2013) 116002.

[7] K. Aamodt, et al., JINST 3 (2008) S08002.

*Work supported by GSI, BMBF, Helmholtz Alliance HA216/EMMI, H-QM, and HGS-HIRe

DOI:10.15120/GR-2017-1

J/ψ measurements in pp collisions at $\sqrt{s}$ = 13 TeV using EMCal-triggered events with ALICE at LHC*

C. Jahnke† [1,2], *T. Dahms*[1,2], *and the ALICE Collaboration*

[1]Excellence Cluster Universe, Technische Universität München, Garching, Germany; [2]Physik Department, Technische Universität München, Garching, Germany

Introduction

Measurements of J/ψ production in proton-proton (pp) collisions provide important information on perturbative and non-perturbative quantum chromodynamics. The production of the heavy-quark pairs can be described perturbatively while their hadronisation into quarkonium state is a non-perturbative process [1, 2]. These processes are not fully understood yet and additional experimental data are necessary to further constrain the theoretical model calculations. Additionally, pp measurements provide a baseline for proton-nucleus and nucleus-nucleus collisions allowing studies of the quark-gluon plasma properties.

In this work we study the J/ψ production in pp collisions at a centre-of-mass energy of $\sqrt{s}$ = 13 TeV at mid-rapidity with ALICE [3].

Analysis strategy

The data set used in this analysis were recorded using the Electromagnetic Calorimeter (EMCal) trigger [4], which is used to measure high-p_{T} electrons and photons. The availability of a high-p_{T} electron trigger enhances significantly the sampled luminosity relative to the available sample of minimum bias (MB) triggered data, extending the reached p_{T} for the J/ψ measurement. Fig. 1 shows the cluster energy distribution for two different trigger thresholds (at 5 GeV (EGA2) and at 7 GeV (EGA1)) compared to a MB triggered data.

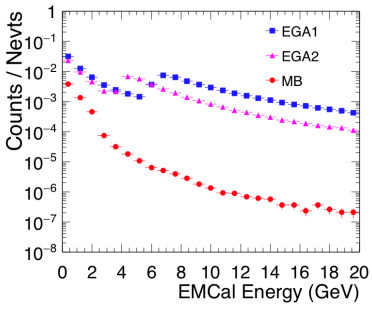

Figure 1: Cluster energy distribution for EMCal-triggered data (EGA1 at 7 GeV and EGA2 at 5 GeV) and for MB-triggered data.

The J/ψ are reconstructed via their dielectron decay channel in events where at least one of the decay electrons triggered the EMCal. The electrons/positrons are identified using the Time Projection Chamber (TPC) [3] and we require at least one of the legs of J/ψ in the EMCal, with a cluster energy above the trigger threshold and a ratio of energy over momentum (E/p) around unity. The J/ψ measurement is performed in the transverse momentum interval $5 < p_{\mathrm{T}} < 20$ GeV/c. In Fig. 2, the invariant mass spectrum is shown for two different trigger threshold: $E > 5$ GeV (left) and $E > 7$ GeV (right). For both thresholds a clear peak is observed around the expected mass for J/ψ.

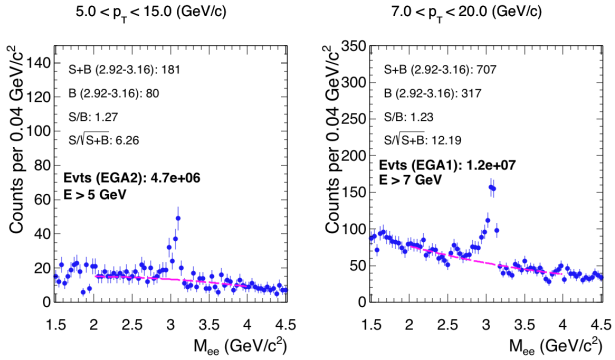

Figure 2: Invariant mass spectrum for trigger data with threshold at 5 GeV (left) and 7 GeV (right).

The J/ψ yield is obtained after subtracting the combinatorial background, which is described by a second-order polynomial.

We are currently working on the efficiency corrections and the evaluation of the systematic uncertainties of the results. Our goal is the measurement of the inclusive J/ψ cross-section as well as the separation of prompt and non-prompt J/ψ. Using this data, it should also be possible to study the dependence of high p_{T} J/ψ production on the charged particle multiplicity, which is an interesting observable to assess possible multi partonic interactions and the interplay between the hard and soft mechanisms in charmonia production.

References

[1] H. Fritzch, Phys. Lett. **B67** (1977) 217.

[2] R. Baier and R. Ruckl Phys. Lett. **B102** (1981) 364.

[3] ALICE Collaboration, JINST **3** (2008) 08002.

[4] ALICE EMCal Group, ArXiv:1008.0413 (2010).

* Work supported by GSI, BMBF, and the DFG cluster of excellence "Origin and Structure of the Universe".

† cristiane.jahnke@cern.ch

Measurements of low-mass dielectrons in pp collisions at $\sqrt{s} = 13$ TeV with ALICE *

I. Vorobyev[†1,2], *A. Chauvin*[1,2], *T. Dahms*[1,2], *A. Dashi*[1,2], *O. Vazquez Doce*[1,2], *and the ALICE Collaboration*

[1]Excellence Cluster Universe, Technische Universität München, Garching, Germany; [2]Physik Department, Technische Universität München, Garching, Germany

The hot and dense system created in ultra-relativistic heavy ion collisions is believed to be a deconfined state of quarks and gluons. Electromagnetic probes such as electron-positron pairs are a unique tool to investigate the whole space-time evolution of such a system. In proton-proton collisions, measurements of dielectron production serve as important vacuum reference to quantify modifications observed in heavy ion collisions. Measurements of low-mass dielectrons could also shed light on the underlying physics processes in those proton-proton collisions with high charged-particle multiplicities.

The current analysis focuses on a comparison of raw dielectron mass spectra in minimum bias events and in events collected with a trigger on high charged-particle multiplicities. To this purpose, the ratio of properly normalised dielectron spectra in high multiplicity (HM) and minimum bias (MB) events is calculated:

$$\frac{\langle N_{\rm ch}({\rm MB})\rangle}{\langle N_{\rm ch}({\rm HM})\rangle} \times \frac{1/N_{\rm HM}\,{\rm d}N_{\rm ee}/{\rm d}m_{\rm ee}|_{\rm HM}}{1/N_{\rm MB}\,{\rm d}N_{\rm ee}/{\rm d}m_{\rm ee}|_{\rm MB}}, \qquad (1)$$

where $\langle N_{\rm ch}\rangle$ is the average charged particle multiplicity and $N_{\rm HM}$ ($N_{\rm MB}$) is the number of recorded high-multiplicity (minimum bias) events.

The dielectron analysis is performed in the central barrel spectrometer of ALICE [1]. Event selection for both multiplicity classes is based on the information from the V0 detectors. Charged particle tracks are reconstructed with the help of the central barrel tracking detectors ($|\eta| < 0.8$) : the Inner Tracking System and the Time Projection Chamber (TPC). Specific energy loss in the TPC and time-of-flight information from the TOF detector are used for electron identification.

Electron and positron candidates from the same event are combined to pairs forming the unlike-sign spectrum. The combinatorial background is estimated via the geometric mean of like-sign pairs within the same event. Conversions of real photons in the detector material (e.g. beam pipe and support structures) are removed from the raw signal by their orientation relative to the magnetic filed.

A cocktail of several dielectron sources is used to estimate the expected ratio (1) as a function of the invariant mass. For the light flavour part, the different hadronic sources of dielectrons via Dalitz or two-body decays are taken into account using a fast Monte-Carlo simulation. Simulations of high-multiplicity events are based on measurements of ratios of charged-particle $p_{\rm T}$ distributions as a function of multiplicity [2].

The contribution of correlated semileptonic decays of open charm and bottom mesons is estimated with PYTHIA simulation. For the multiplicity dependence, the results on D-meson production as a function of multiplicity [3] bracket the expectation for the ratio (1) between 1 and 2.5.

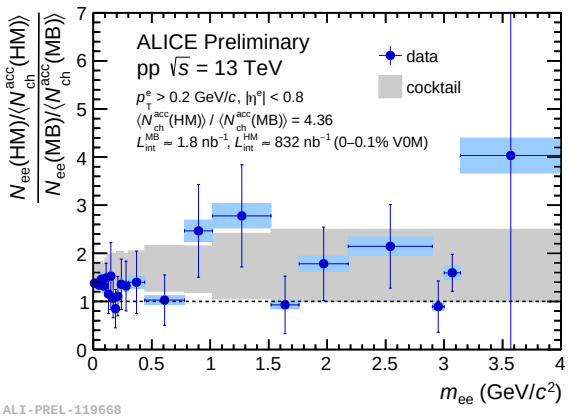

Figure 1: Ratio of dielectron spectra scaled with charged particle multiplicity.

In Fig. 1 the results for the ratio of the dielectron spectra in high multiplicity over minimum bias events scaled by multiplicity factor $\langle N_{\rm ch}\rangle|_{\rm HM}/\langle N_{\rm ch}\rangle|_{\rm MB}$ = 4.36 are shown. The data are in agreement with the expected deviation from a perfect multiplicity scaling over almost the full investigated mass range of 0–4 GeV/c^2. Beyond ≈0.2 GeV/c^2 the data are also consistent with unity, i.e. multiplicity scaling. Higher precision data are necessary to investigate possible modifications of the dielectron spectrum in more details. For this purpose, approximately 5 times more proton-proton data from 2016 will be analysed, and the reduction of systematic uncertainties as well as improvements in cocktail calculations are expected.

References

[1] ALICE Collaboration, JINST **3** (2008) 08002.

[2] ALICE Collaboration, Phys. Lett. B **753**, 319 (2016)

[3] ALICE Collaboration, JHEP **09**, 148 (2015)

* Work supported by GSI, BMBF, HGS-HIRe, Technische Universität München and the DFG cluster of excellence "Origin and Structure of the Universe".

† ivan.vorobyev@tum.de

DOI:10.15120/GR-2017-1

Hadronic cocktail of dielectron sources in pp collisions at $\sqrt{s} = 13$ TeV *

O. Vázquez Doce[†1,2], *A. Chauvin*[1,2], *T. Dahms*[1,2], *A. Dashi*[1,2], *I. Vorobyev*[1,2], *and the ALICE Collaboration*

[1]Excellence Cluster Universe, Technische Universität München, Garching, Germany; [2]Physik Department, Technische Universität München, Garching, Germany

In the study of low mass dielectrons produced in heavy ion collisions, experimental data are usually compared to a hadronic cocktail, that is the sum of all known hadron sources contributing to the dielectron spectrum.

We have obtained for the first time the dielectron mass spectrum from high multiplicity triggered pp collisions at $\sqrt{s} = 13$ TeV, The ratio between this spectrum and the one from minimum bias (MB) events, after normalization by the average charged particle multiplicity, has been compared to a hadronic cocktail expectation. The goal is to search for possible deviations in the mass spectrum when the charged particle multiplicity rises. It is expected an enhancement in the low mass region that is acceptance related, caused by modifications of the p_{T} spectra of hadrons [1]. The region dominated by heavy flavour sources should be enhanced as well, due to higher production yields of charm and bottom mesons in the high multiplicity events [3]. Any other effect like modifications in the relative contributions of different mesons, suppression of short lived vector mesons due to final state interaction with comovers or enhancement due to resonance production in π-π annihilation can be studied.

For the light flavour part of the hadronic cocktail, the different hadronic sources of dielectrons are taken into account using a fast MC simulation. Acceptance, resolution and relative efficiency effects of the ALICE spectrometer are taken into account. The cocktail inputs are based on ALICE measurements in pp collisions at $\sqrt{s} = 13$ TeV. For π^0 the used input parametrization is a Tsallis fit of the p_{T} measured spectra of charged pions by ALICE [2]. Other light hadron spectra are generated via m_{T} scaling.

For the simulation of the high multiplicity events, we apply to the minimum bias cocktail two different weights based on measurements of ratios of p_{T} distributions of charged particles as a function of multiplicity [1], in order to obtain a lower and upper limit for the high multiplicity cocktail. The lower limit is based in the p_{T} spectra of multiplicities $N_{\mathrm{ch}}^{\mathrm{acc}} \geq 2\langle N_{\mathrm{ch}}^{\mathrm{acc}}\rangle$, corresponding to an increase in the average multiplicity by a factor 3. For obtaining the weight of the upper limit case, we use the previous p_{T} spectra divided by the one from low multiplicities $1 \leq N_{\mathrm{ch}}^{\mathrm{acc}} < \langle N_{\mathrm{ch}}^{\mathrm{acc}}\rangle$, in order to account for an increase in the average multiplicity by a factor 6.

With these ingredients, the expected ratio of high multiplicity over minimum bias events from light flavour sources after acceptance cuts can be seen in Fig. 1, represented as a band between the lower and upper multiplicity increases considered for the High multiplicity (HM) cocktail. The effect of the efficiency is shown as well. Both minimum bias and high multiplicity cocktails are normalised using as normalization parameter the number of dielectrons from π^0 Dalitz decays before acceptance cuts.

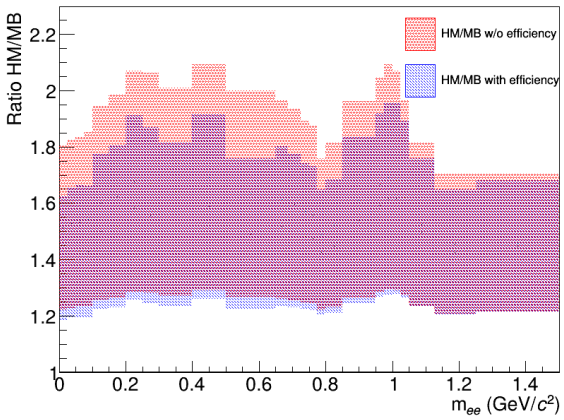

Figure 1: Ratio of the dielectron mass spectrum after acceptance cuts from HM and MB cocktail for the light flavour sources. The blue band represents the ratio HM/MB varying from the lower to the higher multiplicity increases considered for the HM cocktail. The red band represents this ratio when the efficiency weight is not applied.

For the heavy flavour part of the cocktail, we estimate the contribution of correlated semileptonic decays of open charm and bottom mesons making use of a PYTHIA simulation based on the official MC production with enhanced open heavy-flavour contributions of ALICE. We have used this simulation to check the average D meson p_{T} as a function of dielectron invariant mass, and measured values of the enhancement factor of D mesons as a function of its mean p_{T} [3] are used for simulating the high multiplicity dependence.

References

[1] J. Adam et al. (The ALICE Collaboration), Phys. Lett. B **753** (2016) 319.

[2] A. Ortiz Velasquez, ALICE Analysis Note, ALICE-ANA-3034.

[3] J. Adam et al. (The ALICE Collaboration), J. High Energ. Phys. **09** (2015) 148.

* Work supported by GSI, BMBF, HGS-HIRe, Technische Universität München and the DFG cluster of excellence "Origin and Structure of the Universe".

† oton.vazquez.doce@cern.ch

Machine learning for the analysis of low-mass dielectrons in Run II data with ALICE

A. Chauvin[*†1,2], *T. Dahms*[1,2], *A. Dashi*[1,2], *O. Vasquez Doce*[1,2], *I. Vorobyev*[1,2], *and the ALICE Collaboration*

[1]Excellence Cluster Universe, Technische Universität München, Garching, Germany; [2]Physik Department, Technische Universität München, Garching, Germany

Dielectron pairs are an experimental tool to investigate the Quark Gluon Plasma (QGP), which is expected to be created during ultra-relativistic heavy-ion collision. The measured electron-positron pairs are created at different stages of the evolution of the hot and dense medium and do not interact strongly with the latter. Hence, dielectron pairs can probe the full space-time evolution of the system, thereby allowing us to investigate the predicted restoration of chiral symmetry as well as the initial temperature of the QGP.

Machine Learning is a statistical tool that allows combining a large number of variables to perform classification and regression analysis known as Multi-Variate Analysis(MVA) [1]. Combined with complementary analyses, such as overtraining studies and reweighting, a Multi-Variate Analysis can be performed in our analysis e.g. for background rejection and electron identification.

Photon conversions contribute to the background of the dielectron signal. Besides contributing to the combinatorial background, electron pairs from photon conversions contaminate our signal in the very lowmass region ($<$100 MeV/c^2). So far a cut on φ_V (the pair orientation relative to the magnetic field direction) [2] is applied. A cut of φ_V $<$2 rad leads to a signal efficiency of 61% and a background rejection of 99%. The Multi-Variate Analysis allows us to consider a total of 16 track and pair variables which are then combined using Boosted Decision Trees. The optimal cut to apply is found when performing over-traing. This consists of looping over the hyperparameter phase-space to look for the first local maximum of the Receiver Operating Characteristic curve of the test sample as shown in Figure 1. This way, one can ensure the selected parametrisation does not depend on the training sample. Thus, for the same background rejection of 99%, a signal efficiency of 89% is achieved by a cut on the newly computed variable.

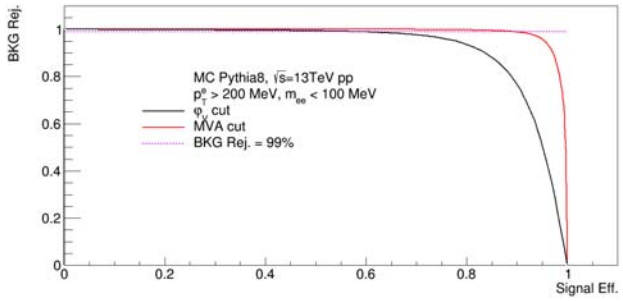

Figure 1: Receiver Operating Characteristic curve for cuts on φ_V and on the MVA output, the background rejection is plotted as a function of the signal efficiency

On top of conversion pairs, MVA can also be used to reject combinatorial background and to perform electron identification. In order to tune Monte-Carlo simulation to match data, reweighting methods [3] can be applied on different types of pairs to be classified. This way, an estimation of the different contributions from the different classes to the spectrum can be evaluated [4]. A MVA relying on Monte-Carlo simulation can be performed for electron identification. In ALICE [5] particle identification is performed using three main detectors: the Inner Tracking System, the Time Projection Chamber and the Time Of Flight detector. So far, cuts are applied separately on the signals in these different detectors. A MVA can combine these signals on top of the other track variables. To do so, Monte-Carlo simulation need to be reweighted in order to correct the different detectors responses [6]. In this case one can expect an increase of the efficiency and the purity, which would reduce the statistical and systematic errors.

References

[1] A. Hocker *et al.*, PoS ACAT (2007) 040 [physics/0703039 [PHYSICS]].

[2] T. Dahms, arXiv:0810.3040 [nucl-ex].

[3] A. Rogozhnikov, J. Phys. Conf. Ser. **762** (2016) no.1, 012036 doi:10.1088/1742-6596/762/1/012036 [arXiv:1608.05806 [physics.data-an]].

[4] S. Lehner, ALICE-ANA-3478.

[5] K. Aamodt *et al.* [ALICE Collaboration], JINST **3** (2008) S08002. doi:10.1088/1748-0221/3/08/S08002

[6] A. Capon, ALICE-ANA-3486.

*Work supported by the DFG cluster of excellence "Origin and Structure of the Universe"

† alex.chauvin@cern.ch

DOI:10.15120/GR-2017-1

Measurement of low-p_{T} electrons from heavy-flavour hadron decays at mid-rapidity in Pb–Pb collisions at $\sqrt{s_{\mathrm{NN}}}$ = 2.76 TeV with ALICE *

S. Hornung †[1,2], *R. Averbeck*[1], *A. Dubla*[1,2], *S. Masciocchi*[1], *and the ALICE collaboration*

[1]GSI, Darmstadt, Germany; [2]Heidelberg University, Germany

Transverse momentum (p_{T}) spectra and the nuclear modification factor (R_{AA}) of electrons from heavy-flavour hadron decays are measured in the most central (0–10%) and in semi-central (20–40%) Pb–Pb collisions at $\sqrt{s_{\mathrm{NN}}}$ = 2.76 TeV. The modification of the p_{T} spectra is studied at mid-rapidity ($|y| < 0.8$) in the p_{T} interval 0.5–3 GeV/c. The R_{AA} is calculated using a new proton-proton (pp) reference cross section.

In ultra-relativistic Pb–Pb collisions at the Large Hadron Collider (LHC) strongly-interacting matter, characterised by high energy density and temperature, is produced. Under these conditions, the formation of a deconfined state of quarks and gluons, the Quark-Gluon Plasma (QGP), is predicted by Quantum ChromoDynamic (QCD) calculations on the lattice. Heavy quarks, i.e. charm and beauty, are produced on a timescale which is smaller than the QGP thermalization time. Heavy quarks interact with the QGP and suffer energy loss while propagating through it.

The modification of the p_{T}-spectra in Pb–Pb collisions with respect to those in pp collisions at the same energy is quantified by the nuclear modification factor R_{AA}:

$$R_{\mathrm{AA}} = (\mathrm{d}N_{\mathrm{AA}}/\mathrm{d}p_{\mathrm{T}})/(\mathrm{d}\sigma_{\mathrm{pp}}/\mathrm{d}p_{\mathrm{T}}) \cdot (1/\langle T_{\mathrm{AA}}\rangle), \quad (1)$$

where $\mathrm{d}N_{\mathrm{AA}}/\mathrm{d}p_{\mathrm{T}}$ is the measured yield in Pb–Pb collisions and $\mathrm{d}\sigma_{\mathrm{pp}}/\mathrm{d}p_{\mathrm{T}}$ is the corresponding cross section in pp collisions. The average nuclear overlap function, $\langle T_{\mathrm{AA}}\rangle$, is estimated via Glauber model calculations and is proportional to the average number of binary nucleon–nucleon collisions in a given Pb–Pb centrality class.

Low-p_{T} heavy-flavour measurements are crucial to test the binary scaling of heavy-quark yields in heavy-ion collisions. In addition, they allow to extract information about potential initial state effects, such as the modification of the parton distribution functions in nuclei with respect to nucleons. They also give information about different hadronisation mechanisms, namely fragmentation in the vacuum and coalescence in the medium. At high p_{T}, heavy quark are sensitive to the medium density, through the mechanism of parton energy loss.

For this analysis, a data sample recorded with ALICE at $\sqrt{s_{\mathrm{NN}}}$ = 2.76 TeV is used. Fig. 1 shows the R_{AA} of electrons from heavy-flavour hadron decays at mid-rapidity ($|y| < 0.8$) as a function of p_{T} in the 10% most central Pb–Pb collisions at $\sqrt{s_{\mathrm{NN}}}$ = 2.76 TeV. The new low-p_{T} measurement (open markers) is shown together with the high p_{T} results obtained using the TPC+EMCal detectors of ALICE to identify the electrons (closed marker) [1]. The statistical and systematic uncertainties are shown as error bars and boxes, respectively. The normalisation uncertainties of the low (high) p_{T} measurements are indicated by empty (filled) box at R_{AA} = 1.

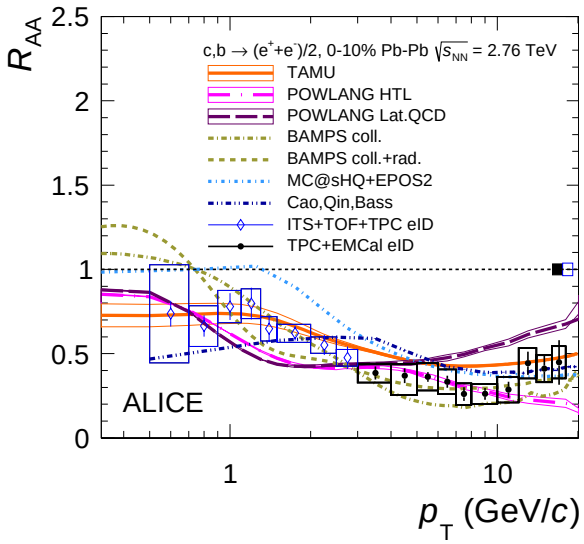

Figure 1: Heavy-flavour decay electron R_{AA} at mid-rapidity as a function of p_{T} in the 10% most central Pb–Pb collisions at $\sqrt{s_{\mathrm{NN}}}$ = 2.76 TeV compared to model calculations [1].

At hight p_{T}, R_{AA} is less than one, showing a suppression of the yield of electrons from heavy-flavour hadron decays in Pb–Pb collisions due to the energy loss of heavy quarks in the QCD medium. For $p_{\mathrm{T}} < 1.5$ GeV/c, R_{AA} is compatible with unity within systematic uncertainties, consistent with binary collision scaling. Models which include shadowing, such as TAMU and POWLANG, predict an R_{AA} smaller than one even at low p_{T}, and are in better agreement with the data compared to other models not including shadowing.

References

[1] ALICE Collaboration, J. Adam et al., arXiv:1609.07104 [nucl-ex].

* Work supported by GSI, Heidelberg University, BMBF and HGS-HIRe

† S.Hornung@gsi.de

The nuclear modification of charged particles in Pb-Pb at $\sqrt{s_{NN}}$ = 5.02 TeV measured with ALICE *

J. Gronefeld[1], *A. Andronic*[1], *P. Huhn*[4], *M.L. Knichel*[2], *J. Otwinowski*[3], *E. Pérez-Lezama*[1,4], *F. Sozzi*[1,2], *A. Toia*[1,4] *for the ALICE Collaboration*

[1]GSI Darmstadt; [2]Universität Heidelberg; [3]The Henryk Niewodniczanski Institute of Nuclear Physics, Polish Academy of Sciences, Cracow, Poland ; [4]Universität Frankfurt

Introduction

Transverse momentum spectra measurements at RHIC at $\sqrt{s_{NN}} = 200$ GeV [1, 2] have shown that charged-particle yields in heavy-ion collisions are suppressed compared to a superposition of independent nucleon-nucleon collisions (binary collision scaling). This observation is related to parton energy loss in the hot and dense QCD matter created in the collision of heavy ions, leading to a modification of transverse-momentum (p_T) distributions of the resulting particles, as initially suggested by Bjorken in 1982 [3].
Results from ALICE [4] show that hadron yields at high p_T in central Pb–Pb collisions at $\sqrt{s_{NN}} = 2.76$ TeV are suppressed even stronger than at RHIC, indicating a hotter and denser medium. This suppression is present up to very high p_T and can also be seen in jets [5].
The suppression is quantified in terms of the nuclear modification factor:

$$R_{AA}(p_T) = \frac{1}{\langle T_{AA} \rangle} \frac{dN_{AA}/dp_T}{d\sigma_{pp}/dp_T}.$$

Here, dN_{AA}/dp_T represents the p_T-differential charged-particle yield in nucleus-nucleus (AA) collisions, while $d\sigma_{pp}/dp_T$ stands for the p_T-differential cross section in proton-proton (pp) collisions. The average nuclear overlap function $\langle T_{AA} \rangle$ is determined by Glauber Monte-Carlo calculations for each class of centrality. It relates to the number of binary collisions $\langle N_{coll} \rangle$ ($\langle T_{AA} \rangle = \langle N_{coll} \rangle / \sigma_{inel}^{NN}$) and is strongly dependent on the collision centrality. In absence of medium effects, the nuclear modification factor will be equal to unity, while $R_{AA} < 1$ indicates a suppression of charged-particle yields compared to binary collision scaling.

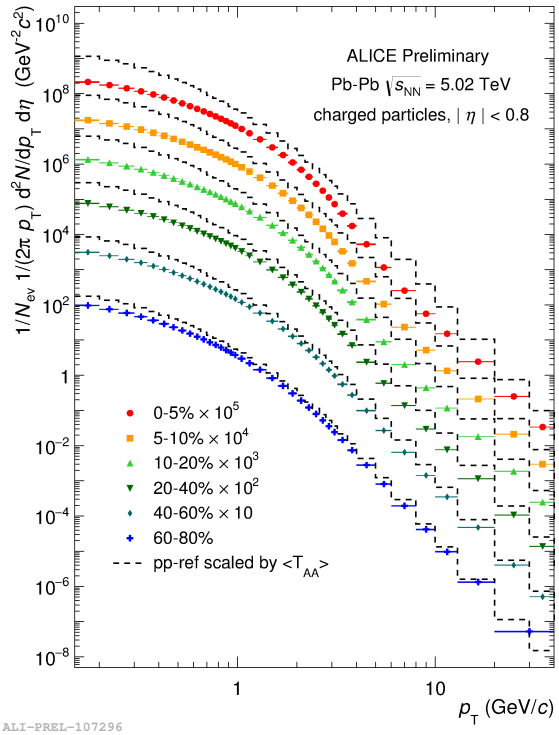

Figure 1: Transverse- momentum distribution of charged particles measured in Pb–Pb collisions for different classes of centrality. The dotted curves represent the measured p_T distribution in pp collisions scaled by the nuclear overlap functions (T_{AA}).

Analysis

Primary charged particles are defined as all prompt charged particles produced in the collision including all decay products, except for products from weak decays of strange hadrons such as K_S^0 and Λ.
To obtain the charged-particle yield as a function of p_T, corrections are made for tracking efficiency and acceptance ($\sim 70\%$), for contamination by secondary particles from weak decays or secondary interactions ($\sim 10\%$, important at low p_T) and for p_T resolution ($\sim 2\%$, important at $p_T > 20$ GeV/c). To account for differences in the particle composition of event generators and the data, the charged-particle reconstruction efficiency was calculated from the particle-dependent efficiencies weighted by the relative abundances of each particle measured in pp at 7 TeV and Pb–Pb at 2.76 TeV . The correction for contamination with secondary particles is taken from Monte-Carlo simulations. The abundances of secondary particles in data and MC is estimated by analyzing the distance of closest approach of tracks to the event vertex (DCA). It is found that the contamination correction from Monte Carlo has to be scaled up by about 30% to match the data.

The total relative systematic uncertainties are in the range range 3.3-7% for pp and 2-6% for central Pb–Pb col-

* Work supported by GSI, BMBF, EMMI, H-QM, and HGS-HIRe

DOI:10.15120/GR-2017-1

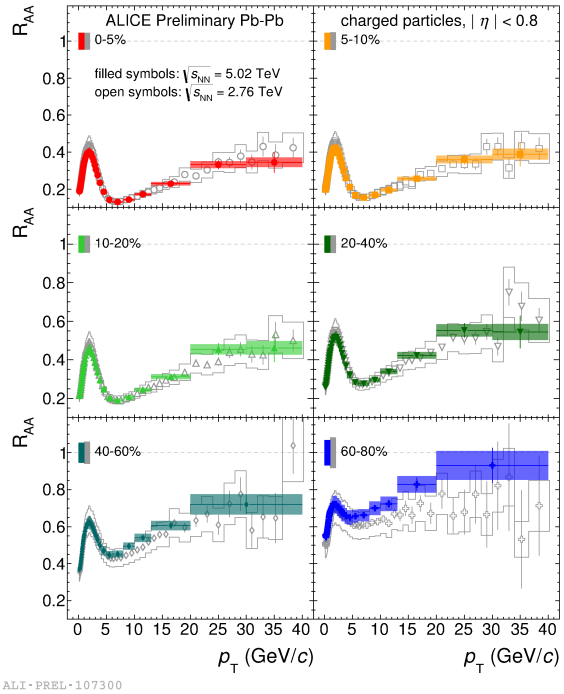

Figure 2: The nuclear modification factor R_{AA} as a function of transverse momentum, p_T, for different centrality classes in Pb–Pb collisions. The filled symbols represent the measurement at $\sqrt{s_{NN}} = 5.02$ TeV while the open symbols stand for the measurement at $\sqrt{s_{NN}} = 2.76$ TeV [4]. The normalisation uncertainty is shown for both energies as a box around unity.

lisions (0-5%) and 4-5.5% in peripheral Pb–Pb collisions (60-80%). Overall, the systematic uncertainties in the current analysis were reduced by about 50% compared to previous analyses, owing to an improved reconstruction and calibration procedure in Run2, as well as to improved track selection methods.

Results

The transverse momentum distribution of charged particles from Pb–Pb collisions is shown in Fig. 1 for six classes of centrality. The spectra are compared with the pp measurement scaled by the nuclear overlap function. Comparing the spectra one observes that the p_T distribution in peripheral collisions is similar to the scaled spectrum in pp collisions while the difference increases towards more central collisions.

The nuclear modification factors as a function of p_T for six centrality intervals are shown in Fig. 2. The filled symbols represent the measurement at $\sqrt{s_{NN}} = 5.02$ TeV, while the open symbols represent the published measurement at $\sqrt{s_{NN}} = 2.76$ TeV [4]. Both measurements exhibit similar features, showing only moderate suppression ($R_{AA} \sim 0.6 - 0.7$) for peripheral collisions (60-80%). In more central collisions, a pronounced minimum at about $p_T \sim 6 - 7$ GeV/c develops, while for $p_T > 7$ GeV/c there is a significant rise of the nuclear modification factor. Within their systematic and statistical uncertainties the measurements at 2.76 TeV and 5.02 TeV agree. Having in mind that the spectra tend to harden for higher center-of-mass energies, this agreement could hint at a stronger energy loss in a hotter and denser medium.

Summary

The strong suppression of charged-particle yields observed in Pb–Pb collisions at $\sqrt{s_{NN}} = 5.02$ TeV exhibits the same characteristics as at $\sqrt{s_{NN}} = 2.76$ TeV. A strong suppression is observed in central collisions, with the maximum suppression around $6 - 7$ GeV/c becoming smaller towards higher p_T. Compared to the previous measurement it was possible to significantly reduce the systematic uncertainties. ALICE is currently analyzing the full 5.02 TeV dataset. In addition, the improved analysis method is being extended to the $\sqrt{s_{NN}} = 2.76$ TeV dataset, in order to further improve the precision in the comparison of the results at the two collision energies.

References

[1] PHENIX Collaboration, *Suppression of hadrons with large transverse momentum in central Au+Au collisions at* $\sqrt{s_{NN}} = 130$ *GeV*, *Phys. Rev. Lett.* **88** (2002) 022301, *arXiv:* 0109003.

[2] STAR Collaboration, *Centrality dependence of high /pt hadron suppression in Au+Au collisions at* $\sqrt{s_{NN}} = 130$ *GeV*, *Phys. Rev. Lett.* **89** (2002) 202301, *arXiv:* 0206011.

[3] J. Bjorken, *Energy loss of energetic partons in quark - gluon plasma: Possible extinction of high* p_T*jets in hadron–hadron collisions*, Preprint **FERMILAB-PUB-82-059-THY** (1982) .

[4] ALICE Collaboration, *Centrality dependence of charged particle production at large transverse momentum in Pb-Pb collisions at* $\sqrt{s_{NN}} = 2.76$ TeV, *Phys.Lett.* **B720** (2013) 52-62, *arXiv:* 1208.2711.

[5] ALICE Collaboration, *Measurement of jet suppression in central Pb-Pb collisions at* $\sqrt{s_{NN}} = 2.76$ *TeV*, Phys. Lett. B **746** (2015) 1,*arXiv:* 1502.01689.

[6] P. Skands, S. Carrazza and J. Rojo,*Tuning PYTHIA 8.1: the Monash 2013 Tune*, Eur. Phys. J. C **74** (2014) no.8, 3024, *arXiv*:1404.5630.

[7] T. Pierog, I. Karpenko, J. M. Katzy, E. Yatsenko and K. Werner, *EPOS LHC: Test of collective hadronization with data measured at the CERN Large Hadron Collider*,Phys. Rev. C **92** (2015) no.3, 034906, *arXiv:*1306.0121.

Hypertriton measurements with ALICE at the LHC

L. Kreis[1,2], *A. Andronic*[1], *B. Dönigus*[3] *for the ALICE Collaboration*

[1]GSI Helmholtzzentrum für Schwerionenforschung, Darmstadt, Germany; [2]Institut für Kernphysik, Technische Universität Darmstadt, Darmstadt, Germany; [3]Institut für Kernphysik, Goethe-Universität Frankfurt, Frankfurt, Germany

Hypernuclei are unstable bound systems of hyperons and nucleons. The hypertriton consists of a proton, a neutron and a Λ baryon. It is the lightest known hypernucleus with a mass of $m = 2.992\,\mathrm{GeV}$.

The lifetime is expected by theory to be close to the lifetime of the free Λ baryon [1]. Recent measurements in heavy-ion collision experiments give a hint of a shorter lifetime. However clarification of this effect needs new measurements with higher precision.

Antihypertriton and hypertriton are rarely-produced particles. Benefiting from the large particle multiplicities in Pb–Pb collisions at the LHC (anti-)hypertriton can be reconstructed in the two particle decay channel using the excellent particle identification capabilities.

$$^{3}_{\Lambda}\mathrm{H} \rightarrow {}^{3}\mathrm{He} + \pi^{-}$$
$$^{3}_{\Lambda}\overline{\mathrm{H}} \rightarrow {}^{3}\overline{\mathrm{He}} + \pi^{+}$$

The hypertriton candidates are reconstructed from their decay products, which are identified by their specific energy-loss in the Time Projection Chamber. Figure 1 shows the invariant mass distribution of the hypertriton candidates in the rapidity interval $|\eta| < 0.9$. It was reconstructed in 43×10^6 Pb–Pb collisions at a center-of-mass energy per nucleon-nucleon pair of $\sqrt{s_{\mathrm{NN}}} = 5.02\,\mathrm{TeV}$ for the $0-80\%$ most central collisions. This is the first measurement of hypertriton in data from LHC Run 2, recorded in 2015. The maximum likelihood fit consists of a Gaussian signal and a polynomial background. An uncorrected (anti-)hypertriton signal of 132 ± 23 counts with a significance of 7.1σ is observed.

Results on the hypertriton in Pb-Pb collisions at $\sqrt{s_{\mathrm{NN}}} = 2.76\,\mathrm{TeV}$ have been published by the ALICE Collaboration in 2016 [2]. A binned method was used for the lifetime extraction. The present feasibility study represents an ongoing effort to improve the precision by using an improved lifetime extraction method based on an unbinned maximum likelihood estimation procedure.

The decay vertex can be reconstructed with the Inner Tracking System. Its six layers of silicon detectors allow to precisely determine the primary vertex of the collision and the position of the displaced vertices.

The invariant mass fit is used to determine the signal- and sideband-ranges. The lifetime τ is calculated from the distance L between the displaced decay vertex and the primary vertex of the collision. It can be extracted with the exponential decay $N(t) \approx \exp(t/\tau)$. The proper decay length can be expressed as $ct = L \cdot cm/p$, where m is the mass and p is the momentum. It can be inserted into the exponential decay

$$N(ct) = \exp\left(-L\frac{m}{\tau \cdot p}\right).$$

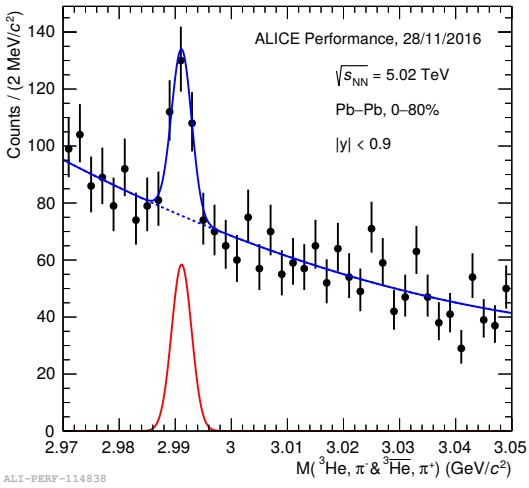

Figure 1: Fit to the invariant mass of hypertriton candidates. The continuous line shows the total fit to the data, the dashed line shows the background fit

The number of counts for the signal and the background in the signal region is determined in the fit to the invariant mass. The shape of the background is evaluated in the sidebands by a fit of the sum of two exponential decay functions. The maximum likelihood fit is performed simultaneously in the signal and sideband regions for the signal and background, and background-only fit functions, respectively. The reconstruction efficiency of hypertriton depends on the decay vertex position. A ct-dependent correction is introduced to correct for this effect. The signal fit function is weighted with this correction, which is calculated in a dedicated Monte-Carlo simulation. This newly-developed method will allow improved measurements of the hypertriton lifetime by the ALICE Collaboration. This may allow to resolve the current ambiguity of the hypertriton lifetime.

References

[1] H. Kamada et. al., "π mesonic decay of hypertriton", Phys. Rev C 57, 1998

[2] ALICE Collaboration, "$^{3}_{\Lambda}\mathrm{H}$ and $^{3}_{\Lambda}\overline{\mathrm{H}}$ production in Pb-Pb collisions at $\sqrt{s_{\mathrm{NN}}} = 2.76$ TeV", Phys. Lett. B 754, 2016

DOI:10.15120/GR-2017-1

Study of the strong interaction with baryon femtoscopy in pp collisions at 7 TeV with ALICE*

O. Arnold[1,2], *L. Fabbietti*[1,2], *and the ALICE collaboration*

[1]Physik Department E62, Technische Universität München, James-Franck-Str. 1, D-85748 Garching, Germany;
[2]Excellence Cluster Universe, Technische Universität München, Boltzmannstr. 2, D-85748, Garching, Germany

Motivation

The understanding of the hyperon-nucleon interaction is an important ingredient for the description of various physical systems. On the one hand side, it helps to better understand the mechanism of the binding of Λ hyperons inside of nuclei. On the other side, the information about the strength of the interaction is of importance to describe heavy astronomical objects like neutron stars. It is expected that in the interior of heavy neutron stars hyperons are produced, since this leads to an energetically more favored configuration. This appearance leads in various model calculations often to a strong softening of the equation of state, usually that strong that the models have a hard time to describe such heavy objects. Since the scattering data on the Λ-p interaction is rather scarce it would be beneficial to study it in more details.

With help of the femtoscopy technique one can access such pair interactions. Femtoscopy is based on the measurement of a two-particle correlation function at low relative momenta. Experimentally, the latter is constructed by a ratio of pairs from the same $A(k^*)$ and from mixed event $B(k^*)$. The mixed event sample does not contain correlations from femtoscopic origin and is thus just an uncorrelated yield of pairs [1]:

$$C(k^*) = \frac{A(k^*)}{B(k^*)}\,, \qquad (1)$$

where $k^* = \frac{1}{2}|\mathbf{p}_1^* - \mathbf{p}_2^*|$ is the momentum of the particles in the rest frame of the pair $\mathbf{p}_1^* + \mathbf{p}_2^* = 0$. At small relative momenta $k^* < 150$ MeV/c the correlation function deviates from unity if the pairs are correlated due to e.g. strong final state interactions. The size of the emission region can be reconstructed with this method.

Analysis strategy

For the femtoscopy study, the pp 7 TeV ALICE data sample was analyzed, which was recorded in 2010. The events were selected with the minimum bias trigger condition. The z-position of the primary vertex was required to lie within 10 cm of the center of the ALICE detector. The goal was to obtain the correlation function among proton pairs as well as p-Λ pairs, where the p-p correlation function serves as benchmark to extract the source size of the pp collision system. Protons are identified with the TPC for momenta below p<0.75 GeV/c. Above this threshold also the TOF information is required to reject contaminations from other species. The hyperons were identified by their decays involving charged particles $\Lambda \rightarrow p\pi^-$ using the invariant mass technique. To reject contributions from combinatorial background, several topological cuts were applied to reduce the source of particles not stemming from the hyperon decay. Around 6M Λ hyperons ($S/B \sim 20$) were reconstructed.

The goal was to investigate the sensitivity of the measured p-Λ correlation function when it is compared to model calculations [2] with different scattering parameters. As an example we tested parameters predicted by chiral effective field theory calculations at leading order (LO) and next-to-leading-order (NLO) expansion [3]. The p-p and p-Λ correlation functions were fitted simultaneously using the NLO parameters for p-Λ. After the fit converged the LO parameters were plugged in to investigate the difference. This is displayed in Fig. 1. One can see that the p-Λ correlation function develops a sensitivity on the scattering parameters. However, the current statistics is not enough to perform a clear separation of the two parameter sets.

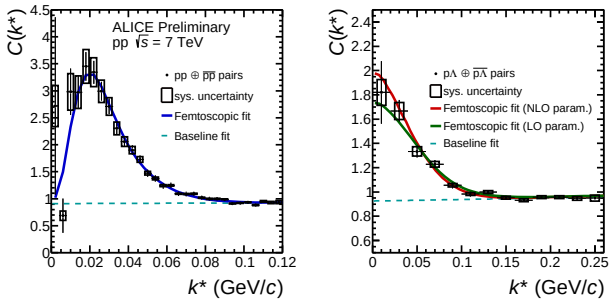

Figure 1: Simultaneous fit of the p-p and p-Λ pair. The p-Λ pair was fitted using the NLO parametrization. Afterwards the LO parametrization was plugged in.

References

[1] M. Lisa *et al.*, "Femtoscopy in relativistic heavy ion collisions", Ann. Rev. Nucl. Part. Sci. (2005) 357-402

[2] R. Lednicky, V.L. Lyuboshits, "Final State Interaction Effect on Pairing Correlations Between Particles with Small Relative Momenta", Sov. J. Nucl. Phys. 35 (1982) 770

[3] J. Haidenbauer *et al.*, "Hyperon-nucleon interaction at next-to-leading order in chiral effective field theory", Nucl. Phys. A 915 (2013) 24-58

* Work supported by GSI, FIAS, HIC4FAIR, HGS-HIRe, BMBF

New flow observables: Symmetric Cumulants*

L. Fabbietti[1,2], *A. Bilandzic*[1,2], *and the ALICE Collaboration*

[1]Physik Department E62, Technische Universität München, 85748 Garching, Germany; [2]Excellence Cluster 'Origin and Structure of the Universe', 85748 Garching, Germany

A measurement of new flow observables, so-called Symmetric Cumulants, which quantify the correlations between event-by-event fluctuations of two different flow harmonics, provide stronger constraints for the medium properties of Quark-Gluon Plasma (QGP), a new state of matter produced in heavy-ion collisions.

Introduction

The key measurement in the exploration of QGP properties is the measurement of anisotropic flow phenomenon. In non-central heavy-ion collisions the initial volume containing the deconfined nuclear matter is anisotropic in the coordinate space. Interactions within this anisotropic volume cause the anisotropy to be transferred from the coordinate space into the momentum space. The resulting anisotropy in momentum space will cause an anisotropic distribution of particles recorded in the detector after each heavy-ion collision, and is therefore an observable quantity. Anisotropic flow is quantified via so-called flow harmonics v_n, which are coefficients in the Fourier series expansion of particle yields in the momentum space.

Anisotropic flow harmonics v_n directly reflect the properties of produced QGP. Their measurements have demonstrated that the QGP produced at the LHC is one of the best examples of a perfect fluid, i.e. the ratio of its shear viscosity to entropy density (η/s) is very close to a universal lower bound of $1/4\pi$ which is obtained from theoretical arguments based on the AdS/CFT conjecture, the fundamental duality between general relativity and conformal field theory.

Symmetric Cumulants

What remains completely unknown is how the η/s of QGP depends on temperature, and this study has been just initiated by the theorists [1]. This question triggered among the experimentalists the development of new flow observables, since the effect of the η/s temperature dependence in individual flow harmonics v_n is masked by other contributions. One recent example are Symmetric Cumulants, which quantify the relationship between event-by-event fluctuations of two different flow harmonics, v_m and v_n [2].

In Fig. 1 a first measurement is shown of these new observables by the ALICE Collaboration [3] and comparison to the theoretical HIJING model. The HIJING model was used to estimate the strength of non-flow correlations. For the data, the positive results of SC(4,2) (red markers) suggest a positive correlation between the fluctuations of v_2 and v_4. The negative results of SC(3,2) (blue markers) predict that finding v_2 larger than average $\langle v_2 \rangle$ enhances the probability of finding v_3 smaller than average $\langle v_3 \rangle$, i.e. a negative correlation between fluctuations of v_2 and v_3. Taking everything into account, SC observables are the least biased measure of the correlation between event-by-event fluctuations of two different harmonics v_m and v_n.

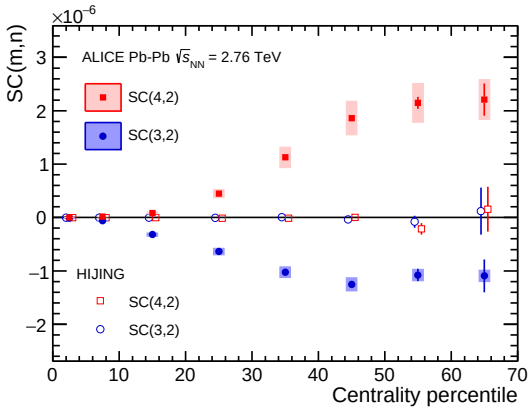

Figure 1: Centrality dependence of observables SC(4,2) (red filled squares) and SC(3,2) (blue filled circles) in Pb–Pb collisions at lower energy of 2.76 TeV. Systematic errors are represented with boxes. Results for theoretical HIJING model are shown with hollow markers.

Remarkably, it was shown [3] that these new correlation observables are sensitive both to the fluctuations of the initial conditions and to the transport properties of QGP, with the potential to discriminate between the two respective contributions. Together with individual flow harmonics v_n, they will allow for verification of theoretical predictions for each individual stage of heavy-ion evolution.

References

[1] H. Niemi, K. J. Eskola, R. Paatelainen and K. Tuominen, Phys. Rev. C **93** (2016) no.1, 014912 doi:10.1103/PhysRevC.93.014912

[2] A. Bilandzic, C. H. Christensen, K. Gulbrandsen, A. Hansen and Y. Zhou, Phys. Rev. C **89** (2014) no.6, 064904 doi:10.1103/PhysRevC.89.064904

[3] J. Adam *et al.* [ALICE Collaboration], Phys. Rev. Lett. **117** (2016) 182301 doi:10.1103/PhysRevLett.117.182301

*Work supported by BMBF Verbundsprojekt ALICE at HIG rate 05P15WOCA1.

DOI:10.15120/GR-2017-1

Using event-shape-engineering in the search for the Chiral Magnetic Effect *

J. Onderwaater[1,2], A. Dobrin[3], J. Margutti[4], I. Selyuzhenkov[1], S. Voloshin[5] for the ALICE Collaboration

[1]GSI; [2]Heidelberg University; [3]CERN; [4]Utrecht University; [5]Wayne State University

The event-shape-engineering technique (ESE) is used to study charge-dependent correlations in classes of events with different flow magnitude. Results for Pb-Pb collisions at $\sqrt{s_{\rm NN}} = 2.76$ TeV recorded with ALICE at the LHC are used to constrain the contribution from the Chiral Magnetic Effect.

The postulated chiral magnetic effect (CME) in heavy ion collisions is a result of parity violation in strong interactions that create a chiral imbalance for fermions in the produced medium, which in combination with an extremely strong magnetic field (B) leads to a charge separation [1]. An observable that is commonly used to measure the charge separation is the two-particle correlation with respect to the reaction plane, $\gamma_{\alpha\beta} = \langle\cos(\varphi_\alpha+\varphi_\beta-2\Psi_{\rm RP})\rangle$, where φ is the azimuthal angle of particles with electric charge α, β, and $\Psi_{\rm RP}$ is the reaction plane angle [2]. In this correlation the contribution from reaction-plane independent background correlations cancels, while other sources of background as well as the CME signal are still present. The ALICE Collaboration has previously observed a significant charge dependence [3]. In order to better understand the origin of the observed correlations, now $\gamma_{\alpha\beta}$ has been measured in event classes with different magnitude of elliptic flow v_2 for fixed centrality ranges using the ESE technique [4,5]. The varying magnitude originates from fluctuations in the initial state of the colliding nuclei. The contribution from CME is assumed to scale with the square of the magnitude of the direction of the magnetic field projected on the event plane. The variation of the magnetic field for different initial states is calculated for different initial conditions. The contribution from background is assumed to scale linearly with v_2. Within the range of v_2 observed for each centrality class, the dependence of the CME contribution on v_2 is approximated to be linear with a different slope. Using this information about the signal and background dependence on v_2, the following function is constructed for a fit to the data and the model calculations with B:

$$F_1(v_2) = p_0(1 + p_1(v_2 - \langle v_2\rangle)/\langle v_2\rangle).$$

The function is constructed such that for data normalized to unity at $\langle v_2\rangle$, p_0 is fixed at 1. If only background is present, $p_1 = 1$ and $F(0) = 0$. The fits and the data are shown in Figure 1. In combination with a fit to the models to estimate $p_{1,\rm CME}$, we can extract an estimate for the CME fraction $f_{\rm CME}$:

$$f_{\rm CME}\, p_{1,\rm CME} + (1 - f_{\rm CME}) = p_{1,\rm data}.$$

Figure 2 shows the extracted values for $f_{\rm CME}$. The statistical errors in 0-10% centrality and 50-60% are too large to reveal any information about the possible presence or absence of a CME signal. For 40-50% the fraction is negative . In the 10-40% range, the indication is that the CME, if present, represents a small fraction of the observed charge dependence of $\gamma_{\alpha\beta}$.

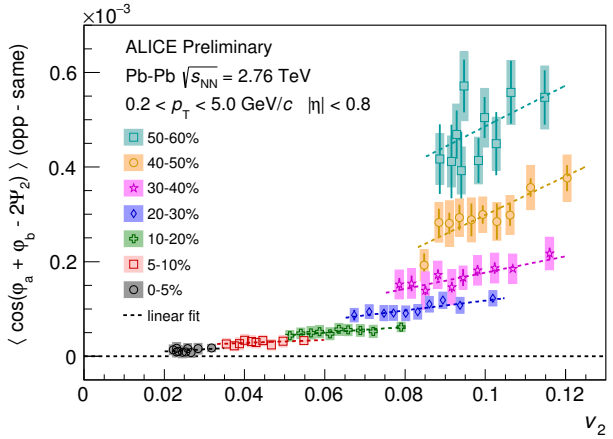

Figure 1: $\gamma_{+-} - \gamma_{++/--}$ as a function of v_2 for various centrality classes.

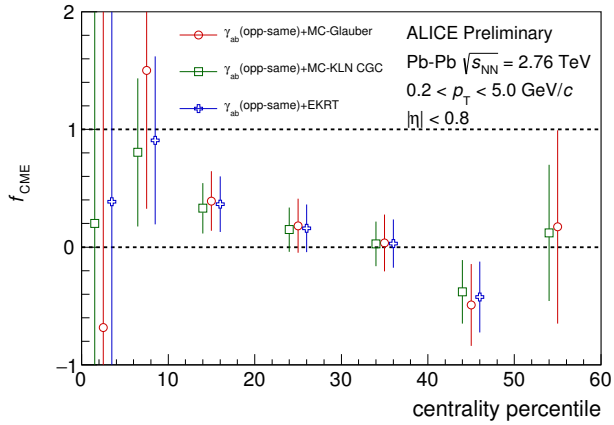

Figure 2: The observed fraction $f_{\rm CME}$ as a function of centrality assuming different initial state models.

References

[1] D. Kharzeev, Phys. Lett. B633 (2006) 260-264

[2] S. Voloshin, Phys. Rev. C70 (2004) 052901

[3] J. Schukraft, Phys. Lett. B719 (2013) 394-398

[4] ALICE Collaboration, Phys. Rev. Lett 110 (2013) 012301

[5] Quark Matter 2017, presentation by A. Dobrin for the ALICE Collaboration, https://indico.cern.ch/event/433345/

* Work supported by GSI, BMBF and TU Darmstadt.

Experience with the upgraded ALICE TPC readout system (RCU2)

C. Lippmann and the ALICE collaboration*
GSI, Darmstadt, Germany

The readout of the ALICE TPC comprises 557 568 electronics channels on 4 356 Front-End Cards (FECs). The FECs are grouped in 216 readout partitions, distributed in 18 sectors each on the two sides of the TPC. Within each partition, a Readout Control Unit (RCU) interfaces the FECs to the trigger processor, to the Data Aquisition System (DAQ) and to the Detector Control System. The readout bus to the FECs is implemented as a 40 bit wide parallel bus.

Figure 1: The RCU2 board.

The new version of the Readout Control Unit, the RCU2 (see Fig. 1) was installed in 2016. It increases the segmentation of the readout bus from two to four separate branches, each reading between 4 and 7 FECs. All functionality is incorporated into a single FPGA. The Microsemi SmartFusion2 was chosen, even though it had only just been released. It integrates an inherently reliable and radiation tolerant FLASH-based FPGA fabric, a 166 MHz ARM Cortex processor and high-performance communication interfaces all on a single chip. As bandwidth of the optical readout link to the DAQ system 300 MByte/s was chosen (was 160 MByte/s). A secondary FPGA (Microsemi ProAsic 3) is responsible solely for radiation monitoring. It counts Single Event and Multi Bit Upsets in dedicated memories and is not required for the basic operation of the RCU2.

The upgrade to the new RCU2 system was performed during the extended winter technical stop of the CERN Large Hadron Collider (LHC) in January and February 2016. Replacing the 216 RCUs and 1080 backplane and adapter cards took about 3 weeks. The newly installed boards were tested immediately for the basic functionality. More time was spent correcting errors and commissioning the system. With the new system, the first physics collisions were recorded in April 2016.

During the course of the year 2016 the performance of the RCU2 was optimized by implementing new features into the RCU2 firmware. The firmware on the 216 installed cards can be updated remotely using ethernet.

- Data ordering following the pad row structure of the readout chambers was implemented to allow optimal speed of the online cluster-finding algorithm in the High Level Trigger system.
- A double buffer structure was implemented for each of the four readout branches. This allows to write the raw data from a channel on a FEC into one buffer while at the same time reading and clearing (reformatting) the other buffer. The buffers are switched once both processes are done.
- In sparse readout mode only channels on the FEC that actually contain some data are adressed. This feature reduces the time needed to read out data from low occupancy events.
- Usage of a Multi Event Buffering scheme allows to accept a new trigger even though not all data from the previous event has been read out.
- Improvements in the protocol on the readout bus were applied, significantly reducing the time needed for a single bus transaction.

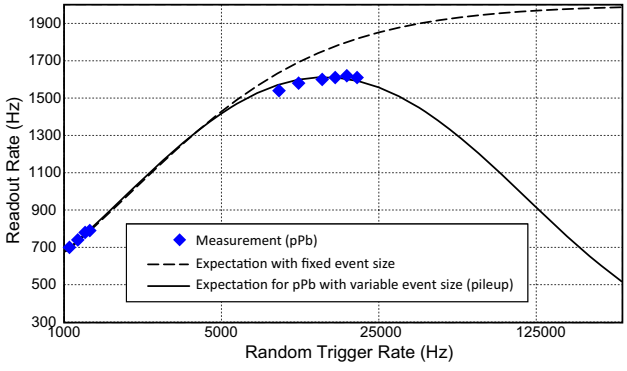

Figure 2: Expected and measured readout rates. Note that the data size and thus the readout time increases at high interaction rates due to event pileup in the TPC drift volume.

During the p–Pb campaign at the LHC in autumn 2016 minimum bias collision events have been recorded at an unprecedented rate (for a TPC) of 1.6 kHz (see Fig. 2). Moreover, a very stable operation without interruptions due to e.g. radiation effects is observed.

* C.Lippmann@gsi.de

DOI:10.15120/GR-2017-1

Space-charge distortion corrections in the ALICE TPC*

H. Appelshäuser[1], M. Arslandok[2], C. Garabatos[3], E. Hellbär[1], M. Ivanov[3], C. Lippmann[3], R. Münzer[1], K. Schweda[3], R. Shahoyan[4], J. Wiechula[1]
for the ALICE Collaboration
[1]IKF, Frankfurt, Germany; [2]PI, Heidelberg, Germany; [3]GSI, Darmstadt, Germany; [4]CERN, Geneva, Switzerland

The ALICE TPC [1] was operated during the first period of data taking at LHC, commonly denoted as Run 1, from 2009–2013 with two different gas mixtures: Ne-CO_2-N_2 (90-10-5) until 2010 and Ne-CO_2 (90-10) from 2011 on. For reasons of operational stability, the gas mixture was changed to Ar-CO_2 (88-12) during the LHC first long shutdown, before the start of Run 2 in 2015. The operational stability turned out to be excellent, even at high luminosities.

At high collisions rates and large charged-particle multiplicities, the TPC drift volume contains a large number of positive ions that pile up due to the slow ion drift velocity. The resulting field distortions modify the electron drift lines, introducing drift field distortions that have to be corrected. In most of the TPC drift volume, the observed distortions in neon and argon, i.e. the *bulk* distortions, are as expected from the known gas properties of the Ar- and Ne-based mixtures, such as primary ionization and ion mobility. In Run 1, small *local* space-charge distortions of up to a few mm were observed in neon. However, in Run 2, these local distortions exceed the simple extrapolation from neon to argon by a factor of up to 10–20 and reach up to several centimeters, see Fig. 1. This is of similar magnitude as the distortions expected for Run 3 after the ALICE TPC upgrade with GEM-based readout [2] at lead-lead collision rates of 50 kHz. However, in Run 3 the distortions are expected to be continuous, with relatively small gradients, as they are resulting from space charge distributed over a large volume. The distortions encountered in Run 2, on the other hand, have large gradients.

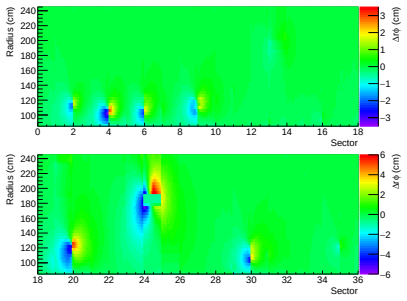

Figure 1: Measured space-charge distortions near the central electrode $\Delta r\phi$ in Pb-Pb collisions at 4.5 kHz interaction rate as a function of the TPC sector and the radius for the A (top) and C side (bottom).

These dynamic distortions were measured as 3 dimensional maps by interpolating tracking information from external detectors, i.e. the silicon-based inner tracking system (ITS) at inner radii as well as the transition radiation detector (TRD) and the time of flight detector (TOF) which are located at outer radii when compared to the TPC. Reconstructed TPC clusters are compared with their expected position obtained from the interpolated reference tracks.

In order to collect sufficient statistics, a distortion map is created as the average of the measured distortions over a time interval of typically 20 minutes. Changes in the interaction rate and thus the amplitude of the distortions are accordingly scaled by the instantaneous luminosity. This procedure does not take into account local fluctuations of space charges which amount to up to 20 - 30 %. During track reconstruction, the coordinate of each TPC cluster is corrected according to these parameterized maps. The quality of the *average* distortion correction can be appreciated from the bias of the mean signed distance of the closest approach (DCA) of TPC tracks to the primary vertex before and after correction shown in Figure 2.

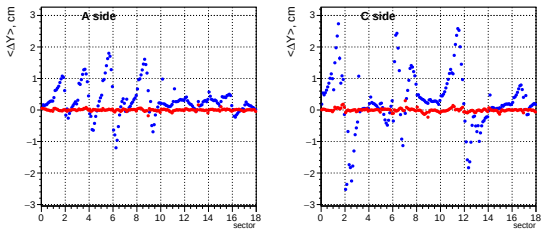

Figure 2: Bias of the mean distance of closest approach of TPC tracks ($p_T > 2$ GeV/c) to the primary vertex in Pb-Pb collisions at 4.5 kHz interaction rate before (blue) and after (red) distortion correction.

For the next data taking period, starting in May 2017, the same gas mixture as used in Run 1 (Ne-CO_2-N_2 (90-10-5)), for which the observed distortions were small, will again be injected into the TPC. The higher ion mobility should lead to a reduction of the space-charge distortions by a factor of two. Possibly a larger reduction will be observed. Already with a factor 2 reduction of the distortions, the challenges related to event-by-event fluctuations in the space-charge distortions, which are not taken into account, will become negligible and the tracking and PID performance will be further improved.

References

[1] ALICE TPC Collab., Nucl. Instr. Meth. A 622 (2010) 316.
[2] ALICE Collab., CERN-LHCC-2013-020 (2013).

* Work supported by GSI, BMBF, EMMI, H-QM, and HGS-HIRe.

Upgrade of the ALICE Time Projection Chamber*

T. Rudzki[†1,2], *U. Frankenfeld*[1], *J. Hehner*[1], *M. Jahn*[1], *L. Karayan*[1], *S. Masciocchi*[1,2], *D. Miśkowiec*[1], *T. Morhardt*[1], *R. Patra*[3], *and B. Voss*[1]

[1]GSI, Darmstadt, Germany; [2]Physikalisches Institut, Heidelberg, Germany; [3]Variable Energy Cyclotron Centre, Kolkata, India

Introduction

ALICE (A Large Ion Collider Experiment) is one of the four large experiments at the CERN LHC. It was designed and built with the aim of studying collisions between lead ions and learning about the properties of the extreme matter created therein. The experiment successfully took data from pp, Pb–Pb, and p–Pb collisions during the LHC Run 1 at half of the nominal LHC beam energy, and continues its studies at (nearly) full energy in the Run 2. A significant increase of luminosity is planned for Run 3.

The Time Projection Chamber (TPC) is the main tracking and particle-identification detector of the ALICE Central Barrel which covers midrapidity $-0.9 \leq \eta \leq 0.9$ and the full azimuth $0 < \varphi < 2\pi$ (Fig. 1). The TPC volume is divided in two halves by a central cathode kept on a potential of -100 kV. The charged particles traversing the gas volume (Ne-CO_2) ionise the gas. The released electrons drift towards the TPC endplates which are equipped with 18 inner and outer readout chambers (IROCs and OROCs). There, the signal is amplified and information about position, timing and charge is digitised and provided to the data acquisition system.

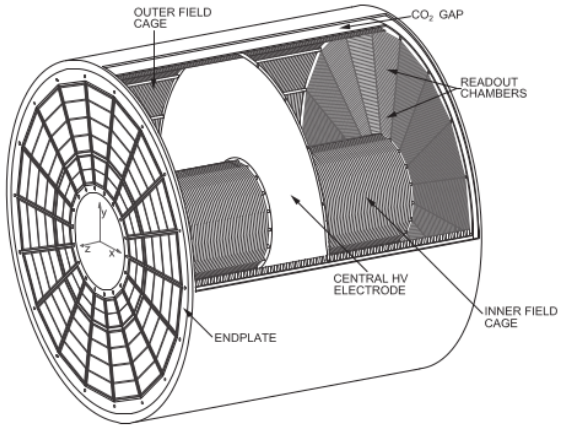

Figure 1: The ALICE TPC at the Large Hadron Collider. Each endplate is equipped with 36 readout chambers.

In 2019-2020, the ALICE experiment will be upgraded to cope with high rates (50 kHz) of Pb-Pb collisions expected in the LHC Run 3. Therefore, the current readout chambers of the TPC – multi-wire proportional chambers (MWPCs) with a gating grid which are capable for rates below 3 kHz – will be replaced by ones equipped with GEMs [1, 2].

GEMs, Gas Electron Multipliers, are 50 μm thick kapton foils, covered on both sides with a copper layer, with small holes. A potential difference of 200–400 V between the two sides of the foil is applied resulting in a strong electric field inside the holes. In this field, the incoming electrons are accelerated and ionise the gas. In an ALICE TPC OROC, the foils are arranged in three stacks of four GEMs (Fig. 2) which are operated at a gain of 2,000 and an ion backflow below 1 % [1].

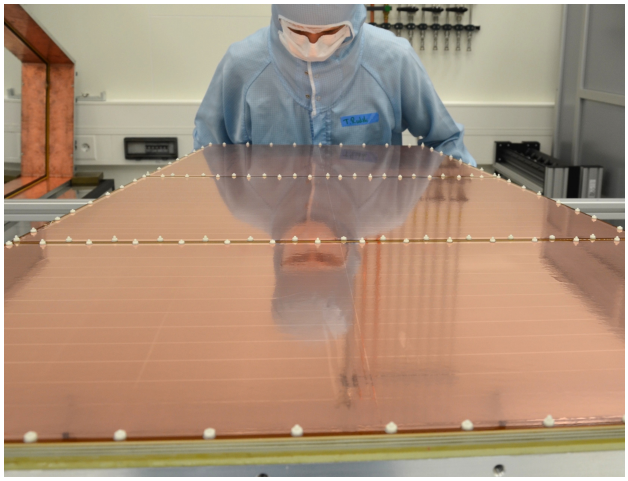

Figure 2: OROC equipped with three stacks of 4 GEMs.

First fully operational GEM OROC

The TPC Upgrade is an international project with many participating institutions. In this collaborative work, GSI fulfills two tasks: framing GEMs for the largest, outermost stack (OROC3) and assembly of OROCs. For this purpose, the test stand for gain uniformity measurements, formerly used to test the Transition Radiation Detector chambers of ALICE, was moved to the clean room and a second test setup, originally designed for the planar GEM-tracker of PANDA, was adapted to perform high-irradiation tests.

In 2016, the QA and framing of GEM foils started. The foils are already tested once and optically scanned at HIP, Helsinki. Arriving at GSI, a basic QA is repeated to make sure that the foils did not get damaged during transport.

* Work supported by GSI, BMBF, EMMI, H-QM and HGS-HIRe
† t.rudzki@gsi.de

DOI:10.15120/GR-2017-1

The leakage current of each foil segment, normalised to its area, is recorded to rate their quality [3].

At the end of 2016, the first fully functioning GEM-based OROC was assembled and commissioned in the lab at GSI. The supplied voltages were tuned such that all stacks have the nominal gain of 2,000. This was reached with minor deviations of 50, 100 and 0 V (for the three GEM stacks, respectively) from the nominal voltage of 4.2 kV (Fig. 3).

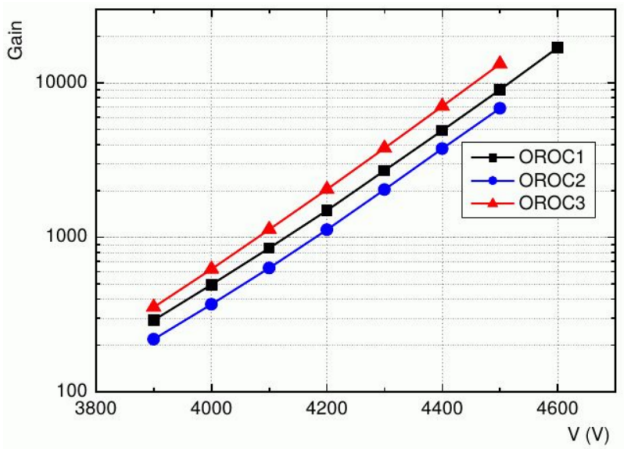

Figure 3: Gain curve of the three GEM stacks of the first OROC, obtained with an ^{55}Fe source.

The upgrade should preserve the performance of the current TPC. This results in the following requirements:

- Gain uniformity with an RMS below 20 %.
- $\frac{\sigma_E}{E}$ of ^{55}Fe photopeak below 12 %.
- Ion backflow below 1 %.
- Operation stability at high radiation rates (ALICE conditions).

In Fig. 4 the gain uniformity map of the OROC is shown. The blue bars are either transition regions between the stacks or in the lowest stack floating segments in two different foils leading locally to a significant reduction in gain. The RMS of the remaining part of the scan is 20 % of the mean and fully satisfying. The ion backflow was found to be at around 0.6 % which is comparable to the values of small prototypes (Fig. 5).

The energy resolution was measured for each stack using an ^{55}Fe source. All three results of $\frac{\sigma_E}{E}$ were around 14 % which will be a subject of further optimisation.

Finally, the chamber was mounted inside the PANDA box and was exposed to x-ray irradiation leading to a pad current of 10 nA/cm^2 which is expected for Run 3 in the TPC. The chamber behaved well and the resolution did not deteriorate.

Conclusion and outlook

The first OROC, described in this note, successfully passed the required tests. In addition, another chamber has been assembled at GSI in 2017. This chamber represents the final design and has an even better performance.

The TPC Upgrade group at GSI is ready for the mass production of OROCs. This is scheduled to begin in summer 2017 and to continue until autumn 2018.

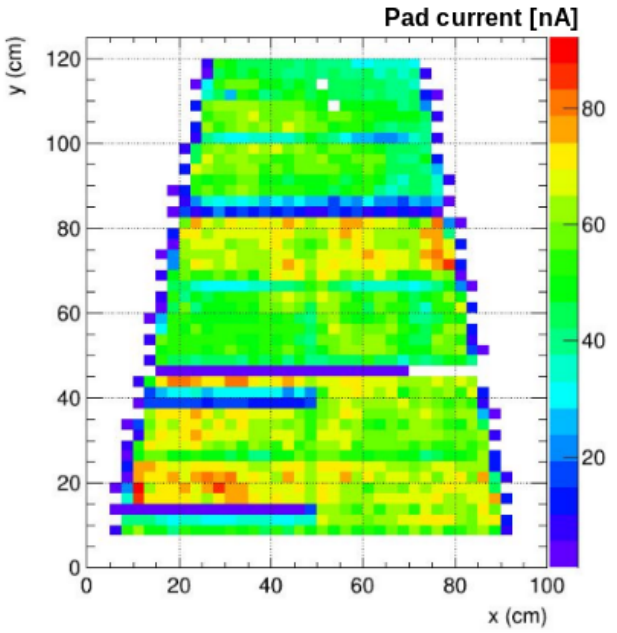

Figure 4: Gain uniformity scan of the OROC. The 3 GEM stacks are clearly visible.

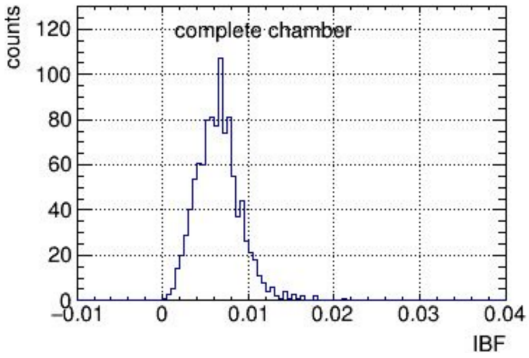

Figure 5: Ion backflow of the OROC - the required value of 1 % is achieved.

References

[1] ALICE Collaboration, Technical Design Report for the Upgrade of the ALICE TPC, CERN-LHCC-2013-020, https://cds.cern.ch/record/1622286

[2] ALICE Collaboration, Addendum to the Technical Design Report for the Upgrade of the ALICE TPC, ALICE-TDR-016-ADD-1, https://cds.cern.ch/record/1984329

[3] Jahn, M. "Quality assurance for gas electron multipliers with the leakage current test", Bachelor thesis, University of Heidelberg, 2017.

DOI:10.15120/GR-2017-1

Study of secondary discharges in Ar-CO_2 (90-10) and Ne-CO_2-N_2 (90-10-5)*

A. Deisting† [1,2], *C. Garabatos*[1], *and S. Masciocchi*[1,2]

[1]GSI Helmholtzzentrum für Schwerionenforschung GmbH, Darmstadt, Germany; [2]Physikalisches Institut, Ruprecht-Karls-Universität Heidelberg, Heidelberg, Germany

Introduction

The Large Hadron Collider (LHC) will provide lead-lead collisions at an interaction rate of 50 kHz from 2021 onwards. To exploit the full rate, the ALICE Time Projection Chamber (TPC) [1] will be upgraded with new ReadOut Chambers (ROCs). These ROCs will utilise stacks of four Gas Electron Multipliers (GEMs) [2] and hence allow for continuous read-out, while preserving the energy and momentum resolution of the current Multi-Wire Proportional Chambers [3]. The discharge mechanism of GEM foils was studied to ensure stable operation of the ROCs at LHC.

Study of secondary discharges

This study has been conducted with a set-up of two 10×10 cm^2 GEM foils mounted with an inter GEM distance of 2 mm. The distance of the last GEM (GEM2) to the anode plane is as well 2 mm. While the electric field between GEM1 and GEM2 is referred to as transfer field (E_{T}), the field between GEM2 and the anode plane is called induction field (E_{Ind}). During a discharge in one of the two GEMs a signal is induced on the anode plane and, after some attenuation, read out with an oscilloscope. The active volume of the detector is flushed with Ar-CO_2 (90-10) or Ne-CO_2-N_2 (90-10-5), enriched with ^{222}Rn. While a high voltage difference (ΔU_{GEM2}) was applied across GEM2, ΔU_{GEM1} was kept at a moderate value. Hence the ionisations produced by the α-decays of Rn trigger discharges in GEM2. A more detailed description of the set-up used here can be found in [4, 5].

In previous studies the phenomenon of *secondary discharges* ("secondaries") was discovered [6]. Two parameters have been found to characterise these discharges: First, they occur always after an initial discharge and the corresponding measured signal is higher than the signal of the original discharge. Second, these discharges are only observed starting from a certain E_{Ind} value [7].

To quantify the onset of secondary discharges, the probability to observe one of them after an initial discharge is measured by: $P_2 = \frac{\#\text{ secondary discharges}}{\#\text{ initial discharges}}$. Plotting P_2 versus e.g. E_{T} (figure 1) shows a clear onset of the secondary discharges for a given electric field. In our work we showed that secondary discharges are caused by a discharge of the induction (transfer) gap if E_{Ind} (E_{T}) is high enough [4]. However the underlying mechanism is not yet understood.

Secondaries in different gas mixtures

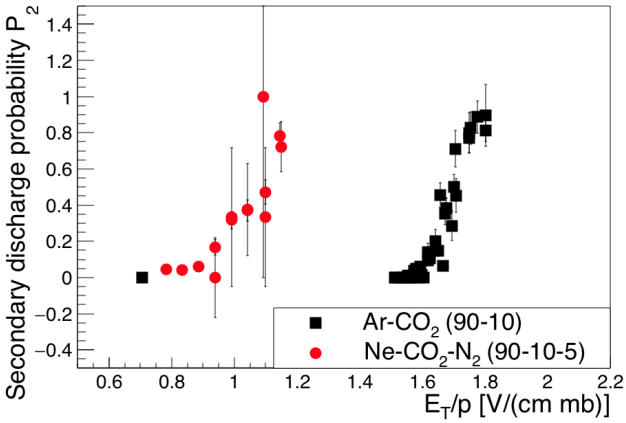

Figure 1: Both measurements were done with the same set-up. For the Ar-CO_2 (Ne-CO_2-N_2) measurement ΔU_{GEM2} was set to 423 V (455 V). ΔU_{GEM1} was varied in both cases in the range between 260 V and 290 V.

Fig. 1 shows P_2 for secondary discharges in the transfer gap between the two GEMs. For Ar-CO_2 (90-10) and Ne-CO_2-N_2 (90-10-5) a steep rise of P_2 from 0 to 1 can be seen. Defining the onset field as the field at which $P_2 = 0.5$, an onset field of 1.69 ± 0.05 V cm^{-1} mb^{-1} and of 1.05 ± 0.08 V cm^{-1} mb^{-1} is observed for the Argon- and Neon-based gas-mixture, respectively. For the ALICE TPC upgrade, Ne-CO_2-N_2 (90-10-5) is foreseen as the baseline gas mixture as well as transfer fields of 4 kV cm^{-1}. Since these foreseen transfer fields are higher than the observed onset of the secondary discharges, measures to mitigate secondaries are needed. A promising ansatz is the use of decoupling resistors as shown in [5].

References

[1] *Nucl. Instr. Meth. Phys. Res. A* **622** (2010) 316–367

[2] *Nucl. Instr. Meth. Phys. Res. A* **386** (1997) 531–534

[3] *CERN-LHCC-2013-020*

[4] A. Deisting, C. Garabatos, *JINST* **12** Nb. 05 (2017) C05017

[5] A. Datz, *Bachelor thesis Uni. Heidelberg* (2017)

[6] V. Peskov, P. Fonte, arXiv:0911.0463

[7] P. Gasik, RD51 Collaboration meeting (2016-03)

* Work supported by GSI, BMBF, H-QM, HGS-HIRe, and University of Heidelberg

† alexander.deisting@cern.ch

DOI:10.15120/GR-2017-1

Quadruple GEM PCB simulator *

P. Gasik† [1,2] *and the ALICE TPC collaboration*

[1]Physik Department E62, TU München, 85748 Garching, Germany; [2]Excellence Cluster 'Origin and Structure of the Universe', 85748 Garching, Germany

A major upgrade of the ALICE TPC is foreseen during the LHC Long Shutdown 2 (2019-20) when the existing MWPC-based readout chambers will be replaced with detectors employing the Gas Electron Multiplier (GEM) technology. The key parameter for a long-term operation of the GEM-based TPC is the stability against electrical discharges. A thorough investigation of the discharge properties of GEM-based detectors has been already reported by the Collaboration in e.g. [1].

The next important goal is the final assessment of the HV supply scheme planned to be used with the upgraded readout chambers. Behaviour of the system in case of a spark occurrence, propagated discharges or an emergency trip of a power supply is of a great importance. The possibility of an over-voltage across any GEM foil must be avoided as it may lead to the development of a destructive discharge. In order to test the reaction of the powering scheme on the violent events, as listed above, we have designed and built a GEM detector simulator based on the conventional electronic elements.

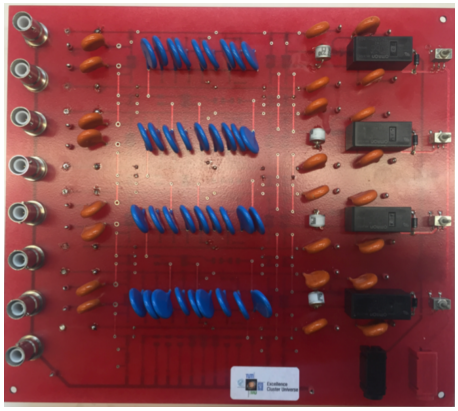

Figure 1: Quadruple GEM PCB simulator.

Figure 1 shows a picture of a double-layer PCB (top view) equipped with capacitors and resistors corresponding to the realistic values of a quadruple GEM Inner Read-Out Chamber for the upgraded ALICE TPC. HV is applied to 8 channels (corresponding to 8 GEM electrodes) via SHV connectors. The device allows for the simulation of a short in one of the GEM segments (in each layer) using HV relays or a spark occurrence by employing a Gas Discharge Tube (GDT) which creates a spark after a breakdown voltage is reached. GDTs can simulate a discharge across one segment of GEM (its equivalent capacitor) or between GEMs in one of the transfer or induction gaps and their breakdown voltage corresponds to the realistic settings applied to the detectors. Voltages on electrodes in question can be monitored on a scope using standard 1:10 probes via decoupling HV capacitors, included in the design.

An example of operation of the PCB simulator is presented on figure 2, where a GEM discharge signal recorded with a real detector (top panel) is compared to the one recorded with the GEM PCB simulator (bottom panel, scope screenshot). The signal waveform shows modulations which are due to the inductance of the system, resulting in periodic oscillations. The signal from the simulator nicely reproduces main features of the real detector signal, such as amplitude ($\sim$ 500 mV), oscillation frequency ($\sim$ 10 MHz) or signal damping ($\sim$ 1 μs).

The device presented in this report can serve as a testing tool for the assessment of the HV scheme without a need to use a real detector.

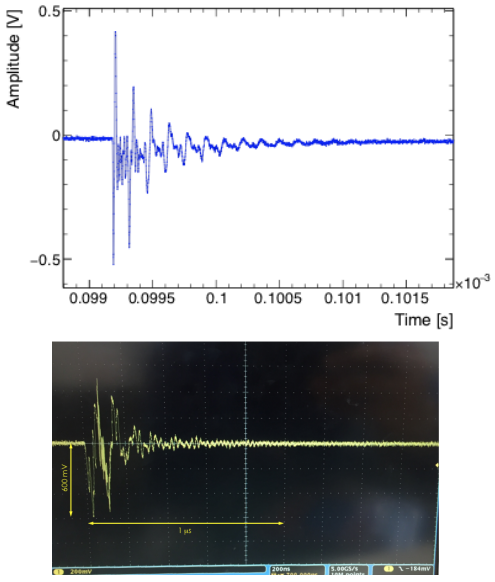

Figure 2: Discharge signal recorded on the oscilloscope with a real detector (top) and with the GEM PCB simulator (bottom).

References

[1] ALICE Collaboration, CERN-LHCC-2015-002 (ALICE-TDR-016-ADD-1) 2015.

* Work supported by BMBF 05P15WOCA1, Excellence Cluster 'Universe'

† p.gasik@tum.de

Digitization for the ALICE GEM TPC*

A. Mathis[†1,2], *J. Wiechula*[3], *L. Fabbietti*[1,2], *P. Gasik*[1,2], *and the ALICE collaboration*

[1]Physik Department E62, Technische Universität München, Garching; [2]Excellence Cluster 'Origin and Structure of the Universe', Garching; [3]Institut für Kernphysik, Goethe-Universität, Frankfurt am Main

The ALICE Collaboration is planning a major upgrade of its central barrel detectors to benefit from the significantly increased LHC luminosity beyond 2019 [1]. In order to record at an increased interaction rate of up to 50 kHz in Pb-Pb collisions, the TPC, the main device for charged-particle tracking and particle identification (PID) in ALICE, will be upgraded with GEM-based (Gas Electron Multiplier [2]) readout chambers [3] allowing for continuous operation in an ungated mode. The increase in interaction rate and the requirements of a trigger-less, continuous readout demand for significant upgrades of the front-end cards, the computing system and the corresponding calibration, reconstruction and simulation framework.

Event generators, such as HIJING [4], are powerful tools to obtain a deeper insight into the particle production mechanisms at the highest energies, and the corresponding final state interactions. A meaningful comparison of such models to experimental data is, however, only possible when the full process of signal formation in the detector is properly modelled in the simulation. Consequently, the upgraded readout scheme of the ALICE TPC demands for a complete re-design of the *digitization*, in which these processes are handled.

The first step after the simulation of the incident particle traversing the detector and the conversion of the corresponding energy deposit into number of electron-ion pairs, is the electron transport in the active volume of the detector. The electrons drift up to 250 cm from the point of their creation until the readout chambers on both ends of the TPC, during which diffusion and attachment occurs. Having reached the readout chambers, the electrons are amplified in the stack of four GEM foils. Fluctuations of the amplification process are modelled according to the findings reported in [5]. The electrons extracted from the last GEM in the stack induce a signal on the pad plane during their drift. Due to the charge spread in the GEM stack and the Coulomb field exerted by the resulting electron cloud, a signal may as well be induced on adjacent pads. These effects are incorporated in the *pad response function*, as displayed in Fig. 1. The latter is computed using a Garfield [6, 7] / COMSOL [8] simulation of the movement of the electrons in the field between the pad plane and the last GEM. The induced current for different starting positions of the electron cloud is calulated and normalized to that expected in the centre of the pad.

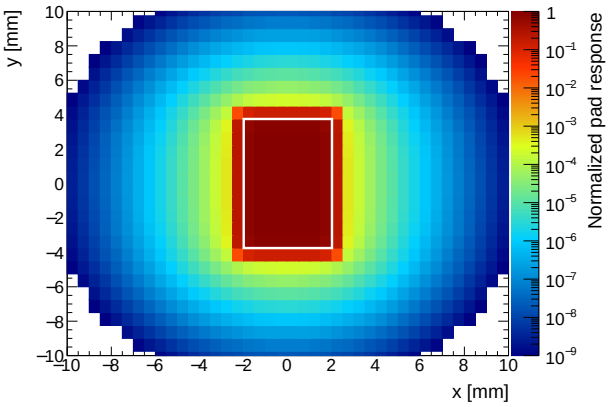

Figure 1: Pad response function of an Inner Readout Chamber of the ALICE GEM TPC for different starting points of the electron avalanche. The white shape indicates the outline of the pad.

The bottom side of the last GEM couples capacitively to the readout anode and thus upon extraction of electrons from the GEM, a signal of opposite polarity is induced on all pads of the readout chamber. This *common mode effect* leads to an effective baseline shift and hence to additional noise in the system. Furthermore, the signal processing in the front-end cards is modelled, during which the avalanche is convoluted with the Gamma4 shaping function and the resulting signal sampled with 5 MHz. The final entity, a *Digit*, which is defined as an ADC value on a given pad and time bin, is then written to disk for further processing.

The simulation framework allows to run in triggered and continuous mode. A first validation will be possible with data measured in a beam test at CERN in May 2017 with a final readout chamber and final front-end cards. Long term tests of the stability and the powering scheme of the readout chambers will be continued in the ALICE cavern.

References

[1] B. Abelev *et al.*, CERN-LHCC-2012-012 (2012).

[2] F. Sauli, NIM A **386** (1997) 531.

[3] B. Abelev *et al.*, CERN-LHCC-2013-020 (2013).

[4] X.-N. Wang and M. Gyulassy, Phys. Rev. D44 (1991) 3501.

[5] A. László *et al.*, JINST 11 (2016) P10017.

[6] R. Veenhof, http://garfield.web.cern.ch.

[7] T. Gunji, private communication.

[8] COMSOL Multiphysics® v. 5.2.

* This research was supported by the DFG cluster of excellence 'Origin and Structure of the Universe' and the BMBF Verbundprojekt 'ALICE at high rate' 05P15WOCA1.

† andreas.mathis@ph.tum.de

DOI:10.15120/GR-2017-1

Hadron Physics at GSI

K. Peters[1], Head of Hadron Physics
[1]GSI, Darmstadt, Germany; Goethe-University Frankfurt

The hadron physics division is embedded in a strong international network and its main focus is the development, construction and completion of the PANDA experiment at FAIR. In addition, the group is involved in running the BESIII experiment in Beijing, PRChina and the GlueX experiment in Jefferson Lab, Newport News, USA.

PANDA

PANDA is a modern multi-purpose detector for a large variety of hadron physics experiments using an antiproton beam with an incident momentum between 1.5 and 15 GeV/*c*. Hadron physics is a very active field with a lot of important questions on the effective degrees of freedom of QCD at low energies, thus which states exist and what structure they obey. With a luminosity of up to $10^{32}/cm^2/s$ and a momentum spread of $\delta p/p$ being less than 10^{-4} ground-breaking experiments in hadron spectroscopy, hadron structure and hadron dynamics are possible with unprecedented statistics and precision.

PANDA at GSI concentrates, apart from particular detector components, on technical integration, coordination, infrastructure (hostlab activities) and software trigger and core software developments.

GSI is also responsible for R&D and construction of the Barrel DIRC (Detector for internally reflected Cherenkov light). The corresponding TDR was submitted to FAIR in 2016. In addition, groups at GSI are working on APD screening, customized ASIC design (PANDA preamplifier ASIC APFEL, and the PANDA-flash-ADC), the R&D of the GEM detectors and physics analysis and their respective tools. For details please refer to subsequent reports.

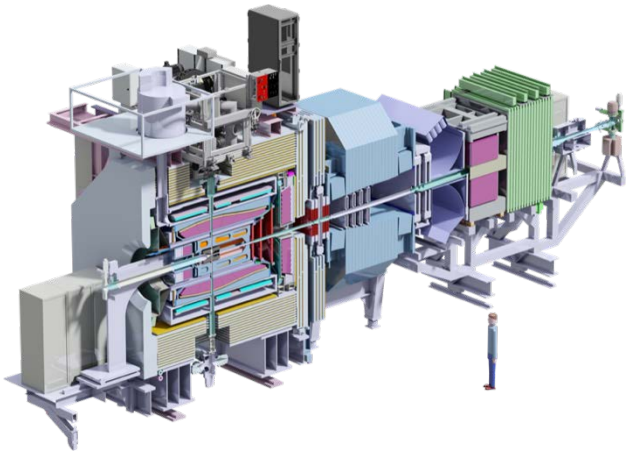

Figure 1: The PANDA detector (cut) for hadron physics experiments at HESR at FAIR.

The GSI group played also a central role in all the various PANDA activities (management, workshops, task forces, reviews) which strengthened the scientific case and underlined the technical competitiveness of the detector layout, which manifested its important role as a first day experiment at FAIR. For those first day experiments a reduced setup including a modified DAQ/Online system with adapted processing power is being proposed to reduce initial detector costs.

BES

The BES3 experiment is investigating all kinds of reactions from e^+e^- annihilations of colliding beams with invariant masses from 3 to 4.6 GeV/c^2. The special interest of GSI is the overlap of the open and hidden charm spectroscopy topics with PANDA and in particular the search for exotic mesons. The previous years were governed by the discovery of various Z_c-States which have a minimum quark-content of at least four quarks, with two of them being a charm-anticharm-pair. GSI is involved in the search for more states and a deeper understanding of the properties and the nature of these states. Particularly η_c yields in Y(4260) decays and the recoil spectra of light mesons or light meson pairs.

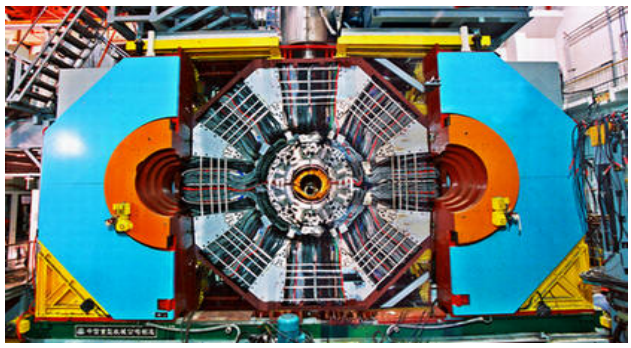

Figure 2: The BES3 detector at IHEP Beijing/China.

GlueX

The GlueX-Experiment in Hall-D at CEBAF at Jefferson National Lab (USA) facilitates a (polarized) photon-beam to produce normal and exotic hadrons of a proton or nuclear target and was successfully commissioned and started physics data taking in 2016.

GlueX will use the coherent bremsstrahlung technique to produce a linearly polarized photon beam. A solenoid-based hermetic detector will be used to collected data on

DOI:10.15120/GR-2017-1

meson production and decays with statistics after the first year of running that will exceed the current photoproduction data in hand by several orders of magnitude. These data will also be used to study the spectrum of conventional mesons, including the poorly understood excited vector mesons and strangeonium. In order to reach the ideal photon energy of 9 GeV for this mapping of the exotic spectrum, 12 GeV electrons are required. Thus, GlueX is part for the JLab12 upgrade being finished recently and is ready for regular operation.

Hybrid mesons, and in particular exotic hybrid mesons, provide the ideal laboratory for testing QCD in the confinement regime since these mesons explicitly manifest the gluonic degrees of freedom. Photoproduction is expected to be particularly effective in producing exotic hybrids. This is due to the fact, that the quantum numbers of the lowest predicted excited modes of the flux tube, when combined with that of a virtual photon, yield exotic JPC. However, there is little data on the photoproduction of light mesons.

The emphasis of the GSI group in GlueX is the development of the GlueX-DIRC together with MIT, JLab, and Indiana University and the search for exotic strangeonium systems and the determination of their static properties, like spin-parity and decays. Significant progress was achieved in 2015 for many systems, which are summarized in the following paragraphs.

The current plan is to place BABAR DIRC bar boxes in front of forward calorimeter to allow for additional PID capabilities. The GlueX PID requirements are rather similar to those of BABAR, thus the concept is comparable but updated in some important technical aspects. Currently the work is focused on prototype optics and software and R&D shall be finalized in 2017.

Figure 3: The GlueX detector at Jefferson Lab.

DOI:10.15120/GR-2017-1

Search for charmonium-like (exotic) states with the BESIII experiment

F. Nerling[1,2], *K. Götzen*[1], *R. Kliemt*[3], *S. Nakhoul*[1,2], *K. Peters*[1,2], *and the BESIII Collaboration*[4]
[1]Goethe Univ. Frankfurt, Germany; [2]GSI, Darmstadt, Germany; [3]HIM, Mainz, Germany; [4]IHEP, Beijing, China

The BESIII experiment [1] at BEPCII at IHEP in Beijing/China has collected the world largest data sets in the τ-charm region, and it is well suited to cover a rich hadron physics programme, including charmonium and open-charm spectroscopy, R-scan and electromagnetic form factor measurements. Especially in the "XYZ" region above 3.8 GeV, BESIII has accumulated unique data sets to explore the still-unexplained XYZ states.

For understanding the nature of some of these states, a precise measurement of the line-shapes is needed as it is only possible in a direct formation experiment. Moreover, complete multiplets also of higher spin states are mandatory. As discussed earlier [2], the $p\bar{p}$ annihilation experiment PANDA/FAIR will provide unique and complementary measurements in view of both, see e.g. [3], as a matter of principle not possible with an e^+e^- annihilation experiment like BESIII.

Apart from the first charged charmonium-like state $Z_c(3900)$ discovered at BESIII in the reaction $e^+e^- \to J/\psi\pi^+\pi^-$ at $\sqrt{s} = 4.26$ GeV, corresponding to the the $Y(4260)$ resonance, also a second has been observed, the $Z_c(4020)^\pm$ decaying to $h_c\pi^\pm$. Together with the neutral isospin partners decaying to $J/\psi\pi^0$ and $h_c\pi^0$, respectively, two isospin triplets have been established [4]. Further decay channels are under investigation. At GSI, we are exploring possible decay channels of the Z_c states involving η_c together with various recoil particles — first results are in preparation for internal review and planned to be published soon.

The $Y(4260)$ and the $Y(4360)$ had firstly been observed using initial state radiation (ISR) decaying to $J/\psi\pi^+\pi^-$ and $\psi(2S)\pi^+\pi^-$, respectively, by BABAR [5]. Based on the "high luminosity" (8.2 fb^{-1}) and the "low luminosity" (0.8 fb^{-1}) XYZ data, we performed a precision measurement of the energy dependent cross-section $\sigma(e^+e^- \to J/\psi\pi^+\pi^-)$ in the energy range of $3.77 < E_{\rm cms} < 4.60$ GeV recently published [6]. The result obtained by a simultaneous fit to both data sets is shown in Fig. 1. The signal yields are determined using an unbinned maximum-likelihood fit ("high luminosity" XYZ data) and a simple counting method ("low luminosity" scan data), for the latter the background counts from sidebands are subtracted. The cross-section appears inconsistent with a single peak just for the $Y(4260)$ — two resonances to describe two peaks is favoured over one by the data at high statistical significance of more than 7 σ. Given the much larger statistics by BESIII, the $Y(4260)$ and the $Y(4360)$ are resolved here for the first time, and the $Y(4360)$ is first observed decaying to $J/\psi\pi^+\pi^-$. At GSI, we contribute to the clarification of this important cross-section via the inclusive measurement of $Y(4260) \to J/\psi\pi^+\pi^-, h_c\pi^+\pi^-$ and further recoil systems. First promising results will be presented internally to the collaboration still this year.

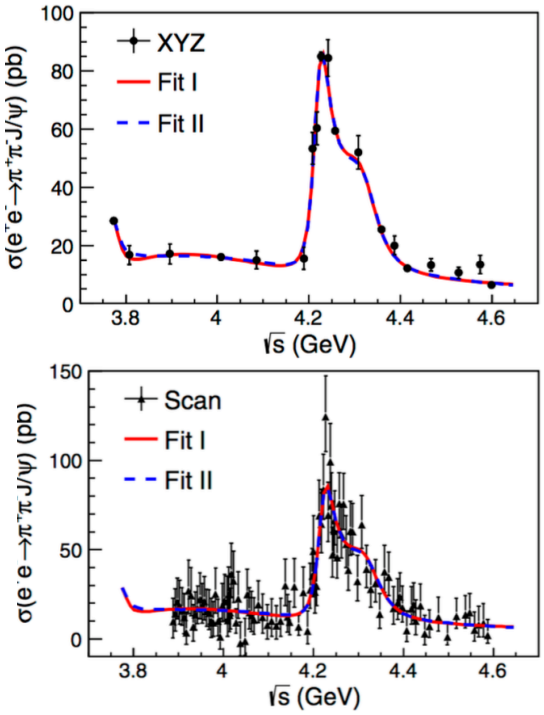

Figure 1: Precision cross-section measurement of the $J/\psi\pi^+\pi^-$ production in e^+e^- annihilation as obtained from a simultaneous fit to both: "high luminosity" (top) XYZ data and "low luminosity" (down) scan data (reprinted with kind permission of APS from [6], copyright 2017 American Physical Society).

Before PANDA starts, there is the great chance to complete the observation of entire (low spin) multiplets and to explore further decay channels of XYZ states with BESIII, offering a perfect preparation of physics analysis of PANDA data, and thus keeping and gaining important experience on this newly very active field of research.

References

[1] BESIII Collab., M. Ablikim *et al.*, NIM **A614** (2010) 345.
[2] F. Nerling *et al.*, GSI Scientific Report 2015-1, (2015) 117.
[3] F. Nerling *et al.*, *A precision line-shape measurement of the $X(3872)$ with PANDA/FAIR*, this Scientific Report (2017).
[4] BESIII Collab., M. Ablikim *et al.*, PRL **110** (2013) 252001, and PRL **111** (2013) 242002; PRL **115** (2015) 112003, and PRL **113** (2014) 212002.
[5] BABAR Collab., B. Aubert *et al.*, PRL 95 (2005) 142001, and PRL 98 (2007) 212001.
[6] BESIII Collab., M. Ablikin *et al.*, PRL 118 (2017) 092001.

DOI:10.15120/GR-2017-1

Search for exotic mesons with the GlueX/JLab experiment

F. Nerling[1,2], K. Götzen[2], A. Hamdi[1,2], K. Peters[1,2], and the GlueX Collaboration[3]
[1]Goethe Univ. Frankfurt, Germany; [2]GSI, Darmstadt, Germany; [3]Jefferson Lab, Newport News, USA

The GlueX experiment is located at the Jefferson National Accelerator Facility (JLab). The primary focus is to understand the nature of confinement in QCD by mapping the spectrum of exotic mesons generated by the excitation of the gluonic field binding the quarks. Using photoproduction to produce exotic states, the experiment probes new areas. The GlueX detector was installed in the new Hall-D at JLab as part of the 12 GeV energy accelerator upgrade. After the first commissioning run in 2014, and first received 12 GeV electrons in 2015, GlueX has begun first physics data taking in 2016.

As compared to $\bar{p}p$ and e^+e^- annihilation, cf. [1], and also pion beam experiments like COMPASS, photoproduction represents another complementary probe and production mechanism for (exotic) hadrons. Given the overlap in accessible invariant masses in GlueX (up to $\sim$2.5 GeV/c^2) and PANDA (up to $\sim$5.5 GeV/c^2, also BESIII up to $\sim$4.6 GeV/c^2), the charmonium, strange and light spectroscopy studies planned with PANDA are complementarily completed with the strange/light quark sector the GlueX experiment is designed for.

At GSI, we are especially interested in searches for tetraquark and hybrid candidates decaying to $K\bar{K}\pi(\pi)$ final states, for which a good K/π identification is needed that later will be improved by the major detector upgrade of an additional DIRC detector we are majorly involved in, see also [2]. Apart from planned physics analysis, a present service work task is to improve the dE/dx measurements for particle identification — first promising results have been obtained and appreciated by the collaboration.

Based on the spring 2016 data, a measurements of the photon beam asymmetry Σ for the reactions $\vec{\gamma}p \to p\pi^0$ and $\vec{\gamma}p \to p\eta$ using a 9 GeV linearly-polarised, tagged photon beam incident on a liquid hydrogen target in Hall-D has been performed, recently accepted for publication [3], and representing not only the first measurement by GlueX but also the first one with a 12 GeV electron beam at JLab[1].

The resultant asymmetries (Fig. 1) as a function of the proton momentum transfer have been measured at higher precision than previous π measurements and are the first η measurements in this energy regime [3]. The black filled circles are the measured asymmetries, the black error bars represent the combined statistical and systematic uncertainties, and the grey bars indicate the uncorrelated systematic errors. Also shown are the previous SLAC results at 10 GeV (blue open circles) along with various Regge theory calculations. The results are compared with theoretical predictions based on t-channel, quasi-particle exchange

[1]12 GeV electrons are required to reach the photon energy of 9 GeV.

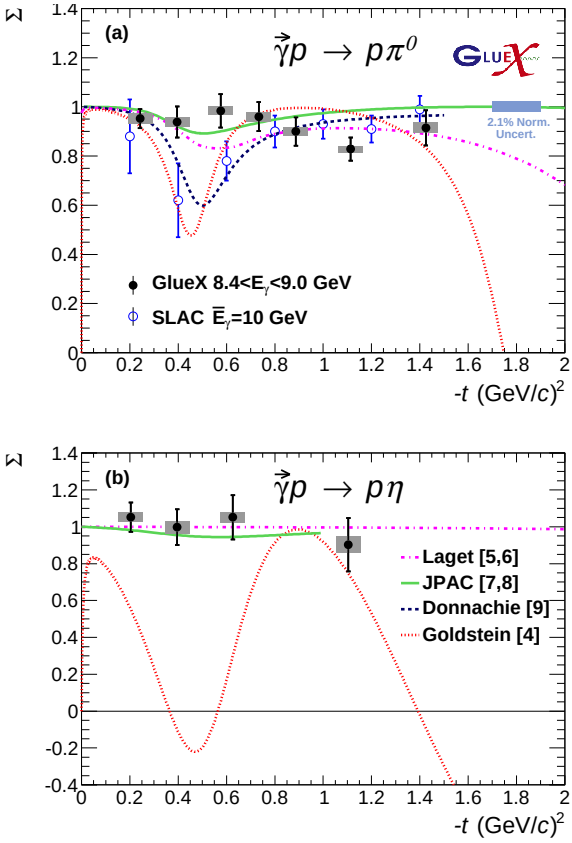

Figure 1: Beam asymmetry Σ for (a) $\vec{\gamma}p \to \pi^0$ and (b) $\vec{\gamma}p \to p\eta$ (reprinted with kind permission of APS from [3], copyright 2017 American Physical Society).

and constrain the axial-vector component of the neutral meson production mechanism in these models.

Before PANDA starts, there is the great chance to already explore the strangeonium spectrum and search for exotic hybrid states using photoproduction, offering a perfect preparation of physics analysis of PANDA data, including reconstruction software for e.g. particle identification, and thus keeping and gaining important experience.

References

[1] F. Nerling, *et al.*, *A precision lineshape measurement of the $X(3872)$ with PANDA/FAIR*; and F. Nerling, *et al.*, *Search for charmonium-like (exotic) states with the BESIII experiment*, this Scientific Report (2017).

[2] R. Dzhygadlo, *et al.*, *The DIRC Upgrade for the GlueX Experiment*, DPG Münster (2017).

[3] GlueX Collab., H. Al Ghoul, *et al.*, Phys. Rev. C95 (2017) 042207, DOI:https://doi.org/10.1103/PhysRevC.95.042201.

DOI:10.15120/GR-2017-1

DIRC-based PID for the EIC Central Detector*

R. Dzhygadlo† [1], *K. Peters*[1,2], *C. Schwarz*[1], *and J. Schwiening*[1]
[1]GSI, Darmstadt, Germany; [2]Goethe-Universität, Frankfurt, Germany

The Detector of Internally Reflected Cherenkov light (DIRC) is expected to be a key element of the PID system for the future Electron-Ion Collider (EIC) central detector [1]. The EIC PID consortium (eRD14 [2]) investigates the feasibility of a high-performance DIRC that would extend the momentum coverage well beyond state-of-the-art, providing 3 standard deviations separation of π/K up to 6 GeV/c, e/K up to 1.8 GeV/c and p/K up to 10 GeV/c.

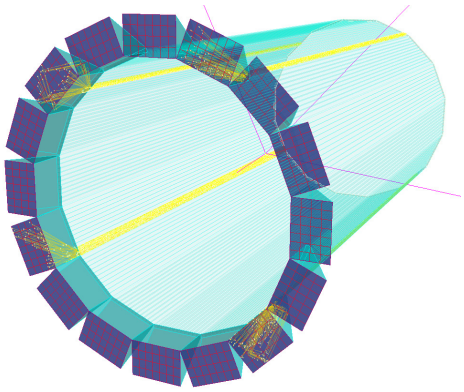

Figure 1: Geant-based simulation of the EIC DIRC using narrow bars as radiators together with prisms as expansion volumes. Cherenkov photon trajectories from 4 GeV/c kaons are shown in yellow.

Geant4 simulations are used to optimize the design configuration of the DIRC counter in terms of the performance and the best integration with the EIC detector. Fig. 1 shows the Geant4 implementation of the baseline design of a DIRC with narrow bars, sherical focusing lenses, and compact fused silica prisms. Possible improvements on the current DIRC design include multi-anode sensors with smaller pixels, providing fast single-photon timing in high magnetic fields, and chromatic dispersion mitigation.

Two different reconstruction approaches have been developed to evaluate the detector resolution for various design optimizations [3]. An example of such an optimization is shown in Fig. 2, where the impact of the pixel size on the Cherenkov angle resolution per photon (SPR) is shown for several polar angles.

To evaluate the PID performance of the design the track Cherenkov angle resolution σ_{θ_C} is defined as $\sigma^2_{\theta_C} = \mathrm{SPR}^2/N_\gamma + \sigma^2_{track}$, where N_γ is the number of detected photons per track and σ_{track} is the uncertainty of the track direction in the DIRC, dominated by multiple scattering and the resolution of the tracking detectors.

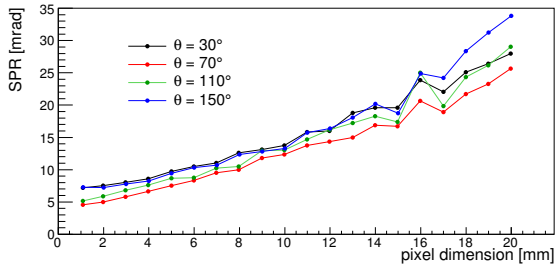

Figure 2: Single photon Cherenkov angle resolution as a function of the pixel dimension. Colors indicate different polar angles of the charged particle.

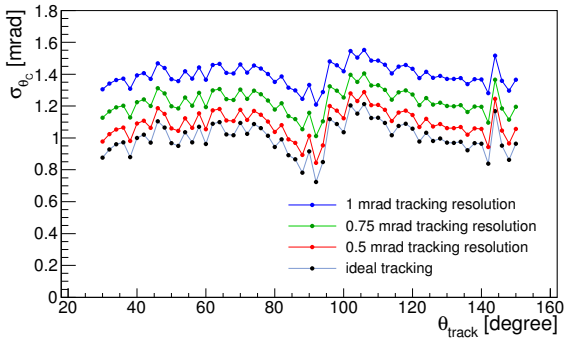

Figure 3: Cherenkov angle resolution per particle for different tracking resolutions.

The optimized design, featuring pixels of 3 mm size, narrow radiators, and 3-layer spherical lenses, is expected to achieve a Cherenkov angle resolution per particle of 1.2 mrad or better for all polar angles, assuming a tracking resolution of 0.5 mrad (see Fig. 3). This corresponds to at least 3 s.d. π/K separation up to 6 GeV/c momentum for forward-going particles, which satisfies the DIRC@EIC performance goal.

References

[1] A. Adare et al., arXiv:1402.1209 [nucl-ex]

[2] G. Kalicy et al., 2016 JINST 11 C07015

[3] R. Dzhygadlo et al., Nucl. Instr. and Meth. Phys. Res A 766 (2014) 263

* Work supported by HGS-HIRe, HIC for FAIR, and by BNL under eRD4 and eRD14.

† R.Dzhygadlo@gsi.de

Performance of the PANDA Barrel DIRC Prototype*

C. Schwarz[†1], *J. Schwiening*[‡1], *A. Ali*[1,2], *A. Belias*[1], *R. Dzhygadlo*[1], *A. Gerhardt*[1], *M. Krebs*[1,2], *D. Lehmann*[1], *K. Peters*[1,2], *G. Schepers*[1], *and M. Traxler*[1]

[1]GSI, Darmstadt, Germany; [2]Goethe Universität Frankfurt, Germany

Charged Particle Identification (PID) for the barrel section of the PANDA target spectrometer [1, 2] will be provided by a DIRC (Detection of Internally Reflected Cherenkov light) detector. This counter will cover the angular range of 22–140° and cleanly separate charged pions from kaons for momenta up to 3.5 GeV/c with a separation power of at least 3 standard deviations (s.d.).

The design of the PANDA Barrel DIRC detector is based on the successful BABAR DIRC [3] and the R&D for the SuperB FDIRC with several important improvements to optimize the performance for PANDA, such as a focusing lens system, fast timing, and a compact synthetic fused silica prism as expansion region.

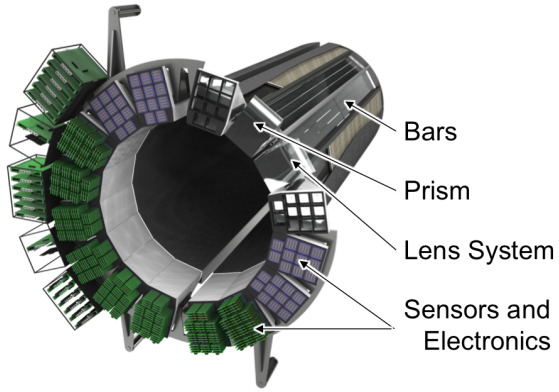

Figure 1: The PANDA Barrel DIRC baseline design in the Geant4 simulation.

In the PANDA Barrel DIRC baseline design, shown in Fig. 1, the barrel of 47.6 cm radius comprises 16 flat sections with 3 fused synthetic silica radiator bars ($17 \times 53 \times 2400$ mm^3) each. A flat mirror is attached to the forward end of each bar to reflect photons towards the readout end, where they are focused by a multi-component spherical lens onto the back of a 30 cm-deep solid synthetic fused silica prism, serving as expansion volume. An array of lifetime-enhanced Microchannel Plate Photomultiplier Tubes (MCP-PMTs) is used to detect the photons and measure their arrival time with a precision of about 100 ps in the magnetic field of about 1 T.

Due to the tight optical and mechanical tolerances, the cost of radiator fabrication is, together with the cost of the photon detectors, the dominant contribution to the Barrel DIRC construction cost. Replacing the 3 radiator bars per section by one 16 cm-wide plate would significantly reduce the radiator fabrication cost since fewer pieces have to be produced. However, the optical quality of such plates and the PID performance of a design with wide plates need to be validated before this option can be considered for PANDA.

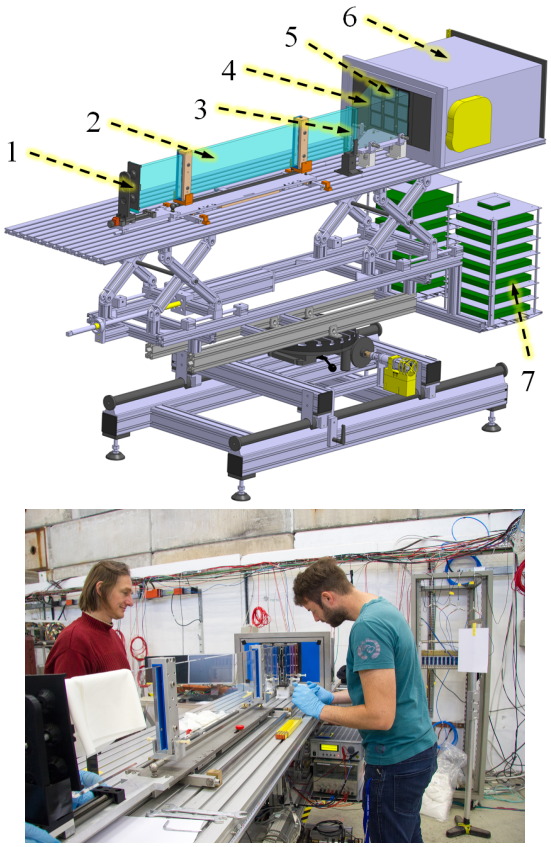

Figure 2: *T*op: Schematic of the prototype used at CERN in 2016, with 1: flat mirror, 2: radiator plate, 3: lens, 4: expansion volume, 5: array of 3×3 MCP-PMTs, 6: readout unit, and 7: TRB stack. *B*ottom: Photograph of the prototype in the T9 beamline.

In the fall of 2016 the latest Barrel DIRC prototype, shown in Fig. 2, was evaluated in a mixed hadron beam at the CERN PS. The setup comprised a synthetic fused silica plate ($17 \times 175 \times 1225$ mm^3) as radiator with an optional 2-layer cylindrical lens attached to one end and a flat mirror to the other end as well as a large synthetic fused silica prism as expansion volume. The plate, lens, and prism were coupled to each other using optical grease and placed into a light-tight container on a remote-controlled rotating stage.

*Work supported by HGS-HIRe, HIC for FAIR, and BNL grant eRD14.

†C.Schwarz@gsi.de

‡J.Schwiening@gsi.de

DOI:10.15120/GR-2017-1

The location and arrival time of photons were measured with a precision of about 2 mm and 180 ps, respectively, using an array of 9 PHOTONIS XP85012 MCP-PMTs, coupled with optical grease to the back surface of the prism. The data acquisition was performed using PADIWA frontend cards and TRB3 boards [4].

During 18 days of data taking a total of some 4.9×10^8 triggers were recorded in the mixed hadron beam at the T9 area of the CERN PS. Most of the time the beam was set to a π/p momentum of 7 GeV/c and to beam/plate polar angles below 40° to evaluate the π/K separation performance[1] of the wide plate for the high momentum range of final state particles in the forward direction of PANDA, the most challenging phase space region for the Barrel DIRC.

The time-based imaging method was used to determine the PID performance of the wide plate, in particular the π/p separation power. This method is based on the approach used by the Belle II Time-Of-Propagation (TOP) counter [5] and compares the measured arrival time of Cherenkov photons in each single event to the expected photon arrival time for every pixel and for every particle hypothesis, yielding the PID likelihoods. Using a time-of-flight system to cleanly tag the pions and protons in the beam, the log-likelihood difference for the pion and proton hypotheses were calculated for the two tagged samples.

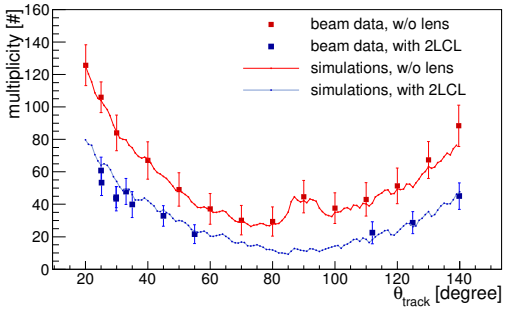

Figure 3: Photon yield as a function of the track polar angle for the wide plate without lens (red) and with the 2-layer cylindrical lens ("2LCL", blue) for tagged protons at 7 GeV/c beam momentum in data (points) and Geant4 prototype simulation (lines).

The reconstructed photon yield as a function of the track polar angle is shown in Fig. 3 for the configuration with the wide radiator plate, with and without the 2-layer cylindrical lens. The simulation describes the experimental data well, with remaining differences of up to 10%. The photon yield for the 2-layer cylindrical lens is, as expected, substantially lower than the yield for the plate coupled directly to the prism. While most of this difference is due to the loss of photons inside the lens, a significant fraction of the photons are lost at the interface of the lens and the prism due to a size mismatch between the prototype lens and the synthetic fused silica prism.

[1]The π/p Cherenkov angle difference at 7 GeV/c (8.1 mrad) is close to the π/K Cherenkov angle difference at 3.5 GeV/c (8.5 mrad).

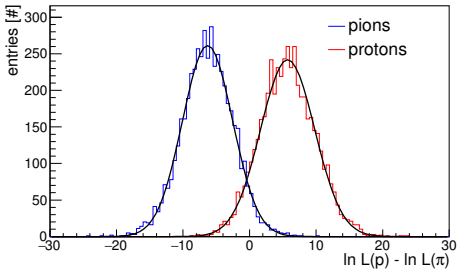

Figure 4: Proton-pion log-likelihood difference distributions for proton-tagged (red) and pion-tagged (blue) beam events from 2016 as a result of the time-based imaging method. The distributions are for the wide plate with the 2-layer cylindrical lens, a beam with 7 GeV/c momentum and 25° polar angle. The separation power value from the Gaussian fits is 3.1 ± 0.1 s.d..

The result of the unbinned likelihood calculation for the plate with the 2-layer cylindrical lens at 7 GeV/c momentum and 25° polar angle is shown in Fig. 4. The observed π/p separation power is $3.1^{+0.1}_{-0.1}$ s.d., in good agreement with the Geant4 simulation of the prototype, which predicts a $3.3^{+0.1}_{-0.1}$ s.d. separation value.

The result of the 2016 beam test validates the plate with a cylindrical focusing lens as a potential design for the PANDA Barrel DIRC. However, the PID performance of the previous prototype, which used a narrow bar and a 3-layer spherical lens, was significantly better during a beam test at CERN in 2015 [6]. Furthermore, the design with narrow bars provides a larger margin for error and can be expected to have a significant performance advantage during the initial phase of the PANDA experiment due to the dependence of the wide plate geometry on excellent timing precision. Therefore, the geometry with narrow bars and 3-layer spherical lenses was selected as the baseline design for the PANDA Barrel DIRC.

References

[1] PANDA Collaboration, *Technical Progress Report, FAIR-ESAC/Pbar*, (2005).

[2] PANDA Collaboration, *Physics Performance Report for PANDA: Strong Interaction Studies with Antiprotons*, arxiv:0903.3905.

[3] I. Adam et al., *Nucl. Instr. and Meth. Res. Sect. A* **538** (2005) 281.

[4] M. Cardinali et al., *Nucl. Instr. and Meth. Res. Sect. A* **766** (2014) 231

[5] M. Staric et al., *Nucl. Instr. and Meth. Res. Sect. A* **639** (2011) 252

[6] J. Schwiening et al., "The PANDA Barrel DIRC," 9th International Workshop on Ring Imaging Cherenkov Detectors (RICH 2016).

Measurement results of the optical quality of prototype radiators for the PANDA Barrel DIRC detector*

M. Krebs[†1,2], *K. Peters*[1,2], *G. Schepers*[‡1], *C. Schwarz*[1], *and J. Schwiening*[1]
[1]GSI, Darmstadt, Germany; [2]Goethe-Universität, Frankfurt, Germany

In the barrel region of the target spectrometer of the PANDA experiment, a fast focusing Cherenkov counter using the DIRC (Detection of Internally Reflected Cherenkov light) principle will provide charged hadronic particle identification (PID). In order to meet the PANDA PID requirements, the Barrel DIRC has to provide precise measurements of the Cherenkov angle, which is the crucial quantity for identifying charged particles that traversed the radiators. The Cherenkov photons propagate through the radiators by total internal reflection until they reach the detection plane, which is equipped with an array of photon sensors.

The Cherenkov angle resolution and the photon yield are critical figures of merit for the PID performance of the DIRC. Thus the radiators, rectangular bars made from synthetic fused silica, have to fulfill very strict optical and geometrical requirements as Cherenkov photons can undergo up to several hundred reflections before they reach the readout end. To ensure high transport efficiency and maintain the magnitude of the Cherenkov angle during all reflections, properties such as highly polished surfaces, parallelism of the sides, and sharp corners have to meet the requirements.

The optical quality of the radiators is assured with two setups, measuring the roughness of surfaces (Fig. 1) as well as the rectangularity and parallelism (Fig. 3). In order to determine the surface roughness of one radiator, it is necessary to measure firstly the bulk transmission and secondly the transmitted intensity after many internal reflections. Hence, an optical setup using lasers of four different wavelengths and a computer-controlled motion system is operated in the optics lab. For the bulk transmission measurement, the laser beam is coupled straight into the radiator measuring the attenuation of the intensity in the bulk material. This intensity loss is related to the attenuation length reaching several hundred meters for synthetic fused silica in the visible wavelength range.

Depending on the length and orientation of the radiator, the beam is reflected from the faces (wide sides) up to 50 times, until it leaves the bar and hits the (value) photo diode. A reference diode is used to correct for fluctuations from the laser system. The fraction of light lost during all internal reflections is translated into a reduction of the coefficient of total internal reflection, which in turn can be related to the surface roughness via the scalar scattering theory. An extensive prototype radiator program had been started resulting in about a total of 30 prototype radiators from various manufacturers. These manufacturers use different materials and techniques for radiator production, hence quality assurance measurements at GSI are needed to qualify vendors for the production stage. Figure 2 shows results for the reflection coefficients from different prototype bars and plates built by five manufacturers such as Carl Zeiss Jena GmbH, InSync Inc., Nikon Corp., Zygo Corp., and Aperture Optical Sciences/Okamoto. For instance, showing a surface roughness of 3 Å, InSync # 2 (InSync Inc.) exceeds the PANDA Barrel DIRC radiator specifications of 10 Å for the large sides of the radiator. Nikon Corp. and InSync Inc., who have built the prototype plates, also fulfill the PANDA Barrel DIRC specifications for the roughness of the surfaces. The measured reflection coefficients (points) and expectations from scalar scattering theory (lines) can be seen in Fig. 2. The surface roughness values are found to be in good agreement with the quality assurance data from the vendors. As vendors measure the surface roughness using an interferometric approach, they can only determine the outer roughness of the radiator surfaces, while the inner surface roughness is more important for DIRC applications as photons propagate via total internal reflection. Expanding the Barrel DIRC optical setup by adding a 266 nm (ultra-violet) laser, lead to an increase in sensitivity of measuring possible sub-surface damage inside the material. Yet the 266 nm laser was only available for the plate measurements. The cause for the deviation of the 266 nm data points from the prediction of the scalar scattering theory is under investigation.

The parallelism and squareness of the radiator sides and faces have to fulfill strict requirements, too. Simulation studies showed that the deviation of the side-to-face angles $\Delta\Phi$ from the nominal 90° value must not exceed 0.25 mrad and the non-parallelism $\Delta\Theta$ required to be smaller than 0.5 mrad to keep the angular smearing due to the large number of reflections as small as possible. For the quality assurance of the rectangularity and parallelism of the radiator surfaces, a Nikon 6D autocollimator (see Figs. 3 and 4) is used. This optical instrument has the capability to measure small angular displacements with an accuracy of 0.002 mrad without making contact with the very sensitive surfaces of the radiators. Fig. 3 shows a sketch of the autocollimator setup and the principle of the measurement. In combination with a pentaprism, the deviation of the angle between a face and a side of the radiator

* Work supported by HGS-HIRe
† m.krebs@gsi.de
‡ g.schepers@gsi.de

DOI:10.15120/GR-2017-1

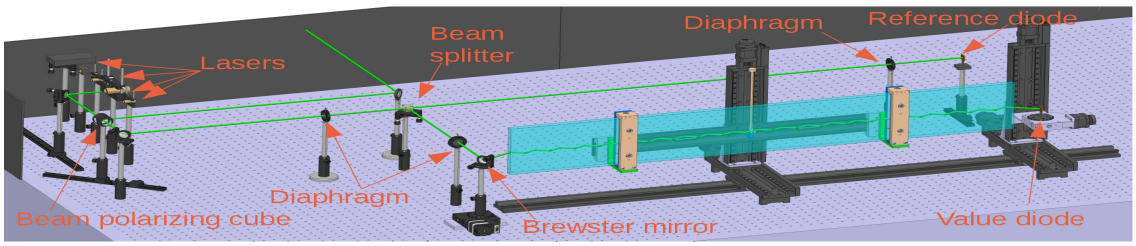

Figure 1: Catia drawing of the setup used for the surface roughness measurement of the Barrel DIRC radiators. The setup accommodates the wide plate radiator in this example.

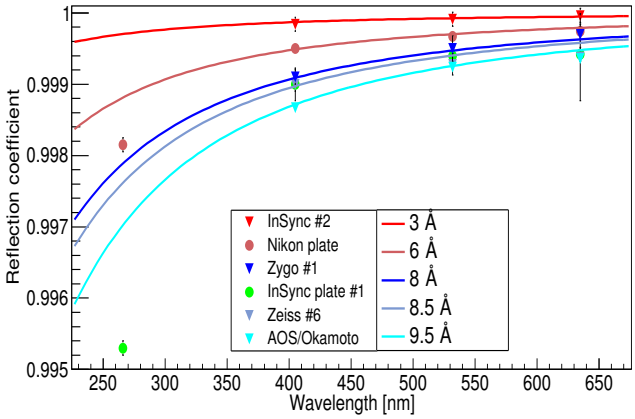

Figure 2: Reflection coefficients for several prototype radiators including 2 wide plates. The lines represent the expected reflection coefficients for defined surface roughness values from the scalar scattering theory.

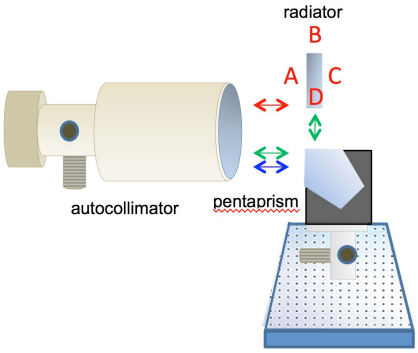

Figure 3: Measurement principle for obtaining the squareness and parallelism of the prototype radiators.

from 90° can be measured precisely. The parallelism of two sides (faces or ends) behind eachother can be read directly. Since each property is read off as a deviation of two simultaneous measured lines additional systematic errors are excluded. The setup allows to place the bars and autocollimator independently from each other and thus enables the detection of variations of the squareness and parallelism (thickness variation). So far, two bars were studied in detail, including measurements at several points along the length of the bars, and the results are shown in Tab. 1. The first prototype bar measured in this setup was produced by Zeiss and all angles were found to deviate from the nominal 90° value by less than 0.024 mrad in agreement with the manufacturers data, thus meeting the production specifications and proving the quality assurance data of the company. While the Zeiss bar is found to have excellent values of non-squareness and parallelism, easily meeting the PANDA Barrel DIRC requirements, the LZOS bar fails the $\Delta\Phi$ production tolerances by a factor of 2-4. The remaining prototype bars/plates will be similarly evaluated in the two setups in the future.

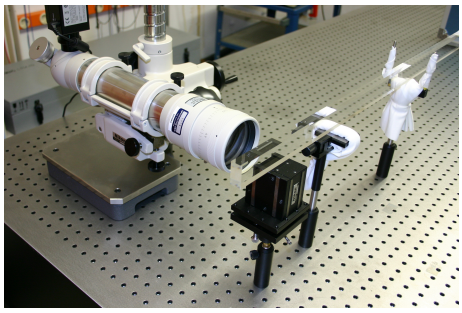

Figure 4: Photograph of the autocollimator setup in the lab.

Angle between sides	Zeiss $\Delta\Phi$ [mrad]	LZOS $\Delta\Phi$ [mrad]
A/B	0.073 ± 0.005	-1.098 ± 0.005
B/C	0.036 ± 0.005	1.037 ± 0.005
C/D	0.007 ± 0.005	-0.541 ± 0.005
D/A	0.075 ± 0.005	0.582 ± 0.005
	$\Delta\Theta$ [mrad]	$\Delta\Theta$ [mrad]
A/C	0.023 ± 0.005	0.041 ± 0.005
B/D	0.030 ± 0.005	0.492 ± 0.005

Table 1: Results from the autocollimator measurements for prototype bars from LZOS and Zeiss

References

[1] M. Krebs, "Quality Assurance Measurements for the PANDA Barrel DIRC Quartz Radiators", HK27.55, DPG Spring Meeting, Muenster, Germany, March 2017

[2] J. Schwiening for the PANDA Cherenkov group, "The PANDA Barrel DIRC Detector", RICH2016, Bled, Slovenija, September 2016

[3] R. Hohler, "Prototyp-Radiatoren eines Barrel-DIRC für das PANDA-Experiment", PhD thesis, Frankfurt, Germany, 2011

DOI:10.15120/GR-2017-1

Latest results with microchannel plate PMTs*

A. Lehmann†[1], *M. Böhm*[1], *W. Eyrich*[1], *D. Miehling*[1], *M. Pfaffinger*[1], *S. Stelter*[1], *and F. Uhlig*[1]

[1]Physikalisches Institut IV, Universität Erlangen-Nürnberg, Erwin-Rommel-Str. 1, D-91058 Erlangen

Microchannel-plate (MCP) PMTs will be the most adequate sensors for the PANDA DIRC detectors. They are available as multi-anode devices (e.g., 8×8 pixels) with a sensitive area of 2"×2" and an active area ratio of up to 80%. With ≤10 μm pores they are operable in magnetic fields of 2 Tesla and they provide an excellent time resolution of <50 ps. For a long time the main drawback of MCP-PMTs was severe photo cathode (PC) aging due to ion feedback which led to very short lifetimes. Recently this obstacle has been overcome by coating the MCPs with an atomic layer deposition (ALD) technique. This significantly reduces the flux of ions and the lifetime of MCP-PMTs was increased drastically by a factor of >50 [1].

The lifetime of an MCP-PMT is usually determined by measuring its quantum efficiency (QE) as a function of the integrated anode charge (IAC). In the last years our group has done long-term illuminations of all available lifetime-enhanced MCP-PMT models with the goal of measuring their lifetime under comparable conditions. Every few weeks the gains, dark count rates and QE spectra are measured and plotted as a function of the IAC. In addition a QE scan across the PC surface is performed every few months. The QE results at 400 nm are shown in Fig. 1 for all ALD-coated MCP-PMTs and compared to one tube with a protection film instead of ALD. This illustrates that the 2" XP85112 and the 1" R10754X MCP-PMTs are performing well, while the recently developed 2" Hamamatsu R13266 prototype tubes still need more tuning. The best performing MCP-PMT is currently the PHOTONIS 9001393 with two ALD layers; it reaches 12 C/cm^2 without a deterioration in any performance parameter. At full luminosity this tube would survive 24 years in the PANDA barrel DIRC.

The performance parameters of four new 2" Hamamatsu R13266 MCP-PMTs were further investigated (see also [2]) and in August 2016 they were included in the lifetime setup. On the negative side we observed that the QE across the PC is not yet homogeneous, the gain is varying by almost a factor 10 across the active surface, and the rate capability is only <10^6 photons/cm^2. On the positive side we found a very low dark count rate of well below 100 Hz/cm^2 at most positions and an excellent time resolution of <50 ps even including tails from recoil electrons [3].

A special focus was put on the behavior of the new R13266 inside a magnetic field. Using the high granularity MCP-PMT (128×6 anode pixels) the behavior of the charge cloud was studied. We observed that the charge cloud width at the anode plane decreases from 0.7 at no B-field to 0.3 mm at 1.0 Tesla. The cross talk among the anodes turned out to be problematic in this tube and requires further studies. By tilting the PMT axis against the B-field direction at an angle ϕ the Lorentz shift inside the MCP-PMT was determined. With an appropriate setup the cloud centroid shifts along the direction of the high pixelation. By calculating the charge weighted position of the charge cloud the Lorentz shift can be determined. It is specific to every MCP-PMT type and depends upon the inner structure of the tube. In the case of the Hamamatsu R13266-M768 MCP-PMT we observe a maximum shift of 1.7 mm at ϕ = 30° (see Fig. 2). This corresponds to 4 pixels and has to be taken into account in a later analysis of experimental data.

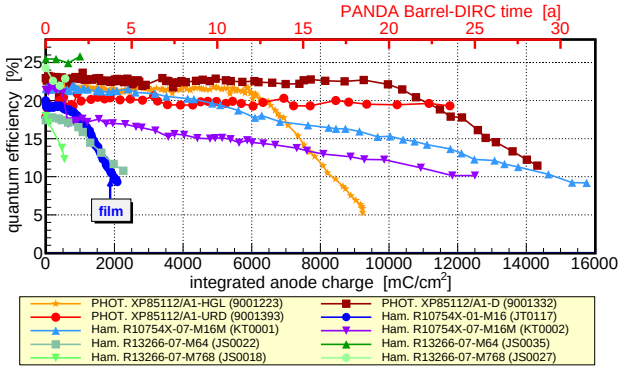

Figure 1: Results of our lifetime measurements for different ALD MCP-PMTs (compared to a tube with film): QE as a function of the IAC at 400 nm (status Jan. 2017).

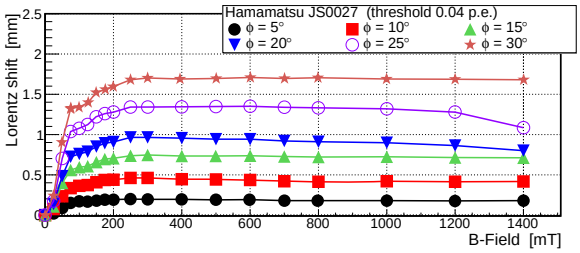

Figure 2: Lorentz shift for different tilt angles ϕ measured inside the 6×128 pixel Hamamatsu R13266 MCP-PMT.

References

[1] A. Lehmann et al., Nucl. Instr. and Meth. A 845 (2017) 570

[2] A. Lehmann et al., https://doi.org/10.15120/GR-2016-1, p. 89

[3] A. Lehmann et al., http://dx.doi.org/10.1016/j.nima.2016.12.063

* Work supported by GSI (contracts EREYRI1416 and ERANTO1419) and BMBF

† Albert.Lehmann@physik.uni-erlangen.de

DOI:10.15120/GR-2017-1

Thickness determination at the cluster-jet target for $\overline{\mathrm{P}}$ANDA*

A.-K. Hergemöller[†1], *D. Bonaventura*[1], *S. Grieser*[1], *B. Hetz*[1], *M. Seifert*[1], *and A. Khoukaz*[1]
[1]Westfälische Wilhelms-Universität, Münster, Germany

The first internal target which will be operated at the $\bar{\mathrm{P}}$ANDA experiment at FAIR is a cluster-jet target. The final $\bar{\mathrm{P}}$ANDA cluster source has been built up [1] in a $\bar{\mathrm{P}}$ANDA-like test setup in combination with the final cluster target beam dump at the University of Münster and has successfully been set into operation as well. Within this kind of target the cluster beam itself is formed by the expansion of pre-cooled gases within a Laval nozzle (further information on Laval nozzles can be found in [2]). To prepare the cluster beam from the surrounding gas-jet two moveable orifices are used, the skimmer and the collimator. Above that, the cluster source includes a nozzle tilting system consisting of a spherical joint with the narrowest point of the Laval nozzle as point of rotation (for more information see [3]). With this feature it is possible to extract highly intense core beams [4], which correspond to regions of higher thicknesses within the cluster beam. For $\bar{\mathrm{P}}$ANDA a target thickness of more than $10^{15}\,\frac{\mathrm{atoms}}{\mathrm{cm}^2}$ in a distance of $2.2\,\mathrm{m}$ behind the nozzle is required to achieve the designated luminosity. With the target prototype, operating successfully for years at the University of Münster, it is routinely possible to provide these thicknesses in the required distance. To determine the thickness at the final cluster-jet target for $\bar{\mathrm{P}}$ANDA two different monitor systems are included in the setup. The first one, which will be available later at the $\bar{\mathrm{P}}$ANDA experiment, is an optical monitor system installed in the so called transition vacuum chamber in a distance of $37\,\mathrm{cm}$ behind the Laval nozzle. There, the cluster beam is illuminated by a diode laser and is observed by two CCD cameras, which are installed in an angle of 90° to each other. The resulting images of the cluster beam yield information on the position and width of the cluster beam and the intensity distribution corresponds to the relative thickness distribution [5]. To determine the

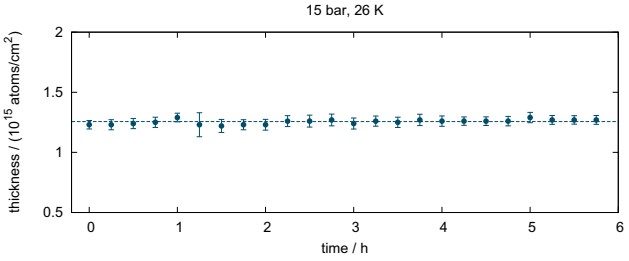

Figure 1: Hydrogen cluster beam stability at stagnation conditions of $15\,\mathrm{bar}$ and $26\,\mathrm{K}$ at the nozzle inlet.

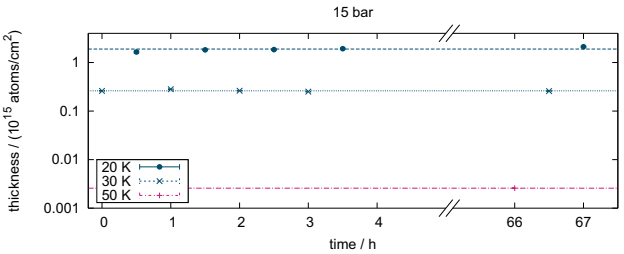

Figure 2: Stability and reproducibility of the target thickness.

absolute target thickness an additional monitor system has been developed and was installed in an interaction chamber in a distance of $1.22\,\mathrm{m}$ behind the nozzle. It consists of two rods, which can be moved through the chamber horizontally and vertically. The impinging clusters on the rods affect a pressure increase in the chamber which can be measured for each step of the rod. With this method a profile of the cluster beam is recorded which also yield information on the position and size of the cluster beam. Furthermore, the determination of the maximum pressure increase allows for the measurement of the absolute target thickness [4]. First studies on the thickness and the stability of the cluster beam have been performed successfully. These measurements show that the target thickness is stable over several hours (see Fig. 1) and can be reproduced easily (Fig. 2). Furthermore, the target thickness is easily adjustable over several orders of magnitude by changing the hydrogen stagnation conditions (see Fig. 2). By these measurments the cluster-jet target is proved to meet the expectations and will be installed at the COSY accelerator in Jülich mid 2017 for extensive tests in an experimental environment.

References

[1] A.-K. Hergemöller, "Initial Operation of the Cluster-Jet Target for $\overline{\mathrm{P}}$ANDA", GSI Scientific Report 2015 (2016).

[2] S. Grieser, "Glass Laval Nozzle Prototypes for Cluster-Jet Targets", GSI Scientific Report 2015 (2016).

[3] B. Hetz, Master Thesis, University of Münster, Germany, 2017.

[4] E. Köhler, PhD Thesis, University of Münster, Germany, 2016.

[5] M. Seifert, Bachelor Thesis, University of Münster, Germany, 2016.

* Work supported by HGS-HIRe for FAIR, BMBF and GSI.
† a.hergemoeller@wwu.de

Jet beam analysis with a Mach-Zehnder Interferometer*

S. Grieser†[1], *D. Bonaventura*[1], *A.-K. Hergemöller*[1], *B. Hetz*[1], *L. Lessmann*[1], *C. Westphälinger*[1], *and A. Khoukaz*[1]

[1]Institut für Kernphysik, Westfälische Wilhelms-Universität Münster, Germany

Cluster-jet targets are highly suited for storage ring experiments due to the fact that they provide high and constant beam thicknesses, i.e., up to 10^{15} $\frac{\text{atoms}}{\text{cm}^2}$ in a distance of 2.1 m [1]. Nevertheless, the thickness is adjustable over several orders of magnitude. Therefore, a cluster-jet target is planned to be the first internal target for the $\overline{\text{P}}$ANDA experiment at FAIR. A cluster source generates a continuous flow of cryogenic solid clusters by the expansion of precooled gases within fine Laval nozzles. For the production of clusters and their properties ,i.e., mass distribution, velocity, and formation of high intense core beams, the geometry of the nozzle is crucial. Therefore, an improved nozzle production process based on the initial CERN production was developed and is now established at the University of Münster [2]. To test and ensure the high performance of the Laval nozzles, a Mach-Zehnder interferometer was built up. In this kind of interferometer, one beam is directed through a vacuum chamber, where the Laval nozzle and the cluster-/gas-jet is located, and merges at last with the reference beam. This causes an interference pattern with horizontal interference bands. The expanding jet beam leads to a change in the phase shift (see Fig. 1). The setup is used to visualize the jet beam and also the surrounding gas directly behind the nozzle. Furthermore, the target density and the shape of the beam can be investigated. With this information the geometry of the nozzle, the production process which is influenced by the nozzles geometry, and the stagnation conditions at the nozzle can be optimized and adapted to the experimental requirements.

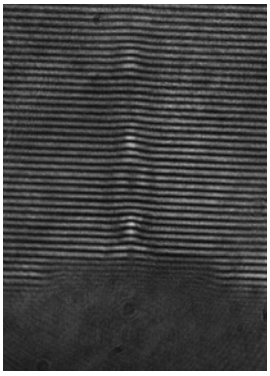

Figure 1: Picture of the interference figure recorded with a CCD camera. At the bottom the shadow of the Laval nozzle exit is visible. Above the nozzle the impact of the gas-jet on the interference bands is observable.

* Work supported by HGS-HIRe for FAIR, BMBF, and GSI

† s.grieser@uni-muenster.de

Above that, an analysis program was created, which calculates the target thickness distribution out of the phase shift from the interference pattern [3]. In a first measurement a nozzle with an inner diameter of 0.5 mm and an outlet diameter of 2 mm was used, which was produced with the new production process at the University of Münster. The applied gas was nitrogen at a temperature of 288 K and a pressure of 20 bar in front of the nozzle. The pressure in the vacuum chamber was varied to study the influence of the pressure in the vacuum chamber on the gas-jet (see Fig. 2). The gas-jet beam expanding into ambient pressure shows the typical shock diamonds which result from the reflection of the jet beam with the surrounding gas in the chamber. Whereas, the expansion into vacuum shows a more divergent and homogeneous shaped beam.

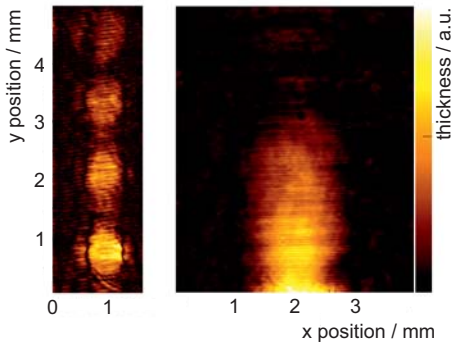

Figure 2: Nitrogen gas-jet, produced at gas pressure of 20 bar and a temperature of 288 K, expands into ambient pressure (left) and vacuum (right).

The Mach-Zehnder interferometer is a powerful analysis system, which offers the possibility to investigate the properties of the jet beam directly behind the nozzle. This leads to a better insight of the formation of clusters and provides more information for the Laval nozzle geometry and their prodction process which is influenced by the nozzles geometry. Additionally, more Laval nozzles with different geometries and their influence on the jet beam will be investigated by this setup in order to provide an optimized set of nozzles for the $\overline{\text{P}}$ANDA experiment.

References

[1] A.-K. Hergemöller, GSI Scientific Report 2016 (2017).

[2] S. Grieser, GSI Scientific Report 2014 (2015).

[3] L. Lessmann, Master thesis, University Münster, Germany, 2016.

DOI:10.15120/GR-2017-1

Gain surface homogeneity of avalanche photodiodes produced in large scale

J. Bailey[1], *A. El Mosleh*[1], *F. Himburg*[1], *D. Scharnberg*[1], *C. Warneke*[1], *P. Wicke*[1], *H. Al-Turany*[1], *I. Retkovac eelja*[2], *and A. Wilms*[1]

[1]GSI, Darmstadt, Germany; [2]Department of Physics, Faculty of Science, University of Zagreb

Introduction

Large area avalanche photodiodes (APDs) are proposed to be used as readout devices of high energy physics electromagnetic calorimeters. According to the high requirements of particle experiments some APD parameters have to be measured to ensure stable conditions of operation. One of them is the homogeneity of the APD surface regarding the internal gain M, whereby the values of M are strongly dependent on applied voltage and temperature.

Gain surface homogeneity of APD

The measured photocurrent of an APD is strongly dependent on the applied bias voltage. In general an amount of 60 to 90 rectangular APDs is cut out of one silicon wafer and several wafers make up one lot. Each wafer or lot will have slightly different characteristics in various parameters, although these differences should not be considerable. Nevertheless it is important to know the profile of eventually occuring current variations over the entire APD surface as well as their possible dependence on lot and wafer number. For this reason the photocurrent homogeneity profile was determined.

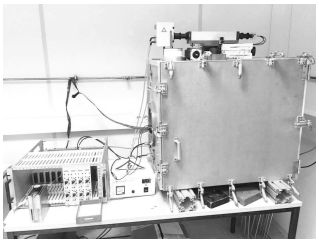

Figure 1: Experimental setup for gain uniformity measurement

Measurement setup

The measurement-stand consists of test chamber, light source and the electronic device transmitting data to a PC via RS232 interface. All components are shown in fig.1. Data acquisition and analysis are done within the ROOT software framework. The needed incident light (420 nm) is provided by a lamp with computer-controlled monochromator mounted on the chamber and guided through a light-fiber bundle into the light-tight chamber. Single APDs are mounted on the x-y-measuring table under one fixed light-fiber. The dark and illumination current are measured for each single diode. The bias voltage values applied are chosen in a regime between 70V to 380V.

Measurements

Measurements were conducted for six wafers originating from different production lots and two wafers of the same lot determined by the specific serial number. We can divide diodes into three district groups - those without direct wafer-neighbours, those with wafer-neighbours on all sides and those originated from the cutting edges of a wafer. The selected APDs represent all three groups. Possible variations of the current over the APD surface could be assigned to the lot/wafer properties or eventually to problems occured during the APD cutting or packaging process.

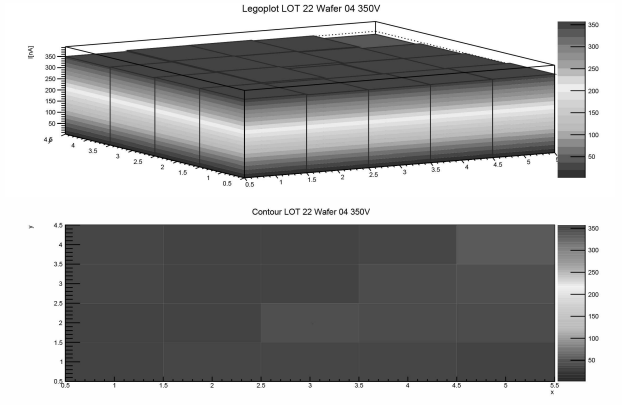

Figure 2: Profile of position-depending APD photocurrent at an applied voltage of 350V (M>30, LOT 22 , Wafer 04, originating from the wafer border).

Based on the prepared measurements the APD photocurrent can be mapped as a function of position, exemplarily shown in figure 2: The x-y plane represents the position on the APD surface and the z axis represents the measured photocurrent in nA. The variation of current over the surface was found to be on the level of a few percent of the mean value.

Preliminary results

The homogeneity of the APD photocurrent over the device surface was determined. The tested APDs originated from different lots and for each lot subsamples of a few wafers were picked out. The determined photocurrent values were found to be nearly constant, independent of surface position or of the applied bias voltage value. APDs from the cutting edges of a wafer seem to apparently show a slightly higher deviation in the measured photocurrent. Further measurements have to be prepared for confirmation.

DOI:10.15120/GR-2017-1

Large area avalanche photo diode irradiation at Giessen*

M. Moritz†[1], *K.-Th. Brinkmann*[1], *H.-G. Zaunick*[1], *and for the* $\overline{P}ANDA$ *collaboration*[1]
[1]II. Physikalisches Institut, Justus-Liebig-Universität Giessen, Germany

The electromagnetic target calorimeter (EMC) [1] of the future $\overline{P}ANDA$ detector has the challenging aim to detect high energy photons with excellent energy resolution from 15 GeV down to a few tens of MeV. To reach this goal, improved $PbW0_4$ scintillator crystals, cooled down to $-25°C$ and read out with two precisely matched large area avalanche photo sensors (APD) each, have been choosen. In order to ensure the stable and reliable high precision operation over the whole envisaged lifetime, the radiation hardness of each photo sensor has to be verified. Furthermore, the parameters of a matched pair, especially the high voltages for each APD, have to develop in a very similar way under the radiation dose which will be accumulated during the whole lifetime of the experiment. To fulfill these requirements, the APDs have to undergo a sophisticated screening and matching procedure. One main step of this procedure is therefore the irradiation with a high intensity ^{60}Co γ-source at the irradiation facility in Giessen.

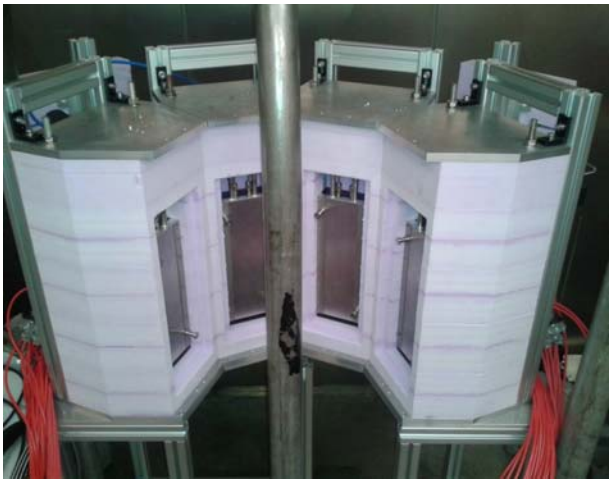

Figure 1: APD irradiation setup at the ^{60}Co irradiation facility at Justus Liebig University Giessen.

The customized setup, as partly shown in figure 1, allows a well controlled irradiation procedure. Four so-called grids, holding twenty APDs each, can be irradiated simultaneously under individual bias for every single APD. Due to the temperature-dependent bias voltage for a certain gain, each grid sits in a separate temperature-isolated box. These boxes are equipped with a liquid-based cooling system in order to facilitate a temperature-stable environment at $20°C$ and are located at a distance of $25.5\ cm$ around the source. The γ-source, which can be mechanically moved into the vertical metal tube in front of the setup, provides nowadays a dose rate of $37\ Gy/h$ at the distance of the setup. The integrated dose of one hour corresponds to the maximum dose which one APD should accumulate within 10 years of $\overline{P}ANDA$ operation.

On the background of the future mass production for the whole calorimeter, which requires processing of nearly 30.000 APDs, the following procedure was iteratively elaborated. After a first screening procedure via the Photo Sensor Laboratory (PSL) [2], the APDs are delivered for irradiation to Giessen. Before each irradiation, the electronic contact of all APDs is verified by measuring the generated current under illumination at 0 Volts bias. After a few minutes for temperature equalization, the dark currents are measured. Furthermore, the dark currents during and after irradiation with $37\ Gy$ under bias were recorded. The present irradiation procedure allows to irradiate up to 400 APDs within a normal working day. In the end, all delivered APDs and the corresponding data are sent back to the PSL for a second screening procedure. The second procedure includes an annealing process for recovering radiation damages. During the second half of 2016, all APDs for the first EMC barrel slice went trough the whole procedure of the irradiation in Giessen. The integrated total screening procedure throughput with an increasing slope can be seen in figure 2.

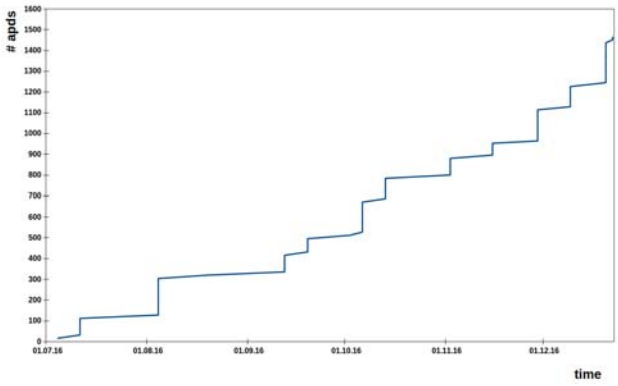

Figure 2: Amount of APDs which passed the screening process since the beginning of the first slice assembly project in 2016.

* This Work is supported by BMBF, GSI and HIC4FAIR.
† markus.moritz@exp2.physik.uni-giessen.de

DOI:10.15120/GR-2017-1

References

[1] PANDA COLLABORATION, Technical Design Report for the $\overline{P}ANDA$ Electromagnetic Calorimteter. arXiv:0810.1216 [physics.ins-det], 2008.

[2] https://www.gsi.de/work/forschung/detector_laboratory/psl.htm

DOI:10.15120/GR-2017-1

Investigation of aging effects in GEM detectors*

B. Ketzer† [1], *M. Ball*[1], *C. Dreisbach*[2], *and R. Schmitz*[1]

[1]Universität Bonn, Helmholtz-Institut für Strahlen- und Kernphysik, 53115 Bonn, Germany; [2]Technische Universität München, Physik Department, 85748 Garching, Germany

An element-specific analysis of depositions on GEM foils exposed to a high-intensity particle beam has been performed. We identify traces of Si and S in the affected regions. Several materials such as glue and conformal coating used in the construction of the detectors are tested for their composition in order to identify the source of the deposition. A setup to systematically study the influence of outgassing from materials on GEM detectors is presented.

Introduction

Detectors based on charge amplification in micropattern structures such as the Gas Electron Multiplier (GEM) [1] exhibit a much higher rate capability than conventional multi-wire proportional chambers (MWPC). Particle rates beyond $1 \cdot 10^6\,\mathrm{mm^{-2}s^{-1}}$ have been reached without noticeable gain reduction [2, 3]. Spatial resolutions of the order of $70\,\mu\mathrm{m}$ are routinely achieved with a projective strip readout in high-intensity environments [4]. In addition, GEM detectors can be built with an extremely small material budget of the order of 2–3 per mill of a radiation length [3]. It is for these reasons that three stations of large planar GEM detectors are foreseen as forward trackers in the PANDA barrel spectrometer [5]. An application as particle beam monitors is also conceivable. When operating such detectors for a long time in a high-intensity particle beam, even tiny contaminations of the gas from outgassing materials used for detector construction or in the gas lines can severely compromise the performance. The foreign molecules will be ionized in the avalanche process and the resulting ions will follow the electric field lines to an electrode, where they are neutralized and deposited. In order to avoid this, it is vital to carefully investigate the outgassing properties of all materials used in the construction of a GEM detector and thus qualify them for their suitability.

Depositions on GEM foils

A set of planar triple-GEM detectors with pixel readout [6] have been subjected to high-intensity muon and hadron beams at CERN. After accumulating a total charge of more than $10\,\mathrm{mC/mm^2}$, significant inefficiencies became visible in the region exposed to the beam, caused by severely reduced signal pulse heights. Opening the detector, a change of color correlated with the inefficient region clearly indicated that depositions of unwanted contaminations on the GEM foils are responsible for the effect.

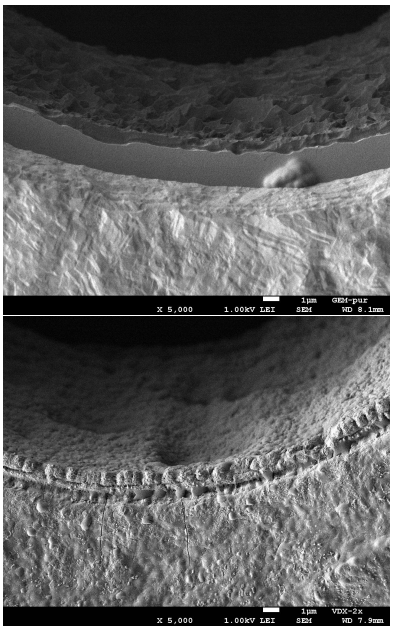

Figure 1: Scanning electron microscope picture of GEM holes, (top) of a new foil, (bottom) of a foil after accumulation of more than $10\,\mathrm{mC/mm^2}$.

In order to further study the depositions, samples of a damaged foil were investigated using a scanning electron microscope (SEM, type JEOL - JSM 7500F) and compared to a new one. Fig. 1 shows (top) a GEM hole in an unused foil and (bottom) a hole in the foil exposed to the beam. While the Cu surface and the Polyimide insulator are clearly visible on the top figure, the damaged hole at the bottom figure clearly depositions of material around and inside the hole, rendering the edge of the metal surface indistinguishable from the insulator.

Energy-dispersive X-ray spectroscopy

The elemental composition of the deposits was analyzed by detecting the X-rays which are emitted following the bombardment of the foil by electrons in the SEM (Energy dispersive X-ray spectroscopy, EDX). Figure 2 shows the EDX spectra (top) for the new foil, and (bottom) for the damaged foil. There are clear traces of Silicon (Si) and Sulfur (S) on the damaged foil, corresponding to an atomic fraction of 1.5% and 5.3%, respectively.

* Work supported by GSI cooperation with University of Bonn, contract no. BNKETZ1416

† Bernhard.Ketzer@uni-bonn.de

DOI:10.15120/GR-2017-1

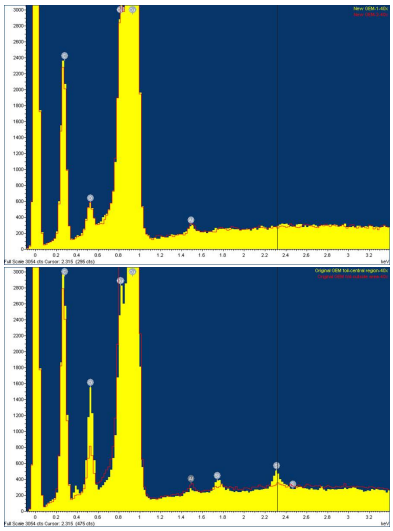

Figure 2: EDX spectra of (top) a new GEM foil and (bottom) a damaged GEM foil. Clear traces of Si and S are found on the damaged one.

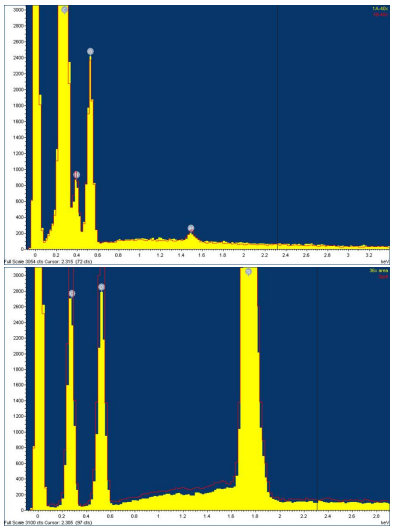

Figure 3: EDX spectra of (top) Araldit AY103-1/HY991 (glue/hardener) and (bottom) Dow Corning 1-2577 conformal coating.

In the following, we analyzed several materials used in the construction of the detectors in the same device, including glue (Araldit AY103-1/HY991), and a conformal coating (Dow Corning 1-2577) used to seal the detector from the outside. The corresponding EDX spectra are shown in Fig. 3. The results indicate that the Silicon originates from the conformal coating. The origin of Sulfur is not yet fully understood, but could be due to sulfuric acid (H_2SO_4) used for cleaning during the production process of the readout circuit.

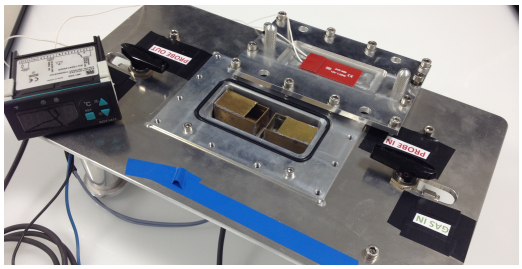

Figure 4: Temperature-stabilized sample box for the controlled introduction of impurities into a gaseous detector through the input gas line.

Setup for aging measurements

A dedicated setup was built to systematically analyze the outgassing properties of materials and their influence on the performance of GEM detectors. Figure 4 shows a photograph of a sample box developed for material tests. The device is mounted in the input gas line to the detector, such that any outgassing molecules are transported to the detector. The cavern is temperature-stabilized up to 70° to accelerate outgassing. It can also be used to add ppm-amounts of other pollutants like H_2O in a controlled way to the detector gas [7]. The device will be used in a measurement campaign dedicated to study the aging effects induced by different materials.

Summary

The results of the aging investigations revealed a clear deposition of Si and S on GEM foils after their exposure to a high particle flux. The contaminations stem from materials used for the construction of the detector, noticeably from a conformal coating which apparently crept into the detector. Also agents used in the production process of special components like readout circuits may be critical. Further investigations will be performed to clarify the origin of Sulfur. These results are relevant for all applications where GEM detectors are exposed to high particle fluxes, like in the PANDA experiment.

References

[1] F. Sauli, Nucl. Instr. Meth. A 386 (1997) 531.

[2] J. Benlloch et al., Nucl. Instrum. Meth. A419 (1998) 410.

[3] COMPASS, P. Abbon et al., Nucl. Instr. Meth. A 779 (2015) 69, 1410.1797.

[4] B. Ketzer et al., Nucl. Instr. Meth. A 535 (2004) 314.

[5] PANDA Collaboration, M. Lutz et al., (2009), 0903.3905.

[6] B. Ketzer et al., Nuclear Science Symposium Conference Record, 2007. NSS '07. IEEE Vol. 1, pp. 242–244, Piscataway, NJ, 2007, IEEE.

[7] S. Urban, Development of QA procedures for large-area GEMs, Master's thesis, Rheinische Friedrich-Wilhelms-Universität Bonn, 2016.

DOI:10.15120/GR-2017-1

Performance study of the $\overline{\text{P}}$ANDA GEM-tracker in the physics simulation*

N. Divani Veis[†1,2,3], *R. Karabowicz*[1], *T. Saito*[1,2], *B.Voss*[1], *and the $\overline{\text{P}}$ANDA collaboration*[1]

[1]GSI, Darmstadt, Germany; [2]HIM, Mainz, Germany; [3]University of Birjand, Iran

To provide measurement of charged particles trajectories with high resolution over the solid angles, one of the inner tracking system is the $\overline{\text{P}}$ANDA GEM-tracker to cover the forward solid angles below 22 degrees. A gas electron multiplier (GEM) is a type of the gaseous ionization detector which will be used as a first forward tracking detector behind the central tracker in the $\overline{\text{P}}$ANDA experiment. This work is investigation of the influence of the GEM-tracker to improve the track finding efficiency and track momentum resolution in the $\overline{\text{P}}$ANDA setup.

Investigation of the track finding efficiency and track momentum resolution

In this investigation is used the realistic pattern recognition for track reconstruction procedure in order to understand the behaviour of the $\overline{\text{P}}$ANDA GEM-tracker in different momenta and angles of emitted particles in the forward directions of interest (below 22 degrees). The particles tracking approach is aimed to reconstruct the particles trajectories in all the inner trackers system (STT, MVD, and GEM tracking detectors) in the target spectrometer of the $\overline{\text{P}}$ANDA setup simultaneously [1]. Briefly, this algorithm loops over all the hits created in different detectors and matches them first to already existing tracks and subsequently to unused hits. This algorithm focuses on the primary trajectories, that is the ones emerging from or around the interaction point. The comparison between the true and the reconstructed momenta allows to determine the track momentum resolution as well [2].

To investigate the track finding efficiency and track momentum resolution, fifty thousand events of the single charged particles (pions) are propagated for two selected values of the momentum 0.5, and 5 GeV/c using the current implemented GEM geometry with three stations [3]. The particles are emitted in the range of the polar angles (θ) between 2 to 45 degrees and the azimuthal angles (ϕ) between 0 to 360 degrees. For each values of the theta and momentum of pions the simulation is done separately in two cases: the full $\overline{\text{P}}$ANDA setup with GEM-tracker (with contributions of the three inner trackers STT, MVD, and GEM together) and without GEM-tracker (with contributions of the two inner trackers STT and MVD only) for track finding procedure. To check and compare the influence of the GEM-tracker to improve the quality of the track finding efficiency, Figure 1 and Figure 2 show the polar angular distribution of the track finding efficiency and track momentum resolution respectively. The contributions and performance of the GEM-tracker are visible at the plots for the 0.5, and 5 GeV/c at the covering polar angles below 22 degrees. Of course, the contributions of the other trackers (STT and MVD) are large to reconstruct tracks for the large angles which are not related to the region of the GEM-tracker.

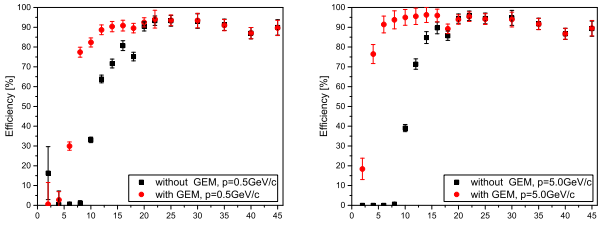

Figure 1: The polar angular distribution of the track finding efficiency for two selected values of pions momenta 0.5 GeV/c (left), and 5 GeV/c (right) in two cases: $\overline{\text{P}}$ANDA setup with (circular points) and without (squared points) the GEM-tracker. The single pions are propagated in the range of the θ polar angles between 2 to 45 degrees and the ϕ azimuthal angles between 0 to 360 degrees. The rounded points indicate the good track finding efficiencies in the forward directions of interest.

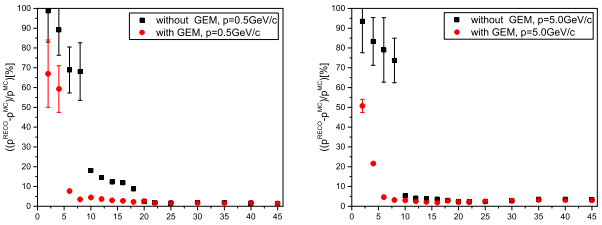

Figure 2: The track momentum resolution versus θ polar angles for two selected values of pions momenta 0.5 GeV/c (left), and 5 GeV/c (right) in two mentioned cases.

References

[1] B. Voss, GSI Scientific Report 2008(2009) 242.

[2] R. Karabowicz, GSI Scientific Report 2010(2011) 117.

[3] N. Divani Veis et al., GSI Scientific Report 2015(2016) 92.

* Work supported by HI Mainz (GEM Technologies (4316))

† n.divani@gsi.de

DOI:10.15120/GR-2017-1

Estimation of the fractional radiation length for the current designed geometry of the $\overline{\text{P}}$ANDA Planar-GEM tracker*

N. Divani Veis† [1,2,3], *R. Karabowicz*[1], *T. Saito*[1,2], *B.Voss*[1], *and the $\overline{\text{P}}$ANDA collaboration*[1]
[1]GSI, Darmstadt, Germany; [2]HIM, Mainz, Germany; [3]University of Birjand, Iran

In the $\overline{\text{P}}$ANDA experiment, charged particles proceeding to the forward directions with the polar angles approximately between 2 to 22 degrees will be measured by a set of large-area planar gaseous micro-pattern detectors equipped with GEM foils as amplification stages. This study presents the estimation of the fractional radiation length for the implemented $\overline{\text{P}}$ANDA GEM-Tracker in Monte-Carlo simulation. This includes the current conceptual technical design of the realistic GEM geometry.

Detector description for the $\overline{\text{P}}$ANDA GEM-tracker

The $\overline{\text{P}}$ANDA GEM-tracker stations are in form of circular planes (disk shape). The geometry of the $\overline{\text{P}}$ANDA GEM detectors in the simulation was transported from the designed geometry implemented in the CAD software [1, 2]. The tracking system contains three stations of planar GEM including main layers and holding support structures. Each station realizes a complex series of multi-layers with aluminium windows, cathodes, GEM foils, sensitive pad planes, Ar/CO_2 gas containers, cooling support and electronic devices. Each of GEM foils and pad planes consists of three thin layers with the copper-kapton-copper configuration.

The double-sided read-out pad planes are located in the centre of each station providing strip information about crossing particles in four projections: radial and circular in front side, horizontal and vertical in back side. The total radius and the Z position (along the beam line in the Cartesian coordinate originating from the target center) of each station respectively are 45 and 119.4 cm for the first station, 56 and 155.4 cm for the second station and 74 and 188.5 cm for the last one. The Riddle shell with its rigid and light-weight supporting structures which holds all the GEM-tracker stations have also been implemented with carbon fiber [3, 4]. The entire GEM system with three stations and the supporting structure is shown in Figure 1.

Estimation of the Fractional Radiation Length for the $\overline{\text{P}}$ANDA GEM-tracker

To study about the effect of the material of the GEM stations for charged particles passing through the detectors, one of the beneficial concepts is to estimate the radiation length. It adds up in all the traversed volumes, depending on the specific radiation length ($X0$) and the density of the materials defined for the volumes corresponding to the traversed path length therein [5].

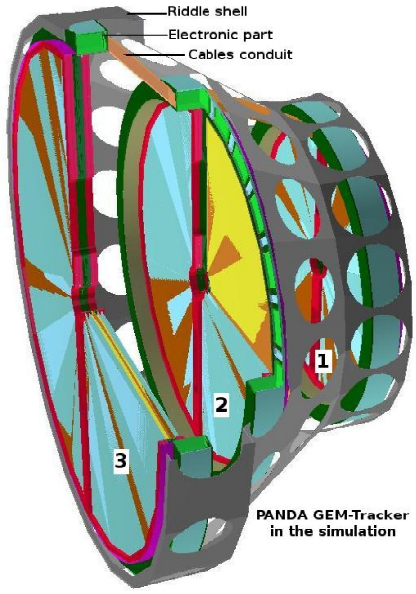

Figure 1: The entire layout of the $\overline{\text{P}}$ANDA GEM-tracker with the current realistic geometry implemented in the PandaRoot. It includes three stations with the main layers in aluminium, kapton and copper, the drift layers with Ar/CO_2 mixed gas, the support structures in carbon and glass fiber, the electronic parts in copper, the cables conduit in copper, and also the Riddle shell in carbon fiber to hold all parts of the detector together.

The introduction of the detailed geometry provides precise quantification of the amount of material introduced the detector in different regions. As the GEM is located in front of the detectors in upstream in the Target Spectrometer as well as of the all the detectors of the Forward Spectrometer, it will influence the track reconstructions with these detectors in forward directions. Thus, we studied the effect of the GEM components by means of the radiation length.

For estimating of the GEM materials budget and extracting of the GEM materials map, the virtual particles "Geantinos" [6] were propagated through the detector using Geant4 simulation engine. These fictitious particles undergo no physical interactions but flag boundary crossings along their straight trajectories and counting the number of the radiation lengths crossed by them within the GEM.

* Work supported by HI Mainz (GEM Technologies (4316))
† n.divani@gsi.de

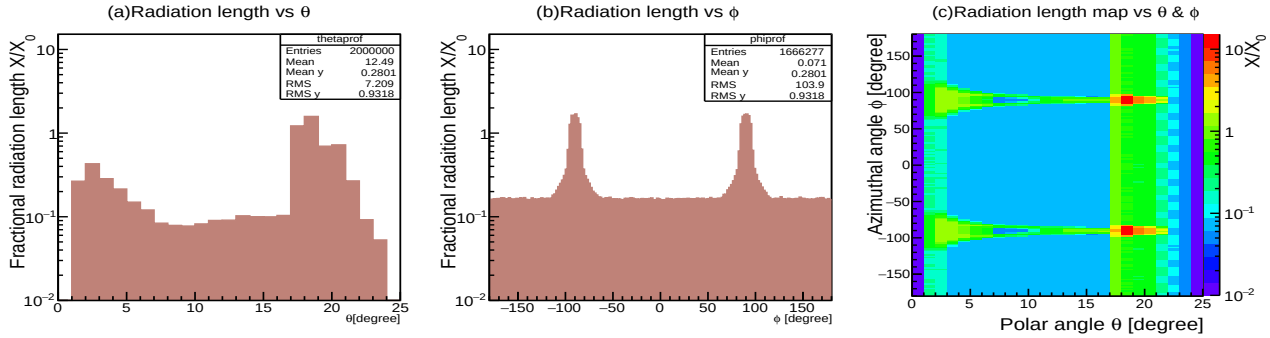

Figure 2: The results of the radiation length for the entire $\overline{\text{P}}$ANDA GEM-tracker geometry. This figure consists of: (a) the fractional radiation length versus polar angle,θ, (b) the fractional radiation length versus azimuthal angle, ϕ, and, (c) the map of the radiation length, θ versus ϕ. They are evaluated by propagating two million Geantinos in ranges from 0 to 25 degrees for θ and from 0 to 360 degrees for the ϕ. In addition, the radiation length map shows the changes which are belonged to the main layers, holding support structures and electronics sections placed in this regions. The changes displayed in red belong to the cables conduit and the changes in blue inside the green belong to the shape of the holding structures and their vertical holes in both side in the GEM geometry).

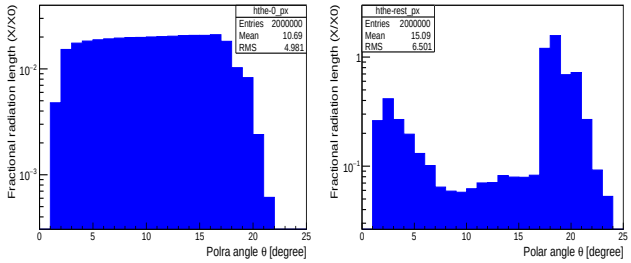

Figure 3: The results of the radiation length separately for the main layers and holding support structures and electronic parts of the $\overline{\text{P}}$ANDA GEM-tracker geometry. This figure consists of: (left) the fractional radiation length versus polar angle,θ for main layers, and, (right) the fractional radiation length versus polar angle, θ for the holding support structures and electronic parts. They are evaluated by propagating two million Geantinos in ranges from 0 to 25 degrees for θ and from 0 to 360 degrees for the ϕ.

In order to have more exact information, profiles of the polar angle (θ) and the azimuthal angle (ϕ) are provided for the contribution of the different GEM components. Two millions of particles were generated at the target position with the polar angle (θ), and the azimuthal angle (ϕ), respectively distributed flatly in ranges from 0 to 25 degrees, and from 0 to 360 degrees. Figure 2 and 3 demonstrate the results of the fractional radiation length for the presented $\overline{\text{P}}$ANDA GEM-tracker geometry.

Figure 2 shows the distributions of the radiation length defined as $X/X0$ as functions of θ and ϕ respectively in the left and middle panels for the entire GEM geometry with three stations. A two-dimensional distribution of $X/X0$ in the θ-ϕ plane (as a map of the radiation length) is also shown in the right panel in the figure. In most of the regions, the radiation length $X/X0$ is below 10^{-1}. However, larger $X/X0$ values exceeding one are distributed around $\theta = 18^{\circ}$ and $\phi = \pm 90^{\circ}$. In order to specify the contributions to those large $X/X0$ values, distributions of $X/X0$ as functions of θ and ϕ are separately studied for the main layers and support structures (the holding structures, electronics and cables conduit), as shown in Figure 3. The study of radiation length for the GEM detector and their associated structures has shown that the $X/X0$ values are below 10^{-2} for the main layers of the GEM stations.

References

[1] B. Voss et al., GSI Scientific Report 2008(2009) 242.

[2] B. Voss et al., GSI Scientific Report 2009(2010) 338.

[3] R. Karabowicz et al., GSI Scientific Report 2009(2010) 12.

[4] N. Divani Veis et al., GSI Scientific Report 2015(2016) 92.

[5] S. Bianco et al., "The CAD model of the $\overline{\text{P}}$ANDA Micro-Vertex-Detector in physics simulation", Nuclear Instrument and Methods in physics Research A, 654(2011)630-633.

[6] Geant4 Toolkit, Webpage: http:geant4.cern.chsupport/proc_mod_catalog/particles .

DOI:10.15120/GR-2017-1

Investigation of the $\Lambda\ \overline{\Lambda}$ invariant mass reconstruction with the $\overline{\mathrm{P}}$ANDA Planar-GEM tracker*

N. Divani Veis† [1,2,3], *R. Karabowicz*[1], *T. Saito*[1,2], *B.Voss*[1], *and the $\overline{\mathrm{P}}$ANDA collaboration*[1]

[1]GSI, Darmstadt, Germany; [2]HIM, Mainz, Germany; [3]University of Birjand, Iran

One important part of the physics program of the $\overline{\mathrm{P}}$ANDA experiment is to study about hyperons and their structures. Hyperons decay weakly and they have a long life time and mean decay length. This causes to have also the hyperons decay in the outer part of the central tracker of the $\overline{\mathrm{P}}$ANDA setup. In this work, simulation have been fulfilled for the $\overline{\mathrm{P}}$ANDA GEM-tracker with $\overline{\Lambda}\Lambda$ decay channel in order to perform acceptance studies. $\overline{\mathrm{P}}$ANDA GEM-tracker is a set of large-area planar gaseous micro-pattern detectors equipped with GEM foils which will measure charged particles proceeding to the forward directions with the covering polar angles approximately between 2° to 22°.

$\Lambda\ \overline{\Lambda}$ Mass resolution

$\Lambda\ \overline{\Lambda}$ channel has been chosen because Λ is the lightest hyperon which is easiest to produce and all final state particles are charged. The full $\overline{\mathrm{P}}$ANDA setup based on the PandaRoot framework has been used in two cases with the GEM-tracker (with contributions of the three inner trackers STT, MVD, and GEM together) and without GEM-tracker (with contributions of the two inner trackers STT and MVD only) in order to study and compare the behaviour and the performance of the current designed GEM-tracker [1, 2] in this physics decay channel. The mentioned reaction was simulated at beam momenta of 2GeV/c of the boosted antiprotons by generating fifty thousand events to study real state of interaction as the forward peaking. The simulations have done with the realistic pattern recognition for the track finding procedure [3]. Figure 1 shows the invariant mass reconstruction and the polar angular distribution for the simulated Λ and $\overline{\Lambda}$ with (red) and without (black) GEM-tracker in the $\overline{\mathrm{P}}$ANDA setup. In right panel (up and down) of this Figure is demonstrated the Λ and $\overline{\Lambda}$ mass reconstruction for all possible combinations of the related particles in this decay channel. The mean values and the mass resolutions of two cases are shown in Table 1. In left panel of this Figure is also implied a big improvement using GEM-tracker to show the reconstructed Λ and $\overline{\Lambda}$ in forward directions of interest (below 22 degrees). The influence of the GEM-tracker in order to improve the mass reconstruction in this channel are also visible in the Armenteros plots in Figure 2. In these plots, the transverse momentum of the decay products in the Λ rest frame is plotted as a function the asymmetry α, where $\alpha = \frac{p_{L+}-p_{L-}}{p_{L+}+p_{L-}}$ and $p_{L+(-)}$ is the longitudinal momentum of the positive (negative) particles produced in this decay. In this Figure the Armenteros plots obtained for both setups without (left) and with (right) GEM-tracker.

Table 1: The mass resolutions and reconstruction efficiency for the Λ and $\overline{\Lambda}$ invariant mass reconstruction with and without GET-Tracker in the $\overline{\mathrm{P}}$ANDA setup.

for all combination of particles	without GEM Λ	with GEM Λ	without GEM Λ (antiΛ)	with GEM Λ(antiΛ)
Mean Value [GeV/c^2]	$1.118\pm3.164\times10^{-4}$	$1.116\pm2.075\times10^{-4}$	$1.120\pm4.966\times10^{-4}$	$1.115\pm1.538\times10^{-4}$
Mass Resolution [GeV/c^2]	$0.020\pm4.828\times10^{-4}$	$0.018\pm2.255\times10^{-4}$	$0.026\pm6.934\times10^{-4}$	$0.017\pm1.733\times10^{-4}$
Reconstruction Efficiency[%]	15.57	27.35	19.34	62.37

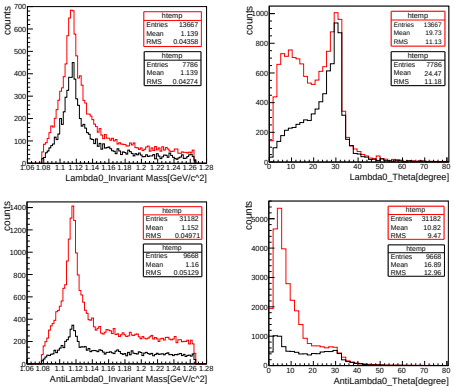

Figure 1: The invariant mass reconstruction and polar angular momentum of the simulated Λ and $\overline{\Lambda}$ with (red) and without (black) the GEM-tracker in the $\overline{\mathrm{P}}$ANDA setup.

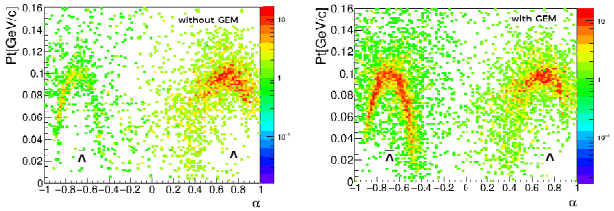

Figure 2: The Armenteros plots obtained with (right) and without (left) the GEM-tracker in the $\overline{\mathrm{P}}$ANDA setup at the beam momentum of 2GeV/c.

References

[1] B. Voss et al., GSI Scientific Report 2009(2010) 338.

[2] N. Divani Veis et al., GSI Scientific Report 2015(2016) 92.

[3] R. Karabowicz et al., GSI Scientific Report 2009(2010) 117.

* Work supported by HI Mainz (GEM Technologies (4316))

† n.divani@gsi.de

A precision lineshape measurement of the $X(3872)$ with PANDA/FAIR

F. Nerling[1,2], *K. Götzen*[1], *R. Kliemt*[3], *K. Peters*[1,2], *and the PANDA Collaboration*[1]
[1]Goethe Univ. Frankfurt, Germany; [2]GSI, Darmstadt, Germany; [3]HIM, Mainz, Germany

The first of the new charmonium-like states discovered since 2003, the $X(3872)$ [1], is still one of the most puzzling ones concerning the properties. Since the mass is indistinguishable close to the sum $m(D^0) + m(\bar{D}^{*0})$, it is unclear whether it lays above or beneath the DD^* threshold. Furthermore, the natural width is very small and basically unknown up to a rather rough upper limit of Γ_X<1.2 MeV/c^2 [2]. Due to these extra-ordinary properties, this state is frequently suggested to be an exotic hadron, possibly featuring a different and more complex internal structure than a simple conventional mesonic $q\bar{q}$ state. In particular, several theoretical models (e.g. [3]) relate not only the mass m_X and the Breit-Wigner-like width Γ_X to the internal structure, but explicitly also the lineshape of the resonance.

This offers another experimental handle to identify the nature of the $X(3872)$, however, a precise measurement is beyond the scope of currently running experiments. Due to typical detector resolutions (∼8 MeV), the precision needed to resolve this very narrow structure in subsequent decays is not reached, unless the $X(3872)$ with $J^{PC} = 1^{++}$ is created in a formation reaction $A+B \to X$ with excellent beam energy precision as it will be delivered by HESR/FAIR, allowing for a resonance energy scan. This is not possible for resonances with $J^{PC} \neq 1^{--}$ in an e^+e^- experiment — in $\bar{p}p$ annihilation reactions, however, all $q\bar{q}$-like spin-parity states can directly be produced in formation, see also [4].

We have studied the expected sensitivity of energy scans of narrow resonances performed with the HESR in combination with the PANDA detector at FAIR [5] under various assumptions of signal cross sections, input widths and luminosities. Apart from the quantification of the prospected sensitivity for the width and lineshape measurement of the example of the $X(3872)$, this exemplary analysis serves as a proof of principle for high precision spectroscopy using the energy scan method with the PANDA experiment in general.

The projected sensitivity for a Breit-Wigner like width as obtained for a PANDA/FAIR phase-1 measurement (i.e. HESRr mode, reduced luminosity) based on 20 energy scan points (two days of data taking per point) within a 1.4 MeV window around the nominal mass is summarised in Fig. 1. The scanned cross-section after de-convolution of the known beam profile together with the Breit-Wigner fit is exemplarily shown for an assumed input width of $\Gamma_0 = 130$ keV (Fig. 1, top) together with the obtained relative uncertainties that will be achieved for a range of assumed input widths Γ_0 beneath 1 MeV. A twenty percent relative uncertainty is achieved for an input width of

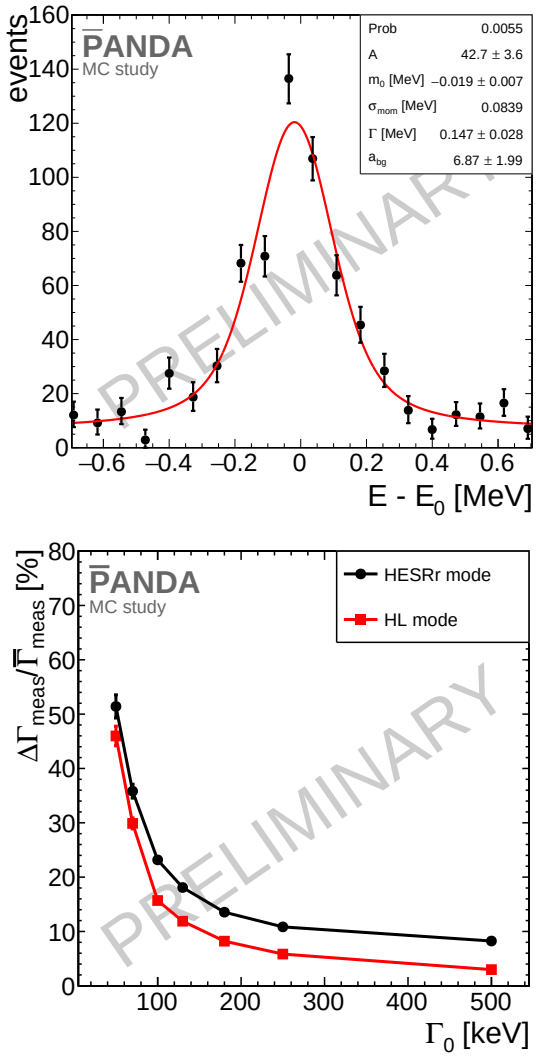

Figure 1: Full MC simulation study of a resonance energy scan using the example of the very narrow $X(3872)$.

Γ_0=100 keV, and the obtained resolution is better for the high luminosity (HL) mode (Fig. 1, low). These results have been released by the PANDA Collaboration and are planned to be published in a journal article soon.

References

[1] Belle Collab., S.-K. Choi *et al.*, PRL 91 (2003) 262001.

[2] K.A. Olive *et al.* (Particle Data Group), Chin. Phys. C 38, 090001 (2014), and 2015 update.

[3] C. Hanhart *et al.*, PRD 76 (2007) 034007.

[4] F. Nerling *et al.*, GSI Scientific Report 2015-1, (2015) 117.

[5] PANDA Collab., W. Erni *et al.*, arXiv:0903.3905 [hep-ex].

DOI:10.15120/GR-2017-1

Chiral anomaly in the baryonic sector of the eLSM *

L. Olbrich[1], *M. Zétényi*[2,3], *F. Giacosa*[1,4], *and D. H. Rischke*[1]

[1]Institute for Theoretical Physics, Goethe University, Frankfurt am Main, Germany; [2]Wigner Research Center for Physics, Budapest, Hungary; [3]ExtreMe Matter Institute EMMI, GSI Helmholtzzentrum für Schwerionenforschung, Darmstadt, Germany; [4]Institute of Physics, Jan Kochanowski University, Kielce, Poland

We consider the so-called extended linear sigma model (eLSM). For the case of $N_f = 3$, it contains (pseudo)scalar and (axial-)vector mesonic degrees of freedom [1] as well as glueballs [2, 3]. In order to reproduce known properties of the strong interaction, it features explicit and spontaneous breaking of chiral symmetry, as well as the $U(1)_A$ anomaly. Only recently, this model has been further extended to include also three-flavor baryonic fields describing four spin-$\frac{1}{2}$ baryon multiplets [4]. These additional fields allow to introduce a further chiral anomaly term in the baryonic sector, which will be investigated in this work.

Since every effective model should (to some extent) show the pattern of flavor symmetry, we first consider a simple model which features *only* the symmetry under $U(N_f)_V$ transformations. Although a model like this is very limited due to the lack of chiral symmetry, it appears to be useful to set a framework for further studies. We construct a Lagrangian which is flavor symmetric, as well as invariant under parity and charge-conjugation transformations. This allows to study the decays of negative-parity baryonic resonances into ground-state positive-parity baryonic states and one pseudoscalar meson. In fact, we investigate two distinct models, where in each one a different negative-parity baryon octet is described: first the octet $\{N(1535),\ \Lambda(1670),\ \Sigma(1620),\ \Xi(?)\}$, and second the heavier states $\{N(1650), \Lambda(1800), \Sigma(1750), \Xi(?)\}$.
As a result of the first model, we found that the flavor symmetry works well to describe most of the decay widths, but with important mismatches: flavor symmetry clearly underestimates (values are too small by around one order of magnitude) the decay widths of the octet resonances $\{N(1535),\ \Lambda(1670),\ \Sigma(1620),\ \Xi(?)\}$ into ground-state baryon states and one η meson.
On the contrary, in the second model where the excited states describe the heavier resonances $\{N(1650), \Lambda(1800), \Sigma(1750), \Xi(?)\}$, the decays into the η meson are in agreement with the experimental data.
The inability to describe certain decays into η properly shows that an additional component is needed when the η meson is considered.

A possible approach to solve this problem is the inclusion of the $U(1)_A$ anomaly. To investigate this idea in detail, we introduce a chiral anomaly term in the baryonic sector of eLSM. To this end, we use the baryonic fields and their properties as introduced in Ref. [4] to extend the Lagrangian by a term that is invariant under parity and charge conjugation, as well as $SU(3)_L \times SU(3)_R$ transformations. It contains two parameters of dimension [energy^{-2}], each one of them describing the coupling of either two equal- or different-parity baryon fields to the object

$$\det \Phi - \det \Phi^\dagger \ , \tag{1}$$

where the 3×3 matrix Φ describes the nonet of (pseudo)scalar mesons. The determinants in Eq. (1) ensure the explicit breaking of the symmetry under $U(1)_A$ transformations. Using the matrix form of Φ (as given in Ref. [1]) we obtain that the expression of Eq. (1) is proportional to the fields η_N and η_S (plus further terms with more than one meson field). Consequently, the anomaly term, which is the coupling of two baryon fields to this object, enhances the interactions with η and η' (being the physical fields that arise from admixtures of η_N and η_S).

As a further test, we incorporated this anomaly term (with only two baryonic fields and one parameter) into the flavor-only model described at the beginning. After fitting the parameter to the decay width of $N(1535) \to N\eta$, the improved model now reproduces also the decay width of $\Lambda(1670) \to N\eta$. This shows that the increase caused by the anomaly term is in agreement with the data from experiment. Furthermore, the model predicts an enhanced coupling to η' through the inclusion of the anomaly.

* Work supported by HGS-HIRe / HQM, the Hungarian OTKA Fund No. K109462, ExtreMe Matter Institute EMMI, and NCN OPUS project 2015/17/B/ST2/01625.

References

[1] D. Parganlija, P. Kovacs, G. Wolf, F. Giacosa and D. H. Rischke, Phys. Rev. D **87** (2013) 1, 014011 [arXiv:1208.0585 [hep-ph]].

[2] W. I. Eshraim, S. Janowski, F. Giacosa and D. H. Rischke, Phys. Rev. D **87** (2013) no.5, 054036 doi:10.1103/PhysRevD.87.054036 [arXiv:1208.6474 [hep-ph]].

[3] W. I. Eshraim, S. Janowski, A. Peters, K. Neuschwander and F. Giacosa, Acta Phys. Polon. Supp. **5** (2012) 1101 doi:10.5506/APhysPolBSupp.5.1101 [arXiv:1209.3976 [hep-ph]].

[4] L. Olbrich, M. Zétényi, F. Giacosa and D. H. Rischke, Phys. Rev. D **93** (2016) 3, 034021 [arXiv:1511.05035 [hep-ph]].

Investigation of a charmed scalar tetraquark candidate*

J. Berlin†[1] *and M. Wagner*[1]

[1]Goethe-Universität Frankfurt am Main, Institut für Theoretische Physik, Max-von-Laue-Straße 1, D-60438 Frankfurt am Main, Germany

The discovery of the positive parity charmed mesons $D^*_{s0}(2317)$ [1] and $D_{s1}(2460)$ [2, 3] at the BaBar, Belle and CLEO has attracted much interest as a structure beyond conventional quark-antiquark states might apply. For our first lattice study we investigate a $D^*_{s0}(2317)$ candidate regarding a possible four-quark structure. This state is of lower mass than predicted by many quark models and the $D^*_{s0}(2317) - D^*_0(2400)$ mass difference is too small to account for the s-u/d quark mass difference.

Utilizing the variational method we aim to study the heavy tetraquark candidate $D^*_{s0}(2317)$, close to the neighboring $D_s\pi$ and $D\bar{K}$ thresholds. We compute two-point correlation functions of two-quark and four-quark interpolating operators of different structure including quark-antiquark type, mesonic molecule type, diquark-antidiquark type and two-meson type, i.e.

$$\begin{aligned}
\mathcal{O}^{q\bar{q}} &= \frac{1}{\sqrt{V_s}} \sum_{\mathbf{x}} \Big(\bar{c}(\mathbf{x})s(\mathbf{x})\Big), \\
\mathcal{O}^{D\bar{K},\,\text{point}} &= \frac{1}{\sqrt{V_s}} \sum_{\mathbf{x}} \Big(\bar{c}(\mathbf{x})\gamma_5 u(\mathbf{x})\Big)\Big(\bar{u}(\mathbf{x})\gamma_5 s(\mathbf{x})\Big), \\
\mathcal{O}^{D_s\pi,\,\text{point}} &= \frac{1}{\sqrt{V_s}} \sum_{\mathbf{x}} \Big(\bar{c}(\mathbf{x})\gamma_5 s(\mathbf{x})\Big)\Big(\bar{u}(\mathbf{x})\gamma_5 u(\mathbf{x})\Big), \\
\mathcal{O}^{Q\bar{Q}} &= \frac{1}{\sqrt{V_s}} \sum_{\mathbf{x}} \epsilon_{abc}\Big(\bar{u}_b(\mathbf{x})(C\gamma_5)\bar{s}^T_c(\mathbf{x})\Big) \\
&\qquad \epsilon_{ade}\Big(c^T_d(\mathbf{x})(C\gamma_5)u_e(\mathbf{x})\Big), \\
\mathcal{O}^{D\bar{K},\,\text{2part}} &= \frac{1}{V_s} \sum_{\mathbf{x},\mathbf{y}} \Big(\bar{c}(\mathbf{x})\gamma_5 u(\mathbf{x})\Big)\Big(\bar{u}(\mathbf{y})\gamma_5 s(\mathbf{y})\Big), \\
\mathcal{O}^{D_s\pi,\,\text{2part}} &= \frac{1}{V_s} \sum_{\mathbf{x},\mathbf{x}} \Big(\bar{c}(\mathbf{x})\gamma_5 s(\mathbf{x})\Big)\Big(\bar{u}(\mathbf{y})\gamma_5 u(\mathbf{y})\Big).
\end{aligned}$$

This is done by employing the most efficient lattice techniques or combination of techniques [4] to provide the best possible signal at comparable computational costs.

The resulting correlation matrix C yields of a tower of states with the quantum numbers of interest ($J^P = 0^+$)

$$C_{jk}(t) = \langle \mathcal{O}_j \mathcal{O}^\dagger_k \rangle = \sum_{n=0}^{\infty} \langle 0|\mathcal{O}_j(t)|n\rangle \, \langle n|\mathcal{O}^\dagger_k(0)|0\rangle \, e^{-E_n t}.$$

These states can be extracted from the eigenvalues after solving a generalized eigenvalue problem

$$C(t)\, v_n(t,t_0) \;=\; \lambda_n(t,t_0)\, C(t_0)\, v_n(t,t_0),$$

$$E_n = \lim_{t\gg a} E^{\text{eff}}_n(t,t_0) = \lim_{t\gg a} \frac{1}{a} \log \frac{\lambda_n(t,t_0)}{\lambda_n(t+a,t_0)}.$$

The so-called *effective masses* that are obtained from various operator bases regarding our correlation matrix are shown in Figure 1.

We observe a third low-lying state with an indication of a structure beyond the conventional quark-antiquark interpretation. Although the state is dominated by a $q\bar{q}$ signal (violet), it is also observed without employing two-quark structures (yellow). In the presence of both dominating contributions is a four-quark component is still sizeable.

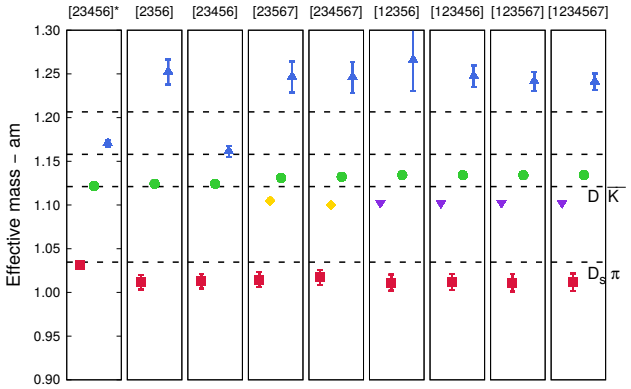

Figure 1: Observed states for $m_\pi \approx 300$ MeV from various interpolator bases, referring to $1 \equiv q\bar{q}$, $2;3 \equiv D\bar{K}$, point; $D_s\pi$, point, $5;6 \equiv D\bar{K}$, 2part; $D_s\pi$, 2part, $4;7 \equiv$ light; heavy $Q\bar{Q}$ interpolating field operators.

References

[1] B. Aubert *et al.* [BaBar Collaboration], Phys. Rev. Lett. **90**, 242001 (2003) doi:10.1103/PhysRevLett.90.242001 [hep-ex/0304021].

[2] K. Abe *et al.* [Belle Collaboration], Phys. Rev. Lett. **92**, 012002 (2004) doi:10.1103/PhysRevLett.92.012002 [hep-ex/0307052].

[3] D. Besson *et al.* [CLEO Collaboration], Phys. Rev. D **68**, 032002 (2003) Erratum: [Phys. Rev. D **75**, 119908 (2007)] doi:10.1103/PhysRevD.68.032002, 10.1103/PhysRevD.75.119908 [hep-ex/0305100].

[4] A. Abdel-Rehim, C. Alexandrou, J. Berlin, M. Dalla Brida, J. Finkenrath and M. Wagner, arXiv:1701.07228 [hep-lat].

* Work support by — the Emmy Noether Programme of the DFG (German Research Foundation), grant WA 3000/1-1 — the Helmholtz International Center for FAIR within the framework of the LOEWE program launched by the State of Hesse

† berlin@th.physik.uni-frankfurt.de

DOI:10.15120/GR-2017-1

Timing test of the NeuRad neutron detector prototype*

D. Kostyleva[1,2,3], *A. Bezbakh*[2,4], *V. Chudoba*[2,5], *A. Fomichev*[2], *A. Gorshkov*[2,4], *O. Kiselev*[3], *S. Krupko*[2,4], *I. Mukha*[3], *and I. Muzalevsky*[2,6]

[1]JLU Giessen, Germany; [2]FLNR JINR Dubna, Russia; [3]GSI Helmholtzzentrum, Darmstadt; [4]FSBI NRC "Kurchatov Institute" - ITEP, Moscow, Russia; [5]Silesian University in Opava, Czech Republic; [6]Dubna State University, Russia

The NeuRad neutron detector is constructed out of scintillation fibers and is aimed on measuring the neutron - heavy fragment angular correlations from exotic neutron decays. The results of the first test of NeuRad prototype timing properties are presented in this report.

The EXPERT (EXotic Particle Emission and Radioactivity by Tracking) is a part of the physics program of the Super-FRS Experiment Collaboration [1]. The EXPERT experiments are aimed at studies of the unknown exotic nuclear systems beyond the proton and neutron drip-lines. These experiments will use the first half of the Super-FRS as a radioactive beam separator and its second half as a high-resolution spectrometer. NeuRad detector will provide precise information on angular correlations between nuclear-decay neutrons and the charged decay products measured by the rest of EXPERT setup. An information on angular correlations will be used to determine the decay energy of the precursor, its life time and mode of the decay.

The detector is designed in order to provide sufficient detection efficiency and fine position resolution for neutrons at expected energies about 200-800 MeV interacting with the material of fibers, in particular, via elastic scattering. The detector will be constructed of scintillating fibers ($\approx 10^3$ units) with 3x3 mm^2 cross section and the length of 1 m each, which will be grouped into bundles. Two multi-anode PMT's will be mounted on each side of bundle, each side of fiber will be read out by one pixel. Bundles will be oriented along beam axis meaning that the frontal PMT will be penetrated by neutrons. The detector will be placed at distance of $\approx$ 30 m from the focal plane FRF1. Such setup will ensure total angular acceptance of the detector up to $\pm$6 mrad which reflects low transfer momentum, corresponding to the decay energy expected at the range of 0.1-100 keV.

One of the significant NeuRad characteristics is the time resolution. The first neutron hit has to be determined in order to distinguish between one multi-scattered neutron and the event with multiple neutrons. The longitudinal (z) position, which enhances angular resolution, will be extracted from the time difference between the signals collected on both sides of the detector. In order to obtain required angular resolution, a position resolution about 6 cm is needed. This corresponds to the time-uncertainty of $\sim$ 0.5 ns. Test measurements of timing characteristics has been performed with NeuRad detector demonstrator at FLNR JINR recently.

The demonstrator consists of one bundle of BCF12 fibers 25 cm long coupled with two PMT's H9500. It has been irradiated with a γ-source ^{60}Co in a shielded black box. Unamplified signals from the PMTs were collected by DRS4 digitizer board [2] and Tektronix MSO7354 oscilloscope for further offline analysis. Qualitative difference between signals acquired by both devices, despite differences in sampling rate (5 GS/s of DRS4 board and 10 GS/s of the oscilloscope), bandwidth (750 MHz of DRS4 and 2 GHz of the oscilloscope) and amplitude resolution (12 bit and 10 bit correspondingly), has not been observed.

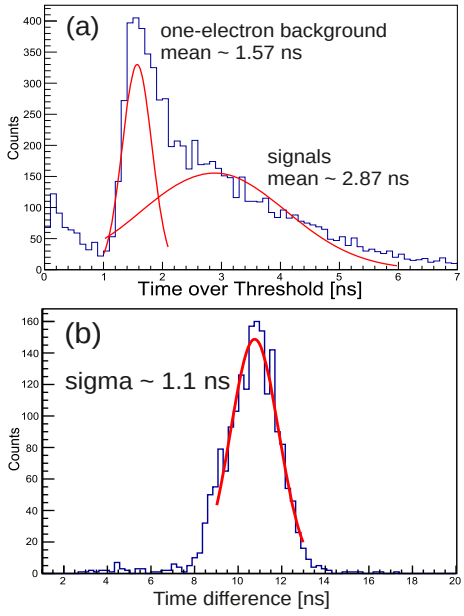

Figure 1: (a) Time-over-threshold spectra of PMT signals, (b) difference between times of γ-ray registration from opposite sides of NeuRad obtained using time-over-threshold selection.

Data have been processed using time difference measurement techniques (Constant Fraction Discrimination, Leading Edge Analysis, fitting the shape of rising edge etc.) which were implemented in ExpertRoot software [3]. Time-over-threshold spectra allowed to implement signal selection avoiding noise and one-electron PMT background, see Fig.1(a). Time uncertainty between two opposite ends of one fiber was determined to be of about 1 ns (σ), see Fig.1(b).

A reference measurement conducted with the same con-

* The work was partly supported by grants provided by MEYS Czech Republic (projects LTT17003 and LM2015049) and RSF (project No. 17-12-01367), A.B., A.G. and S.K have been supported by FAIR-Russia Research Center as well.

figuration of the setup but a thin (4 mm thick) BC-420 square scintillator has shown that the time resolution can be improved down to $\sigma \approx$ 0.5 - 0.7 ns.

The next test of NeuRad prototype is planned with the multi-channel electronics from the company PET SYS Electronics [4].

References

[1] J. Aysto et al. Nucl. Inst. Meth. in Phys. Res. B376 (2016) 111

[2] https://www.psi.ch/drs/evaluation-board

[3] http://er.jinr.ru

[4] http://www.petsyselectronics.com/web/

DOI:10.15120/GR-2017-1

Time-of-Flight measurements with a liquid Cherenkov detector as a possible TOF detector for the Super-FRS

N. Kuzminchuk-Feuerstein[*1], *B. Voss*[1], *E. Fiks*[2], *and the SFRS collaboration*[1]
[1]GSI, Darmstadt, Germany; [2]National Research Tomsk Polytechnic University, Tomsk, Russia

Aiming to develop a system with a precision down to about 50 ps in time and resistant to a high radiation rate of relativistic heavy ions of up to 10^7 per spill (at the second focal plane), we have shown a conceptual design for a Cherenkov detector envisioned for the future TOF measurements employing a fluid radiator. After search of suitable radiator an Iodine-Naphthalene liquid ($C_{10}H_7I$) is proposed [1]. The choice of the radiator was motivated by its high refractive index (n=1.7003) and relatively low density allowing to detect low-energetic particles with minimized deterioration of the beam quality.

The first proof of principle experiment with a Cherenkov TOF prototype detector using a $C_{10}H_7I$ radiator was performed at the experimental place CaveC of the SIS facility at GSI in April 2014 with ^{58}Ni beam at 300 - 1500 MeV/u [2] [3]. In the summer 2016 a time-of-flight was measured with ^{124}Xe ions with 600 MeV/u at CaveC.

Fig. 1 shows a layout of our experimental setup used in the measurements with xenon ions. A quadratic plastic scintillator (S) is used as a start detector for time-of-flight measurements. Scintillator has a size of 5.5 x 5.5 x 2 cm^2 and placed in the vacuum chamber perpendicular to the beam direction, directly at the beginning of HTD-beam line. The scintillation light is directly read out by 4 PMTs (S_u, S_d, S_l, S_r), placed on the top, bottom, left and right sides of the scintillator. For high accuracy timing measure-

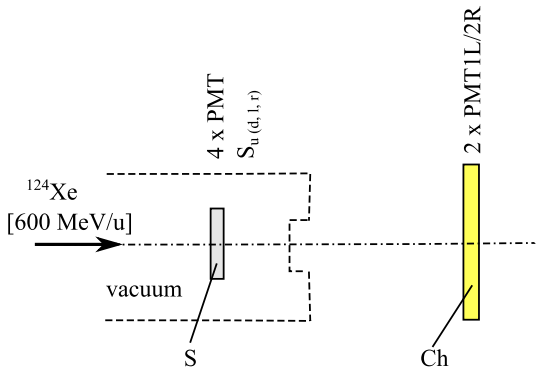

Figure 1: Detector arrangement used in timing measurements with xenon ions at CaveC.

ments the VME - Module VFTX (VME-FPGA-TDC) [4] was used. First, the signals from two ends of the Cherenkov detector (PMT1L, PMT2R) and four ends of the scintillator counter were delivered to CFD. Then the TOF between (Ch) and (S) was recorded by TDC.

The timing of the detectors is calculated by taking the average time detected by four PMTs of a plastic scintillator $< T_S >$ and by two PMTs of a Cherenkov detector $< T_S >$. Time-of-flight distribution between (Ch) and (S) detectors was measured as:

$$TOF(Ch-S) =< T_{Ch} > - < T_S > \quad (1)$$

The width of the time distribution is given by

$$\sigma_{TOF} = \sqrt{\sigma^2_{T_{Ch}} - \sigma^2_{T_S}} \quad (2)$$

where σ is the accuracy of the TOF measurement. Fig. 2 shows resulting time-of-flight distribution $TOF(Ch-S)$.

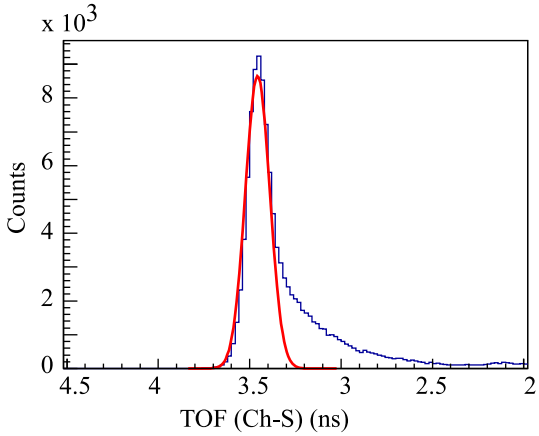

Figure 2: Time-of-flight spectra TOF(C-S) measured with xenon ions between Cherenkov detector and plastic scintillator. The Gaussian fit is indicated with a red solid line. The width of the distribution equals 63 ps.

References

[1] N. Kuzminchuk-Feuerstein et. al., GSI Scientific Report 2013, 103.

[2] N. Kuzminchuk-Feuerstein et. al., GSI Scientific Report 2014, 141.

[3] N. Kuzminchuk-Feuerstein et. al., First beam test of a liquid Cherenkov detector prototype for a future TOF measurements at the Super-FRS, submitted to Nucl. Instrum. and Meth. A (2017).

[4] J. Frühauf et. al., GSI Scientific Report 2012, 300.

* n.kuzminchuk@gsi.de

Systematic investigations of charge states and purity of projectile and fission fragments extracted from the stopping cell of the (Super-)FRS *

I. Miskun[1], *A.-K. Rink*[1], *F. Greiner*[1], *S. Ayet*[1,2], *S. Bagchi*[2], *J. Bergmann*[1], *P. Constantin*[3], *T. Dickel*[2], *J. Ebert*[1], *A. Finley*[4], *H. Geissel*[1,2], *E. Haettner*[2], *C. Hornung*[1], *S. Kaur*[5], *W. Lippert*[1], *I. Mardor*[6,7], *B. Mei*[3], *I. Moore*[8], *J.-H. Otto*[1], *S. Pietri*[2], *A. Pikhtelev*[9], *W. R. Plaß*[1,2], *I. Pohjalainen*[8], *A. Prochazka*[2], *S. Purushothaman*[2], *C. Rappold*[2], *M. P. Reiter*[4], *C. Scheidenberger*[1,2], *Y. Tanaka*[2], *H. Toernqvist*[2], *H. Weick*[2], *J. S. Winfield*[2], *X.Xu*[2], *and M. Yavor*[10]

[1]JLU, Gießen, Germany; [2]GSI, Darmstadt, Germany; [3]ELI-NP, Bucharest, Romania; [4]TRIUMF, Vancouver, Canada; [5]Saint Mary's Univ., Halifax, Canada; [6]Tel Aviv University, Israel; [7]Soreq NRC, Yavne, Israel; [8]Univ. of Jyväskylä, Finland; [9]Inst. for Energy Problems of Chem. Phys., RAS, Chernogolovka, Russia; [10]IAI, RAS, St. Petersburg, Russia

The prototype of the cryogenic stopping cell (CSC) [1] for the Low-Energy Branch of the Super-FRS has been developed and successfully commissioned as a part of the FRS Ion Catcher experiment [2] at GSI. In several experiments various ^{238}U and ^{124}Xe projectile and fission fragments were produced, separated and range-bunched in the FRS, thermalized, extracted from the CSC and identified. The measured charge states of the extracted ions are shown in the bottom section of each element in Fig.1. In the top section of each element the predicted charge states are presented, based on the assumption that charge exchange processes in the CSC are defined by the ionization potential of its contaminants and dominated by N_2 molecules, which are present in trace amounts in the He buffer gas. The results indicate that this assumption is correct and there are no contaminants such as O_2, oil, water, etc. in the CSC. Further purification of the buffer gas can result in the survival of higher charge states of the thermalized ions and, therefore, limitations of the mass range of the ions transmitted by the RF carpet. In the future [3] trace gases will be used to control the charge state of thermalized ions.

Operation with high intensity beams causes high ionization and reveals contaminants introduced together with the He buffer gas. These are light molecules containing noble gases, which do not harm ion survival, but can still spoil the measurement. An example can be seen in Fig.2a, where a time-of-flight spectrum of ^{124}Xe primary beam taken with the multiple-reflection time-of-flight mass spectrometer (MR-TOF-MS) [4] is dominated by Kr molecules. These contaminants can be removed by using a collision induced dissociation (CID) process [5] together with two-stage mass separation [6] in the RFQ beamline downstream of the CSC. It proved to be a universal and effective tool for beam purification. In Fig.2b a spectrum is shown, where this method was applied. It can be seen that all of the contaminants are removed from the spectrum, including the isobar of ^{124}Xe with a mass difference of only $\approx$ 300 keV. This enables a precision measurement of ^{124}Xe, the ion of interest in this case.

*This work was supported by the BMBF under contracts No. 05P12RGFN8 and 05P16RGFN1, by the HMWK through the LOEWE Center HICforFAIR, by HGS-HIRe, by JLU Gießen and GSI under the JLU-GSI strategic Helmholtz partnership agreement.

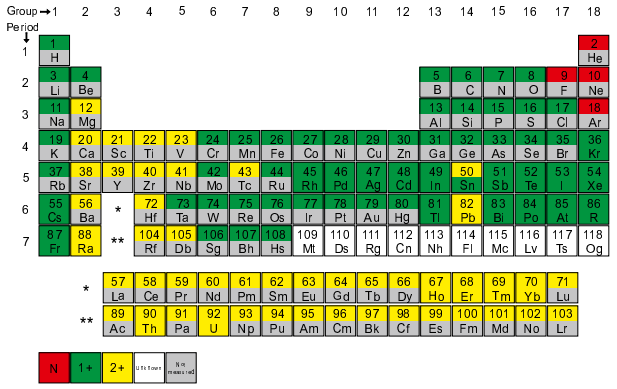

Figure 1: Periodic table showing the charge states in which the ions are extracted from the CSC. Upper section of each element: predicted; lower section: measured.

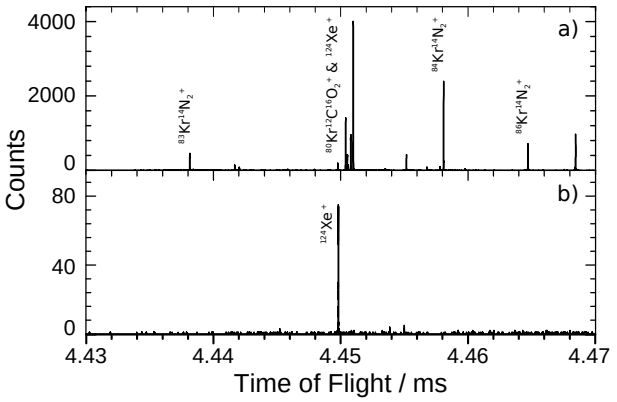

Figure 2: Multi-turn TOF spectra of ^{124}Xe primary beam: (a) no CID applied, the spectrum is dominated by contaminants; (b) CID applied, the contaminants are removed.

References

[1] M. Ranjan et al., Europhys. Lett. 96 (2011) 52001.

[2] W.R. Plaß et.al., NIM B 317 (2013) 457-462.

[3] T. Dickel et al., NIM B 376 (2016) 216.

[4] T. Dickel et al., NIM A 777 (2015) 172-188.

[5] F. Greiner, Master thesis, JLU, Gießen, Germany, 2017.

[6] I. Miskun, Diploma thesis, TPU, Tomsk, Russia, 2015.

DOI:10.15120/GR-2017-1

Complete ion identification by proton and mass number via high-resolution mass spectrometry at the (Super-)FRS *

C. Hornung[1], S. Ayet[1,2], S. Bagchi[2], J. Bergmann[1], P. Constantin[3], T. Dickel[2], J. Ebert[1], A. Finlay[4], H. Geissel[1,2], F. Greiner[1], E. Haettner[2], S. Kaur[5], W. Lippert[1], I. Mardor[6], B. Mei[3], I. Miskun[2], I. D. Moore[7], J.-H. Otto[1], S. Pietri[2], A. Pikhtelev[8], W. R. Plaß[1,2], I. Pohjalainen[7], A. Prochazka[2], S. Purushothaman[2], C. Rappold[2], M. P. Reiter[4], A.-K. Rink[1], C. Scheidenberger[1,2], Y. Tanaka[2], H. Toernqvist[2], H. Weick[2], J. S. Winfield[2], X. Xu[1,2], and M. I. Yavor[9]

[1]JLU, Gießen, Germany; [2]GSI, Darmstadt, Germany; [3]ELI-NP, Bucharest, Romania; [4]TRIUMF, Vancouver, Canada; [5]Astronomy and Phys. Dep., Saint Mary's Univ., Halifax, Canada; [6]Soreq NRC, Yavna, Israel; [7]Univ. of Jyväskylä, Finland; [8]Inst. for Energy Problems of Chem. Phys., RAS, Chernogolovka, Russia; [9]IAI, RAS, St. Petersburg, Russia

Ion identification and separation are important at all present and future rare-isotope facilities. The in-flight separators FRS / Super-FRS [1, 2] use the $B\rho - \Delta E - B\rho$ method to achieve isotopic-spatial separation. At relativistic velocities the verification of the particle identification (PID) by proton number (Z) and mass number (A) of the selected bare ions can be easily performed with particle detectors via velocity, energy-deposition and magnetic rigidity measurements in coincidence. Still the separation and identification require both an elaborated absolute calibration. At lower velocities (300 MeV/u), the fragments emerge from the target in different ionic charge states which makes an unambiguous PID very difficult. Here, we demonstrate that high-resolution mass spectrometry represents a universal method to provide an unambiguous PID at the final focal plane of the FRS.

In our previous FRS experiments we reached a mass resolving power (MRP) of 450000 with the multiple-reflection time-of-flight mass spectrometer (MR-TOF-MS) [3]. It is part of the FRS Ion Catcher [4], which is a test bench for the Low-Energy-Branch (LEB) of the Super-FRS [2] at FAIR. Together with a cryogenic gas-filled stopping cell (CSC) the MR-TOF-MS has the capability to perform a complete PID of exotic nuclei based on their mass-to-charge ratio only.

In Fig. 1 we illustrate the ensemble of isotopes which enters the CSC for two experiments centered either on ^{94}Ag or ^{202}Os fragments. Although the number of possibly implanted isotopes is relatively large due to the applied monoenergetic degrader and the selected kinetic energy domain of 300 MeV/u, all ions involved can be uniquely identified with the achieved MRP.

In our latest experiment uranium projectile fragments were produced at 300 MeV/u, spatially separated in-flight, energy bunched and efficiently stopped in the CSC, fast extracted and finally analyzed with the MR-TOF-MS. The 300 MeV/u corresponds to the energy at the LEB. The nuclides could be identified unambiguously already with a modest MRP of 75000 (Fig. 2).

*This work was supported by the BMBF under contracts No. 05P12RGFN8 and 05P16RGFN1, by the HMWK through the LOEWE Center HICforFAIR, by HGS-HIRe, by JLU Gießen and GSI under the JLU-GSI strategic Helmholtz partnership agreement.

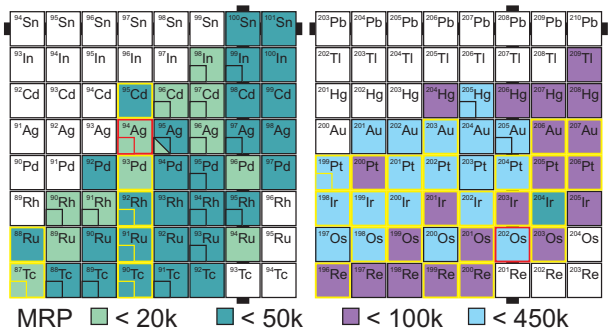

Figure 1: Required MRP to achieve unique PID in two typical isotope domains (^{94}Ag and ^{202}Os). An MRP corresponding to twice the mass difference between adjacent isobars has been assumed. The fragments were produced and separated at 300 MeV/u. All fragments which are stopped together with the goal fragment (red frame) in the CSC got a yellow frame.

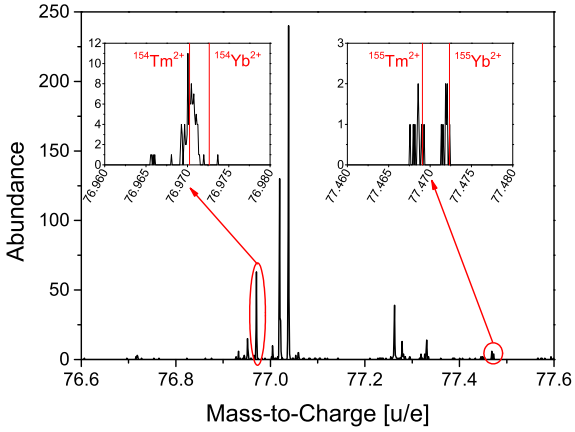

Figure 2: Measured mass-to-charge-spectrum of the uranium fragments under LEB conditions.

References

[1] H. Geissel et al., Nucl. Instrum. Methods B 70 (1992) 286.
[2] H. Geissel et al., Nucl. Instrum. Methods B 204 (2003) 71.
[3] T. Dickel et al., Nucl. Instrum. Methods A 777 (2015) 172.
[4] W.R. Plaß et al., Nucl. Instrum. Methods B 317 (2013) 457.

Excitation of baryonic resonances in projectiles of ^{124}Xe at 600A MeV

J.L. Rodríguez-Sánchez[1], J. Benlliure[1], S. Bagchi[2], J. Díaz-Cortes[1], H. Geissel[2], E. Haettner[2], H. Lenske[3], A. Prochazka[2], C. Scheidenberger[2], Y. Tanaka[2], I. Vidaña[4], H. Weick[2], and J.S. Winfield[2]

[1]University of Santiago de Compostela, Spain; [2]GSI, Germany; [3]Justus-Liebig-Universität Giessen, Germany; [4]University of Coimbra, Portugal

The structure of baryons, such as the Δ and Roper (N*) resonances, and their excitation spectrum is one of the unsolved issues of strong interaction physics. Recently, the early appearance of Δ-isobars in dense nuclear matter has inspired many studies relevant to neutron stars [1] and heavy-ion collisions [2]. In particular, very compact stellar configurations are reached due to the introduction of Δ-isobars [1]. However, the in-medium properties of baryon resonances are not well understood. Up to now, the in-medium effects of Δ-isobars have been studied in heavy-ion collisions at kinetic energies above the production threshold using pion-nucleus and nucleon-nucleus reactions [3, 4], where there is not a good control over the production of residual fragments and thus over the number of collisions. Further investigations were performed with isobar charge-exchange reactions at SATURNE using nucleus-nucleus collisions [5]. This kind of reaction allows us to constrain the nucleus-nucleus collision to one nucleon-nucleon reaction at the surface of both nuclei. However, the experiments carried out at SATURNE did not permit to measure the pion emitted in the decay of the resonances in coincidence with the isobar charge-exchange reaction.

To go a step further, we propose to perfome complete kinematics measurements of isobar charge-exchange reactions, detecting the residual nucleus in coincidence with pions in order to separate the quasi-elastic and inelastic componets observed in the missing-energy spectrum [6]. The GSI experimental facilities provide us unique conditions to perform these measurements with high quality allowing us to identify the isobaric charge-exchange reactions from the determination of the atomic and mass number of the residual fragments event-by-event. For the measurement of the pions, a specific setup (based on a solenoid magnet and tracking detectors) will be installed in the middle focal plane of the fragment separator FRS in order to deflect and trace the pions. We plan to perform this measurement with the WASA detector [7].

In this work we report on the results from a experimental test carried out at the FRS in July of 2016 for the phase 0 of this new generation of experiments. We measured the excitation of isobar charge-exchange reactions in stable projectiles of ^{124}Xe impinging in a carbon target of 89 mg/cm^2 placed in the intermediate focal plane of the FRS, using vacuum in the experimental areas S0, S1, S2, and S3 in order to reduce the energy and angular straggling of the projectiles and residual fragments. In Fig. 1 we display the missing-energy spectrum for the isobar charge-exchange reaction ^{12}C(^{124}Xe, ^{124}Cs)X at 600A MeV. The peak close to zero corresponds to the quasi-elastic channel (n, p) and the peak around -300 MeV represents the inelastic contribution due to the excitation of the Δ and Roper (N*) resonances. Thanks to the thin carbon target and the use of vacuum we obtained this spectrum with an energy resolution of 7 MeV, improving the resolution in a factor two with respect to previous experiment performed at FRS [8] or at SATURNE [5].

The new generation of experiments at the FRS will help us to separate the quasi-elastic and inelastic componets observed in the missing-energy spectrum, leading to a full identification of the baryonic resonances excited in the nuclear medium.

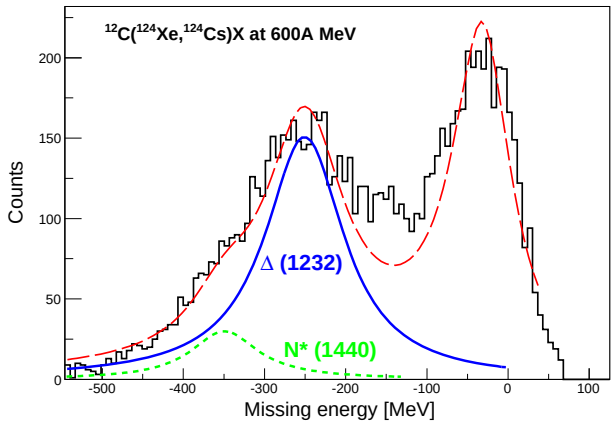

Figure 1: Missing-energy spectrum for the isobar charge-exchange reaction ^{124}Xe + ^{12}C at 600A MeV going to ^{124}Cs. Solid and short-dashed lines show the Δ and Roper (N*) contributions obtained by fitting the spectrum to Breit-Wigner distributions, respectively.

References

[1] A. Drago et al., Phys. Rev. C **90**, 065809 (2014).

[2] Z.-Q. Feng, Phys. Rev. C **94**, 054617 (2016).

[3] S. B. Kaufman et al., Phys. Rev. C **20**, 2293 (1979).

[4] J. Chiba et al., Phys. Rev. Lett. **67**, 1982 (1991).

[5] D. Bachelier et al., Phys. Lett. B **172**, 23 (1986).

[6] I. Vidaña et al., EPJ Web of Conferences **107**, 10003 (2016).

[7] C. Bargholtz et al., Nucl. Instrum. Meth. A **594**, 339 (2008).

[8] J. Vargas et al., Nucl. Instrum. Meth. A **707**, 16 (2013).

DOI:10.15120/GR-2017-1

Measurements of hypernuclear decay fragments at FRS for Phase0-FAIR hypernuclear experiment

C.Rappold[*1,2], *T.R. Saito*[1,3,4], *and C. Scheidenberger*[1,2]

[1]GSI, Darmstadt, Germany; [2]Justus-Liebig-Universität Giessen, Germany; [3]Johannes Gutenberg-Universität, Mainz, Germany; [4]The Helmholtz Institute Mainz, Mainz, Germany

The first experiment of the HypHI collaboration demonstrated the feasibility of the hypernuclear spectroscopy by means of heavy ion beam induced reactions. The phase 0 experiment was performed with a ^{6}Li beam at 2AGeV impinged on a stable ^{12}C target material. The main results of the experiment showed the reconstruction and identification of decay vertexes of Λ particle and $^{3}_{\Lambda}$H, $^{4}_{\Lambda}$H [1, 2, 3].

A novel experiment at the FRS fragment separator for the FAIR-Phase 0 beam-time period is proposed in order to assess the existence of the nnΛ possible bound state. A new experimental concept have been under development and their designs have been already reported [4, 5]. In order to assess if this experimental method is viable, a experiment with similar conditions of the previously successful experiment will be performed. Light hypernuclei $^{3}_{\Lambda}$H, $^{4}_{\Lambda}$H and nnΛ will be the species of interest that will be aimed to be reconstructed and identified by invariant mass method.

After the two-body decay, a narrow magnetic rigidity acceptance window will be set for the FRS in order to measure precisely the momentum of outgoing decay fragment. The detection apparatus at the S2 experimental area will be responsible for the measurement of a large portion of the emitted π^{-}. The acceptance and measurement efficiency of the S2-S4 section of the FRS is assessed by means of MOCADI simulations.

The full phase-space distribution in position and momentum is simulated by Geant4 simulations. The Geant4 simulation code is responsible for the detail treatment of the hypernuclear decay, the tracking within the experimental apparatus placed in the S2 area, and the hit digitalization within the different detection systems in the S2 area. decay π^{-} and other light particles produced in the reaction and in the hypernuclear decay are measured in the dedicated apparatus in S2, while fragments continue up to the S2 exit.

Detectors placed at the S2 exit register the full phase-space of the outgoing fragments. Specific code for loading Geant4 events as input event into MOCADI simulations was implemented and allowed a event by event simulations in the continuity of Geant4 simulations. A Bρ scanning is then possible in order to assess the decay fragment measurement efficiency of the S2-S4 section of the FRS. Fig. 1a shows the phase-space distribution as a function of Bρ of decay ^{3}He of $^{3}_{\Lambda}$H at the entrance and exit of the S2-S4 section of the FRS.

Fig. 1b shows the differential efficiency of S2-S4 section for FRS setting center at Bρ of 12.6 Tm for ^{3}He decay fragment of $^{3}_{\Lambda}$H. After performing the Bρ scanning over the full phase-space, the maximum efficiency of measurement between S2-S4 was determined. The average measurement efficiency for ^{3}He, ^{4}He and d are around 40% respectively.

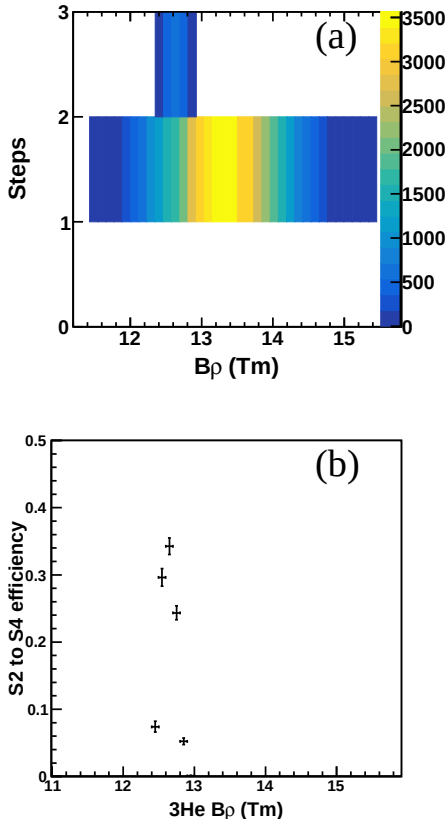

Figure 1: Differential efficiency of the S2-S4 section of the FRS for the momentum measurement of decay ^{3}He of $^{3}_{\Lambda}$H. The central Bρ of 12.6 Tm was set in the MOCADI simulations.

References

[1] C. Rappold *et al.*, Nucl. Phys. A **913**, 170 (2013).

[2] C. Rappold *et al.*, Phys. Rev. C **88**, 041001 (2013).

[3] C. Rappold *et al.*, Phys. Lett. B **747**, 129 (2015).

[4] C. Rappold *et al.*, GSI Scientific Report 2014 [GSI Report 2015-1] (2015) p. 135.

[5] C. Rappold *et al.*, GSI Scientific Report 2014 [GSI Report 2015-1] (2015) p. 136.

* c.rappold@gsi.de

Particle identification using cylindrical detector system for Phase0-FAIR hypernuclear experiment

C.Rappold[*1,2], *T.R. Saito*[1,3,4], *and C. Scheidenberger*[1,2]

[1]GSI, Darmstadt, Germany; [2]Justus-Liebig-Universität Giessen, Germany; [3]Johannes Gutenberg-Universität, Mainz, Germany; [4]The Helmholtz Institute Mainz, Mainz, Germany

The feasibility of the hypernuclear spectroscopy by means of heavy ion beam induced reactions was demonstrated by the results obtained in the first experiment of the HypHI collaboration. A ^{6}Li beam at 2AGeV impinged on a stable ^{12}C target. The main results of the experiment showed the measurements of Λ hyperon and $^{3}_{\Lambda}$H, $^{4}_{\Lambda}$H. Results on the invariant masses, lifetime and production cross sections were published [1, 2, 3].

For the FAIR-Phase 0 beam-time a new hypernuclear spectroscopy experiment is proposed in order to assess the existence of the nnΛ possible bound state. This novel experiment will take place at the FRS fragment separator. The section TA-S1-S2 of FRS will use to deliver the stable beam with a energy of 2AGeV to the S2 experimental area. In the S2 area, the possibility to install a cylindrical detector system that involved a solenoid magnet is considered as described in [4]. A target will placed around 40 cm to 60 cm upstream to this detection system. The light hadrons, π^-, π^+, K$^+$, K$^-$, and protons will be able to be measured by the cylindrical system. A central drift chamber and hodoscope barrel will be responsible for the main tracking system for the momentum measurement. Additional planar tracker stations will be placed in the upstream area of the detection system. The most important aspect of this cylindrical detector system will be to precisely measure the decay π^- from the nnΛ and other produced hypernuclei. As well the produced kaons from the strangeness s-$\bar{\text{s}}$ production will be possible to be measured and identified. After the hypernuclear two-body decay, a narrow magnetic rigidity acceptance window will be set for the S2-S4 section of FRS in order to measure precisely the momentum of outgoing decay fragment.

The full phase-space distribution in position and momentum is simulated by Geant4 simulations. The Geant4 simulation code is responsible for the detail treatment of the hypernuclear decay, the tracking within the experimental apparatus placed in the S2 area, and the hit digitalization within the different detection systems in the S2 area. The MOCADI simulations are then used for the study of the S2-S4 section of FRS efficiency. Decay π^- and other light particles produced in the reaction and in the hypernuclear decay are measured in the dedicated apparatus in S2, while fragments continue up to the S2 exit. Fig. 1 shows the results of the particle identification of track reconstruction of the Geant4-simulated events. The tracking is based on Kalman Filter and the framework developed for full data analysis of the Phase 0 experiment. A time-of-flight resolution of 150 ps was assumed in the simulations. Fig. 1a shows the β-momentum correlation while the mass distribution, $m = p\sqrt{\beta^{-2}-1}$, of the reconstructed light hadrons is shown in Fig. 1b. A clear identification and separation between π, kaon and proton is visible in each plot.

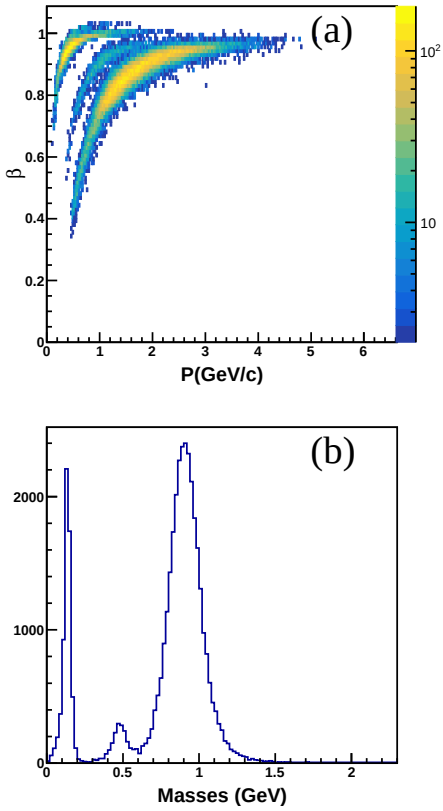

Figure 1: Particle identification plots for light hadrons within the cylindrical detector system. (a) The β-momentum correlation shows clear distinction between π, kaons and protons. (b) The mass distribution spectrum of light hadrons calculated from β and momentum.

References

[1] C. Rappold *et al.*, Nucl. Phys. A **913**, 170 (2013).

[2] C. Rappold *et al.*, Phys. Rev. C **88**, 041001 (2013).

[3] C. Rappold *et al.*, Phys. Lett. B **747**, 129 (2015).

[4] C. Rappold *et al.*, GSI Scientific Report 2014 [GSI Report 2015-1] (2015) p. 135.

* c.rappold@gsi.de

DOI:10.15120/GR-2017-1

Simulations of RCE, ChR & HWC channeling

H. Geissel[1], *O.V. Bogdanov*[*2], *C. Scheidenberger*[1], *Yu.L. Pivovarov*[2], *N. Kuzminchuk-Feuerstein*[1], *E.I. Rozhkova*[2], *T.A. Tukhfatullin*[2], *and the Super-FRS Experiment Collaboration*[1]

[1]GSI, Darmstadt, Germany; [2]National Research Tomsk Polytechnic University, Russia

The perspective atomic physics experiments are the part of Super-FRS collaboration program [1], in particular for the first time to observe the nuclear Okorokov effect of resonant coherent excitation (RCE) of relativistic nuclei passing through a crystal [2]. The RHI beam energy at Super-FRS is up to 1500 MeV/u, and perturbation harmonic energy at axial channelling in a crystal is equal to $\hbar\omega_n = (2\pi\hbar c/d) \cdot \gamma \cdot \beta \cdot n$, n=1,2,.., where d is the spacing between atoms in the crystal axis, γ is the relativistic factor and $\beta = v/c$, with v being RHI velocity. For RCE, the transition energy between ground and excited state of projectile nucleus should match perturbation harmonic energy. For a case of ¡100¿ channelling in W crystal, the harmonic energy equals $\hbar\omega_n = 3.92 \cdot \gamma \cdot \beta \cdot n$ keV [2]. Therefore, at $\gamma\beta \cong 2$ the energies of the first three strong perturbation harmonics are $\hbar\omega_1$=7.84 keV, $\hbar\omega_2$=15.68 keV and $\hbar\omega_3$=23.52 keV. At Super-FRS, RCE experiments will be performed with exotic nuclei. Detailed simulations of nuclear RCE using the BCM-2.0 code [3] are in progress.

The first measurements of the Cherenkov radiation (ChR) from RHI with the present FRS have revealed that the well known Tamm-Frank theory cannot describe the observed results [4]. The new models [5] [6] predict that at the Super-FRS energies the slowing-down of the ions in the radiator leads to broadening and complex diffraction structures of the spectral and angular distributions (Fig. 1). These distributions are very sensitive to the charge and

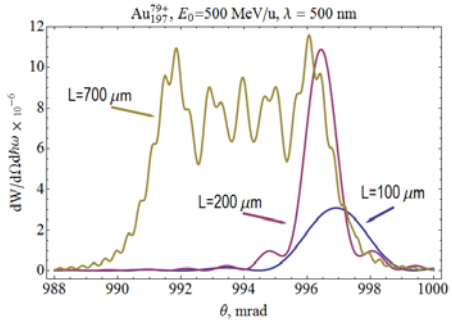

Figure 1: ChR angular distribution from 500 MeV/u Au ions in a 100, 200, and 700 μm diamond radiator.

velocity of RHI, and radiator thickness [7], thus the experiments with the Super-FRS will contribute to the detailed understanding of ChR from RHI ions and will lay the ground for improved and novel detector developments, like velocity selector [8]. These studies will be performed

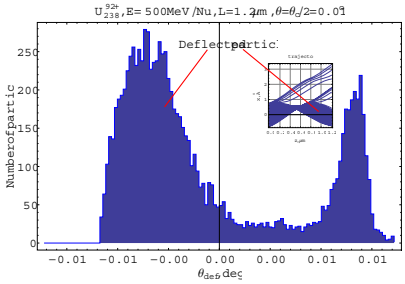

Figure 2: Deflection of 500 MeV/u uranium ions by (200) tungsten HWC. Critical channelling angle θ_C = 0.02 °.

in close collaboration with the detector laboratory at GSI, which investigate ChR in liquid radiator as a diagnostic tool for RHI [9].

The FRS research division is already active in channelling experiments [10], all the necessary equipment exists and can be used to continue these experiments at the Super-FRS. We suggest to include into experimental program the studies of channelling in a Half-Wave Crystal (HWC), which is the very recent trend in high-energy physics [11]. According to the simulations, achievable deflection angle through the mirror effect is of the order of critical channelling angle θ_C (Fig. 2). The possible applications are: effective beam deflector and even charge/velocity selector.

References

[1] I. Tanihata, H. Geissel et. al., 'Conceptual Design Report for the Scientific Program of the Super FRS Experiment Collaboration', GSI Report 2016, 3.

[2] Yu.L. Pivovarov, H. Geissel, C. Scheidenberger. Nucl. Instrum. and Meth. B 256 (2007) 109.

[3] S.V. Abdrashitov, O.V. Bogdanov, B. Korotchenko et. al., Nucl. Instrum. and Meth. B 402 (2017) 106.

[4] J. Ruzicka, et. al., Vacuum 63, Issue 4 (2001) 591.

[5] E.I. Fiks, et. al., Nucl. Instrum. and Meth. B 309 (2013) 146.

[6] E.I. Fiks, et. al., Nucl. Instrum. and Meth. B 314 (2013) 51.

[7] E.I. Fiks, Yu.L. Pivovarov, Phys. Lett. A 380 (2016) 2386.

[8] T. Yamaguchi et. al., Nucl. Instrum. and Meth. B 766 (2014) 123

[9] N. Kuzminchuk-Feuerstein et. al., Nucl. Instrum. and Meth. A 866 (2017), 207.

[10] D. Dauvergne et al., Phys. Rev. A 59 (1999) 2813.

[11] W. Scandale et. al., Phys. Lett. B 734 (2014) 1.

* bov@tpu.ru

A gas degrader for the low-energy branch of the Super-FRS at FAIR *

S. Purushothaman[1], *T. Dickel*[1,2], *S. Ayet*[1,2], *S. Bagchi*[1], *K.-H.Behr*[1,2], *J. Bergmann*[2], *T. Blatz*[1,2], *P. Constantin*[5], *J. Ebert*[2], *A. Finley*[6], *H. Geissel*[1,2], *F. Greiner*[2], *E. Haettner*[1], *C. Hornung*[2], *S. Kaur*[10], *W. Lippert*[2], *B. Lommel*[1], *I. Mardor*[8,9], *B. Mei*[5], *I. Miskun*[1,2], *I. Moore*[3], *J.-H. Otto*[1], *S. Pietri*[1], *A. Pikhtelev*[7], *W. R. Plass*[1,2], *I. Pohjalainen*[3], *A. Prochazka*[1], *C. Rappold*[1,2], *M. P. Reiter*[6], *A.-K. Rink*[2], *C. Scheidenberger*[1,2], *B. Szczepanczyk*[1], *Y. Tanaka*[1,2], *H. Weick*[1], *and J. S. Winfield*[1]

[1]JLU, Gießen, Germany; [2]GSI, Darmstadt, Germany; [3]Univ. of Jyväskylä, Finland; [4]IAI, RAS, St. Petersburg, Russia; [5]ELI-NP, Bucharest, Romania; [6]TRIUMF, Vancouver, Canada; [7]Inst. for Energy Problems of Chem. Phys., RAS, Chernogolovka, Russia; [8]Tel Aviv Univ., Tel Aviv, Israel; [9]Soreq NRC, Yavna, Israel; [10]Astronomy and Phys. Dep., Saint Mary's Univ., Halifax, Canada

At the Low Energy Branch (LEB) of the Super-FRS at FAIR the exotic nuclei produced and separated at relativistic energies are thermalised (∼eV) and delivered to dedicated experimental setups to perform spectroscopy and decay studies (MATS/LaSpec). The only universal technique available for this procedure is to slow the nuclei down to few MeV·u^{-1} in degraders, thermalise them in a noble gas filled stopping cell and then extract using a combination of electric fields and gas flow. The magnetic rigidity of the main-separators of the Super-FRS is 20 Tm whereas it is 7 Tm at the LEB. Therefore, the ion beam must first be slowed down (e.g. $\leq$300 MeV·u^{-1} for ^{238}U) using a homogeneous degrader. The stochastic processes during the production and slowing down of exotic nuclei introduce a momentum spread which is orders of magnitude larger than that of the primary beam. To overcome this problem the ion beam is spatially dispersed according to the momentum using a magnetic stage and the difference is then compensated by passing through a wedge-shaped degrader [1].

A final fine tuning of ion energy is required for an efficient implantation in a gas stopping cell. A thickness-tunable homogeneous degrader which can achieve areal densities lesser than that is possible using a technically feasible aluminum degrader is required for this purpose. Due to the large beam size at the LEB and the requirement of a large dynamic range of tuning, a gas-based degrader is proposed. A prototype of such a density controllable gas degrader was tested at the FRS Ion Catcher (FRSIC) setup [2] during the 2016 beam time at GSI. A Multiple-Reflection Time-of-Flight Mass-Spectrometer (MR-TOF-MS) was used to identify and quantify the thermalized ions extracted from the stopping cell.

The prototype gas degrader consists of a cylindrical stainless steel chamber of 1500 mm length and 125 mm radius. The beam entrance and exit windows were made of 100 μm Kapton foils. The dimensions of the windows were 200 mm$\times$100 mm. The Kapton beam windows were coated with a thin layer of carbon to avoid beam induced charging up and destruction of the beam windows by electrical discharge. These two windows contribute 2$\times$20 mg·cm^{-2} to the total areal density of the gas degrader. Dry nitrogen was used as the degrader material. The areal density of the nitrogen gas inside the chamber can be tuned between 0–160 mg·cm^{-2} with an accuracy of $\pm$0.2 % using a pressure controller.

For the test measurements the FRSIC setup was equipped with a tunable homogeneous aluminum degrader besides the gas degrader. Tests were performed for two gas degrader pressure settings (525 mbar and 800 mbar). The optimal ion energy for the efficient stopping in the gas cell was found by scanning the thickness-tunable homogeneous aluminum degrader. To study the effect of the curvature of the gas degrader beam window on the areal density a scan was also repeated for off-axis beams. No noticeable effect of the window curvature was found. The results of these tests (see Figure 1) show the technical feasibility of a gas degrader system for the LEB of the Super-FRS.

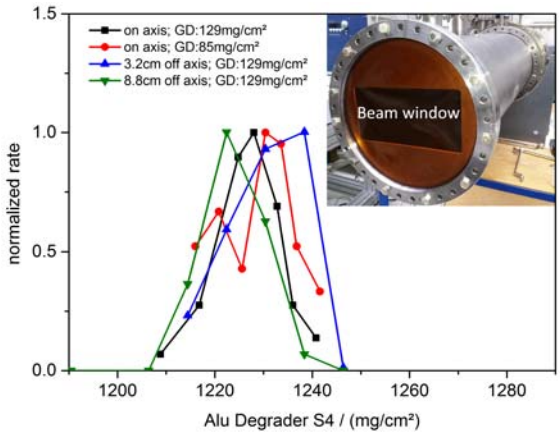

Figure 1: Stopping efficiency of ions in the gas stopping cell as a function of the sum of the areal densities of the thickness-tunable homogenous degrader and the gas degrader (GD) in aluminum equivalent. Photograph of the gas degrader chamber is shown in the inset.

*This work was supported by the BMBF under contracts No. 05P12RGFN8 and 05P16RGFN1, by the HMWK through the LOEWE Center HICforFAIR, by HGS-HIRe, by JLU Gießen and GSI under the JLU-GSI strategic Helmholtz partnership agreement.

References

[1] H. Weick et al., NIMB 164 (2000) 168-179

[2] W.R. Plaß et al., NIMB 317 (2013) 457-462

DOI:10.15120/GR-2017-1

Systematic measurement of total interaction cross sections in medium mass nuclei

J. Díaz-Cortés[1], *J.L. Rodríguez-Sánchez*[1], *J. Benlliure*[1], *D. Dragosavac*[1], *D. Pérez*[1], *H. Álvarez-Pol*[1], *B. Blanck*[2], *E. Casarejos*[1], *V. Fohr*[3], *M. Gascón*[1], *W. Gawlikowicz*[4], *A. Heinz*[5], *K. Helariutta*[6], *L. Pienkowski*[4], *M. Staniou*[3], *K. Subotic*[7], *K. Summerer*[3], *B. Pietras*[1], *J. Taieb*[8], *A. Trzcinska*[4], *D. Rossi*[6], *H. Simon*[6], *J. Vargas*[1], *and B. Voss*[6]

[1]University of Santiago de Compostela, Spain; [2] Centre d'Etudes Nucleaires,Bordeaux-Gradignan Cedex, France; [3]GSI, Darmstadt, Germany; [4]University of Warsaw, Poland; [5]University of Chalmers, Sweeden; [6]University of Helsinki, Finland; [7]Institute of Nuclear Science Vinca, Belgrade, Serbia; [8]CEA DAM, Bruyeres-le-Chatel, France

Radial distributions of protons and neutrons are fundamental properties of nuclei that are fairly well understood for stable nuclei, but in neutron-rich nuclei signatures of unconventional behavior have been reported [1].

Several methods can be used to determine the matter distribution in nuclei, but in general they are all model dependent. X-ray spectroscopy of anti-protonic atoms [2] or the probability for collective excitation as the giant-dipole resonances (GDR) or the spin-dipole resonance (SDR) [3] are some of them.

Interaction cross sections (σ_I) of relativistic projectiles can give access to matter radii and nuclear density distributions [4]. One of the most interesting features of unstable nuclei is the existence of skins [5]. These data provide a unique opportunity to systematically investigate the evolution of neutron-skin structures in medium-mass nuclei.

The experiment took place at the GSI facility where we used secondary beams produced in the fragmentation of ^{132}Xe and fision of ^{238}U at energies around 1000 MeV/A to produce nuclei between Cadmium and Xenon over a broad range in isospin. The FRagment Separator was used as a two-independent magnetic spectrometers, each with a different magnetic setting. In the first part of the FRS, fission and fragmentation fragments produced by the primary beams were unambiguously identified in mass and charge. At the intermediate focal plane of the FRS, a beryllium target of 2591 $\pm$ 7 mg/cm^2 was placed in order to induce the fragmentation reactions. Then, the second part of the FRS was used to identify the fragmentation products.

Total interaction cross sections were determined using the transmission method, counting the number of projectiles impinging in the fragmentation target and the number of projectiles arriving at the final focal plane of the FRagment Separator. The number of counts were corrected by the optical transmission of the ions along the spectrometer, detection efficiency and reactions in other layers of matter by using measurements without the fragmentation target.

These cross sections will be compared to Glauber model calculations in order to investigate the evolution of the neutron and proton density distributions along the isotopic chain [6]. By comparing the spread of the neutron density to that of the proton density for the most neutron-rich nuclei, the difference between the neutron (r_n) and proton (r_p) radii can be obtained. The thickness of the neutron skin is defined as the differrence between the matter radii of the two different nucleon species ($S_n = r_n - r_p$), so this measurements will allow us to evaluate the existence of a neutron skin in medium-mass neutron rich nuclei .

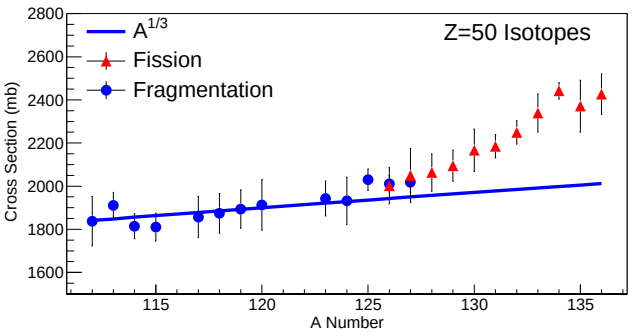

Figure 1: Total interaction cross sections for different tin isotopes (Z=50) from N = 63 to N = 85. The blue line shows the A$^{1/3}$ dependence.

In Fig. 1 we depict the preliminary total interaction cross sections for different tin isotopes measured in this work (points) as a function of the projectile mass number. The blue line shows the A$^{1/3}$ dependence normalized to the ^{112}Sn.The total interaction cross sections for the most neutron deficient tin isotopes increase slowly with the mass but for the most neutron-rich isotopes this increase is much faster. This increment would indicate that the size of the most neutron-rich tin isotopes is bigger than predicted and this could be a signature of the existence of a neutron skin.

References

[1] R.Kanungo et al., Phys. Rev. C **83**, (2011).

[2] A. Trzcinska et al., Phys. Rev. Lett. **87**, 082501 (2001)

[3] T. Kasznahorkay et al., Nucl. Phys. A **731**, (2004)

[4] A.Ozawa et al., Nucl. Phys. A **709**, (2002).

[5] A.Ozawa et al., Nucl. Phys. A **693**, (2001).

[6] T.Suzuki et al., Phys. Rev. Lett. **75**, 3241 (1995).

DOI:10.15120/GR-2017-1

DOI:10.15120/GR-2017-1

Offline analysis of Beam Spill structure measurement at GSI

S. Saha [*1,2], *M. Reese*[1], *H. Schaffner*[1], *J. Vesic*[1,3], *J. Gerl*[1], *and M. Górska*[1]

[1]GSI, Darmstadt, Germany; [2]Technical University Darmstadt, Darmstadt, Germany; [3]Jozef Stefan Institute, Ljubljana, Slovenia

Uniform spill structure of high energy ion beams is required for various spectroscopy experiments carried out in GSI fragment separator. We have carried out an offline analysis of the Beam spill structure from beam obtained at Cave C during an experiment in June 2016.

Resonance extraction of particles from SIS can have some fluctuations from various non-coherent as well as coherent sources [1]. These fluctuation leads to non uniformity of the beam current. The random fluctuations in the beam current can significantly lower the detection efficiency of events in slow response detectors like HPGe.

The incoming particles of a steady beam current can be considered as homogeneous Poisson events occurring at a uniform rate. The time of occurrence of each event is independent of the time of a previous event. The waiting time distribution of such events should fall exponentially with increasing time interval. The rate of beam current is given by the decay time of this distribution.

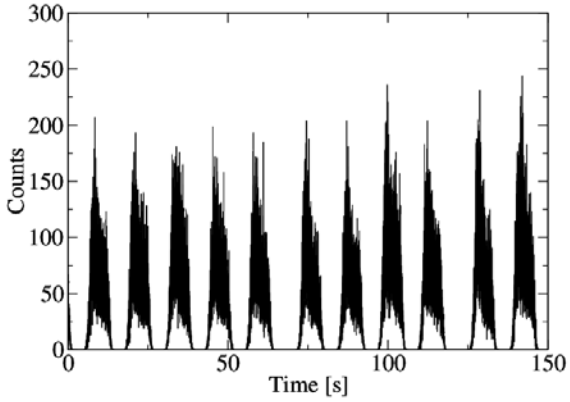

Figure 1: Beam Spill structure over a time period during experiment.

The data was taken during the GSI beam time in June 2016. The ^{124}Xe primary beam at 600 MeV/u energy was extracted from the SIS. The count rate at the detector was maintained at 10 kHz. The signal from the incident events were collected when the beam particles pass through a plastic scintillator detector placed across the beam direction. The event by event time information was collected using a discriminator and a VME time stamper module [2].

The events recorded in the experiment is first sorted with respect to an increasing time stamp. Then the average number of events recorded per 5 milliseconds is plotted against

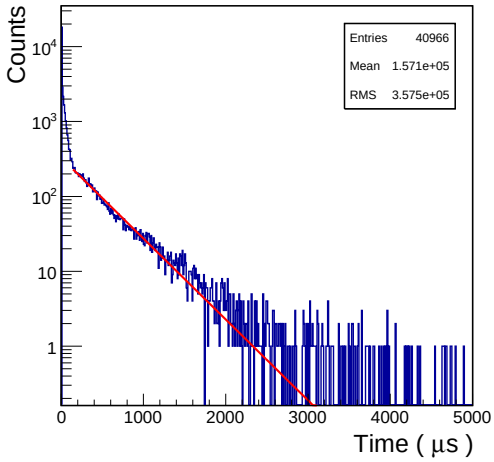

Figure 2: Waiting time statistics over a duration of beam time. The exponential fit to the distribution is shown in red.

time to obtain the spill structure as shown in Figure 1. The figure clearly shows the fluctuation in beam current over a given spill structure. The data was further analysed by extracting the waiting time distribution of all events with respect to the previous event over a given run time. In Figure 2 the statistics of the waiting time distribution for a typical run time is plotted. The data is fitted with an exponential function to obtain the avarage event rate. The Figure 2 clearly shows that the beam current cannot be regarded as uniform over time as the exponential distribution exhibits a steeper ascent within a time window of 100 μs. The rate of the wait time distribution is constant over time beyond 200 μs. More than two orders of magnitude higher statistics is observed within a wait time of 100 μs.

The experiment and subsequent analysis concludes the presence of random fluctuation in the beam current. The fluctuation can be more than two order of magnitude higher than the avarage current. As 100 μs is also the typical event processing time, an excessive number of events in this time domain reduces the trigger throughput.

References

[1] U. Blell, "A feedback system to improve the spill structure of a synchrotron." GSI, Darmstadt, Germany.

[2] VULOM (VME Universal Logic Module with 48 ECL I/Os), GSI.

* ssaha@gsi.de

DOI:10.15120/GR-2017-1

Neutron flux mapping in an ion-beam environment employing an improved neutron activation technique using thick foils

P. Koseoglou[1,2,*], M.L. Cortés[1,2], J. Gerl[2], T. Habermann[1,2], I. Kojouharov[2], C. Lizarazo[1,2], N. Pietralla[1], H. Schaffner[2], S. Stoulos[3], E. Vagena[3], J. Vesic[2]

[1] *Institut für Kernphysik, Technische Universität Darmstadt, 64289 Darmstadt, Germany*
[2] *GSI Helmholtzzentrum für Schwerionenforschung GmbH, 64291 Darmstadt, Germany*
[3] *Nuclear Physics Lab., School of Physics, Aristotle University of Thessaloniki, 54124 Thessaloniki, Greece*
(Dated: 13/02/2017)

* *Corresponding author. E-mail address: pkoseoglou@ikp.tu-darmstadt.de*

Purpose and method:

Measurements have been performed during summer 2016 at GSI in order to determine the neutron background in the ion beam environment. An advanced neutron activation method has been used to allow determination of low neutron fluxes [1][2]. Thick foils, instead of thin, have been used in the past for the determination of the neutron flux spectrum on the sub nuclear assembly-reactor of Aristotle University of Thessaloniki [1] and on a medical LINAC environment [2]. Due to the thickness of the samples low neutron fluxes can be "detected", at the same time, corrections for the self-shielding of the neutrons and the gammas by the materials have been applied [2]. In previous studies, the sensitivity of the technique has been proven to be lower than 3000 thermal neutrons/s/cm^2 [1]. The main purpose of the experiment performed was to test the applicability of the specific method in an ion-beam environment in order to investigate the neutron background of it.

Experiment:

The measurements have been performed using three different ion beams, uranium, xenon and carbon. The samples have been irradiated in several position near the ion beam and not in it. These positions were along FRS (S1, S2, S3 and S4, for S4 in both the exit of the last dipole and in the AGATA frame) and in Cave C (HTC and HTD) (see Figure 1). Limitations on the number of foils did not allow simultaneous irradiation in more than three to four areas. In Table 1 the activated samples are shown for each combination of beam and area tested, the combinations of beam and irradiation areas that were not tested are mark with a "-".

Being a parasitic measurement, the beam parameters changed according to the needs of other experiments. An estimation we can make at this point for the average energy of the beam (e.g. for uranium beam) during the activations is ~300MeV/u and for the average intensity ~10^8pps. The exact values of each beam during the irradiations will be considered on the analysis.

Early results:

Some "in-beam" observations are the following:

- Only (n,γ) reactions and no threshold reactions were detected.
- The activated samples were: Au, As, In, Ir, Mn, Sn and W (see Table 1). The expected reactions was occurred; the ones with the higher cross-section.
- The fluxes of the thermal neutrons were lower than 100 n/cm^{2}s, so a "weak" activation of the samples was achieved. This estimation was derived from the comparison of the count rates from these measurements with the ones obtained during the experiment in the sub-critical nuclear assembly [1].
- The technique can be used in an ion-beam environment.

Further analysis:

In the on-going analysis the activation of each reaction will be studied and the neutron flux spectrum will be calculated using the SAND-II unfolding code [3]. The conclusions will be connected to the different beams and beam intensities during the irradiations.

DOI:10.15120/GR-2017-1

Table 1. Samples activated per beam and irradiation area. The combinations of beams and irradiation areas that were not tested are mark with a "-".

Beam\Area	FRS				Cave-C	
	S1	S2	S3	S4	HTC	HTD
U	-	Au, In, Ir, Mn, W	-	In, Ir, Sn	-	-
Xe	-	In	-	W	Au, In, W	No activation
C	Au	Ir	Au, As, Ir	-	-	-

This work is supported by Helmholtz Graduate School for Heavy Ion Research for FAIR.

References

[1] Koseoglou, P.; Vagena, E.; Stoulos, S.; Manolopoulou M. Neutron spectrum determination in a sub-critical assembly using multi-disc neutron activation technique. Radiation Effects and Defects in Solid, **2016**, 171, 9-10, 766-774. (http://dx.doi.org/10.1080/10420150.2016.1262370)

[2] Vagena, E.; Stoulos, S.; Manolopoulou M. Analysis of improved neutron activation technique using thick foils for application on medical LINAC environment. Nuclear Instr. Methods A, **2016**, 806, 271-278. (http://www.sciencedirect.com/science/article/pii/S0168900215012346)

[3] SAND II, (https://rsicc.ornl.gov/codes/ccc/ccc1/ccc-112.html)

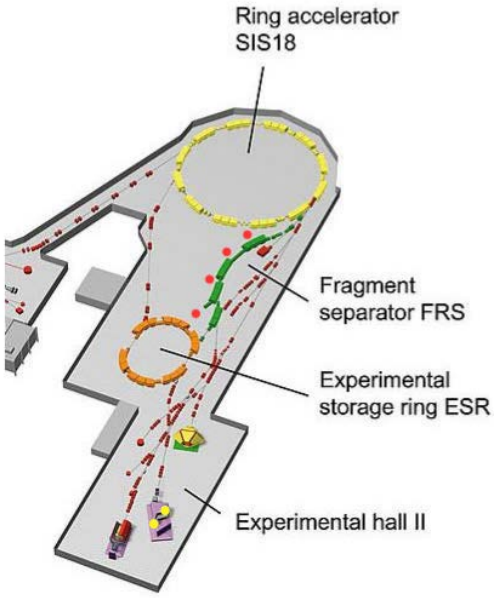

Figure 1. Areas of irradiation. The red bullets represents the areas along FRS where the samples were placed. And the yellow in Cave-C.

Tests of Sunpower CryoTel CT Stirling cooling engine for DEGAS*

W. Witt[1,2], *P. Koseoglou*[1,2], *I. Kojouharov*[2], *and J. Gerl*[2]
[1]IKP TU Darmstadt, Darmstadt, Germany; [2]GSI, Darmstadt, Germany

Introduction

As one of the four pillars of the FAIR project the NUSTAR collaboration aims at investigating exotic beams provided by the Super-FRS to study NUclear STructure, Astrophysics and Reactions. High-resolution DEcay SPECtroscopy of short-lived nuclei and isotopes is performed within the DESPEC experiment, which is located at the low-energy branch of the facility. γ-decays following the ion implantation in the active silicon detector (AIDA) are to be detected using the DEGAS germanium-array making DEGAS a key instrument of DESPEC. It is currently under development and planned to be used starting at the SIS/FRS beam-time 2019 as part of the NUSTAR phase-0 program.

Cooling of DEGAS Ge-crystals

Based on γ-ray interactions in semi-conducting matter, high-purity Germanium (HPGe) detectors such as DEGAS operate at temperatures around 90K, which makes cooling an essential aspect of the operation and for design considerations. Previous studies have shown a need for cooling power of $<$ 8W per DEGAS triple-Ge-cluster [1]. As opposed to the usual liquid nitrogen cooling, free-piston Stirling cooling (i.e. a heat engine operated within the Stirling circle to transfer heat) was chosen for DEGAS cooling. The main reason for that is the box geometry of the array adapted to the focal plane of the Super-FRS that would require a specifically tailored dewar too small for reliable operation and difficult to find. Next to smaller size and mass and lack of failures due to refilling (lifetimes of 10 years have been achieved), electrical coolers offer a cooling power of up to 10W at 77K, which satisfies the needs for DEGAS cooling. However, the piston's motion causes vibrations of the cooler, which affect the detector performance. The CryoTel CT cooler from Sunpower [2] is one of such electric coolers and was taken into operation at GSI for the planned investigation of the vibration effects and for testing counter-measures.

Ongoing tests of CryoTel CT cooling engine

The cooling engine was delivered by Sunpower around mid of 2016 including an active vibration cancellation system (AVC by Ametek) to reduce the vibrations typical for such coolers. A holding structure as well as a flange adapter for connection with a DEGAS cluster-cryostat were designed and constructed. The cooling engine, the AVC, the thermal Pt-100 sensors, the power supply and the corresponding controller were connected and the system was taken into operation by the end of 2016 (see fig. 1). Cooler vibrations too strong for reliable operation of the Ge detector excluded further tests and the system was moved to Helmholtz-Institute Mainz early 2017, where it is currently being set up.

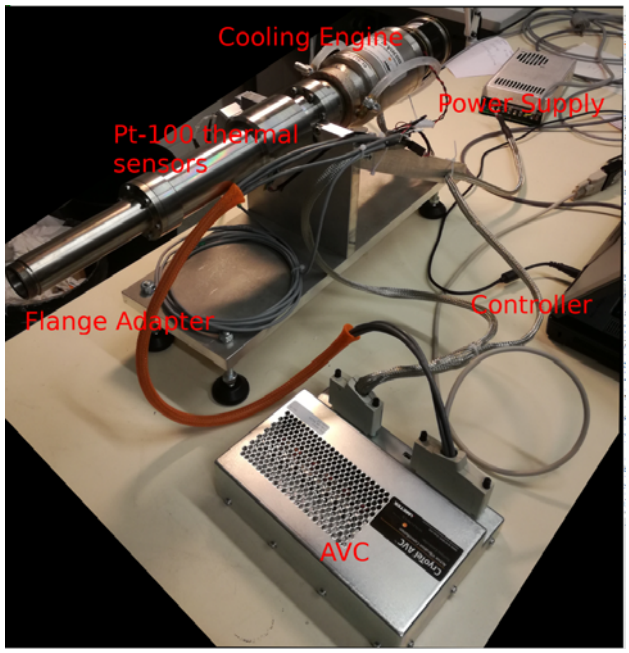

Figure 1: Cooler system setup at GSI end of 2016 including AVC, controller and temperature sensors and power supply

Perspective

The cooler will be taken into operation at the Mainz lab in the near future to verify and quantify the observed vibrations. If a defect or wrong setting of the AVC can be excluded it is foreseen to study the vibrations employing acceleration sensors at different positions of the cooling system. For the readout a BeagleBone plug-in board will be used.
After quantification of the oscillations a reduction of them is a considered option.
Operation of such coolers for astronomical detectors [3] encountered vibration problems as well and solved this issue by mechanically decoupling (see fig. 2) the cooler from

* Work supported by Helmholtz Graduate School for Hadron and Ion Research at FAIR.

DOI:10.15120/GR-2017-1

the rest of the system (i.e. here the holding structure and the cryostat connection). Using leaf-springs and vacuum bellows a mechanical low-pass filter can be created to reduce oscillations for certain frequencies. In the mentioned case a reduction of the oscillations caused by the piston's movement by a factor of 500 was achieved.

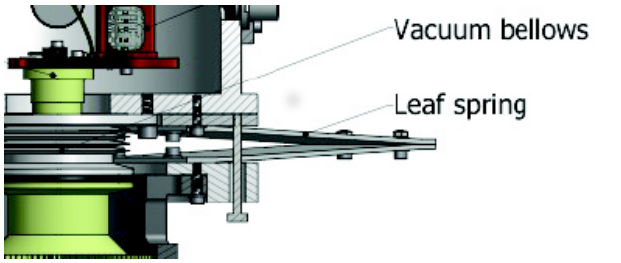

Figure 2: Mechanical decoupling of cooler vibrations from holding structure via vacuum bellows and leaf springs as done in ref. [3]. Shown in green is the cooling engine.

Conclusion

As it currently stands the Sunpower CryoTel CT cooling engine is unfit to be used as planned for DEGAS due to too strong vibrations. In case of a previous AVC malfunction, minor (e.g. frequency) setting changes could solve this problem.
However, should the oscillation reduction of the AVC remain insufficient, oscillation measurements and simulations followed by design and construction of changes to the mechanical structure would be necessary.
The consideration of another electrical cooling engine could be a valid option.

References

[1] Technical Design Report for DEGAS (2014)

[2] Sun Power CryoTel User Manual V.7, http://sunpowerinc.com/cryocoolers/ cryotel-family/ct/ (2012)

[3] G. Raskin et al., Compact Stirling cooling of astronomical detectors, https://arxiv.org/pdf/1311.0685.pdf (2013)

Bayes-Tracking – A novel approach to γ-ray tracking

P. Napiralla[1,2], H. Egger[3], P. R. John[2], N. Pietralla[2], M. Reese[1], and C. Stahl[2]

[1]Institut für Kernphysik, TU Darmstadt, Darmstadt, Germany; [2]GSI, Darmstadt, Germany; [3]AG Numerik und wissenschaftliches Rechnen, TU Darmstadt, Darmstadt, Germany

The Advanced GAmma Tracking Array AGATA [1] will be the key instrument for nuclear structure investigations in the upcoming HISPEC and DESPEC experimental campaigns at the Facility for Antiproton and Ion Research FAIR.
In the photon energy range of $0.2 - 8$ MeV, the Compton-scattering is the dominating interaction process in HPGe detectors. This leads to numerous Compton-escaped photons, which are typically suppressed or appear as background in the γ-ray spectra. Although it is possible to reconstruct photon paths between different HPGe detectors of AGATA using *Pulse Shape Analysis* [5] and γ-ray tracking algorithms [3], photons that have Compton-scattered and subsequently left the array still only contribute to the background of the γ-ray spectra. Using Bayesian inference, some of these events can be reconstructed via a new type of γ-ray tracking algorithm, called *Bayes-Tracking*, when it is most likely that they originate from Compton-escape.

In contrast to existing γ-ray tracking algorithms based on the Forward/Back-Tracking method [3], the *Bayes-Tracking* algorithm quantifies the probability of an initially incident photon, given the measured hit pattern in the detector. It is based on Bayes' Theorem [2, 4]

$$P(B|A) = \frac{P(A|B) \cdot P(B)}{P(A)} . \tag{1}$$

The conditional probability for two arbitrary events A and B is defined as

$$P(A|B) := \frac{P(A \cap B)}{P(B)} . \tag{2}$$

The incident photon energy E_γ can be identified in the case of full energy absorption (photoelectric effect at last interaction point) **and** in the case of a Compton-escaped photon. In contrast to existing tracking algorithms, the latter events can be partially recovered.

Using Bayes' theorem and the measured deposited energies $\{E_{\text{dep}_1}, \ldots, E_{\text{dep}_N}\}$ at the corresponding interaction points $\{\vec{x}_1, \ldots, \vec{x}_N\}$ identified via *Pulse Shape Analysis* [5], a conditional probability distribution P for hypothetical incident photon energies e_0 can be derived

$$\begin{aligned} &P\left(e_0 | \left\{\{\vec{x}_1, E_{\text{dep}_1}\}, \ldots, \{\vec{x}_N, E_{\text{dep}_N}\}\right\}\right) \\ &\propto \sum_\pi \mathcal{L}\left(\pi\left(\{\vec{x}_1, E_{\text{dep}_1}\}, \ldots, \{\vec{x}_N, E_{\text{dep}_N}\}\right) | e_0\right) . \end{aligned} \tag{3}$$

π denotes the permutation function over all possible permutations of the measured energies E_{dep_i} (at interaction points $\vec{x}_i$) and $\mathcal{L}$ the corresponding *likelihood function* (corresponds to $P(A|B)$ in Equation (1)). By using the principle of so-called *marginalization* [4], a calculable form of the likelihood function can be derived.

A *Geant4* simulation of a simplified cubic Germanium detector (edge length 8 cm) with incident photon energy $E_\gamma = 1.5$ MeV has been used to firstly realize Bayes-Tracking and test its performance. The amount of interactions inside the detector has been limited to $N = 3$. Altogether, 5055 photons (4000 Compton-escaped, 1055 photo-absorbed) have been used. The Bayes-tracked photon spectrum compared to the Add-Back energy spectrum (traditional detector response) is shown in Figure 1.

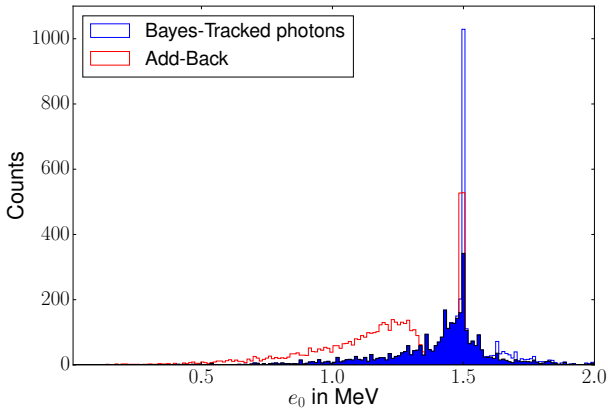

Figure 1: Comparison of Add-Back energy spectrum (red) to Bayes-tracked photon energy spectrum (blue). The tracked photon energies of the Compton-escaped photons are shown in solid blue.

The Peak-to-Total ratios in this simulated detector are:

- Add-Back: 20.77 %
- Bayes-tracked: 24.35 %

Hence, a gain in the Peak-to-Total ratio by around 3.6 percentage points absolute has been achieved by simply using the Bayes-Tracking on this dataset.

Future work on the Bayes-Tracking algorithm will include testing on real data sets taken with AGATA detectors, the incorporation of pair-production and embedding

DOI:10.15120/GR-2017-1

the algorithm into the AGATA framework *Femul* to enable the usage of the Bayes-Tracking on upcoming AGATA experiments.

Especially for radioactive ion beam experiments with limited intensities, this algorithm can be applied with the aim to increase the statistics in the γ-ray peaks. It will potentially decrease the statistical uncertainties of future HISPEC experiments with very exotic relativistic radioactive ion beams using AGATA at FAIR.

References

[1] A. Akkoyun et al., AGATA – Advanced GAmma Tracking Array, *Nuclear Instruments and Methods in Physics Research A*, 668:26–58, March 2012.

[2] H.-O. Georgii. *Stochastik – Einführung in die Wahrscheinlichkeitstheorie und Statistik*, volume 4. Walter de Gruyter, Berlin, 2009.

[3] A. Lopez-Martens et al. γ-ray tracking algorithms: a comparison. *Nuclear Instruments and Methods in Physics Research A*, 533:454–466, 2004.

[4] D. Sivia and J. Skilling. *Data Analysis – A Bayesian Tutorial*, volume 2. Oxford University Press, Oxford, 2006.

[5] R. Venturelli and D. Bazzacco. Adaptive Grid Search as Pulse Shape Analysis Algorithm for γ-Tracking and Results. *LNL Annual Report*, 2004.

DOI:10.15120/GR-2017-1

Upgrade and commissioning of the Lund-York-Cologne CAlorimeter*

B. Fu[1], *K. Wolf*[1], *P. Reiter*[1], *M. A. Bentley*[2], *P. Coleman-Smith*[4], *S. Fox*[2], *C. Goergen*[1], *P. Golubev*[3], *I. Lazarus*[4], *C. Lorenz*[3], *D. Rudolph*[3], *L. Scruton*[2], *and S. Thiel*[1]

[1]IKP, Universität zu Köln, Germany; [2]University of York, UK; [3]Lund University, Sweden; [4]STFC Daresbury Laboratory, UK

Introduction

The Lund-York-Cologne CAlorimeter (LYCCA) is a charged-particle detector for the FAIR/NUSTAR collaboration, to discriminate heavy ions produced in nuclear reactions of relativistic radioactive-ion beams (RIB). The charge number Z and mass number A of the reaction products can be determined measuring their Time-of-Flight (ToF), energy loss and total energy. Employing the position sensitivity of LYCCA the flight paths of the reaction products can be tracked event-by-event, enabling the HIgh-resolution in-beam γ-ray SPECtropscopy (HISPEC) far from the line of stability (concept and design of LYCCA see Ref. [1]).

Upgrade of Electronics

The precursor LYCCA-0 using 12 ΔE-E telescopes and analog electronics was employed in the PreSPEC campaign from 2009 to 2014. A high resolution of Z and A was proven for proton number around 33 and mass region around 100 [2,3,4]. Afterwords the major upgrade from analog to digital electronics for LYCCA was carried out by the STFC Daresbury Laboratory. Using high-integrated Front-End Electronics (FEE) with Application-specific Integrated Circuits (ASICs), the electronic arrangement and data-acquisition process were significantly simplified. As

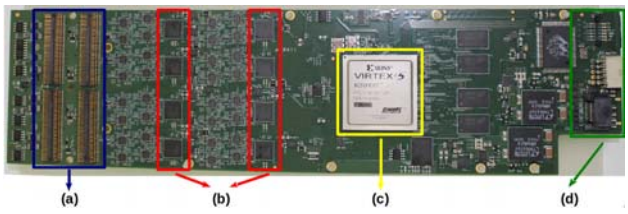

Figure 1: The view of a FEE-card. (a) four 16-channel ASICs; (b) eight 14-bit ADCs; (c) Virtex-5 PowerPC; (d) Connections: HDMI (Clock), Power and Gbit-Ethernet.

shown in Fig. 1, each FEE card contains four 16-channel ASICs, which amplify the signals from all 64 channels of one Double-Sided Silicon Strip Detector (DSSSD). The ASIC is optimized for high dynamic range with excellent linearity and noise performance. Each ASIC covers three energy ranges: (i) high gain up to 20 MeV, (ii) medium gain up to 1 GeV, and (iii) low gain up to 20 GeV. The pre-amplified signals are digitalised in ADCs, processed in the Virtex-5 PowerPC and then stored in a LYCCA-Server. A master-slave control delivers a synchronous time stamp via HDMI-cables on all FEE cards in use. The Multi-Instance Data-Acquisition System (MIDAS) ensures the hardware configuration, experiment control, data merging and data storage.

Commissioning at IKP Cologne

Since 2016 the LYCCA setup is located at the Cologne tandem accelerator. A new three-stage beam tube was built for LYCCA, which allows for three different distances between target position and the DSSSD-wall (cf. Fig. 2). Thus, the corresponding opening-angles range from 1.5 to 16 degree. Currently 25 FEE modules and 14 ΔE-E telescopes are installed on LYCCA. In order to check the specifications and energy resolutions of the DSSSDs with the new digital FEE modules, measurements were performed with a triple-alpha source. Employing the Multi-Instance-Data-Acquisition System (MIDAS) experiment data were stored, sorted event by event and analyzed using the data-analysis framework ROOT. The results show that more than 99% DSSSD-channels were working successfully. A consistent energy resolution of around 1.1% at 5.8 MeV was obtained for all 14 DSSSDs in use. At the IKP several in-beam experiments were also curried out to test the performance of the LYCCA system. In collaboration with the University of York, a 2 mm thick plastic scintillator for later ToF-measurement was tested on the LYCCA setup in March 2016. A ^{12}C beam with an en-

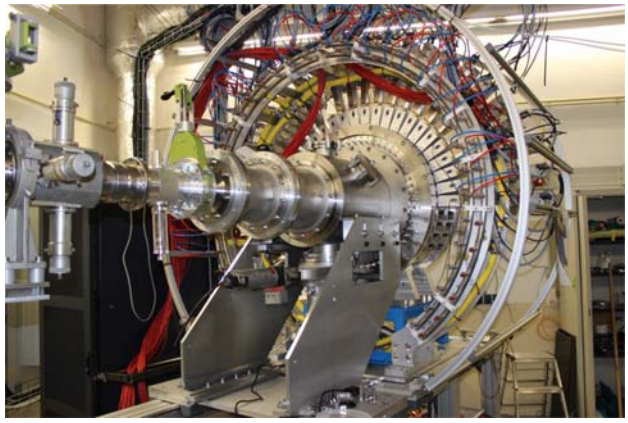

Figure 2: The current LYCCA-construction in the IKP Cologne. With the 25 installed FEE-modules all DSSSDs can be operated.

* This work supported by the German BMBF (05P12PKFNE TP5) and GSI F&E KREITE 1416.

DOI:10.15120/GR-2017-1

ergy of 60 MeV was scattered on the ^{197}Au target with a thickness of 0.2 mg/cm^2, and stopped in the ToF-detector. The generated light signals were detected with 32 photomultipliers (PMTs) mounted around the plastic scintillator. Together with the Lund University in May 2016, another beam time was scheduled to test the performance of the ΔE-E telescopes. A proton beam with an energy of 18 MeV was scattered on a thin gold foil and then detected in the DSSSDs and CsI-detectors. In November 2016 a further in-beam experiment of elastic scattering of heavy ions was conducted. In this measurement the medium-gain range (up to 1 GeV) of the FEE modules was tested successfully for the first time. A ^{12}C beam with a kinetic energy of 60 MeV was scattered on the ^{197}Au target with a thickness of 0.17 mg/cm^2. At a distance of 120 cm between the target and the DSSSDs, a continuous scattering-angle coverage of 1.5 to 9.5 degrees was obtained. The measured Full Width at Half Maximum (FWHM) of the DSSSDs are 350 keV to 400 keV at approximately 60 MeV. In order

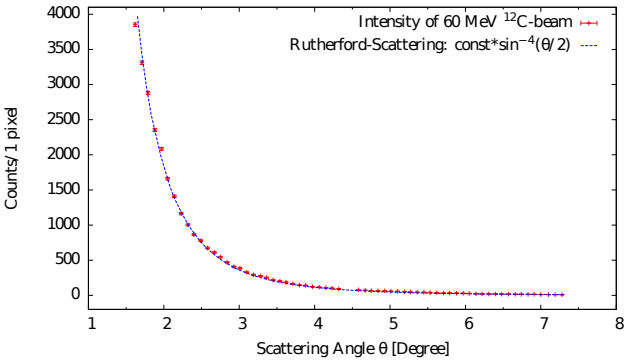

Figure 3: The measured intensity distribution of the elastically scattered ^{12}C-nuclei on ^{197}Au-target follows the expected distribution of the Rutherford scattering.

to investigate the exact angular distribution of the beam intensity after the elastic scattering, the measured data of the p- and n-side were correlated and, thus, the events in the DSSSDs were analyzed pixel by pixel. Figure 3 shows the intensity distribution of 64 contiguous pixels from two DSSSDs located vertically below the beam axis. The measured values, covering a range of 1.5 to 7.2 degree, reproduced the theoretically expected scattering-angle dependence of $\sin^{-4}(\theta/2)$ nicely.

Outlook

For further in-beam experiments at the Cologne tandem accelerator, a modified mechanical construction of the LYCCA chamber was realized by IKP's mechanical workshop. The new design consists of two octagon brackets and a back wall, which support up to 24 ΔE-E telescopes in operation (see Figure 4). The target ladder is located between the octagon brackets. This new construction increases the scattering-angle coverage from a maximum of 16 to a maximum of 120 degree, as well as the solid-angle coverage up to 60% of 4π significantly, which means that LYCCA can be used to further examine elastic and inelastic particle scattering. This configuration will be shortly installed and tested for the first time.

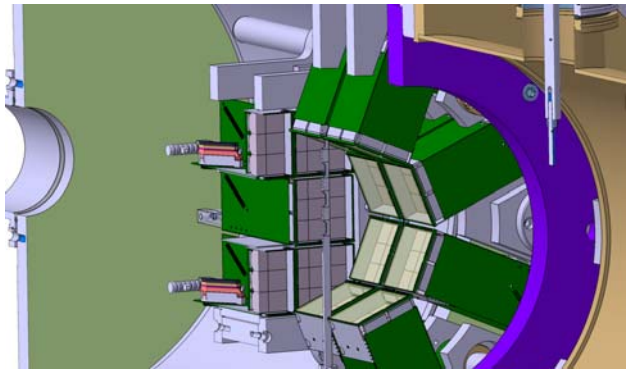

Figure 4: The new mechanical design of the LYCCA chamber. Each octagon bracket and the back wall support 8 ΔE-E telescopes.

References

[1] P. Golubev *et al.*, Nucl. Instr. & Meth. A 723 (2013).

[2] G. Guastalla *et al.*, Phys. Rev. Lett. 110, 172501 (2013).

[3] A. Wendt *et al.*, Phys. Rev. C 90, 054301 (2014).

[4] K. Moschner *et al.*, Phys. Rev. C 94, 054323 (2016).

DOI:10.15120/GR-2017-1

Collective behaviour of p-rich nuclei around A = 70

T. Arici [*1,2], *J. Gerl*[1], *and W.Korten*[3]

[1]GSI, Darmstadt, Germany; [2]Justus-Liebig University, Giessen, Germany; [3]CEA-Saclay, DAPNIA/SPhN, France

In N = Z nuclei, neutrons and protons occupy the same orbitals. This creates an opportunity to study the effect of the nucleon sequence on deformation changing effects caused by proton-neutron correlations. Moreover, in this region towards the proton drip line, nuclei experience a low binding energy which results in a shape change and in the vicinity of N = Z and around A = 70 this becomes even more rapidly due to the large shell gaps in the Nilsson diagram for nucleon numbers 34, 36 and 38. The ^{70}Kr, ^{72}Kr, ^{70}Br and ^{68}Se isotopes of this region were studied, where the valence protons and neutrons occupy these shells and let us to answer the fundamental questions of nuclear physics, such as the charge symmetry, independence of nuclear force and the collectivity.

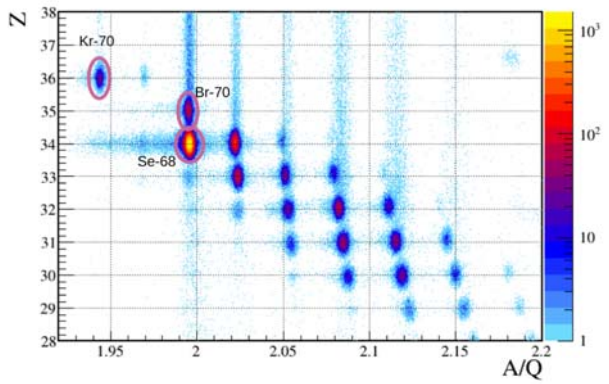

Figure 1: BigRIPS particle identification plot for ^{70}Kr setting. The circles show the particle gates used for each isotope of interest.

Exotic beams with intermediate energy have been used as a spectroscopic tool through inelastic scatterings. The inelastic scattering of ^{72}Kr, ^{70}Kr, ^{70}Br and ^{68}Se isotopes on ^{9}Be and ^{197}Au targets has been studied. Production of these very exotic nuclei, through the proton drip-line, was achieved at the Radioactive Isotope Beam Factory (RIBF) [1]. A ^{78}Kr primary beam with an energy of 345 MeV/u was impinged on a ^{9}Be target to produce the ions of interest as a secondary beam. The BigRIPS fragment separator was used in order to deliver the secondary beam isotopes, ^{72}Kr, ^{70}Br, ^{68}Se and ^{70}Kr at around 175 MeV/u to the secondary target for the measurements. Particle identification plot for selected isotopes is given in Figure 1 for ^{70}Br, ^{68}Se and ^{70}Kr. The reaction products were identified in the ZeroDegree Spectrometer (ZDS) employing the Bρ-ΔE-TOF method and γ-rays emitted due to the excitation were measured by an array of γ-ray detectors, DALI2, that was placed around the secondary target. Firstly, the exotic beam was scattered through the electromagnetic field of a heavy target gold. In this process, Coulomb excitation and nuclear interaction interfere. The fraction of these two kinds of excitation was identified. In order to separate these two interactions, the same setting was repeated to scatter the beam off a Beryllium target to increase the relative strength of nuclear scattering. For each isotope, the experimental conditions were simulated to obtain the response functions of the transitions. Experimental results were then fitted to these response functions from the simulations in order to determine the number of emitted γ-rays. The excitation cross-sections were deduced for both cases and used in order to determine the deformation lengths δ_n and δ_c, for nuclear and Coulomb excitation, respectively. These deformation lengths were obtained using ECIS-97 code [2]. In the even-even nuclei, degree of the deformation in the nucleus is related to reduced transition probability, B(E2) values with the following equation:

$$\beta = \frac{4\pi}{3ZR_0^2}\sqrt{B(E2\uparrow)/e^2} \qquad (1)$$

where A and Z mass and charge numbers, respectively, β is the deformation parameter and R_0 is the nuclear radius.

The chain for the experimental knowledge on Kr isotopes was extended with this study. Results also allow to make a direct comparison with ^{70}Se which gives important new information about the shape coexistence phenomenon (the existence of two stable shapes at the same excitation energies) across the N = Z line. We deduced the B(E2) value for the $2_1^+ \rightarrow 0_1^+$ transition of ^{70}Kr, T_z = - 1 for the first time. This quantity for the other measurements was determined before within different experiments and shows and aggrement with our results. The B(E2;$2_1^+ \rightarrow 0_1^+$) value for ^{70}Kr showed a rapid increase among these values. It was even approximately twice higher compared to its isobaric triplet members. This variation indicates an increase in the deformation in this isotope.

References

[1] T. KUBO, D. KAMEDA, H. SUZUKI, ET AL. BigRIPS separator and ZeroDegree spectrometer at RIKEN RI Beam Factory. Progress of Theoretical and Experimental Physics, 2012(1), 2012

[2] J. RAYNAL. Coupled channel code ECIS97. Unpublished.

* t.tarici@gsi.de

DOI:10.15120/GR-2017-1

Geant4 Simulations of the novel γ-ray detector array DEGAS *

C. Lizarazo[1,2], G. Li[2,3], N. Pietralla[1], J. Gerl[†2], and the PreSPEC Collaboration [1]

[1]Institut für Kernphysik, Technische Universität Darmstadt, Germany; [2]GSI, Darmstadt, Germany; [3]Institute of Modern Physics, CAS, Lanzhou, China

The performance of the novel HP-Ge detector array DEGAS that will be used at FAIR has been studied through GEANT4 simulations using real geometries of most of the detector components. Different possibilities of ancillary background shields were simulated and compared, showing that a system of active BGO Compton-suppressor back-catchers combined with additional side shields, provide a clear improvement of the photo-peak efficiency and the Peak-to-Total ratio in comparison to previous decay-spectroscopy arrays. Large differences in the performance of different clusters in DEGAS reveals that, due to geometrical effects, some particular positions in the array contribute stronger than others to achieve a superior performance.

Introduction. In the future FAIR facility, very exotic nuclei not yet accessible will be produced to perform RI-beams experiments that will allow to understand their nuclear structure and address open questions in astrophysical phenomena of high relevance such as the r-process. The DEcay SPECtroscopy experiments (DESPEC) are intended to measure and understand the decay processes of the exotic nuclei that will be studied at FAIR [1]. For this purpose, the beams will be slowed down and stopped into the implantation detector AIDA [2], a stack of 24×8 cm^2 Si-based 2-mm thick layers where the stopped nuclei eventually decay. The novel HP-Ge detector array DEGAS [3] is a key device for DESPEC, since it will be used as the high energy resolution γ-ray spectrometer device to detect the delayed γ-rays emitted by the stopped nuclei after isomer or beta decay. DEGAS must have a sensitivity good enough in order to detect with high efficiency the γ-rays emitted by the implanted nuclei and discriminate the intense background expected from the secondary radiation produced at RI-beams environments.

Simulations of complex detector systems are a powerful tool to get insights on their performance otherwise not possible to obtain, so they can help to improve the detector design beforehand its actual construction. In this report, we summarize the simulation studies of the DEGAS array using the Geant4 toolkit [4].

Simulation Description. The simulated experiment consists of an AIDA-shape γ-ray source surrounded by 72 HP-Ge crystals arranged in 26 triple-clusters (DEGAS configuration Phase-0), for extra details see Ref [5]. Besides the active Ge detector volume, additional elements of each crystal capsule such as the aluminum housing, mechanical components and the cooling rod were included. Realistic dimensions for these elements were achieved by using GDML geometry files based on the original CAD design of the detector. The translation from CAD to GDML format was done using the software FASTRAD [6] . For all the simulations performed, add-back energy reconstruction between crystals of the same cluster was conducted (e.g. *intra-cluster* add-back).

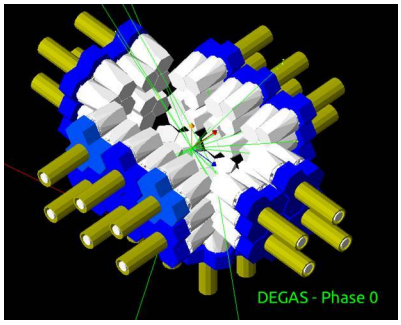

Figure 1: Snapshot of a simulated experiment. The 26 DEGAS triple-clusters in a squared-box geometry (grey) surround the source, the BGO back-catchers (blue), and additional elements (gold/grey). The AIDA-source lies in the x-z plane (red-blue axis). The trajectory of few γ-rays (green) emitted from the origin are shown.

The photo-peak efficiency (ϵ_{ph}) of the full DEGAS array and of each triple-cluster were obtained in the range of 25 keV to 3 MeV, see Figs. 2 and 3. For each energy value of the source, 2×10^6 γ-rays were simulated, isotropically emitted from a random point inside the volume of an AIDA layer centered at the origin.

In order to study the influence of an external γ-ray background, a second set of simulations was performed. Background γ-rays were emitted randomly from a spherical surface containing the experimental setup. A cosine-law angular emission distribution was used in order to have isotropic fluence inside the sphere volume [7]. A double decreasing exponential function was used as energy distribution in the range [25 keV, 3 MeV], using parameters to mimic a background distribution previously measured in decay spectroscopy experiments with the EURICA array. The ratio between background and γ-rays emited from the AIDA-source was chosen to be 1000:1. The DEGAS Peak-to-Total ratio in the range of 25 keV to 3 MeV was measured for each one of the following ancillary shield systems added to the setup:

* Work supported by T. U. Darmstadt in cooperation with GSI.

† j.gerl@gsi.de

- Compton-suppressor BGO back-catchers.
- BGO back-catchers and lead side-shields placed at the edges of the "Ge-faces" defined in the DEGAS-0 Configuration.
- Passive lead back-catchers and lead Side shields.

For a more detailed description of each one of these configurations, see Ref. [5].

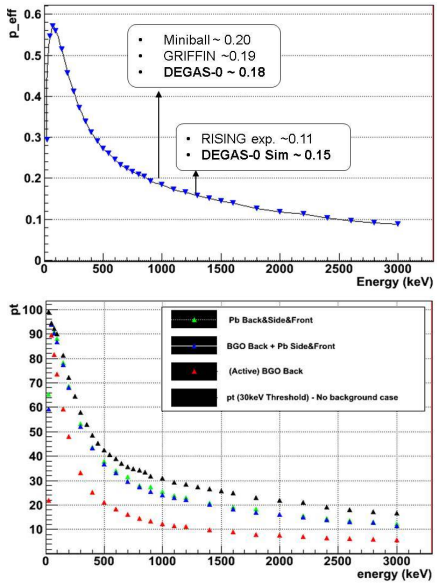

Figure 2: DEGAS ϵ_{ph} (top) and P/T ratio (bottom) in the range [25 keV, 3 MeV]. The P/T ratio is compared not only between different shields, but also to the background-free case, as it is the scenario with the best possible P/T value.

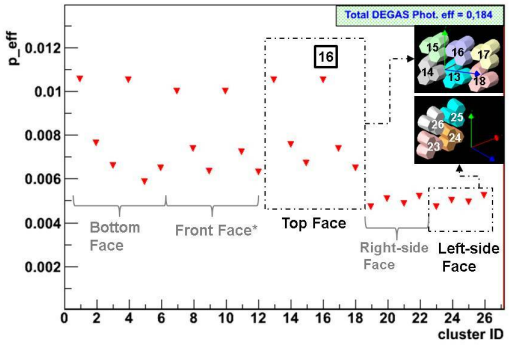

Figure 3: ϵ_{ph} of individual triple-clusters. Due to the geometry of the AIDA+DEGAS setup, cluster positions such as 13 or 16, double the performance of others like 19-26.

Results. The ϵ_{ph} obtained with inter-cluster addback, shown in Fig. 2, The obtained values are comparable to current state-of-the-art decay-spectroscopy arrays such as GRIFFIN (TRIUMF, Canada). As shown in Fig. 2 the DEGAS ϵ_{ph} at 1.3 MeV was found to be 0.15, in comparison to the measured value of 0.11 of EUROBALL during the RISING experiments, leading to an improvement of almost 40%. This is a direct consequence of the squared-box design of DEGAS since it is more suited than a spherical one (such as EUROBALL) for an implantation detector with the AIDA geometry. It is worth to mention that add-back reconstruction between neighbouring crystals regardless their cluster number (*inter-cluster* addback) can potentially double the impact of the add-back analysis on the efficiency, as it is not limited to only to the two adjacent crystals that belong to the same cluster.

In Fig. 3 it can be observed how the ϵ_{ph} changes drastically with the cluster position. Particular positions such as 16 and 13 double the ϵ_{ph} of clusters 19-26, and are even almost 40% bigger than the ϵ_{ph} for neighbouring positions 14,15,17,18. The reason for this phenomenon lies in the larger solid angle covered by clusters in central positions with respect to the AIDA-source, revealing them as determinant for the superior performance of DEGAS. This represents a challenge since all the beam-induced background particles emitted in the forward beam direction have larger probabilities to impact these central positions during the ion implantation process, worsening their performance. To overcome this limitation, it is expected to use AGATA type detectors at these forward positions in DEGAS Phase-2.

The P/T ratio has been used to evaluate the effectiveness of a shield system to allow DEGAS to identify a "good" γ-ray emitted from the AIDA-source against an intense external background. The results in Fig. 2 reveal that as soon as the external background is plugged into the simulation, the P/T ratio is strongly affected, decreasing from the black curve (no background case) to the red one (DEGAS+BGO). When Additional Pb Side shields are added, the P/T ratio improves considerably (blue curve), being almost similar to the case where only Pb is used as a shield (green curve). However, Compton-suppression allows in addition to discriminate events where a γ-ray escapes from the Ge detector and hits the Shield and viceversa. A further simulation with a new configuration of the clusters is currently under development, showing already an improvement in the total efficiency. Background components such as the known prompt-flash emitted during the stopping of the ions or, as well as beam-induced background particles such as high energetic protons or neutrons, can be studied in further simulations.

References

[1] http://www.fair-center.eu/for-users/experiments/nustar/experiments/hispecdespec.html

[2] http://www2.ph.ed.ac.uk/ td/AIDA/

[3] J. Gerl et. al. "Technical report for the design, construction and commissioning of the DESPEC Germanium Array DEGAS", v12.3, August 2014,

[4] http://geant4.cern.ch/

[5] G. Li, C.Lizarazo, et. al. "Simulation on the performance of the DEGAS gamma detector array", GSI Scientific Report 2015, DOI:10.15120/GR-2016-1

DOI:10.15120/GR-2017-1

[6] http://www.fastrad.net/

[7] G. Santin, ESA / ESTEC and RheaTech Ltd - Seminar at "Ecole Geant4", Annecy, 18-21 and 25-28 Nov 2008.

DOI:10.15120/GR-2017-1

DOI:10.15120/GR-2017-1

Superheavy element research – Status report 2016

M. Block[1,2,3], P. Chhetri [2,4], H. David[2], A. Di Nitto[1,2], C. Droese[6], Ch.E. Düllmann[1,2,3], F. Giacoppo[2,3], M. Götz[1,2,3], S. Götz [1,2,3], F.P. Heßberger[2,3], E. Jäger[2], O. Kaleja[1,5], J. Khuyagbaatar[2,3], J. Krier[2], M. Laatiaoui[2,3], L. Lens[1,2], A. Mistry[2,3], V. Pershina[2], S. Raeder[2,3], J. Runke[1,2], P. Scharrer[1,2,3], B. Schausten[2], A. Yakushev[2,3]for the SHE Physics and SHE Chemistry Departments

[1]Johannes-Gutenberg University Mainz, Germany; [2]GSI, Darmstadt, Germany; [3]Helmholtz-Institute Mainz, Germany; [4]TU Darmstadt, Germany; [5]Max-Planck Institute Heidelberg, Germany; [6]University Greifswald, Germany

The main activity at GSI was the ^{48}Ca UNILAC beamtime, where the experiments were devoted to the continuation of the laser spectroscopy study in No [1] and to the chemical investigation of element 113, which was recently named nihonium (Nh).

In 2015, for the first time optical spectroscopy of nobelium atoms was performed at SHIP, making nobelium the heaviest elements for which such studies were feasible. A strong atomic ground state-transition and several Rydberg states in the nobelium atom were identified by resonance ionization laser spectroscopy [1]. The data showed good agreement with theoretical predictions using relativistic coupled cluster and multi configuration Dirac-Fock approaches. Among the atomic and nuclear properties, a limit for the first ionization potential (IP) of nobelium was obtained. However, a more accurate determination of the IP from the convergence of a Rydberg series was hampered by quenching collisions with buffer gas atoms populating also lower-lying metastable states. In 2016, the laser spectroscopy in nobelium thus focused on the identification of different Rydberg series. To this end, measurements in which the second laser pulse (exciting to a Rydberg state) was delayed compared to the laser for the first excitation step were performed for different pressures in the optical cell. The decay of the RIS signal is indicative of the lifetime of the populated state and allowed us to identify different Rydberg series originating from either the $^1P_1$ state or the metastable $^3D_1$ state. From the convergence of the Rydberg series now the IP of nobelium can be determined with high precision. The data analysis is close to completion and the results will be subject of a forthcoming publication. A rate equation model describing the quenching process was developed and showed good agreement with the data. In addition, the location of the $^3D_1$ state that cannot be excited directly from the ground state was determined indirectly [2]. In the second part of the beamtime, first steps towards laser spectroscopy in the next heavier element, lawrencium, were performed. The stopping and neutralization followed by the evaporation from different filaments was investigated to optimized the conditions for the level search in Lr. In addition, the feasibility of producing ^{255}No by EC decay of ^{255}Lr for laser spectroscopy was demonstrated. This will allow us to extend the measurements of nuclear properties in the nobelium isotope chain.

Besides the laser spectroscopy experiment, the SHE physics department was engaged in several technical developments and upgrades of the setup. The relocation of the

SHIPTRAP setup was completed to fully integrate the new cryogenic stopping cell. The new gas cell operated at 40 K will boost the overall efficiency of SHIPTRAP by up to an order of magnitude and extend the reach for Penning trap mass measurements to heavier elements available with lower yield. In 2016, extensive commissioning experiments with radioactive source (offline) and in parasitic beamtime with ^{254}No were performed. In addition, the recently developed novel phase imaging method (PI-PICR) was further improved by installing new extraction optics. First online mass measurements with upgraded SHIPTRAP system are foreseen for 2018.

The new focal plane detector system for decay spectroscopy at SHIP was characterized in parasitic beamtime by measuring α- and α-γ – decay of ^{253,254}No produced in irradiations of ^{207,208}Pb with ^{48}Ca. The measurements were followed by studies of neutron-deficiency Np isotopes, produced in irradiations of ^{181}Ta with ^{48}Ca where specific emphasis was devoted to the isotopes ^{225,226}Np. The investigation of nuclides in this region near the N=126 shell at the proton drip line can be extended with the new detector system. This system features practically dead time free digital electronics and thus gives access to short-lived nuclides. The data analysis is ongoing. The further analysis of the decay studies of ^{257}Rf and ^{258}Db performed in 2014 resulted in confirmation of two low-lying isomeric states in ^{258}Db, the identification of two short-lived isomeric states in ^{258}Rf, populated by EC decay of ^{258}Db [3], and a low-lying isomer in ^{257}Lr, populated by EC decay of ^{257}Rf [4].

At TASCA, a first attempt on the chemical study of Nh (nihonium, element 113) was performed in 2016. The nuclear fusion reaction ^{48}Ca + ^{243}Am, recently investigated at TASCA in the Mc (moscovium, element 115) decay spectroscopy experiment [5], was selected for the production. The ^{288}Mc recoils were guided through TASCA to an exit window, and were thermalized in a gas flow inside a recoil transfer chamber. The short-lived ^{288}Mc ($T_{1/2}$ = 0.17 s) isotope decayed via alpha-particle emission to ^{284}Nh ($T_{1/2}$ = 0.97 s), the lifetime of which is long enough for the transport to the detection setup. A similar detection setup as in the recent experiments on Fl chemistry was used [6].

DOI:10.15120/GR-2017-1

However, to account for the expected higher reactivity of Nh compared to Fl, the first half of the first COMPACT detector array was covered with a SiO_2 surface, while the second half as well as the full second COMPACT array with gold. The latter was cooled to low temperature with a liquid nitrogen cryostat. Fl chemistry experiments at TASCA have demonstrated that one Fl decay chain per week can be observed. Similar cross sections for the production of Fl [7] and Mc [5], as well as comparable beam intensities and target thicknesses led us to expect the observation of about two to three decay chains originating from ^{288}Nh, if the volatility and reactivity of Nh is similar to that of Fl. However, no Nh atoms were detected. The final data analysis is ongoing.

A second chemical system, where studies continued in 2016, is that of carbonyl compounds of transition metal complexes, with $Sg(CO)_6$ having been first synthesized in 2013 [8]. Current techniques include the Sg synthesis, its isolation in a recoil separation, followed by chemical synthesis of the compound behind the separator [8]. A next step included an experiment designed to measure the thermal stability of the compounds in the spirit of [9], which was performed under the lead of the heavy element group from Paul Scherrer Institute (PSI), Villingen, Switzerland, at the RIKEN Nishina Center, Wako, Japan. The focus of the work of our group was on further developments to extend studies of carbonyl compounds of the heaviest elements to those beyond Sg. Fusion products from the asymmetric nuclear fusion reactions, as needed for the carbonyl studies with Sg, Bh, and Hs, have a relatively large angular and energy spread, thus the transmission efficiency through an on-line recoil separator is relatively low. In case of TASCA or GARIS (which was used in [8]), the efficiencies are in order of 13% for Sg [10]. Thus, the overall efficiency of the synthesis of carbonyl complexes in combination with physical preseparation is rather low. For future experiments, the possibilities for chemical investigation of the metal carbonyl complexes of SHE without using a preseparation stage are currently being explored, with the goal to avoid the corresponding losses of close to 90%. First experiments performed at the Tandem accelerator at JAEA Tokai, Japan, suggested the successful the synthesis of Os and W carbonyl complexes also without a preseparator to be feasible, if the thermalization of the evaporation residues is spatially decoupled from the chemical synthesis. The latter is required to occur in a beam-free environment [11]. Further experiments were performed at the research reactor TRIGA Mainz [12].

With the aim to support gas-phase experiments on study of stability and volatility of carbonyls of the heaviest elements, calculations of the electronic structure and properties of group-6 $M(CO)_6$ [13] and group-8 $M(CO)_5$ [14] have been performed using the most advanced relativistic quantum-chemical methods (ADF BAND, X2c-DFT, DIRAC). The results have shown that in contrast to earlier published works the carbonyls of Sg and Hs should be less stable than those of the lighter 5d-homologs. This finding is valuable for fixing the right conditions in measurements of the first bond dissociation energies of these complexes. In addition, using results of these calculations, volatilities of goup-8 carbonyls as adsorption energies on inert surfaces have been predicted via a model of mobile adsorption. It was shown that $Hs(CO)_5$ should slightly more strongly adsorb on neutral surfaces than $Os(CO)_5$.

To render assistance to gas-phase experiments on study of reactivity of elements 112 through 114 with various surfaces, calculations of the adsorption energies of these elements and their lighter homologs on a hydroxylated quartz surface have been performed using a periodic ADF BAND code [15, 16]. Such periodic calculations of adsorption energies have been performed for the first time for superheavy element systems. The results have shown that Cn should be indeed the most volatile element out of those under consideration. Also, Fl should not interact with quartz at room temperature. Element 113, Nh, on the contrary should strongly interact with quartz [16]. Such a different adsorption behavior allows for a good separation between all these elements using a combination of quartz and gold surfaces.

A further activity of the SHE Chemistry division concerned the development of a new detector system for ALpha-BEta-Gamma (ALBEGA) multicoincidence spectroscopy for chemically separated samples [17]. Efforts in 2016 were mainly dedicated to the study and development of the new alpha/beta detector. The new version will be characterized by a more densely packed configuration and a thinner dead-layer on the side in contact with the gas flux. The production of the device was performed at the ITE, Warsaw (Poland), for which an ad hoc technological development for its assembling was required. The new alpha/beta detector will not only provide a higher energy resolution and efficiency, but will also feature increased mechanical stability to sustain the pressure difference inside and outside of the gas channel.

Presently, one of the hot topics in the superheavy element research is the synthesis of elements beyond Og (Z=118). The lack of sufficient amounts of heavier actinides prevents a continuation beyond Og with ^{48}Ca-induced reactions. An obvious path is to continue with fusion-evaporation reactions, but with projectiles heavier than ^{48}Ca. Several experiments have already been performed to synthesize Z=119 and 120 by using the reactions ^{50}Ti+^{249}Bk (TASCA, GSI), ^{64}Ni+^{238}U (SHIP, GSI), ^{58}Fe+^{244}Pu (DGFRS, FLNR, JINR), ^{54}Cr+^{248}Cm (SHIP, GSI), and ^{50}Ti+^{249}Cf (TASCA, GSI). In total, about one year of accelerator beam time has been spent for these search experiments. However, none of them led to the discovery of a new element, suggesting that cross sections are significantly lower than for ^{48}Ca-induced reactions. To get a better guidance for future search experiments, a better understanding of the fusion reaction is needed. Therefore, to understand the reaction mechanism better, an intensive experimental campaign involving various heavy

DOI:10.15120/GR-2017-1

projectiles and actinide targets was carried out by a collaboration of scientists from GSI, HIM Mainz, Johannes Gutenberg University Mainz, and the Australian National University (ANU), Canberra, Australia at the ANU's Heavy Ion Accelerator Facility. Suitable actinide targets like ^{244}Pu, ^{248}Cm, and ^{249}Cf were produced at the Institute of Nuclear Chemistry at the Johannes Gutenberg University Mainz, and were irradiated with a variety of beams between ^{34}S and ^{64}Ni at energies around the Coulomb barriers. The mass and angular distribution of fission fragments originating from the nuclear reactions were measured, in many reactions for the first time. The data analysis is ongoing and preliminary results already show a difference in dynamics of reactions involving different projectiles.

Further studies of the fission mechanism were performed, e.g., a study of fission induced by ^{18}O+^{249}Cf multi-nucleon transfer reactions at 8 MeV/A, in which the SHE Chemistry department participated. The experiment was performed at the Tandem accelerator at JAEA Tokai (Japan). Such reactions, acting as surrogate of n-induced fission reactions, allow populating in a single experiment several isotopes at low angular momentum and at low excitation energy. The excitation energy of the fissioning system can be determined by the kinematical reconstruction of the binary process, by measuring the mass and kinetic energy of light ejectile of the transfer reaction. In particular, this experiment was performed with the aim to extend the current systematics of fission fragment mass distribution nearby the region of transition from asymmetric to symmetric fission.

A further activity, which led to widespread recognition, was the contribution of GSI, HIM, and Johannes Gutenberg Mainz scientists and technicians to the direct detection of the exotic low-lying nuclear isomer in ^{229}Th [18]. For this, ^{233}U targets, which yield the ^{229m}Th after alpha decay of ^{233}U, as well as ^{234}U targets (for control experiments serving to exclude an origin other than that of ^{229m}Th decay to the ground state as a source for the observed signal) were produced. They were used in these joint experiments, which were led by the group of P. Thirolf at the Ludwigs-Maximilians-University Munich, Germany.

Some further activities, also including contributions of the SHE Chemistry department to the upgrade of the UNILAC Accelerator, are detailed in individual contributions to this GSI Scientific Report 2016 (J. Konki et al., A. Di Nitto et al., S. Götz et al., M. Götz et al., V. Pershina et al., as well as P. Scharrer et al.)

References

[1] M. Laatiaoui et al., Nature 538, 495 (2016).
[2] P. Chhetri et al., Eur. Phys. J. D (submitted).
[3] F.P. Heßberger et al. EPJ A 52, 328 (2016).
[4] F.P. Heßberger et al. EPJ A 52, 192 (2016).
[5] D. Rudolph et al., Phys. Rev. Lett. 111, 112502 (2013).
[6] A. Yakushev et al., Inorg. Chem. 53, 1624 (2014).
[7] Ch.E. Düllmann et al., Phys. Rev. Lett. 104, 252701 (2010).
[8] J. Even et al., Science 345, 1491 (2014).
[9] I. Usoltsev et al., Radiochim. Acta 104, 141 (2016).
[10] H. Haba et al., Phys. Rev. C 85, 024611 (2012).
[11] Y. Wang et al., Radiochim. Acta 102, 69 (2014).
[12] V. Wolter, Master's Thesis, Johannes Gutenberg University Mainz, 2016.
[13] M. Ilias and V. Pershina, Inorg. Chem. 56, 1638 (2017);
[14] V. Pershina and M. Ilias, J. Chem. Phys. 146, 184306 (2017).
[15] V. Pershina, Phys. Chem. Chem. Phys. 18, 17750 (2016).
[16] V. Pershina, J. Phys. Chem. C 120, 20232-20238 (2016).
[17] A. Di Nitto, GSI Sci. Rep. 2014, p. 184 (MU-NUSTAR-SHE-C-06).
[18] L. von der Wense et al., Nature 533, 47 (2016).

DOI:10.15120/GR-2017-1

DOI:10.15120/GR-2017-1

The new isotopes ^{240}Es and ^{236}Bk

J. Konki[*1], *J. Khuyagbaatar*[2,3], *J. Uusitalo*[1], *P. T. Greenlees*[1], *K. Auranen*[1], *H. Badran*[1], *M. Block*[2,3,4], *R. Briselet*[5], *D. M. Cox*[6], *M. Dasgupta*[7], *A. Di Nitto*[3,4], *Ch. E. Düllmann*[2,3,4], *T. Grahn*[1], *K. Hauschild*[8], *A. Herzán*[1], *R.-D. Herzberg*[6], *F. P. Heßberger*[3], *D. J. Hinde*[7], *R. Julin*[1], *S. Juutinen*[1], *E. Jäger*[3], *B. Kindler*[3], *J. Krier*[3], *M. Leino*[1], *B. Lommel*[3], *A. Lopez-Martens*[8], *D. H. Luong*[7], *M. Mallaburn*[9], *K. Nishio*[10], *J. Pakarinen*[1], *P. Papadakis*[1], *J. Partanen*[1], *P. Peura*[1], *P. Rahkila*[1], *K. Rezynkina*[8], *P. Ruotsalainen*[1], *M. Sandzelius*[1], *J. Sarén*[1], *C. Scholey*[1], *J. Sorri*[1], *S. Stolze*[1], *B. Sulignano*[5], *Ch. Theisen*[5], *and A. Ward*[6]

[1]University of Jyväskylä, Finland; [2]Helmholz-Institut Mainz, Germany; [3]GSI, Darmstadt, Germany; [4]University of Mainz, Germany; [5]CEA Saclay, France; [6]University of Liverpool, UK; [7]ANU, Canberra, Australia; [8]CSNSM Orsay, France; [9]University of Manchester, UK; [10]JAEA, Tokai, Japan

Two new neutron-deficient nuclei ^{240}Es and ^{236}Bk were synthesised in an experiment carried out at the Accelerator Laboratory of the Department of Physics (JYFL), University of Jyväskylä, Finland [1]. The hitherto unknown isotopes were identified by their radioactive decay chains starting from ^{240}Es produced in the fusion-evaporation reaction ^{209}Bi(^{34}S,3n)^{240}Es.

Evaporation residues (ER) recoiling out of the target were separated from the primary beam and transfer reaction products by the gas-filled recoil separator RITU [2]. The ERs passed through a Multi-Wire Proportional Counter (MWPC) and were implanted in the two adjacent double-sided silicon detectors (DSSDs) of the GREAT focal plane spectrometer [3] where their subsequent decays were measured.

The energies of all signals from the detectors were time stamped and recorded using the triggerless Total Data Readout (TDR) data-acquisition system [4]. The spatial and temporal correlations in the data between the detectors were analysed using the GRAIN software package [5].

The results of this experiment were reported in Physics Letters B [1] in detail. Two groups of α particles with energies E_α=8.19(3) MeV and 8.09(3) MeV were assigned to ^{240}Es from correlated ER-α events. The new isotope ^{236}Bk was identified from its electron-capture delayed fission (ECDF) branch. Half-lives of 6(2) s and 22^{+13}_{-6} s were obtained for ^{240}Es and ^{236}Bk, respectively. The ECDF probabilities (P_{ECDF}) of ^{240}Es and ^{236}Bk were determined from correlated ER-fission and ER-α-fission events to be 0.16(6) and 0.04(2), respectively. The proposed decay schemes for the new ^{240}Es and ^{236}Bk isotopes are shown in Fig. 1.

The ECDF probabilities of the heavier odd-odd isotopes $^{242-248}$Es and ^{238,240}Bk have been measured previously (see e.g. [6] and the references therein). The new data from this work extend the systematics of the Es and Bk isotopes and show a continuation of the exponential increase of P_{ECDF} as a function of the Q-value of the EC decay (Q_{EC}) and the spontaneous fission barrier (B_{sf}) in more neutron-deficient isotopes. No deviations from this trend

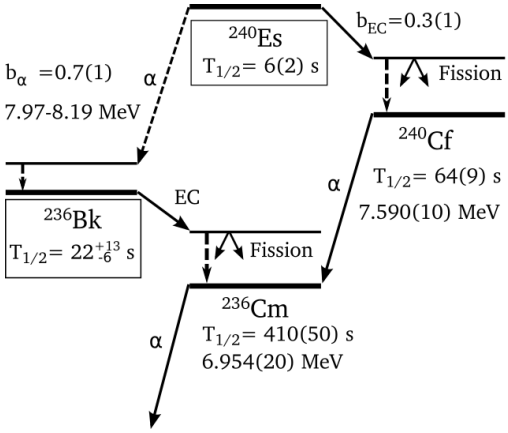

Figure 1: The proposed decay scheme of the new isotopes ^{240}Es and ^{236}Bk. The measured values for ^{240}Es and ^{236}Bk are from this work.

are observed. We note that P_{ECDF}-values for the new isotopes ^{240}Es and ^{236}Bk are the highest ones so far for Es and Bk isotopes, respectively.

The simple dependence of P_{ECDF} on $Q_{\mathrm{EC}} - B_{\mathrm{sf}}$ is not yet fully understood. There is a relative difference between Es and Bk isotopes in P_{ECDF} that could be attributed to the shape of the total fission barrier. In more neutron-deficient isotopes the P_{ECDF} is expected to approach saturation and more experimental data are needed there to shed a light on this complex decay process.

References

[1] J. Konki et al., Phys. Lett. B **764**, 265 (2017).

[2] M. Leino et al., NIM. B **99**, 653 (1995).

[3] R. D. Page et al., NIM. B **204**, 634 (2003).

[4] I. H. Lazarus et al., IEEE Trans. Nucl. Sci. **48**, 567 (2001).

[5] P. Rahkila et al., NIM. A **595**, 637 (2008).

[6] A. Andreyev et al., Rev. Mod. Phys. **85**, 1541 (2013).

*joonas.konki@jyu.fi

Hexacarbonyls of Mo, W, and Sg: Electronic Structure and Bonding

V. Pershina[1] and M. Iliaš[2,3]
[1]GSI Helmholtzzentrum für Schwerionenforschung, Darmstadt, Germany; [2]Helmholtz Institute Mainz, Germany;
[3]Matej Bel University, Banská Bystrica, Slovakia

The class of carbonyl compounds has recently been enriched by a new species, a hexacarbonyl of a superheavy element with Z=106, $Sg(CO)_6$ and its volatility has been studied both experimentally [1] and theoretically [2]. Now, experiments are under way to measure the First Sg-CO Bond Dissociation Energy (FBDE) [3]. Earlier predictions based on RECP calculations have indicated that the Sg-CO bond should be stronger than the W-CO one due to relativistic effects on the 6d AOs [4]. With an aim to prove these earlier predictions on a higher level of theory and to have an own set of data, in this work, we have calculated various properties of the group-6 hexa- and pentacarbonyls and have newly determined FBDEs. The following decomposition reaction was considered

$$M(CO)_6(O_h) \rightarrow M(CO)_5(C_{4v}) + CO.$$

The calculations were performed using a variety of nonrelativistic (NR), relativistic scalar (SR) and spin-orbit (SO) methods, such as ZORA-ADF, X2c+AMFI-CCSD(T) and Dirac-Coulomb-DFT one. The uncontracted Dyall vdz basis sets in the DIRAC CCSD(T) calculations were utilized. The present results for the FBDEs in comparison with those of the work [4] and experimental data for $Mo(CO)_6$ and $W(CO)_6$ [5] are given in Table 1.

Table 1. First M-CO Bond Dissociation Energies at various levels of theory (in kJ/mol)

Method	$Mo(CO)_6$	$W(CO)_6$	$Sg(CO)_6$
ADF (NR)	155.07	218.47	223.81
ADF (SR)	163.63	191.19	181.09
ADF (SO)	163.49	190.73	180.22
DC-DFT	163.20	189.83	177.42
X2c+CCSD(T)	158.19	181.45	176.22
RECP-CCSD[a]	170.71	197.90	204.59
RECP-CCSD(T)[a]	182.00	207.94	212.13
ZPT[b]	-5.17	-5.43	-5.59
Exp.[c]	167.4±8	192.5±8	-

[a]Ref. [4]; [b]Zero point and thermal contribution; [c]Ref. [5].

The main difference between the present relativistic ADF, ReSpect and DIRAC calculations on the one hand and the RECP ones [4] on the other hand is an opposite trend in the vibrational frequencies of the M-CO bond and FBDE from $W(CO)_6$ to $Sg(CO)_6$: all the former show a decrease in this direction, while the latter an increase (Fig. 1).

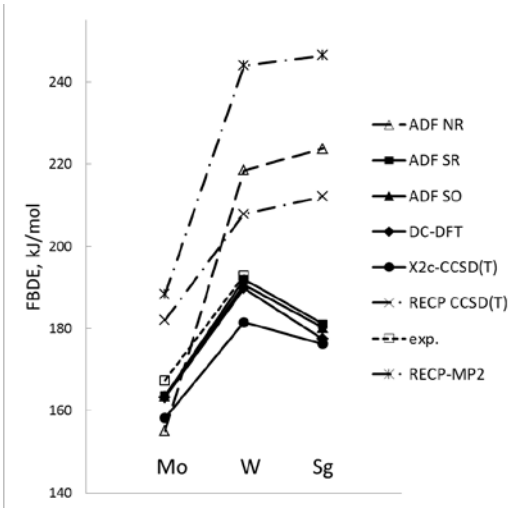

Figure 1. First Bond Dissociation Energies of $M(CO)_6$, where M = Mo, W and Sg, calculated using various methods in comparison with experimental data for the Mo and W carbonyls (open squares).

To find a reason for such a difference, a bond analysis of $M(CO)_6$ (M = Mo, W, and Sg) was performed using ADF Hirshfeld effective charges, q_M, Mulliken MO analysis based on the M and CO fragments and the DIRAC projection analysis. The obtained smaller relativistic q_M(Sg) than q_M(W) means that the electron density is not shifted so much in $Sg(CO)_6$ from Sg to CO as in $W(CO)_6$, so that the Sg-CO electrostatic interaction is smaller than the W-CO one, meaning that bonding is weaker in $Sg(CO)_6$. Non-relativistically, it is just the other way around: the largest q_M on Sg is the source of its largest ionic bonding with CO in the row of homologs. Thus, in difference to the earlier predictions [4], the decomposition of $Sg(CO)_6$ should occur at lower temperatures than those of $W(CO)_6$ [6], with a reversal of the trend from Sg to W.

References

[1] J. Even, et al. Science **345**, 1491 (2014).
[2] V. Pershina and J. Anton, J. Chem. Phys. **138**, 174301 (2013).
[3] R. Eichler, private communication.
[4] C. Nash and B. E. Bursten, J Am. Chem. Soc. **121**, 10830 (1999).
[5] K. E. Levis, et al. J. Am. Chem. Soc. **106**, 3905 (1984).
[6] I. Usoltsev, et al. Radiochim. Acta **104** (3) (2015).

DOI:10.15120/GR-2017-1

Identification of reaction products in ^{50}Ti + ^{249}Cf reactions at TASCA *

A. Di Nitto †[1,2], *J. Khuyagbaatar*[2,3], *D. Ackermann* ‡[2], *J.Adamczewski-Musch*[2], *L.-L. Andersson*[3,4], *E. Badura*[2], *M. Block*[2], *H. Brand*[2], *D.M. Cox*[4], *Ch.E. Düllmann*[1,2,3], *J. Dvorak*[3], *K. Eberhardt*[1], *P.A. Ellison*[5], *N.E. Esker*[5], *J. Even*[1,3], *C. Fahlander*[6], *U. Forsberg*[6], *J.M. Gates*[5], *P. Golubev*[6], *O. Gothe*[5], *K.E. Gregorich*[5], *W. Hartmann*[2], *R.D. Herzberg*[4], *F.P. Heßberger*[2,3], *J. Hoffmann*[2], *R. Hollinger*[2], *A. Hübner*[2], *E. Jäger*[2], *J. Jeppsson*[6], *B. Kindler*[2], *S. Klein*[1], *I. Kojouharov*[2], *J.V. Kratz*[1], *J. Krier*[2], *N. Kurz*[2], *S. Lahiri*[7], *S.Linev*[2], *B. Lommel*[2], *M. Maiti*[7], *R. Mändl*[2], *E. Merchan*[2], *S. Minami*[2], *A. Mistry*[4], *Ch. Mokry*[1], *H. Nitsche*[5], *J.P. Omtvedt*[8], *G.K. Pang*[5], *I. Pysmenetska*[2], *D. Renisch*[1,3], *D. Rudolph*[6], *J. Runke*[2], *L.G. Sarmiento*[6,9], *M. Schädel*[2,10], *H. Schaffner*[2], *B. Schausten*[2], *A. Semchenkov*[8], *J. Steiner*[2], *P. Thörle-Pospiech*[1], *T. Torres De Heidenreich*[2], *N. Trautmann*[1], *A. Türler*[11], *J. Uusitalo*[12], *D. Ward*[6], *M. Wegrzecki*[13], *P. Wieczorek*[2], *N. Wiehl*[1], *A. Yakushev*[2], *and V. Yakusheva*[3]

[1]U. Mainz, Germany; [2]GSI, Darmstadt, Germany; [3]HIM, Mainz, Germany; [4]U. Liverpool, UK; [5]LBNL+UC Berkeley, CA, USA; [6]Lund U., Sweden; [7]SINP, Kolkata, India; [8]U. Oslo, Norway; [9]UNAL Bogotá, Colombia; [10]JAEA Tokai, Japan; [11]U. Bern+PSI Villigen, Switzerland; [12]U. Jyväskylä, Finland; [13]ITE, Warsaw, Poland

During the last decades heavy ion induced reactions were applied to explore the chart of nuclei up to the superheavy elements (SHE), which has resulted in the discovery of the SHE up to Og ($Z = 118$) in complete fusion reactions [1]. Alternatively, recent model calculations suggest the possibility to produce exotic nuclei including SHE in non-fusion channels of heavy ion induced reactions [2]. Pioneering studies on the possible production of such exotic nuclei in non-fusion reactions were performed in the late 1970s by applying chemical separation techniques [3], which are suitable for longer-lived nuclei ($\gtrsim$1 h). Many properties of the multi-nucleon transfer reactions have been established, but still detailed information on the reaction mechanism/kinematics is missing [5, 6, 4].

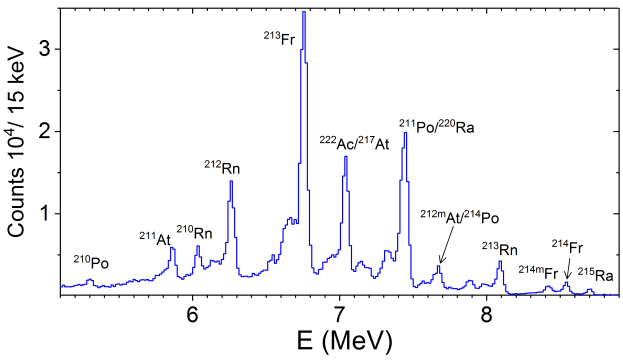

Figure 1: Energy spectrum measured with the focal plane detector during beam-off periods for the ^{50}Ti + ^{249}Cf reaction. Isotopic identification of some lines is given.

Recently, at the velocity filter SHIP new short-lived (down to 10^{-6} h) neutron-deficient nuclei of heavy elements have been synthesized in the ^{48}Ca + ^{248}Cm reaction [7]. These and other results at SHIP (see [8]), benefiting of the kinematic separation, demonstrate the relevance of the forward angle measurements for the investigation of the reaction dynamics.

At the gas-filled recoil separator TASCA, non-fusion products of the ^{50}Ti $+^{249}$ Cf reaction have been investigated. They were produced during the experiment for searching the SHE with $Z = 120$ [9]. The magnetic settings of TASCA were tuned to collect the products of fusion-evaporation reactions, but even under these conditions some amount of non-fusion products were passing through TASCA and were implanted into the focal plane detector. Here their subsequent radioactive decays were measured. A typical energy spectrum containing lines from the α decay of the implanted nuclei is shown in Figure 1. By exploiting the α decay properties, the identification of nuclei was performed employing a position and time correlation analyses between implantation and/or α-like events. In total, 57 isotopes with $Z = 83 - 90$ were identified.

Experimental details and the final analysis will be given in a forthcoming publication [10].

References

[1] Y. T. Oganessian and V. K. Utyonkov, Rep. Prog. Phys. 78, 036301 (2015).
[2] V. I. Zagrebaev and W. Greiner PRC **83**, 044618 (2011).
[3] M. Schädel et al., PRL **41**, 469 (1978), and **48**, 852 (1982).
[4] L. Corradi et al., Jour. of Phys. G **36**, 113101 (2009).
[5] J.V. Kratz et al., NPA **944**, 117 (2015).
[6] M. Götz et al., NPA **961**, 1 (2017).
[7] S. Heinz et al., EPJA **52**, 278 (2016).
[8] S. Heinz et al., EPJA **51**, 140 (2015).
[9] Ch. E. Düllmann et al. to be published.
[10] A. Di Nitto et al., to be published.

* We thank the ion-source and accelerator staff at GSI. Work supported by BMBF contract-No. 06MZ7164.
† a.dinitto@gsi.de
‡ Present address: GANIL, Caen, France

Speeding up gas-phase chemistry to access elements beyond Fl

S. Götz[*1,2,3], *S. Raeder*[1,2], *M. Block*[1,2,3], *Ch. E. Düllmann*[1,2,3], *P. Chhetri*[1,5], *F. Giacoppo*[1,2], *M. Götz*[1,2,3], *O. Kaleja*[1,3,4], *Ch. Mokry*[2,3], *J. Runke*[1,3], *P. Thörle-Pospiech*[2,3], *and A. Yakushev*[1,2]

[1]GSI, Darmstadt, Germany; [2]HIM, Mainz, Germany; [3]Johannes Gutenberg-University, Mainz, Germany; [4]MPIK, Heidelberg, Germany; [5]TU Darmstadt, Darmsatdt, Germany

The electronic structure of the heaviest elements is strongly influenced by relativistic effects, which may lead to chemical properties that deviate from those expected based on an extrapolation of trends present in the periodic table [1]. Chemical properties have been reproducibly studied for all elements up to Hs (Z=108) as well as for Cn (Z=112). Current research activities in the field focus on the elements Nh (Z=113) and Fl (Z=114) [2]. Due to the low production rates and short half-lifes, $T_{1/2}$, only single atoms are available in chemical experiments. Nevertheless, the required sensitivity can be achieved, best by combining chemical setups with electromagnetic preseparators [3]. Gas phase chemical methods have proven most successful for the heaviest elements, as they give access to isotopes with half-lifes of the order of at least about one second [2]. The successful gas-chromatography studies of Fl demonstrate the potential of the combination of the chromatography detector array COMPACT with the gas-filled separator TASCA at an one-atom-at-time level [4]. The most time-consuming step in the experiments performed with the current TASCA-COMPACT setup as it was used for the Fl experiments is the thermalization of the fusion-evaporation reaction products in the Recoil Transfer Chamber (RTC) [3] and their transport to the connected COMPACT detector array. Besides Cn and Fl, also Nh is in reach with this technique. The extraction time is, however, significantly longer than the half-lifes of the most long-lived isotopes of all elements wit $Z > 114$. For Mc (Z=115), for example, the most long-lived currently known isotope is ^{288}Mc with $T_{1/2}$ = 170 $\binom{+40}{-30}$ ms [5]. To overcome this limitation, exploratory experiments on the coupling of COMPACT to an existing gas-catcher operating with electric fields [6] were carried out.

To get access to shorter-lived isotopes, it is crucial to speed up the transport time, while maintaining a high efficiency of the setup [5]. To this end, a faster and more effective transport technique is currently being developed. For future experiments with Mc and beyond, the current RTC will be replaced by a gas-catcher, which uses electric fields to extract the ions [6, 7, 8, 9].

In 2016, first off-line measurements were performed with ^{223}Ra ($T_{1/2}$ = 11.43 d) and ^{225}Ac ($T_{1/2}$ = 10 d) recoil ion sources. The used sources were placed in axial symmetry in the center of the direct current electrodes-system (DC-cage), which is located within the gas-catcher. The DC-cage contains the stopping volume for the ions inside the gas-catcher. The system consists of 5 cylindrical electrodes with an outer diameter of 180 mm and an inner diameter of 160 mm. From the source the recoil ions ^{219}Rn$^+$ ($T_{1/2}$ = 3.96 s) or ^{217}At$^+$ ($T_{1/2}$ = 32.34 ms) are guided by the electric fields through the segmented DC electrode towards a funnel structure. This funnel guides the ions by applied DC and AC (RF: 140 V, gradient 7 V cm^{-1}) fields to the exit hole (5 mm diameter). After exiting, the ions are neutralized by collisions with the walls of a Teflon-tube. This neutralization section facilitates gas-chromatography studies of the element of interest in elemental form. After the neutralization zone the atoms are directed by a gas flow into the subsequent COMPACT-detector array [4]. The gas-catcher-COMPACT-setup was flushed with helium gas and kept at a pressure of 50 to 100 mbar. This ensured a viscous flow and allowed performing gas phase chromatography studies in COMPACT. For ^{219}Rn, only decay in-flight was observed as COMPACT was operated at ambient temperature. Due to the high adsorption tendency of ^{221}Fr no atoms of this element were observed in COMPACT in a first test, ^{217}At, however, was observed in the first COMPACT-detector. We studied the efficiency for transporting ^{217}At from the source to the COMPACT detector as well as the transport time. For the efficiency quantification, the measured rate in COMPACT was compared with the effective source strength, which was determined in a separate measurement of the rate at which ^{217}At$^+$ ions are recoiling from the source. To measure the transport time, the potential, at which the source was kept, was cyclically switched rapidly from negative (to avoid release of ^{217}At$^+$ ions) to positive. This was used as the start of a time-of-flight measurement. The stop signal was given by measured decay in COMPACT. Transport times well below 100 ms were measured, which would be fast enough for applications to, e.g., Mc.

References

[1] M. Schädel (Ed.), The Chemistry of the Superheavy Elements, Kluwer Academic Publishers, Dordrecht, The Netherlands, 2003.

[2] A. Türler et al., Nucl. Phys. A **944**, 640 (2015).

[3] J. Even et al., Nucl. Instrum. Meth. A **638**, 157-164 (2011)

[4] A. Yakushev et al., Inorg. Chem. **53**, 1624 (2014).

[5] D. Rudolph et al., AIP Conf. Proc. **1681**, 030015-1 (2015).

[6] J. Neumayr et al. Nucl. Instr. and Meth. B **244** (2006) 489.

[7] M. Wada et al., Nucl. Instrum. Methods B **204**, 570 (2003).

[8] G. Savard et al., Nucl. Instrum. Methods B **204**, 582 (2003).

[9] M. Block et al., Eur. Phys. J. D **45**, 39 (2007).

* s.goetz@gsi.de

DOI:10.15120/GR-2017-1

Radiochemical investigation of the kinematics of multi-nucleon transfer reactions

M. Götz[1,2,3], S. Götz[1,2,3], J. V. Kratz[1], Ch. E. Düllmann[1,2,3], Ch. Mokry[1,3], J. Runke[1,2], P. Thörle-Pospiech[1,3], N. Wiehl[1,3], M. Schädel[2], J. Ballof[4], H. Dorrer[1], J. Grund[1], E. Jäger[2], O. Keller[1], J. Krier[2], J. Khuyagbaatar[2,3], L. Lens[1,2], B. Lommel[2], M. Mendel[1], K. J. Moody[5], B. Schausten[2], M. Schmitt[1], D. Shaughnessy[5], J. Steiner[2], N. Trautmann[1], A. Yakushev[2,3], and V. Yakusheva[2]

[1]Institute of Nuclear Chemistry University Mainz, 55099 Mainz, Germany; [2]GSI Helmholtz Center for Heavy-Ion Research, 64291 Darmstadt, Germany; [3]HIM Helmholtz Institute Mainz, 55128 Mainz, Germany; [4]Advanced Science Research Center JAEA, Tokai-mura Ibaraki 319-1195, Japan; [5]Lawrence Livermore National Laboratory, Livermore CA, USA

Renewed interest in multi-nucleon transfer reactions as a promising tool for the production of neutron-rich transactinide isotopes [1] has motivated us to perform a ^{48}Ca+^{248}Cm bombardment at an incident energy 10% above the Coulomb barrier to study emission-angle resolved kinetic energies of isotopes of Bk through Fm [2]. The isotopes of interest were implanted into a stack of Ni foils mounted behind the target. They were isolated off-line using radiochemical separations and detected by alpha spectroscopy. This way, long-lived isotopes with mass numbers between 246 and 256 were accessible. Angular distributions and kinetic energies corresponding to recoil ranges in the Ni foils were evaluated and weighted mean values in the center of mass system were used to construct deflection functions, total kinetic energy TKE vs. Θ_{cm}. Fig. 1 shows the location of the centroid of the Fm activities in the TKE vs. Θ_{cm} plane corresponding to an average total kinetic energy loss TKEL = 70 $\pm$ 10.5 MeV at Θ_{cm} close to the grazing angle. Taking into account the ground state Q value for the most probable primary fragment results in an excitation energy corresponding within the uncertainty in the measured TKEL to the missing mass, i.e. the mass difference between the most probable secondary mass number and the most probable primary mass number calculated with Volkov's generalized Qgg systematics [3] (minimum potential energy corrected for the breaking of nucleon pairs in the multi-nucleon transfer process) indicating that the number of evaporated neutrons is 1.3 on the average. For products closer to the target, e.g. for Cf, the values of TKE spread much wider than for Fm, see Fig. 2. Here, TKEL values of ≈9, ≈34, and ≈54 MeV corresponding to the evaporation of 0, 1, and 3 neutrons are observed in the corresponding range bins.

Thus, values of TKE reach from quasi-elastic to completely damped values. For multi-nucleon transfer products (Fm), the distributions are peaked close to the grazing angle with laboratory kinetic energies close to 80 MeV. These are benchmarks for the design of a large acceptance separator for the separation and detection of short-lived neutron-rich transactinide isotopes.

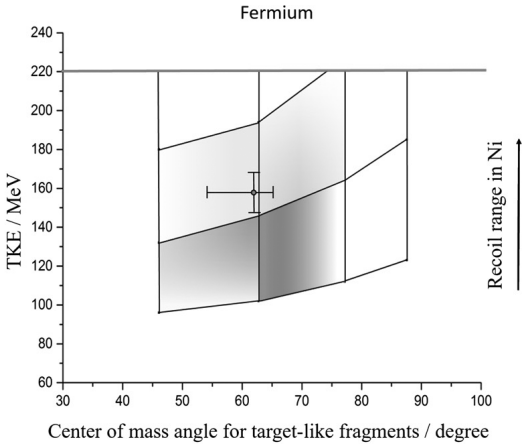

Figure 1: Centroid of the Fm distribution with standard deviations. The shades are meant to indicate the approximate width of the distribution.

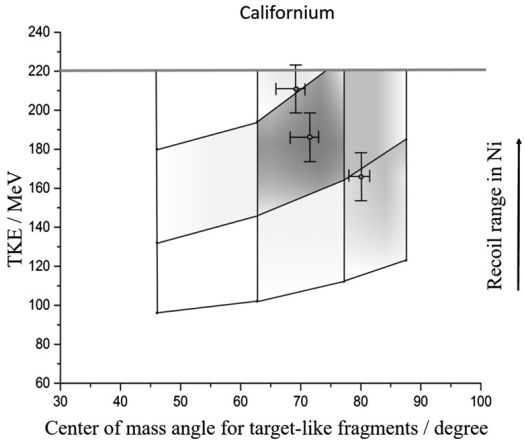

Figure 2: Same as Fig. 1 but for the Cf isotopes.

References

[1] V. Zagrebaev et al,. Nucl.Phys. A834, 366c (2010)

[2] M. Götz et al., Nucl. Phys. A961, 1 (2017)

[3] V.V. Volkov, Int. Conf. on Reactions between Complex Nuclei, Nashvillle 1974, (North Holland, Amsterdam) Vol. II, 363 (1974)

DOI:10.15120/GR-2017-1

DOI:10.15120/GR-2017-1

NeuLAND - from the demonstrator to the start version*

K. Boretzky† [3], *G. Alkhazov* [1], *L. Atar* [2,3,4], *T. Aumann* [2,3], *C. Beinrucker* [13], *D. Bemmerer* [5], *C. Caesar* [3], *M. Cherciu* [6], *L. Chulkov* [7], *T. Cowan* [5,8], *C.A. Douma* [9], *Z. Elekes* [10], *J. Enders* [2], *J. Frühauf* [3], *D. Galaviz Redondo* [11], *I. Gašparić* [12], *N. Gruzinsky* [1], *K. Göbel* [13], *T. Heftrich* [13], *H. Heggen* [3], *M. Heil* [3], *A. Heinz* [14], *J. Hoffmann* [3], *M. Holl* [2], *A. Horvat* [2], *Á. Horváth* [15], *H.T. Johansson* [14], *B. Jonson* [14], *J. Kahlbow* [2], *N. Kalantar-Nayestanaki* [9], *A. Kelić-Heil* [3], *K. Koch* [3], *N. Kozlenko* [1], *D. Kresan* [3], *N. Kurz* [3], *V. Kuznetsov* [1], *D. Körper* [3], *C. Langer* [13,3], *S. Lindberg* [14], *J. Mayer* [16], *M. Najafi* [9], *T. Nilsson* [14], *G. Nyman* [14], *A. Pelizza* [14], *S.G. Pickstone* [16], *R. Plag* [3], *M. Pohl* [13], *P. Potlog* [6], *R. Reifarth* [13], *S. Reinhardt* [8], *S. Reinicke* [5], *C. Rigollet* [9], *S. Röder* [5], *D. Rossi* [2], *D. Savran* [17], *H. Scheit* [2], *F. Schindler* [2], *P. Schrock* [2], *H. Simon* [3], *E. Stan* [6], *R. Thies* [14], *H. Törnqvist* [2], *L. Uvarov* [1], *S. Volkov* [1], *A. Wagner* [5], *V. Wagner* [2], *A. Zilges* [16], *K. Zuber* [8], *and the R^{3}B Collaboration* [1]

[1]Petersburg Nuclear Physics Institute Gatchina, Russia; [2]Technische Universität Darmstadt, Darmstadt, Germany; [3]GSI Helmholtzzentrum für Schwerionenforschung, Darmstadt, Germany; [4]University of Guelph, Canada; [5]Helmholtz-Zentrum Dresden-Rossendorf, Dresden, Germany; [6]Institute of Space Sciences, Magurele, Romania; [7]NRC Kurchatov Institute, Moscow, Russia; [8]Technische Universität Dresden, Germany; [9]KVI - CART, University of Groningen, The Netherlands; [10]ATOMKI Debrecen, Hungary; [11]Laboratory for Instrumentation and Experimental Particle Physics, Lisbon, Portugal; [12]RBI Zagreb, Croatia; [13]Johann Wolfgang Goethe-Universität Frankfurt, Germany; [14]Chalmers University of Technology, Gothenburg, Sweden; [15]Eoetvoes Lorand University, Budapest, Hungary; [16]Universität zu Köln, Germany; [17]Extreme Matter Institute, Darmstadt, Germany

Introduction

NeuLAND (New Large Area Neutron Detector) [1] is one of the key elements of the R^{3}B experiment, designed to measure fast neutrons with energies of typically 100 to 1000 MeV, and to determine their four-momenta with high precision. Acting primarily as a time-of-flight spectrometer with a time resolution of $\sigma_t \leq 150$ ps and spatial resolutions of $\sigma_{x,y,z} \approx 1.5$ cm, the calorimetric properties of this detector are essential for the reconstruction of multi-neutron events. NeuLAND with its front size of 2.5x2.5 m^2 and a total depth of 3 m is built from organic scintillator bars arranged in a double-plane structure. For details we refer to the GSI annual reports [2, 3]. In this document, we report about the achievements in the last two years. The two major activities are the continous production of further detector components, and the experimental campaign carried out at RIKEN with the NeuLAND demonstrator.

Production Status

Double Planes The final NeuLAND detector will consist of 30 double planes, each with a depth of 10 cm constitutes an independent subunit of 100 scintillators and 200 photomultipliers, see figure 1. The read-out electronics and the high voltage supply are mounted on each double plane frame, the form factor enables the dense packing of double planes, limited only by the depth of the scintillator bars.

The NeuLAND demonstrator, consists of four double-planes, which are still supplied by a commercially available high voltage system and the read-out system TacQuila [4] previously used for LAND. While it was shipped to RIKEN in 2014, the production of new double planes at GSI continued and big steps were made towards the final design. At the time of writing this report, a total of 11 double planes are complete. One to two more double planes will be built during 2017, thus providing a 40% detector.

Readout Electronics The read-out electronics for NeuLAND (NeuLAND-TAMEX) is a GSI in-house development based on the former TacQuila electronics. It delivers a very precise time measurement from an FPGA TDC and a charge measurement using the Time-over-Threshold (ToT) method. After in-beam tests of the first prototypes [5], major improvements in terms of compactness and performance were implemented. The functionality of the former frontend electronics (LANDFEE), the charge measuring board (QTC), and the monitoring and controls board (TRIPLEX) have been combined into one newly designed board (FQT). Together with the improved FPGA TDC board (TAMEX3), a very compact and cost-effective design has been established. This setup was tested in a GSI beam time in 2016 as read-out for the new Time-of-Flight wall for R^{3}B and demonstrated excellent performance with respect to timing and charge resolution, far beyond the needs for NeuLAND. The pre-series of the new read-out electronics (200 channels) was mounted inside the electronic boxes of one double-plane (see figure 1) and successfully taken into operation. The timing properties of the double-plane, determined using cosmic rays, exhibit results of typically $\sigma_t^{mean} \approx 120$ ps similar to earlier extracted val-

*This work is supported by the BMBF projects 05P15RDFN1, 05P2015PKFNA,05P15RFFN1, University of Groningen, the Croatian Science Foundation project SR-ETNo, HIC for FAIR and GSI (KZILGE1416)

† k.boretzky@gsi.de

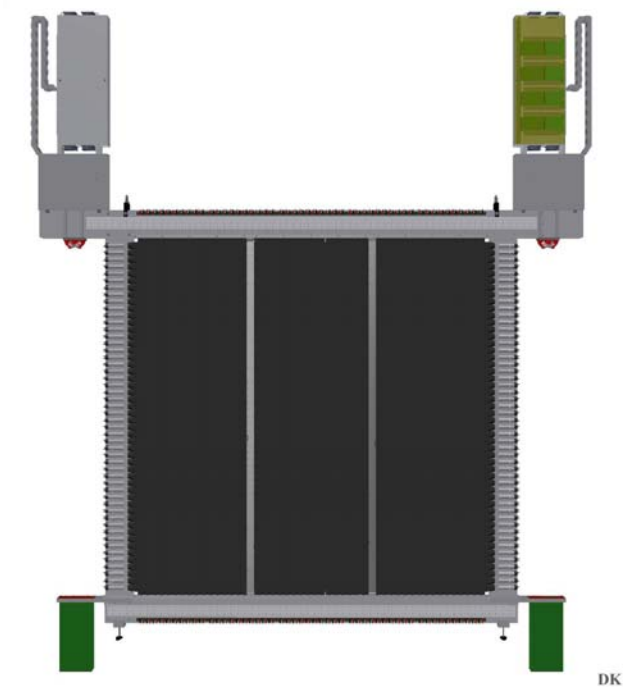

Figure 1: Schematic drawing of one double plane in a front view. Visible are the 50 horizontal bars read out on both sides by photomultipliers. The high-voltage modules (DB50) are mounted in the lower right and left corner, while the boxes on the top corners are hosting the cables and the read-out electronics. The 50 vertical bars are mounted on the backside of the horizontal bars.

ues using the former TacQuila electronics. The series production of the NeuLAND-TAMEX electronics is underway (3000 channels) and the installation and commissioning is scheduled for the end of 2017.

High Voltage Distribution System NeuLAND will be supplied with high voltage from two high voltage distribution systems (HVDS) called HV3200, each connected to up to 3200 photomultipliers (PMT). These systems are produced and delivered by PNPI, Russia, and their design has been optimized for usage with NeuLAND. The principle of operation of the HV3200 is based on individual down-regulation of a primary power supply output for each PMT. Each voltage regulator is located on an individual daughter-board. The 50-channel distribution board DB50 carries 50 regulators. Thus, four DB50 modules serve exactly one NeuLAND double plane. The communication with each individual channel, in order to adjust the high voltage and to monitor voltage and current, is provided via control monitor boards. Up to 16 DB50 boards can be daisy-chained. The pre-series (200 channels) and the first series delivery (1000 channels) have been taken into operation successfully. Together with the second series delivery (2000 ch) in autumn 2017, all existing NeuLAND double planes can be supplied, starting from 2018.

Support Structure The design of the support structure for the full-size NeuLAND was finalized, see figure 2. It consists of two identical supports, of which each can host up to 20 double planes. The two supports can be placed adjacent to each other, avoiding any gap between the double planes of the first and second support frame. Each of the supports consists of a frame to hold the double planes, and a platform on top which allows to access the electronics and PMTs from the top for maintenance. One of the support frames has been built, the existing double planes will be put into the frame after the delivery and installation of the maintenance platform.

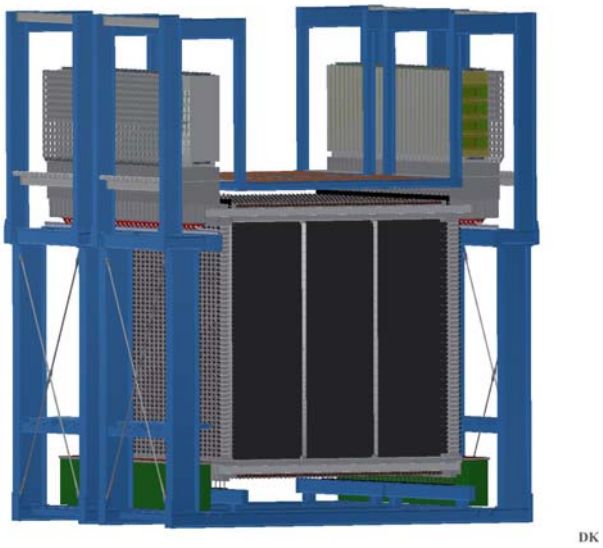

Figure 2: NeuLAND with 30 double-planes placed in the support structure, which is composed of two adjacent identical support frames and platforms.

NeuLAND Demonstrator at RIKEN

In the beginning of 2015, the NeuLAND demonstrator (4 double planes) arrived at RIKEN and was installed in the SAMURAI experimental hall [6], see figure 3. In the standard configuration, it is located in front of the NEBULA neutron detector from RIKEN [7, 8] at 0° with respect to the beam line downstream from the SAMURAI magnet, see figure 4. The NeuLAND demonstrator increases the neutron efficiency and improves the resolution in several experiments in a two year campaign.

Prior to the first experiment with NeuLAND@RIKEN, a one-day measurement was performed to study the neutron efficiency of NeuLAND at typical RIKEN beam energies, i.e. 100 and 250 MeV, using quasi mono-energetic neutrons from a ^{7}Li(p,n)^{7}Be reaction [9].

This calibration run was directly followed by an experiment aiming at identifying resonance states of the extremely neutron-rich oxygen isotopes ^{27}O and ^{28}O [10].

In spring 2016, experiments studying the nuclear EOS in central collisions of Sn isotopes were performed. Neu-

DOI:10.15120/GR-2017-1

Figure 3: Transportation of the NeuLAND demonstrator to the underground SAMURAI experimental hall at RIKEN.

Figure 4: The downstream area of the SAMURAI setup. The NeuLAND demonstrator, equipped with a VETO detector from RIKEN, is located in front of NEBULA. Neutrons impinging on NeuLAND come from the left.

LAND was placed at an angle of 30° with respect to the beam line in order to measure light charged particles, such as hydrogen and helium ions in addition to neutrons and γ-rays. In order to distinguish between neutral and charged particles, a RIKEN VETO detector in front of NeuLAND was used. Figure 5 presents the particle identification with NeuLAND, based on time of flight (ToF) and deposited energy (E_{dep}) in the first NeuLAND plane. In the upper part the spectrum is displayed without any condition on the VETO counter, in the lower part with rejection of events with a valid VETO hit. A clear signature of the various

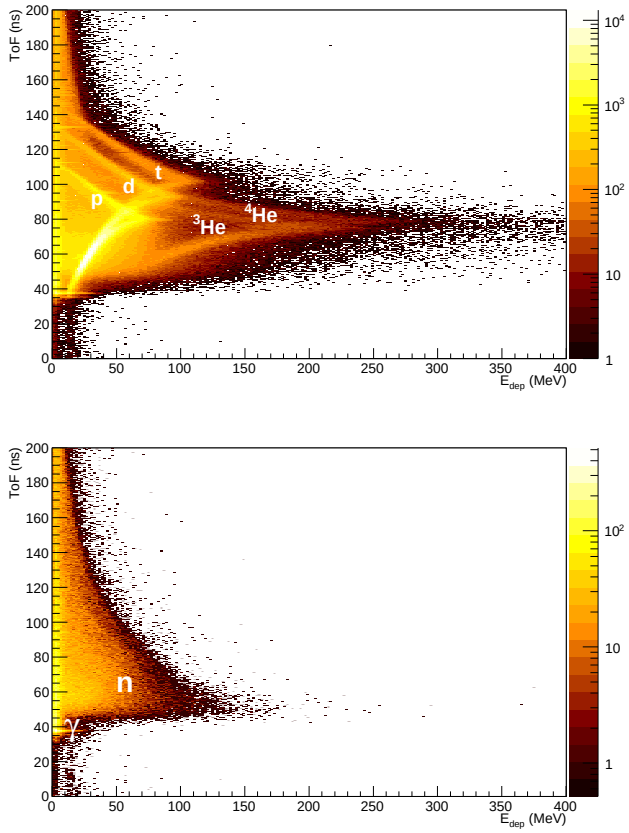

Figure 5: Particle identification in the first NeuLAND plane without (upper panel) and with VETO condition (lower panel).

charged isotopes is observed in the first case, and a clean suppression of these charged particles in case of the strict VETO condition [11]. Note, that the need for a VETO detector for NeuLAND at GSI/FAIR was studied recently with simulations [18].

For the autumn 2016 measurement campaign at SAMURAI, the NeuLAND demonstrator was moved back to its position at 0° to the beam line. Three experiments were carried out using light ions, comprising a study of the unbound states and ground-state properties of ^{31}Ne [12], an investigation of the level structure of ^{22}C combined with the search for ^{21}B [13], and an experiment exploiting a new technique to determine the neutron-decay lifetime of the ^{26}O ground state [14].

Five more experiments with NeuLAND participation are scheduled for the first half of 2017 at RIKEN. After these experiments the NeuLAND demonstrator will be moved back to GSI.

Preparation for Phase-0 Experiments at GSI

For the first phase-0 experiments of the R^{3}B setup in Cave C at GSI, about 40% of NeuLAND will be completed. The necessary calibration tools have been prepared [15],

DOI:10.15120/GR-2017-1

using the data taken in 2014 with the former electronics, and will be customized after the commissioning of the NeuLAND-TAMEX electronics. Detailed simulation studies using R3BRoot [16] are underway, investigating the NeuLAND response as a function of detector volume [17]. The 40% detector cannot provide the full design parameters with respect to efficiency, resolution and multi-neutron recognition capabilities. Multi-neutron detection is especially hampered due to the limits in calorimetric properties. The tools for neutron reconstruction need to be optimized for this scenario, depending on the demand of the physics cases to be investigated in the phase-0 campaign. In addition, the setup in Cave C does not allow a distance larger than 14 m between NeuLAND and the target, thus excluding high resolution performance, as laid out in the technical design report [1] for a distance of 35 m to the target. However, due to the excellent timing properties, the large granularity and the fully active converter material, the 40% detector will provide a major advance in the detection of fast neutrons.

References

[1] NeuLAND@R3B: A Fully-Active Detector for Time-of-Flight and Calorimetry of Fast Neutrons, NeuLAND Technical Design Report, http://www.fair-center.de/fileadmin/fair/experiments/NUSTAR/Pdf/TDRs/NeuLAND-TDR-Web.pdf

[2] K. Boretzky et al., NeuLAND - from Prototypes to Double-Planes, GSI Report 2014-1, 346-350 p. (2014) [10.15120/GR-2014-1-FG-S-FRS-11]

[3] K. Boretzky et al., NeuLAND - from double-planes to the demonstrator, GSI Report 2015-1, 200-202 p. (2015) [10.15120/GR-2015-1-MU-NUSTAR-NR-12]

[4] K. Koch et al., A New TAC-Based Multichannel Front-End Electronics for TOF Experiments With Very High Time Resolution, IEEE Trans. Nucl. Sci.52, 745 (2005)

[5] C. Ugur et al., A compact readout system for the R3B High-Resolution Neutron Time-of-Flight Spectrometer (NeuLAND), GSI Report 2015-1, 204-205 p. (2015) [10.15120/GR-2015-1-MU-NUSTAR-NR-14]

[6] T. Kobayashi et al., SAMURAI spectrometer for RI beam experiments, NIMB 317, 294 (2013)

[7] T. Nakamura and Y. Kondo, Large acceptance spectrometers for invariant mass spectroscopy of exotic nuclei and future developments, NIM B 376 (2016) 156–161

[8] Y. Kondo et al., Calibration methods of the neutron detector array NEBULA, RIKEN Accel. Prog. Rep. 45, 131 (2012)

[9] J. Kahlbow et al., Efficiency study of the NeuLAND demonstrator, contribution to this annual report

[10] Y. Kondo et al.,Spectroscopy of unbound oxygen isotopes II, RIKEN Accel. Prog. Rep. 49 (2016) 42, http://www.nishina.riken.jp/researcher/APR/APR049/pdf/42.pdf

[11] I. Gašparić et al., NeuLAND demonstrator performance in EOS experiments, submitted to RIKEN Accel. Prog. Rep. 50 (2017)

[12] T. Tomai et al., Search for unbound excited states of deformed halo nucleus ^{31}Ne using breakup reactions, submitted to RIKEN Accel. Prog. Rep. 50 (2017)

[13] SAMURAI36 and NeuLAND Collaborations, Exploring the N=16 sub-shell closure: level structure of ^{22}C and search for ^{21}B, submitted to RIKEN Accel. Prog. Rep. 50 (2017)

[14] C. Caesar et al., submitted to RIKEN Accel. Prog. Rep. 50 (2017)

[15] V. Wagner et al., Automated NeuLAND calibration in R3BRoot, contribution to this annual report

[16] D. Kresan et al., Status of the R3BRoot framework, contribution to this annual report

[17] J. Mayer et al., Neutron reconstruction with NeuLAND in FAIR Phase 0, contribution to this annual report

[18] C.A. Douma et al., Simulation studies of a NeuLAND VETO wall, contribution to this annual report

DOI:10.15120/GR-2017-1

Efficiency study of the NeuLAND demonstrator

J. Kahlbow[*1,2], *I. Gašparić*[3,2], *T. Aumann*[1,4], *K. Boretzky*[4,2], *Y. Kondo*[5,2], *T. Nakamura*[5,2], *H. Otsu*[2], *A. Saito*[5,2], *H. Simon*[4], *Y. Togano*[5,2], *H. Törnqvist*[1,2], *T. Uesaka*[2], *and the NeuLAND-SAMURAI Collaboration*[4,2]

[1]Institut für Kernphysik, TU Darmstadt, Germany; [2]RIKEN Nishina Center, Tokyo, Japan; [3]Ruder Bošković Institute, Zagreb, Croatia; [4]GSI, Darmstadt, Germany; [5]Department of Physics, Tokyo Institute of Technology, Japan

The NeuLAND demonstrator has been used for several experiments studying exotic (multi-)neutron unbound nuclear systems at SAMURAI, see K. Boretzky *et al.* [1]. An essential quantity in understanding this new detector and its response is the one-neutron detection efficiency. It has been studied in a one-day machine-study experiment using quasi-monoenergetic neutrons from the ^{7}Li(*p*,*n*)^{7}Be reaction at the beginning of the campaign at RIKEN.

NeuLAND was placed under zero degree $10.87\,\mathrm{m}$ downstream from the target followed by the two NEBULA subdetectors. In front of NeuLAND, a layer of eight $1\,\mathrm{cm}$ thin plastic scintillators was placed to veto charged-particle events. The active depth of the detector itself is $40\,\mathrm{cm}$ of organic scintillator material. The 800 PMT channels were read out with TacQuila electronics.

The charge-exchange reaction ^{7}Li(*p*,*n*)^{7}Be$(\mathrm{g.s.} + 430\,\mathrm{keV})$ produces almost monoenergetic neutrons as either the ^{7}Be ground state or excited state at $430\,\mathrm{keV}$ is directly populated. The zero-momentum transfer center-of-mass cross section for this reaction has been measured by Taddeucci *et al.* [2] and is used for the analysis here.

The proton beam was produced as a secondary beam from ^{48}Ca and delivered to SAMURAI after separation in BigRIPS. The incident proton beam with a rate of about $1\,\mathrm{MHz}$ impinged on the $1.05\,\mathrm{g/cm^2}$ thick natural Li target. Two plastic-scintillator veto-counters with a hole diameter of $3\,\mathrm{cm}$ were installed to determine the beam-spot size. The proton energies at the middle of the target were $109\,\mathrm{MeV}$ and $253\,\mathrm{MeV}$ leading to neutron energies of $106.8\,\mathrm{MeV}$ and $250.5\,\mathrm{MeV}$, respectively. The neutrons were emitted in the forward direction and detected by NeuLAND, whereas the unreacted protons were bent in the SAMURAI dipole magnet.

In order to identify one-neutron events in NeuLAND, the neutron velocity spectrum, shown in Fig. 1, is considered. The spectrum is obtained under the following conditions: The neutron velocity is determined from the time difference of the first valid hit in NeuLAND to the start detector. For NeuLAND the time is calculated from the two PMT times above threshold $\gtrsim 2\,\mathrm{MeVee}$ of one scintillator bar. The background from the empty-frame measurement is subtracted. In order to match the zero-momentum transfer condition in the lab frame, the position distribution is limited to a cone of $\pm 40\,\mathrm{mrad}$ in the x-y-plane.

The sharp peak marked by the fitted curve in the histogram is associated with the response to quasi-monoenergetic neutrons; the continuum is mainly caused by neutrons from other break-up reactions as ^{7}Li(*p*,x*n*). The uncertainty in determination of the prompt neutrons due to the overlap of the continuum and peak region is small in comparison to the 3% uncertainty arising from the uncertainty of the used cross section. For $250\,\mathrm{MeV}$ the acceptance cut was reduced to $\pm 14\,\mathrm{mrad}$ to reduce the continuum background further. By integrating the peak the number of detected neutrons is obtained. To calculate the efficiency, this value is normalized by the number of incident neutrons, corrected for the trigger efficiency. For a threshold energy cut $E > 5\,\mathrm{MeVee}$ the *preliminary* obtained one-neutron detection efficiency accounts for $(27.8 \pm 1.2)\%$ and $(26.6 \pm 1.1)\%$ at the neutron energies of $110\,\mathrm{MeV}$ and $250\,\mathrm{MeV}$, respectively. A first comparison to simulation data is provided by J. Mayer *et al.* [3].

A detailed study of the detector response is needed to provide final results. With the results from this calibration experiment, cross sections from measurements using NeuLAND at SAMURAI can be calculated.

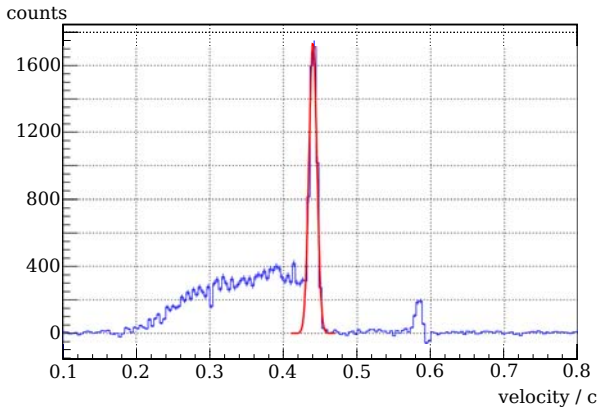

Figure 1: Experimental velocity spectrum of NeuLAND for $\approx 110\,\mathrm{MeV}$ neutrons with veto condition on charged particles, background subtraction, spatial cut, and an energy cut $E > 5\,\mathrm{MeVee}$.

References

[1] K. Boretzky *et al.*, contribution to this annual report and references therein

[2] T. N. Taddeucci *et al.*, Phys. Rev. C 41 (1990) 2548

[3] J. Mayer *et al.*, contribution to this annual report

*jkahlbow@ikp.tu-darmstadt.de

Work supported by the BMBF contract no. 05P15RDFN1.

Neutron reconstruction with NeuLAND in FAIR Phase 0

J. Mayer[*1], *K. Boretzky*[2], *M. Heil*[2], *D. Kresan*[2], *S.G. Pickstone*[1], *A. Zilges*[1], *and the R^3B collaboration*[2]

[1]Institut für Kernphysik, Universität zu Köln; [2]GSI Helmholtzzentrum für Schwerionenforschung GmbH, Darmstadt

The NeuLAND[1] simulation and analysis modules for the R3BRoot software package [2] have been rebuilt and extended. The data work flow can be separated into three main components, namely experimental mapping and calibration from raw data to hits, simulation specific inputs with detector response leading up to hit level, and shared neutron multiplicity and energy reconstruction.

Total detection efficiency

The 1n total detection efficiency for four double planes was studied during experiments with the NeuLAND@SAMURAI setup for neutron energies of 110 MeV and 250 MeV in 2015 [3, 4]. Several GEANT3 settings and GEANT4 physics lists were investigated together with the NeuLAND TacQuila Digitizer. This combination of simulation settings and detector response can be compared to experimental data [4]. Adjusting the hit energy threshold exposes differences in the energy deposition of the different physics lists. After applying equivalent acceptance cuts to both simulation and experiment, the preliminary comparison shows good agreement both for the adopted GEANT3 settings and GEANT4 physics lists which do not use the Bertini cascade.

For different detector depths, the total detection efficiency ϵ_{tot} can be described by a probabilistic approach. If n_{in} neutrons are impinging on n_{DP} double planes and the the hit energy acceptance threshold is low (up to $\approx$ 10 MeV), one finds:

$$\epsilon_{\mathrm{tot}} = 1 - (1 - p(n_{\mathrm{DP}}))^{n_{\mathrm{in}}}$$

where $p(n_{\mathrm{DP}}) = 1 - (1 - p_{\mathrm{DP}}))^{n_{\mathrm{DP}}}$, with the *double plane efficiency factor* p_{DP} as single free variable. For 600 MeV neutrons and 2 MeV threshold p_{DP} is ≈ 0.11.

Reconstruction

For FAIR Phase 0 experiments, at least 12 of the 30 proposed double planes will be available. A similar binomial approach can be made for the probability of different multi-neutron interaction channels. In the case of four incoming neutrons impinging on 30 double planes, all four will react in about 90% of all cases. For 12 double planes, this 4n-4n channel drops down to about 33% and competes with the 4n-3n and 4n-2n channels.

* jan.mayer@ikp.uni-koeln.de

Supported by the BMBF (05P2015PKFNA) and the GSI (KZILGE1416). J.M. is supported by the Bonn-Cologne Graduate School of Physics and Astronomy.

Reconstruction of the neutron multiplicity and the four-momentum for each neutron can be carried out using the combination of deposited energy and energy spread in the detector [1]. For limited detector depth, the capability of this calorimetric method is significantly reduced. Simulations show that while this method is still applicable to a reasonable degree for low multiplicities, the 4n reconstruction capability is not sufficient. Monte Carlo data shows that a reasonable four neutron reconstruction efficiency could be obtained, if the first hits in the active material could be distinguished with higher precision, displayed in Fig. 1 for a breakup scenario of ^{8}He to ^{4}He + 4n with a relative energy of E_{rel} = 100 keV.

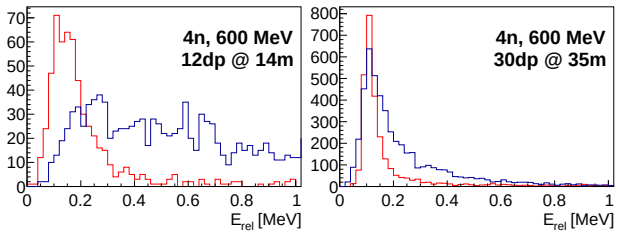

Figure 1: Simulated reconstructed relative energy spectra for 12 double planes at 14 m and 30 double planes at 35 m distance, gated on four neutrons (blue) obtained with the basic calorimetric method compared to the equivalent spectra using Monte Carlo data for reconstruction (red).

Reconstruction methods for 12 double planes at short distances are currently under revision for Phase 0 experiments.

References

[1] NeuLAND@R3B: A Fully-Active Detector for Time-of-Flight and Calorimetry of Fast Neutrons, NeuLAND Technical Design Report (2011)

[2] D. Kresan *et al.*, "R3BRoot: a FAIRRoot-based development for the analysis and simulation of the R3B experiment", GSI Report 2013-1 205 (2013)

[3] K. Boretzky *et al.*, "NeuLAND - from the demonstrator to the start version", contribution to this annual report.

[4] J. Kahlbow *et al.*, "Efficiency study of the NeuLAND demonstrator", contribution to this annual report.

DOI:10.15120/GR-2017-1

Simulation studies of a NeuLAND VETO wall

C. A. Douma[1], K. Boretzky[*2], I. Gasparic[3], N. Kalantar-Nayestanaki[1], D. Kresan[2], J. Mayer[4], C. Rigollet[1], and the R^{3}B collaboration[2]*

[1]KVI-CART, University of Groningen, The Netherlands; [2]GSI Helmholtzzentrum für Schwerionenforschung, Germany; [3]Ruđer Bošković Institute, Zagreb, Croatia; [4]Institut für Kernphysik, Universität zu Köln, Germany

Simulation Procedure

Simulations were carried out to investigate a possible layout and need of a VETO detector in front of NeuLAND (New Large Area Neutron Detector) [1] in order to reduce the background from charged particles.

All simulations were performed with R^{3}BRoot [2] according to the multi-neutron simulation procedure [1, 3]. The Geant4 Monte Carlo engine was chosen to include nucleus-nucleus collisions (like the target reaction) [3]. The physics list was benchmarked against the S438 experiment [4] to provide a production ratio of charged and uncharged particles close to reality.

The full R^{3}B setup in cave C was simulated, including a simplified model of the scattering chamber behind the GLAD magnet. This model included all tracking detector materials and the 4 mm thick stainless steel neutron exit flange. The simulation geometry is displayed in figure 1. The source code is available upon request.

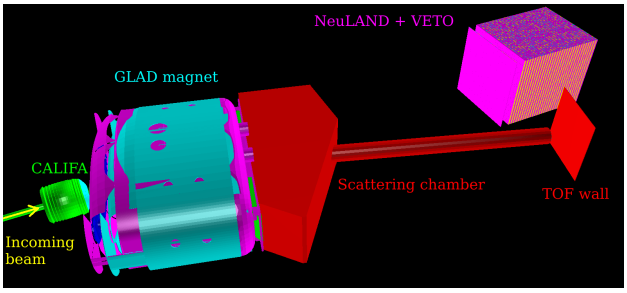

Figure 1: Simulated Geometry in R^{3}BRoot.

Several physics cases were investigated: a 1 GeV/u ^{208}Pb on a 500 mg/cm^2 lead target and a 600 MeV/u ^{48}Ca-beam on a 1.0 g/cm^2 carbon target and on a 2.2 g/cm^2 lead target. Results were evaluated by counting the number of successful events: events where the neutron multiplicity was correctly determined and all neutron interactions were correctly reconstructed and identified properly.

Design of the VETO wall

The VETO wall in the simulation was designed as a 250 cm $\times$ 250 cm wall of 16 distinct non-overlapping scintillators constructed from the same materials as NeuLAND [1] with 1.1 cm active scintillation crystal thickness, a time resolution below 300 ps and an energy deposition threshold below 1 MeV. This wall should be placed 30 cm in front of NeuLAND. Charged particles can then be eliminated by removing one neutron interaction point for each VETO signal. Our simulations show that this is the optimal design for the geometry and the position of the VETO detector.

Time Cuts

The background in NeuLAND originates from secondary scattering of projectiles (fragments) in the downstream detectors of the R3B setup. The neutron background was more than 50% higher than the charged background. To eliminate this neutron background, time cuts were applied on the raw data. This reduced the neutron background with a factor of 3.7 and the charged particle background with a factor of 5.7 while only 4% of the neutrons stemming from reactions in the target were lost. As a result, the number of successful events increased by 5%-25% (depending on neutron multiplicity). However, these time cuts influence the calorimetric properties of NeuLAND. This problem was solved by adjusting the neutron separation matrix accordingly [1].

VETO results

Our simulations show that about 1% of the target neutrons were eliminated by the VETO, while 46%-73% (depending on neutron multiplicity) of the contaminated events were turned into successful events. Due to the low number of charged background particles, this resulted in a small decrease in the total number of successful events in the configuration where the scattering chamber and the fragment arm are under vacuum making the VETO detector not very useful

However, with air in the scattering chamber, our ^{208}Pb physics case showed a significant increase in signal-to-noise ratio when using the VETO.

References

[1] The R^{3}B collaboration 2011 *Technical Design Report of NeuLAND* `http://www.fair-center.eu/fileadmin/fair/publications_exp/NeuLAND-TDR-Web.pdf`

[2] D. Bertini 2011 *J. Phys.: Conf. Series* **331** 032036 (2013) 56

[3] D. Kresan *R^{3}BRoot* `http://r3broot.gsi.de/`

[4] K. Boretzky *et al.* 2015 *NeuLAND - from double-planes to the demonstrator* GSI Report vol. 2015-1 MU-NUSTAR-NR-12

* k.boretzky@gsi.de

DOI:10.15120/GR-2017-1

Automated NeuLAND calibration in R3BRoot*

V. Wagner† [1,2], *D. Kresan*[2], *J. Enders*[1], *I. Gašparić*[3], *M. Heil*[2], *H.T. Johansson*[4], *and the R*^{3}*B Collaboration*[1]

[1]Institut für Kernphysik, TU Darmstadt, Germany; [2]GSI, Darmstadt, Germany; [3]RBI, Zagreb, Croatia; [4]Chalmers University of Technology, Göteborg, Sweden

Within the R3BRoot framework [1], an automated calibration chain for NeuLAND [2] has been developed and tested. The calibration is divided into three consecutive steps, from unpacked data to the fully calibrated hit level data, which is described below in detail.

Pedestal offset

The readout electronics used in NeuLAND have arbitrary zero energy channels, the so-called pedestals. These are determined by using a pedestal run, where all modules fire and record their readout value at zero energy deposit. In all following events these pedestal values are subtracted from the measured ones to get the proper values.

Time calibration

NeuLAND readout electronics has different time channel widths for each bin. To determine the width of each channel, any uncorrelated data, e.g. from cosmics, can be used. For uncorrelated data the events are uniformly distributed in time, thus the width of each channel is proportional to its number of counts and the calibration is derived from that.

The NeuLAND electronics has a walk effect, i.e. the time measurement of each hit is influenced by its amplitude. The dependency was determined by using an UV laser with variable amplitude and therefore the measured time can be corrected. Note that the signal from each PMT is time calibrated after this step but not synchronized yet. An automated synchronization is performed in the next step.

Position calibration, time synchronization and energy calibration

For the position calibration, time synchronization and energy calibration cosmic muons are used. The former two are based on the cosmic1 algorithm from the land02 software package [3]. The muons create long tracks inside NeuLAND and because of its design with alternating plane orientations, these tracks can be reconstructed in case enough planes were hit. After the reconstruction the coordinates of the hits alongside the bars are known. The time difference of the two signals in one bar linearly depends on the position of the hit, with the effective speed of light in the bar as its slope. For hits in the center of a bar the time difference between the signals of the two PMTs originates from different cable lengths. This effect is accounted for and removed in the synchronisation. With the offset and the effective speed of light, the position of each hit can be determined from the time difference. In the second step of synchronisation, the time relations of signals in different bars are adjusted. The time difference between the hits in the bars caused by the finite speed of the muons is calculated and subtracted and the remaining time difference is added to an overdetermined linear equation system which is solved at the end. For the gain calibration using muons, the deposited energy from a muon is divided by its path-length inside the bar. Since cosmic muons are minimum ionizing particles, the mean value corresponds to the well known energy deposition per length for the material. Thus the gain for each module can be determined.

The dataflow of the calibrations is shown in fig. 1.

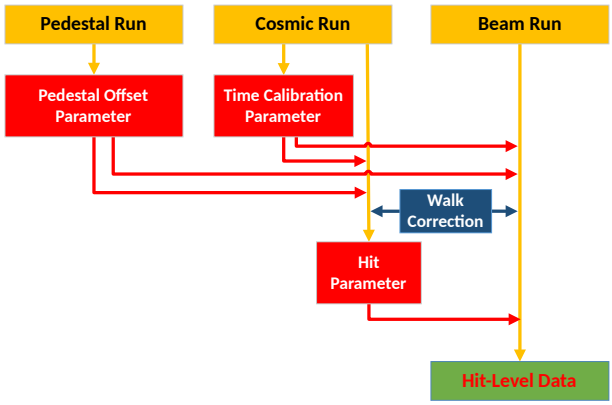

Figure 1: Dataflow of NeuLAND calibration.

Calibration Quality

The quality of the time calibration routine has been checked by determining the time resolution for high-energy gamma-rays stemming from reactions of ^{48}Ca reactions on a polyethylen target at 650 AMeV. The time resolution $\sigma = (144.6 \pm 5.6)$ ps without energy cut was below the goal of $\sigma = 150$ ps, specified in the TDR.

References

[1] R3BRoot : https://r3broot.gsi.de/

[2] K. Boretzky et al, "NeuLAND from the demonstrator to the start version", contribution to this annual report

[3] H. T. Johansson, The DAQ always runs, Chalmers, 2006

* Work supported by BMBF (05P15RDFN1)

† vwagner@ikp.tu-darmstadt.de

DOI:10.15120/GR-2017-1

Performance of PSP detectors for the R^{3}B setup *

I. Syndikus[1], S. Storck[1], D. Rossi[1], L. Atar[1], T. Aumann[1], R. Gernhäuser[2], M. Heil[3], B. Heiss[2], A. Ignatov[1], A. Inglessi[4], H. Johansson[5], J. Kahlbow[1], A. Kelic-Heil[3], O. Kiselev[3], P. Klenze[2], A. Krivshich[4], D. Körper[3], Y. Litvinov[3], B. Löher[3], C. Nociforo[3], S. Paschalis[6], M. Petri[6], R. Plag[3], H. Scheit[1], S. Scholl[1], H. Simon[3], J. Tscheuschner[1], H. Törnqvist[1], F. Wamers[3], and the R^{3}B collaboration[1]

[1]Institut für Kernphysik, TU Darmstadt, Germany; [2]TU München, Garching, Germany; [3]GSI, Darmstadt, Germany; [4]Petersburg Nuclear Physics Institute Gatchina, Russia; [5]Chalmers University of Technology, Göteborg, Sweden; [6]University of York, United Kingdom

A kinematically complete measurement of nuclear reactions is possible with the R^{3}B setup. To do so, several detectors are positioned in the beam tracking the incoming and outgoing isotopes. Position Sensitive Pin diodes (PSP) are used to determine the position of the passing particles and to measure their energy loss in the detector, respectively their charge.

Continuing the work of the previous years [1,2], we tested PSP detectors using the charge-division method to determine the interaction position of passing ions. This method has the advantage of a small number of electronic channels compared to micro-strip detectors providing a similar position resolution. After promising tests with detectors segmented into strips, reducing the noise and increasing the rate capability, we now tested new prototypes.

During a beam time in June 2016, several detectors were tested using a ^{124}Xe beam at $E = 600\,\mathrm{AMeV}$. We tested two different prototypes of X5 detectors from Micron Semiconductor Ltd. This model has strips on both sides perpendicular to each other, providing position information with a design goal of $100\,\mu\mathrm{m}$ in both directions and an active area of $10 \times 10\,\mathrm{cm}^2$. In addition, we used X1 detectors (same manufacturer, with strips only on one side and a smaller active area of $5 \times 5\,\mathrm{cm}^2$), to determine the influence of radiation damage from previous tests on the detector performance. All PSP detectors were read out with MPR-32 preamplifiers from Mesytec and their signals were digitized using the FEBEX3 [3] read-out system.

The focus of the ongoing analysis lies on the traditional prototype with read-out along the strips, while the analysis of the prototype with strips read out along the long edge is pending. During the beam time, the X5 detectors showed an unreasonably high leakage current. Still, the position and energy resolution of the detector were determined. Results are shown in Table 1 together with the results for the X1 detectors.

For the position resolution of the X5 detector, a cut on the interstrip events on the opposite side of the detector was applied. While the back side showed nice peaks and a promising resolution of $130 - 170\,\mu\mathrm{m}$, the front side showed a double-peak structure for every interstrip area. This structure lead to an unacceptably large position resolution of $350 - 800\,\mu\mathrm{m}$. The investigation of this phenomenon is still ongoing. Figure 1 shows the reconstructed positions for the interstrip events.

Table 1: Detector performance for Micron X1 detectors and X5 prototype.

Detector	X1	X1	X5 back	X5 front
$\Delta x/\mu\mathrm{m}$	90	120	150	> 350
$\frac{\Delta E}{E}/\%$	2.1	3.6	1.3	

For the energy resolution, only an upper limit can be given. Due to the presence of inhomogeneous material in the beam path for tests of other detectors, the PSP detectors require a position-dependent correction of the energy-loss, which cannot be performed yet at this time.

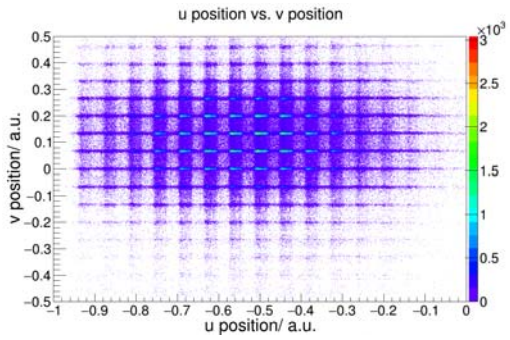

Figure 1: Position information from one Micron X5 prototype. The reconstructed lines in one direction correspond to the interstrip region of the opposite side of the detector.

References

[1] S. Paschalis and the R^{3}B collaboration, "Heavy-ion tracking detectors for the R^{3}B setup", GSI Scientific Report 2013 (2014) p.147, DOI:10.15120/GR-2014-1-NUSTAR-KR-10

[2] S. Paschalis and the R^{3}B collaboration, "The in-beam tracking detectors of R^{3}B", GSI Scientific Report 2014 (2015) p.206, DOI:10.15120/GR-2015-1-MU-NUSTAR-NR-15

[3] FEBEX3 homepage: https://www.gsi.de/work/forschung/electronics/digitalelektronik/digitalelektronik/module/lwl/febex/febex3a.htm

* Work supported by BMBF contract 05P15RDFN1, HGS HIRe and GSI-TU Darmstadt cooperation agreement.

Developing a fiber-detector for in-beam tracking at the R^{3}B-setup *

S. Scholl[1], J. Tscheuschner[1], D. Rossi[1], L. Atar[1], T. Aumann[1], R. Gernhäuser[2], M. Heil[3], B. Heiss[2], A. Ignatov[1], A. Inglessi[4], H. Johansson[5], J. Kahlbow[1], A. Kelic-Heil[3], O. Kiselev[3], P. Klenze[2], A. Krivshich[4], D. Körper[3], Y. Litvinov[3], B. Löher[3], C. Nociforo[3], S. Paschalis[6], M. Petri[6], R. Plag[3], H. Scheit[1], H. Simon[3], S. Storck[1], I. Syndikus[1], H. Törnqvist[1], F. Wamers[3], and the R^{3}B collaboration[1]

[1]Institut für Kernphysik, Technische Universität Darmstadt, Darmstadt, Germany; [2]Technische Universität München, Garching, Germany; [3]GSI, Darmstadt, Germany; [4]Petersburg Nuclear Physics Institute Gatchina, Gatchina, Russia; [5]Chalmers University of Technology, Göteborg, Sweden; [6]University of York, United Kingdom

The R^{3}B (**R**eactions with **R**elativistic **R**adioactive **B**eams) setup at FAIR is intended for kinematically complete measurements of reactions with relativistic heavy-ion beams up to 1 AGeV. In order to track the ions before and after the target, five plastic fiber detectors with active areas between 10×10 cm^2 and 120×80 cm^2 are foreseen. These detectors will provide position measurements perpendicular to the trajectory of charged particles to determine, *e.g.*, the magnetic rigidity $B\rho$ of the ions, and hence their mass-to-charge ratio. The light from the scintillating fiber is sensed using, for instance, SiPMs (silicon photomultipliers) and Multi-anode Photomultiplier Tubes. One advantage of such plastic fibers is the capability of handling beam rates up to several MHz.

Two prototype detectors were built to test the performance of the fibers and of the associated read-out system. These detectors were tested during a beam time in June 2016 at GSI. The first detector, made of 2×64 square fibers, had an active area of 1.28×1.28 cm^2 and consisted of two planes of fibers for measurements in the x and y directions. The fibers were individually coupled to 3×3 mm^2 Hamamatsu multi-pixel photon counters (MPPCs) [1] and read out with the FEBEX [2] system. The MPPCs are photon-counting devices using multiple avalanche photodiode pixels and have a very good acceptance for light emerging from the fiber. In normal operation, the MPPCs are operated in Geiger mode. The other detector was made of 2×8 fibers oriented vertically to measure the x-position. These fibers were coupled on one end to 3×3 mm^2 Hamamatsu MPPCs and to SiPMs from SensL [3] on the other, providing correlated data to compare the performance of both MPPC types directly. The read-out used PADI [4] combined with a VFTX2 TDC [5] with a time resolution of about 10 ps.

One of the results from this test is the capability to detect 600 AMeV ^{12}C ions using 200 μm plastic scintillating fibers. In figure 1 is shown the response of the different MPPCs. One can recognize the single pixels and a strong linear correlation between the detected photons on both sides. Here, no selection criteria were used. The time resolution between both ends is approximately 0.5 ns.

Although the fibers are rather thin, this test shows that if the dark rate is sufficiently low, it might be possible to track ions with even lower charge than carbon. The choice of read-out electronics is currently under investigation, with the goal of simplifying the electronics chain and reducing the cost per channel when compared to the present situation. Two different read-out systems will be tested in the near future, namely the GEMEX [6] (charge integration) read-out system and a PADI+TDC system, using a time-over-threshold approach.

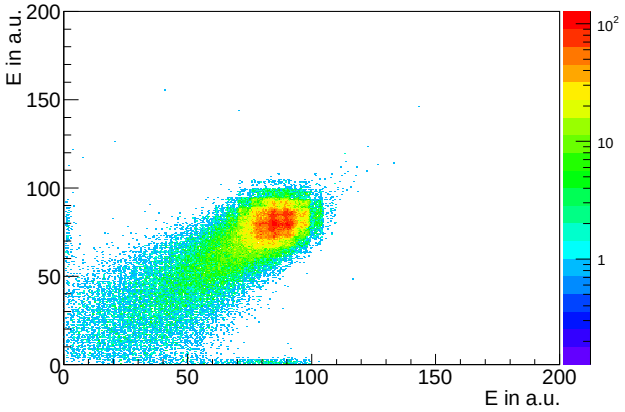

Figure 1: Energy signals from both sides of one fiber of the prototype detector using VFTX2 TDC + PADI with SensL SiPMs.

References

[1] http://www.hamamatsu.com/jp/en/4113.html

[2] https://www.gsi.de/en/work/research/experiment_electronics/digital_electronic/digital_electronics/modules/font_end_module/febex.htm

[3] http://sensl.com/products/c-series/

[4] M. Ciobanu et al., IEEE Transactions on Nuclear Science (2014), p.1015-1023, DOI:10.1109/TNS.2014.2305999

[5] https://www.gsi.de/fileadmin/EE/Module/Dokumente/vftx1_8.pdf

[6] B. Voss et al., 2012 IEEE NSS/MIC (2012), p.678-679, DOI:10.1109/NSSMIC.2012.6551191

* Work supported by BMBF (05P15RDFN1).

DOI:10.15120/GR-2017-1

Preliminary results of the PAS prototype test with a ^{12}C beam*

A. Krivshich[1], G. Alkhazov[1], V. Andreev[1], L. Atar[2], T. Aumann[2], R. Gernhäuser[3], M. Heil[4], B. Heiss[3], A. Ignatov[2], D. Ilin[1], A. Inglessi[1], H. T. Johansson[5], J. Kahlbow[2], A. Kelic-Heil[4], O. A. Kiselev[4], P. Klenze[3], D. Körper[4], Y. Litvinov[4], B. Löher[2], D. Maisuzenko[1], A. Nadtochiy[1], C. Nociforo[4], S. Paschalis[6], M. Petri[6],R. Plag[4], D. M. Rossi[2], H. Scheit[2], S. Scholl[2], N. Shvetsova[1], H. Simon[4], S. Storck[2], I. J. Syndikus[2], J. M. Tscheuschner[2], H. T. Törnqvist[2], F. Wamers[4], V. Yatsyura[1], and the R^{3}B collaboration

[1]Petersburg Nuclear Physics Institute Gatchina, Orlova Roscha, Leningrad district 188300, Gatchina, Russia; [2]Institut für Kernphysik, Technische Universität Darmstadt, 64289 Darmstadt, Germany; [3]Technische Universität München, James-Franck-Str 1, 85748, Garching, Germany; [4]GSI Helmholtzzentrum für Schwerionenforschung, Planckstraße 1, 64291, Darmstadt, Germany; [5]Chalmers University of Technology, Kemivagen 9, 412 96, Göteborg, Sweden; [6]University of York, United Kingdom

To test the operability of the PAS detector [1], we have fabricated a prototype of the detector module, structurally corresponding to the STW-X2 station. The performance of this prototype was studied at PNPI (using β-sources ^{90}Sr and photon source ^{55}Fe) and at a high-energy (600 MeV/u) beam of carbon ions at GSI. PAS is designed to measure precisely trajectory coordinates of protons emitted in nuclear reactions. The coordinate resolution of PAS is expected to be about 200 μm. The final version of PAS will be located in the vacuum chamber of the dipole magnet GLAD.

The PAS prototype consists of 96 thin-wall aluminum drift tubes (straws), which are arranged in three layers. Each layer is shifted by one tube radius with respect to the previous layer. All the tubes are of 110 cm length, diameter 10 mm and the wall thickness being 0.2 mm. The straw anode is a gold-plated tungsten wire with the diameter of 35 μm. The gas mixture is Ar+30%C_2H_6. The scheme of the experimental setup is presented in Fig. 1a. The general view of the detector and its location on a carbon beam at GSI is shown in Fig. 1b.

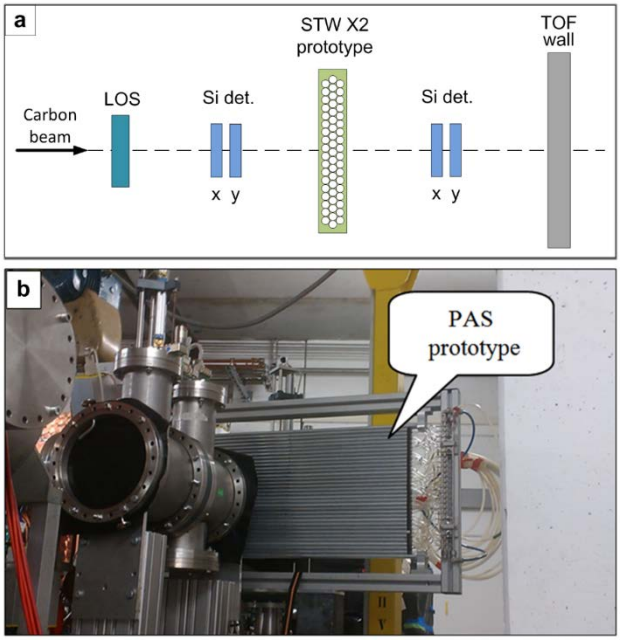

Figure 1: Scheme of the experimental setup (a); general view of the detector on a carbon beam (b).

During the beam test, data sampling and readout was performed using the VFTX-2 VME TDC module with the 10 ps time resolution. All events included a timestamp code which was distributed throughout all active detectors (LOS, TOF, PSP) providing synchronization of the time with other systems of the setup. A preliminary analysis was performed via standalone ROOT scripts, while an activity to integrate the Prototype in the R3BRoot framework is on the way.

The observed structure of the beam profile (Fig. 2a) and the dependence of the counting rate (Fig. 2b) on the high voltage do not match the same characteristics which are generated by monoenergetic particles (emitted protons). The map of the straw arrangement and the beam position are presented in Fig. 2c.

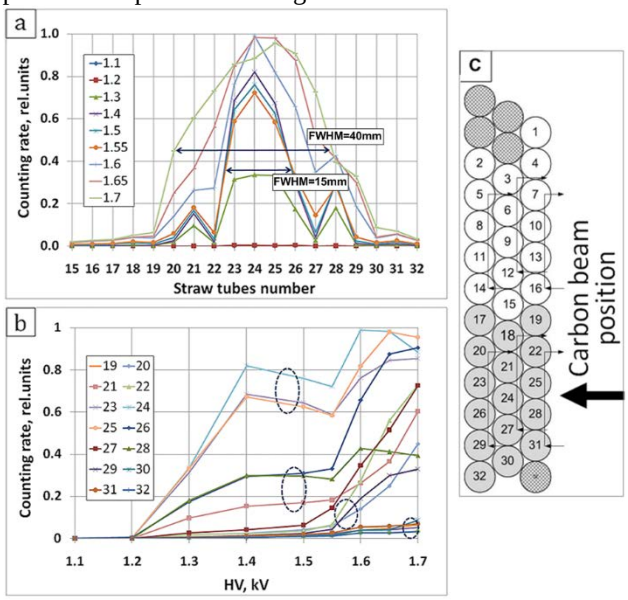

Figure 2: Counting rates of different straws for different high voltages (a); the counting rates via high voltage for different straws (b); straw map in the STW-X2 prototype and the beam position (c).

These results indicate that the carbon beam had a pronounced halo which contained a lot of accompanying particles (including delta-electrons) with different ioniz-

* Work supported in part by BMBF contracts 05P15RDFN1 and 05P15WOFNA, HGS HIRe and GSI-TU Darmstadt cooperation agreement.

ing power, which resulted in different counting rates from different straws. Such groups of particles are highlighted by dotted circles in Fig. 2b. This halo distorted the obtained time spectra due to a significant time dispersion of the detected signals with respect to the LOS trigger signal.

It was shown that for correct selection of particle tracks, special algorithms are required. Two of them were applied for the off-line data analysis (Fig.3), which allowed us to select events using information from either two or three layers of the detector straws.

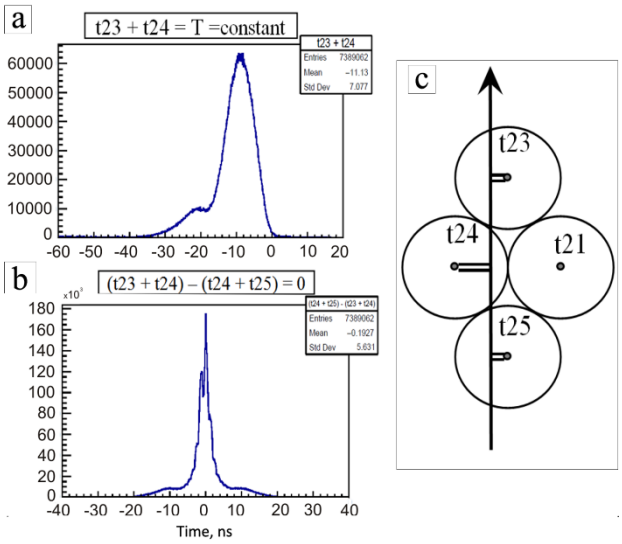

Figure 3: Time spectra and special algorithms for particle selection. Straw map and drift time information (c).

Both algorithms are based on the fact that the sum of the drift times of electrons from the single particle track to the anodes of two adjacent straws which are placed in two neighboring layers is a constant equal to the maximum electron drift time from the cathode to the anode (about 100 ns). The first algorithm (t23+t24=constant), which was initially used, was not sufficient to perform effective selection of events (Fig. 3a). To improve the particle selection, the third straw layer should be involved in the analysis. As one can see, the second algorithm ((t23 + t24) – (t24 + t25) = 0) makes it possible to detect most of particles within the time jitter of about ±8 ns, which corresponds to fluctuations in the measurement of the absolute coordinate of the particle track in the ±400 μm range (Fig. 3b). This data analysis has shown that the three layer design of each STWs was a proper choice.

A further development of the algorithms should include two following stages: (a) selection of useful events from PAS by using the scintillator wall TOFD; (b) synchronization of our data with the data from position-sensitive Si detector PSP. This will allow us to select the required events and to carry out measurements of the spatial resolution and the X-T relation of the PAS detector.

References

[1] Technical Report for the Design, Construction and Commissioning of the Tracking Detectors for R3B, pages 101-117, November 20.

DOI:10.15120/GR-2017-1

In-beam test of a CALIFA Demonstrator segment of R3B *

P. Cabanelas[†1,2], *P. Teubig*[3], *P. Remmels*[4], *P. Klenze*[4], *E. Galiana*[1,2], *H. Álvarez-Pol*[1,2], *E. Alves*[5], *J. M. Boillos*[1,2], *R. C. da Silva*[5], *D. Cortina-Gil*[1,2], *J. Cruz*[7], *D. Ferreira*[3], *M. Fonseca*[7], *D. Galaviz*[3,6], *R. Gernhäuser*[4], *D. González*[1,2], *A. Henriques*[3], *A.P. Jesus*[7], *H. Luís*[5], *J. Machado*[7], *L. Peralta*[3,6], *J. Rocha*[5], *A. M. Sánchez-Benítez*[8], *H. Silva*[7], *P. Velho*[3], *and the R3B Collaboration*

[1]Dpt. de Física de Partículas, Universidade de Santiago de Compostela, E-15782 Santiago de Compostela, Spain; [2]Instituto Galego de Física de Altas Enerxías (IGFAE), E-15782 Universidade de Santiago de Compostela, Spain; [3]Laboratório de Instrumentação e Física Experimental de Partículas (Lip), Av. Prof. Gama Pinto 2, 1640-003 Lisbon, Portugal; [4]Technische Universität München, 80333 Garching , Germany; [5]Campus Tecnológico e Nuclear, Instituto Superior Técnico, Universidade de Lisboa, 2695-066 Bobadela LRS, Portugal; [6]Departamento de Física, Faculdade de Ciências da Universidade de Lisboa, Campo Grande, P-1749-016 Lisbon, Portugal; [7]Laboratório de Instrumentação, Engenharia Biomédica e Física da Radiação (LIBPhys-UNL), Departamento de Física, Faculdade de Ciências e Tecnologia, Universidade Nova de Lisboa, P-2829-516 Caparica, Portugal; [8]Departamento de Ciencias Integradas, Facultad de Ciencias Experimentales, Campus de El Carmen, Universidad de Huelva, 21071 Huelva, Spain

Introduction

A devoted experiment to test the CALIFA [1] Barrel Demonstrator together with its Data Acquisition Chain was carried out in November of 2016. Two modules of the CALIFA Demonstrator, also known as petals, were exposed to gamma-rays up to 15 MeV coming from reactions of a proton beam with Al and LiF thin targets. A High Purity Germanium detector was included in the setup. The performances of the full detection system are being analyzed, and the physics of the produced nuclear reactions is being studied as well.

In this report, a complete description of the experiment is provided, together with a short summary on the status of the data analysis and the simulations of the experimental setup.

Experimental setup

Each of the two CALIFA modules consist of a petal box made of high resistance 5083 Aluminium with a 3 μm thick mylar window in the interaction point direction. Inside, a total of 64 CsI(Tl) scintillator crystals, with different shapes in groups of four, are located. The light collection and signal creation is made with Large Area Avalanche Photo Diodes (LAAPDs) directly coupled to the crystals, so that one read-out channel per crystal is available. The crystal + APD system used has an average energy resolution of $\Delta E/E < 6\%$ for 1 MeV gamma rays and very good light output uniformity. In this experiment, each petal had an approximate coverage of 30° in polar angle and 20° in azimuthal angle.

After a first pre-amplification stage, the signals were sent to a FEBEX-based Data Acquisition and trigger system [2], with 9 FEBEX boards available with 16 channels each (144 channels in total). The signal from the HPGe detector was read out with the FEBEX boards as well. The online data unpacking was done using a stand-alone program based on a MBS event structure [3]. The online monitoring was performed with Go4 [4]. A preliminary calibration was done and applied to the data on flight. In total, about 2 TB of data were recorded.

The experiment was performed at the 3 MV Cockcroft-Walton Tandem accelerator of the LATR (Laboratório de Aceleradores e Tecnologías de Radiação) facility located at the CTN/IST (Campus Tecnológico e Nuclear) campus near Lisbon, Portugal. Negatively charged hydrogen ions were produced in a duoplasmatron ion source and were injected with 14 keV energy into the Tandem accelerator. The final proton energies considered during this experiment ranged between 2 and 3 MeV. Following the two-step acceleration process, the positively charged ions were directed via an analysing magnet (90 degree) and further guided towards the reaction line where the detectors were mounted. Typical beam intensities of 100 - 300 nA were achieved throughout the experiment.

For this experimental campaign the nuclear reaction line was adapted to include a reaction chamber from the Technische Universität München. The reaction targets prepared for this experiment consisted in thin pure ^{27}Al foils as well as evaporated LiF foils (with thicknesses lower than 1 μm in both cases). A view of the experimental setup with the position of the CALIFA modules around the reaction chamber can be observed in figure 1.

The HPGe detector (40% relative efficiency) was also installed around the reaction target, positioned at 90 and 180 degrees from the nominal position of the two CALIFA petals. This detector provides a higher resolution of the energy lines observed during the measurements, and will also allow correlation studies between the CALIFA petals and the photons measured with this device.

Prior to the start of the experiment, calibration sources were used to verify the response of the detectors as well as

* Work supported by project No. POS-B/2016/015 of Xunta de Galicia, Grant 654002, ENSAR2, H2020-INFRAIA-2014-2015 of European Commission and Grant POCI-01-0145-FEDER-007334

† pablo.cabanelas@usc.es

Figure 1: Top view of the experimental setup during the experiment at the Tandem accelerator of the CTN/IST laboratory. The reaction target, at the end of the beam line, is surrounded by the two CALIFA petals used in the experiment, as well as by the HPGe detector.

a basis for energy calibration of the individual crystals. The sources used before and after the experiment were ^{60}Co, ^{137}Cs, and ^{152}Eu. A spectrum of the response of one single CALIFA crystal exposed to the ^{60}Co source can be observed in figure 2. The sufficiently good energy resolution allows as well for the separation and measurement of the natural background line from the ^{40}K decay, as shown in the figure.

The reactions studied during this experiment are listed in table 1. The two first reactions, ^{27}Al(p,γ)^{28}Si and ^{19}F(p,α)^{16}O, were chosen based on its high Q-value, allowing for the production of high energy photons (above 6 MeV) and thus providing a convenient tool to expose the CALIFA modules to energies similar to those expected in the future R^{3}B setup. The reaction ^{27}Al(p,α)^{24}Mg was also produced in the target, resulting in the emission of a photon of 1368.63 keV from the decay of the first excited state of ^{24}Mg. In addition to the particle capture reactions, the inelastic reaction ^{27}Al(p,p')^{27}Al* was also populated, resulting in the emission of the decay from the two first excited states in ^{27}Al at 843.79 keV (1/2$^+$) and 1014.56 keV (3/2$^+$) [5]. The spectrum obtained for this channel with one of the CALIFA modules can also be seen in figure 3.

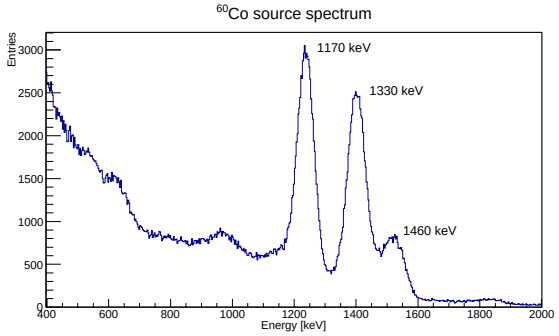

Figure 2: Spectrum measured by a single CsI(Tl) unit exposed to a ^{60}Co source during the preparations of the experimental campaign. The two gammas of 1.17 and 1.33 MeV from ^{60}Co are detected, together with the natural background 1.46 MeV peak from ^{40}K.

Table 1: List of reactions measured during the experimental campaign

Reaction	Q-value (MeV)
^{27}Al(p,γ)^{28}Si	11.6
^{19}F(p,α)^{16}O	8.1
^{27}Al(p,α)^{24}Mg	1.6
^{27}Al(p,p')^{27}Al*	< 0

Ongoing work

Experimental Data Analysis

The analysis of the experimental data is on-going. At the time of this internal report, the energy calibration of all individual modules is close to be finished. This will allow to explore the capabilities of the CALIFA modules in its petal configuration to reconstruct high energy photons in similar conditions as those to which they will be exposed in the future R^{3}B setup. Whereas the reconstruction of the full energy photon peak is one of the goals of the experiment,

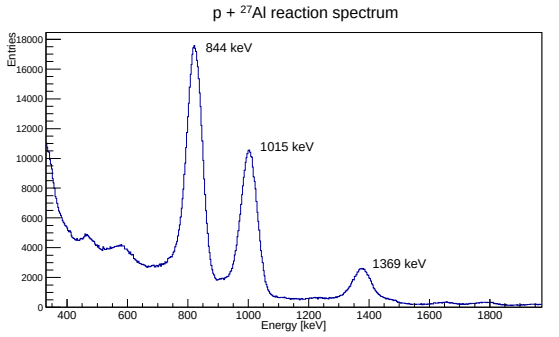

Figure 3: Spectrum measured by a single CsI(Tl) unit during the irradiation of protons on a ^{27}Al target. The two photons of 843.79 keV and 1014.56 keV from the inelastic reaction ^{27}Al(p,p')^{27}Al* are clearly observed, together with the 1368.63 keV photon from the first state of ^{24}Mg.

DOI:10.15120/GR-2017-1

the study of the clustering behaviour as a function of the photon energy will provide very valuable data for the upcoming experimental campaigns at GSI/FAIR. Additional outcomes from this experiment will be the data analysis tools that will be available for the first series of experiments with the CALIFA modules at the R^3B setup.

Simulation

At the same time, the full experiment is being simulated within the EnsarRoot framework [6]. The geometries of the CALIFA petals used in the experiment have been created, together with the reaction chamber and the HPGe detector, and placed in the space in their relative positions, as it is shown in figure 4. By means of simulation, the solid angle covered by the detection system was determined to be 12%. Figure 5 shows a detail of the CALIFA petals where the frame and the crystals inside the box are visible. Also, a dedicated event generator for this kind of proton induced reactions is under construction.

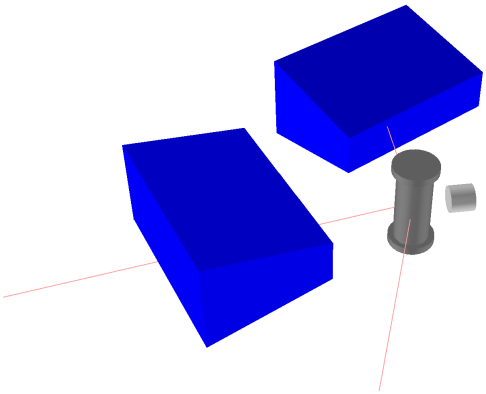

Figure 4: Simulated Setup for the experiment: the two CALIFA petals (big blue boxes), the HPGe detector (small light grey cylinder) and the reaction chamber are located in the space reproducing their real positions. An event with tree gammas coming from the interaction point inside the chamber is shown.

Conclusions

A segment of the CALIFA Barrel Demonstrator has been tested successfully under gamma-rays up to 15 MeV in a beam environment. Two demonstrator modules, or petals, with 64 CsI(Tl) crystals each (128 channels in total), were fully instrumented and the acquisition was performed with a FEBEX-based system of 144 channels. Also, a HPGe detector was included and data was sent to the same DAQ system. The data was unpacked and monitored online. The data from nuclear reactions of a proton beam on Al and LiF targets is now being analyzed. In addition, a complete simulation of the experiment is currently being performed.

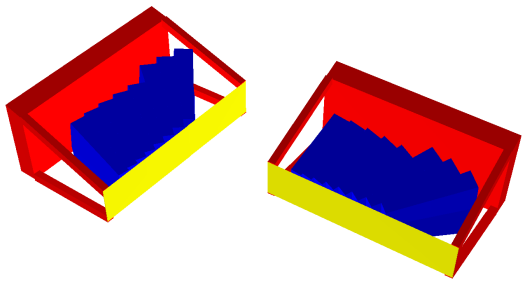

Figure 5: Detail of the CALIFA petals where the frame of the boxes and the 64 crystals inside each box are clearly observed.

References

[1] D. Cortina-Gil et al.,“CALIFA, a Dedicated Calorimeter for the R^3B/FAIR”, Nucl. Data. Sheets, Vol. 120, June 2014, p. 99-101

[2] See the dedicated contribution in this Annual Report

[3] https://www.gsi.de/mbs/

[4] http://go4.gsi.de

[5] National Nuclear Data Center. http://www.nndc.bnl.gov

[6] https://github.com/EnsarRootGroup/EnsarRoot, http://igfae.usc.es/satnurse

EPICS collector - making control parameters stick*

B. Löher[1], *H. Simon*[1], *H. T. Törnqvist*[1,2], *and H. T. Johansson*[3]

[1]GSI, Darmstadt, Germany; [2]Technische Universität Darmstadt, Darmstadt, Germany; [3]Chalmers Tekniska Högskola, Göteborg, Sweden

During experiment preparation and runtime, many important aspects of the experimental setup are controlled by adjusting parameters that may have an influence on the analysis of experimental data. Those parameters may include for example voltages, currents, and thresholds. To facilitate collection and long-term storage of these parameters and their chronological sequence, a helper library was created. Within the NuSTAR collaboration, all experiment control systems rely on EPICS[1] as a backend. Therefore, the helper library introduces an interface between the EPICS channel access protocol and the LMD data format used for detector data storage. This interface allows for timestamped correlation of control parameter values with detector data and gives the user direct access to these parameters during analysis.

Today, EPICS is already successfully in use in several experiments throughout GSI, mainly in the HADES, R3B, CBM and PANDA groups. However, the EPICS servers (IOC) and related software are mainly tailored to a specific use case and either no or only isolated infrastructural components exist. What is needed for future operations in the NuSTAR collaboration besides the IOCs and user interfaces for the individual device are therefore common infrastructural components.

The EPICS collector library focuses on monitoring a set of EPICS process variables (PVs) for changes of their state and value. Any change of state or value is then serialised into a binary format, receives a timestamp, and is written to an LMD data stream. The main benefit of this mechanism is the tight correlation between recorded detector data and control parameters, which makes these parameters directly available and reproducible when analysing data both online and at a later stage. Treating control parameter data similar to detector data automatically ensures also the same level of data protection, reducing the risk of data loss.

To guarantee that PVs have the state and value that was reported by the IOCs at a given time, any change is actively checked after a short time interval has passed. A confirmation flag is written to the data stream, if the PV can be guaranteed to be valid in this time interval. The PV is marked as valid if no further change was seen. Otherwise, the PV cannot be guaranteed to be valid for the interval and therefore receives no confirmation in the data.

The library allows the user to select the source for time information that is used when writing the data to file. Predefined time sources are the system time of the PC where the EPICS collector is running on, and any EPICS PV that exposes a timestamp.

By default, the EPICS collector reads a file `pv_list` or files in a directory named `pv_list.d` to load the list of PVs to track. PVs in the single file are treated as a single group (id $= 0$) and written to a single LMD subevent. Files in the `pv_list.d` directory must have a name starting with a unique group number (> 0, e.g. `01_los_hv`). This group number is used to generate the LMD subevent identifier and ensures that PVs from separate groups are written to separate subevents. The files contain a plain list of PV names, one per line.

Functional example clients, which use the library, are part of the distribution. The `standalone` client shows how the important parts of the library are used and outputs all available information to the terminal. The `watcher` client allows text-based monitoring of the value and state of PVs. The `lmd_source` client runs in an untriggered loop and produces LMD files. Additional clients include an `f_user.c` to show how the EPICS collector can be used from within an MBS node.

The LMD events written by the `lmd_source` and `f_user.c` clients are not marked with the standard type:subtype combination of 10:1, but instead with the proposed combination of ST:KY for so-called *sticky events*. Sticky events are a proposed extension to the LMD data format and represent a core concept for guaranteed delivery of information in a tree of data acquisition, transport, and analysis nodes. Information contained in sticky (sub-)events is cached at each node and delivered to any connecting client before sending any normal events. The cached information is stored until it is either overwritten by a sticky subevent with the same identifier or until it is actively revoked.

Careful consideration should be applied when choosing, which PVs are tracked by the EPICS collector. The persistent nature of information written to LMD files also applies to incorrect information or information that is falsified at a later stage. This means, that only information which is known to be correct is tracked by the EPICS collector and stored in sticky events. Information which is likely to change must not be stored in this way. It is strongly advised to store information organised by hardware (physical) name instead of any logical name. Physical to logical mappings are prone to contain errors, which are clearer to resolve when all mapping is done during analysis.

[1] A. Johnson, et al., Epics - experimental physics and industrial control system (2011).

* For the Common NUSTAR WG

DOI:10.15120/GR-2017-1

A FEBEX based real time high level trigger system

P. Klenze[1], M. Bendel[1], R. Gernhäuser[1], B. Heiss[1], P. Remmels[1], F. Stark[1], and M. Winkel[1]
[1]Physik Department, Technische Universität München

The CALIFA calorimeter with its 2600 scintillator crystals will be one key component for the upcoming R^3B experiment. In kinematically complete measurements, its large acceptance, efficiency and granularity will allow for a detailed event characterization. In addition the particle identification in the frontend electronics [1] and the spectroscopic quality energy measurement provide a substantial information for high level event selection.

The CALIFA trigger system is currently extended to allow for complex trigger conditions such as the total energy deposit, the gamma multiplicity or specific geometrical pattern, like "two protons in planar geometry", for the existing FEBEX readout platform developed at the GSI in Darmstadt [2]. This development will thus be useful for many NUSTAR experiments.

The aggregation of trigger information from the full detector is done in multiple layers using a newly developed low latency protocol named Trigger Transfer Tree Protocol (T^3P). On the lowest level of a tree structure (see figure 1), each FEBEX board sends information collected from its 16 channels to a Collector FEBEX Addon Board (C-FAB) module using a serial bus.

The C-FAB is a dedicated Addon Board for the FEBEX module which hosts one FPGA (Lattice MachXO2 featuring 334 IOs) which processes the information of eight FEBEX boards (128 channels) and sends it to a Receiver FEBEX Addon Board (R-FAB).

On the next level level, the R-FAB combines information from eight C-FABs in a similar manner. Already at the next layer, the information from the whole detector is collected in a single R-FAB and can be used for trigger decisions. Triggers are sent to the FPGA on its FEBEX card which then asserts a MLVDS trigger line on the crate's backplane connected to the EXPLODER [2]. From there, it can be used either to trigger CALIFA itself only or to sent out a signal to the R3B central trigger.

To accomodate trigger generation for auxilary detectors without long event buffers, these trigger decisions should not exceed a latency of $1\,\mu$s.

The only difference between the C-FAB and the R-FAB is the cabling used to connect different layers: For local collection on the first tree layer, the FEBEX boards will be connected using high density ribbon cable on the front side. For the global aggregation in the upper layers, where intercrate connections and longer distances are needed, CAT 7 cables with standard 8P8C connectors will be used.

Each tree connection features three point to point LVDS lines: a leafwards clock signal and two rootwards data signals. Each data line transmits a serialized word (typically one byte) describing the type of current trigger information. In the C-FAB and R-FAB, these informations are aggregated on the fly to decrease the overall latency. This works by receiving the least significant bit and then sending the resulting least significant bit of the operation out in the next clock cycle while processing the next bit. Any eight bits of trigger information can thus transferred from the FEBEX cards to the top level in 18 clock cycles.

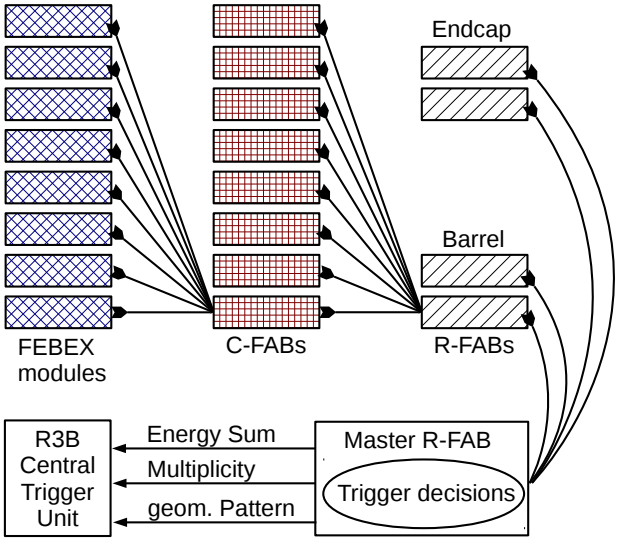

Figure 1: The Trigger Transfer Tree for the CALIFA Calorimeter in R3B

Prototypes for the C-FAB module were designed, produced and tested in the lab. For the FEBEX 3B modules, new branches of the CALIFA firmware were created: one which allows sending T^3P data from standard FEBEX cards and one which allows slow control access to the C-FAB FPGA via I^2C over GOSIP [2]. Additionally, firmware for the C-FAB FPGA was also developed – including HDL components for sending, combining and receiving trigger information. The transmission has been tested extensively in lab conditions and could be operated at a clock frequency of up to $66.5\,\mathrm{MHz}$. This results in an internal trigger delay of less than $300\,\mathrm{ns}$.

References

[1] CALIFA/R^3B Collaboration, Technical Report for the Design, Construction and Commissioning of The CALIFA Endcap, 2014

[2] https://www.gsi.de/en/work/research/electronics/digital_electronic/digital_electronics/modules/lwl.htm

DOI:10.15120/GR-2017-1

Implementation of the deexcitation model ABLA07 in GEANT4

J.L. Rodríguez-Sánchez[1], *A. Kelić-Heil*[2], *J. Benlliure*[3], *J.-C. David*[1], *and S. Leray*[1]

[1]IRFU, CEA, Université Paris-Saclay, Gif-sur-Yvette, France; [2]GSI, Darmstadt, Germany; [3]University of Santiago de Compostela, Spain

GEANT4 (for GEometry ANd Tracking) [1] is a platform for the simulation of the passage of particles through matter, using Monte Carlo methods. *GEANT4* software was the first in the use of object oriented programming and is written in C++. Therefore, in the last decades different codes, for example the intranuclear cascade model *INCL* [2], have been completely redesigned and rewritten in C++ [3] for their incorporation to the *GEANT4* software package.

The *INCL* model was developed to describe spallation reactions at kinetic energies from a few MeV to ∼3 GeV. Spallation reactions at relativistic energies are often described by means of a two-step process [4]: the collision itself, where part of the mass is removed from projectile and target nuclei and excitation energy is gained by the surviving remnants, and subsequent deexcitation processes by evaporation of particles or fission. For the description of the deexcitation stage, *INCL* is usually coupled to the *ABLA07* model [5] developed at GSI. However, *ABLA07* is written in *FORTRAN* and it cannot be used in *GEANT4*. For this reason, we have decided to rewrite *ABLA07* in C++.

The *ABLA07* model describes the deexcitation of an excited nucleus emitting γ-rays, neutrons, light-charged particles, and intermediate-mass fragments (*IMFs*) according to Weisskopf's formalism. For a more realistic description of the deexcitation, the separation energies and the emission barriers for charged particles are also considered according to the atomic mass evaluation from 2012 and the Bass potential, respectively. In addition, deexcitation by fission is also included according to a dynamical picture described in Ref. [6]. The coupling of *INCL+ABLA07* has been benchmarked in several works by using isotopic distributions of evaporation residues and fission fragments produced in spallation and fragmentation reactions of nuclei from iron to uranium, providing a satisfactory description of many observables [7, 8, 9, 10]. In what follows, the version of *ABLA07* rewritten in C++ will be called *ABLA++* and both models contain exactly the same physics and same input parameters.

In figure 1 we show the comparison of experimental data obtained for ^{238}U (1000A MeV) + p with calculations where *INCL* was coupled to different versions of *ABLA*. The dashed and solid lines correspond to *ABLA07* and *ABLA++* calculations, respectively, while the dotted line corresponds to a calculation using the previous version of *ABLA* implemented in C++, the so-called *ABLAv3p*. This version of *ABLA* only includes the evaporation of neutrons, protons, and α-particles, and the fission probability is described according to the Kramers picture [11]. As can be seen, *ABLAv3p* underestimates the production of light and intermediate residual nuclei and overestimates the production of fission fragments, while ABLA07 and ABLA++ provide a good description.

The new version of *ABLA07* in C++ will be included in the next *GEANT4* software package in order to describe the deexcitation of the compound nuclei produced in all kind of reactions, such as spallation, abrasion, fusion, etc.

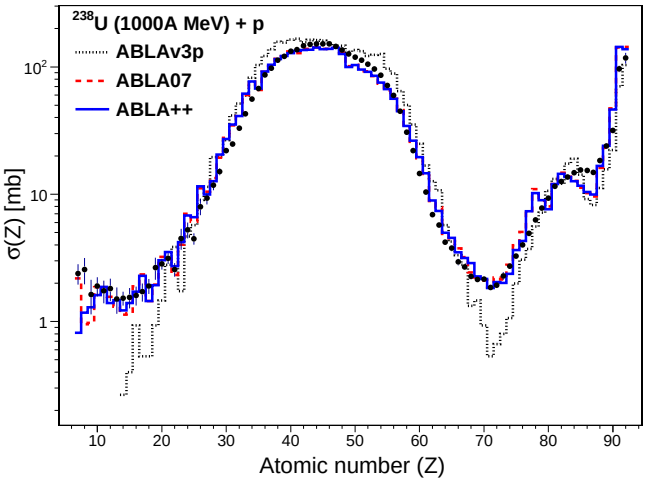

Figure 1: Comparison of *ABLAv3p* (dotted line), *ABLA07* (dashed line), and *ABLA++* (solid line) predictions with experimental data for proton-induced spallation reactions on ^{238}U.

References

[1] http://geant4.cern.ch

[2] A. Boudard et al., Phys. Rev. C **87**, 014606 (2013).

[3] D. Mancusi et al., Phys. Rev. C **90**, 054602 (2014).

[4] J.-C. David, Eur. Phys. J. A **51**, 68 (2015).

[5] A. Kelić, M. V. Ricciardi, and K.-H. Schmidt, Proceedings of Joint ICTP-IAEA Advanced Workshop on Model Codes for Spallation Reactions, ICTP Trieste, Italy, 4–8 February 2008, edited by D. Filges, S. Leray, Y. Yariv, A. Mengoni, A. Stanculescu, and G. Mank (IAEA INDC(NDS)-530, Vienna, 2008), pp. 181-221.

[6] B. Jurado et al., Nucl. Phys. A **747**, 14 (2005).

[7] C. Schmitt et al., Phys. Rev. C **81**, 064602 (2010).

[8] J. L. Rodríguez-Sánchez et al., Phys. Rev. C **91**, 064616 (2015); Phys. Rev. C **92**, 044612 (2015).

[9] Y. Ayyad et al., Phys. Rev. C **91**, 034601 (2015).

[10] J. Alcántara-Núñez et al., Phys. Rev. C **92**, 024607 (2015).

[11] H. A. Kramers, Physica **7**, 284 (1940).

DOI:10.15120/GR-2017-1

Hyperfine splitting in ^{209}Bi^{80+}, ^{209}Bi^{82+} and beyond*

R. Sánchez †[1], J. Ullmann[2,3], Z. Andelkovic[1], C. Brandau[1,4], A. Dax[5], W. Geithner[1], Ch. Geppert[3], C. Gorges[3], M. Hammen[6,7], V. Hannen[8], S. Kaufmann[3], K. König[3], Y. Litvinov[1], M. Lochmann[3], B. Maass[3], J. Meisner[9], T. Murböck[10], M. Schmidt[9], S. Schmidt[3,7], M. Steck[1], Th. Stöhlker[1,2], R. C. Thompson[11], C. Trageser[4], J. Vollbrecht[8], C. Weinheimer[8], and W. Nörtershäuser[3]

[1]GSI Helmholtzzentrum für Schwerionenforschung, Darmstadt, Germany; [2]HIJ, Jena, Germany; [3]IKP, TU Darmstadt, Germany; [4]I. Physikalisches Institut, JLU, Germany; [5]PSI, Villigen, Switzerland; [6]HIM, Mainz, Germany; [7]IKC, Universität Mainz, Germany; [8]IKP, Universität Münster, Germany; [9]PTB, Braunschweig, Germany; [10]IAP, TU Darmstadt, Germany; [11]QOLS Group, Department of Physics, Imperial College London, UK

The specific difference between the ground state hyperfine splittings (hfs) in hydrogen-like and lithium-like ions of the same isotope was suggested about fifteen years ago as the ultimate tool to prove bound-state QED in the strong magnetic field generated by the heavy nucleus [1].

The isotope of bismuth, ^{209}Bi, exhibits both ground-state hyperfine transitions very close to the visible spectrum and therefore they can be probed by laser spectroscopy. The $1s$ hfs in hydrogen-like bismuth (^{209}Bi^{82+}) was measured by direct laser spectroscopy at the experimental storage ring (ESR) in 1994 [2]. Seventeen years later and using an improved laser spectroscopic technique [3] at the same ring we found the $2s$ hfs in lithium-like bismuth (^{209}Bi^{80+}) [4]. Combined with a new measurement of the $1s$ hfs in the hydrogen-like bismuth we found good agreement with the theoretical prediction. Yet the accuracy of our result was limited at that time by the calibration of the electron-cooler voltage, determining the velocity of the ions in the ring [4].

We have repeated this experiment in 2014. This time we were able to monitor the electron-cooler voltage *in situ* using a voltage divider provided by PTB Braunschweig. First results on the $1s$ hfs in hydrogen-like bismuth using a coasting beam have been already published in [5].

After two years of studying potential systematic errors we have now achieved relative accuracies at the 10^{-5} level for both hyperfine transitions [6]. These are the most accurate transition wavelengths measured in a heavy highly charged ion so far. This improvement has finally allowed us to improve the accuracy on the specific difference by an order of magnitude. A significant fact is that our new result shows now a 7σ-difference to the latest theoretical prediction [7]. Such a large discrepancy was not expected by theory and therefore it has put the specific difference into question as a tool to test QED in strong fields.

It has, however, been pointed out that the specific difference is still sensitive to the nuclear magnetic moment of $\mu(^{209}\mathrm{Bi})$ [7, 8]. A small variation from the tabulated value could bring theory and experiment into agreement. Therefore, there is also a need to remeasure this ground state nuclear property. A new measurement of $\mu(^{209}\mathrm{Bi})$ via nuclear magnetic resonance is in preparation at TU Darmstadt and on a long-term perspective, a measurement of the hfs in both ion species is planned at the SpecTrap Penning trap and of the magnetic moment directly on hydrogen-like bismuth at the Penning trap ARTEMIS, which are both installed at HITRAP/GSI.

In order to confirm both, the reliability of the proposed nuclear structure independence in the specific difference as well as any assumption of a different nuclear magnetic moment value, we are now considering to measure the hfs in hydrogen-like and lithium-like ions of a second isotope. Two candidates are envisaged: ^{207}Bi and ^{208}Bi. Their magnetic moments are ascribed to the single proton outside the ^{208}Pb-core and the additional neutron holes below the $N = 126$ shell-closure. The specific difference in ^{207}Bi is expected to have a deviation that scales with the magnetic moment compared to that in ^{209}Bi because of the similar magnetic moment and spin. In the case of ^{208}Bi, a new measurement of the magnetic moment relative to $\mu(^{209}\mathrm{Bi})$ has recently been performed at COLLAPS/ISOLDE by collinear laser spectroscopy [9]. If the moment of ^{209}Bi is really different from the literature value, then we expect a similar disagreement for the specific difference in the case of ^{208}Bi. In case that our disagreement with theory is an artefact due to an incomplete cancellation of the Bohr-Weisskopf effect in the specific difference, the deviation for ^{208}Bi should not scale with the magnetic moment since a considerably different Bohr-Weisskopf effect is expected for this isotope with a different spin and nuclear magnetism distribution. Bound-state strong-field QED can only be proven if this cancellation works as proposed in [1].

References

[1] V. Shabaev *et al.* Phys. Rev. Lett **86** (2001) 3959.
[2] I. Klaft *et al.* Phys. Rev. Lett. **73** (1994) 2425.
[3] R. Sánchez *et. al.* J. Phys. B. **50** (2017) 085004.
[4] M. Lochmann *et al.* Phys. Rev. A **90** (2014) 030501.
[5] J. Ullmann *et al.* J. Phys. B **48** (2015) 144022.
[6] J. Ullmann *et al.* Nat. Commun. **8** (2017) 15484.
[7] A. V. Volotka *et al.* Phys. Rev. Lett. **108** (2012) 073001.
[8] A. V. Volotka *priv. comm.* (2016).
[9] S. Schmidt *et al.* to be published.

*Work supported by BMBF under Contract 05P15RDFAA, 05P12PMFAE, 06GI947 and 05P12R6FAN, by the Helmholtz-Association under Contract HGF-IVF-HCJRG-108, the Helmholtz International Center HIC4FAIR, and by HGS-HiRe. Also part of the Annual Report 2016, Helmholtz Institut Jena.

† r.sanchez@gsi.de

Asymmetries of the electron cusp in heavy-ion atom collisions*†

P.-M. Hillenbrand‡[1,2], *S. Hagmann*[1], *D. Banaś*[3], *M. Benis*[4], *C. Brandau*[5], *E. De Filippo*[6], *O. Forstner*[1,7,8], *T. Gassner*[1,7,8], *J. Glorius*[1], *R. Grisenti*[1], *A. Gumberidze*[1], *D. Guo*[9], *B. Hai*[9], *M. O. Herdrich*[7,8], *C. Kozhuharov*[1], *M. Lestinsky*[1], *Yu. A. Litvinov*[1], *E. V. Pagano*[10], *N. Petridis*[1], *S. Sanjari*[1], *D. Schury*[1,5], *U. Spillmann*[1], *C. Trageser*[1,5], *S. Trotsenko*[1], *M. Vockert*[7,8], *G. Weber*[8], *and Th. Stöhlker*[1,7,8]

[1]GSI, Darmstadt, Germany; [2]Columbia University, New York City, USA; [3]Jan Kochanowski University Kielce, Poland; [4]University of Ioannina, Greece; [5]Justus-Liebig-Universität Giessen; [6]INFN Catania, Italy; [7]Friedrich-Schiller-Universität, Jena, Germany; [8]Helmholtz Institut, Jena, Germany; [9]IMP Lanzhou, China; [10]INFN-LNS, Catania, Italy

The well-known experimental technique of zero-degree cusp electron spectroscopy has been extended towards heavy-ion atom collisions at near-relativistic collision velocities, at which new effects of asymmetries in the electron cusp arise.

In collisions of heavy highly-charged projectile ions with atomic targets, the energy distribution of the emitted electrons is a characteristic observable for the underlying elementary charge-transfer processes [1]. At the experimental storage ring ESR of the heavy-ion accelerator facility GSI, a dedicated magnetic electron spectrometer was installed downstream from the supersonic gas-jet target, which enables the measurement of high-energetic electrons emitted in ion-atom collisions, with electron velocities similar to the projectile velocity, emitted within a small cone in the forward direction (Figure 1). This technique provides the ability to extend the well known study of zero-degree cusp electrons towards heavy-ion atom collisions at near-relativistic projectile energies.

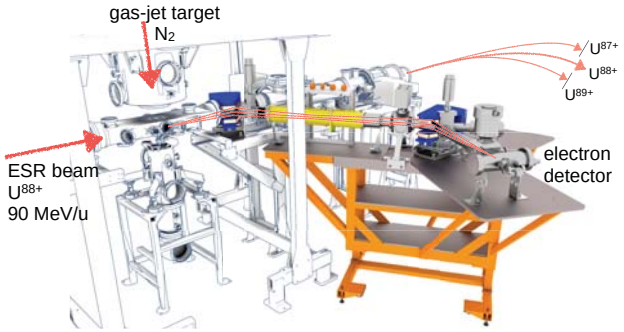

Figure 1: Magnetic electron spectrometer at the ESR.

Through the electron-loss-to-continuum (ELC) cusp, double-differential cross sections of projectile ionization can be studied even for the heaviest few-electron projectiles [2]. But also a new channel opens up, the radiative electron capture to continuum [3], which can be directly compared to its non-radiative counterpart [4]. Using the electron spectrometer in combination with detectors for emitted x rays and charge-exchanged projectiles, the study of the collision system $U^{88+}(1s^22s^2) + N_2$ @ 90 MeV/u revealed all three processes, each characterized by a unique shape of the electron cusp [5].

Furthermore, the process of electron loss to continuum was investigated for multi-electron projectiles in the collisions of U^{28+} with gaseous targets of H_2, N_2, and Xe at collision energies of 30 and 50 MeV/u. The experimental data revealed a significant electron cusp asymmetry, which increases towards heavier targets. This observation is inconsistent with presently available theories [6].

As a next step, the electron spectra for $U^{89+}(1s^22s)$ ions colliding with gaseous targets of N_2 and Xe have recently been measured in the beamtime of 2016, at a projectile energy of 76 MeV/u, i.e., just above the threshold for electron impact ionization of the L-shell of uranium. In these measurements, the studied electron emission energy was extended considerably, stretching both over the full electron cusp and the binary-encounter peak. At the studied collision velocity, relativistic continuum-distorted-wave (CDW) calculations of projectile ionization show a deviation of the electron energy distribution from first-oder perturbation theory due to attraction of the electron emitted from the projectile by the target nucleus. The experimental results motivate further developments of relativistic theories describing charge-changing processes in heavy-ion atom collisions.

References

[1] D. H. Jakubaßa-Amundsen 2003 *J. Phys. B* **36** 1971

[2] P.-M. Hillenbrand *et al.* 2014 *Phys. Rev. A* **90** 042713

[3] P.-M. Hillenbrand *et al.* 2014 *Phys. Rev. A* **90** 022707

[4] P.-M. Hillenbrand *et al.* 2015 *Phys. Rev. A* **91** 022705

[5] P.-M. Hillenbrand *et al.* 2015 *J. Phys. Conf. Ser.* **635** 012011

[6] P.-M. Hillenbrand *et al.* 2016 *Phys. Rev. A* **93** 042709

* also part of the Annual Report 2016, Helmholtz Institute Jena.

† This work was supported by the Helmholtz-CAS Joint Research Group HCJRG-108. C.B. acknowledges support by BMBF (contracts 05P12R6FAN and 05P15RGFAA). This project has received funding from GSI Helmholtzzentrum für Schwerionenphysik GmbH under the grant number GSI-TNA-002.

‡ p.m.hillenbrand@gsi.de

DOI:10.15120/GR-2017-1

High-resolution wavelength-dispersive spectroscopy of K-shell transitions in hydrogen-like gold

T. Gassner[1,2], M. Trassinelli[3], R. Heß[2], U. Spillmann[1,2], D. Banaś[4], K.-H. Blumenhagen[1], F. Bosch[2], C. Brandau[2,5], W. Chen[2], Chr. Dimopoulou[2], E. Förster[1,6], R.E. Grisenti[2,7], A. Gumberidze[2], S. Hagmann[2,7], P.-M. Hillenbrand[2], P. Indelicato[8], P. Jagodzinski[4], T. Kämpfer[1], Ch. Kozhuharov[2], M. Lestinsky[2], D. Liesen[2], Yu. A. Litvinov[2], R. Loetzsch[1], B. Manil[9], R. Märtin[1], F. Nolden[2], N. Petridis[2,7], M. S. Sanjari[2], K.S. Schulze[1], M. Schwemlein[1], A. Simionovici[10], M. Steck[2], Th. Stöhlker[1,2,6], C. I. Szabo[11], S. Trotsenko[1], I. Uschmann[1,6], G. Weber[1,6], O. Wehrhan[1], N. Winckler[2], D.F.A. Winters[2], N. Winters[2], E. Ziegler[1,2], and H.F. Beyer[2]

[1]Helmholtz-Institut Jena, Jena, Germany; [2]GSI Helmholtzzentrum, Darmstadt, Germany; [3]Institut des NanoSciences de Paris, CNRS-UMR 7588, Sorbonne Universités, UPMC Univ Paris 06, 75005, Paris, France; [4]Institute of Physics, Jan Kochanowski University, PL-25-406 Kielce, Poland; [5]Institut für Atom und Molekülphysik, Justus-Liebig-Universität, Gießen, Germany; [6]Inst. für Optik und Quantenelektronik, Friedrich-Schiller-Universität, Jena, Germany; [7]Institut für Kernphysik, Goethe-Universität, Frankfurt am Main, Germany; [8]Laboratoire Kastler Brossel, CNRS-UMR 8552, Collège de France, ENS-PSL Research University, Sorbonne Universités, UPMC Univ Paris 06, 75005, Paris, France; [9]Laboratoire de Physique des Lasers (LPL) UMR 7538 CNRS - Université Paris 13, Villetaneuse, France; [10]ISTerre, Observatoire des Sciences de l'Univers, BP 53, 38041 Grenoble, France; [11]Laboratoire Kastler Brossel, Sorbonne Universités, UPMC Univ. Paris 06, Case 74; 4, place Jussieu, 75005 Paris, France; [12]ESRF, Grenoble, France

Aiming for an accurate testing of the QED effects on the ground state binding energy in high-Z, H-like ions, novel high resolution x-ray spectrometer apparatus has been developed for experiments at the Experimental Storage Ring (ESR) at GSI, Darmstadt. Namely, the twin crystal-spectrometer assembly, Bi-FOCAL, operated in the FOcusing Compensated Asymmetric Laue geometry has been arranged for accurate x-ray spectroscopy at the ESR gas jet [1]. In a dedicated beamtime at the ESR, Lyman-α transitions of H-like Au^{78+} were measured in high resolution via spectroscopy of the corresponding x rays located near 63 keV in the laboratory system [2].

This experiment represents the first high-resolution wavelength-dispersive measurement of hard x-rays stemming from a high-Z H-like ion. It demonstrates the feasibility of this method at heavy-ion storage rings, such as ESR and represents an important milestone towards achieving a sensitivity to higher-order QED effects.

Since this is a new measurement method dealing with crystal spectroscopy of relativistic high-Z ions, for obtaining an accurate result, particular attention has to be paid to systematic effects. Therefore, in the aftermath of the main experiment, few auxiliary measurements have been conducted each of the them addressing different possible sources of systematic uncertainties [3, 4, 5].

In table 1, we show a summary of the different systematic effects and the associated uncertainties on the Lyman-α_1 transition energy which is used to deduce the 1s Lamb shift in H-like gold. As one can see from the table, the statistical uncertainty (stemming from the determination of the peak position) of only 2.2 eV has been achieved which is unique for a crystal spectrometer operated in the region of hard x rays of H-like high- Z ions. The systematic effects give the main contribution to the total uncertainty and have to be reduced in future runs. The ion-beam velocity can already be determined with a much higher accuracy using a high-voltage divider from the Physikalisch-Technische Bundesanstalt (PTB) in the electron-cooler terminal. With a slightly modified assembly it will also be possible to measure the gas-target position relative to the detector-crystal position in situ, which will almost entirely eliminate these systematic uncertainties avoiding supplementary experiments alltogether.

Table 1: Different systematic effects and the associated uncertainties on the total Lyman-α_1 transition energy (preliminary results).

Contribution	Value (eV)
Preliminary Transition Energy	$71\,539.8(2.2)$
Temporal Drift	(2.8)
Gas-Target Position	(13.0)
Ion-Beam Velocity	(4.3)
Detector-Crystal Position	(5.1)

References

[1] H. F. Beyer, *et al.* 2015 *J. Phys. B* **48** 144010

[2] H. F. Beyer, *et al.* GSI Report 2013-1, 310 p. (2013)

[3] H. F. Beyer, *et al.* GSI Report 2014-1, 155-156 p. (2014)

[4] T. Gassner, H. F. Beyer GSI Report 2015-1, 216 p. (2015)

[5] T. Gassner, *et al.* GSI Report 2016-1, 135 p. (2016)

[1]Also part of the Annual Report 2016 / Helmholtz Institute Jena

[2]supported by contract ENSAR 262010

Sympathetic cooling in two-species ion crystals at SpecTrap

S. Schmidt[1,2], *T. Murböck*[3], *Z. Andelkovic*[4], *G. Birkl*[3], *W. Nörtershäuser*[1], *and M. Vogel*[4,5]

[1]Institut für Kernphysik, TU Darmstadt; [2]Institut für Kernchemie, Johannes Gutenberg-Universität, Mainz; [3]Institut für Angewandte Physik, TU Darmstadt; [4]GSI Helmholtzzentrum für Schwerionenforschung, Darmstadt; [5]Helmholtz-Institut Jena

Following our previous studies of single-species ion Coulomb crystals in the SpecTrap Penning trap [1], we have investigated two-species ion crystals formed by sympathetic cooling of a second ion species injected into previously confined and laser-cooled Mg^+ ions from a dedicated external source [2].

The present experiments have been performed with the SpecTrap Penning trap setup [1, 3, 4], located at the HITRAP facility [5]. It uses a cylindrical, open-endcap Penning trap located in the center of a superconducting magnet for dynamic capture and confinement of externally produced ions, see figure 1. These ions can either be obtained from our dedicated pulsed source of singly charged ions [2], from other sources along the HITRAP low-energy beamline such as an electron beam ion source (EBIS), or, in future the HITRAP deceleration facility [5].

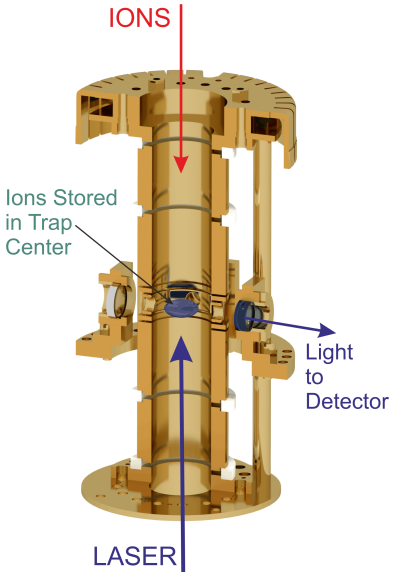

Figure 1: Sectional view of the SpecTrap Penning trap.

Formation of pure Mg^+ ion Coulomb crystals has previously been achieved by a combination of buffer gas cooling and laser cooling of externally produced Mg^+ ions from energies of several hundreds of eV to energies of the crystalline state below μeV within seconds [1]. We have further imaged the temporal evolution of the ion crystal structures upon injection of singly charged ions of mass-to-charge ratios $m/q = 2$ u/e (H_2^+), $m/q = 12$ u/e (C^+), $m/q = 28$ u/e (N_2^+), and $m/q = 44$ u/e (CO_2^+) into the same confinement region, see figure 2. In each case, sympathetic cooling can be observed and the results are in agreement with expectations from theory and previous experiments on centrifugal separation of ion species in a Penning trap. With ion numbers of up to 10^5 and ion temperatures far below 1 K, these molecular ion Coulomb crystals represent ideal tools for sympathetic cooling. Such cooling is favourable when ions without suitable transitions for laser cooling are to be cooled significantly below ambient temperature, for example for precision optical spectroscopy. In particular for highly charged ions, it allows to enter the Lamb-Dicke regime in which Doppler-free spectroscopy becomes possible. The presented method and results are valuable for precision spectroscopy of medium-mass ions such as Ar^{13+} and heavy ions of even higher charge states such as Bi^{82+} as foreseen in the SpecTrap experiment.

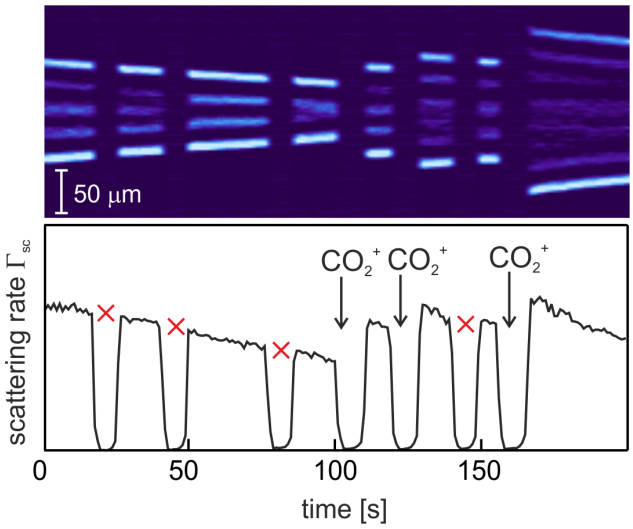

Figure 2: Top: observed layer structure of the mixed-ion crystal as a function of time. Bottom: observed fluorescence signal rate as a function of time, with injection gates for CO_2^+ ions indicated.

This work has been supported financially by BMBF (05P12RDFA3, 05P12RDFA4, and 05P12PMFAE), DFG, EPSRC, GSI and HIC for FAIR.

References

[1] T. Murböck et al., Phys. Rev. A **94** (2016) 043410
[2] T. Murböck et. al., Rev. Sci. Inst. **87** (2016) 043302
[3] Z. Andelkovic et al., Phys. Rev. A **87** (2013) 033423
[4] M. Vogel et al. Rev. Sci. Inst. **76** (2005) 103102
[5] H.-J. Kluge et al., Advances in Quantum Chemistry **53** (2008) 83

DOI:10.15120/GR-2017-1

Proton and α capture studies for nuclear astrophysics at GSI storage rings*

Jan Glorius[1,#], C. Langer[2], Z. Slavkovská[2], Y. Litvinov[1], R. Reifarth[2], C. Brandau[1,7], B. Brückner[2], X. Cheng[3], T. Davinson[4], P. Erbacher[2], S. Fiebiger[2], T. Gaßner[1], A. Gumberidze[1], G. Gyürky[5], K. Göbel[2,1], M. Heil[1], R. Hess[1], P. M. Hillenbrand[1], O. Hinrichs[2], B. Jurado[6], C. Kozhuharov[1], D. Kurtulgil[2], G. Lane[8], C. Lederer-Woods[4], M. Lestinsky[1], S. Litvinov[1], B. Löher[1], F. Nolden[1], N. Petridis[1], U. Popp[1], M. Reed[8], S. Sanjari[1], H. Simon[1], U. Spillmann[1], M. Steck[1], T. Stöhlker[1,9], T. Szücs[5], B. Thomas[2], M. Träger[1], H. Törnqvist[1], S. Torilov[10], C. Trageser[1], S. Trotsenko[1], M. Volknandt[2], M. Weigand[2], C. Wolf[2] and P. J. Woods[4]

[1]GSI Darmstadt, Germany, [2]Goethe University Frankfurt, Germany, [3]Institute of Modern Physics, Lanzhou, China, [4]University of Edinburgh, UK, [5]ATOMKI Debrecen, Hungary, [6]CENBG, France, [7]JLU Gießen, Germany, [8]Australian National University, Australia, [9]HI Jena, Germany, [10]Saint Petersburg State University, Russia

The ^{124}Xe(p,γ) reaction has been measured for the first time at energies around the Gamow window by using stored ions at the ESR facility. The desired beam energies below 10 MeV/u introduced new experimental challenges like windowless ions detection under UHV conditions, extremely short beam lifetimes and efficient beam deceleration and cooling, all of which have been successfully met.

In the nucleosynthesis of the so-called *p* nuclei radiative capture reactions like (p,γ) or (α,γ) play an important role to model the reaction network and to explain the stellar production yields in different explosive scenarios [1]. Most of the key reactions involve radioactive nuclei [2] and can be studied solely in inverse kinematics. The GSI facility offers the unique possibility to produce such exotic ions and to store them in the experimental storage ring, ESR, and eventually in the CRYRING. This setting allows one to use the limited intensities available for radioactive ions with maximum efficiency.

In a first step, fully-stripped ions are stored at beam energies below 10 MeV/u. Subsequently, nuclear reactions are introduced by colliding the stored ions with the internal jet target that consists of either hydrogen or helium gas for (p,γ) or (α,γ) reactions, respectively. Ions, which capture a proton or an α particle at the target, are separated from the stored beam in the next dipole magnet and are detected by UHV compatible double-sided silicon-strip detectors (DSSSD) with a 100% efficiency. Due to atomic interactions the lifetime of the highly charged beam is on the order of seconds. The dominant process responsible for this is the well-known radiative electron capture (REC), which can be used for cross section normalization by employing x-ray spectroscopy around the target.

The very first measurement in the ESR was performed with a beam of stable $^{124}Xe^{54+}$ ions decelerated to and stored at energies between 5.5 MeV/u and 8 MeV/u to study the reaction ^{124}Xe(p,γ)^{125}Cs. The spacial resolution of the employed DSSSD allowed a clear identification of the (p,γ) signal sitting on a background of elastically scattered ions, as shown in Fig. 1. Similar signals could be identified for five different beam energies in the aforementioned energy range. The analysis of the data set is ongoing within a phd project.

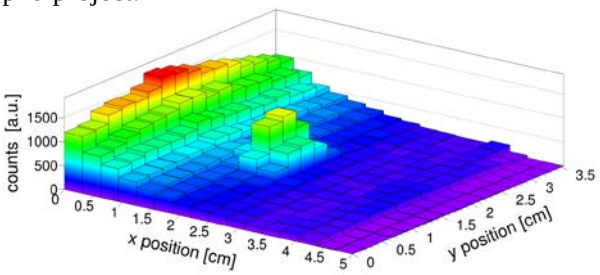

Figure 1. 2D map of the DSSSD data taken at 7 MeV/u. The peak contains the (p,γ) products sitting on a background distribution of elastically scattered ions.

In the future, first reaction studies on radioactive nuclei are planned and will be carried out using the ESR setup [3] described above. For energies below 4 MeV/u the newly installed CRYRING facility [4] is ideally suited to serve as a low-energy extension of the ESR. Corresponding experimental equipment is already being designed and will be ready for first experiments in 2018.

This project has received funding from the European Research Council (ERC) under the European Union's Horizon 2020 research and innovation programme (grant agreement No 682841 "ASTRUm")

References

[1] M. Pignatari *et al.*
Int. J. Mod. Phys. E **25** (2016) 1630003
[2] T. Rauscher *et al.*
Mon. Not. R. Astron. Soc. **463** (2016) 4153
[3] C. Brandau *et al.*
GSI Report 2014-1, 160 p.
[4] M. Lestinsky *et al. EPJ ST* **255** (2016) 5

* also part of the Annual Report 2016, Helmholtz Institute Jena
# j.glorius@gsi.de

A continuous data logger for the ESR current transformer*

S. Sanjari†[1], *Yu. A. Litvinov*[1], *H. Reeg*[1], *and Th. Stöhlker*[1,2,3]
[1]GSI Helmholtzzentrum Darmstadt; [2]Helmholtz-Institut Jena; [3]IOQ, Friedrich-Schiller-Universität Jena

In this work we introduce a new read-out electronics for the existing DCCT current transformer of the ESR.

Motivation

As long as coherent effects are not dominant in the beam, which is the case for beams of very high intensity, the integral power within Schottky bands are proportional to the ion beam current and hence the number of particles [1]. So a measured absolute value of current intensity is needed so that the integral power of Schottky spectra can be normalized to it. To this end usually a DC current transformer (DCCT) or alternatively a cryogenic current comparator (CCC) can be used.

This approach has two advantages: in the absense of a CCC, sensitivities out of reach to the DCCT can be realized by properly designed resonant Schottky detectors. Furthermore, using time resolved Fourier analysis it is possible to quickly follow the beam intensity within the same injection cycle. This method has been tested at the ESR storage ring at GSI using the resonant Schottky pickup [2] and the DC Current Transformer [3]. Results are available in [4].

The Hardware

The GSI DCCT electronics provides an analog signal, which after passing through a differential to serial converter in GSI operation area BG2.009, reaches the main control room. Additionally a second output was connected to a circuit based on a voltage to frequency converter, in order to make the signals available in the atomic physics data acquisition system over a 50 ohm transfer line [5]. A third low impedance output was left unused. The circuit described here has been designed to sample this output, after adaptation, using a 12-bit serial successive approximation analog to digital converter MCP3208. As the main controller, a single board computer (Raspberry Pi) running Linux (Raspbian) operating system has been utilized. The circuit is placed directly underneath the DCCT in the ESR in order to keep a short analog signal path. The digitized values are transferred over the network.

The Software

The code is written entirely in Python using a client/server structure [6]. The circuit acts as a message queue (ZeroMQ) server in the publisher/subscriber mode and broadcasts the value of the DCCT current to any subscriber available on the network. The sampling rate is set to 5 sps. Any number of clients can subscribe to the publishing server, either using the command line or the GUI and can run on any number of computers inside the network. The command line interface can be set to write out files of certain length, thereby allowing practically unlimited and continuous monitoring of ESR current over weeks of beam time. While providing a unique time stamp for every recorded sample, the server updates its clock regularly using an internet time server. The resulting data can be easily plotted or processed offline together with Schottky spectra. During the beam time of 2016, this device was successfully tested, where data were stored directly on GSI central computing cluster.

Future extensions

The electronics of the DCCT allow for certain amplification ranges. Although already implemented in the software, currently the ranges are set manually. In order to receive the ranges automatically set by the control system, an optically decoupled module has been designed in order to separate ground loops from that of the ESR. The test of this module is planned for a future beam time. The proper connection to the FAIR Control System still needs to be implemented. A similar design may be planned for experimental purposes in future storage rings of FAIR.

References

[1] S. Chattopadhyay, CERN-1984-011 (1984)
[2] S. Sanjari et. al., Phys. Scr. (2013) 014088
[3] H. Reeg, N. Schneider, Proc. DIPAC Grenoble (2001) PS08
[4] S. Sanjari, GSI Scientific Report (2012) PNI-ACC-03
[5] R. Steiner, private communication (2016)
[6] S. Sanjari, *https://github.com/xaratustrah/rasdaq* (2016)

* Also part of the Annual Report 2016, Helmholtz Institute Jena
† s.sanjari@gsi.de

DOI:10.15120/GR-2017-1

Status of the HILITE Penning trap experiment*

S. Ringleb[1], *N. Stallkamp*[1,2], *M. Vogel*[2,3], *S. Kumar*[4], *M. Kiffer*[1], *W. Quint*[5], *G. Paulus*[1,3], *and Th. Stöhlker*[1,2,3]

[1]Universität Jena; [2]GSI, Darmstadt; [3]Helmholtz-Institut Jena; [4]Inter-University Accelerator Centre, New Delhi; [5]Ruprecht Karls-Universität Heidelberg

The HILITE Penning trap is an ion trap developed to capture, detect and confine ions in order to provide well-defined ion-targets for laser-ion interaction studies. Therefore we apply several techniques for ion detection, ion selection and ion confinement.[1]
We have implemented the SWIFT (Stored waveform inverse Fourier transform) technique to be able to form ion targets of only one ion species. This technique has been tested at the similar ion trap ARTEMIS [2]. Based on the results of this test we have adapted our electronic circuits for noise-reduction such that we enable fast switching of the electrodes with time constants of the order of nanoseconds. These modified filters have been built and connected to the trap electrodes.

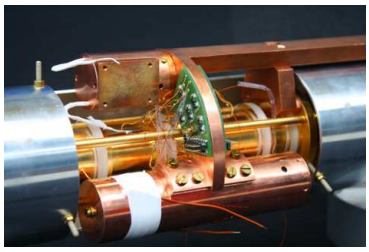

Figure 1: Picture of the assembled Penning trap - electrodes inside inner tube with applied filter boards and resonators.

For non-destructive ion detection we use resonant amplification of image currents induced in the trap electrodes by ion oscillations. To improve the sensitivity of the detection of stored ions inside the Penning trap we have built two resonators and tested them at cryogenic temperatures. To enlarge the ion spectrum, that can be detected by the resonant circuit, we will employ a varactor-diode for each resonator. We have tested the varactor-diode concerning its behaviour in the magnetic field at temperatures down to 4 K. Based on the results we have built dedicated varactor diode boards, which also support a wide tunability even at low temperatures and high magnetic fields.

In order to achieve long ion storage times the design residual gas pressure is better than 10^{-12} mbar. To compromise the open-endcap design of the Penning trap with a sufficient vacuum in the interaction region, a set of baffles at cryogenic temperatures is applied on each side of the trap-electrodes. As these baffles will also be used as a pulsed drift tube for ion deceleration, they are electrically isolated from the inner shield by ceramic spacers, which also support good thermal conductivity.

Figure 2: Picture of the assembled baffle system for vacuum improvement and ion deceleration.

As an ion source for the first commissioning experiments we have set up an EBIT and verified its functionality. We have produced ions inside the EBIT and have measured the extraction with a faraday cup. The next steps will be the connection of the EBIT with our ion trap to capture ions produced inside the EBIT and check the functionality of the measurement principles of the ion trap.

Figure 3: Experimental stand with the equipped device rack.

Our recent results and the status of our experiment have been presented at the PSAS conference in Jerusalem, at the SPARC workshop in Krakow and at the MML workshop in Hamburg.

References

[1] S. Ringleb, M. Vogel, S. Kumar, W. Quint, G. Paulus, Th. Stöhlker, Journal of Physics Conference Series **635** (2015) 092124

[2] Vogel M. et al. (2017) Extreme-field physics in Penning traps The ARTEMIS and HILITE experiments. In: Wada M., Schury P., Ichikawa Y. (eds) TCP 2014. Springer, Cham

* Also part of the Annual Report 2016, Helmholtz Institute Jena

DOI:10.15120/GR-2017-1

Status of the ARTEMIS experiment: Purification of highly-charged ion clouds and their months-long storage

M.S. Ebrahimi[1,2], *G. Birkl*[3], *Z. Guo*[1,2], *M. Wiesel*[1,2,3], *A. Martin*[3], *W. Quint*[1,2], *and M. Vogel*[1,4]

[1]GSI, Darmstadt; [2]Ruprecht Karls-Universität Heidelberg; [3]Institut für Angewandte Physik, TU Darmstadt; [4]HI Jena

We are currently upgrading and commissioning the ARTEMIS experiment, a Penning trap setup located at the HITRAP facility, and designed for precision microwave spectroscopy of highly charged ions [1]. In combination with optical spectroscopy, this will be used to determine the magnetic moment of the electron in the presence of the extreme fields in the vicinity of the core of a highly charged ion. Within the theory of bound-state quantum electrodynamics, magnetic moments can be calculated to high accuracies. With the foreseen measurements at relative accuracies on the ppb level and beyond, it is possible to test such calculations with high stringency. The method of choice is the so-called laser-microwave double-resonance spectroscopy, utilizing the fact that for medium-heavy few-electron ions the fine structure, and for some heavy highly-charged ions the hyperfine-structure splitting is in the optical regime. These ions, such as $^{207}Pb^{81+}$ and $^{209}Bi^{82+}$, are foreseen to be available within the framework of the HITRAP facility. For efficient light collection, the Penning trap features a dedicated half-open design [2].

For first off-line tests, the $^{40}Ar^{13+}$ ion has been chosen. It has a spinless nucleus, so that the magnetic moment (g-factor) of the $2p$-electron can be measured. Due to the high magnetic field of 7 T also first laboratory measurements of higher-order Zeeman effects can be performed [2]. To that end, we have successfully and routinely operated an in-trap source of highly charged ions, similar to a miniature electron beam ion trap, and have created ions up to Ar^{16+} and W^{26+}.

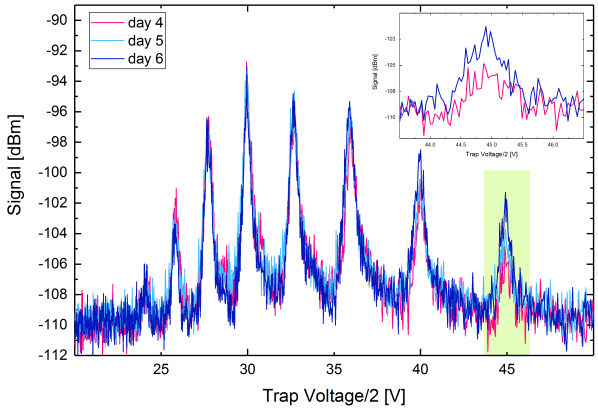

Figure 1: Detected argon ion charge state spectrum for different storage times. The inset indicates small changes, used for the residual gas pressure measurements.

We are able to store these ions over the course of many days, detect them non-destructively by use of dedicated radio-frequency resonators [4], and to cool their motion. We have used the cooled ion cloud to perform a residual gas pressure determination in our trap chamber. With a measured half-life of 78 days, an upper limit of the residual gas pressure of 9×10^{-16} mbar has been estimated. Such a measurement is depicted in figure 1.

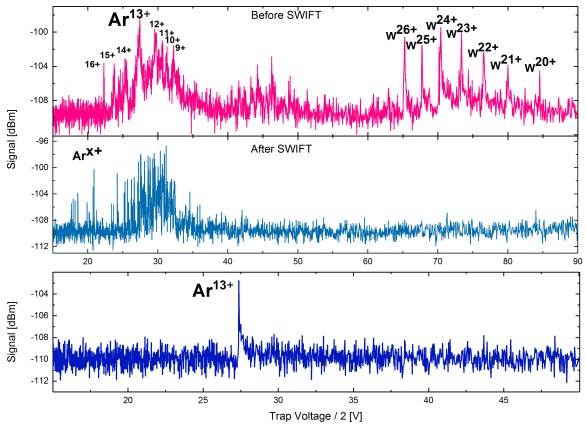

Figure 2: The SWIFT cleaning technique performed on an ion cloud in the creation trap of ARTEMIS.

We have demonstrated preparation of pure ion clouds by application of the Stored Waveform Inverse Fourier Transform technique (SWIFT). It enables selective excitation of different charge states in order to remove unwanted ion species from the trap. Figure 2 demonstrates the procedure required to achieve a pure cloud of Ar^{13+} from a rather extreme example of an ion cloud in our trap.

This work has been supported in part by DFG (Grants VO 1707/1-2 and BI 647/4-1), by GSI, HGS-HIRe, and by the IMPRS for Quantum Dynamics Heidelberg.

References

[1] W. Quint, D. Moskovkin, V.M. Shabaev and M. Vogel, Phys. Rev. A **78** (2008) 032517.

[2] D. von Lindenfels, M. Vogel, G. Birkl, W. Quint and M. Wiesel, Hyp. Int. **227** (2014) 197

[3] D. von Lindenfels, W. Quint, D. Glazov, V.M. Shabaev, G. Birkl and M. Vogel, Phys. Rev. A **87** 023412 (2013).

[4] M.S. Ebrahimi, N. Stallkamp, W. Quint, M. Wiesel, M. Vogel, A. Martin, and G. Birkl, Rev. Sci. Inst. **87** (2016) 075110

DOI:10.15120/GR-2017-1

Progress of experimental systems for CRYRING@ESR*†

M. Lestinsky‡ [1], *F. Herfurth*[1], *S. Schippers*[2], *Th. Stöhlker*[1,3,4], *and the APPA collaborations*[1]
[1]GSI, Darmstadt, Germany; [2]JLU Gießen, Gießen, Germany; [3]HI Jena, Germany; [4]IOQ, FSU Jena, Germany

CRYRING@ESR is a new heavy ion storage ring facility at GSI/FAIR and is presently under construction [1-2]. The former Swedish CRYRING was modernized and adapted to its new location. After almost two years, reassembly of the ring in general has been completed and vacuum pumping could be started. Also, the beam transport from ESR to CRYRING has been completed. Figure 1 shows a photograph of the injector beamline and the ring at the end of 2016. During the course of 2016, already the first two beamtime campaigns were dedicated to the commissioning of CRYRING@ESR. During these periods, the low-energy beam extraction from ESR and transport towards CRYRING, as well as — using a beam produced in the local injector of CRYRING — the "first turn" of ions in the ring could be successfully demonstrated. More details about the commissioning are given in [3]. For the machine, the directions are set for going from first turn to a long-lived stored beam. Thus, next steps will be establishing the required ultrahigh vacuum conditions for a long ion beam lifetime, as well as electron cooler operation.

With the machine gradually progressing into regular operation, the experimental systems are presently also being prepared, and CRYRING@ESR in fact offers exciting research opportunities for research on highly charged ions for a large range of scientific fields. In the future, all ions presently available from the GSI accelerator chain can be transported and stored at low energies, between ~ 0.05 to 15 MeV/u with ion beam lifetimes between few seconds to $\sim$ 15 minutes, depending on charge state and energy. Hence, SPARC and FLAIR, but also NuSTAR have formulated extensive research programmes for this facility [4]. The low energy conditions will allow for precision spectroscopy and thus, e.g., allow one to test non-perturbative strong field QED, or to study transient quasi-molecular systems. Further, at the border between atomic and nuclear physics, nuclear size effects, hyperfine interactions or exotic couplings between the electronic shell and the nucleus of an ion may be explored. In nuclear physics, storage of bare nuclei at low energies permits to determine fragment distributions unmasked by atomic physics. Under these conditions, e.g., nuclear reactions at the Coulomb barrier or nucleosynthesis of heavy elements in the Gamow window of the p-process may be analyzed.

A first generation of experiments at CRYRING@ESR is being prepared by the German APPA R&D collaboration [5,6] (supported by BMBF Verbundforschung). This instrumentation comprises various installations for a wide range of atomic physics experiments (SPARC collaboration): Electron-ion collision spectroscopy at the electron cooler and an intense transverse electron target, laser- and fluorescence spectroscopy from the visible to the VUV regime, particle detectors, and precise systems to measure electron- and ion energies. Most systems shall be ready for at least rudimentary operation in first experiments during the 2018-2019 beamtime campaings. Also, details of further international projects are presently being worked out. Finally, in order to coordinate the efforts by and resources for the various experiment groups, a new mailing list and a monthly regular meeting have been established (see [1] to sign up).

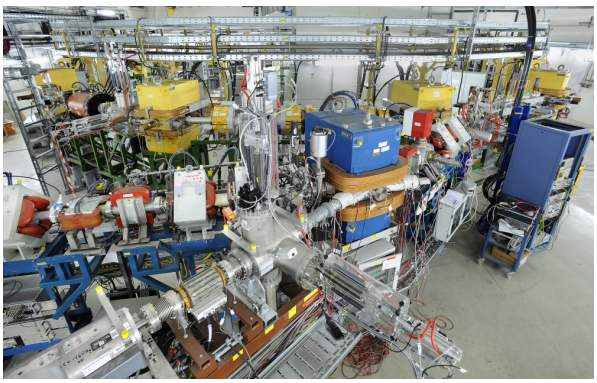

Figure 1: CRYRING@ESR overview. Ions are injected from the local injector or from ESR (diagonally from the lower left) and the ring is in the back (yellow dipole magnets). Photo by G. Otto, GSI, Dec. 2016.

References

[1] `http://www.gsi.de/cryring/`

[2] W. Geithner, et al., "Status and outlook of the CRYRING@ESR project", 2017, Hyperfine Interact., 238, 13

[3] F. Herfurth, et al., "The status of CRYRING@ESR – first turn", GSI annual report 2016, GSI Darmstadt, in print.

[4] M. Lestinsky, et al., "Physics book: CRYRING@ESR", 2016, Eur. Phys. J. Spec. Top. 225, p. 797

[5] `http://appa-rd.fair-center.eu`

[6] Z. Andelkovic, et al. and the SPARC collaboration, "Technical Design Report: Experimental Instrumentation of CRYRING@ESR", 2015, FAIR Darmstadt

*CRYRING@ESR is supported by GSI, HI Jena, Stockholm Univ., Jagiellonian Univ. Kraków, and BMBF Verbundforschung under various contracts

† Also part of the Annual Report 2016, Helmholtz Institute Jena

‡ m.lestinsky@gsi.de

SPARC experiments with highly charged ions at the HESR of FAIR

O. Kovalenko[1,#], Yu. A. Litvinov[1], Th. Stöhlker[2]
[1]GSI, Darmstadt, Germany;[2]Helmholtz-Institut Jena, Germany.

Introduction

One of the aims of the SPARC collaboration [1] at FAIR is to perform precision atomic physics experiments with highly charged heavy ions at the High Energy Storage Ring (HESR).

An internal target is indispensably an integral part for many such experiments. Ions with different charge states, which are obtained as a result of interaction of an ion beam with the target, need to be effectively separated and detected. In this work we present ion optical studies unambiguously showing the feasibility of SPARC experiments at the HESR.

Target location

The SPARC collaboration at FAIR [1] aims at atomic physics research with highly charged ions (HCI) in energy domains previously not accessible for precision experiments [2,3]. Here, the High Energy Storage Ring (HESR) will allow for storing stochastically and/or electron cooled HCIs up to energies of ~5 A GeV.

The missing dipole concept in the HESR enables an installation of internal target stations [4] in two arcs (ROI 1 and 2) [5] (see Figure 1).

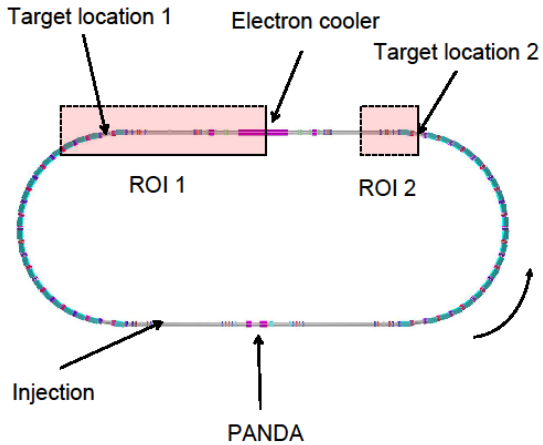

Figure 1: Two target locations in the HESR and the corresponding regions of interest (ROI) can be seen.

The experimental conditions in the ROI 1 region, which was initially proposed for the SPARC target location [6], have a complication: ions, recombined in the electron cooler and the rest gas along the long straight section, will produce an unwanted background. This situation is avoided in the ROI 2 case resulting in much cleaner experimental conditions. However, only one dipole magnet is then available for charge state separation [5].

Figure 2 shows a separation of the primary fully ionized $^{238}U^{92+}$ uranium beam (2-sigma emittance) and two charge states ($^{238}U^{91+}$, $^{238}U^{90+}$) obtained after the reaction in the target (ROI 2). The ion optical computations prove that the resolution of the charge states at the particle detector, which is placed 3 m after the last defocusing quadrupole, is more than sufficient. For experiments with lighter beams, the separation improves further since ΔQ/Q increases [5]. As a conclusion, the experiments with internal target, placed in the missing dipole gap in ROI 2, are feasible [7]. Examples of the growing number of the proposed precision experiments in the HESR, which will thus be enabled, can be found in [8-14].

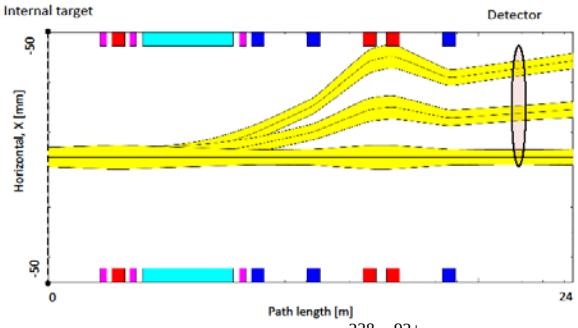

Figure 2: Propagation of primary ($^{238}U^{92+}$) and secondary charge exchange reaction products ($^{238}U^{91+}$, $^{238}U^{90+}$) after interaction with the target. The dipole magnets, focusing and defocusing quadrupoles are shown by cyan, red and blue colors, respectively [5].

References

[1] T. Stöhlker*et al.* 2011 AIP Conf. Proc. 1336 132
[2] T. Stöhlker*et al.* 2015 Nucl. Instr. Meth. B365 680
[3] T. Stöhlker*et al.* 2013 Phys. Scr. T156 014085
[4] N. Petridis *et al.* 2015 Phys. Scr. T166 014051
[5] O. Kovalenko 2015 PHD Thesis, Heidelberg
[6] T. Stöhlker*et al.* 2014 Hyperf. Interact. 227 45
[7] O. Kovalenko *et al.* 2015 Phys. Scr. T166 014042
[8] S. Hagmann *et al.* 2013 Phys. Scr. T156 014086
[9] F. Bosch2013 *Prog. Part. Nucl. Phys.*73 84
[10] Y. Litvinov *et al.*2013 *Nucl. Instr. Meth. B*317 603
[11] T. Stöhlker*et al.* 2015 Phys. Scr. T166 014025
[12] A. Gumberidze *et al.* 2015 Phys. Scr. T166 014076
[13] P. Hillenbrand *et al.* 2015 Phys. Scr. T166 014026
[14] W. Nörtershäuser 2015 Phys. Scr. T166 014020

#okovalenko@gsi.de

DOI:10.15120/GR-2017-1

Ion trajectory simulations for the purification system of the FISIC experimental program

A. Kumar[1], *A. Méry*[2], *J.M. Ramillon*[2], *L. Adoui*[2], *J.-Y. Chesnel*[2], *A. Lévy*[1], *S. Macé*[1], *C. Prigent*[1], *J. Rangama*[2], *P. Rousseau*[2], *J.-P. Rozet*[1], *S. Steydli*[1], *M. Trassinelli*[1], *D. Vernhet*[1], *A. Gumberidze*[3], *Th. Stöhlker*[3,4,5], *A. Bräuning-Demain*[3], *C. Hahn*[4], *U. Spillmann*[3], *G. Weber*[4,5] and *E. Lamour*[1]

[1]Institute des Nanosciences de Paris, Sorbonne Universtités UPMC Paris 6; [2]CIMAP, CEA/CNRS/ENSICAEN/Université de Caen Basse-Normandie, Caen; [3]GSI, Darmstadt, Germany; [4]Friedrich-Schiller-Universität Jena, Germany; [5]Helmholtz-Institut Jena, Germany.

With the Fast Ion-Slow Ion collisions (FISIC) experimental program [1], we propose an experimental crossed-beam arrangement in the so-called intermediate regime (the regime in which the ion stopping power is maximum) for a wide range of projectile-target combinations with an ultimate control of experimental conditions to measure absolute cross-sections of fundamental atomic processes. Up to now, only a few crossed-ion-beam experiments have been performed for light ions in the low energy-energy domain [2].

Simulation results

Crossing two multi-charged ion beams, under well-controlled conditions, has always been a very challenging task, whatever the physics under consideration. For such a challenging experimental project, many technical barriers have to be overcome. For the low-energy beam line, one of them is to prevent pollution mainly due to electron capture from the residual gas before the collision point. To control the charge state of keV/u ions, a new Omega type purification system has been developed. This system consists of four cylindrical deflectors with Matsuda plates allowing us to generate toroidal electric fields. This particular arrangement allows to get the exit beam back on the initial beam axis. Ion trajectory simulations have been performed with the SIMION 8.1 version software in order to optimize the geometry of the purification system. To test different configurations, we have used the batch mode operation of SIMION with a Lua code. In the simulations, we generate an ion beam with an energy of 20 keV/q and a large emittance of 60 π mm.mrad with a Gaussian spatial distribution ($\sigma_x = 0$, $\sigma_y = \sigma_z = 2$mm, x being the ion propagation axis). To test the purification system, we generate ions having the same mass but with different charge states. The voltages on the cylindrical deflectors are set in such a way that only the desired charge state is allowed to pass through the purification system while the other charge states are stopped. As an example, simulated ion trajectories for Ar^{q+} with q = 15, 16, 17 and 18 are shown in Fig. 1 with voltages that permit only the transmission of Ar^{17+} ions. Therefore, a clean Ar^{17+} ion beam is obtained just before the collision with the fast ion beam. Simulations for different ion species such as C^{5+}, N^{6+}, O^{7+}, and Ne^{9+} have also been carried out with success showing the versatility of this purification system.

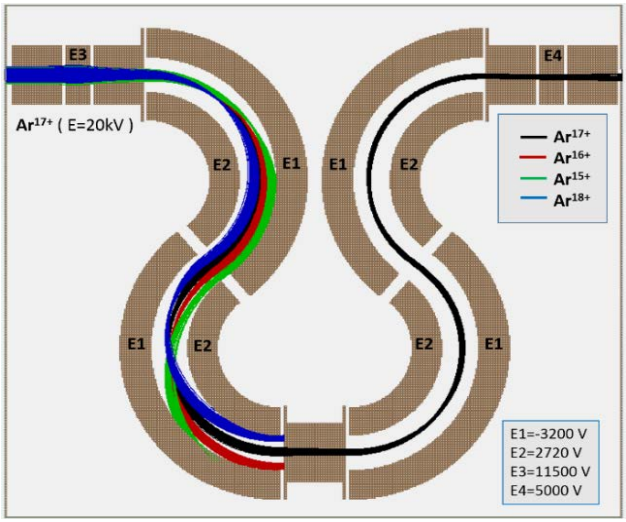

Figure 1: Ion trajectory simulations in the omega-type purification system. The voltages are set to permit only the transmission of Ar^{17+} ions.

Future work

A dedicated chamber for the purification system has been designed and is under construction. Experimental tests are scheduled first at the ARIBE facility at Caen. Meanwhile, simulations of the collision zone together with the post-collision electrostatic charge state analyser of the low-energy ions are under progress.

References

[1] E. Lamour *et al.* Fast ion-slow ion collision – FISIC project at http://www.agence-national-researche.fr/?Project=ANR-13-IS04-0007 and htpp://pro.ganilspiral2.eu/sprial2/instrumentation/s3/working-docments/loi-day-1-experiments/fast-ion-slow-ions-collisions2013fisic-project/view.

[2] S. Meuser *et al.* 1996, Rev. Sci. Instrum. **67** (8) 2752-2759 ; A. Diehl *et al.* 2001, J. Phys. B **34** 4073-4081 ; C.Y. Chen *et al.* 2001, J. Phys. B **34** 469-475

DOI:10.15120/GR-2017-1

Parallel plasma description of ions stored in Penning traps*

A. Henkel[1,2,3], *F. Herfurth*[1], *R. Pinnau*[2], *and T. K. Strempel*[3]

[1]GSI Helmholtzzentrum, Darmstadt, Germany; [2]University, Kaiserslautern, Germany; [3]University of Applied Sciences, Darmstadt, Germany

The HITRAP (Highly Charged Ions Trap) facility at the GSI allows to investigate slow highly charged ions up to U 92+. The most important part of the facility is the Penning trap, which allows the trapping of charged ions.

A microscopic simulation of the ion cloud is only possible to a limited extent. Because of the computational effort of $O(N^2)$ a system of 10^5 ions, as occurs in the ion trap, leads to long simulation times, which makes long-term simulations impossible. Even if we parallelize the problem and have access to an infinite number of resources, a simulation would take about 15 years [1].

Plasma description

The macroscopic description provides further access [2]. The ion-ion interaction is avoided and we look at the system of ions as a continuum similar to a charged liquid. We use a statistical approach in which the positions and velocities of the ions are given by a probability. This means that the dynamics of the ion cloud is described by the dynamics of the density $f(r, v, t)$ in the phase space, which describes the probability of finding an ion with a given velocity at a certain point in space.

The dynamics of the single particle density $f(r, v, t)$ is given by the Vlasov equation

$$\frac{\partial f}{\partial t} + \mathbf{v} \cdot \frac{\partial f}{\partial \mathbf{r}} + \frac{\mathbf{F_{ext}}}{m} \cdot \frac{\partial f}{\partial \mathbf{v}} = 0 \qquad (1)$$

which is an exact description of non-interacting particles. The force F is given by the external electromagnetic fields. The interaction of the ions among each other is described by an mean-field $\Phi(r, t)$. This is given by the charge density $\rho = q \int f \, \mathrm{d}^3 \, \mathbf{v}$ which is given by the iondensity, where Φ is the solution of the Poisson's equilibrium $\Delta\Phi\varepsilon = \rho$. Together with the associated force $-q\nabla\phi$ and the Vlasov equation (1), we obtain the non-linear Vlasov-Poisson equations

$$\begin{aligned} \frac{\partial f}{\partial t} + \mathbf{v} \cdot \frac{\partial f}{\partial \mathbf{r}} &= -\frac{q}{m}(-\nabla\phi + \mathbf{F_{ext}}) \cdot \frac{\partial f}{\partial \mathbf{v}}, \\ \Delta\Phi = -\frac{\rho}{\varepsilon} &= -\frac{q}{\varepsilon} \int f \, \mathrm{d}^3 \, \mathbf{v}. \end{aligned} \qquad (2)$$

Parallelisation

The Vlasov-Poisson equations (2) have to be solved numerically for practical applications. A grid-based hybrid MPI / OpenCL solution called *TRAPSim* was implemented to run the simulations on the GSI *Green IT Cube* in order to minimize the computational effort.

The *L-CSC* cluster consists of 160 compute nodes, each with four AMD FirePro S9150 GPUs, two CPUs and 256 GB memory.

The implementation was tested with a system of 2^{17} ions and a grid of $64 \times 64 \times 128$ points. In Table 1 we see the measurement data of the runtime for an iteration. g is the number of GPUs and t the runtime in seconds. s the speedup, f the serial fraction and e the efficiency, as defined in [3].

g	1	2	4	8	16
t	115.355	59.316	29.857	15.083	7.664
s	-	1.94	3.86	7.64	15.05
f	-	2.84E-2	1.17E-2	6.57E-3	4.2E-3
e	-	0.97	0.96	0.95	0.94

Table 1: Measuring of the parallel GPU Performance.

We see that the serial fraction f decreases. The reason for this is that by increasing the number of GPUs we get more cache and memory bandwidth that reduces the overhead.

Which maximum speed-up can be expected? Due to Amdahl's law [4] we can calculate the maximum speed-up with the limit

$$\lim_{g \to +\infty} s(g) = \frac{1}{f}. \qquad (3)$$

If we choose for $f = 4.2\mathrm{E}{-3}$, the limit is $s_\infty \approx 238$. The runtime of the simulation depends strongly on the selected grid. A detailed analysis is needed to find the minimal grid that still describes physics.

References

[1] Henkel, A. et al. GSI Scientific Report 146, 2015.

[2] Blaum, K. and Herfurth, F. Trapped charged particles and fundamental interactions. Springer, 2008.

[3] Karp, A. H. and Flatt, H. P. Measuring parallel processor performance. Communications of the ACM 33.5 (1990): 539-543.

[4] Amdahl, G. M. Validity of the single processor approach to achieving large scale computing capabilities. Proceedings of the April 18-20, 1967, spring joint computer conference. ACM, 1967.

* Work supported by FE, Project-Number DAGROS1416.

DOI:10.15120/GR-2017-1

Backscattered electron emission from gold nanoparticle after protons impact: Experiments and simulations*

F. Hespeels[1], AC.Heuskin[1], S. Lucas[1], T.Tabarrant[1], E. Scifoni[2], M.Kraemer[3]
[1]University of Namur , Namur, Belgium; [2]TIFPA-INFN, Trento, Italy. ; [3]GSI, Darmstadt, Germany;

It has been shown that the presence of gold nanoparticles (GNPs) can increase cell damage during radiotherapy treatment, possibly due to emission of low energy electron around GNPs. Reproducing the interaction between protons beam and GNPs by Monte Carlo simulation requires cross section data which are still incomplete. In this context, theoretical models need experimental validation. This work aims at a comparison of simulation results calculated with the TRAX code and with experimental data obtained from irradiation of GNPs deposited on Carbon thin film.

The TRAX code is dedicated to the description of low-energy electron emission and transport in solids after proton irradiation [1]. Sets of interaction cross sections for electron with energies down to 1 eV are available for different materials and allows us to reproduce ionization, excitation and elastic scattering. Standard elastic scattering cross sections can be calculated using the screened Rutherford approximation or the Partial Wave Analysis method, respectively, for low and high Z. Ionization induced by electron is taken into account by applying the binary encounter Bethe model. Auger electron emission probabilities are implemented in the code using Livermore Evaluated Atomic Data Library.

Experimental data were gathered at the University of Namur. GNPs were deposited on thin Carbon films using the magnetron sputtering method developed in Namur [2]. Gold nanoparticles size and distribution were observed with transmitted electron microscopy (see Figure 1). The experimental setup dedicated to the secondary electron emission is described in our paper published in Nuclear Instruments and Methods in Physics Research Section B [3]. This paper presented secondary electron emission result obtained from carbon thin film (50 nm and 100 nm thick) and gold thin film (200 nm thick).

Electron energy spectra resulting from 2 MeV proton bombardment on carbon and gold nanoparticles deposited on carbon substrate are displayed on Figure 2. Preliminary TRAX simulation of GNPs deposited on carbon are also presented. As expected, presence of GNPs increase the secondary electron yield. It turns out that the simulation is quite similar to the experimental results at low energy (< 270 eV). The Auger peak at ~270 eV appears more pronounced in TRAX simulation. The difference in electron yield above 270 eV has to be studied. As it is a preliminary simulation, this could be due to geometrical errors. This will be discussed in further works.

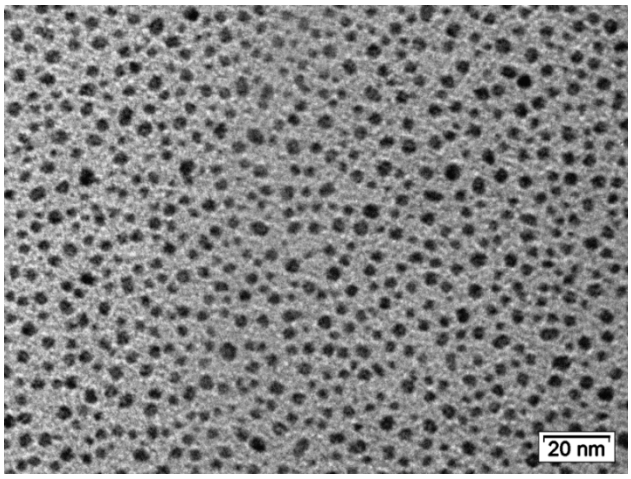

Figure 1: Gold nanoparticles (~4nm) deposited on 100 nm carbon foil.

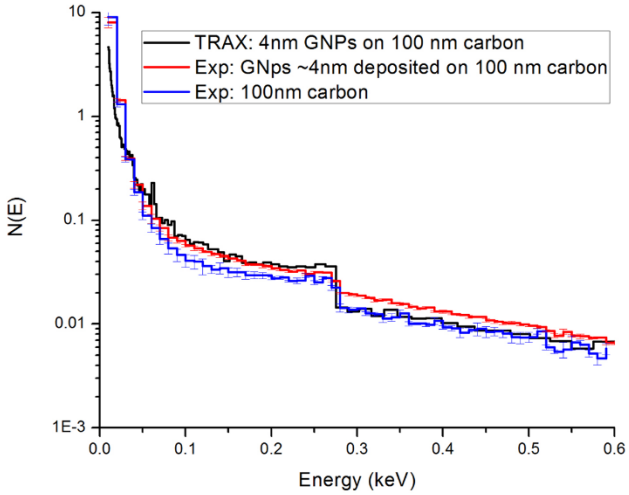

Figure 2 : TRAX and experimental secondary electron spectrum of carbon thin film and GNPs deposited on carbon film.

References

[1] M. Krämer, G. Kraft, Calculations of heavy-ion track structure, Radiat. Environ. Biophys. 33 (1994) 91–109.

[2] V. Bouchat and al, On the use of radioisotopes to study the possible synthesis by magnetron sputtering of bimetallic nanoparticles, Surf. Coatings Technol. 205 (2011) 4934–4940.

[3] F. Hespeels and al. Geant4, M. Carlo, Backscattered electron emission after proton impact on carbon and gold films: Experiments and simulations, (2017).

*: F.Hespeels is supported by the Belgian Fund for Industrial and Agricultural Research (FRIA).

Test of a new silicon microcalorimeter array at the ESR *

S. Kraft-Bermuth[1], *V. Andrianov*[2], *A. Echler*[1,3,4], *P. Egelhof*[3,4], *O. Kiselev*[3], *and P. Scholz*[1]

[1]I.Physics Institute, Justus-Liebig-University, Giessen, Germany; [2]Lomonosov Moscow State University, Moscow, Russia; [3]GSI Helmholtz Center for Heavy Ion Reserach, Darmstadt, Germany; [4]Institute of Physics, Johannes Gutenberg University, Mainz, Germany

Silicon microcalorimeters for high-precision X-ray spectroscopy have been developed at GSI and the University of Mainz since more than two decades [1]. These microcalorimeters are based on arrays of silicon thermometers [2] and X-ray absorbers of lead or tin [3] to obtain high quantum efficiency for X-ray energies of around 100 keV. With such detectors, an excellent energy resolution of $\Delta E_{FWHM} = 40 - 60$ eV for a X-ray energy of 60 keV has been demonstrated [3, 4]. Two detector arrays were applied in two successful experiments at the ESR for the determination of the 1s Lamb Shift on hydrogen-like lead and gold ions [4].

For experiments at FAIR, a new detector array with a larger detector solid angle is currently developed within the SPARC collaboration. As microcalorimeters detect the energy of a photon as a heat signal, low operating temperatures of below 100 mK are mandatory to obtain high energy resolution. Accordingly, these detectors are operated in a ^{3}He/^{4}He dilution refrigerator. In the past, a cryostat with a specially adapted side-arm was used which fits to the gas-jet target geometry at the ESR and allows bringing the detectors as close to the interaction region of ion beam and gas jet as possible [3]. This cryostat has been used in the above-mentioned Lamb Shift experiments and performed well at the ESR, but the use of liquid helium and nitrogen as coolants make its application cost-intensive. In addition, interruptions of beamtime for refilling the cryogenics are unavoidable. To overcome this disadvantage, a new dry cryostat, which is equipped with a pulse-tube cooler to reach 4 K and a ^{3}He/^{4}He dilution stage, was designed in cooperation with the company BlueFors[1] and commissioned in Giessen in the last three years [5]. In spring 2016, this new cryostat was for the first time set up at the ESR gas-jet target to test its performance.

The side arm of the cryostat has to fit into one of the vacuum pockets at the gas-jet target, which limits its outer diameter to about 90 mm. Therefore, the detector array has to be compact enough to fit inside this limited space under the consideration that several cryogenic shields have to be mounted in order to limit the heat radiation from the environment. The detector design of Bleile et al. [3, 4] was too large to be extended to more than 32 detector pixels, whereas the goal of the new design is to deploy 96 detector pixels. Accordingly, a new, more compact detector was designed and produced as a prototype for the larger array. It is displayed in figure 1. In addition, a new data acquisition system was set up which is extendable to 96 detector channels. The goal of the test run in spring 2016 was to test all components of the new setup.

The test run was performed at the ESR in combination with several other detector systems which are developed within SPARC. Our detector system was set up at the 145° port of the ESR gas-jet target, similar to the setup of the Lamb Shift experiments [4]. The cryostat performed flawlessly at the ESR over six weeks, during which several cooldown cycles were completed. The quick cooling and warming up as well as the remotely controlled operation provided a great advantage because several adjustments of the setup were found to be necessary.

In the test experiment, X-rays were detected which had been produced by interaction of an ion beam with a gas-jet target. This experimental setup has been described in detail in many publications, i.e. in [4]. A beam of bare or highly-charged ions is injected into the ESR, stored and cooled. After the cooling cycle is finished, a gas-jet, which is oriented perpendicular to the ion beam, is switched on.

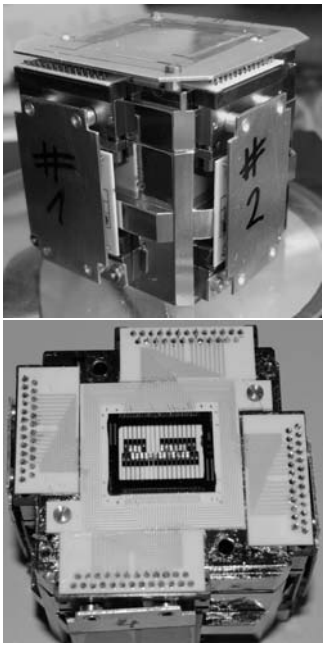

Figure 1: The upper panel displays a photograph of the new, more compact detector which was tested in 2016 at the ESR in the first campaign with uranium ions. The lower panel shows the actual microcalorimeter array without its protective aluminum cover.

* Work supported by the German Research Council under Emmy-Noether-Grant KR3721/1 and by the Ministry of Research and Education (BMBF) under grant 05P15RGFAA.

[1]BlueFors Cryogenics, Arinatie 10, 00370 Helsinki, Finland

DOI:10.15120/GR-2017-1

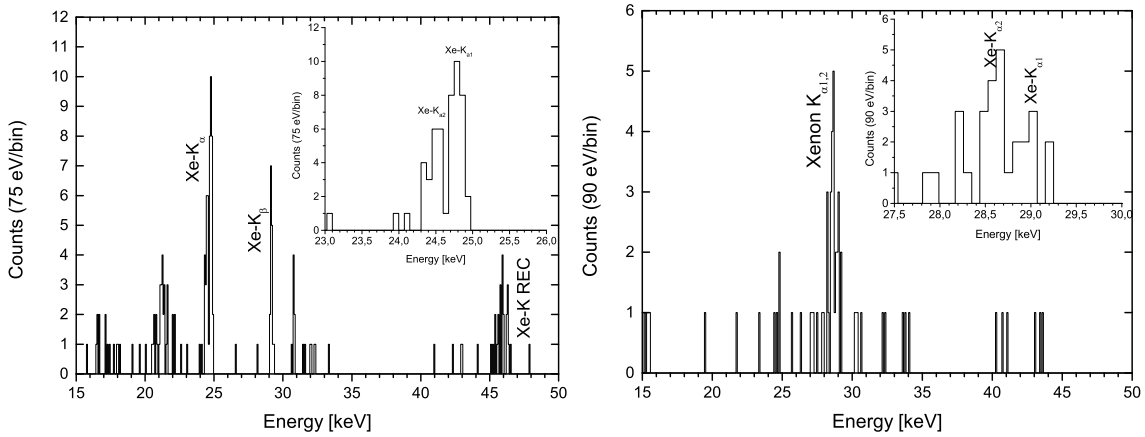

Figure 2: Left: X-ray spectrum from the interaction of a 30.85 MeV/u ($\beta \approx$25.1%c) $^{124}Xe^{54+}$ beam with a N_2 target, not corrected for the Doppler shift. The displayed spectrum was measured with one microcalorimeter pixel within 12.5 hours. The Xe-K$_{\alpha1,2}$, K$_\beta$ and K-REC could be assigned. The insert shows the region of the K lines in an amplified scale. Right: X-ray spectrum from the interaction of a 5.95 MeV/u ($\beta \approx$ 11.2%c) $^{124}Xe^{54+}$ beam with a H_2 target, not corrected for the Doppler shift. The displayed spectrum is the sum of six microcalorimeter spectra which were recorded within 22 hours. The Xe-K$_{\alpha1,2}$ can be identified in the spectrum. The K-REC is not visible because the probability for this process is low at low ion energies. The insert shows the region of the K lines in an amplified scale. These spectra were obtained with the old detector array described in [4] which was mounted in the new dry dilution refrigerator for the second measurement campaign.

While the ions cross the gas-jet, part of them may capture an electron and emit X-rays, which are detected by our microcalorimeter. The test experiment consisted of two campaigns: The first campaign provided a beam of helium-like uranium which interacted with a gas-jet of molecular nitrogen. Accordingly, X-rays from lithium-like uranium were detected. This was not optimal for our detector, because the X-ray energies were of the order of 15 keV or below, with the most prominent line at 4.5 keV. Our setup is optimized for energies around 100 keV. Accordingly, our sensitivity for these low X-ray energies is rather small. X-ray energies below 10 keV cannot pass the current windows of our cryostat. Nonetheless, we could distinguish X-rays coming from the interaction of ion beam and gas-jet, but the energy resolution was unexpectedly low. It was found that the observed signal amplitude was considerably smaller than expected. The reasons for this behavior are currently under investigation.

To investigate if the low energy resolution was only due to the low signal-to-noise ratio or if other aspects contributed as well, in the break between first and second campaign we exchanged the new detector with the old detector which had been used in former experiments [4]. In the second campaign, hydrogen-like xenon ions interacted with a gas-jet of hydrogen. This configuration in combination with a very low beam energy resulted in very small count rates, which in turn caused us to remove the calibration sources that we usually observe in parallel to the actual experiments in order to have a permanent energy calibration. This removal was possible because the cryostat maintained a very stable operation temperature over all times.

Example spectra for two different ion energies are displayed in figure 2. Despite the low count rates, we observed Lyman-α transitions from hydrogen-like xenon with energies around 30 keV as well as X-rays from direct radiative recombination into the K shell (K-REC). The energy resolution obtained was around 200 eV, which is comparable to the energy resolution obtained in past experiments [4]. Optimization and further data analysis is currently in progress. In parallel, the next-generation microcalorimeter array with 96 pixels and an active area of approximately 1 cm^2 is in preparation. We expect that this larger array with the designed performance will be available for experiments in 2018.

Acknowledgements

We thank T. Gassner, J. Glorius, P.M. Hillenbrand, Y. Litvinov and the ESR and accelerator groups of GSI for the good cooperation during the experiment.

References

[1] P. Egelhof et al., Nuclear Instruments and Methods A 370, 263 (1996)

[2] C. Stahle et al., Nuclear Instruments and Methods A 370, 173 (1996)

[3] A. Bleile et al., AIP Conference Proceedings 605, 409, (2002)

[4] S. Kraft-Bermuth et al., Journal of Physics B 50, 055603 (2017)

[5] P. Scholz et al., Journal of Low Temperature Physics 184, 576 (2016)

Recent developments for the CRYRING@ESR transverse electron target*

C. Brandau†[1,2], *A. Borovik, Jr.*[1], *B.M. Döhring*[1], *B. Ebinger*[1], *C. Kozhuharov*[2], *M. Lestinsky*[2], *T. Molkentin*[1], *A. Müller*[1], *S. Schippers*[1] *for the SPARC working group "Electron Targets"*

[1]Justus-Liebig-Universität Gießen, Germany; [2]GSI Helmholtzzentrum für Schwerionenforschung, Darmstadt, Germany

As part of the instrumentation of the upcoming storage ring CRYRING@ESR a ribbon-shaped free-electron target for atomic physics electron-ion collision studies is presently being developed and constructed [1, 2, 3, 4]. The target operates in crossed-beams collision geometry, i.e., with an interaction angle of 90° with respect to the ion beam circulating in the ring.

Within the last year, simulations for the electrode configuration were carried out. The according design is based on a multi-electrode electron gun [5, 6] originally developed for the Giessen low-energy single-pass electron-ion collision facility [7]. Yet, the present electrode layout has been substantially altered in order to adapt the electron target to the experimental environment at CRYRING@ESR. The electron gun has several advantages, among others: (i) the possibility to set the electrode potentials to a large extent independently from each other, yielding a higher flexibility in operation modes, (ii) a very homogeneous electron density (n_e) in the interaction region, (iii) minimization of angular misalignments with respect to the ion beam, (iv) clearing electrodes in order to avoid trapping of slow ions from ionization of residual gas, (v) a new decelerating collector with lower heat dissipation, (vi) a large interaction gap to provide space for the circulating ion beam, and, (vii) the realization of a high density mode with $n_e > 1 \cdot 10^9$ cm^{-3}.

In addition, the major features of the mechanical and vacuum layout have been worked-out (Fig. 1). The electron target can be fully retracted behind a gate valve and, thus, can be separated from the ring vacuum. This allows maintenance work to be carried out without breaking of the ring vacuum. A turbo pump (Pfeiffer HIPACE 300H) with high compression for light gases and a cryo pump will be used to fulfill the stringent vacuum requirements ($p \approx 10^{-11}$ mbar) of CRYRING@ESR. Two large viewing ports will provide spectroscopic access to the interaction region.

The experimental electron target station has been optimized to enable a joint installation with the gas-jet target in the experimental section YR09 (Fig. 1). The concurrent setup allows for a more flexible usage of test and experimental beam times since no vacuum-breaking changes of setups needs to be performed. Additional synergies such as for diagnosis or instrumentation or even joint experiments are currently being investigated. At present, still a few details and short-noticed changes need to be clarified. It is planned that an off-line version of the target will be available in the first half of 2018, and, depending on additional funding, the target will be available in CRYRING@ESR in 2021.

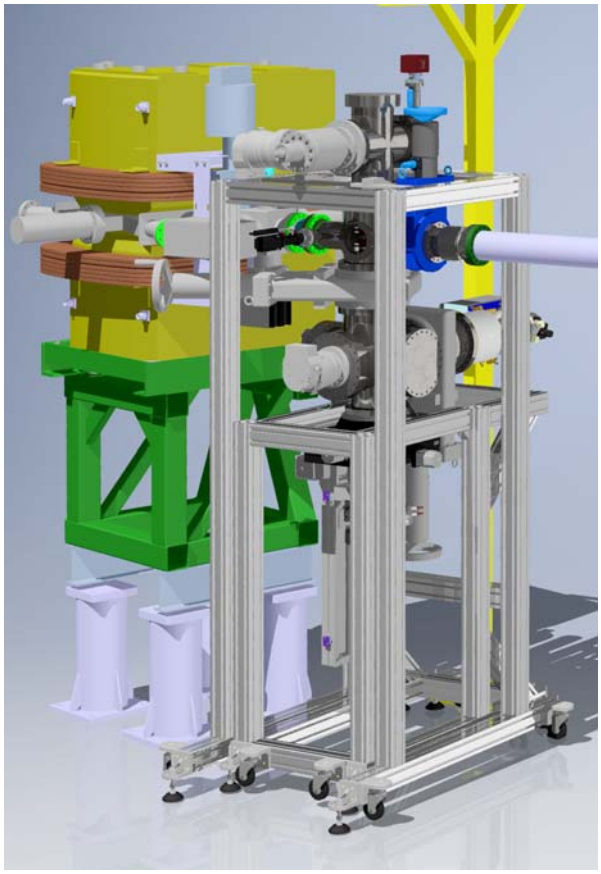

Figure 1: Transverse electron target at the beginning of the CRYRING@ESR experimental section YR09 according to the current status of planning. The set-up allows for a joint installation with the internal gas-jet target.

*Work is supported by BMBF (contract 05P15RGFAA), and by HIC for FAIR. PSP code:1.3.1.5.9

† c.brandau@gsi.de

References

[1] Z. Andelkovic et al., *Technical Design Report: Experimental Instrumentation of CRYRING@ESR*, 2015, http://www.fair-center.eu/en/en/for-users/experiments/appa/documents.html.

[2] M. Lestinsky et al., Phys. Scr. **T166** (2015), 014075.

[3] M. Lestinsky et al., Eur. Phys. J Spec. Top. **225** (2016), 797.

[4] C. Brandau et al., GSI Scientific Report 2015, p. 143.

[5] W. Shi et al., Nucl. Instrum. Meth. B **205** (2003), 201.

[6] A. Borovik Jr. et al., J. Phys.: Conf. Ser. **488** (2014), 142007.

[7] A. Müller, Adv. At. Mol. Opt. Phys. **55** (2008), 293.

DOI:10.15120/GR-2017-1

Dynamic compression of diffractograms for an improved convergence in ptychography

F. Tuitje[1,2] *and C. Spielmann*[1,2]
[1]Friedrich-Schiller-University Jena; [2]Helmholtz Institute Jena

The quality of ptychographic reconstructions mainly depends on the signal redundancy of the diffractograms. We present a method for improving diffraction images used for ptychography to enhance the convergence time and object visibility.

Dynamic compression of redundant fringes

Ptychography uses redundant data from overlapping illumination spots to overcome the isolation constraint known from classical CDI. The amount of redundant information in the diffractograms gives a criterion for quality of reconstruction and time of convergence [1].

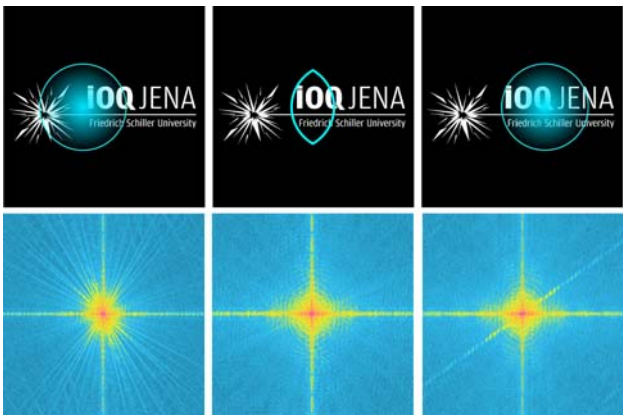

Figure 1: Different ptychographic scan positions (left and right) of an object (top) lead to varying diffractograms (bottom). The overlapping area of these two scan points (middle row) leads to a diffractogram, which consists of redundant fringes.

The usage of a Gaussian intensity profile for the illumination spot leads to lower intensities of the redundant illuminated parts of the object. Therefore the intensity of the supernumerous fringes in the fourier space decreases. We use a method called dynamic compression (DC) or tone mapping to amplify these weak information in the diffractogram. Due to the ambiguity of the diffraction pattern, it is difficult to selectively identify and amplify the redundant pattern. Because of the low intensity in the overlapping area, it is more probable to find redundant information in the weak fringes. Thus weak signals of the diffractograms getting increased with respect to high intensity fringes under usage of an adapted local gradient tone mapping operator [2] (fig. 2).

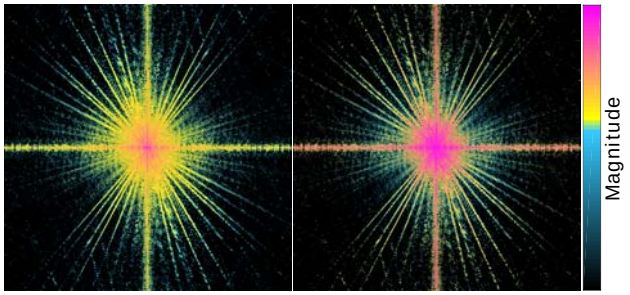

Figure 2: Dynamic compression (right) of a diffractogram (left) with background subtraction.

Ptychographic reconstruction

The ptychographic reconstruction with the ePIE-algorithm [3] of the object from fig.1 is shown in fig.3. For both reconstructions the number of iterations was fixed to 10. Whereas the object without dynamic compressed signals are barely visible, the algorithm using enhanced diffractograms was able to converge to a solution, which is more similar to the scanned object.

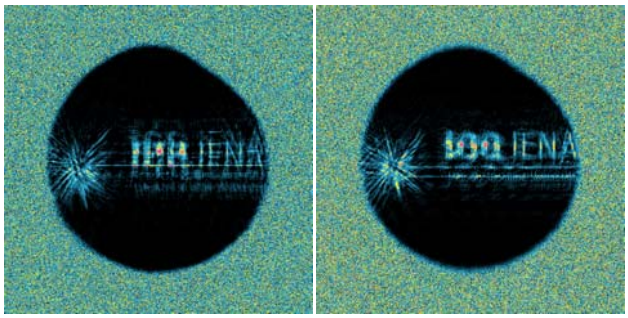

Figure 3: Reconstruction of the object shown in fig.1 without DC (left) and with DC (right).

References

[1] Fienup, J., “Phase retrieval algorithms: a comparison”, Applied Optics 21.15 (Aug. 1982), pp. 2758–2769

[2] Ok, J., Lee, C., “HDR tone mapping algorithm based on difference compression with adaptive reference values”, Journal of Visual Communication and Image Representation, Vol. 43 (February 2017), pp.61-76

[3] Maiden, A.; Rodenburg, J., “An improved ptychographical phase retrieval algorithm for diffractive imaging”, Ultramicroscopy 109.10 (Sept. 2009), pp. 1256–1262

DOI:10.15120/GR-2017-1

Online monitoring of XUV spectra from high-harmonic generation by surface reflectivity measurements with particle detectors*†

A. Hoffmann‡ [1], *C. Egelkamp*[2], *D.F.A. Winters*[3], *Th. Kühl*[3,4], *and C. Spielmann*[1,4]

[1]Institute of Optics and Quantum Electronics, Abbe Center of Photonics, Friedrich Schiller University Jena, Max-Wien-Platz 1, 07743 Jena, Germany; [2]Institut für Kernphysik, Westfälische Wilhelms Universität, Wilhelm-Klemm-Straße 9, 48149 Münster, Germany; [3]GSI Helmholtz Centre for Heavy Ion Research, Planckstrasse 1, 64291 Darmstadt, Germany; [4]Helmholtz Institute Jena, Fröbelstieg 3, 07743 Jena, Germany

We present reflection measurements of cesium iodide (CsI)-coated and uncoated steel surfaces with shaped XUV pulses. We measure the spectrally integrated signal from both surfaces and show that the ratio of the two measured signals is a sensitive probe of changes in the incident XUV spectrum. Additionally, a disagreement between the measured ratio and the calculated number can be explained by a leakage of IR radiation through one of the metal filters. This simple setup allows for the monitoring of the IR leakage and spectral stability simultaneously. The benefits of our approach are a spectrally sensitive diagnosis of the XUV radiation at the interaction place of time-resolved XUV experiments and the detection of infrared leak light though metal filters in high-harmonic generation (HHG) experiments. Our obtained results are of interest for time-resolved XUV experiments presenting an additional diagnostic directly in the interaction region and for small footprint XUV beamline diagnostics. For the experiments we

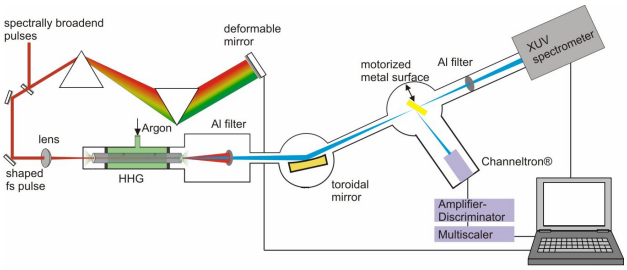

Figure 1: Experimental setup

used spectrally shaped XUV pulses from high-harmonic generation in an argon-filled capillary (Fig. 1, detailed experimental description in [1] and [2]). The XUV radiation is either directly launched into an XUV spectrometer or detected with a Channeltron after reflection from an uncoated or CsI-coated stainless steel plate. The polished surfaces were coated by a vacuum evaporation process with a 300-nm-thick layer of high purity CsI [3]. The secondary electron signal from the Channeltron is amplified, discriminated and measured by a multiscaler with sub-nanosecond resolution. From the XUV spectra (Fig. 2a) the reflectivity ratio between the two surfaces can be calculated using tabulated values [4]. A comparison with reflection measurements using a Channeltron shows agreement with less than 3% difference to the calculation (Fig. 2b), but in case of residual IR light a stronger deviation is visible (∼10%).

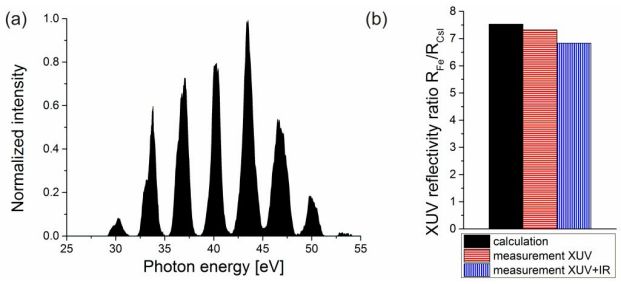

Figure 2: For an XUV spectrum (a), the reflectivity ratio between an uncoated stainless surface and a CsI-coated surface (b) can be calculated from tabulated values (black) or measured. Depending on the residual IR content in the XUV emission from HHG, a deviation from the calculation can be observed (red horizontally dashed, blue vertically dashed).

Further investigations with high-harmonics with residual IR light showed, that the Channeltron signal is sensitive to femtosecond laser light in an XUV-beam, although the Channeltron is regarded as solar blind. In the temporally resolved secondary electron signal from the Channeltron the interaction with femtosecond IR pulses can be clearly attributed to certain time windows [1].

References

[1] A. Hoffmann et al.: Online Monitoring of Laser-Generated XUV Radiation Spectra by Surface Reflectivity Measurements with Particle Detectors, Appl. Sci. 2017, 7, 70.

[2] A. Hoffmann et al.: Extremely Nonlinear Optics Using Shaped Pulses Spectrally Broadened in an Argon- or Sulfur Hexafluoride-Filled Hollow-Core Fiber, Appl. Sci. 2015, 5, 1310-1322.

[3] C. Egelkamp et al.: Detection system for forward emitted XUV photons from relativistic ion beams at ESR, GSI Scientific Report 2015 (2016)

[4] B.L. Henke et al.: X-ray interactions: photoabsorption, scattering, transmission, and reflection at E=50-30000 eV, Z=1-92, Atomic Data and Nuclear Data Tables Vol. 54 (no.2), 1993, 181-342

*Work supported by BMBF under contract numbers 05P15PMFAA and 05P15SJFFA.

† This GSI scientific report has also been published as a scientific report 2016 of the Helmholtz-Institute in Jena.

‡ andreas.hoffmann.3@uni-jena.de

DOI:10.15120/GR-2017-1

YAP:Ce-based scintillation devices for heavy ion detection within the Fit-FISIC project*

C. Hahn[†1,2], *P. Pfäfflein*[1,2], *G. Weber*[1,3], *and Th. Stöhlker*[1,2,3]

[1]Helmholtz Institute Jena, Germany; [2]FSU, Jena, Germany; [3]GSI, Darmstadt, Germany

With the advancing realization of the novel FAIR accelerator and ion storage complex, in particular the impending commencement of CRYRING operations (*FAIR Phase 0*), planned experiments such as the Franco-German Fit-FISIC project (***Fi**rst steps **t**owards atomic physics of **F**ast **I**on–**S**low **I**on **C**ollisions*, [1,2]) depend on the availability of robust ion detectors. Among the quite extensive variety of established detection methods, the use of scintillation detectors provides a solution that is both economical as well as versatile with respect to the ion energies and species accessible [3]. While common plastic scintillators usually suffer from fatal radiation damage due to the localized nature of ion energy deposition – the so-called *Bragg peak* –, crystalline substances such as YAP:Ce (cerium-doped yttrium aluminium perovskite) have been known to exhibit a significant degree of radiation hardness [4].

Commonly the readout of such scintillator detectors is accomplished with a photomultiplier tube of suitable spectral sensitivity. However, some experiments require position resolution that this approach fails to provide, e.g. to distinguish the trajectories taken by different charge states. A promising alternative is the use of so-called silicon photomultiplier (SiPM) devices. This novel detector type, sometimes called "multi-pixel photon counters", can be described as an array of parallelly connected avalanche photodiodes with a typical size of $25\,\mu\mathrm{m}$, and provides a compact, low-voltage and easily tileable readout solution. In addition, the devices' inherent high gain affords single-particle detection efficiency.

Pursuing this approach, a demonstrator setup is presently investigated at Helmholtz Institute Jena. It consists of an 8×8 assembly of square SiPM devices with an edge length of $6\,\mathrm{mm}$ each, manufactured by SensL Technologies Ltd., and readout electronics furnished by Vertilon Corporation. A dedicated breakout board allows for custom signal processing, e.g. for use in experiments where timing information is critical. The actual YAP:Ce scintillator crystal has a thickness of $1\,\mathrm{mm}$ and was manufactured by CRYTUR spol.s.r.o. It is attached to the SiPM array with an aluminium frame for easy mounting; a photograph of this detector head is reproduced as an inset in figure 1. At the scintillator's primary emission wavelength of $370\,\mu\mathrm{m}$, the photon detection efficiency of the SiPMs is on the order of a favorable 40%, on par with typical values achieved with conventional photomultiplier tubes.

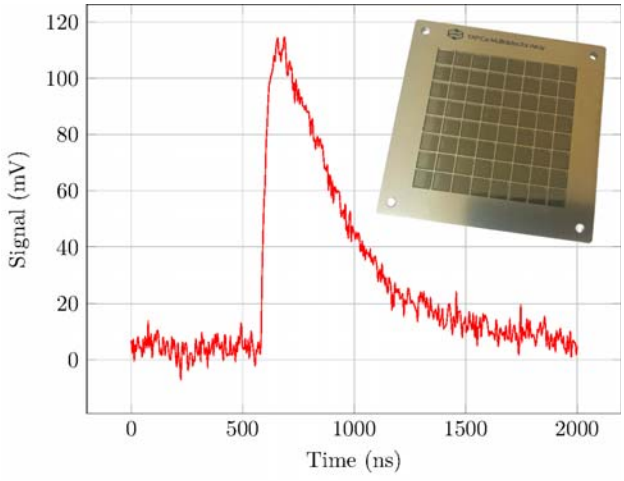

Figure 1: Oscilloscope signal from the SiPM readout of a $1\,\mathrm{mm}$-thickness YAP:Ce crystal scintillator, irradiated with $662\,\mathrm{keV}$ photons from a ^{137}Cs source. The inset shows the scintillator array bonded to the SiPM detector head, of which only the 8×8 segmentation is visible.

Figure 1 also displays the oscilloscope trace of the observed signal when the scintillator–SiPM assembly is irradiated with $662\,\mathrm{keV}$ photons from a ^{137}Cs γ source. The peak exhibits a steep rising flank with a rise time of approximately $50\,\mathrm{ns}$ (10%–90% of maximum signal). The falling flank, on the other hand, is decidedly longer, with its slope primarily determined by the quenching resistors that halt the avalanche. In any case, operation at a maximum event rate of some $100\,\mathrm{kHz}$ is obviously feasible.

Pending availability of the necessary vacuum components, a characterization measurement with ion energies of ca. $10\,\mathrm{MeV}$ is currently being set up at HI Jena.

References

[1] Fit-FISIC Collaboration, ed., "Project Fit-FISIC: Scientific Document" (2013)

[2] C. Hahn et al., "Development of ion detectors for the 1–10 MeV/u energy range", GSI Scientific Report 2014 (2015) 228

[3] W. Klamra et al., "Response of BaF_2 and YAP:Ce to heavy ions", Nucl. Instrum. and Meth. A 444 (2000) 626

[4] M. Tokman et al., "Towards a Determination of QED Effects in Cu-Like Pb Recombination Resonances Near Threshold", Phys. Scripta 2001 (2001) 406

* We gratefully acknowledge support by the DFG under grant no. STO 346/4-1. This report is also part of the Annual Report 2016, Helmholtz Institute Jena.

† christoph.hahn@uni-jena.de

Status report on a Si(Li)-Compton polarimeter of SPARC - 3D-readout of a thick double-sided Si(Li) strip detector

U. Spillmann[1], Th. Krings[4], M. Vockert[2,3], G. Weber[2], and Th. Stoehlker[1,2,3], on behalf of the SPARC collaboration

[1]GSI, Darmstadt, Germany;[2]HI Jena, Germany;[3]IOQ, FSU Jena, Germany; [4]IKP, FZ Jülich, Germany

The x-ray polarization and spectroscopy research program of the SPARC collaboration [1] at FAIR and GSI depends strongly on the performance of the available Compton polarimeter instruments within the community. During the last years we applied our Si(Li)- and Ge(i)-Compton polarimeters in several accelerator-based beam time campaigns [2,3] at GSI, DESY, ESRF, etc.. A consequent development of the detector and readout techniques led to the design and realization of our first Si(Li)-DSSD (double-sided strip detector with 1.0mm² spatial resolution) with 64 preamplifiers with a 1st-stage at cryogenic temperature. This change in readout technique improves the energy resolution to 850eV-900eV at 60keV (ground-side) and 1200eV at 60keV (HV-side) compared to 2000eV at 60keV with a readout with all parts (except the DSSD) kept at room-temperature. The improved energy resolution decreased the lower energy threshold for a reliable event reconstruction with respect to linear polarization detection of incident photons from 70keV down to 40keV. With this progress we are now able to study a huge variety of transitions in atomic systems that were not accessible for us up to now. Recently we studied, with a focus on future experiments at FAIR higher event complexities and rates, the possibilities of a reliable identification of the point of interaction within the detector crystal (z-component). The relatively simple geometry of the DSSD allows for identification of the x- and y- position by superposition of the front side and back side strips of the detector. The z-position may be measured by the time of arrival of the electron cloud (hole cloud respectively) at the strip contacts. For our 9.0mm thick Si(Li)-DSSD we measured an electron drift velocity of 37µm/ns in the depleted bulk. This result agrees well with the values known from literature. From the edges of the drift time spectrum one can derive a time resolution of 20-30ns for the measurement of the z-component. This corresponds to a measurement with a collimated photon fan beam (approx. 1mm FWHM width at the detector surface) hitting the detector at an angle of 35 degree with respect to the surface (figure 1). With the knowledge of the z-component the quality of polarization measurements can be improved with the respect to background suppression. The same is true if we turn the argument of the z-component around. The typical time coincidence resolution with a fast (typically 10ns resolution) external signal is in the order of 80-120ns due to the different path length of the charge depending on the location of the point of interaction inside the bulk. With the z-information this uncertainty in time can be reduced significantly resulting in an improved event identification efficiency.

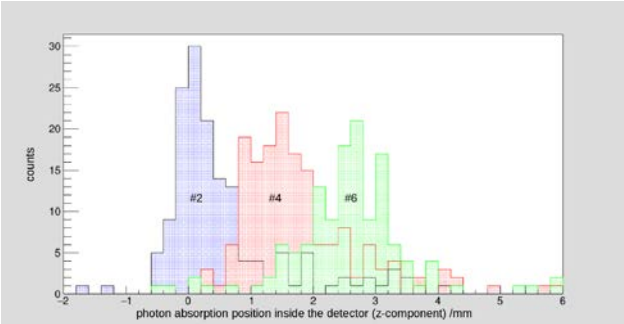

Figure 1: Photon absorption position in the bulk as function of the measured detector position (z-component, which is derived from the time of arrival differences of the charge between the backside contacts and the front side contacts #2, #4, #6)

References

[1] Technical Report of the SPARC collaboration, http://www.gsi.de/sparc

[2] R. Märtin et al., Phys. Rev. Lett. **108**, 26480 (2012)

[3] K.-H. Blumenhagen et al., New Journal of Physics **18**, 103034 (2016)

[4] M. Vockert et al., within this scientific report

Work supported by BMBF Verbundprojekt 05P2015 R&D Beschleuniger/HI Jena/GSI(ESR, SIS, UNILAC).

This report is also part of the HI Jena Annual Report 2016 (DOI:10.15120/GSI-2017-00708)

DOI:10.15120/GR-2017-1

Commissioning of a detection system for forward emitted XUV photons*

D. Winzen[†1], *M. Bussmann*[2], *A. Bußß*[1], *C. Egelkamp*[1], *L. Eidam*[3], *V. Hannen*[1], *Z. Huang*[4], *D. Kiefer*[5], *S. Klammes*[5], *Th. Kühl*[6,7,8], *M. Loeser*[2], *X. Ma*[4], *W. Nörtershäuser*[9], *H.-W. Ortjohann*[1], *R. Sánchez*[6,9], *M. Siebold*[2], *Th. Stöhlker*[6,7,10], *J. Ullmann*[7,9,10], *J. Vollbrecht*[1], *Th. Walther*[5], *H. Wang*[4], *Ch. Weinheimer*[1], *and D. Winters*[6]

[1]Institut für Kernphysik, Uni Münster; [2]Helmholtz-Zentrum Dresden-Rossendorf; [3]Institut für Theorie Elektromagnetischer Felder, TU Darmstadt; [4]Institute of Modern Physics, Chinese Academy of Sciences; [5]Institut für Angewandte Physik, TU Darmstadt; [6]GSI, Darmstadt; [7]Helmholtz-Institut Jena; [8]Institut für Physik, Uni Mainz; [9]Institut für Kernphysik, TU Darmstadt; [10]Institut für Optik und Quantenelektronik, Uni Jena

The Institut für Kernphysik in Münster has developed a system for in-vacuum detection of forward emitted fluorescence photons created in laser-spectroscopy experiments with highly-charged ions at the experimental storage ring (ESR) [1]. The detector is optimized for XUV photons in a wavelength region around 10 nm. It will be used in an anti-collinear laser-spectroscopy measurement of the $^3P_0$ – $^3P_1$ splitting in beryllium-like krypton [2]. Since ions in the ESR are stored at relativistic velocities, the emission of fluorescence photons is forward peaked due to the Lorentz boost. Therefore, the detector consists of a movable cathode plate with a central slit that can be positioned around the ion beam axis collecting mainly forward emitted photons (figure 1, left). Secondary electrons emitted from the CsI-coated cathode are guided via electric and magnetic fields provided by two solenoid coils and a system of ring electrodes to a multi-channelplate detector (MCP) placed inside the ultra-high vacuum of the ESR (10^{-11} mbar).

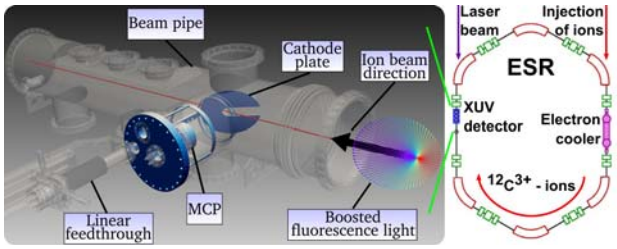

Figure 1: Left: CAD drawing of the XUV detector setup at the ESR. Right: Schematic of the laser spectroscopy setup for the test beam time conducted in summer 2016.

For tests of the pulsed laser system for laser cooling, and for commissioning of the XUV detection system, three days of ESR beam time with $^{12}C^{3+}$-ions could be used in summer 2016. In an anti-collinear laser-spectroscopy setup (figure 1, right) the $2s_{1/2} - 2p_{1/2}$- and $2s_{1/2} - 2p_{3/2}$-transitions at $\lambda \approx 155\,\mathrm{nm}$ were investigated. The ions were stored at $\beta \approx 0.47$ which results in a fluorescence wavelength Doppler shifted to approx. 93 nm. To excite the transitions, two laser systems were available: a pulsed laser system from HZDR/TU-Dresden at $257\,\mathrm{nm}$ [3], and

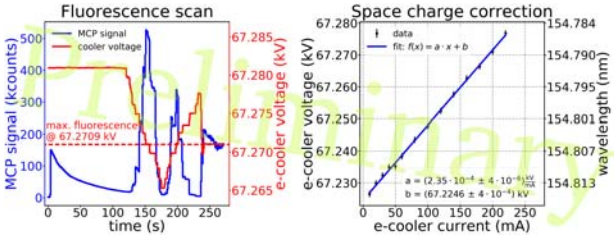

Figure 2: Preliminary analysis of the $2s_{1/2} - 2p_{3/2}$-transition in $^{12}C^{3+}$-ions. Left: MCP signal and electron cooler voltage of an exemplary fluorescence scan (for $I_{ecool} = 200\,\mathrm{mA}$). Right: Space charge correction of the electron cooler voltage.

a tunable cw laser system from TU-Darmstadt, also at $257\,\mathrm{nm}$ [4]. Each transition was measured by varying the electron cooler voltage, thus changing the velocity of the stored ions inside the ESR (exemplary measurement shown in figure 2, left). As can be seen from the MCP signal, the flurescence is clearly distinguishable from the background, despite the detector not being optimized for a wavelength region around $93\,\mathrm{nm}$. The maximum in the fluorescence yield, occurring when the ions are in resonance with the laser, was determined for different values of the electron cooler current. This way, space charge effects shifting the ion velocity, caused by the intense electron beam of the e-cooler, could be investigated systematically. A preliminary result for the $2s_{1/2} - 2p_{3/2}$-transition is shown in figure 2, right. In conclusion, the XUV detection system was successfully commissioned and both fine structure transitions in $^{12}C^{3+}$-ions could be measured. The XUV detector was found to be very sensitive to the fluorescence from the ions, but also susceptible to background coming from the ion beam and laser stray light. Therefore, background reduction methods are being investigated for a detector upgrade in prospect of a possible ESR beam time in 2018 or 2019.

References

[1] V. Hannen *et al.*, GSI Scientific Report 2015.
[2] D.F.A. Winters *et al.*, GSI Experiment E104.
[3] M. Siebold *et al.*, DOI 10.1002/lpor.201600063.
[4] T. Beck *et al.*, DOI 10.1364/OL.41.004186.

* Supported by BMBF under contract number 05P12PMFAE.987
† d.winzen@uni-muenster.de

Test beamtime for laser spectroscopy and laser cooling at the ESR

D. Winters[*1], *O. Boine-Frankenheim*[†1,2], *M. Bussmann*[3], *A. Bußmann*[4], *C. Egelkamp*[4], *L. Eidam*[2], *V. Hannen*[4], *Z. Huang*[‡5], *D. Kiefer*[2], *S. Klammes*[2], *Th. Kühl*[1,6], *M. Loeser*[3,7], *X. Ma*[‡5], *F. Nolden*[1], *W. Nörtershäuser*[2], *R. Sanchez*[1], *U. Schramm*[†3,7], *M. Siebold*[3], *P. Spiller*[1], *M. Steck*[1], *J. Ullmann*[2,6,8], *Th. Walther*[†2], *H. Wang*[‡5], *W. Wen*[‡5], *D. Winzen*[4], *and Th. Stöhlker*[1,6,8]

[1]GSI Helmholtzzentrum, Darmstadt; [2]Technische Universität Darmstadt; [3]Helmholtz-Zentrum Dresden-Rossendorf; [4]Westfälische Wilhelms-Universität Münster; [5]Institute of Modern Physics-CAS, Lanzhou, China; [6]Helmholtz Institut Jena; [7]Technische Universität Dresden; [8]Friedrich-Schiller-Universität Jena

In July 2016, during a test beamtime of 3 days, test experiments concerning laser spectroscopy and laser cooling of Li-like carbon ion beams could be performed at the ESR. The new XUV detector system (Münster university) for fluorescence measurements could be tested, as well as the new pulsed laser system (HZDR/TU Dresden) and the cw laser system (TU Darmstadt) for laser cooling of the stored and bunched ion beams. Both laser systems have been used for laser spectroscopy and laser cooling. A high-voltage divider (TU Darmstadt) was used to record the voltage of the electron cooler during laser spectroscopy measurements.

The laser system from the TU Darmstadt is a fast and broad scanning cw-laser system [1]. The system from the HZDR/TU Dresden is a pulsed laser system with a repetition rate up to 1 MHz, delivering short pulses (∼ps) [2]. The group in Münster has designed and built an XUV detector for the ESR [3]. A pure beam of up to 1 mA of carbon ions was injected into the ESR at an energy of 122 MeV/u. The $2s_{1/2} - 2p_{1/2,3/2}$ transitions in these Li-like carbon ions have a wavelength around 155 nm and can, due to the Doppler boost at the ion velocity $\beta = v/c = 0.47$, be excited by the 257 nm laser systems.

During the first part of the test beamtime, we focussed on tests of the XUV detector system. Firstly, the system was able to move *in* and *out* of the beam without disturbing it. Secondly, the voltages and magnetic field were applied and the fluorescence from the laser-excited ions was seen. Thirdly, the *resonance* (=transition frequency) was sought by searching for the maximum in the fluorescence whilst scanning the high-voltage from the ESR electron cooler in the smallest steps over the expected value. A typical result, for a fixed value of the electron cooler current, is shown in figure 1. Here, time is plotted vertically, the (189^{th} harmonic of the) ion revolution frequency horizontally, and the Schottky power density of the signal in color. This scan was performed for many different values of the electron cooler current to account for space charge effects (see [3]). This way, both transitions in carbon have been determined precisely. The data analysis is still ongoing.

The second part of the test beam time concentrated on laser cooling using the cw laser, and especially the pulsed laser. The ion beam was moderately bunched (10-15 bunches) by the exciter. In figure 2, using the cw laser,

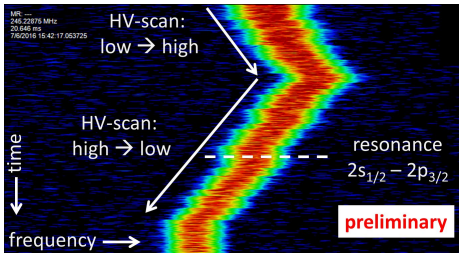

Figure 1: Schottky image of a stored C^{3+} ion beam. The high-voltage of the electron cooler is changed over the resonance condition. At resonance (dotted line), the ions have the correct velocity and are excited [3]. [Preliminary]

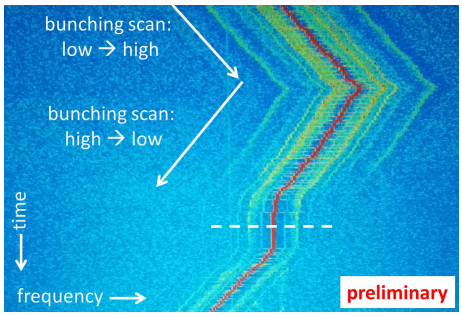

Figure 2: Schottky image of a stored C^{3+} ion beam. The bunching frequency was changed to search for the laser cooling condition. The dotted line indicates the possible point for a proper bunching frequency. [Preliminary]

it can be seen that the ion velocity changes as the bunching frequency is being varied. At the optimal point, the many sidebands around the central line (red) should vanish, indicating that the amplitudes of the synchrotron oscillations are very small. In contrast to the beamtime in 2012, no laser cooling could be observed in 2016, mainly due to time contraints. The data is still under analysis. However, for the first time, a clear interaction of the ion beam and the pulsed laser has been observed. This important result motivates further studies with pulsed laser systems.

References

[1] T. Beck *et al.*, DIO 10.1364/OL.41.004186

[2] M. Siebold *et al.*, DOI 10.1002/lpor.201600063

[3] D. Winzen *et al.*, GSI scientific report 2016.

* d.winters@gsi.de

† Work supported by BMBF.

‡ Work supported by BMBF-WTZ.

DOI:10.15120/GR-2017-1

Recent Work on the Darmstadt laser systems for laser cooling of relativistic ion beams at SIS100*

D. Kiefer[1], *S. Klammes*[1], *B. Rein*[1], *and T. Walther*[1]
[1]Institute of Applied Physics, TU-Darmstadt, Darmstadt, Germany

We are developing two laser systems for laser cooling of highly relativistic ion beams at the SIS100. The first is a continuous wave system with fast and broad tuning capabilities, the second is a pulsed system with variable pulse duration and a high repetition rate. In this contribution we discuss recent progress in the development of these systems.

Laser cooling of relativistic ion beams was successfully demonstrated at the ESR during beam times in 2004, 2006 and 2012 [1]. With this technique a relative longitudinal momentum spread of less than $\Delta p/p = 10^{-6}$ was achieved [2]. It was shown that intra beam scattering is a potential source of heating [3]. Simultaneous cooling with cw and pulsed lasers is a possible solution to overcome this limitation and will be implemented as the sole source of beam cooling at the SIS100 of FAIR.

The cw laser system was described in detail in a recent publication [6]. In brief, we use the radiation from an external cavity diode laser (ECDL), amplify it in a fiber amplifier and then use two build-up cavities in order to convert the IR radiation into the UV range using LBO and BBO crystals, respectively. A second ECDL locked to a wavemeter is employed to off-set lock the first and guarantee smooth and fast tuning. While the performance of the system during the beamtimes in 2012 and 2016 was very reliable, the system employs several locking and control circuits in order to operate. Therefore, a goal has been in our recent work to simplify the setup.

In light of this goal we have improved upon the performace of the fiber amplifier and replaced the first build-up cavity by a single pass configuration using a periodically poled $LiNbO_3$ crystal (PPLN). Overall efficiency was lower than in the previous setup. However, we managed to generate up to 2.4 W of green radiation at 514 nm compared to 5 W in the previous setup. We need to reduce the green power entering the second cavity in order not to exceed the damage threshold of the BBO crystal. The tuning capabilities are slightly narrower due to the limited temperature acceptance of PPLN, but for a combined cw-pulsed laser cooling this is not an issue.

Our pulsed system has the capability of generating pulses between 70 and 740 ps. The basic laser system was introduced in [4]. We showed that the generated pulses are nearly Fourier transform limited [5]. The entire system consists of an ECDL with several fiber amplifiers in series. After the first fiber amplifier, the pulses are generated with an electro-optic modulator from the cw radiation. In the consecutive stages the pulses are amplified.

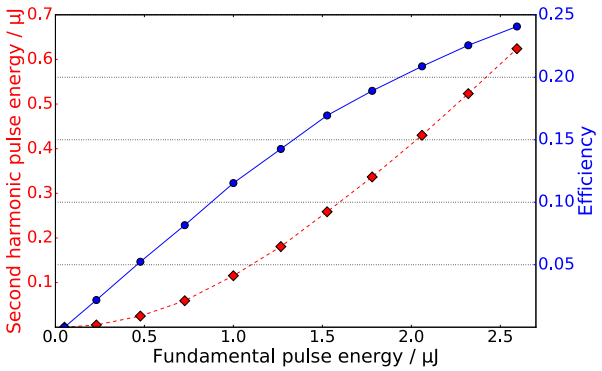

Figure 1: Second harmonic pulse energies (diamonds) and conversion efficiencies (circles) versus fundamental pulse energies.

We focussed on increasing the output energy of the pulses while maintaining the spectral properties. To this end we have increased the efficiency of the first pulsed stage and added a second. Currently, our pulses have an energy of up to 2.6 μJ depending on the pulse duration. In a first test of the second harmonic generation of the pulses we obtained conversion efficiencies exceeding 20 % (cf. fig. 1). Outgoing from that first test we anticipate that a third pulsed amplifier stage is necessary in order to fulfill the requirements.

References

[1] D. Winters et al, "Laser cooling of stored relativistic C^{3+} ions at the ESR", GSI Scientific Report 2013

[2] T. Beck, B. Rein and Th. Walther, "An all solid-state based laser system for laser cooling of relativistic ion beams", GSI Scientific Report 2013

[3] S. N. Atutov et al, "White-light Laser Cooling of a Fast Stored Ion Beam", Phys. Rev. Lett. 80 (1998) 2129

[4] T. Beck and Th. Walther, "A flexible pulsed ps/ns laser system for ion beam cooling at the ESR/SIS100", GSI Scientific Report 2014

[5] D. Kiefer, T. Beck and Th. Walther, "Flexible Picosecond Master Oscillator Fiber Amplifier System for Ion Beam Laser Cooling at ESR/SIS100", GSI Scientific Report 2015

[6] T. Beck, B. Rein, F. Sörensen, and Th. Walther, "Solid-state-based laser system as a replacement for Ar^+ lasers", Opt. Lett. 41, 4186-4189 (2016)

* Work supported by BMBF Grant No. 05P12RDRB2

S-EBIT facility: status report*

S. Trotsenko[1,2], N. Bauer[3], A. Gumberidze[3,4], G. Vorobjev[3], D. Racano[3], C. Kozhuharov[3], F. Herfurth[3], R. Schuch[5], and Th. Stöhlker[1,2,3,4]

[1]Friedrich-Schiller-Universität Jena, D-07743 Jena, Germany; [2]Helmholtz-Institut Jena, D-07743 Jena, Germany; [3]GSI Helmholtzzentrum für Schwerionenforschung, D-64291 Darmstadt, Germany; [4]ExtreMe Matter Institute EMMI, GSI, D-64291 Darmstadt, Germany; [5]Department of Physics, Stockholm University, SE-10691 Stockholm, Sweden

S-EBIT [1] facility currently installed at GSI shall facilitate research and development works for SPARC experiments at FAIR. This accelerator-independent source of HCI shall provide ions necessary for R&D of HITRAP [2] experimental stations and serve as a standalone device for research and R&D activities (e.g. development of x-ray spectrometers, calorimeter detectors, x-ray optics etc. [3]). Furthermore, the combination of S-EBIT with the available laser infrastructure e.g. JETI200 will be a unique platform for the study of highly charged ions subject to intense laser radiation [4]. During the FAIR construction related shutdown period of the GSI accelerator complex, when little to no beam time can be provided, such an accelerator-independent source of ions is of particular importance (Fig. 1).

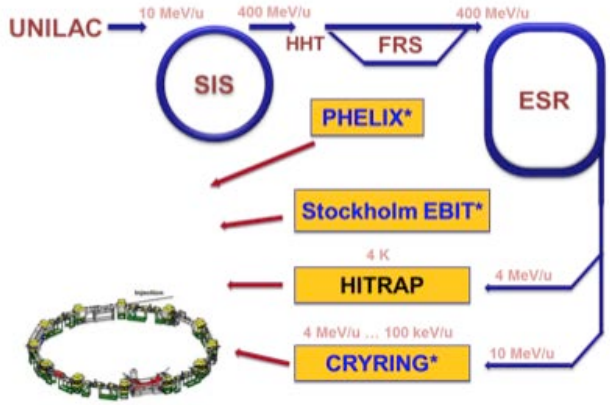

Figure 1: *Schematic of interrelated experimental arrangements (for description compare text).*

The EBIT-I of the S-EBIT facility [5] has been succsessfully commissioned at the Helmholtz Institute Jena/GSI and can be stably operated. This EBIT is equipped with a few windows providing line of sight to the middle drift tube (trap) region at an angle of 90◦ with respect to the electron beam axis. On one of the windows a gas injection is realized in a colimated differentially pumped drift region, which is providing an atomic beam that is pointed directly on the electron beam. A buffer volume of the gas injection can be filled by a leak valve and/or a pulsed valve allowing for mixing a cooling gas. The trap pressure during the continuous gas injection is lower than 10^{-10} mbar. Another port, equiped with a Be-window, was used in ordert to characterize the EBIT by recording spectra of the x-rays emitted from interactions between the ions and electrons inside the trap region. A Si-pin diode detector (Amptek XR-100CR) with a measured resolution of about 300 eV at 10 keV was used for these measurements.

A typical x-ray spectrum with Xe and Ar injection is shown in figure 2 with the relevant peaks labeled. The spectrum was taken with the electron beam of a 10kV energy (and a current of 30 mA), which was compressed by 1 Tesla magnetic field provided by the superconducting coils. The Ar-K and Xe-L peaks can be seen along with the peaks due to radiative recombination (RR) into the xenon L-, M- etc shells.

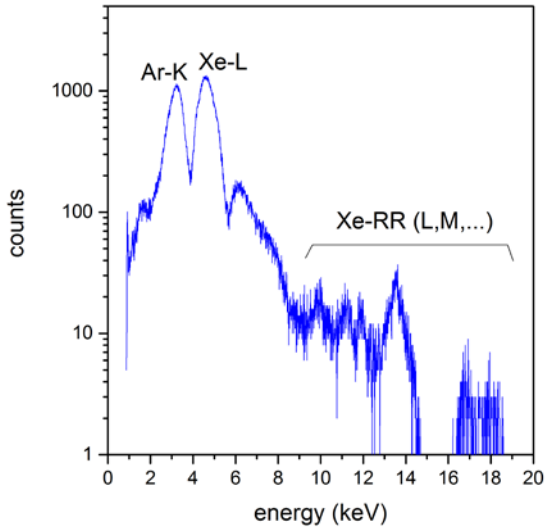

Figure 2: *X-ray spectrum of Xe and Ar from the EBIT-I (for description compare text).*

Currently a fast multi-parameter data acquisition system is being prepared for the future x-ray measurements that will combine the EBIT with a dedicated Si(Li) detector as well as with novel techniques based on combination of crystal- and microcalorimeter-spectroscopy up to the hard x-ray regime [3]. Moreover, a time-resolved x-ray measurements is being prepared, which is necessary for a characterization of the charge breeding process. This along with the time of flight (and/or magnet scan) for the evaluation of the charge state distribution of extracted ions is also vital for the experiments where the EBIT can serve as a source of ions, e.g. HITRAP, CRYRING.

References

[1] R. Schuch et al., JINST5, C12018 (2010)
[2] F. Herfurth et al., Phys. Scr. T166, 014065 (2015)
[3] D. Hengstler et al., Phys. Scr. T166, 014054 (2015)
[4] M. Vogel et al., Nucl. Instr. Meth. B 285, 65 (2012)
[5] S. Trotsenko et al., HIJ/GSI Sci. Rep. 2015 (2016)

**Also a part of the HI-Jena Scientific Report 2016*

DOI:10.15120/GR-2017-1

Ionoacoustic monitoring of high energetic ions at SIS-18*

S. Lehrack[1], *W. Assmann*[1], *K. Parodi*[†1], *M. Bender*[2], *D. Severin*[2], *and C. Trautmann*[2]
[1]Lehrstuhl für medizinische Physik, Garching b. München, Germany; [2]GSI, Darmstadt, Germany

As heavy ions are stopped in water, their energy is distributed in the form of the well-know Bragg curve. For a short pulse width, this can be considered a spatially confined, adiabatic heating, and the resulting temperature gradient results in a pressure wave containing temporal and spatial information about the beam puls. It has been shown before, that this signal is the spatial derivative of the energy distribution. Usually studied in the context of medical physics as an in-vivo range determination[1-3], in this work the feasibility of an ionoacoustic detector for high energetic ions has been investigated with ^{238}Ur, ^{124}Xe, and ^{12}C at various energies and intensities.
A lead-zirconate-titanate crystal (PZT) ultrasound transducer (Videoscan, Olympus) was placed in a water basin axial to the beam facing a kapton entrance window. The transducer was positioned by a 3-dimensional motorized stage. After an amplification of 60 dB, the signals were acquired by a digital oscilloscope. With this rather high amplification, we were able to measure beam intensities down to 200 uranium ions, 5000 xenon ions, and 3×10^7 carbon ions per single pulse. The data acquisition was triggered by an accelerator "beam-on" signal (SIS18 extraction kicker). A typical waveform is shown in figure 1. The signal can be separated in 3 distinct parts deriving from different source locations. A *direct signal*, which is the pressure directly from the distal Bragg peak front. Also, a *reflection signal* being the reflection of the pre-distal part of the Bragg peak at the entrance window. Between those two is a *window signal*, which is resulting from the temperature gradient at the interface between water and the entrance window. With this identification of the signal, the time differences between those signals multiplied by the speed of sound in water (1.488 mm/μs at 22 °C) is the range in water. For a correct value of the speed of sound and density of the water, its temperature was measured during every shot. As a comparison value, we calculated the expected range of the used ions in water from a GEANT4 simulation including all used parts in the beam path.
As an example, selected results of all used ion types at 300 MeV/u for uranium and xenon and 180 MeV/u for carbon are displayed in table 1. The measured data is very stable in time as indicated by the low standard variation σ, providing a sub-millimeter-precise measurement of the range over several shots. For all used energies and ion types, we are in good agreement with the simulated ranges. The evaluation is ongoing and sophisticated methods to exploit the rich frequency content of the signals are being developed. With this further understanding, an ionoacoustic detector can be a simple, fast, and precise monitor for high energy ions even at high beam intensity, since this method is not suffering from e.g. EMP or pile-up effects as seen in standard particle detectors.

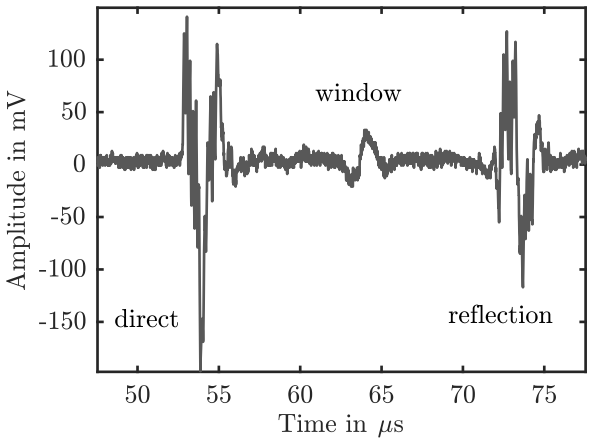

Figure 1: Example waveform measured at a uranium beam with 300 MeV/u and about 200 particles per pulse. The distinct parts of the signal are indicated (see text).

Ion type	Simulated range in mm	Ionoacoustic range in mm	σ in μm
Uranium	14.28	14.43	74.5
Xenon	21.00	21.12	8.4
Carbon	70.43	71.03	7.7

Table 1: Results from ionoacoustic range measurements. The given ionoacoustic value is half of the time difference between direct and reflection signal multiplied with the proper speed of sound in water. The used energies were 300 MeV/u for uranium and xenon, and 180 MeV/u for carbon. The standard variation of the measured ranges are fitted to a normal distribution and are given as σ.

References

[1] K. Parodi and W. Assmann, "Ionoacoustics: A new direct method for range verification," *Modern Physics Letters A*, vol. 30, no. 17, p. 1540025, 2015.

[2] W. Assmann et al, "Ionoacoustic characterization of the proton Bragg peak with submillimeter accuracy," *Medical physics*, vol. 42, no. 2, pp. 567–574, 2015.

[3] S. Kellnberger et al, "Ionoacoustic tomography of the proton Bragg peak in combination with ultrasound and optoacoustic imaging," *Scientific Reports*, vol. 6, p. 29305, 2016.

* Work funded by DFG Cluster of Excellence Munich Centre for Advanced Photonics (MAP). We thank the GSI beam instrumentation group.
† katia.parodi@physik.lmu.de

Radioresistance of nucleobases to cosmic rays*

Gabriel S. Vignoli Muniz[1], A. N. Agnihotri[1], B. Augé[1], M. Bender[2], Ph. Boduch[1], A. Domaracka[1], C. Mejía[1,3], R. Martinez[1,4], H. Rothard[1,#] D. Severin[2], C. Trautmann[2,5]

[1]CIMAP-CIRIL-Ganil, Caen, France; [2]GSI, Darmstadt, Germany; [3]Universidad de Cuenca, Cuenca, Ecuador; [4]Universidade Federal do Amapá, Macapa, Brasil; [5]TU Darmstadt, Germany

Introduction and Experiment

Complex organic molecules (COMs) have been observed in space, e.g., in interstellar clouds or Solar system objects such as comets. They can be synthesized following irradiation of ice layers on grains at low temperature by cosmic rays or Solar wind [1]. Organic matter is constantly delivered to earth from space (micrometeorites) and thus may have contributed to the emergence of life. It is thus of great interest to study the radiation resistance of COMs in order to determine their survival times in space.

In this project, we studied the radiolysis of nucleobases (adenine, cytosine, thymine, guanine) in solid phase at low temperature exposed to swift heavy ion beams. This allows us to simulate in the laboratory cosmic ray irradiation of COMs in space. The destruction of the initial molecules and the appearance of radiolytic products were monitored by in situ infrared absorption spectroscopy. Experiments were performed with 190-MeV Ca beams at the M-Branch of UNILAC as described in [2,3].

Radioresitance of Adenine

As shown in [1-3], the apparent disappearance cross sections σ_d can be determined from the fluence dependence of molecular column densities. An important information, needed e.g. for estimating life times of molecules exposed to cosmic rays in space, is the dependence of the cross sections on the amount of deposited energy, as shown in Figure 1 for adenine. The cross sections are found to follow a power law as a function of the electronic stopping power, $\sigma_d \sim S_e^n$ with n = 1.17.

With this information, taking into account the flux distribution of cosmic rays, the half life time of molecules can be estimated [1, 3]. Deep inside a dense molecular cloud, where primary UV radiation cannot penetrate and only secondary UV photons induced by cosmic rays are present, the survival time of adenine exposed to cosmic rays would be of the order of 10 million years [3].

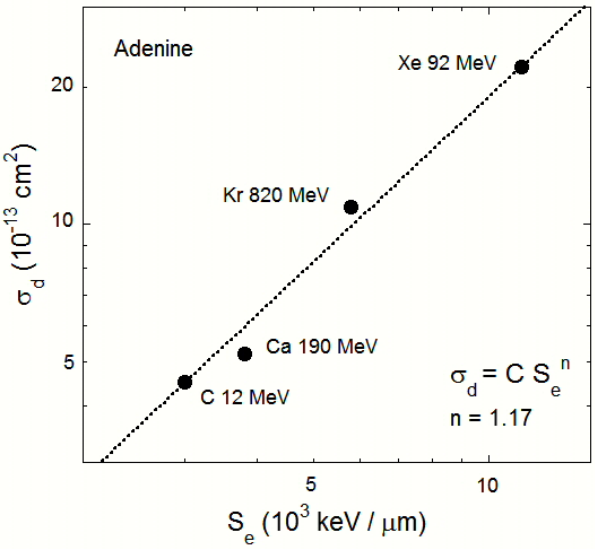

Figure 1: Cross section for disappearance of adenine as a function of electronic energy loss.

10 Mys is comparable to the lifetime of such molecular clouds. Therefore, it seems likely that adenine could survive in those "nurseries" of star formation. However, in the outer regions of dense clouds, photolysis by UV radiation is dominant. A further interesting finding is that a water layer on top of the adenine sample does not significantly reduce or enhance the radiosensitivity [3].

References

[1] H. Rothard, A. Domaracka, P. Boduch, M. Palumbo, G. Strazzulla, E.F. da Silveira, E. Dartois, J. Phys. B: At. Mol. Opt. Phys. 50 (2017) 062001

[2] C. Mejía, M. Bender, D. Severin, C. Trautmann, Ph. Boduch, V. Bordalo, A. Domaracka, X.Y. Lv, R. Martinez, H. Rothard, Nucl. Instrum. Meth. B365 (2015) 477

[3] G.S. Vignoli Muniz, C.F. Mejía, R. Martinez, B. Auge, H. Rothard, A. Domaracka, P. Boduch, Astrobiology 17 (2017) 298

*This work was supported by Brazilian agencies CNPq (INEspaço and Science without Borders) and FAPERJ, the CAPES-COFECUB French-Brazilian exchange program, the European Commission, FP7 for RTD Capacities Programme (Contract No. 262010, ENSAR), and the EU's Horizon 2020 Research and Innovation Programm (grant No. 654002 ENSAR2)

rothard@ganil.fre

DOI:10.15120/GR-2017-1

Role of composition, bond covalency, and short-range order in the disordering of stannate pyrochlores by swift heavy ion irradiation*

C.L. Tracy[1,#], C. Trautmann[2,3], F. Zhang[4], S. Park[1], R.C. Ewing[1], J. Shamblin[5], M. Lang[5]
[1]Stanford University, Stanford, CA 94305, USA; [2]GSI, Darmstadt, Germany; [3] Technische Universität Darmstadt, Darmstadt, Germany; [4]ORNL, Oak Ridge, TN 37831, USA; [5]University of Tennessee, Knoxville, TN 37996, USA

$A_2B_2O_7$ materials with the pyrochlore structure exhibit complex order-disorder transformations in response to irradiation with swift heavy ions. Either an amorphous phase, a defect-rich fluorite-structured phase, or a mixture of both form within individual ion tracks. The propensity of a material to amorphize or to adopt the fluorite structure is typically attributed to the ratio of its cation ionic radii, r_A/r_B. To date, most work has focused on the zirconate and titanate pyrochlores (B = Zr, Ti), due to their widely differing ionic radii. However, both elements exhibit similar ionic bonding. Thus, the role of bond covalency on the radiation responses of pyrochlore materials remains unclear.

To elucidate this role of B-O bond covalency, various stannate pyrochlores (A = Y, Nd, Sm, Gd, Er, Yb; B = Sn) were irradiated with 2.2 GeV Au ions, as the Sn-O bond is highly covalent. The resulting structure changes were characterized by transmission electron microscopy (TEM), x-ray diffraction (XRD), and Raman spectroscopy [1].

Atomic structure in the ion tracks

TEM images showed continuous cylindrical tracks for all compounds. XRD revealed the loss of the pyrochlore structure with increasing ion fluence and the accumulation of amorphous or fluorite material, indicated by attenuation of the initial diffraction peaks and the growth of new peaks corresponding to the latter two phases.

The rate at which these new phases accumulate, as a function of ion fluence, is proportional to the fraction of each phase produced within an ion track. Because the cylindrical tracks are nearly homogeneous in the axial direction, these phase fractions can be expressed in terms of the cross-sectional areas of a single track that are transformed to each phase. Assuming that track formation occurs by amorphization following ion impact and subsequent recrystallization of the fluorite phase at the amorphous/crystalline interface, the following expression was developed:

$$f_A(\Phi) = \frac{1 - e^{-\sigma_A \Phi + \sigma_D \Phi}}{1 - \left(\frac{\sigma_D}{\sigma_A}\right) e^{-\sigma_A \Phi + \sigma_D \Phi}} \quad (1)$$

where f_A is the amorphous phase fraction, Φ is the ion fluence, and σ_D and σ_A are the cross-sectional areas for the defect-rich fluorite and amorphous phases, respectively. Fits of equation 1 to the phase fractions obtained from the XRD data are illustrated in Figure 1.

A clear dependence of the extent of amorphization on r_A/r_B is observed. The rate of amorphization in the stannates is less than that of similar titanates [2], which have larger r_A/r_B values and less covalent bonding. This confirms that the pyrochlore radiation response is governed largely by the ionic radius ratio, rather than the bond type.

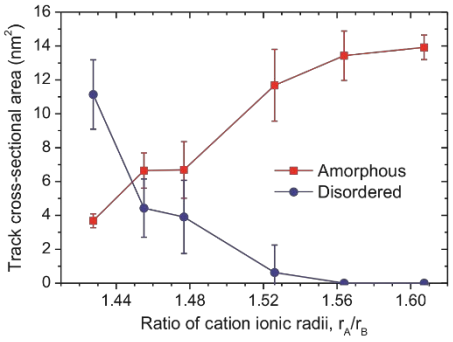

Figure 1: Cross-sectional areas of the amorphous and defect-rich fluorite regions as a function of r_A/r_B.

Local ordering in the irradiated region

The initial Raman spectra of these materials correspond to pyrochlore structures, but they are modified by irradiation. At high ion fluence the spectra of all compounds become nearly identical(Figure 2), although the XRD results indicate different long-range structures. These results agree with recent study of the local structures of irradiated pyrochlores, which indicated short-range weberite-type ordering in those disordered to the fluorite long-range structure [3]. The spectra shown here are consistent with weberite-type local ordering. These results show that this local order is present not only in pyrochlores disordered to the fluorite structure, but also those that have been fully amorphized.

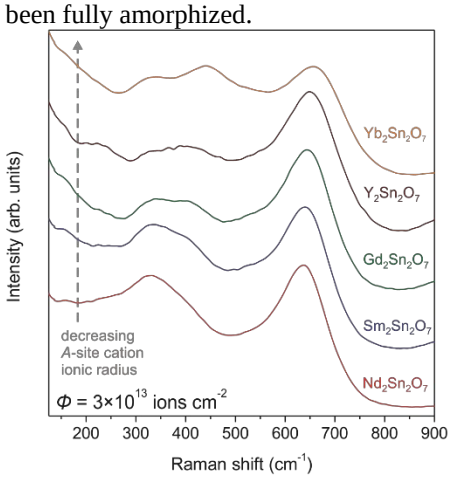

Figure 2: Raman spectra of irradiated pyrochlores.

[1] C.L. Tracy *et al.*, Phys. Rev. B 94 (2016), 064102
[2] J. Shamblin *et al.*, Acta Mater. 117 (2016), 207
[3] J. Shamblin *et al.*, Nat. Mater. 15 (2016), 507

* Work supported by US DOE, BES grant No. De-SC0001089.
#cltracy@stanford.edu

Swift-heavy ion irradiation and annealing of A_2TiO_5 (A = Nd, Gd, and Yb)

Sulgiye Park[1], Cameron L.Tracy[1], Fuxiang Zhang[2], Raul I. Palomares[3], Changyong Park[4], Christina Trautmann[6], Maik Lang[3,#], Wendy L. Mao[1], Rodney C. Ewing[1]

[1] Department of Geological Sciences, Stanford University, Stanford, CA 94305-2115, USA; [2] Materials Science and Technology Division, Oak Ridge National Laboratory, Oak Ridge, TN 37831, USA; [3] Department of Nuclear Engineering, University of Tennessee, Knoxville, TN 37996, USA; [4] (HPCAT), Geophysical Laboratory, Carnegie Institution of Washington, Argonne, IL 60439, US; [5] GSI Darmstadt & Technische Universitat Darmstadt, Germany.

The structural responses of A_2BO_5 (A = Nd, Gd, and Yb; B = Ti) compositions irradiated with 2.2-GeV Au ions were investigated using transmission electron microscopy (TEM), synchrotron X-ray diffraction (XRD) and Raman spectroscopy. The extent of irradiation-induced amorphization of three titanate compositions is shown to depend on the size of the A-site cation, with smaller lanthanides leading to a lower susceptibility to the accumulation of radiation damage (Fig. 1) [1].

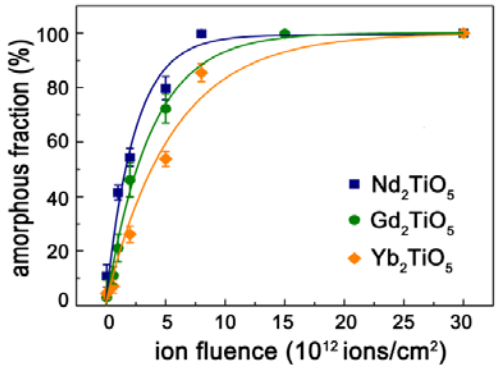

Fig. 1: Calculated amorphous phase fractions as a function of fluence for three compositions. The lines represent the fit of the data to a direct impact model (Eq. 1: $f_A(\Phi) = (1 - e^{-\sigma\Phi})$). Error bars were derived from repeated deconvolutions of the XRD patterns.

In the track-overlapping regime, complete amorphization occurs in all three compounds, despite the ability of Yb_2TiO_5 to incorporate a great deal of structural disorder into its initial defect-fluorite structure (*Fm-3m*). The reduced stability of Yb_2TiO_5 (as compared with $A_2B_2O_7$-type compounds with similar structure) is attributed to the high cation stoichiometric ratio (A:B = 2:1), which results in a local distortion due to random arrangements of the dissimilarly-sized cations, as well as different defect energetics from the difficulty in fitting a large Yb in a small Ti site. Such stuffing of A-site cations causes the material to exhibit a defect-fluorite periodicity on a long-range, but a pyrochlore-like local ordering, which inherently leads to a lowered susceptibility to radiation damage. The morphology of the ion track, as observed from TEM indicates a disordered crystalline phase without a distinct core-shell structure (Fig. 2).

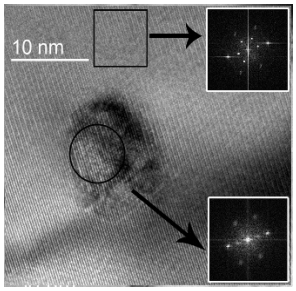

Fig. 2: HRTEM image of cross section of single ion track revealing the heterogeneous damage morphology of Yb_2TiO_5. The insets represent the FFT analysis of the in-track and surrounding matrix phases.

Fully-amorphized samples were then isochronally heated at temperature intervals from 100 to 850°C. XRD analysis indicated a consistent damage recovery in Nd_2TiO_5 and Gd_2TiO_5, where both compositions recover their original structures (*Pnma)*, with the degree of recrystallization being more efficient for the material that was more easily amorphized under ion irradiation. In contrast to the orthorhombic A_2TiO_5, Yb_2TiO_5 exhibited recrystallization of a metastable, non-equilibrium orthorhombic phase prior to a transformation to the stable defect-fluorite phase. The multi-phase transition pathway can be attributed to the fact that the transition from the amorphous to the orthorhombic phase requires a lower activation energy than would the immediate formation of the stable defect-fluorite phase, due to fewer topological constraints from the smaller degree of atomic connectivity of the orthorhombic structure.

[1] S.G.Y. Park, C. L. Tracy, F.X. Zhang, R. I. Palomares, C.Y. Park, C. Trautmann, M. Lang, W. L. Mao, R. C. Ewing, to be submitted (2017).

* Work supported by US DOE, BES grant No. DE-SC0001089
#mlang2@utk.edu

DOI:10.15120/GR-2017-1

Thermal defect annealing of swift heavy ion irradiated ThO_2*

R.I. Palomares[1], C.L. Tracy[2], J. Neuefeind[3], R.C. Ewing[2], C. Trautmann[4,5], M. Lang[1,#]
[1]University of Tennessee, Knoxville, TN 37996, U.S.A.; [2]Stanford University, Stanford, CA 94305, U.S.A.; [3]Spallation Neutron Source, Oak Ridge National Laboratory, Oak Ridge, TN, 37831, U.S.A.; [4]GSI, Darmstadt, Germany; [5]Technische Universität Darmstadt, Darmstadt, Germany, 64287

ThO_2 has been proposed as a nuclear fuel alternative to UO_2 in which ^{232}Th breeds fissile ^{233}U. Thorium-based fuels offer several advantages over conventional uranium-based fuels, such as high chemical durability and improved thermophysical properties. Despite the international interest in ThO_2-based fuels, there exist few data regarding the structural stability of ThO_2 under extreme conditions encountered in a reactor core environment. In this study, the effects of dense electronic excitation from 2-GeV Au ion irradiation were investigated in order to simulate the electronic energy loss component from fission-fragment irradiation and elucidate the high-temperature stability of irradiation-induced defects [1].

A compacted powder sample of microcrystalline ThO_2 was irradiated to a fluence of 1×10^{13} ions/cm^2 with 2-GeV Au ions at the X0 beamline of the UNILAC at GSI. ThO_2 is non-amorphizable and does not undergo any phase transformations under swift heavy ion irradiation; therefore, local probe techniques were applied to characterize ion-induced structural disorder caused by point defects. The ion-irradiated sample was characterized using neutron total scattering and Raman spectroscopy as a function of isochronal annealing temperature.

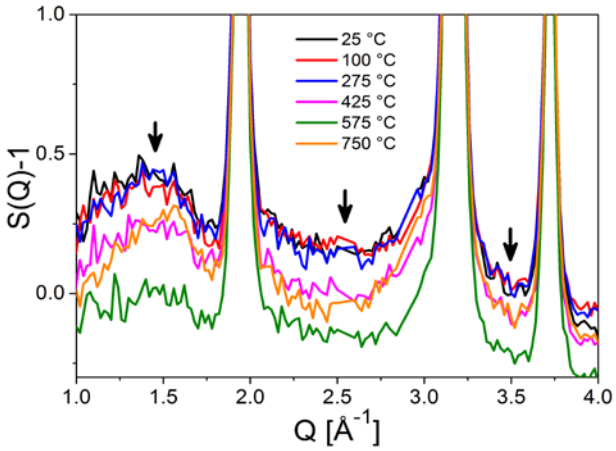

Figure 1: Total scattering function of irradiated ThO_2 after annealing at different temperatures

Neutron total scattering yields information from both Bragg and diffuse scattering. The Bragg contribution was characterized by Rietveld analysis of neutron diffraction and gave information about the crystalline fraction of the material. The diffuse signal represents the atomic disorder in the system. In order to characterize the disorder and defects that were produced in the irradiated sample, the level of diffuse scattering was monitored. Figure 1 shows the level of diffuse scattering, as indicated by the arrows, after heating the irradiated sample to different temperatures for 20 minutes.

The diffuse scattering and shift in peaks in the diffraction patterns (not shown) demonstrated that a significant annealing event occurred after heating to 425 °C. Using Raman spectroscopy, which is sensitive to the CeO_8 polyhedra coordination environment, it was shown that the abrupt drop in diffuse scattering level is concomitant with a shift in the T_{2g} Raman mode (see Figure 2 inset). Therefore, the structural change occurring between ~300–400 °C is attributed to the annealing of small oxygen-interstitial-type defects.

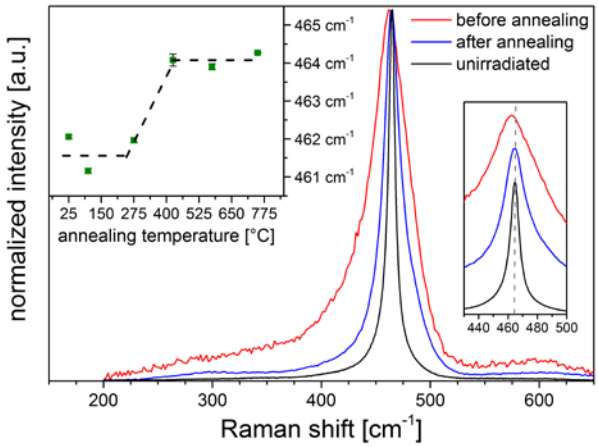

Figure 1: Raman spectra of irradiated ThO_2 after annealing at different temperatures

The defect annealing trend observed for swift heavy ion irradiated ThO_2 is in agreement with the defect annealing behavior of alpha- and neutron-irradiated UO_2 and PuO_2 [2]. In addition, the study demonstrated the ability to use neutron total scattering to investigate point defect phenomena in homogeneously-irradiated powders.

References

[1] R.I. Palomares *et al.*, *Thermal defect annealing of swift heavy ion irradiated ThO_2*, Nuclear Instruments and Methods Section B 405 (2017) 15.

[2] Weber, W.J., *Alpha-Irradiation Damage in CeO_2, UO_2 and PuO_2*, Radiation Effects and Defects in Solids 83 (1984) 145.

* Work supported by US DOE, BES grant No. DE-SC0001089,
The research at ORNL's Spallation Neutron Source was sponsored by the Scientific User Facilities Division, BES/DOE
#mlang2@utk.edu

Thermal diffusivity degradation of heavy ions irradiated isotropic graphite*

A. Prosvetov[1,2], *C. Trautmann*[1,2], *M.Tomut*[1,#]
[1]GSI, Darmstadt, Germany; [2]TU Darmstadt, Germany

Polycrystalline graphite (PG) is one of the most used materials for application in extreme radiation environments in high power accelerators because of its high thermal conductivity, thermal shock resistance and low activation. PG is considered as the material of choice for the beam catchers and the production target at the Super-FRS at FAIR. However, since radiation damage can cause severe structural changes, it is important to quantify the degradation of graphite properties under high intensity ion beam exposure.

Thermal diffusivity α is a material-specific property describing the rate of transfer of heat from the hot to the cold side of a material. Together with the specific heat C_P and density ρ it defines the thermal conductivity λ by

$$\lambda(T)=\alpha(T)\times C_P(T)\times\rho(T).$$

The method for measuring thermal diffusivity was originally developed by Parker [1]. The rear side of a plane-parallel sample is exposed to a short laser pulse and the temperature rise on the front side of the sample is monitored by an IR detector. For thin and for high conductive samples the in plane measurement provides more reliable results [2].

A series of 20-mm PG discs with average thickness of 50 µm were irradiated at the M-branch of the UNILAC with 4.8 and 5.9 MeV/u Ca and Au ions. The average flux during irradiation was 2×10^9 ions/(cm$^2\times$s) and the accumulated fluence on series of samples was between 1×10^{11} and 5×10^{13} ions/cm^2.

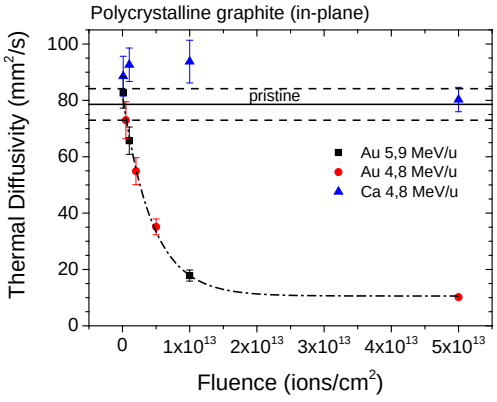

Figure 1: Thermal diffusivity of polycrystalline graphite as a function of fluence for Au and Ca ions. The dash-dotted line is an exponential fitting to the data.

Before and after irradiation the in plane thermal diffusivity of the samples was measured using a NETZSCH LFA42. Figure 1 shows the thermal diffusivity of irradiated graphite samples as a function of accumulated fluence. The irradiation with Au ions leads to a significant drop of the thermal diffusivity, while lighter Ca ions have a smaller contribution at similar fluences.

Beam-induced structural changes of the samples were analysed by Raman spectroscopy (Fig. 2). The G-band is caused by vibrations of the ideal crystal lattice of graphite, and the D-band is due to defects in the material. With increasing irradiation the intensity I_D of the D-peak grows. A quantitative analysis of the defect density n_d is obtained by using the following formula [3], with I_G being the G-band intensity:

$$n_d(cm^{-2}) = \frac{(1.8\pm0.5)\cdot10^{22}}{\lambda_{Laser}{}^4}\cdot\left(\frac{I_D}{I_G}\right)$$

The increase of the defect density (Fig. 3) confirms the stronger effect of the Au -ion irradiation on the degradation of the thermal diffusivity of polycrystalline graphite.

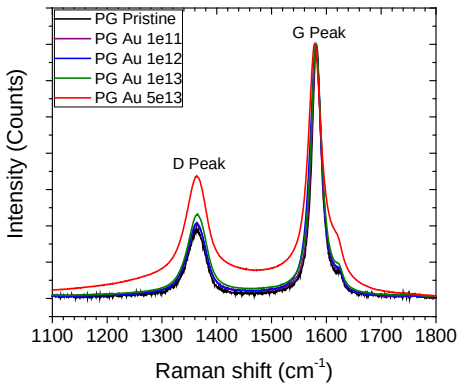

Figure 2: Raman spectra of PG irradiated with Au ions at different fluences. The spectra are normalized to the intensity of the G-peak.

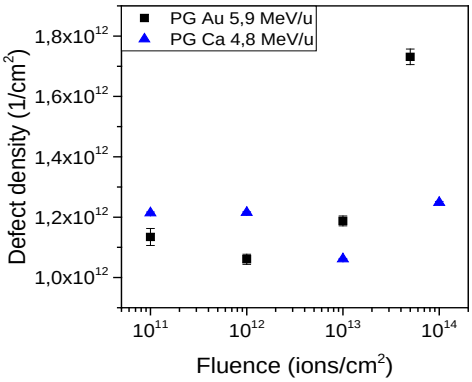

Figure 3: Defect density of Ca and Au ions irradiated PG deduced from Raman spectroscopy data.

* Work supported by HGS-HIRe and the GSI F&E cooperation with TU Darmstadt.
#m.tomut@gsi.de

[1] W.J. Parker, et al, J. Appl. Phys. 32 (1961) 1679
[2] F.I. Chu, et al, J. Appl. Phys. 51 (1980) 336
[3] L.G. Cançado et al, Nano Lett. 11 (2011) 3190

DOI:10.15120/GR-2017-1

Study of high-energy ion beam induced dimensional changes in high density isotropic graphite

Ph. Bolz[1,2], M. Tomut[2,#], F. Kopietz[1,2], A. Dunlap[1,2], A. Prosvetov[1,2], C. Trautmann[1,2]
[1]TU Darmstadt, Germany; [2]GSI, Darmstadt, Germany

Polycrystalline graphite (PG) is the material of choice for the target wheel and as beam catchers at the Super-Fragment Separator and for the beam dumps of experimental caves at FAIR. In the context of increased beam intensities and high accumulated doses, these FAIR components will experience structural changes [1] leading to swelling and to thermal and irradiation creep. From low-doses neutron irradiation of graphite it is known that Frenkel pair generation leads to dimensional increase perpendicular and decrease parallel to the basal planes. The growth in normal direction to the planes is accommodated by the existing pores in the material. As a result, at low doses, the neutron irradiated isotropic graphite experiences an initial shrinkage. After most of the pores are closed, the swelling normal to basal planes starts to dominate and the graphite sample expands again until it finally fails.

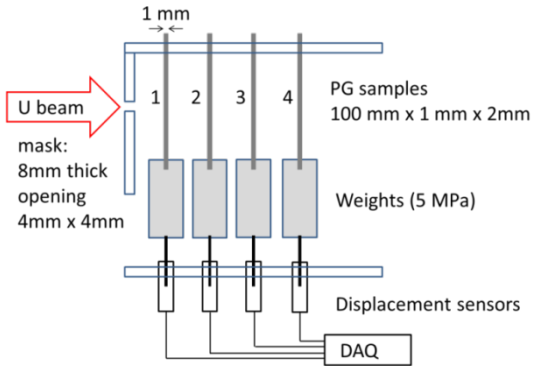

Figure 1: Scheme of online experimental set up for creep measurements at cave A at SIS 18 accelerator at GSI.

To investigate the behaviour under high energy heavy ion irradiation an online set up for monitoring sample dimensional changes was built (Fig.1). Four fine-grained isotropic PG bars were clamped in special holders. The applied load consisted of 1.02 kg weights, resulting in an applied stress of 5 MPa. The weights were connected to displacement transducers that measured the dimensional changes online during irradiation. The irradiation was performed in cave A at SIS-18 using 230-MeV/u uranium ions with a pulse frequency of 0.5 Hz. The average flux was 4-5×10^8 ions/cm²s and the total accumulated fluence was 1.23×10^{13} ions/cm². A mask with an opening of 4×4 mm² was used to define a beam spot that covers the whole sample width but only a small part of the length. The mechanical creep was measured for 2 h and 20 min before the start of the irradiation. It was assumed to be constant during the irradiation and subtracted from the measurement signal to obtain the beam induced dimensional change (Fig.2).

The mechanical creep before the irradiation is much smaller compared to the beam-induced strain. During the irradiation, despite the applied load, a two-step shrinking process is observed. In the first step the dimensional change proceeds with a larger initial rate up to ~2×10^{12} ions/cm². Above this fluence, the contraction rate decreases. This might be associated with clustering of irradiation-induced vacancies once a critical density is reached, leading to a decrease of the contraction rate or to an increase of the creep strain. Sudden elongations of the samples (e.g. at ~7.5×10^{12} ions/cm²) are associated with beam failures, as shown in figure 3. When the beam stops, the sample cools down leading to a small contraction. Afterwards the sample expands due to mechanical creep.

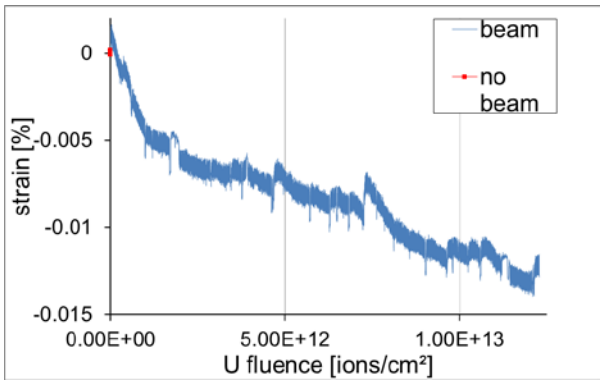

Figure 2: Strain as a function of accumulated fluence for an isotropic graphite sample applied to a tensile load of 5 MPa and exposed to 230-MeV/u ^{238}U ions.

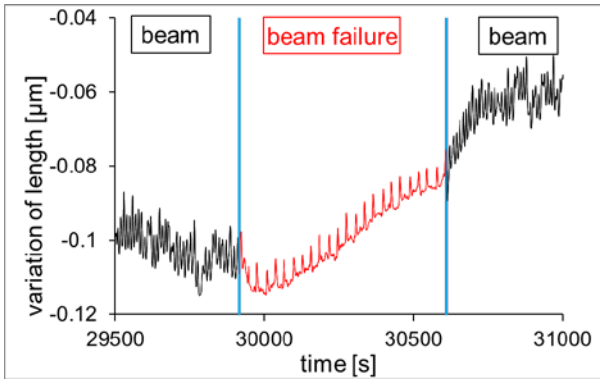

Figure 3: Blow-up of variation of sample length during a beam failure interval; the accumulated fluence reached 7.3×10^{12} U ions/cm² at an applied tensile load of 5 MPa.

References

[1] C. Hubert et al., Nucl. Instr. Meth. B 365 (2015) 509.

#m.tomut@gsi.de

DOI:10.15120/GR-2017-1

Upgraded *in situ* Raman spectroscopy system at UNILAC beamline M3*

S.Dedera[1,#], M. Burchard[1], U.A. Glasmacher[1], D. Severin[2], C. Trautmann[2,3]
[1]Institute of Earth Sciences, Heidelberg University,; [2] GSI Helmholtzzentrum, [3] TU Darmstadt, Germany

Introduction

Raman spectroscopy is widely used in materials research as well as in geosciences. It has proved to be an excellent method to analyze structural changes of solids exposed to high-energy ions available at large accelerator facilities. *In situ* investigations have the great advantage that the modification induced by the ion beam can be followed on a given sample spot by stepwise increasing the fluence without removing the sample from the irradiation chamber. This is of particular interest for natural materials that are often inhomogeneous and/or anisotropic. By analyzing the same spot after each irradiation step, crystal orientation effects are excluded because the sample remains in a fixed position.

A first version of a confocal Raman spectrometer was integrated at the M3 beamline of the UNILAC and successfully used for *in situ* analysis during beamtimes in 2014 and 2015 [1]. In the meantime several improvements were installed and tested during irradiation experiments in 2016.

System Upgrade

The main improvement of the upgraded system is a high-precision 3-axis stage consisting of three piezo stages (*Physik Instrumente* Q521-330) with a precision of 30 nm. The new stage has the advantage that it is equipped with a multiple-sample holder. This allows the irradiation of a series of samples without venting the irradiation/spectroscopy chamber and thus saves valuable beamtime. Moreover, it is now possible to precisely position the location of a sample spot to be analyzed. Also tiny samples such as for example nanofibres can be studied. For geological samples this is of great advantage in case of microanalysis of zoned samples.

In the upgraded version, the laser of the system is now operated by remote control providing a better possibility to monitor beam-induced iono-luminescence of samples. This allows us to cross-check the exact position and shape of the beam on luminescent samples like calcite ($CaCO_3$).

First irradiations with 4.8 MeV/u Au ions in combination with Raman spectroscopy on calcite ($CaCO_3$), dolomite $CaMg(CO_3)_2$ nanofibers and graphene were demonstrating the very useful improvements of the upgraded system.

References

[1] S. Dedera, et al., On-line Raman spectroscopy of calcite and malachite during irradiation with swift heavy ions, *Nucl. Instr. Meth. B* 365 (2015) 564; DOI: 10.1016/j.nimb.2015.09.079.

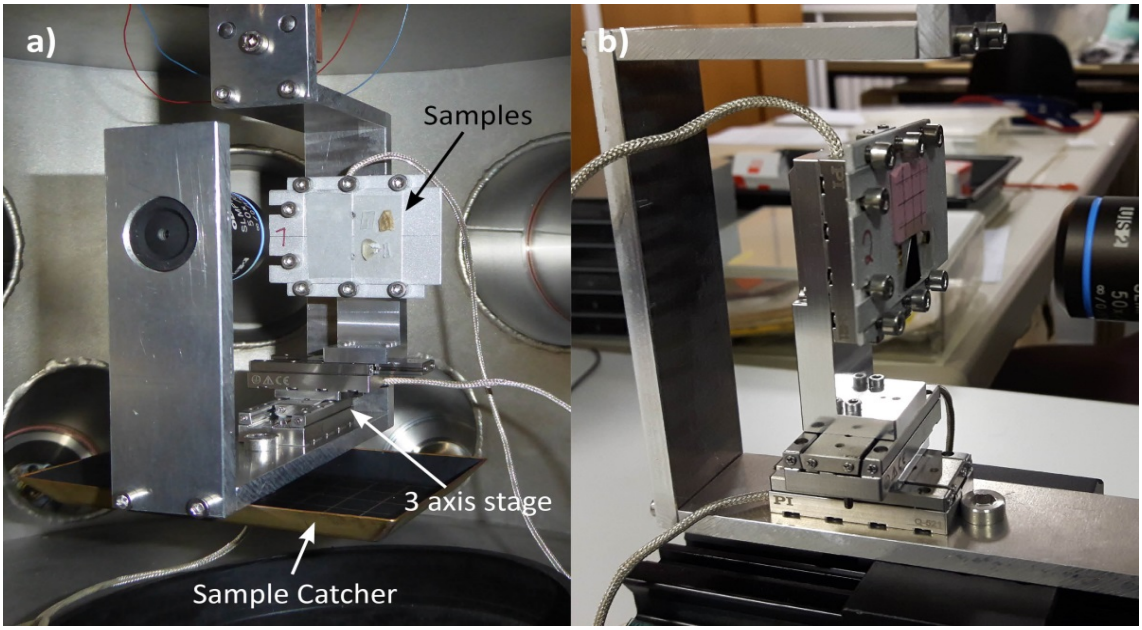

Figure 1: a) Raman-System inside the irradiation chamber at the M3-beamline of the UNILAC, consisting of a Horiba Jobin Yvon iHR 320 spectrometer with a Pelletier cooled camera and a 532 nm laser (90mW power);
b) new 3-axis piezo stage with a holder for several samples.

* Work supported by BMBF Verbundprojekt (05K16VHA).
#Sebastian.Dedera@geow.uni-heidelberg.de

DOI:10.15120/GR-2017-1

Chemical track etching of ion-irradiated siderite

Baldur Knörr[1,#], Ulrich A. Glasmacher[1], Sebastian Dedera[1], Michael Burchard[1], Christina Trautmann[2]

[1]Institute of Earth Sciences, Heidelberg University; [2]GSI and Technische Universität Darmstadt, Germany

In geosciences, fission-track dating is one of the main methods of thermochronological analysis. Mineral samples are etched to convert tracks of fission fragments into surface etch pits that can be viewed and quantified under an optical microscope. Below a mineral specific temperature, tracks accumulate over time due to the mineral's natural uranium content [1].

Siderite ($FeCO_3$) is an important mineral formed during diagenetic processes and hydrothermal activity. In order to test the viability of track etching methods, we used siderite crystals from Grube Pfannenberger Einigkeit, Siegerland and irradiated them with 5.9 MeV/u ^{197}Au ions to a nominal fluence of 1×10^6 ions/cm^2. During irradiation the crystals were covered with a hexagonal mask to create irradiated and non-irradiated areas on the crystal surface. A thin polycarbonate foil simultaneously irradiated was etched to determine the exact fluence applied.

Track etching of the irradiated siderite samples was performed in a solution of sulfuric acid (10%). The temperature of the etchant was thermally stabilized to 50 (± 0.1) °C using a heated water bath. The etchant was stirred with a magnetic stir bar.

The etch pits were counted and their dimensions measured using a reflected light Olympus BX 50 microscope and Stream Enterprise software. The etch pits exhibited a roughly hexagonal shape and reached a diameter of 3-4 µm after 60 min of etching (Fig. 1).

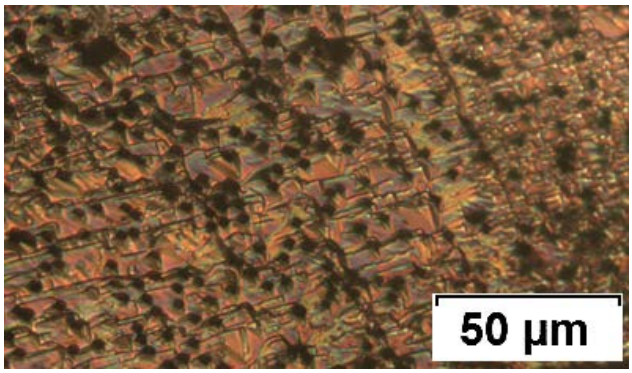

Figure 1: Etch pits on surface of irradiated siderite (60 min, 50°C, 10% H_2SO_4, 20x magn., reflected light).

The topography of the surface of natural siderite is rough and has small natural pores/orifices, which can have diameters of several µm. They will also be enlarged by the etching process, which makes it difficult to see the etch pits of the ion tracks under reflected light. However, when using sufficiently thin samples, transmitted light can be used to distinguish etched ion tracks from the background (Fig. 2).

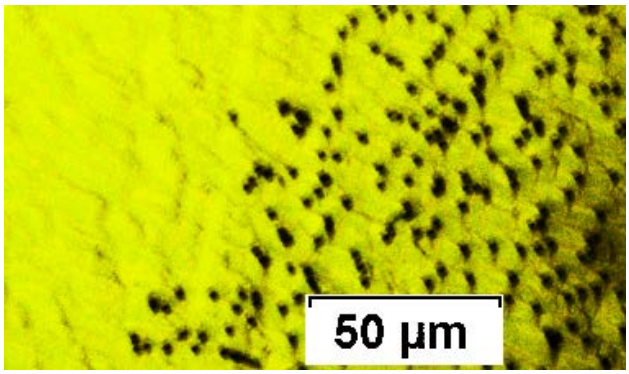

Figure 2: Etch pits on surface of irradiated siderite (60 min, 50°C, 10% H_2SO_4, 20x magn., transmitted light).

The polymer reference foil covering the siderite samples during irradiation was etched in aqueous 6 mol/l NaOH solution for 90 min at 50 (± 0.1) °C. When exposed to the etchant, all ion tracks in the foil are converted into open channels that can easily be counted (Fig. 3).

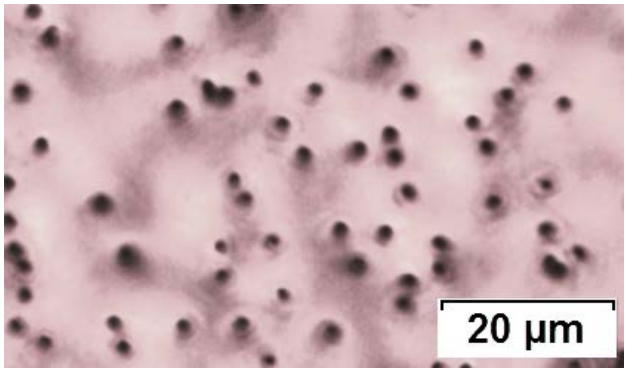

Figure 3: Etch pits on surface of irradiated polymer foil (90 min, 50 °C, 6 mol/l NaOH, 50x magnification).

The analysis of several microscope images yields an areal density of 2.14 (± 0.17) × 10^6 etch pits/cm^2 for siderite and 2.10 (± 0.11) × 10^6 pores/cm^2 for the polymer foil. Within the experimental error, the amounts of etch pits matches the fluence applied.

In conclusion, sulfuric acid is a useful etchant for visualizing ion tracks in siderite created by swift heavy ions. The etching solution applied converts all tracks into countable etch pits. Experiments with fission tracks induced by covering siderite samples with zircon grains, which emit fission fragments when irradiated with thermal neutrons, are in progress.

[1] K.G. Bell, Uranium in carbonate rocks, Shorter contributions to general geology, 474-A (1963).

*Work supported by BMBF-Verbundprojekt 05KK7VH1 and 05K13VH1.

Baldur.Knoerr@geow.uni-heidelberg.de

The role of osmotic effects in asymmetric track etching

P.Y. Apel[1,2,#], I. Blonskaya[1], N.Lizunov[1], O.Orelovitch[1] and C. Trautmann[3]
[1]JINR, Dubna, Russia, [2]Dubna State University, Dubna, Russia, [3]GSI and TU Darmstadt, Germany

The ion track technology provides unique opportunities for developing tailored micro- and nanoporous membranes with fine-tuned transport properties. In the last decade, special attention was given to so-called conical pores. Their fabrication includes the irradiation of a poymer foil with high energy ions followed by asymmetric chemical track etching. Recently it was evidenced that under such conditions an intense osmotic flux develops and has a strong effect on the nanopore geometry [1]. Here we report on experiments aimed at better understanding the role of osmotic phenomena in asymmetric track-etched nanopores.

Polyethylene terephthalate (PET) biaxially oriented foils (12-µm-thick Hostaphan RNK) were irradiated with 11 MeV/u Au ions at the UNILAC (GSI, Darmstadt) and with 1.2 MeV/u Xe and Kr ions at the IC-100 cyclotron (FLNR, JINR, Dubna). All samples were additionally exposed to ultraviolet radiation to stabilize the track-to-bulk etch rate ratio. Chemical etching was performed in an electrolytic cell at room temperature. One compartment of the cell was filled with 9 M NaOH and the other compartment contained a stopping solution (either neutral 1M KCl or acidic 2 M KCl + 2 M HCOOH, 50:50, v/v). The cell was equipped with a capillary (2 mm inner diameter) inserted into the compartment with the alkaline etchant. The etched area of the foil samples was 1 cm^2. The geometry of the obtained asymmetric pores was investigated using field emission electron microscopy (FESEM).

Because the electrolyte concentrations on the two sides of the asymmetrically etched foil are significantly different, a gradient of the chemical potential of water generates a flow from the stopping solution to the etchant. Figure 1 shows the etching solution build-up in the capillary as a function of the etching time. For Au ion tracks, a pronounced osmotic flow starts at 90-100 and 140-200 min for neutral and acidic stopping solutions, respectively. Tracks of lighter ions (Kr) are etched through slower, however the resulting pores show a similar osmotic flow. The influence of acidity of the stopping solutions on the track etch rate indicates that unetched tracks are less permeable for electrolyte at low pH [2].

Due to osmotically driven flow of water into the pore, the alkali concentration gradient in the pore is essentially non-linear. The concentration is almost constant along the wide part of the pore and dramatically decreases in the pore tip region. This effect results in the conservation of the tip radius at a level of few nanometers after the etching and stopping solutions meet each other (see Fig. 2).

To our knowledge, clear osmotic effects caused by inorganic salts in track-etched membranes have not been observed before.

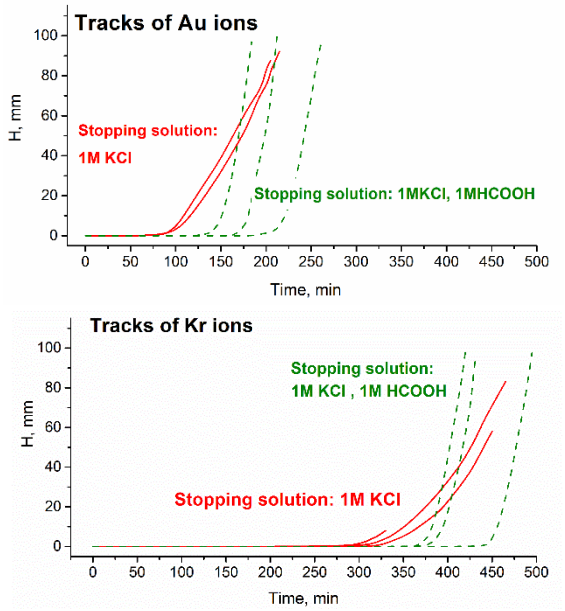

Figure 1:Build-up of the alkaline solution level H as a function of time for asymmetric etching of PET foils with·10^8 cm^{-2} Kr (bottom) or Au (top) ion tracks. Solid and dashed lines show the respective data for neutral and acidic stopping solutions. Results of several parallel experiments for each ion are shown.

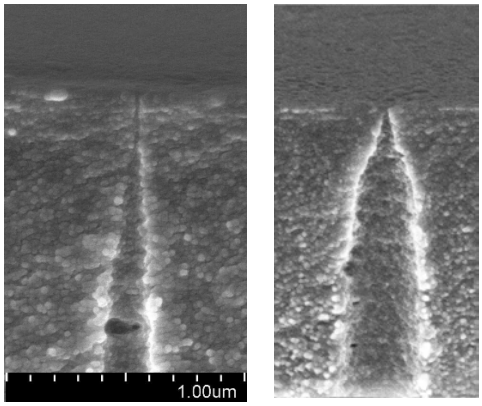

Figure 2: Track-etched pore tip ~20 min (left) and ~70 min (right) after breakthrough. One-sided etching of Au ion tracks continued after osmotic flow had been detected.

References

[1] P.Yu. Apel, V.V. Bashevoy, I.V. Blonskaya, N.E. Lizunov, O.L. Orelovitch, C. Trautmann, Phys. Chem. Chem. Phys. 18 (2016) 25421.

[2] Q. Wen, D. Yan, F. Liu, M. Wang, Y. Ling, P. Wang, P. Kluth, D. Schauries, C. Trautmann, P. Apel, W. Guo, G. Xiao, J. Liu, J. Xue. and Y. Wang, Adv. Funct. Mater. 26 (2016) 5796.

#apel@jinr.ru

DOI:10.15120/GR-2017-1

Nanoconfinement effects on solid-state, gel electrolyte systems *

T. S. Plett[1], W. Cai[1], M. Le Thai[2], I. Vlassiouk[3], R. M. Penner[2], Z. S. Siwy[1,2,4,#]
[1]Dept. of Physics, UC Irvine; [2]Dept. of Chemistry, UC Irvine; [3]Oak Ridge National Laboratory; [4]Dept. of Biomedical Engineering, UC Irvine, U.S.A.

Recent findings demonstrating remarkable cyclability of MnO_2 mesowires in gelled $LiClO_4$-PMMA (poly(methyl) methacrylate) [1] motivated our research to understand how nanoconfinement affects the gel electrolyte. Because MnO_2 possess tendril and nanovoid structures, nanopores can be used to explore the effects of nanoconfinement on the $LiClO_4$-PMMA gel electrolyte. In this report, we demonstrate a nanoscale solid-state ionic diode using $LiClO_4$-PMMA gel electrolyte. This was accomplished by infiltrating a polyethylene terephthalate (PET) conical nanopore with $LiClO_4$-PMMA gel. [2] Other experiments in cylindrical PET pores served to confirm fundamental characteristics of the ion transport in the solid electrolyte.

Our nanopores were fabricated by the track-etching 12-µm PET films irradiated at the UNILAC with single Au ions (11.4 MeV/u). Cylindrical pores were subjected to symmetric etch conditions while conical pores were prepared by asymmetric etch conditions. After etching, pores were characterized by I-V curves in $LiClO_4$/propylene carbonate and then drop-cast with the $LiClO_4$-PMMA gel.

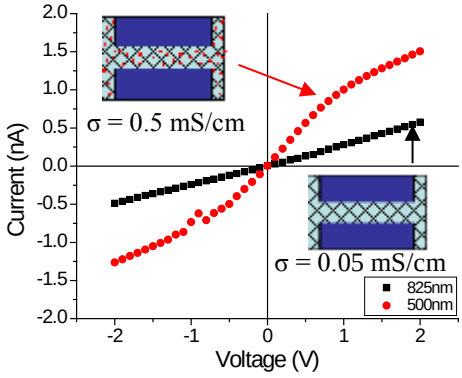

Figure 1. I-V curves for cylindrical pores with both Li^+ doped and undoped PMMA gels.

Initial experiments in cylindrical pores with the gel electrolyte demonstrated many properties of ion transport observed at the bulk scale translated to sub-micron confinement. Previous measurements of conductivity and ion transfer number [3] were confirmed in cylindrical pores by comparing doped and undoped (Fig. 1) PMMA gels. We also showed that PMMA fully infiltrated nanopores using simple drop-cast.

Experiments in conical pores demonstrated classic ion current rectification behaviors (Fig. 2). Current-voltage curves and long pulse (20 s) measurements confirmed the effect was robust. We hypothesize the macroscopic drop of $LiClO_4$-PMMA on the surface of the membrane served as an ion reservoir, preventing ion depletion for the long pulse measurements. Furthermore, we were able to demonstrate switching of the diode for a 0.1Hz, 2V amplitude square wave [2].

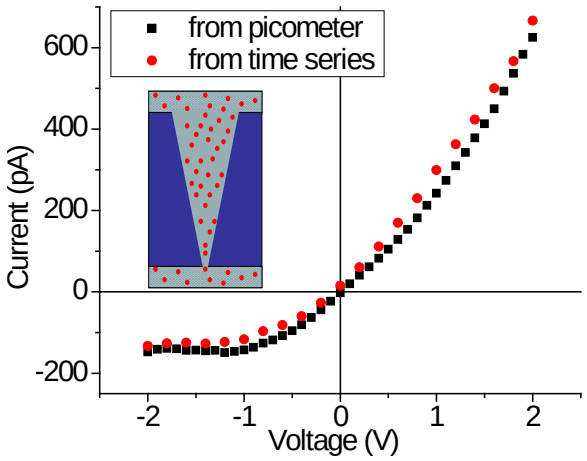

Figure 2. I-V curves from a 100mV/s pulse scan and a 20s long pulse measurement

The standard model for ion current rectification requires ion selectivity which, in nanopores, commonly results from presence of surface charge in nanoconfinement, leading to voltage-dependent conductive states. In the case of a solid-state electrolyte, elucidating mechanisms is not as straightforward, as no charges are expected on the nanopore surface. However, ionic selectivity can be contributed to other factors i.e. Li^+ complexing with the PMMA to generate positive volume charge [4] (in agreement with Fig. 2) and confinement dependent conductivity [5].

These results detail the first, to our knowledge, nanoscale solid-state ionic diode and extends the range of electrolytes capable of testing with PET nanopores. Solid-state ion transport phenomena in nanoconfinement showed similarity to liquid counterparts, despite possessing different mechanisms for achieving them.

References

[1] M. L. Thai et al., ACS Energy Lett. 1 (2016) 57
[2] T. Plett et al., J. Phys. Chem. 121 (2017) 6170
[3] Z. Osman et al Results Phys. 2 (2012) 1
[4] C.M. Mathew et al, Int. J. Electrochem. 2015 (2015) 494308
[5] S. Vorrey et al, Electrochim. Acta. 48 (2003) 2137

* Work supported by US Department of Energy, DESC001160.
#zsiwy@uci.edu

Conical ion-track etched nanopores in SiO_2*

A. Hadley[1,#], C. Notthoff[1], P. Mota-Santiago[1], U.H.Hossain[1], S. Mudie[2], M.E. Toimil-Molares[3], C. Trautmann[3,4], and P. Kluth[1]

[1]Australian National University (ANU), ACT, Australia; [2]Australian Synchrotron, VIC, Australia; [3]GSI, Darmstadt, Germany, [4]Technische Universität, Darmstadt, Germany

The ion-track etching method can be used to produce nanopores in a variety of materials. The aim of this work is to develop a better understanding of the ion-track etching process in SiO_2 and its dependence upon the un-etched track structure. To achieve this goal, we performed advanced synchrotron-based small-angle x-ray scattering (SAXS) measurements.

Films of 2 µm thick SiO_2 were irradiated with 1.1-GeV Au ions (10^8 cm^{-2}) at the GSI UNILAC accelerator and alternatively with 185-MeV Au ions at the ANU ion accelerator facility. Samples were subsequently etched in concentrations of 10, 5, and 2.5% hydrofluoric acid (HF) at room temperature for times ranging from 60 to 30 min.

After etching, some samples were investigated by scanning electron microscopy (SEM) revealing parallel oriented, conical pores of uniform size and morphology (Fig. 1). Obtaining cross-section images is, however, time consuming and the samples have to be broken.

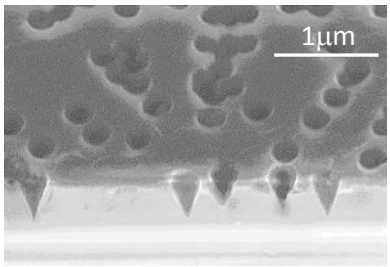

Fig. 1: Cross-section SEM image of conical nanopores in SiO_2 obtained after 8 min etching in 5% HF. The pores display a base of ~160 nm and a very small tip size.

In contrast to SEM, SAXS is a non-destructive technique and it enables leveraging statistics, since many uniform structures are measured at once. Here, we apply SAXS to extract information about the morphology of the nanopores including base and tip diameters as well as opening angle of the cones.

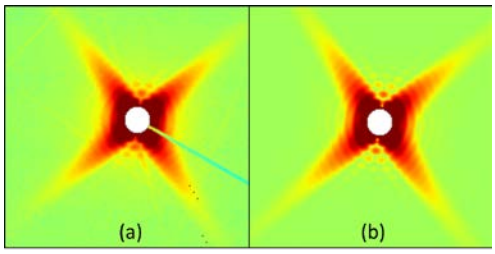

Fig. 2: (a) SAXS image measured at the SAXS/WAXS beamline of the Australian Synchrotron; (b) calculated fit.

* Work supported by the Australian Research Council (ARC) and the Australian Synchrotron.

andrea.hadley@anu.edu.au

Figure 2(a) shows the SAXS image of the same SiO_2 membrane SEM-imaged in fig. 1. The complex image contains details about the pore morphology. Figure 2(b) shows the calculated fit to the image attained using a semi-analytical model for the cone form factor. This fit allows us to extract the length, opening angle and base radius of the etch cones averaged over millions of cones. Subsequently, we calculated the axial as well as the radial track etching rates. Figure 3 displays the base radius as a function of etching time obtained in 10% (blue), 5% (green), and 2.5% (red) HF. From the slope, a respective radial etching rates of 29, 12 and 7 nm/min is deduced. Plotting the cone length as a function of etching time (not shown), we obtain corresponding axial etching rates of 146, 62, and 33nm/min. As expected the etching rates vary roughly linearly with etchant concentration.

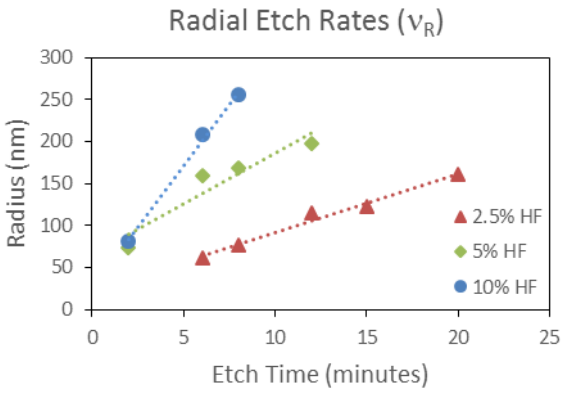

Fig. 3: Radius of cone base as a function of etching time in different HF concentrations at room temperature.

Linear extrapolation of the radial etch rates for the lower concentrations of 5 and 2.5% suggest non-linear behaviour at the early stages of etching because they do not intercept the radius axis at zero. The early stages of the etching process are interesting because the channel opening within the first few nm is influenced by the damage structure of the track. Planned experiments combining short etching times and in-situ SAXS studies will allow us to improve existing etching models and achieve a higher control on tailoring particularly small nanopores for specific applications such as nanoscale filtration and biosensing.

References

[1] D. Nikezic, K.U.Yu, Mat. Sci. Eng. R 46 (2004) 51

DOI:10.15120/GR-2017-1

The *iNAPO*-project: etched swift heavy ion damage tracks in polymers as bio-mimetic ion conducting nanopores for electrochemical sensors

W. Ensinger[1,#], M. Ali[1,2], S. Nasir[1], I. Duznovic[1], C. Trautmann[1,2], M.E. Toimil-Molares[2], G.R. Distefano[1,2], B. Laube[1], M. Bernhard[1], M. Mikosch-Wersching[1], H.F. Schlaak[1], M. El Khoury[1]

[1]TU Darmstadt, Germany; [2]GSI, Darmstadt, Germany.

In nature, ion conducting nanopores play a vital role for the function of living cells. They undergo gating processes where they open and close upon an external stimulus, such as the presence of a particular biomolecule, the ligand. When the gating process is observed and is quantitatively measured, one can derive data about the presence and the amount of the ligand. Hence, the nanopores can be utilized for specific sensing. However, biological nanopores are embedded in a biological cell membrane that is fragile and unstable with respect to storage and application. The LOEWE project *iNAPO* (**i**on conducting **NA**no **PO**re) aims at combining robust polymer-based nanopores with protein-based biological nanopores, thus combining the selectivity and sensitivity of the latter with the stability and processability of the first ones. In the final step of the project, the biologically modified polymeric nanopores will be incorporated into a *Lab-on-Chip* system, creating a new type of device for applications, e.g., in medical diagnostics and environmental analysis. The whole bottom-up process is schematically shown in Fig. 1.

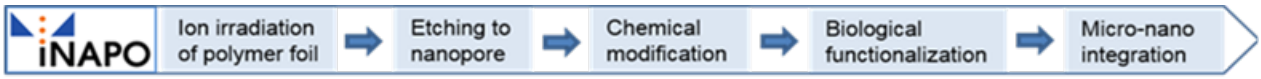

Figure 1: The *iNAPO* project: Fabrication steps of a micro sensing device for ion conducting nanopores.

The first essential step in the process of fabricating synthetic nanopores is the formation of a straight well defined damage track in a polymer. A single heavy ion, e.g. gold, accelerated in the UNILAC to a kinetic energy of several MeV/u, is directed perpendicularly towards the polymer foil, mostly polycarbonate or polyethylene terephthalate, that has a typical thickness of 10 to 20 µm. The ion passes the target in a straight line and producing a cylindrical zone of a few nm in diameter. This damage track consists of broken chemical bonds and reduced density. Due to the enhanced chemical reactivity, the track can be converted into an open channel by chemical etching in a suitable etchant cylindrical as well as conical channels can be produced. Their size is adjusted by the etching time and can be tailored between few nanometers and micrometers.

In the next step, the nanopore walls are chemically modified, i.e. specific molecules are attached to the surface. These molecules are able to specifically react with counterpart molecules, in a key-lock type reaction. This reaction is accompanied by a reduction in pore diameter. The process is monitored electrochemically by mounting the polymer foil (containing in most cases one single nanopore) between two compartments of an electrochemical cell. The cell is filled with an aqueous electrically conductive salt solution. When a voltage is applied between two electrodes placed in each of the cell compartments, an ionic current flows through the nanopore. When the nanopore surface is electrically neutral, the flow is the same in both directions, irrespective of the polarity of the electrodes. If, however, the surface is charged, the asymmetric shape of a conical nanopore results in a potential distribution yielding rectification, i.e. the ion flow in one direction is larger than in the other direction. The nanopore thus becomes a nanofluidic diode. The resulting current/voltage curve shows a steep line for a positive applied voltage and a flat one under negative voltage, or vice versa, depending on the sign of charge of the nanopore surface.

The following example of a biomolecular nanopore sensor deals with the analysis of pyrophosphate ($P_2O_7^{4-}$), an anion that plays an important role in biochemistry. In elevated quantities, it may cause various diseases, such as arthritis. Therefore, monitoring is of importance. For a nanopore-based pyrophosphate -sensor, di(2-picolyl)amine groups are chemically coupled to the nanopore wall. Zinc ions are added and form a bis(Zn^{2+}-DPA) complex. This complex specifically reacts with pyrophosphate while there is no reaction with other phosphates such as monohydrogen phosphate (HPO_4^{2-}), dihydrogen phosphate ($H_2PO_4^-$), and adenosine mono-, di- and tri-phosphate (AMP, ADP, ATP). Fig. 2 shows schematically the complexation reaction between the zinc-DPA complex and the pyrophosphate (shown in green).

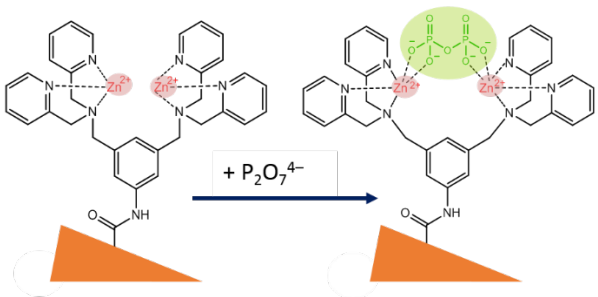

Figure 2: bis[Zn^{2+}-DPA] complexes (red) coupled to the nanopore surface selectively react with $P_2O_7^{4-}$(green).

DOI:10.15120/GR-2017-1

The current/voltage curves in Fig. 3 show that the ion current through the nanopore is hardly changed when various phosphate ions are added to the electrolyte solution. In contrast, the addition of pyrophosphate causes a strong reduction of the current at negative voltages, and an increase at the positive voltage branch. This effect is due to the coupling of pyrophosphate with its 4 negative charges that influence the cation flow, leading to a diode-like effect. While the presence of other phosphates does merely change the nanopore current, pyrophosphate can be measured specifically, even down to submicromolar quantities. This example illustrates that ion-track based nanopores in polymer foils can be used as molecular sensors with a certain sensitivity and selectivity.

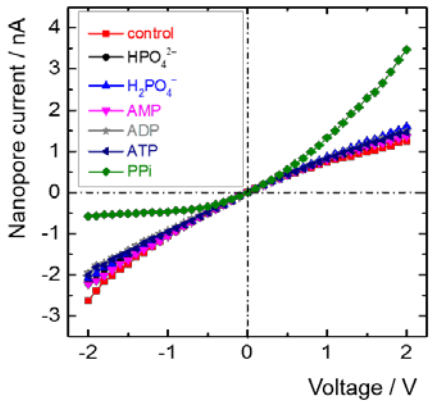

Figure 3: The ion current through the nanopore is changed in the presence of pyrophosphate (PP_i) but not when other phosphates (e.g., mono- and di-hydrogen phosphate or adenosine mono-, di- and tri-phosphate are added [1].

As mentioned before, an ongoing further step in the development is the combination of polymer nanopores with biological nanochannels. Figure 4 shows how binding proteins are used as a base for biological protein-based nanopores. In these hybrid pores, the second generation of functional nanopores, the distinct selectivity of the biological nanopores to ligands, i.e the biomolecules to be analyzed, will lead to a further improvement in the functionality of the sensors.

So far, laboratory set-ups have been used for the electrochemical measurements. They consist of an electrochemical cell of some 10 to 15 cm length, connected via cables to a voltage source and a sensitive current meter. The project *iNAPO* comprises the fabrication of a compact *lab-on-chip* micro device with the polymer foil embedded in it by means of micro-nano-integration techniques. The polymer foil containing the nanopore is embedded into a microfluidic system with integrated electrodes. The foil is glued between two 200 µm thick sheets of an epoxy-based photoresist containing three microfluidic channels formed by photolithography. The lower polymer plate is placed on a glass substrate with two evaporated gold electrodes; the upper plate is covered with a glass plate. For operation, the microdevice will be connected to a power supply and an amperometer that are located in a compact unit where the microdevice is fitted in.

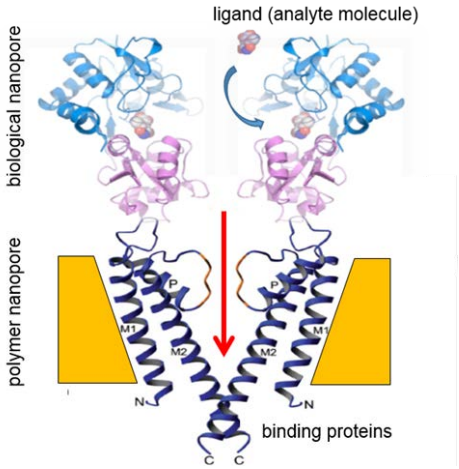

Figure 4: Schematic cross-section of a polymer nanopore with binding proteins included (dark blue) that are coupled to biological nanopores on top. These are gated by the presence of a specific analyte biomolecule (the ligand, reacting with the receptor) leading to an ion flux (red) [1].

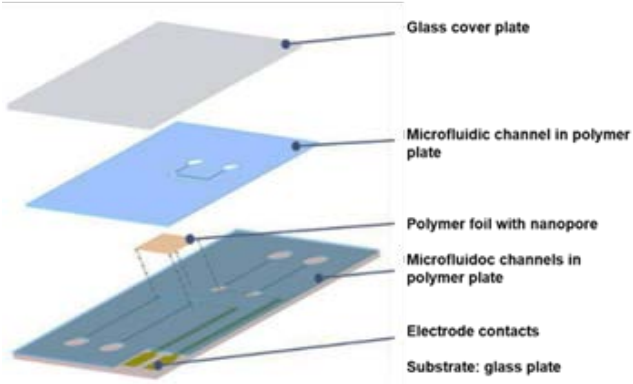

Figure 5: Setup of microfluidic *lab-on-chip* system with integrated nanopore [1].

The microchannels are filled with electrolyte, and an amperometric reference value is recorded at a given voltage. Then, the electrolyte with the analyte molecules is added and the current response is measured again. In a calibrated system, the concentration of the analyte can be determined quantitatively, if it is within the measurement range of the system.

With such a compact set-up with low power input, it will be possible to carry out fast low-cost analyses, e.g. for medical diagnostics or for environmental tests.

[1] W. Ensinger et al., Proceedings of the 2nd World Congress on Recent Advances in Nanotechnology (RAN'17), Barcelona, Spain, April 4 – 6, 2017, Paper No. ICNNFC 141: 141-1, International ASET Inc., Ottawa, ISSN: 2371-5308

* Work supported by supported in the frame of the LOEWE project *iNAPO* by the Hessen State Ministry of Higher Education, Research and the Arts.
#ensinger@ma.tu-darmstadt.de

DOI:10.15120/GR-2017-1

Redox-responsive ionic conduction through single conical nanopores*

M. Ali[1,2,#], S. Nasir[2], C. Trautmann[1], and W. Ensinger[2]

[1]GSI, Darmstadt, Germany; [2]TU Darmstadt, Germany.

Ion channels are pores embedded in cell membrane that regulate the passage of ions and signaling molecules.[1] Natural ion channels are precisely controlled structures with defined interfacial chemistry. However, the fragility of the supporting lipid bilayer restrains their suitability for practical purposes. Conversely, synthetic nanopores have recently attracted interest because their geometry and surface pore properties can be tuned on demand.[2]

Particularly, track-etched single conical nanopores (produced by irradiating polymer membranes with one individual ion at the UNILAC) exhibit remarkable transport properties such as permselectivity, voltage-dependant gating mechanism and current rectification, similarly to biological ion channels.[3] To date, a variety of responsive molecules and functional groups that respond to different external stimuli have been immobilized on the pore surface to tune ion transport properties. To broaden the scope of nanoporous systems, the synthesis and anchoring of more complex functional molecules, *e.g.*, oxidation-reduction (redox) sensitive moieties, on the pore surface is a challenge for current techniques.

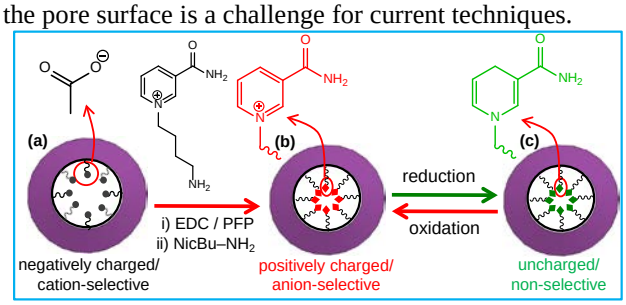

Figure 1: Scheme representing the changes in pore surface chemistry (a) as-prepared pore, (b) modified with nicotinamidemoities in oxidized state, and (c) pore with dihydronicotinamide moieties in reduced form.

Here, we demonstrate the redox-sensitive ionic conduction through a nanofluidic diode based on single asymmetric nanopores fabricated in polyethylene terephthalate (PET) membranes.[3] To achieve this goal, 1-(4-aminobutyl)-3-carbamoylpyridinium (Nic-BuNH$_2$) is synthesized and anchored onto the pore surface via carbodiimide coupling chemistry (Figure 1).[4] The single conical pore exhibits current rectification because of the ionized carboxylate groups on the pore surface (Figure 1a). The modification process resulted in the switching of pore surface charge from negative to positive due to the presence of positively charged quaternary pyridinium units (Figure 1b). This fact caused a reverse in the current rectification, *i.e.*, the Nic-modified pore preferentially transported anions from the tip to the base (Figure 2A).[4]

Once the nanopore surface was successfully functionalized with nicotinamide moieties, we proceeded to study the redox reactions inside the confined environment. The immobilized nicotinamide moieties were in oxidized state (quaternary pyridinium form) and the net charge on pore surface was positive. For the reduction of nicotinamide moieties, the modified pore was exposed to sodium dithionite ($Na_2S_2O_4$) prepared in sodium bicarbonate solution in dark for a time period. During the course of the reduction process, the oxidized (positively charged) pyridinium ring of nicotinamide was converted to 1,4-dihydropyridine (uncharged/ neutral) form (Figure 1c). This process resulted in the loss of pore surface charges, and the nanopore behaved like an ohmic resistor as shown in Figure 2B. Hence, the reduction process switched the nanopore from an "*ON*" state characterized by a high rectified ion flux to an "*OFF*" state with a low non-rectified current. The dihydronicotinamide can be reoxidized to nicotinamide by exposing the modified pore to a solution of an oxidizing agent such as hydrogen peroxide (H_2O_2). The oxidation process resulted in the generation of positive charges on the pore walls, and concomitant current rectification inversion.

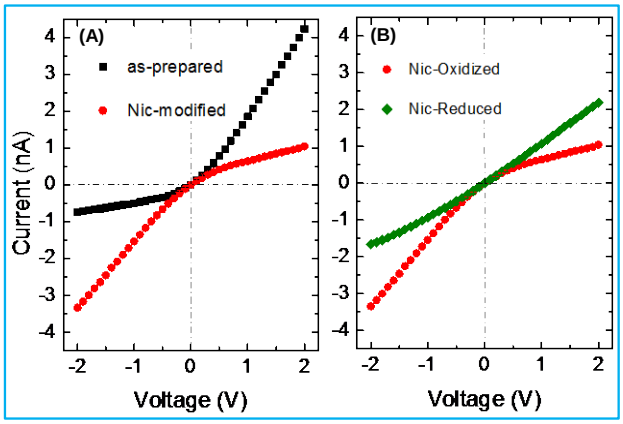

Figure 2: (A) *I–V* curves of single conical nanopore (d ~ 24 nm and D ~ 400 nm) prior to and after modification with nicotinamide. (B) *I–V* curves of the modified pore exhibiting the switching of oxidized (positively charged) nicotinamide moieties into reduced (uncharged) states.

In summary, we have demonstrated the fabrication of a redox-sensitive nanofluidic diode whose transport properties can be tuned via oxidation and reduction processes occurring inside the pore. The redox reactions allowed us to reversibly switch the nanopore inner environment from hydrophilic and conducting ("*ON*" state) to a hydrophobic and nonconducting ("*OFF*" state).

References

[1] B. Hille, *Ionic channels of excitable membranes*, 3rd ed., Sinauer Associates Inc., Sunderland, MA, 2001.
[2] S. Howorka and Z. Siwy, *Chem. Soc. Rev.* 38 (2009) 2360.
[3] P. Y. Apel *et al. Nucl. Instrum. Methods Phys.* 184 (2001) 337.
[4] M. Ali *et al. Sens. Actuators B;* 240 (2017) 895

*Work supported by the LOEWE project iNAPO.
M.Ali@gsi.de

Ion transport through single conical nanochannels synthesized by ion-track technology and atomic layer deposition of Al_2O_3, TiO_2 and SiO_2 *

N. Ulrich[1,2], A. Spende[1,2], N. Sobel[2], C. Hess[2], C. Trautmann[1,2] and M. E. Toimil-Molares[1,#]
[1]GSI, Darmstadt, Germany; [2]Technische Universität Darmstadt, Darmstadt, Germany

Solid state nanochannels exhibit unique transport properties for electrolytes including ion selectivity, ion current rectification and responsive behaviour to external stimuli such as pH value, temperature, or ion concentration [1].

The ion flux through a nanochannel can be described by nanofluidic models. At the nanochannel surface a layer of immobile and mobile ions is formed. The type of ions in this so-called electrical double layer (EDL) depends on the surface charge, which in turn is influenced by the pH value of the employed electrolyte. For each material, there is a specific pH value, called point of zero charge (PZC), where no surface charges and thus no EDL are present [2].

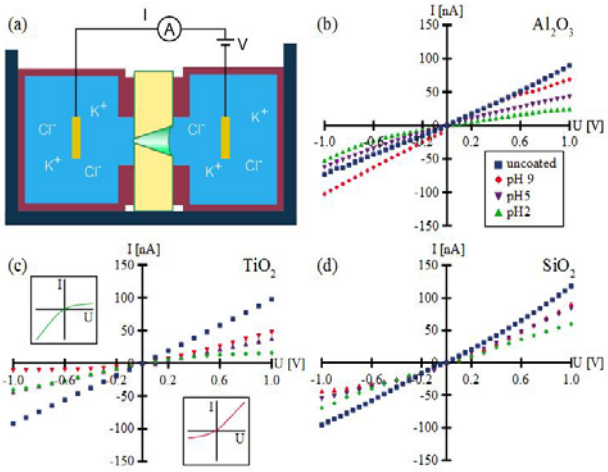

Figure 1: Setup employed for *I-V* measurements (a) and *I-V* curves recorded across single conical channels coated with a 15 nm thin layer of Al_2O_3 (b), TiO_2 (c), and SiO_2 (d). Each channel was characterized at three different pH-values (legend shown applies for b-d). The insets in (c) show typical curves for preferred anion- (top left) and cation-flow (bottom right).

Single conical nanochannels were fabricated by ion-track technology. This includes the irradiation of a 30-µm thick polycarbonate (PC) foil with one individual high-energy ion (e.g. 2-GeV Au ions) followed by chemical track etching. The irradiated PC foil containing the single ion track is mounted into an electrochemical cell exposing one side of the tracked foil, e.g., to a 9 M NaOH solution and the other side to water [3]. For this project, etching was performed at 30 °C for 15 min converting the ion track into an open conical channel with a base diameter of about 3 µm and a tip size of ~100 nm. Afterwards, the polymer foils were coated by atomic layer deposition (ALD) with 15 nm Al_2O_3, TiO_2, or SiO_2. The employed ALD reaction parameters have been previously adjusted to achieve homogeneous and conformal inner coating along the full length of the nanochannels [4].

Figure 1 shows the electrolytical cell (a) and the *I-V* characteristics (b-d), measured across the single nanochannels using 1 M KCl solution with pH values of 2 (green), 5 (purple), and 9 (red) together with the linear *I-V* characteristics measured across uncoated nanochannels (blue) at pH 5 (PZC of PC). The ion currents of uncoated channels are higher due to the larger tip diameter. After ALD, the Al_2O_3-coated channel (Fig. 1b) exhibits a linear *I-V* curve at pH 9, which is the PZC of Al_2O_3 [5] while at lower pH values, the channel surface charges positively resulting in a preferential anion flow from tip to base. The SiO_2-coated channel (PZC = pH 2) [5] exhibits a linear *I-V* curve at pH 2 (Fig. 1d). Increasing the pH value of the electrolyte increases the negative surface charges and the *I-V* curve reveals a preferential cation flow from tip to base. Finally, the TiO_2 (PZC = pH 5) [5] coated channel exhibits symmetric ion flow at pH 5 (Fig. 1c). The surface charge can be either tuned positively (pH 2) or negatively (pH 9), resulting in either preferred anion- or cation flow.

After the ion transport measurements, each polymer foil was dissolved and free-standing, stable single conical nanotubes were imaged by scanning electron microscopy (SEM) (Fig. 2). The images reveal a conformal ALD deposition and a smooth nanochannel surface. We observed that the ALD coating improved the long term stability of the nanochannels, supposedly by prohibiting “closure” due to random polymer chain rearrangements.

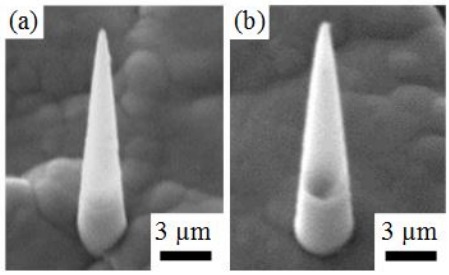

Figure 2: SEM images of free-standing single conical nanotubes obtained by selectively dissolving the track-etched PC membrane after ALD coating with Al_2O_3 (a) and TiO_2 (b).

References

[1] Perez-Mitta G., et al., Chem. Sci. 8 (2017) 890
[2] Schoch R, et al., Rev. Mod. Phys. 80 (2008) 839
[3] Siwy Z., et al. Europhys. Lett. 60 (2002) 349
[4] Spende A., et al., Nanotechnology 26 (2015) 5301
[5] Barry Carter C.; Grant Norton M., Ceramic Materials: Science and Engineering; Springer Science, New York, 2007

* Work supported by Deutsche Forschungsgemeinschaft (DFG-FOR 1583)
# M.E.ToimilMolares@gsi.de

DOI:10.15120/GR-2017-1

Graphene/Polymer Composite Membranes by ion-track technology*

L. Madauß[1$], J. Schumacher[2$], M. Ghosh[3], O. Ochedowski[1], J. Meyer[2], H. Lebius[4], B. Ban-d´Etat[4], M.E. Toimil-Molares[5], C. Trautmann[5,6], R.G.H. Lammertink[3], M. Ulbricht[2], M. Schleberger[1,#]

[1] Faculty of Physics and CENIDE, University of Duisburg-Essen, Duisburg, Germany; [2] Technical Chemistry II and CENIDE, University of Duisburg-Essen, Essen, Germany; [3] Soft matter, Fluidics and Interfaces, MESA+ Institute for Nanotechnology, University of Twente, Enschede, The Netherlands; [4] CIMAP (CEA-CNRS-ENSICAEN-UCN), Caen, France; [5] GSI Helmholtzzentrum, Darmstadt, Germany, [6] TU Darmstadt, Darmstadt, Germany

Membranes can be used in a large variety of different applications, e.g., as separating agent for nano- and ultrafiltration processes [1]. The requirements for high-performance membranes are manifold including crucial characteristics such as excellent mechanical stability, high flow rates, and narrow pore-size distribution. Graphene, a monolayer of carbon atoms, exhibits all of these criteria. Due to its infinitesimal thickness of 0.3 nm and chemical inertness it is a promising material for filter applications.

In this work, we apply swift heavy ions (SHI) as an efficient tool to nanostructure graphene, i.e. to introduce defects of adjustable size and shape [2,3]. Our concept of fabricating high performance membranes is depicted in Fig. 1. A single graphene layer is transferred onto a mechanically stable polyethylene terephthalate (PET) support foil (thickness ~13 µm) which allows handling the membrane without damaging the graphene (Fig. 1a). By applying SHI irradiation, nm-sized pores are directly formed in the graphene and chemically modified tracks are created in the supporting polymer foil (Fig. 1b). By exposing the whole composite to a suitable etchant such as NaOH, the tracks in the PET foil are converted into open channels (Fig. 1c), which will serve as supply pipes to guide the fluid towards the nanoporous graphene where the filtering process takes place.

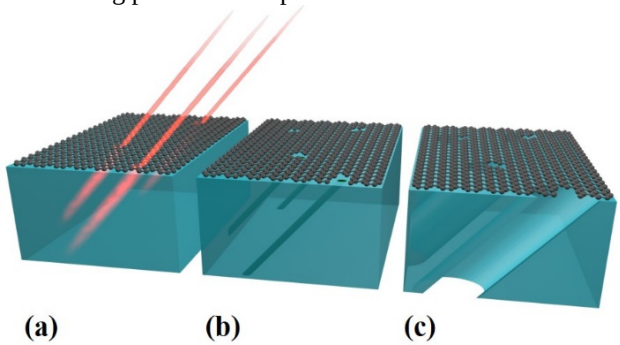

Figure 1: Schematic of fabrication process to produce graphene/polymer composite membranes: (a) SHI irradiation of graphene on PET foil, (b) generation of nanopores in graphene and ion tracks in PET foil, (c) converting ion tracks into open nanopores in PET by chemical etching. The graphene pores remain unaltered.

Figure 2 shows a representative scanning electron microscopy (SEM) image of a track-etched graphene/PET composite membrane. The sample was irradiated with 1.1-GeV Au ions at the X0 beamline of the UNILAC, applying a fluence of 1×10^8 ions/cm^2. Subsequent etching was performed in a 3 mol/L NaOH solution at 50 °C for 50 min. Under these conditions, the ion-tracks were converted into open channels of diameter 640 ± 40 nm. The absence of charging effects during the SEM studies demonstrates the presence of the conductive graphene on top of the isolating PET foil. The inset presents a scanning force microscopy (SFM) image of a single ion-induced nanopore in graphene. The pore size distribution of the nanopores in graphene is narrow with a mean diameter of 12± 0.8 nm.

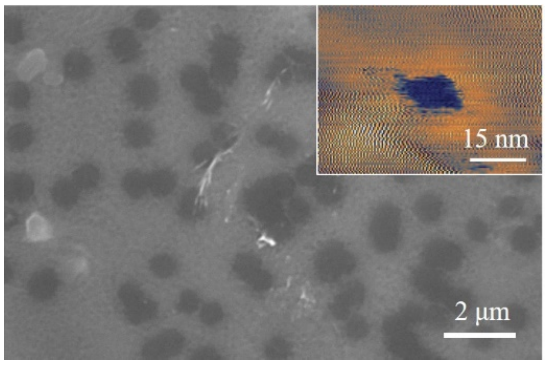

Figure 2: SEM image of a track-etched graphene/PET composite membrane. Inset presents a SFM image of a single ion-induced nanopore in the suspended graphene.

References

[1] M. A. Shannon, P.W. Bohn, M. Elimelech, J.G. Georgiadis, B.J. Marinas, A.M. Mayes, *Science and technology for water purification in the coming decades*, Nature 452 (2008**)** 301

[2] O. Ochedowski, O. Lehtinen, U. Kaiser, A. Turchanin, B. Ban-d'Etat, H. Lebius, M. Karlusic, M. Jaksic, M. Schleberger, *Nanostructuring graphene by dense electronic excitation*, Nanotech. 26 (2015) 465302

[3] L. Madauß, J. Schumacher, M. Ghosh, O. Ochedowski, J. Meyer, H. Lebius, B. Ban-d´État, M.E. Toimil-Molares, C. Trautmann, R. Lammertink, M. Ulbricht, M. Schleberger, *Fabrication of Nanoporous Graphene/Polymer Composite Membranes*, accepted in Nanoscale (2017)

$ Both authors have contributed equally

* Work supported by DFG (SPP 1459 Graphene, DFG-Schl 384/16-1, DFG Ulbr 113/10-1, NU-TEGRAM) and LOEWE project iNAPO (HMWK).

marika.schleberger@uni-due.de

Lithographic editing-system based on track-etched conical pores in glass *

P. Kohli[1], R.R. Pradeep[1], M. Dasari[1], Chuanhong Zhou[1], K.O. Voss[2], and C. Trautmann[2,#]
[1]Southern Illinois University Carbondale, IL 62901, U.S.A; [2]GSI, Darmstadt, Germany; [3] Technische Universität, Darmstadt, Germany

A new lithographic editing system with the ability to erase and rectify errors on a microscale with real-time optical feedback is demonstrated. The erasing probe is a conically shaped hydrogel (tip size ~500 nm) template-synthesized from track-etched conical pores in glass wafers (Fig. 1). Our "nano-sponge" hydrogel probe "erases" patterns by hydrating and absorbing molecules into a porous hydrogel matrix via diffusion analogous to a wet sponge. The presence of an interfacial liquid water layer between the hydrogel tip and the substrate during erasing enables frictionless uninterrupted translation of the eraser on the substrate. The erasing capacity of the hydrogel is extremely large due to large free volume of the hydrogel matrix. The fast frictionless translocation and interfacial hydration results in a high erasing rate (~785 $\mu m^2/s$) which is two to three orders of magnitude higher than AFM-based erasing (~0.1 $\mu m^2/s$) experiments.

The Polymeric Lithography Editor (PLE) pens and erasers were fabricated by means of template-assisted synthesis. In a first step, 70-µm-thick borosilicate glass substrates were irradiated with 2.2-GeV Au ions at the UNILAC of GSI. The created ion tracks were converted into conical channels by chemical etching in hydrofluoric acid. In a second step, a polydimethylsiloxane (PDMS) and agarose replica of the glass pore was generated.

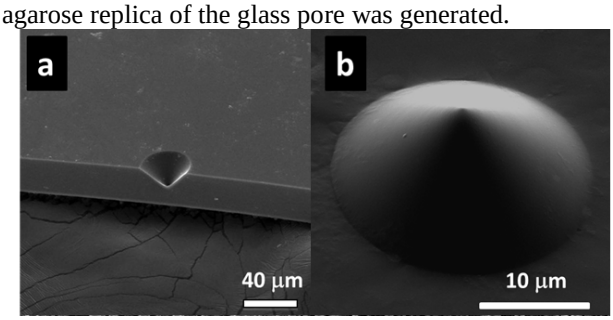

Figure 1: Scanning electron micrographs of (a) cross-section of a single track-etched pore in a glass substrate. (b) PDMS replica fabricated by using a conical glass pore as template (tip diameter 500±100 nm, base diameter 22±1 µm, pore length 38±1 µm).

The high precision and accuracy of our PLE system is obtained by coupling piezoelectric actuators to an inverted optical microscope (Fig. 2). Subsequently after erasing the patterns using agarose erasers, a PDMS probe fabricated from the same conical track-etched template was used to precisely re-deposit molecules of interest at the erased spots. The system also provides a continuous optical feedback throughout the entire molecular editing process including writing, erasing, and rewriting. To demonstrate its potential in device fabrication, we used PLE to electrochemically erase a metallic copper thin-film, forming an interdigitated array of microelectrodes for the fabrication of a functional micro-photodetector device (Fig. 2). High throughput, dot and line erasing, writing with the conical "wet-nano sponge" and continuous optical feedback, makes PLE complementary to the existing catalogue of nano/micro lithographic and 3D printing techniques. This new PLE technique will potentially open up many new and exciting avenues in lithography which have been unexplored due do the inherent limitations in error rectification capabilities of the existing lithographic techniques.

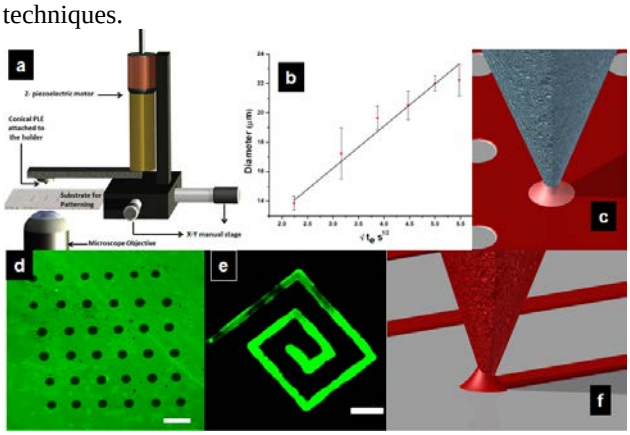

Figure 2. (a) Schematic of custom built PLE system with XYZ stage coupled to an inverted optical microscope. (b) Linear increase of the pattern diameter (in µm) with the square root of the erasing time (in s). (c) Schematic of absorption of molecules upon contact with the PLE tip with a contact time of ~1.8 s. (d) Fluorescence micrograph of PLE erasing with a 5 w/w% of agarose after gelation. The diameter of the erased patterns is 11.7 ± 0.7 µm. (e) Continuous line deposition with agarose PLE equilibrated in a 2% fluorescein solution. (f) Schematic of line pattern deposition of fluorescein using agarose encapsulated with fluorescein. Both the deposition and erasing occurred via the water meniscus formed upon contact between the conical hydrogel tip and the substrate. Scale bar in (e) and (d): 30 µm.

References

[1] Pradeep Ramiah Rajasekaran, Chuanhong Zhou, Mallika Dasari, Kay-Obbe Voss, Christina Trautmann, Punit Kohli, Science Advances 3 (2017) e1602071; doi: 10.1126/sciadv.1602071

[2] R.R. Pradeep, J. Wolff, Justin, Chuanhong Zhou, M.°Kinsel, C. Trautmann, S. Aouadi, P. Kohli, *Two-dimensional pore gradient in tracked glass*, Journal of Materials Chemistry 19 (2009) 8142

* Work supported by NSF (CHE-0748676 and CHE-0959568) and NIH (GM 106364 and GM 080711).
#pkohli@chem.siu.edu

DOI:10.15120/GR-2017-1

Seebeck coefficient measurements of $Bi_{1-x}Sb_x$ nanowire arrays

M. Cassinelli[1,2], K.-O. Voss[1], F. Völklein[3], C. Trautmann[1,2], M.E. Toimil-Molares[1,#]

[1]GSI, Darmstadt, Germany,[2] TU Darmstadt, Germany,[3] Hochschule RheinMain, Germany.

Thermoelectric (TE) devices are considered attractive potential pollution-free sources of energy, since they are able to convert thermal energy into electrical energy by means of the Seebeck effect. Moreover, supplying current through a TE device generates a temperature gradient by means of the Peltier effect, making TE devices suitable also for applications e.g. in cooling systems. The efficiency of a TE material is described by the figure of merit $Z = S^2\sigma/\lambda$, where S denotes Seebeck coefficient, σ electrical and λ thermal conductivity, the latter including contributions of charge carriers and phonons. Theoretical calculations predicted an enhancement of the TE efficiency in $Bi_{1-x}Sb_x$ nanowires (NWs) due to the presence of finite- and quantum-size effects compared to the bulk systems [1]. Moreover, a further enhancement of ZT is predicted when decreasing the NW diameter and adjusting the composition. In fact, a high value of ZT ~2.5 was calculated for 40 nm diameter wires with 13% Sb concentration. Despite these promising predictions, comprehensive and systematic measurements of the TE properties of $Bi_{1x}Sb_x$ NWs as a function of wire diameter and orientation are scarce. The difficulties include the synthesis of $Bi_{1-x}Sb_x$ NWs of controlled diameter and the task to contact single NWs to measure the value of S, σ and κ without affecting their chemical and mechanical properties [2]. Here, we present measurements of the Seebeck coefficient of arrays of $Bi_{1-x}Sb_x$ NWs with controlled composition and diameters ranging from ~750 down to ~40 nm.

Polycarbonate foils (Makrofol N, thickness 30 µm) were irradiated with ~2 GeV Au ions at the GSI UNILAC. Track etching in a 6M NaOH solution at 50°C, converted the tracks into open pores with controlled diameter between ~40 and ~750 nm. The $Bi_{1-x}Sb_x$ NWs were subsequently electrodeposited in the pores using a three-electrode cell with a saturated calomel reference electrode at room temperature. The electrolytes were based on hydrochloric acid and different concentrations of Bi(III)- and Sb(III)-chloride [2,3].

Since the TE properties of the synthesized $Bi_{1-x}Sb_x$ NWs depend on both crystallographic orientation and composition, systematic investigations by both X-ray diffraction (XRD) and energy dispersive X-ray analysis (SEM-EDX) were performed as a function of electrolyte composition (i.e. using different concentrations of Bi(III)- and Sb(III)-chloride) and average wire diameter. The results revealed that both crystallographic orientation and composition do not vary significantly as a function of wire diameter. Subsequently, different arrays of $Bi_{1-x}Sb_x$ NWs were inserted in a setup specifically developed for measurements of the Seebeck coefficient from room temperature down to 20 K.

Figure 1 shows the Seebeck coefficient values measured on Bi, $Bi_{0.85}Sb_{0.15}$ and Sb NW arrays at room temperature as a function of the wire diameter. The data allow us to distinguish three different regimes: (Zone 1) wire diameter larger than ~130 nm, S is similar to values of bulk materials (red area); (Zone 2) when decreasing NW diameter from ~130 nm to ~60 nm, S decreases monotonically (green area); (Zone 3) for nanowires with diameter below ~60 nm, the absolute value of S increases with decreasing wire diameter (blue area).

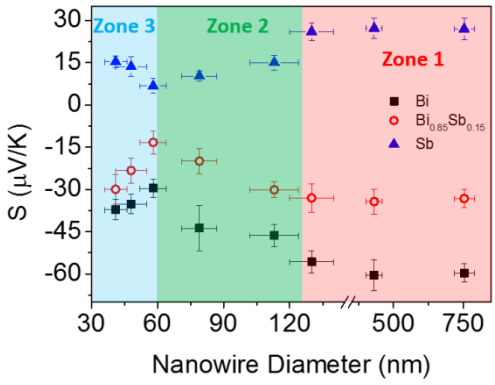

Fig. 1: Room temperature Seebeck coefficients of Bi (black squares), $Bi_{0.85}Sb_{0.15}$ (red circle) and Sb (blue triangles) nanowires as a function of their diameter.

Given that composition and crystallographic orientation of the NWs do not vary significantly as a function of wire diameter, we attribute the monotonic decrease in zone 2 to the complementary contribution to the total Seebeck coefficient of the wire of both bulk- and surface states. The analysis of the data using a two-channel model supported this assumption [4]. Only for wires thinner than ~60 nm the Seebeck coefficient raises possibly due to quantum size-effects on both NWs surface and bulk states of the nanowires.

To conclude, these measurements demonstrate the possibility to tailor and eventually further increase the Seebeck coefficient in thin nanowires due to modifications in the electronic structure of both surface and bulk states of the material. This may lead to a further increase of ZT for even thinner wires, making them suitable for thermoelectric applications such as sensing.

References

[1] L.D. Hicks and M.S. Dresselhaus, Phys. Rev. B: Condens. Matter 47 (1993) 16631, and Phys. Rev. B: Condens. Matter47 (1993) 12727
[2] M. Cassinelli, PhD Thesis, TU Darmstadt (2016)
[3] M. Cassinelli et al., NIMB 365 (2015) 668.
[4] M. Cassinelli et al., Nanoscale, 9 (2017) 3169.

* Work supported by DFG SPP1666.
# M.E.Toimilmolares@gsi.de

A new setup for the investigation of stimulated desorption

V. Velthaus[1], *J. Schall*[1], *M. Bender*[*2], *and F. Völklein*[1]
[1]Hochschule RheinMain, Rüsselsheim, Germany; [2]GSI, Darmstadt, Germany

A new laboratory setup for investigations on beam and temperature desorption processes was established. To compare the amounts of released gas, different stimuli such as thermal desorption, ion-, electron- and laser-induced desorption are possible. During future beamtimes the setup is planned to be impemented into the M3 beamline at the UNILAC or the CRYRING.

During the 2016 beamtime with swift heavy ions it was found ion-induced desorption to origin not only from the surface, but diffusion from the bulk is also significant [1, 2]. One aim of the new setup is to investigate the contribution of the bulk more detailed. The investigations with different stimulations allow to distinguish the influence of surface and bulk separately, because of different ranges of ions and electrons. While running the setup on the accelerator, ion-induced desorption at different sample temperatures and beam parameters will be investigated. Additionally measurements on cryogenic surfaces are possible. By varying the thickness of frozen gas layers, the influence of the substrate to desorption can be analyzed.

The setup (figure 1) consists of two vacuum chambers, which are separated by an aperture. The temperature of this section must be constant to reduce thermal desorption form the aperture. Therefore it is water-cooled and a smaller aperture, made out of ceramics, is mounted to decrease the thermal conduction. For the measurements, the sample is moved in front of the aperture, so it is closed by the sample and only molecules desorped from the sample surface get into the measuring chamber. For the analysis a residual gas analyzer with m/q up to 200 and a sensitivity of $5 \cdot 10^{-14}$ mbar ist used. The sample can be fixed on a heating assembly or a cryostat. Thus, a temperature range from 10 K up to 800 °C can be applied. In addition there are flanges for the connection to the accelerator and the installation of an electron and a keV-ion source. A pumping system evacuates the setup to a pressure of $1 \cdot 10^{-10}$ mbar. A load lock for quick sample exchange is included.

First investigations on thermal desorption spectroscopy (TDS) are shown in figure 2. The gases desorb on different temperatures. Hydrogen has the highest desorption temperature due to diffusion from the bulk. In contrast the other gases desorb form layers close to the surface and show lower desorption temperatures [3].

The measurements on thermal desorption spectroscopy will be continued. In future the cryostat, the electron and the ion source will be mounted to do investigations on electron- and ion-induced desorption.

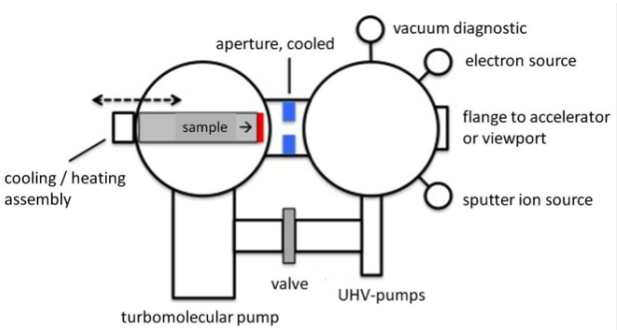

Figure 1: Schematic sketch of the installed setup. The cooling / heating assembly denotes either the heater or the cryostat. The loadlock is not displayed.

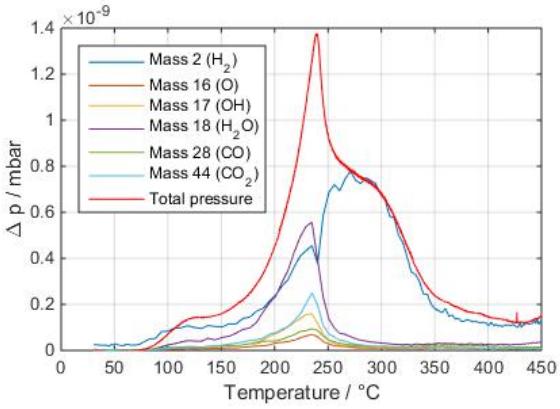

Figure 2: First measurement of thermal desorption from a copper sample.

References

[1] A. Warth, "Vorbehandlungs-Prozeduren zur Minimierung Ionenstrahl-induzierter Desorption", Master Thesis, Hochschule RheinMain (2016)

[2] A. Warth et al., "Ion-induced desorption and cleaning processes", GSI Scientific Report 2015

[3] V. Velthaus, "Untersuchung thermisch-induzierter Desorptions- und Diffusionsvorgänge"; Bachelor Thesis, Hochschule RheinMain (2017)

* m.bender@gsi.de

DOI:10.15120/GR-2017-1

Thermal pre-treatment to minimize ion-induced desorption

A. Warth[1], *M. Bender*[*2], *D. Severin*[2], *and F. Völklein*[1]
[1]Hochschule RheinMain, Rüsselsheim, Germany; [2]GSI, Darmstadt, Germany

Heavy ion-induced desorption is a major intensity limitation for particle accelerators. Due to interaction of the particle beam with gas molecules, ions can hit the beam tube wall and stimulate the release of gas. At high beam intensities it is of most interest to develop new solutions to minimize the amount of desorbed gas molecules per incident ion, the so-called desorption yield.
In 2015, we tested the desorption yield (desorbed gas molecules per incident ion) for different accelerator-specific materials exposed to different cleaning procedures and revealed thermal annealing as the most effective treatment [1]. Last year we have systematically investigated desorption under thermal annealing between 200 °C and 600°C for variuos annealing times [2]. The reduction of the desorption yield can be described as an exponential decay as:

$$\eta = \eta_0 + ae^{-bX} \quad (1)$$

with X being the annealing time or the annealing temperature, η_0 is the ultimate desorption yield value and a and b are constant values. The decrease of the desorption yield as a function of annealing time at 200 °C is shown in figure 1. At this temperature the yield decreases down to about 18 % of the initial value. The annealing affects all desorbed gas species, H_2, CO and CO_2 to similar amounts.
Increasing the annealing temperature also leads to an exponential decay of the desorption yield as shown in figure 2 for oxygen-free copper samples, all annealed for 24 h. Also here, a limit is reached at 550 °C, where an increase of the temperature is not further effective. However, the desorption yield can be reduced down to about 3 % of the initial value which means an important improvement for dynamic vacuum effects in particle accelerators.

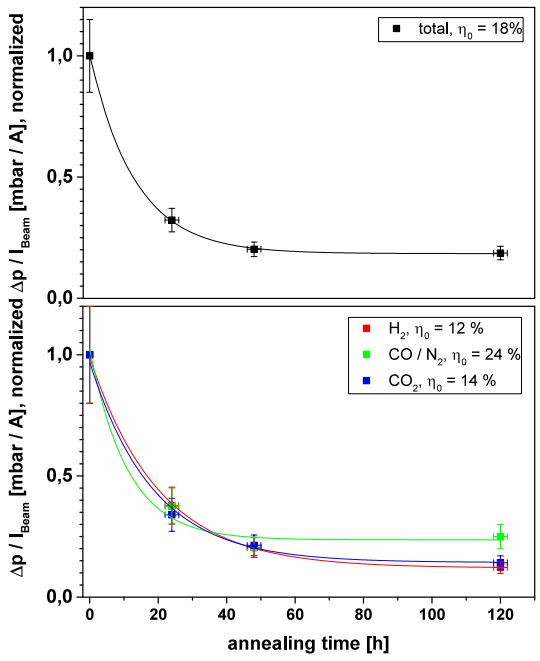

Figure 1: Normalized desorption yield of gold-coated copper as a function of annealing time. The annealing temperature for each sample was 200 °C. η_0 indicates the saturation value compared to the initial desorption yield.

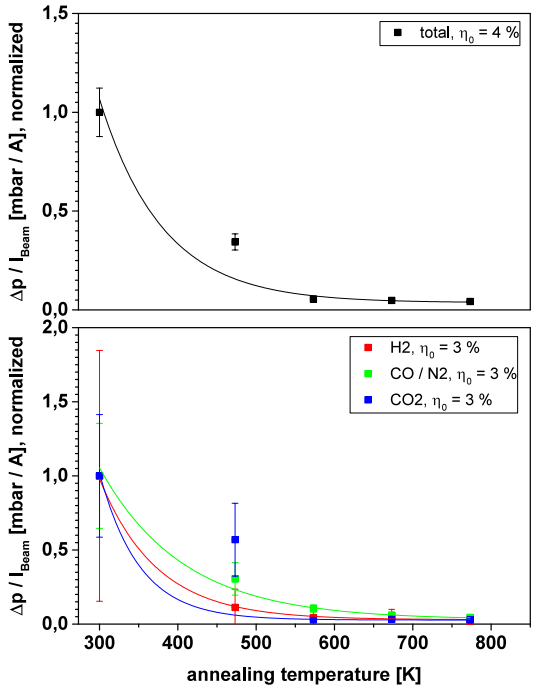

Figure 2: Normalized desorption yield as function of annealing temperature. The annealing time was 24 h for each sample.

References

[1] A. Warth, et al., "Ion-induced desorption and cleaning processes", GSI Scientific Report 2015

[2] A. Warth, "Vorbehandlungs-Prozeduren zur Minimierung Ionenstrahl-induzierter Desorption", Master Thesis, Hochschule RheinMain (2016)

* m.bender@gsi.de

DOI:10.15120/GR-2017-1

ESD setup for desorption yields investigation on various metals

P.M. Suherman, M.C. Bellachioma, J. Kurdal, E. Renz
GSI, Darmstadt, Germany.

Introduction

A new ESD (electron stimulated desorption) experimental setup has been developed at the vacuum lab CSVS (Common System Vacuum System) Division. The existing setup from previous work [1] has been reconstructed, in order to investigate the desorption yields of various metals used in UHV (ultra-high vacuum) chambers. The desorption yield plays an important role in understanding the interactions between the chamber surface and charged particles such as ions and electrons.

ESD Experimental Setup

The new ESD setup consists of two vacuum chambers separated by a ceramic insulator. The first chamber consists of a pumping system with a known aperture, residual gas analyser, extractor gauge, and gas inlet. The second chamber is dedicated for loading and placement of the sample. Figure 1 shows a schematic of the configuration of the ESD experimental setup

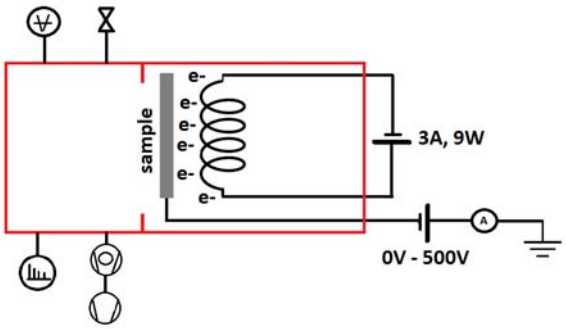

Figure 1: Schematic configuration of the ESD experimental setup at Vacuum Lab CSVS Group.

The main new feature of this setup is a new sample holder that has been designed in such a way to allow investigation of desorption yields of various metals more efficiently. Figure 2 shows the sample holder involving the filament, sample head, and electrical feedthrough.

The filament used for this work was a tungsten filament as electron source. The sample, located at the sample head, was placed above the filament and biased at positive voltage to attract the electrons from the filament. The electrical feedthrough on the sample holder allowed a current flow through the filament, voltage bias on the sample, current measurement on the sample, and ground connection.

The current through the filament was normally around 3 Amp, 9 Watt power. The voltage for the sample was biased from +0 V to + 500 V. The current due to the electron bombardment on the sample was measured using a Picoammeter.

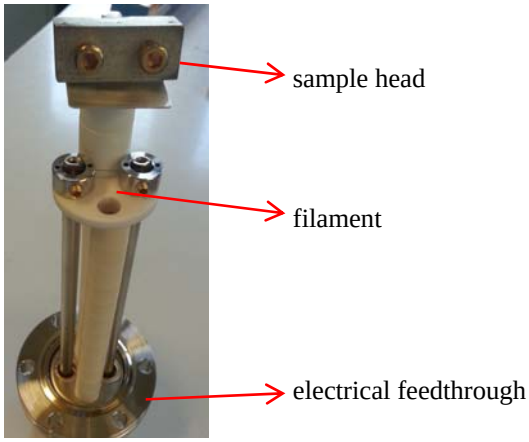

Figure 2: A new design of sample holder for the ESD experimental setup at Vacuum Lab CSVS Group

Figure 3 shows preliminary data obtained from the ESD measurement. As shown in Figure 3, the ion current measured on the samples was polarised into minus current due to the electron bombardment on the sample. At the same time, there was a change on the ion current for residual gas composition and the chamber pressure. The desorption yield can be calculated from the data of ion current and partial pressure measurements. This will be conducted in the future work.

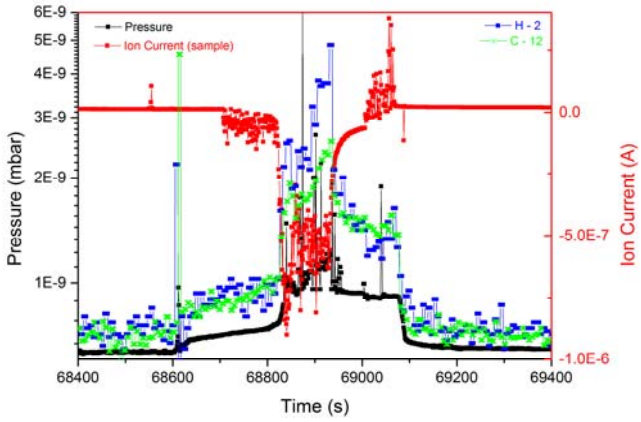

Figure 3: Preliminary results showing the effect of electron bombardment on the sample, chamber pressure, and residual gas compositions.

References

[1] K. Wetzel, Diplomarbeit, 2002

***Acknowledgement*:** A. Coronato, G. Savino, S. Strohmenger, H. Rittelmeyer

DOI:10.15120/GR-2017-1

Operation and improvements of PHELIX

S. Götte[1], *C. Brabetz*[1], *C. Bruske*[1], *U. Eisenbarth*[1], *M. Kreutz*[1], *S. Kunzer*[1], *D. Reemts*[1], *D. Schumacher*[1], *L. Tymura*[1], *F. Wagner*[1,2], *B. Zielbauer*[1,2], *and V. Bagnoud*[*1,2]

[1]GSI, Darmstadt, Germany; [2]Helmholtz Institute Jena, Germany

The *P*etawatt *H*igh *E*nergy *L*aser for heavy *I*on E*x*periments (PHELIX), a user facility of GSI, has been serving an international user community for nine years as the main experimental capability of the plasma physics department. PHELIX is a versatile nanosecond and sub-picosecond laser delivering pulses above 100 J and in a peak-power range up to 500 TW. In 2016 a major upgrade of the pre-amplifier section has been performed without a significant impact of the beam-time: As planed, ten experiments were conducted. Three of experiments were made at the UNILAC experimental area, where one was done in combination with the ion beam available at this site. The rest was done at the in-house experimental area at the PHELIX building. Details about the various experimental beam times delivered by the laser are described in the plasma physics section of this annual report [1 ... 9]. Additionally, one internal experiment was done in-house. Basing on results of experiments performed at PHELIX, several peer-reviewed articles were published in 2016 [10 ... 16]. Since it takes time to publish results afterwards, most of these took place in the year(s) before. One of the worldwide unique aspects of PHELIX lies in its very good temporal contrast, whose characteristics and most recent developments have been published in [17].

Operation and improvements

As illustrated in Fig. 1, about half of time was spent to prepare and to perform external and internal beam-times. The PHELIX shot data base registered 414 shots on target. 5.1 % (in total: 21) of these are marked as failed: 16 due to problems with hardware, four caused by the experimentalists, one due to an operator failure. The experimentalists got compensation for all failed shots.

Most of the shut down time was spend to rearrange the pre-amplifier section. Details can be found in [18]. Additionally, simulations were started to develop a new main amplifier head design for higher repetition rate operation [19], and two in-house developed measurement devices were brought to daily operation [20, 21].

Outlook

The increase of the repetition rate of the pre-amplifier section to somewhat of a few shots per minute for dedicated high repetition rate experiments with energies at the Joule level will be continued after the optical setup has been changed successfully.

* v.bagnoud@gsi.de

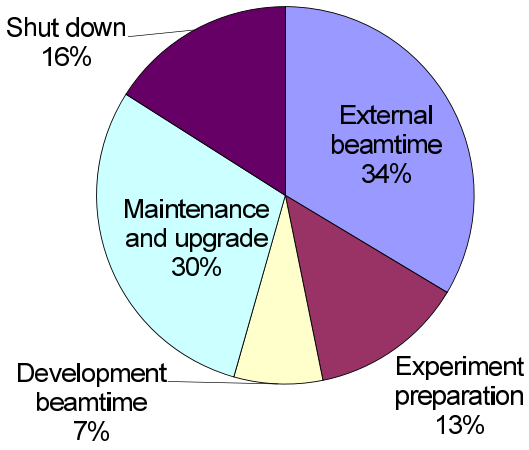

Figure 1: Usage of PHELIX in 2016

References

[1] M. Ehret et. al., this report
[2] A. Tebartz et al., this report
[3] B. Borm et al., this report
[4] P. Hilz et al., this report
[5] D. Jahn et al., this report
[6] W. Cayzac et al., this report (Charge-state equilibration ...)
[7] J Hornung et al., this report (Time resolved measurement ...)
[8] P. Neumayer et al., this report
[9] D. Khaghani et al., this report
[10] B. Borm at al., Review of Scientific Instruments **87** 9 (2016)
[11] W. Cayzac et al., Journal of Physics: Conference Series **688** 012009 (2016)
[12] I. Engin et al., Proceedings of Science, PSTP2015 **002** (2016)
[13] A. Ortner at al., Journal of Physics: Conference Series **688** 012081 (2016)
[14] A. Schönlein et al., Europhysics Letters **114.4** 45002 (2016)
[15] F. Wagner et al., Physical Review Letters **116** 205002 (2016)
[16] F. Wagner et al., High Power Laser Science and Engineering **4** e45 (2016)
[17] V. Bagnoud and F. Wagner, High Power Laser Science and Engineering **4** e39 (2016)
[18] U. Eisenbarth et al., this report
[19] M. Patrizio et al., this report
[20] V. A. Schanz et al., this report
[21] J. Hornung et al., this report (Development of a FROG ...)

DOI:10.15120/GR-2017-1

Implementation of the upgraded PHELIX pre-amplifier *

U. Eisenbarth†[1], *S. Götte*[1], *S. Kunzer*[1], *D. Reemts*[1], *B. Zielbauer*[1], *and V. Bagnoud*[1,2]
[1]GSI, Darmstadt, Germany; [2]HIJ, Jena, Germany

In the past year, significant progress has been achieved at the PHELIX laser facility on the way towards higher pulse repetition rates. After detailed studies on the characterization of a flashlamp-based amplifier head and improvements of the optical layout the new pre-amplifier system has been implemented at the PHELIX facility. This step represents an important milestone on the way towards higher performance in terms of output energy and shot repetition rate.

The PHELIX Pre-Amplifier is a flashlamp-based Nd:glass laser amplifier system with a typical pulse output energy of up to 10 J and a repetition rate of one shot every 3 minutes. This limitation mainly arises from thermal wavefront deformations such as defocus, astigmatism, and higher order aberrations as well as birefringence effects. However, some experiments using only the pre-amplifier would greatly benefit from a higher repetition rate. In addition, the design of the 100 J laser to be built for the plasma physics collaboration at FAIR includes a pre-amplifier with the same characteristics as the one of PHELIX but this amplifier should operate at a higher repetition rate. For this reason, it was decided to upgrade the PHELIX pre-amplifier to a repetition rate of 3 shots per minute not only to serve the greater user community but also to gather hands-on experience for the FAIR 100 J laser.

The project follows two lines: at first, a new amplifier layout had to be implemented to overcome the thermal loading limitations of the previous design and second, individual components have been improved. The 45 mm amplifier has been redesigned, which includes a new 45 mm head as well as a new power supply using low voltage (2 kV) and off-the-shelf components. The newly designed optical layout consists of two amplifier heads (19 mm and 45 mm diameter) in double-pass configuration combined with Faraday rotators (Fig. 1 top). The new system needed to be inserted in an existing laser system which led to many layout constraints such as the position of object and image planes, input and exit beam diameters as well as various space limitations.

In a two month shutdown phase in summer 2016, the new system was successfully installed (Fig. 1 bottom). First measurements demonstrated output energies up to 17 J with considerable margin in terms of flashlamp voltages. Hence the design value of 20 J should be easily reachable. In addition, particular attention was paid to the optimization of the passive transmitted wavefront through the system. Precise alignment in combination with a strongly enhanced Shack-Hartman wavefront sensor (developed at PHELIX) allowed for an overall wavefront error of less than $\lambda/4$. After correction of astigmatic aberrations using controlled deformation of a polarizer plate in the beam path the residual wavefront error corresponds to spherical aberration as the most prominent contribution. During a shot the defocus aberrations is by far the dominating contribution to the wavefront deformation. This effect is compensated using a motorized lens at one of the relay telescopes. Higher order aberrations are compensated by a deformable mirror.

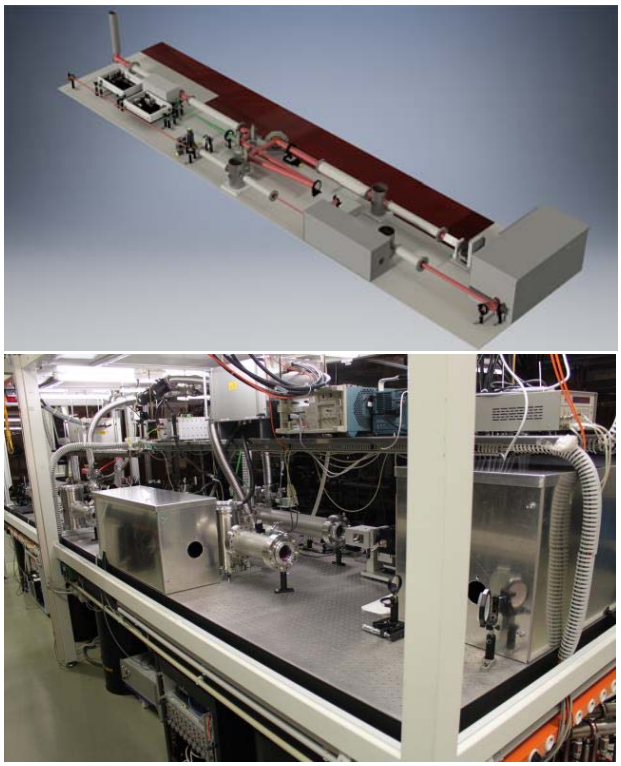

Figure 1: The new PHELIX pre-amplifier as planned (top) and implemented (bottom).

First tests also showed that the magnification of a telescope led to unexpected aperture clipping at the 45 mm head which lead to very little alignment margin and turned out to be critical for daily system usage. Hence, slight modifications of the magnification of telescopes before and after the 45 mm head will easily overcome the limitation. The new lenses will be installed in an upcoming maintenance period. Meanwhile several beamtimes have been performed since the implementation of the new system. The next step will focus on an operation at higher repetition rates on the order of one shot every 20 to 30 s.

* This report is also published in the HIJ Scientific Report 2016
† u.eisenbarth@gsi.de

DOI:10.15120/GR-2017-1

Development of an actively cooled glass amplifier at PHELIX

M. Patrizio[1,2], *V. Bagnoud*[1], *B. Zielbauer*[1], *and M. Roth*[2]
[1]GSI, Darmstadt, Germany; [2]TU Darmstadt, Darmstadt, Germany

To improve the repetition rate of the *H*igh *E*nergy *L*aser for heavy *I*on Experiments (PHELIX) a cooling system for the main amplifier is required. In preparation for this task several simulations have been conducted to optimize the coolant flow, identify promising cooling agents and to improve the cooling time by using a time dependent temperature profile for the coolant.

Coolant flow

To ensure the wavefront of the Laser to be as undisturbed as possible after passing through the amplifier, it is important to reduce temperature gradients inside the glass to a minimum. This can only be achieved if the coolant is applied to the glass homogeneously. Using *CADFEM ANSYS* to run 3D fluid dynamics simulations it was possible to develop a concept to distribute the coolant evenly over the total width of the glass plate as can be seen in Figure 1. To facilitate the removal of potential bubbles the coolant was injected from the bottom and extracted from the top while the overall design is a sandwich of glass - coolant - glass.

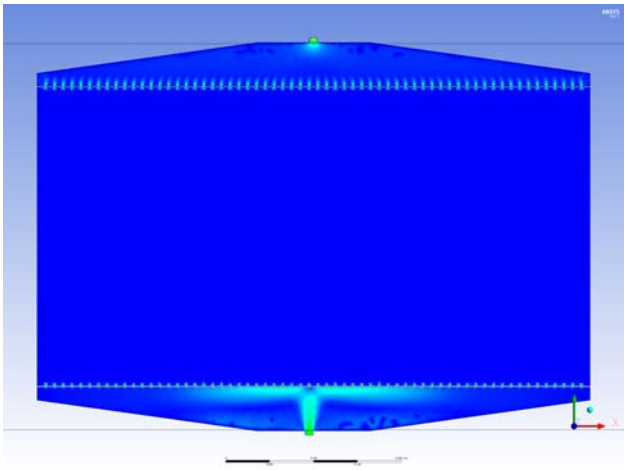

Figure 1: Fluid velocity inside the amplifier

Coolant temperature profile

Simulations have shown that the thermal conductivity of glass is too low to achieve the goal of reducing thermal gradients below 0.01 K within 10 minutes if the coolant is injected at a constant temperature. To counter this problem we devised a plan to inject the coolant at a lower temperature during the initial phase of the cooling cycle to induce higher thermal gradients between the glass and the coolant and thus increase the thermal flux. To stabilize the temperature at the specified design point of the amplifier the coolant temperature is raised to the design point temperature in the second phase of the cooling cycle. This concept was again simulated using *CADFEM ANSYS* (an example can be seen in Figure 2) and the durations and temperatures of the phases were optimized.

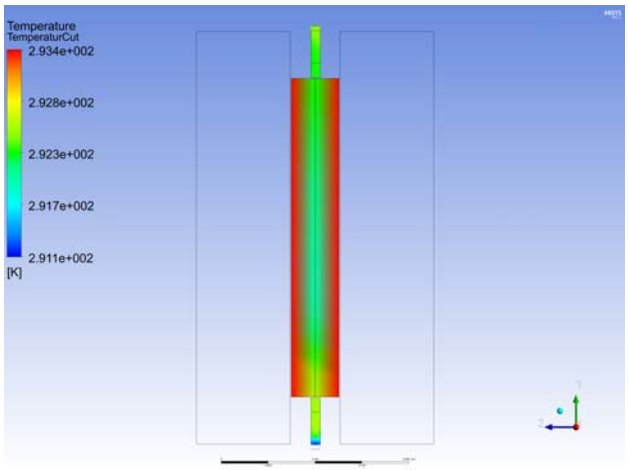

Figure 2: Temperature distribution inside the glass and fluid (cut view from the side @ t = 10s)

Wavefront construction

Based on the previous simulations it is possible to calculate the deformations of the wavefront caused by the remaining thermal gradients left in the glass after one cooling cycle. This is caused by the differences in the optical path due to the thermal dependency of the refractive index and the thermal expansion of the glass. The constructed wavefronts were used as a benchmark for comparing different cooling agents and to further improve the temperature profile of the coolant.

Outlook

The development of the amplifier requires experimental data to complement the information gained from the simulations. Therefore experiments have been planned to test the chemical compatibility of the cooling agent with the glass as well as improving the cooling of our flash lamps and develop a design for the amplifier that is coolant tight.

DOI:10.15120/GR-2017-1

Noise reduction technique for high dynamic range temporal laser pulse profile measurement *

V.A. Schanz[1,2], *F. Wagner*[3], *M. Roth*[1,4], *and V. Bagnoud*[2]

[1]GSI, Darmstadt, Germany; [2]TU Darmstadt, Darmstadt, Germany; [3]HI Jena, Jena, Germany; [4]FAIR, Darmstadt, Germany

At the PHELIX laser a novel technique is proposed which enlarges the dynamic range of temporal laser intensity pulse profile measurement devices by several orders of magnitudes.

In today's laser-plasma experiments it is essential to know the whole temporal intensity profile of a high intensity laser pulse. The intensity range of interest spans over twelve orders of magnitude, from the ionization threshold of matter, around 10^9 W/cm^2, up to the maximum achievable peak intensity. Unfortunately available measurement devices are limited to nine to eleven orders of magnitude dynamic range. Temporal high dynamic range measurements are typically done by third order cross-correlators, a scheme of such a device is shown in fig. 1. The limits for the dynamic range are formed by the maximum signal strength and noise photons, generated in the sum-frequency-generation (SFG) process.

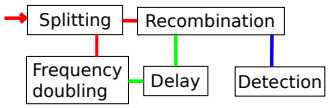

Figure 1: Scheme of a third order cross-correlator: The pulse to be measured enters the device (arrow) and splits in two. One part is frequency doubled, delayed and afterwards is recombined with the other partial beam in a nonlinear crystal. In this, a sum-frequency generation of both beams takes place and the generated signal is detected.

Noise photons can be generated by interaction of the beam of the fundamental frequency ω with itself. This is a two step process, illustrated in fig. 2, where parts of this beam are frequency doubled and scattered into the direction of the frequency doubled beam. In this case the same optimized conditions apply for the SFG of such a frequency doubled, scattered photon with the fundamental beam to noise as it applies for the SFG of the signal.

Calculations show that the signal to noise ratio (SNR) depends on the phase mismatch of the frequency doubling (Δk), the nonlinear optical coefficient (d_{eff}) of the 1ω beam in the recombination crystal and the scatter distribution S of the generated 2ω noise light into the direction of the 2ω beam, which all depend on the angles of incidence of the fundamental and frequency doubled beam α_1 and α_2, respectively, and the cutting angle of the crystal Θ.

$$SNR = \frac{I_{3\omega}}{I_{3\omega,noise}} \propto \frac{\Delta k^2}{S d_{eff}} \qquad (1)$$

* Work supported by GSI(PHELIX) /HI Jena /TU Darmstadt /Eurofusion.

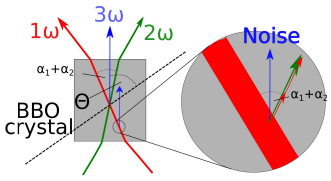

Figure 2: The left side of the scheme shows a nonlinear crystal and the both interacting beams. The right side shows a magnified area of the fundamental beam (1ω), which generates frequency doubled photons (2ω) and interacts with these photons to noise photons (noise).

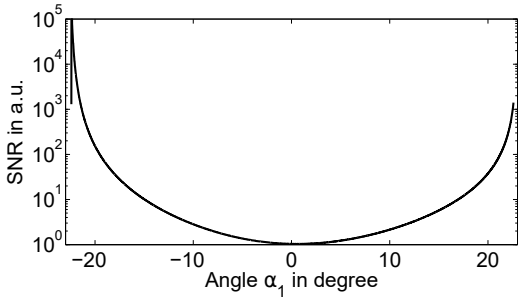

Figure 3: For a BBO-crystal, predicted signal to noise ratio enhancement as a function of the angle of incidence of the fundamental beam.

To maintain phasematching for the SFG of the signal these three angle have to be matched to each other. With this the increase of SNR depending on the angle of incidence α_1 was calculated. The result is shown in figure 3.

A prototype device was built to validate this technique. The published results [1] show the first measurement of a laser pulse over 12.5 orders of magnitude and therefore experimentally validates the proposed technique.

References

[1] V. A. Schanz et al, "Noise Reduction in Third Order Cross-Correlation by Angle Optimization of the Interacting Beams", Opt. Express **25**(8), 9252–9261 (2017).

DOI:10.15120/GR-2017-1

Improvement of the homogeneity of the laser-driven proton beam within the LIGHT project *

D. Jahn[1], *D. Schumacher*[2], *C. Brabetz*[2], *S. Weih*[1], *J. Ding*[1], *F. Kroll*[3,4], *F.E. Brack*[3,4], *U. Schramm*[3,4], *T. E. Cowan*[3,4], *V. Bagnoud*[2,5], *A. Blazevic*[2,5], *and M. Roth*[1]

[1]Technische Universität Darmstadt, Darmstadt, Germany; [2]GSI Helmholtzzentrum für Schwerionenforschung, Darmstadt, Germany; [3]Technische Universität Dresden, Dresden, Germany; [4]Helmholtzzentrum Dresden-Rossendorf, Dresden, Germany; [5]Helmholtz-Institut Jena, Jena, Germany

Laser-driven ion acceleration is an emerging and promising field in which the Laser Ion Generation Handling and Transport (LIGHT) project makes a significant contribution. LIGHT combines the laser-driven ion acceleration with conventional accelerator technology realized in a worldwide unique test beamline [1] and leads to developments of experimental and applied science capability for e.g. FAIR and radiography. The project is based on a Target Normal Sheath Acceleration (TNSA) source driven by the Petawatt High-Energy Laser for Heavy Ion EXperiments (PHELIX) 100 TW beam resulting in a continuous proton energy spectrum. The generated ions are captured by a high-field solenoid for energy selection of protons of 9±1 MeV via chromatic focusing and transported into a radiofrequency double spiral resonator operating at -90 degrees synchronous phase which is used for phase rotation of the single ion bunch. Behind the resonator, the beam is transported into a second target chamber. This transport can optionally be supported with two permanent quadrupole doublets. In the second target chamber a second high-field solenoid system was installed for steep focusing to access highest proton peak intensities. The beamtime in April 2016 aimed to improve the proton beam homogeneity. This goal is essential to enable the time-resolved imaging capability of the laser-driven proton beam and for the determination of a density distribution of a sample. In this beamtime, the so called Radiochromic Imaging Spectroscopy (RIS) was chosen as the detection method in which several radiochromic films (RCF)enable a spectral and spatial analysis of the beam profile. Due to the Bragg behaviour of the protons connected to a corresponding position in the film, an energy resolution is possible. Based on the transverse spectrum, the so called normalized beam uniformity factor (isonorm 13694:2015) can be calculated, which describes whether the beam has an uniform distribution (U_η = 0 completely uniform).

We have shown already the successful generation of sub-nanosecond focused proton bunches [2], this time compression enables the resolution of fast dynamic processes. Now we will improve the beam homogeneity. Figure 1 a) shows the beam profile recorded on a RCF film (Bragg peak at 7.4 MeV) at 6 m distance from target and shows low particle numbers but has a good homogeneity (U_η = 0.27). Based on TraceWin simulations, the remove-

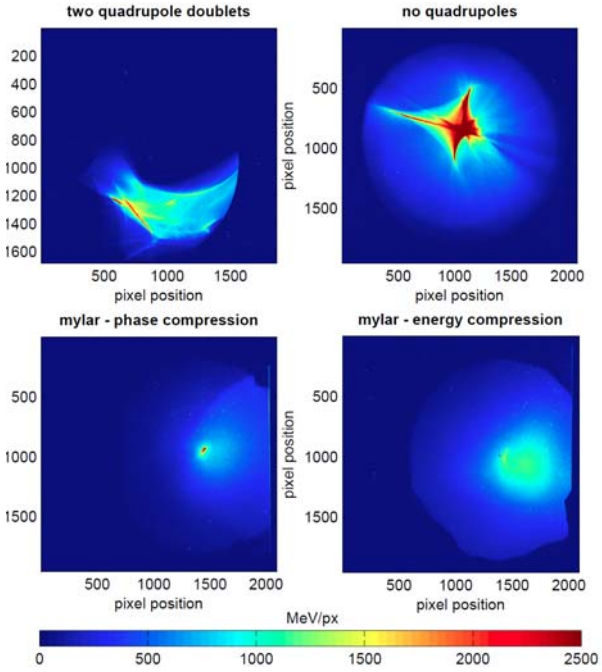

Figure 1: Beam profiles at 6 m distance from the target: a) beam with the installed quadrupole doublets, b) beam without the quadrupole doublets, c) time compressed beam with a mylar foil, d) energy compressed beam with a mylar foil.

ment of the quadrupole doublets within the beamline improved the transport efficiency. Figure 1 b) demonstrates a higher energy deposition at 6 m distance from target and a star shaped inhomogeneity leading to U_η = 0.50. In the next step, a 1.25 μm thin mylar foil for transverse scattering (negligible energy loss of 10%) was placed between the first solenoid and the rf cavity leading to significant improvements. Figure 1 c) shows the beam profile of a beam which is compressed in time with a beam uniformity U_η = 0.38. Figure 1 d) shows the profile of an energy compressed beam with a beam uniformity U_η = 0.25. This beam uniformity value in combination with the increased particle number describes an essential improvement in our beam transport quality.

References

[1] S. Busold *et al.*, NIMA **740**, 94-98 (2014)

[2] S. Busold *et al.*, Scientific Reports **5**, 12459 (2015)

* This report is also published in *News and Reports from High Energy Density generated by Heavy iOn and Laser Beams 2016.*

DOI:10.15120/GR-2017-1

Further steps towards the generation of intense, subnanosecond heavy ion bunches at LIGHT *

J. Ding[1], *D. Schumacher*[2], *D. Jahn*[1], *C. Brabetz*[2], *F.E. Brack*[3,4], *F. Kroll*[3,4], *S. Weih*[1], *U. Schramm*[3,4], *T.E. Cowan*[3,4], *V. Bagnoud*[2,5], *A. Blazevic*[2,5], *and M. Roth*[1,6]

[1]TU Darmstadt, Darmstadt, Germany; [2]GSI, Darmstadt, Germany; [3]TU Dresden, Dresden, Germany; [4]HZDR, Dresden, Germany; [5]HI Jena, Jena, Germany; [6]FAIR, Darmstadt, Germany

The LIGHT collaboration has been founded to provide a testbed for Laser Ion Generation, Handling and Transport [1]. The laser ion generation is based on the Target Normal Sheath Acceleration (TNSA) mechanism and is driven by the PHELIX 100 TW beam line at GSI. A pulsed solenoid captures and collimates a part of the divergent ion beam with a continous energy spectrum by means of achromatic focusing. The resulting collimated beam can be compressed in phase or energy in a radiofrequency (rf) cavity, which is situated two meters behind the ion source. The resulting ion beam is then diagnosed with a diamond detector for a temporal depiction of the achieved phase focus at a distance of six metres from the target.

After a succesful first demonstration of the generation, handling and transport of fluorine ions in 2015 [2] a subsequent campaign was launched in 2016 to optimise the resulting ion beam. One of the main differences to the generation of intense subnanosecond proton pulses [3] using the same setup is, that the central energy of the transported fluorine ion bunch is only a tenth of the central energy of the proton bunch. Therefore the fluorine ion beam is longitudinaly much longer at the entrance of the rf cavity than the proton beam and exceeds the cycle duration of the rf cavity. This leads to the formation of multiple ion bunches with varying degrees of phase compression.

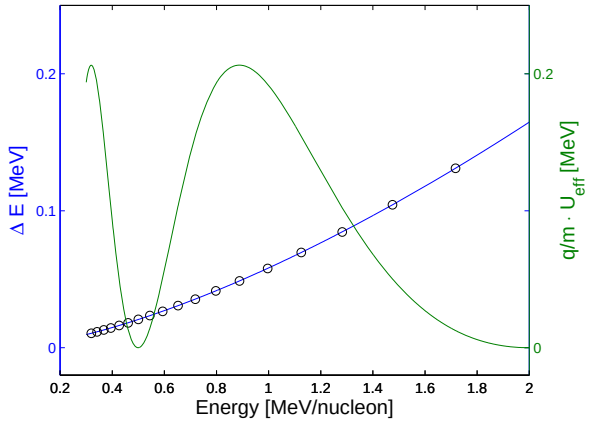

Figure 1: The energy necessary to achieve a temporal focus of F^{7+} ions is plotted as ΔE (distance between the circles indicate Δt=9.2 ns at cavity entrance), whereas $q/m \cdot U_{eff}$ demonstrates the effective gap voltage for F^{7+} ions.

The utilised rf cavity is a three gap spiral resonator and is designed for particles with kinetic energies of 8 MeV/u. The effeciveness of the bunching depends on the kinetic energy of the particles which can be seen in figure 1. The gap voltage in gap two has a phase difference of π with respect to gap one and three. This means for maximum effectiveness, the particles must have travel times from gap to gap of 9.2·(n+1)/2 ns (standing waves f_{rf}=108.4 MHz).

To reduce the number of intense ion bunches one can exploit the characteristics of the cavity. By increasing the energy of the collimated F^{7+} ions from 0.95 MeV/u to 1.31 MeV/u and adjusting the rf power to achieve temporal focussing one strongly overcompensates the temporal divergence at lower energies and undercompensates at higher energies. The result of such a configuration can be seen in figure 2, where also the result of 2015 is depicted. It shows, that in the campaign 2016 we were able to suppress all other bunches when compared to the maximum intensity bunch at around 1.3 MeV/u. The steep slope of U_{eff} equals a high sensitivity of the minimum FWHM temporal width to the phase of the cavity and therefore the high intensity bunch is still in the order of nanoseconds.

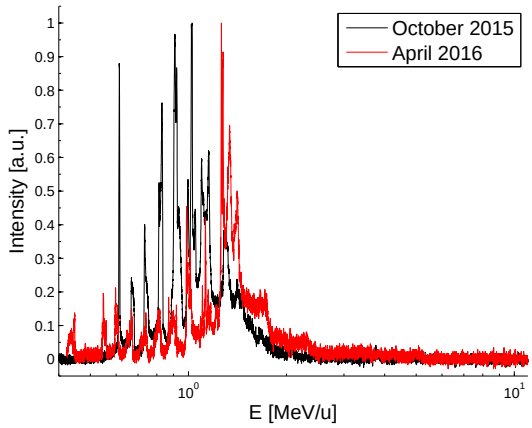

Figure 2: Time of flight data of diamond detector converted to energy per nucleon

References

[1] S. Busold et al., NIMA 740, 94-98 (2014).

[2] J. Ding et al., HEDgeHOB annual report 2015.

[3] S. Busold et al., Sci. Rep. 5, 12459; (2015).

* also published in 'News and Reports from High Energy Density generated by Heavy Ion and Laser Beams'

DOI:10.15120/GR-2017-1

Energy selective focusing of TNSA proton beams by picosecond-laser driven ultra-fast EM fields* †

M. Ehret‡ [1,2], *J.I. Apiñaniz* [3], *M. Bailly-Grandvaux* [1], *V. Bagnoud* [4], *C. Brabetz* [4], *S. Malko* [3], *A. Morace* [5], *M. Roth* [2], *G. Schaumann* [2], *L. Volpe* [3], *and J.J. Santos* [1]

[1] Centre Lasers Intenses et Applications (CELIA), UMR 5107, Université de Bordeaux, Talence, France; [2] Institut für Kernphysik, Technische Universität Darmstadt, Darmstadt, Germany; [3] Scientific area of Pulsed Laser Center C.L.P.U., Salamanca, Spain; [4] Plasmaphysik/PHELIX, GSI Helmholtzzentrum für Schwerionenforschung GmbH, Darmstadt, Germany; [5] Institute of Laser Engineering (ILE), Osaka University, Japan

Abstract

This work demonstrates efficient micro-lensing of laser-accelerated proton beams by transient electromagnetic (EM) fields in coil targets. In an all-optical principle, high intensity ps-laser pulses are used to charge solid density targets and induce EM target-discharges [1]. The strong transient EM-fields are guided by the target geometry. Such EM-mode propagation along wire targets [2] has already been used for the guiding of a proton beam [3]. Our collaboration aims at a more easily tunable energy-selective collimation and focusing with independent discharge and particle source targets: A sub-mm coil shaped part of the discharge target's rod produces lensing effects. Protons within an energy range of approximately ± 2 MeV, with energies up to 12 MeV, are focused over cm-scale distances.

Experiment

A 50 % subdivision of the Petawatt High Energy Laser for Heavy Ion Experiments (PHELIX) with 500 fs, 50 J focused at 5×10^{18} W/cm^2 into a 10 μm diameter focal spot drives the discharge of a flat 50 μm-thick Cu disc. Targets comprise such a disc as well as a coil of 500 μm diameter. In Capacitor-Coil-Targets (CCT) the disc is part of a capacitor, linked via the coil. Such geometry, shown in figure (1a), allows comparison to previous experiments in the ns-laser pulse regime [4]. With Disc-Coil-Targets (DCT), we conduct a first test of flat targets of simple geometry, depicted in figure (1b).

Main diagnostic is ps-time-resolved imaging of mm-sized areas by proton deflectometry, detected by a a stack of Radiochromic Films (RCF), see figure (1c) and (1d). Proton acceleration from 10 μm thick Au foils is driven by the second 50 % subdivision of the PHELIX beam, we obtain a proton cutoff energy of 18 MeV.

Two experimental configurations are applied to both target types. A first setup, depicted in figure (1c), for field strength determination where the coil's axis z is perpendicular to the proton beam symmetry axis $\langle \vec{v} \rangle$ and a second setup, depicted in (1d), for micro-lensing where $\langle \vec{v} \rangle \parallel z$.

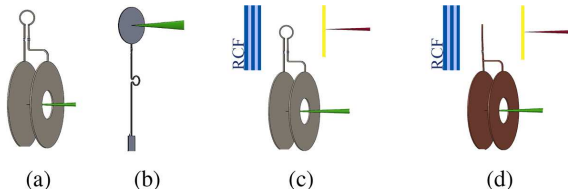

Figure 1: The ps-driver laser (green) hits (1a) the CCT on the capacitor part passing through the front plate via a hole and (1b) the DCT on the top disc. Setups (1c) for field strength determination by deflectometry and (1d) for micro-lensing, with particle source using a ps-pulse (red).

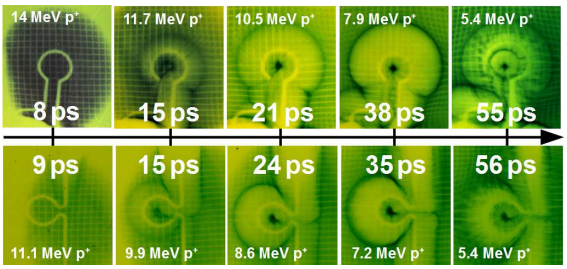

Figure 2: RCF imprints for probing times relative to the short pulse bang time. A EM mode causes comparable deflections on CCT (top) as well as on DCT (bottom).

Results

Proton deflectometry reveals the propagation of transient EM-fields following the target geometry with a phase speed of $(0.95 \pm 0.05) \times c$. Figure 2 shows results from both CCT and DCT in lensing configuration, with the discharge streaming around the coil over $\approx$ 25 ps which produces efficient focusing of the protons passing inside it. Up to 12 MeV-protons are collimated over distances of $\approx$ 5 cm and the beam emittance is reduced by a factor $\approx$ 3 compared to cases without driving the coil. A closer look on straight conductor sections makes it possible to estimate the E-field component to a peak value of several 10 GV/m.

References

[1] A. Poyé et al., Physical Review E 92(4-1):043107 (2015)

[2] K. Quinn et al., PRL 102, 194801 (2009)

[3] S. Kar et al., Nat. Com. 7, 10792 (2016)

[4] J. J. Santos et al., New Journal of Physics 17, 083051 (2015)

* ACK: POPRA Proj. 29910; IdEx U-BOR LAPHIA ANR-10-IDEX-03-02; ToIFE EuroFusion No. 633056; CRA-ARIEL

† This report is also submitted to the Report 'News and Reports from High Energy Density generated by Heavy Ion and Laser Beams 2016'

‡ michael.ehret@u-bordeaux.fr

Picosecond-laser driven ultra-fast EM fields propagating along coil targets for proton beam micro-lensing*

M. Ehret† [1,2], *J.I. Apiñaniz* [3], *M. Bailly-Grandvaux* [1], *V. Bagnoud* [4], *C. Brabetz* [4], *S. Malko* [3], *A. Morace* [5], *M. Roth* [2], *G. Schaumann* [2], *L. Volpe* [3], *and J.J. Santos* [1]

[1] Centre Lasers Intenses et Applications (CELIA), UMR 5107, Université de Bordeaux, Talence, France; [2] Institut für Kernphysik, Technische Universität Darmstadt, Darmstadt, Germany; [3] Scientific area of Pulsed Laser Center C.L.P.U., Salamanca, Spain; [4] Plasmaphysik/PHELIX, GSI Helmholtzzentrum für Schwerionenforschung GmbH, Darmstadt, Germany; [5] Institute of Laser Engineering (ILE), Osaka University, Japan

Abstract

Efficient micro-lensing of laser-accelerated proton beams by transient electromagnetic (EM) fields in coil targets has been demonstrated [1, 2]. In an all-optical principle, high intensity ps-laser pulses are used to charge solid density targets and induce EM target-discharges [3]. The strong transient EM-fields are guided by the target geometry [4]. A sub-mm coil shaped part of the discharge target's rod produces lensing effects: protons within an energy range of approximately ± 2 MeV, with energies up to 12 MeV, are focused over cm-scale distances. Our collaboration aims at the better understanding of such EM-mode propagation and its pulse shape.

Experiment

A 50 % subdivision of the Petawatt High Energy Laser for Heavy Ion Experiments (PHELIX) with 500 fs, 50 J focused at 5×10^{18} W/cm^2 into a 10 μm diameter focal spot drives the discharge of a flat 50 μm-thick Cu disc. Transient EM-fields propagate with a phase speed of $(0.95 \pm 0.05) \times c$ through the target rod. The discharges follow the target geometry and stream around the coil of 500 μm diameter over $\approx$ 25 ps, then producing efficient focusing of the protons passing inside it (see figure 1). Up to 12 MeV-protons are collimated over distances of $\approx$ 5 cm and the beam emittance is reduced by a factor $\approx$ 3 compared to cases without driving the coil: for example from initially (1.59 ± 0.05) mm mrad to (0.5 ± 0.1) mm mrad for 6.3 MeV protons.

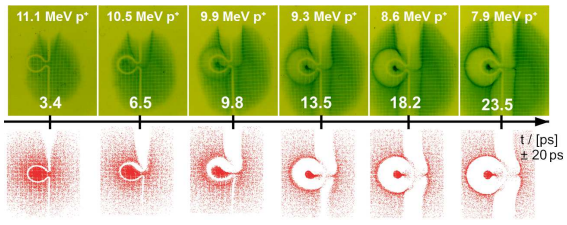

Figure 1: RCF proton imprints for different probing times within one shot (top) - the corresponding synthetic images are obtained by PAFIN simulations (bottom).

* ACK: POPRA Proj. 29910; IdEx U-BOR LAPHIA ANR-10-IDEX-03-02; ToIFE EuroFusion No. 633056; CRA-ARIEL

† michael.ehret@u-bordeaux.fr

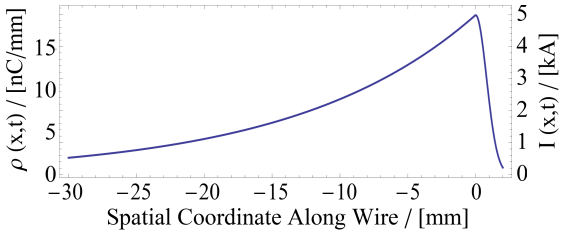

Figure 2: Charge density and displacement current.

Discussion

Rapid laser-induced target charging leads to a positive potential close to the front surface [3] and a supplementary positive potential at the target rear side [5]. Inside the target, neutralization currents form on a timescale of fs.

The positive potential attracts adjacent electrons and propagation of a positive charge distribution starts along the target surface. Using the transverse E-field component around straight conductor sections, a charge-density distribution $\rho(\vec{x}, t)$ is deduced from deflectometry data and Poisson equation. It can be described as a reduced Cristal Ball Function [6] with a rising edge of $\approx$ 3 ps and a peak value of several nC/mm. Charge density and displacement current, shown in figure 2, are linked by continuity equation assuming constant phase speed.

Simulation of such a EM-mode propagation with the Particle Field Interaction (PAFIN) code [7] reproduces fairly well the proton deflectometry data, revealing E-fields of the order of the GV/m and B-fields of a few tens of T at the coil center. Comparison of RCF films with synthetic images is shown in figure 1. We find a good agreement with experimental results for a total discharge of $\approx$ 250 nC.

References

[1] S. Kar et al., Nat. Com. 7, 10792 (2016)

[2] M. Ehret et al., HEDgeHOB FAIR Report 2016 (2017)

[3] A. Poyé et al., Physical Review E 92(4-1):043107 (2015)

[4] K. Quinn et al., PRL 102, 194801 (2009)

[5] K. Kanaya et al., Journal of Physics D: 5 43 (1972)

[6] S. Das, "A simple alternative to the Crystal Ball function", University of Florida (2016)

[7] M.Ehret, Master Thesis, TU Darmstadt (2016), [DOI: 10.13140/RG.2.1.3855.7847]

DOI:10.15120/GR-2017-1

Particle acceleration from levitated targets at Phelix

P. Hilz[1], J. Gebhard[1], D.Haffa[1], J.Hartmann[1], F.H.Lindner[1], T. M. Ostermayr[1], T. Rösch[1], B. Borm[3], P. Neumayer[2], B. Zielbauer[2]

[1]Ludwig-Maximilian Universität, München, Germany; [2]GSI, Darmstadt, Germany; [3]Goethe-Universität, Frankfurt, Germany;

Experiment

The vast majority of laser ion acceleration experiments relies on thin foils as targets. In the experiment P108 we used isolated spheres with micrometer extent as targets. An electrodynamic trap (Paul Trap) was used to levitate spheres made of copper and plastic (PS). By an electro-optical damping method the trapped particles' residual motion could be reduced to sub-micron extent and allowed overlapping the laser focus and target reliably. The PHELIX laser delivered 150 J in 500 fs resulting in peak intensities larger than 10^{20} W/cm^2. For enhanced contrast the uOPA front end of PHELIX was used. A magnetic slit spectrometer (covering +-4°) under 0° served as particle diagnostics. Due to the sub focus dimensions of the target, part of the focal spot is modulated by the target in amplitude and/or phase. The resulting diffraction images were measured via a scatter screen in front of the ion spectrometer. These diffraction images deliver valuable information about the plasma size during the main interaction. In the horizontal plane, at 20° we used a permanent magnet quadrupole doublet to refocus the accelerated ions. Normal to the laser axis X-ray diagnostics were applied (X-ray spectrometer, X-ray edge source size measurement (for details see progress report of experiment P109)). Reflected light from the target was re-collimated by the parabola and analysed behind a beam line mirror. The setup is shown in Fig. 1.

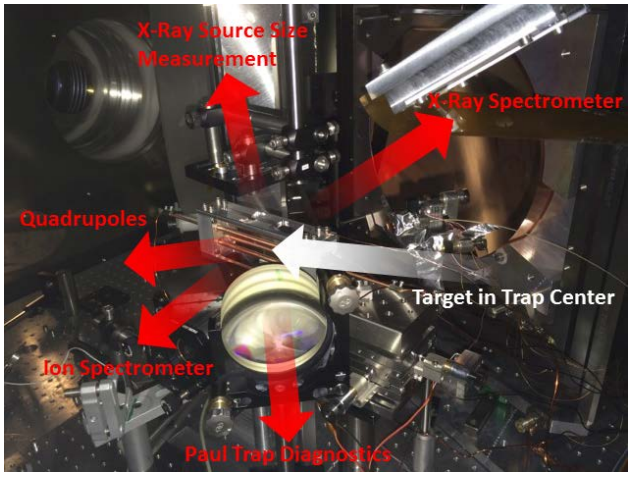

Fig. 1: Experimental setup.

Preliminary results

We were able to reproduce the experimental findings of our previous beam time for 1µm plastic spheres (experiment P65 in 2013). For 1 µm plastic spheres we again obtained quasi monoenergetic proton spectra with peak energy around 25 MeV and a few MeV bandwidth.

For 2 µm diameter spheres preliminary analysis indicate much higher proton energies of 40-50 MeV. The spectra for even larger targets with 6 µm diameter depended on the hit "quality". A "full hit" (no transmitted light, i.e. dark scatter screen) delivered a strongly modulated spectrum with about 100% energy spread. A "grazing shot" showed mono-energetic behaviour, indicating the strong influence of pre-plasma expansion on proton acceleration. Copper spheres with 1.5 µm diameter delivered energetic copper ions with a few MeV/u.

The spectrum of the recorded light reflected from a plastic sphere is given in Fig 2. The yellow and green lines depict the expected positions for the second and third harmonic, respectively. The spectrum of the third harmonic is trimmed by the transmission characteristics of the beam line mirror at short wavelengths. The spectra

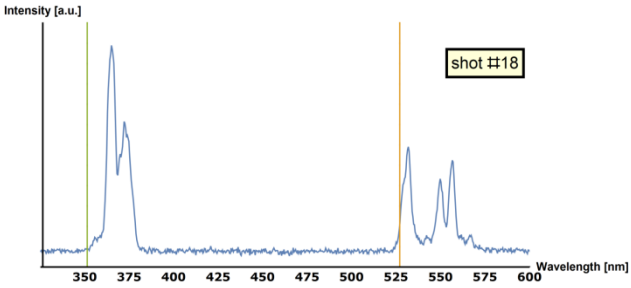

Fig.2: Spectrum of the reflected light

exhibit significant redshift up to 7% of the respective center wavelengths (527 and 351 nm). The observable peaks in the second and third harmonic show the same relative redshift. Transmission screen data indicates that the observed redshift is attributed to the mean electron drift velocity of all target electrons.

We demonstrated the refocusing of energetic copper ions with a set of permanent magnetic quadrupoles. Hereby we observed ion energies which we did not detect in the slit spectrometer.

Conclusion

Sub focus sized targets show remarkable source properties such as quasi monoenergetic spectra with large amounts of particles contained in the target being accelerated in forward direction. Due to the finite size of the target the experimental signatures are very clean and without almost any background. This renders levitated targets as an ideal tool for the investigation of laser plasma interactions. All given values are preliminary and currently evaluated in more detail.

DOI:10.15120/GR-2017-1

Laser-driven acceleration of deuterium ions from cryogenic targets

A. Tebartz[1], *M. Hesse*[1], *A. Alejo*[2], *J. Hornung*[1], *A. Kleinschmidt*[1], *N. Neumann*[1], *V. A. Schanz*[1,3], *G. Schaumann*[1], *F. Wagner*[3], *V. Bagnoud*[3], *and M. Roth*[1,4]

[1]Technische Universität Darmstadt, Institut für Kernphysik, Schlossgartenstraße 9, 64289 Darmstadt, Germany;
[2]Centre for Plasma Physics, School of Mathematics and Physics, Queen's University Belfast, Belfast BT7 1NN, UK;
[3]GSI Helmholtzzentrum für Schwerionenforschung GmbH, Planckstraße 1, 64291 Darmstadt, Germany;
[4]Facility for Antiproton and Ion Research in Europe GmbH, Planckstraße 1, 64291 Darmstadt, Germany

Cryogenic Targets

In the research of laser-driven ion acceleration, a multitude of different materials and designs have been used as the matter sample (*target*). Gaseous materials pose a special challenge due to their volatility. While gas jet targets are often used, solid targets have a much higher density. Cryogenic targets offer the possibility to use gaseous materials for targets at solid density.

When a target interacts with the laser, not all of it is accelerated as an ion beam. Some material evaporates and some parts remain solid but move as high velocity debris particles. Thus, as opposed to gas jet targets, solid targets carry the risk of damaging optics or other equipment around the interaction point through debris. In addition, vaporized material solidifies again on surfaces at room temperature. As more and more laser systems with repetition rates in the range of Hz are developed, the issue of vaporized target material coating optical elements should be addressed. Cryogenic targets open up the possibility of debris-free solid state targets whose remains can be removed by vacuum pumps.

Deuterium as Target Material

Hydrogen as target material is the only substance that, once ionized, is a pure proton source. Its low triple point temperature of 13.9 K [1] poses a special challenge regarding the needed cooling power.

The hydrogen isotope deuterium can be advantageous due to its higher triple point temperature of 18.7 K. Deuterium ion beams are applicable for e.g. the production of laser-driven neutron beams [2]. In addition, due to their charge-to-mass-ratio of 1:2, deuterium ions can be separated from protons in ion spectrometers, so a distinction of ions regarding their source is possible: Target material (deuterium) ions are discernible from contamination ions such as protons from residual water.

Target Creation

Cryogenic targets are fundamentally different from conventional solid state targets, as they need constant cooling and thus have to be produced and characterized in-situ. A condensation method was developed at the Target Laboratory of the Institute for Nuclear Physics of Technische Universität Darmstadt. Instead of moving through the phase diagram from gaseous directly to solid, a path via the liquid phase was chosen. This entails pressure above the triple point. A setup was developed to combine temperature and pressure control, which was then moved to the target chamber for a beamtime at the PHELIX laser system, conducted in February 2016.

The target is created in an aperture of 1 mm diameter in a cooled copper frame. The required pressure for liquidation is reached by enclosing the frame with a motorized growth chamber, which is filled with gas. Liquid covers the aperture and is solidified through cooling below triple point temperature. The growth chamber is then removed to allow access for the laser beam.

As the PHELIX target chamber is larger than the test vacuum chamber at the Target Laboratory and is equipped with more powerful vacuum pumps, we found a difference concerning target survival (see [3]).

Target Characterization

Target thickness characterization, just like target creation, needs to be conducted in-situ. Chromatic-confocal sensors produce axial chromatic aberrations through a set of dispersive lenses. If the sensor is placed in front of a reflective surface, analysis of the wavelength of the reflected image can be processed to the distance between surface and sensor. Thickness values were deduced from distance values to the target surface, under utilization of the geometry of the setup (see [3]).

As the sensors are placed directly in front of the target and thus in the laser beam path, they need to be removed before laser interaction.

Ion Acceleration

Deuterium ions were successfully accelerated during the experiment in 2016 at PHELIX. A detailed publication with results and analysis is in preparation.

References

[1] P. Souers, *Hydrogen Properties for Fusion Energy*, University of California Press, 1986.

[2] A. Alejo et al., Plasma Physics and Controlled Fusion **59** (2017).

[3] A. Tebartz et al., *Creation and characterization of free-standing cryogenic targets for laser-driven ion acceleration*, submitted to Review of Scientific Instruments.

DOI:10.15120/GR-2017-1

Resonance spectroscopy with a laser-driven neutron source*†

A. Kleinschmidt‡[1], *A. Favalli*[2], *J. Hornung*[1], *A. Tebartz*[1], *G. Wurden*[2], *V. A. Schanz*[1], *and M. Roth*[1,3]

[1]Institut für Kernphysik, TU Darmstadt, Germany; [2]Los Alamos National Laboratory, New Mexico, USA; [3]FAIR - Facility for Antiproton and Ion Research, Darmstadt, Germany

Laser-driven neutron sources have been a topic of intense research and development over the last years. They provide an exponentially decaying energy spectrum with cut-off energies of a few 10 MeV up to over 100 MeV [1,2]. However, there are applications where neutrons with thermal or epithermal energies are preferable. To maximize the neutron yield in this energy range, a moderting material is used to slow down high-energy neutrons. The preferred material should scatter neutrons without absorbing them. Thus, it should contain light elements, like hydrogen or carbon, to maximize the energy loss per collision.

Amongst many other things, neutrons can be used to probe materials. One example of such a measurement is neutron resonance spectroscopy (NRS). This technique utilizes the unique resonance structure in neutron reaction cross sections of elements, which serves as a fingerprint for instance to identify the elemental composition of bulk materials. To investigate the applicability of a laser-driven neutron source for NRS, we conducted an experiment at the Trident laser facility at Los Alamos National Laboratory, USA.

NRS on a static indium sample

During the experimental campaign, thin deuterated polystyrene foils of a few 100 nm were irradiated by the Trident short pulse laser with an energy of 80 J and a pulse length of 600 fs. The laser was focused to intensities above 10^{20} W/cm^2 with a f/1.5 off-axis parabola. The accelerated ions from the target impinged on a 30×30 mm cylindrical beryllium catcher (converter) that had a 15×15 mm cylindrical hole drilled into it. The hole is directed towards the incoming ion beam. Neutrons that are emitted in the direction of the laser, are scattered back into the catcher to maximize the neutron yield. To moderate the generated neutrons, the beryllium catcher was surrounded by a high density polyethylene (HDPE) block with a length of 13.8 cm and a width of 7 cm. Regarding the setup, there are four main points to be considered:

- Very fast neutrons with energies of several 10 MeV and above (depending on the moderator material and length) are able to pass the moderator without being scattered and thus are not moderated.
- Moderated neutrons change their propagation direction, because they are scattered out to the sides of the moderator.
- The thicker the moderator, the more high energy neutrons get slowed down.
- The moderator dimension in line of sight to the NRS detector is to be kept as small as possible, because the moderator thickness causes a temporal spread of the neutron pulse.

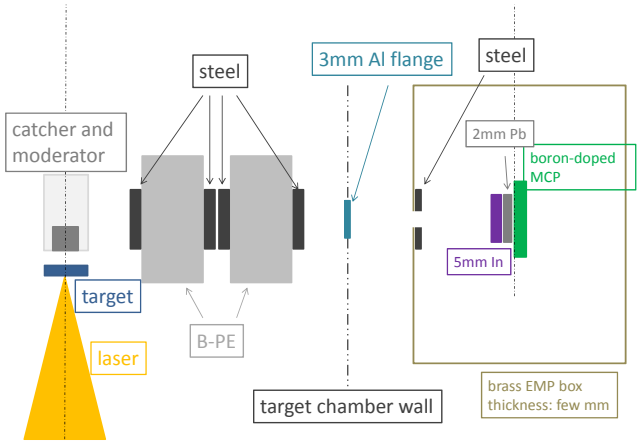

Figure 1: Sketch of the experimental setup for neutron resonance spectroscopy at Trident.

Considering all these conditions, it is advantageous to set up the detector in a sideward direction. The full experimental setup is sketched in figure 1. The neutrons were collimated with a set of boron-treated polyethylene (B-PE) blocks and steel disks. The sample was an indium sheet with 5 mm thickness placed at 1.67 m directly in front of a boron-doped microchannel plate (MCP) detector, which was additionally shielded with 2 mm lead to stop gamma rays from the interaction of neutrons with the indium sample, and B-PE to all sides to avoid detection of scattered neutrons.

With this setup, we were able to measure the 1.45 eV ^{115}In resonance and thus could successfully demonstrate the feasibility of a laser-driven neutron source for NRS.

References

[1] S. Kar *et al.*, "Beamed neutron emission driven by laser accelerated light ions", New J. Phys., 18, 053002, (2016)

[2] M. Roth *et al.*, "Bright Laser-Driven Neutron Source Based on the Relativistic Transparency of Solids", Phys. Rev. Let., 110 (4), (2013)

* Work supported by LANL, GSI and HIC4FAIR

† This report is also published in 'News and Reports from High Energy Density generated by Heavy Ion and Laser Beams 2016'

‡ a.kleinschmidt@gsi.de

Laser pulse amplification by Stimulated Brillouin Scattering (SBS) and cell radiation damage caused by laser accelerated protons*

M. Blecher[1], *S. Spickermann*[1], *and O. Willi*[†1]
[1]Institut für Laser- und Plasmaphysik, Heinrich-Heine-Universität Düsseldorf

Introduction

Strong light pulse amplification by Stimulated Brillouin Scattering (SBS) is a new, prospecting way to realize a laser gain medium that is able to sustain much higher intensities than a solid state body, as commonly used today. Hence, short pulse amplification by SBS could be used to reach extreme laser intensities with a relatively compact and inexpensive laser setup. This will allow accelerating particles to energies that significantly exceed values achieved in present laser particle acceleration.
In 2015, a successful experiment was carried out at the Düsseldorf Arcturus Laser Facility. The Arcturus laser system generates three synchronized beams, with variable pulse durations $\geq$ 25 fs and energies up to 5J. The two 200 TW beams were used for ionization of the gas target and as a pump whereas the third 3 TW beam line was used as a seed pulse for amplification. The goal of the SBS campaign was to study the SBS process with ultra-short pulses for the first time and find optimal parameters to trigger SBS amplification. In 2016, a second experiment was carried out again at the Arcturus Laser Facility in the so-called strongly coupled regime.
In addition, a study was performed in order to distinguish the biological effectiveness and cellular responses upon irradiation with two types of proton deliveries namely the laser accelerated protons by the Arcturus laser system and conventionally accelerated protons by PTB Braunschweig. High-energy protons induce DNA damage in the form of double stranded and single-stranded DNA breaks (DSB and SSB), DNA base damage and clusters thereof (complex DSB). DNA damage is either induced by direct energy deposition to the 2-deoxyribode moiety or the bases of DNA (direct effects), or the generation of radicals through water radiolysis, which then interact with DNA (indirect effects). The biological effectiveness of protons is mostly a function of the frequency and complexity of the DNA breaks resulting from direct and indirect effects.

Results

For the SBS experiment, three counter-propagating laser beams, having pulse durations between 30 and 800 femtoseconds and energies up to 800 mJ, were focused onto a gas target. The interaction region was probed by seven diagnostics, that measured energy, frequency and duration of the outcoming laser light. A preliminary analysis of the data shows that a relative amplification of SBS by a factor 6 or more was observed, which is an improvement of factor 4 compared to 2015.
In the second study a remarkable difference between the two types of sources of accelerated protons was observed at the same dose level. Cellular nitroxidative stress response is significantly lower after exposure of cells to laser-driven than to conventionally accelerated protons. The results were published in Ref. [1]. The salient finding of our study is that laser accelerated protons (LAP) and conventionally accelerated protons (CAP) have a similar effectiveness to induce DSB. However, LAP exhibited a far lower potential than CAP to induce nitroxidative stress leading to tyrosine-nitration (see Fig. 1). The most likely explanation for this unique property of LAP is the excessively high dose rate. It appears as if redox chemistry changes when dose deposition occurs as an ultra-short pulse, with similar duration as the lifetime of the primary radicals thereby generated (as is the case with LAP).

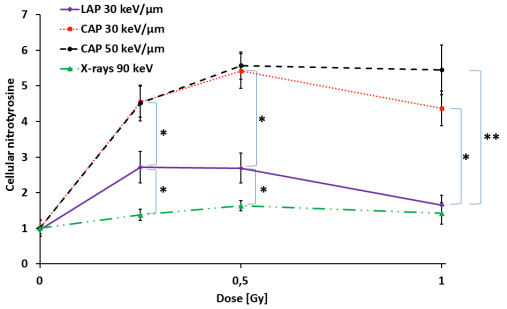

Figure 1: Comparison of mean fluorescence intensity (MFI) as a measure of nitroxidative stress between the proton source for laser-accelerated protons (LAP) at ILPP in Düsseldorf and a source for conventionally accelerated protons (CAP) at PTB in Braunschweig. The two CAP curves (dotted and dashed line) show MFI for two proton beams with a different energy. The solid purple line shows MFI in cell samples treated with different dose exposures of laser-accelerated protons. In the case of CAP, nitroxidative stress is clearly higher than in the case of LAP, over the entire range of dose exposure.

References

[1] S. Raschke, S. Spickermann, T. Toncian, M. Swantusch, J. Böker, U. Giesen, G.Iliakis, O.Willi, F. Boege, *Ultra-short laser-accelerated proton pulses have similar DNA-damaging effectiveness but produce less immediate nitroxidative stress than conventional proton beams*, Scientific Reports **6**, 32441 (2016)

* Work supported by GSI Darmstadt, Germany
† oswald.willi@hhu.de

DOI:10.15120/GR-2017-1

Platform development for laser accelerated particle induced nuclear reaction studies utilizing RC methods*

P. Neumayer[1,2], A. Yakushev[1,3], K. Jadambaa[1,3], V. Bagnoud[1,6], Ch. Brabetz[1], B. Borm[1,2], J. Hornung[1,5], F. Wagner[1], T. Kueh1[1,4,6], T. Stoehlker[1,6], J. Despotopulos[7], D. Sayre[7], D. Schneider[7]

[1]GSI, Darmstadt, Germany; [2]Goethe University, Frankfurt, Germany; [3]Helmholtz Institute Mainz, Mainz, Germany; [4]Johannes-Gutenberg University, Mainz, Germany; [5]TU Darmstadt, Darmstadt, Germany; [6]Helmholtz Institute Jena, Jena, Germany; [7]Lawrence Livermore National Laboratory, Livermore, USA

Introduction

A team of GSI and LLNL researchers successfully completed a platform development experiment to enable future nuclear science experiments at short-pulsed laser facilities. The experiment is a joint effort between Plasma Physics group led by V. Bagnoud and radiochemists from the Super Heavy Element research group at GSI led by A. Yakushev. This first experiment demonstrated an efficient collection of isotopes produced in nuclear reactions with laser driven MeV proton beams. The proposed experiment was awarded the requested run-time of 20 shifts and 40 shots have been used to demonstrate the isotope collection efficiency and reproducibility.

Experiment

The experiment utilizes laser accelerated proton beams (5 – 20 MeV) in combination with radiochemistry based isotope analysis to study nuclear reactions. In particular, the ^{63}Cu(p,n)^{63}Zn reaction was used to measure the proton activated radioactive ^{63}Zn via its β^+ decay and subsequent 511 keV gamma emission identified by its $T_{1/2}$ = 38 sec half-life.

The proton beams were produced through the TNSA (Target Normal Sheath Acceleration) mechanism utilizing GSI's PHELIX laser facility. Laser pulses at 90 J and 500 fs impinging on a thin gold target (the observation of laser accelerated protons has first been reported from experiments at LLNL laser facilities [1,2]. After various tests to identify the spatial, time and energy distribution the accelerated protons were used to activate thin ^{63}Cu-foils and to measure the level of activation, which was found to be consistent with known milli-barn cross sections for 5 – 20 MeV protons. Due to the divergence of the accelerated protons over about 30 mm, the spot size at the interaction with the target foils is around 10 mm. The spot size of the accelerated protons at the exit of the conversion foil is less than 1 mm due to the small source emittance.

After passing through a thin capton foil as debris shield and a thin Ti-foil as window in the gas filled (in flow mode) target cell inside the main target chamber, the protons interacted with ^{63}Cu target foils (1-5 stacked foils) inside the target cell. The produced ^{63}Zn recoil isotopes were stopped in a He/aerosol gas mixture at about 1 bar gas pressure, and transported to a filter through a thin tube. The decay of the ^{63}Zn was identified by measuring the 511 keV annihilation gammas following the β^+ decay with a half-life of 38 min (Fig. 1). The reaction ^{63}Cu(p,n)^{63}Zn and gas transport wsas verified by comparing shots with and without ^{63}Cu foils and with and without carrier gas. The length of the transport line was varied from a 20 to 1 m distance resulting in a transport efficiency varying between 10 to 60%.

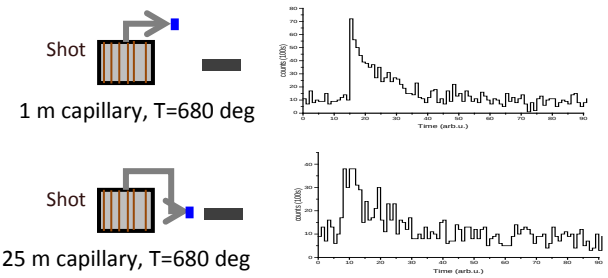

Figure 1: 511 keV gamma emission following the β^+-decay of ^{63}Zn after gas collection utilizing a 1 m (top) and 25 m (bottom) capillary transport line; the decay of the 511 keV gamma line confirms the 38 sec half-life of the ^{63}Zn isotope.

The presented experiment at PHELIX with laser accelerated MeV protons and a pulse duration of around 1 ps opens up new domains of studies through the detection of short lived isomers. The experiments provide critical experimental input for future experiments at FAIR (Facility for Antiproton and Ion Research), but also at laser facilities as ELI (Extreme Light Infrastructure) [3,4]. The collaborative experimental research is part of an agreement between LLNL (DOE) and the GSI (BMBF).

References

[1] R. A. Snavely et al., PRL 85, 2954 (2000)
[2] D. A. Shaughnessy *et al.*, Rev. Sci. Instrum. 85, 063508 (2014).
[3] ELI-NP White Book, eds. D. Habs et al. (2010), http://www.eli-np.ro/documents/ELI-NP-WhiteBook.pdf
[4] FAIR Green Paper - The Modularized Start Version, (2009)

* This report was also submitted for the Annual Report of HIJ and "News and Reports from High Energy Density generated by Heavy Ions and Laser Beams 2016".

DOI:10.15120/GR-2017-1

Development of a high-resolution x-ray spectrometer for laser-generated hot dense plasma emission *

D. Khaghani[†1], *B. Borm*[2,3], *P. Neumayer*[3], *and C. Spielmann*[1,4]

[1]Friedrich-Schiller-University, Jena, Germany; [2]Goethe-University, Frankfurt, Germany; [3]GSI, Darmstadt, Germany; [4]HIJ, Jena, Germany

In last year's *GSI Scientific report* we reported on the generation of ultra-high energy density conditions irradiating tailored micro-pillar arrays at high laser-drive energy [1]. We carried on further experiments to better characterize these extreme plasma conditions. A high-resolution x-ray spectrometer was developed so as to measure the variety of K-shell emission lines providing accurate information about the time evolution of both temperature and density. We report here on the technical design of that instrument.

In our experiments, the target material chosen for spectroscopy purposes is copper. For this element, the K-shell transition lines of interest are emitted between 8000 and 9000 eV, ranging from quasi-neutral species' K_α ($\sim$ 8040 eV) to highly-ionized ion emission (8370 and 8680 eV for He_α and Ly_α, respectively). Furthermore, many intermediate lines from various charge states and so-called dielectronic configurations can provide accurate estimates for the plasma parameters. In order to differentiate these spectrally-close lines, we need high quality crystals which are able to perform high-resolution diffraction. α-Quartz silicon dioxide (SiO_2) crystals are commonly used for this application [2] and are widely characterized [3]. These quartz crystals are available with various lattice cuts, which has to be chosen in accordance with the corresponding Bragg angle. The ideal choice for the spectral window of interest is the lattice $22\bar{4}3$ with a $2d$-spacing of 2.024 Å. Finally, increasing the signal-to-noise ratio is made possible with spherically curved crystals which focus the spectrum into a thin line.

A commercial crystal (Golem IMS GmbH) is used. It consists of a 12×48 mm^2 quartz crystal ($22\bar{4}3$) applied onto a concave spherical glass substrate with a radius of curvature of 150 mm. We designed a holder to position the crystal onto the spectrometer board (Fig. 1). The crystal is mounted on a kinematic platform (Thorlabs KM100B/M) equipped with two tip-tilt adjusters for fine alignment of the crystal pointing. The platform is attached to an assembly of two translation stages (OptoSigma TSDH-251S and TSDS-253): one along the x-axis parallel to the spectrometer board in the crystal focus direction and another one along the z-axis for crystal height adjustment. The spectrometer board is a 10 mm-thick Delrin plate which extends in the direction of the central axis of the crystal so as to mark the position of two alignment reference points with the help of pointy metal dowel pins. These two reference points are: (**1**) the center of the Rowland circle (focus of the crystal at 0°), and (**2**) the center of curvature. They are located at 75 and 150 mm from the center of the crystal surface, respectively. Finally, the spectrometer board is mounted onto a rotation stage (Newport M-UTR80SA) whose rotation axis passes through the center of the crystal surface in order to maintain the crystal in the right position while adjusting the Bragg angle by turning the plate. The detector, an imaging plate (Fujifilm BAS-SR), is place in an enclosed aluminium box. An alignment hole (**3**) is located on the side of the box so that a laser diode shining through it would span the surface of the detector across its long side, thus symbolizing the detector axis. This method is used to finely tune the focus of the spectrum as the geometrical configuration requires that the radiation source and the center of curvature of the crystal are placed on the detector axis.

In the framework of the BMBF project "Development of x-ray spectroscopy for 'Day One' plasma physics experiments at FAIR", we will delve into further designing of similar spectrometers.

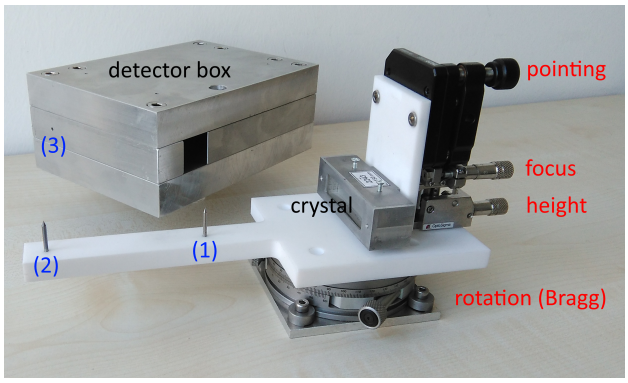

Figure 1: Photograph of the spectrometer describing its alignment features: reference points (blue) and optomechanics (red)

References

[1] D. Khaghani *et al.*, "Proton acceleration and matter at ...", GSI Scientific Report 2015 (2016) 179

[2] F.P. Condamine *et al.*, "M-shell resolved high-resolu- ...", AIP Conf. Proceedings (2017) Vol. 1811 No. 1 p. 060001

[3] L. Antonelli *et al.*, "Measurement of reflectivity of spher- ...", Review of Scientific Instruments (2015) 86(7) 073507

* This work will also be published in *Annual Report 2016 – HI Jena*

† d.khaghani@gsi.de

DOI:10.15120/GR-2017-1

Ultra-high energy density conditions produced in free-floating micron-size targets by intense laser irradiation

B. Borm[1], D. Khaghani[2], P. Neumayer[3], J. Gebhard[4], P. Hilz[4], T. M. Ostermayr[4], J. Schreiber[4], L. Gremillet[5]

[1]Goethe-Universität, Frankfurt, Germany; [2]Friedrich-Schiller-Universität, Jena, Germany; [3]GSI, Darmstadt, Germany; [4]Ludwig-Maximilian Universität, München, Germany; [5]CEA, DAM–DIF, Arpajon, France

In relativistic laser-matter interaction a large fraction of the laser energy is converted to a population of energetic (MeV) electrons. When using "mass-limited" targets with dimensions smaller than the hot electron range the hot electrons are confined to the target by electrostatic sheath fields, leading to the generation of matter at ultra-high energy density (see e.g. [1,2]). While individual mounting of such targets has been realized by e.g. using spider-silk threads, the holding structure constitutes a possible source for return currents and drain for the hot electrons. Avoiding any nearby material, truly mass-limited targets can be realized using droplet-targets formed by the Rayleigh-decay of a liquid jet [3].

In the experiment described here we have made use of a Paul-trap setup, developed at the LMU, Munich [4]. Solid spheres with diameters of order 1 μm were charged up with an ion-gun and held freely floating by the electrostatic fields in the trap. Employing active damping allowed overlapping the few-micron laser spot with the targets.

At the PHELIX laser facility we have subjected micron-sized solid copper spheres to short (~500 fs), energetic (150 J) laser pulses, focused to intensities above 10^{20} W/cm^2. We have made use of the uOPA front-end amplifier system, providing laser pulses with ultra-high temporal contrast, to limit heating and expansion of the target before the arrival of the peak of the laser pulse.

Energetic electrons generated in the laser-matter interaction penetrate the solid target, simultaneously heating the material by collisional energy loss and producing inner-shell ionization. The latter is followed by the emission of K-shell radiation which can serve as a diagnostic of the target state. We have developed a highly efficient broadband crystal spectrometer based on a large cylindrical crystal of highly-oriented pyrolytic graphite. The spectral range of the spectrometer from 7.5…12 keV covers the entire copper KL-emission spectrum, from neutral K-alpha up to Ly-alpha from hydrogen-like copper ions. The spectrometer was designed such that the passive detector (Fuji imaging plate) is located outside the target chamber to allow easy exchange of the detector between shots without breaking the vacuum.

The x-ray emission source size was measured by means of a knife-edge setup. A laser-cut gold foil was positioned at a distance of 25 mm from the target and the edge projected onto an image plate detector located at a distance of ~2.5 m outside the target chamber. The resulting magnification of ~100x provided a resolution of approx. 1 μm. With the spot size of the laser focus of 5 μm significantly larger than the targets, the laser pulse energy intercepted by the target amounts to less than 2 J. Nevertheless, due to the small dimensions this results in a laser energy per target volume of 10^9 J/mm^3, at least 2 orders of magnitude larger than previous experiments at kJ short-pulse laser facilities [5].

K-shell emission x-ray spectra show strong emission from the H-like and He-like resonance lines. The complete absence of any emission from lower charge states indicates rapid ionization of the entire target during the time of interaction with the laser pulse. This is supported by particle-in-cell calculations of the laser-target interaction and subsequent target evolution. The simulations show rapid volumetric heating within the first half of the laser pulse to bulk temperatures of 3-4 keV, concomitantly with ionization to charge states exceeding 27+. Atomic kinetic calculations of K-shell emission spectra at these conditions agree well with the measured spectra. The simulations also show the fast hydrodynamic expansion of the target. However, during the few hundred femtoseconds laser pulse duration the rarefaction wave, although at sound speeds of several hundred km/s, has only progressed into the target by a fraction of the target radius.

The x-ray emission source size is measured to be comparable to the initial target size, indicating negligible expansion of the target during peak emission. This could be explained by a rapid relaxation of the hot electron distribution, for example by adiabatic cooling.

Bulk temperatures of several keV are reached while most of the target mass is still at solid density, corresponding to pressures exceeding 10 Gbar. This opens a path towards studying matter at ultra-high energy densities in the laboratory. Upcoming x-ray free electron lasers will be ideally suited to probe structure and dynamic of these highly excited states of matter. At our conditions the high densities and charge states yield a strongly coupled ion system, however with non-degenerate electrons due to the high temperatures.

References

[1] P. M. Nilsen et al., Phys. Rev. E 79, 016406 (2009)
[2] P. Neumayer et al., High Energy Density Physics 5, 244 (2009)
[3] R. A. Costa Fraga et al., Rev. Scient. Instr. 83, 025102 (2012); P. Neumayer et al., Phys. Plasmas 19, 122708 (2012)
[4] T. M. Ostermayr et al., Phys. Rev. E, 94, 033208 (2016)
[5] P. M. Nilson et al., Phys. Rev. Lett. 105, 235001 (2010)

DOI:10.15120/GR-2017-1

Time-resolved measurement of the relativistic interaction of an ultra-intense laser pulse with sub-micrometer-thick targets*

J. Hornung[1], *F. Wagner*[2,3], *N. Schröter*[1], *J. Ding*[1], *B. Zielbauer*[2], *C. Brabetz*[2], *P. Hilz*[4], *M. Haug*[4], *J. Schreiber*[4], *T. Stöhlker*[2,3], *M. Roth*[1,5], *and V. Bagnoud*[2,3]

[1]TU-Darmstadt, Darmstadt, Germany; [2]GSI, Darmstadt, Germany; [3]HI-Jena, Jena, Germany; [4]LMU, München, Germany; [5]FAIR, Darmstadt, Germany

Motivation

For a better understanding of the interaction between laser and thin foils during experiments at the PHELIX laser and general laser-plasma experiments temporally resolving the interaction dynamics can bring a new insight. Conventional diagnostics are too slow to resolve those interactions, but the method of frequency resolved optical gating (FROG, [1]), could be used as a ultra fast diagnostic. Such a FROG-device has been specifically designed for this type of experiment [2].

Experimental Setup

The experimental setup can be seen in figure 1. The pulse of the PHELIX laser is focused on sub-micrometer-thick CH_2 targets. A part of the pulse is reflected at the critical plasma density, which is picked up and back-collimated by the focusing parabola. After leaking through a mirror, the back-reflected pulse is split up in two parts and sent to the FROG-device, as the main diagnostic, as well as a 1 ω spectrometer. For the measurement of the transmitted part of the pulse a sub aperture of the beam is taken, which is collimated and imaged on to a second FROG-device and a spectrometer. The rest is blocked by a glass-screen which is used to determine the amount of transmitted light.

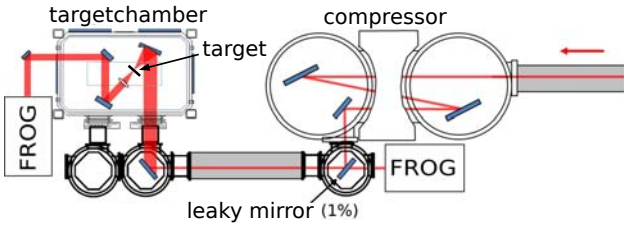

Figure 1: Experimenal Setup

Experiment

The experiment (P126) involved 47 shots with different target thickness and laser parameters. The thickness of the targets ranged from 50 nm up to 15 μm and the laser energy was varied from 10 to 130 J, with a constant pulse duration of 500 fs. Additionally to shots with a single pulse an innovative double pulse configuration was used where a replica of the first pulse has been created as a post pulse with approximately 10 % of the energy and a time delay of approximately 3 ps. [3]

Preliminary Results

For both reflection- and transmission diagnostic, different modulations of the pulse could be observed, which can be explained by different physical effects. Preliminary results for the spectra can be seen in figure 2. The back-reflected spectrum experiences a larger red shift than the transmitted spectrum. This can be attributed to the doppler-effect of the laser-hole-boring [4], whereas both spectra are broadened due to relativistic self-phase-modulation. [5] A reconstruction of those pulses with a FROG-algorithm [1] can now show the temporal behaviour of the pulses, which is currently ongoing.

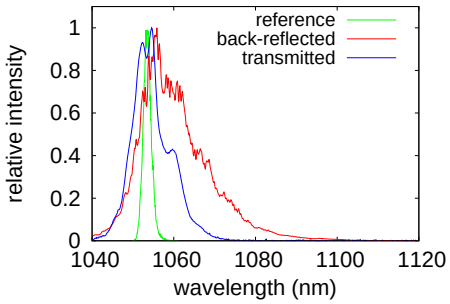

Figure 2: Spectra of the transmitted and reflected part of the laserpulse compared to the incoming reference pulse.

For thin targets in the order of a few hundred nanometer a measurement of the transmitted double pulses show a clear retarding effect on the post pulse, which rises up to 500 fs for 200 nm thin targets. This retardation can be used to gain additional information about the pre-expansion of the target before the main pulse arrives. A more detailed analysis of this double pulse setup can be found in [3].

Conclusion

Both the use of FROG as main diagnostic and the double pulse configuration show promising results which will be further evaluated and also used in upcoming experiments.

References

[1] K.W. DeLong, et. al., J. Opt. Soc. Am. B 11, 2206–2215 (1994).

[2] F. Wagner, et. al., Rev. Sci. Instrum. 88, 023503 (2017)

[3] V. Bagnoud, et. al., Accepted at Phys. Rev. Lett. (2017)

[4] M. Zepf, et. al., Phys. Plasmas 3, 3242–3244 (1996).

[5] I. Watts, et. al., Phys. Rev. E 66, 036409 (2002).

*This report is also published in *News and Reports from High Energy Density generated by Heavy iOn and Laser Beams 2016*

DOI:10.15120/GR-2017-1

Development of a FROG for temporal resolution of laser-plasma interactions*

J. Hornung[1], *F. Wagner*[2,3], *C. Schmidt*[4], *M. Eckhardt*[5], *T. Stöhlker*[2,3], *V. Bagnoud*[2,3], *and M. Roth*[1,6]

[1]TU-Darmstadt, Darmstadt, Germany; [2]GSI, Darmstadt, Germany; [3]HI-Jena, Jena, Germany; [4]Hochschule Darmstadt, Darmstadt, Germany; [5]TH-Mittelhessen, Friedberg, Germany; [6]FAIR, Darmstadt, Germany

Motivation

During typical relativistic laser-plasma experiments, a complex interaction between the laser and the plasma takes place. For experiments employing thin foils, a part of the pulse can be transmitted and/or reflected by the plasma generated by the interaction. Due to effects such as relativistic self-phase-modulation [1] and doppler-effect [2] the laser pulse is distorted after the interaction. This distorted pulse carries some information on the interaction conditions, and therefore the different effects can then be identified by spectrally and temporally resolving the pulse, which can be achieved by the technique of frequency resolved optical gating (FROG) [3].

Setup

The FROG setup consists of a second-harmonic autocorrelator, an imaging system and a self-constructed 2D-spectrometer with a high dynamic range. Our experimental implementation can be seen in figure 1. The device is designed to resolve the pulse of the PHELIX laser with a pulse duration (FWHM) of 500 fs and a spectral window of 14 nm, as well as pulses with a high spectral broadening of up to 200 nm and slightly stretched pulses up to 2 ps. The self-constructed 2D-spectrometer is able to resolve these ranges with a spectral resolution of up to 0.07 nm and a temporal resolution of up to 15 fs.

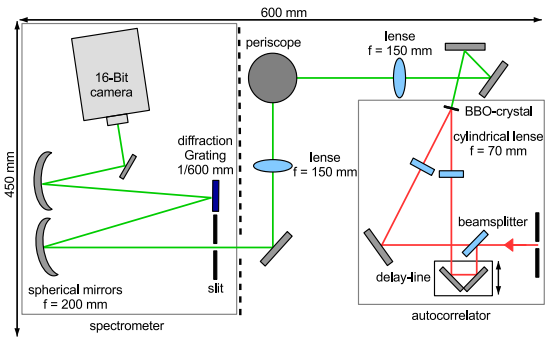

Figure 1: Setup of the FROG

Verification

As a verification of the FROG, nearly transform-limited pulses as well as highly linearly chirped pulses, have been measured. With the help of a FROG-algorithm the pulses could be reconstructed temporally and spectrally. The behaviour of the spectral phase for different linear chirps was in good agreement with the expected behaviour. A result for the reconstructed spectrum of two pulses, including the spectral phase, can be seen in figure 2.

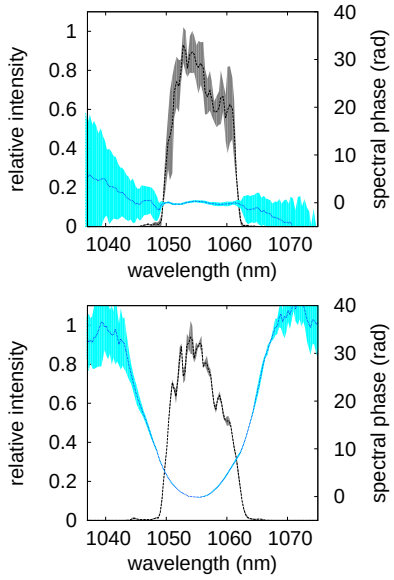

Figure 2: Reconstructed spectra for the PHELIX laser for a nearly transform-limited (upper) and strong linear chirped (lower) pulse. The black line shows the spectral intensity and the blue line shows the spectral phase. The light areas indicate the uncertainty given by the algorithm.

Conclusion

The FROG has been implemented at the Petawatt target area of the PHELIX building, where it can be used as a diagnostic for back-reflected and transmitted laser pulses during laser-plasma experiments [4]. Furthermore it can be used to measure the unmodified pulse of the PHELIX-laser with a higher precision than the standard autocorrelators.

References

[1] I. Watts et. al., Phys. Rev. E 66, 036409 (2002).

[2] M. Zepf et. al., Phys. Plasmas 3, 3242–3244 (1996).

[3] K.W. DeLong et. al., J. Opt. Soc. Am. B 11, 2206–2215 (1994).

[4] F. Wagner et. al., Rev. Sci. Instrum. 88, 023503 (2017)

*This report is also published in *News and Reports from High Energy Density generated by Heavy iOn and Laser Beams 2016*

Generation of keV hot near solid density plasma at high contrast laser-matter-interaction * †

S. Zähter[1], *A. Schönlein*[1], *O. N. Rosmej*[1,2], *Z. Samsonova*[3,4], *D. Khaghani*[3], *C. Arda*[1], *N. Andreev*[5], *A. Hoffmann*[3], *S. Höfer*[3], *M. Kaluza*[3,4], *D. Kartashov*[3], *L. Pugachev*[5], *I. Uschmann*[3,4], *and C. Spielmann*[3,4]

[1]Goethe Universität, Frankfurt, Germany; [2]GSI, Darmstadt, Germany; [3]Friedrich-Schiller-Universität, Jena, Germany; [4]Helmholtz-Institute Jena, Germany; [5]Joint Institute for High Temperatures, Moscow, Russia

Laser accelerated electrons play a major role in the process of laser energy transfer into matter. Electron energies can usually be described by a maxwellian-like distribution function with one or more temperatures. In this work, we investigate relativistic laser-matter interaction at high laser contrast and show that a large amount of relatively "slow" keV electrons play a dominant role in the target heating process leading to the creation of a high energy density plasma state. The experiment was carried out at the JETI-40 laser system delivering a high contrast (10^{-8}) frequency doubled ($400\,nm$), $45\,fs$ relativistic ($10^{19}\,W/cm^2$; $a_0 \approx 1$) laser pulse. The $180-200\,mJ$ laser pulse was focused to a $5\,\mu m$ spot onto the target ($25\,\mu m$-thick Ti-foils) at $45\,\mathrm{deg}$. The diagnostic setup used in the experiment included an X-ray spectrometer with a cylindrically bent HOPG-crystal ($2d = 6.71\,\AA$) ensuring a wide spectral window of $4.4-7.9\,keV$ and a spectral resolution of $\lambda/\delta\lambda = 1000$. For analysis of the bremsstrahlung radiation up to $0.5\,MeV$ a hard X-ray detector (HXRD) based on a filter attenuation method and a Timepix detector operated in the single hit regime were used.

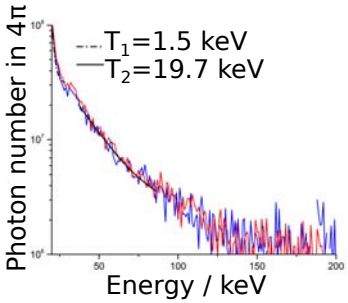

Figure 1: Bremsstrahlung radiation measured by Timepix.

Spectral distribution of the bremsstrahlung radiation of suprathermal electrons traversing the target measured using the Timepix detector is presented in Fig. 1. It can be well approximated by a two temperature electron energy distribution with $T_1 = 1.5 \pm 0.2\,keV$, $T_2 = 19.6 \pm 0.1\,keV$ and the corresponding hot electron fraction f_2 of nearly 3%.
Fig. 2 presents a Ti spectrum containing several K-shell transitions: $K\alpha$- and $K\beta$- transitions of weakly ionized Ti-atoms, K-shell transitions of intermediate charge states with vacancies in the M- and L-shell (F- up to Be-like ions) and K-shell transitions from one and double excited states in Li- and He-like Ti ions. While the intermediate charge states occur at plasma temperatures of 200–300 keV, the Li- and He-like states originate from a hot surface layer with keV temperatures. Both, a large number of low-energy electrons and a small interaction volume lead to high energy density plasmas with keV temperatures and near-solid densities. As shown in [1], the analysis of the $K\alpha$-profile broadening, that incorporates K-shell transitions of weakly ionized Ti-ions, allows to determine a plasma temperature in "warm" foil regions heated by laser accelerated electrons. In our case, this method leads to temperatures of $20-50\,eV$. The fit of the experimental spectrum in 2 was made using FLYCHK [2] for an optically thin plasma case with a bulk electron temperature of $T_1 = 1250\,eV$. Diagnostics of the electron density was based on the relative intensities of the $He\alpha$ resonance and intercombination ($1s^2(^1S_0)$–$1s2p(^3P_1)$) transitions.

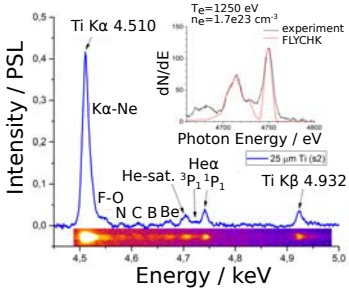

Figure 2: Measured Ti-spectrum and FLYCHK fit.

According to the fit made for the optical thin case, we obtain $n_e = 1.7 \cdot 10^{23}\,cm^{-3}$ or 15 % of the Ti solid density. Corrections for optical thickness $\tau = R/L_{ph}$ (see FLYCHK) lead to a higher bulk plasma temperature $T_1 = 1450\,eV$ and electron density $n_e = 2 \cdot 10^{23}\,cm^{-3}$.

References

[1] A. Schönlein et al, "Generation and characterization of warm dense matter isochorically heated by laser-induced relativistic electrons in a wire target", EPL, June 2016, p. 45002

[2] http://nlte.nist.gov/FLY/

* Work supported by HI Jena/HIC4FAIR/HGShire

† This report is also submitted to the Helmholtz Institute Jena Annual Report 2016 and News and Reports from High Energy Density generated by Heavy Ion and Laser Beams 2016

DOI:10.15120/GR-2017-1

2D simulation of a hohlraum backlighter for opacity measurements*

S. Faik[1,#], J. Jacoby[1], O. Rosmej[1,2], and An. Tauschwitz[1]
[1]Goethe-Universität, Frankfurt, Germany; [2]GSI, Darmstadt, Germany

Multidimensional codes, which combine the solution of the fundamental hydrodynamic equations with the spectral transfer equation for thermal radiation and with an accurate scheme for thermal conduction, provide an indispensable tool for the design and the analysis of experiments as well as for the understanding of physical phenomena at high energy density. The radiation-hydrodynamics code RALEF-2D [1] and the equation-of-state / opacity codes FEOS [2] and THERMOS [3] support the research at GSI and at the upcoming FAIR facility. Furthermore, code development is still in progress [4].

In the past, measurements of the heavy-ion stopping in laser-generated dense plasmas at high temperatures at GSI were of crucial importance for the indirect drive scenario of heavy-ion fusion and for the ion-driven fast ignition concept. The corresponding RALEF-2D simulation results [5,6] for the hohlraum X-ray spectra as well as for the plasma column densities were essential for understanding the measurements and for optimization of the experimental setup. Now, current research for planned warm dense matter experiments at GSI and FAIR focusses on the design of diagnostical options, especially of backlighter sources for opacity measurements.

For opacity measurements of expanding laser-heated plasmas an intense “smooth” backlighter option is needed where the spectrum should not be tainted with dominating spectral lines. For such purpose hohlraum targets are a well-suited option. Fig. 1 shows a simulation of a cylindrical gold hohlraum backlighter target with length 0.8 mm and diameter 0.8 mm heated by the short pulse (10 ps pulse duration and 50 J total deposited energy) option of the PHELIX laser at GSI. In contrast to the “old” above mentioned hohlraum simulations for combined laser-ion-beam experiments, the much shorter laser pulse demands for a better and more complicated numerical mesh structure. The figure demonstrates the ablated plasma from the left hohlraum wall by the laser beam and from the right wall by thermal radiation. Both plasma fronts collide and form a hot filament close to the hohlraum center.

Fig. 2 shows the calculated X-ray spectrum as would have been observed through the lower hohlraum hole at three times and in comparison to a Planckian fit for T = 33 eV. At t = 5 ns the spectrum comes close to the Planckian one with a peak maximum of the spectrum at 100-120 eV. At t = 20 ns, both the matter and radiation temperature close to the hohlraum center drop down only by ~ 15% compared to the temperatures at t = 5 ns. This shows that the hohlraum can be used over a long time period with T ≈ 28–33 eV for the opacity measurements.

* Work supported by BMBF project No. 05P15RGFAA.
This report is also submitted to the report “News and Reports from High Energy Density generated by Ion and Laser beams 2016”.
#faik@physik.uni-frankfurt.de

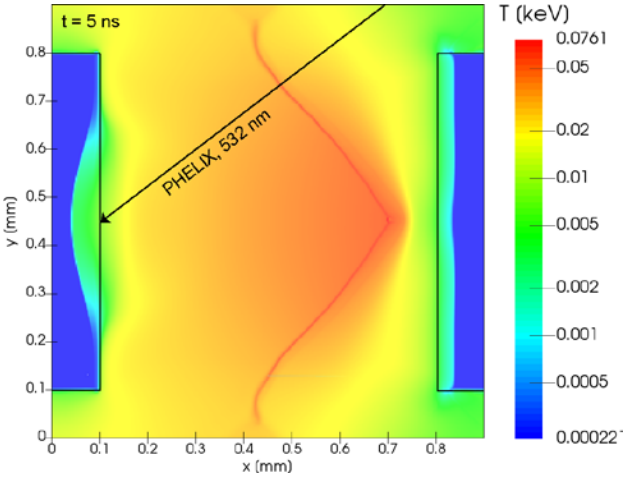

Figure 1: Simulated temperature inside a 0.8 mm long gold hohlraum with diameter 0.8 mm at t = 5 ns. The hohlraum is heated by the short pulse of the PHELIX laser. Black lines indicate the boundary of the hohlraum walls and the direction and spot of the laser at t = 0 ns.

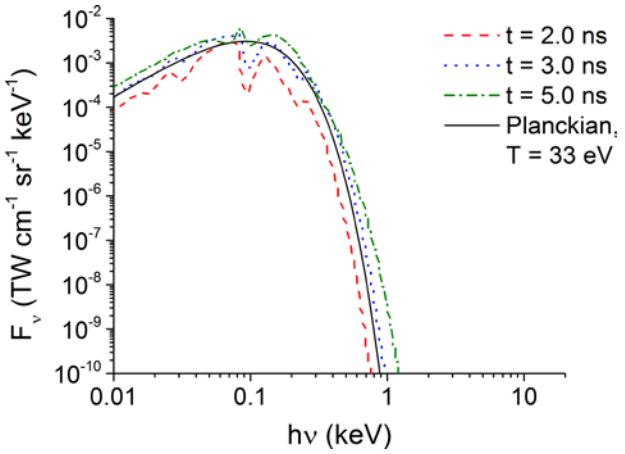

Figure 2: Calculated X-ray spectrum as would have been observed through the lower hohlraum hole at t = 2, 3, and 5 ns. The solid line shows a Planckian fit for T = 33 eV.

References

[1] M. M. Basko, J. A. Maruhn, An. Tauschwitz, GSI Report 2010-1 410.
[2] S. Faik, M. M. Basko, An. Tauschwitz, I. Iosilevskiy, J. A. Maruhn, HEDP 8 (2012) 349.
[3] A. F. Nikiforov, V. G. Novikov, V. B. Uvarov, Quantum-Statistical Models of Hot Dense Matter (2005).
[4] M. M. Basko, I. P. Tsygvintsev, Computer Physics Communications (2017) 6128.
[5] S. Faik, An. Tauschwitz, M. M. Basko, J. A. Maruhn et al., HEDP 10 (2014) 47.
[6] A. Ortner, S. Faik, D. Schumacher, M. Basko, et al., NIMB 343 (2015) 123.

Charge-state equilibration of a carbon beam at 0.65 MeV per nucleon energy in thin solid carbon foils*

W. Cayzac[1], *V. Bagnoud*[2,3], *A. Blaževic*[2,3], *S. Busold*[3], *O. Deppert*[4], *J. Ding*[4], *P. Fiala*[4], *S. Frydrych*[4], *D. Jahn*[4], *N. Neumann*[4], *A. Ortner*[4], *G. Schaumann*[4], *D. Schumacher*[2], *F. Wagner*[2], *S. Weih*[4], *and M. Roth*[4]

[1]CEA, DAM, DIF, Arpajon, France; [2]GSI, Darmstadt, Germany; [3]Helmholtzinstitut Jena, Jena, Germany; [4]Institut für Kernphysik, Technische Universität Darmstadt, Darmstadt, Germany

We report on measurements of the charge-state distribution of carbon ions at a 0.65 MeV per nucleon energy behind thin solid carbon foils obtained within the experiment U303. In this low-energy range of the beam-target interaction, the collision processes that rule charge-exchange cross sections cannot be described within a first-Born approximation. The prediction of the charge-state distribution is therefore challenging. Moreover, the experimental database is still very incomplete. Here, we use carbon foils with thicknesses in the range 2–10 µg/cm^2 for which the beam charge is expected to reach equilibrium [1]. By measuring not only equilibrium but also non-equilibrium charge-state distribution, we are able to absolutely determine the electron capture and loss cross sections.

The experimental setup at the Z6 area of the UNILAC accelerator is shown in Fig. 1. The carbon ion beam at an initial energy of 3.7 MeV per nucleon, after passing through a 1 mm diameter pinhole for beam collimation, was decelerated through a 40 µm thick aluminum degrader foil. This resulted in a beam energy of $E_p = 0.65 \pm 0.015$ MeV per nucleon that was measured using the time-of-flight method with a semiconductor detector based on chemical-vapour-deposition (CVD) diamond [2].

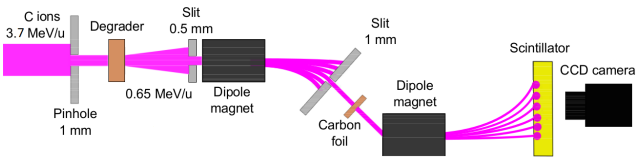

Figure 1: Setup for the charge-state measurements

The ion slowing down also created a charge-state distribution of the carbon beam. One of the charge states was then selected using a dipole magnet featuring a length of 60 mm and a magnetic field of 1.2 T strength and employed as a probe for the thin carbon foils. The resulting beam charge-state distribution behind the thin foils was split spatially using another dipole with a length of 60 mm and a strength of 0.8 T and subsequently registered on a scintillator screen with the help of a CCD camera. The charge states 5+, 4+ and 3+ of the carbon beam were successively selected as initial charge states for the measurements. Most foils were produced at the Target Laboratory of GSI and their thickness was measured by means of Raman backscattering spectroscopy at Helmholtzinstitut Jena with a precision of about 3–5 % for each foil. Additional carbon foils of 2–4 µg/cm^2 thickness were made at the Target Laboratory of Technische Universität München and measured in thickness with a precision of 5 % with the help of a quartz crystal microbalance.

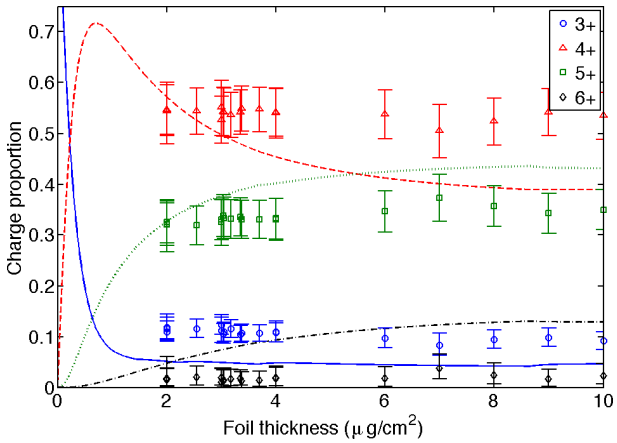

Figure 2: Measured charge-state distributions for the carbon beam at 0.65 MeV per nucleon energy as a function of the thickness of the carbon foil, for an initial beam charge state of 3+, compared with the predictions of the ETACHA code (3+: plain line, 4+: dashed line, 5+: dotted line, 6+: dash-dotted line)

The measured charge-state-distributions are compared with the predictions of the ETACHA code [3] that solves rate equations for the projectile ions. The results for the initial charge state 3+ are presented in Fig. 2. A preliminary analysis suggests that, firstly, the ETACHA code over-estimates the electron loss cross section compared to the electron capture cross section and that, secondly, the charge-state equilibrium is reached for foil thicknesses smaller than predicted. A detailed analysis considering the presence of contaminants on the foils surface is in progress.

References

[1] H. D. Betz, in Applied Atomic Collision Physics, Volume 4: Condensed Matter, Vol. 4, edited by S. Datz (1983)

[2] W. Cayzac, Rev. Sci. Instrum. 84, 043301 (2013)

[3] E. Lamour et al., Phys. Rev. A 92, 042703 (2015)

*This report was also submitted to News and Reports from High Energy Density generated by Heavy Ions and Laser Beams 2016"

DOI:10.15120/GR-2017-1

A light gas accelerator for studies on dynamic material properties with PRIOR*

M. Endres †[1], *S.Udrea*[2], *and D.H.H. Hoffmann*[1]
[1]TUD, Darmstadt, Germany; [2]GSI, Darmstadt, Germany

At FAIR a novel diagnostic system, the proton microscope (PRIOR), will use high energy protons for radiography [1]. The ion accelerator will be used for accelerating the protons for diagnostics, thus an external driver for dynamic experiments is needed. At the Technische Universität Darmstadt the design and realisation of a two stage light-gas driver for shockwave experiments is ongoing. The parts and the design of the accelerator are shown in figure 1 and 2. The first stage consists of four pistons driven by methane combustion. These pistons compress and heat up Helium in the second stage. The Helium then is supposed to accelerate a sabot carrying a flyer. According to present estimations the two stage device could accelerate 3 g loads up to about 3 km/s. The flyers will shock load different types of targets. The resulting material states should be investigated by a combination of proton radiography and other means.

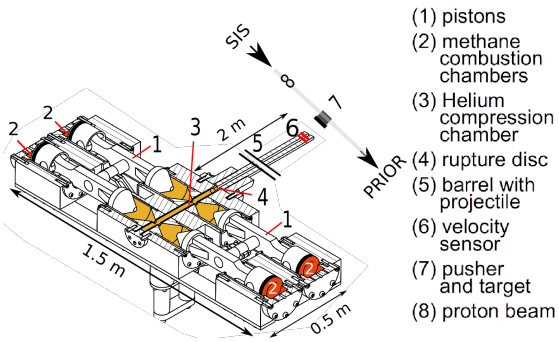

Figure 1: Not to scale scheme of the proposed setup.

The basic experiment setup consists of the light-gas accelerator and PRIOR (see Figure 1). A flyer accelerated with the driver impacts into a pusher or directly into a target. The target then is irradiated by the protons so the proton microscope could serve as an in situ diagnostic of the shock wave inside the target,. According present estimations the shockwave and proton pulse should be synchronised with accuracy of 50 ns.
The ignition of the accelerator will have a quite large jitter of about 1ms. Also the velocity of the flyer is not precisely predictable. Thus the velocity of the flyer will be measured at the end of the barrel with a light barrier to produce a trigger signal for the kicker magnet. This kind of inverse triggering means that the accelerated protons have to been stored inside the synchrotron up to the arrival of the trigger signal. For a 4 mm target and a shock velocity of 3km/s the shockwave inside the target will need about 1.3μs. To get a picture of the shockwave itself the proton beam has to illuminate the target in this time. Typically a beam with 4 bunches in one Proton pulse (0.7μs) should be used. To adjust the flight time of the projectile after the measurement between 2.5 and 200μ s the flight distance will be adjustable. The possible precision is limited by the distance between the bunches in the synchrotron and the accuracy of the velocity measurement.

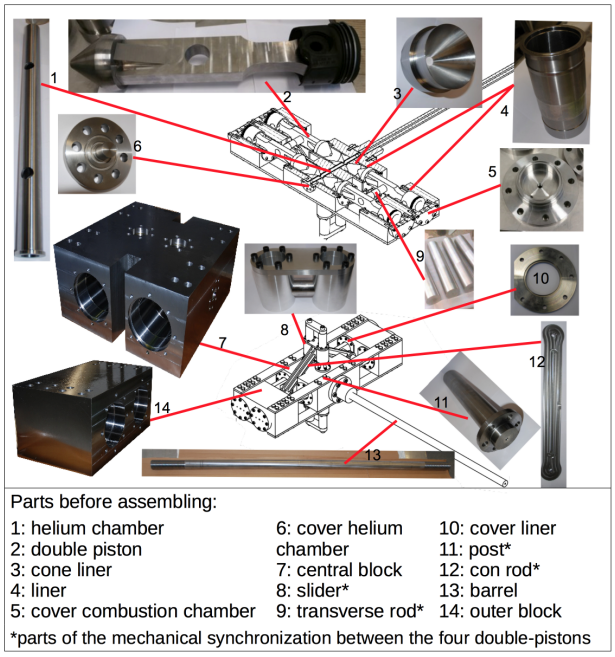

Figure 2: Overview of the design of the light-gas accelerator and its parts.

The goal of the planned experiments is to investigate material properties under shock wave loading. Also it is possible to study the behaviour of different kind of surfaces. The proton radiography will allow to measure the density distribution inside the shocked materials. Targets for this kind of experiments are currently developed and tested at IPCP RAS.

References

[1] D. Varentsov et al., "Commissioning of the PRIOR proton microscope", Rev. Sci. Instrum. 87, 023303 (2016), doi: 10.1063/1.4941685

* Work supported by BMBF. This report is also submitted to *News and Reports from High energy Density generated by Heavy Ion and Laser Beams 2016*.
† m.endres@gsi.de

Investigation on the theta pinch plasma as application for an ion stripper for FAIR*

K. Cistakov[1,†], Ph. Christ[1], A. Fedjuschenko[1], G. Xu[1,2,3], M. Iberler[1], T. Ackermann[1], T. Rienacker[1], A. Blazevic[4], K. Weyrich[4], O. Rosmej[4], A. Schönlein[1], J. Wiechula[1], T. Manegold[1], S. Zähter[1], and J. Jacoby[1]

[1]Goethe Universität, Frankfurt, Germany; [2]IMP, Lanzhou, China; [3]UCAS, Beijing, China; [4]GSI, Darmstadt, Germany

Important results concerning the beam transfer and the charge distribution were published after finishing the Plasma stripper experiment at GSI (Helmholtzzentrum für Schwerionenforschung) in April 2014 ([1], [2], [3]). In spite of the good results, it was determined that the electron density required to get appropriate charge states was not obtainable. Different solutions for the optimization of the experiment were researched, having as principal challenges the deposition of more energy into the plasma without increasing the parasitic magnet field, the conservation of the beam transfer without exceeding the geometrical sizes of the experiment and the protection against flash-overs in the presence of the increased energy.

As a result of the simulations and analysis of the new plasma stripper concept, a new cylindrical theta-pinch cell was constructed instead of a spherical one. The advantages of a cylindrical design are: The plasma obtained at the z-axis sufficiently protects the ion beam against the impact of parasitic magnet fields. Despite of the increased current, simulations have shown that the parasitic magnetic fields have remained on the same level. This fact allows an even better beam transfer through the stripper cell. Finally, the new configuration raises the magnetic field, which triggers higher particle density.

Compared to the previous plasma stripper with a discharge energy of approx. 6 kJ, the new capacitor bank is equipped with 16 parallel-connected capacitors of 5 μF each and is driven at a voltage of 35 kV, which provides a discharge energy up to 50 kJ. Additionally, the frequency of the circuit remains below 10 kHz. In contrast to the last design, which has shown a very high efficiency up to 85 %, the efficiency of the new design is only 40 to 50 %. Nevertheless, the energy stored into the plasma will be increased up to a factor of 4, raising the electron density accordingly.

The first attempts of constructing the new configuration have been very positive. However, new solutions are still required, addressing the increased inductance due to the new capacitor bank, the energy supply and the discharge coil. Higher inductance causes a lower frequency of the LCR-circuit, which leads to difficulties affecting the plasma ignition. This problem can be solved by an improved coaxial circuit. Moreover, an additional support for the coil must be developed to protect it from vibrations during the current flow.

Further experiments are planned for March-April due to the technical difficulties in the creation and manufacture of the new circuit.

For the determination of the stripping characteristics, it is vital to estimate the electron density of the pinch plasma time-resolved along the beam line. To cover this task, a Mach-Zehnder-Interferometer has been successfully built and tested at IAP Frankfurt. The interferometer operates with a He/Ne-Laser at 632.8 nm wavelength and is based on a heterodyne measurement method with a frequency shift of 80 MHz between the interfering waves, which defines a time-resolution of 12.5 ns. Figure 1 shows the schematic structure of the interferometer.

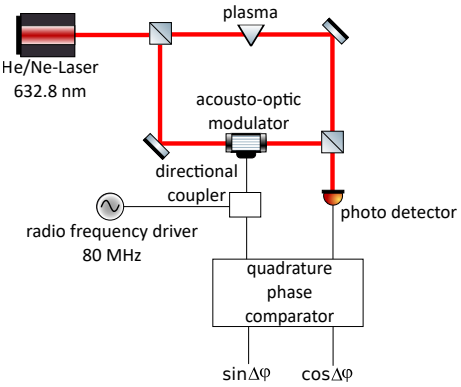

Figure 1: Schematic structure of the interferometer

The preliminary testing of the interferometer has been done without a plasma source by estimating the angle of a glass wedge in a fall experiment to explore basic functionality. The used wedge is indicated with an angle $\alpha = (3.883 \pm 0.017)^\circ$ by the manufacturer, which has been reproduced within the error margin with a deviation of only $0.12\,\%$ from the optimum value. Additionally, a maximum phase error of 0.08 rad has occurred ordinarily during the testing, what implies a lower limit of the measurable line-integrated electron density of $4.48 \cdot 10^{19}\,\mathrm{m}^{-2}$.

References

[1] G. Xu *et al.*, GSI SCIENTIFIC REPORT 2014, APPA-MML-PP-16.

[2] G. Loisch, G. Xu, A. Blazevic, B. Cihodariu-Ionita und J. Jacoby, Physics of Plasmas 22, 053502 (2015).

[3] G. Loisch, IEEE Transactions on Plasma Science 42(5):1163-1172 (2014).

* This report is also submitted to 'News and Reports from High Energy Density generated by Heavy Ion and Laser Beams 2016'.

† Cistakov@iap.uni-frankfurt.de

DOI:10.15120/GR-2017-1

Construction, characterization and optimization of a plasma window based on a cascade arc design for FAIR, Status update*

B. Bohlender[1#], J. Wiechula[1], M. Iberler[1], A. Michel[1], M. Dehmer[1] O. Kester[2] and J. Jacoby[1]
[1]Goethe University, Frankfurt, Germany; [2]TRIUMF, Vancouver, Canada

Introduction

As described in the last GSI Scientific Report [1], the plasma window is a device designed to shield two different pressure areas such that a particle beam may move unhindered through. Since the last report, a lot of effort has been put into determining the operational characteristics, which include the erosion behavior which links strongly to the estimated lifetime of the window, spectra for information about the plasma characteristics e.g. temperature, density, operational pressure and the electrical conditions for ignition and CW burning of the arc. First results prove that a shielding of the gas flow can be achieved with this setup.

Constructional remarks

With the first stable CW-mode of the window established in November 2016, it became obvious that the used cathode material (Tungsten 80%, Copper 20%) proved to be not temperature resistant enough for this application, see Figure 1. Figure 1 shows two cathodes: one brand new (left) and one after the usage of approx. *15min @45A* of discharge current.

Figure 1: Unused Cathode (left) used cathode (left) with additional isolator (white). The cathodes are aligned such that the tips would be on the same height.

To encounter this phenomenon, new cathode tips made from pure tungsten were constructed and are tested. Figure 2 shows a first impression of the increased stability for pure tungsten cathode tips. While the W-Cu tip has already melted, the W tip has held its geometry.

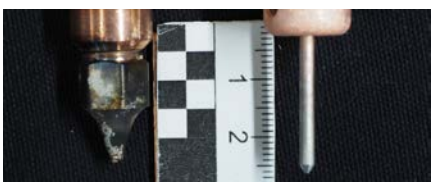

Figure 2: W80Cu20 tip (left), pure W tip (right) after approx. 20 ignitions with I < 50A, t<20ms per shot

Another rather big constructional effort has proved to be necessary: The sealing (hard solder) of the water cooling channels is heavily attacked during the discharge and loses its stability. Thus, several designs including ceramic isolators between the cooling plates, smaller gaps in between are being tested.

Experimental Data

With the establishment of the CW mode, first spectra were taken to determine an approximation of the plasma temperature. Figure 3 shows such a spectrum, from which an electron temperature of about $T_e \approx 6900K$ can be calculated. This Temperature is less than expected, which might be explained by the composition of the plasma (Ar, C, W, Cu, H).

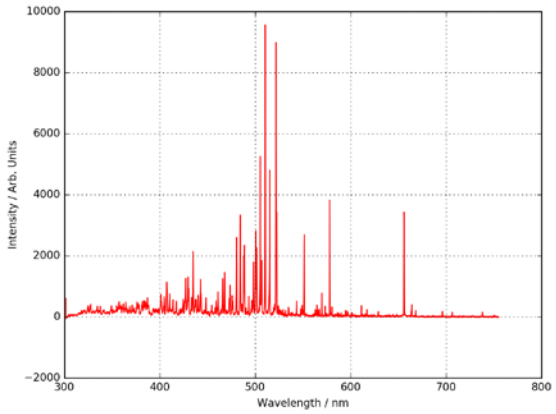

Figure 3: Spectrum taken @ I=50A, p=1mbar

The usual ignition voltage for pressures around 0.1…10mbar is around 300-600V with an arc current of $I_{Arc} \geq 36A$ for Argon gas.

Status and outlook

The present setup has shown to be capable of shielding two different pressure areas from another without the usage of solid shielding. While the basic proof of principle is adducted, a lot of work is still ahead, especially to increase the lifetime of the cathodes and the discharge channel, e.g. the cooling plates. Right now, several new designs are being tested which should result in reproducible data and CW mode operation throughout this year.

References

[1] B. Bohlender et al: GSI Scientific Report 2015, p 352

* Work supported by BMBF contract No. 05P2015.
# bohlender@iap.uni-frankfurt.de
* This report is also submitted to 'News and Reports from High Energy Density generated by Heavy iOn and Laser Beams 2016'

Generation of core conditions of Earth and Super–Earths using LAPLAS scheme at FAIR *

N.A. Tahir[1], I.V. Lomonosov[2], B. Borm[1], A.R. Piriz[3], A. Shutov[2], P. Neumayer[1], V. Bagnoud[1], and S.A. Piriz[3]

[1]GSI, Darmstadt, Germany; [2]IPCP, Chernogolovka, Russia; [3]UCLM, Ciudad Real, Spain

Planetary physics research is an important part of the FAIR High Energy density (HED) physics program. For this purpose, a unique experimental scheme named LAPLAS, has been developed, as shown in Fig. 1. A sample material is enclosed in a High–Z, High–ρ cylindrical shell that is facially irradiated by an intense ion beam with an annular focal spot. Such a scheme leads to a low–entropy compression of the sample that generates super–high densities, ultra–high pressures, but low temperatures. Previously, we simulated compression of hydrogen [1] and water [2] using an intense uranium beam with parameters that will be available at the FAIR. The simulations were done using a 2D hydrodynamic code. BIG2 [3]. This work predicted that using LAPLAS scheme, one can generated the physical conditions similar to those which exist in the interior of hydrogen rich (Jupiter and Saturn) and water rich (Uranus and Neptune) planets respectively.

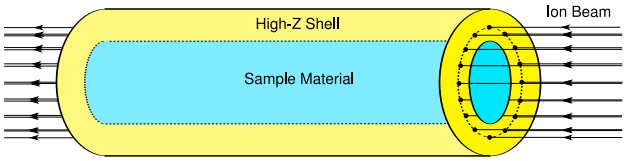

Figure 1: Beam–target configuration for LAPLAS scheme.

In the present contribution we report calculations of compression of an Fe sample enclosed in a W shell. Studies of Equation of State, transport and constitutive properties of Fe under extreme conditions is key to understanding the interior structure of the Earth and more massive extra–solar rocky planets, the "Super–Earths". The target length is 4 mm, the radius of the iron sample is 0.2 mm and the outer radius of the W shell is 3 mm. The inner radius of the focal spot ring, R_i = 0.2 mm and the outer radius, R_o = 1.2 mm while the beam is comprised of 1.5 GeV/u uranium ions. Three different beam intensities including 10^{11}, 2.5 $\times$ 10^{11} and 5 $\times$ 10^{11} ions per bunch, respectively, are considered. The bunch length is assumed to be 75 ns.

In Fig. 2 we present the pressure distribution in the target on a length–radius plane at t = 75 ns using an intensity of 2.5 $\times$ 10^{11} ions per bunch. It is seen that a driving pressure of about 2 Mbar is generated in the W absorption region that drives an inmoving and an outgoing radial shock wave. This is shown in Fig. 3, where we present the corresponding density distribution. The optimum compression leads to a pressure of about 4 Mbar, a temperature of around

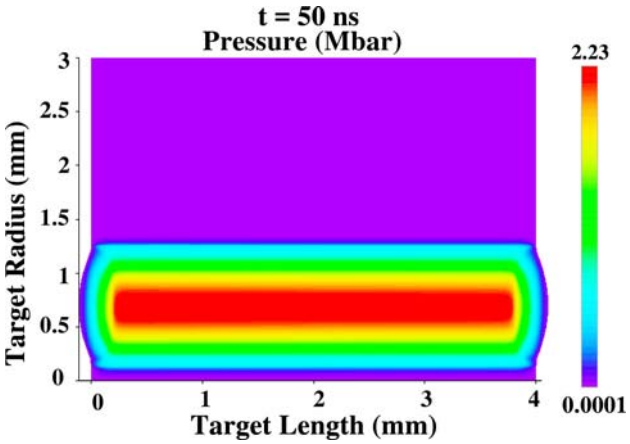

Figure 2: Pressure distribution in the target at t = 75 ns.

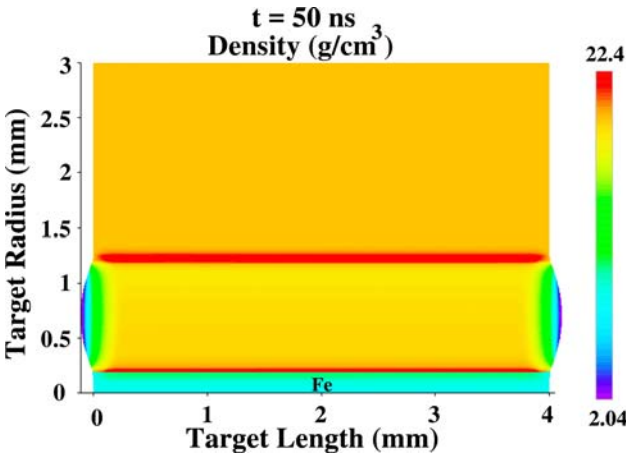

Figure 3: Density distribution in the target at t = 75 ns.

6000 K and a density of the order of 15 g/cm^3, which are expected Earth core physical conditions. Calculations done using 5 $\times$ 10^{11} ions per bunch predict pressures of around 7.5 Mbar, temperatures of the order of 10000 K and densities of about 18 g g/cm^3. Models predict that these extreme conditions may exist at the core of solid rocky planets, 4 – 5 times more massive than the Earth [4].

References

[1] N.A. Tahir et al., PRE 63 (2001) 016402.

[2] N.A. Tahir et al., New J. Phys. 12 (2010) 073022.

[3] V.E. Fortov et al., Nucl. Sci. Eng. 123 (1996) 169.

[4] D. Valencia et al., Astrophysical J. 665 (2007) 1413.

* Work supported by BMBF.

DOI:10.15120/GR-2017-1

Generation of High Energy Density Fe sample at FAIR employing LAPLAS scheme using a circular beam focal spot *

N.A. Tahir[1], *I.V. Lomonosov*[2], *B. Borm*[3], *A.R. Piriz*[4], *A. Shutov*[2], *P. Neumayer*[1], *V. Bagnoud*[1], *and S.A. Piriz*[4]

[1]GSI, Darmstadt, Germany; [2]IPCP, Chernogolovka, Russia; [3]Goethe–Uninversität Frankfurt, Frankfurt, Germany; [4]UCLM, Ciudad Real, Spain

The schematics of the proposed experiment is shown in Fig. 1. The sample material "S" which is Fe in this case, is enclosed in a thick cylindrical shell of W and the target is facially irradiated by the ion beam which has a circular focal spot with a Gaussian transverse intensity distribution. We have carried out hydrodynamic simulations of the target implosion using the 2D code, BIG2 [1] which are reported in this contribution. Previously, we did similar calculations

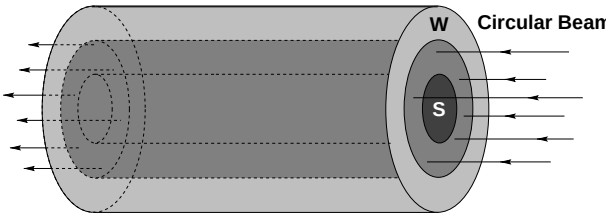

Figure 1: Beam–target configuration for LAPLAS scheme.

using hydrogen [2] and water [3], respectively, as sample material. It was found in the simulations that although the sample materials were directly heated by the beam, the pressure in the surrounding heated part of the outer high–Z shell was still much higher due to the very high density. Therefore, despite the strong preheating of the sample, the sample material was significantly compressed by the outer pressure. Typically, hydrogen was compressed by a factor 10, while a compression of factor 3 was achieved in case of water. In case of Fe, however, the density is about a factor 2 less than that of W. The pressure in the preheated region becomes too high to achieve any noticeable compression. The sample is strongly heated and becomes a hot high pressure liquid at solid density that is confined by the W shell.

In the present simulations, we have used a wide range of beam parameters including the "Day–One" as well as the maximum design values. Four different values have been considered for the beam intensity including 5×10^{10}, 10^{11}, 2.5×10^{11} and 5×10^{11} ions per bunch, respectively. Three different bunch lengths, namely, 50, 75 and 100 ns, respectively, have been used. Moreover, three different values for the focal spot size characterized with full width at half maximum (FWHM), respectively, have been taken into account.

In Fig. 2 we plot ρ, T and P vs radius at L = 2 mm at optimum conditions using a bunch intensity of 2.5×10^{11} ions/bunch, a bunch length = 75 ns and FWHM = 1 mm. It

* Work supported by BMBF.

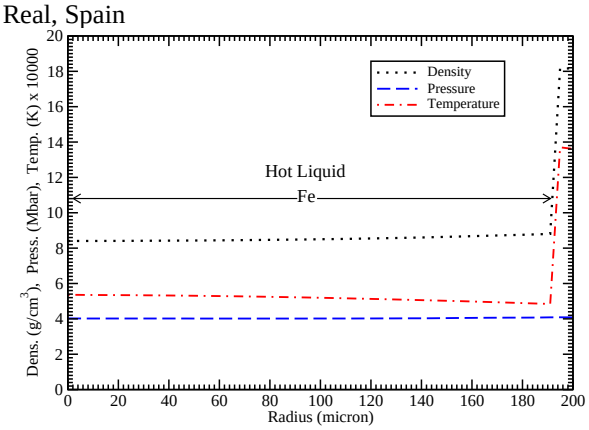

Figure 2: ρ, T and P vs radius at L = 2 mm at optimum conditions, 2.5×10^{11} ions/bunch, bunch length = 75 ns and FWHM = 1 mm.

Table 1: Optimum physical conditions in Fe, τ = 75 ns, FWHM = 1 mm, N: intensity, t_o: time for optimum conditions, PS: physical state and HL: hot liquid.

N (10^{11})	t_o(ns)	ρ(g/cc)	P(Mbar)	T(10^4 K)	PS
0.5	70	8.8	1.4	1.4	HL
1	64	8.7	2.3	2.5	HL
2.5	52	8.5	4.0	5.2	HL
5	45	8.4	5.7	8.3	HL

is seen that the physical conditions are fairly uniform along the radius and Fe sample is in a hot liquid state. Table I shows optimum sample physical parameters in case of different beam intensities. In all these cases, the Fe has been coverter into a hot liquid state. These samples can be used to study the EOS and transport properties, especially the viscosity of HED liquid Fe.

References

[1] V.E. Fortov et al., Nucl. Sci. Eng. 123 (1996) 169.

[2] N.A. Tahir et al., PRE 63 (2001) 016402.

[3] N.A. Tahir et al., New J. Phys. 12 (2010) 073022.

High energy resolution spectroscopy of the target and projectile X-ray-fluorescence * †

S. Zähter[1], *C. Arda*[1], *P. Beloiu*[1], *B. Borm*[1,2], *M. El Houssaini*[1], *D. Khaghani*[3], *D. Lyakin*[4], *O. N. Rosmej*[1,2], *A. Schönlein*[1], *J. Jacoby*[1], *and A. Golubev*[4]

[1]Goethe Universität, Frankfurt, Germany; [2]GSI, Darmstadt, Germany; [3]Friedrich-Schiller-Universität, Jena, Germany; [4]Institute for Theoretical and Experimental Physics (ITEP), Moscow, Russia

Intense uranium beams, that will be available after commissioning of the new synchrotron SIS100 in Darmstadt, can be used for volumetric heating of any type of material and generation of extreme states of matter with Mbar pressures and some eV of temperature. Investigation of their EOS is one of the main goals of the plasma physics program at FAIR. Diagnostic of such extreme states of matter demands development of new diagnostic methods and instruments, which are capable to operate in an environment with a high level of radiation damage. The precise knowledge of the energy density distribution caused by the U-beam in the target is a very important input parameter for numerical simulations of the hydrodynamic response of the target on deposited energy. Simulations are crucial during the planning of experiments and for the interpretation of obtained experimental data. To investigate the energy density distribution, we propose to use the target and heavy ion beam X-ray fluorescence for imaging of the target expansion and mapping of the heavy ion beam distribution in the interaction region with a high spatial resolution of at least $100\,\mu m$. The obtained results can be scaled to high heavy ion energies available at SIS18 and SIS100.

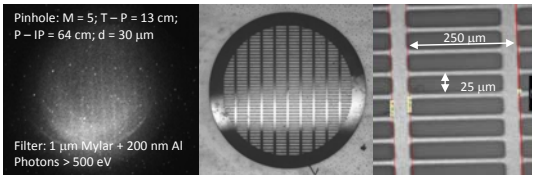

Figure 1: Pinhole Image of interaction between Au^{26+} beam and Cu-mesh. Picture of used Cu-mesh. Microscopical picture of Cu-mesh.

First pilot experiments on measurements and characterization of the heavy ion and target fluorescence using pinholes, X-ray CdTe-diodes and dispersive systems have been carried out in 2016 at the Z6 experimental area which is situated after the UNILAC. A 6.5 MeV/u Au^{26+}-Beam passed through different foil-targets (Al, Cu, Ta) of $6-10\,\mu m$ thickness.

X-ray radiography of Cu-meshes with fluorescence radiation shows a spatial resolution of at least $250\,\mu m$ (see Fig. 1). It is intended to use this diagnostic to measure the projectile X-ray fluorescence to map the ion-beam distribution on the target.

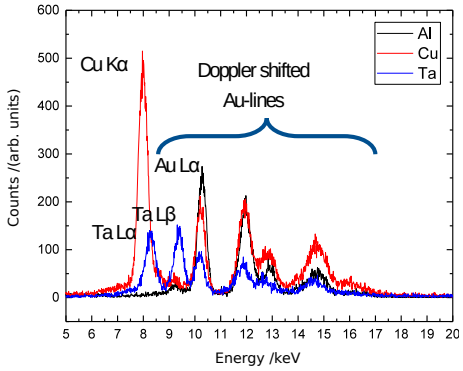

Figure 2: Fluorescence spectrum measured by CdTe-spectrometer.

This experiment demonstrated a big potential of X-ray fluorescence as a diagnostic tool for future FAIR-experiments. We observed intense radiation of ionized target atoms (K-shell transitions in Cu at 8-8.3 keV and L-shell transition in Ta) as well as Doppler shifted L-shell transitions of Au projectiles passing through foils in the photon energy region of 10 keV (see Fig. 2). This radiation can be used for monochromatic (dispersive element) or polychromatic (pin-hole) X-ray mapping of the ion beam intensity distribution in the interaction region. Using data obtained by means of CdTe X-ray spectrometer and a faraday cup, we could estimate the number of Au-Lα photons per 1 C of the Au-charge passing through Al, Cu and Ta foils and per $1\,\mu m$ target-thickness in 4π. This number allows us to conclude that 10-100 fold amplification of the signal is required in order to apply this method for U-beam intensities between $10^{10}-5\cdot10^{11}$ particles/pulse. 2D X-ray pinhole image of the Cu-grating excited by Au-ion beam, obtained with $200\,\mu m$ spatial resolution, is the first promising result that can be improved in future experimental campaigns.

* Work supported by GSI (UNILAC)/ HIC4FAIR/ HGS-Hire/ BMBF (Förderkennzeichen 05P15RFFA1)

† This report is also submitted to the Annual Report 'News and Reports from High Energy Density generated by Heavy Ion and Laser Beams'

DOI:10.15120/GR-2017-1

High energy density physics issues related to FCC beam*

N.A. Tahir[1], *F. Burkart*[2], *R. Schmidt*[2], *A. Shutov*[3], *D. Wollmann*[2], *and A.R. Piriz*[4]

[1]GSI, Darmstadt, Germany; [2]CERN, Geneva, Switzerland; [3]IPCP, Chernogolovka, Russia; [4]UCLM, Ciudad Real, Spain

To study the affect of an accidental release of one FCC beam on equipment and accelerator components, we carried out simulations of the full impact of the beam on a cylindrical Cu target that has a radius of 2 cm and is 5 m long. The beam is comprised of 10600 bunches of 40 TeV protons with a bunch intensity of 10^{11} particles. Bunch length is 0.5 ns and bunch separation is 25 ns. The focal spot has a σ = 0.2 mm. The simulations have been done using an energy deposition code, FLUKA and a 2D hydrodynamic code, BIG2, iteratively. The beam is transversely incident of one face of the cylinder so that the beam and the target axis coincide. In Fig. 1 we present isolines of

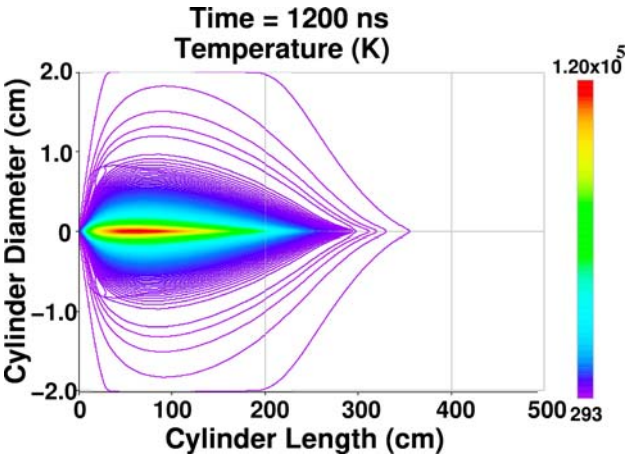

Figure 1: T distribution at t = 1250 ns

temperature at t = 1200 ns [48 bunches delivered] in the target provided by the BIG2 code. It is seen that the maximum temperature at the axis is 1.2 $\times$ 10^5 K. Fig. 2 shows that the corresponding pressure has a maximum value of about 46 GPa. The high pressure generates an outgoing radial shock wave that leads to significant density depletion at and around the axis. As a result of this, the protons that are delivered in the subsequent bunches penetrate deeper in the target, which makes the range of the protons and their shower much longer than the static range, which is called, "the hydrodynamic tunneling effect". For example, according to our present calculations, the static range of a single 40 TeV proton and its shower is about 1.5 m in Cu, but the full FCC beam will penetrate up to 295 m in the target [1].

In Fig. 3, we plot profiles of density, temperature and pressure along the target axis. It is seen that the material that lies between L = 0 – 1 m is converted into a weekly

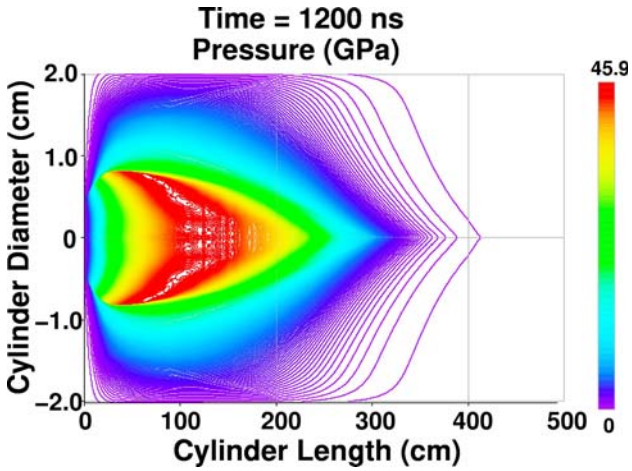

Figure 2: P distribution at t = 1250 ns

ionized plasma, whereas material between L = 1 – 3 m is in liquid state. This shows that a large part of the target has been converted into different phases of HED matter including Warm Dense Matter and strongly coupled plasma. One may conclude that issues of HED matter are inherent to every powerful accelerator that generates intense ion beams.

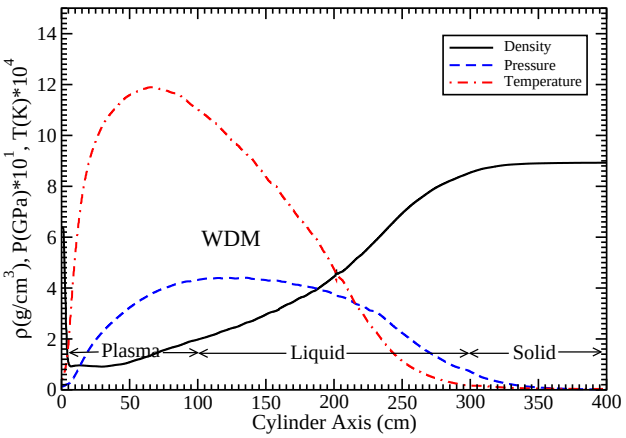

Figure 3: ρ, T and P vs axis at t = 1250 ns

References

[1] N.A. Tahir et al., Phys. Plasmas (2017) Accepted.

* Work supported by CERN and BMBF

Feasibility study of a water beamdump for the 50 TeV FCC proton beam*

N.A. Tahir[1], *F. Burkart*[2], *R. Schmidt*[2], *A. Shutov*[3], *D. Wollmann*[2], *and A.R. Piriz*[4]

[1]GSI, Darmstadt, Germany; [2]CERN, Geneva, Switzerland; [3]IPCP, Chernogolovka, Russia; [4]UCLM, Ciudad Real, Spain

After the unprecedented success with the Large Hadron Collider (LHC), a design study is being conducted to assess the feasibility of a much more powerful hadron collider named, Future Circular Collider (FCC). According to this design study, the FCC will be installed in a circular tunnel with a circumference of 100 km and will accelerate two counter rotating proton beams with a particle energy of 50 TeV. Each beam is comprised of 10600 proton bunches while the intensity is 10^{11} protons per bunch. Each bunch is 0.5 ns long and the bunch separation is 25 ns.

Safe disposal of the beam after experiment is a very important part of the operation. For the LHC, a carbon beamdump is being used. The beam is diluted before it reaches the beamdump and the bunches are delivered on an extended spiral shaped path so that the energy is distributed over a large volume of the beamdump to avoid material damage. For the FCC beam, such a scheme will require 20 m long spiral path for the bunches, which is very challenging. An alternate beamdump design that uses ordinary water to absorb the beam energy, has been studied with the help of numerical simulations done employing the energy deposition code, FLUKA and a 2D hydrodynamic code, BIG2, iteratively. First results are reported in this contribution.

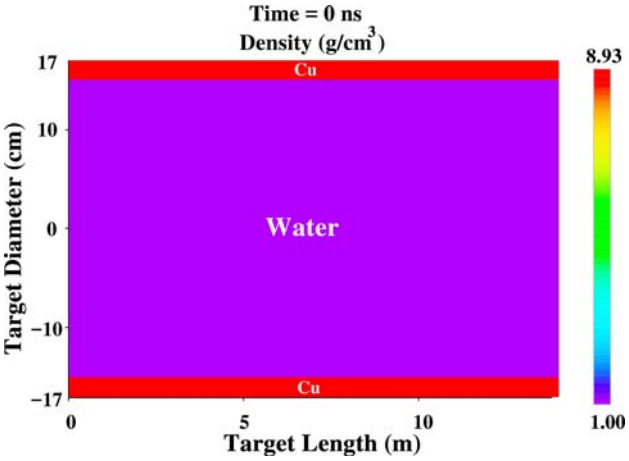

Figure 1: Target geometry.

It is a Cu pipe with an inner radius of 15 cm, an outer radius of 17 cm and is 14 m long (Fig. 1). It is filled with ordinary water and the beam is incident on the left face of the cylinder along its axis. The focal spot is circular with a Gaussian transverse intensity distribution with σ = 0.4 mm.

* Work supported by CERN and BMBF

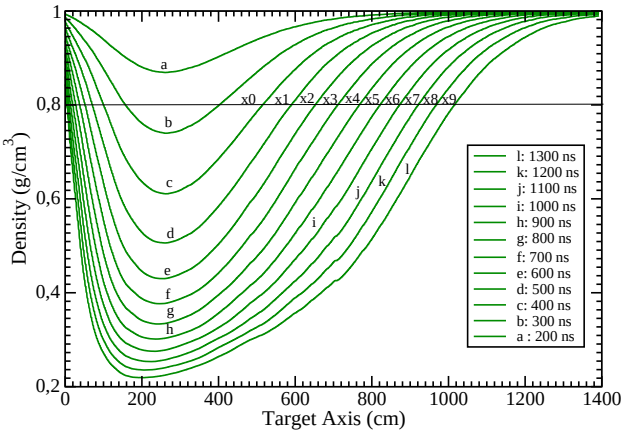

Figure 2: ρ vs axis at different times.

In Fig. 2 we present ρ along the target axis at different times. It is seen that a density depletion front propagates towards the right which is due to the outmoving radial shock wave. This leads to the hydrodynamic tunneling of the primary beam and the shower [1]. In table I we present the position and the propagation speed of the depletion front at different times. It is seen that the speed decreases with time and achieves a constant value of about 4.80 $\times$ 10^6 m/s. Since the duration of the bunch train is 265 μs, the total penetration distance of the beam and the shower will be about 1.3 km, which should be the length of the beamdump. It is interesting to note that the static range of a single 50 TeV proton and its shower is about 7 m in water.

Table 1: Position, x, Distance traveled in 100 ns, Δx and speed, v of depletion front

Time (ns)	x (cm)	Δx (cm)	v (m/s)
700	713.00		
800	769.70	56.7	5.67×10^6
900	822.80	53.1	5.31×10^6
1000	872.6	49.8	5.31×10^6
1100	920.5	47.9	4.79×10^6
1200	968.7	48.2	4.82×10^6
1300	1016.7	48.0	4.80×10^6

References

[1] N.A. Tahir et al., PRAB 19 (2016) 081002.

DOI:10.15120/GR-2017-1

Establishment of a psoriatic skin model for radon treatment*

J. Wiedemann[1], *C. L. Witzler*[1], *M. Kovacs*[2], *M. Podda*[2], *and C. Fournier*[1,3]
[1]GSI, Darmstadt, Germany; [2]Department of Dermatology, Darmstadt Hospital; [3]Hochschule Darmstadt, Germany

Introduction

Psoriasis is a common chronic inflammatory skin disease [1] which is on the indication list for the therapy in radon galleries [2], but the mechanisms underlying the clinical benefit are still unclear. The disease is characterized by red plaques with white scales at elbows, knees and scalp and triggered by many factors like injury and trauma. In general it is due to an overshooting and persisting activation of the immune system. For the manifestation IL-17, IL-22, TNF-α and IFN-γ released from Th17, Th1 and Th22 cells are essential to contribute to the inflammatory cytokine milieu and to trigger an amplifying feedback loop, which is responsible for the pathogenesis [3, 4].
The access to skin biopsies from psoriasis patients and patients treated in radon galleries is limited. Therefor a model system which is close to the in vivo situation is needed for radon exposure experiments (Figure 1).

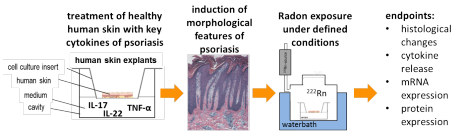

Figure 1: Experimental setup for induction of a psoriatic skin model and exposure in the radon chamber [5]

Material and Methods

Human skin from surgeries (FF136/2014) is cultured as explant at the air liquid interface (ALI) and treated with IL-22, IL-17 and TNF-α (100 ng/ml) alone or in combination for 24 or 48 hours. Then the samples are prepared for histology, immunostainings and qPCR; medium is collected for cytokine analysis. A H&E staining and an antibody staining of Psoriasin and Keratin 16 is performed.

Results and Discussion

Hematoxylin & Eosin staining of human skin treated with key cytokines of psoriasis (Figure 2) shows parakeratosis, an unsharp connection between stratum granulosum and stratum corneum and an impaired tissue organisation [6]. Immunostaining of Psoriasin (S100A7) (Figure 3) revealed a slight expression in controls and an enhancement after treatment with IL-22 or IL-17. A combined treatment with IL-22, IL-17 and TNF-α shows a synergetic effect. These results show that treatment with IL-17, IL-22 or a combination of IL-17, IL-22 and TNF-α can induce an impaired differentiation and an enhanced expression of Keratin 16 and Psoriasin which are key markers of Psoriasis. These are first hints to a successful induction of psoriatic features.

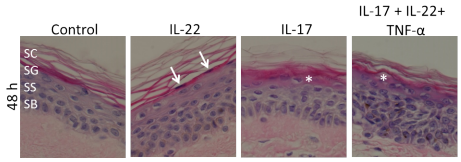

Figure 2: H & E staining of human skin explants 48 h after treatment with IL-22, IL-17 or a combination of IL-22, Il-17 and TNF-α; arrows mark parakeratosis, stars mark the unsharp connection between SG and SC

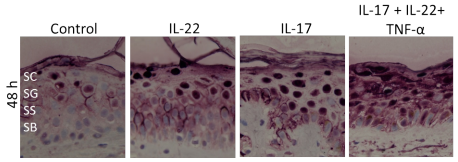

Figure 3: Psoriasin (S100A7) staining of human skin explants 48 h after treatment

References

[1] Lowes MA et al.; Nature (2007) 445:866–73. doi:10.1038/nature05663
[2] Gasteiner Kur- Reha- und Heilstollen Betriebsges.m.b.H. Indikationen; www.gasteiner-heilstollen.com
[3] Johnson-Huang LM et al.; Dis Model Mech (2012) 5:423–33. doi:10.1242/dmm.009092
[4] Chu C-C et al.; Semin Immunol (2011) 23:28–41. doi:10.1016/j.smim.2011.01.006
[5] Maier A et al.; Nucl.Instrum.Meth.(2015); 362, 187-193; doi10.1016/j.nimb.2015.09.042
[6] Simoniello P. et al.; Front. Oncol. (2015) 5:294.; doi: 10.3389/fonc.2015.00294

*Work supported by Forschungsinstitut Bad Gastein (FOI-15/08-031WIE), EURADON, the Radon Gallery of Bad Gastein and GREWIS (02NUK017A)

Contribution of radon decay products to lung dose*

A. Maier[1], *S. Sternkopf*[1,2], *H. Schmidt-Böcking*[2], *G. Kraft*[1], *C. Fournier*[1]
[1]GSI, Darmstadt, Germany; [2]Goethe Universität Frankfurt a. M., Germany

Introduction

Radon is one of the main contributors to annual dose from natural sources. Additionally radon exposure is associated with an increased risk for lung cancer [1]. The lung dose arises from radon and its decay products that can be attached to aerosols. The formation of radioactive aerosols is shown in figure 1. The radon decay products can react with vapour and form unattached progeny. Subsequently they can form clusters with dust particles (attached progeny). The deposition mechanism depends on the size of the aerosols but will not be investigated in this work. In this study we want to quantify the contribution of the radon decay products to the lung dose in relation to the radon concentration and independent from the size of the particle.

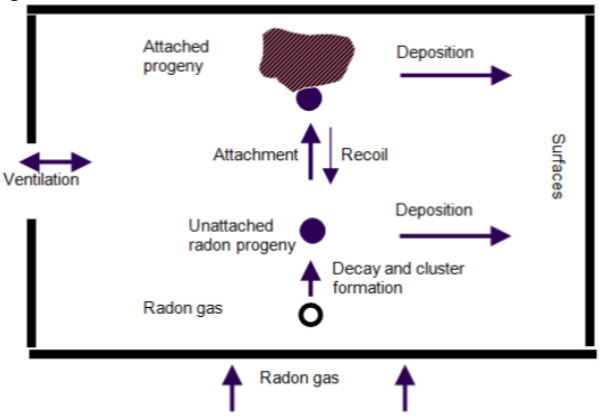

Figure 1: Formation of radioactive aerosols [2]

Measurement setup

For the experiments we developed a mechanical lung model (see figure 2). The radon progeny are deposited on a glas fibre filter and radon is absorbed on activated coal, both inside a small tube. The flow through the model is regulated by a pump and measured by a flow-meter. The whole setup is placed in a big radon chamber. For variation of the aerosol concentration we changed the relative humidity in the measurement setup.

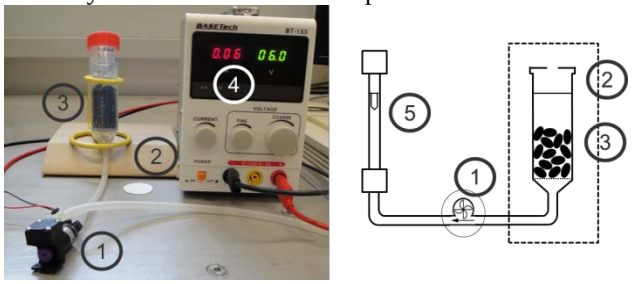

Fig. 2: Overview of the lung model with: 1 pump, 2 filter, 3 tube with activated coal, 4 power supply, 5 flowmeter

After exposure the activity of the decay products and radon were determined by gamma- spectroscopic measurements and the dose caused by the attached aerosols was determined as function of humidity [3].

Results

The results of our first measurements are shown in figure 3 where we plotted the dose of the filter over the relative humidity during the experiments. The results are normalised to a radon concentration inside the big radon chamber of 400 kBq/m^3. With these measurements we could show the feasibility of our method. But the scatter of the data points is too large to identify a clear increase.

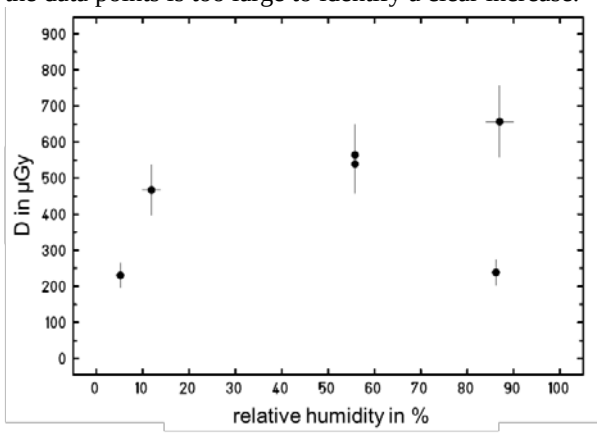

Fig. 3: Calculated dose from radon progeny in dependence of the relative humidity [3]

Outlook

For future work there are several improvements of the measurement setup. Amongst others we want to construct a more anatomical correct lung model and a reproducible variation of the aerosol concentration. In combination with a certain size distribution of the aerosols, the deposition mechanism at different sites in the lung can be investigated.

References

[1] S. Darby et al. Residential radon and lung cancer – detailed results of a collaborative analysis of individual data on 7148 persons with lung cancer and 14208 persons without lung cancer from 13 epidemiologic studies in Europe, Scand. J. Work Environ. Health, 32, 1-84, 2006

[2] Committee on Health Risks of Exposure to Radon, National Research Council, Health Effects of Exposure to Radon (BEIR VI), National Academy Press, 1999

[3] S. Sternkopf, Dosisbeitrag von Radonzerfallsprodukten in der Lunge, Bachelor Thesis, Goethe University, Frankfurt, 2016

* Work is supported by BMBF project funding reference number 02NUK017A

DOI:10.15120/GR-2017-1

Towards the multi-ion treatment planning with ^{16}O beams

O. Sokol[*1], *E. Scifoni*[2], *S. Hild*[2], *M. Durante*[2], *and M. Krämer*[1]

[1]GSI, Helmholtz Centre for Heavy Ion Research, Darmstadt, Germany; [2]TIFPA Trento Institute for Fundamental Physics and Applications, Trento, Italy

It was recently demonstrated theoretically and experimentally [1] that ^{16}O ions might be able to produce lower damage to residual tissue in several cases of hypoxic (with partial oxygen pressure $pO_2 < 21\%$) tumors irradiation. Meanwhile, the cell kill in the normally oxygenated regions ($pO_2 = 21\%$) is expected to be higher due to the increased LET and, consequently, RBE values of ^{16}O. These two statements allow one to expect further dose decrease for the residual tissue when combining light and heavy ion modalities inside one plan, e.g. by forwarding high-LET ^{16}O ions only to the hypoxic parts of the target, while covering the rest with lighter particles (p, ^{4}He).

TRiP-98 multiion

The current 'mainstream' version of GSI in-house treatment planning system TRiP98 allows including several ion modalities inside one plan. Another 'proof-of-concept' version TRiP98-OER [2, 3] accounts for tumor hypoxia by means of kill-painting approach, but only for single-ion fields. In order to test the hypothesis mentioned above, TRiP98 was expanded by merging these two versions.

^{16}O + ^{4}He combined planning

Figure 1 describes the geometry of the test treatment plan. The target of 40×40×60 mm with hypoxic (pO_2 = 0.15%) central region of 28 mm was placed at 80 mm depth inside the 160 mm CT cube. The RBE tables for CHO cells [1] with α/β = 11 were used for the calculations of biological effects with LEM IV. Figure 2 represents the tests of plans optimized for a uniform target survival level of 10%. Three cases were analyzed: single-ion optimizations with opposite ^{4}He or ^{16}O fields, and quadruple-field optimization with two pairs of opposite fields (^{16}O + ^{16}O and ^{4}He + ^{4}He).

Table 1 shows the corresponding survival values in the entrance channel (EC) region at depths of 5 mm (beam entrance) and 45 mm (target border region). For the combined plan ^{16}O + ^{4}He these values are the highest with the same damage to the target. At 5 mm depth the relative increase of EC survival will be 12.1% and 19.6% compared to pure ^{16}O and pure ^{4}He irradiations, accordingly. At a higher depth of 45 mm the difference increases towards 26.8% and 34.6%, accordingly.

Revealing the conditions for the highest benefit from applying this method, and its experimental verification are subjects of further investigation.

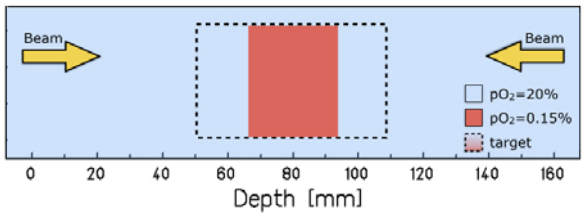

Figure 1: Geometry, oxygenation distribution and fields directions for the test plan. Target borders are marked with a dashed line.

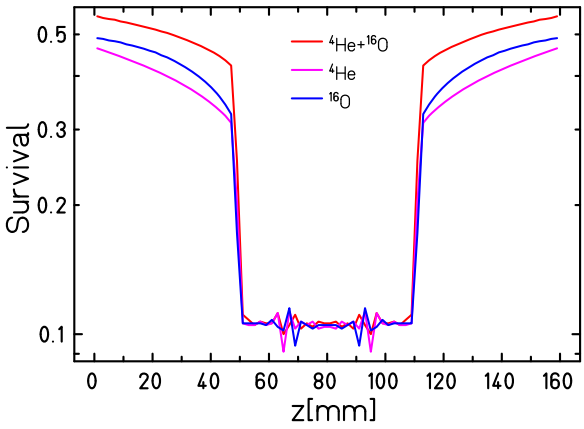

Figure 2: Survival distribution for single-ion double-field optimizations (^{4}He + ^{4}He and ^{16}O + ^{16}O), and multiion quadruple-field optimization (^{16}O + ^{16}O + ^{4}He + ^{4}He).

Depth (mm)	EC survival, %		
	O	He	O+He
5	48.4	45.4	54.3
45	34.3	32.3	43.5

Table 1: Numerical values of EC survival at different depth for three cases of irradiation shown in Figure 2.

References

[1] O. Sokol et al, submitted to Phys. Med. Biol.

[2] Scifoni et al, Including oxygen enhancement ratio in ion beam treatment planning: model implementation and experimental verification, Phys. Med. Biol. 58 (2013)

[3] W. Tinganelli et al, Kill-painting of hypoxic tumours in charged particle therapy, Sci. Rep. 5 (2015).

* o.sokol@gsi.de

Influence of Poly(ADP)ribosylation on radiation-induced chromatin decondensation

A. Heselich[1], L. Pack[1], G. Taucher-Scholz[1,2] and B. Jakob[1]
[1]GSI, Darmstadt, Germany; [2] TU Darmstadt, Darmstadt, Germany

Motivation

Aim of our project is the identification of factors responsible for the observed chromatin changes in proximity of heavy ion induced clustered lesions [1]. First we focussed on Heterochromatin protein 1 (HP1), which showed no significant influence on the condensation and relocation of heterochromatic damages after targeted irradiation of mammalian cells [2]. This finding was in contrast to data published using *Drosophila* cells [3], but goes in line with very recent publications using CRISPR/Cas9-mediated heterochromatic (HC) DNA DSB induction [4]. New publications using UV laser micro-irradiation have recently shown that inhibition of the repair factor PARP1 has a significant influence on chromatin expansion [5]. Since this is a first indication that PARP1, possibly via its PARylation activity, could also play a role in chromatin decompaction at complex damages we started to analyse the effect of PARP inhibition on chromatin decondensation after heavy ion irradiation.

Materials & Methods

Murine fibroblasts (NIH/3T3) or U2OS-NBS1-GFP2 were treated with PARP inhibitor PJ34 prior to DNA damage induction. Inhibitor efficiency was checked via PAR staining after treatment with H_2O_2 as positive control. U2OS-NBS1-GFP2 cells were stained with Hoechst 33342 and irradiated with a 337 nm UV-laser to analyse the influence of PARPi on chromatin expansion and at the same time to check for accumulation of GFP-tagged NBS1 to verify efficient DNA-DSB induction. NIH/3T3 cells were irradiated with Helium ions (76 keV/µm) at the UNILAC accelerator and decondensation of heterochromatin at DNA-DSBs was evaluated 5 min post IR.

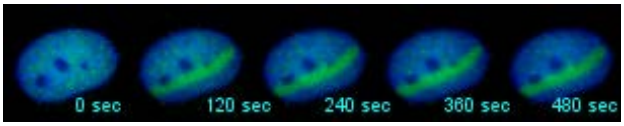

Figure 1: Laser irradiation showed efficient DNA-DSB induction in U2OS-NBS1-GFP2 as verified via NBS1 recruitment (green = NBS1; blue = DNA).

Results

First we verified that PARP1 inhibition was able to influence the chromatin expansion after DNA-DSB induction via laser irradiation under the applied conditions (Fig. 1,2). PARPi treated U2OS showed a reduced chromatin expansion compared to control cells (Fig 2). In preliminary experiments using Helium ion irradiation the vast majority of HC areas traversed by He ions still showed a signature of radiation induced decondensation. We could only find tendency of slightly increased number of chromocenters showing no decondensation at the DNA damage site in PARPi treated NIH/3T3 cells (Fig. 3). This is in contrast to the general inhibition of chromatin opening in the UV-laser experiments using PARP inhibition.

Summary

We could show an influence of PARP1 activity on chromatin decondensation after DSB-induction after UV-laser irradiation, which was hardly visible after ion irradiation. It is possible that different remodelling factors are predominatly used for lesion of different complexity.

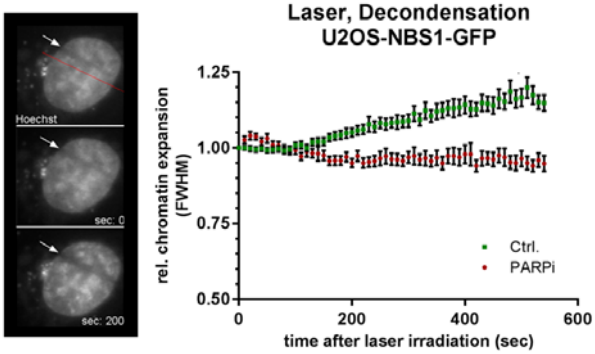

Figure 2: Decondensation measured via chromatin expansion showed an inhibited expansion in U2OS cells treated with PARPi (PJ34, 10µM). Left panel shows an example of chromatin expansion after laser irradiation over time. Right panel represents analysis (FWHM) of relative chromatin expansion (mean±SEM, n ≥45 nuclei).

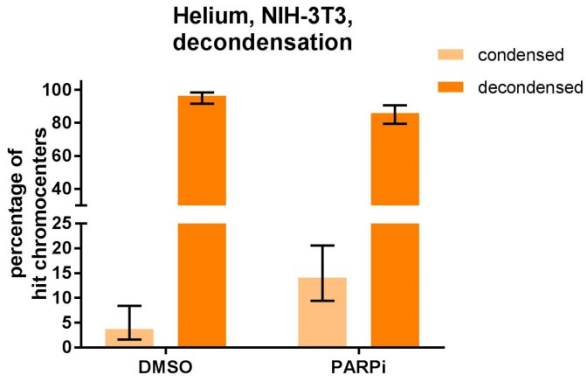

Figure 3: PARPi treated NIH/3T3 cells show a tendency to less decondensed chromocenters (CC) after heavy ion irradiation (He, 76 keV/µm). Data represent percentage of hit CC (n ≥ 135 CC) 5 min post irradiation, error bars represent 95% confidence interval based on binomial distribution.

References

1. Jakob, B., *et al.* NAR **39**, 2011.
2. Heselich, A., *et al.* Scientific Report, 2015.
3. Chiolo, I., *et al.* Cell **144**, 2011.
4. Tsouroula, K., *et al.* Mol Cell **63**, 2016.
5. Strickfaden, H., *et al.* J Biol Chem **291**, 2016.

We thank C. Lukas (University of Copenhagen) for kindly providing the U2OS-NBS1-GFP2- cells.
This work is supported by the German federal ministry of education and research (BMBF). Grant#: 02NUK037A.

DOI:10.15120/GR-2017-1

Measurement of neutron production by high energy protons in space radiation shielding materials

F. Horst[*1,2], *C. Schuy*[1], *M. Rovituso*[3], *M. Giraudo*[4], *K. Zink*[2], *and U.Weber*[1]

[1]GSI, Darmstadt, Germany; [2]THM, Giessen, Germany; [3]TIFPA, Trento, Italy; [4]Thales Alenia Space, Turin, Italy

Introduction

An experiment was carried out at the Trento proton therapy center within the ROSSINI-2 project funded by ESA [1]. The aim of this experiment was to measure and to compare the neutron production by high energy protons in different space radiation shielding materials (LiH, moon concrete, polyethylene, aluminum).

Methods and Materials

Targets of the different materials were irradiated with $228\ \mathrm{MeV}$ protons delivered at high intensities ($100\ \mathrm{nA}$ cyclotron current) with at least 10^{12} protons per measurement. Three passive dosimeters, usually applied for radiation monitoring at GSI [2] were used for the measurements. They consist of a TLD cartridge (two TLD600H chips sensitive to photons and thermal neutrons and two TLD700H chips only sensitive to photons) inside a polyethylene moderator with a lead layer. They were placed at $15\,°$, $65°$ and $90°$ at a distance of $1\ \mathrm{m}$ from the target. A $21 \times 21\ \mathrm{cm}^2$ air-filled parallel plate ionization chamber was used to monitor the proton fluence. After traversing the targets, the protons were stopped within a water beam dump. For every material three different target thicknesses were irradiated. The experimental setup is illustrated in Figure 1.

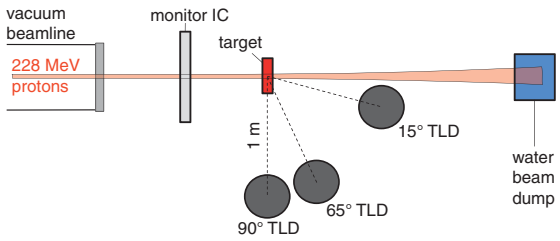

Figure 1: Experimental setup used at the Trento proton therapy center to measure neutron production in different space radiation shielding materials.

All TLDs were individually calibrated beforehand using a $^{137}\mathrm{Cs}$ source for absorbed dose and the conversion factor to neutron ambient dose equivalent was obtained by calibration measurements with an $^{241}\mathrm{AmBe}$ neutron source. The TLDs were readout within 3 days after irradiation using an automated TLD reader (Harshaw 6600 Plus Automated TLD reader) and corrected for background dose using four unirradiated cartridges. The neutron dose originating from the water beam dump (see experimental setup in Figure 1) was measured in a no-target run and was appropriately subtracted from the target-in measurements. The neutron ambient dose equivalent was then calculated by averaging the two TLD-600H readings (neutron + photon dose), subtracting the average of the two TLD-700H readings (only photon dose) per cartridge and applying the conversion factor obtained at the $^{241}\mathrm{AmBe}$ neutron source. The summed relative standard deviation of each averaged dose reading was used as estimated experimental error.

Results

Figure 2 shows exemplary the dataset obtained for the moon concrete targets, in particular the measured neutron ambient dose equivalent $\mathrm{H}^*(10)_n$ in $1\ \mathrm{m}$ as a function of the angle to the beam axis for three different thicknesses. The given neutron dose values are normalized per 10^{12} primary protons striking the target as obtained from the charge reading of the monitor ionization chamber.

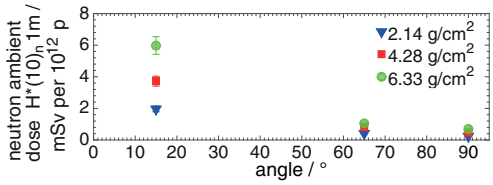

Figure 2: Neutron ambient dose $\mathrm{H}^*(10)_n$ in $1\ \mathrm{m}$ at $15°$, $65°$ and $90°$ generated by $228\ \mathrm{MeV}$ protons in moon concrete measured for three different target thicknesses.

As expected, the generated neutron dose is roughly proportional to the thickness of the irradiated target. The angular dependence shows that there is a forward trend in the emission direction of the neutrons.
Further work will be done to compare the measured neutron production within the different materials together with predictions by different Monte Carlo codes.

References

[1] C. Schuy, M. Rovituso, R. Pleskac, C. La Tessa, M. Durante "The ROSSINI project at GSI", GSI Scientific Report 2013 (2014)

[2] G. Fehrenbacher, F. Gutermuth, E. Kozlova, T. Radon and R. Schuetz "Neutron dose measurements with the GSI ball at high-energy accelerators", Rad. Prot. Dos. 125 (2007)

* f.horst@gsi.de

Commissioning of the MIMOSA28 for radiotherapy application

C.-A. Reidel[1,2], *C. Schuy*[1], *Ch. Finck*[2], *and U. Weber*[1]
[1]GSI, Darmstadt, Germany; [2]IPHC, Strasbourg, France

Introduction

In radiotherapy, monitoring the deposited dose in a patient is a critical issue. MIMOSA28 – also called ULTIMATE – [1] is used for the tracking of charged particles. With a readout of 185.6 μs and a spatial resolution < 5 μm, MIMOSA28 is a good candidate for online monitoring of the Bragg peak. In this case, the sensor would be placed on the side of the target for the detection of the lighter fragments.

Motivations

The sensors will be used in different places for different experiments with different configurations. Therefore it is important to have a setup relatively easy to build up while maintaining a precise and reproducible mechanical alignment in order to do a good track reconstruction.

The setup is composed of five electronic boards. Around 30 cables have to be connected properly between the boards and the sensors. Since the boards and the cables are not on a fixed support, it is easy to have a wrong connection and to damage the sensors. The sensors are placed in a holder which also has to be optimized to avoid unwanted interactions like nuclear fragmentation.

The positioning of the set of sensors (telescope) is an important step to be able to have a precise analysis. Before track reconstruction of the produced fragments in a target, the sensors need to be aligned using an alignment run at low intensity without target. The alignment of the sensors is done to mitigate mechanical inaccuracies and placement mistakes (Fig.1).

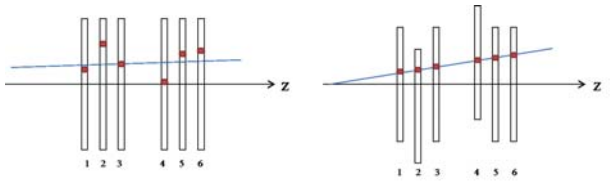

Figure 1: Reconstruction of a track before the alignment (left) and after the alignment procedure (right).

However, the alignment procedure can only be done if the misalignment is smaller than 3° for the rotation for simplifications of the alignment algorithm. It is also important to know the coordinates of the telescope compared to a global system of coordinates. The room where the telescope is placed is then defined as the global system.

Setup optimizations

The first improvement was to build a new holder for the sensor based on an existing design. The main goal of the new holder is to prevent unwanted interactions. Therefore, the holder (made of plastic) has a reduced amount of matter compared to the old design to avoid the interactions between the particle from the beam and the holder which could be detected by the sensor. Moreover, the sensors will be placed on an optical bench to have a good initial position.

Since the setup is intended to be used for different experiments, the optimization of the cabling time needed to be improved. A new box integrating all the 5 boards fixed inside and cabled together has been designed. Around 20 cables are already connected inside the box and the connection to the sensors is relatively fast and easy using feedthrough connectors.

The sensors placed on the optical bench is shown in Figure2.

Figure 2: 6 MIMOSA28 sensors placed the optical bench.

References

[1] Baudot, J. et al., First Test Results Of MIMOSA-26, A Fast CMOS Sensor With Integrated Zero Suppression And Digitized Output.

DOI:10.15120/GR-2017-1

Primary beam attenuation in innovative shielding materials*

C. Schuy[1], F. Horst[1], and U. Weber[1]
[1]GSI, Darmstadt, Germany

Overview

High energetic protons from solar particle events (SPE), HZE ions of the galactic cosmic rays (GCR) as well as trapped particles in the magnetic field of earth pose a serious health risk to astronauts [1]. A possible space radiation mitigation technique is the use of passive shielding [2]. The *ROSSINI2* project (**R**adiati**O**n **S**hielding by I**S**RU and/or **IN**novative mater**I**als for EVA, Vehicle and Habitat) is a common effort of Thales Alenia Space, Trento Institute for Fundamentals Physics Applications, NASA Space Radiation Laboratory, GSI and ESA to select and benchmark the space radiation shielding capabilities of novel materials using ground based accelerator facilities as well as different Monte Carlo codes. The accelerator based experiments include dose attenuation, attenuation of the primary beam, neutron ambient dose as well as cross section measurements.

Experiment

The primary beam attenuation of several materials was tested in Cave A at GSI with 600 MeV/u carbon ions. As shown in Figure 1 the primary beam particles were counted by a 1 mm plastic scintillator before impinging on the target. Surviving carbon ions as well as the produced fragments were monitored by a dE/E telescope consisting of a 5 mm plastic scintillator and a 20 cm long BaF2 crystal scintillator.

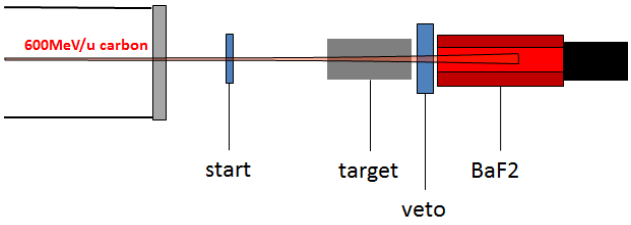

Figure 1: Schematic of the used experimental setup.

After identifying the amount of carbon ions behind the target using correlated 2D scatter plots of the telescope data and correction of the fragmentation introduced by the detectors themselves the resulting number of surviving carbon ions was calculated. Offline data analysis was performed using the ROOT data analysis framework.

Preliminary results

First preliminary results for sintered moon substitute [3] are presented exemplary in Figure 2. As expected the surviving fraction of primary beam particles is decreasing for increasing target thickness resulting in a more complex radiation field due to nuclear fragmentation. A precise knowledge of the composition of this target dependent complex radiation field is essential for space radiation risk assessment. It is important to note that the experimental error is largely dominated by the uncertainties related to the areal density of the different target thicknesses.

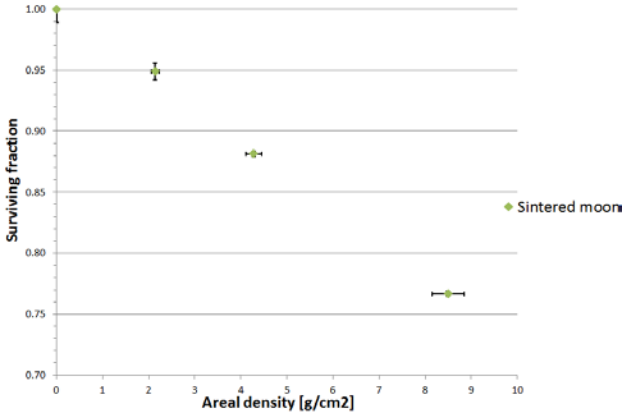

Figure 2: Preliminary results for the surviving fraction of 600MeV/u carbon ions impinging on different thicknesses of sintered moon substitute.

Status and outlook

All datasets of the different ROSSINI2 measurement campaigns are currently analyzed and compared to the widely used Monte Carlo codes PHITS and Geant4. Final results for a wide variety of different materials and beams are expected for later this year.

References

[1] M. Durante and F. A. Cucinotta, “Physical basis of radiation protection in space travel”, Rev. Mod. Phys (2011).
[2] M. Durante, “Physical and biomedical countermeasures for space radiation risk”, Z. Med. Phys (2008).
[3] Giovanni Cesaretti, et al., “Building components for an outpost on the Lunar soil by means of a novel 3D printing technology”, Acta Astronautica (2014).

* Work supported by ESA(Contr. No. 4000112525/14/NL/LF) and NASA.

Differentiation of (pre)adipocytes following irradiation*

K. Shreder[1], V. Rzeznik[1], P. Fischer-Posovszky[2], M. Wabitsch[2], C. Fournier[1]

[1] Helmholtzzentrum für Schwerionenforschung GSI, Darmstadt, [2] Universitätsklinik für Kinder- und Jugendmedizin, Sektion Pädiatrische Endokrinologie und Diabetologie, Ulm

Introduction

Rheumatoid arthritis (RA) is a chronic inflammatory disease, which affects the joints. RA patients are treated primarily with drugs, but also ionizing radiation is used. The patients are exposed either locally to low doses of photons or to Radon. Adipocytes, the dominant cell type of adipose tissue, are known to support inflammatory processes and cartilage degradation in RA by release of different cytokines and adipokines [1]. As there are no data available about the radiation response of adipocytes, we investigated in this study the effect of X-ray irradiation on the differentiation process of human (pre)adipocytes.

Materials and methods

SGBS cells were derived from subcutaneous fat of a patient with Simpson-Golabi-Behmel syndrome [2]. The cells were grown in the DMEM/F12 medium, containing 10% FCS until reaching confluence. Adipogenic differentiation was induced by addition of a defined adipogenic cocktail, including insulin and rosiglitazone. Mature adipocytes were identified by Oil Red O staining. Irradiation was performed with X-rays (1Gy/min). Gene expression was analyzed using real-time PCR.

Results and discussion

Proliferation of SGBS pre-adipocytes after X-ray irradiation

In order to assess the radiation response of pre-adipocytes, the cells were irradiated with 0.5 and 2 Gy, and the proliferation capacity was monitored over 21 days. The cell numbers of irradiated SGBS-pre-adipocytes were dose-dependently reduced (Fig. 1), which was detectable from day 12 on.

Effect of X-ray irradiation on the expression of differentiation markers

To investigate the impact of X-ray irradiation on the differentiation process of adipocytes, SGBS pre-adipocytes were irradiated with 0.5 and 2 Gy and the differentiation was initiated. Gene expression analysis of important adipogenic transcription factors PPARγ (Fig. 2) and C/EBPα (Fig. 3) revealed only slight trends towards reduced expression levels.

Our results demonstrate radiation-induced changes in the proliferation capacity of SGBS pre-adipocytes, but based on the expression of crucial adipogenic genes (PPARγ and C/EBPα) this is not accompanied by changes in differentiation.

Our data is in agreement with Nicolay et al, who showed that the expression of adipogenic genes in mesenchymal stem cells (adipocyte precursor cells) after irradiation remained unchanged [3].

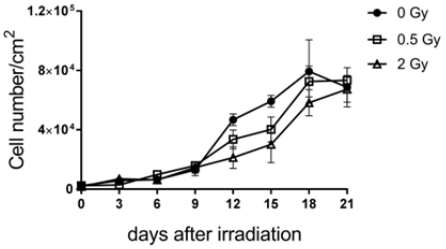

Figure 1: Proliferation of SGBS pre-adipocytes after X-ray irradiation, Mean±SEM, N=3

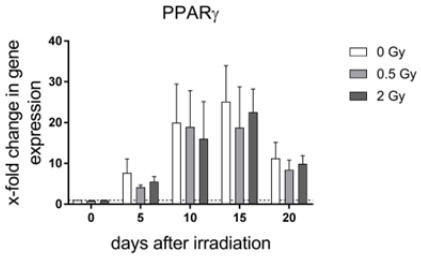

Figure 2: Gene expression of PPARγ in SGBS adipocytes following X-ray irradiation, Mean±SEM, N=3

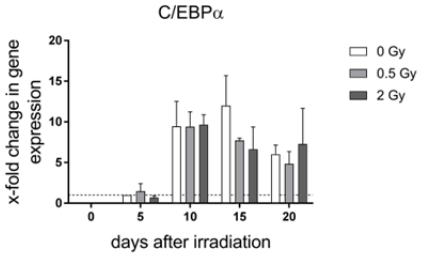

Figure 3: Gene expression of C/EBPα in SGBS-adipocytes following X-ray irradiation, Mean±SEM, N=3

References

[1] S. Vielma et al, Int. Immunopharmacol. 2013 Jun, 16(2): 224-231
[2] M. Wabitsch et al, Int. J. Obes. 2001, 25: 8-15
[3] N. Nicolay et al, Oncotarget 2014 Dec

*Work supported by BMBF (02NUK017A GREWIS)

DOI:10.15120/GR-2017-1

Low-dose irradiation reduces inflammatory reactions in endothelial cells*

Felicitas Rapp[1], Nadine Erbeldinger[1], Stephanie Hehlgans[3], Svetlana Ktitareva[1], Bianca Bertulat[2], M. Cristina Cardoso[2], Franz Rödel[3], Claudia Fournier[1]

[1]GSI, Biophysik; [2] Fachbereich Biologie, Zellbiologie und Epigenetik, TU Darmstadt; [3]Klinik für Strahlentherapie und Onkologie, Molekulare Strahlenbiologie, Goethe-Universität Frankfurt

Introduction

Patients with chronic inflammatory diseases can be treated with low doses of irradiation, either with classic X-rays or α-particles from Radon-containing water or air. Treatment leads to pain relief and anti-inflammatory effects [1, 2]. During inflammation, stimulation with cytokines (e.g. TNF-α) or irradiation, endothelial cells (EC) regulate expression of surface molecules. This fosters adhesion of peripheral blood lymphocytes (PBL), followed by transmigration through the blood vessel wall into injured tissue [3]. We have previously shown that PBL adhesion to EC is decreased after low dose exposure under laminar shear stress (blood flow) conditions, and have started to elucidate underlying mechanisms like ROS (reactive oxygen species) production and NF-κB signaling.

Methods

PBL adhesion was measured as described before [4, 5]. The production of ROS was measured in endothelial hybridoma cells (Ea.hy926) as well as primary human microvascular cells (HMVEC) via flow cytometry using an intracellular dye [1]. NF-κB translocation as an indicator for induction of gene expression was measured in Ea.hy926 and HMVEC by a high-content/high-throughput imaging routine (Operetta) 1 or 24 h after addition of TNF-α and/or photon irradiation [4, 5].

Results

Decreased PBL adhesion after low LET He-ion irradiation (76 keV/µm), comparable to α-particles, could be verified in two experiments (Fig. 1). Under laminar conditions resembling blood flow (B), this effect was more pronounced as compared to static conditions (A).

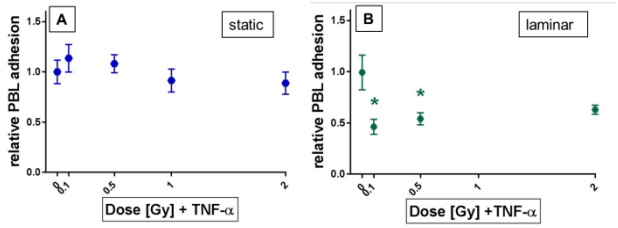

Fig. 1: Reduced adhesion of PBL to HMVEC under static (A) and laminar (B) conditions after low doses of He ions (89 keV/µm, 0.1 and 0.5 Gy, 24h). Laminar culture conditions seem to enhance the anti-inflammatory effect of low dose irradiation. Results are mean ± SEM; N=2, n=6; * p= 0.05 vs. 0Gy+TNF- α

ROS production in Ea.hy926 as wells as HMVEC follows a non-linear dose-response relationship after low doses of He-ions (Fig. 2), while the hybridoma cells show a stronger reaction than primary cells.

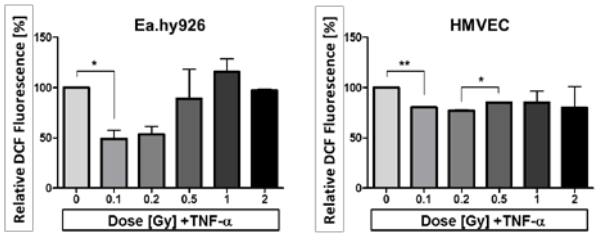

Fig. 2: Ea.hy926 or HMVEC cells were cultivated under static conditions, irradiated with He- ions (76 keV/µm) and analyzed for intracellular ROS production by flow cytometry 24 h later. ROS production is decreased at 0.1 Gy. Results are mean ± SEM; N=2, n=6; *$P < 0.05$; ** $P < 0.01$.

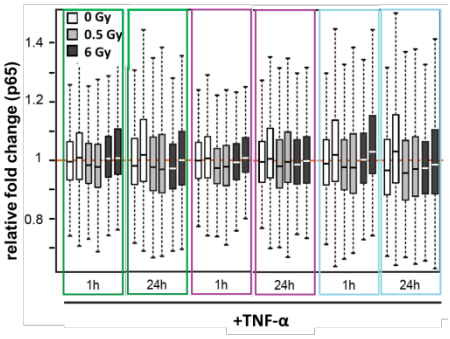

Fig. 3: Nuclear translocation of NF-κB subunit p65 after static cultivation of HMVEC, X-irradiation and TNF-α stimulation. N=1, n=3, median ± SEM.

NF-κB p65 nuclear translocation under static conditions is enhanced in the presence of TNF-α, but not further modified by low dose exposure (Fig. 3; [4]).

Discussion

We showed previously that low doses of photons reduced TNF-α- induced PBL adhesion to Ea.hy926 [1]. Here, we used low LET He-ion irradiation on primary HMVEC to mimic Radon treatment. Choosing more physiological culture conditions (Fig. 1 B) resulted in a stronger decrease of PBL adhesion to primary cells. The underlying mechanism of adhesion molecule expression is regulated by components of the antioxidative system. ROS production after He-ion exposure also showed a non-linear dose-response relationship (Fig. 2, [1]). Investigations on the respective impact of He-ion exposure, as well as on the activation of adhesion molecules, are under work.

References

[1] Large M et al., (2015) Strahlenther Onkol. 191(9):742-9.
[2] Rühle PF et al., (2017) Autoimmunity. 50(2):133-140.
[3] Schnoor et al., (2015) Mediators Inflamm. 2015:946509.
[4] Erbeldinger et al., GSI report 2015
[5] Erbeldinger et al., (2017) Front. Immunol. 8:627. (in press)

*Financed by BMBF (GREWIS 02NUK017A and 02NUK17D), DFG (GRK 1657) and HGS-HIRe
DOI:10.15120/GR-2017-1

RNF138 stimulates DNA-end resection upon heavy-ion-irradiation in human G1-phase cells

C. Barent[1,2], L. Niederreiter[1,3], L. Pack[1], A. Heselich[1], B. Jakob[1], G. Taucher-Scholz[1,2], and N. B. Averbeck[1]

[1]GSI Helmholtzzentrum für Schwerionenforschung, Darmstadt, Germany; [2]Technische Universität Darmstadt, Germany; [3]Hochschule Darmstadt University of Applied Sciences, Germany

Cells have evolved multiple DNA repair pathways to preserve genome integrity when damage arises. The most serious form of DNA damage are double-strand breaks (DSBs). Among other factors the repair pathway choice is influenced by the complexity of the break as well as the cell-cycle phase. Simple DSBs are repaired resection dependent only in the S/G2 cell-cycle phase, whereas at complex DSBs resection dependent repair occurs also in G1-phase cells [1]. It was recently shown that the ubiquitin ligase RNF138 is required for DNA-end resection in S/G2 phase in the context of RNF138-dependent Ku removal from DSBs [2]. Moreover, the ubiquitination of the resection factor CtIP by RNF138 is essential for the recruitment of CtIP to DSB sites [3]. Hence, we investigate whether RNF138 is required for resection in G1-phase cells upon induction of complex DSBs as well.

To study a possible function of RNF138 in G1 phase, it is required to be expressed in this phase. Hence, we applied the Hela.S-Fucci cell system to evaluate the RNF138-expression level in G1-phase cells in comparison to S/G2-phase cells. The Hela.S-Fucci system allows to easily distinguish and separate G1- (red) and S/G2/M-cells (green) [4] (Fig. 1 A, B, D). Protein expression studies of RNF138 showed no difference between the indicated cell cycle phases (Fig. 1 C).

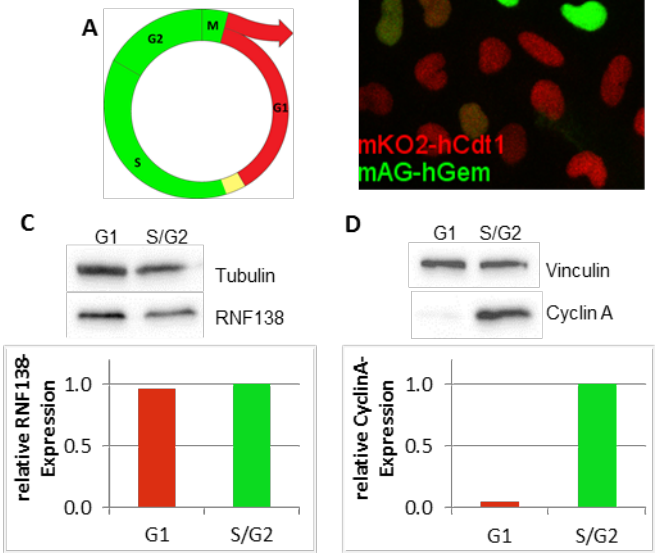

Figure 1: Hela.S-Fucci cells express RNF138 in G1- and in G2-phase cells. (A) In the Hela.S-Fucci system individual G1-phase nuclei are labelled in red and S/G2/M-phase nuclei in green. **(B)** Typical fluorescence image of HeLa.S-Fucci cells expressing mKO2-hCdt1 and mAG-hGeminin in G1 and S/G2/M-phase, respectively. **(C)** Expression of RNF138 in G1 and S/G2 HeLa.S-Fucci cells isolated via a flow cytometric sort. **(D)** The correct sorting was verified by the expression of the S/G2-marker Cyclin A. Tubulin and Vinculin served as a loading control, respectively. The quantitative evaluation was carried out with the ImageJ software. The Hela.S-Fucci cell line was kindly provided by the RIKEN BRC through Atsushi Miyawaki (RIKEN Brain Science Institute, 2-1 Hirosawa, Wako, Saitama 351-0198, Japan).

In addition, human cells depleted for RNF138 by RNAi were irradiated with carbon ions to investigate the recruitment of the resection marker RPA to DSBs. The decreased fraction of Rad51-positive cells upon irradiation (data not shown) proved the successful RNF138 knockdown. RNF138 depleted cells showed less RPA-positive cells regardless of the cell cycle phase (Fig. 2). These data suggest that RNF138 stimulates resection of complex, ion-induced DSBs in G1-phase cells. Future experiments will characterise the role of RNF138 in the repair of ion-induced DSBs in human G1-phase cells.

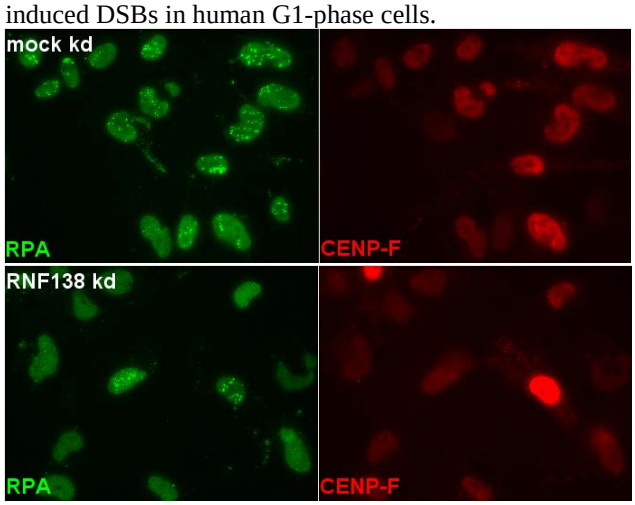

Figure 2: Depletion of RNF138 decreases the fraction of resection positive cells regardless of the cell cycle phase. Human, immortalized fibroblasts (NFFhTERT cells) depleted for RNF138 (RNF138 kd) or mock depleted (mock kd) were irradiated angular with carbon ions (6,5 MeV/u, LET: 325 keV/µm). In RNF138 depleted cells the fraction of RPA-positive cells was reduced 1 h post irradiation, regardless of the cell cycle phase. CENP-F served as a cell cycle marker (G1: CENPF-negative; S/G2: CENP-F-positive).

References

[1] Averbeck, N. B. et al. (2014). Cell Cycle **13**: 2509-2516
[2] Ismail, I. H. et al. (2015). Nat Cell Biol **17**: 1446-1457
[3] Schmidt, C. K. et al. (2015). " Nat Cell Biol **17**: 1458-1470.
[4] Sakaue-Sawano, A. et al. (2008). Cell **132**: 487-498.

* This work is supported by the DFG GRK1657 and the German federal ministry of education and research (BMBF), Grant # 02NUK037A.

DOI:10.15120/GR-2017-1

Impact of the lateral dose profiles on scanned dose distribution in particle therapy

M. Rovituso[*1,2], *C. Schuy*[1], *S. Brons*[3], *and U. Weber*[1]
[1]GSI, Darmstadt, Germany; [2]TIFPA, Trento, Italy; [3]HIT, Heidelberg, Germany

The delivery of the prescribed dose to the tumor volume is, often, realized by active techniques which consist in scanning the tumor volume slice-by-slice, with a narrow pencil beam over a matrix of single positions (raster points). The complex task to delivery an uniform dose to the tumor volume is performed by the Treatment Planning System (TPS), which needs detailed information on the beam energy, symmetry and size. The beam profile has to be parametrize with certain function in the TPS in order to be able to reproduce the core of the distirbution given by multiple Coulomb scattering and the halo given by the nuclear interaction of the beam projectile with the target nuclei. Recently a great effort is devoted to enhance the accuracy of the parametrization inside the TPS in order to better describe the contribution of the nuclear interactions in the halo region [1, 2].

This work wants to show the impact of the lateral beam shape in a scanned field. Therefore, measurements of radial dose distribution of a scattered protons and Helium beams have been performed at the Heidelberg Ion Therapy (HIT) center. The used experimental setup is explained in [2].

The data obtained for proton and ^{4}He beam at 200 MeV/u impinging on 13.96 cm H_2O have been fitted with a simple gaussian and a double Gaussian + exponential function. The result for the proton case is shown in Fig.1.

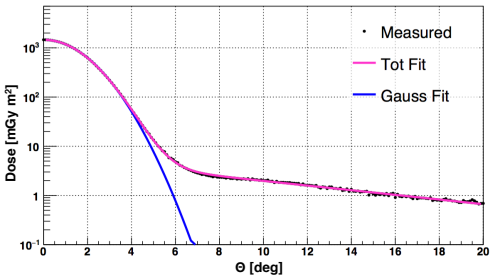

Figure 1: Fit of the radial dose distribution of 200 MeV/u proton beams impinging on 13.96 cm H_2O.

In order to quantify the effect of the parametrization on a scanned field, a 2D dose distribution was built by superimposing the beam projection distribution and shifting the beam spot in steps of 2.5 mm in x- and y-direction inside a square (target volume) size of 100x100 mm^2 and in a smaller square of 60x60 mm^2. This provides a simplified estimation for a real scanning procedure in therapy, allowing a qualitatively description of the contribution of dose transported outside the target volume due to the tail of the radial dose distribution. The results are shown in Fig.2. In order to be able to compare the Gaussian and the measured dose profile, the beam spots were superimposed with the same constant weights. It can be observed in Fig.2(a) and (c) how the effect of a single Gaussian approach affects the border of the distribution, being more pronounced for the helium dose distribution (Fig.2(a)) than for the proton one. By decreasing the target volume (Fig.2(b) and (d))the effect increases also in the plateau of the distribution, reducing significantly the dose accuracy in the target volume.

Even though the dose fall off at the border of the dose distribution for the proton beam is larger compared to ^{4}He ions, the tail contribution due to secondary fragments is higher [3], demonstrating how important is a correct parametrization of the lateral beam profile in the TPS beam models.

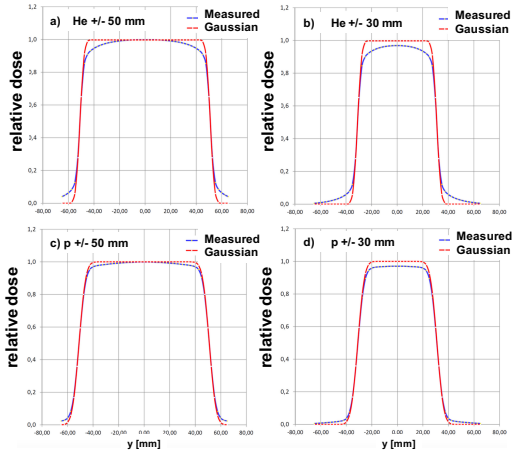

Figure 2: Dose profile through the mid plane of the scanned dose distribution for 200 MeV/u ^{4}He and proton beams.

References

[1] V.E. Bellinzona et al., "On the parametrization of lateral dose profiles in proton radiation therapy", Phys Medica, vol.31,pp.484-492, February 2015

[2] M. Rovituso et al , "Lateral scattering of 120 and 200 MeV/u ^4He ions in water", GSI Annual Report, APPA-HEALTH-36, 2016 (2013) 56

[3] M. Rovituso et al. , "Fragmentation of 120 and 200 MeV/u ^4He ions in water and PMMA targets ", Phys. Med. Biol., 62, 2017

* Work supported by HGS-HIRe

Effective cell killing following spread-out Bragg peak Carbon-ion irradiation despite efficient DNA double-strand-break rejoining

N.B. Averbeck[1], J. Topsch[2], M. Scholz[1], W. Kraft-Weyrather[1], B. Jakob[1], G. Becker[1], G. Taucher-Scholz[1,3]

[1]GSI Helmholtzzentrum für Schwerionenforschung, Darmstadt, Germany; [2]IZKS, Universitätsmedizin der Johannes-Gutenberg-Universität, Mainz, Germany, [3]TUD, Darmstadt, Germany

Radiotherapy of solid tumours aims at destructing the cancer while sparing healthy tissue. On the molecular level, DNA damage and in particular DNA double-strand breaks (DSBs) represent a crucial factor of cell killing and thus radiation effectiveness. In order to study the DSB-repair capacity and cell survival in tumour compared to healthy tissue under radiotherapy conditions with Carbon ions, we developed an irradiation setup that mimics a two-field configuration typical for patient irradiation (Fig. 1). Positions close to the beam entrance ("entrance channel", EC) represent those of healthy tissue in tumour therapy; those in the spread-out Bragg peak (SOBP) represent the tumour. Cells in the EC are exposed to a relative homogenous radiation field of high-energy ions, cells in the SOBP are exposed to a wide spectrum of Carbon ions with different individual energies and LET. Hence, DNA damage in the EC is rather simple, while damage in the SOPB ranges from simple to complex lesions.

We analysed the clonogenic cell survival and DSB repair at the EC and SOBP. Clonogenic survival is clearly lower in the SOBP compared to the EC (Fig. 2, bottom, circles). This data agrees well with the calculated survival from the local effect model (LEM) [1] (Fig. 2, bottom, line).

DSB-repair was analysed by measuring the immunofluorescence signal of the DSB marker γH2AX at different time points after irradiation by flow cytometry. Upon 2 Gy irradiation, DSBs were rejoined efficiently (Fig. 3).

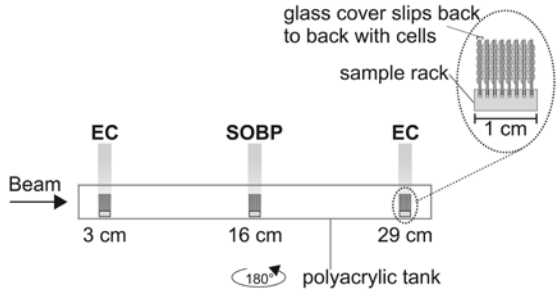

Figure 1[#]: Experimental setup for a two-field irradiation that mimics therapy-like carbon-ion irradiation. Confluent, human fibroblasts (AG1522D) were exposed at different positions from the beam entrance side within a medium filled tank at the SIS, GSI Darmstadt. To simulate a two-field configuration, the tank was irradiated with a horizontal turn of 180°. The irradiation was done with an SOBP of 2.4 cm at a water equivalent depth of 16 cm. The dose in the SOBP was 2 Gy (dose-averaged LET: 70 – 85 keV/µm), typical for a therapeutic fraction. Samples in the EC region were irradiated with a corresponding dose of 0.6 Gy (dose-averaged LET: 13 keV/ µm; see Fig. 2, top).

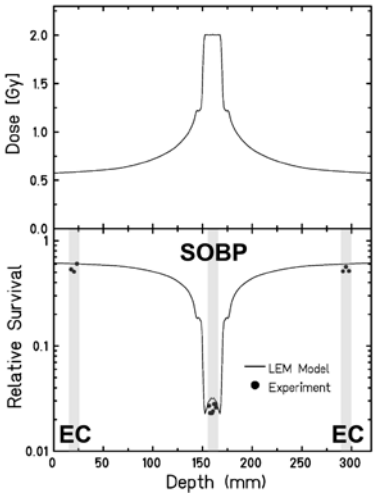

Figure 2[#]: Dose distribution and cell survival upon therapy-like irradiation as in Fig. 1. Top: Distribution of the absorbed dose. Bottom: Corresponding calculated (line; LEM) and measured (circles; n=1) cell survival. Grey boxes: position of the samples during irradiation.

The γH2AX signal declined almost to control values within 48 h in the EC and SOBP despite the increased fraction of complex lesions in the latter. Only, in the SOBP the process was slower within 24 h after irradiation. Since the lesions in the SOBP are well rejoined and yet seem to cause low survival, we assume that misrepair plays a non-negligible role in the increased cell killing in the SOBP.

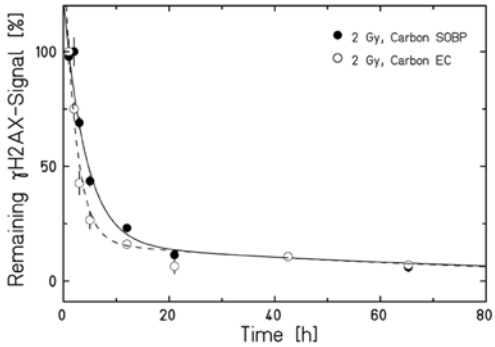

Figure 3*: Comparison of the DSB-repair capacity in human fibroblasts after 2 Gy carbon-ion irradiation in the EC or SOBP (for irradiation conditions see Fig. 1A). The global immunofluorescent γH2AX-signal was analysed by flow cytometry as described earlier [2].

References

[1] T. Elsässer *et al.*, Int J Radiat Oncol Biol Phys (2010) 78: 1177 - 1183

[2] F. Tommasino *et al.*, PLoS One (2015) 10 (6): e0129416

[3] N. Averbeck *et al.*, Front. Oncol. (2016) 6: 28

#modified version of Fig. 2 in [3]; *modified version of Fig. 3 in [3]

DOI:10.15120/GR-2017-1

Changes in cellular organization leading to the interruption of conductivity in a pig model after exposure to high doses of carbon ions

N. Erbeldinger[1,4]; P. Simoniello[1,6]; F. Rapp[1]; H. I. Lehmann[2]; P. Lugenbiel[3]; A. Eichhorn[1]; D. Thomas[3]; D. L. Packer[2]; M. Durante[5]; C. Graeff[1] and C. Fournier[1]

[1]GSI, Darmstadt, Germany; [2]Mayo Clinic/St. Marys Hospital, Rochester, MN, USA; [3]Heidelberg University Hospital, Heidelberg, Germany; [4]Darmstadt University of Technology, Darmstadt, Germany; [5]TIFPA Trento Institute for Fundamentals Physics Applications, Trento, Italy; [6]University of Naples Parthenope, Naples, Italy

Introduction

The increasing age of the population of developed countries entails higher prevalence of cardiac arrhythmias (CA). Most common CA is atrial fibrillation and ventricular tachycardia[1,2]. The first line of treatment of CA is mainly based on anti-arrhythmic and anti-coagulant medication[3]. If CA still occurs frequently, the established therapy is a minimally-invasive catheter ablation[3]. However, the efficiency of this treatment is often limited (60-75%) and comprises risks for unfavorable complications[3].

These circumstances motivated investigations on a non-invasive alternative treatment[4]. As carbon ion irradiation is well-established in cancer therapy, its benefits were exploited for this approach. First macroscopic examinations revealed scar formation in target areas in parallel to morphologically unaltered myocardium.

Based on these results, the organization of irradiated myocardium, elicited by scanned carbon ions, were investigated as cause for electrophysiological changes.

Material and Methods

The long-term effects of high dosed carbon ion irradiation on cardiac substructures were investigated in a porcine model. For this approach, targets were irradiated with single doses of 25 - 55 Gy. Follow up studies on manifold changes were performed up to six months after irradiation. For histological analyzes, tissue biopsies were obtained three and six months after irradiation during final follow-ups.

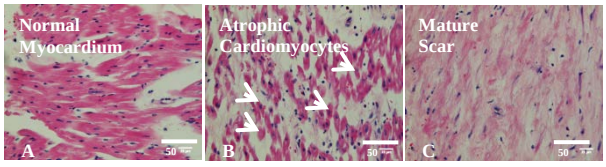

Figure 1: Different stages of cardiac fibrosis in target areas until at least 6 months after irradiation. Target areas from sham (A) and 40 Gy irradiated pigs (B, C) were stained with H&E three and six months after irradiation. Modified after[5].

Work is financed by GRK 1657 and BMBF (GREWIS, 02NUK017A)

Results

Several stages of tissue remodeling occurred in parallel in target areas. A replacement of cardiomyocytes with fibrotic tissue was observed three and six months after irradiation (Figure 1) indicating ongoing tissue remodeling. Furthermore, surviving cardiomyocytes in target areas displayed structural abnormalities. One example for those abnormalities was vacuolization (Figure 2B), which is presumably related to cell death[6]. Moreover, the distribution of the structural protein troponin the cytoplasm was inhomogeneous, indicating an altered structure of the cytoskeleton (Figure 2C, D).

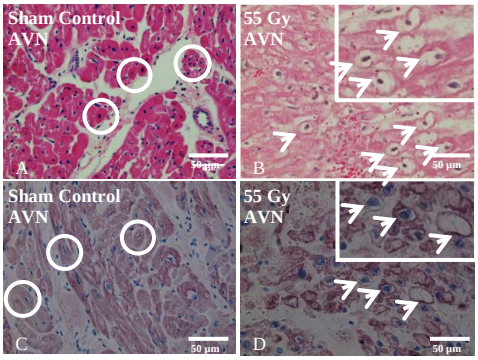

Figure 2: Vacuolization of cardiomyocytes is related to an abnormal distribution of the cytoskeleton. AVN target areas from sham (A, C) and 40 Gy irradiated pigs (B, D) were stained with H&E (A, B) and for troponin (C, D) six months after irradiation. Healthy cardiomyocytes (circles) and their vacuolization (arrows) is indicated.

Discussion

The structural abnormalities (vacuolization and distribution of troponin) of surviving cardiomyocytes point might be related to cell death during ongoing fibrosis, at late time points. In addition, cardiac fibrosis is known to cause changed electrophysiological signaling as observed in the irradiated animals. Both tissue responses (cell death and fibrosis) might underlie these changes.

References

1 Verdino J Saudi Heart Assoc. 2015 Jan; 27(1): 44–49.
2 Grant et al. Clin Geriatr Med. 2012 November ; 28(4): 539–553.
3 Cappato, Circ Arrhythm Electrophysiol. 2010 Feb;3(1):32-8.
4 Lehmann et al, Sci Rep. 2016 Dec 20;6:38895.
5 Erbeldinger, doctoral dissertation, submitted 2017
6 Vigliano et al,, J Am Coll Cardiol. 2011 Apr 5;57(14):1523-31.

TRAX-CHEM*

D. Boscolo†[1], *E. Scifoni*[2], *M. Krämer*[1], *and M. Durante*[2]
[1]GSI, Darmstadt, Germany; [2]TIFPA, Trento Italy

Although it is well known that the indirect effect of radiation plays a very important role on the radiation effect on biological systems and many dosimetrical technique are based on the detection of chemical reactions with radiation induced free radicals, still little is known on water radiolysis and on radicals diffusion and reaction along a particle track. For this reasons in the last two years the particle track structure code TRAX [1] has been extended to the pre-chemical and chemical stage of radiation damage [3][4]. It is now possible to use this extension of the code in order to simulate the time-dependent yields of the most important products of water radiolysis e^-_{aq}, $\cdot OH$, $H^{\cdot}$, H_3O^+, H_2, OH^- and H_2O_2 for different ion radiation and different energies. In Figure 1 the computed time dependent G-values for different radical species generated by a 750keV electron are compared with experimental data.

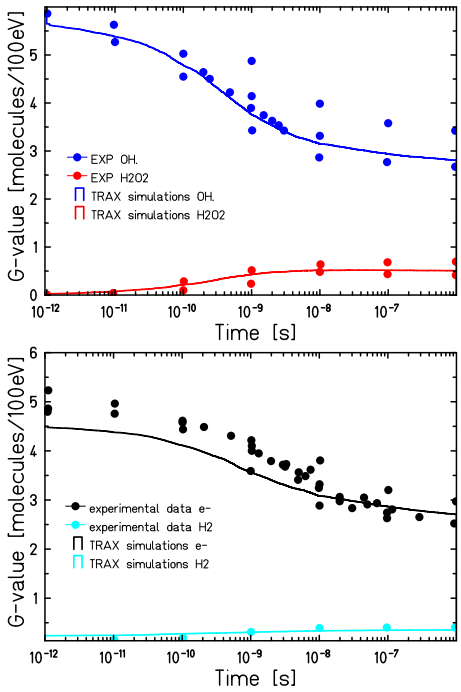

Figure 1: Time-dependent radiolytic yields for 750keV electron in a water cube of 5 μm side for the species $\cdot OH$ and H_2O_2(top panel) and e^-_{aq} and H_2 (bottom panel). Experimental data from [2].

With the increase of the LET the particle track becomes more dense increasing the probability or radical recombination. This will lead to a decrease of the G-values of radical species generated immediately after the water dissociation, such as $\cdot OH$ and e^-_{aq} and to an increase of the radical generated by the interaction of the former ones, such as H_2O_2 and H_2. A comparison of the LET dependent G-values at the end of the chemical stage with experimental data is shown in Figure 2 for different radical species. The OH radical yield depending on both time and LET seems to be in very good agreement with the experimental data while for the other radicals some refinements are still required especially to predict their yield for high LET radiation.

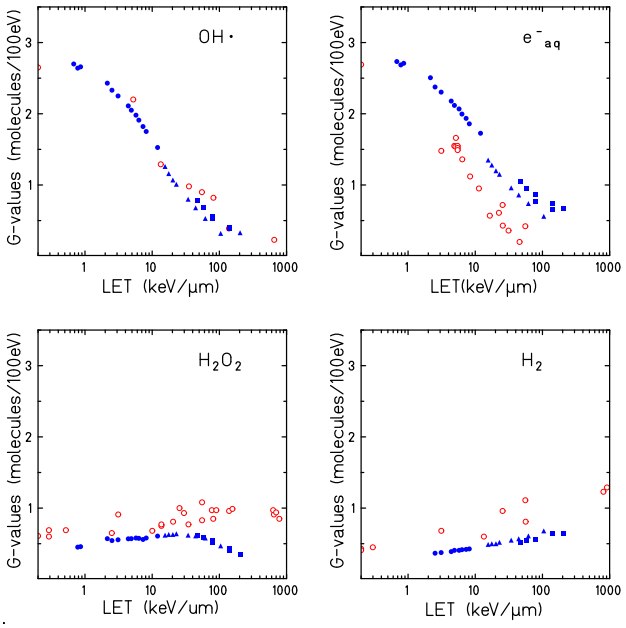

Figure 2: LET dependence of G values in pure water for the species $\cdot OH$(top left) , e^-_{aq} (top right), H_2O_2(bottom left) H_2 (bottom right). Solid blue symbols :TRAX simulations (circle 1H, triangle 4He, square 12C). Open red circles: collection of experimental data from [2]

References

[1] C.Wälzlein et al., Phys. Med. Biol. ,59:1441-1458(2014).
[2] M.S.Kreipl et al., Radiat. Environ. Biophys. ,48:11-20(2009).
[3] D.Boscolo, et al. "Chemical stage implementation in TRAX", GSI Scientific Report 2015 (2016)
[4] M.Bolsa, et al. Chapter in book: "Nanoscale Insights into Ion-Beam Cancer Therapy", pp.379-434, (2017)

*The research leading to these results has received funding from the European Union Seventh Framework Programme [PEOPLE 2013 ITN-ARGENT project] under grant agreement n [608163].
† d.boscolo@gsi.de

DOI:10.15120/GR-2017-1

Advanced IMPT algorithm for multiple targets of late stage lung cancer

K. Anderle[1], *J. Stroom*[2], *S. Viera*[2], *N. Pimentel*[2], *C. Greco*[2], *M. Durante*[3] and *C. Graeff*[1]
[1]GSI, Darmstadt, Germany; [2]Champalimaud Centre for the Unknown, Lisbon, Portugal; [3]TIFPA, INFN, University of Trento, Povo (TN), Italy;

Introduction

Patients with late stage lung cancer have extremely poor prognosis, with median survival rate less than a year, therefore new treatments are warranted. Recent studies have shown promising results with stereotactic body radiation treatment (SBRT) for such patient patients [1], however patients still exhibit several radiation-induced side effects.

With better physical properties for radiotherapy, intensity modulated particle therapy (IMPT) could better spare normal tissue. However, creating a treatment plan for moving tumours in complex geometries is challenging, due to range changes and interplay effects.

To address these challenges, an algorithm was developed to create IMPT treatment plans for late stage lung cancer patients. To asses the developed algorithm, the generated plans were compared to SBRT ones, which were used in an actual treatment.

Materials and Methods

Our algorithm was implemented in the GSI's treatment planning software, TRiP98 [2]. Firstly, modifications were made to the raster point setup, where previously only one target was supported. Raster point setup was expanded in a way that every field is designated to a specific target. Raster points for each field are created only around the designated target. Afterwards optimization takes into account contributions from all fields. The opti mization function was adapted so that strict stereotactic treatment planning objective could be respected.

By optimizing over all motion states, range changes are already included [3]. Rescanning was used to address interplay changes. After successful optimization, a time-resolved (4D) dose was calculated, to quantify motion effect on the treatment. Furthermore, dose was calculated on 4 different motion variations to estimate plan robustness.

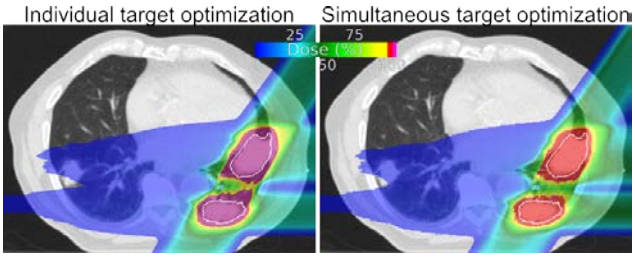

Figure 1 - Comparision between individual and simultaneous target optimization.

To test the algorithm, IMPT treatment plans for 8 patients with 24 lesions in total were generated. Patients were actually treated with SBRT at Champalimaud Center for the Unknown, Lisbon, Portugal. Intended dose regimen for SBRT was 24 Gy in 1 fraction, but lower fractionated doses had to be delivered in 3 cases due to OAR constraints. Besides adopting the fractionation regimes for IMPT, additional dose escalation of 1x24Gy was explored for these 3 cases.

Results

A comparison between IMPT and SBRT treatment plans for two patients is shown on Figure 2. Patient 2 has no critical OARs in close vicinity to the target and both modalities deliver the same dose to 5 targets. IMPT for Patient 5 has poorer target coverage for two targets close to the heart. Both patients receive less integral dose in the whole body with IMPT.

Overall, there was no significant difference in target coverage between SBRT and IMPT. However, the IMPT on averaged deposited 44% and 70% less dose to OARs for maximum point dose and dose to critical volume, respectively.

A dose escalation was possible for one patient with large overall target volume, where an IMPT plan of single fraction could be created and SBRT was limited due to high heart dose. This shows the potential of IMPT for late stage lunge cancer patient.

Conclusions

An advanced optimization algorithm was developed and used to achieve superior IMPT treatment plans for late stage lung cancer patients. Furthermore, IMPT could be used in a single fraction regime for some patients, where SBRT was limited.

References

[1] Iyengar P, et al: Phase II Trial of Stereotactic Body Radiation Therapy Combined With Erlotinib for Patients With Limited but Progressive Metastatic Non–Small-Cell Lung Cancer. Journal of Clinical Oncology 32, 2014
[2] Krämer M, et al: Treatment planning for heavy-ion radiotherapy: calculation and optimization of biologically effective dose. Physics in Medicine and Biology 45, 2000
[3] Graeff C, et al: Motion mitigation in intensity modulated particle therapy by internal target volumes covering range changes. Med. Phys 39, 2012

DOI:10.15120/GR-2017-1

Ionizing radiation alters signalling pathways affecting the maintenance and endodermal differentiation of embryonic stem cells.*

S. Luft[1], O. Arrizabalaga[1], Ireen Kulish[1,2], E. Nasonova[1,3], M. Durante[4], S. Ritter[1], I. Schroeder[1,#]

[1]GSI, Darmstadt, Germany; [2]Technical University Darmstadt, Darmstadt, Germany; [3]Laboratory of Radiation Biology, Joint Institute for Nuclear Research, Dubna, Russia; [4]Trento Institute for Fundamentals Physics Applications (TIFPA), Trento, Italy.

We investigated the impact of ionizing radiation (IR) on the properties of human embryonic stem cells (hESCs) and their capability to differentiate into definitive endoderm (DE) that will eventually give rise to organs such as the lung, pancreas and liver. The usage of hESCs allowed us to mimic early development *in vitro* (Figure 1). Thus, the study addressed a very radiation-sensitive period of the embryogenesis as the ability of hESCs to preserve genomic integrity and to form any tissue of the body is crucial for proper embryonic development. Any disturbance of this process may lead to functional defects, malformations, cancer or premature death. IR is a known disturbing factor in early development but the underlying mechanisms have yet to be elucidated in detail.

In the above mentioned study we identified for the first time the mechanism that led to altered stem cell properties and impaired capacity to differentiate into DE of irradiated hESCs. Exposing hESCs to X-ray irradiation (1Gy and 3 Gy, respectively) led to immediate responses such as a cell cycle arrest in G2/M phase, elevated apoptosis and increased chromosomal aberrations. However, these effects were transient and mostly overcome within 24h.

In contrast, stem cell signalling analyses revealed changes in the TGF beta-, Wnt-, and Hedgehog pathways that persisted up to four days in case of irradiation with 3Gy. Remarkable was the down-regulation of activin receptors. They not only regulate the maintenance of pluripotency, the ability to form all tissues of the body, but also the differentiation of hESCs into DE. Accordingly, surviving hESCs, which were differentiated 4 days post-irradiation, showed a lower efficiency to form DE than their mock-irradiated counterparts. This was conclusively demonstrated by a reduced expression of the key regulator of DE formation, SOX17 and the microRNA miR-375.

However, the study also revealed that hESCs responded differently to IR depending on the culture conditions chosen for maintenance (Figure 2): enzymatically passaged cells, representing the most commonly used hESCs, were less sensitive than mechanically passaged ones and showed fewer apoptotic events, fewer changes in stem cell signalling but also higher levels of chromosomal aberrations.

From our results we conclude that the enzymatically passaged cells are more inhomogeneous hampering the identification of an IR impact. Thus, careful choice of appropriate culture conditions and vigorous monitoring of the stem cell quality are mandatory for the use in radiation biology and the assessment of a radiation risk during early development.

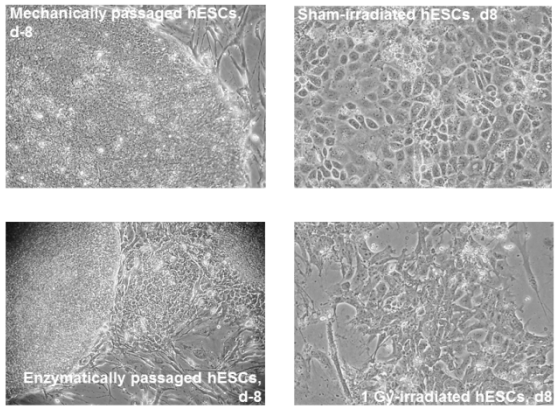

Figure 2: Morphology of cells before (d-8) and after (d8) differentiation.

The study has demonstrated that exposure to IR influences the properties of hESCs even when the immediate radiation effects are overcome. This warrants consideration in the risk assessment of radiation effects during the earliest steps of human development. For further details see Luft et al. [1].

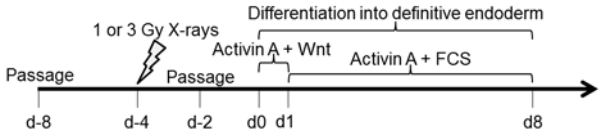

Figure 1: Differentiation and irradiation scheme

References

[1] S. Luft et al., "Ionizing Radiation Alters Human Embryonic Stem Cell Properties and Differentiation Capacity by Diminishing the Expression of Activin Receptors, Stem Cells and Development 26 (2017) 341.

* Work supported by BMBF (02NUK025A).
#i.schroeder@gsi.de

DOI:10.15120/GR-2017-1

Impact of ionizing radiation on cardiac differentiation – an update*

S. Nitsch[‡,1], *F. Braun*[1/2], *J. Kunz*[1], *S. Ritter*[1], *M. Scholz*[1], *I. Schroeder*[#,1]
[1]GSI, Darmstadt, Germany, [2]Hochschule Darmstadt, Germany

Currently embryo- and cardiotoxicity of drugs or medical treatments, like ionizing radiation, are mostly investigated in animal models. However, due to species-specific differences, data obtained from these studies are difficult to extrapolate to the human organism. Therefore, human embryonic stem cells (hESC) are one of the most important models to study embryo- and cardiotoxic effects during human development.

Previous studies of our lab used the wildtype hESC line WA09 (H9) which was differentiated into cardiomyocytes by using two different protocols [1, 2]. In 2014, Wrighton et al. established a genetically modified H9-cell line called H9-cTnT-GFP [3] which we now established in our laboratory. In these cells, GFP is under the control of the cardiac specific troponin T (TNNT2) promoter leading to green fluorescence when TNNT2 is expressed. Thereby, cardiac cells can easily be distinguished from non-cardiac cells that develop during the differentiation process to support the cardiac differentiation.

First experiments confirmed that H9-cTnT-GFP cells can be successfully differentiated into beating cardiomyocytes and express typical cardiac markers during differentiation (Figure 1). Compared to wildtype H9-cells their marker gene expression is higher.

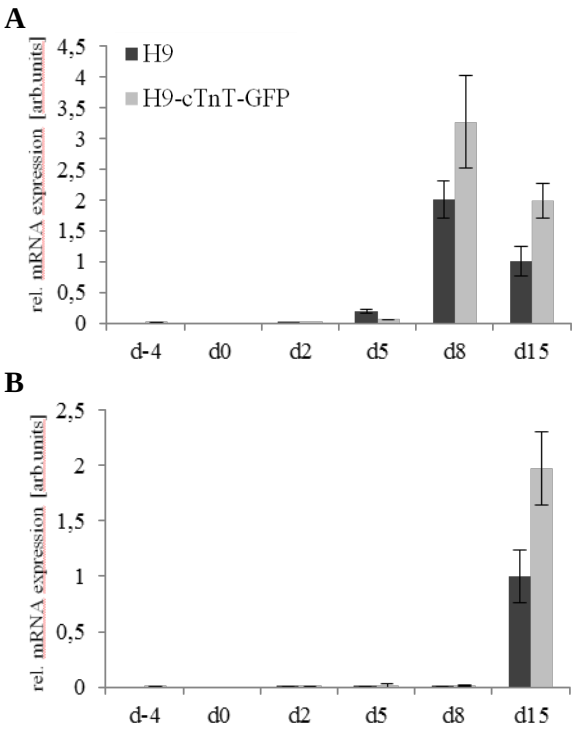

Figure 1: Relative mRNA expression of cardiac marker genes cTnT (A) and MLC2v (B) during differentiation. d=day, d0=initiation of differentiation.

Wildtype and H9-cTnT-GFP derived cardiac clusters respond to the beta-adrenoreceptor agonist isoproterenol visualized by an increased beating rate (Figure 2), thereby confirming the presence and functionality of these receptors and their ability to respond to exogenous factors.

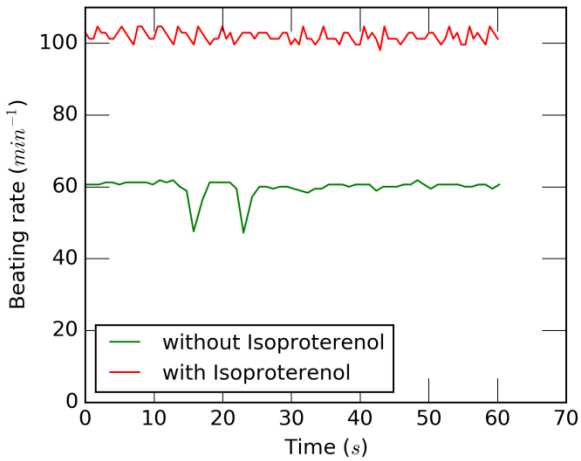

Figure 2: Beating rate of one cardiac cluster derived from H9-cTnT-GFP before (lower line) and after (upper line) stimulation with 1 µM isoproterenol.

Based on their fluorescence signal, cardiac cells derived from H9-cTnT-GFP can be separated from the supporting, non-fluorescent cells by Fluorescence Activated Cell Sorting (FACS). This allows for the specific analysis of these cell types regarding their marker gene expressions.

In conclusion, H9-cTnT-GFP cells behave similar to the wildtype cells and are therefore suitable to investigate effects of ionizing radiation on the differentiation of hESC.

References

[1] Kadari et al., Robust Generation of Cardiomyocytes from Human iPS Cells Requires Precise Modulation of BMP and WNT Signaling. Stem Cell Rev and Rep 2015, 11:560

[2] Lian et al., Directed cardiomyocyte differentiation from human pluripotent stem cells by modulating Wnt/β-catenin signaling under fully defined conditions. Nature Protocols 2013, 8:162

[3] Wrighton et al., Signals from the surface modulate differentiation of human pluripotent stem cells through glycosaminoglycans and integrins. PNAS 2014, 51:18126

* Work supported by BMBF (02NUK025A).
‡ S. Nitsch is supported by HGS-HIRe.
#i.schroeder@gsi.de

Nonlinear robust optimization methods for 4D treatment planning in carbon ion therapy*

M. Wolf[1,2], *K. Anderle*[1], *and C. Graeff*[1]
[1]GSI, Darmstadt, Germany; [2]TUD, Darmstadt, Germany

Introduction

We introduced robust optimization into non-linear biological optimization of GSI's TRiP4D to avoid internal IMPT dose inhomogeneities. Here we present a conformal robust 4D optimization delivering a homogeneous dose to each motion phase resulting in a plan library [1]. The delivery of this set of plans has to be synchronized to the motion.

Materials and methods

The implemented worst case scenario method currently considers 9 different scenarios in the optimization process: nominal scenario, 2 range error scenarios (shifting water-equivalent path length (WEPL) by $\pm 3.5\,\%$) and 6 positioning error scenarios (shifting the patient's iso-center by ± 5 mm target in S-I, A-P and L-R direction) [2]. In every iteration step LEM-based RBE-weighted doses are calculated for all scenarios from the current set of beam fluences respecting fragment spectra and LET. Within the conformal 4D optimization approach, robust IMPT on the CTV is compared to conventional IMPT on the PTV using 5 mm isotropic margins regarding 4D dose distributions for different uncertainty scenarios. Each phase of the 4DCT is optimized individually.

Results

Using robust IMPT in a patient case with a lung tumor in close proximity to the heart, a motion amplitude larger than 2 cm and a target dose of 9.4 GyE, an increased target dose of 9.6 GyE due to the steeper falloff and smaller spread in the robust DVHs was enabled. Thus the target coverage (V95) could be increased from $87.6 \pm 10.6\,\%$ to $98.0 \pm 2.7\,\%$ averaged over all scenarios by slightly increasing mean heart dose from 0.7 ± 0.1 GyE to 0.9 ± 0.1 GyE compared to conventional IMPT (see fig. 1). The dose spread of the DVH bands could be reduced from $6.3\,\%$ to $4.5\,\%$ on the V50 value using robust IMPT.

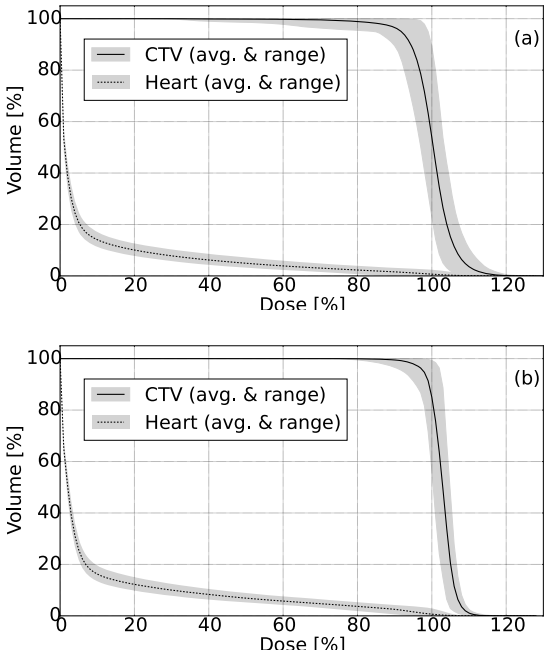

Figure 1: Dose volume histogram (DVH) for the 4D dose distribution of several error scenarios comparing for (a) conventional IMPT and (b) robust IMPT used in conformal 4D optimization. The gray bands show the uncertainties due to the error scenarios. The black lines give the DVH values averaged over all scenarios.

Conclusion

An initial patient simulation shows the feasibility and the importance for robust (4D) optimization methods for moving targets in carbon ion therapy. A further extension of the algorithm to a full 4D robust optimization where all phases of the 4DCT are optimized simultaneously using deformable image registration in every iteration step will follow, completed by an expanded patient study comparing different robust 4D optimization methods.

References

[1] C. Graeff, "Motion mitigation in scanned ion beam therapy through 4D-optimization", Phys. Med. (2014) 30, p.570-577

[2] W. Liu et al., "Robust optimization of intensity modulated proton therapy", Med. Phys. (2012) 39 (2), p.1079-1091

* Work supported by HGS-HIRe.
[1]mo.wolf@gsi.de

DOI:10.15120/GR-2017-1

BRCA1's function at complex heavy-ion induced DNA double strand breaks may include regulation of resection

T. Syzonenko[1,2], B. Jakob[1], G. Becker[1], G. Taucher-Scholz[1,2] N. B. Averbeck[1]

[1]GSI Helmholtzzentrum für Schwerionenforschung, Darmstadt, Germany; [2]TUD, Darmstadt, Germany

We observed repair relevant resection of heavy-ion induced DNA double-strand breaks (DSBs) in G1-phase cells [1]. Studying the regulation of this resection, we found earlier that BRCA1, required for break resection in G2-phase [2], is recruited to heavy-ion induced DSBs in G1-phase cells [3].

In order to study BRCA1's possible function in the resection of heavy-ion induced DSBs in G1-phase cells, we on the one hand depleted cells for BRCA1 by RNAi (Fig. 1A) and on the other hand increased the BRCA1 level by depletion of HUWE1, a negative regulator of BRCA1 [4] (Fig. 1B).

Neither increase nor decrease of the BRCA1 level had an effect on the fraction of resection positive cells upon heavy ion irradiation (Fig. 2A and B).

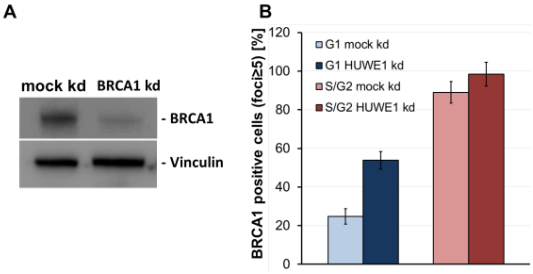

Figure 1: Decrease and increase of the BRCA1-protein level by BRCA1 knockdown (BRCA1 kd) and HUWE1 knockdown (HUWE1 kd) in U2OS cells, respectively. (A) Western analysis to proof the successful decrease of the BRCA1-protein level by RNAi. Mock depleted cells (mock kd) were treated as BRCA1 kd cells but without siRNA. **(B)** Increase of the BRCA1-protein level by RNAi driven HUWE1 depletion in G1 cells. U2OS cells were mock depleted or depleted for HUWE1 and irradiated with oxygen ions (LET 610 keV/µm, 6.5 MeV/nucleon, 5 x 10^6 p/cm^2). 1 h post-irradiated samples were fixed and stained against BRCA1 and the cell cycle marker CENP-F. BRCA1 positive cells (foci number ≥ 5) in HUWE1 depleted cells were quantified in G1 (CENP-F negative cells) or in S/G2 (CENP-F positive cells). More than 100 cells were counted in each sample. The number of BRCA1 positive cells in non-irradiated cells was subtracted. Error bar: binomial error.

Yet, determining the number of RPA foci upon irradiation of BRCA1 depleted cells revealed a resection defect in S/G2- and G1-phase (Fig. 3). Taken together, these data suggest that although BRCA1 is not a critical factor of resection of complex ion induced DSBs it is involved in regulation of their resection not only in S/G2-phase cells but also in G1-phase cells.

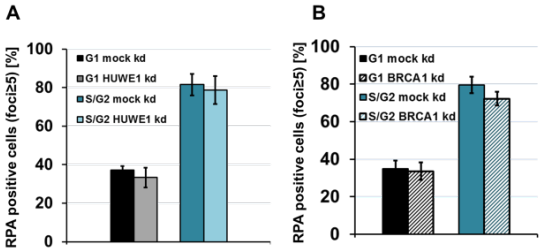

Figure 2: Fraction of resection positive cells is not influenced by modifying the BRCA1 protein level. U2OS cells were mock depleted (mock kd), depleted for HUWE1 (HUWE1 kd) **(A),** or depleted for BRCA1 (BRCA1 kd) **(B)** by RNAi and irradiated with oxygen ions (LET 610 keV/µm, 6.5 MeV/u, fluence 5 x 10^6 p/cm^2). 1 h post irradiation, the samples were fixed and stained against RPA (resection marker) and CENP-F (cell cycle marker). RPA positive cells (foci ≥ 5) were quantified in G1 (CENP-F negative cells) or in S/G2 phase (CENP-F positive cells). Graph shows mean number of RPA positive cells; n=1, error bars: binomial error.

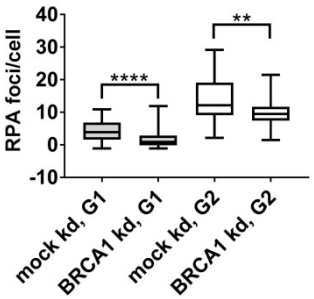

Figure 3: BRCA1 depletion decreases the RPA foci number in S/G2 and G1 cells. U2OS cells were mock depleted (mock kd) or depleted for BRCA1 (BRCA1 kd) by RNAi and irradiated with carbon ions (LET 325 keV/µm, 4.05 MeV/u, 5 x 10^6 p/cm^2). 1 h post irradiation, the samples were fixed and stained against RPA (resection marker) and CENP-F (cell cycle marker). RPA foci per nucleus were counted in at least 50 cells per sample. n=1, whiskers: minimum and maximum. Mann-Whitney test: (****) indicates P<0.0001, (**) indicates P<0.01. The average number of foci measured in non-irradiated cells was subtracted.

References

[1] N. Averbeck *et al.*, Cell Cycle (2014) 13(16): p. 2509-16.
[2] C. Escribano-Diaz *et al*., Molecular Cell (2013) 49, 1-12.
[3] T. Syzonenko *et al.*, GSI, Scientific Report 2015.
[4] Wang *et al.*, BBCR (2014) 444, 549-554.

* This work is part of the Helmholtz Graduate School for Hadron and Ion Research "HGS-HIRe for FAIR" and supported by Graduate College 1657 "Molecular and cellular responses to ionizing radiation".

Comparison of X-ray and ion irradiation dependent protein recruitment to DNA lesions using online microscopy

E. Janiel[1], *G. Becker*[1], *G. Taucher-Scholz*[1, 2], *B. Jakob*[1]
[1]GSI, Darmstadt, Germany; [2]Technical Universität Darmstadt, Germany;

Introduction

The repair of DNA lesions, especially double strand breaks (DSBs), is an essential process for maintaining genome integrity. It is tightly controlled by a complex network of DNA repair factors. Beamline microscopy of living cells with fluorescently tagged DNA repair factors revealed LET dependent recruitment kinetics for the factor NBS1, but almost no LET dependency for 53BP1 recruitment[1,2]. In the following, these findings are compared to X-ray dependent protein recruitment measurements through temporal resolved analysis of NBS1 and 53BP1 accumulation at DNA DSBs.

Materials and Methods

Living U2OS cells expressing fluorescently tagged DNA repair factors, NBS1-GFP2 or 53BP1-GFP (all kindly provided by Dr. Claudia Lukas, Danish Cancer Society, Copenhagen, Denmark), were irradiated with 0.92Gy X-rays inside a stage incubation system on the microscope. Images were captured before and immediately after irradiation, every ten seconds. The relative intensity of irradiation induced foci (IRIF) was measured above the background (average per individual nucleus) and plotted as a function of time.

Results

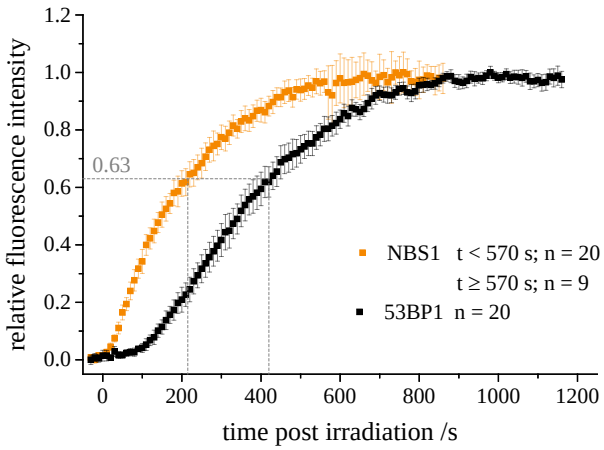

Figure 1 – Kinetics of NBS1 and 53BP1 accumulation after X-rays . X-ray irradiation at ~ 1 Gy revealed faster recruitment of NBS1 to DSBs and shorter delay than that of 53BP1 (mean intensities ± 95% confidence interval).

The live-cell recruitment measurements at X-ray induced DSBs revealed an assembly of 53BP1 in IRIFs that lags behind NBS1 accumulation (Figure 1). Average recruitment of 53BP1 exhibits a lag phase of approximately two minutes whereas average NBS1 accumulation already starts within the first 30 seconds. As shown by Tobias et al. 2013, fast protein accumulation after irradiation can approximately be described by a mono-exponential saturation curve yielding a single time constant, representing the time when 63% of the final foci intensity is reached. For NBS1 recruitment this time constant was ~220s whereas for 53BP1 a similar level was reached after ~440s due to the lag phase (dotted lines, Figure1). As compared in Tab. 1, the NBS1 mono-exponential time constants for X-ray and carbon ions are similar whereas the time constant for NBS1 recruitment at higher LET induced damage was much shorter. Concerning 53BP1, a direct relation between damage density and time constant was not observed.

Table 1 – X-ray and ion irradiation dependent recruitment times of NBS1 and 53BP1 to DNA DSBs.

	X-rays	Carbon	High LET
NBS1	220±25 s	235±25 s [(1)]	80±10 s [(1), A]
53BP1	420±35 s	640±80 s [(1)]	580±80 s [(1), B]

[(1)] Tobias F. et al. 2013
[A] V ions, LET = 2460 keV/µm
[B] Au ions, LET = 13000 keV/µm

Conclusions

The accumulation of the DNA DSB repair factors NBS1 and 53BP1 could be observed after X-ray irradiation in real-time. The time constant of NBS1 recruitment was lower than that of 53BP1 for all compared radiation qualities. This is in agreement with the findings that NBS1 acts upstream of 53BP1[3]. NBS1 recruitment kinetics at moderate LET and X-ray induced DNA damage sites were fairly similar supporting a model of predominantly binding to the surroundings of the actual DSBs at low local DSB numbers [1]. Concerning 53BP1, the recruitment showed a pronounced delay in the order of 2 min and was rather independent of the LET. The apparently slightly faster recruitment after X-rays might be due to a more transient nature of recruitment. The different LET dependent behaviour indicates that NBS1 recruitment is not the rate limiting step for a subsequent 53BP1 accumulation.

[1] F. Tobias et al., *PLoS One* **2013**, *8*
[2] V. Hable. et al., *PLoS One* **2012**, 7
[3] S. Panier and S. J. Boulton, *Nat Rev Mol Cell Biol* **2014**, *15*, 7-18

* This work is supported by the German federal ministry of education and research (BMBF), Grant#: 02NUK037A.

DOI:10.15120/GR-2017-1

High energy proton imaging for medical applications at FAIR

M. Schanz[*1], *T. Berger*[3], *M. Krämer*[1], *N. Peters*[2], *B. Przybyla*[3], *and D. Varentsov*[1]
[1]GSI, Darmstadt, Germany; [2]Universität Halle-Wittenberg, Halle, Germany; [3]DLR, Cologne, Germany

Flash Proton Radiography with high energy protons in the GeV-range is a diagnostics technique developed in the 1990s at the Los Alamos National Laboratory (LANL) for investigations on high energy density states of matter [1]. Recent experiments have shown that it is also very sensitive in the low-density-regime making this method an ideal tool for biomedical applications such as the imaging of patients during heavy ion radiotherapy [2]. The fast data acquisition will enable live tracking of the patient which is a key feature for the treatment of moving tumors.

Experiments at LANL

In order to demonstrate and quantify the performance of proton radiography for biomedical applications, several targets were manufactured at GSI in 2016 and irradiated with 800 MeV protons at the pRad facility of the LANL. Fig. 1 shows the setup that has been used for most of the measurements. Although an unknown amount of scattering and energy straggling due to three windows, a tungsten diffuser and the air gap of 1 m where the target was placed occured, a spatial resolution of 65.3 μm was achieved. The evaluation of the data is not yet completed, but a density resolution of 1 % or less is to be expected.

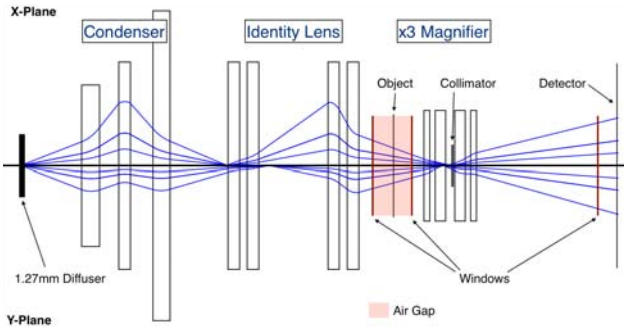

Figure 1: Ion optical scheme of the pRad facility at the LANL.

For further investigations a PMMA head phantom with different insets made of tissue equivalent plastics (see Fig. 2) was irradiated. The corresponding dose for a single projection was measured with thermoluminescence dosimeters situated in a separate target on top of the phantom (see upper part of radiograph in Fig. 2). Although the measured dose is comparably high ($D_{avg} = 52$ mGy per projection / $1.92 \cdot 10^{10}$ protons), the low noise in the acquired images indicates that a reduction of the proton dose by a factor of 100 will not affect the accuracy of the density resolution, thus permitting the operation in a clinically feasible dose range.

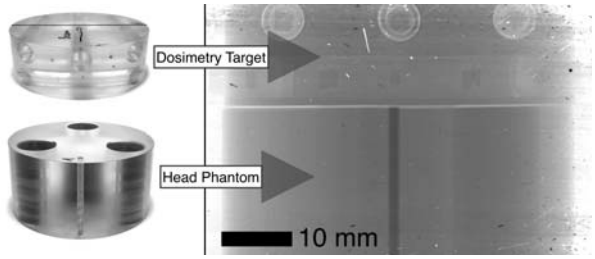

Figure 2: Head phantom and dosimetry target (left) and proton radiography (right). The insets from tissue equivalent plastic are designed to imitate soft tissue with small deviations in density from 0.36 % up to 7.56 %.

Biophysics at FAIR

During the 2018 beam time further experiments with low density static targets are planned at the HHT cave where the new PRIOR-II facility will be commissioned.

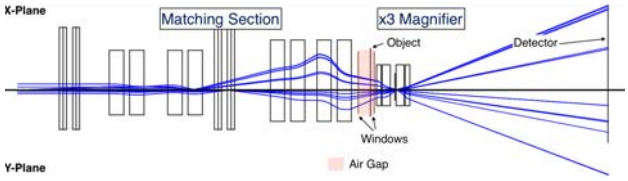

Figure 3: Ion optical scheme of the PRIOR-II facility at FAIR.

Following these investigations PRIOR-II will be transferred to the FAIR site and installed as a permanently available diagnostic system at the HEDgeHOB beam line [3]. Continuing the collaboration with the plasma physics department in the APPA cave, this facility will also be available for biophysics experiments. The new facility offers a 2.1 m gap for the installation of various experiments allowing also the examination of larger body phantoms (see Fig. 3).

References

[1] C.L. Morris et. al., “Charged particle radiography”, Rep. Prog. Phys. **4**, 2013.

[2] M. Prall et. al., “High-energy proton imaging for medical applications”, Scientific Reports **6**, 2016.

[3] M. Schanz, “High Energy Proton Microscopy at FAIR”, Master thesis, TU Darmstadt, 2016

* m.schanz@gsi.de

Inspection of counting loss and pile up effect on fluorescence lifetime recording of radiation-induced chromatin decompaction*

E. Abdollahi[1], *L. Pack*[1], *G. Taucher-Scholz*[1, 2], *B. Jakob*[1]
[1]GSI, Darmstadt, Germany; [2]Technical Universität Darmstadt, Germany;

Introduction

Recently, we provided evidence that densely ionizing radiation induces chromatin decondensation, which most probably originates as a biological consequence of DNA double strand break (DSBs) formation [1]. However, the lack of a sensitive method of detection of chromatin compaction by intensity based measurements introduced a need for the establishment of a new approach to obtain a more reliable readout. Employing fluorescence lifetime imaging microscopy (FLIM), we recently showed that chromatin compaction probes based on single organic dyes can be used to demonstrate a local radiation-induced chromatin relaxation at sites of ion traversals [2]. However, we experienced an unexpected lifetime dependency on the fluorescence and laser intensity at moderate average detector count rates. At high count rates, counting loss and pile-up effect due to detection deadtime have been reported to impair results of TCSPC FLIM [3] readout. Thus, we analyzed how these effects impact on photon numbers and lifetime distribution in our spatially inhomogeneous emitting samples under the applied conditions. In addition, we investigated in how far the detected radiation induced chromatin decompaction was impaired by the applied deadtime correction.

Material and Methods

TCSPC FLIM measurements of formaldehyde-fixed murine NIH-3T3 cells were carried out using an Olympus IX71 microscope equipped with a 60x 1.2 NA water immersion lens and a Becker&Hickl DCS-120 FLIM Scanner. Staining was done with 1 µM of Hoechst34580. Photon counting was performed over a period of 20s at 80 MHz laser repetition rate.

Results and Discussion

One of the hallmarks of fluorescence lifetime imaging is its independency on the non-quenched fluorescence intensity. Surprisingly, a fluorescence lifetime correlation to the recorded photon numbers became apparent in our FLIM measurements upon changing laser intensity. Loss of recorded photons is likely to occur due to the dead time of the FLIM detection (in the order of 100 ns) even at relatively low count rates in the order of 1 MHz [3]. In case of inhomogeneous samples, local count rates might exceed average values by far, leading to a decrease in intensity contrast (Fig 1a). At high counting rates exceeding 10% of the laser pulse rate of 80MHz the preferential detection of the first (early) photon gives rise to a loss of a potential second photon in the same signal period leading to a so-called pile-up effect. This yields a deformation of the excitation decay curve and in turn, results in an underestimation of the calculated lifetime.

As we faced high local count rates (6 MHz) due to bright areas in the detection field, we applied a pixel-wise mathematical correction of counting loss and pile-up (using the corrected incident photon rates up to 20 MHz). Figure 1 (a) and (b) show the impact of counting loss correction on the intensity images of ion-hit NIH 3T3 cells stained with 1 µM Hoechst34580. Fig. 1 (c) depicts the uncorrected lifetime image recorded at an average count rate of 2.7 MHz. An average lifetime correction of 2 % was calculated, but correction values of 3 % for bright areas were determined. The corresponding lifetime image with pile-up correction is shown in panel (d). Adopting the color LUT (insert) the compaction dependent lifetime as well as the radiation induced decompaction (insert) are still visible. Hence, our investigation proved that although pile-up effect affected the lifetime, the observed chromatin compaction dependent lifetime and radiation changes were not introduced by instrumental artifacts.

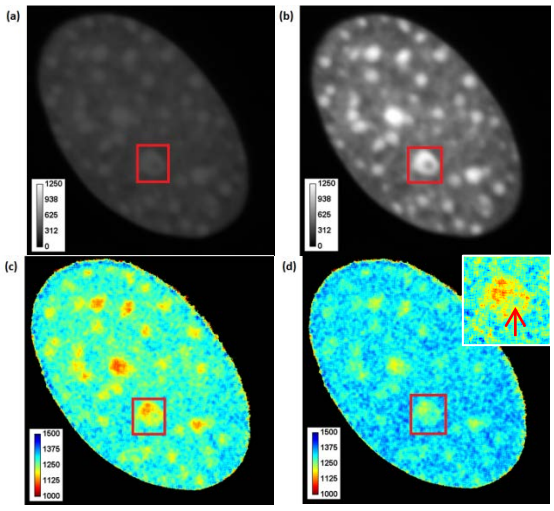

Figure 1: Confocal FLIM image of an irradiated NIH-3T3 cell nucleus stained with Hoechst 34580. Uncorrected (a, c [2]) and corrected (b, d) intensity and lifetime images. The ion-hit chromocenter is enclosed in the red rectangular and magnified with adjusted LUT in 1d. Arrow marks position of ion traversal.

References

[1] B. Jakob et al., NAR, 39, 6489-99 (2011).
[2] E. Abdollahi et al., NIMB. 365, 626-630 (2015).
[3] W. Becker, The bh TCSPC handbook 6th , 2014.

* This work is supported by the German federal ministry of education and research (BMBF), Grant#: 02NUK037A and DFG GRK1657.

DOI:10.15120/GR-2017-1

Imaging chromatin under near native conditions using transmission electron microscopy*

S. Tonnemacher[1], M. Eltsov[2], D.Grewe[2], A. Frangakis[2], G. Becker[1], G. Taucher-Scholz[1,3] and B. Jakob[1]

[1]GSI, Darmstadt, Germany; [2]BMLS, Frankfurt, Germany; [3]Technical Universität Darmstadt, Germany

Introduction

The resolution of optical microscopy has its limitation due to the diffraction barrier defined by the wavelength of the light. Besides recent approaches circumventing the diffraction barrier by a more precise determination of the signal origin, electron microscopy (EM) provides a traditional tool to obtain a much higher resolution. However structural modifications introduced by the chemical fixation methods needed for the preparation of biological samples are noticeable at this high resolution. To study radiation damage or other radiation induced changes in cells, it is necessary to develop and use fixation methods that largely preserve the structures of interest (i.e. chromatin) in a near native state. The method applied here for the future study of charged particle induced chromatin changes High-Pressure-Freezing (HPF) and subsequent Freeze-Substitution (FS) [1, 2].

Materials and Methods

NIH-3T3 cells were cultured on 3mm sapphire glasses coated with carbon at the GSI Target Lab glass was put in a flexiPrem (Sarstedt, Nürnberg) chamber in a petri dish (Fig.1a). HPF and all following steps were done at the BMLS in Frankfurt. The HPF was done with the Leica HM HPM100 in a sample cartridge (Fig.1b). FS with Lowicryl was done using a Leica EM AFS2.

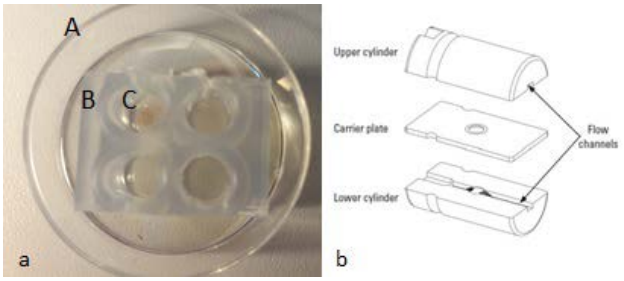

Figure 1: a) 35mm plastic petri dish (A) with a modified flexiPrem (B). Each chamber has a diameter of 5mm; inside each chamber is a 3mm sapphire (C). b) Sample cartridge for HPF consists of three parts. While freezing the sample is placed in the carrier plate (figure from [3]).

During HPF living cells are frozen rapidly to the temperature of liquid nitrogen while simultaneously exposed to a very high pressure of 2100bar within 20ms [1]. This procedure prevents the formation of ice crystals in wet biological samples and favours the formation of amorphous ice. The lack of crystalline ice and the absence of chemical fixation preserve internal structures much better than using other fixation methods. Following the HPF the frozen cells were immersed in acetone (containing 0.1% uranyl acetate (UA) to contrast membranes and nucleic acids) at -90°C for more than 24h to substitute the water molecules. After substitution, the samples were slowly warmed to room temperature while displacing the acetone by HM20, a Lowicryl resin. For imaging at a transmission EM (TEM) thin sections (200nm) were cut using an ultramicrotome and contrasted with uranyl acetate (UA) and lead citrate (LC).

Results

Using this HPF protocol, it is possible to image the cellular chromatin in a near native state. Due to the contrasting with UA and LC the chromatin was well visible and different stages of compaction (e.g. heterochromatin) could be observed. In addition nucleoli could be easily recognised (Fig. 2).

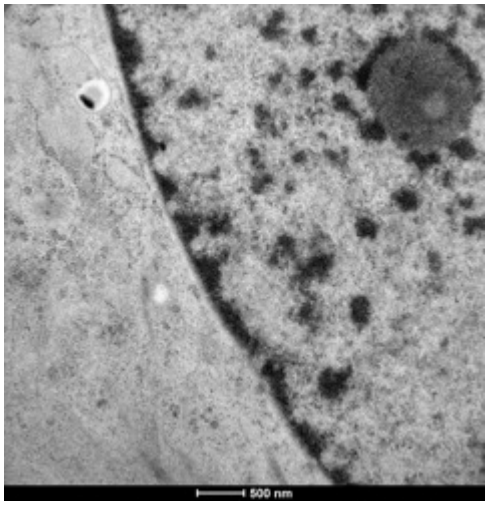

Figure 2: TEM image of a part from a NIH 3T3 cell. The nuclear membrane is visible in the middle of the figure; it goes from the top to the bottom. On the left side is the cytoplasm, on the right side the nucleoplasm with the heterochromatin (black structure) and the nucleoli (dark grey area on the top right). Section was cut, stained and imaged by Mikhail Eltsov.

Outlook

The quality of structural preservation and the obtained resolution might allow analysing radiation induced changes in the chromatin structure after irradiation with x-rays and ions.

References

[1] D. Studer et al., Histochem Cell Biol., 130, 877- 89 (2008)

[2] E. Johnson et al., Sci Rep, 5 (2015)

[3] Leica EMHPM100 Brochure

* This work was supported by BMBF Grant 02NUK037A and the graduate school HGS-HIRe.

Measurement of the time response of the beam monitors used for fast raster scanning

U. Weber[1], B. Voss[1], C. Schuy[1], K. Zink[2], C. Graeff[1]
[1]GSI, Darmstadt, Germany; [2]University of Applied Sciences Mittelhessen – THM (IMPS)

Speed improvement of the raster scanning is one of the most important prerequisites for the treatment of moving tumours such as lung or liver. One bottle neck in the existing raster scanning systems was turned out to be the gas filled beam monitors used for control of the scanning. Even when using fast amplifiers and fast data processing of the detectors, the relatively slow drifting time of the positive ions remains and significantly delays the signal. In this work we modelled and measured the time response of the integral parallel plate ionization chambers (PPIC) from the GSI pilot project [1]. They were tested with four different types of gas fillings: Ar/CO_2 (80%/20%), air, Helium, Nitrogen. The output signals from the PPICs were amplified using fast current amplifiers (Stanford-SR570m) and recorded via a fast storage oscilloscope. In order to measure the time response from a short beam pulse we used fast beam pulses (<3µs) from a 6 MeV Photon Linac or from the GSI synchrotron (^{12}C, 300 MeV/u) with fast extraction mode. The voltage of the detectors was varied from 100 to 2000 V.

The measured signals induced by the short beam pulses show a fast contribution from the fast drifting electrons and a much slower signal from the positive ions due to their much lower mobility [2].

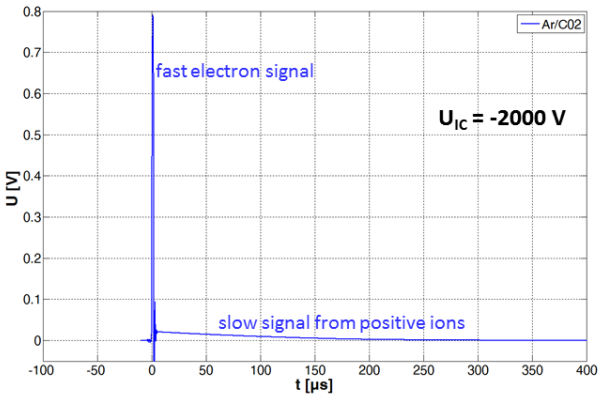

Figure 1: Measured time response of a parallel-plate ionization chamber filled with Ar/CO_2 for a short ion-beam pulse (^{12}C 300 MeV/u, <3µs). Shown is the signal at a voltage of 2000 V.

Furthermore, the type of gas has a strong influence on the response time. Especially, helium as detector gas strongly accelerates the time-response, because the mobility µ of helium ions is much higher compared to that of the other gases [2][3]. The time $t_{80\%}$ - until 80% of the charge is collected - is more than two times faster for Helium than for Ar/CO_2, air or Nitrogen (see figure 2). On the other hand, helium gas has the drawback, that due to its lower density the total signal is about 5-8 times smaller than for the other gases, which could result in higher noise, especially for low intensity beams (e.g. for scanning of proximal slices and/or for rescanning techniques).

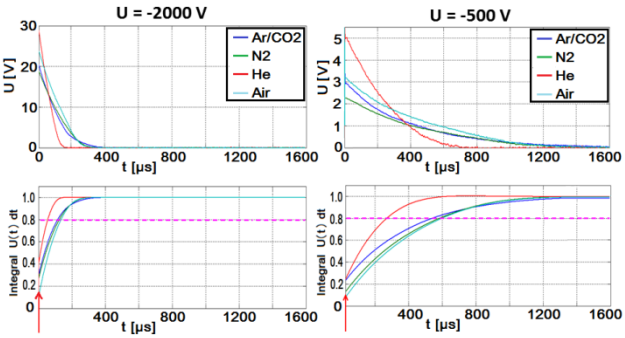

Figure 2: The upper diagram shows the pulse-answer signals for four different gases at voltages of 2000 V (left) and 500 V (right). The lower diagrams show the corresponding integrated signals normalized to 1. The $t_{80\%}$ values (intersection with dashed line) are useful parameters for the evaluation of the detector delay due to the ion drift time. The red arrow depicts the point in time of the beam pulse

We can conclude from figure 2 that the time response of the beam monitors can be dramatically improved by increasing the voltage. This requires a design of the ionization chambers which is resistant to high voltages [1]. A further improvement by a factor of two can be yielded by using helium gas. However, especially for low beam intensities, this requires a careful design of the amplifiers and good noise-shielding of the chambers.

References

[1] H. Stelzer, B. Voss , “Ionization chamber for ion beams and method for monitoring the intensity of an ion beam”, US patent, 6,437,513 B1, 2000.
[2] F. Sauli, “Principles of Operation of Multiwire Proportional and Drift Chambers”, 10.5170/CERN-1977-009, 1977.
[3] K. Kleinknecht: “Detectors for Particle Radiation”, Cambridge University Press, ISBN 0521640326, 1998.

DOI:10.15120/GR-2017-1

Nanoparticles radio-enhancement of ion beams at different oxygenation conditions*

M. Bolsa[1, #], D. Boscolo[2], E. Porcel[1], S. Lacombe[1], O. Sokol[2] , J. Wiedemann[2] , E. Scifoni[3], W. Tinganelli[3], B. Jakob[2], S. Roux[4], G. Jimenez[4], M. Durante[3] M. Kraemer[2]

[1]Institut des Sciences Moléculaires d'Orsay (UMR 8214) Bât 351, Université Paris Sud, CNRS, 91405 Orsay, France.
[2]Biophysics, GSI Helmholtzzentrum für Schwerionenforschung GmbH, Planckstr. 1, 64291 Darmstadt, Germany.
[3]Trento Institute for Fundamental Physics and Application (TIFPA-INFN), 38123, via Sommarive 14, Trento, Italy.
[4]Institut UTINAM, Université de Franche-Comté, CNRS, UMR6213, 25030 Besançon cedex, France.

Low oxygen concentration in cancer cells results in significantly lower cell death after exposure to ionizing radiation. It has been observed that heavy ion therapy under certain conditions would favour the treatment of hypoxic tumours as compared to conventional radiotherapy [1]. However, the irradiation of healthy tissues at the entrance channel remains a major limitation. A new strategy based on the combination of high-Z nanoparticles (NPs) with ion radiation has been developed by the group of S. Lacombe to improve the performance of heavy ion therapy [2, 3]. The addition of NPs increases the radiation effects within the tumour allowing ultimately the reduction of the dose deposited in healthy tissues. The group has studied the physico-chemical events that take place at nanoscale. In particular, it was shown that water radicals play a major role [3]. In the present work, the possibility of using AuNPs to increase radio-induced cell killing also in the case of hypoxia was addressed. The results of a series of experiments performed at HIT and GSI investigating the effect of AuNPs on HeLa (human cervical cancer) cells in oxic and anoxic conditions are presented in this report.

HeLa cells were gassed with a mixture of 95% N_2 and 5% CO_2 inside the exposure chamber 2 hours prior irradiation to achieve anoxic conditions (0% O_2). In oxic conditions, cells were kept in the exposure chamber but without gassing. Cells were incubated with AuNPs 6 h before gassing at a concentration of 1 mM in Au. At this concentration, AuNPs are not toxic. AuNPs, synthesized by S. Roux and co-workers, are composed of a gold core (2.5 nm) and encapsulated within an organic shell of DTDTPA [4]. Cells were irradiated with carbon ion beam at fixed <LET> (dose averaged linear energy transfer) values of 50 and 100 keV/µm. The combined effect of radiation and NPs on cells was quantified by the measurement of the mitotic survival, and by the quantification of radiation-induced nuclear DNA double strand breaks (DSB).

The surviving fraction of cells for <LET>=100 keV/µm can be reduced in the presence of AuNPs by 25% at 2 Gy in oxic and anoxic conditions and up to 45% at 4 Gy in anoxic (Figure 1). For <LET>=50 keV/µm, we did not find any NPs-induced radio-enhancement (NRE). We thus observed that the NRE seems to increase with LET. The nucleic DNA repair assay has demonstrated that AuNPs have no impact on DNA damage whatever the oxygenation condition without irradiation. However, the number of DSBs produced by radiation differs in between oxic and anoxic conditions in the absence of NPs but not in the presence of NPs (data not shown).

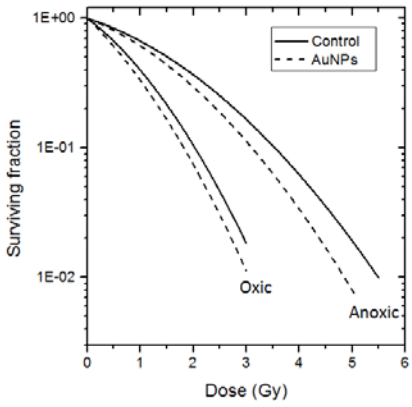

Figure 1: Surviving fraction of cells after irradiation by carbon ion beam (<LET> = 100keV/µm) versus the dose in oxic and anoxic conditions in presence or absence of AuNPs.

However, an exhaustive nanoscopic model able to describe the mechanism underlying the radio-induced effects of NPs and the role of oxygen concentration is still missing. For this reason both a Monte Carlo track structure and a LEM like model are in development in order to interpret these experimental results.

References

[1] Scifoni, E., et al. Phys Med Biol 58.11 (2013): 3871.
[2] Porcel, E., et al. 2014, Nanomedicine vol 10, Issue 8, p1601-1608
[3] Porcel, E., et al. Nanotechnology 2010; 21(8):85103.
[4] Debouttière, P-J., et al. Adv. Funct. Mater. 2006, 16, 2330-2339.

*The research leading to these results has received funding from the European Union Seventh Framework Programme [PEOPLE 2013 ITN ARGENT project] under grant agreement n [608163] and the BMBF Grant 02NUK037A.
marta.bolsa-ferruz@u-psud.fr

DOI:10.15120/GR-2017-1

Characterization of neurospheres generated from irradiated human embryonic stem cells*

M. Mayer[1], *O. Arrizabalaga*[2], *J. Kunz*[2], *S. Ritter*[2], *S. Sadeghi*[†2], *and C. Thielemann*[1]

[1]University of Applied Sciences, BioMEMS Lab, Aschaffenburg, Germany; [2]GSI, Biophysics, Darmstadt, Germany

Cognitive dysfunctions as well as malformations of the brain have been observed after *in utero* exposure to ionizing radiation (IR) [e.g. 1]. Further, *in vitro* studies reported on altered neuronal and synaptic excitability induced by IR [2]. Therefore an assessment of radiation-effects on the developing central nervous system, especially on the electrophysiological properties, is needed. To address this topic we chose human embryonic stem cell (ESC)-derived neural stem cells as a model system. For further proliferation and differentiation neural stem cells (NSC) were grown as three-dimensional aggregates (neurospheres, NS) [3].

To characterize the formed NS, quantitative RT-PCR was performed demonstrating the expression of NSC markers NES, PAX6 and SOX2, as well as markers of neuronal progenitors such as DCX, MAP2, NR2F2 and TJP1, among others (data not shown).

To study the effect of IR on neural development, human ESC were irradiated with 1 Gy X-rays (250 kV, 16 mA). Controls were sham-irradiated. Four days later neural differentiation was initiated.

The proliferative capacity of the stem cells that form the sphere is reflected in the diameter. Previous studies on mouse ESC reported on a reduced diameter of spheres generated from irradiated cells [4]. To evaluate if NS derived from irradiated human ESC show an altered diameter compared to the control, the area of the NS was determined from microscopic images (Nikon Eclipse, TS100) using the NIS-Elements Documentation software™ (Fig. 1a).

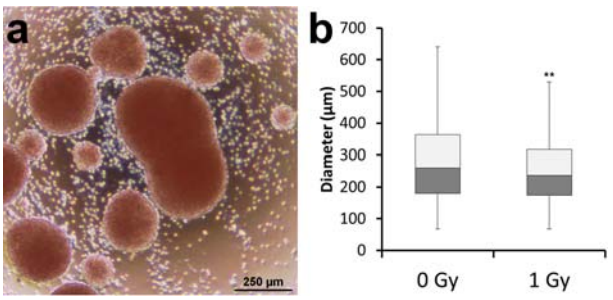

Figure 1: Diameter of NS. (a) An exemplarily image of NS 14 days after formation. NIS-Elements Documentation software™ was used to measure the area and automatically calculate the diameter. (Scale bar = 250 μm) (b) Boxplot showing NS diameter in quartiles, whiskers show minimum and maximum values (after discarding the outliers, which were calculated by "Outlier = Q3 + 1.5 x interquartile range") (n= 413 for 0 Gy, n= 257 for 1 Gy, ** $P < 0.01$).

* Funding for this project was provided by the Federal Ministry of Education and Research (02NUK025C and 02NUK034C).

† S. Sadeghi received funding from "Verein für Tumortherapie".

The mean diameter of NS originated from irradiated human ESC was smaller than the respective control, i.e. 251 +/- 97 μm compared to 274 +/- 119 μm. As displayed in Fig. 1b, the quartile-distribution of the diameters also showed a statistically significant difference between sham and 1 Gy irradiated samples.

To evaluate if irradiated human ESC-derived NS are electrically active, we used microelectrode arrays (MEAs) as previously described [3]. NS within the interquartile range size were placed onto MEA chips. Electrophysiological recording started 1 day after plating. The results clearly showed that irradiated human ESC are still able to form electrophysiologically active NS. Noteworthy in both groups a comparable number of spikes per minute (365,6 +/- 130,92 for 0 Gy, 438,2 +/- 178,45 for 1 Gy) was recorded on day 1 of electrical activity (Fig. 2). On day seven the number of spikes increased about threefold in sham irradiated samples, while the amount of signals in NS derived from irradiated human ESC increased only by a factor of 1,42 +/- 0,5. These preliminary data indicate that exposure of human ESC to IR affects the electrophysiological properties of their progeny.

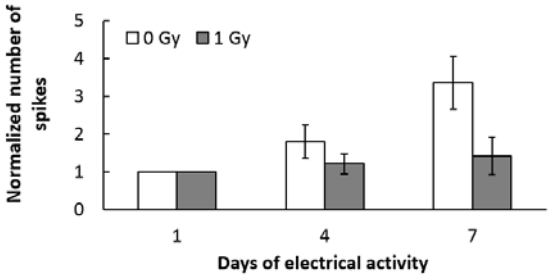

Figure 2: Number of spikes recorded from single NS. NS derived from 0 Gy or 1 Gy X-ray irradiated human ESC were cultured on MEAs. The number of spikes was examined for 60 seconds on day 1, 4 and 7 of electrical activity. Data are represented as mean normalized to day 1 (n = 5 for 0 Gy, n = 5 for 1 Gy) +/- SEM.

Currently, further electrical recordings of NS are being generated and analyzed to validate the data obtained so far. Moreover, gene expression studies are being carried out, in order to determine the cellular and molecular composition of the NS. The exposure of human ESC to IR could influence their differentiation capability, i.e. forming non-functional neurons or other types of neural cells.

References

[1] Verreet, T. et al., JNeurodevDisord. 2015, 7: p. 17-21
[2] Ordy, J.M. et al., JNeurochem. 1968, 15: p. 1245-1256
[3] Mayer, M. et al., GSI Scientific Report 2015, p. 205
[4] Helm, A. et al., Stem Cells Dev. 2016, 25:p. 178-188

DOI:10.15120/GR-2017-1

Semi-automatic analysis of dicentric chromosomes for cytogenetic risk assessment of low radiation doses*

C. Hartel[1], Y. Knies[1] and S. Ritter[1]
[1]GSI, Darmstadt, Germany.

In the context of the GREWIS project, we aim to determine the cytogenetic risk associated with the therapeutic exposure to very low doses of (densely or sparsely) ionizing radiation. The scoring of dicentric chromosomes (DCs) is a standard technique for biological dosimetry and the assessment of genotoxic risk [1]. To determine the cytogenetically equivalent dose, the frequency of DCs in a sample of peripheral blood lymphocytes is compared to a reference dose-effect curve. DCs can be scored manually; yet, to achieve an adequate resolution in the low-dose range, analysing a high number of metaphases is essential. Therefore, a software-based image acquisition and a semi-automatic analysis system was established in our laboratory and a dose-effect curve was generated.

Irradiation and chromosome preparation were performed as described previously [2]. Briefly, peripheral blood lymphocytes were exposed *in vitro* to X-rays (dose range 0-6 Gy). Metaphase spreads were prepared and were stained with Giemsa dye. DC scoring was performed using an Axio Imager Z2 microscope (Zeiss, Germany) and the DCScore/Metafer software (Metasystems, Germany). The automatically detected DCs were reviewed by an experienced scientist and false positives were removed. We accept as true positive DCs only those which clearly have the typical shape and are accompanied by an acentric fragment. Examples of a true DC as well as a false positive DC are shown in figure 1. In the unexposed control, the vast majority (98.5%) of all automatically detected DCs are false-positives, this value drops to 11.9 % of false positives at a dose of 4 Gy. This is in good agreement with literature data [3].

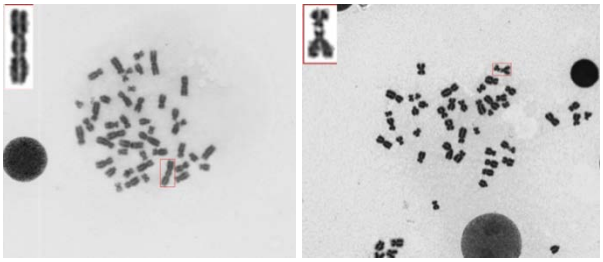

Figure 1: Left: Metaphase with a true DC, the acentric fragment is also visible in the metaphase spread. Right: Metaphase with a false positive DC, two aligned chromosomes are scored by the software as one DC.

The resulting dose effect curve for the *in vitro* induction of DCs in peripheral blood lymphocytes is shown in figure 2. We observed 0.103±0.017 DCs per 100 analysed metaphases in the unexposed control and 0.156±0.020 in the sample exposed to the lowest dose of 25 mGy (each based on 35 000 analysed metaphases), showing that the exposure to a dose of 25 mGy can be distinguished from the background level. For higher doses, a lower number of analysed metaphases was sufficient. The calibration curve constructed so far is based on 100 000 analysed metaphases (figure 2).

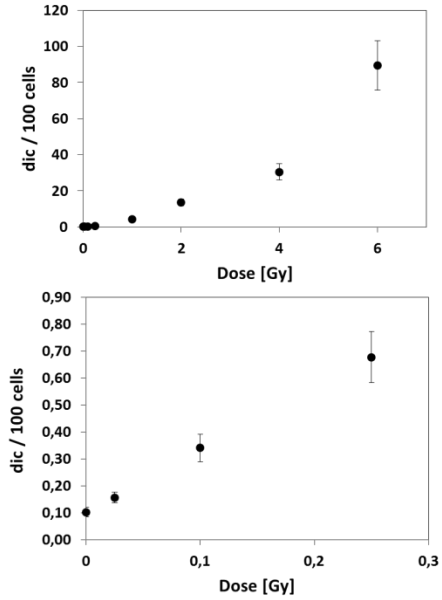

Figure 2: Dose-effect curve for the induction of DCs by X-rays in peripheral blood lymphocytes. The low-dose range (0-0.25 Gy) is shown in the lower panel.

The analysis of DCs is currently used to determine the cytogenetic effect of *in vitro* exposure to radon gas on lymphocytes. Furthermore, we will apply the semi-automatic scoring of DCs to assess the cytogenetic risk of the therapeutic exposure to low doses of sparsely (low dose radiotherapy, LDRT) or densely (radon therapy) ionizing radiation *in vivo*.

References

[1] IAEA Technical Report Series No 105: Cytogenetic Analysis for Radiation dose Assessment. International Atomic Energy Agency 2001.

[2] Lee *et al.* Chromosome aberration measurements in mitotic and G2-PCC lymphocytes at the standard sampling time of 48 h underestimate the effectiveness of high-LET particles. Radiat Environ Biophys 50 (2011) p371-381.

[3] H. Romm *et al.* Automatic scoring of dicentric chromosomes as a tool in large scale radiation accidents. Mutat Res 756 (2013) p174-183.

* Work supported by the Federal Ministry of Education and Research (Bonn, Germany) under contract number 02NUK017A.

Pharmacological augmentation of heavy ion cancer therapy *

Norman Reppingen[1], *Marco Durante*[2], *and Claudia Fournier*[1]

[1]GSI Helmholtzzentrum für Schwerionenforschung; [2]Trento Institute for Fundamental Physics and Applications - TIFPA

Our ongoing *in vitro* efforts (see previous reports)[1] aim to find a most versatile pharmacological augmentation of heavy ion cancer therapy. Recently, we evaluated a multimodal pharmacological approach in the murine cell lines CT26.WT, B16-F10 and 4T1. Using the 4T1 cells (metastatic breast cancer), we extended this evaluation to a mouse model with and without x-ray irradiation. One of the pharmacological entities did demonstrate impressive efficacy with strongly reduced tumor growth. This reveals our model of choice as a potentially useful test system to demonstrate the versatility of heavy ion cancer therapy.

In vitro progress

In the CT26.WT cells (colon carcinoma) and in the B16-F10 cells (melanoma) we were able to induce apoptotic cell death also in conjunction with irradiation. The evaluation of our approach with the 4T1 cell line was reflecting the known high treatment resistance of this model. We were able to show the activity of a tyrosine kinase inhibitor to at least partly antagonize this treatment resistance, inducing tumor cell death. These in *in vitro* results, although encouraging, were limited by the absence of an immune system and tumor stroma, which is known to influence tumor *in vivo* behavior and to contribute heavily to treatment resistance.

In vivo results

To gain more insights on immunological mechanisms and to validate overall efficacy, we evaluated our pharmacological approach in an immune competent mouse model with 14 Gy of x-ray irradiation confined to the tumor. Irradiation with x-ray alone led to a minor reduction in tumor growth (see figure 1). The tyrosine kinase inhibitor reduced tumor growth efficiently. The tumor shrinkage took place without any signs of toxicity under close monitoring of health status and individual mouse weight. As the remaining tumors were small but visible, there still remains room for improvement to evaluate the versatility of heavy ion cancer therapy in this particular and potentially other combined applications.

* Work supported by HGShire. In vivo animal work was carried out by TRON GmbH.

Outlook

One of the next steps is to find new interesting drug candidates. Also, we need to gain deeper insights into cell death mechanisms, as e.g. 4T1 cells are p53 negative and -as many other cancer cell types- unlikely to succumb to apoptosis. Histological analysis of the experimental specimens gained from the animal experiments will hopefully hint to further pharmacological optimization strategies to maximize carbon ion cancer therapy efficacy. As we have reasons to assume that carbon ion irradiation could lead to a more pronounced decrease in tumor growth, a further validation of a combined regimen including heavy ions is one of the upcoming aims.

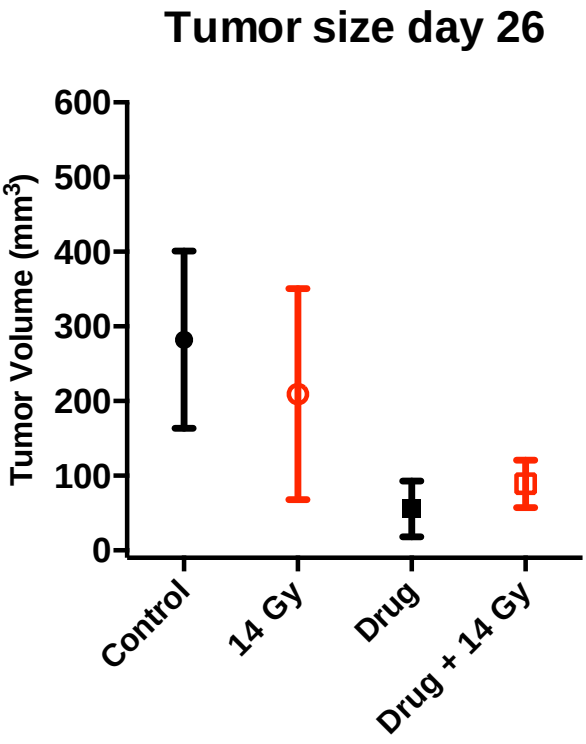

Figure 1: Representative tumor sizes (sample groups between 7 and 13 animals) with drug treatment beginning at day 5 and 14 Gy of x-ray irradiation (tumor) at day 14.

References

[1] N. Reppingen, M. Durante, C. Fournier, Scientific Reports 2014

DOI:10.15120/GR-2017-1

Comparison of relative biological effectiveness of proton radiation for regeneration of intestinal crypts in mice with the Local Effect Model*

R. Grün[1], T. Friedrich[1], M. Krämer[1] and M. Scholz[1]
[1]GSI, Darmstadt, Germany

Introduction

The role of relative biological effectiveness (RBE) consideration in proton radiotherapy different from the dogma of a constant RBE is gaining interest for clinical application. In a previous report [2], we were comparing proton RBE predictions by the Local Effect Model (LEM) [1] to experimental RBE values for clonogenic cell survival (*in-vitro* data). To further demonstrate the capabilities and limitations of LEM for proton irradiation along the spread out Bragg peak, here we focus now on the comparison to experimental *in-vivo* data. The endpoint intestinal crypt regeneration in mice after single fractions of proton irradiation was chosen since the intestinal crypt assay is an established and widely studied endpoint with a sufficient amount of data available in the literature.

Methods

Ten *in-vivo* experiments for the survival of intestinal crypts in mice were considered for the comparison. We compared the RBE for 10 and 20 surviving crypts to the RBE prediction by the LEM in dependence on dose-mean linear energy transfer (LET_D). The treatment planning software TRiP98 was used to optimize the passive proton SOBP of each experiment. For the comparison with *in-vivo* data, mainly single fraction experiments with high doses exceeding 10 Gy were examined. The LEM is based on the so-called single particle approximation (SPA), which is expected to show limitations for high doses. Therefore, we additionally used the so-called 'full simulation' version (FS) of the LEM for the comparison to account for the potential limitations of the SPA at higher doses [3]. More detailed information about the analysis can be found in [4].

Results & Conclusion

The RBE values predicted by the LEM (SPA) were evaluated using the photon dose given in the publications, which leads to 10 and 20 surviving crypts, respectively. A systematic shift to lower RBE values for the LEM (SPA) and LEM (FS) prediction as compared to the experimental RBE is observed (fig. 1). The deviation of the RBE values for 10 surviving crypts is of the order of 5% for LEM (SPA) and 2.5% for LEM (FS). For 20 surviving crypts the deviations are only slightly higher. The constant underestimation was attributed to the high doses of around 13–16 Gy needed to study this endpoint. Regarding the 95% confidence interval, the LEM (FS) prediction as well as a constant RBE of 1.1 seem to be in good agreement with the experiments. Nevertheless, the trend of an increasing RBE with increasing LET_D as observed in the experiments is better described by the predictions of both LEM (SPA) and LEM (FS).

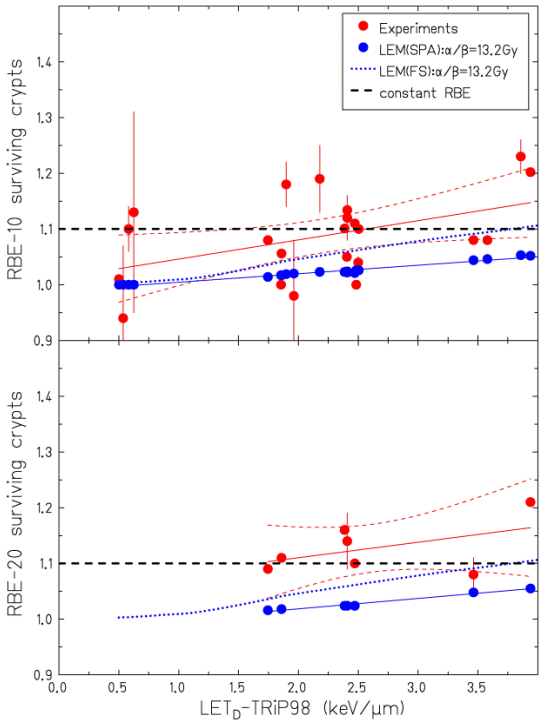

Figure 1: RBE vs. LET_D for 10 and 20 surviving intestinal crypts in mice. The blue data points and solid blue line (fit curve) correspond to the LEM prediction with the SPA. The red line represents a fit to the experimental values (red circles). Note that for the fit no error bars were considered. Thin red dashed lines show the 95% confidence interval for the experimental values. For the LEM predictions the 95% confidence interval coincides with the fitted curve (solid blue line).

References

[1] T. Elsässer et al., Int J Radiat Onc Biol Phys (2010)
[2] R. Grün et al., GSI Scientific Report 2015 (2016)
[3] Friedrich et al., Int J Radiat Biol (2012)
[4] R.Grün et al., Phys Med Biol (2017)

* Work supported by RaySearch Laboratories AB

Influence of ionising radiation on the capacity of neural stem cells to form neurospheres*

O. Arrizabalaga[1], L. Muñoz-Rizzo[1], D. Ney[1] and S. Ritter[1].
[1]GSI, Darmstadt, Germany

Human embryonic stem cell derived neural stem cells (hNSC) are a powerful model system to study the effects of ionizing radiation (IR) on neurogenesis [1], a fundamental part of brain development and homeostasis. The method of choice to determine the ability of a cell to survive radiation exposure is the colony forming assay that measures the ability of a single cell to form a colony in a culture dish. Yet, colonies cannot be grown from single hNSC in adherent culture. An alternative approach is the cultivation of NSC in suspension as 3-dimensional aggregates, called neurospheres (NS).

As culture dish and cell density are critical parameters that influence the NS formation efficiency, we optimized the technique for two types of suspension culture vessels, i.e. T25 flasks and 96-well round-bottom plates. In T25 a larger number of NS can be grown (e.g. for further molecular biological analyses), whereas in microplates a single NS can be grown per well. First, different seeding densities were tested from 100 cells/µl down to 1 cell/µl. These experiments showed that an appreciable number of NS with a comparable size is generated by seeding 5 cells/µl in T25 flasks, while a seeding density of 1 cell/µl for 96-well plates results in one single NS per well.

NS were allowed to grow for 2 weeks, and then their number and size (diameter) was determined. NS formed in T25 flasks were analysed using an in-house developed automatic counter recognizing objects greater than 35 µm [2], while NS grown in 96-well plates were analysed using a Nikon Eclipse TS100 microscope and the NIS Elements Documentation software™.

Having established these techniques, a first radiation experiment was performed. hNSC were exposed to 1 or 2 Gy X-rays (250 kV, 16 mA) and seeded 1 or 2 days after exposure for NS formation. Analyses of NS number and size were performed 14 days later (Figure 1).

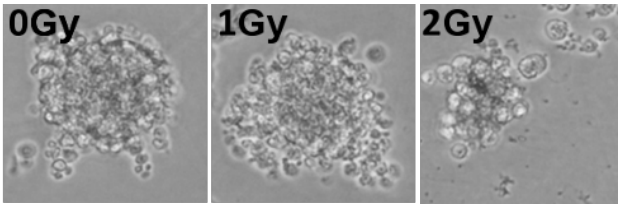

Figure 1: Representative images of NS generated from X-ray irradiated hNSC in 96-well plates. NS formation was initiated 1 day after exposure.

As shown in Figure 2, in each experimental set up the NS formation capacity of irradiated NSC was found to be affected by dose and post-irradiation incubation time. Yet, the data obtained for NS grown in T25 flasks shows a higher inter-experimental variability.

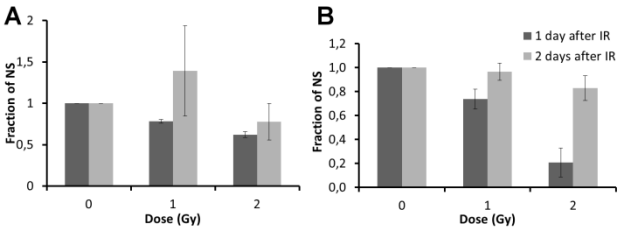

Figure 2: Fraction of NS formed in T25 flasks (**A**, n = 2) or 96 well plates (**B**, n = 7). Cells were seeded 1 or 2 days after X-ray exposure. Data was normalized to the sham irradiated control (mean ± SD).

Noteworthy, in control samples the diameter of NS grown in T25 flasks was 54 ± 7 µm and was not significantly affected by radiation (Figure 3 A). On the other hand, the diameter of control NS formed in 96 well plates was larger (91 ± 13 µm). Irradiation of hNSC with X-rays resulted in slightly smaller NS compared to the control. This effect showed a dose-dependency, but no substantial difference was observed between NS formation 1 or 2 days after X-ray exposure (Figure 3 B).

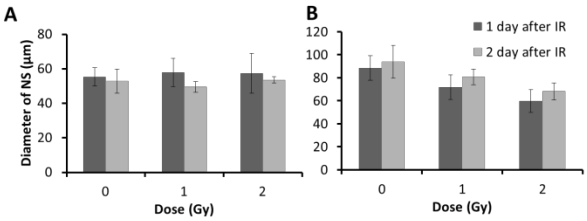

Figure 3: Mean diameter of NS (± SD) generated in T25 flasks (**A**) or 96-well plates (**B**). Cells were seeded 1 or 2 days after X-ray exposure.

In summary, our data show that the neurosphere formation assay can be applied for assessing the effects of IR on hNSC, resembling the classical colony forming assay for adherent cells. Moreover, our results suggest that 96-well plates possess a number of advantages in comparison with T25 flasks, e.g. the inter-experimental variation in the NS formation efficiency is lower. If this is due to the fact that in each well only one sphere is formed and thus fusion and aggregation of NS cannot take place remains to be elucidated.

References

[1] Arrizabalaga et al., GSI Report 2016-1, p. 201
[2] Sonnemann et al., GSI Report 2014-1, p. 43

* Funding for this project was provided by the Federal Ministry of Education and Research (02NUK034C) and Verein für Tumortherapie.

DOI:10.15120/GR-2017-1

Cluster analysis of ionization patterns after ionizing radiation*

J. Renner[1], *M.Scholz*[1], *T. Friedrich*[1]
[1]GSI, Darmstadt, Germany

One determinant for the enhanced biologic effectiveness of ion radiation is the concentrated accumulation of ionization events delivered to the tissue. Ionization clusters facilitate the promoted induction of double strand breaks and possibly more severe lesions to the DNA. The Ripley J function provides a convenient tool to compare cluster properties of such ionization patterns of different radiation qualities, which is of relevance for biophysical models like the Local Effect Model (LEM).

The LEM is used to predict the biologic effectiveness of ion radiation for therapy in its original version. Its latest improved version (LEM IV) is now used for research purposes at GSI. It assumes that in any subvolume of cell nuclei covered by the track structure of ions as many double strand breaks (DSB) are induced to the DNA as if the local dose in that subvolume was deposited by high energetic photon radiation, for which the DSB yield is known. The notion of local dose is here based on an amorphous track description and falls off with the radial distance to the ion path. This approach does not explicitly consider the point like nature of radiation induced ionization sites. As the DSB is a consequence of clustering of at least two ionizations on opposite DNA strands within the spatial scale of a few nm, the amorphous track structure approach in LEM therefore requires that on this scale the clustering properties of ionizations in ion tracks and high energy photon radiation fields are comparable. While assessed by performance, reliability and robustness the LEM is validated in numerous ways, a full theoretic consideration of this assumption has not been attempted so far.

For a theoretic analysis of ionization patterns which can be obtained by Monte Carlo transport calculations, a method to characterize the clustering properties of an arbitrary ionization pattern (or, more abstract, point process) is needed. A formalism derived in ecology by Ripley allows quantifying the number of observed points in a given area in comparison to a complete random distribution of points [1]. This formalism was modified to three dimensions and adapted for describing ionization patterns. The quantity

$$J(L) = \sqrt[3]{\langle n \rangle - \rho_e L^3}$$

can be calculated for any ionization point pattern, where ρ_e is the overall density of points in the simulation volume, and $<n>$ is the average number of additional points within small cubic volumes of length L, centred around an arbitrary point. Hence J directly parameterizes the number of points exceeding the expected number by a random homogeneous distribution within the entire simulation volume. If the point pattern is free of any spatial correlation, no clustering is visible and $J(L) = 0$ for all L. Instead, if ionization points are clustered, e.g. as on secondary electron tracks ionizations occur in an organized way (like 'pearls on a string'), then clustering is visible as accumulation of ionizations along these tracks, leaving space in between tracks. In this case J is larger than 0 and rises with L, eventually getting constant when entire clusters are covered by the cubes of site length L.

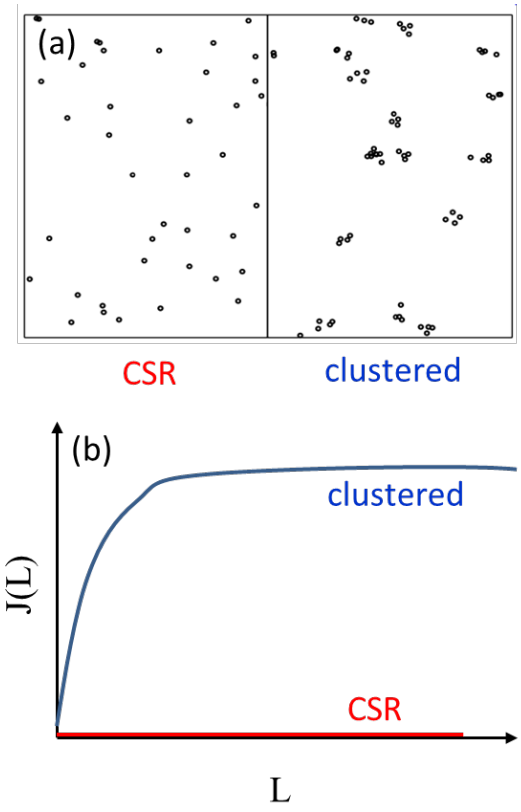

Figure 1: (a) Schematic 2D sketch of a point pattern following complete spatial randomness (CSR, left) and showing cluster agglomeration (right). (b) Ripley's J function allows a distinction between these cases for every probe size L.

On the relevant size for DSB induction of a few nm the function $J(L)$ can now be used to determine the degree of clustering in comparison to CSR for any radial distance to the ion path within its track structure formed by δ-electrons, and for high energetic photon radiation fields of equal dose. While a broader investigation is planned, first results at selected situations indicate a general similarity of the cluster properties of these cases.

References

[1] A.J. Baddeley and B.W. Silverman, Biometrics **40**, 1089 (1984).

DOI:10.15120/GR-2017-1

Nanodosimetry with quantum dots: Proton track structure simulations

M. Borghesi[*1], *M. Dapor*[1,2], *M. Krämer*[3], *I. Abril*[4], *R. Garcia-Molina*[5], *A. Quaranta*[6], *M. Durante*[1], *and E. Scifoni*[1]

[1]TIFPA, Trento, Italy; [2]ECT*, Trento, Italy; [3]GSI, Darmstadt, Germany; [4]Universitat d'Alacant, Spain; [5]Universidad de Murcia, Spain; [6]Università di Trento, Italy

Introduction

Ion beam nanodosimetry is an emerging method for radiation field characterization in particle therapy. Such a different dosimetry cannot substitute the standard methods, but is necessary to deal with as small volumes as DNA convolutions. Different phenomena must be taken into account at the nanoscale than those studied on a macroscopic level.

Dealing with these small volumes is very difficult on the experimental level. Several apparatuses have been built, e.g. [1], to measure the number of ionizations inside tissue-proportional gas chambers, which gave very good results (see e.g. [2]). However, such apparatuses are too large and lack of portability. As a consequence, new nanoscopic dose-measuring devices are needed for the evaluation of nanodoses. Recently [3], in the context of INFN experiment NADIR, quantum dots have been proposed as an alternative nanometric ionization-counting device due to their luminescence properties [4].

We performed a track structure analysis to characterize proton induced ionizations in these systems through the GSI code *TRAX* [5].

Cross section assessment

Two ionization cross section models have been compared: the binary encounter approximation or BEA, already implemented into the code *TRAX*, which only accounts for two-body collisions, thus neglecting all solid state interactions between target atoms; the dielectric response formalism, which includes empirical solid state effects by construction from optical limit measurements, extended to $k \neq 0$ regime via the Mermin model [6] which will be called MELF, i.e. Mermin energy loss function.

A comparison between these two models is depicted in figure 1, where every single differential cross section (SDCS) for proton projectile at kinetic energy $T = 1$ MeV is shown. The difference is restricted to low secondary electron energy $W < 20$ eV, while at higher energy the two curves almost perfectly overlap.

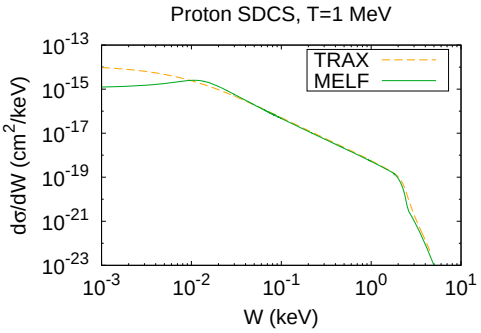

Figure 1: Ionization cross sections for 1 MeV proton on amorphous carbon, accounting (MELF) or not (BEA, labeled *TRAX*) for solid state effects.

Quantum dot nanodosimetry

When evaluating the number of ionizations produced inside an aC-dot, two components should be taken into account: the ionizations produced by direct traversal of the dot and those produced when ions pass aside the dot.

For what regards the former case, which turns out to produce many more ionizations, making the other one negligible, the number of ionizations is plotted in figure 2.

Such analysis served as a basis to design experimental conditions for aC-dot irradiation tests [7].

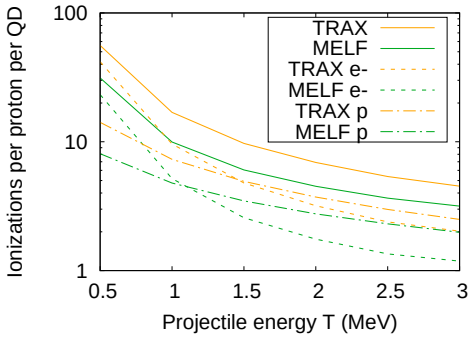

Figure 2: Ionizations produced by direct traversal of an aC-dot as a function of ion energy. Solid, dashed and dash-dotted lines represent respectively total, secondary electron and primary (i.e. ion induced) ionizations.

References

[1] Pszona S. *et al*, *Nucl. Instrum. Methods A*, 447(2000)601-607
[2] Conte V. *et al.*, *New Journal of Physics*, 14(2012)093010
[3] Pancheri L. *et al.*, *Radiother. Oncol.*, 118(2016)S88
[4] Kelarakis A., *MRS Energy & Sustainability*, 1(2014)E2
[5] Krämer M. & Durante M., *Eur. Phys. J. D*, 60(2010)195–202.
[6] Heredia-Avalos S. *et al.*, *Phys. Rev. A*, 72(2005)052902
[7] Borghesi M., *Master thesis*, University of Trento (2017)

*mauro.borghesi@tifpa.infn.it

DOI:10.15120/GR-2017-1

Space shielding simulations with TRiP98 for the ROSSINI-2 project*

M. Krämer[1#], E. Scifoni[2], M. Giraudo[3] and M. Durante[2]
[1]GSI, Darmstadt, Germany; [2]TIFPA-INFN, Trento, Italy; [3] Thales Alenia Space, Turin, Italy.

Introduction: a Space-TRiP?

The possibility of using TRiP98, the GSI in-house treatment planning system for particles [1] also for space radiation protection studies was already mentioned and discussed in a publication several years ago [2]. This was because his fully modular structure, and extensibility towards different regions of validity, e.g. of nuclear interaction cross sections. Here for the first time we realize modifications of the code dedicated to this purpose and perform several test of radiation shielding with different monochromatic and spectral particle radiation sources, in the context of the ESA ROSSINI-2 project[3].

Simulation tests

A series of tests were performed by modifying the internal transport code of TRiP98, normally used for beam model generation in particle therapy, extending it for handling different materials, and compound multi-layers of them. The shielding simulations were thus carried on with a numerical pencil beam monodimensional transport model. The same experimental setup described in the dedicated ROSSINI-2[3] technical notes, for the Monte Carlo transport codes (GEANT4 and PHITS), have been simulated. i.e., for the particle spectra a couple of ionization chambers were simulated before and after a layer of varying thickness of material. The complete setup was simulated packed, i.e., no air between the different layers of material.
Results have been presented for 2 different SPE proton spectra (ESP and "worst hour", August 72 (Aug72)) as well as for the carbon beam measured at HIT (430.1 MeV/u) by the GSI team [3].

Summary and Outlook

With these initial results, we show that TRiP98 may be efficiently used for dose reduction analysis in different materials, even if further efforts will be needed for a closer reproduction of the experimental data. A high energy extension of the transport code, i.e. in the GeV region, allowing description of GCR scenarios, is one of the next steps to take.

Material	*Aeric density (g/cm²)*	*Absolute depth (mm)*	*DR (%) (TRiP98)*	*DR (%) (Exp)*	*DR/masss (%/(g/cm2)) (TriP98)*
No target	0	0	100	100	
Water	3.49	35	95.0	97.74	1.43
PMMA	3.57	30	94.7	97.42	1.48
LiH	0.58	11	98.0	99.05	3.44
"	2.33	44	93.2	96.03	2.91
"	5.82	110	85.0	90.65	2.57
Alu2024	0.56	2	99.3	99.99	1.25
"	2.82	11	97.0	99.78	1.06
"	8.47	32	93.0	99.13	0.82

Table 1: Dose reduction (DR) for a carbon ion beam at 430.1 MeV/u with different shielding materials obtained with TRiP98 and compared to HIT experiments [3]

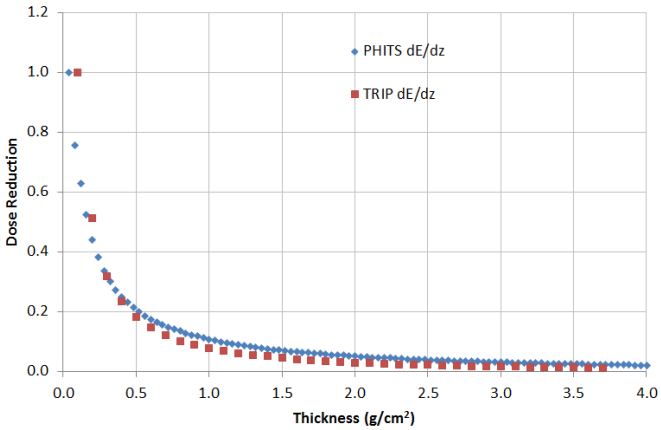

Figure 1: Comparison of depth dose profile of the Aug72 proton Spectrum in water as computed by TRiP98 and PHITS.

References

[1] M. Krämer and M. Durante, Ion beam transport calculations and treatment plans in particle therapy, Eur. Phys. J. D **60**, 195 (2010).
[2] M. Krämer, TRiP98 (TReatment PlannIng for Particles), THREE - Heal. Risk Extraterr. Explor. 2012, 1 (2012).
[3] U. Weber et al., Dose attenuation measurements in the ROSSINI-2 project for space research, GSI Sci-Rep 2016-1, Biophysics-46, p. 234 (2014).

* ROSSINI-2 is supported by ESA (Contr. No.4000112525/14/NL/LF)

#m.kraemer@gsi.de

DOI:10.15120/GR-2017-1

Entanglement of pygmy skin and core polarization modes in ^{206}Pb

N. Tsoneva and H. Lenske
Institut für Theoretische Physik, Universität Gießen

In this report we present our recent theoretical results on dipole response in the neutron-rich ^{206}Pb. The calculations are obtained in advanced microscopic theory of high predictive power, based on energy-density functional (EDF) and three-phonon quasiparticle-phonon model (QPM) [1, 2, 3]. In the focus of our studies are electric and magnetic dipole excitations with energies up to 25 MeV. Of special interest is the Pigmy Dipole Resonance (PDR) mode [3, 4] which incorporates the dynamics of the nuclear isospin at the nuclear surface. Thus, the PDR may provide useful information on fundamental properties of the nucleus such as neutron and proton root-mean-square radii, nuclear skin thickness and symmetry energy [5]. Despite of many experimental and theoretical evidences on the close relation between the PDR and the neutron skin, presently a direct method to extract experimentally the neutron skin thickness from the PDR does not exist [4]. This could be related to the fact that at excitation energies below the neutron separation energy the PDR coexists with a variety of modes, such as the tail of the GDR, magnetic dipole and multi-phonon excitations [2, 3]. So far the low-energy distribution of the GDR is elusive. The question that arises in this connection is how to differentiate the contributions of different origin to the low-energy photoabsorption spectra and in particular the PDR and GDR modes which are supposed to have the largest impact, in addition to other modes [3]. Theoretically, the problem could be solved within our three-phonon EDF+QPM approach which is one of the most elaborated multi-quasiparticle and multi-phonon approaches that has been proven successful in various scenarios [1, 2, 3, 6, 7].

Spectral distribution of the newly studied low-energy E1 and M1 strengths in ^{206}Pb (S_n = 8.087 MeV) are shown in Fig. 1. It is found that the fragmentation of the E1 strength is due to the interaction of the QRPA PDR states with those from the GDR tail and also with multi-phonon configurations with different spin and parities. The detailed EDF+QPM analysis of the E1 transition matrix elements strongly suggests that the PDR dominates the distribution of the dipole strength up to about 7 MeV, at which point the tail of the GDR starts making an important contribution. Overall, the PDR and the GDR account for about 77% and 12% of the $E1$ strength below the neutron separation energy in ^{206}Pb, respectively. Also significant is the impact from multi-phonon states to the total E1 strength—and to a lesser extent to the M1 strength. The theoretical cumulative electric and magnetic dipole strengths are compared to recent high-resolution ($\vec{\gamma}$,$\vec{\gamma}'$) experiment from the HI$\vec{\gamma}$S facility which provides spins, parities, branching ratios, and decay widths of excited states [5]. From the EDF+QPM

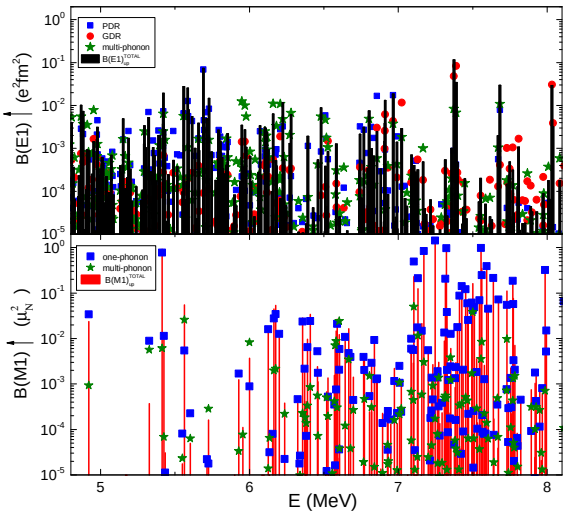

Figure 1: (Color online) B(E1) and B(M1) strength distributions of ^{206}Pb related to different counterparts of the transition matrix elements obtained from three-phonon EDF+QPM calculations.

calculations of both, E1 and M1 strengths up to 25 MeV in ^{206}Pb, we obtained also the total dipole polarizability α_D(^{206}Pb)=18.3 (fm^3/e^2) which is in good agreement with the HI$\vec{\gamma}$S data and earlier photonuclear experiments above the neutron threshold [5]. The comparison of the α_D value with the one obtained in ^{208}Pb [8] shows a decrease of ≈3% in ^{206}Pb. This is found correlated with the decrease of the neutron skin thickness of ^{206}Pb which value is ≈4% less than that of ^{208}Pb.

References

[1] N. Tsoneva *et al.*, **B586**, 213 (2004).

[2] N. Tsoneva, H. Lenske, Phys. Rev. C **77**, 024321 (2008).

[3] N. Tsoneva, H. Lenske, Physics of Atomic Nuclei, Vol. 76, pp. 885-903 (2016) and refs. therein.

[4] D. Savran *et al.*, Prog. Part. Nucl. Phys. **70**, 210 (2013).

[5] A. Tonchev *et al.*, Phys. Lett. B, submitted.

[6] N. Tsoneva, H. Lenske, Phys. Lett. B **695**, 174 (2011).

[7] N. Tsoneva *et al.*, Phys. Rev. C **91**, 044328 (2015).

[8] A. Tamii *et al.*, Phys. Rev. Lett. **107**, 062502 (2011).

DOI:10.15120/GR-2017-1

Gogny-HFB self-consistent blocking for odd-A and odd-odd nuclei*

A. Arzhanov[1,2], *G. Martínez Pinedo*[1,2], *L. M. Robledo*[3], *and T. R. Rodríguez*[3]

[1]Institut für Kernphysik, TU Darmstadt, D-64289 Darmstadt, Germany; [2]GSI Helmholtzzentrum für Schwerionenforschung, D-64291 Darmstadt, Germany; [3]Departamento de Física Teórica, UAM, E-28049 Madrid, Spain

Self-consistent blocking within Gogny-HFB

A self-consistent description of odd-A and odd-odd nuclei breaks the time-reversal symmetry. This makes their study more involved than the one of even-even nuclei in different aspects. In the case of Gogny energy density functional (EDF), the Hartree-Fock and pairing fields possess both T-even and T-odd components. For even-even nuclei the T-odd terms intricately vanish in the nuclear ground state calculations of $J^\pi = 0^+$ configurations, and therefore can be disregarded in numerical computations. However, for odd nuclei the T-odd fields have to be treated explicitly in the calculations. This fact lifts the two-fold Kramer's degeneracy of the HFB quasi-particles (q.p.) states, thereby at least doubling the computational effort already in this aspect. Moreover, a fully self-consistent variational calculation for odd nuclei usually requires to block multiple low-lying q.p. states separately to later identify the configuration leading to the lowest ground state energy solution, thereby making the calculation scheme even more sophisticated and time-consuming. Because of the heavy computational burden, most of the recent calculations either ignored the T-odd fields completely, or involved approximative blocking techniques while keeping the benefits of time-reversal symmetry.

Global survey

We have performed a large-scale self-consistent calculation including all T-odd components of Gogny EDF to calculate both odd-A and doubly odd nuclei up to the neutron drip lines from $Z = 8$ up to $Z = 134$. We have also employed the widely used perturbative quasiparticle addition (PQPA) approximative method, and compared the results from both methods with the experimental values.

Both PQPA and T-odd global calculations exhibit a common trend of decreasing spread of the neutron pairing gaps for heavier elements. In the case of PQPA, the gaps tend to decrease in their strength for heavier isotopic chains, which is not visible in the T-odd calculations. The systematic decrease of the gap strength with the mass number is also present for the experimental gaps (gray regions on the Fig.), which follow a general trend $\Delta_n^{(3)} \approx 12/\sqrt{A}$ MeV based on the global fit. Another feature on the global scale is the occurrence of many narrow dips in the PQPA results – particularly noticeable in the region $N \approx 50 - 120$. The T-odd gaps appear to be more smeared out, with only a couple of major well-established dips occurring in vicinity from the magic numbers $N = 28, 50, 82, 126$. Besides the fact that the PQPA approximation overall yield larger gaps than T-odd calculations, there is an apparent tendency of odd-Z gaps having weaker strength than in the even-Z chains. This feature is qualitatively visible in the Figure, where the odd-Z chains (blue) are shifted downwards with respect to the even-Z chains (red), whereas the PQPA calculatations clearly do not exhibit this feature. This is quantitatively verified: the calculated number of 1985 even-Z and the same number of odd-Z pairing gaps have an identical average of 0.95 MeV, whereas the T-odd calculations for the same nuclei have 0.73 MeV and 0.62 MeV for even-Z and odd-Z cases, respectively. This dependence on proton number parity is also established experimentally, where the total number of 556 even-Z gaps are found to have 1.06 MeV, while the 508 established odd-Z gaps yield 0.76 MeV on average. Interestingly, the standard deviation in all the cases of calculated gaps is found to be $\sim$0.28 MeV.

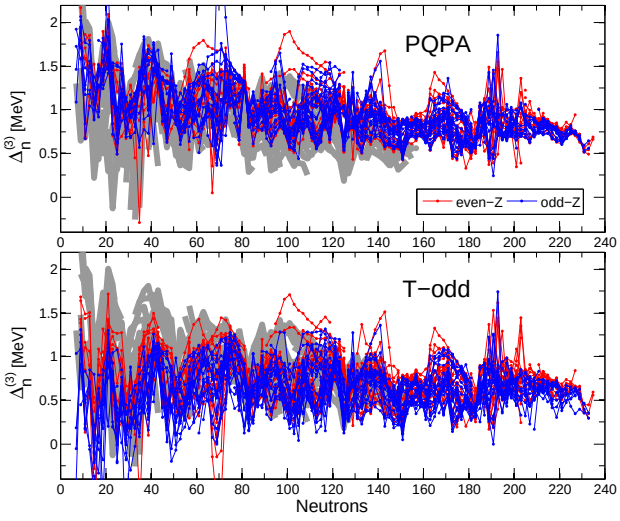

Figure 1: Pairing gaps from PQPA (upper panel) and T-odd (lower panel) even-Z (red) and odd-Z (blue) calculations. Gray region represents experimental pairing gaps.

Overall, the pairing strength of D1S functional is adequate to describe important qualitative features of the experimentally known gaps, but their mass dependence is not very well reproduced in T-odd calculations. Ultimately, in order to improve the theoretical results, the T-odd interaction should be re-examined, while also exploring the impact of beyond-mean-field correlations.

* Work supported by Helmholtz Association through Nuclear Astrophysics Virtual Institute (VH-VI-417 /HGF/ NAVI GSI).

DOI:10.15120/GR-2017-1

The Wigner function of the deuteron

T. Neff[1] *and H. Feldmeier*[1,2]
[1]GSI, Darmstadt, Germany; [2]FIAS, Frankfurt, Germany

Short-range correlations in nuclei are induced by the strong repulsion and the strong tensor force found in realistic nucleon-nucleon interactions. They are usually investigated in coordinate space where they are reflected in a suppression of the two-body density at short distances or in momentum space where they manifest themselves in high-momentum components of one- and two-body densities [1]. This short-range physics is usually contrasted with the low momentum part that contains mainly long-range correlations which are describable by superpositions of a smaller number of uncorrelated Slater determinants.

To provide a better intuitive picture for how long- and short-range or low- and high-momentum physics are connected we decided to investigate the Wigner function of the deuteron. The Wigner function or Wigner representation is the quantum mechanical analogue of the classical phase space distribution [2] and contains the full information about the system as given by its wave function or the density matrix.

$$W(\vec{r},\vec{p}) = \frac{1}{(2\pi)^3}\int d^3s\, \left\langle \vec{r}+\tfrac{1}{2}\vec{s}\right| \widehat{\rho} \left|\vec{r}-\tfrac{1}{2}\vec{s}\right\rangle e^{-i\vec{p}\cdot\vec{s}} \quad (1)$$
$$= \frac{1}{(2\pi)^3}\int d^3\varkappa\, \left\langle \vec{p}+\tfrac{1}{2}\vec{\varkappa}\right| \widehat{\rho} \left|\vec{p}-\tfrac{1}{2}\vec{\varkappa}\right\rangle e^{i\vec{\varkappa}\cdot\vec{r}}$$

The Wigner function furthermore makes a comparison with the classical picture possible and highlights the quantum-mechanical nature of short-range correlations.

The Wigner functions $W(r,p)$ obtained with realistic AV8' and N3LO interactions show a characteristic behavior. One can distinguish between a dominant low-momentum region that is unaffected by short-range correlations and a high-momentum region that shows a shoulder at distances up to 1.5 fm and that extends to high relative momenta. Another characteristic feature is an oscillating behavior of the Wigner function extending to large arguments $rp \approx \text{const.}$. The contribution of short-range correlations is highlighted when the Wigner functions for the bare AV8' and N3LO interactions (as shown in Fig. 1 are compared to those obtained with softened interactions in the SRG approach. The SRG transformation decouples low- and high-momentum modes and essentially eliminates short-range correlations. This is reflected in the Wigner functions that are very similar to those obtained with the bare interactions in the low-momentum region, but that become more and more suppressed in the high-momentum region with increasing flow parameter. If the Wigner function is interpreted as a quasi-probability distribution one can define partial momentum distributions that are obtained by integrating over pairs at small and large distances respectively.

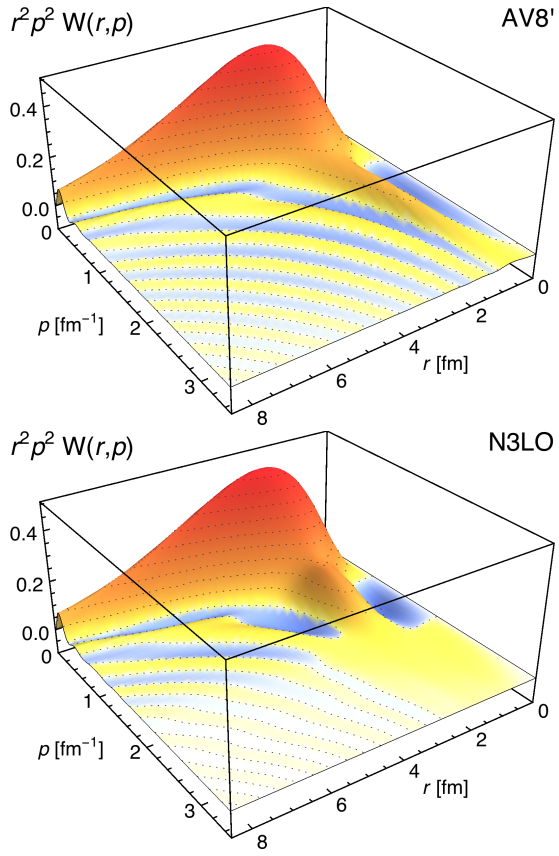

Figure 1: Wigner functions of the deuteron scaled with phase space volume element $r^2p^2W(r,p)$ for the AV8' interaction (top) and the chiral N3LO interaction (bottom).

In case of the AV8' interaction there is a clear separation between a small- and large distance scale. Pairs at small distances generate the high-momentum components. This separation is not so clear for the N3LO interaction. This interaction contains regulators that affect the wave function even at large distances and generate high-momentum components.

References

[1] T. Neff, H. Feldmeier, W. Horiuchi, Phys. Rev. C **92**, 024003 (2015).

[2] E. Wigner, Phys. Rev. C **40**, 749 (1932).

[3] T. Neff, H. Feldmeier, arXiv:1610.04066

DOI:10.15120/GR-2017-1

The ν process in core-collapse supernova nucleosynthesis *

A. Sieverding[†1], *G. Martínez-Pinedo*[1,2], *and K. Langanke*[2,1]

[1]Institut für Kernphysik (Theoriezentrum), Technische Universität Darmstadt, Schlossgartenstraße 2, 64289 Darmstadt, Germany; [2]Gesellschaft für Schwerionenforschung Darmstadt, Planckstr. 1, D-64259 Darmstadt, Germany

Supernova explosions mark the end of the lives of stars that are born more massive than 8-10 $M_\odot$ and are accompanied by the emission of a large number of neutrinos of all flavors from the collapsing stellar core which are not only important for the explosion itself but also interact with the bulk of the stellar material which is finally ejected. Neutrino-nucleus interactions can lead to inverse beta-decay (charged-current) and nuclear excitations above particle separation threshold (charged- and neutral-current). Emitted light particles then provide additional fuel for further thermonuclear reactions. These direct and indirect effects of neutrinos are referred to as the ν process. Compared to previous studies of this process [1] that have assumed average neutrino energies of $\langle E_{\nu_e}\rangle = 13$ MeV, $\langle E_{\bar{\nu}_e}\rangle = 15$ MeV and $\langle E_{\nu,\bar{\nu}_{\mu,\tau}}\rangle = 19$ MeV recent progress in supernova simulations has corrected the expected neutrino energies significantly downward to values around $\langle E_{\nu_e}\rangle = 9$ MeV, $\langle E_{\bar{\nu}_e}\rangle = \langle E_{\nu,\bar{\nu}_{\mu,\tau}}\rangle = 13$ MeV. This results in a general reduction of the effect of the ν process but also in a larger sensitivity to charged-current reactions that proceed through low-lying transitions. This has motivated the effort to derive charged-current neutrino nucleus cross sections from experimentally measured data [2]. We have performed a set of nucleosynthesis calculations for a range of supernova progenitor models with initial masses between 13-30 $M_\odot$ presented in [4] using parametric explosion models based on the hydrodynamics code KEPLER which is a significant improvement compared to the results presented in [3]. The model is tuned to achieve an explosion energy of 1.2×10^{51} erg for all progenitor models and we assume that 3×10^{53} erg are emitted as neutrinos equally distributed over all 6 flavors.

Nucleus	no ν	Low energies	High energies
^{7}Li	0.002	0.07	0.45
^{11}B	0.008	0.36	1.54
^{19}F	0.12	0.19	0.33
^{138}La	0.12	0.55	1.15
^{180}Ta	0.19	0.49	0.88

Table 1: Production factors relative to solar abundances normalized to ^{16}O production without neutrinos, with our choice of neutrino energies ("Low energies"), and with the choice of ref. [1] ("High energies"). For ^{180}Ta we assume that 35% survive in the long-lived isomeric state

Table 1 shows the production factors we have obtained comparing calculations without neutrinos to the probably more realistic low energy neutrinos and also the "canonical" neutrino energies averaged over the progenitor mass with progenitor masses distributed according to the empirical Salpeter initial mass function $\mathrm{d}n_*/\mathrm{d}m_* \propto m_*^{-1.35}$. With the low neutrino energies the ν process cannot account for the production of the light elements ^{7}Li and ^{11}B and ^{19}F to full solar abundance. However, for ^{7}Li and ^{11}B irradiation by galactic cosmic rays can provide an additional contribution. ^{138}La and ^{180}Ta remain as the most sensitive to neutrino interactions and could be produced predominantly by the ν process. We have also explored the production of the radioactive isotopes ^{26}Al, ^{44}Ti and ^{60}Fe that are important for γ-ray astronomy that are summarized in table 2. Especially for low energies we find only minor effects for ^{26}Al and almost no effect for ^{44}Ti and ^{60}Fe. However, we find quite a significant enhancement of the production of ^{22}Na that has been found in pre-solar grains of supernova origin.

Nucleus	no ν	Low energies[1]	High energies[2]
^{22}Na	2.41×10^{-6}	3.02×10^{-6}	3.74×10^{-6}
^{26}Al	4.29×10^{-5}	4.64×10^{-5}	5.27×10^{-5}
^{44}Ti	1.48×10^{-5}	1.49×10^{-5}	1.56×10^{-5}
^{60}Fe	7.58×10^{-5}	7.53×10^{-5}	7.56×10^{-5}
^{92}Nb	4.53×10^{-11}	9.69×10^{-11}	16.73×10^{-11}
^{98}Tc	2.84×10^{-11}	3.38×10^{-11}	4.10×10^{-11}

Table 2: Yields of of radioactive isotopes in $M_\odot$ averaged over progenitor masses for different choices of neutrino energies

References

[1] A. Heger, E. Kolbe, W. Haxton, K. Langanke, G. Martínez-Pinedo, S. E. Woosley, "Neutrino nucleosynthesis", Phys. Lett. B 606, 258

[2] A. Sieverding, , G. Martínez-Pinedo, T. Marketin, K. Langanke , "Charged-current neutrino-nucleus cross-sections for the ν process" , GSI Scientific Report 2015 (2016), 242

[3] A. Sieverding , G. Martínez-Pinedo, K. Langanke "Neutrino Nucleosynthesis of radioactive nuclei in supernovae" , GSI Scientific Report 2014 (2015), 341

[4] A. Heger, S. E. Woosley, "Nucleosynthesis and remnants in massive stars of solar metallicity" Physics Reports 442 (2007), 269

* Work supported by NAVI and by the DFG through SFB 1245

† a.sieverding@gsi.de

DOI:10.15120/GR-2017-1

r-process abundances from BCPM fission properties*

S. A. Giuliani[†1], *G. Martínez-Pinedo*[1,2], *L. M. Robledo*[3], *and M.-R. Wu*[4]

[1]Institut für Kernphysik (Theoriezentrum), Technische Universität Darmstadt, Schlossgartenstraße 2, 64289 Darmstadt, Germany; [2]GSI Helmholtzzentrum für Schwerioneneforschung, Planckstraße 1, 64291 Darmstadt, Germany; [3]Departamento de Física Teórica, Universidad Autónoma de Madrid, E-28049 Madrid, Spain.; [4]Niels Bohr International Academy, Niels Bohr Institute, Blegdamsvej 17, 2100 Copenhagen, Denmark

The r-process is invoked in order to explain the existence of nuclei heavier than iron that are observed in the Universe. Even though its astrophysical site is not (yet) known, recent simulations suggest the merger of two neutron star (NSM) as a likely candidate. In such astrophysical site seed nuclei can capture a large number of free neutrons reaching the fissioning region by successive neutron-captures and beta-decays. In this case fission plays a crucial role by terminating the r-process path, shaping the second peak and providing a mechanism for robust abundances [1]. In this report, we present the results of r-process calculations for dynamical ejecta in NSM based on the fission properties computed using the Barcelona-Catania-Paris-Madrid (BCPM) energy density functional (EDF) [2, 3].

In a recent publication we studied the fission properties of r-process nuclei predicted by the BCPM EDF [4]. We consistently computed fission barriers, collective inertias and neutron separation energies and used them as a nuclear input for the calculation of stellar reactions rates of neutron-induced reactions relevant for r-process in the region $84 \leq Z \leq 120$ and $118 \leq N \leq 250$. The rates were obtained within the statistical theory using the Back-shifted Fermi gas model for level densities and the Kopecky-Uhl generalized Lorentzian gamma-ray strength functions implemented in the TALYS code. Fig. 1 shows the final r-process abundances obtained from the BCPM neutron-induced stellar rates for a single standard trajectory simulating the dynamic ejecta in neutron star mergers. For comparison, the plot also shows the abundances obtained from the neutron-induced stellar rates computed by Panov *et al.* [5] based on the FRDM nuclear masses and Thomas-Fermi fission barriers.

Our calculations predict larger barriers and shell gaps for nuclei around the magic number $N = 184$. This results in a larger accumulation of material in the region $A \sim 280$. Lately this material decays by fission enhancing the abundances above the second peak ($A \sim 150$). Conversely, the larger shell gap predicted by the FRDM mass model around $N = 172$ induces an accumulation of material at $A \sim 257$ that enhances the abundances below the second peak $A \sim 110$. These results prove the extreme sensitivity of the r-process abundances to local variations in the binding energies and to the fission properties of the r-process nuclei. On the other hand, comparing the ratio of the ^{232}Th and ^{238}U cosmochronometers and the radioactive energy emitted at timescales relevant for macronova observations we did not find a significant difference between both models. This suggests that in both calculations the production of actinides during the build up of heavy nuclei is similar [6], which is due to the fact that we only changed the rates of nuclei with $Z \geq 84$.

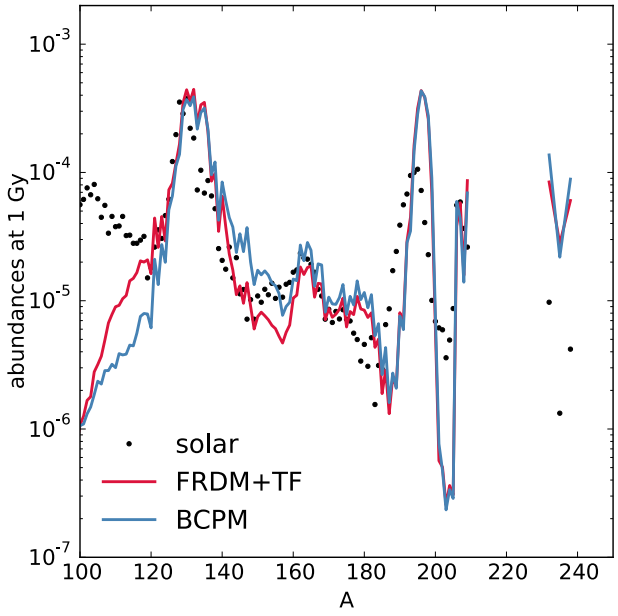

Figure 1: r-process abundances for two different sets of neutron-induced stellar rates: BCPM (blue line) and Panov et al. [5] (red line) at 1 Gy. Circles represent the solar r-process relative abundances.

References

[1] J. J. Mendoza-Temis et al., Phys. Rev. **C92**, 055805 (2015).

[2] M. Baldo et al., Phys. Rev. **C87**, 064305 (2013).

[3] S. A. Giuliani et al., Phys. Rev. **C88**, 054325 (2013).

[4] S. A. Giuliani, G. Martinez-Pinedo and L. M. Robledo, arXiv:1704.00554 [nucl-th].

[5] I. V. Panov et al., *Astron. Astrophys.* **513**, A61 (2010).

[6] J. Barnes et al., Astrophys. J. **829**, no. 2, 110 (2016)

* SAG, GMP and MRW acknowledge support from the the Helmholtz Association through the Nuclear Astrophysics Virtual Institute (VH-VI-417), and the BMBF-Verbundforschungsprojekt number 05P15RDFN1. MRW acknowledges support from the Villum Foundation (Project No. 13164) and the Danish National Research Foundation (DNRF91). The work of LMR was supported in part by the Spanish Ministerio de Economía y Competitividad (MINECO), under Contracts Nos. FIS2012-34479, FPA2015-65929, FIS2015-63770 and by the Consolider-Ingenio 2010 Program MULTIDARK.

† giuliani@theorie.ikp.physik.tu-darmstadt.de

Form-factor dependence of neutrino-nucleon interactions in supernova environment*

A. Lohs[1] *and G.Martinez-Pinedo*[1]
[1]GSI, Darmstadt, Germany

Highly energetic neutrinos in compact stellar objects are able to probe the weak form factor of (quasi)free nucleons to a sizeable extent. We present an implementation of this form factor dependence in the computation of the neutrino inverse mean free path in order to model more accurately the transport of neutrinos in dense baryonic matter.

Introduction

In semileptonic neutrino-nucleon reactions, such as (anti)neutrino absorption or scattering, the momentum transfer dependence of the weak nucleon form factors modifies the cross-section at 2nd order in neutrino energy over nucleon mass, $(E_\nu/m_N)^2$. For highly energetic supernova neutrinos in the range of several tens of MeV, these corrections need to be considered to accurately model many aspects of neutrino transport e.g. neutrino spectra formation or the neutrino driven wind (see e.g.[1]).

For the conditions which are present in astrophysical scenarios such as core-collapse supernovae or neutron star mergers, the dominating weak neutrino-nucleon interactions can be sufficiently described by a current-current Lagrangian with effective weak nucleon couplings. These nucleon couplings are sensitive to the momentum transfer, since highly energetic neutrinos are able to probe the nucleon's structure. The corresponding weak nucleon form factors can be directly related to the electromagnetic ones which are experimentally better accessible. For the important axial-vector coupling one finds

$$G_A(q^2) = G_A(0)\left(1-\frac{q^2}{m_A^2}\right)^{-2}, \text{with } m_A \simeq 1.206\,\text{GeV}$$

where m_A is the so called axial mass. Similar relations are found for the vector coupling G_V and the tensor coupling F_2.

Recently we were able to explicitly include this behaviour in the semianalytic computation of the cross sections for these reactions, i.e. into the phase space integration over the reaction matrix element. Describing the strong interaction among the nucleons in the framework of *relativistic mean field*, one can show that for all the different couplings in the effective nucleon current the form factor dependence is well approximated by the relation

$$G_X G_Y(q^2) = G_X G_Y(0)\left(1+\frac{4q^2}{m_{XY}^2}\right)$$

The pure vector component G_V^2 for example is described by $1/m_{VV}^2 = 1/M_V^2 - F_2(0)/8m_N$, where $M_V \simeq 0.84\,\text{GeV}$ is the so called vectorial mass.

Results

Using the above relation one can compute the inverse mean free path $1/\lambda(E_\nu)$ from a simple 2D-numerical integral, without the need for further simplifications regarding the kinematics or the degree of relativity of any of the participating particles. For representative conditions at the neutrinosphere, the quenching of the energy dependent inverse mean free path is shown in Fig.1 for (anti)neutrino absorption on neutrons (protons) by the solid (dashed) curve.

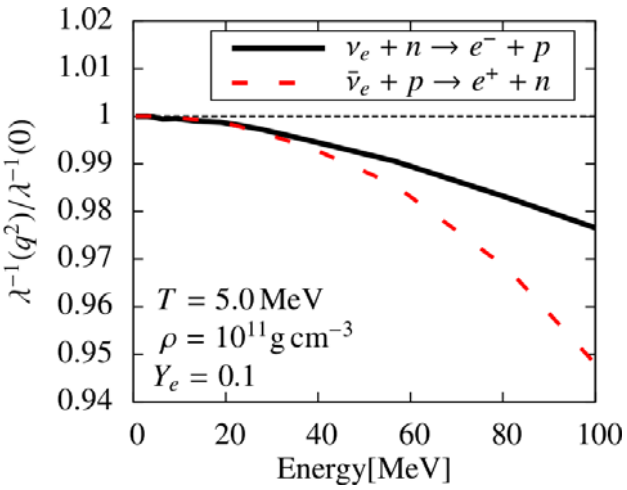

Figure 1: Quenching of neutrino inverse mean free path due to weak nucleon form factor.

The quenching is larger for $\bar{\nu}_e$ compared to ν_e. In general it is smaller than 1% for neutrino energies below $40-50\,\text{MeV}$, and it just reaches 5% for antineutrinos with $E_{\bar{\nu}_e} \sim 100\,\text{MeV}$. While we expect a rather small impact on the emerging neutrino spectra, we still recommend the inclusion of this effect when considering nucleon recoil effects, since it adds no further numerical complexity.

References

[1] C.J. Horowitz,"Weak magnetism for antineutrinos in supernovae", Phys.Rev. D65 (2002) 043001

* The work of A.L. is partly supported by GSI, University of Basel, and by the Helmholtz Association through the Nuclear Astrophysics Virtual Institute (VH-VI-417).

DOI:10.15120/GR-2017-1

High-mass twin neutron stars with hybrid equations of state and the existence of a critical end point in the QCD phase diagram*

S. Typel[†1,2], *D. Alvarez-Castillo*[3], *and D. Blaschke*[3,4,5]

[1]IKP, TU Darmstadt, Darmstadt, Germany ; [2]GSI, Darmstadt, Germany; [3]BLTP, JINR, Dubna, Russia; [4]National Research Nuclear University (MEPhI), Moscow, Russia; [5]ITP, University of Wrocław, Wrocław, Poland

The equation of state (EoS) of strongly interacting matter at almost vanishing temperature and baryon densities above the nuclear saturation density determines fundamental properties of neutron stars and in particular their mass-radius relation. The observation of compact stars with precisely determined masses around two solar masses [1, 2, 3] puts already severe constraints on models for high-density matter [5] requiring a rather stiff EoS. In contrast, present-day measurements of neutron star radii give ambiguous results and still suffer from large uncertainties. Future x-ray satellite mission like NICER [4] are expected to provide more precise constraints on compact star radii.

A sufficiently strong first-order phase transition from hadronic to deconfined quark matter could affect the mass-radius relation with the possible existence of a third family of compact stars. The observation of "mass twins", i.e. compact stars with the same mass but a measurable radius difference of about $1 - 2$ km, and a gap in the mass-radius relation would support the existence of at least one critical end point (CEP) in the QCD phase diagram [6] because lattice QCD calculations established that the transition from hadronic to quark matter is a crossover on the temperature axis at zero baryochemical potential, see, e.g., [7, 8].

The consequences of a first-order phase transition on the structure of compact stars can be explored by providing suitable EoSs of the hadronic and quark matter phases for the construction of the phase transition with the conditions of β equilibrium and charge neutrality. A generalized relativistic density functional with well calibrated density dependent couplings [9], which fulfills most current constraints from nuclei and nuclear matter, is used for the microscopic description of the hadronic phase. Excluded-volume effects are considered at suprasaturation densities in the thermodynamically consistent approach of Ref. [10] that can model a stiffening or softening of the EoS employing effective, density-dependent degeneracy factors. This homogeneous neutron star matter EoS is supplemented by an appropriate crust EoS at densities below nuclear saturation. Quark matter is described in a QCD motivated extended Nambu–Jona-Lasinio model with higher-order interactions [11] that allows a stiffening of the EoS by a variation of the eight-quark coupling parameter. The two-phase/hybrid EoS is prepared from the two models using the standard Maxwell construction assuming a coexistence of both phases with macroscopic size neglecting surface effects. The Tolman-Oppenheimer-Volkoff equations are solved to generate sequences of compact stars and the resulting mass-radius relations for various parameter sets.

A Bayesian analysis of the parameter dependence for the hybrid EoSs has been performed with given observational constraints for the mass and radius of compact stars [12]. It was shown that the observation of high-mass twin stars would have the power to discriminate between hybrid EoS models with strong first-order phase transitions and alternative EoS models. In addition, it was observed that there is a correlation between the maximum radius of the horizontal branch in the mass-radius diagram and the pressure at the onset of the hadron-to-quark matter transition. This is likely a quantity of utmost relevance for upcoming experiments with heavy-ion collisions (HICs) at FAIR and NICA. It is in striking agreement with the "universal" hadronization pressure extracted from the analysis of chemical freeze-out in HICs [13].

In the future, the robustness of the high-mass twin-star phenomenon with respect to the precise form of the hadron-to-quark phase transition has to be investigated, in particular by considering a mixed phase where pasta-like structures appear [14] similar as at the crust-core boundary in neutron stars.

* Work supported by COST action MP 1304 "NewCompStar", Polish NCN under grant No. UMO-2014/13/B/ST9/02621, Heisenberg-Landau programme, Bogoliubov-Infeld programme, LOEWE, HIC for FAIR, HGF, and NAVI (VH-VI-417).

† s.typel@gsi.de

References

[1] P. Demorest *et al.*, Nature **467** (2010) 1081

[2] J. Antoniadis *et al.*, Science **340** (2013) 6131

[3] E. Fonseca *et al.*, Astrophys. J. **832** (2016) 167

[4] K. C. Gendreau *et al.*, Proc. SPIE **9905** (2016) 99051H

[5] M. Oertel, M. Hempel, T. Klähn and S. Typel, Rev. Mod. Phys. **89** (2017) 015007

[6] D. Alvarez-Castillo, S. Benic, D. Blaschke, S. Han and S. Typel, Eur. Phys. J. A **52** (2016) 232

[7] S. Borsanyi *et al.*, Phys. Lett. B **730** (2014) 99

[8] A. Bazavov *et al.* [HotQCD Collaboration], Phys. Rev. D **90** (2014) 094503

[9] S. Typel *et al.*, Phys. Rev. C **81** (2010) 015803

[10] S. Typel, Eur. Phys. J. A **52** (2016) 16

[11] S. Benic, D. Blaschke, D. E. Alvarez-Castillo, T. Fischer and S. Typel, Astron. Astrophys. **577** (2015) A40

[12] D. Alvarez-Castillo, A. Ayriyan, S. Benic, D. Blaschke, H. Grigorian and S. Typel, Eur. Phys. J. A **52** (2016) 69

[13] M. Petran and J. Rafelski, Phys. Rev. C **88** (2013) 021901

[14] D. E. Alvarez-Castillo and D. Blaschke, Phys. Part. Nucl. **46** (2015) 846

DOI:10.15120/GR-2017-1

Matter in neutron star mergers vs. matter in heavy ion collisions*

A. Mukherjee[†1], *J Steinheimer*[1], *S. Schramm*[1,2], *and H. Stöcker*[1,2,3]

[1]Frankfurt Institute for Advanced Studies; [2]Institut für Theoretische Physik, Goethe Universität, Frankfurt am Main; [3]GSI Helmholtzzentrum für Schwerionenforschung GmbH

Gravitational waves (GWs) have been recently observed from a pair of merging black holes (BHs) by the LIGO detectors [1] and GWs emitted from merging neutron star (NS) binaries are on the verge of their first detection. The equation of state (EOS) of elementary matter might be deduced by a frequency analysis of the GW [2, 3], which is interesting, as the EOS of quantum chromo dynamics (QCD) is mainly investigated by high energy heavy ion collisions. In heavy ion experiments at particle accelerators, heavy nuclei collide to create a small system which is expected to have a Temperature of $T \geq 80$ MeV and densities several times the nuclear ground state density. It is therefore very intriguing to study QCD matter at similar temperatures and densities in two rather different 'experimental' setups, in neutron star mergers and heavy ion collisions.

Densities in NS mergers and nuclear collisions

In order to determine the temperature of the system at given densities, one requires knowledge on the effective degrees of freedom of the system, encoded in the equation of state. Depending on the EOS used, the Temperatures reached in these relativistic collisions and neutron star mergers may vary significantly. It is consequently most important to employ an EOS that entails a realistic set of degrees of freedom as well as interactions.

The model we employed is the so called Quark-Hadron Chiral Parity Doublet Model (QχP) [4, 5]. This approach describes the thermodynamics of the transition from a hadronic chiral model to a deconfined quark phase.

A straight forward way of consistently connecting the features of the EOS with the maximally achievable compression of a relativistic collision is by employing the so called Rankine-Hugoniot-Taub-Adiabat [6]. If the EoS, i.e. the connection between pressure, energy density and baryon density is know (as p(ϵ,ρ)), then one can calculate the maximum compression in a collision by solving the following Taub-equation:

$$(\rho_0\, X_0)^2 - (\rho\, X)^2 - (p_0 - p)(X_0 + X) = 0 \quad (1)$$

with $X = (\epsilon + p)/\rho^2$, the generalized volume. For simplicity we assume $p_0 = 0$. One can furthermore connect the center of mass gamma factor $\gamma_{\rm c.m.}$ of the colliding slabs to the densities created using $\gamma^2_{\rm c.m.} = \left(\frac{\epsilon\ \rho_0}{\rho\ \epsilon_0}\right)^2$. The resulting beam energy dependence of the net-baryon density and temperatures reached is shown in figure 1 (left) for two different scenarios:

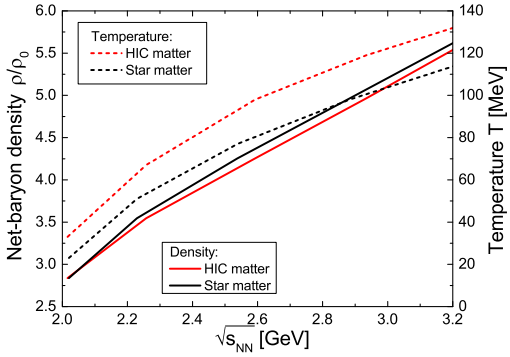

Figure 1: Largest net-baryon density (solid lines) and Temperatures (dashed lines) achieved in collisions of heavy ions and compact stars at a given center of mass beam energy $\sqrt{s_{\rm NN}} = 2 \cdot \gamma_{\rm c.m.} \cdot m_N$. Due to the different properties of the EoS as function of iso-spin the temperatures in heavy ion collisions are larger and densities slightly smaller, at the same relative velocities.

1. The EOS for heavy ion collisions, i.e. with conserved strangeness and no beta-equilibrium
2. The EOS for compact stars, i.e. in beta-equilibrium

Figure 1 presents, for different center of mass energies, the compressions achieved, using the Rankine-Hugoniot-Taub-Adiabat with the QχP EOS. This figure highlights the difference in the compression in collisions of projectiles with iso-spin symmetric matter (heavy ion collisions) and asymmetric matter (NS mergers).

References

[1] B. P. Abbott *et al.* [LIGO Scientific and Virgo Collaborations], Phys. Rev. Lett. **116**, no. 6, 061102 (2016).

[2] K. Takami, L. Rezzolla and L. Baiotti, Phys. Rev. Lett. **113**, no. 9, 091104 (2014).

[3] L. Rezzolla and K. Takami, Phys. Rev. D **93**, no. 12, 124051 (2016).

[4] A. Mukherjee, J. Steinheimer and S. Schramm, arXiv:1611.10144 [nucl-th].

[5] J. Steinheimer, S. Schramm and H. Stocker, Phys. Rev. C **84**, 045208 (2011)

[6] A. H. Taub, Phys. Rev. **74**, 328 (1948).

* Work supported by GSI, BMBF, HIC4FAIR and HGShire.

† mukherjee@fias.uni-frankfurt.de

DOI:10.15120/GR-2017-1

Equation of state dependence of directed flow in a microscopic transport model*

Yasushi Nara[†1,2], *Harri Niemi*[3], *Jan Steinheimer*[2], *and Horst Stöcker*[2,3,4]

[1]Akita International University, Yuwa, Japan; [2]Frankfurt Institute for Advanced Studies; [3]Institut für Theoretishe Physik, Johann Wolfgang Goethe Universität; [4]GSI Helmholtzzentrum für Schwerionenforschung GmbH

The collective transverse flow measured in the heavy ion collisions is considered to be sensitive to the equation of state (EoS) of QCD matter. The softest region in the EoS with a (first-order) phase transition is expected to have significant influence on the directed flow $v_1 = \langle \cos\phi \rangle$ of nucleons [1, 2].

In this work [3], we shall examine effects of the EoS on the directed flow within the microscopic transport approach JAM by modifying the scattering style in the two-body collision term [4, 5]. In JAM [6], particle production is modeled by the excitation and decay of resonances and strings. In the standard cascade approach the two body collision term is implemented so that it does not generate additional pressure. Namely, the azimuthal angle in the two-body collision is randomly chosen. It is well known that the pressure can be controlled by changing the scattering style. Here we employ a method similar to that proposed in Ref. [4] in which the momentum change in each two-body collision between particle i and j at the space-time coordinates of q_i and q_j is related to the pressure $\Delta P = P - P_f$, where P_f is the free streaming part of the local pressure. The formula is given by $\Delta P = -\frac{\rho}{3(\delta\tau_i+\delta\tau_j)}(p_i' - p_i)^\mu (q_i - q_j)_\mu$, where ρ is the Lorentz invariant local particle density, $\delta\tau_i$ is the proper time interval between successive collisions, and $p_i' - p_i$ is the energy-momentum change of the particle i. P_f can be computed from the energy-momentum tensor $T^{\mu\nu}$: In this way, we control the pressure such that P coincides with any given EoS at an energy density $e = u_\mu T^{\mu\nu} u_\nu$.

In Fig. 1 we present the beam energy dependence of the slope of the directed flow dv_1/dy of protons in mid-central A+A collisions. The standard JAM cascade calculation predicts a minimum at around AGS energy. In the case of the EoS with the first order phase transition (JAM-1.Opt), we also see the minimum in the excitation function of the proton directed flow at almost the same beam energy as the cascade model. In addition, the slope is now negative as predicted by hydrodynamical approaches.

We therefore have shown that our approach provides an efficient method to control the EoS in a microscopic transport model, and our result yields qualitatively similar result as the pure hydrodynamical predictions. As predicted by hydrodynamical approach, the minimum of the directed flow, from a strong first order phase transition, is located at much lower beam energy than the STAR data.

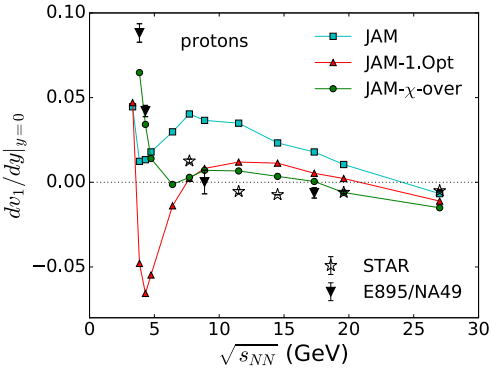

Figure 1: Beam energy dependence of the slope of the directed flow of protons in mid-central Au+Au collisions (10-40%) from JAM cascade mode (squares), JAM with first-order EoS (triangles) and with crossover EoS (circles) in comparison with the STAR/NA49/E895 data [7, 8, 9, 10, 11]. Local energy densities are computed by taking into account the contributions of constituent quarks.

References

[1] D. H. Rischke, Y. Pursun, J. A. Maruhn, H. Stoecker and W. Greiner, Heavy Ion Phys. **1**, 309 (1995)

[2] H. Stoecker, Nucl. Phys. A **750**, 121 (2005)

[3] Y. Nara, H. Niemi, J. Steinheimer and H. Stöcker, doi:10.1016/j.physletb.2017.02.020

[4] H. Sorge, Phys. Rev. Lett. **82**, 2048 (1999)

[5] Y. Nara, H. Niemi, A. Ohnishi and H. Stöcker, Phys. Rev. C **94**, no. 3, 034906 (2016)

[6] Y. Nara, N. Otuka, A. Ohnishi, K. Niita and S. Chiba, Phys. Rev. C **61**, 024901 (2000).

[7] L. Adamczyk *et al.* [STAR Collaboration], Phys. Rev. Lett. **112**, no. 16, 162301 (2014).

[8] P. Shanmuganathan [STAR Collaboration], Nucl. Phys. A **956**, 260 (2016)

[9] H. Liu *et al.* [E895 Collaboration], Phys. Rev. Lett. **84**, 5488 (2000);

[10] H. Appelshauser *et al.* [NA49 Collaboration], Phys. Rev. Lett. **80**, 4136 (1998);

[11] C. Alt *et al.* [NA49 Collaboration], Phys. Rev. C **68**, 034903 (2003).

*This work was supported in part by the Grants-in-Aid for Scientific Research from JSPS (Nos. 15K05079 and 15K05098), H. N. has received funding from the European Union's Horizon 2020 research and innovation programme under the Marie Sklodowska-Curie grant agreement no. 655285 and from the Helmholtz International Center for FAIR within the framework of the LOEWE program launched by the State of Hesse.

† nara@aiu.ac.jp

Traces of non-equilibrium dynamics in relativistic heavy-ion collisions*

P.Moreau[1,2,3], *Y. Xu*[4], *T. Song*[1,2,5], *M. Nahrgang*[4,6], *S. A. Bass*[4], *and E. Bratkovskaya*[2,3]

[1]Frankfurt Institute for Advanced Studies, Johann Wolfgang Goethe Universität, Frankfurt am Main, Germany; [2]Institute for Theoretical Physics, Johann Wolfgang Goethe Universität, Frankfurt am Main, Germany; [3]GSI Helmholtzzentrum für Schwerionenforschung GmbH, Planckstrasse 1, 64291 Darmstadt, Germany; [4]Department of Physics, Duke University, Durham, NC 27708, USA; [5]Institut für Theoretische Physik, Universität Gießen, Heinrich-Buff-Ring 16, 35392 Gießen, Germany; [6]SUBATECH UMR 6457 (IMT Atlantique, Université de Nantes, IN2P3/CNRS), 4 rue Alfred Kastler, 44307 Nantes, France

In this contribution, we summarize our work from [1] where we performed a comparison of two prominent models for the evolution of bulk QCD matter. The first one is a non-equilibrium transport approach, the Parton-Hadron-String-Dynamics (PHSD) [2, 3, 4], and the second one a 2D+1 viscous hydrodynamical model, VISHNew [5, 6] which is based on the assumption of local equilibrium and conservation laws. Both approaches give an excellent agreement with numerous experimental data, despite the very different assumptions inherent in these models. In PHSD, quasi-particles are treated in off-shell transport with thermal masses and widths which reproduce the lattice QCD equation of state and are determined from parallel event runs in the simulations. Hydrodynamics assumes local equilibrium to be reached in the initial stages of heavy-ion collisions and transports energy-momentum and charge densities according to the lattice QCD equation of state and transport coefficients such as the shear and bulk viscosity.

We have tried to match the hydrodynamical evolution as closely as possible to quantities like viscosities as obtained within PHSD. In general we find that the ensemble averages over PHSD events follow closely the hydrodynamical evolution. The major differences between the macroscopic near-(local)-equilibrium and the microscopic off-equilibrium dynamics can be summarized as:

1. The hydrodynamical response to changing transport coefficients, especially the bulk viscosity, has a strong impact on the time evolution of the momentum anisotropy. In PHSD these transport coefficients can be determined but remain intrinsically linked to the interaction cross sections. Although there are indications for a substantial bulk viscosity in PHSD, it does not show the same sensitivity to the momentum space anisotropy as in hydrodynamical simulations.

2. Event-by-event fluctuations might be of similar magnitude in quantities like the spatial and momentum anisotropy but while they remain smooth functions of time in hydrodynamics significant variations are observed within in a single event in PHSD as a function of time (Fig. 1).

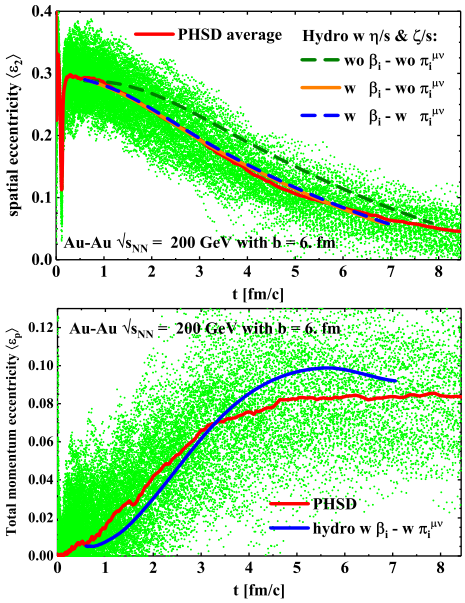

Figure 1: (Color online) Event-by-event averaged spatial eccentricity ϵ_2 of 100 PHSD events and 100 VISHNU events with respect to proper time, for a peripheral Au+Au collision ($b = 6$ fm) at $\sqrt{s_{NN}} = 200$ GeV. The green dots show the distribution of each of the 100 PHSD events used in this analysis. The solid red line is the average over all the green dots. (Top) The green, orange and blue lines correspond to hydrodynamical evolution taking different initial condition scenarios. (Bottom) The blue line corresponds to the standard hydrodynamical evolution taking the 100 initial conditions which are generated from PHSD events.

References

[1] Y. Xu, P. Moreau, T. Song, M. Nahrgang, S. A. Bass and E. Bratkovskaya, arXiv:1703.09178 [nucl-th].

[2] W. Cassing and E. L. Bratkovskaya, Phys. Rev. C **78**, 034919 (2008).

[3] W. Cassing and E.L. Bratkovskaya, Nucl. Phys. A **831**, 215 (2009).

[4] E. L. Bratkovskaya, W. Cassing, V. P. Konchakovski and O. Linnyk, Nucl. Phys. A **856**, 162 (2011).

[5] H. Song and U. W. Heinz, Phys. Rev. C **77**, 064901 (2008).

[6] C. Shen, Z. Qiu, H. Song, J. Bernhard, S. Bass and U. Heinz, Comput. Phys. Commun. **199**, 61 (2016).

* This work in part was supported by the LOEWE center HIC for FAIR and the HGS-HIRe as well as by BMBF and DAAD. The computational resources have been provided by the LOEWE-CSC. SAB, MG and YX acknowledge support by the U.S. Department of Energy under grant no. DE-FG02-05ER41367.

DOI:10.15120/GR-2017-1

Particle production in nucleus-nucleus collisions at SIS energies*

Vinzent Steinberg[1,2], *Dmytro Oliinychenko*[1,3], *and Hannah Petersen*[1,2,4]

[1]Frankfurt Institute for Advanced Studies, Frankfurt am Main, Germany; [2]Institute for Theoretical Physics, Goethe University Frankfurt, Germany; [3]Bogolyubov Institute for Theoretical Physics, Kiev, Ukraine; [4]GSI, Darmstadt, Germany

In this report some results for particle production in heavy-ion reactions at $E_{\mathrm{kin}} = 0.4 - 2A\,\mathrm{GeV}$ with a new microscopic, hadronic transport approach SMASH (Simulating Many Accelerated Strongly-interacting Hadrons) [1] are shown.

56 mesons and 60 baryons (+ anti particles) are implemented in the model and can perform $2 \leftrightarrow 2$ and $2 \leftrightarrow 1$ reactions using the geometric collision criterion, effectively solving the relativistic Boltzmann equation. In SMASH, particle production in nucleus-nucleus collisions mainly happens via $NN \rightarrow NR, RR$ with subsequent decays of the formed resonances R. To test that resonances are implemented correctly, the elementary cross sections are compared to experimental data and detailed balance in an equilibrated box is verified.

To be able to compare to experimental data from heavy-ion collisions, it is necessary to implement additional physics. The effects of these features can be seen in Figure 1: Soft nucleon-nucleon potentials (Skyrme and symmetry) decrease the pion multiplicity while Fermi motion increases it significantly. Pauli blocking inhibits some reactions, resulting in a slightly lower multiplicity. In the end, the total pion multiplicity is overestimated (similar to some other transport models), but the ratio agrees rather well with the FOPI measurements. Only at the lowest energies the ratio is influenced by Fermi motion, potentials and Pauli blocking.

This shows that heavy-ion collisions at SIS energies can be reasonably well described with the resonance approach. However, to extend SMASH to higher energies relevant for FAIR, it is necessary to model the cross sections with a different approach. Future work includes integrating string fragmentation into SMASH by using PYTHIA [3] and exploring effective many-particle interactions via forced thermalization [4].

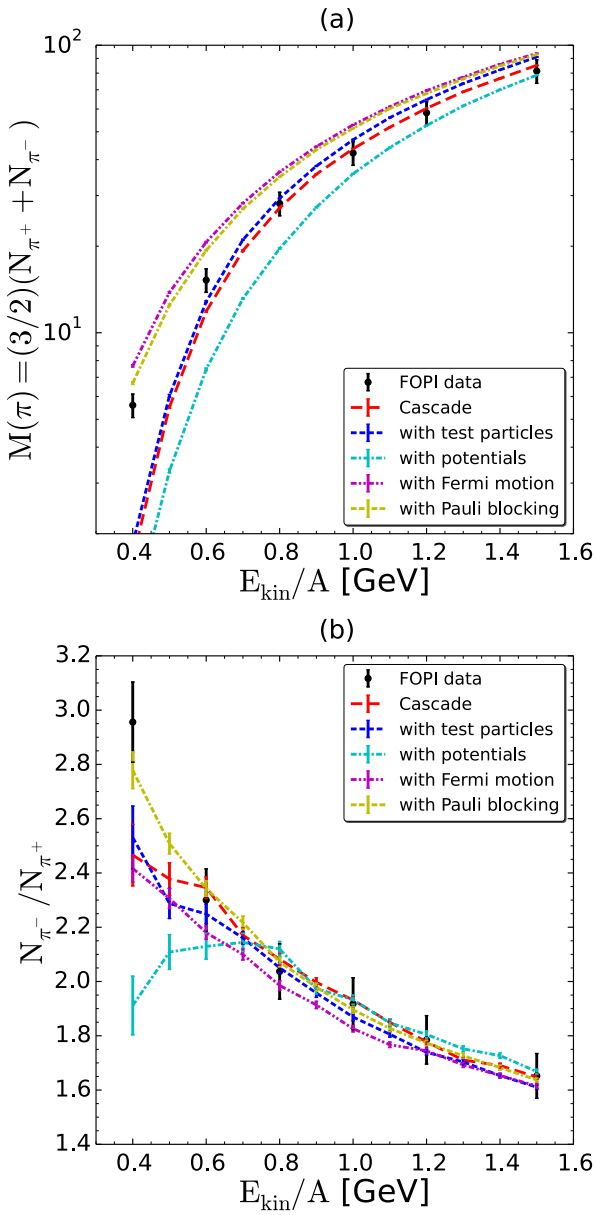

Figure 1: Pion production in gold-gold collisions at kinetic energies ranging from $0.4A\,\mathrm{GeV}$ to $1.6A\,\mathrm{GeV}$, as measured by FOPI [2] (markers), in comparison to SMASH (lines). Plot (a) shows the excitation function of π^+ and π^- multiplicities, plot (b) shows the ratio. The following features are successively switched on: 20 test particles per real particle, Skyrme and symmetry potentials, Fermi motion, Pauli blocking.

References

[1] J. Weil *et al.*, Phys. Rev. C **94** (2016) no.5, 054905. doi:10.1103/PhysRevC.94.054905

[2] W. Reisdorf *et al.* [FOPI Collaboration], Nucl. Phys. A **781** (2007) 459 doi:10.1016/j.nuclphysa.2006.10.085

[3] T. Sjöstrand *et al.*, Comput. Phys. Commun. **191**, 159 (2015) doi:10.1016/j.cpc.2015.01.024

[4] D. Oliinychenko and H. Petersen, J. Phys. Conf. Ser. **832** (2017) no.1, 012052. doi:10.1088/1742-6596/832/1/012052

*Work supported by GSI and the Helmholtz Association with the Helmholtz Young Investigator Group VH-NG-822, HIC for FAIR, LOEWE, HGS-HIRe, and the Deutsche Telekom Stiftung

$K^*/\bar{K}^*$ dynamics in the nuclear medium*

Andrej Ilner[†1,2], *Daniel Cabrera*[‡1,2], *Christina Markert*[§3], *and Elena Bratkovskaya*[¶1,2]

[1]Frankfurt Institute for Advanced Studies, Ruth-Moufang-Straße 1, 60438 Frankfurt am Main, Germany; [2]Institut für theoretische Physik, Johann Wolfgang Goethe-Universität, Max-von-Laue-Straße 1, 60438 Frankfurt am Main, Germany; [3]The University of Texas at Austin, Physics Department, Austin, Texas, USA

We study the in-medium properties and dynamics of the vector-mesons $K^*/\bar{K}^*$ in a dense and hot nuclear medium within the Parton-Hadron-String Dynamics (PHSD) transport approach. By $K^*/\bar{K}^*$ we are referring to all of the isospin channels, i.e. $K^* = [K^{*+}, K^{*0}]$ (vector mesons with a $\bar{s}$ and a u and d quark, respectively) and $\bar{K}^* = [K^{*-}, \bar{K}^{*0}]$ (vector mesons with a s and a d and u quark respectively). The in-medium properties of the $K^*/\bar{K}^*$ have been calculated on the basis of the G-Matrix approach, a unitary self-consistent chiral model, as complex self-energies and have been implemented in PHSD in the form of density- and temperature-dependent widths and effective masses through the relativistic Breit-Wigner spectral function, defined as

$$A_V\left(M,\rho_N\right) = \frac{\frac{2}{\pi}\cdot C_1 \cdot M^2 \cdot \Gamma_V^*\left(M,\rho_N\right)}{\left(M^2 - {M_V^*}^2\left(\rho_N\right)\right)^2 + \left(M\Gamma_V^*\left(M,\rho_N\right)\right)^2}. \quad (1)$$

The invariant mass of the meson $V = [K^*, \bar{K}^*]$ is denoted as M, ρ_N is the nuclear baryon density and C_1 is a normalisation constant which is determined through the normalisation of the spectral function, i.e. $\int_0^\infty A_V\left(M,\rho_N\right)\, dM = 1$.

The G-Matrix specral function contains the in-medium properties of the $K^*/\bar{K}^*$ in terms of the complex self-energy obtained by solving the Bethe-Salpeter equation. We can relate the real and imaginary parts of the self-energy to the width and the mass shift of the Breit-Wigner spectral function such that the real part of the self-energy is related to the mass shift

$$\mathrm{Re}\left(\Pi_i\left(M_V^*,\rho_N\right)\right) = M_V^2 - \left(M_V^*\right)^2, \quad (2)$$

whereas $M_V = M_{K^*/\bar{K}^*} = 0.892$ GeV is the vacuum mass of the $K^*/\bar{K}^*$ meson, and the imaginary part of the self-energy to the width

$$\mathrm{Im}\left(\Pi_V\left(M,\rho_N\right)\right) = -\Gamma_V^*\left(M,\rho_N\right)\cdot M \quad (3)$$

with a vacuum width for the $K^*/\bar{K}^*$ of $\Gamma_V^0 = 42$ MeV.

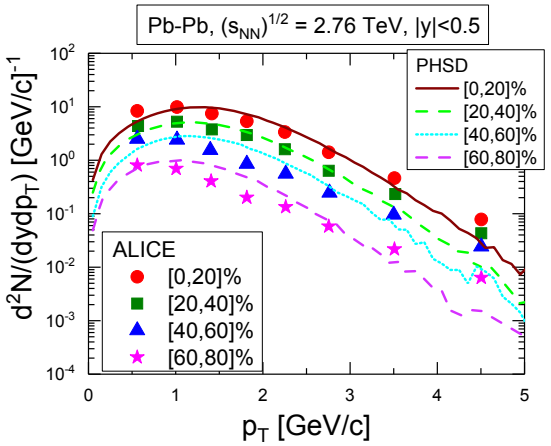

Figure 1: The transverse momentum spectrum $d^2N/\left(dydp_T\right)$ is shown at midrapidity for a PbPb collision at a centre of mass energy of $\sqrt{s_{NN}} = 2.76$ TeV for different centralities. The lines show results from PHSD while the symbols show data from ALICE [3].

The spectral function was implemented into PHSD in the form of cross sections for the $K^*\bar{K}^*$ and also in the hadronisation process of the quarks [1]. Experimental data from RHIC can be described very successfuly within PHSD and the implemented $K^*\bar{K}^*$ in-medium effects for pp and AuAu collisions at different centralities. However, we found a sizable difference between the spectra as taken from the decay point of the $K^*\bar{K}^*$ and the spectra as reconstructed from the final kaon and pion pairs [2]. Furthermore, we have performed additional studies within PHSD and $K^*/\bar{K}^*$ in-medium effects at higher and lower energies. In figure 1 the p_T spectrum for a PbPb collision at LHC can be seen. PHSD describes these data very well, if the final $K\pi$ pairs are taken and experimental cuts to the invariant mass spectrum are taken into account. However, just like for RHIC [2], we find that this spectrum differs from the measured spectrum at the $K^*/\bar{K}^*$ decay point, i.e. the spectrum is lower and softer.

References

[1] A. Ilner, D. Cabrera, P. Srisawad and E. Bratkovskaya, Nucl. Phys. A **927** (2014) 249

[2] A. Ilner, D. Cabrera, C. Markert and E. Bratkovskaya, Phys. Rev. C **95** (2017) no.1, 014903

[3] B. B. Abelev *et al.* [ALICE Collaboration], Phys. Rev. C **91** (2015) 024609

*Work supported by the Helmholtz International Center for FAIR within the framework of the LOEWE program. A.I. acknowledges support by GSI, HGS-HIRe for FAIR and H-QM. D.C. acknowledges support by BMBF (Germany).

† ilner@fias.uni-frankfurt.de
‡ cabrera@fias.uni-frankfurt.de
§ cmarkert@physics.utexas.edu
¶ Elena.Bratkovskaya@th.physik.uni-frankfurt.de

DOI:10.15120/GR-2017-1

Dilepton production in proton-proton collisions in comparison to HADES measurements*

J. Staudenmaier[†2,3], *J. Weil*[2], *and H. Petersen*[1,2,3]

[1]GSI, Darmstadt, Germany; [2]Frankfurt Institute for Advanced Studies (FIAS), Frankfurt am Main, Germany; [3]Johann Wolfgang Goethe-Universität, Frankfurt am Main, Germany

Lepton pairs are clean probes for strongly-interacting matter, since they only interact electromagnetically. They are directly emitted from the hot and dense medium created in a heavy-ion collision, whereas hadronic probes are rescattered or absorbed. It is therefore possible to extract medium properties and medium modifications of resonances from dileptons over the whole lifetime of such collisions. Dileptons are measured for low beam energies by the HADES collaboration at GSI [1].

Describing heavy-ion collisions theoretically remains challenging, since no calculation from first principles is able to model strongly-interacting many-body systems. Therefore an effective model based on the relativistic Boltzmann equation is used in this work. SMASH (=Simulating Many Accelerated Strongly-interacting Hadrons) is a new hadronic transport approach, which has been developed with the intention to provide a standard reference for hadronic systems with vacuum properties [2].

The approach describes all resonances with dilepton decays which are relevant in the low invariant mass region. Dileptons in SMASH [3] are produced by decays either through direct decays of the vector mesons ρ, ω and ϕ or through Dalitz decays from the pseudoscalar mesons π^0 and η or the ω and Δ resonances. In order to obtain better statistics the so called *Time-Integration-Method* or also called *Shining-Method* [3] is used.

Figure 1 shows the di-electron invariant mass spectrum for proton-proton collisions at a kinetic energy of 3.5 GeV. The thick black line represents the total dilepton contribution, which is the sum of all the different decay contributions (coloured lines). The spectrum looks qualitatively as expected. The invariant mass region below 400 MeV is dominated by the Dalitz decays of the pseudoscalar mesons π^0 and η, whereas in the invariant mass region above 400 MeV the vector mesons ρ and ω are dominant. Since those are direct decays, features of the resonance properties, e.g. the width, can be seen. The ω has a much smaller width and therefore also the sharper peak in the dilepton spectrum compared to the ρ meson, which has a very broad peak structure. The Dalitz decays of the ω and the Δ resonances also contribute to the total spectrum, but are always smaller than the dominant yields.

Also plotted in Figure 1 in order to compare with experimental results is data from HADES [1]. The overall agreement with the data is good, which not only validates the dilepton production, but also the description of hadronic resonances within SMASH. In particular the lower invariant mass region is in good agreement. However, it is important to note that there is tension with the data in the vector meson dominated region. The data hints at a ϕ peak around 1 GeV, which is lacking in SMASH, since no ϕ mesons are produced in elementary collisions yet. Furthermore, the total yield overshoots the data in the region below and above the ω peak. Both can be attributed to a high ρ yield in these regions, which needs further investigation. One possibility are overestimations of the branching ratios of baryonic resonances (N^*, Δ^*) decaying into ρ mesons. New results [5] report substantial lower branching ratios, which would decrease the ρ yield in the relevant region.

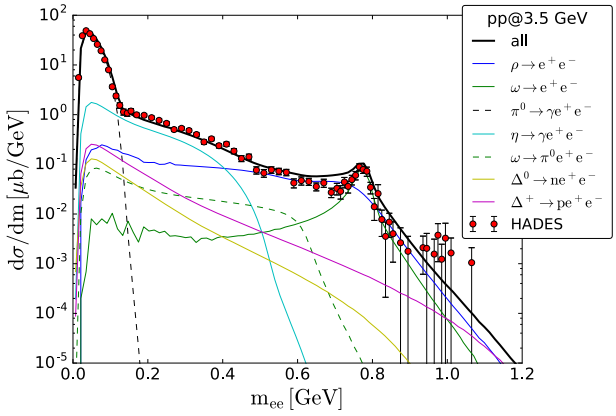

Figure 1: Invariant mass spectrum of di-electrons produced by pp collisions at $E_{kin} = 3.5$ GeV compared to HADES data from [1].

References

[1] Agakishiev G et al (HADES), Eur. Phys. J. A48 (2012) 64

[2] Weil J et al, Phys.Rev. C94 (2016) no.5, 054905

[3] Staudenmaier J et al, J.Phys.Conf.Ser. 832 (2017) no.1, 012037

[4] Schmidt K et al, Phys. Rev. C79 /2009) 064908

[5] Agakishiev G et al (HADES), Eur. Phys. J. A 50 (2014) 82

* Work supported by Helmholtz Nachwuchsgruppe VH-NG-822, by the LOEWE Initiative HIC for FAIR of the State of Hesse and GSI. Computational resources have been provided by the Center for Scientific Computing (CSC) at the Goethe- University of Frankfurt.

† staudenmaier@fias.uni-frankfurt.de

The production of primordial J/ψ in p+p and relativistic heavy-ion collisions*

T. Song[†1,2,3], *E. Bratkovskaya*[2,4], *and J. Aichelin*[3,5]

[1]Universität Gießen, Germany; [2]Institute for Theoretical Physics, Johann Wolfgang Goethe Universität, Frankfurt am Main, Germany; [3]FIAS, Frankfurt am Main, Germany; [4]GSI, Darmstadt, Germany; [5]Subatech, Nantes Cedex 3, France

Quarkonium production is special in the respect that it includes both, perturbative and non-perturbative, processes, where the former corresponds to the production of a heavy quark pair and the latter to the formation of a bound state from the pair. Though the former process is well described by pQCD, the latter needs a model.

We show that charmoninum production in p+p collisions can be described by projecting the position and momentum of the charm and anticharm quarks onto the Wigner density of the charmonium. The energy and momenta of the initial charm and anticharm quarks are given by the PYTHIA event generator, which has been tuned to reproduce the FONLL calculations. The radius of each charmonium state is a parameter to fit the experimental data on the total yield of J/ψ as well as the feed-down from the excited states of charmonium. We show in Fig. 1 that the experimental data in p+p collisions at $\sqrt{s} = 200$ GeV and 2.76 TeV are reproduced with the rms radii of 0.5, 0.55, and 0.9 fm respectively for J/ψ $(1S)$, χ_c $(1P)$ and ψ' $(2S)$, which are close to those calculated in a potential model. The distinguished feature of our approach is that it takes into account the spatial information of charm and anti-charm quarks.

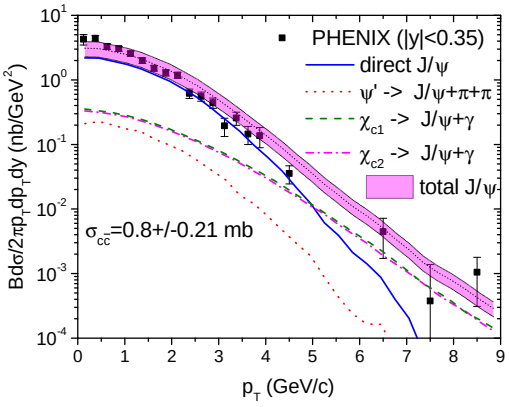

Figure 1: J/ψ production in p+p collisions at $\sqrt{s} = 200$ GeV including the feed-down from χ_c and ψ' in comparison with the experimental data from the PHENIX Collaboration [1].

While in p+p collisions mostly only one pair of charm quarks is produced, in relativistic heavy-ion collisions many charm quark pairs are produced in a small volume. Since many charm quark pairs are produced nearby in coordinate space, there is a probability for charm and anticharm quarks from two different initial pairs to form a charmonium. Using the same approach as in p+p collisions but allowing for the formation of charmonium from two different initial charm quark pairs, we find 46 % enhancement of primordial J/ψ in 0-20 % cental Au+Au collisions at $\sqrt{s} = 200$ GeV and an enhancement of a factor of 2.7 in 0-20 % cental Pb+Pb collisions at $\sqrt{s} = 2.76$ TeV, as shown by dotted line in Fig. 2.

The properties of charmonia change in the QGP matter produced in relativistic heavy-ion collisions. To estimate this effect we simply increase the radius by a factor of two and find that the production of primordial J/ψ reduces to 32 % in 0-20 % central Au+Au collisions at $\sqrt{s} = 200$ GeV, and to 86 % in 0-20 % central Pb+Pb collisions at $\sqrt{s} = 2.76$ TeV. It implies that the nuclear matter effects are important to describe J/ψ production in relativistic heavy-ion collisions.

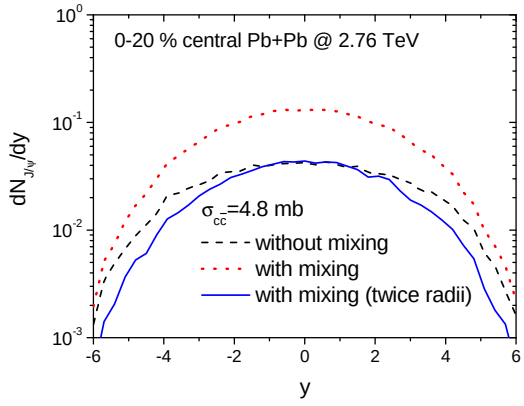

Figure 2: Rapidity distributions of J/ψ in $0-20$ % central Pb+Pb collisions at $\sqrt{s} = 2.76$ TeV. For the dashed curve the creation of charmonium from c and $\bar{c}$ from different initial collisions is excluded. For the dotted line we do not exclude this mixing. The solid lines show calculations in which the Wigner density has been modified to simulate QGP effects.

References

[1] A. Adare and PHENIX Collaboration, "J/ψ production versus transverse momentum and rapidity in p^+p collisions at $\sqrt{s}$ = 200-GeV", Phys. Rev. Lett. **98** (2007) 232002.

* Work supported by HIC4FAIR/DFG.

† song@fias.uni-frankfurt.de

DOI:10.15120/GR-2017-1

Numerical relativistic magneto-hydrodynamics for heavy ion collisions*

G. Inghirami[†1,2,3,4], *L. Del Zanna*[5,6,7], *A. Beraudo*[8], *M. Haddadi Moghaddam*[9,8], *F. Becattini*[5,6], *and M. Bleicher*[1,2,3,4]

[1]FIAS, Frankfurt am Main, Germany; [2]Goethe-Universität, Frankfurt am Main, Germany; [3]GSI, Darmstadt, Germany; [4]J. von Neumann Institute for Computing, Jülich, Germany; [5]Università degli Studi di Firenze, Firenze, Italy; [6]INFN - Sezione di Firenze, Firenze, Italy; [7]INAF - Osservatorio di Arcetri, Firenze, Italy; [8]INFN - Sezione di Torino, Torino, Italy; [9]Hakim Sabzevari University, Sabzevar, Iran

In the context of heavy ion collisions, the huge magnetic fields ($e|\vec{B}| \approx 10\, m_{\pi_0}^2$) generated by the fast moving electric charges contained in the nuclei might produce many interesting phenomena, like the chiral magnetic effect [1], changes in the directed and elliptic flows of the emitted charged particles [2, 3], a modification of the QCD equation of state [4, 5] or a mass shift of the light mesons [6, 7]. We modified the ECHO-QGP code [8, 9] to include the effects of such strong magnetic fields into the hydrodynamical description of the expanding fireball created after the collision, in the limit of an infinite electrical conductivity of the fluid and adopting the massless particles equation of state $p = e/3$. We executed several tests to validate the code, then we performed a 2D+1 simulation of an Au+Au collision at $\sqrt{s_{NN}} = 200\,\text{GeV}$ A. The initial energy distribution has been computed using the Glauber model with an impact parameter $b = 10\,\text{fm}$, while the magnetic field has been initialized according to the model described in Ref.([10]), assuming that the electrical conductivity of the medium before starting the hydro evolution was $5.8\,\text{MeV}$. The time evolution of the magnetic field at the center of the grid is shown in Fig.(1): due to the fluid expansion on the transverse plane, it decays a bit faster than in the case a pure Bjorken expansion, but still much slower than in the case of a magnetic field generated by particles freely streaming in the void. With these initial conditions, we did not appreciate any change in the elliptic flow of the charged pions, computed with the "standard" Cooper Frye prescription. However, more realistic and extensive simulations are needed before drawing any reasonable conclusion, e.g. 3D+1 runs with lattice QCD + hadron gas EoS, taking into account viscous effects and a finite electrical conductivity, at different collision energies, using more sophisticated methods to compute the initial conditions, varying the impact parameters and performing a final hadronic rescattering. The present work should be considered just a necessary, but still preliminary step toward a more complete magneto-hydrodynamical description of the quark-gluon plasma evolution in heavy ion collisions.

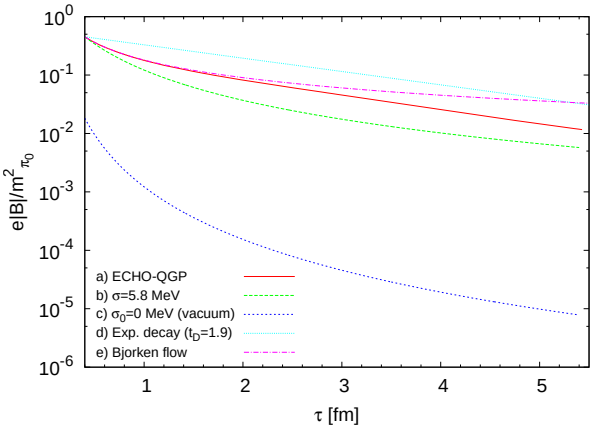

Figure 1: Comparison of the time evolution of the magnitude of the magnetic field (in neutral pion mass units squared) at the center of the grid. In the plot are depicted five different cases: a) ECHO-QGP, computing the initial $\vec{B}$ field assuming $\sigma = 5.8\,\text{MeV}$ b) magnetic field generated by the electric charges of the two colliding nuclei moving in a medium with uniform and constant electrical conductivity $\sigma = 5.8\,\text{MeV}$ c) same as in case b), but assuming zero electrical conductivity $\sigma = 0\,\text{MeV}$ (vacuum) d) assuming an exponential decay of the magnetic field with a characteristic decay time $t_D = 1.9\,\text{fm}$ e) Bjorken flow.

References

[1] K. Fukushima, D. E. Kharzeev and H. J. Warringa, Phys. Rev. D **78** (2008)

[2] U. Gursoy, D. Kharzeev and K. Rajagopal, Phys. Rev. C **89** (2014)

[3] G. S. Bali, F. Bruckmann, G. Endrodi, F. Gruber and A. Schaefer, JHEP **1304** (2013)

[4] G. S. Bali, F. Bruckmann, G. Endrődi, S. D. Katz and A. Schäfer, JHEP **1408** (2014)

[5] G. S. Bali *et al.*, JHEP **1202** (2012)

[6] J. O. Andersen, Phys. Rev. D **86** (2012)

[7] E. V. Luschevskaya and O. V. Larina, JETP Lett. **98** (2014)

[8] G. Inghirami, L. Del Zanna, A. Beraudo, M. H. Moghaddam, F. Becattini and M. Bleicher, Eur. Phys. J. C **76** (2016)

[9] L. Del Zanna *et al.*, Eur. Phys. J. C **73** (2013)

[10] K. Tuchin, Phys. Rev. C **88** (2013)

*G.Inghirami was supported by a GSI grant in cooperation with the John von Neumann Institute for Computing. G. Inghirami also gratefully acknowledges support from the H-QM and HGS-HIRe graduate schools. The computational resources were provided by the INFN-FI, by the FIAS and by the Center for Scientific Computing of the Goethe University. This work was also supported by the University of Florence grant "Fisica dei plasmi relativistici: teoria e applicazioni moderne".

† inghirami@fias.uni-frankfurt.de

Identifying QCD transition with deep learning *

L.-G. Pang[1,5], *K. Zhou*[1], *N. Su*[†1], *H. Petersen*[1,2,3], *H. Stöcker*[1,2,3], *and X.-N. Wang*[4,5]

[1]Frankfurt Institute for Advanced Studies, 60438 Frankfurt am Main, Germany; [2]Institut für Theoretische Physik, Goethe Universität, 60438 Frankfurt am Main, Germany; [3]GSI Helmholtzzentrum für Schwerionenforschung, 64291 Darmstadt, Germany; [4]Key Laboratory of Quark and Lepton Physics (MOE) and Institute of Particle Physics, Central China Normal University, Wuhan, 430079, China; [5]Lawrence Berkeley National Laboratory, Berkeley, CA 94720, USA

Introduction

One primary goal of ultra-relativistic heavy-ion collision experiments – currently carried out at RHIC (BNL) and LHC (CERN), and the forthcoming one at FAIR (GSI) – is to study the QCD transition, which is conjectured to be a crossover at small density (and moderately high temperature), and 1st order at moderate density (and lower temperature), with a critical point separating the two. Although it is believed that strongly coupled QCD matter can be created in these collisions, a direct access to the bulk properties of the matter such as the equation of state (EoS) and transport coefficients is impossible due to the highly dynamical nature of the collisions. What directly measured in experiments are the final-state particle spectra $\rho(p_T, \Phi)$, where p_T is the transverse momentum and Φ is the azimuthal angle of the final charged hadrons. So far, there has been no establishment of noticeable and unique correspondence between $\rho(p_T, \Phi)$ and the bulk properties during the evolution, which has thus posed a pressing challenge in testing the non-perturbative nature of QCD for the high-energy-physics community.

Deep learning is one branch of machine learning, which aims at understanding high-level representations of data using a deeper structure of multiple processing layers. Its features suggest that it could be adopted to uncover hidden information from the highly implicit data of heavy-ion experiments. Here we review a recent exploratory study, which provided a first step in directly connecting QCD bulk properties and raw data of heavy-ion collisions using state-of-the-art deep-learning techniques [1].

Results and discussions

The evolution of strongly coupled QCD matter can be well described by 2nd-order dissipative hydrodynamics. The EoS of the medium is a crucial input in solving the hydrodynamic equations, and the nature of the QCD transition (crossover or 1st order) strongly affects the hydrodynamic evolution. The final $\rho(p_T, \Phi)$ are obtained from the Cooper-Frye formula for particle i at mid-rapidity

$$\rho(p_T, \Phi) \equiv \frac{dN_i}{dY p_T dp_T d\Phi} = g_i \int_\sigma p^\mu d\sigma_\mu f_i \,, \qquad (1)$$

where N_i is the particle number density, Y is the rapidity, g_i is the degeneracy, $d\sigma_\mu$ is the freeze-out hypersurface element, f_i is the thermal distribution.

We found unique encoders of the EoS inside $\rho(p_T, \Phi)$ in terms of high-level representations using deep-learning techniques, which are not captured by conventional observables. This was achieved by constructing a convolutional neural network (CNN) and supervisedly training it with labeled $\rho(p_T, \Phi)$ of charged pions generated by the event-by-event hydrodynamic package CLVisc [2] with two different EoSs as input: crossover and 1st order. We then used $\rho(p_T, \Phi)$ generated by independent simulations (CLVisc with different setup parameters and another hydrodynamic package iEBE-VISHNU [3]) for testing. The performance of our method is surprisingly robust against other simulation parameters and an overall $\gtrsim 97\%$ testing accuracy was obtained, see Tab. 1 for the testing results and please check Ref. [1] for further details.

TESTING RESULTS	GROUP 1		GROUP 2	
	EOSL	EOSQ	EOSL	EOSQ
Number of Events	3349	3994	4164	4752
Accuracies	98.5%	91.6%	99.2%	99.2%

Table 1: Testing accuracies for two groups (iEBE-VISHNU and CLVisc with the IP-Glasma-like initial condition) of the testing dataset.

Our method yields a novel perspective on identifying the nature of the QCD transition in heavy-ion collisions. By adopting deep CNNs, we firmly demonstrated that discriminative and traceable projections – "encoders" – from the QCD transition onto the experimentally direct accessible $\rho(p_T, \Phi)$ do exist in the complex and highly dynamical heavy-ion collisions. The deep CNN provides a powerful and efficient "decoder" from which the EoS information can be extracted directly from the $\rho(p_T, \Phi)$. In this way, the high-level representations, which help decoding the EoS information in our method, act as an "EoS-meter" for the QCD matter created in heavy-ion collisions. Our study might provide a key to the experimental determination of QCD EoS and search for the critical end point.

References

[1] L.-G. Pang, K. Zhou, N. Su, H. Petersen, H. Stöcker, and X.-N. Wang, arXiv:1612.04262 [hep-ph].

[2] L.-G. Pang, Q. Wang, and X.-N. Wang, Phys. Rev. C **86**, 024911 (2012).

[3] C. Shen, Z. Qiu, H. Song, J. Bernhard, S. Bass, and U. Heinz, Comput. Phys. Commun. **199**, 61 (2016).

* Work supported in part by GSI.

† nansu@fias.uni-frankfurt.de

DOI:10.15120/GR-2017-1

Higher-order baryon number susceptibilities: interplay between the chiral and the nuclear liquid-gas transitions*

J. Steinheimer[†1], *A. Mukherjee*[1,2], *and S. Schramm*[1,2]

[1]Frankfurt Institute for Advanced Studies, Ruth-Moufang-Straße 1, D-60438 Frankfurt am Main, Germany; [2]Institut für Theoretische Physik, Goethe Universität Frankfurt, Max-von-Laue-Straße 1, D-60438 Frankfurt am Main, Germany

Theoretical studies employing lattice QCD methods have already established that the transition from hadrons to quarks proceeds as a smooth crossover in the case of vanishing net baryon number density [1, 2]. For finite net baryon density, the use of standard lattice QCD methods is limited by the so-called fermion sign problem. One proposed universal characteristic of a possible critical point of QCD is that higher-order fluctuation moments of observables diverge, at least for an infinite system size and relaxation time [3, 4]. We use an improved version of the SU(3) flavor parity-doublet quark-hadron model to investigate the higher order baryon number susceptibilities near the chiral and the nuclear liquid-gas transitions. We observe a strong interplay between the chiral and liquid-gas transition at intermediate baryo chemical potentials [5].

Model Description

We use the so called Quark-Hadron Chiral Parity Doublet Model (QχP) for a consistent description of strongly interacting matter which undergoes a chiral and deconfinement transition. The model parameters can be chosen so the model gives a good description of nuclear ground state and compact star properties as well as zero baryon density lattice QCD data. For a detailed description see [5]. Figure 1 shows the resulting phase diagram with both the nuclear liquid-gas transition and the chiral transition as function of T and μ_B.

To quantify the effect of the liquid-gas transition on the net-baryon susceptibilities we extract the cumulant ratio χ_4/χ_2 as function of the beam energy, using the freeze out curve obtained from a thermal fit to particle multiplicities [6], shown in figure 2.

In summary we have found that the interplay between liquid-gas and chiral transition has an effect on the equation of state and the extracted susceptibilities in a significant range of the phase diagram. This means that the influence of dense nuclear matter on the phase structure, even at large temperatures and moderate chemical potentials, cannot be neglected.

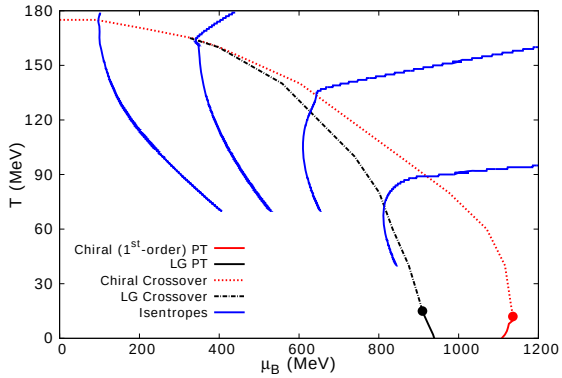

Figure 1: T-μ_B diagram showing the 1st-order liquid-gas (LG) phase transition (bold, black line), the 1st-order, chiral phase transition (bold, red line), the LG crossover (dashed, black line), the chiral crossover (dashed, red line), the LG Critical Point (black dot), the chiral Critical Point (red dot). Lines of constant entropy per baryon are shown as blue solid lines.

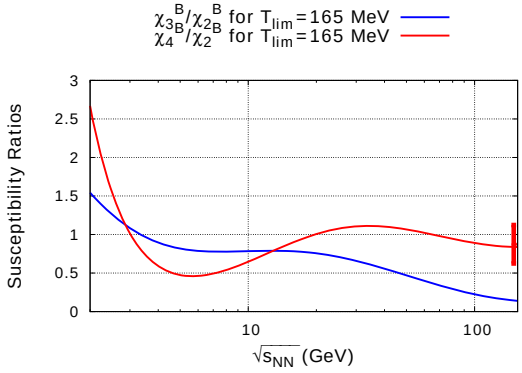

Figure 2: Susceptibility ratios as function of beam energy along the freeze-out line with $T_{\rm lim}$ = 165 MeV; with the value of $\chi_4^{\rm B}/\chi_2^{\rm B}$ for $\mu_{\rm B} \approx 0$, obtained from lattice data [7], represented by the thick, red bar.

References

[1] S. Borsanyi *et al.*, JHEP **1011**, 077 (2010)

[2] A. Bazavov and P. Petreczky [HotQCD collaboration], J. Phys. Conf. Ser. **230**, 012014 (2010)

[3] M. A. Stephanov, Phys. Rev. Lett. **102**, 032301 (2009)

[4] M. A. Stephanov, K. Rajagopal and E. V. Shuryak, Phys. Rev. Lett. **81**, 4816 (1998)

[5] A. Mukherjee, J. Steinheimer and S. Schramm, arXiv:1611.10144 [nucl-th].

[6] A. Andronic, P. Braun-Munzinger and J. Stachel, Phys. Lett. B **673**, 142 (2009) [Erratum-ibid. B **678**, 516 (2009)]

[7] R. Bellwied, S. Borsanyi, Z. Fodor, S. D. Katz and C. Ratti, Phys. Rev. Lett. **111**, 202302 (2013).

* Work supported by GSI, BMBF, HIC4FAIR and HGShire.

† steinheimer@fias.uni-frankfurt.de

Van der Waals interactions in hadron resonance gas: from nuclear matter to lattice QCD

V. Vovchenko[1,2,3], *M.I. Gorenstein*[2,4], *and H. Stoecker*[1,2,5]

[1]ITP, Goethe University, Frankfurt, Germany; [2]FIAS, Frankfurt, Germany; [3]Taras Shevchenko University, Kiev, Ukraine; [4]BITP, Kiev, Ukraine; [5]GSI, Darmstadt, Germany

Extension of the ideal hadron resonance gas (Id-HRG) model is constructed which includes attractive and repulsive van der Waals (VDW) interactions between hadrons [1]. The model employs a novel multi-component quantum statistical VDW approach which incorporates the Fermi-Dirac and Bose-Einstein effects in the system of interacting particles [2]. In the present minimalistic setup we include the VDW interactions for all baryon-baryon and all antibaryon-antibaryon pairs. At the same time, the VDW interactions between all other hadron pairs are explicitly omitted. The VDW parameters of baryon-baryon interaction are assumed to be the same for all baryon pairs, and are fixed by the ground state properties of nuclear matter ($a \simeq 329$ MeV fm^3 and $b \simeq 3.42$ fm^3). This VDW-HRG model yields the nuclear liquid-gas transition at low temperatures and high baryonic densities with a critical point located at $T_c \simeq 19.7$ MeV and $\mu_c \simeq 908$ MeV ($n_c \simeq 0.07$ fm$^3 = 0.45\, n_0$).

The predictions of the model are confronted with the lattice QCD calculations at zero chemical potential. The inclusion of the VDW interactions between baryons does not spoil the existing agreement of the Id-HRG model with lattice data on the pressure and energy density, and it leads to an improved description of the speed of sound. Moreover, the VDW interactions lead to a qualitatively different behavior of cumulants of fluctuations of conserved charges, for many observables closely resembling the lattice QCD results. For instance, the VDW-HRG model predicts the drop of the χ_4^B/χ_2^B cumulant ratio for the net baryon number fluctuations in the crossover region, which is also seen on the lattice (see Fig. 1). The VDW interactions are found to have a substantial influence on the higher orders of fluctuations of conserved charges at finite chemical potential, in the regions where chemical freeze-out in heavy-ion collisions is expected to occur. For example, the region of negative χ_4^B/χ_2^B at small μ_B is smoothly connected to the region of the liquid-vapor phase transition in nuclear matter (Fig. 2), and seems relevant for "chemical freeze-out" in heavy-ion collisions (see dashed line). Thus, the nuclear liquid-gas transition manifests itself into non-trivial net-baryon fluctuations in heavy-ion collisions.

These results hint towards crucial importance of the VDW interactions in the hadron gas, and indicate that commonly performed comparisons of the Id-HRG model with the lattice data may result in misleading conclusions. In particular, our results suggest that hadrons do not melt quickly with increasing temperature, as one could conclude on the basis of the Id-HRG model analysis.

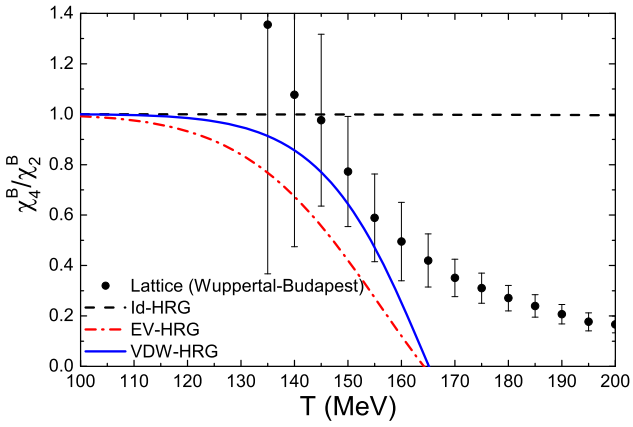

Figure 1: The temperature dependence of the χ_4^B/χ_2^B cumulant ratio for the net baryon number fluctuations. Calculations are done within the Id-HRG model (dashed lines), EV-HRG model with $b = 3.42$ fm^3 (dash-dotted lines), and VDW-HRG model with $b = 3.42$ fm^3 and $a = 329$ MeV fm^3 (solid lines). The lattice QCD results of the Wuppertal-Budapest collaboration [3] are shown by symbols.

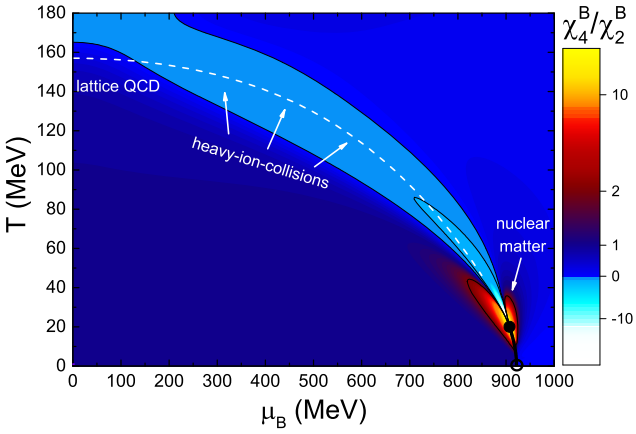

Figure 2: The χ_4^B/χ_2^B ratio calculated in the VDW-HRG model is exhibited in the T-μ_B plane.

References

[1] V. Vovchenko, M. I. Gorenstein, and H. Stoecker, Phys. Rev. Lett. **118**, 182301 (2017).

[2] V. Vovchenko, D. V. Anchishkin, and M. I. Gorenstein, Phys. Rev. C **91** (2015) 064314.

[3] R. Bellwied, S. Borsanyi, Z. Fodor, S. D. Katz, A. Pasztor, C. Ratti, and K. K. Szabo, Phys. Rev. D **92** (2015) 114505.

DOI:10.15120/GR-2017-1

New scenarios for hard-core interactions in a hadron resonance gas

L. M. Satarov[*1,2], *V. Vovchenko*[1,3,4], *P. Alba*[1], *M. I. Gorenstein*[1,5], *and H. Stoecker*[1,3,6]

[1]FIAS, Frankfurt am Main; [2]Kurchatov Institute, Moscow; [3]Goethe University, Frankfurt am Main;
[4]Taras Shevchenko University, Kiev; [5]BITP, Kiev; [6]GSI, Darmstadt

To describe realistically the equation of state (EoS) of a hot and dense hadronic matter, one should take into account finite sizes of hadrons. In Ref. [1] we investigate thermodynamic properties of a hadron resonance gas (HRG) with a hard-core repulsion of particles. It is assumed that that hard core radii of all baryons (B) and antibaryons ($\overline{B}$) are equal (below they are denoted by r_B), but mesons (M) are point-like. In the Boltzmann approximation, introducing the excluded volume corrections one can write the following relation for the pressure P of HRG [2]:

$$P = T\left[\frac{n_M}{1-\eta} + \frac{n_B + n_{\overline{B}}}{1-4\eta}\right]. \qquad (1)$$

Here T is temperature, $n_M, n_B, n_{\overline{B}}$ are total densities of mesons, baryons, and antibaryons, respectively. The packing fraction $\eta = (n_B + n_{\overline{B}})\,v$ is proportional to the hard-core volume of a single (anti)baryon $v = 4\pi r_B^3/3$. The calculation are done for the baryon-symmetric case $n_{\overline{B}} = n_B$.

The conditions of chemical equilibrium lead to the transcendental equation for $n_B = n_B(T)$. By solving this equation one obtains partial densities of different hadrons at given T. We found that the equilibrium nucleon to pion ratio is a nonmonotonic function of T with a maximum in the temperature range $170 - 200$ MeV at $r_B = 0.3 - 0.5$ fm. This explains the appearance of the second high-temperature minimum of χ^2 obtained from the thermal fit of ALICE data in Ref. [3].

The above model (CI) assumes that the BB and $B\overline{B}$ interaction are the same and mesons do not penetrate into hard cores of (anti)baryons. We also consider two other scenarios: CII where antibaryons do not interact with baryons, and CIII where the $B\overline{B}$, MB and $M\overline{B}$ interactions are neglected. The EoS in the CII model is obtained by replacing $\eta \to n_B v = n_{\overline{B}} v$ in the second term of (1). In the CIII scenario, one should additionally omit the denominator in the first term. At fixed r_B the N/π ratio increases in the transition from CI to CII, and from CII to CIII.

We performed the fit of midrapidity yields of hadrons measured by the ALICE collaboration in the central Pb+Pb collisions at $\sqrt{s_{NN}} = 2.76$ TeV. This was done for the ideal HRG as well as for the CI, CII and CIII models. At each freeze-out temperature the system volume was determined by minimizing the χ^2 values of the fit.

The results for hard-core radii $r_B = 0.3 - 0.6$ fm are shown in Fig. 1. One can see that introducing the hard-core repulsion improves the fit quality. Also the structure of the $\chi^2/N_{\rm dof}$ curves is very different form the ideal gas case. As compared to the calculation with $r_B = 0$, the corresponding curves in the CI, CII and CIII models are noticeably wider and in many cases two minima appear. According to our results, omitting the meson-baryon and antibaryon-baryon interactions strongly influences the hadronic yields and their ratios.

This shows that extracting the chemical freeze-out temperature from the hadron yield data is a rather delicate and model-dependent procedure. The improved excluded volume calculations should take into account the difference between the BB and $B\overline{B}$ interactions.

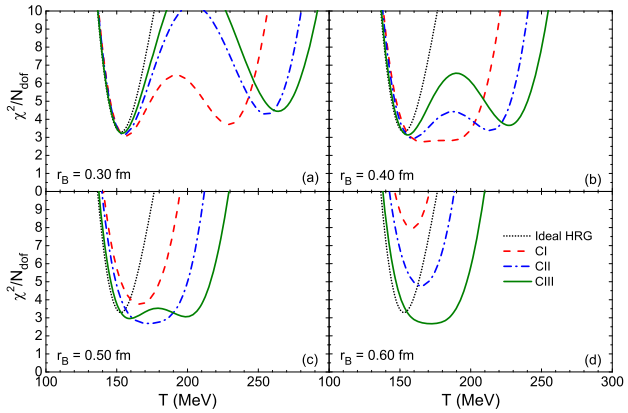

Figure 1: The temperature dependence of χ^2/N_{dof} for fitting the ALICE data on hadron yields in 0-5% central Pb+Pb collisions at $\sqrt{s_{NN}} = 2.76$ TeV. The dashed, dash-dotted, and solid curves correspond, respectively, to the models CI, CII, and CIII. The dotted lines are calculated in the ideal gas limit $r_B = 0$.

References

[1] L. M. Satarov, V. Vovchenko, P. Alba, M. I. Gorenstein, H. Stoecker, Phys. Rev. C 95 (2017) 024902

[2] L.M. Satarov, K.A. Bugaev, I.N. Mishustin, Phys. Rev. C 91 (2015) 055203

[3] V. Vovchenko, H. Stoecker, J. Phys. G 44 (2017) 055103; arXiv: 1512.08046 [hep-ph]

* satarov@fias.uni-frankfurt.de

Effective size of glueballs in Yang-Mills theory*

P. Alba† [1], *W.M. Alberico*[2], *A. Nada*[2], *M. Panero*[2], *and H. Stöcker*[1,3,4]

[1]FIAS, Frankfurt am Main, Germany; [2]University of Turin & INFN, Turin, Italy; [3]Goethe Universität Frankfurt, Frankfurt am Main, Germany; [4]GSI, Darmstadt, Germany

It is well known that the confined phase of QCD matter is well described by the standard version of the Hadron-Resonance Gas (HRG) model, which however neglects repulsive interactions among hadrons. These can be easily implemented in the model through an Excluded Volume (EV) approach, in which every hadron has an effective radius r_j. In order to crosscheck the results found in the fit to particle yields [1], here we analyze the interaction measure for SU(2) and SU(3) Yang-Mills theories calculated by means of Monte-Carlo lattice simulations [2,3]. The pure gauge sector is a good benchmark, since here we have only one physical scale, much lower computational costs, and none of the problems related to the implementation of fermionic fields; in particular in SU(2) there is no ambiguity in the definition of the Hagedorn temperature T_H with respect to the critical temperature T_c.
In figure 1 we show the HRG calculations in comparison to the lattice results; it is clear how the introduction of EV effects drastically reduces the reduced χ^2, table 1 and table 2, giving a consistent description between the two theories, with the radius of the lightest glueball r_0 in the ballpark of 0.5-0.9 fm depending on the EV scheme.

	r_0 (fm)	Δr_0 (fm)	χ^2_{red}
point-like	0	0	8.16
fixed radius	0.65	0.12	0.74
direct prop.	0.47	0.19	1.87
inverse prop.	0.82	0.14	0.39

Table 1: Best-fit results of lattice data for the SU(2) interaction measure, to the glueball-gas model with different EV scenarios.

	r_0 (fm)	Δr_0 (fm)	χ^2_{red}
point-like	0	0	84.3
fixed radius	0.73	0.08	2.33
direct prop.	0.55	0.07	5.41
inverse prop.	0.91	0.10	0.82

Table 2: Best-fit results of lattice data for the SU(3) interaction measure, to the glueball-gas model with different EV scenarios.

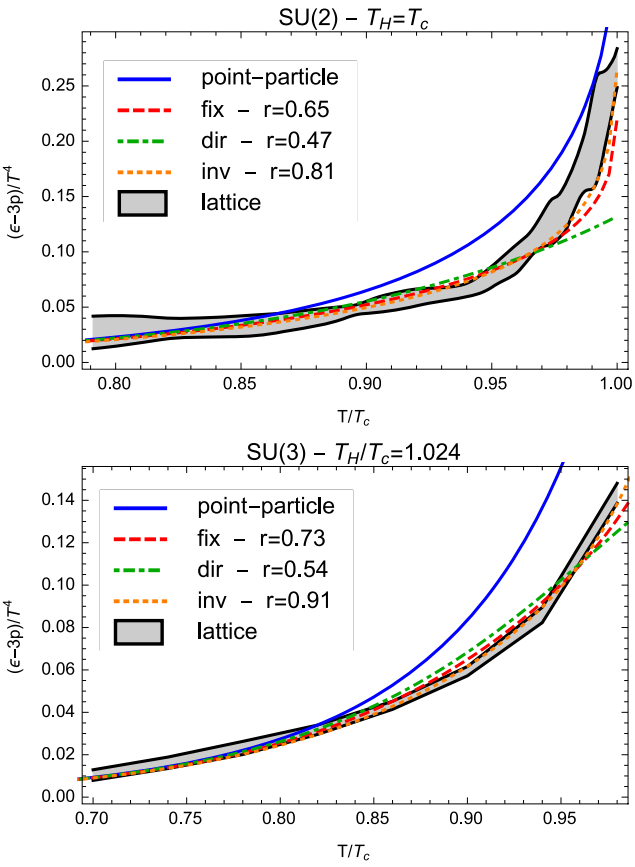

Figure 1: Interaction measure for SU(2) (upper panel) and SU(3) (lower panel) from lattice simulations [2,3] (band) and a gas of glueballs with the point-particle assumption (continuos line) and effective volume fixed (dashed), directly proportional (dot-dashed) and inversely proportional (dotted) to glueball masses.

References

[1] P. Alba, V. Vovchenko, M. I. Gorenstein and H. Stoecker, arXiv:1606.06542 [hep-ph].

[2] S. Borsanyi, G. Endrodi, Z. Fodor, S. D. Katz and K. K. Szabo, JHEP **1207**, 056 (2012) doi:10.1007/JHEP07(2012)056 [arXiv:1204.6184 [hep-lat]].

[3] P. Alba, W. M. Alberico, A. Nada, M. Panero and H. Stcker, arXiv:1611.05872 [hep-lat].

*This research is partially supported by HIC for FAIR within the LOEWE program of the state of Hesse.

† alba@fias.uni-frankfurt.de

DOI:10.15120/GR-2017-1

Electromagnetic probes of a pure-glue initial state in nucleus-nucleus collisions at LHC energies

V. Vovchenko[1,2,3], *Iu. Karpenko*[4,5], *M.I. Gorenstein*[2,5], *L.M. Satarov*[2,6], *I.N. Mishustin*[2,6], *B. Kämpfer*[7,8], *and H. Stoecker*[1,2,9]

[1]ITP, Goethe University, Frankfurt am Main, Germany; [2]FIAS, Frankfurt am Main, Germany; [3]Taras Shevchenko University, Kiev, Ukraine; [4]INFN, Firenze, Italy; [5]BITP, Kiev, Ukraine; [6]Kurchatov Institute, Moscow, Russia; [7]HZDR, Dresden, Germany; [8]TU Dresden, Germany; [9]GSI, Darmstadt, Germany

Partonic matter produced in the early stage of ultrarelativistic nucleus-nucleus collisions is assumed to be composed mainly of gluons, while quarks and antiquarks are produced at later times. The implications of this chemical non-equilibrium scenario are studied within the ideal (2+1)–dimensional hydrodynamics with a time dependent (anti)quark fugacity [1]. We use the explicit parametrization for the quark fugacity, $\lambda(\tau) = 1 - \exp\left(\frac{\tau_0 - \tau}{\tau_*}\right)$, where τ is the proper time, τ_* is the quark chemical equilibration time, τ_0 is the initial time of hydrodynamic evolution. The chemically equilibrium scenario ($\lambda = 1$) corresponds to the limit $\tau_* \to 0$. We use the equation of state which interpolates linearly between the lattice data for the purely gluonic Yang-Mills plasma and the lattice data for the (2+1)-flavor chemically equilibrated QCD matter. The modified vHLLE code [2] is used in numerical calculations.

We perform simulations for central Pb+Pb collisions at LHC energy of $\sqrt{s_{\rm NN}} = 2.76$ TeV. The initial energy density at $\tau_0 = 0.1$ fm/c is fixed to reproduce the hadronic observables in the chemical equilibrium ($\lambda = 1$) scenario. Figure 1 shows the density plot of the temperature in the coordinates (x, τ) for a simulation with $\tau_* = 5$ fm/c. The dashed curves correspond to $\tau_* = 0$. The chemically undersaturated matter is hotter as compared to the equilibrium case, which is a consequence of a reduced number of degrees of freedom in such a medium. A small region of first-order phase transition (FOPT) is also seen.

The spectra of electromagnetic probes – photons and dileptons – are also considered in the chemical non-equilibrium scenario. The QGP thermal photon emissions rates are modified by additional fugacity factors in undersaturated QGP. The calculated photon elliptic flow v_2^γ is exhibited in Fig. 2. In the chemical non-equilibrium scenario the momentum anisotropy of thermal photons is greatly enhanced at large p_T. The enhancement of the v_2^γ is also suggested by the preliminary data of the ALICE collaboration for direct photons [3]. The sensitivity of the results to chemical non-equilibrium effects, however, is greatly reduced when contributions from the prompt photons to the total direct photon spectrum are taken into account.

Stronger effects of are found for the thermal dilepton spectra, especially at large invariant masses $M \gtrsim 2$ GeV, where the deviations between two scenarios can reach one to two orders of magnitude. The corresponding experimental data are not available yet.

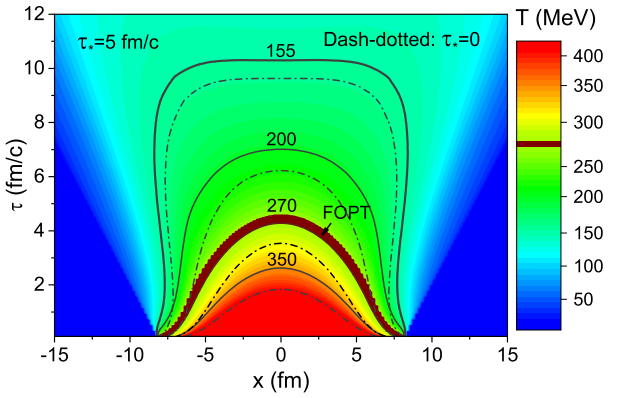

Figure 1: Contour plot of the temperature in the $x-\tau$ plane for the 0–20% most central Pb+Pb collisions at $\sqrt{s_{\rm NN}} = 2.76$ TeV for quark equilibration time $\tau_* = 5$ fm/c. The dash-dotted curves depict isotherms calculated for equilibrium matter with $\lambda = 1$.

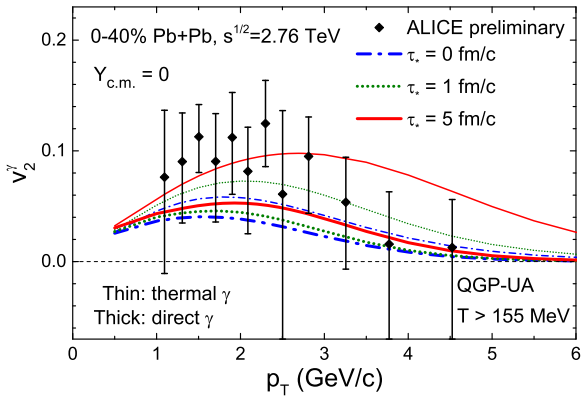

Figure 2: Elliptic flow v_2^γ of direct (thick lines) and thermal (thin lines) photons as a function of transverse momentum p_T in the $0-40\%$ central Pb+Pb collisions at $\sqrt{s_{\rm NN}} = 2.76$ TeV for different quark equilibration times τ_*. Experimental data are taken from Ref. [3].

References

[1] V. Vovchenko et al., Phys. Rev. C **94** (2016) 024906.

[2] I. Karpenko, P. Huovinen, and M. Bleicher, Comput. Phys. Commun. **185** (2014) 3016.

[3] D. Lohner [ALICE Collaboration], J. Phys. Conf. Ser. **446** (2013) 012028.

DOI:10.15120/GR-2017-1

Equations of state for real gases on the nuclear scale

V. Vovchenko[1,2,3]

[1]ITP, Goethe University, Frankfurt am Main, Germany; [2]FIAS, Frankfurt am Main, Germany; [3]Taras Shevchenko University, Kiev, Ukraine

Classical models of equation of state for real gases are generalized to include quantum statistical effects [1]. The free energy of the system reads

$$F(T,V,N) = F^{\rm id}(T, V f(\eta), N) + N\, u(n), \qquad (1)$$

where $F^{\rm id}(T,V,N)$ is the free energy of the corresponding quantum ideal gas. Function $f(n)$ quantifies the fraction of the total volume which is available for particles to move in at the given value of the packing fraction $\eta \equiv bn/4$, where b is the eigenvolume parameter. The function $f(\eta)$ has to take values in the range $0 \leq f(\eta) \leq 1$, and it corresponds to a generalized excluded-volume (EV) procedure. The quantity $u(n)$ in Eq. (1) is the self-consistent density-dependent mean field, corresponding to intermediate-range attractive interactions. All other quantities are calculated from free energy via standard thermodynamic identities (see [1] for details).

A family of two-parameter models, consistent with van der Waals (VDW) equation in low-density limit, is considered. Variations on the EV mechanism include van der Waals (VDW) and Carnahan-Starling models, while the considered attractive mean fields are based on VDW, Redlich-Kwong-Soave (RKS), Peng-Robinson (PR), and Clausius equations of state, giving a total of eight different VDW-like models. All considered models are consistent with the VDW equation of state in the low-density limit and, augmented with quantum statistical effects, give a fair description of properties of symmetric nuclear matter.

The VDW parameters a and b of nucleon-nucleon interaction are fitted in each model to the properties of ground state of nuclear matter, and the following range of parameters is obtained: $a = 330 - 430$ MeV fm^3 and $b = 2.5 - 4.4$ fm^3. Fits within standard VDW model are found to underestimate the value of the attraction parameter a. In the context of excluded-volume approach, the fits to the nuclear ground state disfavor values of the effective hard-core radius of nucleon significantly smaller than 0.5 fm in the nuclear matter region of phase diagram.

All considered models provide qualitatively similar description of nuclear matter, in particular regarding the critical parameters and critical fluctuations. Differences between models are more pronounced if one compares stiffness between the resulting equations of state. This is illustrated by the density dependence of the binding energy per nucleon E/A at $T = 0$ shown in Fig. 1: The behavior of E/A is changes significantly between different real gas models at densities above the saturation density n_0. The VDW model yields the stiffest equation of state, with the nuclear "incompressibility" factor $K_0 = 9\,(\partial P/\partial n)_T \cong 763$ MeV at the saturation density. This is well above the empirical range $250 - 315$ MeV [2]. On the other hand, the model with Carnahan-Starling EV term and Clausius attraction term yields $K_0 \cong 333$ MeV, much closer to empirical estimates, and better than the $K_0 \cong 550$ MeV value obtained in the standard Walecka model [3].

The present approach allows a straightforward generalization to a multi-component hadron gas. This, in turn, opens new applications in physics of heavy-ion collisions and QCD equation of state. As an illustration, the generalization to include the baryon-baryon interactions in the full hadron resonance gas model is performed. The preliminary calculations show that the behavior of the baryon-related lattice QCD observables at zero chemical potential is strongly correlated to the nuclear matter properties.

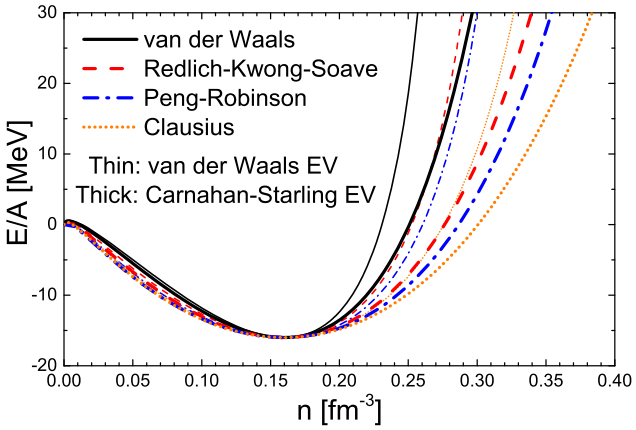

Figure 1: The nucleon number density dependence of the binding energy per nucleon E/A in symmetric nuclear matter calculated within eight different real gas models at $T = 0$. The thin lines denote calculations within four models with the VDW EV term, i.e. they correspond to VDW (solid black line), Redlich-Kwong-Soave (dashed red line), Peng-Robinson (dash-dotted blue line), and Clausius (dotted orange line) models. The thick lines correspond to models with the Carnahan-Starling EV term.

References

[1] V. Vovchenko, arXiv:1701.06524 [nucl-th].

[2] J. R. Stone, N. J. Stone, and S. A. Moszkowski, Phys. Rev. C **89** (2014) 044316.

[3] M. Dutra *et al.*, Phys. Rev. C **90** (2014) 055203.

DOI:10.15120/GR-2017-1

Shear viscosity of a pion gas*

J.B. Rose[1,2], *D. Oliinychenko*[1,3], *J.M. Torres-Rincon*[2], *and H. Petersen*[1,2,4]

[1]Frankfurt Institute for Advanced Studies, Frankfurt, Germany; [2]Institute for Theoretical physics, Goethe University, Frankfurt, Germany; [3]Bogolyubov Institute for Theoretical Physics, Kiev, Ukraine; [4]GSI, Darmstadt, Germany

Shear viscosity is an important transport property of strongly interacting matter. While it was first shown to play a significant role in explaining the high levels of elliptic flow observed at RHIC or the LHC in an hydrodynamical framework, there has been far fewer such investigations at lower temperatures such as will be explored at FAIR. In particular on the hadron gas side of the phase transition, these show conflicting results [1-3]. The ultimate goal of this work is to extract the shear viscosity over entropy ratio as a function of temperature and net baryon chemical potential in a full hadron gas. Here, the formalism is introduced and validity checks for a pion gas are displayed.

The viscosity calculation is based on the Green-Kubo formalism. This formalism relates so-called auto-correlation functions with themselves at a later point in time to extract transport coefficients. Viscosity can thus be expressed as

$$\eta = \frac{V}{T}\int_0^\infty C^{xy}(t)dt, \qquad (1)$$

where V is the volume and T is the temperature of the system. $C^{xy}(t)$, the auto-correlation function, is computed as a discrete average over N fixed time steps:

$$C^{xy}(t) = \frac{1}{N}\sum_s^N T^{xy}(s)T^{xy}(s+t), \qquad (2)$$

with T^{xy} an off-diagonal spatial component of the energy-momentum tensor.

The model used in all calculations is SMASH [4], a new transport approach. Since a constant temperature over a long period of time is required by the previously described formalism, all calculations are performed in a box with periodic boundary conditions simulating infinite matter.

As a test on the calculation, we reproduce analytical calculations for a gas of pions with constant isotropic cross-sections (figure 1). All plots show the computed shear viscosity from SMASH and compare it to calculations within a high order Chapman-Enskog approximation [5]. The three plots in the left column show the viscosity as a function of the physical parameters which come into play in the analytical calculations, namely the temperature, cross-section and mass of the pions, and agree with analytical calculations up to a difference of no more than 3%. The three plots on the right show that the calculation is very stable against large variations of other technical parameters. Specifically, these are the number of box calculations

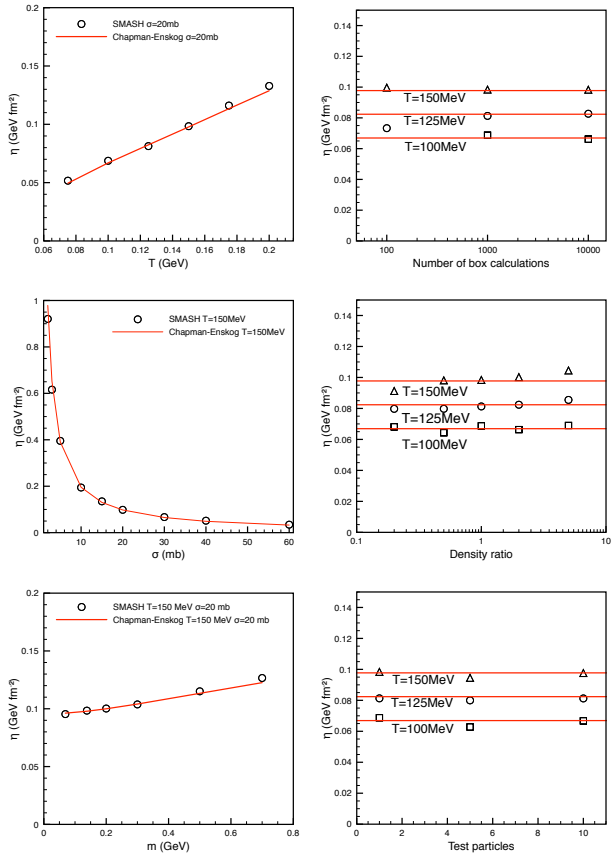

Figure 1: Pion box systematics.

(which does not strongly affect results if one uses more than a thousand), the density ratio (the ratio of the current density to the thermal density for $\mu = 0$, for which a very slow dependence is shown, with a maximum error of about 6%) and the number of used test particles (which remains relatively stable within 4% of the Chapman-Enskog value).

Following this detailed verification of the method, the calculation of the shear viscosity of the complete hadron gas is ongoing.

References

[1] N. Demir, S. Bass, Phys.Rev.Lett. 102 (2009) 172302

[2] H. Song, S. Bass, U. Heinz, Phys.Rev. C83 (2011) 024912

[3] P. Romatschke, S. Pratt, arXiv:1409.0010 [nucl-th]

[4] J. Weil et al., Phys. Rev. C94 (2016) no.5, 054905

[5] J. Torres-Rincon, PhD dissertation (2012)

* Work supported by HIC4FAIR/HGS-Hire/Helmholtz Young Investigator Group VH-NG822

Spectral functions of the quark-meson model within the functional renormalization group approach beyond the local potential approximation*

A. Stegemann†[1], *R.-A. Tripolt*[3], *L. von Smekal*[2], *and D.-H. Rischke*[1]

[1]Johann Wolfgang Goethe-Universität Frankfurt am Main; [2]Justus-Liebig-Universität Gießen; [3]European Centre for Theoretical Studies in Nuclear Physics and Related Areas (ECT*) Trento

Introduction

In order to study the low-energy regime of quantum chromodynamics (QCD), where quarks and gluons are confined into hadrons, it is necessary to employ non-perturbative methods. In this work, we use the functional renormalization group (FRG) which, in contrast to lattice calculations, does not exhibit a sign problem at finite quark-chemical potential. We apply this method to the quark-meson-model, an effective theory for low-energy QCD that incorporates quarks (ψ) as well as scalar (σ) and pseudoscalar (π) mesonic degrees of freedom.

Functional renormalization group

The FRG approach aims at calculating the effective action Γ which is the generating functional of the one-particle irreducible diagrams in the considered theory. Therefore, the scale (k)-dependent effective average action Γ_k is introduced. It interpolates between the classical action S in the ultraviolet and the full effective action in the infrared. This behavior is described by the FRG flow equation, also known as Wetterich equation [1].

The Wetterich equation is a functional differential equation. In order to solve it, one needs to expand the effective average action and truncate this expansion which yields a finite set of coupled differential equations. One possibility is the derivative expansion which corresponds to an expansion in momenta and reads for a scalar field ϕ [2]

$$\Gamma_k = \int \mathrm{d}^D x \left[U_k\left(\phi^2\right) + \frac{1}{2} Z_k\left(\phi^2\right)\left(\partial_\mu \phi\right)^2 + \mathcal{O}\left(\partial^4\right) \right].$$

In the lowest order derivative expansion, usually called local potential approximation (LPA), the only scale-dependent quantity is the effective potential U_k. The next order, denoted as LPA′, additionally incorporates a scale-(but not yet field-)dependent wave function renormalization Z_k.

Spectral functions from the FRG

When performing calculations in quantum field theory at finite temperature, it is convenient to work in Euclidean space-time. However, this causes the need for an analytic continuation when trying to calculate real-time quantities like spectral functions.

Within the FRG framework, such an analytic continuation procedure is possible already on the level of the flow equations. This method has been applied to the 2-flavor quark-meson-model in previous studies [3,4].

However, these calculations, which were restricted to the LPA, show a large difference between the pion pole and curvature masses at vanishing quark-chemical potential and small temperature. It is presumed that the use of higher truncations can solve this problem. Evidence was found that the LPA′ can already be sufficient [5].

Extension to LPA′

In our recent calculations, we included mesonic wave function renormalizations $Z_{\sigma,k}$ and $Z_{\pi,k}$. At finite temperature, they split up into a longitudinal and transversal part with respect to the heat bath. Thus, our ansatz contains five scale-dependent quantities.

We derived the flow equations for the effective potential as well as for the wave function renormalizations and for the spectral functions. Currently, we are occupied with the numerical solution; first results look promising.

In the near future, we will complete the numerical solution of the flow equations. Later, we plan to include additionally a fermionic wave function renormalization $Z_{\psi,k}$ and a scale-dependent Yukawa coupling.

References

[1] C. Wetterich, "Exact evolution equation for the effective potential", Phys. Lett. B 301, 90 (1993).

[2] H. Gies, "Introduction to the functional RG and applications to gauge theories", Lect. Notes Phys. 852, 287 (2012).

[3] R.-A. Tripolt, N. Strodthoff, L. von Smekal, and J. Wambach, "Spectral Functions for the Quark-Meson Model Phase Diagram from the Functional Renormalization Group", Phys.Rev. D89, 034010 (2014).

[4] R.-A. Tripolt, L. von Smekal, and J. Wambach, "Flow equations for spectral functions at finite external momenta", Phys.Rev. D90, 074031 (2014).

[5] A. J. Helmboldt, J. M. Pawlowski, N. Strodthoff, "Towards quantitative precision in the chiral crossover: masses and fluctuation scales", Phys.Rev. D91, 054010 (2015).

* A. S. thanks GSI F&E and HIC for FAIR for funding.

† stegemann@th.physik.uni-frankfurt.de

DOI:10.15120/GR-2017-1

Scaling violation and the magnetic equation of state in chiral models*

G. A. Almasi†[1], *B. Friman*[1,2], *K. Redlich*[2,3,4], *and W. Tarnowski*[5]

[1]Gesellschaft für Schwerionenforschung, GSI, D-64291 Darmstadt, Germany; [2]ExtreMe Matter Institute (EMMI), D-64291 Darmstadt, Germany; [3]University of Wrocław - Faculty of Physics and Astronomy, PL-50-204 Wrocław, Poland; [4]Department of Physics, Duke University, Durham, NC 27708, USA; [5]Faculty of Physics, Astronomy and Applied Informatics, Jagiellonian University, PL-30-348 Cracow, Poland

In this work, the scaling behavior of the order parameter at the chiral phase transition, the so-called magnetic equation of state, of strongly interacting matter is studied within effective models. We explore universal and nonuniversal structures near the critical point. We consider two models in the mean-field approximation, the quark-meson (QM) and the Polyakov loop extended quark-meson (PQM) models, and compare their critical properties with a purely bosonic theory, the $O(N)$ linear sigma (LS) model in the $N \to \infty$ limit. In these models the order parameter scaling function is found analytically using the high temperature expansion of the thermodynamic potential. The effects of a gluonic background on the nonuniversal scaling parameters are studied within the PQM model.

Fig. 1 shows that in the quark-meson model the scaling violation is small up to physical pion mass, in agreement with recent lattice calculations [2]. The coupling of quarks to the Polyakov loop enhances the scaling violation, as seen in Fig. 2. This is particularly apparent in the broken phase.

The difference in strength of the scaling violation found in the QM and PQM models is even more pronounced in the $O(N)$ sigma model. As shown in Fig. 3, the $O(N)$ model exhibits stronger deviations from the universal scaling curve for the corresponding strength of the symmetry breaking field and scaling is preserved only for a very weak external field. The qualitative differences in the universal scaling curves and in the strength of the scaling violation indicate that fluctuations of the meson fields, not accounted for in the mean-field models, play an important rôle. The strong violation of scaling obtained in this model is consistent with previous studies within the FRG approach [3].

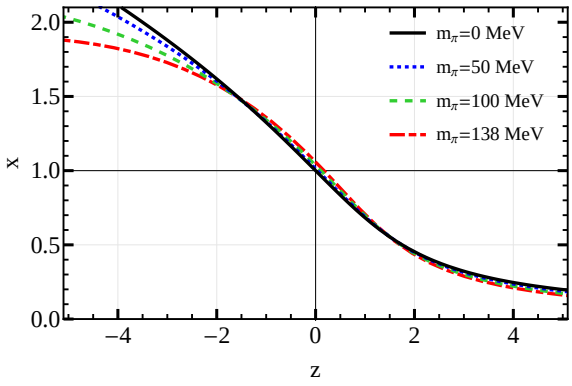

Figure 1: The magnetic equation of state for the QM model. The black line corresponds to the universal scaling curve.

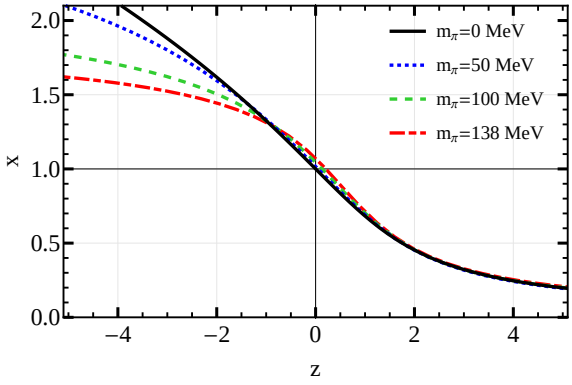

Figure 2: The magnetic equation of state for the PQM model.

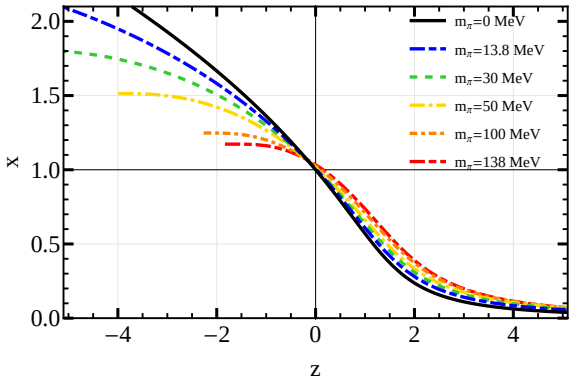

Figure 3: The magnetic equation of state for the $O(N)$ linear sigma model in the $N \to \infty$ limit.

References

[1] G. A. Almasi, B. Friman, K. Redlich and W. Tarnowski, Phys. Rev. D **95**, 014007 (2017)

[2] H.-T. Ding and P. Hegde. 2015. (Bielefeld-BNL-CCNU), Proc. Sci. LATTICE, 161 (2016).

[3] J. Braun, B. Klein and P. Piasecki, Eur.Phys.J. C **71**, 1576 (2011).

*The work of B.F. and K.R. was partly supported by the Extreme Matter Institute EMMI. K. R. also acknowledges partial supports of the Polish Science Center (NCN) under Maestro Grant No. DEC-2013/10/A/ST2/00106, and the U.S. Department of Energy under Grant No. DE-FG02-05ER41367. W.T. is grateful to GSI for the hospitality during the Summer Student Programme. G. A. acknowledges the support of the Hessian LOEWE initiative through the Helmholtz International Center for FAIR (HIC for FAIR).

† g.almasi@gsi.de

Coherent hypernucleus production in $\bar{p}A$ interactions as a test of κ meson exchange*

A.B. Larionov[1,2] *and H. Lenske*[1]

[1]Institut für Theoretische Physik, Universität Giessen, D-35392 Giessen, Germany; [2]National Research Center "Kurchatov Institute", 123182 Moscow, Russia

Coherent annihilation of antiprotons on nuclei to hyperonic channels is an efficient mechanism of populating discrete states of hypernuclei. We have studied the

$$\bar{p} + {}^{A}Z \to {}^{A}_{\Lambda}(Z-1) + \bar{\Lambda} \qquad (1)$$

annihilation reaction on a target nucleus ${}^{A}Z$ leading to the production of the hypernucleus ${}^{A}_{\Lambda}(Z-1)$. The amplitude of the $\bar{p}p \to \bar{\Lambda}\Lambda$ reaction was evaluated by considering t-channel exchange of the light strangeness-carrying mesons, i.e. pseudoscalar K, vector K^*, and the hypothetical scalar $\kappa/K_0^*(800)$, modelling correlated πK exchange in the 0^+ $I = 1/2$ channel. The parameters of the elementary $\bar{p}p \to \bar{\Lambda}\Lambda$ amplitude, i.e. vertex coupling constants, form factor cutoffs and the attenuation factor due to initial/final state interaction (ISI/FSI), were adjusted to describe the $\bar{p}p \to \bar{\Lambda}\Lambda$ cross section for beam momenta $p_{\rm lab} \simeq 1.5 - 8$ GeV/c. In this way we have defined two sets of parameters: without κ exchange (set 1) and with κ exchange (set 2). Both parameter sets reproduce the angle-integrated $\bar{p}p \to \bar{\Lambda}\Lambda$ cross section reasonably well. The corresponding angular distributions, however, are better described with κ exchange which significantly rises the cross section at forward scattering angles. We have evaluated the amplitude of the process Eq.(1) in second order perturbation theory by impulse approximation as discussed in detail in [1], also including antibaryon-nucleus ISI and FSI effects similar to our investigations in [2]. The wave functions of the initial nucleon and final Λ bound states were obtained numerically as stationary solutions of the corresponding Dirac equations. Self-energies were approximated by scalar and vector relativistic mean-field potentials with pre-chosen Woods-Saxon form factors. The nucleonic potential parameters were adjusted to the total binding energy of the target nucleus and the r.m.s. radii of proton and neutron HFB ground state matter densities. As in [3] the Λ single particle states were obtained by potential fits to the energy spectrum of the final hypernucleus.

Numerical calculations have been performed for the reaction $\bar{p} + {}^{40}\mathrm{Ar} \to {}^{40}_{\Lambda}\mathrm{Cl} + \bar{\Lambda}$. The choice of the ^{40}Ar target was motivated by the future PANDA experiment at FAIR where noble gases will be used as targets. In order to assure that after the reaction the residual ^{39}Cl core nucleus carries as little excitation energy as possible, we consider only strangeness creation processes on protons of the ^{40}Ar $1d_{3/2}$ valence shell. As we see from Fig. 1, the cross section of coherent hypernucleus production grows rapidly with orbital angular momentum of the Λ state. The inclusion of κ exchange leads to almost one order of magnitude larger hypernucleus production cross sections. A closer inspection shows that the enhancement due to κ exchange is, in fact, a result of a general property of bound state Dirac wave functions. Their low energy characteristics lead to a strong suppression of the lower components which, in turn, suppresses any kind of pseudoscalar vertices involving the γ^5 matrix – which mixes upper and lower components – as encountered in the K-meson exchange. Thus, the apparent in-medium enhancement of the κ exchange amplitude is in fact related to a relative suppression of the pseudoscalar K exchange amplitude. As a consequence, the coherent hypernucleus production reactions proceed predominantly via K^* and κ exchange where the latter – when included – dominates, especially at beam momenta of interest for the PANDA experiment, irrespective of the quantum state in which the Λ hyperon is produced. Hence, we conclude that coherent hypernucleus production in $\bar{p}A$ collisions could serve as a test for κ-meson exchange in the underlying $\bar{p}p \to \bar{\Lambda}\Lambda$ transition amplitude.

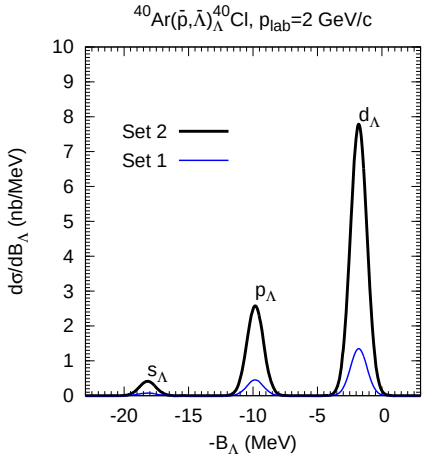

Figure 1: The Λ binding energy spectrum of the ${}^{40}_{\Lambda}$Cl hypernuclei coherently produced in $\bar{p}$ ^{40}Ar collisions at $p_{\rm lab} = 2$ GeV/c. The calculated spectrum was folded by Gaussians of a width $\Gamma_{FWHM} = 1.5$ MeV.

References

[1] A.B. Larionov, H. Lenske, PLB (submitted); arXiv:1703.02073.

[2] A.B. Larionov and H. Lenske, Nucl. Phys. **A957**, 450 (2017).

[3] S. Bender, R. Shyam, H. Lenske, Nucl. Phys. **A839**, 51 (2010).

* Work supported by DFG under Grant No. Le439/9.

DOI:10.15120/GR-2017-1

Investigation of heavy tetraquarks by means of lattice QCD*

A. Peters[1], *K. Cichy*[1,2], *B. Wagenbach*[1], *and M. Wagner*[1]

[1]Goethe-Universität Frankfurt am Main, Institut für Theoretische Physik, Max-von-Laue-Straße 1, D-60438 Frankfurt am Main, Germany; [2]Adam Mickiewicz University, Faculty of Physics, Umultowska 85, 61-614 Poznań, Poland

Tetraquark systems are expected to be studied in more detail in the near future by experimental collaborations, e. g. with the PANDA experiment at FAIR. Therefore it is important to gain theoretical understanding of these systems. Moreover, quite a number of mesons observed experimentally (e.g. at LHCb and Belle) are theoretically not well understood yet.

In a recent study [1] we investigate static-light $\bar{b}\bar{b}ud$ four-quark states in the Born-Oppenheimer approximation. The potential of a pair of B mesons is computed using Wilson twisted mass lattice QCD with two flavours of degenerate dynamical quarks. Using the fit function $V(r) = -\frac{\alpha}{d}\exp(-(r/d)^2)$ we provide fits to the ground state potentials in the attractive channels and discuss the potentials in the repulsive and excited channels. The attractive channels are most important since they can possibly lead to a bound four-quark state, i.e. a $\bar{b}\bar{b}ud$ tetraquark. Using these attractive potentials in the Schrödinger equation, we find indication for such a tetraquark state of two static bottom antiquarks and two light u/d quarks with mass extrapolated down to the physical value (cf. Figure 1). In another study [2, 3] of the same four-quark system we investigate the dependence of the binding of the four quarks on the mass of the light quarks. While we find strong indication for a bound four-quark state for $qq = (ud-du)/\sqrt{2}$, i.e. isospin $I = 0$, which is stable with respect to QCD, i.e. can only decay weakly, we find clear evidence against the existence of corresponding tetraquarks with $qq \in \{uu, (ud+du)/\sqrt{2}, dd\}$, i.e. isospin $I = 1$, $qq = ss$ and $qq = cc$. In a follow-up study [4] we investigate heavy-light four-quark systems $\bar{b}\bar{b}ud$ with bottom quarks of finite mass which are treated in the framework of NRQCD. We focus on $I(J^P) = 0(1^+)$, where we recently found evidence for the existence of a tetraquark state using static bottom quarks.

One example for an experimentally measured but not well understood system is the $Z_c^{\pm}$. It contains a $c\bar{c}$ pair, which one can infer from both its mass and decay products. Because it carries electromagnetic charge, there must be additional quarks, most likely a light quark-antiquark pair, i.e. the minimal quark content of $Z_c^{\pm}$ is $c\bar{c}q\bar{q}$ with $q = u, d$. For this reason they are subject of many recent experimental and theoretical investigations. Such $c\bar{c}$ studies are expected to be measured by PANDA. In our study [5] we investigate as a first step the $Z_b^{\pm}$ which is quite similar to $Z_c^{\pm}$. We assume a four-quark structure $b\bar{b}u\bar{d}$ using lattice QCD. Again, we work with b quarks in the static approximation. We compute the potentials of the static quarks in the presence of the light quarks, which can be interpreted as the potentials of a B and a $\bar{B}$ meson. To check, whether the four quarks may form a bound state, we use the Born-Oppenheimer approximation, i.e. we solve the Schrödinger equation with the computed potentials. We find first evidence that $B\bar{B}$ with light quarks $qq = u\bar{d}$ and quantum numbers $I(J^P) = 1(1^+)$ is a candidate for a stable tetraquark. In the future we plan to replace the heavy b quarks by lighter c quarks.

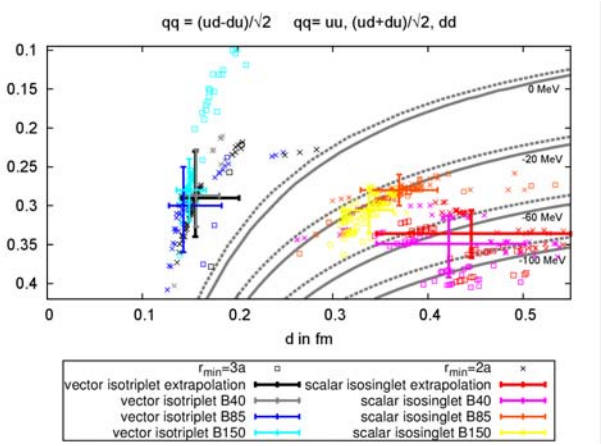

Figure 1: Binding energy isolines $E_B(\alpha, d) = \text{const}$ in the $\alpha - d$ plane for the scalar isosinglet ($I = 0$, $j = 0$) and vector isotriplet ($I = 1$, $j = 1$) channels and four pion masses: 140 MeV (extrapolated), 340 MeV, 480 MeV and 650 MeV. The error bars represent combined systematic and statistical errors. The area below the 0 MeV line corresponds to a bound state, the area above corresponds to a two-meson state.

References

[1] P. Bicudo, K. Cichy, A. Peters and M. Wagner, Phys. Rev. D **93** (2016) [arXiv:1510.03441 [hep-lat]].

[2] P. Bicudo, K. Cichy, A. Peters, B. Wagenbach and M. Wagner, Phys. Rev. D **92** (2015) [arXiv:1505.00613 [hep-lat]].

[3] A. Peters, P. Bicudo, K. Cichy, B. Wagenbach and M. Wagner, PoS LATTICE **2015** (2016) 095 [arXiv:1508.00343 [hep-lat]].

[4] A. Peters, P. Bicudo, L. Leskovec, S. Meinel and M. Wagner, PoS LATTICE **2016** (2016) 104 [arXiv:1609.00181 [hep-lat]].

[5] A. Peters, P. Bicudo, K. Cichy and M. Wagner, J. Phys. Conf. Ser. **742** (2016) [arXiv:1602.07621 [hep-lat]].

* Work supported by HIC4FAIR/HGS-HIRe

DOI:10.15120/GR-2017-1

Improved operation for the ALICE Tier2 Centre at GSI

K. Schwarz, S. Fleischer, R. Grosso, J. Knedlik, T. Kollegger[1]
[1]GSI, Darmstadt, Germany

This article describes the improvements implemented in 2016 to increase the reliability and performance of the ALICE Tier2 Computing Centre at GSI.

ALICE Tier2 centre at GSI and ALICE Grid in Germany

The ALICE Tier2 centre and the National Analysis Facility at GSI provide a computing infrastructure for ALICE Grid and for the local usage of the German ALICE groups.

The storage resources pledged to the global ALICE community (2300 TB) are provided via a Grid Storage Element which consists of a set of xrootd daemons running on top of the Lustre file system.

The main elements are the xrootd redirector in combination with three xrootd data servers as well as two xrootd forward proxy servers, also for redundancy. The redirector of the GSI storage element is using the split directive of xrootd and redirects external clients to the external interfaces of the xrootd data server machines and internal clients to the internal interfaces which are directly connected to the local Infiniband Cluster. The xrootd forward proxy servers provide the possibility to Grid jobs running inside the protected HPC environment to read input data from external data sources using the proxy interface. Writing to external storage elements is possible via the same technique. The complete setup can be seen in fig. 1.

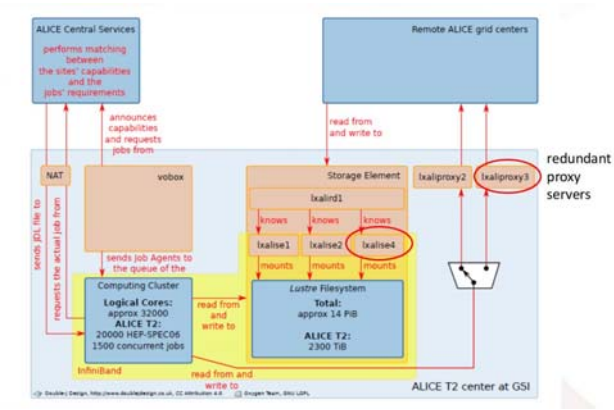

Figure 1: ALICE tier centre at GSI

Throughout the year GSI participates in centrally managed ALICE Grid productions and data analysis activities, but also analysis jobs of individual users are running on the ALICE Tier2 centre. The overall job share of successfully computed jobs in 2016 contributed by the German Grid sites, the GSI Tier2 centre and Forschungszentrum Karlsruhe (ALICE tier1 centre) has been 6.3% of all ALICE Grid jobs worldwide. This corresponds well with the pledged CPU resources for 2016: 16000 HEP-SPEC06 for GSI Tier2 (7% of the global Tier2 requirements) and 39250 HEP-SPEC06 for FZK (25% of the global T1 requirements)

Since Spring 2016 the ALICE Tier2 centre is running within GSI's Green IT Cube.

Singularity

A specific container technology - Singularity - has been adopted in the ALICE Tier2 centre at GSI in order to encapsulate ALICE jobs in an experiment specific system image. This made it possible to run ALICE Grid jobs smoothly in their standard Scientific Linux environment on top of the Debian based host system of the local HPC cluster. A detailed description of the related configuration and workflow can be found in [1].

Key Performance Indicator

High-level performance indicators, such as delivered computing wall time or Storage Element availability are being monitored and show the overall status of the ALICE Tier2 centre. Furthermore, a tool has been developed which identifies how jobs performed before and after they have been submitted to GSI. This helps putting the absolute job success rate into context and makes it easier to recognize if the GSI ALICE Tier2 centre is performing well.

XRootD Plugins

In order to optimise the current storage infrastructure, namely the access to Lustre through XRootD data servers, several XRootD Plugins have been developed. One solution provided is a client and a server based Plugin which is able to redirect XRootD file operations directly to Lustre thus bypassing the need for Grid jobs running at GSI to double the network traffic by first communicating with the XrootD data servers. A second solution provided is a Plugin which reports to the central ALICE Grid Monitoring the ALICE Grid quota on Lustre instead of the full Lustre capacity provided at GSI as it did before. The implementations are described in [2].

References

[1] R. Grosso, M. Bauer, S. Fleischer, J. Knedlik, T. Kollegger, K. Schwarz, "Use of Singularity containers for the ALICE T2", GSI Scientific Report 2016

[2] J. Knedlik, P. Kramp, "Adapting XRootD to the site specific infrastructure at GSI", GSI Scientific Report 2016

DOI:10.15120/GR-2017-1

Adapting XRootD to the site specific infrastructure at GSI

J. Knedlik[1] *and P. Kramp*[1]
[1]GSI, Darmstadt, Germany

Abstract

Operating an XRootD service, the established software standard for WAN data access in HEP and HENP, to access the scientific data stored on-top of the HPC infrastructure at the ALICE Tier 2 centre at GSI revealed multiple challenges and requirements. This article describes the current state of development for XRootD based solutions, especially XRootD client & server plug-ins.

ALICE Tier 2 & XRootD

GSI is operating the only German ALICE Tier 2 centre. In this context GSI provides a computing infrastructure and storage to the ALICE community. In ALICE's AliEn Grid framework data is accessed through the XRootD protocol. XRootD enables the use of this data through a scalable federated storage system. At GSI, instead of operating XRootD servers with local storage, the shared HPC Lustre filesystem is used as storage backend of the XRootD servers. In AliEn, Grid jobs requiring the same data are preferably scheduled on the same site to lower the need for traffic between sites. This means, that local data is reused many times and therefore it is essential to optimize the I/O performance.

Improving the I/O performance at GSI using XRootD plug-ins

With the current storage infrastructure at GSI, namely the access to Lustre through the XRootD data servers, the following room for improvement has been identified: The three XRootD dataservers can provide limited I/O bandwidth and all data read locally via XRootD from Lustre needs to be sent over the network twice (Lustre to XrootD server & XrootD server to client), effectively doubling the network traffic for an I/O operation.

We considered two kinds of plug-ins in order to improve I/O performance, namely a client plug-in and a server plug-in. The XRootD client plug-in API offers a way to overwrite XRootD file operations. Being configurable via a local configuration file, the plug-in replaces specified remote URLs with local file paths. The current plug-in, in contrary to the version specified in last year's report[1, p. 280], uses XRootD file operations. A requirement for this version is a modified XRootD client source[2], which has been developed in cooperation with the XRootD development team and shall be integrated into the main base soon. It introduces a new component for handling local file operations, which is also necessary for a redirection to the local file system by using a server or client side plug-in. The server plug-in has the same purpose as the client plug-in. A redirector server may load this plug-in, to redirect clients to locally available files, if both client and redirection target are inside a private network, as this guarantees local availability of the required file at GSI. In order to allow a redirector to redirect to a local file, additional changes needed to be implemented into the XRootD base code. Therefore notification of the XRootD client component responsible for file operations, about accessing the file locally instead of remotely, had to be added. We also modified XRootD's communication message handling interface in order to enable the aforementioned notification. The remaining operations are handled in the same way as in the client plug-in.

Lustre quota as XRootD file space statistics using an XRootD plug-in

One of ALICE's monitoring tools reported wrong space usage statistics to CERN. It uses the onboard XRootD executable xrdfs in order to get space usage statistics from local storage elements. Since XRootD runs on top of the local Lustre filesystem, the XRootD data server returned statistics referring to the whole Lustre file space instead of ALICE's Grid quota at GSI. This in turn gave misleading information to ALICE's distributed data management system. Our deployed solution was to use the XRootD - data server - plug-in API to create a plug-in that feeds Lustre quota statistics collected by using the Lustre C-API to our data servers instead of using the base XRootD calls.[3]

Conclusion

In conclusion we have implemented XRootD plug-ins redirecting client I/O to data on Lustre which has the capability to significantly improve the I/O performance. We proposed implementation changes in the core XRootD code to allow robust usage of such plug-ins. A data server plug-in for Lustre quota statistics has been deployed. The current tests give promising results and show that plug-ins can be used to adapt XRootD to our site's specific needs.

References

[1] "GSI Scientific Report 2015", doi = 10.15120/GR-2016-1, http://dx.doi.org/10.15120/GR-2016-1

[2] https://github.com/pkramp/xrootd/tree/local-file-impl_localfilehandler

[3] https://github.com/jknedlik/XrdLustreOssWrapper

DOI:10.15120/GR-2017-1

Use of *Singularity* containers for the ALICE Tier2 at GSI

R. Grosso[1], *M. Bauer*[1], *S. Fleischer*[1], *J. Knedlik*[1], *T. Kollegger*[1], *and K. Schwarz*[1]
[1]GSI, Darmstadt, Germany

A specific container technology - *Singularity* - has been adopted in the GSI ALICE Tier2 site to encapsulate ALICE jobs in an experiment-specific system image, thus allowing to run in the locally shared HPC environment. The use of *Singularity* in this context and the resulting benefits are presented.

Container technologies and Singularity

As an ALICE Tier2 site, GSI provides storage and computational resources integrated in the Grid of the experiment via its middleware, *AliEn*. This assumes a standard environment, notably a specific operating system. Appropriately chosen container technologies can help considerably to fit these requirements into a shared cluster.

Containers are a thin layer encapsulating a system environment, from a user perspective looking like lightweight virtual machines. The user can install his own software in a container, without affecting other containers or the host environment, on which the container runs. Since containers include neither hardware virtualization nor a kernel, their footprint is significantly smaller than that of a virtual machine and applications in a container run at the same level as native applications.

Containers have become very popular in the last years as an enterprise solution for running many isolated instances of a definite working environment on a single machine. They could in addition effectively satisfy a strong demand in the science domain too, offering a way to insure application and environment compatibility. The most popular container system, *Docker*[1], which is at the origin of the dissemination of container technology of the last years, has not yet matched this request in HPC environments, mostly due to security issues. A relatively new container framework - *Singularity*[2][3] - overcomes these problems. The strongest point for the adoption of *Singularity* as a container solution on a shared HPC cluster is **security**. The user inside a *Singularity* container is the same as the user on the host. Privilege escalation within the container is not possible and there is no root-owned container daemon, which are all important points in favor of this technology both in terms of security and of effective resource management. In addition the image is provided as a single file, which makes it very portable.

Implementation at the GSI ALICE Tier2 site

Prerequisite for running jobs within a *Singularity* image is the installation of *Singularity* on the cluster. The node requesting the resource manager to launch jobs on behalf of ALICE (VOBox) must prepend the script call with the `singularity` command and its flags. This is implemented in a wrapper command taking precedence over the default command for launching batch scripts (`sbatch`).

On a building host a definition file describes the system image, specifying for example the list of packages which have to be installed, and is used by `singularity bootstrap` to make the image. By adapting the definition file to ALICE-specific requirements, we can provide within the *Singularity* image expected packages and the expected environment (e.g. we had to correct the definition of locales via environment variables). Correspondingly adapting the system and the environment on a dedicated cluster would have required considerably more work, but would not even have been possible on a shared HPC cluster, as is our case.

AliEn jobs running in the container need to read also from a CernVM File System mounted on the cluster. That is possible by means of the `--bind` option, with which the specified destination is bind mounted in the container. AliEn jobs also need to write output to a specified location, within the `/tmp` directory. These did not require any additional setting, as *Singularity* automatically shares `/tmp` into the container. However we needed to set the user home directory in the container to a valid path. That is achieved by means of the `--homedir` flag, requiring only that the directory exists in the container to serve as a mount point. This is just one additional line in the definition's file. To keep synchronized with the experiments standard running environment, the definition file has to be updated when needed, and the image must be regenerated and newly deployed on the CernVM File System, where it is seen by jobs from all worker nodes. In case, the `singularity` command line in the sbatch wrapper on the VOBox machine is also updated.

This workflow has allowed to operate the ALICE Tier 2 site at GSI, transparently running AliEn jobs in their standard Scientific Linux 6 environment on top of the Debian host system of the local HPC cluster and substantially reducing possible causes for failing jobs together with the load of debugging and fixing them.

References

[1] https://www.docker.com

[2] G. M. Kurtzer, "Singularity 2.1.2 - Linux application and environment containers for science", August 2016, doi = 10.5281/zenodo.60736, https://doi.org/10.5281/zenodo.60736

[3] http://singularity.lbl.gov

DOI:10.15120/GR-2017-1

Machine learning based monitoring of HEP computing infrastructures*

A. Gomez Ramirez[1], *C. Lara*[1], *and U. Kebschull*[1]
[1]Infrastructure and Computer Systems for Data Processing (IRI), Goethe-University Frankfurt

Introduction

Computing infrastructures used in High Energy Physics (HEP) need tools to monitor, analyze and react to potential security incidents. These tools should collect data such as resource consumption, system logfiles and sequence of system calls for detecting and analyzing anomalies caused by security problems. They should also be able to perform automated actions when an attack is detected without the administrator intervention. We are working in a framework that accomplishes these requirements, with a proof of concept implementation for the AliEn Grid used by the LHC experiment ALICE, also used in the Grid site at GSI. We show how we achieve a fully virtualized environment that improves the security by isolating services and jobs. We describe a collected dataset for Machine Learning based Intrusion Prevention and Detection Systems. This dataset is composed of resource consumption (such as CPU, RAM and network traffic), system logfiles, and system call data collected from production jobs running in a Grid test site and a big set of malware. This malware was collected from security research sites. Based on this dataset, we will proceed to develop Machine Learning algorithms able to detect malicious jobs.

Implementation

We have deployed a Grid site based on AliEn [1] in a local Linux cluster, with 5 Ubuntu 14.04 nodes. To orchestrate and run the jobs inside Linux Containers (LC) we have tested 3 different tools: Google Kubernetes, Apache Mesos and Docker Swarm.

We have decided to work with Docker Swarm, given its more simplistic setup. As LC engine we use Docker with Centos 6 container images. We have developed AliEn interfaces for the mentioned resource management system. CVMFS [2] is installed at the hosts and shared as a volume inside the AliEn container, to allow access to HEP libraries. Currently we execute one Job per container. This is useful to increase the traceability between different jobs. Also, this is the natural micro service model for LC.

We have used Prometheus [3] and Sysdig [4] as the monitoring infrastructure for collecting data from normal Grid jobs. Prometheus allows to take resource usage data directly from containers and collect it by a RESTful interface. Sysdig enables system call capture in Linux OS, in a fast and reliable way. We have developed a custom Python library to integrate these tools, and make them fit our needs. This infrastructure has been utilized for the execution and measurement of AliEn production jobs, that are tagged as normal jobs.

A network isolated machine for malware data collection was used, with the same setup as the Grid worker nodes. We have downloaded a set of 10000 Linux malware samples from a security research web site [5]. We ran the samples and collected the same information as for the normal jobs (logfiles, sequence of system calls, resource usage data). At the end we obtained a dataset that allows to train and test our selected Machine Learning algorithms: SVM, Radial Basis Function NN and Deep Learning NN. Figure 1 shows a representation of the proposed framework.

Next steps

Using the described dataset, we will proceed to test the selected Machine Learning algorithms to find the one that offers the best accuracy and performance.

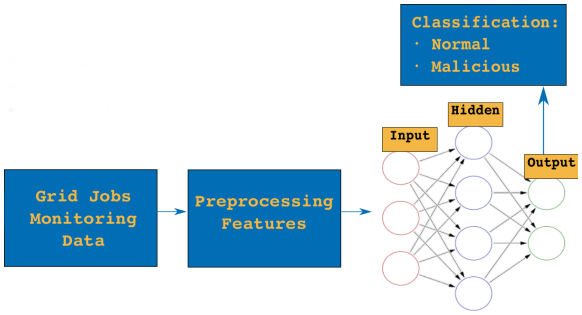

Figure 1: Data obtained from the monitored Grid jobs is processed to extract feature that feed a ML algorithm. This algorithm decides whether a job is normal or malicious.

References

[1] A. Gomez Ramirez, C. Lara and U. Kebschull, "Intrusion Prevention and Detection in Grid Computing - The ALICE Case". JPCS 2015

[2] P Buncic et al., "CernVM - a virtual appliance for LHC applications". Proceedings of the XII. International Workshop on Advanced Computing and Analysis Techniques in Physics Research (ACAT08), Erice, 2008 PoS(ACAT08)012

[3] https://prometheus.io/

[4] http://www.sysdig.org/

[5] https://virusshare.com/

* Work supported by HGS-HIRe, BMBF and the ALICE offline group.

DOI:10.15120/GR-2017-1

FairMQ status

A. Rybalchenko[1] *and M. Al-Turany*[1]
[1]GSI, Darmstadt, Germany

The FairRoot framework provides a set of tools for simulation, reconstruction and data analysis for particle physics experiments [1]. A message queue aware package (FairMQ) has been introduced to FairRoot that enables reconstruction and analysis of free streaming data [2] [3]. Moreover it makes it possible for user code to run in a distributed and heterogeneous environment with minimum effort from the user. FairMQ devices are independent processes that can be coordinated and synchronized (if necessary) by an external mechanism through the internal state machine of the device. Furthermore, processes using FairMQ can be configured via extensible configuration system. The communication layer in FairMQ has an abstract interface that hides the transport implementation from the user code, which allows changing the transport layer without changing the user code. In addition to two existing transport implementations (with ZeroMQ [4] and nanomsg [5]) a new one, using shared memory, has been introduced. Following is a brief description of this and other FairMQ developments:

Shared memory transport

A new implementation of the transport interface using shared memory has been introduced. The shared memory transport becomes relevant when devices on the same node want to transport/share large messages. The implementation avoids copying of the message body, which can significantly improve performance and reduce CPU usage with large messages. The implementation uses Boost.Interprocess [6] library for the management of the shared memory and ZeroMQ [4] library for the transfer of the meta data associated with every message. Fig. 1 shows the transfer rate between two processes on the same node using the shared memory transport implementation. In addition to high performance, the shared memory transport also has much lower CPU usage compared to existing TCP/IPC transports.

Multiple transports per device

Introduction of the shared memory transport provided an important use case for combining more than one transport implementation within the same device: a device might want to receive data over network and send it further via shared memory. To support this use case FairMQ now allows to configure the transport on a per-channel basis.

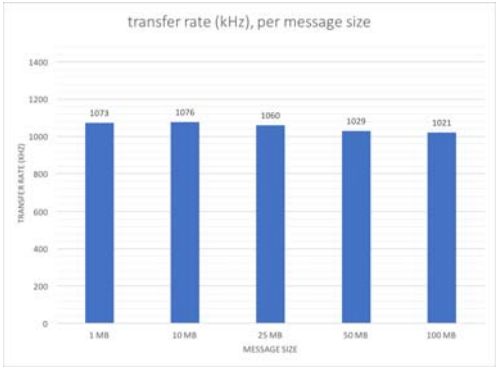

Figure 1: Shared memory transport transfer rate

Callback-based API

A new set of APIs has been introduced to FairMQ with the goal to simplifiy implementation of common device use cases. These APIs allow the device developers to provide callbacks to device channels, that will be called whenever data arrives on the corresponding channel. FairMQ manages the callback with respect of the state machine, ensuring they are called only during allowed states.

Boilerplate reduction

To further simplify the work of device developers FairMQ now supplies a common header file that provides a main() function that handles the necessary setup and control of the device. The device developer only needs to include this file and implement two functions - one returning the device class to use and another to extend the command line options (if necessary).

References

[1] M. Al-Turany et al.: The FairRoot framework, Journal of Physics: Conference Series (2012)

[2] M. Al-Turany, A. Rybalchenko: GSI Scientific Report: Streaming data processing with FairMQ (2013)

[3] M. Al-Turany, D. Klein, A. Manafov, A. Rybalchenko, F. Uhlig: Extending the FairRoot framework to allow for simulation and reconstruction of free streaming data. Accepted for publication by Journal of Physics: Conference Series (2013).

[4] ZeroMQ: http://zeromq.org/.

[5] nanomsg: http://nanomsg.org/.

[6] Boost.Interprocess: http://www.boost.org/doc/libs/1_63_0/doc/html/interprocess/.

DOI:10.15120/GR-2017-1

Message based reconstruction example in FairRoot

R. Karabowicz[1], *M. Al-Turany*[1], *D. Klein*[1], *T. Kollegger*[1], *D. Kresan*[1], *A. Lebedev*[1], *A. Manafov*[1], *A. Rybalchenko*[1], *F. Uhlig*[1], *and N. Winckler*[1]

[1]GSI, Darmstadt, Germany

Introduction

The big scale data analysis in the FairRoot will be based on the message queue transport ([1] [2]), which provides asynchronous exchange of data packets between running processes, be it on one or multiple computing nodes. The communication between processes is realized by a transport layer, FairMQ, which currently builds on ZeroMQ or nanomsg transport.

The performance achieved for the previously implemented examples [3] encouraged the introduction of a new example that shows the transition from the single process data analysis (default in FairRoot) to multiprocess reconstruction.

FairMQ devices

The base component of FairMQ is a device. The device encapsulates tasks, provides simple functionalites and runs as a single process. The FairMQ framework offers set of general devices, that may be used to peform basic services, like splitting or merging of the data streams, enabling access to the reconstruction parameters (parameter server).

As a part of the presented example (FairRoot/examples/MQ/9-PixelDetector) several devices have been implemented:

- FairMQEx9Sampler - reads the root file (standard output FairRoot file with data organized in branches of a ROOT tree), packs the data from requested branches into TMessage, and sends the created message to a transport layer;
- FairMQEx9TaskProcessor - templated class, which unpacks data from the received message, runs the attached FairRoot task to process the data, packs the reconstructed data into messages, and finally moves the created message into transport layer; it also gives possibility to connect to the parameter server to access the reconstruction parameters needed by tasks;
- FairMEx9Sink - unpacks data from the received message to store it in the output ROOT file, which mimics the output of a standard single-process FairRoot program.

These devices are able to read and write any FairRoot file, as requested by the user. The processor device is compatible with the FairRoot tasks, provided that they implement three FairMQ-specific functions: GetParList(), InitMQ() and ExecMQ(). This functionality is enabled by using the ROOT's TMessage container class, however it comes with throughput penalty, and thus increases execution time.

The step to enhance performance is to transport data without unnecessary oherheads. In the presented example a set of three similar devices shows the implementation of data transport using simple stl vectors of binary data. This shortens execution time twofold, but comes at a price of reduced generalization. In order to read or send different types of data, appropriate devices would have to be written.

Topology

The list of the FairMQ devices that run as a group together with the intended communication channels between them is called a topology. The user specifies the devices and their properties (file names, branch names, task types, etc.) in a shell script, while the attributes of communication channels (like IP and port addresses, communication type: push-pull, publish-subscribe, request-reply) are set via JSON configuration file. The schematic plot depicting simple topology is presented in Figure 1.

Figure 1: Simple topology example.

In the example, several topologies have been prepared to ilustrate various development strategies, like adding more analysis levels (first set of processors run hit finding, tracks are reconstructed on the second level and fitted on third). The user may run the devices in the interactive mode, when all devices start in separate windows, and may be steered with key combination or in the static mode, when the devices run as subprocesses in the background and need some level of automatization to at least be able to stop themselves on completion.

References

[1] A.Rybalchenko, and M.Al-Turany, "Streaming data processing with FairMQ", GSI Scientific Report 2013

[2] M. Al-Turany et al., "ALFA: A new Framework for ALICE and FAIR experiments", GSI Scientific Report 2013

[3] N. Winckler et al., "FairMQ application example in CbmRoot", GSI Scientifi Report 2014

DOI:10.15120/GR-2017-1

Status of the R3BRoot framework

D. Kresan[*1], *R. Plag*[1], *B. Löher*[1, 2], *M. Heil*[1], *V. Wagner*[2], *the R*^{3}*B collaboration*[1], *and the FairRoot group*[1]

[1]GSI, Darmstadt, Germany; [2]Institut für Kernphysik, TU Darmstadt, Germany

Reactions with Relativistic Radioactive Beams (R^{3}B) [1] is one of the future experiments at the FAIR facility. It will focus on studies of nuclear dynamics and astrophysics by performing reactions in inverse kinematics. The setup for detection of heavy fragments, protons, neutrons and gammas will be placed downstream the high-energy branch of the Super-FRS. The data coming from 10 complex detectors will be collected by a dedicated DAQ system and sent further to multiple client-side nodes running the analysis software R3BRoot. The R3BRoot framework [2] was designed to perform the calibration of the detectors and reconstruction of the reactions kinematics, completed by the high-level physics analysis. It also provides the functionality to calculate the interaction of particles with the pre-defined volumes of the R^{3}B setup and to simulate the response of the detectors. This is important during both stages: planning and design of the experiment as well as evaluation and understanding of the measured data.
The R^{3}B software is based on FairRoot [3] - a common software framework for FAIR experiments, developed at GSI. Figure 1 shows the schematic structure of R3BRoot, which functionality is delivered by the FairRoot framework and the UCESB software package.

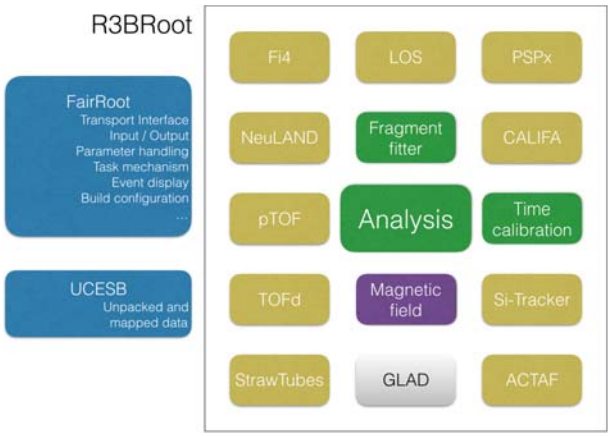

Figure 1: Basic components of the R^{3}B software. Yellow blocks for detectors include the code for calibration, reconstruction, and analysis. The analysis block is the combined high-level physics analysis. Green boxes are the additional algorithms.

R3BRoot is distributed under open-source license using GitHub and currently has 12 active contributors. The C++ code contains 38510 lines of code, 38% of which are automatically tested on a nightly basis. There is a dedicated forum for the user support and a website [2] with regularly updated instructions, selected documentation, and how-tos. In July 2015 and March 2017 two "R3BRoot Development Workshops" with approximately 30 participants each were held at GSI, focused on practical exercises in software writing and aiming at education of students.

Analysis of experimental data

The setup during the last test experiment in June 2016 at GSI SIS18 contained the start counter LOS, the tracking strip detectors PSPx, the fragment time-of-flight wall TOFd and the fiber tracking detector Fi4. Raw data in MBS format was unpacked and hardware channels were mapped to physical detector indices using the UCESB (Unpack and Check Every Single Bit) software tool. The experiment resulted in a successful test of the reconstruction chain up to the HIT level for LOS, PSPx and TOFd detectors. The online histogram server was configured and used for monitoring in online mode. Fi4 still requires both hardware and software development. Previously, based on the data from s438b experiment in 2015, the fully automated calibration procedure for NeuLAND neutron detector was developed [4]. Work is ongoing towards completion of the list of detectors with calibrated and reconstructed HIT data in order to proceed to the high-level physics analysis.

Status of simulations

The level of the simulations for detectors like CALIFA (gamma spectrometer), NeuLAND (neutron detector) [5] and VETO wall is advanced (including granular and detailed geometry description) and the results have previously contributed to the Technical Design Reports of the first two. Improvement of the description of the geometry and calculation of the response for other detectors is in progress and is currently focused on the preparations for the upcoming beam-time in 2018 at SIS18. There are also ongoing activities on the selection and validation of a Geant4 physics list suitable for the R^{3}B physics as well as on the design of classes for data levels in order to merge simulation and data analysis on the framework level.

References

[1] R^{3}B: https://www.gsi.de/r3b

[2] R3BRoot: https://www.r3broot.gsi.de

[3] M. Al-Turany *et al.* J. of Phys. Conf. Ser **396** (2012) 022001

[4] V. Wagner *et al.*, this annual report

[5] J. Mayer *et al.*, this annual report

* d.kresan@gsi.de

DOI:10.15120/GR-2017-1

DDS: The Dynamic Deployment System

A. Manafov[1] *and A. Lebedev*[1]
[1]GSI, Darmstadt, Germany

The Dynamic Deployment System (DDS) [1] is a toolset that automates and significantly simplifies a deployment of user defined processes and their dependencies on any resource management system (RMS) using a given topology.

During 2016 DDS development has been focused on improvements of the core code and main modules.

Shared memory communication. In the initial implementation dds-agents used to have only a network connection transport for communication with user tasks. This introduced certain implications, for instance, there was no guarantee that all key-value updates or custom command messages will be delivered to the user. As a fallback solution a shared memory was used to cache messages comming from network channels, to make sure that all messages are actually delivered to the user tasks. In order to improve and simplify this algorithm we have implemented a generic shared memory channel. The channel has similar API as DDS network channel, it supports two way communication, asynchronous read and write operations. Its implementation is based on the boost::message_queue library [2], on the DDS protocol which is used for message encoding and decoding and on the boost::asio library [2] for thread poolling and implementation of the proactor design pattern. The shared memory channel is used for communication between dds-agents and user tasks which significantly simplifies and secures the implementation (see Figure 1). There is no need to cache messages any more as we now can guarantee the delivery. All messages are stored directly in the shared memory and managed by the message queue. The new implementation shows a factor of 2 better performance in our test case where 40 tasks intensively exchanging key-values on a single node with 40 logical cores. It is also forseen that the new shared memory channel will be used in other parts of DDS, for example, for communication between dds-agents on the local machine.

New dds-intercom library API. With the release of the shared memory channel we have also introduced a new version of the dds-intercom library API.

Versioning in key-value propagation. In DDS a single property in the topology results in multiple keys at runtime, namely, each task gets its own key for a certain property. A given task can only change a key it owns. But in some edge cases a versioning of key-value pairs is required to protect against key updates with an obsolete values. For instance, if task sends a key-value, crashes and then restarts and sends it again. In some cases the key update which was send first can be processed after the key update which was send last. As a result there will be a wrong value assigned to the key.

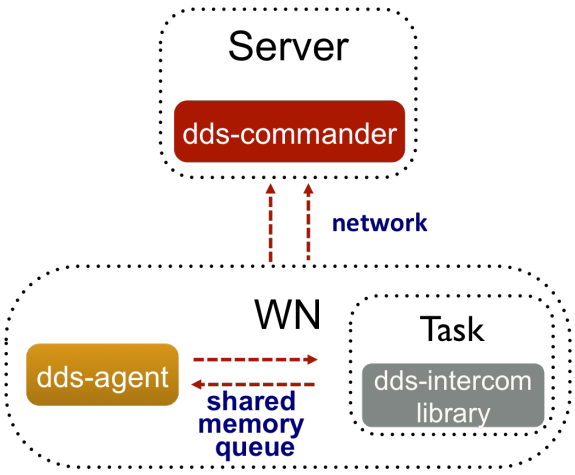

Figure 1: New shared memory communication.

The versioning prevents such situations. Its implementation is completely hidden from the user, all versioning algorithms are processed by DDS behind the scene.

Runtime topology update. In 2016 we have also introduced a runtime topology update feature to offer users a possibility to make changes in a currently running topology without stopping it. The algorithm determines the difference between old and new topologies on the fly. As a result it creates lists of tasks and collections that has to be added and removed. These lists are passed to DDS scheduler which then applies required changes by sending commands to corresponding DDS agents.

RMS plugins. Newly developed LSF and PBS plugins were added to the list of supported DDS RMS plugins.

Automated tests using dds-octopus. Growing complexity of DDS requires powerful functional tests, as most of issues can only be detected during runtime when multiple agents are in use. Unit tests can't cover all edge cases. We therefore introduced a dds-octopus tool chain - a full blown functional test machinery for DDS. dds-octopus features a rapid development of test cases with minimum code duplication. The tool chain is designed to run fully automatic without human intervention. Since DDS 1.4 it runs as a part of continues integration builds.

References

[1] The Dynamic Deployment System (DDS), http://dds.gsi.de.

[2] The BOOST C++ Libraries, http://boost.org

DOI:10.15120/GR-2017-1

FairDb status

D. Bertini[1]
[1]Scientific Computing, GSI, Darmstadt, Germany

FairDb is a virtual database library which extends the FairRoot[1] framework initialization scheme to any SQL compliant database systems. This report describes the present FairDb status.

Introduction

FairDB provides the user with a well-defined and uniform API for database manipulation. Using internally the ROOT `TSQLServer` class [2], the same user code can be executed independently on Oracle, MySQL, PostGreSQL and even SQLite SQL database engines (Fig. [1]).

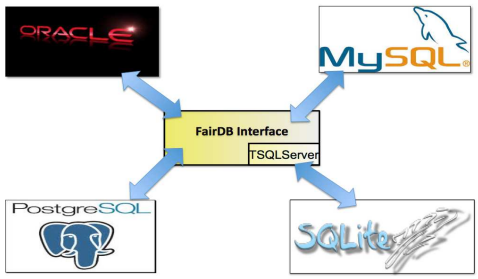

Figure 1: FairDB supported SQL-Database engines.

Generic parameter template

A new generic paremeter interface has been implemented in order to ease the writing of parameter container. The new interface uses the Curiously Recurring Template Pattern (CRTP[4]) to automatically generate all the neccessary functions to perform input and output operations. The user can then focus on the more important task of choosing and designing the parameter data model.

Caching

In order to reduce the response time FairDb stores the data in a client cache memory or cache file using a dedicated serialization procedure. When queries are executed repeatedly, the user application retrieves results directly from the client cache, resulting in faster query response time (Fig. [2]).

Sts Qa web interface

The Sts Qa web interface has been completely redesign to cope with automatically attributed sensor unique identifier. The query of sensor quality information is done via the vendor production batch number. Fig. [3] shows a snapshot of the new Sts Qa web interface.

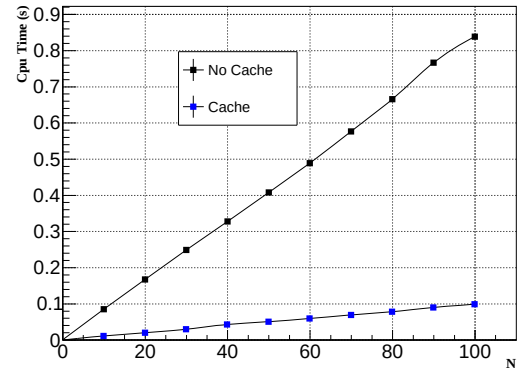

Figure 2: Query response time as a funtion of the number of parameter initialised with and without caching mechanism.

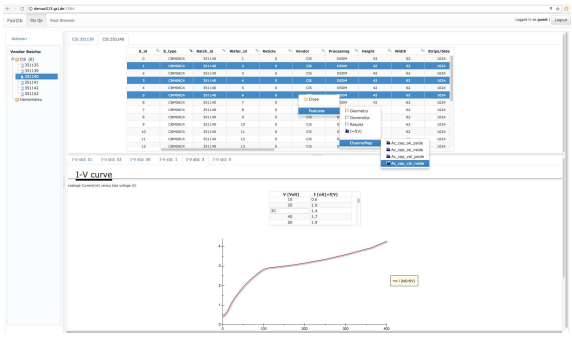

Figure 3: Sts Qa interface

References

[1] The FAIR simulation and analysis framework 2008 J. Phys.: Conf. Ser. 119 032011

[2] R. Brun, F. Rademakers, P. Canal, I.Antcheva , D. Buskulic, O. Couet, A. and M. Gheata *ROOT User Guide* CERN, Geneva 2005.

[3] FairRoot Virtual Database (User Manual) `https://cbm-wiki.gsi.de/foswiki/pub/STS/STSComponentsDatabase/FairDB_Manual.pdf`

[4] `https://en.wikipedia.org/wiki/Curiously_recurring_template_pattern`

DOI:10.15120/GR-2017-1

Lattice QCD Dslash operator implementation on FPGA accelerator with data-flow computing*

T. Janson, and U. Kebschull[1]
[1]IRI Goethe University, Frankfurt, Germany

Introduction

In this work we investigate new methodologies to compute Lattice QCD algorithms using data-flow computing. The algorithm is described and programmed as a graph that models the data movement through arithmetic compute nodes. This can be seen as the opposite of programming the control flow for traditional von Neumann computers, where one programs or models the flow of control commands. The concept data-flow programming is also discussed in [1, 2]. Such a graph is programmed with MaxJ from Maxeler and will run on DataFlow machines from the same company. For this, Maxeler provides a framework to develop, simulate, and run such applications. The goal is to figure out if we can accelerate Lattice QCD simulation with this framework.

Data-flow computing is not a new approach and goes back to works from Jack B. Dennis and many others since the beginning of 1970s [3]. We use the concept developed from Maxeler called Multiscale DataFlow Computing [4] that combines approaches like static and dynamic data-flow principles, and vector or array processing to scale the features of a compute problem on different levels of computation finding an optimal solution.

The Framework

The framework consists of a data-flow machine node (MPC-X) and a CPU host computer [5]. Both are interconnected with Infiniband. Figure 1 shows the architecture. Further, the software part is divided into a data-flow compiler, which compiles the MaxJ code into a configuration bit file for the MPC-X node, and a run time system that controls and schedules the configuration and execution of data-flow engines (DFE). Each MPC-X can host eight DFEs, where each has 96 GByte DDR3 memory over six channels connected, which is called large memory (LMem). In addition, all DFEs form a ring structure to stream data between data-flow engines. It is possible to connect several CPU host computers and MPC-X nodes over an Infiniband network to form a supercomputer. This study is done on one CPU host and one MPC-X with four DFEs.

Dslash Operator as Data-Flow Graph

We use the Wilson Dirac operator described in [7, p.115] that performs $\Psi'(n) = (1 - \kappa H)\,\Psi(n)$, where the hopping matrix H collects all nearest neighbour terms. Here, n is a

* Work supported by HIC for FAIR and HGS-HIRe

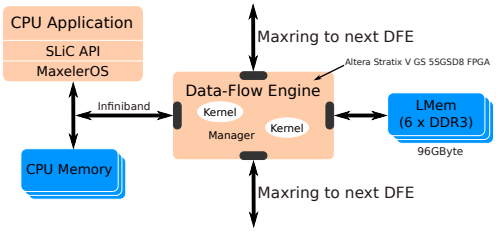

Figure 1: Maxeler System Architecture

four dimensional vector (x, y, z, t) and labels lattice sites. For each site index n we compose a data structure with one spinor and its four link variables to be held in LMem as an array of structure (AoS). Read or write commands to the LMem fetch these data structures in bursts of 384 Byte using a linear access pattern. The indexing scheme of the data-flow stream and also the storage order in LMem is given by $n = x + y * N_s + z * N_s^2 + t * N_s^3$ with spatial lattice extent parameter N_s.

The implemented data-flow kernel graph for one direc-

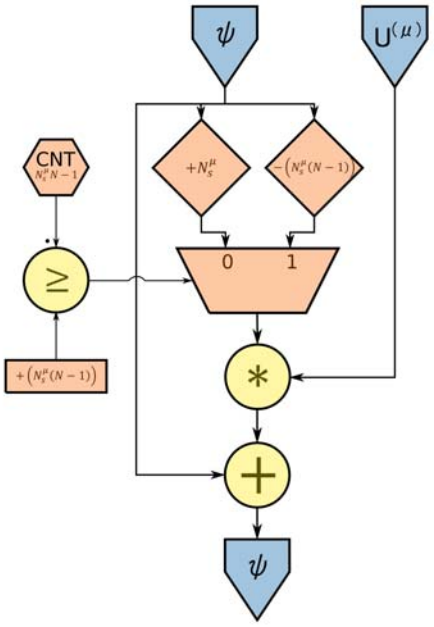

Figure 2: Data-flow graph for one lattice coordinate in forward direction which collects one neighbour term

DOI:10.15120/GR-2017-1

tion μ is shown in figure 2. Such a directed kernel graph contains a small set of node types and arcs [5]. Data flows along the arcs and through the fully pipelined nodes. Circles in a graph are arithmetic and logic operations, rectangles provide constant parameters, and diamonds implement the offset operator. In addition, there are multiplexer nodes, counter cores, and last I/O nodes. A program describes the graph with MaxJ/Java syntactic code [5, 6]. As in Java, one can define methods for complex operations like matrix vector multiplications which are then sub graphs in a kernel. This way, we have implemented the Dslash as shown partly in figure 2 to collect all neighbours simultaneously. Here, the offset operator picks up the nearest neighbour terms within the data-flow stream. All arithmetic operations down to simple additions and multiplications are pipelined. Each core is running fully parallel on hardware. The offset parameters are derived from lattice extents and known at compile time. These parameters express data locality and the offset core allocates BRAM on an FPGA for larger offsets. It is the MaxJ compiler which creates VHDL code from the graph and distributes the local memory resources in a optimal way near to the compute cores.

Implementation Results and Outlook

We have implemented the Wilson Dirac operator in single precision, which fits completely on an Altera Stratix V FPGA (MAX4) using fixed-point arithmetic. The resource usage is shown in table 1. It should be noted that the algorithm is implemented as a full data-flow graph that collects all nearest neighbour terms to perform all vector and matrix multiplications as well as additions in one kernel tick. This allows us to update one spinor collecting all neighbour terms in one clock cycle. The so implemented operator is memory bound with an equivalent arithmetic intensity of 0.92 FLOPs/Byte. With 133 MHz kernel clock frequency, we get a equivalent theoretical peak performance of 176 GFLOPs. We use the term "equivalent" here, because our implementation is using fixed-point arithmetic. Each site is read or written only once from or to the LMem using a linear access pattern to get the best possible memory bandwidth. To collect all neighbours, it is necessary that the lattice fits completely into BRAM, which restricts our size to $16^3 \times 4$. Thus, we have developed a custom memory command generator to access the LMem also for any bigger lattice divided into tiles, where one tile will be computed with the Dslash implementation described above. The communication with neighbour tiles is performed over halo buffers. The focus is to improve the memory access to get the highest possible performance. Each tile as well as the lattice itself is a four dimensional hypercube. The surrounding next neighbour tiles, the surface for such a cube, are three dimensional volumes. There are eight neighbours. The idea is to stream the tiles through a DFE in one direction that way to get the best possible linear memory access on the LMem, where we need six halo buffers to the other directions. Tests have shown that we can reach a peak performance of 25 GByte/s using a custom memory command generator which is only the half LMem peak performance of 48 GByte/s. Therefore, we have to improve the LMem interface, which is still an ongoing process. In addition, a first test against a given data set show a relative error of $10^{-4}\%$ compared to exact values computed with Mathematica.

Resource Usage				
Logic utilization	114771	/	262400	(43.74%)
Primary FFs	203944	/	524800	(38.86%)
Secondary FFs	5810	/	524800	(1.11%)
Multipliers	2304	/	3926	(58.69%)
DSP blocks	1152	/	1963	(58.69%)
Block Memory	2489	/	2567	(96.96%)

Table 1: Resource usage of implemented Dslash operator processing $\Psi'(n) = (1 - \kappa H)\,\Psi(n)$ to collect all neighbour terms

References

[1] F. Gruell and U. Kebschull, "Accelerating of Biomedical Image Processing with Dataflow on FPGAs", River Publishers, 2016, ISBN 978-87-93379-36-7

[2] V. Milutinović, J. Salom, N. Trifunovic, R. Giorgi, "Guide to DataFlow Supercomputing", Springer, 2015, ISBN 978-3-319-16229-4

[3] J. B. Dennis and D. P. Misunas, "A preliminary architecture for a basic data-flow processor", ISCA'75, ACM, 1974, p. 126–132

[4] O. Pell (Maxeler), "Keynote: Multiscale Dataflow Computing", 6th International Workshop on Multi-/Many-core Computing Systems (MuCoCoS-2013), Edinburgh, UK, 2013

[5] Maxeler Technologies, "Programming MPC Systems", White Paper, June 2013

[6] OpenSPL Consortium, "OpenSPL: Revealing the Power of Spatial Computing", White Paper, Dec 2013

[7] C. Gattringer and C. B. Lang, "Lecture Notes in Physics 788: Quantum Chromodynamics on the Lattice", Springer, 2010, ISBN 978-3-642-01849-7

DOI:10.15120/GR-2017-1

Testing of new sensitive TLD cards

E.Kozlova[1], A. Sokolov [1], M. Pyshkina [2], and T. Radon[1]
[1]GSI, Darmstadt, Germany; [2]Ural Federal University, Yekaterinburg, Russia

Introduction

During the GSI accelerator facility operation the radiation fields outside the shielding are dominated by the neutron component which is monitored among others with a passive thermoluminescent based dosimeter. The sensitive elements are thermoluminescent crystals. They are situated in the center of a polyethylene moderator. In order to improve the response to high energy neutrons the moderator is equipped with a lead layer. Each sphere is equipped with one card carrying pairs of TL 600/700 crystals [1].

In some cases it is required to measure small doses which can hardly be distinguished from the natural background. In this work, the sensitivity threshold for new TLD cards and previously used TLD cards was determined.

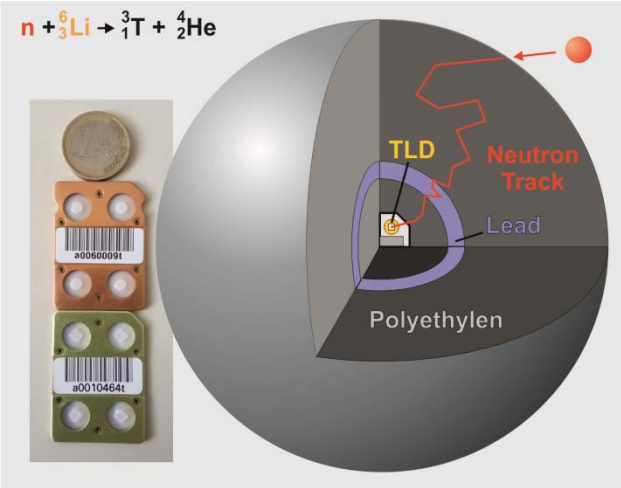

Figure 1: Schematic view of the GSI sphere with a TLD card. The radius of the sphere equipped with lead is 16,25 cm. Previously used TLD (yellow) and new (orange) TLD cards are shown in comparison with a one Euro coin.

Measurements

Spheres containing two type of TLD cards were positioned in one meter distance from a 37 GBq (1 Ci) ^{241}Am(α,n)Be neutron source. An ambient dose equivalent of 21,1 µSv per hour was delivered by the source at the position of the spheres. The cards inside the spheres were irradiated for 15 minutes, 30 minutes, 1 hour, 2 hours and 4 hours. The new TLD cards were additionally irradiated for 7 minutes.

Results

The results of the experiment are presented in Fig 2. Relative deviations of the measured ambient dose equivalent from the expected are calculated for old and new TLD cards. The deviations are plotted versus the expected doses. It can be clearly seen that the old TLD cards might be used for doses above 20 µSv only and the new TLD cards might be used for smaller dose measurement down to ~2 µSv. Thus new TLD cards are more suitable for the area monitoring with low dose rates. Similar results are produced by the spheres without lead layer.

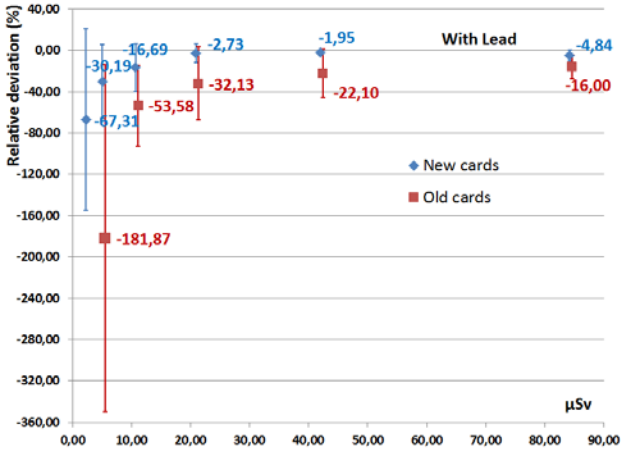

Figure 2: Relative deviation of measured ambient dose equivalent values from calculated values.

The calibration of the detectors was performed by also using a ^{241}Am(α,n)Be neutron source. The energy dose response of the bare thermoluminescent elements was determined with a ^{137}Cs γ-source before the cards can serve as neutron detectors. The corresponding values are stored for every card in the automatic TLD reader [2]. The calibration factors for the spheres with lead and without lead with two types of the TLD cards are listed in Table 1. The calibration factor is defined as the ratio of the measured energy dose response in Gy and the expected dose equivalent from the source in Sv.

Table 1. Calibration factors for the TLD cards situated in the spheres with and without lead layer.

Detector	New	Old	unit
With Lead	0,83±0,05	2,40±0,03	Gy/Sv
Without Lead	0,88±0,05	2,82±0,09	Gy/Sv

References

[1] F. Gutermuth et al., The response of various neutron dosemeters considering the application at a high energy particle accelerator, Kerntechnik, 68, 172-179 (2003)

[2] Thermo Scientific Harshaw 6600 PLUS TLD Reader, https://tools.thermofisher.com/content/sfs/brochures/Harshaw-6600-Brochure.pdf

DOI:10.15120/GR-2017-1

Neutron dosimeters for the high energy accelerators

A. Sokolov[1],G. Fehrenbacher[1,2], E. Kozlova[1], T. Radon[1]
[1]GSI, Darmstadt, Germany; [2]now at Uni. Tübingen, Germany

High energy accelerator facilities are sources of harmful radiation which should be continuously surveyed during operation. Neutrons in a wide energy range are one of the main contribution factors to the radiation, thus a reliable neutron dosimeter for radiation control is required. The present passive neutron dosimeter "GSI Ball" [1] is sufficient for the measurement of doses caused by neutrons from thermal up to 100 GeV energies; still it has a rather large size and weight.

Recently we have used the Monte Carlo code FLUKA [2] to study different layouts of passive neutron dosimeters. The passive dosimeter signal is proportional to the absorbed energy in the sensitive element, in our case it is a thermoluminescence detector (TLD) card. The response function in terms of absorbed energy of the TL chips irradiated in neutron fields has been calculated. The simulations revealed a possibility to create a compact neutron dosimeter [3]. The chosen design was manufactured and tested at the CERF [4] facility at CERN. The results approved the simulation approach and confirmed the possibility to use the dosimeter in high energy neutron fields [5].

Our further design developments improving the dosimeter response brought us to the dosimeter depicted in fig.1 (left).

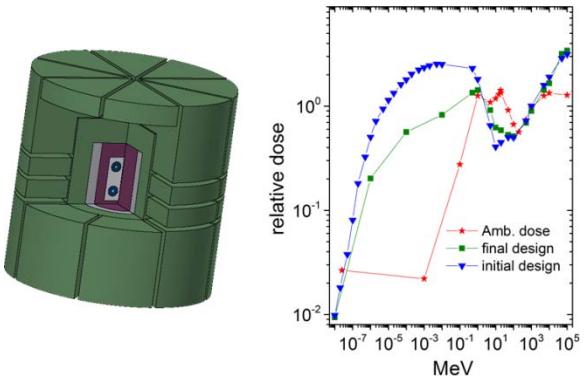

Figure 1. Left: Neutron dosimeter in 3D view (obtained using Flair [6]) with openings in the outer PVC layer (green). The inner lead (grey) and PE (purple) layer with a TLD card in the middle can be seen. Right: The final dosimeter response in comparison to the required ambient dose values and additionally the response function for the dosimeter from [3] are shown.

The initial design [3] was slightly increased to 20 cm in height and 20 cm in diameter. Openings were cut into the highly absorptive PVC layer to make the dosimeter more transparent to thermal neutrons. The final response is improved in comparison to the previous design fig.1 (right) and can even be further improved increasing the size of the dosimeter.

FLUKA is capable to calculate isotope production rates under neutron irradiation. Several simulations were performed to count the number of ^{3}H and α-particles produced in TLD chips during the detection time. In the TL chips the Li^{6} element is used to detect neutrons via the ^{6}Li(n,α)^{3}H reaction. The calculated amount of tritium and alphas revealed the same dosimeter response function as the first method, which takes into account the absorbed energy.

The method calculating the amount of e.g. ^{3}H – particles is very suitable to estimate the dose reading of the active detectors, where the dose is calculated as a number of pulses. Each pulse corresponds to a neutron capture event. In a couple of tests we have also performed some simulations calculating the tritium production for the active ^{3}He dosimeters. The neutrons are detected here via the ^{3}He(n,p)^{3}H reaction. Again we additionally used the absorption energy for detection and both methods gave the same response, within a statistical uncertainty of around 5 %.

After the response calculations of the passive dosimeters with a TLD card, as the sensitive element, we wanted to check the studied layouts to be used for the active neutron dosimeters with a ^{3}He counter tube as the sensitive element. The energy dependency of the capture cross sections for ^{3}He and ^{6}Li are pretty similar, thus it is interesting to check the response of a possible neutron dosimeter with a ^{3}He proportional counter instead of the TL chips.

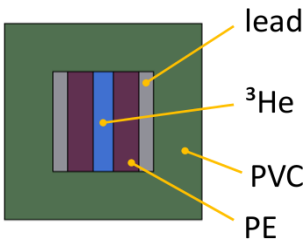

Figure 2. Compact dosimeter with a PVC layer and a ³He tube in the centre.

The readings of the dosimeters shown in Fig. 2 containing a cylindrical volume, 1.4 cm in diameter, filled with ^{3}He gas at 1 bar pressure shows identical readings as the one with a TLD card from [3]. The readings for the active dosimeters were obtained counting the neutron capture reactions as was described above, still in simulations the steel tube containing the ^{3}He gas and connections were not included and in reality can slightly influence the response characteristics, as well as the different gas pressures of the counter. Exchanging the sensitive element of the dosimeter in all layouts studied in [7], including the one from fig.1, should provide almost the same read-out

DOI:10.15120/GR-2017-1

values. The active dosimeter prototypes are to be tested in the near future.

The new design from fig.1, though it is larger than the initially proposed one [3], is still only half as heavy as the currently used dosimeter. In comparison to the initial design, which showed around 20 % higher dose values at the CERF experiment [5], the new design should provide exact values.

References

[1] G. Fehrenbacher, F. Gutermuth, E. Kozlova, T. Radon and R. Schuetz, Neutron dose measurements with the GSI ball at high-energy accelerators, Radiation Protection Dosimetry (2007), Advance Access publication 16 September 2007, Vol. **125**, No. 1-4, pp. 209-212.

[2] A. Fasso', A. Ferrari, J. Ranft and P. R Sala, FLUKA: a multi-particle transport code, CERN-2005-10 (2005), INFN/TC 05/11, SLAC-R-773.

[3] A.Sokolov, G. Fehrenbacher, E.Kozlova, T.Radon, "ANDREA, a Compact Neutron Dosimeter", GSI Scientific report 2014

[4] A. Mitaroff and M. Silari, The CERN-EU high-energy Reference Field (CERF) facility for dosimetry at commercial flight altitudes and in space, Radiation Protection Dosimetry 102, 7-22, 2002.

[5] I.A. Zahradnik, Development of the passive neutron dosimeter, ANDREA, for high energy accelerators, verification measurements and simulation of the dose response using the Monte Carlo code , bachelor thesis, THM Giessen (2015).

[6] V. Vlachoudis, FLAIR: A Powerful But User Friendly Graphical Interface For FLUKA Proc. Int. Conf. on Mathematics, Computational Methods & Reactor Physics (M&C 2009),, Saratoga Springs, New York, 2009.

[7] "Design Development of a passive neutron dosimeter for the use at high energy accelerators", A. Sokolov, G.Fehrenbacher, T. Radon, Radiation Protection Dosimetry 2015;doi: 10.1093/rpd/ncv489

DOI:10.15120/GR-2017-1

DOI:10.15120/GR-2017-1

Accelerator operation report

S.Reimann[1], A.Bloch-Späth[1], P. Schütt[1], M. Sapinski[1], O.Geithner[1]
[1]GSI, Darmstadt, Germany

This report describes the operation statistics of the GSI accelerator facility of the year 2016. The information is based on the data of the new GSI electronic log-book OLOG [1], which allows a detailed evaluation of operation statistics especially for the time-sharing operation mode of the GSI accelerators.

General Overview

After a 4.5-month long shutdown and maintenance period, the re-commissioning of the UNILAC started in April. From end of April till July, a single beam time block was scheduled and in comparison to the previous year, the GSI accelerator facility was completely operational again with one exception. Since the UNILAC RF-System is under construction, the maximum energy of the Alvarez section was defined to 5.89 MeV/u. So the synchrotron had to be operated with higher RF-harmonic number, what in the end was limiting the maximum revolution frequency and therefore the SIS18 extraction energy.

In total the UNILAC has been in operation for 2448 hours and the SIS18 for 1776 hours (504 hours are included for the commissioning of each accelerator after shutdown).

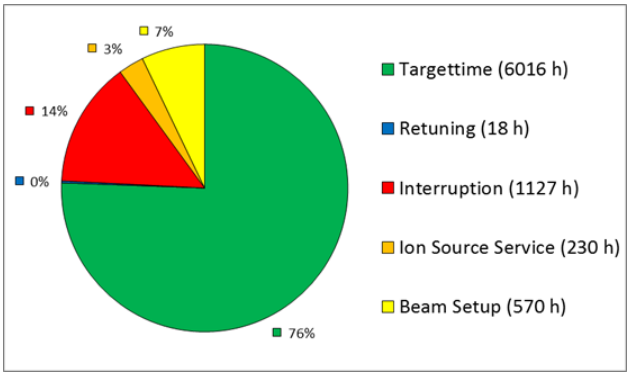

Figure 1: Distribution of overall beam time for all beam modes and experiments (parallel operation, no standby).

Figure 1 shows the overall beam time of the whole facility with respect to the parallel operation modes. In total 6016 hours of beam-on-target-time were successfully delivered to the different experiments, which is 76% of total beam time (the same as in 2015).

The percentage of interruption time increased drastically from 8% in 2015 to 14%. Fortunately this loss was completely compensated by a decreasing time for setup and retuning. Main reason was the very efficient beam time schedule which was developed in close cooperation of the experiments with the accelerator division under consideration of the limitations of the machines and the personnel situation. The dedicated hands-on operator training shifts [2], which we established this year at GSI, may also have had influence on this improvement.

Since the SIS18 was not operated in 2015, Table 1 shows also the beam time statistics of 2014, when SIS18 was last time fully operational. In comparison to the 2014 beam time both, percentage of setup- and interruption times, could be reduced this year.

Table 1: Overall beam time of the GSI accelerator facility

	2014	2015	**2016**
Integral target time	12000 h	5000 h	**6016 h**
	70%	76%	**76%**
Setup & Retuning	2300 h	873 h	**588 h**
	13%	13%	**7%**
Ion Source Service	514 h	218 h	**230 h**
	3%	3%	**3%**
Time for interruption	2391 h	533 h	**1127 h**
	14%	8%	**14%**
Total beam time	17133 h	6624 h	**7960 h**

Experiments

Figure 2 gives an overview of target time for different experimental areas. The fraction of the beam branches of the UNILAC are marked in blue, the ESR in green and the different experimental caves behind the SIS are displayed as orange slices. Details corresponding to the different experimental programs are given in [3].

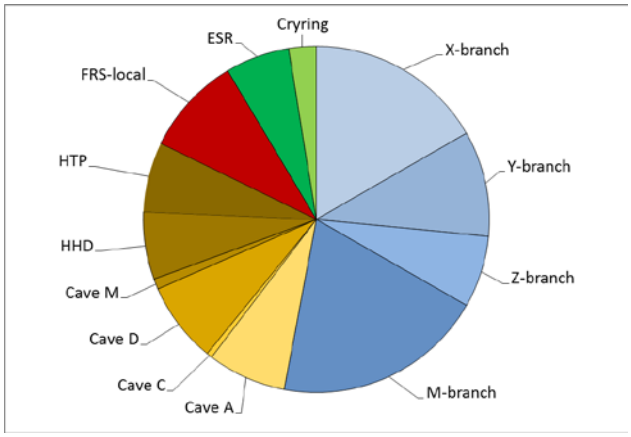

Figure 2: Distribution of target time to the different experimental areas.

DOI:10.15120/GR-2017-1

Over the year, the UNILAC delivered beams to 29 different experiments. Main user was the Material Science at the M-branch. In addition 25 fixed target experiments for FAIR detector tests have been performed behind the SIS18 and at the ESR internal target. Besides, the transfer line from the ESR to the CRYRING has been commissioned during this beam time.

Breakdown Statistics

Table 4 shows all unscheduled down time events in more detail. Problems with the RF-System and structures (especially UNILAC) are dominating this statistics again and are now responsible for 56% of overall downtime. The UNILAC RF-Transmitter-System is replaced at the moment and is expected to be fully operational again in beam time 2018. Nevertheless the replacement of the post stripper section is a necessary long term task to be done.

Table 4: Sum of all unscheduled down time events per category (parallel operation is not taken into account)

	Duration	No. of events
Power Supplies	200 h	112
Vacuum and RF-Structures	154 h	49
Beam Instrumentation	70 h	10
Operation	3 h	4
Safety-/ Interlock System	73 h	14
Ion Sources	21 h	31
RF-System	382 h	146
Controls	9 h	9
Infrastructure	26 h	6
Others / Ambiguous	10 h	17
Total	**948 h**	**398**

Isotope Statistic

During 2016, 11 different isotopes have been accelerated from 6 different ion sources.

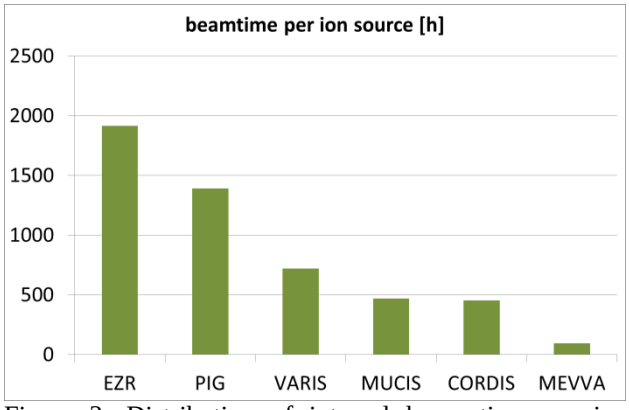

Figure 3: Distribution of integral beam time per ion source.

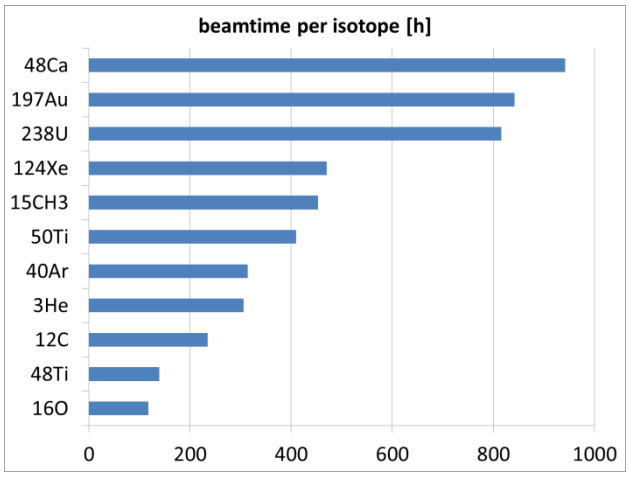

Figure 4: Distribution of integral beam time per isotope.

Figure 3 shows the distribution of the beam time per ion source and figure 4 shows the distribution of the integral beam time (parallel operation) per isotope. Calcium (from ECR), Gold (from PIG) and Uranium (from VARIS) are dominating both statistics.

Summary

Even though half of the Alvarez-Section was not operational this year and the SIS18 has been operated in an unusual mode, the beam time was a success for both the accelerator division and the experiments. The limitation of the parallel operation modes at the SIS18 to few elements and the close cooperation with the experiment speakers helped, to completely process the ambitious beam time schedule.

Outlook

For 2017 no beam time is scheduled as the site construction project GAF (German, GSI Connection to FAIR) forces GSI accelerators into a 2 years shutdown period. Within this shutdown many maintenance and upgrade measures on all accelerators will be performed.

Until next beam time in 2018 the main control room has to be refurbished and upgraded, to fit the needs of the new operation software and control system which is planned to be installed during the controls retrofitting project next year. In addition it is planned, to go first steps into automation and digitalization.

We are also working on a new way to analyse and present statistical data on machines operation, which will help to have a more complete picture of the availability of the GSI accelerator complex.

References

[1] P. Schuett, the GSI Operation Logbook OLog, WAO 7th, Seoul, Korea, 2010
[2] M. Vossberg and S. Reimann, Operator Training Shift Experience, WAO 10th, China, Shanghai, 2016
[3] Report of beam time coordinator, this report

DOI:10.15120/GR-2017-1

Shutdown report

P.Schütt, M.Vossberg, S.Reimann
GSI, Darmstadt, Germany

This report describes the main service and upgrade measures of the GSI accelerator facilities, which were started in 2016 and will be continued until mid-2018. The presented information is based on the work of the shutdown coordination and the corresponding MS-Project shutdown schedules.

General Overview

In July 2016 began the longest shutdown GSI has ever seen. It is expected to end in May 2018. The planning started well in advance [1] with a collection of the major tasks planned by the respective machine coordinators.

The most important projects have been fit into a common time line (see Figure 1). It is derived from a detailed MS-Project schedule comprising more than 1500 individual tasks. This way, conflicts were identified and the individual schedules were synchronized. Weekly meetings are organized with the machine coordinators and representatives of all involved departments, including civil construction and infrastructure. There, the actual progress is monitored, pending work and critical incidents are discussed and the overall schedule is adapted accordingly.

Work Packages

The largest work package is the civil construction project GAF (GSI Anbindung an FAIR, Link of GSI to FAIR), which comprises additional shielding of SIS18, fire protection measures, as well as the connection of the new beam line tunnel towards FAIR to the existing TR hall (s. Figure 2).

The GAF project implies that SIS accelerator components are inaccessible during most of the construction work. Therefore, maintenance and repair work on the kicker and on RF cavities was scheduled at the beginning of the shutdown and was finished, before the start of GAF.

The largest project at the UNILAC is the modernization of post-stripper RF systems, which started in 2015. It needs regular test periods with full infrastructure available. This is in conflict with the refurbishment of the Heating, Ventilation and Air Conditioning (HVAC) system of the UNILAC tunnel. Careful coordination of these projects is mandatory to finish in time for the beam time 2018.

Ion source development requires several test periods. The electrostatic acceleration section of terminal north will be renewed.

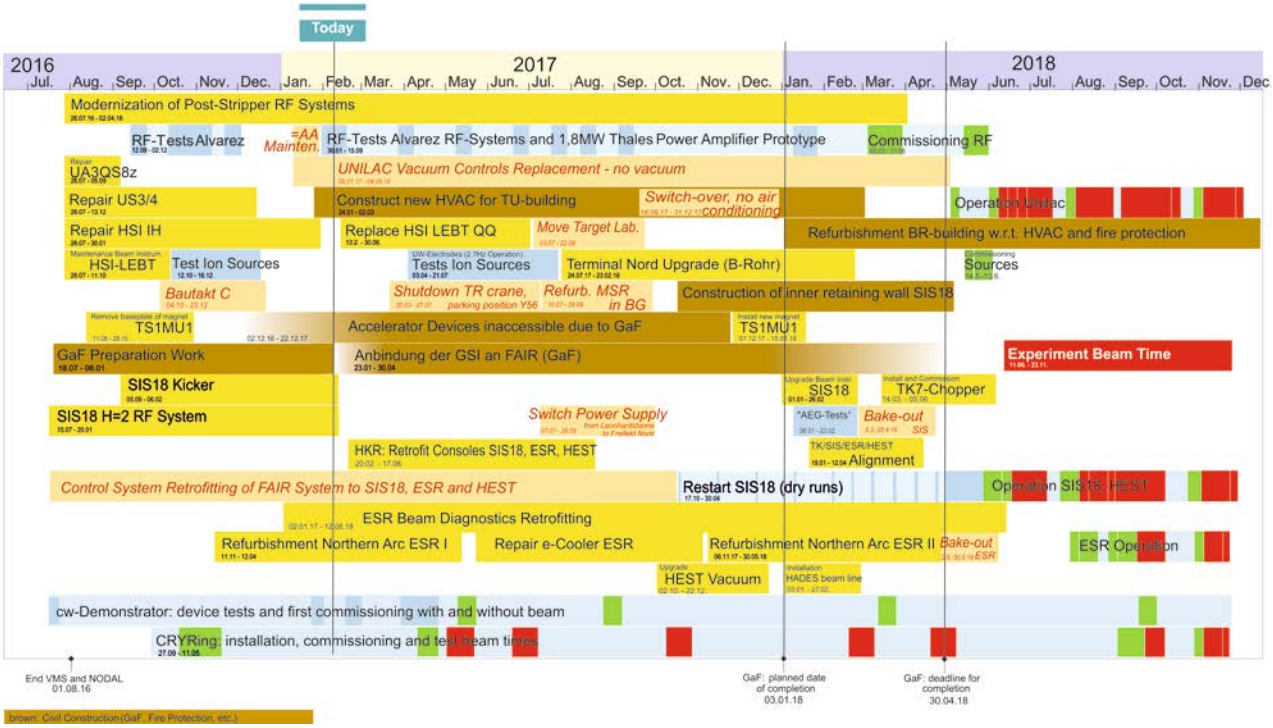

Figure 1: Timeline of the long Shutdown 2016-2018, status February 2017.

DOI:10.15120/GR-2017-1

Another important project is the retrofitting of the FAIR control system to SIS18, ESR and HEST: the previous control system was finally shut down after the beam time 2016. In order to ensure smooth commissioning of the new control system, dry runs are scheduled half a year before the next beam time. These interfere with the GAF project. The control system refurbishment also implies beam diagnostics upgrades and the implementation of modern consoles for SIS18 and ESR in the main control room. These consoles shall have the same layout as the planned consoles for FAIR.

ESR requires a vacuum refurbishment of the northern arc, following the respective work on the southern arc in the last shutdown 2015. Repair of a short-circuit fault in the electron cooler of the ESR will need several months, for this work the cooler must be almost completely dismantled.

The shutdown work in the HEST concentrates on the upgrade of the HADES beam line with respect to the aperture and beam diagnostics and the refurbishment of some vacuum components.

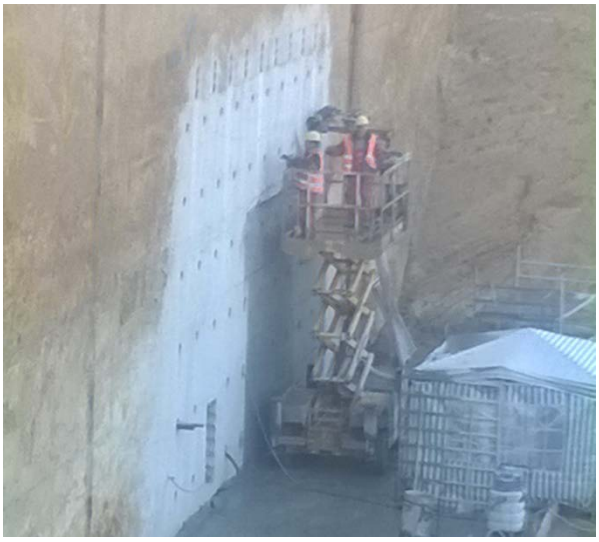

Figure 2: Construction Area of GAF: wall of existing hall is opened to connect new beam line tunnel towards FAIR.

The pulsed power connection for the main magnets of SIS18 and ESR will be switched from Leonhardstanne to “Freifeld Nord” in FAIR. Afterwards, the SAT of the new power supplies needs to be performed.

Due to civil construction not only in GAF but also for the new FAIR buildings, the accelerator tunnel floors will move and the corresponding accelerators components accordingly. Therefore, a thorough survey is scheduled and alignment will be necessary.

Development of the cw-demonstrator is on-going. The power coupler is delivered and the amplifier is ready. First tests with beam will take place end of June.

CRYRing was set up and adjusted, first tests took place in December 2016 and commissioning with beam is planned until 2018.

Critical Path

The end of the beam time 2016 was determined by the need to prepare for the GAF civil construction project. The deadline for this project is April 2018, with all work inside the accelerator tunnels finished in January 2018, in order to enable timely recommissioning for the beam time 2018.

Other projects with long duration are:

- modernization of post-stripper RF systems
- UNILAC vacuum controls replacement
- refurbishment of HVAC of the UNILAC tunnel
- retrofitting of the FAIR control system

Status and Outlook

At the end of 2016, SIS18 and HEST were prepared for GAF. The actual construction work was delayed by several weeks which could be used for completion of work on kicker and RF systems, which had originally been planned for 2018.

UNILAC vacuum controls replacement had to be postponed to the next shutdown because of shortage of manpower: with the available workforce, the project could not be started early enough to be finished before the scheduled beam time 2018.

Not all proposed projects can be fully supported during this shutdown for reasons of capacity. This includes e.g.

- replacement of the UNILAC personal safety system TVS (windows NT based server)
- refurbishment of the chopper in front of injection into SIS18
- ionization profile monitors (IPM) for SIS and ESR
- vacuum upgrade measures in the HEST
- upgrade of beam line FRS to ESR
- upgrade of HADES beamline
- preparation of beam line and cave C for Mini CBM
- upgrade of FRS

For a timely completion of these tasks, a decision in the first quarter of 2017 is mandatory.

Due to personal shortage in all involved departments and high priority tasks for the FAIR project, the progress in many tasks is slower than expected. Nevertheless, a timely completion for the beam time 2018 is still feasible.

References

[1] S. Reimann, P. Schütt, Scheduling and Tracing of Maintenance Tasks in Long Shutdowns, ARW 5th, Knoxville, Tennessee, USA, 2015

DOI:10.15120/GR-2017-1

R&D Status of the new CH cavities for the sc cw Heavy Ion LINAC@GSI

M. Basten[#,1], K. Aulenbacher[3,4], W. Barth[2,3], M. Busch[1], F. Dziuba[1,3], V. Gettmann[3], M. Heilmann[2], M. Miski-Oglu[3], H. Podlech[1], M. Schwarz[1], S. Yaramyshev[2]

[1]Goethe University, 60438 Frankfurt am Main, Germany; [2]GSI Helmholtzzentrum, 64291 Darmstadt, Germany; [3]Helmholtz-Institut Mainz (HIM), 55099 Mainz, Germany; [4]KPH Mainz University, 55128 Mainz, Germany

Presently cavity 2 and 3 of the advanced cw linac demonstrator at GSI is under construction at Research Instruments (RI). After the successful beam test of the demonstrator at GSI-HLI in 2017 this is the next milestone realizing a new sc heavy ion cw-LINAC at GSI. The demonstrator cavity had been successfully rf tested at cryo conditions at Frankfurt University [1] and GSI [2]. The recent design of the sc cw-LINAC comprises the demonstrator and cavity 2 and 3 as first cryomodule and up to 4 additional cryomodules each equipped with three short CH-cavities. The overall design of this standard cryomodule will be used for all following cavities. The recent short cavity with 8 accelerating cells is designed for high power applications at a design gradient of 5 MV/m. Its resonant frequency is the second harmonic of the High Charge Injector (HLI) at GSI, Darmstadt. Table 1 shows the main parameters of the short sc 217 MHz CH-cavity. In Figure 1 the layout of this cavity is depicted.

Design of the short CH-Cavity

The design of the cavity is based on 8 equidistant gaps without girders and with stiffening brackets at the front and end cap to reduce pressure sensitivity. Avoiding high fabrication costs and extended fabrication duration the short cavity design is without girders. In a final step the design has been changed to provide for constant welding depths at the stems. As a consequence the cavity is flattened around the stems. Also the design of the bellow tuner was changed to reduce mechanical stress and the number of parallel segments.

Parameter	Unit	
β		0.069
Frequency	MHz	216,816
Accelerating cells		8
Length (βλ-definition)	mm	381.6
Cavity diameter (outer)	mm	400
Cell length	mm	47.7
Aperture diameter	mm	30
Static tuner		3
Dynamic bellow tuner		2
Wall thickness	mm	3-4
Accelerating gradient	MV/m	5
E_p/E_a		5.2
B_p/E_a	mT/(MV/m)	<10
G	Ω	50
R_a/Q_0		1070

Table 1: Specifications of the 217 MHz short CH-cavity

Figure 1: Final design of the sc 217 MHz CH-cavity.

Status

The final design of the 217 MHz short CH-cavity was finished at the beginning of 2015; the construction started end of 2015. Several simulations with CST-Microwave-Studio [3], as well as ANSYS Workbench [4] have been performed to determine crucial parameters and eigenfrequencies. The niobium raw material was delivered to RI company at the end of 2015. The construction phase was scheduled till 2017. Recently RI faces several difficulties concerning the flattened parts around the stems. Problems during the mechanical process of pressing the cylindrical cavity have to be solved. The center of the flattened parts reach 0.4 mm out of in the cavity while the edges are facing 0.7 mm inside the cavity. RI has to correct these parts assuring for alignement of all stems after the welding process. First frequency measurements are already performed confirming consistent results between measurements and simulations.

References

[1] F. Dziuba et al., First Performance Test on the Superconducting 217 MHz CH Cavity at 4 K, LINAC 2016, East Lansing, USA, THPLR033

[2] F. Dziuba et al., First cold tests of the superconducting cw demonstrator at GSI, RuPAC2016, St. Petersburg, Russia, WECBMH01

[3] CST Microwave Studio; http://www.cst.com

[4] ANSY, Inc.; www.ansys.com

[#]Basten@iap.uni-frankfurt.de

DOI:10.15120/GR-2017-1

Horizontal RF tests of the superconducting 217 MHz CH cavity for the HIM/GSI-cw LINAC

F. Dziuba[*1,2], *M. Amberg*[1,3], *K. Aulenbacher*[1,4], *W. Barth*[1,2,5], *M. Basten*[3], *M. Busch*[3], *V. Gettmann*[1], *M. Heilmann*[2], *M. Miski-Oglu*[1], *H. Podlech*[3], *J. Salvatore*[2], *A. Schnase*[2], *M. Schwarz*[3], *and S. Yaramyshev*[2,5]

[1]HIM, Mainz, Germany; [2]GSI, Darmstadt, Germany; [3]IAP, Frankfurt, Germany; [4]KPH, Mainz, Germany; [5]MEPhI, Moscow. Russia

Introduction

The continuous wave (cw) demonstrator is the first prototype of a new superconducting (sc) cw linac, which is proposed to keep the Super Heavy Element (SHE) research program at GSI competitive. The demonstrator consists of a sc 217 MHz crossbar-H-mode (CH) multigap cavity embedded by two sc 9.3 T solenoids mounted in a horizontal cryomodule. At the end of 2016 the rf performance of the cavity has been extensively tested at 4.2 K with low level rf power.

Measurement results

A first rf test of the sc 217 MHz CH cavity (without helium vessel) at the Institute of Applied Physics (IAP) of Goethe University Frankfurt has been performed beginning of 2016 [1]. At that time the performance of the cavity was limited by field emission caused by insufficient surface preparation. Nevertheless, a maximum accelerating gradient of $E_a = 6.9$ MV/m at $Q_0 = 2.19 \cdot 10^8$ was reached (see Figure 1).

After the final assembly of the helium vessel and further High Pressure Rinsing (HPR) preparation, the cavity was delivered to GSI and prepared for a second rf test in a horizontal cryomodule (see Figure 2) [2]. A 50 W broadband amplifier was used to deliver the required rf power. The cavity runs as a generator driven resonator directed by an rf control system. Further equipment, namely a network analyzer, three power meters and a scope has been used for rf measurements. Initially, the cavity has been passively precooled down to 218 K by the N_2 shield of the cryostat. Hereafter, the temperature was quickly lowered (3 K/min in average) applied by liquid helium to 4.2 K avoiding hydrogen related Q-disease. Subsequently, rf conditioning has been performed. All multipacting barriers up to 4 MV/m could be surmounted permanently. In a next step the rf performance of the cavity was reviewed. Figure 1 shows the related Q_0 vs. E_a curves measured in vertical position (without helium vessel, red curve) and in horizontal orientation (with helium vessel, blue curve), respectively. The maximum Q-value at a low field level (Q_0^{low}) was measured as $1.37 \cdot 10^9$. Recently, the cavity showed an improved performance due to an advanced HPR treatment. The initial design quality factor at 5.5 MV/m has been exceeded by a factor of 4. Furthermore, a maximum accelerating gradient of $E_a = 9.6$ MV/m at $Q_0 = 8.14 \cdot 10^8$ was reached, which increases the cw linac capabilities in terms of operation with heavy ions as well of higher beam energies.

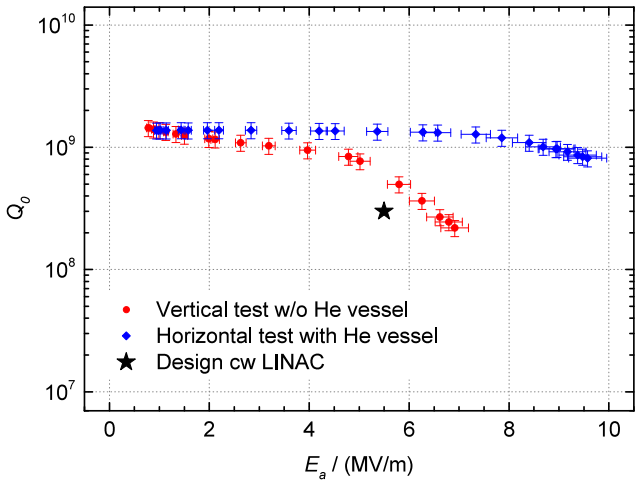

Figure 1: Q_0 vs. E_a curves at 4.2 K [2].

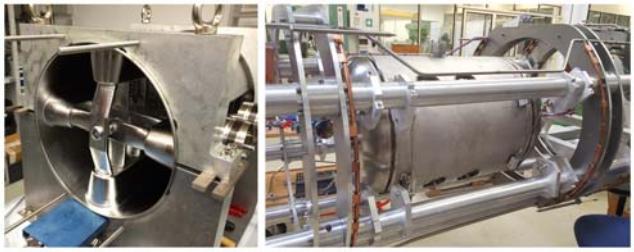

Figure 2: Superconducting 217 MHz CH cavity during manufacturing (left) and finally mounted into the support frame of the horizontal cryomodule (right) [2].

References

[1] F. Dziuba et al., in Proc. of LINAC2016, East Lansing, Michigan, USA, THPLR044, 2016, (to be published).

[2] F. Dziuba, "First Cold Tests of the Superconducting CW Demonstrator at GSI", RuPac'16, St. Petersburg, Russia, November 2016, p. 83–85

* f.dziuba@gsi.de

DOI:10.15120/GR-2017-1

Preparation work at the 325 MHz test stand at GSI for Klystron FAT and SAT

A. Schnase, M. Helmecke, E. Plechov, S. Pütz, G. Schreiber
GSI, Darmstadt, Germany

In 2016 the 325 MHz test stand was used to continue high power testing [1] of a CH prototype cavity for the FAIR proton Linac. Finally up to 2.7 MW forward power were delivered to find out the limits and to condition this CH cavity [2]. It was confirmed that the whole high power signal chain from klystron via circulator to the cavity coupler works as expected. This klystron system was also used to evaluate the RF power limits of a prototype 325 MHz ladder-RFQ [3]. Here up to 487 kW of forward power could be send to the cavity.

Short afterwards the Klystron HV modulator, which was a loan from CERN Linac 4, had to be returned. In order to restart Klystron operation in 2018 the design process for Klystron modulators for the pLinac was started [4]. The 45 kW buncher amplifiers are prepared to be connected to the CH prototype cavity to check the result of remodeling work and to conduct the related SAT.

The test stand will be used for cavity testing and conditioning, and also for SAT (Site Acceptance Test) of RF transmission line components as:

Circulators, rectangular waveguides, coaxial RF power transmission lines, transitions from WR 2300 waveguide to coaxial and high power loads. Of equal importance are tests of HV modulators, Klystrons and LLRF systems.

Two In-Kind contracts between GSI/FAIR and the laboratory CNRS were prepared. One contract covers RF components used at the test stand. The other covers the series production of Thales TH 2181 klystrons, which after delivery to GSI/FAIR need to be tested (SAT) before installation to the pLinac klystron gallery.

Directional coupler remodeling work

For the FAT (Factory Acceptance Test) of the TH 2181 klystrons at Thales, the RF power is measured with directional couplers. We already noticed that their directivity was below requirements and developed an external cure [5]. The 4 dual directional couplers for the test stand and the 7 dual directional couplers for the pLinac itself contain different versions of loop couplers as shown in fig. 1. The geometry on the left provides directivity not better than 23 dB. The geometry in the center provides a better directivity in the range of 30 dB.

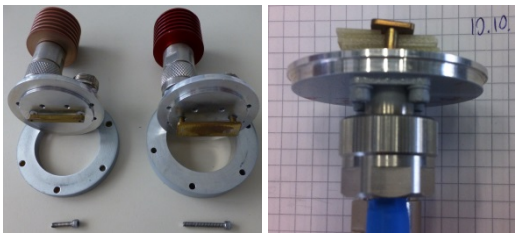

Figure 1: Different coupling loop geometries.

The measured reflection S_{11} on the Type N port was only in the order of -20 dB. Calculations show that the geometry behaves like a PCB stripline that matches to 50 Ω, when filled with FR4 circuit board material. With the loop filled with FR4 (right geometry in Fig. 1), and a selected precise termination, S_{11} improves to -40...-50 dB. This modified loop leads to an improved directivity in the order of 40...50 dB. The modifications before (left) and after (right) are shown in Fig. 2 for the dual coupler serial #1119-987. The directivity improves from 22 to 42 dB.

Figure 2: Modification process for coupler #1119-987.

These modifications were applied to all 4 dual directional couplers of series #1119. The results (before / after upgrade) are displayed in figure 3. Two of these modified dual couplers were handed to Thales for next FATs.

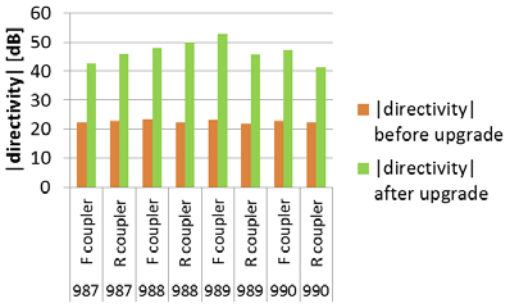

Figure 3: Comparison of improved directivity.

Outlook

Next 7 dual direction couplers and 7 6-port couplers will be upgraded. This requires machined FR4 inserts and a calibration procedure, improved by driving the movable short with an embedded system controlled stepper motor.

References

[1] A. Schnase, et. al. “Progress of the 325 MHz Test Stand at GSI in 2015”, GSI sci. report 2015, p. 340

[2] G. Schreiber, et. al., “First High Power Tests at the 325 MHz RF Test Stand at GSI”, Proc. 28th Linear Acc. Conf. (LINAC'16), East-Lansing, MI, USA, Sep. 2016, MOPLR067, pp. 273-275

[3] M. Schütt, et. al., “Development and Measurements of a 325 MHz RFQ”, Proc. 28th Linear Acc. Conf. (LINAC'16), Sep. 2016, TUPLR053, pp. 543-545

[4] S. Pütz, A. Schnase, G. Schreiber “Design and Production of Klystron Modulators for the pLINAC”, this scientific report

[5] A. Schnase, E. Plechov, G. Schreiber “Development of a procedure for directional coupler calibration at the 325 MHz test stand, GSI sci. report 2015, p. 341

DOI:10.15120/GR-2017-1

New simulation code for ionization profile monitors

D. Vilsmeier[*1,2], *P. Forck*[1], *and M. Sapinski*[1]
[1]GSI, Darmstadt, Germany; [2]Universität Regensburg, Germany

Ionization Profile Monitors (IPMs) are devices for non-invasive beam profile measurement. They make use of phenomena of rest gas ionization by the beam. Electrons or ions produced in the ionization process are extracted from the region of interaction between the beam and the rest gas, and transported, using external electric and magnetic fields (called guiding fields), towards a detection device. The detection device is usually based on a phosphor screen or a segmented anode. The distribution of the positions of electrons or ions on the detector allow for reconstruction of the beam profile.

Although the principle of the IPM operation is simple, the reconstructed beam profile can be distorted due to various effects. Those effects include the nonuniformities of the guiding fields, initial kick given to electrons during the ionization (initial velocities) or the influence of the bunch fields on the trajectories of particles. Most of those effects cannot be treated analytically and specialized simulation program is needed. Such a program typically incorporates particle generation in the ionization process, calculation of the beam fields and tracking of charged particles in a superposition of transient bunch fields and constant guiding fields.

Surprisingly, none of the investigated available codes (CST and Geant4) has an ability to perform this kind of simulations therefore, in almost every laboratory which uses IPMs, researchers wrote their own codes [1,2]. Those codes are tuned to particular needs of the laboratories and are usually designed for specific cases only. Nevertheless, they contain a lot of common aspects.

In this situation we decided to create a modern, universal simulation code [3], which is easy to set up and which contains algorithms adequate for most of the investigated IPMs. The program, written in Python, has a modular structure and is easily extendable (it is being extended to Beam Induced Fluorescence monitor case). The main components are: ionization, guiding fields, bunch fields and tracking. Currently those components contain the following methods:

- Ionization: zero velocities, Voitkiv analytical formula [4] and phenomenological parametrization of double differential cross-section. This component is an independent package, so it can be used by other projects.
- Guiding fields: uniform fields and CST field map.
- Bunch field: analytical expression for special cases (Basetti-Eriskine, etc.) and numerical Poisson solvers (2D, 3D).
- Tracking: Runge-Kutta method, Boris algorithm and analytical expression (for parallel electric and magnetic fields only).

Additional components describe the detector part, the rest gas properties and manage the simulation output. The Graphical User Interface to the simulation program is written using Qt libraries and the simulation configuration, as well as the simulation output, can be handled using XML format. The code is open source and accessible via Python Package Index (virtual-ipm package).

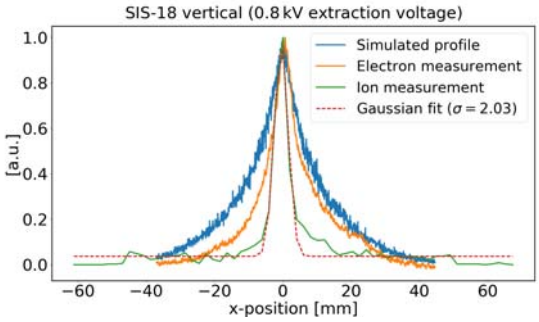

Figure 1: Measurement and simulation results for SIS18 IPM: measured beam profile (green), simulated beam profile distorted by the initial velocities of electrons and bunch field (blue) and the corresponding measurement (orange).

Figure 1 presents an example of results of the simulation program. The data were measured on June 28th, 2016 during $^{124}Xe^{43+}$ beam time using vertical IPM in SIS-18. The device was working in electron collection mode and the extraction voltage was decreased from 4 kV to 800 V in order to investigate the profile distortion. The beam had asymmetric shape, what has not been taken into account by the simulation, therefore a good agreement is seen only for half of the profile.

References

[1] M. Sapinski et al.,"Ionization Profile Monitor Simulations - Status and Future Plans", IBIC 2016, Barcelona, September 2016, TUPG71
[2] https://twiki.cern.ch/twiki/bin/view/IPMSim
[3] https://gitlab.com/IPMsim/Virtual-IPM/
[4] A. Voitkiv et al., J.Phys.B: At.Mol.Opt.Phys.**32**(1999) p. 3923

* d.vilsmeier@gsi.de

DOI:10.15120/GR-2017-1

BIF profile monitor development for electron lenses

S. Udrea[1], P. Forck[1], E. Barrios Diaz[2], N. Chritin[2], O. R. Jones[2], P. Magagnin[2], G. Schneider[2], R. Veness[2], V. Tzoganis[3], C. Welsch[3], H. Zhang[3]
[1]GSI, Darmstadt, Germany; [2]CERN, Geneva, Switzerland; [3]Cockcroft Institute, Warrington, UK

Electron lenses (e-lens) [1] have been proposed and used to mitigate several issues related to the beam dynamics in high current synchrotrons. As part of the collimation upgrade for the high luminosity upgrade of LHC a hollow electron lens system is presently under development. Moreover, at GSI an electron lens system also is proposed for space charge compensation in the SIS-18 synchrotron to decrease the tune spread and allow for the high intensities at the future FAIR facility. To ensure for a precise alignment between the ion beam and the low energy electron beam a transverse profile monitor based on an intersecting gas sheet and the observation of beam induced fluorescence (BIF) is under development within a collaboration between CERN, Cockcroft Institute and GSI [2], as schematically shown in Fig. 1.

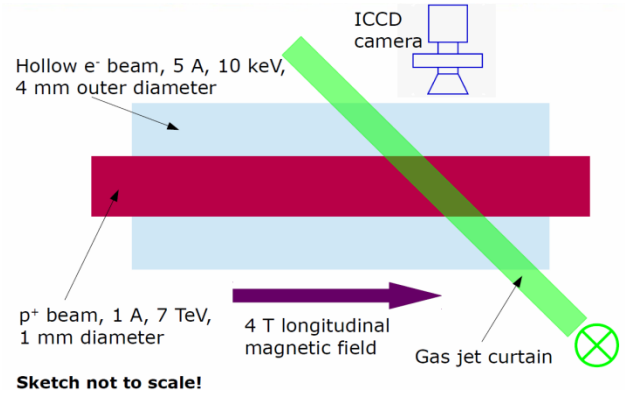

Figure 1: A schematic of the e-lens system planned at CERN for the collimation of the HL-LHC proton beam and the associated transverse beam diagnostics.

Fluorescence cross-sections and photon yield

For the gas jet curtain both neon and molecular nitro-gen are under consideration. While N_2 is known for its high fluorescence efficiency, Ne has a better compatibility with high vacuum systems. Moreover the most prominent nitrogen lines originate from the N^{2+} ion, while neutral Ne has strong emission in the visible. This is relevant, since ion movement may get strongly affected by the electric and magnetic fields of the charged particle beams and the solenoid of the electron lens, in contrary to neutrals. Thus an extensive study has been conducted to predict the detectable photon rates to be expected for nitrogen and neon [2]. The results are summarized in Table 1.

First experimental results

Experiments with an electron beam and a nitrogen supersonic gas jet have been performed at the Cockcroft Institute. The gas jet setup generates gas sheets with a width of several millimetres, sub-millimetre thickness and a particle density of about 10^{10} cm^{-3} [3]. An electron gun delivering up to 10 µA and a maximum energy of 5 keV is employed. BIF diagnostics is performed with an ICCD camera and a filter wheel with interference filters having a 10 nm bandwidth and central wavelengths at 337, 391, 431 and 471 nm.

Projectile	Jet	λ [nm]	σ [cm^2]	I [A]	N_γ [s^{-1}]
electron	N_2	337.1	$1.5\cdot10^{-23}$	5	1.2
electron	N_2^+	391.4	$9.1\cdot10^{-19}$	5	$7.5\cdot10^4$
proton	N_2^+	391.4	$3.7\cdot10^{-20}$	1	$6.1\cdot10^2$
electron	Ne	585.4	$1.4\cdot10^{-20}$	5	$2.9\cdot10^2$
proton	Ne	585.4	$4.7\cdot10^{-22}$	1	1.9

Table 1: Cross-sections σ and detectable photon rates for relevant nitrogen and neon lines. Protons are considered to have an energy of 7 TeV. The average proton beam current is 1 A. Electrons have an energy of 10 keV. The electron beam current is 5 A.

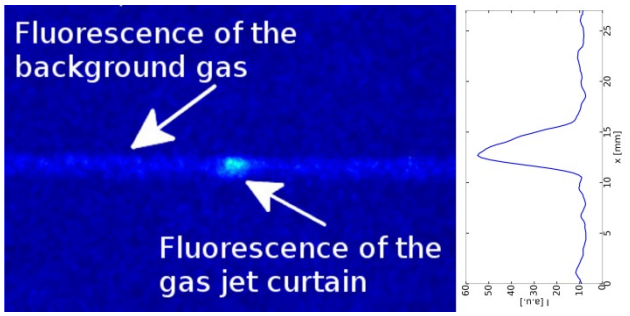

Figure 2: Profile of a 3.5 keV electron beam obtained due to the interaction with a supersonic N_2 gas jet curtain.

The profile of a 3.5 keV electron beam obtained due to the interaction with a nitrogen jet is shown in Fig. 2. The filter at 391 nm was used. Due to the very low electron beam current the integration time needed for good image quality has been 8000 s. Further investigations are planned for 2017.

References

[1] V. Shiltsev et al., Phys. Rev. STAB, **2**, 071001, 1999.
[2] S. Udrea et al., Proc. IBIC 2016.
[3] V. Tzoganis, and C.P. Welsch, Appl. Phys. Lett., **104**, 204104, 2014.

DOI:10.15120/GR-2017-1

DOI:10.15120/GR-2017-1

Ion source operation at GSI

R. Hollinger, K. Tinschert*, A. Adonin*, R. Berezov*, M. Brühl, B. Gutermuth, F. Heymach, S. Jung, R. Lang, J. Mäder, F. Maimone, K. Ochs, P. T. Patchakui, M. Raupach, P. Schäffer, S. Schäffer, C. Ullmann, C. Vierheller, A. Wesp, S. Zulauf*
GSI, Darmstadt, Germany

High Current Ion Sources

During the beamtime in 2016 a wide experimental program has been accomplished (realized) due to the parallel operation. High current ion sources from Terminal North (MUCIS and VARIS) and Penning ion sources from Terminal South were supplying the experiments with various types of ions. The following Table 1 gives an overview of the ion species, which were delivered for physics and accelerator development experiments. A representative value for delivered intensity to the linear accelerator UNILAC is the analysed beam current in front of the RFQ.

Table 1: Ion beam intensities generated with high current ion sources in 2016; filament driven volume type ion sources: MUCIS, vacuum arc ion sources: VARIS, Penning type ion sources PIG.

Ion species	Duration (days)	Ion source	Beam for experiment	Analyzed intensity (emA)
$^{15}CH_3^+$	18	MUCIS	UNI/SIS/ESR	2.4
$^{50}Ti^{2+}$	7	PIG	UNI	0.04
$^{124}Xe^{3+}$	19	MUCIS	SIS/ESR	2.6
$^{197}Au^{8+}$	23	PIG	UNI	0.07
$^{238}U^{4+}$	27	VARIS	UNI/SIS/ESR	16

The main requested ion species from the Penning Ion Source was gold $^{197}Au^{8+}$ for material research (UMAT) and for biophysics (UBIO) experiments. The PIG source was operated with high duty cycle (50 Hz / 3-4.5 ms) with the lifetime of approximately 24 hours during the beamtime.

One of the main highlights of the beamtime in 2016 was further performance optimization of VARIS ion source with multi aperture (7-holes, ø 4 mm) triode extraction system for $^{238}U^{4+}$ beam. A new record for the beam brilliance in front of the HSI-RFQ has been achieved. An intensity of 13.5 mA (90% from full beam) was obtained inside the beam emittance of 178π mm·mrad horizontally and 175π mm·mrad vertically. Measured beam emittances for both planes are shown in Fig.1. Emittance measurements have been performed in UH1-section. In combination with tuning of the UNILAC high current injector (HSI) and the pulsed gas stripper [1] during the machine experiment campaign that results in a new record intensity of 11.5 mA for U^{29+} beam in the post-stripper section (US4-section) [2].

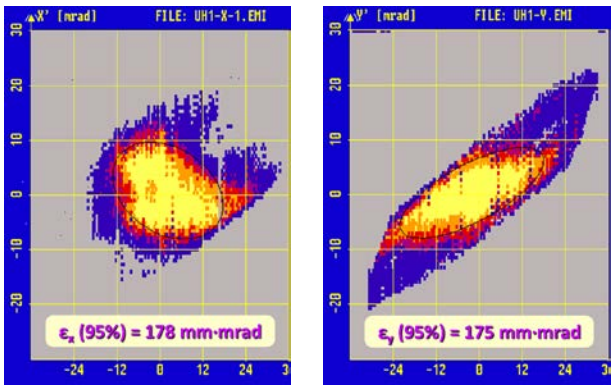

Figure 1: Measured emittances: horizontal (*left*) and vertical (*right*) of intense (15 mA) U^{4+} ion beam in front of the RFQ (UH1-section)

Another notable highlight is further development of molecular ion beams from Terminal North for production of intense proton and carbon beams behind the gas stripper [3]. A new separate gas-exhaust system for flammable gases has been developed and installed on terminal North. Due to this the production of CH_3^+ molecular ion beam from MUCIS ion source using methane gas has been established as standard operation. The optimization of the operation mode and the ion source parameters results in notably increased lifetime of MUCIS with methane.

In the frame of following elaboration of higher duty cycle (2.7 Hz) uranium operation for FAIR the investigation of possible ways of thermal load reduction of cathodes as well as the concept of using U-W composite materials in the cathodes is ongoing. The first set of test cathodes with U-W(5% Wt.) and U-W(12% Wt.) alloys will be manufactured by AREVA company [4] and delivered in the nearest future to GSI for performance tests with VARIS ion source on terminal North.

In the frame of the program of development of the new projectiles for FAIR experiments seven elements (including four new metals) have been successfully tested in various operation modes on terminal North in 2016 [5].

The further renewing and development of the Penning ion sources is in process. The five sputter PIG sources are completely renewed and successfully put into operation during this beam time. For the gas operation the renewing of PIG sources has been started. The first gas PIG source is ready and will be tested in the new constructed PIG test bench. Also the optimization and performance tests of compact PIG ion source are ongoing on the dedicated new test bench. The first results with argon beams are obtained.

* Corresponding authors

DOI:10.15120/GR-2017-1

High Charge State Injector HLI

The CAPRICE ECR ion source (ECRIS) at the High Charge State Injector (HLI) experienced a major damage due to a lack of cooling during a test run at the end of 2015. In order to be prepared for the beam time of 2016 starting in April a big effort was made to reconstruct the ion source within the first quarter of the year. Due to the excessive temperature 3 of 6 coils of the ion source solenoids were destroyed, while the permanent magnet hexapole showed an intolerable decrease of magnetic remanence. Consequently these major components of the ion source had to be replaced. Fortunately most of the essential spare components were available for the required replacement. However, a complete disassembly of the ion source was inevitable and further components had to be refurbished or to be re-fabricated.

Table 1 shows the ion species delivered from the ECRIS during the regular beam time.

Table 1: Ion beam operation of the HLI-ECRIS in 2016

Ion species	Auxiliary gas	Duration (days)	Analysed intensity (eμA)
$^{3}He^{1+}$	He	12	500
$^{12}C^{2+}$	O_2	12	160
$^{40}Ar^{9+}$	O_2	19	100
$^{48}Ca^{10+}$	He	40	90-130

After the implementation of the CAPRICE-ECRIS at the HLI-LEBT a $^{40}Ar^{9+}$ ion beam was used for its recommissioning at the HLI before the first beam time period. Subsequently this ion beam was used for tests and experiments scheduled at the cw-LINAC demonstrator [6] at the local experimental area of the HLI working at beam energies of 1.4 MeV/amu. A second period of experiments at the cw-LINAC demonstrator with $^{40}Ar^{9+}$ followed at the end of the beam time block.

Several short periods of biophysics experiments in 2016 were provided with ion beams of $^{12}C^{2+}$, and of $^{3}He^{1+}$, respectively.

A major part of the beam time was occupied by $^{48}Ca^{10+}$ beam which was delivered to various experiments on Super Heavy Element (SHE) research which were performed at TASCA and at SHIPTRAP, respectively. Most of the time a typical ion beam intensity of 90 eμA was provided while maximum intensities of 130 eμA could be achieved. The consumption of ^{48}Ca sample material was as low as 130 μg/h (including material recycling) in the first run and about 440 μg/h (without material recycling) during the high intensity period.

While for most of the elements produced as ion beams from the ECRIS a stable equilibrium can be found for a favourable working point the situation can be more critical for the operation of ^{48}Ca. Occasionally the plasma is characterised by an unstable equilibrium but the response time for optimisation is very slow. For visual control purposes the plasma is continuously observed by means of a CCD camera equipped with a telephoto lens and looking through the straight beam line into the extraction aperture of the ion source which allows a close-up view of the plasma. Experiences obtained from ^{48}Ca beam times in the past years had shown that the colour of the plasma is mainly determined by the amount of Ca in the plasma. This is a critical parameter as it is correlated with the occurrence of instabilities. Moreover it could be verified that a change of colour already appears before an instability occurs. Therefore the monitoring of the colour could be helpful to anticipate instabilities early in order to intervene via re-optimisation. As the human eye is not capable to perceive small changes in colour the RGB values of the CCD-pixels are used. A small software tool has been set up which monitors the averaged RGB values of an area in the image which can be set by the software tool (yellow area in Figure 1a). A diagram visualises the trend of the RGB values over time (Figure 1b).

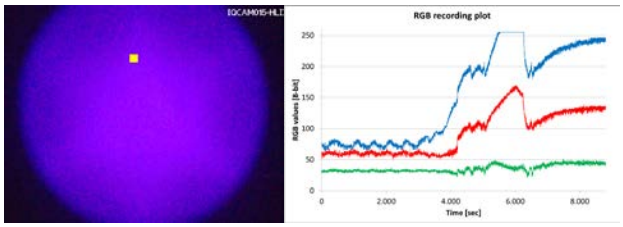

Figure 1: Camera image of the ^{48}Ca-plasma (a, left) and continuous RGB recording plot (b, right).

The application of this software tool during the last phase of the ^{48}Ca beam time showed promising results and turned out to be very helpful to simplify the optimisation of the ion beam.

References

[1] W. Barth et al., U^{28+}-intensity record applying a H_2-gas stripper cell, Phys.Rev.STAB, **18**, 040101 (2015).
[2] W. Barth et al., High Brilliance Uranium Beams for FAIR, Phys. Rev. Acc. Beams, in print 2017.
[3] A. Adonin et al., Production of high current proton beams using complex H-rich molecules at GSI, Rev. of Sci. Inst. **87**, 02B709 (2016).
[4] AREVA GmbH, 91058 Erlangen.
[5] A. Adonin, R. Hollinger, this report.
[6] M. Miski-Oglu et al., GSI Scientific Report 2015, GSI Report GR-2016-1 (2016) 345.

DOI:10.15120/GR-2017-1

UNILAC status report

P. Gerhard[1]
[1]GSI, Darmstadt, Germany

General remarks

As in 2015, the maximum ion energy of the UNILAC was restricted to 5.9 MeV/u due to the (planned) upgrade activities relating to the rf transmitters of the Alvarez tanks 3 and 4. The six operable single gap resonators were used for post acceleration several times, especially for synchrotron injection. Energy gains of up to $5.2(q/A)$ MeV/u were realized. For the first time the pulsed gas stripper was used over an extended period of four weeks in total, three of them during a regular ^{238}U beam time, successfully.

Operation

UNILAC operation started with machine checkout and commissioning on 4$^{\mathrm{th}}$ April, regular operation began on 25$^{\mathrm{th}}$ April and ended on 21$^{\mathrm{st}}$ July. During commissioning ^{40}Ar beam was delivered for tests at the cw linac demonstrator. ^{3}He and ^{48}Ti were used for training and for commissioning of the ROSE setup in the transfer channel.

Regular beam time started with ^{197}Au (PIG), and with ^{3}He and ^{16}O (both ECRIS). This block was terminated early by a severe water incident in the HSI RFQ rf power amplifier, which was put out of operation for 10 days. Operation was resumed with ^{238}U (MeVVA) and ^{50}Ti (PIG) for UNILAC machine experiments. This was followed by the first block of ^{48}Ca (ECRIS) mainly for SHE experiments and ^{238}U^{63+} for the synchrotron and material sciences. After this, ^{197}Au, ^{12}C and again ^{197}Au were used alternately for three weeks by different users at the UNILAC, while ^{124}Xe^{43+} (MUCIS) was accelerated for the SIS. At the end of the Xe operation, another block of ^{48}Ca began. This was accompanied by ^{12}C made from CH_3^+ (CORDIS) cracked by the gas stripper. ^{12}C^{3+} and ^{12}C^{6+} were accelerated for the synchrotron. Later ^{12}C^{n+} together with ^{1}H^{+} also made from CH_3^+ were used for machine experiments at the UNILAC and SIS. The beam operation ended with ^{40}Ar for beam tests at the cw linac demonstrator and machine experiments with ^{238}U and ^{50}Ti.

Aged capacitors in magnet power converters caused a number of breakdowns, including one severe incident were all IGBT modules of a kicker magnet PC were damaged. This almost terminated the beam time. A failure of a power supply of the UNILAC emergency stop caused a shutdown of the complete accelerator, and one day was lost.

Despite the several serious failures, the beam operation of the UNILAC was quite successful, thanks to the great effort of all colleagues involved.

Shutdown Activities

The renewal of the power converter for the Alvarez tank 3 rf transmitter was continued throughout the year. The replacement of the Alvarez tank drift tubes no. 30 of tank 1 and no. 15 of tank 3 started in November 2015 and was finished end of February 2016. In January a water leakage occurred at a baffle in the HLI beam line. It was not immediately noticed, because the vacuum system was switched off for maintenance reasons. A gate valve was erroneously opened, probably due to a defective vacuum controller. This caused flooding of a larger part of the beam line up to the gas stripper section, including two rf cavities and several vacuum pumps. The whole beam line was dismounted, disassembled, inspected and cleaned. One turbo pump was damaged. In spring, the field stabilization of all dipole magnets at the TK charge state separator was improved by new Hall probes.

After the beam time, the exchange of the last inner tank triplet of the first IH tank at the high current injector (HSI) began (ground fault). The adaptor plate was damaged during copper plating, a new plate will be delivered in May 2017. Several breakdowns of magnet power converters happened during operation (s. a.). A major replacement and maintenance programme will be executed until 2018.

The 108 MHz buncher TK4BB11 was out of operation, because its rf power line had been flooded partly by water from a defective coupling loop before the beam time. This was no constraint for operation, the repair is ongoing.

Machine Experiments

Machine experiments with the pulsed gas stripper were conducted in May and July, using ^{238}U, ^{50}Ti, and ^{1}H and ^{12}C^{n+} from CH_3^+ [1, 2]. The amplitude calibration and beam loading effects of the single gap resonators were investigated with ^{3}He and ^{124}Xe respectively. Several measurements with ROSE were conducted in the transfer channel with ^{3}He and ^{238}U. High current measurements regarding the FAIR beam requirements were performed with ^{238}U and ^{1}H all along the UNILAC [2]. At the entrance to the transfer channel, 5.4 mA of ^{238}U^{28+} and 3.6 mA of ^{1}H^{+} were achieved.

References

[1] P. Scharrer et al. (this report)

[2] Report on UNILAC Machine Experiments, LINAC dept., www.gsi.de

DOI:10.15120/GR-2017-1

Status of the pulsed gas stripper for the UNILAC

P. Scharrer[1,2,3], W. Barth[1,2], M. Bevcic[2], Ch. E. Düllmann[1,2,3], P. Gerhard[2], L. Groening[2], K. P. Horn[2], E. Jäger[2], J. Khuyagbaatar[1,2], J. Krier[2], H. Vormann[2], and A. Yakushev[2]

[1]HIM Helmholtz-Institut Mainz, Mainz, Germany; [2]GSI Gesellschaft für Schwerionenforschung GmbH, Darmstadt, Germany; [3]Johannes-Gutenberg Universität, Mainz, Germany

The GSI UNILAC will be used as part of the injector chain for FAIR [1]. In order to meet the high demands in terms of delivered beam current and quality an extensive upgrade program of the UNILAC is ongoing [2]. In this process a new setup for the gas stripper at 1.4 MeV/u was developed [3] and has been first employed in 2014. A pulsed gas injection is used instead of the continuous gas-jet of the previously existing stripper setup. With this setup, using H_2-gas, and together with additional improvements, significantly increased uranium beam intensities were achieved behind the gas stripper [4].

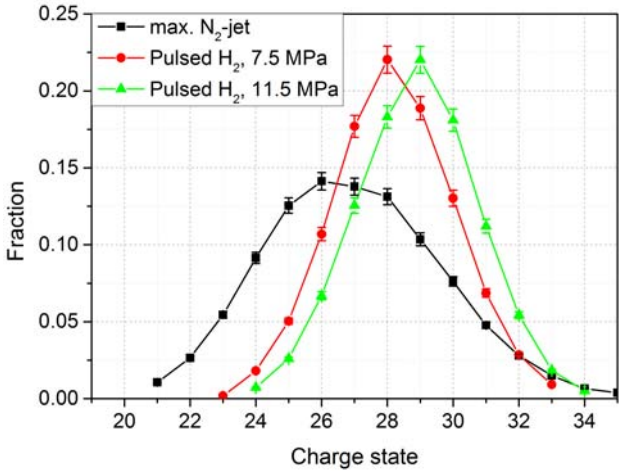

Figure 1: Comparison of the charge state distributions of ^{238}U ions after passing through the charge stripper applying different gas targets and back-pressures on the gas inlet.

Recent measurements

In 2016, additional measurement series were conducted over five days of machine beam time. The main topic was to obtain complete data sets for stripping of uranium and titanium beams, complementing measurements conducted in 2015, and additional measurements of the beam properties behind the gas stripper. For high-current measurements the VARIS-type ion source [5] was used and optimized for high-current operation. With the pulsed gas stripper, using H_2-gas, the target thickness can be adjusted to shift the maximum of the charge state distribution of uranium either to charge state 28 or 29 (see Fig. 1).

Measurements of charge state distributions of uranium and titanium beams after passing through different gases at 0.12 MeV/u and 0.74 MeV/u beam energy were conducted. To enable measurements at lower beam energies, the DTL tanks of the HSI were turned off separately. The corresponding results for 0.74 MeV/u are presented in [6]. At 0.12 MeV/u beam energy, the major part of the charge state distribution could not be measured due to limitations of the magnetic field of the dipole magnet in the charge separation system.

Additionally, the optimal target thickness for operation with the titanium beam was determined to reach maximum yield into a desired charge state. Due to limitations of the differential pumping system, this target thickness is currently not viable in long-pulse operation mode (5 ms pulse length, 50 Hz repetition rate). Alternatively, N_2-gas can be used with the pulsed gas stripper to match the performance of the previously existing N_2-jet stripper setup.

Long-term test

The pulsed gas stripper setup has been used continuously for three weeks during the SIS18 beamtime as a long-term test. During this time, the UNILAC delivered high-intensity U^{28+}-ion beams. A pulsed H_2-gas target with a thickness of about 9 μg/cm^2 was used.

After about two weeks, an increased gas pressure in the adjacent accelerator structures was noticed, which caused the closure of the adjacent gate valves. This was found to be due to a leaky gas valve, which had been in use as the main gas inlet for about 15 days in the course of several beam times and offline measurements in 2015-2016. After switching to the second gas valve, which had significantly less duty time in the past, the beam time continued without any further incidents due to the gas stripper. Additional systematic long-term measurements with the pulsed gas valves are in preparation at a dedicated test stand to identify the cause of this outage.

References

[1] FAIR Baseline Technical Report, Vol. 2, GSI Darmstadt, Germany p. 335 (2006).

[2] L. Groening et al., in proceedings of IPAC2016, Busan, Korea (JACoW) MOPOY017 (2016).

[3] P. Scharrer et al., in proceedings of IPAC2016, Busan, Korea (JACoW) TUPMR058 (2016).

[4] W. Barth et al., Phys. Rev. Accel. Beams 18 040101 (2015).

[5] R. Hollinger et al., Nucl. Instrum. Meth. B 239 p. 227 (2005).

[6] P. Scharrer et al., Phys. Rev. Accel. Beams 20, 043503 (2017).

DOI:10.15120/GR-2017-1

Pressure profile simulations for UNILAC gas stripper

P.M. Suherman, P. Gerhard, M. Maier, M.C. Bellachioma, J. Cavaco, M. Kaiser
GSI, Darmstadt, Germany.

Introduction

A new gas stripper setup based on a pulsed gas injection is being developed at GSI UNILAC. This work is part of an upgrade of the existing gas stripper in preparation for the FAIR project [1]. The inlet pressure of the pulsed gas will be in the order of 100 bar. The gas will flow through the nozzle and disperse through the T-pipe construction in the gas stripper chamber (Figure 1). It is expected that the gas flow will then be directed to the pipes/apertures connecting the gas stripper chamber and the adjacent differential pumping chambers. The purpose of the new gas stripper is to maximise the gas density inside the T-pipe, in order to increase the stripping efficiency. During this process, the gas flow from the stripper chamber to the adjacent chambers connected to the accelerator must be kept as low as possible. A pressure profile simulation is therefore conducted to investigate if a new design of the gas stripper may be used to improve the stripping performance, as well as maintaining a sufficient low pressure for the neighbouring accelerator sections for high duty factors.

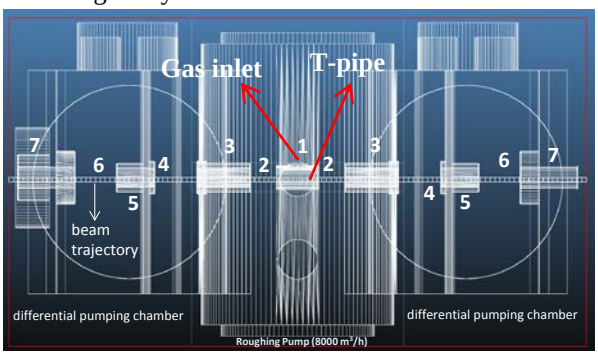

Figure 1: Cross-section of gas stripper chambers.

Pressure Profile Simulations

The gas stripper setup consists of a gas stripper chamber and two differential pumping chambers that are connected to the accelerator sections. All chambers have dimensions of approximately 20 cm diameter and 30 cm long. The chambers are all linked via ~ 2 cm diameter pipes/apertures, which are positioned in the middle of the chambers at the beam trajectory (see Figure 1).

The gas stripper chamber itself consists of a T-pipe construction with a fast switchable nozzle as high pressure gas inlet. The T-pipe is mounted directly in-line with the pipes/apertures connected to the adjacent chambers. A roughing pump with a pumping speed of 8000 m^3/h is mounted directly underneath the T-pipe.

The differential pumping chambers are equipped with 4 turbo pumps (1200 l/s – N_2 equivalent). These high speed pumps are required in order to achieve a sufficiently low pressure (<10^{-6} mbar) in the accelerator sections.

The pressure profile was calculated using a Monte Carlo based simulation for vacuum conditions (Molflow software) [2]. A N_2 gas pulse of 1 Hz repetition rate and 100 µs pulse length and two different gas flow rates were used in the simulation: 1 mbar·l/s and 10^4 mbar·l/s.

Figure 2 shows the pressure profiles along the beam trajectory. The preliminary simulation results show that there should be a sufficient gas density inside the T-pipe, while maintaining low enough pressure in the differential pumping chambers. For a low gas flow rate (1 mbar·l/s), the pressure inside the T-piece pipe is approximately $5x10^{-6}$ mbar. The pressure will increase proportionately with the gas flow rate. The anticipated gas flow rate to be used is in the order of 10^4 mbar·l/s. Therefore, the pressure inside the T-piece will be approximately $5x10^{-2}$ mbar.

The concern with using higher gas flow rates is that the pressure in the differential pumping chambers is increasing above the limit for the accelerator sections. At a gas flow rate of 10^4 mbar·l/s, the pressure in the differential pumping chambers is in the order of 10^{-3} mbar (inside the pipe/aperture) - 10^{-4} mbar (outside the pipe/aperture). This pressure is considerably too high, since these chambers are directly connected to the accelerator sections.

A possible simple solution to obtain a low pressure in the differential pumping chambers while maintaining the optimum gas density in the gas stripper is the use of higher pumping speed for the turbo pumps. This will be investigated in the future simulation work.

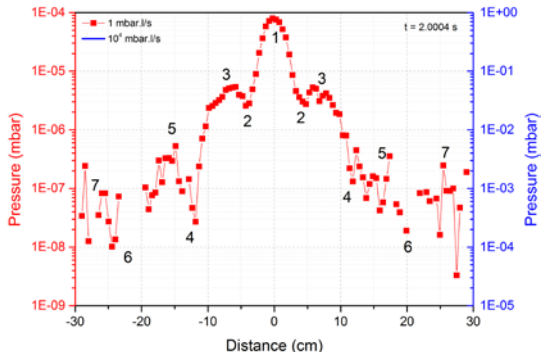

Figure 2: Pressure profile along the cross-section of the chamber for a pulsed N_2 gas

The drawback of using Molflow software for this purpose is the inaccuracy that may be observed in the area of the T-piece by the gas injection, due to a viscous flow. A future work may use ANSYS software to compare the pressure profiles for this setup.

References

[1] P. Scharrer, et. al. J. Radional. Nucl. Chem., 2015.
[2] http://molflow.web.cern.ch/content/about-molflow.

DOI:10.15120/GR-2017-1

Status of the 108 MHz RF system modernisation at the UNILAC

B. Schlitt, J. Catta, T. Eiben, G. Eichler, S. Hermann, M. Hörr, F. Lorenz, M. Müh, S. Petit, M. Pilz, E. Plechov, J. Salvatore, R. Scholz, G. Schreiber, W. Vinzenz, A. Windolf, and J. Zappai
GSI, Darmstadt, Germany

Modernisation of existing RF systems

Various tests of the modernised RF system at the Alvarez tank 3 were successfully performed during 2016. It comprises the rebuilt high power RF amplifier stage (HPA), a new separate control rack (including a newly developed measurement and fast interlock unit and a commercial control grid power supply), and the updated 1 MVA, 24 kV anode power supply equipped with a new PLC control [1, 2].

A specifically developed manual control unit is used for test operation of the HPA. For routine operation, another PLC system based on Siemens S7-1500 is being built and programmed (Fig. 1) [3]. The system handles monitoring and interlocks of all HPA cooling circuits and power supplies, turn-on/off sequences of the supply voltages, system access interlocks, control of the motorized tuning circuits, basic switch-on/off commands of the driver amplifier and of the LLRF output signal, etc. The central part of the PLC is installed in the separate control rack, whereas a subunit is directly installed in the HPA stage comprising the I/O modules for all signals provided there. The PLC system as well as the manual control unit is designed for both amplifiers – the existing HPA as well as the new Thales amplifier (see below). First prototype tests of the new PLC system were performed at a test setup [3]. Tests of the final PLC system installed in the Alvarez 3 RF system are scheduled for summer 2017.

The fully modernised Alvarez 3 RF system as well as the upgraded 1 MVA anode power supplies at Alvarez 1–3 will be used for routine operation during the beam time 2018. The remaining HPA stages will be upgraded in the same way.

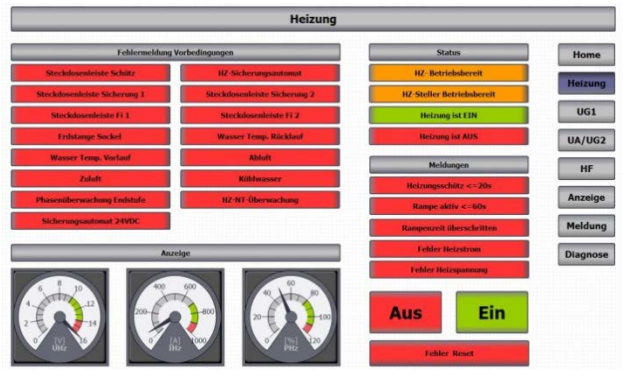

Figure 1: PLC system graphical user interface for filament operation at the Alvarez high power RF amplifiers.

New 1.8 MW cavity amplifier prototype

The new 1.8 MW cavity amplifier prototype [1] was commissioned successfully at Thales Electron Devices [2, 4]. The manual control unit developed by GSI was used for the tests to control interlocks and the motorised tuners. Parasitic oscillations which occurred around 900 MHz could be damped successfully by placing ECCOSORB MF-124 bars at the bottom of the output circuit of the cavity [4]. Further tests and measures were taken to ensure good suppression of parasitic oscillations during pulsed operation [2, 4]. Finally, the factory acceptance tests (FAT) were successfully finished in July 2016 including a 3×8 hour test run at 1.8 MW peak RF output power on dummy load without any trip.

After delivery to GSI, the new amplifier was integrated into the existing equipment at the UNILAC RF gallery (anode power supply, driver amplifier, air and water cooling systems, installation of RF transmission lines, etc.) and a control rack similar to that built for the A3 amplifier was installed (Fig. 2). An existing huge coaxial transmission line switch in the output RF line is used to switch between a water dummy load and the Alvarez tank 4 at the UNILAC. Site acceptance tests (SAT) at GSI are scheduled for July – August 2017. Routine operation of the new amplifier on Alvarez tank 4 is planned during regular beam time from 2018 on.

Figure 2: New 1.8 MW high power cavity amplifier prototype installed at the UNILAC RF gallery plus control rack equipped with grid power supplies, new measurement & fast interlock unit, and further control elements.

References

[1] B. Schlitt et al., GSI Scientific Report 2015, p. 310.
[2] B. Schlitt et al., LINAC2016, THPLR025.
[3] S. Petit, Bachelor Thesis, Darmstadt University of Applied Sciences (Hochschule Darmstadt), Darmstadt, Germany, 2016.
[4] Thales Electron Devices, Thonon-les-Bains, France.

DOI:10.15120/GR-2017-1

Design study for a first of series Alvarez-cavity

M. Heilmann[*1], *X. Du*[1], *P. Gerhard*[1], *L. Groening*[1], *M. Kaiser*[1], *S. Mickat*[1], *A. Rubin*[1], *and A. Seibel*[2]
[1]GSI Helmholtzzentrum, 64291 Darmstadt, Germany; [2]IAP, Frankfurt University, 60438 Frankfurt am Main, Germany

The design study describes the first of series Alvarez tank of the new poststripper section as injector for FAIR. The existing Alvarez linac had an operation period of over 40 years and the repair efforts increase particularly with regard to the drift tubes and the included magnets. The FAIR experiments have new requirements to the linac and a high availability is important for the new main operational injector [1]. The UNILAC at GSI comprises a low energy section with RFQ and IH-DTL with an energy of 1.4 MeV/u and after the stripper section the Alvarez-DTL accelerates the design beam of U^{28+} up to 11.4 MeV/u and delivers the beam to the SIS18. In the first step a first of series Alvarez tank (Table 1) with 11 drift tubes (quadrupole singlets are included) and a total tank length of 1.9 m will be manufactured (Fig. 1). This cavity will implement the new drift tube shape profile to increase the shunt impedance and a new beam dynamics concept [2, 3]. Furthermore it is possible to investigate an optimized stem position to increase the RF-field stability [4]. After low level measurements the prototype will be conditioned and operated with high power.

Table 1: Parameters of the first of series Alvarez tank

Parameter	Unit	Value
Frequency	MHz	108.408
A/q		≤ 8.5
max. Current	mA	16.5
Synchronous Phase	deg.	-30
RF-pulse length	ms	2
Beam repetition rate	Hz	10
Input energy	MeV/u	1.4
Output energy	MeV/u	1.7
Gaps	#	12
Gap length	mm	40.9-44.7
Drift tubes	#	11
Drift tube length	mm	111.3-122.2
Drift tubes diameter	mm	180.0
Aperture	mm	30.0
Tank diameter	mm	1948.9
Tank length	mm	1917.2
Q - Factor		82000

Mechanical Integration

The drift tubes are installed from the top of the tank (Fig. 2), but other combinations are possible [4]. RF coupling and a maintenance hole are installed in the bottom. In the center position on the tank side are installed two vacuum pumps. The Alvarez tanks will all have these parts at the bottom. The frequency range is increased with eight tuners in total (two dynamical tuners).

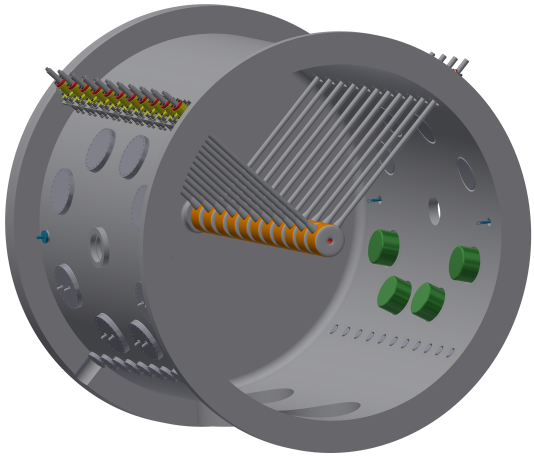

Figure 1: CAD-model of the first of series Alvarez tank with a length of 1.9 m and 11 drift tubes.

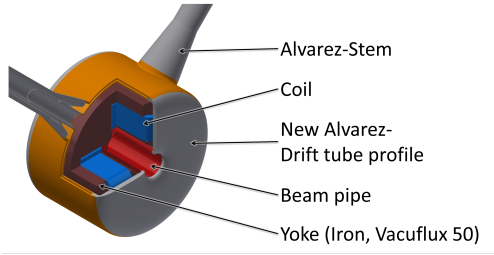

Figure 2: Alvarez-drift tube with the new shape profile. In the drift tube casing a water cooling system is implemented. The power and water supply for the magnet is in one Alvarez-stem only. Both stems and the casing of the drift tube are cooled.

References

[1] L. Groening et al., Upgrade of the Universal Linear Accelerator UNILAC for FAIR, MOPOY017, Proceedings of IPAC'16, Busan, Korea, p. 880 (2016).
[2] X. Du et al. (this report)
[3] A. Rubin et al. (this report)
[4] X. Du et al., DOI: 10.1103/PhysRevAccelBeams.20.032001

* m.heilmann@gsi.de

Status of the beam dynamics design of the new post-stripper DTL

A. Rubin[1], *X. Du*[1], *L. Groening*[1], *and S. Mickat*[1]
[1]GSI, Darmstadt, Germany

Introduction

The GSI UNILAC has served as injector for all ion species since 40 years. Its 108 MHz Alvarez DTL providing acceleration from 1.4 MeV/u to 11.4 MeV/u has suffered from material fatigue and has to be replaced by a new section [1]. The design of the new post-stripper DTL is developed in GSI [2]. Five Alvarez tanks with four intertank sections provide 100% transmission and low emittance growth. The intertank sections allow for a matched solution and provide place for diagnostics [3].

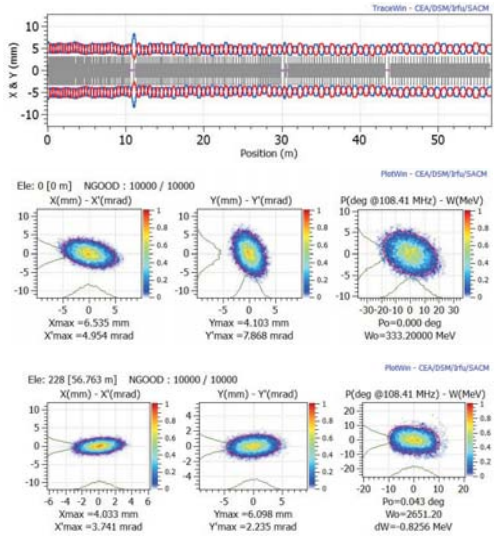

Figure 1: FAIR case: envelopes along the new Alvarez-DTL, input and output distributions.

Beam dynamics simulations for the new Alvarez DTL

The beam dynamics simulations for the new model were done for $^{238}U^{28+}$ using the TraceWin code [4]. The behaviour of the beam in the proposed structure was investigated for different zero current phase advances, as without current, as for the current of 16.5 mA. Input emittances were chosen as E_x=E_y=0.175 mm·mrad and E_z=70 deg·keV/u. Simulations along the complete Alvarez DTL (Fig. 1) were done for the zero current phase advance of $65°$ for each tank. The intertank section for the presented design consists of quadrupoles, one buncher, and spaces between them. These drifts can be filled with other elements (trafo, steerer, grid, probe etc.) The 1^{st} and the 3^{rd} quadrupoles are placed partially in the tank cover, the length of the intertank section is about 1m. The total emittance growth for the whole Alvarez is about 7%. The new DTL serves also for the non-FAIR scenarios. Results of beam dynamics simulations for six different scenarios including the FAIR nominal case and low energy operation are presented in Tab.1.

References

[1] L. Groening, et al. "Upgrade of the Universal Linear Accelerator UNILAC for FAIR", IPAC 2016, Busan, Korea, Mar. 2016, paper MOPOY017, pp. 880-882

[2] X. Du, et al. "Alvarez DTL Cavity Design for the UNLAC Upgrade", IPAC 2015, USA

[3] A. Rubin, et al. " Status of beam dynamics design of the new post-stripper DTL", annual report 2015, GSI

[4] TraceWin http://irfu.cea.fr/Sacm/logiciels/index3.php

Table 1: Six investigated cases for the new Alvarez DTL:

	FAIR case	Zero current	Low Energy	Larger Long.	Smaller Long.	Transvers. Flat
I, mA	16.5	0	0	16.5	16.5	16.5
E_x (rms), mm mrad	0.175	0.175	0.175	0.175	0.175	0.0875
E_y (rms), mm mrad	0.175	0.175	0.175	0.175	0.175	0.35
E_z (rms), MeV/u deg	0.07	0.07	0.07	0.14	0.035	0.07
Energy (out), MeV/u	11.4	11.4	3.3	11.4	11.4	11.4
Transmission	100%	100%	100%	100%	100%	100%
δE_x (tot, 95%)	7%	0%	0%	7%	8%	16%
δE_y (tot, 95%)	7%	0%	0%	10%	7%	3%
δE_z (tot, 95%)	10%	0.7%	1.7%	5%	11%	4%
Bunch Length (95%)	±16 deg	±11 deg	±33 deg	±21 deg	±14 deg	±17 deg

DOI:10.15120/GR-2017-1

Benchmarking of four post-stripper DTL options

S. Mickat, L. Groening, A. Rubin
GSI, Darmstadt, Germany

After more than 40 years of reliable operation the existing post-stripper DTL commences causing an increasing amount of down time of the GSI facility as well as of the amount of resources for repair and maintenance. In 2013 an evaluation of options for refurbishment drew the conclusion that the amount of related resources does not justify this activity. Moreover, in 2013 a dedicated review by external experts stated that the present layout of the post-stripper will not allow for reaching FAIR's requirement to its injector linac. The results from 2013 were confirmed by a 2nd review in 2016, where the listed four post-stripper DTL options were reviewed:

- new Alvarez DTL
- KONUS IH DTL
- synchronous IH DTL
- refurbishment of existing Alvarez DTL

The two first listed DTL concepts passed the review as being feasible from first principles. The required resources for installation of a new post-stripper DTL are similar for the two DTL concepts. The KONUS IH has lower cost but its final beam quality does not comply with the FAIR requirements. Therefore the Alvarez option has been favoured in-house.

In preparation of the review, which took place in October 2016, common rules w.r.t. obtaining information as well as a schedule and deliverables towards a reliable benchmarking were defined three months before. In two dedicated meetings in August chaired by the Accelerator Operation division head, these rules, the data exchange format, and six beam dynamic benchmark scenarios including input particle distributions were communicated to those collaborations that proposed an option.

The most important scenario is conceived to check the option's ability to serve as a dedicated FAIR injector. Two scenarios assume different initial longitudinal beam parameters, while two additional scenarios probe the beam requirements of today's UNILAC experiments. The 6th scenario is on the compliance with future upgrade measures based on flat beam injection into the SIS18. In parallel to the beam dynamics investigations a systematic cost estimate by GSI experts for the four options has been conducted.

The table below presents an extraction of the obtained data and information, which was sent to the review committee prior to the review itself. The complete table lists 43 items and the report on the cost estimate comprises 42 pages. In February 2017 the GSI/FAIR directorate decided that the Alvarez option will be followed exclusively.

Table 1: Extract of the table which summarizes the benchmarking results.

Criteria	New Alvarez	IH (KONUS)	IH (synchronous)	Alvarez (refurbished)
FAIR injection				
Transmission [%]	100%	100%	100%	-
Final emittances (95% tot., norm.)	1.058 mm mrad 1.061 mm mrad 104.19 MeV deg	1.62 mm mrad 1.64 mm mrad 107 MeV deg	1.262 mm mrad 1.228 mm mrad 111.67 MeV deg	-
Final bunch length (95% tot.)	± 16 deg	± 16 deg	± 26 deg	-
Flat beam injection				
Transmission [%]	100%	99.4%	-	-
Final emittances (95% tot., norm.)	0.575 mm mrad 2.033 mm mrad 97.09 MeV deg	1.19 mm mrad 2.36 mm mrad 109.82 MeV deg	-	-
Final bunch length (95% tot.)	± 17 deg	± 14 deg	-	-
General parameters				
DTL length [m]	57 (+4m Transferline)	23 (+38 m Transferline)	35 (+26m Transferline)	
Eff. gradient [MV/m]	1.59	3.76	2.77	
# cavities (Transferline)	5x Alvarez 4x Buncher (-)	5x IH DTL (3x Buncher)	20x IH DTL (1x IH-DTL)	5
Costs				
[M€]	28.4	18.3	40.3	> 25.1

DOI:10.15120/GR-2017-1

Status of the IH-DTL poststripper linac proposal*

H. Hähnel†, *U. Ratzinger, and R. Tiede*
Institut für Angewandte Physik, Goethe Universität Frankfurt

Motivated by the necessary replacement of the GSI UNILAC poststripper linac, a compact and efficient linac design based on IH-type cavities has been developed [1, 2]. Using KONUS beam dynamics, it was possible to design a linac consisting of only five cavities that can be operated by the existing UNILAC RF amplifier structure. The transversal focusing scheme is based on magnetic quadrupole triplet lenses.

The optimized design provides full transmission and low emittance growth for the design current of 15 emA U^{28+}, accelerating the beam from 1.4 MeV/u to 11.4 MeV/u. Extensive error studies were performed to define tolerances and verify the stability of the design with respect to misalignment and injection parameters. With a total length of just 22.8 meters, the design provides a compact and cost effective alternative to a new Alvarez linac.

Error Studies

Extensive error studies were performed on the IH-DTL poststripper linac design using TraceWin. The total number of simulated particles for each simulation run is 10^7 to 10^8. These values were chosen to achieve reproducible results. A detailed description of the error studies can be found in [1], including:

- Sensitivity studies of the individual component errors (magnetic lenses, cavities, RF, beam)
- Error studies of different combined error sets
- Finding the best steering strategy
- Influence of corrective steering on error tolerance

Based on the sensitivity studies, simulations were performed with combined error sets (see Tab. 1). Case A resembles the error limits beyond which significant losses and/or emittance growth were observed in the sensitivity studies. In Case B, only the magnetic triplet errors are reduced to $\Delta xy = 100\,\mu\text{m}$ and $\Delta\phi_{x,y,z} = 1\,\text{mrad}$ to account for strong coupling of singlet and triplet errors. For Case C, all errors were reduced to optimistic achievable values. The resulting additional emittance growth and average transmissions for these three error sets are summarized in Table 2. As expected, the "Case A" error set shows significant average losses. Due to strong coupling between quadrupole singlet and triplet errors, the average transmission of "Case B" is significantly improved. Even without any corrective steering in the linac, an average transmission of 99.76 % is achieved for the Case C.

Table 1: Lens parameters for combined error runs of the poststripper IH-DTL (cavitiy/RF errors not shown [1]).

Error Type	**Case A**	**Case B**	**Case C**
Quadrupole Lenses			
Singlet Δxy	80 µm	80 µm	**50 µm**
Singlet $\Delta\phi_{x,y,z}$	1 mrad	1 mrad	1 mrad
$\Delta B'/B'_0$	0.7 %	0.7 %	**0.1 %**
Triplet Δxy	360 µm	**100 µm**	100 µm
Triplet $\Delta\phi_{x,y,z}$	1.6 mrad	**1 mrad**	1 mrad

After investigation of different steering strategies, it was found that a total of four steerers, set up as two steerer pairs, is sufficient for the proposed linac. With this steering strategy, the average losses can be significantly lowered from 7.21 % to 0.03 % for Case A (see Tab. 2). In combination with strict error tolerances, as in Case C, the losses can be reduced even further to $6 \cdot 10^{-8}$.

Table 2: Resulting additional emittance growth and losses of combined error simulations with and without steerers.

	$\Delta\epsilon_x$ [%]	$\Delta\epsilon_y$ [%]	**Losses [%]**
Case A	1.0 %	0.2 %	7.2 %
Case B	2.1 %	2.1 %	1.5 %
Case C	0.6 %	1.3 %	**0.2 %**
with steerers:			
Case A	1.4 %	2.5 %	**0.03 %**
Case C	0.7 %	0.8 %	$\mathbf{\underline{6 \cdot 10^{-8}}}$

References

[1] H. Hähnel, "Development of an IH-Type Linac for the Acceleration of High Current Heavy Ion Beams", Ph.D. thesis, Phys. Dept., Goethe University, Frankfurt, Germany, 2017.

[2] H. Hähnel, U. Ratzinger, R. Tiede, "Status of the IH-DTL Poststripper Linac Proposal", GSI Scientific Report 2015, p. 300.

* Work supported by BMBF05P15RFRBA
† haehnel@iap.uni-frankfurt.de

DOI:10.15120/GR-2017-1

Simulation of UNILAC BPMs with CST

R. Singh[1], *P. Forck*[1], *W. Kaufmann*[1], *T. Sieber*[1], *T. Reichart*[1], *and J. He*[2]
[1]GSI, Darmstadt, Germany; [2]IHEP, Bejing, China

Several BPMs are installed in GSI UNILAC to monitor beam positions with a desired resolution of atleast 1 mm at a rate of 1 MHz. Initial stages of UNILAC e.g. RFQ and IH structures operate at 36 MHz while the later part i.e. Alvarez part operates at 108 MHz. The processing electronics utilize 72 MHz for one BPM placed at the exit of RFQ and 216 MHz for rest of the BPMs. These BPMs were simulated to calculate the position sensitivity at the processed frequency.

Simulations and results

Figure 1 shows the CST model for top part of the BPM plates. The pick-ups have a rather complex design for reasons such as protection from beam hits, good position sensitivity as well as mechanical stability.

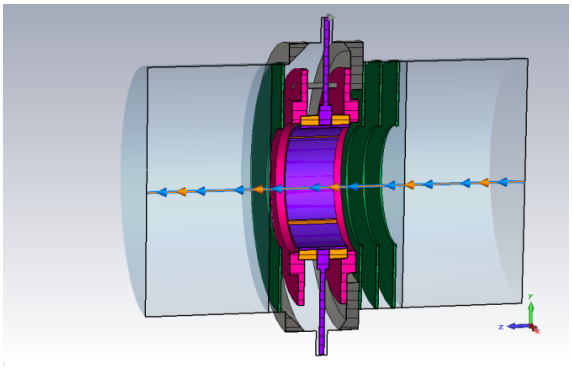

Figure 1: Model of UNILAC BPM as simulated in CST.

Scattering parameters of the structure were measured by a network analyzer as shown in Fig. 2 where S21 represents the coupling to the opposite plate and S31 is the coupling into the another plane, and S11 is the reflection. The corresponding S-parameters derived from the simulation are shown in Fig. 3 and closely matched the measured parameters which confirmed the pick-up model and gave insights into the crucial components of the design. Figure 4 shows the position sensitivity of the pick-up calculated for a relativistic beam; the percentage change in difference signal of the opposite plates as a function of beam position.The coupling between opposite plates (as characterized by S21) increases with frequency which explains the observation that the position sensitivity decreases with increasing frequency. The coupling from one plane to another (S31) has a peak at around 200 MHz which reduces the position sensitivity and modifies the shape of sensitivity curve to bring a non-trivial position dependence. The outlook is to confirm the results with the more relevant case of non- relativistic beams in different sections of UNILAC.

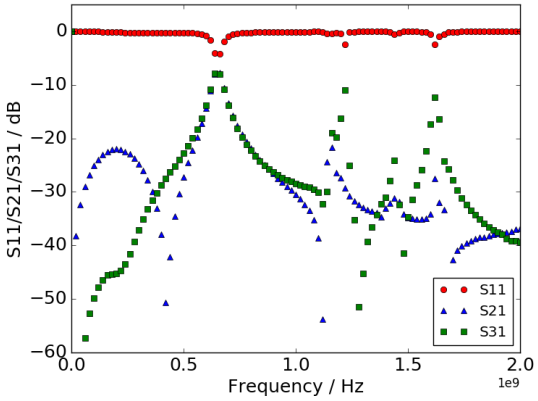

Figure 2: Measured S parameters.

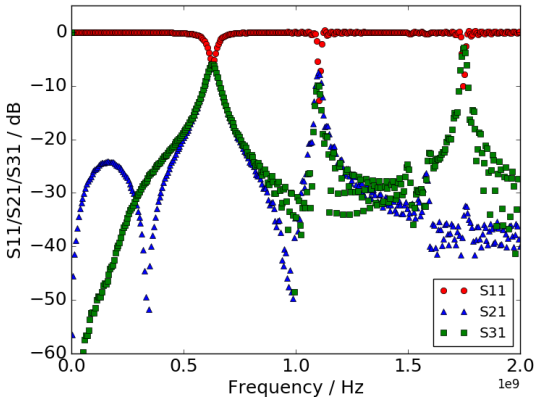

Figure 3: Simulated S parameters.

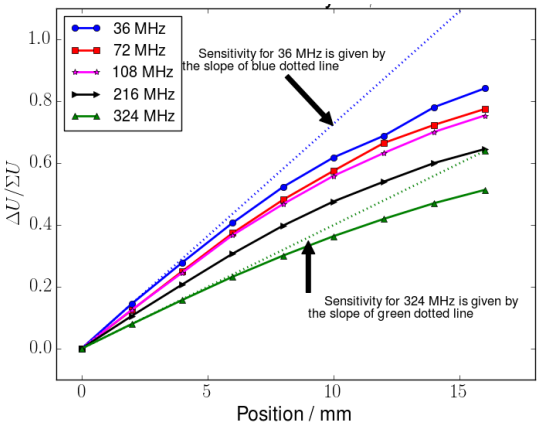

Figure 4: The slope of the curves correspond to position sensitivity at the respective frequency.

DOI:10.15120/GR-2017-1

Structural mechanical simulations for a new 108 MHz CW RFQ for the HLI*

D. Koser† [1], *P. Gerhard*[2], *L. Groening*[2], *O. Kester*[3], *and H. Podlech*[1]
[1]IAP, University of Frankfurt, Germany; [2]GSI, Darmstadt, Germany; [3]TRIUMF, Vancouver, BC, Canada

The currently operated 108 MHz 4-rod RFQ at the HLI was commissioned in 2010 [3]. Unfortunately the structure suffers from strong modulated RF power reflections with a frequency of approximately 500 Hz that severely limit the achievable pulse length and amplitude [2]. Measurements of the velocity profile of the electrodes using a laser vibrometer identified mechanical vibrations as source of the RF modulations and additionally revealed other vibrational modes around 350 Hz that however do not affect the RF behavior [1]. In structural mechanical simulations using ANSYS Workbench the measured frequency spectra could be replicated accurately. Derived concepts for the mitigation of the RF affecting mechanical eigenmodes were implemented in the design of a prototype for a completely revised 4-rod HLI-RFQ.

Mechanical Eigenmodes

It could be shown that the RF affecting vibrations at 500 Hz correspond to radial oscillations of the electrodes that are triggered by the radially acting electric forces of the quadrupole field. Tangential oscillations with eigenmode frequencies of roughly 350 Hz are caused by asymmetries (e.g. dipole component) and are therefore comparatively small, having an negligible influence on the RF properties.

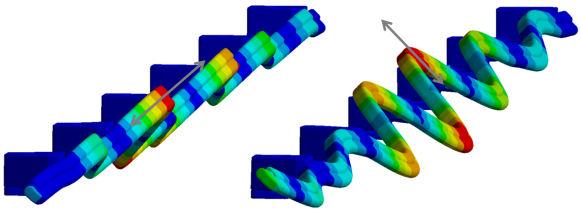

Figure 1: Mechanical eigenmodes of the electrodes

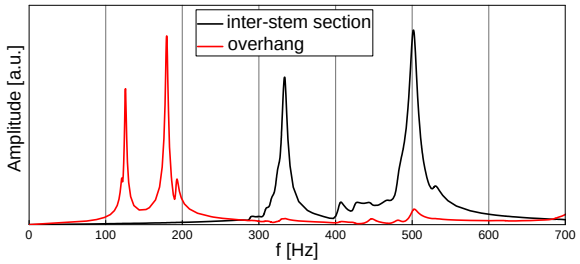

Figure 2: Simulated mechanical resonance spectrum of the inter-stem electrode sections (black) and the overhang (red)

Prototype Development

Starting from the basic FRANZ/MYRRHA-RFQ concept the electrode profile, trapezoidal electrode mountings, stem geometry and stem distance were optimized in view of mechanical rigidity, shunt impedance and electric dipole. The resonance frequencies of the mechanical eigenmodes could be increased by a factor of roughly 4 compared to the existing HLI-RFQ while mostly preserving the value of the shunt impedance of about 100 kΩ·m. The electric dipole is compensated entirely.

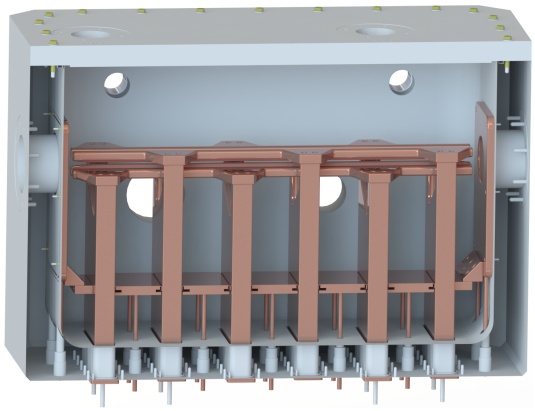

Figure 3: Final 6-stem prototype design

From a previously intended 4-stem design the prototype configuration was upraded to 6 stems in order to reproduce a mechanical resonance mode spectrum of the electrodes that is comparable to a longer structure. The manufacturing of the prototype by NTG, Gelnhausen, is currently in progress and is expected to be completed in Q3 2017.

References

[1] P. Gerhard, L. Groening, K.-O. Voss, "In Situ Measurements of Mechanical Vibrations of a 4-Rod RFQ at GSI", Proc. of LINAC2014, Geneva, Switzerland, p. 553-555 (2014)

[2] P. Gerhard, W. Barth, L. Dahl, W. Hartmann, G. Schreiber, W. Vinzenz, H. Vormann, "Experience with a 4-Rod CW Radio Frequency Quadrupole", Proc. of LINAC2012, Tel-Aviv, Israel, p. 825-827 (2012)

[3] P. Gerhard, W. Barth, L. Dahl, A. Orzhekhovskaya, A. Schempp, K. Tinschert, W. Vinzenz, H. Vormann, M. Vossberg, S. Yaramyshev, "Commissioning of a New CW Radio Frequency Quadrupole at GSI", Proc. of IPAC'10, Kyoto, Japan, p. 741-743 (2010)

* work supported by BMBF Contr. No. 05P15RFRBA
† koser@iap.uni-frankfurt.de

DOI:10.15120/GR-2017-1

Upgrade measures for the UNILAC

L. Groening[*1], *X. Du*[1], *P. Gerhard*[1], *M. Heilmann*[1], *M.S. Kaiser*[1], *S. Mickat*[1], *A. Rubin*[1], *A. Seibel*[2], *H. Vormann*[1], *and C. Xiao*[1]

[1]GSI Helmholtzzentrum, 64291 Darmstadt, Germany; [2]IAP, Goethe University Frankfurt, 60438 Frankfurt, Germany

In 2013 the UNILAC upgrade project [1] has been defined in order to prepare the machine to fulfil the requirements imposed by FAIR on beam quality and on operational reliability. The measures have been grouped into sub-projects and cover the full UNILAC from the installation of a dedicated uranium source up to the replacement of the post-stripper DTL. For each sub-project the target, required resources, schedule, risks, and boundaries have been summarized within a dedicated so-called Fact Sheet.

Handling and operation of uranium sources shall be localized at a dedicated source "terminal West" to be installed between the existing terminals "North" & "South" after the sub-project has been approved. The required fire protection concept for the new terminal is in preparation, now taking into account an overall concept for the ion source operation hall. The terminal will be followed by a short straight LEBT section [2]. This section ends with a new quadrupole quartet that is currently being installed at the entrance to the HSI-RFQ. The power supply for the new quadrupole quartet will be delivered soon.

The re-design of the HSI-RFQ electrodes has been started by A. Lombardi et al. from CERN within the overall CERN/GSI collaboration framework. The re-design aims for an improved envelope matching at the RFQ exit as well as for lowered electric surface fields during operation.

For the subsequent MEBT, providing for proper injection into the pre-stripper IH-DTL, a new design has been proposed already in 2014 [3]. It will notably increase the operational flexibility of the section by decoupling the transverse tuning from the longitudinal one. All components can be procured as soon as the funding has been approved.

During the last years a new gaseous stripper cell has been developed. It aims for replacing the continuous nitrogen jet by a pulsed jet of hydrogen and for an increase of the target density. The new device provided for remarkable improvement of the stripping efficiency of about 68%. It additionally allows for pulse-to-pulse adaption of the jet parameters w.r.t. type of gas, pulse duration, and pressure. A detailed description of its development and performance is given in [4] and the references therein.

The aged post-stripper DTL will be replaced by a completely new DTL based on Alvarez-type cavities. This choice of technology has been made after a systematic and rigorous benchmarking procedure of several DTL-technologies finally commented and evaluated by external experts during a dedicated review [5]. Five independent cavities will provide for acceleration from 1.4 to 11.4 MeV/u. The rf-design includes improved drift tube shapes for maximum shunt impedance [6] as well as a novel scheme for field stabilization [7]. A 1:3 model cavity has been successfully tested [8] and a fully operational prototype cavity section is under preparation [9]. The new beam dynamics design [10] is optimized for delivery of intense uranium beams and will use pulsed quadrupoles inside the drift tubes, thus assuring optimized beam transport for each ion species being provided in quasi-parallel pulse-to-pulse switching mode. The cavities are separated by inter-tank sections, including a re-buncher each. These are required to provide smooth envelopes for provision of high quality beams. The bunchers will also be used to deliver beams of low energy spread for physics experiments at the Coulomb barrier. Extensive error studies w.r.t. machine errors as well as to fluctuations of the initial beam parameters have been performed. The upgrade of the DTL's rf-power alimentation system has been continued. A new 1.8 MW amplifier has been successfully tested at the manufacturer. In parallel the modularization of the alimentation system of the fourth cavity has well advanced [11].

All upgrade measures involving beam dynamics were modelled by front-to-end simulations based on measured beam parameters at the uranium source extraction gap. The fully upgraded UNILAC was modelled up to the entrance to the SIS18 [12]. These simulations provide the set of beam parameters to be achieved during stepwise commissioning of the upgraded UNILAC. The aged UHV control system needs to be modernized and first components have been ordered.

References

[1] L. Groening et al., Proc. of 7$^{\text{th}}$ IPAC Conf. (2016).

[2] C. Xiao et al., NIM A 788 p. 173 (2015).

[3] H. Hähnel et al., Proc. of XXVII Linac Conf. (2014).

[4] P. Scharrer et al., PRAB **20** 043503 (2017).

[5] S. Mickat et al., this report.

[6] X. Du et al., this report.

[7] X. Du et al., PRAB **20** 032001 (2017).

[8] A. Seibel et al., annual report of IAP, Univ. of Frankfurt (2016).

[9] M. Heilmann et al., this report.

[10] A. Rubin et al., this report.

[11] B. Schlitt et al., this report.

[12] C. Xiao et al., this report.

* la.groening@gsi.de

DOI:10.15120/GR-2017-1

DOI:10.15120/GR-2017-1

ESR operation and development

C. Dimopoulou[1], *R. Heß*[1], *M. Kelnhofer*[1], *C.M. Kleffner*[1], *S. Litvinov*[1], *F. Nolden*[1], *C. Peschke*[1], *N. Petridis*[1], *U. Popp*[1], *J. Roßbach*[1], *S. Sanjari*[1], *M. Steck*[*1], *and D. Winters*[1]

[1]GSI Helmholtzzentrum, Darmstadt, Germany

In 2016, the experimental storage ring (ESR) has been operated from May to July for a period of about 5 weeks in total. A variety of interesting physics experiments, addressing different topics and using different new (FAIR-type) detector systems, could successfully be performed.

A new fast current transformer has been installed at the ESR, which allows for measurements of short ion bunches. The software for the ionization profile monitors (IPM), which were installed at the ESR a few years ago, has been updated and greatly improved. Therefore, it was possible to systematically perform measurements of the properties of bunched, electron-cooled ion beams.

From the 25$^{\text{th}}$ to the 29$^{\text{th}}$ of May, a uranium ion beam was offered for experiments at Cave A (HTA). The uranium ions ($^{238}U^{73+}$) extracted from the SIS18 were stripped by a carbon foil (12 mg/cm^2), into the helium-like charge state ($^{238}U^{90+}$), and injected into the ESR at a kinetic energy of 192 MeV/u. After electron cooling, using the cooler as an electron target and exploiting the electron capture process, slow extraction of lithium-like ($^{238}U^{89+}$) ions towards Cave A could be performed. The beam could be delivered under good conditions, enabling precise spectroscopic measurements of the $2s_{1/2} - 2p_{3/2}$ transition in Li-like uranium, using the resonant coherent excitation process of relativistic ions in the *virtual photon field* of a thin silicon crystal. The lifetime of the stored beam was of the order of a few minutes.

From the 30$^{\text{th}}$ of May to the 7$^{\text{th}}$ of June, a uranium ion beam was offered for an atomic physics experiment at the internal target of the ESR. Li-like uranium ions ($^{238}U^{89+}$) were injected into the ESR at an energy of 76 MeV/u. After electron cooling, the ion beam was positioned such (by the *target bump*) that it had maximum spatial overlap with the gas jet. As a target, nitrogen (N_2) and xenon (Xe) gases were used. With the ion beam on target, the lifetime of the stored beam was about 1 minute. During the collisions between the Li-like ions and the target atoms, the ions can (non-)radiatively capture electrons into different states, or are excited, or lose an electron (ionization). Also two novel microcalorimeters have been successfully used to record the radiation emitted from the projectile-target interaction zone. The unique advantage of these microcalorimeters is that they can measure a broad X-ray energy spectrum with a high energy resolution. One microcalorimeter came from Heidelberg university, the other one from Giessen university. Finally, a VUV-spectrometer from Kassel university had been set up to look for specific radiation emitted from the target, during the collisions with the stored ions.

From the 13$^{\text{th}}$ to the 26$^{\text{th}}$ of June, a xenon ion beam was offered for an astrophysics experiment at the ESR. In a scattering process between projectile (Xe) and target (H_2), the projectile can capture a proton from hydrogen directly into the nucleus. The energy of the ions needs to be chosen low enough (Gamow window) to obtain stellar conditions. Special *in vacuo* particle detectors had previously been installed at the ESR to detect the charge-changed ions. The ($^{124}Xe^{54+}$) ions were injected into the ESR at an energy of 100 MeV/u. The experiments, using decelerated and electron-cooled ion beams and the internal target, could be performed at 30, 15, 8, 7, 6.7, 6, and 5.5 MeV/u. Under these conditions, the lifetime of the ion beams was of the order of only a few seconds. Especially the 5.5 MeV/u is very impressive, because it is the lowest energy thus far for an electron-cooled ion beam in the presence of a high-density target (density = 2×10^{14} cm^{-2}).

From the 4$^{\text{th}}$ to the 6$^{\text{th}}$ of July, a Li-like carbon ion beam was offered for laser spectroscopy and laser cooling of stored and bunched ion beams in the ESR. The $^{12}C^{3+}$ ion beam was injected and stored at an energy of 122 MeV/u. The lifetime of the ion beam was of the order of a few tens of seconds, which was long enough for the laser spectroscopy measurements, but rather short for the laser cooling experiments. Stable ESR conditions were offered during the entire test beamtime. The laser systems have been developed by the TU-Darmstadt and the HZDR/TU Dresden and had a very good performance. The XUV detector, used for fluorescence measurements during laser spectroscopy, was installed and operated successfully by the University of Münster. The high-voltage of the electron cooler was recorded by a precision high-voltage divider (TU Darmstadt) and a high-precision digital voltmeter, which were installed inside the Faraday cage of the electron cooler.

From the 7$^{\text{th}}$ to the 11$^{\text{th}}$ of July, a bare carbon ion beam was offered for tests with CRYRING@ESR [1]. The goal was to extract and transport the ions, at very low energies, through the very long beamline towards CRYRING@ESR. The $^{12}C^{6+}$ ions were first electron-cooled inside the ESR, then decelerated, again electron-cooled, and finally extracted from the ESR at two energies, 6 MeV/u and 18 MeV/u, in order to compare results. This endeavor was a great success, and the arrival of ions at the first fluorescent screen inside the ring could be demonstrated.

References

[1] F. Herfurth *et al.*, GSI scientific report 2016.

* m.steck@gsi.de

DOI:10.15120/GR-2017-1

Progress with the barrier bucket system for ESR *

D. Domont-Yankulova†[1], *J. Harzheim*[1], *K.Groß*[1], *H. Klingbeil*[1,2], *and M. Frey*[2]
[1]TU Darmstadt, Germany; [2]GSI, Darmstadt, Germany

Introduction

A new barrier bucket system is designed for the ESR storage ring at GSI. It will be used to precompress or to stack the beam longitudinally [1]. The core part of the system are the RF cavities where single-sine voltage pulses with defined amplitude $\hat{U}_{BB}$ and repetition frequency $1/T_{rev}$ have to be generated . These RF pulses are used as potential barriers. To compress the beam one of the pulses is shifted in time (see figure 1).

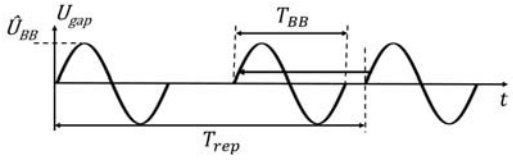

Figure 1: Shifting of the single sine pulses

To achieve pulses with the required high quality a model of the pulse generation system is essential. So in the last year we put efforts into the improvement of a PSpice cavity model and into the nonlinear behavior of the amplifier for high voltage amplitudes.

PSpice model of the cavity

In last year's scientific report [2], we presented a method how to systematically generate an equivalent circuit model for broadband cavities from ring core measurement data. The transfer function of these models showed good agreement with measurements, but the measured impedance still differed from simulation results. In order to improve the model, the coupling windings (see figure 2) were modeled more accurately by a two conductor transmission line and an ideal coupler. The transmission line parameters were estimated analytically from winding geometry and ring core properties.

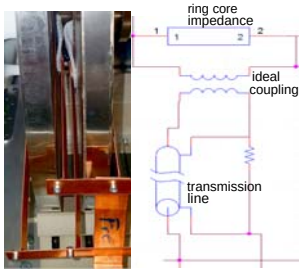

Figure 2: Cavity windings and PSpice model

The refined modeling decreased the difference between measurement and simulation of the impedance (see figure 3) and improved the accuracy of the simulated transfer function even further.

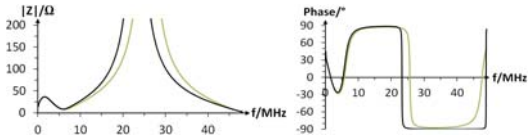

Figure 3: Impedance, comparison beetween measurement and simulation.

Operation in the nonlinear range

As pointed out in the last GSI annual report [3] it is possible to generate single sine gap signals of high quality in a wide voltage range (up to 550 V) by using linear methods. However at high amplitudes, nonlinear effects can be observed and have to be taken into account. Arguing from the setup structure, it is reasonable to assume a static nonlinearity located right after the amplifier entrance. In a first attempt, we determined the nonlinearity by measuring the peak of the gap voltage for sine input signals of different amplitude and smoothened the obtained characteristic by a 4th order polynomial. Figure 4 shows that taking the nonlinearity of the amplifier into account improves the quality of the output signal. Now, amplitudes of up to 760 V can be generated with the same setup and good signal quality.

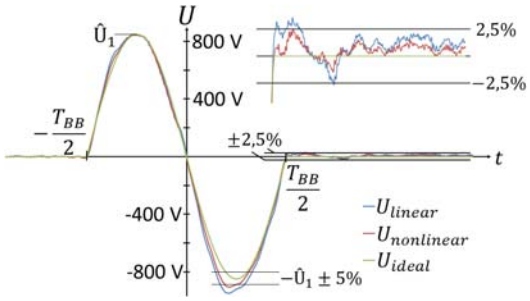

Figure 4: Linear and nonlinear predistortion for $\hat{U} = 820\,\mathrm{V}$

References

[1] M. Steck, et al., "Demonstration of Longitudinal Stacking in the ESR with Barrier Buckets and Stochastic Cooling", Proc. Workshop on Beam Cooling and Relates Topics (COOL'11), Alushta, Ukraine, 2011

[2] J. Harzheim, et al., "Modeling of broadband cavities in PSpice", GSI SCIENTIFIC REPORT 2015

[3] M. Frey, et al., "Status of the Barrier-Bucket system for the ESR", GSI SCIENTIFIC REPORT 2015

* Work supported by GSI
† D.Domont-Yankulova@gsi.de

DOI:10.15120/GR-2017-1

The status of the CRYRING@ESR project - First Turn*

F. Herfurth†[1], *M. Lestinsky*[1], *Z. Andelkovic*[1], *R. Bär*[1], *A. Bräuning-Demian*[1], *S. Litvinov*[1], *O. Dolinskii*[1], *W. Enders*[1], *M. Engström*[1], *S. Fedotova*[1], *B. Franzke*[1], *W. Geithner*[1], *O. Gorda*[1], *A. Källberg*[2], *N. Kotovskiy*[1], *A. Reiter*[1], *A. Simonsson*[2], *T. Sieber*[1], *J. Sjöholm*[2], *M. Steck*[1], *Th. Stöhlker*[1,3], *G. Vorobjev*[1], *and the CRYRING@ESR team*[1]

[1]GSI, Darmstadt, Germany; [2]MSL, Stockholm University, Stockholm, Sweden; [3]HIJ, Jena, Germany

The low energy storage ring LSR [1] will provide highly charged ions and antiprotons at low energy for two collaborations at FAIR, SPARC and FLAIR. Those collaborations intend to perform precision experiments pursuing atomic and nuclear physics questions [2] whose preparation is well on track [3]. The LSR is a Swedish in-kind contribution to the FAIR facility in Darmstadt.

The LSR is the low energy storage ring CRYRING modernized and adapted to the additional needs for injection and ejection of antiprotons and highly charged ions at about 10 MeV/nucleon. CRYRING has been operated at the Manne Siegbahn Laboratory in Stockholm until 2010, was dismantled in 2012 and transported to GSI in the first months of 2013. At GSI it is being installed behind the ESR, as proposed and described in detail in 2012 by a swedish-german working group [4].

CRYRING can decelerate, cool, and store heavy, highly charged ions and antiprotons injected at about 10 MeV/nucleon down to a few 100 keV/nucleon. It provides a high performance electron cooler and a straight section for flexible experiment installations as for instance a gas jet target. It is equipped with it's own injector and ion source, to allow for standalone commissioning.

The ring hardware and all infrastructure is in place and the local injector has been commissioned [5]. In summer the transfer of ions from the ESR to CRYRING@ESR has been succesfully commissioned online. For this, a bunch of C^{6+} ions, decelerated and cooled in the ESR to 6 MeV/nucleon (corresponding to a beam rigidity $B\rho \approx$ 0.7 Tm), was transported to the first diagnostic station in CRYRING@ESR - a fluorescent screen. The modified transport beam line from ESR to Cave B (where CRYRING@ESR has been set up) has been fully operational, including the newly built magnetic septum for fast injection. The successful transport of a beam with such low rigidity is promising when it comes to the robustness of this transfer line even at settings well below the design rigidity. The planned regular transport rigidity is about 1.4 Tm, slightly higher than the one originally designed for protons injected into the LSR. The injection kicker in CRYRING@ESR was upgraded to be able to handle this beam rigidity and tested in summer successfully offline at the vendors factory.

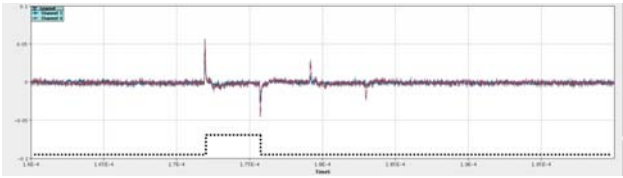

Figure 1: Raw signal as recorded from beam position monitors, i.e. capacitive pickups, that show twice the passage of the injected single bunch. Plotted is the signal amplitude in arbitrary units versus time. The injected ion bunch shape is sketched in the lower part of the plot.

A dedicated off-line commissioning beam time, using the local injector and H_2^+ ions, was used to achieve the first turn. The pressure in the ring was not lower than a few times 10^{-8} mbar because the system has not been baked yet and hence the NEG pumps were not activated. A short ion bunch of about 4 μs has been created with the beam chopper in the injector in order to have a bunch shorter than one turn at the injection energy of 300 keV/nucleon.

With a peak intensity of up to 2 μA the bunch was injected into the ring and after optimising the injection line elements, signals on the installed first turn diagnostics, two fluorescent screens and three faraday cups, have been observed.

The signal displayed in fig. 1 only shows the quickly changing components of the passing ion beam. To be more sensitive to the complete signal the capacitive coupling to the preamplifiers has been adapted. Results of the change will make it easier to detect also weak signals during the upcoming beam tests.

References

[1] H. Danared, et al. (2011) "LSR - Low-energy Storage Ring, Technical design report", MSL, Stockholm University, v 1.3.

[2] M. Lestinsky, et al. (2015), "CRYRING@ESR: Present Status and Future Research", Phys. Scr. T166, 014075 (2015).

[3] M. Lestinsky, et al. (2016), "Progress of experimental systems for CRYRING@ESR", GSI annual scientific report 2016.

[4] M. Lestinsky, et al. (2012) "CRYRING@ESR: A study group report", GSI, Darmstadt,

[5] W. Geithner, et al. (2017), "Status and outlook of the CRYRING@ESR project", 2017, Hyperfine Interact., 238, 13

* Work supported by GSI/HI Jena/FAIR@GSI PSP code:1.3.4.2./The SPARC collaboration/Uni Krakov/KVI Groningen

† F.Herfurth@gsi.de

Installation progress of the electron cooling system at CRYRING

J.Roßbach[1], *C.Dimopoulou*[1], *R.Heß*[1], *M.Bräscher*[1], *M.Kelnhofer*[1], *and J.Krieg*[1]
[1]GSI, Darmstadt, Germany

Activities regarding the CRYRING electron cooler concentrated on completing the media supplies (electrical power, cooling water, cryogenics). The demineralized water cooling system for the normal conducting magnets was equipped with a pressure reducer in order to match the specifications for the cooler magnets operation. Some repairs had to be done to several leaks which occurred during the commissioning of the cooling system. Water hoses had also to be replaced because they caused an electrical short-circuit to earth and disabled the commissioning of the magnet power supplies. The electron cooler uses in total three coldheads/cyropumps, they are driven by two helium cryocompressors. The latter need special cooling water (softened water, not demineralized) which has been provided by a separate cooling system.

The liquid helium transfer line was delivered and installed in May 2016, thus completing the helium supply system. The commissioning of the superconducting gun solenoid took place at the end of 2016. A first successful test with magnetic field strengths up to 3 T was carried out, as required for the cooler operation. (Fig. 1)

Figure 1: Magnetic field of 3 T and corresponding electric current (51 A) in the superconducting magnet during the test. The cold magnet kept its field in persistance mode i.e. after the current power supply was switched off.

Two cryopumps, on the gun and collector side, are essential to improve the vacuum pressure for the cooler operation. They had to be refurbished on site: service of the coldheads, exchange of the absorber inside the cryocompressor, purging of the whole helium system. A similar service was necessary for the coldhead of the solenoid cryostat: Its cooling power was not sufficient to keep the thermal shield within the cryostat cold. This lead to fast liquid helium loss (evaporation) out of the bath of the superconducting coil. After the service the coldhead performs appropriately.

The 3.5 kV high voltage power supply of the collector broke down; due to its age and poor current resolution (3 A) it was replaced by a new device allowing the measurement of the electron beam current reaching the collector with high resolution (16 bits, 0-200 mA). Several other high voltage power supplies were refurbished. To protect the cooler against unsecure operating conditions a hardware interlock system was designed and implemented. It protects the cooler against bad vacuum pressure, loss of cooling water in the collector, loss of the accelerating high voltage, loss of the magnetic field in the gun superconducting solenoid.

The pickups installed within the cooler main solenoid have been successfully tested with ion beam. Furthermore, due to space restrictions, making it difficult to attach and detach them, the RF cables connected to the pickup vacuum feedthroughs were substituted by bakeable ones. For future laser experiments, the scrapers used in Sweden were reinstalled at their ports within the toroid chambers at the gun and collector side.

Regarding the cooler vacuum system, its assembly was completed. Vacuum measurement gauges as well as a high-voltage feedthroughs had to be changed. The electron gun itself was equipped with a new cathode and was installed into the gun vacuum chamber. The cryopumps at gun and collector were mounted. First bake out of the vacuum system took place in April 2017.

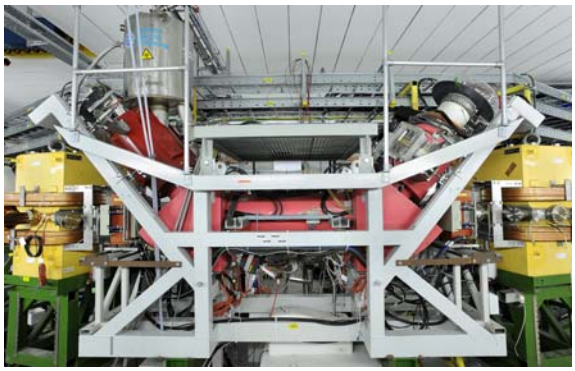

Figure 2: Recent view of the complete electron cooler in the CRYRING cave.

The application program for the remote control and operation of the electron cooler was further developed. All electron cooler magnet and high-voltage power supplies were created as a FESA model, tested and released.

Standalone commissioning of the electron cooler with its electron beam is scheduled for May 2017. Cooler operation with ion beam will follow later in 2017.

DOI:10.15120/GR-2017-1

Beam instrumentation of the RFQ injector at CRYRING

A. Reiter, F. Herfurth, T. Sieber, G. Vorobjev
GSI, Darmstadt, Germany
for the Dept. of Beam Instrumentation and the CRYRING collaboration

Introduction

This contribution reports on the beam instrumentation in the RFQ injector and the experiences gained throughout the linac commissioning in 2016. It completes an earlier report on this topic [1] and provides an update on modifications to beam line and instrumentation.

Ion Source Beam Line

The injector together with the positions of the beam instrumentation is shown in Fig. 1. Continuous beams of light, singly-charged ions of 10 keV/u, mainly H_2^+, have been extracted from a MINIS ion source and cut to pulses of several 100 μs by a chopper. To increase filament lifetime and current, the ion source will be modified for pulsed operation. An isolated iris or AC transformer (ACT) will be added to the current measurement system to monitor the source stability. The plasma around the filament is monitored by a special camera that looks upstream from the 0° port of the dipole chamber into the ion source.

Before and after the 90° spectrometer dipole, current and distribution of the primary beam can be measured with a Faraday cup (FC) or a scintillating screen (SCR) [2]. The combination of multi-channel plate and 25 mm phosphor P43 has turned out to be too sensitive. More robust and larger 50 mm Chromox screens with an anti-static wire mesh will be their replacement.

The beam line, apart from the dipole, is composed of electrostatic elements. Together with beam instrumentation devices they are supplied from a common high voltage (HV) system with FESA software and graphical user interface (GUI). All HV mainframes are network devices with TCP/IP control. An industrial PC hosts a base FESA class which provides access to all HV channels, e.g. to a quadrupole FESA class that converts a field gradient calculated by the ion optics model to HV set values of the four quadrupole electrodes.

At the RFQ entrance a segmented iris, consisting of four isolated plates, aids the optimisation of the beam injection into the linac. The plate currents are fed to a charge-to-frequency converter, and the output pulses are registered in a dedicated VME scaler. A GUI displays left-right and top-bottom asymmetry together with a list of scaler values.

Radio-Frequency Quadrupole Linac

The 108.5 MHz RFQ linac accelerates ions of q/A>0.36 to about 300 keV/u. Beam currents of 1.5 μA for H_2^+ have been routinely achieved with a transmission of 50%. With pulsed source operation the new target value is 10 μA. Behind the RFQ, a quadrupole doublet replaces the debuncher, which - due to its small diameter - caused significant losses and lead to spurious effects in the time-of-flight energy measurements. The bunch monitoring system analyses pairs of signals selected from three pickups or the RFQ tank. A FESA application controls signal gain and readout of a 5 GSa/s digital oscilloscope. The analysis is described in [3]. The GUI displays signals traces and trends of pickup voltages, energy and tank power. The energy of ∼295 keV/u is in good agreement with previous measurements and is reached at the expected power of P=12 kW following the empirical rule P= $3 \cdot (A/q)^2$ kW for this RFQ. The FESA application can be ported to the HITRAP decelerator and serve during linac commissioning, e.g. of the 1.4 MeV/u continuous-wave demonstrator cavity in 2017.

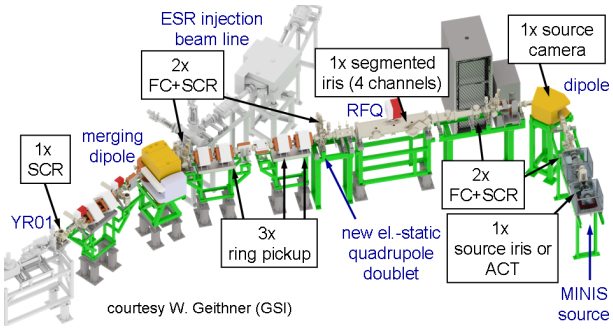

Figure 1: Overview of RFQ injector and diagnostics elements. The total length is ∼10 m. ESR beam line and first ring section YR01 are shown in gray colour.

At the RFQ exit and before the merging dipole the same FC/SCR detector combinations as in the ion source beam line are available. Both detectors are mounted in a compact chamber on a common stepper motor drive. Close to the injection septum, a bakeable Chromox screen on a pneumatic drive acts as injection monitor. The new PLC system has been recently completed with FESA class and GUI. All infrastructure systems (HV, stepper motors, and pneumatic drives) can be fully integrated into the control system.

References

[1] A. Reiter et al., GSI Scientific Report 2013

[2] B. Walasek-Höhne et al., TUPD062, IBIC 2014, Stanford, USA

[3] A. Reiter et al., MOPD35, DIPAC 2011, Hamburg, Germany

DOI:10.15120/GR-2017-1

A detection system for laser spectroscopy experiments at CRYRING *

A. Bußˆ†[1], Z. Andelkovic[3], V. Hannen[1], C. Huhmann[1], W. Nörtershäuser[2], D. Thomas[1], and Ch. Weinheimer[1]

[1]WWU Münster, Institut für Kernphysik, Wilhelm-Klemm-Str. 9, 48161 Münster;
[2]Technische Universität Darmstadt, Institut für Kernphysik, Schlossgartenstraße 9, 64289 Darmstadt;
[3]GSI Helmholtzzentrum für Schwerionenforschung GmbH, Planckstraße 1, 64291 Darmstadt

The low energy storage ring CRYRING is being set up as the first storage ring of the upcoming accelerator facility FAIR at GSI. In order to enable laser spectroscopy experiments with stored ions, a fluorescence detection system is currently being developed at the Institut für Kernphysik in Münster. It will be set up in section 7 of CRYRING. The detector is designed to measure in a broad wavelength regime between 250 nm to 900 nm.

Several ions of interest have transitions in this wavelength regime. For instance Mg^+ (at 280 nm) and Ba^+ (at 313 nm). The latter is a relevant candidate for studying laser induced dielectronic recombination (LIDR).

So far, simulations of the optical system have been performed in order to optimize the detection efficiency for laser-induced fluorescence photons, while - at the same time - reducing the detection probability for background photons.

Geant4 Monte Carlo simulations show [1], that a geometry with a focusing ellipse is a well performing design in order to enhance fluorescence detection, while suppressing detection of background photons uniformly generated in the detector's sensitive volume. The working principle of this geometry is shown in figure 1 in the projection on the ion beam axis. Next to it, the reflectivity of the ellipse's surface material MIRO3® is shown.

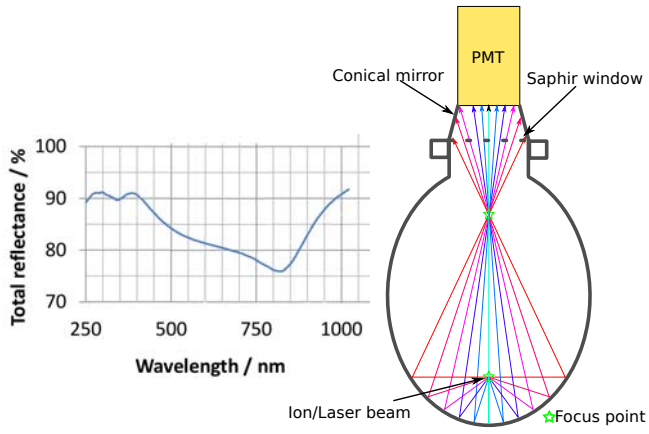

Figure 1: Left: reflectivity of MIRO3®, right: focusing ellipse principle

Both, the ion and the laser beam are passing through the lower focus point of the ellipse. The laser induced fluorescence photons are emitted nearly isotropically (as ions in CRYRING are only slightly relativistic). The geometry of the ellipse reflects photons that hit the elliptical surface through the upper focus point. Eventually, they can be measured by one of three PMTs on the top of the setup. Two sets of PMTs will be procured, one for the UV and one for the long wavelength range ($\lessapprox$ 900 nm). Depending on the wavelength of the observed transition, the PMTs can be interchanged easily, as they are located outside of the vacuum. For the infrared-sensitive PMTs, a cooling housing is needed in order to reduce background from thermal noise.

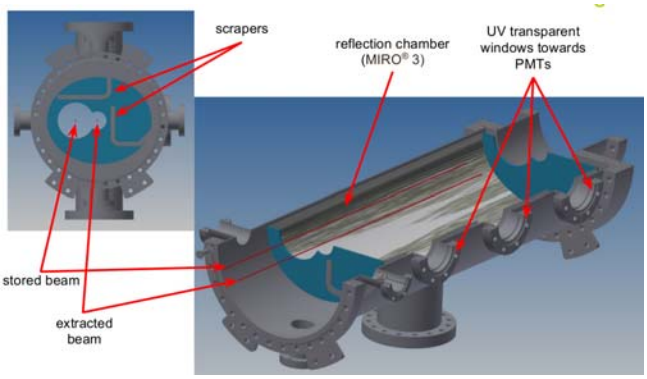

Figure 2: Cross section of the vacuum enclosure and mirror chamber of the detection system.

The estimated collection efficiency of the geometry amounts to 19.5% for beam photons and 2.3% for background photons at a wavelength of 350 nm. This number contains the wavelength-dependent reflectivity and transmission coefficients of the used materials. Not included in the number is the quantum efficiency of the PMTs.

The design of the detector is currently being finalized. First components have been procured.

References

[1] D. Thomas, bachelor thesis, Institut für Kernphysik Münster, 2016

* Supported by BMBF under contract number 05P15PMFAA
† axel.buss@uni-muenster.de

DOI:10.15120/GR-2017-1

Precision high voltage divider for the electron cooler at CRYRING *

D. Winzen†[1], *I. Denesjuk*[1], *V. Hannen*[1], *W. Nörtershäuser*[2], *H.-W. Ortjohann*[1], *O. Rest*[1], *and Ch. Weinheimer*[1]

[1]Institut für Kernphysik, Uni Münster; [2]Institut für Kernphysik, TU Darmstadt

The low energy storage ring CRYRING@ESR is currently being comissioned as the first storage ring for FAIR phase-0 at GSI. CRYRING features an electron cooler in order to cool stored ions and thus achieve a low momentum spread of the beam. To determine the velocity of the ions a precise knowledge of the acceleration voltage of the electron cooler is essential.

Therefore we construct a high-precision divider for voltages up to 35 kV which will be similar to the ultrahigh-precision voltage dividers which have been constructed in Münster in cooperation with PTB for use at the KATRIN experiment [1, 2]. The precision of the divider will be in the low ppm range and will allow for measurement uncertainties in the $< 10^{-5}$ region.

Scale factor	Voltage range
1 : 100.46	≤ 1206 V
1 : 162.71	≤ 1953 V
1 : 268.98	≤ 3228 V
1 : 775.45	≤ 9305 V
1 : 3451.50	≤ 35000 V

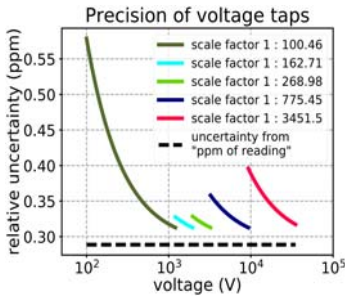

Figure 1: Left: Scale factors of voltage taps. Right: Precision of voltage taps for 8.5 digit DVM resolution (Keysight 3458a).

High-voltage dividers usually consist of many high voltage resistors R_i connected in series to allow for the requested maximum voltage. The available Vishay VHA518 -11 resistors [3] to be installed in the high-voltage divider have been characterized and tested for stability. The output voltage U_{out} is measured using a high-precision digital voltmeter over the low voltage resistance R_{LV}. A voltage divider is characterized by the scale factor M of its voltage tab (1):

$$M = \frac{U_{in}}{U_{out}} = \frac{\sum_i R_i + R_{LV}}{R_{LV}} \qquad (1)$$

The scale factor describes the factor between input and output voltage and has to be matched to the high-voltage range of interest and the most sensitive range of the applied digital voltmeter (< 20 V for commercially available precision 8.5 digit voltmeters). For measurement ranges from 0.1 kV up to 35 kV the high voltage divider will provide different scale factors by implementing different low voltage outputs (figure 1).

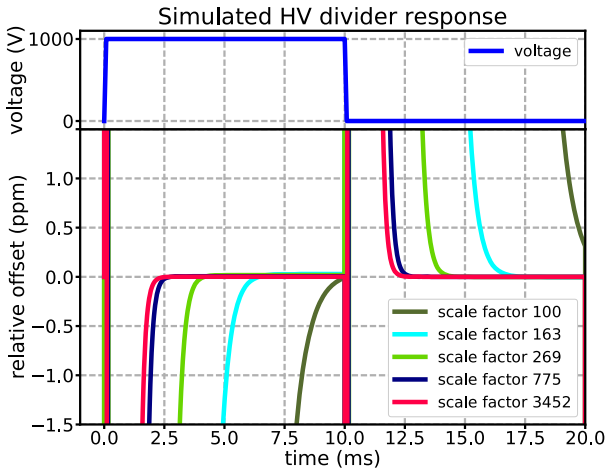

Figure 2: Top: Application of 1000 V detuning voltage with 12V/μs ramping speed. Bottom: High-voltage divider response relative to ideal value (3 ppm window).

Besides static electron cooler voltage measurements, a detuning of the electron cooler voltage for approx. 10 ms is necessary for electron-ion merged-beam experiments [4]. Therefore the high-voltage divider response times have been investigated using LTspiceXVII. In figure 2 the response of the different voltage tabs to a 1000 V offset as provided by a Kepco Bop 1000m are shown. For scale factors > 100 the voltage signal stabilizes in the 10 ms window allowing for DVM integration times of approx. 4-7 ms corresponding to 6.5 digit precision measurements.

The design of the divider has been finalized. Construction is currently ongoing and aimed to be finished in summer 2017. Subsequently calibration measurements will be conducted using a new absolute calibration method developed in Münster. This calibration will also be available for use at GSI to calibrate the divider on a regular basis.

References

[1] T. Thümmler *et al.*, New J. Phys. 11 (2009) 103007

[2] S. Bauer *et al.*, JINST 8 (2013) P10026

[3] Vishay, http://www.vishaypg.com/docs/63006/hmetlab.pdf

[4] Andelkovic Z *et. al.*. Technical Design Report: Experimental Instrumentation of CRYRING@ESR FAIR Facility for Antiproton and Ion Research

* Supported by BMBF under contract number 05P15PMFAA

† d.winzen@uni-muenster.de

DOI:10.15120/GR-2017-1

Overview of the status of the FAIR Project

Dr.- Ing. J. Henschel, Technical Director & FAIR Project Lead; Dr. P. Spiller, SPL SIS 100; Dr. H.Simon, SPL SFRS; Dr. K.Knie, SPL PLinac;Dr. I. Koop, SPL CR; Dr. D.Prasuhn, SPL HESR; Dr.H.Reich Sprenger, SPL Commons; Dr. A.Brauening Demian, APPA; Dr. H.Gerl, APPA; Dr. W.Mueller, CBM; Dr. L.Schmitt, PANDA
[1]GSI, Darmstadt, Germany;.

Summary

The construction of FAIR is one of the four strategic objectives of FAIR GmbH & GSI GmbH in Darmstadt as illustrated in figure 1.

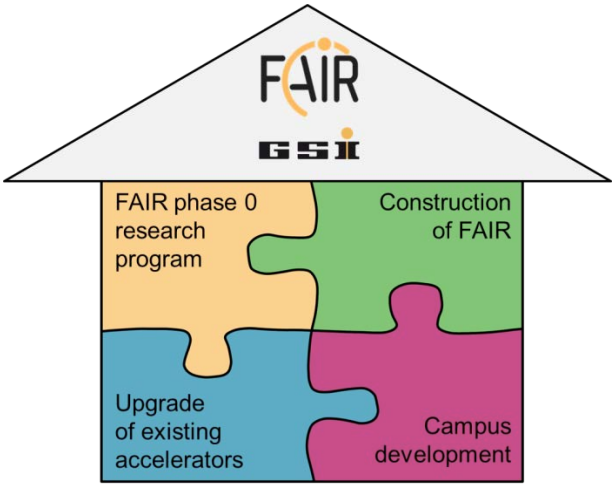

Figure 1: Strategic objectives of GSI & FAIR

For the progress in the FAIR Project the following core activities are worth to mention.
The rework of the complete Project planning after the major review in 2015 was finished on time in late 2016, resulting in the resource loaded and integrated project master time schedule. All three, now integrated areas, Accelerator, Civil construction and the Experiments are progressing according to the expectations documented in this plan.

Most remarkable is the progress in the area of civil construction so far. The target to start preparation work on site was reached already late in 2016. Currently all "connection" tasks from the GSI premises to the FAIR construction site are under execution ("GAF Gebäude Anbindung FAIR").
The enhancement of the SIS 18 (new coverage for increased radiation protection, a supporting wall, and the opening to the FAIR site), the main transformer stations north & south and the preparation of the remaining foundations are in execution. All preparatory and regulatory work for the area north (SIS100 Tunnel & CBM) is on target schedule. All work is aiming towards the start of the excavation of the tunnel 110 in summer 2017.

As remarkable as the progress of the civil construction, the continuity in the design and procurement of the accelerator components has to be highlighted. After the finalization of the new planning setup late 2016, the resources needed for the work packages were identified and committed. The balancing of the resources down to every single name was successfully executed until end of Q1 2017 in a first run. As a result a resource loaded and executable plan is now present, documented and the foundation of the work currently being executed.
The final step to a complete planning rework was done with the major rework on cost. All opportunities and potential threads were re-evaluated and documented. The FAIR Project Risk- and Opportunity report documents the results.
The progress in the experimental areas is as remarkable as the above mentioned ones. All four pillars are in intensive planning work and currently consolidating the procurement activities.
The focus for the remaining year 2017 can be summarized as follows. The major and most visible task will be the start of the excavation of the SIS100 tunnel.
The major contracts closed late 2016 / early 2017 with the In-kind Partners, namely BINP Institute Novosibirsk Russia, CEA and CNRS France and GSI Germany are in ramp up and execution as envisioned. Contract with Industrial partners are alike in status & progress.
The last "Mega-tender" with a value of not less than 30 M€ will be the main Cryogenic plant. Alongside with the planned increase of procurement activity this tender is planned for release during 2017. The award is targeted for late this year. With this tender, the last major component of the machine is in procurement.

Status of the FAIR Project

The Report of the FAIR project status is subdivided in the overview of the six SubProjects (SIS 100, SFRS, PLinac, CR, HESR, and Commons), FAIR Site & Buildings, and the four experimental areas, according to the organizational structure on site.

FAIR Accelerator Subprojects

The progress of the subprojects SIS100, Super Fragment Separator, Proton-Linac and p-bar Target, Collector Ring, High Energy Storage Ring and the cross functional sub-

DOI:10.15120/GR-2017-1

project Commons is documented in the following overview. The activities, progress and current status of civil construction works for the FAIR Project and the experimental areas are made transparent also.

SIS100

The subproject SIS100 owns the responsibility of two major tasks. The primary one is the design and build of the Synchrotron SIS100.
He secondary one is the enabling of the existing Synchrotron SIS18 as injector for FAIR and the connection between the GSI facility and the FAIR buildings.

SIS100
Major progress has been achieved in contracting of new components for SIS100 and developing FOS (First of Series) devices towards serial-production.
After the successful manufacturing and cold testing of the FOS superconducting dipole magnet, the serial production of 110 magnets has been released. The manufacturer, BNG, has just completed its move of the production line to a new dedicated building and released the production of the steel for the yokes and the superconducting coils. Starting in summer this year, one sc. dipole magnet will be delivered per week to GSI for cold testing. Therefore, the set-up of the team for series testing of the dipole magnets over the three years production time is currently in progress.
The manufacturing of the superconducting quadruple magnets in Dubna has progressed with the first two integrated units, consisting of two quadruple magnets, a steerer- and a sextupole magnet. In parallel, the preparation for cold testing of these units is progressing. The set-up of the dedicated NICA-FAIR superconducting magnet test facility could be completed end of November 2016.
The design of the quadrupole modules has been conducted together with industrial partners. The tendering of manufacturing and integration, which is one of the biggest technical efforts for the FAIR accelerators, was launched recently.
The status of design and manufacturing of the radiofrequency systems, used for acceleration and compression of the beam has progressed well. After successful completion and testing of the FOS bunch compression cavity, the series production of the remaining eight cavities has been launched. The design and manufacturing of the FOS acceleration cavity was finalized together with the industrial partner. The cavity undergoes presently an intensive FAT (Factory Acceptance Test) including ramping with targeted machine cycles.
The procurement of several other SIS100 components has been launched. The goal is to complete the procurement according to functional section. All major components of the injection system, the injections kicker modules and the injection septum magnets have been tendered and awarded. As next large system, the components of the extraction system shall be procured, starting with the electrostatic extraction septum in summer 2017.
The local cryogenics system is one of the most complex and unique technical systems of SIS100. Especially the bypass lines, bridging the warm sections of SIS100, differ from conventional cryogenic transfer line by the integrated superconducting bus bar system. A FOS bypass line has been manufactured and delivered. Although the FOS bypass line has been accepted, the internal design had to be further improved for serial production. The design of the overall local cryogenics system, including the end boxes, current feed boxes and all bypass lines segments is progressing very efficient.

SIS18
To finalize the SIS18upgrade program and to enable the execution of major civil construction measures, the machine operation has been interrupted in 2017. In order to prepare SIS18 for the fast cycling FAIR injector operation, in the early project phase of FAIR, an upgrade program has been defined, involving all major technical subsystems. Most of the upgrade program has been successfully implemented trough the last decade. The missing technical items will be completed in the course of 2017. This involves
a) The completion of the new dipole power converter for fast ramping with a ramp rate of 10 T/s, the installation of the missing two of three new MA (magnetic alloy) acceleration cavities.
b) Manufacturing and installation of the IPM (ionization beam profile monitor) system.
c) The manufacturing and installation of a new large bipolar dipole magnet for linking the existing facilities to the transfer line to SIS100.
To cope for the operation with significantly increased average beam intensities, beside the machine upgrade, the SIS18 tunnel construction is presently undergoing a major modification. The so called GAF (Gebäude-Anbindung an FAIR) civil construction project has been launched at the end of 2016 and shall be completed in January 2018. The project involves
a) an enhancement of the soil shielding on top of the SIS18 tunnel, requiring a support structure to cover the additional load.
b) A enhanced air management system.
c) A fire protection system based on Nitrogen flooding.
d) A reinforcement wall at the Northern arc of SIS18.
e) The opening and modification of the Eastern building wall in the experimental hall, generating the interface to the FAIR tunnel 101.
Another major ongoing activity which needs to be completed in 2017 is the retrofit of the accelerator control system. The new control system architecture, including the new timing system, replaces the old VMS based controls hardware and will be implemented and tested for the first time for the re-commissioning of SIS18. The successful completion of this effort is demanding and crucial for the machine operation in 2018. In parallel, upper level controls software, required for generating the set-values for all devices based on physics models and parameterized algorithms, will be completed. This software has

DOI:10.15120/GR-2017-1

been developed in collaboration with CERN, based on the LSA (LHC Software Architecture) over the last decade and is presently tested at commissioning of the CRYRING accelerator at GSI.

Super Fragment Separator

The last six months can be characterized as a period of major targets reached for the progress of the Super Fragment Separator (Super-FRS) development.
In the frame of assembling the ATB ("Along the beamline") List several missing components, in particular the insulating vacuum for cryogenics and cables, were identified. To each element a Work Package was assigned together with a work breakdown structure (PSP Code).
The review of the expected costs was done for all elements of the ATB Elements. In particular the now defined design for the superconducting (SC) dipole magnets, the improvement in the definition of the Local Cryogenics work Package, the robot handling in the Pre-Separator, and the full inclusion of the magnet test facility construction and operation.
The scheduling structure of the sub-project was adapted and embedded into the Integrated Master Schedule structure of the FAIR project. To this aim, three important achievements were reached:
Renewed scheduling for each work package. in addition to the all technical element listed in ATB, also project-related activities were identified and assigned to the new Work Packages. Examples given are: Digital-Mock-Up, Experiment Interface, and Civil Construction Interface. All technical components and project activities were scheduled in individual project-plans according to the work package structure.
The scheduling of the installation of Super-FRS components was established. Side constraints from civil construction as well as common systems were included. The planning yields three time windows for installation of the technical components. The installation scheduling was optimised according to the available of these time frames, which determine the critical path of the Super-FRS machine. The readiness of all three branches of the Super-FRS is given in the overview plan. Since each branch serves different experiments, they could be operated independent of the availability of the other two branches. The timeline for the stepwise implementation of the three branches will be subject of the forthcoming reports.
The overview plan, so called Level-2 plan, was reworked. The plan includes mirror images of the relevant milestones and activities from the Civil Construction plan, from the procurement plans, and from the central FAIR Commissioning plan.
For each activity the assignment of work necessary to carry out the activity was rechecked and defined. The assignment of work was attributed to individual human resources. The mitigation of appearing resource conflicts in the overall project was addressed with the "resource balancing" activity in Q1 2017.

The design phase for the two pre-series SC Multiplets was completed. In December 2016 the Final Design Review (FDR) was successfully concluded which includes in particular also a Quality Control Plan. The Production Readiness Review (PRR) for the Short Multiplet is scheduled for Q2 2017 and for the Long Multiplet in Q4 2017. The existing technical risks in particular the cooldown procedure with a major impact on the schedule will be vastly reduced there. Procurement of most important components like SC wire and yoke steel was initiated. Specimen of some subsystems were built (e.g. quarter yoke of quadrupole magnet, beam tube including cleaning process and μr measurements, coil impregnation, sextupole coil, steerer support structure).
All technical documentation required for the tender of the standard SC dipole magnets were finalized and approved (including detailed specification, Conceptual Design Report (CDR), 3D model and 2D definition drawings). In the meantime all necessary tender documents are established and it was agreed on the criteria for the awarding of the contract.
The beam instrumentation for the LEB has been agreed on with the respective NUSTAR experiments. The Conceptual Design Report (CDR) for the SC magnets of the low-energy Buncher/Spectrometer is in preparation by the magnet experts from VECC Kolkata, India.
The cryogenic system including the 3 satellite boxes and the connecting cryo transfer lines were delivered to the CERN magnet testing facility; the installation is going to be finalized and commissioning of the system is in preparation. The last missing parts to complete the cryogenic system are the magnet interfaces, i.e. the so called cryo jumper lines. The tender of those is currently ongoing.
The construction of the support frame for the radiation resistant dipole magnet was finalized. However, during testing the remote alignment capability it was realized that the required moments of torque are too high. This lead to the action, that the corresponding gears were revised, which is almost completed right now.
The FAT for the First of Series (FoS) x-slit system was completed successfully.
It was agreed that the media connection board required for remote handling in the Pre-Separator will be developed by GSI. The design phase of a prototype board is running.
The FAIR IKC for the time-of-flight (ToF) detectors including the contract documentation was established.
The FAIR IKC for the Delta-E detectors (MUSIC) including the contract documentation was established and it was sent to our collaboration partner.
The Detailed Specification of the Plastic detectors was finalized and approved.
The Detailed Specification for the SC dipole vacuum chamber is finalized and in the approval process.
The Detailed Specification for the Focal Plane Chamber (which will contain all Super-FRS beam instrumentation parts) is close to be finalized. It is planned to prepare and award the in-kind contract still in 2017.

DOI:10.15120/GR-2017-1

The preliminary design of the target chamber and its plug inserts are progressing. The FDR for the plug guidance system was accepted in December 2016 and a full scale mock-up is under preparation. The PDR for the target chamber itself is expected for summer 2017.
It was decided to modify the preliminary design of the shielded transport flask in such a way that all components which have to be transported from the target area of Super-FRS to the Hot Cell complex can be handled by one common flask. In particular this required increasing slightly the cross section of the flask and thus also the docking ports on the Hot Cell roof. A corresponding change request concerning civil construction was established and approved.

Proton-Linac & p-bar Target

As the responsibility for the p-bar Target and the Proton-Linac is allocated to the same Subproject leader, Mr. Klaus Knie, both contents are getting reported in one section.

Proton Linac

According to the baseline schedule the finalization of installation and commissioning of the pLinac was not expected to be earlier than 2025. This fact can endanger the schedule of HESR and PANDA commissioning. Therefore, the construction of the p-Linac building was re-evaluated and subsequently rescheduled to an earlier time. Now the p-Linac will be fully available in 2023 according to this measure.
The contract with our collaboration partner has been signed. The proton source build is close to completion. The first phase of commissioning has been started; an ion-current of 70 mA has been produced, which is close to the design value of 100 mA already. The construction of the low energy beam transport (LEBT) is in progress.
The first Klystrons provided by our collaboration partners passed the FAT successfully.The production of the first-of series-modulator in-house is in progress.
After the very successful power RF tests of the ladder RFQ prototype the design of the full size RFQ, is close to completion.
The layout of the CH and CCH cavities is nearly finished. The production of the internal quadrupole triplets for the CH cavities is delayed due to minor changes in the layout of the cavities.

p-bar Target

An ANSYS working group has been successfully established. Simulations for target, collimators and beam dump are in progress. An experiment at the HiRadMat facility at CERN is in preparation. It is planned to test the mechanical stability of different potential materials for the pbar target and to do a benchmarking of our simulations.
The work on the target station and the alignment system for the magnetic horn is progressing.

Collector Ring

The TDR for the CR is finally ready. 50% of specifications have been approved. The technical design of the full ring has been performed for 80%. The most critical issues: dipole production is still not started; technical design of the vacuum system requires proof-of-principle experiments.
Component status:
a) RF debuncher: readiness – 25%. The first of series RF debuncher is delivered to FAIR. SAT is ongoing.
b) Stochastic cooling: readiness - 22%. The Pick-up prototype of stochastic cooling system is under development.
C) All other CR components (magnets, power supply, diagnostic, vacuum...): readiness – started
Presently 35 BINP experts are working on the CR project. All BINP experts are busy partially from 5 % to 50 % working time for CR project. Totally it corresponds to 11.95 FTE.

High Energy Storage Ring "HESR"

The production of the HESR is in full swing. All deliveries are according to plan. Schedule, Content and Budget is on target. The HESR components are in intermediate storage close to the FAIR site and will be relocated to their final storage area in 2017.

Commons

The status report for the subproject Commons follows the major technical systems used in all other subprojects.
The Subproject Commons takes the responsibility for the major technical systems (listed .psp numbers according Work Breakdown Structure (WBS)):

.psp 2.3. (High Energy Beam Transport (HEBT))
.psp 2.14.1 (Electric Power (EP))
.psp 2.14.8 (Cryogenics (CY))
.psp 2.14.10 (Controls (CO))
.psp 2.14.12 (Transport and Installation (TI))
.psp 2.14.xx (smaller work packages, will not be reported in detail)
.psp 2.3 High Energy Beam Transport (HEBT)

Magnets:
After the first pre-series dipole magnet had successfully passed the SAT Ab in March 2016, the second pre-series dipole magnet was delivered by the end of September 2016. In the meanwhile the dipole magnet passed the SAT Ab and the series production of in total 51 dipole magnets started. At the beginning of March 2017 the first

DOI:10.15120/GR-2017-1

two series dipole magnets passed the FAT. These dipole magnets will be delivered to GSI/FAIR at the end of March. At the same time series dipole magnet number three and four will be ready for the FAT.

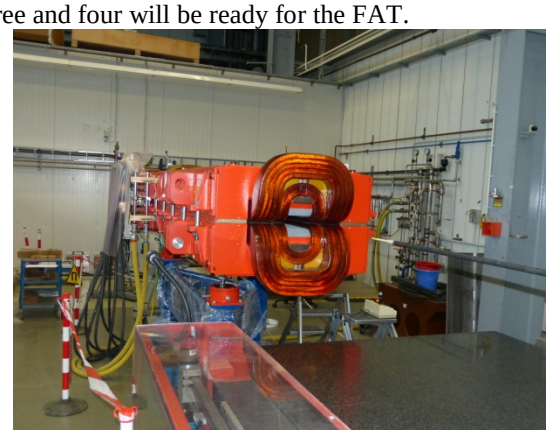

Figure 2: dip13_0 during magnetic measurement at GSI

The magnets of batch2 and 3 (22 dipole, 166 quadrupole, 92 steerer magnets) will be built by the Budker Institute of Nuclear Physics (BINP), Novosibirsk, Russia. While most of the magnet types are currently in the final design phase, stamping lamination and production of yokes of the standard 18Tm quadrupole magnets has already started.

Power Converters:
The power converters for HEBT quadrupole and steering magnets will be mainly built by the Indian company ECIL (Electronics Corporation of India Limited, 152 for quadrupole and 44 for steering magnets). In November 2016 two prototype quadrupole power converters were delivered.

Beam Instrumentation:
The day zero beam instrumentation of the HEBT lines foresees resonant transformers (RT), fast current transformers (FCT), and particle detector combinations (PDC) for intensity measurements and secondary electron emission grids (SEM-Grid) (see figure 3), multi-wire proportional chambers (MWPC) and scintillator screens (SCR) for the determination of the transverse beam profile.
Prototypes of all these instruments have been tested successfully during the GSI beamtime 2016. In addition, the beam loss monitor (BLM) has demonstrated its capability for future requirements.

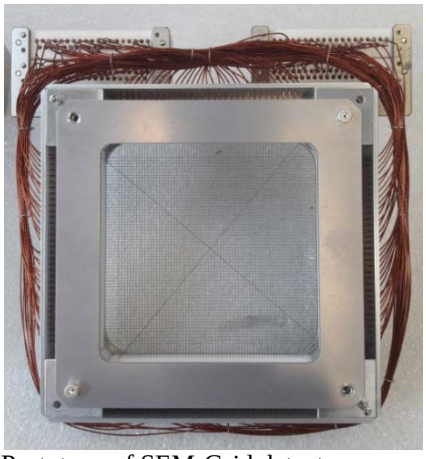

Figure 3: Prototype of SEM-Grid detector
After all prototypes passed the tests, the production of RT, FCT, PDC, SCR, and MWPC started. The purchasing of SEM-Grids and Beam Loss Monitors will follow soon.
Moreover, significant progress was achieved with regard to the auxiliary components related to beam instrumentation detectors.

Vacuum chambers:
The vacuum chambers for the dipole magnets of batch1 will be built. Based on the experiences made with three prototype vacuum chambers which were accepted as prototype only in June 2016, several remedial measures were taken for the series production.

Power Connection to FAIR:
The Technical Department CSEP has successfully supported FAIR Site & Buildings (FSB) in the procurement process and negotiations with energy providers. The construction of the new FAIR transformer fields north and south is on time-schedule (see figure 4). Necessary preparatory work by FAIR S&B was completed in time. Orders for 3 of 4 main items (buildings, transformers, high-voltage cables) have been placed.. The work on the transformer field north has started in February 2017 and will be finished by the end of the year. The work on the transformer field south has started in March 2017. No specific completion date in 2018 required.

Figure 4: FAIR transformer field north

DOI:10.15120/GR-2017-1

Power converters Cables and Machine cable management

PSP-structure and MSP-plans for all technical departments have been created. Cable costs for delivery, cable-laying and assembly were determined on the basis of information provided by the technical departments. Measures have been taken to update the existing data in completeness and quality.

A new work package "coordinating function for cable procurement and cable routing" was established to merge all accelerator related cable data. The aim of this task is to create a complete cable data base, appropriate to go into procurement processes for accelerator cables in synergy with FSB standards for cable planning and purchase.

Cryogenics (CY)

The Technical department Commons Cryogenics (CSCY) is responsible for the GSI and FAIR wide cryogenic helium cooling of superconducting magnets. CSCY is presently operating a prototype test facility (PTF) , a series test facility (STF), the Helium Supply Unit and two more Cryo plants for R3B GLAD magnet testing and for the cooling of the CRYRING electron cooler solenoid. The main customers at FAIR are the SIS100 and the Super-FRS with a total helium inventory of about 8 tons, and CSCY serves additionally small consumers like the final focusing system of APPA and the large scale experiments CBM/HADES and Panda. In addition the department is responsible for the so-called local cryogenics belonging to SIS100 and Super-FRS respectively. In the following different resent activities will be highlighted:

Helium Supply Unit (HeSu):

The HeSu is a liquefier with a decant station, a mobile Dewar parking station and a warm gas recovery system with campus wide helium return lines. The HeSu was taken into operation in 2015 and has delivered more than 7,000 l of LHe to users onside the campus so far. The main purpose is the cryogenic testing of FAIR prototypes. It has a liquefaction capacity of approximately 25 l/h for pure helium gas and 17 l/h in purification mode. A picture of the installation is shown in figure 5. Part of the HeSu project was in addition a universal cryostat for the testing of FAIR components, in particular SIS100 beam pipe vacuum chambers. The universal cryostat has a more than 4 m long cold testing area with an actively cooled table. Two views of the universal cryostat are shown in figure 6. Several different cooling schemas are realized:

(a) LN_2 shield cooling and LHe 4 K cooling with Dewars (using the HeSu)

(b) LHe cooling only, with a boil-off cooling of the shield using again Dewars

(c) connection to the universal connection box of the STF, see below. The planned and realized overall budget for the HeSu, including the universat cryostat and a campus wide recovery system was 1.75 M€.

Figure 5: Helium Supply Facility (HeSu)

Figure 6: Universal cryostat for FAIR components testing

Cryogenic Infrastructure for the Series Test Facility (STF):

The series test facility for SIS100 dipole serial magnet testing was taken into operation in 2015 and continuously running in 2016 for the testing of the first of series (FoS) dipole magnet, but additionally for the test of the SIS100

DOI:10.15120/GR-2017-1

main current leads, for the SIS100 local current leads, for SIS100 cryopumps and for the site acceptance test (SAT) of the first parts of the local cryogenics for SIS100 arrived at GSI in summer 2016. The STF has an overall cooling capacity of 1.5 kW @ 4 K equivalent is equipped with four test benches for magnet testing and one universal connection box. Up to now the plant has about 10,000 h of operation. A picture of the STF cryogenic infrastructure is shown in figure 7.

Figure 7: Serial Testing Facility (STF) in operation

Procurement of the FAIR Cryo Plant CRYO2:

For FAIR one central cryo plant will be installed serving the helium cooling capacity for SIS100, Super-FRS, CBM and HADES. In the first step a 19 kW @ 4 K equivalent cryo plant will be installed, including a campus wide 1.6 km long distribution system. Two industrial studies concerning the cryo plant layout were performed in 2014 and afterwards the specification was progress continuously adapted to future user requirements. According to the present civil construction time schedule the procurement phase is currently in preparation: The specification is under final approval, the budget is released and the official announcement will take place in the second quarter of 2017. Depending on the time for the negotiation with the suppliers, the contract is planned to be signed end of 2017. According to the present time schedule the plant installation will take place in the second half of 2021 and the commissioning will be performed until the end of 2022.

Control Systems (CO)

The activities of the accelerator Controls Department is fully focussed on the development and implementation of the accelerator control system for FAIR.

During the past 6 months significant progress has been made on all control system subprojects. The design of the standard equipment controllers (SCU) for FAIR power converters and many other systems, of which more than 1200 units will be needed, has been successfully completed and production and assembly of the first batch (100 units) has been finalized. Several components of the newly developed White Rabbit protocol-based high precision time and event distribution system, backbone of real-time control in the control system for the full facility, has been further developed and already installed in as a prototype test system for the CRYRING machine. Electronic timing receiver boards (FTRN) in several form factors (PCe, VME, PMC, uTCA), both GSI in-house developments as well as Slovenian in-kind contribution projects are under development. Schematics design and board layout has been checked and prototypes have been produced or are presently under production for test and evaluation. Significant progress has been made in development of the fundamental underlying control system software frameworks for accelerator equipment control (FESA), communication middleware, databases, physics modelling of the machines and beam lines (LSA) as well on user interfaces graphical control room applications. On the industrial controls side, vacuum control with the industrial control SCADA-based UNICOS framework has been developed, installed, commissioned and is presently under testing at. The vacuum bake-out of several sections of the CRYRING has been already successfully tested in the last 2 months, shortcomings and problems being identified and are being addressed in the ongoing development. In respect of cryogenic controls, several cryogenic sensors and actuators have been tested as a sound base for the cryogenic controls system design. Subsequently technical and functional specification documents for the control system of the upcoming tendering of the FAIR central cryo-plant have been worked out and are presently under formal approval.

In January 2017, the IT hardware base of the accelerator control system, both used for development and tests of the new system as well as for operation with the existing GSI accelerators, have successfully been relocated to the new FAIR computing center building, the Green IT Cube (see figure 8). While presently a full row of 14 racks are equipped, the setup is arranged and designed for future extensions to control the full scope of the FAIR accelerator facility.

DOI:10.15120/GR-2017-1

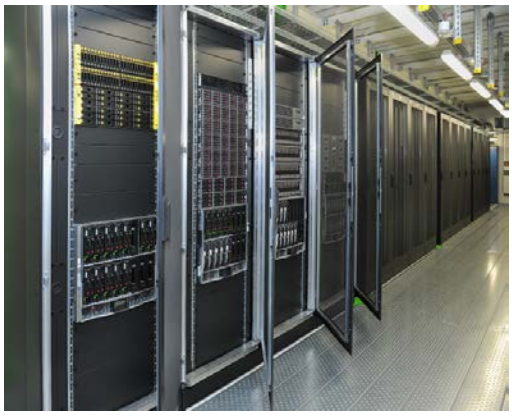

Figure 8: Relocation of accelerator controls hardware to the Green IT Cube

Following the agreed project strategy of the control system subproject, the full control system architecture was implemented at the new CRYRING machine, being used as test-bench for FAIR. During the last 6 months numerous tests have been performed in order to identify bugs and limits. Finally the control system was already used for commissioning the CRYRING local injector with beam and the injection into the CRYRING storage ring itself. Presently a new release of the control system stack is being prepared for beam operation in May. In parallel, the control system team is fully engaged in providing the FAIR control system already for the upcoming beam time of the existing GSI machines in 2018 and 2019. These two applications to existing machines will greatly reduce the time and risk during commissioning of the FAIR machines.

Transport and Installation

Numerous workshops on the topic of accelerator installation have been carried out since Q3/2016, resulting in the creation of dedicated additional work packages and corresponding detailed installation plans.

An overall concept for the intermediate storage of FAIR components is in progress. Measures have been taken to use existing Campus Facilities according increasing requests for adequate component testing and storage. The overall need for intermediate storage leads to leasing of external storehouse areas. Presently the storage of HESR components delivered by Forschungszentrum Jülich (FZJ) is ongoing (see figures 9 and 10).

Figure 9: Unloading of one HESR dipole magnet (weight: 35t) at the site of an external storehouse

Figure 10: Remote positioning of an HESR dipole magnet for intermediate storage.

Engineering /Mechanical Integration

For visualization of beam lines, buildings and technical building services and for facilitation of coordination tasks and test processes of web-based tool, the Kisters 3D viewer, was implemented. This tool allows work package leaders, subproject leaders and management to receive a general review about the content. Independently of CAD tools the configuration of the beam lines will be shown in connection to their position in the buildings. This view can be used on any web-connected unit like computers or mobiles independently of any licence structure. The content will be updated regularly once in a month by the person in charge of DMU group.

Figure 11 shows the screenshot of the Kisters 3D viewer with the detail of the HEBT beam lines and buildings.

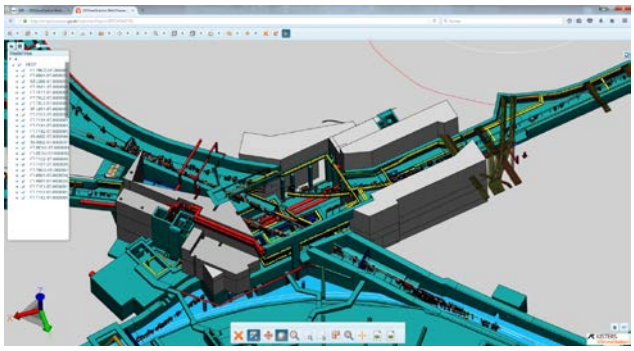

DOI:10.15120/GR-2017-1

Figure 11: Screenshot of that based Kisters 3-D viewer with HEBT

FAIR Site & Buildings

The approval for the tendering and subsequent award of civil works for the construction area North by the BMBF is given mid-September 2016. The reorganization of the S&B department is completed. The development of a staffing plan of S&B department is also completed.
The civil works execution plan for the FAIR project is divided into construction area North and construction area South. The contractual schedules with the civil design companies will be adapted accordingly to next steps. Detailed scheduling of civil work packages is currently progressing in cooperation with the civil designers.
An overall time schedule including defined periods for installation of machine components was developed as part of the integrated project master time schedule.
The tenders for groundwater lowering, trench sheeting and excavation in the construction area North are in the negotiation phase. The award of this contract is planned in Mai 2017. Subsequently it is planned to start site works in July 2017. The tender process for the SIS 100 shell construction works is progressing as per plan aiming at contract award in 4th quarter 2017.
The overall project civil construction permission is issued since 2014 for the entire facility. Some construction permissions for the buildings have to be revised as part of the design process (e.g. for the north and south electrical substations). The revised applications are scheduled in line with the civil construction schedule.

FAIR Experimental Areas

Major developments for the experimental areas of CBM, APPA, NUSTAR & PANDA are described in the following chapters.

APPA
Work on design and construction of the experiment components proceeds as planned. Special attention is devoted to the components which will already be used in the FAIR Phase-0 for experiments. Especially the installation and commissioning of the CRYRING at ESR is a main collaboration activity with strong support from on-site specialists. The realization of the ultra-high vacuum in the ring started according to the planning. The performance of the local injection is continuously improved. The electron cooler was reassembled, cooled down to Liquid-He temperature and demonstrated his superconductivity. In addition, the new FAIR control system is getting implemented and tested in the ring. The next test with beam is planned for May 2017, when also the first training for accelerator operating team with the new control system will take place. The time scheduling and the installation plans of the subprojects were improved in an additional effort by the collaborations.
Within the reporting period, APPA completed and submitted one TDR (Beam line matching section for Plasma physics experiments) to FAIR for the ECE evaluation. A second TDR, Gas-Jet Target for CRYRING, is presently in the stage of internal review and will be submitted soon to FAIR for evaluation.
Concerning the In-kind contracts listed in the previous section the Detailed Technical Specifications and time lines have been defined and are currently in the process of internal collaboration approval and FAIR management check.

CBM
CBM experiment: The CBM magnet has been contacted. The silicon tracker (STS), RICH, time-of-flight (TOF), and muon (MUCH) detector systems have approved TDRs, are in the engineering design phase, and full sized pre-series chambers are verified in test beam campaigns. The STS, as most complex detector project, will structure the production readiness reviews in three parts (sensor, electronics, integration) planned for 2017 and 2018. A cooperation with JINR, which builds 4 silicon tracker planes using the same technology as CBM to augment the BM@N tracking system, will help to widen the manufacturing competence. The photon detector of the RICH is in an advanced stage, 2/3 of the photo multipliers are tested. The RICH readout is a joint CBM, HADES, and PANDA development. This detector component has a modular design and will be used in the context of the HADES experiment at SIS-18 starting 2018. The production of the first batch of TOF chambers will start in April this year.
The PSD detector also has an approved TDR, is already in production phase. The STS, RICH, TOF, and PSD activities at BM@N/JINR, STAR/RHIC and HADES/SIS-18 constitute the CBM FAIR Phase-0 activities which will gain early operational experience for these detectors and generate valuable physics data.

NUSTAR
For all experimental set-ups of the NUSTAR pillar, the list of components and associated Work Breakdown Structure code (PSP Code) was refined and re-confirmed. An intense activity was devoted to the improvement of the time scheduling of the sub-project, which was matched to the Integrated Master Schedule of the FAIR project. For each experiment, the milestone defining the completeness of each component necessary for the installation of the experimental set-up was mirrored in an overview plan, the Level-2 plan. This allowed also the creation of a devoted Installation plan. The time range available for installation is established in the plan of the Civil Construction. Two time windows define the time range available for the assembly of components. The allocated time slot for the installation of NUSTAR experiments is in some cases too early with respect to the foreseen beam availability. The beam availability is scheduled in only one plan (Commissioning plan) for the whole FAIR pro-

DOI:10.15120/GR-2017-1

ject. For this reason, it is foreseen to re-schedule the experiment installation starting backwards from the Commissioning plan. This would be advantageous for some of the experimental groups which could profit from experimental activities at the upgraded GSI facility and other laboratories.
Work has continued on the detailed technical specifications for several In-Kind and Collaboration Contracts. The TDR for the common NUSTAR data acquisition system has been submitted and further TDRs are expected in the next six months. Work on NUSTAR detection systems, electronics, data acquisition and associated infrastructure is proceeding according to the internal planning. Focus is on readiness for FAIR Phase-0 experiments from 2018 onwards. The CDR for the LEB magnets has been updated and the present version is currently under evaluation by internal experts.

PANDA
Electromagnetic Calorimeter (EMC): The first-of-series of 16 modules of the Target Spectrometer Barrel EMC is under construction and is planned to be completed in summer 2017 after the delayed delivery of the PCBs needed for the mounting of readout chips.
The delivery of the high-purity PWO base material funded by Russia has started and will be completed by May 2017. The first two samples showed excellent quality and are stored for further processing. The crystal producer has produced crystals of a pilot series, which show very good quality.
The mass production should resume as soon as possible, to prevent delays. The Forward Endcap EMC is currently under construction in Bonn and Bochum and will be fully assembled until mid 2018. The module design of the Backward Endcap EMC has been revised and is complete now. A full readout chain successfully has been tested with beam.
Superconducting Solenoid Magnet: The PANDA solenoid magnet has been assigned to BINP Novosibirsk (RU) and a collaboration contract for the construction of the complete magnet was signed in March 2017. Work has started and the next step will be a plan review in summer 2017. In addition to the construction contract a service contract for the complete field mapping of the magnet on-site at BINP is being drafted.
Barrel DIRC: The TDR of the Barrel DIRC, was submitted in September 2016. In fall 2016, further test-beam measurements were done with a plate shaped design of the radiator. The detailed analysis of the result is presented in an addendum to the TDR being submitted in April 2017 along with the start of the review of the TDR by ECE.
Luminosity Detector: The Luminosity Detector TDR has received comments from an internal review in 2015, which were addressed in further R&D work during 2015/16. The resulting enhanced version of the TDR was reviewed anew and is now approved for submission to FAIR. A full-scale prototype of the core sensor component, will be tested in summer 2017.
Time-of-Flight (ToF) Detectors: The technical design of the Barrel ToF Detector is based on Silicon Photomultipliers and thin scintillator tiles. The Forward ToF consists of more conventional large area scintillator bars read out by photomultiplier tubes. The TDRs of these detectors were submitted to an internal review at the beginning of 2017. The TDR of the Barrel ToF Detector was approved for submission to FAIR in March 2017, the Forward ToF TDR is supposed to follow soon, at the latest by June 2017.
Infrastructure: Currently the detailed planning of the infrastructure of the PANDA experiment is being brought to the next level of detail in the context of the execution planning of the PANDA hall along with all technical services and the routing of cables and pipes. The experiment infrastructure comprises support structures, rails, gas distribution, electrical power distribution and cooling supplies. In addition, there are service networks and the controls infrastructure.

DOI:10.15120/GR-2017-1

Concept for content and structural quality assurance of CAD models for integration into the DMU models of accelerators developed

L. Heyl[1], *C. Will*[1],
[1]GSI, Darmstadt, Germany.

The sublimation of the CAD models, prepared by GSI and by the collaboration partners, to a high-quality overall model is only possible by consequent structuring. Therefore the qualitative properties of the individual models have to be considered before integration.

As a virtual image of the accelerator systems and their structural embedding, a synthesis of CAD models of buildings, technical building equipment and accelerator systems has been developed in the DMU group, which is part of Engineering Mechanical Integration (ENMI). These CAD models allow the visualization of the components, interfaces and the media supply. Furthermore, transports and assembly tasks can be planned based on the model.

The models have been created using CATIA as CAD program and are based on the ion optical layout and the information of the specialist groups. The product data management functionality of SAP has been used for managing models and drawings.

PDM is defined as "the management of the product and process model with the objective of generating unique and reproducible product configurations" [1]. It provides an increase in productivity due to reuse of models, a considerable time advantage by a fast information access, an improvement of co - operation within and outside the organization and a reduction of throughput times. [2]

Modern PDM functionality (such as implemented in the PLM-systems SAP-PLM, Enovia V6, Oracle Agile or PTC Windchile) ensure, that changes to models, which have already passed an approval cycle, are displayed with a changed revision level. In addition, the structure of models, the designation of parts and the reuse of components are managed.

The contents of the CAD accelerator models have been updated not only by the adaptation of models created by GSI, but also by the integration of CAD models of external collaboration partners. For these models, if not created by CATIA, the STEP format will be used as a system-independent exchange format for 3D CAD models.

To integrate these models into the CATIA SAP, the Enterprise Connector (EnCo) from CENIT is used at the GSI Helmholtz Center.

For integration, EnCo checks the clear identification of the models consisting of the model number and the revision status, as well as the designation. If this information matches with already existing data, the already integrated data are reused.

As changes in the content of the system, which have not been indicated by the change of the revision status, cannot be detected, this will lead to an alienation of the information.

At the latest during the integration of individual models into the overall system of the 3D model of the accelerator systems, erroneously structured data sets lead to a considerable time overload due to the necessary manual reworking. Not all external collaboration partners use a PDM system for managing CAD models and drawings. It is also possible, that the STEP-converters from different CAD-systems cause errors during converting process.

In the DMU group a method has been developed to scan the structural, the content and the orientation-relevant properties of the models. This method is used to check designation, structure, positioning, orientation, completeness and volume of the model components. With this information the Macro identifies the already in SAP stored components and exchange them in the new models.

In the second step, a program checks whether the drawing number of the components of the model matches the supplied drawings. Possible errors can be remedied using the results log. So the EnCo can store the new models and drawings in CATIA SAP correctly. A faulty data exchange can be avoided.

At the same time, the recording of the scan results and a traceable documentation of the made modifications are carried out. The structural agreement between the model and the drawing set is examined and data integration is facilitated.

Based on this concept, the model structures, that are specific to the supplier, can be tested and, if necessary, corrected.

References

[1] M. S. R. Eigner, Product Lifecycle Management – Leitfaden für Product Development und Life Cycle Management, Berlin, Heidelberg: Springer Verlag, 2009.

[2] "Solid System Team PDM Definition," Solid System Team / Worksline, 2017. [Online]. Available: http://www.solid-system-team.de/pdm/smap3d-pdm/pdm-definition.html. [Accessed 26 04 2017].

DOI:10.15120/GR-2017-1

Design studies for Cryogenic Current Comparators (CCC) at FAIR

F. Kurian[1#,2,3], M. Schwickert[1], T. Sieber[1], R. Stolz[4], T. Stöhlker[1,2]
[1]GSI, Darmstadt, Germany; [2]Helmholtz Institute, Jena, Germany; [3]Friedrich-Schiller University, Jena Germany,
[4]IPHT Jena, Germany

For beam intensity measurement in the FAIR accelerator facility, development work for an advanced Cryogenic Current Comparator (CCC-XD) system is ongoing in association with the collaborating partners at TU-Darmstadt, FSU- Jena, CERN-Geneva and IPHT-Jena [1]. There are four major components for the CCC-XD, a suitable cryostat and cryogenic environment, a superconducting beam current to readout current transformer with superconducting shield, a SQUID readout and data acquisition. While the design of a universal cryostat which fulfils the special boundary conditions given in the FAIR beam lines has been worked out, some of its components still undergoing optimization. The focus in this phase of the development lays on the readout using the shield and SQUID which will be described herein.

Optimization of the CCC Design for FAIR

There are obviously contradictory needs for the CCC implementation at FAIR: First of all, the beam installation restricts the size of the cryostat and thus the dimensions of the CCC. Secondly, since the CCC should cope with larger dimensions given by large beam tube diameters (160 mm) of FAIR beam lines which. But as already shown before [2], a larger diameter of the magnetic shield reduces the magnetic shielding factor of the CCC. At the same time, given by the requirement of a compact cryostat with separated insulation vacuum, a minimum possible outer diameter of the shielding has to be achieved. This also limits the sensitivity of the CCC which was approved by simulations.

To ensure minimum temperature fluctuations on the liquid helium surfaces, which were previously shown to cause large drifts in the CCC output signal [3], the thermal load had to be minimized even though a room temperature UHV beam tube needed to be introduced as a 'warm-hole' through the cryostat. The cross-sectional view in figure 1 shows the recent design of the cryostat. Besides a stable operation at FAIR, it also has to provide easy access to all internal parts to allow exchange of CCC components during future development work. Therefore, the isolation vacuum chamber consists of a stainless steel frame with Aluminum windows, which can easily be removed and thus the CCC mounted and serviced in the cryostat.

All these factors led to the development of new concepts for the CCC without magnetic core and with reduced dimensions of the superconducting magnetic shield described in the next section.

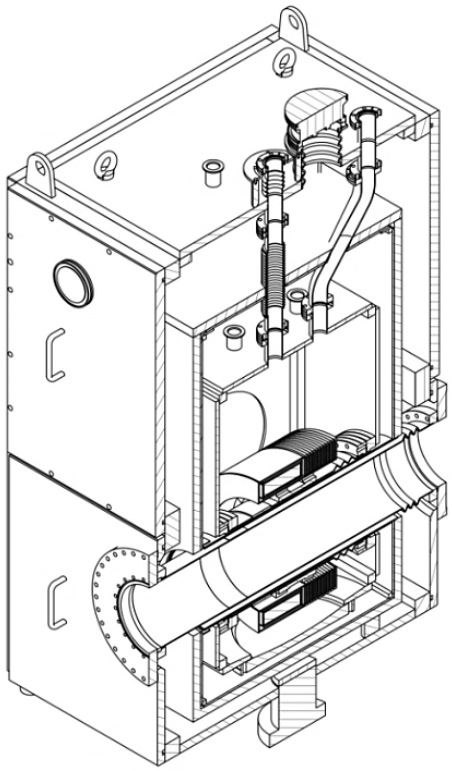

Figure 1: Cross-sectional view of the schematic design of the new CCC system for FAIR

Radially Stacked Magnetic Shield for CCC

For the operation of CCC system as a standard diagnostic instrument in FAIR beam lines, large baseline drifts (long term drifts as well as instantaneous drifts) due to temperature fluctuations has to be minimized. Hence, in order to characterize both types of drifts, detailed experiments on the magnetic shield are still in progress. Preliminary results show clear indications that the high permeability ring core (which acts as a flux concentrator and enhances the magnetic field coupled to the sensor unit) is the main source of the drifts.

In order to achieve better current resolution through enhanced field attenuation and removal of temperature fluctuations of the ring core, which is additionally a source of strong Barkhausen noise, a radially stacked design of magnetic shield is proposed. In this scheme, unlike the magnetic field pickup by the pickup coil, the magnetic shield itself acts as the single turn pickup coil. The superconducting screening current will in this case be inductively coupled to a next generation dc-SQUID with an inductance matched to the shielding. The magnetic shield is radially stacked and thus improves the attenuation factor and reduces dimension at the same time.

DOI:10.15120/GR-2017-1

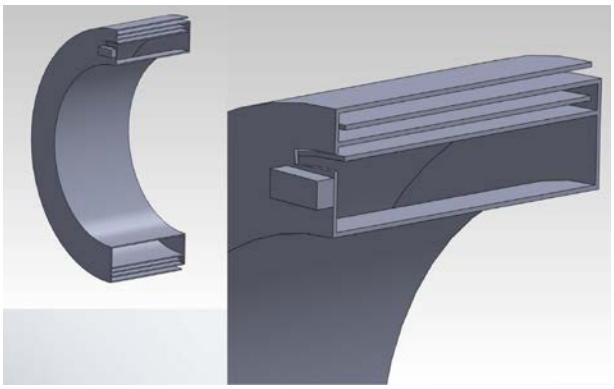

Figure 2: Radially stacked meander CCC.

This new implementation of the CCC is planned to be tested in the new cryostat, which will in installed in the Cryring@ESR storage ring. Depending on the performance compared to the classical solution, application in the FAIR facility is foreseen.

References

[1] T. Sieber, F. Kurian, M. Schwickert et. al, "Optimization studies for an advanced Cryogenic Current Comparator System for FAIR", Proceedings of IBIC 2016

[2] H. De Gersem, N. Marsic, F. Kurian, T. Sieber et al. "Finite-element simulation of the performance of a superconducting meander structure shielding for a cryogenic current comparator", Nucl. Instrum. Methods Phys. Res., Sect. A, 840:77 86, 2016

[3] F. Kurian, "Cryogenic Current Comparator for Precise Ion Beam Current Measurements", PhD thesis, Goethe University, Frankfurt am Main, March 2016

DOI:10.15120/GR-2017-1

Vacuum acceptance test of ferrites for UHV applications

P.M. Suherman, M.C. Bellachioma, J. Cavaco, C. Kolligs
GSI, Darmstadt, Germany.

Introduction

In the last several years, the activities of the vacuum lab, as part of the CSVS (Common System Vacuum System) Division at GSI, have been mainly focused on assisting the realisation of the FAIR project. These mostly involve the vacuum acceptance test for some components used for the FAIR project, such as outgassing rate measurements, leak tests, and residual gas analysis. In addition, the vacuum lab also conducts the fabrication of NEG coatings on vacuum chambers for HESR (High Energy Storage Rings) [1]. This report presents some results obtained from the vacuum acceptance tests of different types of ferrites.

Vacuum Properties of Various Ferrites

The vacuum properties of different types of commercial ferrites (Table 1) have been investigated, as part of a request from SCBC (Stochastic Cooling Beam Cooling) Division, GSI Darmstadt. One of the ferrites is foreseen to be used in the Palmer pick-up and kicker for the CR (Collector Ring).

Table 1: Different Types of Ferrites

No.	Types	Temperature treatment (in a vacuum oven)	Sample Condition
1	Type A1	300 °C, 3 h	Cleaned, as-fired, Not ground
2	Type B	300 °C, 3 h	Cleaned, as-fired, ground
3	Type C	-	As received, as-fired, ground
4	Type D	-	As received, as-fired, ground
5	Type A2	-	As received, as-fired, ground

Figure 1 shows the temperature dependent outgassing rates of the ferrites over the bake-out cycles. The bake-out temperatures in this experiment (80 °C and 150 °C) were chosen based on the demand from the SCBC Division. It was assumed that the temperature of the future setup will increase to such values ((80 °C and 150 °C) during operation.

The results showed that all of the unbaked (as-received) ferrites were not suitable for UHV (ultra-high vacuum) applications due to high outgassing rates (> $1x10^{-10}$ mbar.l/s.cm^2 at room temperature), especially for use at higher temperatures. Even with longer pump down times, the outgassing rates were still slightly higher than the required value. The extrapolated outgassing rate at room temperature after one week pump down time for Type A1 ferrite, for example, was about $1.6x10^{-10}$ mbar.l/s.cm^2.

After bake-out cycles, the outgassing rates of the ferrites were in a marginal acceptance value. The outgassing rates might be improved more significantly with higher bake-out temperature (e.g. 250 °C for 24-48 hours).

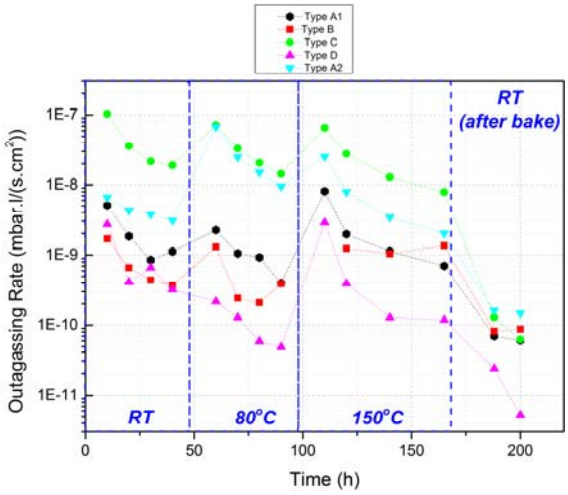

Figure 1: Time dependent outgassing rate of different ferrites over the bake-out temperature ranges.

The RGA (residual gas analysis) scans for all the ferrites at room temperature and after bake-out temperature did not show any concern of contamination or any unwanted chemical elements. Figure 2 shows the RGA scan of one of the ferrites at room temperature after 24 hours pump down.

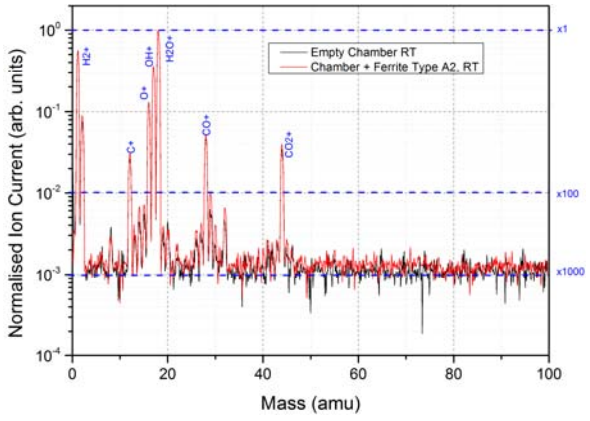

Figure 2: Normalised ion current of the RGA spectra of the empty chamber and the chamber loaded with Type A2 ferrite (as-received, no thermal treatment) after 24 hours pump down.

References

[1] M.C.Bellachioma et. al. GSI Scientific Report 2013.

DOI:10.15120/GR-2017-1

High precise 3D measurements with laser tracker through optical glass under cold-vacuum conditions

A. Junge[1], V. Velonas[1], K. Knappmeier[1], T. Miertsch[1], I. Pschorn[1], C. Schröder[2], F. Walter[3], B. Zielbauer[4],
GSI, Darmstadt, Germany.

Applying an already existing procedure to monitor a cold mass component for deformation and movements with regard to a cryostat covers not all the desired needs. The procedure relies on a combination of two instruments, a theodolite and a laser tracker. The observer performs optical measurements through different optical media which is air, an optical glass and vacuum. The optical glass is mounted on the integrated viewport on the cryostat and represents the window between air and vacuum. The results by using this procedure are very accurate (absolute position of the target is less than ±0.1 mm). The disadvantage is that the yielded results are only 2D and not 3D. This is because of the missing distance between the theodolite and the targets. To overcome this problem a direct replacement of the theodolites by the laser tracker is suggested in order to measure directly a distance contemporaneous with the angles on the targets/spherical mounted reflector (SMR) as shown in Figure 1.

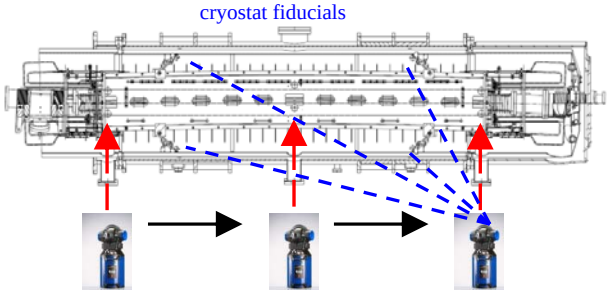

Figure 1: The suggested concept where the theodolite is replaced by the laser tracker

First tests showed that measurements through uncoated optical glass are disturbed by reflection. The laser beam is reflected diffusely on the glass. The superposition of the different laser beams cannot be interpreted by the laser tracker. Therefore a coating of the glass, adapted to the wavelength of the laser tracker, is imperative. The used (coated) optical glass has an actual thickness of 15.10 mm. Its coplanarity is better than 0.01 mm. The surface flatness of both window sides was specified as 1.5 lambda PV (peak to valley) or better.

Before verifying measurements inside a vacuum chamber this coated glass was used for measurements at common conditions on air. The beam transmits the media air, glass and air again. The repeatability of focusing a target behind the glass was about ±0.005 mm in 3D. A comparison of observations accomplished through glass and without it showed range and angle errors. With the aim of error compensation the physical effects which act on the beam were analysed.

Measuring through a glass blank, laser tracker observations are disturbed by several physical effects. Therefore a new complex mathematical model was developed for the calculation of a 3D position behind a coplanar glass by its pseudo observations. As a difference to conventional laser tracker measurements, there is the need to measure the front plane of the glass to define its normal, which is needed for the computation of the angle of incidence. Further the plane gives the distance from laser tracker source to the glass front. Furthermore the value of the glass thickness needs to be known and must be given with an accuracy of ±0.01 mm. By applying this mathematical model the absolute 3D point accuracy is about ±0.015 mm.

Afterwards measurements inside a vacuum chamber were accomplished. Now the laser beam transmits the media air, glass and vacuum (Figure 2). The repeatability of focusing the targets inside the vacuum was ±0.005 mm. Using the mathematical model the absolute 3D point accuracy for measurements inside the vacuum chamber is identical with the measurements through air-glass-air about ±0.015 mm.

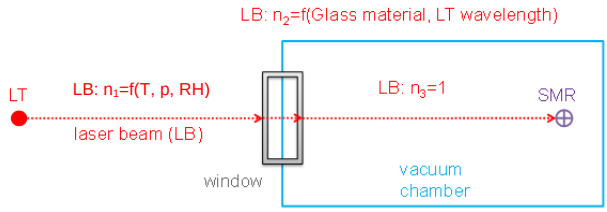

Figure 2: Splitting the distance in separate parts regarding the refractive index of the different optical media

Under cold vacuum conditions (90 K) additional test were performed. Through a second port the observation of the laser tracker was contemporaneous checked by a further independent instrument (theodolite). The investigations showed that the mathematical model works correct under cold-vacuum conditions. 3D point accuracy of 0.01-0.03 mm can be achieved by a laser tracker system.

Absolute 3D Measurements through an optical glass with laser trackers are possible as long as the suitable glass material and coating has been chosen. The mathematical model must be used as a post processing method to eliminate or reduce different errors that yields to absolute coordinates of points measured behind the glass. [1]

References

[1] V. Velonas et al, „Measuring through glass window with laser tracker under cold-vacuum conditions: Investigations and results“, IWAA 2016

[1] alignment@gsi.de
[2] c.schroeder@gsi.de; [3] f.walter@gsi.de; [4] b.zielbauer@gsi.de

DOI:10.15120/GR-2017-1

Development of new projectiles for future FAIR experiments

A. Adonin and R. Hollinger
GSI, Darmstadt, Germany

The upcoming FAIR facility will provide wide opportunities for investigations and research in different branches of science including antiproton physics, bio and material research, nuclear astrophysics and many others. Some of the FAIR experiments require improved quality and intensity of ion beams for certain ion species as well as the new projectiles as primary ion beams. To fulfil these requirements the tests on Terminal Nord with high current VARIS ion source have been performed in 2016.

Seven elements were tested in various operation modes and under different conditions. For three elements (O_2, Mg and Mo) the goal was to improve the performance and another four elements (Al, V, Zr and Ru) have never been performed from high current ion sources before. The main results of the tests are summarized in Table 1. For middle-heavy elements (V, Zr, Mo and Ru) the performance has been tested for various ion charge states optimizing for highest particle current and stability of operation.

Table 1: Ion beam currents achieved with VARIS ion source in front of the RFQ for various charge states and operation modes, using different auxiliary gases.

Element	Provided ions	Duty cycle	Beam current	Auxiliary material
O_2	$^{32}O_2^+$	2 Hz	3.5 mA	V-cathode
Mg	$^{24}Mg^+$	2 Hz	3.5 mA	He-gas
Al	$^{27}Al^+$	2 Hz	2 mA	O_2-gas
V	$^{51}V^+$	2.7 Hz	2.3 mA	O_2-gas
	$^{51}V^{2+}$	2.7 Hz	4.5 mA	–
Zr	$^{90}Zr^{2+}$	1 Hz	8 mA	N_2-gas
	$^{90}Zr^{3+}$	2 Hz	6 mA	He-gas
Mo	$^{98}Mo^{3+}$	2 Hz	5 mA	He-gas
Ru	$^{102}Ru^{2+}$	2 Hz	9 mA	He-gas
	$^{102}Ru^{3+}$	2 Hz	5 mA	–

Plasma generation processes in vacuum arc ion source define a certain distribution of ion charge states in plasma and in extracted beam, respectively. This distribution depends mainly on plasma density and could be changed by tuning the ion source parameters or by changing the operation duty cycle. Normally the ion source is optimized for maximum production efficiency and the distribution maximum is situated on the desired ion charge state. However during the ion source optimization for highest beam current in front of the RFQ the maximum of this distribution could be shifted to higher charge states reducing the production efficiency. The situation could be improved by adding to the plasma a small amount of proper auxiliary gas. Due to varied energy- and charge-exchange schemes in ion source plasma the maximum of the distribution could be returned to the desired ion charge state further increasing the beam intensity (Fig.1). Moreover admixture of the auxiliary gas in most of the cases leads to a more stable vacuum arc and results in noise reduction of the beam pulse and improved pulse-to-pulse repetition. On Figure 1 the influence of auxiliary gas on charge state distribution as well as on the production efficiency for Zr^{2+} and Ru^{2+} ions is demonstrated.

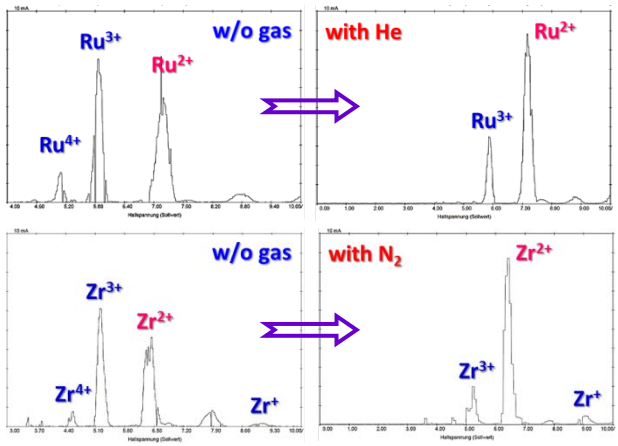

Figure 1: Optimization of the spectrum and production efficiency for desired ion charge state by using auxiliary gas on example of Ru (*upper*) and Zr (*lower*).

Summing up, the production of O_2^+ ions was the most efficient using V-cathodes. It showed very good performance also with 2 Hz repetition rate. Magnesium has shown very good pulse-to-pulse stability. The production efficiency was optimal using helium as auxiliary gas. Aluminium showed average performance with noisy beam pulses and pulse-to-pulse instabilities even with auxiliary gases. Situation became worse by increasing the duty cycle. In contrast to Al vanadium showed extremely good performance also with 2.7 Hz (maximum requested for FAIR experiments) operation. Oxygen is a proper gas for production of V^+ ions. Also one could tune the ion source for production of V^{2+} ions. In this case no gas is necessary. Operation is very stable with the same particle current as for V^+. The highest particle current for zirconium has been achieved with Zr^{2+} ion beam. However the stable operation was possible only with 1 Hz. Switching to charge state of 3+ notably improved pulse-to-pulse stability and allowed higher repetition rates but at the cost of particle current. The similar situation was with ruthenium. Molybdenum has shown much better stability and higher particle current with 3+ charge state compare to 2+.

As the conclusion, four new projectiles from high current ion sources have been developed for FAIR experiments. Operation with three elements has been notably improved. As next steps further performance optimization for considered elements for 2.7 Hz operation as well as tests with Si and Nd are planned.

DOI:10.15120/GR-2017-1

DOI:10.15120/GR-2017-1

SIS18 upgrade and SIS100 status report

P. Spiller, U. Blell, L. Bozyk, T. Eisel, E. Fischer, P. Hülsmann, H. Kollmus, P. Kowina, H. Klingbeil, H.G. König, J.P. Meier, A. Mierau, C. Mühle, C. Omet, D. Ondreka, I. Petzenhauser, I. Pongrac, V. Plyusnin, N. Pyka, P. Rottländer, C. Roux, A. Schuhmann, J. Stadlmann, K. Sugita, P. Streicher, S. Wilfert

GSI, Darmstadt, Germany

SIS18 Upgrade

In order to prepare SIS18 for the operation as fast cycling FAIR injector, a technical upgrade has been conducted and almost completed. This upgrade program has been defined in the early project phase of FAIR [1]. It follows a recipe to control the dynamic residual gas pressure during beam operation and involves almost all major technical subsystems [2]. Most of the upgrade program has been successfully implemented through the last decade. The still missing technical items will be completed in the course of 2017. This involves a) the completion of the new dipole power converter for fast ramping with a ramp rate of 10 T/s, the commissioning of the last two of three new MA (magnetic alloy) acceleration cavities, b) the manufacturing and installation of the IPM (Ionization beam Profile Monitor) system and c) the manufacturing and installation of a new large bipolar dipole magnet for linking the existing facilities to the transfer line to SIS100. Since SIS18 will also be the driver for a major experimental program in the FAIR phase 0, further technical improvements, machine developments and maintenance measures are continuously conducted from institutional funds. E.g. a new cavity is under preparation for smoothing the micro spill structure of slowly extracted ions [fig.1] [3].

Figure 1: A UNILAC single resonator cavity is under modification for smoothing the micro spill structure.

The planned machine developments will provide further insight into critical phaenomena showing up at high current operation or low charge state, heavy ion operation and will enable the development of methods to counteract fundamental issues, e.g. the uncontrolled generation of a microstructure at slow extraction. A major ongoing activity which needs to be completed in 2017 is the retrofit of the accelerator control system. The new control system architecture, including the new timing system, replaces the old VMS based controls hardware and will be implemented and tested for the first time for the recommissioning of SIS18. The successful completion of this effort is demanding and crucial for the machine operation in 2018. In parallel, upper level controls software, required for generating the set-values for all devices based on physics models and parameterized algorithms, will be completed. This software has been developed in collaboration with CERN, based on the LSA (LHC Software Architecture) over the last decade and is presently tested at commissioning of the new Cryring accelerator at GSI.

LINK EXISTING FACILITY – CIVIL CONSTRUCTION

In order to finalize the SIS18upgrade program and to enable the execution of major civil construction measures, the machine operation has been interrupted in 2017.

Figure 2: The soil shielding on top of the SIS18 tunnel is presently enhanced. This requires a table like construction, carrying the additional weight on top of the existing tunnel.

To cope for the operation with significantly increased average beam intensities, beside the machine upgrade, the SIS18 tunnel construction is presently receiving a major modification. The so called GAF (Gebäude-Anbindung-an-FAIR) civil construction project has been launched at the end of 2016 and shall be completed in January 2018. The project involves a) an enhancement of the soil shield-

DOI:10.15120/GR-2017-1

ing on top of the SIS18 tunnel, requiring a support structure to cover the additional load, b) a radioactive air management system, c) a fire protection system based on Nitrogen flooding, d) a reinforcement wall at the Northern arc of SIS18 and e) opening and modification of the Eastern building wall in the experimental hall, generating the interface to the FAIR tunnel 101. The underground pillars acting as foundation of the table are presently constructed (figure 2).

SIS100 STATUS

Major progress has been achieved in contracting of new components for SIS100 and developing FOS (First of Series) devices towards readiness for series-production.

After the successful manufacturing and cold testing of the FOS superconducting dipole magnet, the series production of 110 magnets has been released. The manufacturer, BNG, has just completed its move of the production line to a new dedicated building and released the series production of the steel for the yokes and the superconducting coils. Starting from August 2017, one sc. dipole magnet will be delivered per week to GSI for cold testing. Therefore, the set-up of the team for series testing of the dipole magnets over the three years production time is presently a major issue. The manufacturing of the superconducting quadruple magnets in Dubna has progressed towards two integrated units, consisting of two quadruple magnets, a steerer- and a sextupole magnet. In parallel, the preparation for cold testing of these units is progressing. The set-up of the dedicated NICA-FAIR superconducting magnet test facility could be completed end of November 2016. The commissioning of the test facility has been celebrated as an official ceremonial act. In terms of contracts, all deliverable of JINR for FAIR are covered up to the completion of the FOS devices. The production chain of superconducting units at JINR and the manufacturing and integration of the quadrupole modules is the critical path in the SIS100 schedule. Therefore, a major focus over the last year has been set onto the completion of the design of the cryogenic quadrupole modules and the preparation of the tendering for module production and integration. The design of the quadruple modules has been conducted together with industrial partners. The tendering of manufacturing and integration, which is one of the biggest technical efforts for the FAIR accelerators, could be launched recently. In parallel, possibilities for cryogenics testing of the integrated modules have been evaluated. The status of design and manufacturing of the radiofrequency systems, used for acceleration and compression of the beam has been progressed well. After successful completion and testing of the FOS bunch compression cavity by the company AURION, the series production of the remaining eight cavities has been launched. The company RI (Research Instruments) could complete the design and manufacturing of the FOS acceleration cavity. The cavity receives presently an intensive FAT (Factory Acceptance Test) including ramping with typical machine cycles [figure 3].

Figure 3: First of Series (FOS) SIS100 acceleration cavity at factory acceptance test at Research Instruments (RI).

The procurement of several other SIS100 components has been launched. The goal is to complete the procurement according to functional sections. All major components of the injection system, the injections kicker modules and the injection septum magnets have been tendered and awarded. As next large system, the components of the extraction system shall be procured, starting with the electrostatic extraction septum in summer 2017. The local cryogenics system is one of the most complex and unique technical systems of SIS100. Especially the bypass lines, bridging the warm sections of SIS100, differ from conventional cryogenic transfer line by the integrated superconducting bus bar system. A FOS bypass line has been manufactured and delivered by the Wroclaw University of Technology as Polish inkind contribution. Although the FOS bypass line has been accepted, the internal design had to be further improved for series production. The tendering process for the series production of the bypass lines has launched by WUST (Wroclaw University of Science and Technology). The design of the overall local cryogenics system, including the end boxes, current feed boxes and all bypass lines segments by WUST is progress very efficient. In order to finalize the (inkind) contracting of components of the local cryogenics system, it was necessary to complete and approve the specification for the feed boxes and feed-in lines. The local cryogenics system components are critical items in the overall SIS100 project schedule.

References

[1] P. Spiller et. al, Proc. of EPAC2004,1180(2004)
[2] P. Spiller et. al, Proc. of IPAC2014
[3] P. Hülsmann, Internal note Nr. 20.02.2017.RRF

DOI:10.15120/GR-2017-1

Status of the superconducting magnets for FAIR*

E. Fischer†, M. Becker, V. Bezkorovaynyy, A. Bleile, H. Bouillot, J. Ceballos, E. J. Cho, V. Datskov, N. Fischer, W. Freisleben, R. Jäger, F. Kaether, P. Kosek, V. Marusov, F. Marzouki, S. Mohite, J. P. Meier, A. Mierau, H. Müller, C. Roux, P. Schnizer, F. Seifert, K. Sugita, P. Szwangruber, and H. Weiss
GSI, Darmstadt, Germany

Introduction

Within this report the various and manifold activities and achievements of the superconducting magnets division (SCM) at GSI are summarized. In the context of superconducting magnet modules intended mainly for the SIS100 and Super-FRS, the spectrum of assignments of SCM ranges from the development of particular modules, their procurement, and follow-up of their production to the testing of the devices including the development of sophisticated methods and the set-up of test facilities.

Superconducting Magnets

Rapidly cycling magnets for SIS100

SIS100 Dipoles – status of the series production: In the course of an intensive series of tests of the First of Series (FoS) SIS100 main dipole delivered in 2014 showed excellent results with respect to e.g. quench behaviour, electric properties, powering, and ac losses. The nominal field was reached without any issues. However, the geometrical properties of the yoke aperture were found to be beyond the specified values caused by an inappropriate production technique chosen by the contractor. It was based on a standard welding technique of the yoke followed by the milling of the aperture. As a result the magnetic-field homogeneity showed characteristics which are insufficient for beam operation and the series production could not be released.
After a broad survey for alternative production techniques in cooperation between GSI and the contractor a second yoke was produced with lamination cut to the final cross section geometry, and with a novel laser welding technique (among other changes). Tests of the magnet with the new yoke were finalized in Q1/2016 with positive results. The aperture geometry was well improved with respect to the specified values. Consequently, the magnetic field provides properties suitable for beam operation proven by a sophisticated measurement system developed at GSI [1].
In parallel, about 140 issues between the FoS and the series dipoles concerning design, fabrication, and quality assurance issues were identified in a basic optimization process. With such alteration and the changes of the production technique the supplier's manufacturing concept of the series dipoles was successfully reviewed (FDR) and the series production was released in 07/2016.
In Q3 and Q4 of 2016 the manufacturer started to acquire the required material and tools, and first components of the series dipoles were manufactured. The delivery of the first series dipole is expected to be in 08/2017.

Quadrupole unit production: The Quadrupole units for the SIS100 will be built by Joint Institute for Nuclear Research (JINR) in Dubna as FAIR In-kind-contribution from Russia. The production of two pre-series quadrupole units has started at the beginning of 2016. The first one is the so-called VQD unit built from a defocusing quadrupole magnet (QD) with a vertically focusing sextupole (V) in a common unit assembly. The second one, the SF2B unit, is built from a focusing quadrupole magnet (F2) with a steering magnet (ST) joined in one unit assembly.
The yokes of all magnets have been produced by a subcontractor and delivered to JINR. The coils for both quadrupole magnets and for the sextupole corrector magnet have been manufactured at JINR. The production of the steerer coil, superconducting bus bars and the assembling of quadrupole units is scheduled for the beginning of 2017.
The design of the remaining components needed for the assembling of the quadrupole units – terminal boxes and cold terminals of the 250 A current leads – was finished and the engineering drawings were transferred to JINR. A prototype of the terminal box for the corrector magnets was tested at GSI and has shown reliable operation.

Quadrupole doublet integration: A first version of a SIS100 quadrupole doublet module (QDM) in its final configuration was finished in engineering design in 2016. This QDM located in the SIS100 arc section is named type 2.5 (QDM with type 2 focusing quadrupole magnet (QD) located in ion optical cell no. 5). It is equipped with two different superconducting quadrupole units in the so called VQD-CR-SF2B configuration. In between these two units, a cryo-collimator (CR) is located within the integrated cold mass. The unit SF2B is equipped with a beam position monitor (B). The full module also provides LHe supply for magnet cooling, main current supply for main quadrupole magnet operation, and local current supply for corrector magnet operation as well as the beam vacuum chambers.
The engineering design for the complete series of SIS100 QDMs was derived from the design of the QDM type 2.5. The series consists of four different module classes with, in total, eleven configurations including two special modules for injection and extraction of the beam with very special

* We acknowledge the support of the European Community-Research Infrastructure Activity under the FP7 program CRISP (Grant agreement no: 283745) Work Package 5. We acknowledge the support through the JINR–BMBF contract.
† e.fischer@gsi.de

DOI:10.15120/GR-2017-1

engineering design and configuration [2].
The type 2.5 QDM will be manufactured in 2018 as the first QDM in a series of 83 modules for SIS100. The procurement of the full series of SIS100 QDMs is planned in a process including multiple contractors for the various subsystems. All critical ultra-high vacuum components are planned to be procured separately by specialised manufacturers. For manufacturing of cryostat components and mechanical integration of the SIS100-QDMs a dedicated contractor shall be commissioned. The preparation work for tendering of the module integration was completed in 2016. An according contract for module integration is planned to be signed in 2017.

Magnets for the Super-FRS

The superconducting magnets of the Super-FRS comprises 33 multiplets (assemblies of quadrupole, sextupole and other corrector magnets) and 24 dipoles. The multiplets are being built by ASG, Genoa, Italy. The final design of the first of series multiplets has been approved in December 2016 and the production is about to start. The first multiplet will be available in spring 2018. The design of 21 standard superconducting dipoles by CEA Saclay is finished [3] and the tender has started. The contract signature with a manufacturer is planned for the end of 2017. The design of three special branching dipoles (i.e. dipoles with an additional straight exit) will also be carried by CEA, Saclay.

Magnet testing

Prototype test facilities

The prototype test facility (PTF) at GSI was upgraded to be able to power the high current superconducting dipoles. The new DC power converter is able to provide 20 kA at an output voltage up to 66 V with a current stability of 10^{-4}. Since the cooling power of the cryoplant is limited to 300 W the conventional vapour cooled copper current leads used before were replaced by 14 kA DC HTS-current leads in order to reduce the heat load and guarantee a reliable cooling of the magnet.

One of the main tasks running at the prototype test facility is the development of new and the adjustment of existing measurement systems for testing the SIS100 series dipole magnets.

The new system for magnetic-field measurements was developed in collaboration with CERN. It consists of a shaft of five rotating coil probes, a motor drive with an angular encoder and the data acquisition electronics. Next to this a system to measure the geometry of the magnet's aperture was developed and successfully tested during the measurements on the first of series dipole magnet for SIS100 [1].

Series test facilities

The GSI test facility for SIS100 series dipoles (STF) was built from 2014 to 2015 and is under commissioning. The main use of the STF is to execute the series tests of the SIS100 dipoles and the SIS100 string test, a short part of SIS100 consisting of one dipole and one quadrupole module together with local cryogenic components. Besides this the STF allows for testing of every type of superconducting magnet for SIS100, Super-FRS and later on of Heavy Ion Synchrotron SIS300. Moreover, it provides cooling capacity for operating a superconducting continuous-wave linear accelerator (cw-linac) later on.

The main supply systems such as a cryoplant with a cooling power of 1500 W and two power converters with 20 kA (at 66 V output voltage) were successfully commissioned during 2015 and 2016. The STF is expected to be ready for operating in May 2017.

SIS100 quadrupole unit testing

A facility for testing of superconducting magnets for FAIR and NICA projects has been commissioned and put in operation at Joint Institute for Nuclear Research in Dubna in November 2016. JINR and GSI shared the costs of building the facility. Three of six cryogenic test benches are foreseen for testing of quadrupole units for the SIS100 synchrotron. The testing program will include the power tests of the magnets at helium temperatures, measurements of the magnetic-field quality as well as the adjustment of the hydraulic resistance for each type of the quadrupole unit. Tested units will be shipped to the company responsible for the integration of the units to the Quadrupole Doublet Module (QDM). Cold testing of two pre-series quadrupole units is scheduled for the middle of 2017.

Testing of Super-FRS magnets

The Super-FRS dipoles and multiplets will be tested under cold condition (4 K) at a novel cryogenic test facility in CERN [4]. In accordance with a collaboration agreement between CERN and GSI, refurbishment of the facility and installation of the new infrastructures have been done. The commissioning of the facility is partly started. The handover of the facility from CERN to GSI is planned in the middle of 2017. For completion of the commissioning to be participated by GSI colleagues, and the pre-series multiplet testing starts from 2018.

Current leads

The four pairs of Main HTS Current leads have been delivered to the series test facility (STF) at GSI in 2016. The first pair of current leads in Feedbox1 at STF passed the high voltage tests up to 3 kV and a successful run with 14 kA DC current, 13.2 kA cycling current and up to 17 kA pulsed current. Such test program during two days of tests corresponds to the SIS100 requirements. The design of 250 A local current leads made from HTS was finished

DOI:10.15120/GR-2017-1

and two prototype current leads were tested during three runs at the prototype test facility (PTF). Those current leads with novel concept successfully passed tests with 250 A DC current, cycling of 0-250 A current at 1-3 Hz and training pulses of 0-300 A . For the γ_t-Jump-Quadrupole with 250 A pulses of 100 ms duration the design of conventional copper current leads has been finished and a prototype current lead has been successfully tested at PTF. For the Hedgehob collaboration a modern design of conventional copper current leads cooled by vapor was proposed due to the high risk for HTS with respect to magnetic field and radiation losses.

Quench detection system of SIS100

The quench detection system dedicated to survey the magnets of SIS100 against quench was recently redefined. In order to reduce the impact of parasitic capacitance introduced to the SC dipole and quadrupole circuits by a large number of voltage taps, it was decided to develop a new cabling concept that enables to compare two adjacent magnets of the circuit.
The new cable structure provides a high reliability level since each magnet is surveyed by two quench detectors. For the main magnets either a magnetic amplifier (MA) [5, 6] or classical bridges (BRD) will be utilised. MA provides galvanic insulation at the cryostat level while BRD cards require high voltage cabling between the magnet and quench detection cabinets. The R&D program on MA is ongoing. A number of transductor prototypes were manufactured and tested with a single dipole magnet. The results are very promising. The next experiment will consider a test of 10 identical transductor assembled in the overlapping structure.
For the corrector magnets, it is foreseen to use a new Mutual Inductance Detector. The first prototype was manufactured and successfully tested with the corrector magnet model (solenoid) at cryogenic conditions.

Conclusion

In 2016 many remarkable steps were taken in the various fields of activities of the SCM division. By the release of the series production of the superconducting dipoles a major milestone in the procurement of the components for SIS100 was passed. The start of the pre-series production at JINR, Dubna, complements this process on the quadrupole unit side. There, the unit's yokes are produced and other components are on the track. In parallel, the engineering design of the first quadrupole doublet module formed by an assembly of the quadrupole units was finalized and the further module designs were derived from this concept. Regarding the production of the Super-FRS magnets, the manufacturer's concept of the pre-series multiplet was reviewed and confirmed. The engineering design of the Super-FRS dipole was finished and the tendering for manufacturing will be started soon.
On the testing branch, a novel magnetic-field measurement system for the SIS100 dipole was developed. Moreover, a tool for the precise mapping of the yoke's aperture geometry as a crucial parameter for the field quality of the magnets was engineered. The series test facility for acceptance measures of the SIS100 dipoles is under commissioning at GSI. In parallel, the test facility for the quadrupole units was commissioned and successfully put in operation at JINR, Dubna. The installation and commissioning of the Super-FRS magnets testing site at CERN has partly started. The four pairs of main current leads for the STF successfully passed acceptance tests. Their design will be used for the main current leads for SIS100. Novel developments for local current leads were confirmed.
For the scope of quench detection and magnet protection, the planned system for SIS100 was redefined in terms of a novel cabling concept to minimize parasitic capacitances. A research program on magnetic amplifiers was started in order to open up alternatives to classical bridge detectors.
To summarize, the manifold activities under the responsibility of the SCM division yielded in many crucial milestones and set the basis for further steps to successfully realise the FAIR project.

References

[1] C. Roux et al., IOP Conf. Series: Materials Science and Engineering 171 (2017), 012108, doi:10.1088/1757-899X/171/1/012108

[2] J. Ceballos Velasco et al., IEEE TRANSACTIONS ON APPLIED SUPERCONDUCTIVITY, VOL. 26, NO. 3, APRIL 2016, http://ieeexplore.ieee.org/document/7433400/

[3] J. E. Munoz Garcia et al., IEEE Transactions on Applied Superconductivity 2017, Volume 27, Issue 4

[4] L. Serio and P. Schnizer et al., IEEE TRANSACTIONS ON APPLIED SUPERCONDUCTIVITY, VOL. 27, NO. 4, JUNE 2017

[5] K. H. Mess, Quench Protection at HERA, CH2387-9/87/0000-1474 IEEE, PAC, 1987.

[6] L. Coull, D. Hagedorn, V. Remondino, F. Rodriguez Mateos, LHC Magnet Quench Protection System, CERN Internal Note AT-MA/LC 93-81, July 1993.

Investigations on desorption using the single shot method *

Ch. Maurer[†1,2], *L. Bozyk*[2], *Sh. Ahmed*[2], *P. Spiller*[2], *and D.H.H. Hoffmann*[1]
[1]TU Darmstadt, Institut für Kernphysik, Germany; [2]GSI, Darmstadt, Germany

Introduction

Beam induced gas desorption is a key process that drives beam intensity limiting ionization losses in heavy ion synchrotrons in general and in the upcoming SIS100 in particular. Minimizing this effect by providing low desorption yield surfaces is an important part of maintaining a stable ultra high vacuum, which is required for accelerator operation with medium charge state heavy ions. This necessitates the measurement of beam induced desorption yields for various materials and thermal properties of the target in combination with energy and ion species of the beam. Due to the relevancy of high intensity beams for high energy density physics, previous iterations of this report have contained contributions about the results of these experiments [1] as well as novel methods for data analysis [2].

Experimental Setup

An experimental setup for desorption yield measurement has been devised, constructed and taken into commission at the SIS18 at GSI. Based on the experience gained during operation in the beamtime of 2014, it has been continuously improved and expanded. The new setup was used during a beamtime in 2016. Both versions have been used in single shot mode, since measurement in continuous bombardement mode is unfeasible when using a synchrotron. This technique relies on a time resolved measurement of the pressure peak after beam impact, known as the desorption peak. [3] explains both methods in context of a review of past results.

Data Analysis

The desorption yield η is defined as the relation between the number of incoming beam particles N_{beam} and the number of desorbed gas particles N_{des}. Expanding it with the height of the measured desorption peak Δp yields

$$\eta = \frac{N_{\mathrm{des}}}{N_{\mathrm{beam}}} = \frac{\Delta p}{N_{\mathrm{beam}}} \cdot \left(\frac{\Delta p}{N_{\mathrm{des}}}\right)^{-1}.$$

This way, η can be expressed as a product between two factors. $\Delta p/N_{\mathrm{des}}$ must be measured for every desorption event, while $\Delta p/N_{\mathrm{des}}$ is the pressure peak height caused by a single desorbed particle from the target, regardless of the way the desorption was caused. This value, the gas dynamics factor, is characteristic for the experimental setup and can be calculated in a variety of ways, including the ideal gas law. In this work, the ideal gas approach has been rejected in favour of a technique using 3D Monte Carlo gas dynamics syimulations to account for additional effects, like the pumping of the cryotarget.

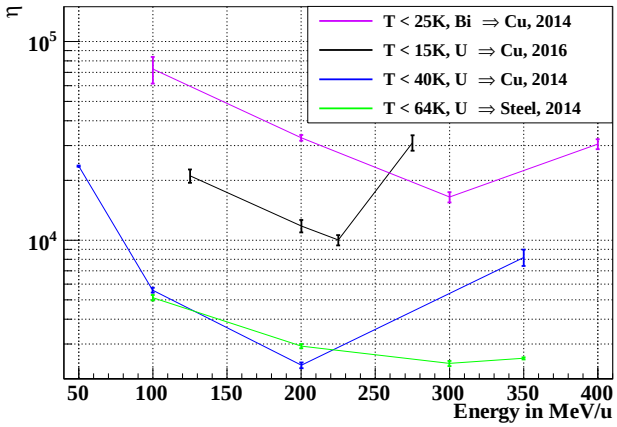

Figure 1: Energy dependance of desorption yields η, measured during the beam times in 2014 and 2016.

Results

Fig. 1 shows a heavily condensed summary of the results obtained with a cryogenic target. While room temperature results show a scaling of eta with the ion's energy loss at the target surface (i.e. a lowering of η with rising energy), the rise in η after a local minimum represents a deviation from this dependancy, which has been observed before [4]. A lower temperature also seems to cause a general rise of η, which suggests the existance of a temperature with a minimum desorption yield. Comparing the data taken with uranium beams suggests a relation between the strength of this deviation and the temperature. However, when taking into account the bismuth curve, one can see that the temperature does not seem to be the only responsible variable.

References

[1] Ch. Maurer et al., "Heavy Ion Induced Desorption on Cryogenic Targets", GSI annual report 2014

[2] Ch. Maurer et al., "Gas Dynamics Simulations for Heavy Ion Induced Desorption Measurements with the Single Shot Method", GSI annual report 2015

[3] E. Mahner, "Review of heavy-ion induced desorption studies for particle accelerators", Phys. Rev. Acc. Beams, Vol. 11, 2008

[4] L. Bozyk et al., "Development of a cryocatcher prototype and measurement of cold desorption", LPB, Vol. 34, 2016

* This report is also submitted to the HEDgeHOB-Report 2016

† christoph.maurer@skmail.ikp.physik.tu-darmstadt.de

DOI:10.15120/GR-2017-1

SIS100 Inspection robot – development and status report

N. Schweizer[*1] *and I. Pongrac*[2]
[1]TU Darmstadt RMR, Darmstadt, Germany; [2]GSI, Darmstadt, Germany

During maintenance work or upgrade measures of large particle accelerator vacuum systems, randomly as well as deliberately introduced foreign objects may inhibit the particle beam significantly, usually leading to a considerable high risk of a complete shutdown of the accelerator. Considering reported incidents from several different particle accelerator laboratories, where e.g. bottles, screws, dropped down inserts, and in the case of SIS18, a crumpled aluminum foil, have been found within the vacuum system, a novel platform for a mobile inspection device is currently being developed and is foreseen to be deployed in SIS100.

Development of the robot design

The vacuum system of SIS100 offers a challenging topography for any mobile inspection robot where a multitude of steps, deep gaps, as well as chambers with limited apertures have to be traversed reliably. Ideally, during each shutdown and prior to closing the vacuum system, the inspection robot shall traverse the complete vacuum system of the SIS100 and visually examine the beam pipe vacuum for any obstacles, damages or anomalies.

In order to design a suitable semi-autonomous robot to be used in the SIS100 vacuum system, the geometries of the different vacuum chambers and pipe sections have been analyzed. The robot is designed in such a way that steps and gaps can be detected and traversed in a safe way. In addition, the robot is able to move forwards and backwards in case an insurmountable obstacle is detected.

The ab initio modular concept of the robot where several modules can be attached successively to increase the total length ensures a high degree of flexibility for the inspection robot to be able to traverse most vacuum chamber topographies. Fig. 1 illustrates the current modular prototype design.

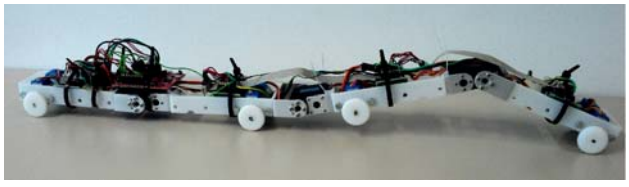

Figure 1: Fully functional prototype model of the SIS100 inspection robot.

* nicolai.schweizer@rmr.tu-darmstadt.de

Simulations and current status

After the determination of the fundamental robot design, extensive 3D simulations have been performed to test and to verify that the robot can traverse as many vacuum sections of SIS100 as possible. Thus, the probability of malfunctions (e.g. the robot gets stuck) can be minimized. Various locomotion strategies have been simulated in realistic test environments based on actual SIS100 CAD data. Additionally, several experiments have been successfully executed with real vacuum chambers or replicas. In Fig. 2 a typical simulation scenario is exemplarily illustrated.

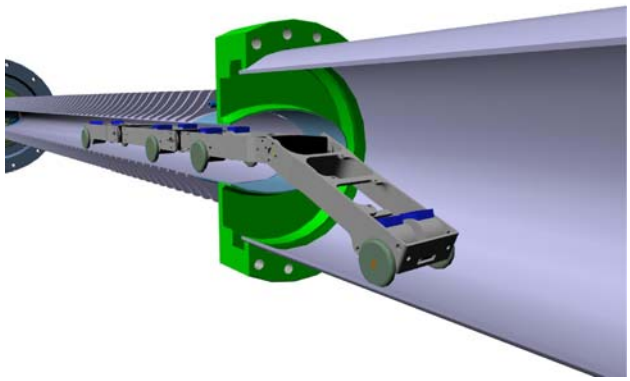

Figure 2: 3D simulation with the Gazebo [1] robotics simulator: A step is traversed as an example of a typical locomotion sequence of the inspection robot.

Outlook and further steps

Consideration of more complex chamber geometries (e.g. double steps), adaptations for curved vacuum chambers (dipole chambers) as well as ongoing maneuver strategy optimizations are currently under development. Battery management, communication possibilities and the implementation of a suitable on-board camera are the principal topics of ongoing work. Further experiments as well as simulations are crucial to allow the SIS100 inspection robot to become a universal tool for particle accelerators.

References

[1] N. Koenig and A. Howard, “Design and use paradigms for Gazebo, an open-source multi-robot simulator”, IEEE/RSJ International Conference on Intelligent Robots and Systems (IROS), pp. 2149-2154, vol. 3, 2004

DOI:10.15120/GR-2017-1

Mechanical interaction of the cryogenic piping system of SIS100*

M.C. Serna Moreno[1], *J. Ceballos Velasco*[† 1,2], *V. Datskov*[2], *and PBMT department*[2]
[1]Universidad de Castilla-La Mancha, Ciudad Real, Spain; [2]GSI, Darmstadt, Germany

The SIS100 superconducting magnetic system consists of different types of modules all along the ring perimeter, containing the main dipole and quadrupole magnets. The modules must be lined up under exigent displacement tolerances, accomplishing the challenging requests on the positioning of the cold masses and vacuum vessels [1]. Due to the hexagonal shape of the synchrotron, there are angular connections between adjacent modules. Traditionally, numerical studies analysing their structural response have been carried out isolating each module. However, the mechanical influence that they could have over each other should not be omitted. The join with a certain angle of modules with different geometries in combination with temperature changes and linkages for displacement compensation could lead to unexpected interaction forces. Their effect should be taken into account in order to avoid any source of misalignment.

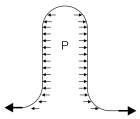

Figure 1: Resulting forces along the expansion joint axis transferred to the pipelines [3]

The piping installation that ensures the cooling to cryogenic temperatures of the magnets is vital to maintain superconducting conditions during the operating phase. In particular, within the conceptual engineering design developed in the Super Conductive Magnets & Testing department of GSI, the analysis of the relative displacements in the connection point between cryogenic pipes from different modules has been recently developed [2,3]. The study has taken into account the angular joint, the thermal shrinkage and the internal pressure withstood. The introduction of universal compensation junctions is essential to absorb the resulting interaction forces and to reduce the undesirable axial, lateral and angular deflections. But these bellows-type elements generate unbalanced loads over the piping system in the axial direction of the linkage (Fig. 1), proportional to the internal pressure and the surface of the crest, which have had to be also accounted in the analysis.

Simulations have been performed with the ANSYS® finite element software under license of GSI. Simplified models from the point of view of the geometry have been considered under the hypotheses of static and linear analysis. In order to assure that the physics of the problem was reproduced, a previous study of the elements accuracy has been performed. The correctness of the numerical estimations have been confirmed by means of comparing the simulation results with those of known situations with analytical solution. As well, sensitivity analyses to the element size have been carried out to ensure that the mesh was ine enough, finding an adequate balance between the computational cost and the degree of precision of the results. This work has been focused on studying the mechanical interaction of the piping systems that ensure the cryogenics of the magnets. As main scenario, the angle of the connection between the cooling tubes which belong to two contiguous modules has been assumed to be equal to 1.67° (Fig. 2). Both pipes have been modelled with the same cross-section and material properties but different lengths, working at temperatures of 4.5 K and supporting internal pressures of 1.1 bar. Besides, the existence of a displacement compensation joint has been considered for completing the definition of realistic conditions. The linear analyses have been developed with simplified 1D geometries, thanks to the use of PIPE188 and MPC184 elements for modelling, respectively, the tubes and the desired rigidity in the connection. Being the variable of interest the mid-point displacements of the system, the results have demonstrated the importance of the flexural deformation of the pipes caused by the angular joint and the induced horizontal movements due to the non-symmetric geometry. These effects could be transmitted to the body of the vacuum vessel at the attachment points, generating a loading hypothesis not contemplated in previous designs. Taking into account that the displacement tolerances of the modules are very restrictive, it is desirable to evaluate its influence at the analysis stage.

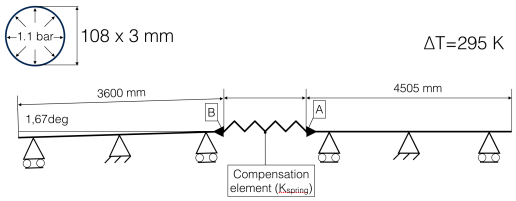

Figure 2: Reference simulation for coupled pipes with a displacement compensation linkage [3]

* Work supported by FAIR@GSI PSP code: G2.08.02.10, the University of Castilla-La Mancha and the grant DPI2016-77715-R from Ministerio de Economía y Competitividad (Spain).

† j.ceballosvelasco@gsi.de

DOI:10.15120/GR-2017-1

References

[1] J.P. Meier, A. Bleile, E. Fischer, G. Hess, J. Macavei, P. Spiller, “Cryo-technical design aspects of the superconducting SIS100 quadrupole doublet modules”, ICEC/ICMC 2014, July 2014, p. 1519.

[2] J. Ceballos Velasco, M.C. Serna Moreno, V. Datskov, E. Fischer, PBMT department, “First Steps of the Development of a Simplified FEM Model for an Arc Section of SIS100 Synchrotron”, GSI Scientific Report 2015, p. 357.

[3] J. Ceballos Velasco, M.C. Serna Moreno, V. Datskov, E. Fischer, “Evaluation of mechanical displacements in superconducting accelerator magnet arrays”, 14th Cryogenics 2017, Dresde, May 2017.

DOI:10.15120/GR-2017-1

Feasibility of RF feedback control loops in heavy-ion synchrotrons by means of derivative estimation *

B. Reichardt[†1], *J. Adamy*[1], *D. Domont-Yankulova*[1,2], *K. Groß*[2], *H. Klingbeil*[2,3], *and D. Lens*[3]
[1]TU Darmstadt RMR, Darmstadt, Germany; [2]TU Darmstadt TEMF, Darmstadt, Germany; [3]GSI, Darmstadt, Germany

Damping of longitudinal coherent bunched-beam oscillations is needed in SIS18 and SIS100 to stabilize the beam, prevent emittance growth and keep beam loss low during acceleration. In last year's work several approaches of digital filters for beam-phase control have been examined. An FIR (finite impulse response) filter with 3 taps, cf. [1], has been successfully used at GSI in several machine experiments for a beam-phase control system and a longitudinal feedback system. In this report an alternative FIR filter approach based on derivative estimation leads to better results as it damps dipole oscillations *within* one oscillation period whereas the former filter approach unveils its full potential only *after* one oscillation period.

Requirements and filter properties

A numerical differentiator approach [2] has been chosen as an alternative to the established 3-tap filter. Both filters share the same control topology, but have different coefficients. The results obtained so far indicate that the optimal filter gain is approximately a constant divided by the synchrotron frequency. Therefore the derivative estimation filter has to be adapted to varying synchrotron frequency.
A filter bank will be used to select different filters based on available parameters such as the synchrotron frequency and bunch length. Alternatively, a continuous tuning of the coefficients will be possible [3].

Experiment, simulations

Both the experiment and the nonlinear tracking simulations were performed for $^{238}U^{73+}$ as ion species at an energy of 300 MeV/u for a stationary operation with a linear synchrotron frequency of 422 Hz at h=2. The beam-phase measurement varies with white Gaussian noise with about $3\sigma = \pm 0.66°$. In this case the derivative estimator has a length of L = 10 non-zero taps without additional zero-taps and is tuned to a high damping rate.
Figure 1 shows the experimental and the simulated results where a disturbance of $2°$ on the beam phase is applied to intentionally excite a feedback reaction. The results indicate that the experiment is in very good agreement with the nonlinear tracking simulation for the derivative estimation approach. Compared to the 3-tap filter approach, there is no overshoot and the dipole oscillation is damped within one oscillation period for the derivative estimation approach. Also the RMS-emittance does not increase while using the derivative estimation approach, which is a second quality criterion besides the damping rate. Furthermore, this approach can be put into practice easily with the existing control topology.

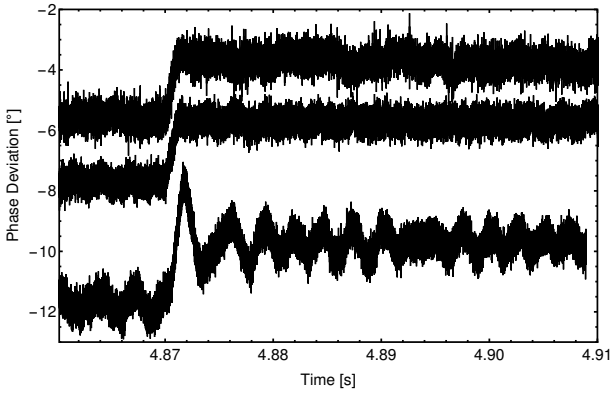

Figure 1: Beam-phase with respect to uncorrected Group-DDS: Experimental data (top), simulated data with arbitrary offset for a controller with derivative estimator (middle) and 3-tap filter (bottom) with a $2°$ distortion at 4.87s.

Outlook

Under current investigation is the critical signal to noise ratio (SNR), at which the derivative estimator approach delivers better results than the 3-tap filter. Another important investigation regards the implementation of the new approach for operation during acceleration ramps.

References

[1] H. Klingbeil et al., "A Digital Beam-Phase Control System for Heavy-Ion-Synchrotrons", IEEE Transactions on Nuclear Science Vol. 54, No. 6, December 2007

[2] M. Mboup et al., "Numerical differentiation with annihilators in noisy environment", Numerical Algorithms, Vol. 50, Issue 4, April 2009

[3] K. Möller et al., "FPGA Based Tunable Digital Filtering for Closed Loop RF Control in Synchrotrons", GSI Scientific Report, 2013

* Supported by the Helmholtz Graduate School for Hadron and Ion Research

† benjamin.reichardt@rmr.tu-darmstadt.de

DOI:10.15120/GR-2017-1

Measurements of incoherent synchrotron frequencies in dual RF bucket

O.Chorniy
GSI, Darmstadt, Germany

The knowledge of the so-called incoherent synchrotron frequencies may be used in different applications: for the RF voltage calibration or studies of the high intensity effects [1]. Future operation in FAIR synchrotrons includes regimes when beam is bunched using two RF harmonics. For such bunches, the incoherent frequencies were obtained using bunch profiles.

In Figure 1 the longitudinal bunch profiles measured using Beam Position Monitor every machine turn in SIS18 is shown. To create the bunch, two RF harmonics were used: one with 10 kV amplitude at h=5 and second 4.6 kV at h=10 (see Figure 1, lower plot). Measurements were done at injection energy of 6.75 Mev/u with 0.4 mA current of Xe^{43+} ion beam.

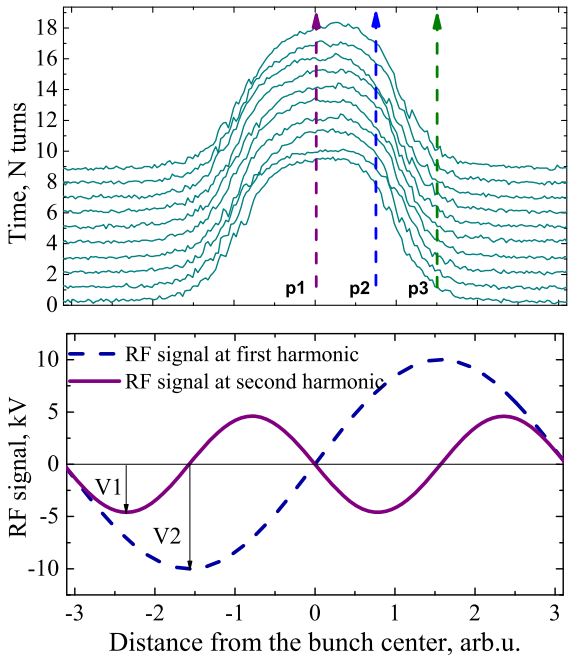

Figure 1: Waterfall of the measured buches (upper plot) created by two RF harmonics (lower plot)

It can be seen that the current at each coordinate of the bunch profile fluctuating with time (as example along the lines p1,p2,p3 on Figure 1). In [1] it was shown that the frequency spectra of these fluctuations must have maximum at specific frequencies (as example see spectra on upper plot of Figure 2). The position of the maximum depends on the bunch coordinate at which the current was measured. Therefore, calculating the current spectrum at different coordinates and correlating the spectrum peaks with these coordinates the incoherent synchrotron frequencies can be obtained. The measured frequencies compared with theory are presented on lower plot of Figure 2.

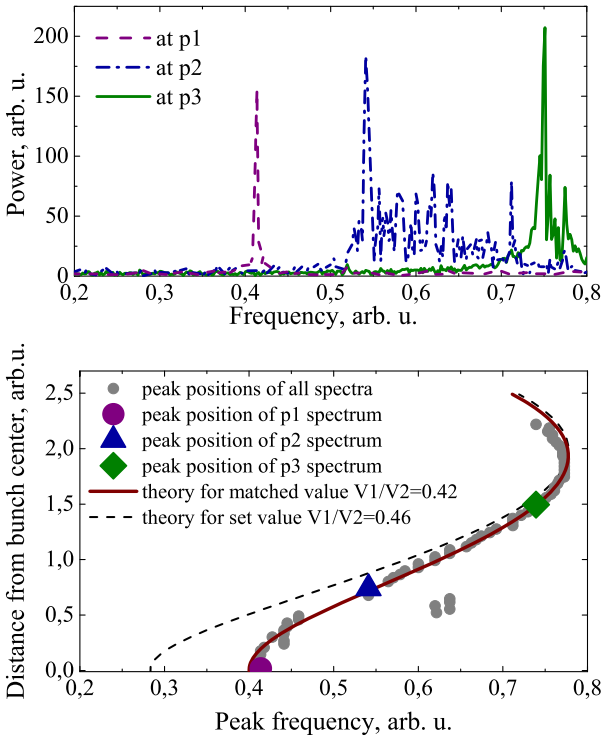

Figure 2: Spectra of current fluctuations measured at three coordinates (upper plot), position of the spectrum peak depending on the coordinate at which the spectrum was obtained and theorethical curves for two cases (lower plot)

In theory, the incoherent synchrotron frequencies can be obtained using formulas in [2]. One of the parameter influencing the incoherent frequencies is the relation of the RF voltage amplitudes. Despite this relation was set to 0.46, the measurements show that the value of 0.42 matches better to the measurements. The reasons for this deviation will be investigated during next beam times.

References

[1] Oleksandr Chorniy and Hansjörg Reeg, A Method To Measure The Incoherent Synchrotron Frequencies In Bunches., Proc. of HB2012, Beijing, China, 2012

[2] S.Y. Lee. Accelerator Physics. World Scientic Publishing Co. Pte. Ltd., second edition, 2004, pages 327-331

DOI:10.15120/GR-2017-1

The SIS100 laser cooling facility*

D. Winters[†1], *T. Beck*[2], *G. Birkl*[‡2], *O. Boine-Frankenheim*[‡1,2], *M. Bussmann*[3], *C. Egelkamp*[4], *L. Eidam*[2], *V. Hannen*[4], *D. Kiefer*[2], *Th. Kühl*[1,5], *M. Löser*[3,7], *X. Ma*[§6], *U. Schramm*[‡3,7], *M. Siebold*[3], *Th. Stöhlker*[1,5,8], *Th. Walther*[‡2], *W. Wen*[6], *D. Winzen*[4], *and P. Spiller*[1]

[1]GSI Helmholtzzentrum, Darmstadt, Germany; [2]Technical University Darmstadt, Germany; [3]Helmholtz-Zentrum Dresden-Rossendorf, Germany; [4]Münster University, Germany; [5]Helmholtz Institute Jena, Germany; [6]Institute of Modern Physics-CAS, Lanzhou, China; [7]Technical University Dresden, Germany; [8]Jena University, Germany

Within POFIII ARD 'Matter and Technologies', the project group 'SIS100 laser cooling' is setting up a laser cooling facility at the FAIR heavy-ion synchrotron SIS100. With the aid of this facility, intense beams of relativistic heavy highly charged ions will be laser-cooled to lowest temperatures, thus providing worldwide unique beams. The project group that deals with this task consists of scientists from GSI and the collaborating partner universities and research centers in Dresden-Rossendorf, Darmstadt, Jena, Münster, and Lanzhou (China) [1].

The laser systems are being developed by the HZDR/TU-Dresden and the TU-Darmstadt, with strong support from the BMBF. These laser systems can be operated at 257 nm or 514 nm, and produce about 100 mW of coherent radiation. The TU-Darmstadt will provide a fast scanning cw-laser system [2], and a pulsed laser system with long (up to 1 ns) pulses and a high repetition rate (up to 1.5 MHz) [3]. The HZDR will provide a pulsed laser system with short pulses (∼ps) and a high repetition rate up to 1 MHz [4]. The Münster group will provide an XUV/X-ray detector for the SIS100, again supported by the BMBF.

The laser lab at the SIS100 will be located 18 m underground in the service tunnel, spatially separated from the accelerator tunnel where the ions circulate. We will need a dedicated laser beamline with sophisticated laser beam steering, stabilization, and diagnostics to ensure an optimal transport and overlap (in space and time) of the laser beam with the ion beam. Currently, we are designing a prototype for the laser beamline, which will have complete laser beam steering and diagnostics. Important components for this beamline, such as a complete set of doubly-coated (257 - 266 nm and 514 - 532 nm) mirrors of the highest quality (reflectivity >99.5%), in 1", 2", and 3" sizes [LayerTec], are already available. These mirrors are compatible with the required vacuum of 10^{-6} mbar of the beamline. The same is true for an entire set of high-quality mirror mounts and prism holders [Liop-Tec]. The mounts incorporate fast piezo drivers, which can be remotely controlled. The new 1" polarizing beam splitter cubes also work for both wavelength ranges [MPO]. Two small green (532 nm) laser systems will be used for tests of the laser beamline. Figure 1 shows a collage of some of the new components.

Figure 1: Collage showing a selection of the components purchased in 2016. Top row, polarizing beam splitter cube and doubly-coated mirrors. Middle row, mirror mounts (vacuum, 2", prism). Bottom row, $\lambda/4$-plate, green laser.

Finally, also two test beamtimes for laser cooling have been performed in 2016: one in April at the CSRe of the IMP in Lanzhou, China, and one in July at the ESR in Darmstadt [5]. The pulsed laser system from the HZDR was shipped over especially for the beamtime at the CSRe. At the ESR, the pulsed laser system was also used, and uniquely exhibited a clear and effective interaction with the stored and bunched ion beam. The cw-laser system from the TU-Darmstadt was also very successfully applied and delivered great results, also for laser spectroscopy of $^{12}C^{3+}$. In addition, the new XUV detector system from Münster university was successfully used for the first time during an experiment [6]. A similar detector is foreseen for the SIS100 vacuum chamber, where also the laser will be coupled in. The design of this vacuum chamber is ready and the chamber can hopefully be delivered in 2017.

References

[1] D. Winters *et al.*, Phys. Scr. **T166** (2015) 014048.

[2] T. Beck *et al.*, Opt. Lett. **41** (18) (2016) 4186.

[3] D. Kiefer *et al.*, GSI scientific report 2015.

[4] M. Siebold *et al.*, Opt. Expr. **20** (2012) 21992.

[5] D. Winters *et al.*, GSI scientific report 2016.

[6] D. Winzen *et al.*, GSI scientific report 2016.

* Work supported by HGF POFIII ARD-ST2.

† d.winters@gsi.de

‡ Work supported by BMBF.

§ Work supported by BMBF-WTZ.

DOI:10.15120/GR-2017-1

Optimization of the multi-turn injection

S. Appel[1], O. Boine-Frankenheim[1,2], L. Groening[1], Y. El Hayek[1], M. Maier[1], C. Xiao[1]
[1] GSI, Darmstadt, Germany, [2] TU, Darmstadt, Germany

The multi-turn injection (MTI) into the SIS18 is one of the bottlenecks for providing ion beams of unprecedented intensities and qualities for FAIR. An optimized injection is also crucial for an excellent interfacing between injector linac and synchrotron. The loss-induced vacuum degradation and associated life-time reduction is one of the key intensity limiting factors for SIS18. Beam loss during injection can trigger the pressure bump instability. An optimized injection can relax the dynamic vacuum problem, but is also crucial to reach the synchrotron intensity limit by a large multiplication of the injected current. For the SIS18 the optimization with genetic algorithms (GA) resulted in a significant improvement of MTI performance and subsequent transmission for intense beams [1]. A loss-free or low-loss injection over many turns were identified. The dependence between gain factor and injection loss is shown in Fig. 1. GA optimization found a much better MTI performance than the previous simulation studies in [2]. Space charge results in a similar MTI performance, but with different injection settings. Using a global residual gas pressure and beam lifetime model together with the optimized multi-turn injection a range of injector brilliance could be defined. This crucial information gives more flexibility for the injector upgrade layout for FAIR [3] and allow an excellent interfacing between injector linac and synchrotron.
One consequence of the single-plane MTI is that the required injection emittance for the injection plane (usually the horizontal one) is very demanding; to the other plane not. Re-partitioning of the injected beam emittances, i.e. round-to-flat transformation would increase the injection efficiency. This benefit effect to the MTI performance of a smaller emittance has been measured as a function of the amount of flatness of the beam. The injection performance has increased significantly up to about 30% shown in Fig. 2. An excellent agreement between simulation and measured injection performance as a function of the injected emittance was achieved thanks to fast adjustment of the beam flatness without changing other beam parameters [4]. The flat beam injection scheme is a scenario for an additional upgrade of the existing UNILAC which may be necessary if the other upgrade measures [3, 5] including a well optimized injection turn out to be not sufficient to reach the beam parameters imposed by FAIR.
Further opportunity to enhance the MTI performance is to injected into both space phase planes. One possibility is to used skew quadruples during injection to couple both planes. The other is to rebuild the SIS18 injection section and transfer channel for the advantage of two-plane injection. Injection optimization simulation studies with this mentioned methods are ongoing. After the undergoing

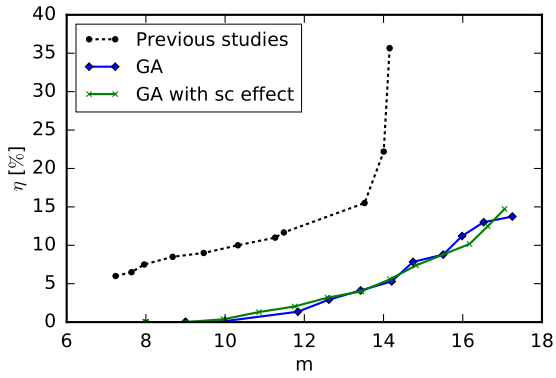

Figure 1: The GA optimization found much better MTI performance than the previous simulation studies [2].

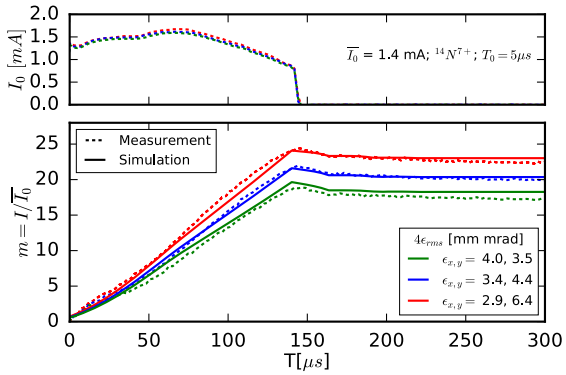

Figure 2: MTI optimization through emittance transfer.

construction work at SIS18 has been finished, it is planned to test an online injection optimization with the new implement and more flexible control system. First online GA optimization test as been already performed at CRYING injector [6].

References

[1] S. Appel, el al, Nucl. Instr. and Meth. A 852 7379 (2017), http://dx.doi.org/10.1016/j.nima.2016.11.069.

[2] S. Appel, O. Boine-Frankenheim, arXiv:1403.5972 (2014).

[3] L. Groening et al, PRL 113, 246802 (2014)

[4] S. Appel, et al, Injection optimization through generation of flat ion beams, submitted to Nucl. Instr. and Meth. A (2017).

[5] L. Groening et al, Upgrade of the Universal Linear Accelerator UNILAC for FAIR, Proc IPAC2016 (2016).

[6] S. Appel et al, Automatized Optimization of Magnet Settings using Evolutionary Algorithms, Proc IPAC2017 (2017).

DOI:10.15120/GR-2017-1

The cryosorption pumps of the SIS 100 – acceptance tests of the first-of series units

St. Wilfert[1] and I. Pongrac[1]
[1]GSI, Darmstadt, Germany

Abstract

The article gives an overview on the production of the SIS100 series cryosorption pumps and their acceptance tests. We also present simulation results on time and position dependent hydrogen density profiles in a SIS100 sector which show why the use of localized cryosorption pumps is crucial for keeping the hydrogen partial pressure in the cryogenic section at an acceptable low level for sufficiently long times.

Introduction

The cryogenic beam vacuum system of SIS100 will be operated at wall temperatures between 5 … 15 K. At such low temperatures, with the exception of hydrogen and helium, all vacuum relevant gas species can effectively be cryopumped by the cold chamber walls with practically infinitive pumping capacity. However, while H_2 can be cryosorbed by the bare chamber walls at least with a limited pumping capacity at these temperatures, no pumping speed is available for He at 15 K. Consequently, additional pumping speed for these both gas species is of crucial importance for long-term maintenance of sufficiently low beam vacuum pressures. Local cryosorption pumps (CSP) are predestined for this purpose and will therefore be used in the cryogenic sections of SIS100 as auxiliary pumps. In total, 14 CSPs are required for each SIS100 sector, 11 of them will be distributed in the cryogenic arc. They will be installed in ~ 13 m intervals between each superconducting (sc) dipole doublet. In addition, each one pump will be integrated in the sc quadrupole doublets on the straight beam line sections of the ring.

In [1] we reported on a prototype of the CSP developed and tested at GSI. The pump was specially designed according to the space and installation conditions in the SIS100 magnet cryostats. The pumping elements are formed by 6 circular charcoal-coated cryopanels, which are uniformly cooled-down to 4.2 K by an axially running liquid helium (LHe) cooling tube. In contrast to the prototype pump described in [1], however, minor technical modifications have been made to the series pumps. First, all panels of the series pumps have the same diameter of 9 cm, achieving a higher pumping capacity. Second, instead of the charcoal type SC2 by Chemviron Carbon, all panels are now coated with the adequate charcoal type Aquacarb 208C (particle size 12x30 US mesh) also produced by Chemviron Carbon. The cryosorption properties of the alternative charcoal type were investigated experimentally in advance, no significant differences in pumping characteristics were found. Each panel is coated with approximately 5 g, i.e. 2.5 g charcoal per panel side. This corresponds to an average coating density of approx. 0.04 g/cm^2. In total, approximately 30 g charcoal contains one pump. The coating was done using a suitable low temperature-resistant epoxy. The central cooling tube was manufactured from a threaded Cu rod. In operation, pressurized liquid helium with a mass flow of minimum 1.0 g_{LHe}/s (at 4.2 K, 2 barg) will be led through the cooling tube. The pump is mounted on a standard D100CF base flange, its housing is formed by a standard stainless steel DN100CF full nipple. In order to avoid charcoal particles from falling out of the pump, a commercially available turbo pump splinter shield with a high optical transparency will be mounted at the pump inlet flange. Figure 1 shows the series pump to be used in the cryogenic beam line sections of the SIS100.

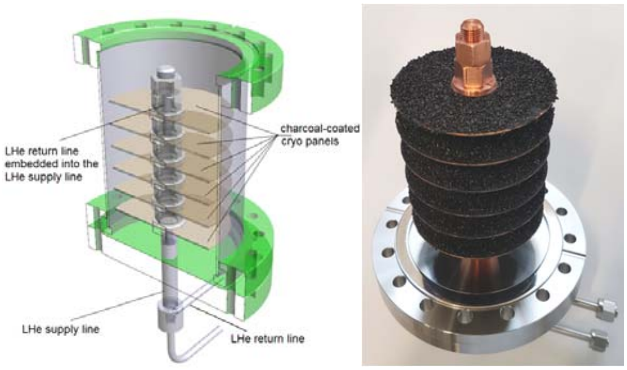

Figure 1: Series cryosorption pump produced by ILK Dresden, Germany.

Acceptance Tests of the First-of Series Units

The production order of the series pumps was granted to ILK Dresden, Germany. The first two pumps, denoted to as first-of-series (FoS) pumps, were subjected to intensive tests at the manufacturer and GSI. Of particular importance is the leak tightness of the central cooling circuit. As the LHe cooling circuit runs through the pump housing and faces directly the beam pipe vacuum system, absolute leak tightness was mandatory. LHe leaking into the pump may disable completely the pumping action of the pump due to rapid He saturation of the panels. In order to prove the leak tightness of the axial cooling tube, the leak test has been conducted for 30 min while the tube circuit was pressurized with 28 barg gaseous helium (GHe). In addition, a GHe flow rate test and a residual moisture test have been carried out successfully. Another important aspect of CSP production was their dust release. Since turbulences can generate and disperse dust from the charcoal-plated panels during roughing, it was crucial to

DOI:10.15120/GR-2017-1

analyse the dust release of the CSP to make sure that no dust contamination of the beam vacuum may occur. Thanks to the optimization of the coating process by means of an epoxy, however, the producer was able to demonstrate experimentally that no dust or charcoal particles with a size of > 100 µm were released from the panels while the pump was roughed. The pumping speed measurements of the FoS pumps were carried out at GSI using a standardized PNEUROP vacuum dome. It was mounted on a test cryostat where the cryosorption pump was built in and cooled down. Details on the measuring procedure can be found in [2]. The tests were carried out with the aforementioned splinter shield which reduces the pumping speed by of about ~ 10%. Results of the measurements are shown in Figure 2.

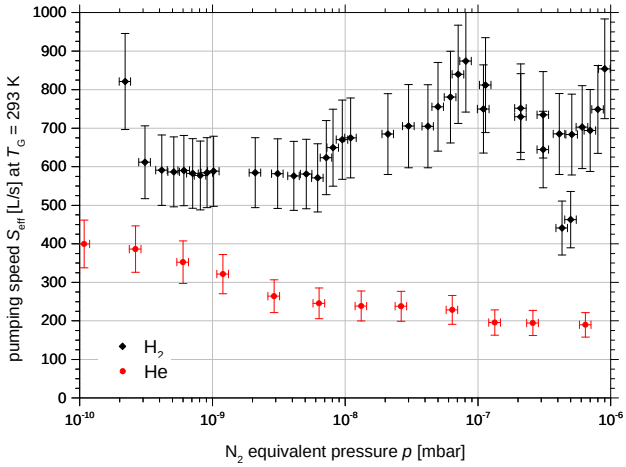

Figure 2: Measured pumping speed, S_{eff}, for H_2 and He

One can clearly see that the CSP provides high pumping speeds for both hydrogen and helium. For H_2 an averaged effective pumping speed of $S_{eff} \approx 600$ ℓ/s was measured in the lower UHV range and for He $S_{eff} \approx 300$ ℓ/s. It must be noted that the real pumping speed of the pump, S, however, is significantly higher than its measured S_{eff} as it is reduced by the conductance of the splinter shield and an upstream installed radiation baffle needed for thermal screening the cold pumping panels during measurement. Both were not taken into account yet in the above presented S vs. p characteristics. Moreover, since the test gas injected was at room temperature, the measured effective pumping speed only holds for $T_G = 293$ K. But what will be the pumping speed of CSP under cryogenic conditions, i.e. at $T_G = 5$ K? From the kinetic gas theory it is known that the pumping speed of a surface, S, depends on the Maxwellian mean velocity of impinging gas molecules, $\bar{c}$,

$$S = \frac{\bar{c}}{4} sA = \frac{1}{4}\sqrt{\frac{8k_B T_G}{m\pi}} sA, \qquad (1)$$

where s is the sticking coefficient, A the surface area, k_B is Boltzmann's constant, T_G the gas temperature, and m the mass of the gas particle. Assuming the sticking probability is temperature-independent, it follows that S is only a function of gas temperature, T_G, and one gets as an approximation

$$\frac{S(T_G = 5\text{K})}{S(T_G = 293\text{K})} = \sqrt{\frac{5\text{K}}{293\text{K}}} \approx 0.13. \qquad (2)$$

Consequently, the pumping speed at $T_G = 5$K is only ~ 1/8 of that at $T_G = 293$ K. Thus, the pump provides under cryogenic conditions a pumping speed for H_2 of $S \geq 78$ ℓ/s and for He $S \geq 40$ ℓ/s.

The effect of CSPs on hydrogen density profile in time in one SIS100 sector

In order to verify the advantage of using the CSPs in the cryogenic beam vacuum system of SIS100, calculations on the long-term hydrogen density distribution in one 180m long sector have been carried out using the novel simulation tool TRANSVAC also developed at GSI [3]. The simulation results are shown in Figure 3. In this Figure, the positions of the CSPs within the cryogenic sections are indicated by blue arrows. The red arrows represent the position of the conventional pumps ($S_{H2} = 2200$ ℓ/s) in the room temperature (RT) sectors. A constant and non-capacity limited H_2 pumping speed of $S_{H2} = 78$ ℓ/s per cryosorption pump was assumed in the simulation. The results indicate that the use of the pumps positively influences the hydrogen density distribution in time. It is interesting to note that the pumping action of the SPCs in the arc (section position $48 \leq l \leq 180$ m) come into real effect particularly in long time scales of a few years, rather than in short time scales. At these times, the H_2 cryosorption capacity of the bare chamber walls has already decreased gradually. Furthermore, the SPCs also limit the H_2 density rise in the cryogenic vacuum system of the sc quadrupole modules on the straight ring sections (section position $0 \leq l \leq 48$m) to nearly the same H_2 density level expected in the adjacent RT sections.

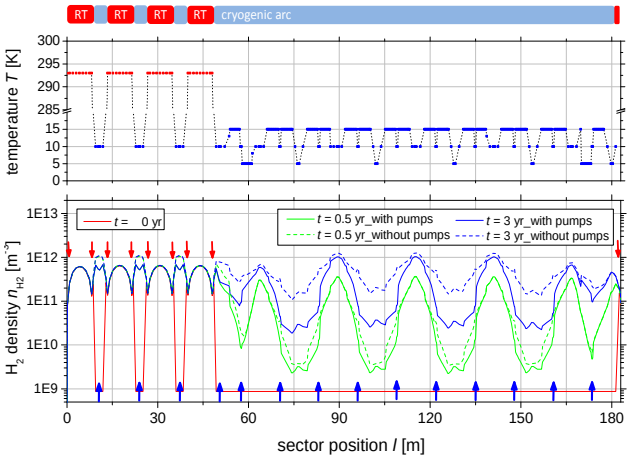

DOI:10.15120/GR-2017-1

Figure 3: Temperature profile of one SIS100 vacuum sector (upper chart) and simulated time and position dependent hydrogen density profiles (chart below).

The simulation neglects any beam dynamical vacuum effects.

The CSPs have an additional advantage. With their installation, a possible small He leak in the cryogenic beam vacuum system can be accepted several times longer as without their use.

References

[1] St. Wilfert, T. Hackler, M. Wengenroth, GSI Scientific Report, PHN-FAIR-16 (2012), 241
[2] International Standard ISO 21360-1
[3] to be published

DOI:10.15120/GR-2017-1

Collimation of primary ion fragments in SIS100

I. Strasik
GSI, Darmstadt, Germany

Introduction

The halo collimation system in the SIS100 synchrotron of Facility for Antiproton and Ion Research (FAIR) must be capable to collimate various ion species from protons up to uranium [1]. For protons and fully stripped ions, a conventional two stage betatron collimation system [2] is going to be applied. The collimation of the primary halo particles is summarized in Ref. [3].

The halo particles, except the scattering and momentum losses, undergo also the inelastic nuclear interaction with the primary collimator. It results in a production of secondary particles due to two processes: (1) hadronic fragmentation and (2) electromagnetic dissociation (EMD).

Probability of inelastic nuclear interaction

The probability P_{in} for the inelastic nuclear interaction (hadronic fragmentation and EMD) of the halo particles with the primary collimator material was calculated using FLUKA code [4]. The P_{in} for various primary ions with magnetic rigidity 18 and 100 Tm, pertaining to injection and extraction in SIS100, are presented in Fig. 1.

The P_{in} shows a substantial increase with increasing mass and atomic number of the primary ions especially taking into account the EMD. A significantly higher growth rate of the P_{in} is observed at 100 Tm with the EMD switched on.

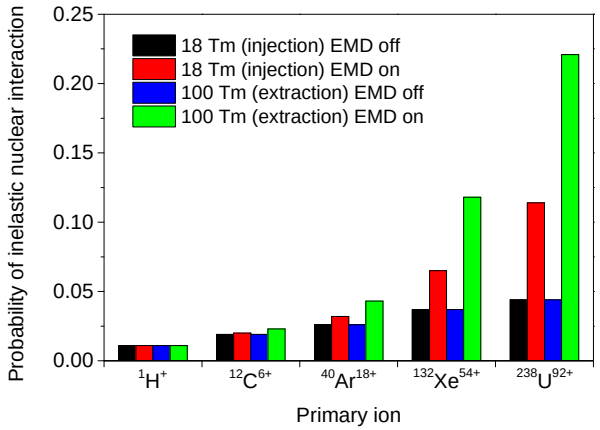

Figure 1: Probability P_{in} for the inelastic nuclear interaction of the halo particles with the primary collimator.

Fraction of the primary ion fragments

Inelastic nuclear interaction of the halo particles with the primary collimator and consequently production of individual secondary fragments was simulated again using FLUKA. A fraction of the individual fragments produced from ^{238}U primary ions after the interaction with the primary collimator is shown in Fig. 2.

The values are normalized by A/238, where A and 238 are the nucleon numbers of the fragment and primary ion, respectively. It can be seen that only the fragments corresponding to the EMD products (isotopes with the lowest and the highest nucleon numbers) have the abundance higher than 10^{-4}.

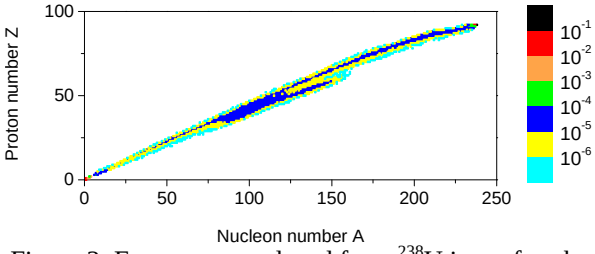

Figure 2: Fragments produced from ^{238}U ions after the interaction with 1 mm tungsten primary collimator.

Collimation of primary ion fragments

Particle tracking simulation in SIS100, for the fragments with the abundance > 10^{-4}, was performed using MAD-X code [5]. The beam loss map of the $^{238}U^{92+}$ halo primary particles together with the secondary fragments is presented in Fig. 3. In general, the calculated collimation efficiency with and without [3] the secondary fragments differ from each other by only a few percent.

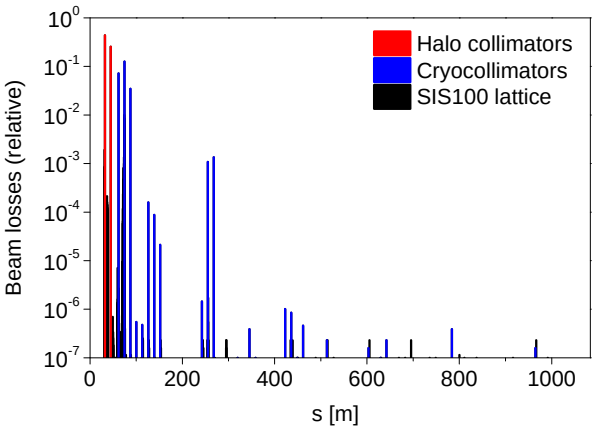

Figure 3: Distribution of the lost $^{238}U^{92+}$ primary beam particles including their secondary fragments in SIS100.

Conclusions

By comparison with the collimation of primary ions in Ref. [3] was shown that the fragmentation in the primary collimator has no significant effect on the efficiency.

References

[1] P. Spiller et al., IPAC'13, Shanghai, China, p. 3782.
[2] J.B. Jeanneret, PhysRev ST AB 1 (1998) 081001.
[3] I. Strasik et al., PhysRev ST AB 18 (2015) 081001.
[4] http://www.fluka.org
[5] http://mad.web.cern.ch/mad

DOI:10.15120/GR-2017-1

Phase calibration of synchrotron RF signals

A. Andreev[*1], *D. Lens*[2], *and H. Klingbeil*[1,2]
[1]TEMF, TU Darmstadt, Germany; [2]GSI, Darmstadt, Germany

Introduction

The RF reference signals for the FAIR synchrotron RF cavity systems are generated by direct digital synthesis modules mounted in so-called Group DDS crates which allow to perform various multiharmonic operations [1]. This means that each DDS unit operates in a certain mode defined by the harmonic number that is generally independent of the module and can be changed during operation. Different harmonic numbers of the DDS modules lead to a different phase response of each module, which results in a phase shift between reference DDS RF signals.

Absolute phase calibration

In the formerly used Group DDS calibration procedure the harmonic numbers of DDS modules are fixed and the calibration is done with respect to the highest harmonic number. If the harmonic number of the DDS module is changed, calibration data stored in calibration electronics modules (CEL) are no longer valid and one has to repeat the process for the new value. With the new proposed method phase correction values stored in CEL stay valid independent of the harmonic number realized by the DDS.

The BuTiS T_0 signal with a 10 μs period is used as one of the clock signals for DDS modules to ensure that reference RF signals are synchronized [2]. Therefore the measurement procedure is synchronized with the T_0 pulse train in order to increase the accuracy of the results. The measurement setup includes (Fig. 1):

- DDS module under calibration
- Scalable Control Unit (SCU) controlled by the PC[1]and forwarding data with the frequency tuning word to the corresponding modules via the backplane
- BuTiS reference signal generator and distributor

All the traces are measured by an oscilloscope and the acquired data are transferred into the PC which performs the subsequent analysis. The resulting phase correction data can finally be stored in a CEL module, which receives telegrams with the DDS frequency via optical fiber link and provides optical telegrams with phase corrections. The first pre-condition to arm the oscilloscope is the output trigger signal of the DDS module, marking the moment when the new frequency tuning word is received by the DDS. The oscilloscope is triggered on one of the next periods of the T_0

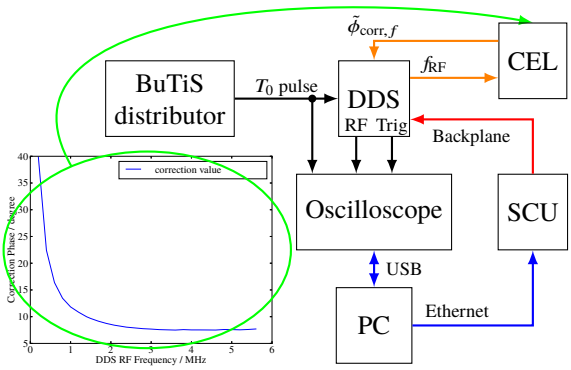

Figure 1: Measurement setup layout.

pulse N_{T_0} and the DDS RF signal portion after the trigger is used for the subsequent analysis.

The DDS RF output signal phase $\hat{\phi}_f$ is precisely estimated with a four-parameter sine wave fit algorithm [3] for each measurement. The phase correction value $\tilde{\phi}_{\mathrm{corr},f}$ for each frequency under calibration is obtained with

$$\phi_{\mathrm{corr},f} = \hat{\phi}_f - 2\pi f\,(N_{T_0} \times 10\mu\mathrm{s} - \tau_\delta)$$
$$\tilde{\phi}_{\mathrm{corr},f} = [(\phi_{\mathrm{corr},f} + \pi) \bmod 2\pi] - \pi,$$

where τ_δ is the dead time of the DDS unit after a T_0 slope to realize the new frequency tuning word settings at the analog RF output, including the delays of digital processing, PCB, filters and cables. The resulting phase correction table can be stored into the CEL module and applied during regular operation. The standard deviation of the obtained phases doesn't exceed 0.2°, allowing to meet the desired phase accuracy requirements.
The measurement as well as the data analysis procedures are automatized by means of Python scripts allowing to perform calibration quickly and comfortably.

References

[1] H. Klingbeil *et al.*, "New digital low-level rf system for heavy-ion synchrotrons", *Phys. Rev. ST Accel. Beams*, vol. 14, p. 102802, 2011.

[2] B. Zipfel and P. Moritz, "Recent progress on the technical realization of the bunch phase timing system BuTiS", in *Proc. IPAC'11*, pp. 418–420.

[3] P. Händel, "Properties of the IEEE-STD-1057 four-parameter sine wave fit algorithm", *IEEE Trans. on Instr. and Meas.*, vol. 49, no. 6, pp. 1189–1193, 2000.

* andreev@temf.tu-darmstadt.de
[1]During regular operation the SCU receives the data from the Central Control System

DOI:10.15120/GR-2017-1

Simulating particle loss for slow extraction from SIS-100*

S. Sorge†[1]
[1]GSI, Darmstadt, Germany

Slow extraction of heavy ion beams will be one of the most important operation modes of SIS-100. The minimisation of uncontrolled particle loss is essential for avoiding damages and irradiation of the machine. For that reason, expected particle losses are estimated with particle tracking simulations. The special focus of the studies is on the impact of magnet imperfections.

Slow extraction from SIS-100 is based on the excitation of the third integer resonance given by $3 \cdot Q_x = 52$ with six resonance excitation sextupoles, leading to the formation of a triangular stable area in the horizontal phase space plane. Rf knock-out (KO) extraction will be applied, where the beam is excited with horizontal rf noise which results in a slow growth of the phase space area of the beam beyond the stable phase space area so that particles will successively become unstable, travel towards the electro-static septum (ESS), and enter the extraction channel after passing the ESS.

Essential for minimising uncontrolled particle loss during slow extraction from SIS-100 is to reduce the large horizontal chromaticity which is

$$\xi_{x,nat} = -20, \tag{1}$$

according to the definition $\Delta Q_x = \xi_x Q_x$, to

$$\xi_{x,corr} = -1 \tag{2}$$

with chromaticity correction sextupoles in order to fulfil the Hardt condition [1]. In doing so, the trajectories of the particles can be adapted to the extraction septa independently of their momenta.

Superconducting dipole and quadrupole magnets will be used which have field errors characterised by the series [2]

$$B_y + \mathrm{i}B_x = B\rho \sum_{n=0}^{\infty} (k_n + \mathrm{i}j_n) \frac{(x+\mathrm{i}y)^n}{n!} \tag{3}$$

of the normal and skew multipole coefficients $k_n = (\partial^n B_y)/(\partial x^n)|_{x=y=0}$ and $j_n = (\partial^n B_x)/(\partial x^n)|_{x=y=0}$. The sextupole contribution k_2 to the field error of the dipole magnets is important because it is relatively strong and induces a significant change of the chromaticities as well as of size and orientation of the stable phase space area. k_2 is as all other coefficients a function of the magnet's excitation current and, consequently, of the beam rigidity $B\rho$, see Figure 1. The resulting horizontal chromaticity without correction for $B\rho = 100$ Tm is $\xi_{x,uncorr} = -27$ and, hence, strongly deviates from the natural chromaticity in Equation (1). Therefore, stronger chromaticity correction sextupoles are necessary for achieving the required horizontal chromaticity of Equation (2) resulting in a decreased stable phase space area and unacceptably high uncontrolled particle loss. By performing particle tracking simulations with 5000 test particles tracked for 15000 turns for conditions of a U^{28+} beam at $E = 2.7$ GeV/u, particle losses ~ 10 % in places anywhere in ring except the ESS [4] were obtained. Applying new settings for the resonance sextupoles, essentially generated by reducing their strengths in order restore the size of the stable phase space area and to re-adjust its orientation, reduced these losses to less than 1 %. In addition, particles losses of about 3 % due to collisions with the ESS were obtained without and with modifications of the settings which is acceptable. Similar amounts of lost particles could be achieved in ongoing tracking studies also for beams of lower energies, where the sextupole settings always had to be adapted to the actual magnet errors. The results indicate that finding proper sextupole settings for each rigidity will be essential for enabling slow extraction from the real machine.

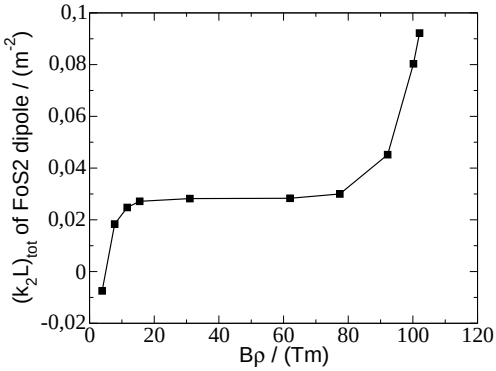

Figure 1: Total integrated coefficient of the sextupole error in the field of the FoS2 dipole [3].

References

[1] W. Hardt, "Ultraslow extraction from LEAR", PS/DL/LEAR Note 81-6, CERN, Geneva, 1981.

[2] A. Wolski, "Maxwell's equations for magnets", arXiv:1103.0713v1 [physics.acc-ph] 3 March 2011.

[3] P. Schnizer, private communication.

[4] S. Sorge, "Slow extraction issues of SIS-100", talk at the Slow extraction workshop, Darmstadt, June 1-3, 2016.

*This report was also submitted to the Annual Report "News and Reports from High Energy Density generated by Heavy Ions and Laser Beams 2016"

† s.sorge@gsi.de

Behavior of the planned RF feedback loops under beam loading during a reference SIS100 cycle*

D. Mihailescu-Stoica[†1], *J. Adamy*[1], *D. Domont-Yankulova*[1,2,3], *H. Klingbeil*[2,3], *and D. Lens*[3]
[1]TU Darmstadt RMR, Darmstadt, Germany; [2]TU Darmstadt TEMF, Darmstadt, Germany; [3]GSI, Darmstadt, Germany

It is well known that beamloading effects in accelerating cavities can have a serious impact on the beam quality. In order to prevent emittance growth and to keep beam loss low during acceleration, detailed simulations are necessary to evaluate the effects on the cavity and its low level RF feedback systems. This situation is aggravated by the fact that in a SIS100 scenario two out of ten buckets have to stay empty. Up to now the closed loop performance of the overall cavity system is still an open topic. Therefore a detailed study has been started.

Planned architecture and requirements

For most operating conditions ferrite-cavities can be well modeled as parallel, time variant RLC-circuits [1]. In order to analyze the influence of beamloading and empty buckets a simulation model has been set up consisting of the cavity itself, its attached control loops and a macro-particle nonlinear tracking simulation. The LLRF systems consist of the amplitude control loop, the resonance frequency control and the cavity synchronization. The amplitude control loop is planned as a linear PI controller in order to achieve stationary accuracy. The resonance frequency controller is as well a PI element and possesses additionally a feed-forward path which maps the desired resonance frequency to the desired bias current. Finally the cavity synchronization is a P-type controller with inherent integral type behavior.

It can be shown that all three control loops are influenced by beam loading. As a phase accuracy of better than $\pm 3^\circ$ and an amplitude accuracy of $\pm 6\%$ are intended to guarantee a satisfactory beam quality [2], beam loading effects must not be neglected. Especially the induced parasitic frequencies due to empty buckets are an open topic up to now and the planned control architecture has to be validated with respect to this issue.

Simulation of the RIB $^{238}U^{28+}$ 2.7GeV cycle

Nonlinear tracking simulations of the full acceleration cycle were performed for 5×10^{11} $^{238}U^{28+}$ ions with an injection energy of 1.976×10^8eV/u and an extraction energy of 2.7×10^9eV/u according to the official SIS100 cycle document [3]. The maximum synchronous phase during the cycle is 59.28° with a maximum gap voltage of 372.53kV. The bunches are injected in groups of two, letting the last two buckets of in total ten empty. The shape of two bunches during acceleration, near flat top, is shown in Fig.1, where the peak beam current reaches about 6 A . The emittance growth depends on the bunch position. While the first bunch growth by 2.1% the sixth bunch shows an emittance growth of 8.4%. Particle losses are hardly noticeable and will be dominated by other effects. The objective of the simulation is to serve as a proof of principle for the closed-loop control systems planned for SIS100. There is still the possibility to improve the beam quality, for example by temporarily de-activating individual cavities.

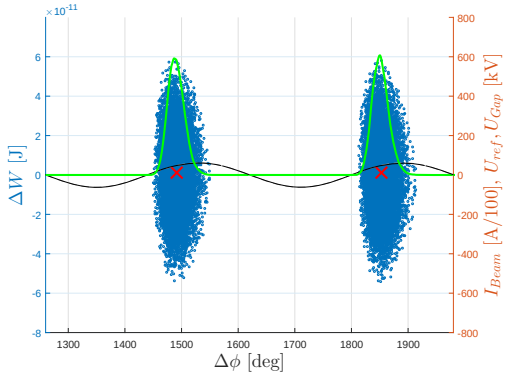

Figure 1: Two filled buckets during acceleration: particles (blue), beam current (green), gap voltage (black) and center of gravity (red)

Outlook

The results obtained in the detailed simulation study described in this contribution show that the planned low level RF control loops are able to deal with beam loading effects during the extremal RIB $^{238}U^{28+}$ cycle and maintain the RF accelerating voltage at the desired set point. Current work focuses on the influence of beam loading on the LLRF systems during a bunch-to-bucket-transfer from SIS18 to SIS100 and the arising transient effects. In future the influence of dipole beam oscillations on the stability and performance of the controlled cavity dynamics is going to be analyzed.

References

[1] H. Klingbeil, U. Laier, D. Lens, "Theoretical Foundations of Synchrotron and Storage Ring RF Systems", Springer, 2015

[2] H. Klingbeil et al., "New digital low-level RF system for heavy-ion synchrotrons", Physical Review Special Topics - Accelerators and Beams, 2011

[3] H.Liebermann, D. Ondreka, "SIS100 Cycles 3.0", Tech. rep. GSI, 2016

* Work supported by GSI
† dinu.mihailescu-stoica@rmr.tu-darmstadt.de

DOI:10.15120/GR-2017-1

Signal processing development for the SIS100 bunch-by-bunch longitudinal feedback*

D. Lens†[1], *M. Hardieck*‡[3], *K. Groß*[2], *H. Klingbeil*[1,2], *M. Kumm*[3], *K. Möller*[3], *and P. Zipf*[3]
[1]GSI; [2]TU Darmstadt, TEMF; [3]University of Kassel, Digital Technology Group

Overview of the System

The bunch-by-bunch longitudinal feedback planned for SIS100 is a broad-band feedback system (BBFB) that will help to stabilize the beam, keeping longitudinal emittance blow-up low and minimizing beam losses [1]. The low-level RF (LLRF) topology of the signal processing part of the system is mainly based on hardware and software components that have already been successfully tested in several machine experiments at SIS18, e.g. [2, 3]. However, some new components have to be developed such as a de-multiplexer and multiplexer (MUX). Here, the progress on the development of the digital MUX is reported.

Digital Multiplexing and Amplitude Modulation

The signal processing chain of the BBFB system is planned in principle as follows. First, the beam current signal is de-multiplexed into 10 channels each representing a single bunch (two channels will be zero for SIS100). For each channel, a DSP system with analog pre-processing is used to detect the bunch phase and amplitude and to calculate correction values (phase and amplitude). The correction values for all channels are converted to in-phase and quadrature components (I/Q) and then forwarded to the MUX. As the BBFB system will use dedicated broad-band kicker cavities, a driver signal for these cavities has to be generated. Therefore, the MUX has to convert the I/Q corrections of all channels into a single analog driver signal. Since the corrections of each channel must act on a particular bunch, it is mandatory that the driver signal is synchronized with the beam. Thus, the MUX also needs reference RF signals as inputs.

Figure 1 shows the inner functionality of the MUX. The signals with the correction values for each bunch are transmitted over a so-called Optical Direct Link (ODL, [4]). They consist of a stream of optical telegrams that contain the I/Q components. The new values are stored in buffers before they are used to avoid parameter switching during operation. The MUX performs a unique bucket numbering by counting periods of two reference RF signals (sine) which correspond to the bunch frequency (analog inputs) and the revolution frequency (harmonic number $h = 1$, Trigger input), respectively. Using these signals, the multiplexer selects the correct pair of I/Q values for the current

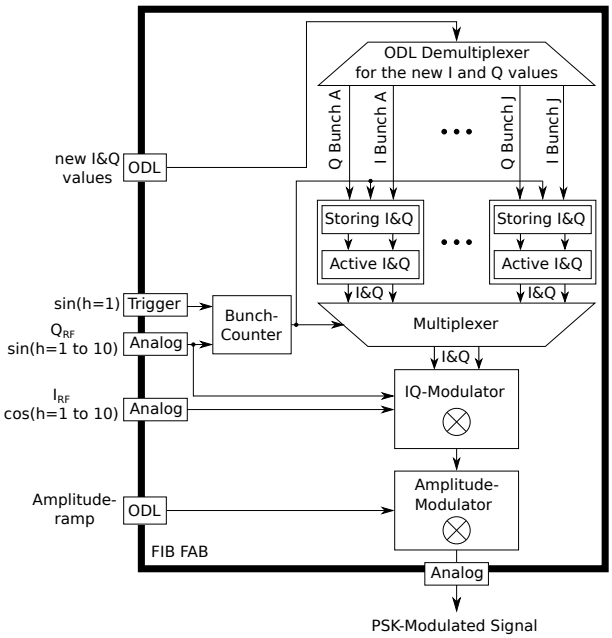

Figure 1: Functionality of the planned MUX module.

bunch and modulates the two analog signals with $h \geq 1$ (sine and cosine) according to I and Q. To obtain the necessary phase and amplitude correction of the beam, the gap voltage of the kicker cavities has to be scaled with respect to the total gap voltage of all other SIS100 cavities. Therefore, a subsequent modulation with an optical amplitude ramp is needed. Finally, the driver signal is generated as an analog signal at the output.

Outlook

The MUX firmware is currently under development and will be tested in a laboratory environment first. As a next step, a machine experiment with beam at SIS18 using one of the h=2 magnetic alloy cavities as dedicated kicker cavity will be necessary to evaluate the setup.

References

[1] K. Groß et al., GSI SR 2014, FG-SIS100-10 (2015).

[2] H. Klingbeil et al., "A digital beam-phase control system for heavy-ion synchrotrons", IEEE Trans. Nucl. Sci. 54(6)2604:2610 (2007).

[3] D. Lens et al., GSI SR 2014, FG-GENERAL-29 (2015).

[4] H. Klingbeil et al., "Generic Data Format for Optical Links", Rev. 1.42, 18.01.2017.

* Work supported by GSI.
† d.e.m.lens@gsi.de
‡ Hardieck@uni-kassel.de

A new bunch-to-bucket transfer technology for FAIR*

T. Ferrand†[1], *H. Klingbeil*[1,3], *O. Bachmann*[1], *and J. Bai*[2]

[1]Technische Universität, Darmstadt, Germany; [2]Goethe Universität, Frankfurt, Germany; [3]GSI Helmholtzzentrum für Schwerionenforschung GmbH

Introduction

In the continuity of [1] and [2], this paper reports the status stand of the Bunch-to-Bucket transfer topology development for FAIR as well as some key results obtained recently. The Bunch-to-Bucket topology for FAIR relies on the BuTiS absolute time frame and White Rabbit high-speed synchronous Ethernet packet exchange.

Implementation

The position of the beam's first bucket is locally and asynchronously measured at the source and at the receiving synchrotron by means of a DSP-based phase measurement system [3].

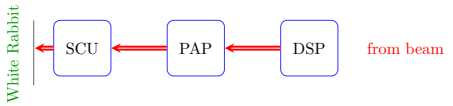

Figure 1: Functional flow of the new Bunch-to-Bucket transfer acquisition chain for FAIR.

As shown in Fig. 1, the Phase Advance Prediction (PAP) module uses the measured phase values to extrapolate a re-synchronized phase value and time-stamp it before it shares it through a separated Virtual LAN of the White Rabbit network by means of a Scalable Control Unit (SCU) [4].

According to the latest measurements, the transfer of synchronized Ethernet packets via the White Rabbit costs less than 30 μs per switch layer. The maximum amount of switch layers depends on the tolerable frame loss rate. The firmware of the White Rabbit switches is still under development at CERN.

New functions such as the PAP function require the development of a new FPGA-based Multi-purpose Hardware Unit (MHU), which is under development in cooperation with the IES Institute at the TU-Darmstadt. The MHU benefits from a modular design and a variety of interfaces, which make it a key stone for a variety of applications foreseen in the framework of the FAIR development.

Phase advance prediction

The DSP-based phase measurement device delivers phase difference values between a RF signal and a BuTiS-based synchronous reference signal through optical telegrams every 3.22 μs with an accuracy of 0.1 ^{o} [5]. According to the technical concept, the maximum absolute frequency difference between the measured signal and the reference signal is 50 kHz.

Phase prediction algorithms have been developed in Python and tested off-line with real phase measurements performed in February 2017 at GSI. The equation

$$\bar{\bar{X}} = \frac{1}{M}\sum_{n=0}^{M-1}\bar{X}_n = \frac{1}{MN}\sum_{n=0}^{M-1}\sum_{i=n}^{N+n-1}X_i. \qquad (1)$$

enables to use a minimum amount (N) of required samples (X_i) to achieve the required prediction stability of 1 ^{o} over the expected 10 ms of synchronization time (see fig. 2). M defines a second averaging window.

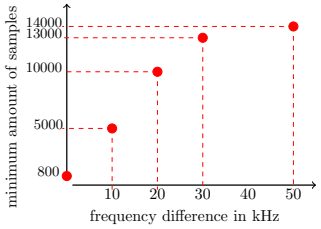

Figure 2: Summarized results of PAP code simulation as function of the frequency difference.

Outlook

Recent results confirm that the averaged phase advance converges towards a final value. The minimum amount of samples that is required to reach the required accuracy is very large but can be optimized.

The phase advance prediction accuracy and the systematic errors must still be investigated.

References

[1] T. Ferrand and J. Bai, "System Simulation of Bunch-to-Bucket Transfer Between Synchrotrons", *GSI SCIENTIFIC REPORT 2014*, 2015.

[2] T. Ferrand, H. Klingbeil, J. Bai and O. Bachmann, "Development of a topology for the bunch-to-bucket Transfer for FAIR", *GSI SCIENTIFIC REPORT 2015*, 2016.

[3] H. Klingbeil *et al.*, "New Digital Low-Level RF System for Heavy-Ion Synchrotrons", *Phys. Rev. ST Accel. Beams*, vol. 14, p. 102802, 2011.

[4] J. Bai and T. Ferrand, "Technical Concept of the Bunch-to-Bucket Transfer for FAIR", EDMS 1514162v.6.

[5] H. Klingbeil, "A Fast DSP-Based Phase-Detector for Closed-Loop RF Control in Synchrotrons", *IEEE Transactions on Instrumentation and Measurement*, vol. 54, no. 3, pp. 1209–1213, 2005.

* Work supported by GSI

† ferrand@temf.tu-darmstadt.de

DOI:10.15120/GR-2017-1

Beam position measurement during multi-turn injection in SIS-18

R. Singh, P. Forck, A. Reiter, and Y. El-Hayek
GSI, Darmstadt, Germany

New asynchronous algorithm for beam position evaluation [1] provided online measurement of beam position of each injected beamlet during the multi-turn injection in SIS-18. Injection bump and decoherence of injected beam were clearly visible. Further, horizontal and vertical tune at injection were measured.

Experiment and results

The multiturn injection in SIS-18 involves painting the UNILAC beam into horizontal transverse phase space by means of injection bumper and appropriate horizontal tune setting over several revolution periods of SIS-18 [2]. The exact temporal length of injection is regulated by the time window of electrostatic chopper. Figure 1 shows the pick-up data recorded immediately after injection. Nine beamlets with 108 MHz structure are injected which decoheres in roughly 1 turn. Since the "chopper window" is not exactly matched to revolution time, an additional longitudinal structure with revolution frequency and harmonics stay for 100-500 turns depending on the exact beam momentum spread. Presence of such a longitudinal structure due to the injection process allows for position calculation in these periods after injection and could be utilized to tune the injection.

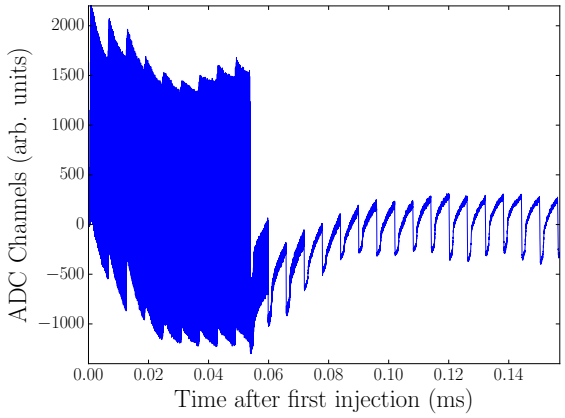

Figure 1: Raw data from top plate of the BPM 3 immediately after the start of multi-turn injection.

Figure 2 shows the horizontal and vertical positions at BPM 3 as a function of number of turns. The horizontal oscillations are expectantly much larger than vertical oscillations and the initial horizontal position at BPM 3 is ≈ 18 mm confirming the injection bump design. An "Injection orbit" is calculated by taking an average of initial 2 turn positions. It is plotted as a function of section number in Fig. 3. BPM 12 was unavailable between 3rd and 40th turn while capacitor charging and discharging transients were observed. The vertical BPM in section 7 was malfunctioning during this experiment and the corresponding data point should be ignored. The orbit bump matches well with designed orbit bump shown in Fig. 7.4 of reference [2]. Further tune was measured by spectral analysis of turn-by-turn data in both planes and the results compared well with the set values during the experiment.

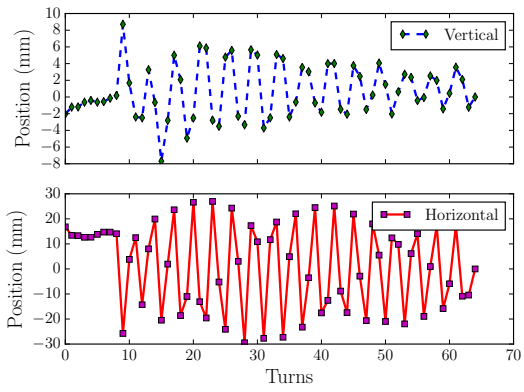

Figure 2: Vertical and horizontal beam oscillations after injection at BPM 3.

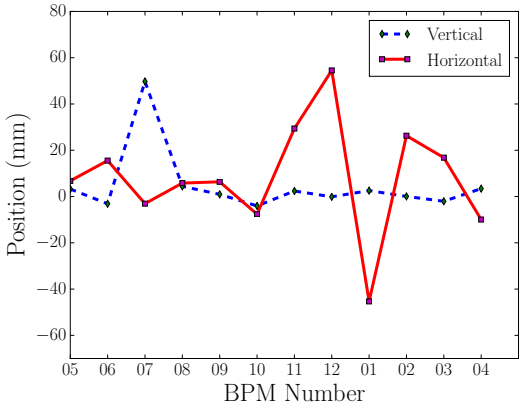

Figure 3: The orbit bump created during injection.

References

[1] A. Reiter et al., "Statistical Treatment of Beam Position Monitor Data", https://arxiv.org/abs/1609.01332 2016.

[2] Y. El-Hayek, "Minimierung der systematischen Anfangsverluste im SIS18", Goethe UNiversity Frankfurt, PhD-Thesis, 2013.

DOI:10.15120/GR-2017-1

Pressure measurement in low temperature vacuum systems – Advances in the development of an extractor ion gauge with CNT cathodes

M. Lotz[1,2], St. Wilfert[1], and O. Kester[1,2]
[1]GSI, Darmstadt, Germany; [2]Goethe University, Frankfurt

Abstract

Pressure measurement in cryogenic UHV and XHV environments is non-trivial. Basically, commercially available hot-filament ion gauges can be used in cryogenic vacuum systems [1], however, one has to accept disadvantages. The operation of their thermionic filament is always associated with a huge heat development. The heat-produced radiation disturbs the thermal equilibrium of the ambient gas and makes the pressure reading erroneous. In a cryogenic environment, moreover, such additional heat load is absolutely unwanted as it must be countered by a higher cooling effort. The problem of thermionic cathodes in ion gauges can be overcome by using non-thermal field emitter cathodes instead. For this reason, we studied a conventional extractor ion gauge type IE514 (INFICON) with a single CNT emitter cathode. Our investigations published in [2-4] confirmed the general functionality of this gauge with a field emission cathode in low temperature vacuum systems. In order to improve the gauge performance by extending its measuring range towards lower pressures, a gauge design with multiple field emitter cathodes was developed and evaluated in numerical simulations [5]. In this gauge design small-sized field emitter cathodes were arranged around the anode grid. Two different emitter types have been tested consecutively with this design: gated field emitter arrays (FEA) and CNT cathode spots.

Gated Mo field emitter array-based gauge

The gated molybdenum field emitter array chips were provided by the Vacuum Nanoelectronics group of PSI, Switzerland. The emission properties of these emitters were studied in [6] and showed emission currents > 1mA at relatively low gate voltages, making their use in an ion gauge interesting. However, during conditioning at GSI, short circuits between substrate and gate occurred in every tested FEA. The reasons are not known. We suppose a chemical reaction of the Mo field emitter tips with the residual gas or a dust particle effect. Also, the emission currents extracted before breakdown were insufficient for the application in our gauge. If they cannot be significantly increased by appropriate measures, these emitters seem to be unsuitable for the use in our modified gauge.

CNT cathode-based gauge

Due to our positive experience with CNT cathodes during our previous studies [2-4], we decided to examine the use of CNT cathodes instead of FEAs in the advanced extractor gauge design. Since CNT cathodes need substantially higher extraction voltages than micro-structured FEAs to generate comparable emission currents, numerical simulations have been carried out first to investigate the impact of the higher potentials on the electron trajectory length and thus on the gauge sensitivity. The results obtained have shown that the electron trajectory length decreases only slightly. This finding suggested that the gauge with 3 individual emitter arranged around the anode grid (each rotated by 120 degrees) can also be used for a gauge with CNT cathodes. However, a new miniature CNT housing had to be developed which fits into the tight space between the anode grid and the surrounding vacuum tube. Furthermore, the housing had to be as small as possible in order to keep the additional gas load due to the outgassing to a minimum. In addition, the housing design had to be such that the extraction potential (< 1kV) is safely insulated against the ground potential (substrate). The gap distance between emissive CNT layer and extraction grid was set to 200 µm. The final CNT housing and its integration into the gauge are shown in Figure 1.

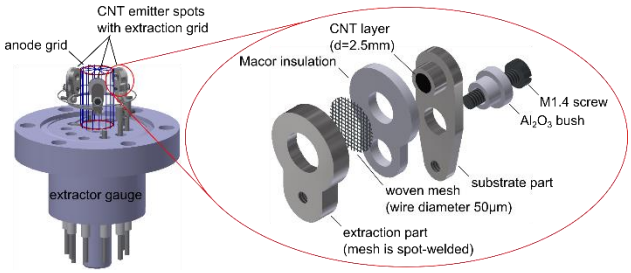

Figure 1: Advanced extractor ion gauge with parallel-wired miniature CNT cathode spots.

The CNT layer deposition and the final assembly of the customized CNT cathodes have been contracted out. The CNT emitter spots were tested and showed sufficient emission current to be suited for the use in an extractor gauge at the expected extraction voltages. Preliminary measurements of the gauge characteristic show a higher gauge sensitivity compared to the former gauge design, as predicted by the numerical simulations.

References

[1] Rao, M. G.: Advances in Cryogenic Engineering Bd. 41, p. 1783 (1996).
[2] Lotz, M. *et al.*, GSI Report 2012, p. 263 (2013).
[3] Lotz, M. *et al.*, Proceedings of IPAC2014, p. 2320 (2014).
[4] Lotz, M. *et al.*, Vakuum in Forschung und Praxis (VIP) 27 (2015), p. 34 (2014) (in German).
[5] Lotz, M. *et al.*, GSI Report 2014, p. 515 (2014).
[6] Kirk, E. *et al.*, J. Vac. Sci. Technol. B 27, p. 1813 (2009).

DOI:10.15120/GR-2017-1

Study of SIS-18 spill structure by introducing external ripples

R. Singh, P. Boutachkov, P. Forck, P. Kowina, P. Schmid, A. Stafiniak, and H. Welker
GSI, Darmstadt, Germany

The slow extraction spill structure from SIS-18 suffers from ripples of the main magnet power supplies which results in a duty factor significantly below the theoretically achievable level given by the Poisson statistics. External ripples were introduced into dipole and quadrupole power supplies and their effect was observed in the spill structure in order to estimate the magnitude and frequency of inherent power supply ripples.

The duty factor within in the time period Δt of the spill is defined as,

$$F(\Delta t) = \frac{\langle N \rangle^2}{\langle N^2 \rangle} = \frac{\langle N \rangle^2}{\langle N \rangle^2 + \sigma^2}$$

where N is the particle count in each measurement bin δt and σ is the std. deviation. It can also be described as the ratio of "DC power" to total power in the spill frequency spectrum. In our measurements, Δt and δt were chosen 10 ms and 10 μs respectively. Figure 1 shows the change in the spill duty factor for bunched and unbunched beams as a function of ripple currents introduced in dipole and quadrupole power supplies at 137 and 177 Hz respectively. The frequencies were chosen such that no overlap happens with harmonics of 150 Hz inherently present in the power supplies. Bunched beams are known to be more robust to power supply ripples as explained in [1].

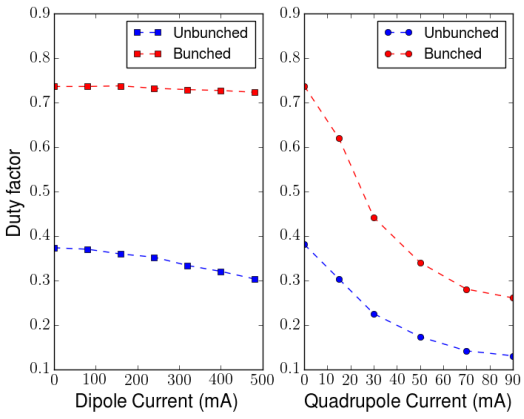

Figure 1: The change in duty factor for increase in ripple amplitude for dipole and quadrupole magnet power supplies.

The quadrupole ripples modulate the tune and therefore the stable phase space area at slow extraction and leads to a strong influence on the spill duty factor. Dipole ripples on the other hand affect the extraction process via change in dispersion and mean orbit which do not strongly translate into spill structure variations. Figure 2 compares the temporal variation of duty factor along the extracted spill

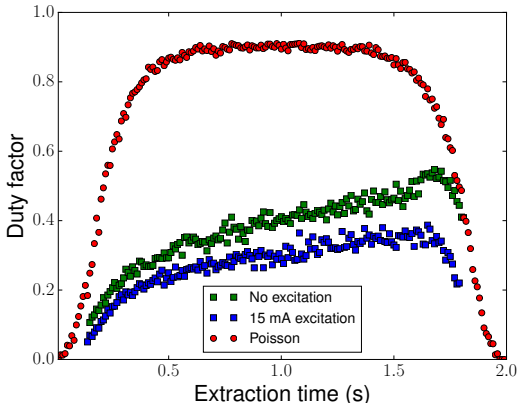

Figure 2: Duty factor of an unbunched beam with no excitation and 15 mA ripple introduced in the quadrupole.

for an unbunched beam without any excitation to the case with 15 mA ripple introduced in the quadrupole. It can be compared to the theoretical "Poisson spill" which also indirectly represents the actual extracted spill profile. Figure 3 shows the spectra of the spill in previous figure. The relative heights of peaks at 177 Hz and 600 Hz gives an estimate of inherent ripple of $\approx$ 5mA present at 600 Hz in the quadrupole power supply. Since the magnet current was set to 500 A at the time, the inherent ripple to total current ratio is 10^{-5}. The full scale dipole current is 3.5 kA and for quadrupoles is 1.75 kA.

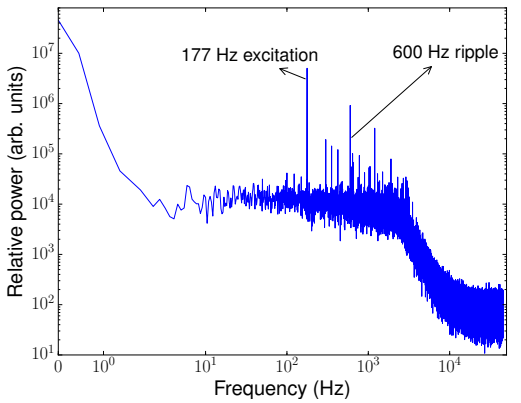

Figure 3: FFT of the spill with 15 mA ripple at 177 Hz introduced in the quadrupole for unbunched beam.

References

[1] P. Forck et al., Proceedings of EPAC 2000, Vienna, Austria (2000)

DOI:10.15120/GR-2017-1

Rf based bunch detection for position calculation in SIS-18

R. Singh, K. Lang, D. Lens, P. Forck, P. Kowina, and A. Reiter
GSI, Darmstadt, Germany

For the calculation of synchronous bunch-by-bunch transverse beam position in SIS-18, the temporal position of the bunches in the pick-up (PU) data stream has to be accurately identified. At present, a bunch detection method based on double threshold crossing of the PU data is used [1]. However, this data based bunch detection approach led to operational issues when the bunches were very short during proton operation (only 1 or 2 ADC samples) or when misformed bunches or unexpected amplifier spikes occur. To overcome these shortcomings, an rf frequency based bunch detection was attempted where the cable lengths and amplifier delays between PU cables and rf signal cables were matched.

The rf signal is strongly correlated to the PU signal due to the fact that bunches are formed as a result of cavity action. The rf cavity feedback system guarantees that the DDS source and cavity phases are precisely matched [2]. Usually the rf cavity signal is required by the BPM acquisition system to convert absolute time into units of synchrotron revolution turns. The signal paths from rf cavity and PUs to the acquisition system are shown in Fig. 1. The

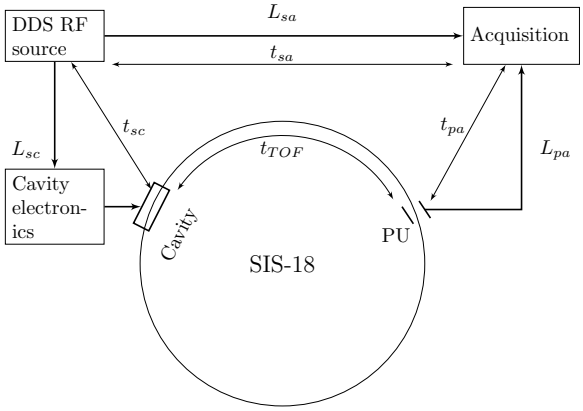

Figure 1: Principle of rf based bunch detection.

time difference Δt between the two paths is a function of rf frequency given by,

$$\Delta t(f_{rf}) = t_{sa} - (t_{sc} + t_{pa} + t_{TOF}) \quad (1)$$

where t_{TOF} denotes the time required by beam to traverse between cavity and PU and scales with beam velocity, t_{pa} and t_{sa} are the path delays between the components highlighted in Fig. 1 taking cables, amplifiers and switching electronics into account and t_{sc} represents the synchronous phase and phase ramp set by the control system. If represented in terms of the phase slip between the two paths,

$$\omega_{rf} \cdot \Delta t(f_{rf}) = \omega_{rf}(t_{sa} - t_{pa}) - \phi_{ramp} - \frac{\alpha \cdot h}{2\pi} \quad (2)$$

where $\alpha \in [0, 1]$ denotes the distance between cavity and the PU normalized to synchrotron circumference, h is the harmonic number. ϕ_{ramp} is assumed to be independent of rf frequency for SIS-18 ramp. However, since the rf frequency changes during acceleration ramp to account for increase in beam velocity, a linear frequency dependent phase slip is expected between rf signal and PU signal unless the condition $\omega_{rf}(t_{sa} - t_{pa}) = 0$ is satisfied. A fixed phase offset which is function of relative locations of cavity and PU denoted by α and frequency harmonic h in accordance to Eq. 2 needs to be individually set at each BPM.

The cavity rf ($h = 6$) for SIS-18 ramps from 850 kHz to 5 MHz. In our experiment, we varied the length mismatch between rf and PU signal cables to compensate the path delay mismatch in order to eliminate the phase slip as a function of frequency for a selected PU. Figure 2 shows

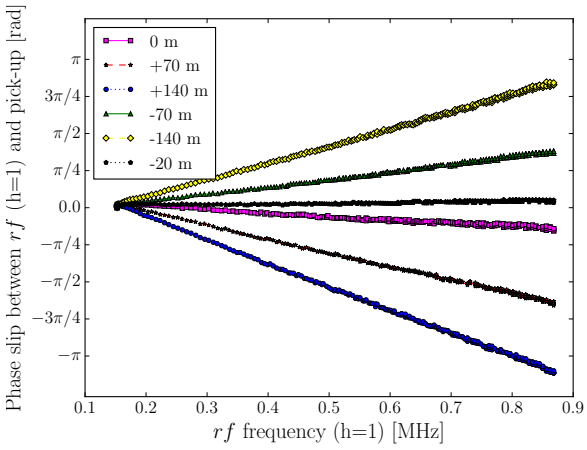

Figure 2: The measured phase slip as a function of frequency for different cable length variations.

the measured phase slip as a function of rf frequency for several variations of relative lengths of rf and PU cables ($t_{sa} - t_{pa}$). The phase slip was minimized when PU cable was appended by a 20 m cable. With this compensation in place, robust bunch detection independent of PU data deformations can be performed under most operational scenarious.

References

[1] U. Springer, "High resolution of betatron tune at SIS-18", PhD thesis, Goethe University Frankfurt (2010)

[2] B. Zipfel et al., Proceedings of IPAC14, Dresden, Germany (2014)

DOI:10.15120/GR-2017-1

Observation of SIS-18 spill structure by systematic parameter variations

R. Singh, P. Boutachkov, P. Forck, P. Kowina, and P. Schmid
GSI, Darmstadt, Germany

Typical slow extraction parameters such as chromaticity, momentum spread, sextupole strength and spill extraction length were systematically varied individually to see their effects of spill structure for the quadrupole driven resonance extraction.

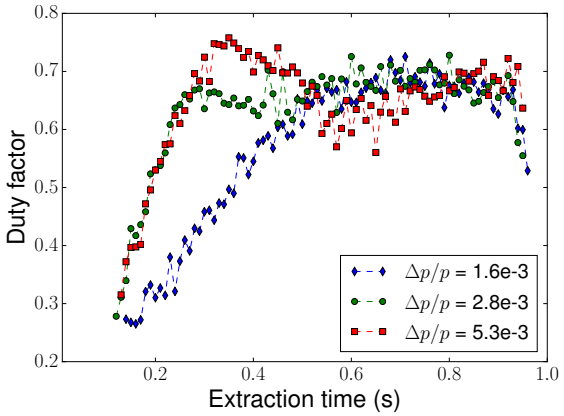

Figure 1: The effect on duty factor for change in momentum spread variation.

Chromaticity and momentum spread of the beam affect the spill structure via their effect on tune spread of the beam. A changed tune spread is not expected to have a significant effect on the spill duty factor for our extraction method where the tune of the beam is moved into resonance using fast quadruples. Thus, any power supply ripples will have a similar effect on the beam irrespective of tune spread. Figure 1 shows the duty factor [1] for three values of beam momentum spread confirming the assertion.

Figure 2 shows the duty factor along the extracted spill for various set sextupole strengths. A clear trend of spill structure improvement as a function of sextupole strength is seen. Figure 3 shows the corresponding spill spectra, where the high frequency components are seen to be drastically reduced for lower sextupole strength. The stable phase space area is inversely proportional to the sextupole strength, and therefore a smaller sextupole strength has two major effects countering the tune ripple. First, it reduces the ability of tune ripple from completely ”squeezing” the phase space area, and second, a larger stable phase space area corresponds to a larger range of transit times for the extracted particles i.e. the time between when they become unstable till the time when they exit the septum. These larger range of transit times are expected to suppress the effect of high frequency ripples on duty factor [2]. One should note that sextupole strength cannot be arbitrarily reduced since the resulting smaller ”spiral step” and ”spiral kick” would lead to higher losses in the septum. Further

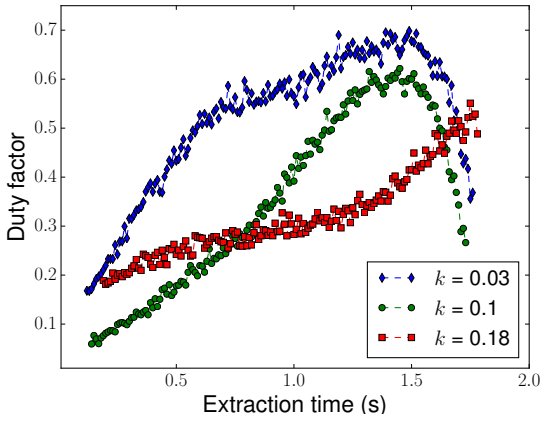

Figure 2: The change in duty factor for variation in sextupole strength. Note: The non uniform shape of duty factor curve do not represent the spill profile/structure.

simulation studies are required to understand these results.

Reduction of spill length is effectively a faster tune movement towards resonance and should reduce the the effect of ripples and improve the duty factor [2]. This was also clearly observed during the experimental campaign.

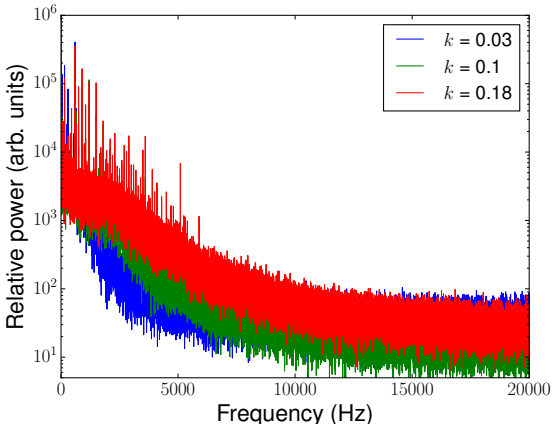

Figure 3: Spectra of the the spill data used in Fig.2.

The observations will be further studied by means of simulations to determine the relative importance of each parameter and obtain hints on their operational usage.

References

[1] R. Singh et al., Proceedings of this annual report (2017)

[2] “PROTON-ION MEDICAL MACHINE STUDY (PIMMS) PART I”,CERN/PS 99-010 (DI), Geneva (1999)

DOI:10.15120/GR-2017-1

DOI:10.15120/GR-2017-1

Super-FRS design status report

M. Winkler[*1], *S. Althoff*[1], *F. Amjad*[1], *K.-H. Behr*[1], *A. Bergmann*[1], *T. Blatz*[1], *E.J. Cho*[1], *W. Freisleben*[1], *H. Geissel*[1,2], *C. Karagiannis*[1], *A. Krämer*[1], *A. Kratz*[1], *J. Kurdal*[1], *H. Leibrock*[1], *H. Müller*[1], *G. Münzenberg*[1], *I. Mukha*[1], *C. Nociforo*[1], *S. Pietri*[1], *A. Prochazka*[1], *S. Purushothaman*[1], *M.V. Ricciardi*[1], *P. Rottländer*[1], *C. Scheidenberger*[1,2], *F. Schirru*[1], *C. Schlör*[1], *H. Simon*[1], *C. Schlör*[1], *P. Szwangruber*[1,3], *K. Sugita*[1], *F. Wamers*[1], *H. Weick*[1], *A. Wiest*[1], *J.S. Winfield*[1], *and Y. Xiang*[1]

[1]GSI, Darmstadt, Germany; [2]JLU Giessen, Germany

System design

The LEB cave could be integrated into the Civil Construction planning to its full extend which includes in particular the floor plan of the beam lines and their technical infrastructure as well as the arrangement of the various experimental areas. A rather short and thus cheap connection of the local cryogenic into the LEB could be found by linking it directly to the separator tunnel. This avoids to install the previously planned long cryo transferline into the supply building. In fact by introducing an additional distribution box in the LEB cave also a simplified and direct cryo connection from the LEB cave to the HEB Cave could be realized.

Magnets

During 2016 an extensive design phase of the SC multiplets was conducted. Our provider ASG Superconductors SpA, Genoa, concentrated on the design of the two pre-series multiplets (one short multiplet and one long multiplet). The long multiplet is the most complex cryo module and contains altogether 9 individual magnets including two types of quadrupoles with superimposed octupole coils, sextupole magnets, and y-steerer magnets. It has a total length of approximately 7 m, a diameter of almost 2.7 m and a total weight of 60 tons. In summer we could release the Preliminary Design Review (PDR) which included the complete magnetic design of all individual magnets, a manufacturing sensitivity analysis, a preliminary mechanical design, as well as the assembly concept. This design was then detailed and in beginning of December we could also release the Final Design Review (FDR) for the pre-series multiplet. The FDR included detailed calculation reports on all relevant subsystems, the quality assurance documentation, the 3D model and the main 2D drawings, a Factory Acceptance Test (FAT) Plan, and the report on already prepared mock-ups and specimen of various sub-components.

The technical documents for the superconducting dipole magnets were approved and also all further tender documents were established. At the time of writing this report the tender of these magnets is running (qualifying phase done already) and tender award is expected for end of 2017.

All revised remote connectors (water, power, etc.) of the radiation resistant pre-series dipole were taken into operation and tested successfully [1] such that the concept will be included into the design of all remaining radiation resistant magnets. The power dissipation of that magnet into air was tested once more in order to be able to finalize the technical infrastructure of civil construction planning (the total electrical power of all NC magnets in the heavily shielded target area tunnel is expected to be about 1 MW).

Local cryogenics

The technical discussions with our In-Kind provider (WUST, Wroclaw, Poland) were initiated. As a result the conceptual design of the feedboxes was modified such that we are turning towards a modularized design (see Fig. 1). In this case each cryo-module is operated by an individual feedbox which increases the feasibility for series production and thus reduces design effort and production time.

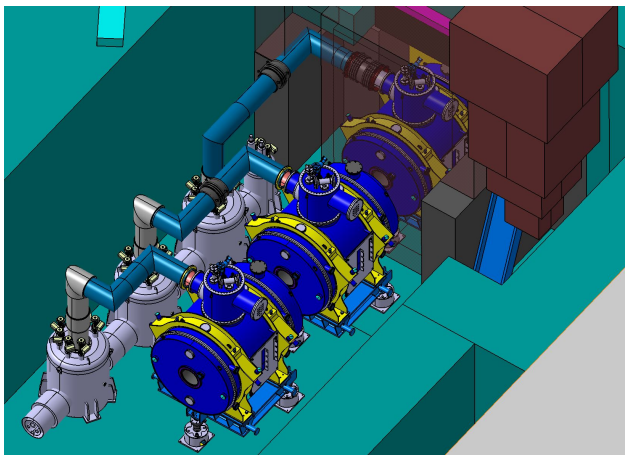

Figure 1: Each cryo-module is operated by an individual feedbox as shown for some short multiplets located in the Pre-Separator.

Beam instrumentation

The detailed specification for various types of detectors could be finalized and approved. This includes the SEM grids (beam profile monitors), the time-of-flight detectors (ToF), the energy-loss detectors (MUSIC) and the plastic

* m.winkler@gsi.de

DOI:10.15120/GR-2017-1

scintillates. For these systems the contract preparation with our In-Kind providers were initiated.

Several prototypes of various detector systems could be tested during the beamtime in 2016. This comprises in particular the GEM-TPC (tracking detector) including its corresponding read-out electronics [2] and silicon detectors which are intended to be used as ToF systems [3].

The slit systems are produced by our collaboration partner KVI-CART. The contract to manufacture 26 blocks of heavy tungsten alloy has been awarded to Plansee. Meanwhile all blocks have been produced and were delivered to KVI. Most of the remaining x-slit purchase parts have been ordered and the manufacturing of the x-slit series is continuing. The prototype of the y-slit has been manufactured, too, and the FAT test of this system is in preparation.

Vacuum

The vacuum system design has been detailed and is described in [4].

The specification of the SC dipole vacuum chambers as well as the specification of the focal plan chambers have been established. Altogether 20 focal plan chambers will be installed in the Super-FRS. These chambers contain all Super-FRS beam instrumentation such as various beam detectors, slit systems, degrader stations, etc. (Fig. 2 shows the focal plane chamber at FPF2, i.e. the midplane of the Pre-Separator). The chambers have a cross section of approximately 1x1 m^2 and a length of up to 4.5 m.

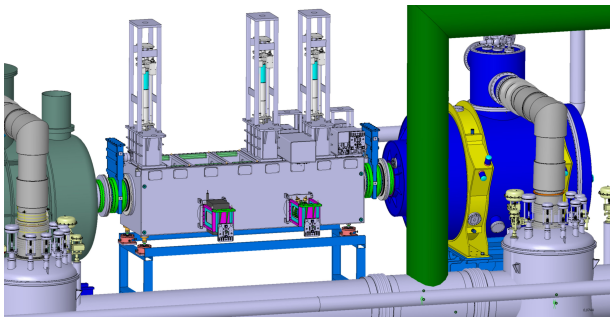

Figure 2: Focal plane chamber at FPF2 with some of its beam instrumentation inserts.

Target area / handling system

In summer 2016 we signed a collaboration contract with KVI-CART to design the Super-FRS target chamber and its plug inserts. A preliminary design of the target chamber is already available and shown in Fig. 3. The chamber will be approximately 2.1 m long and it will comprise five plug inserts including the production target which is a rotating carbon wheel. Each plug insert consists of a functional unit which is shielded to the top by a 1.6 m high iron block. The weight of one plug is up to 4.0 t.

All plug interfaces (electrical power, cooling water, etc.) are located on the top of the plug which will be accessible

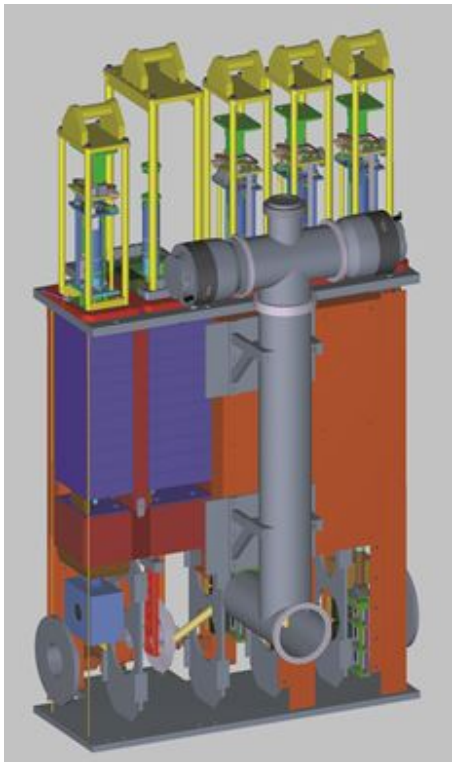

Figure 3: Preliminary design of the Super-FRS target chamber.

by a maintenance tunnel. Here also vacuum pumps will be placed which are coupled to the target chamber by a knee in backward direction to minimize the radiation level on the top of the chamber. The plugs will be inserted into the target chamber from the top by means of a special transport flask (not part of this work package) and must then be guided into the chamber. To demonstrate the feasibility of the plug-guidance system a 1:1 mock-up is in preparation, too. Another feature is the integration of a thermal imaging system for diagnostic purposes of the beam spot on the target. Basically it will consist of a mirror system which will guide the light out of the high-radiation zone where it will be coupled to an IR camera.

References

[1] H. Leibrock et al., “Upgrade of the prototype of a radiation resistant Super-FRS dipole to an operational FAIR-magnet”, this report

[2] F. Garcia et al., “Twin GEM-TPC Prototype (HGB4) Beam Test at GSI – a Tracking detector for the Super-FRS”, this report

[3] O. Kiselev et al., “Performance tests of the Si detectors for TOF beam diagnostics of the Super-FRS”, this report

[4] J. Kurdal et al., “Pressure simulation for the Super-Fragment Separator (Super-FRS) of the GSI future accelerator facility FAIR with various pumping configurations”, this report

DOI:10.15120/GR-2017-1

Upgrade of the prototype of a radiation resistant Super-FRS dipole to an operational FAIR-magnet

H. Leibrock, C. Mühle, T. Blatz, C. Will, A. Bergmann, R. Lotz, O. Zurkan and M. Winkler #
GSI, Darmstadt, Germany .

The areas after the production target of the Super-Fragment-Separator (Super-FRS) will be exposed by high radiation. Integral doses up to $2.8 \cdot 10^8$ Gy (mainly neutrons) within 20 years of operation are expected. Special magnets only consisting of non-organic radiation resistant materials like mineral insulated cables (MIC) must be used to ensure the functionality.

After the operation of the Super-FRS is started, direct access to the magnets is impossible because of the high radiation. Misalignment of the magnets due to settlement must be corrected with remote alignment of the adjustable support frame below the magnet. The remote alignment will be done per hand with rods and angle gears through a 1000 mm thick steel/concrete screen in a service tunnel above the magnets.

A prototype of a radiation resistant dipole has been made in cooperation with the Budker Institute in Novosibirsk [1] (Figure 1). It was successfully tested in the year 2009. The required field quality is achieved. The coils and the yoke of the magnet will withstand the hard conditions in the Super-FRS tunnel. Due to the results of the tests it was decided to use the prototype as one of the three necessary dipoles in the Super-FRS target area.

Figure 1: Prototype of the radiation resistant Super-FRS dipole after delivery to GSI.

Unfortunately not all parts of the prototype of the adjustable support frame below the magnet fulfil the requirements of radiation resistance and operability so a new adjustable support frame has been designed and manufactured (Figure 2). One important requirement besides the radiation resistance is that the adjustment in all directions must be possible with hand wheels. The required torque for adjustment in all directions must be less than 100 Nm. Three feet stand on a 3 m ×3 m baseplate. Roller bearings allow individual horizontal movements of each foot. The top of the feet are fixed on a steel support frame which carries the 90 tons magnet.

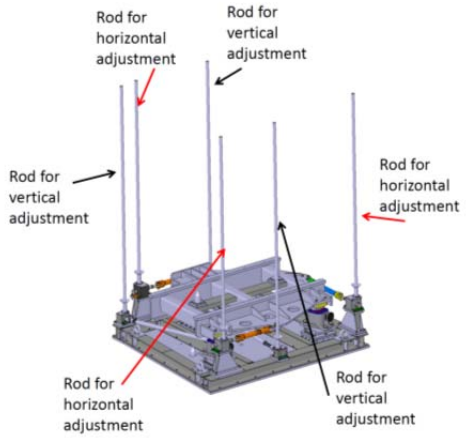

Figure 2: One adjustable support frame for one dipole with the six adjustment rods. This system allows an adjustment for all six degrees of freedom.

The horizontal movement is based on a three strut system. These three struts are connected on one side with an angle gear; the other side is fixed on the support frame (Figure 3).

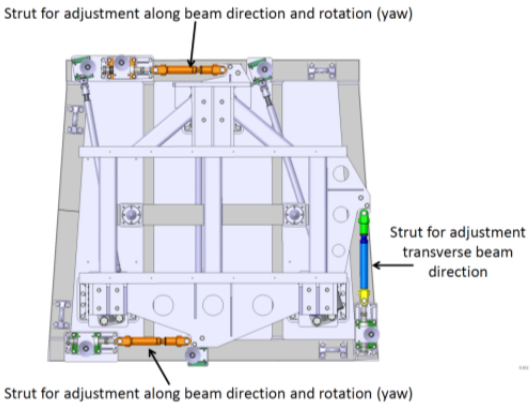

Figure 3: Top view on the support frame. A 3-strut system is used for horizontal adjustments.

The vertical adjustment is based on the principles of the feet of the prototype but with 100 % non-organic material. An angle gear and a gear inside each foot connected with a cardan shaft reduce the required torque for vertical movement to less than 100 Nm. It appeared that the combination of heavy weight (100 tons) and greaseless gears (grease is not radiation resistant) is still a challenge. But after several tests with different materials and coating the problems were solved.

In parallel to the work on the new adjustable support frame new connections for cooling water and electrical current have been designed and manufactured. Long term

DOI:10.15120/GR-2017-1

tests with the 100% powered magnet (140 kW) verified the full functionality of the new connections.

References

[1] C. Muehle et al., “Radiation Resistant Prototype Dipole for the First Stage of Super-FRS”, IEEE Trans. Appl. Supercond., vol. 22, p. 4003304, 2012

DOI:10.15120/GR-2017-1

Pressure simulation for the Super-Fragment Separator (Super-FRS) of the GSI future accelerator facility FAIR with various pumping configurations *

J. Kurdal[1], *A. Bergmann*[1], *and E. Renz*[1]
[1]GSI, Darmstadt, Germany

The Super-FRS will be the most powerful in-flight separator for exotic nuclei up to relativistic energies [1]. These calculations are mandatory to estimate the number of pumps, their pumping speed and the position in the Super-FRS [5].

Simulated Beamlines FMF1 - FMF2

The simulated beamlines consists of multiplet, dipole and focal plane chambers (Figure: 1).

Figure 1: Drawing from FMF1 - FMF2: From left to right, Multiplet, 3 Dipoles, Multiplet, Focal Plane Chamber, Multiplet, 3 Dipoles, Multiplet, and a Focal Plane Chamber.

The Simulation Software

For simulations Molflow+ [2] was used, which is a Test Particle Monte Carlo (TPMC) [3] Software. The code generates a total number of $N_{virtual}$ test particles, each of them represents the number of real particles.

$$K_{\frac{\text{real}}{\text{virtual}}} = \frac{\sum \mathrm{d}N_{\text{real}}/\mathrm{d}t}{N_{\text{virtual}}} \qquad (1)$$

The cosine law of Knudsen is applied as $ds = \frac{d\omega}{\pi} \cdot \Theta$, where ds is the probability that a molecule leaves the surface, $d\omega$ the solid angle and Θ the polar angle. Both angles can be generated in the following way: $\Theta = sin^{-1}\sqrt{r}$ and $\delta = r \leq 2 \cdot \pi$. Where δ is measured from x-axis in xy-plane in spherical coordinates. The random number **r** is uniformly generated in the real interval from (0,1). Fast gas molecules cross more frequently transparent **facets** [2] into the volume as slower ones [4]. If $f(v)_{(gas)}$ is the probability density function in volume (**pdf**), then it's possible to calculate the **pdf** of molecules colliding with the wall in a certain period $f(v)_{(coll)}$ [3,4].

$$f(v)_{coll} = f(v)_{gas} \cdot \nu \cdot C \qquad (2)$$

C is the normalizing factor (the integral of **pdf** must be unitary [4]). The following is obtained after a number of mathematical transformations and simplifications:

$$C = \frac{1}{f(v)_{(gas)}} \Rightarrow f(v)_{(gas)} = \sqrt{\frac{8 \cdot R \cdot T}{\pi \cdot m}} \qquad (3)$$

Results

The results diagrammed in (Figure: 2) reveal that both concepts should work for the Super-FRS (pressure in the range of 10^{-7} mbar is required). Momentary there are mechanical collisions with the 4 ion getter pumps between the multiplets (Figure: 2) blue (diamonds). At the moment 3 ion getter pumps with a pumping speed of 300 l/s each between the multiplets seems to be the best solution [5] (Figure: 2) red (dots).

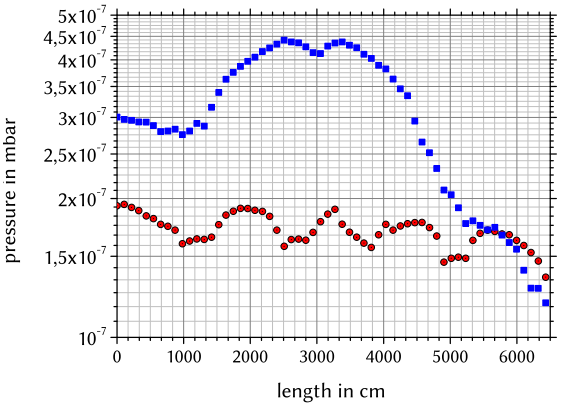

Figure 2: Pressure Profile from FMF1 - FMF2: Blue (diamonds) 4 IGPs between multiplets S=200 l/s per IGP, 1 TMP in the first focal plane and 2 in the second S=1000 l/s each. Red (dots) 3 IGPs between multiplets S=300 l/s per IGP and 1 TMP with S=1000 l/s per chamber.

References

[1] H.Geisel et al., Nucl.Instr. and Meth. in Phys.Res.B 204 (2003) 71-85

[2] M.Ady "Molflow+" https://test-molflow.web.cern.ch

[3] R.Kersevan, J. L. Pons, Journal of Vacuum Science Technology A 27, 1007 (2009)

[4] R.Kersevan, 13th IUVSTA School on Vacuum Gas Dynamics, Thessaloniki, Greece (2015)

[5] J.Kurdal, et al, 14th EVC, Portoroz, Slovenia (2016)

* PSP-Code: 2.4.7

DOI:10.15120/GR-2017-1

Twin GEM-TPC prototype (HGB4) beam test at GSI – a tracking detector for the Super-FRS

F. García[*1], *R. Turpeinen*[1], *J. Äystö*[1,2], *T. Grahn*[1,2], *S. Rinta-Anttila*[1,2], *A. Jokinen*[1,2], *B. Voss*[3], *J. Kunkel*[3], *V. Kleipa*[3],*H. Risch*[3], *C. Caesar*[3], *C. Simons*[3], *A. Prochazka*[3], *C. J. Schmidt*[3], *J. Hoffmann*[3], *I. Rusanov*[3], *N. Kurz*[3], *H.Heggen*[3]

[1]Helsinki Institute of Physics, University of Helsinki, 00014 Helsinki, Finland
[2]University of Jyväskylä, Department of Physics, 40014 Jyväskylä, Finland
[3]GSI Helmholtzzentrum für Schwerionenforschung, Darmstadt 64291, Germany

INTRODUCTION

The GEM-TPC detector will be part of the standard Super-FRS detection system, as tracker detectors at several focal diagnostic stations along the separator and its three branches.

GEM-TPC DETECTOR DEVELOPMENT

A group was created in 2009 for the development of a tracking detector to be located along the Super-FRS. Since then a series of prototypes were built and tested at GSI[1] The main requirements for the operation of those chambers are: close to 100% tracking efficiency at 1 MHz rates and position resolution less than 1 millimeter in the full acceptance on each diagnostic station. In order to, achieve such requirements a new configuration was proposed with two GEM-TPCs enclosed in one vessel; in such a way that one is flipped in the middle horizontal plane against the other one, thus the electric field of the field cages will be in opposite directions. Therefore, constraining the time of arrival of the hits in each GEM-TPC can drastically reduce the ambiguity of association of hits to a single track and therefore achieving the desired tracking efficiency.

BEAM TEST AT GSI & JYVÄSKYLÄ

The twin prototype 2 called HGB4-2, is shown in Fig. 1 was tested at GSI in cave S4 and in Jyväskylä.

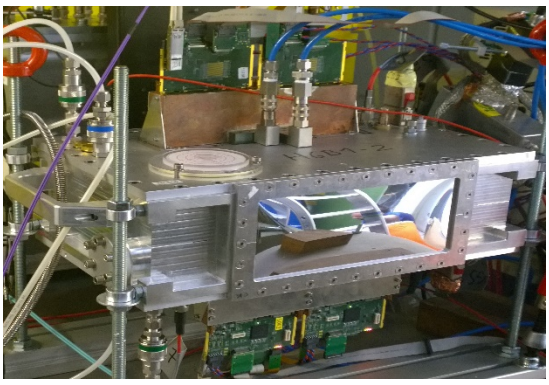

Fig. 1. Super-FRS GEM-TPC prototype HGB4, equipped with four GMX-NYXOR cards.

During these campaigns the readout system was the GMX-NYXOR cards, which contains two n-xyters chips to readout a total of 256 channels per card.

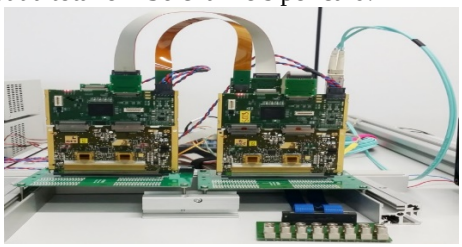

Fig. 2. The readout system GMX-NYXOR cards during testing in the laboratory.

Below is shown a correlation plot of the two GEM-TPCs X-axis projection of the HGB4-2 chamber.

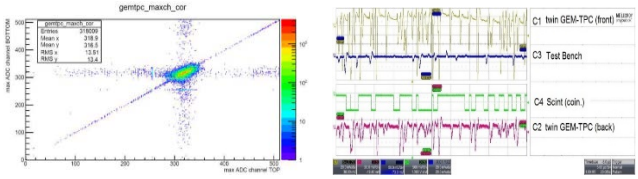

Fig. 3. Position correlation of the Top and Bottom GEM-TPCs of the HGB4-2 prototype for ^{124}Xe projectiles (left) and signals from the Bottom of both GEM #3 at 2.20 MHz rate under Protons at Jyväskylä.

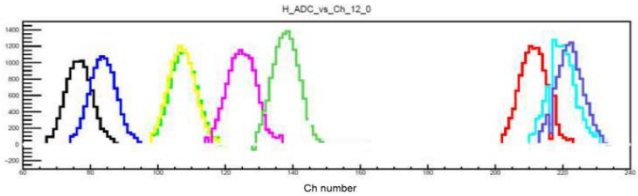

Fig. 4. Single clusters for primary ^{124}Xe @ 660 MeV/u beam.

Results from the test Beam campaign at Jyväskylä and GSI has shown that twin GEM-TPC (HGB4-2) has operated very stable in continuous mode and the concept has been proven to be the final one.

REFERENCES

[1] F. Garcia et al., 2011 IEEE Nuclear Science Symposium conference record, ISSN: 1082-3654, pp. 1788-1792.

DOI:10.15120/GR-2017-1

Performance tests of the Si detectors for TOF beam diagnostics of the Super-FRS*

O. Kiselev[1#], A. Bezbakh[2,3], N. Egorov[4], I. Eremin[5], V. Eremin[5], N. Fadeeva[5], A. Fomichev[2], M. Golovkov[2], S. Golubkov[4], A. Gorshkov[2,3], C. Konkov[4], D. Kostyleva[1,2,6], S. Krupko[2,3], D. Mitina[5], C. Nociforo[1], R. Slepnev[2], P. Sharov[2], Y. Tuboltsev[4] and E. Verbitskaya[5]

[1]GSI, Darmstadt, Germany; [2]JINR, Dubna, Russia; [3]FSBI NRC "Kurchatov Institute" - ITEP, Russia; [4]Research Institute of Material Science and Technology, Zelenograd, Russia; [5]Ioffe Institute, St. Petersburg, Russia; [6]JLU Giessen, Germany

The Time of Flight (ToF) information about the heavy-ion beam is one of the key aspects for the successful ion identification. It is also true for the Super-FRS setup and it's ToF system being designed now. The key parameter of the ToF system is the time resolution ≤30 ps (rms) for the ^{238}U ions. The active area of the largest station should be up to 380 x 60 mm^2 requiring the size of individual sensors to be at least 60 x 60 mm^2. In addition, similar detectors are needed for the experiments within the project EXPERT (EXotic Particle Emission and Radioactivity by Tracking) which is a part of the physics program of the Super-FRS Experiment Collaboration [1]. These experiments are aimed at studies of the unknown exotic nuclear systems beyond the proton and neutron drip-lines and will use the first half of the Super-FRS as a radioactive beam separator and its second half as a high-resolution spectrometer. The ToF information on the secondary ion beam and triggering on certain ion type will absolutely be required.

In summer 2016 a beam test of the few Si strip detector prototypes has been performed using ^{124}Xe and ^{12}C at energy of 600 MeV/u beams. One prototype had an active area 64 x 64 mm^2 and the strip pitch of 1 mm (Fig. 1).

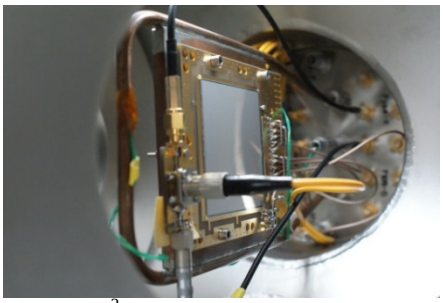

Figure 1: Photograph of the Si strip detector in the vacuum chamber. The small Si pad detector and the fiber-optic cable mounted on the top of it are also visible.

The second prototype had the same strip length but a different strip topology - the strips were arranged in 3 groups of 5 strips in each – with the pitch of 1 mm (2 groups with different width of interstrip gap) and one group with 1.5 mm pitch. A thickness of each detector was 300 µm. A quadrant detector built with 4 pads of 5x5 mm^2 each, was used as a start detector.

In addition, a thin scintillator detector LOS read out by 4 PMTs was provided by the R3B group as a reference start detector. One small Si pad detector illuminated by the red laser via the fiber-optic cable was also mounted for controlling the readout electronics based on the PADI-6 [2] preamplifier/discriminator and FPGA TDC VFTX2.

The time resolution of the large detector prototype has been already measured with U and Au ion beams; this time the main goals were the measurement of the ToF resolution with lighter ions beams, plus testing a different strip topology and confirmation of the previous measurements with U ions. More details about the detectors and setup can be found in [3].

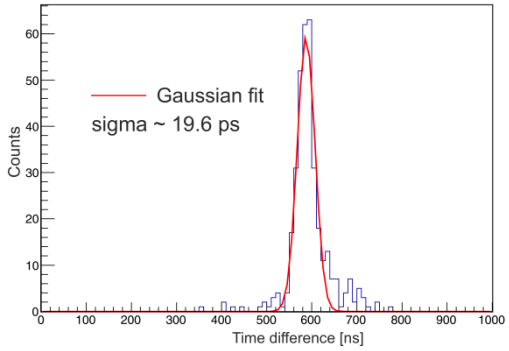

Figure 2: TOF resolution of the Si strip detector with ^{124}Xe beam.

The measured time resolution of the full-size detector prototype with Xe beam was close to 20 ps, including the resolution of the quadrant detector. This fully satisfies the requirements to the ToF system of the beam diagnostics of the Super-FRS. The analysis of the ^{12}C run is still in progress. It is already clear that the time resolution with ^{12}C beam will be worse due to the lower signal to noise ratio. This is not a real problem because the light ions identification is much easier and the requirements to the detector systems are not so severe as in the case of heavy ion beams.

References

[1] J.Aysto et al., NIM B376 (2016) 111.
[2] M. Ciobanu et al., *IEEE Trans. Nucl. Sci.* **61**(2014)1015.
[3] V. Eremin et al., *2017 JINST 12 C03001.*

*Work was carried out with partial support by RSF (project No. 17-12-01367), A.B., A.G. and S.K have been also supported by FAIR-Russia Research Center.
#o.kiselev@gsi.de

Implementation and test of a setting generator for the GSI fragment separator FRS in the LHC Software Architecture LSA*

J.P. Hucka[1,2], J. Enders[1], J. Fitzek[2], H. Huether[2], H. Liebermann[2], D. Ondreka[2], S. Pietri[2], and H. Weick[2]

[1]TU Darmstadt, Darmstadt, Germany; [2]GSI, Darmstadt, Germany

The LSA [1] framework from CERN is used to implement a new control system for accelerators and beam transfers. The fragment separator FRS [2] and - at a later stage - also the superconducting fragment separator Super-FRS at FAIR will be controlled within this framework. The challenge posed by the implementation of the control system for the FRS arises from the interaction of the beam with matter in the beamline and the beam's associated energy loss. This energy loss is determined using input from ATIMA [3] and has been included into the code of the LSA framework. The implemented setting generator was simulated and benchmarked by results of earlier measurements.

Benchmark Setup

The Benchmark was performed with data from the beamtime in October 2014 with 2 beam fragment settings and ^{238}U $^{73+}$ as the primary beam with an energy of 1 GeV/nucl. The used fragment settings are as follows:

- ^{238}U $^{92+}$ on a Cu-target with $90(2)$ mg/cm^2 at TA and degrader with 4200 mg/cm^2 at S2
- ^{134}Te $^{52+}$ on a Be-target with $6333(1)$ mg/cm^2 and Nb-Stripper with $233(1)$ mg/cm^2 at TA and degrader with 4200 mg/cm^2 at S2

Detectors (ionisation chambers, multi wire proportional chambers, TPCs and scintillators) were also taken into account at the positions of S2 and S4. TA means FRS target area, S2 and S4 mean middle and final focal plane respectively.
From given focussing strengths of quadrupole magnets and bending angles of dipole magnets the resulting currents for every single ion-optical element was calculated and compared to the experimental value and the calculated value of the simulation software LISE++ [6].

Results: Simulation vs. Experiment

From the given parameters the resulting values of magnetic rigidity Bρ and current I are used to find the relative deviation from the experimental values. Uncertainties in the calculation are only given by the uncertainty of the thickness of the different targets. It gives the biggest contribution to the resulting energy-loss calculation and delivers a relative deviation in the order of 10^{-5}. The beam energy was taken as given without uncertainty. Other input parameters were taken from MIRKO [7] with the inherent uncertainties, which was negligible.

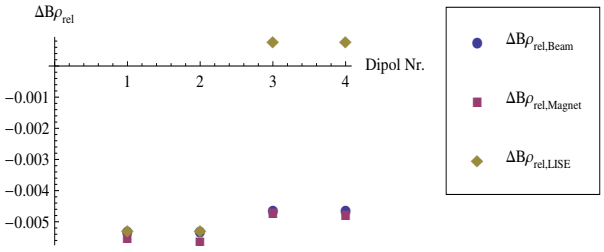

Figure 1: $\Delta B\rho_{rel}$ for $^{238}U^{92+}$ setting

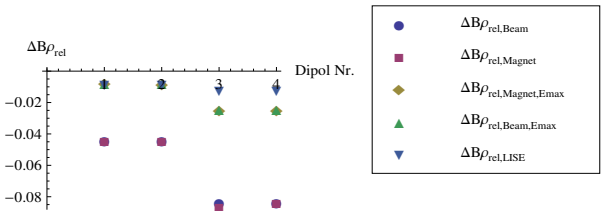

Figure 2: $\Delta B\rho_{rel}$ for $^{134}Te^{53+}$ setting

Conclusion

The machine model was benchmarked in the LSA framework with experimental data, which showed that LSA is better or in accordance with LISE++ calculations for single particle beams, whereas for beams containing secondary particles from fragmentation reactions, the quality of LSA suffers as there are no nuclear reaction models implemented which help the adjustment of the ion optical elements.

References

[1] M. Lamont et al., LHC Project Note 368
[2] H. Geissel et al., NIM B 70, 286 (1992)
[3] H. Weick et al., NIM B 164/165 (2000) 168
[4] J. Lindhard, A.H. Soerensen, Phys. Rev. A53 (1996) 2443
[5] J.F. Ziegler, J.B. Biersack, U. Littmark, The Stopping and Range of Ions in Solids, Vol.1, Pergamon Press (1985)
[6] LISE++ home page, http://lise.nscl.msu.edu/lise.html
[7] B. Franczak, simulation programme MIRKO, GSI Darmstadt. Siehe auch http://www-linux.gsi.de/~redelbac/MIRKO/.

* Work supported by HIC for FAIR and BMBF (05P15RDFN1).

DOI:10.15120/GR-2017-1

Design and production of klystron modulators for the pLINAC

S. Pütz, A. Schnase, G. Schreiber
GSI, Darmstadt, Germany

The pLINAC will be driven by seven identical klystron amplifier systems, each supplying the RFQ and CH accelerating structures with up to 2.5 MW of unsaturated RF-power [1].

Klystron modulators have been designed at GSI to generate pulsed high voltage for the klystron cathode. At their nominal operating point (-115 kV, 54 A, 4 pulses per second), the modulators produce a useable flat-top width of 360 µs (1% droop).

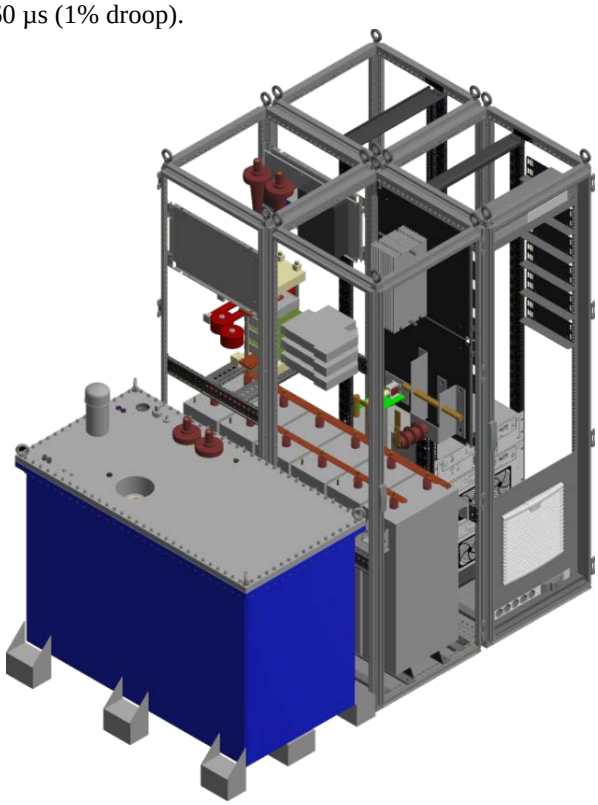

Figure 1: Electromechanical system layout

The modular construction of the power train with simple, well defined interfaces between function blocks provides excellent interchangeability. Components from alternative sources can be easily substituted, should the original component become obsolete or otherwise unavailable over the course of the operational life of the system. Function blocks of the pulse forming system are built from commercial off the shelf components.

Figure 2 shows the principal system structure of the klystron modulator. A capacitor charger supplied from 400 V mains recharges the capacitor bank between pulses to a user-defined voltage. The semiconductor switch assembly generates the output pulse and protects the klystron load in the event of internal arcing.

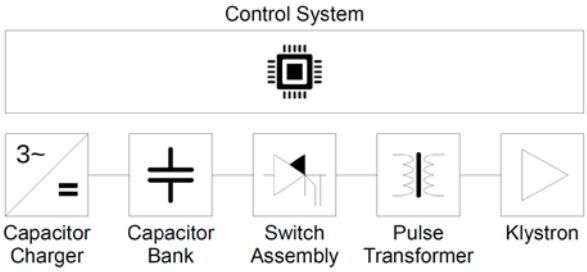

Figure 2: Function block diagram

The pulse transformer sets the intermediate voltage level of the pulse forming system to approx. 3.6 kV, an operating point at which cost optimal power semiconductor devices are available. Its parasitic series inductance limits the rate of rise of current in case of a load short circuit (i.e. klystron arc).

The control system consists of a PLC in combination with in-house designed fast analogue and digital electronics to control the switch assembly and implement active load protection.

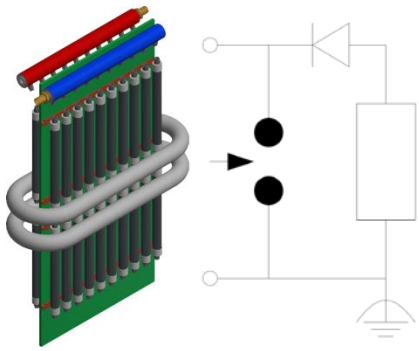

Figure 3: Resistive test load (left);
Arc simulator equivalent circuit (right)

A resistive test load has been designed to replace the klystron during the commissioning phase. A triggered spark-gap simulates a klystron arc which allows practical evaluation of the modulator's load-fault protection performance.

Component procurement for the prototype system is ongoing. Commissioning of the prototype is planned for 2018. Pending successful operation in the GSI RF test stand [2], the series production will follow with the first of series device anticipated ready for installation in the pLINAC building in 2020.

References

[1] "Detailed Specification on the FAIR pLINAC RF Systems", F-DS-RF-01e, 2012

[2] "Progress of the 325 MHz Rf Test Stand at GSI in 2015", FG-GENERAL-25, 2016

DOI:10.15120/GR-2017-1

Status of the modulated 3 MeV, 325 MHz Ladder-RFQ*

M. Schuett†, *U. Ratzinger, and M. Syha*
IAP, Frankfurt, Germany

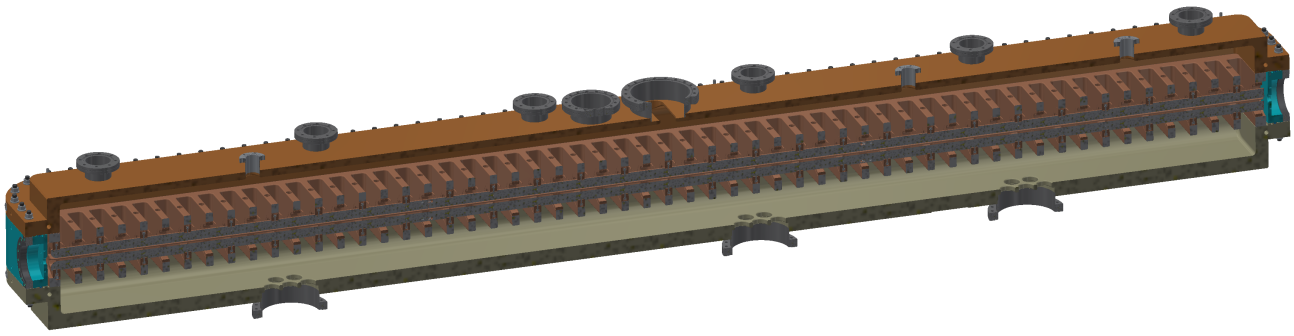

Figure 1: Isometric view of the 3.3 m modulated Ladder-RFQ prototype. The copper carrier-rings guarantee the electrode positioning as well as the RF contact. The ladder structure consists of bulk copper components. Any brazing or welding processes were avoided for the assembly of the main components. For more details cf. [1]. The successful high power tests of the unmodulated prototype motivated the development of a new beam dynamics with an increased electrode voltage of 96 kV [2].

Abstract

Based on the positive results of the unmodulated 325 MHz Ladder-RFQ from 2013 to 2016, a modulated 3.3 m Ladder-RFQ (s. Fig. 1) is currently under construction and will be tested with beam at GSI FAIR, Darmstadt. The 325 MHz RFQ is designed to accelerate protons from 95 keV to 3.0 MeV according to the design parameters of the p-linac at FAIR. The basic design and tendering of the RFQ has been successfully completed in 2016.

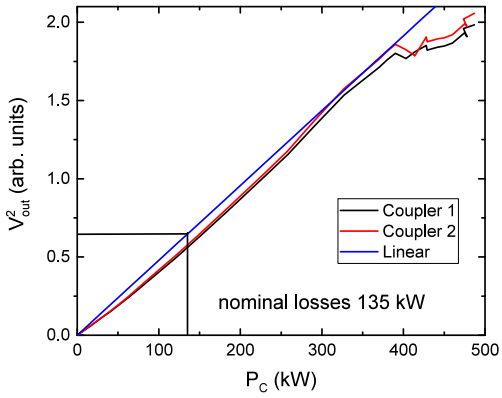

Figure 2: Results of the high power tests of the unmodulated prototype. The forward power up to 487 kW is shown in black. The RFQ accepted the power as the reflected power is stable along the flat top being lower than 3.34 kW.

* Work supported by BMBF 05P12RFRB9, 05P15RFRBA.
† schuett@iap.uni-frankfurt.de

High Power Measurements of the unmodulated Prototype

At the GSI 325 MHz klystron test stand the unmodulated Ladder-RFQ prototype with an electrode length of 630 mm was tested with a forward power up to 487 kW (s. Fig. 2) [3]. That exceeds the designed RF power at an electrode voltage of 80 kV during normal operation by a factor of 3.6. The averaged power reached 200 W, which is about 50% more than the thermal loss during normal operation.

Conclusion

All measurements of the unmodulated Ladder-RFQ such as frequency spectra, tuning, field flatness are in a good agreement with the simulations. The vacuum properties and pump ability has been verified. The design and construction of a full length modulated Ladder-RFQ, which will be tested with beam at GSI, is currently on-going. The completion of manufacturing is aimed until the end of 2017, to be ready for first RF tests in early 2018.

References

[1] M. Schuett, M. Obermayer, U. Ratzinger, M. Syha "Status of the modulated 3 MeV 325 MHz Ladder-RFQ", Proc. of IPAC2017.

[2] M. Syha, M. Obermayer, U. Ratzinger, M. Schuett, "Beam Dynamics for a high Current 3 MeV, 325 MHz Ladder-RFQ", Proc. of IPAC2017.

[3] G. Schreiber, E. Plechov, J. Salvatore, B. Schlitt, A. Schnase, M. Vossberg, "First High Power Tests at the 325 MHz RF Test Stand at GSI", Proc. of LINAC2016, East Lansing, USA, p. 3745.

DOI:10.15120/GR-2017-1

Beam Position Monitor design for the FAIR proton Linac

T. Sieber[1], P. Forck[1], W. Kaufmann[1], M. Almalki[2], C. Simon[3] and A. Bechtold[4]
[1]GSI Darmstadt, Germany; [2]KACST, Riyadh, Saudi-Arabia; [3]CEA, Saclay, France; [4]NTG, Gelnhausen, Germany

In order to achieve a significant intensity increase in the FAIR antiproton chain, the planned FAIR proton Linac will deliver a 70 mA, 70 MeV proton beam with a repetition rate of max. 4 Hz for injection into the SIS18 synchrotron. The 30 m Linac consists of an RFQ, followed by a number of cross-bar H-mode cavities (CH), which are partially combined to doublets, mechanically as well as rf-wise [1].

A key diagnostics for beam alignment during commissioning and also for verification of reproducibility during standard operation is an arrangement of 15 beam position monitors (BPM), which are distributed along the beamline. Nine of them are so-called 'inter-tank' versions (s. fig. 1), designed to be mounted directly to the magnetic triplet housings in between the CH tanks, while the other six are regular 'beamline' BPMs with CF100 flanges for the HEBT section. Both BPM types comprise four button-type capacitive pickups.

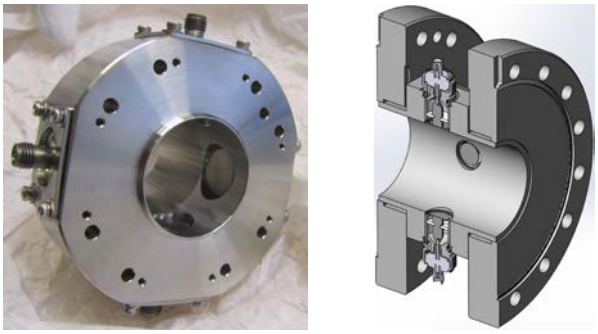

Figure 1: Left: inter-tank BPM prototype (tube radius 15 mm), right: beamline BPM (tube radius 25 mm).

A prototype of the inter-tank version has been built at CEA, using buttons from Kyocera. After extensive simulations [2, 3], and lab tests at GSI, a new button type was developed together with NTG company. The main difference between this button and the so far considered buttons (Kyocera, VACOM) is - besides the smaller button diameter of 12 mm instead of 14 mm - the conical increase in diameter of the inner conductor, starting directly at the SMA type rf-feedthrough.

Figure 2: Button pickup from NTG. Diameter 12 mm, gap width between button and housing 1.5 mm.

This type of geometry leads to a less drastic impedance jump at the position of the button, where the 50 Ω geometry is - unavoidably - no longer preserved. To investigate the effect of this change, time domain reflector (TDR) measurements were performed and compared to earlier results. Figure 3 shows the result of such a TDR measurement.

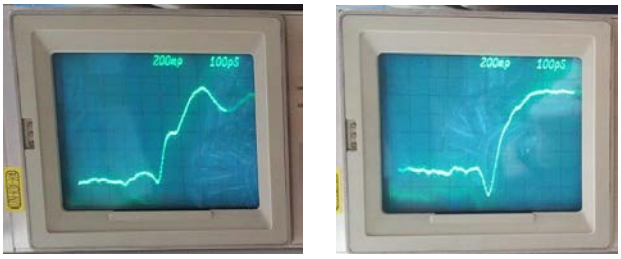

Figure 3: TDR measurements. Left: NTG, right VACOM.

The TDR shows that the new button has a significantly smaller reflection at the button position (negative peak in the curve). At the same time it seems to be more prone to oscillations, which probably derive from the smaller capacitive load.

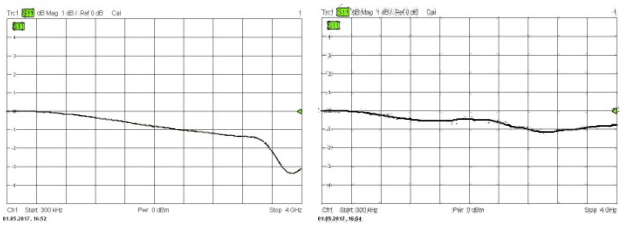

Figure 4: NWA measurement of S_{11}. Left NTG, right VACOM (scaling 1dB/div, span 300 MHz to 4 GHz).

To investigate the frequency range of these oscillations, both buttons were connected to a network analyzer and S_{11} was measured. Figure 4 shows again the comparison between the two buttons. In the frequency range below 3 GHz they show quite similar behavior, while above this value the NTG button has stronger return loss. Since the given measurement range is < 3 GHz, oscillations above this value are considered to be non-critical.

References

[1] L. Groening et al., "Status of the FAIR 70 MeV Proton LINAC", LINAC 2012, p. 927 (2012)
[2] C. Simon et al., "Numerical calculations for the FAIR Proton Linac BPMs", IBIC'14 (2014)
[3] M. Almalki, PhD Thesis, IAP, University of Frankfurt, 2016

DOI:10.15120/GR-2017-1

Status of CH-Cavity Design for the FAIR p-Linac

Ali M. Almomani[#1], Marco Busch[1], Ulrich Ratzinger[1] Carl M. Kleffner[2] and Florian D. Dziuba[2]
[1]IAP – Frankfurt University, Germany, [2]GSI – Darmstadt, Germany

Abstract

The FAIR proton linac will serve as an injector to provide a 70 mA, 68 MeV proton beam. The main acceleration will be performed by six room temperature "Crossbar H-type" CH-cavities which will be operated at 325 MHz. The beam dynamics had been revised by IAP – Frankfurt in collaboration with GSI-FAIR in Darmstadt to further optimize the design. This step was followed by cavity RF design. The mechanical cavity design will begin in 2017, while the quadrupole lenses are under production already. In this paper, an overview of the cavities RF design with integrated focusing triplets will be a main focus.

FAIR Proton Linac

The main accelerator section in the proton linac consists of six room temperature “Crossbar H-type” CH – cavities operated at 325 MHz. Figure 1 shows an overview of the proton linac from the RFQ exit down to the end of the last CH cavity.

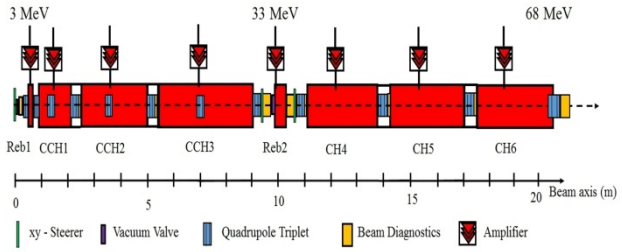

Figure 1: An overview of the FAIR proton linac from the RFQ exit down to the last CH cavity including the positions of the triplet quadrupoles, diagnostics and vacuum elements.

The CH – cavities consist of two sections: the first one is composed of three coupled CH – cavities (CCH1, CCH2 and CCH3) that will accelerate the beam from 3.0 to 33 MeV. The second part will be the high energy section-which consists of three lens-free CH – cavities. This helps to simplify the mechanical design and to tune the cavities besides reducing the total cost.

The main parameters of the CH – cavities are summarized in Table 1.

All cavities have been designed in order to fulfill the revised beam dynamics [1]. This includes the number of gaps, voltage distribution, coupling cell lengths, additional spaces for diagnostic and vacuum elements and the total length.

The Coupled CH – Cavity CCH2

As an example for the cavity RF design, the final layout of the second coupled cavity (CCH2) is presented here. Figure 2 shows a 3D – view on the cavity.

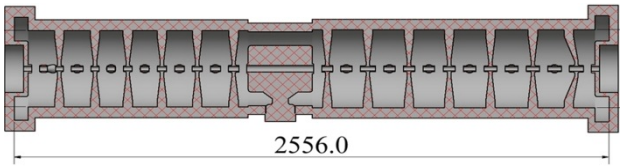

Figure 2: A cross sectional view on the second coupled CH – Cavity.

Table 1: Main Parameters of the FAIR Proton Linac CH – Cavities at 75 mA operation.

Cavity	L (m)	P_{tot} (MW)	Z_{eff} (MΩ/m)	Energy (MeV)	Gap No.
CCH1	1.44	1.33	53.5	3.0 - 9.9	21
CCH2	2.56	1.87	53.2	9.9 - 21.1	27
CCH3	3.66	1.92	44.6	21.1 – 33.0	30
CH4	2.67	2.14	42.4	33.0 - 44.6	20
CH5	3.02	2.12	38.5	44.6 - 56.3	20
CH6	3.31	2.06	36.7	56.3 – 68.0	20
Magnetic Quadrupole Triplets					
Effective Length (mm): 2 units 10 units				38, 60, 38 52, 95, 52	
Effective Gradients (T/m)				45 – 62	
Aperture Diameter (mm)				30	

The rf simulations have shown that an effective coupling is achieved with this geometry as shown in Figure 3.

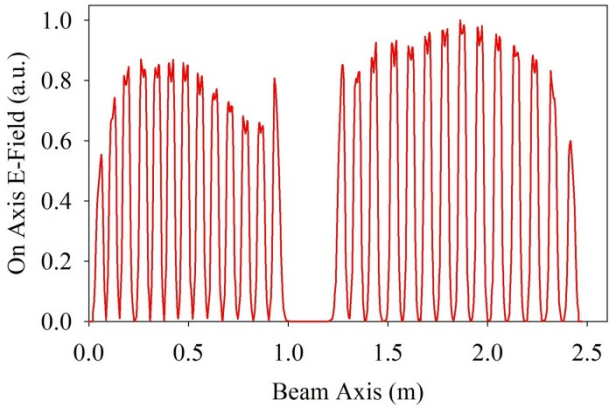

Figure 3: On axis electric field for the second coupled cavity.

Similarly, the final layout for the cavities has almost been finished and the results will be used as the basis for the mechanical layout and cavity construction [1].

References

[1] R. Tiede et al., Proceeding of LINAC16, East Lansing, MI, USA, MOPRC018 (2016).

[2] A. Almomani et al., Proceeding of IPAC17, Copenhagen, Denmark, TUPVA064 (2017).

[#]a.almomani@iap.uni-frankfurt.de

DOI:10.15120/GR-2017-1

Developments for the CR stochastic cooling system

C. Dimopoulou, R. Böhm, M. Bräscher, R. Hettrich, J. Krieg, C. Peschke, A. Stuhl, and S. Wunderlich
GSI, Darmstadt, Germany

Further progress was made in 2016 on in-house developing, engineering and testing for the demanding CR stochastic cooling system in the frequency band 1-2 GHz.

Cryogenic pickup with plunging electrodes

The first metallised ceramic (Al_2O_3) electrode plates have been delivered and tested (Fig. 1), confirming the demanding manufacturing concept. A redesign in-house is now necessary so as to ease the mechanics and reduce the cost of the series.

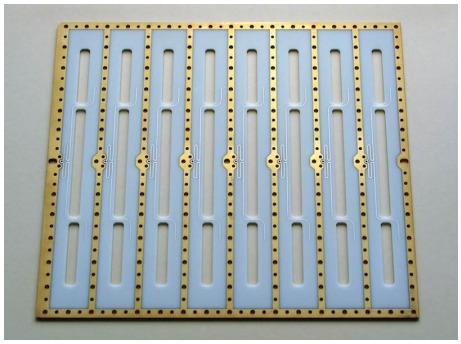

Figure 1: Prototype slotline electrode plate (signal side).

Progress was made towards an improved concept for the critical plunging Ag/BeCu sheets (geometry, manufacturing process). The pure BeCu sheets now sustain several million cycles in the test. Intensive optimization of the silver-plating procedure with the company is underway in order to reach such reliability with the $\approx$ 80 μm Ag layer on the BeCu sheets.

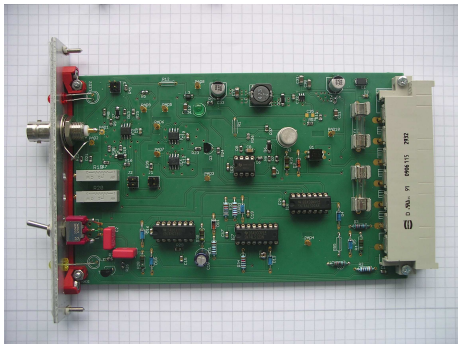

Figure 2: In-house designed comparator electronics ensuring the interlock function in case of over-acceleration of the motor drive units.

In the special chamber for testing motor drive units under pre-vacuum conditions, at room temperature, one linear motor drive unit with the dummy weight of the electrode module was mounted and tested in all 3 possible orientations of movement i.e. horizontal, vertical upwards, vertical downwards. In each case, appropriate springs have thus been specified, the static forces have been measured and benchmarked against theoretical calculations and the corresponding real-time code for the module movement was finalized. Special care is taken for machine protection and personnel safety (e.g. against mechanical crushing): The signal from the accelerator sensor mounted on the motor drive unit is fed into a specially designed comparator (Fig. 2). If the acceleration is beyond a specified range, the comparator initiates an emergency function of the servomechanism of the motors. The latter switches off the electrical power of the motor unit within 4 ms.

RF signal processing components 1-2 GHz

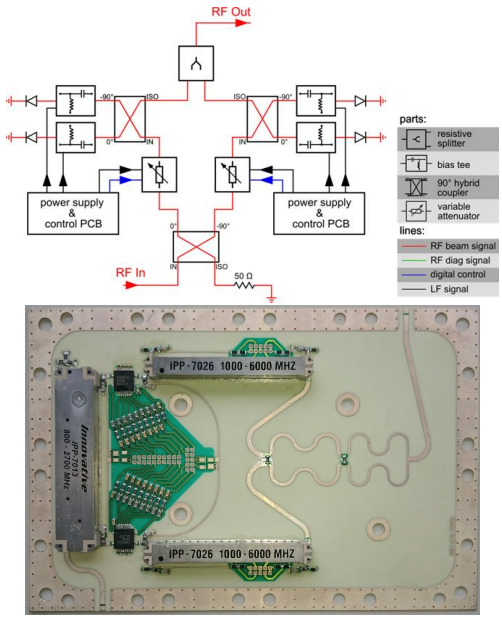

Figure 3: Block diagram and prototype RF PCB of the variable phase shifter.

The in-house design of demanding RF components has been continued: The pickup module controller and the versatile power supply and control unit are under development. The series of variable attenuators has been ordered. A functioning prototype of the variable phase shifter is now

DOI:10.15120/GR-2017-1

available (Fig. 3). The measured data show that the critical values: constant signal delay (1.818 ns $\pm$ 7 ps), high phase resolution ($< 1^0$), minimal phase distortion ($< \pm 3.5^0$), flat amplitude response and fast rampability (>10 kPoints/s) are within acceptable limits. Therefore, the device is only a small imperfection to the signal path.

The preseries unit (mw power 250 W in the 1-2 GHz band, water cooled) of the ordered power amplifiers at the kickers has been tested. The device demonstrates the design concept, nicely complies with the demanding RF properties and the full electrical specification (Fig. 4). However, it is not reliable for long-time operation and not yet mature for series production. Improvements are under way at the manufacturer to meet these reliability goals. A new round of factory and site acceptance tests is planned in 2017.

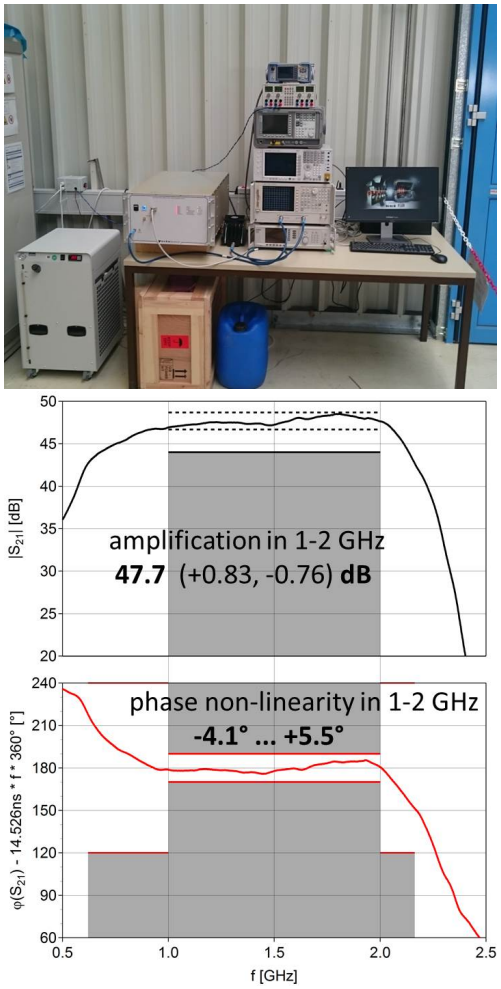

Figure 4: SAT (Site Acceptance Test) of the prototype power amplifier at GSI: test set-up and measured amplitude and phase response compared with the specification.

Expected stochastic cooling performance

New simulations of the stochastic cooling performance for the most demanding case of 10^8 antiprotons at 3 GeV in the CR have been performed taking into account the finalized lattice parameters and the realistic response of the designed slotline electodes. Cooling in all 3 phase space planes, with constant power gain of 150 dB in the longitudinal plane (notch filter momentum cooling with the pickups in sum mode) and constant power gain of 138 dB in both transverse planes (horizontal and vertical betatron cooling with the pickups in difference mode) has been studied, assuming no plunging of the pickup electrodes (Fig. 5). Already with the simple pessimistic assumption of constant transverse gain and no pickup plunging, simultaneous cooling in all 3 planes for 10 s leads to phase space quality close to the design limits for the HESR downstream.

Plunging the pickup electrodes reduces the diffusion in all 3 phase space planes from the beginning. The final emittances and momentum spread are lower by a factor 2-3 compared to the non-plunging case.

Therefore, the demanding pbar momentum spread budget between CR and HESR should be within reach by optimizing the interplay among the long. and transv. cooling in the CR and the rebunching/debunching procedures of the transfer. However, longitudinally there seems to be no safety margin, the high power requirement remains.

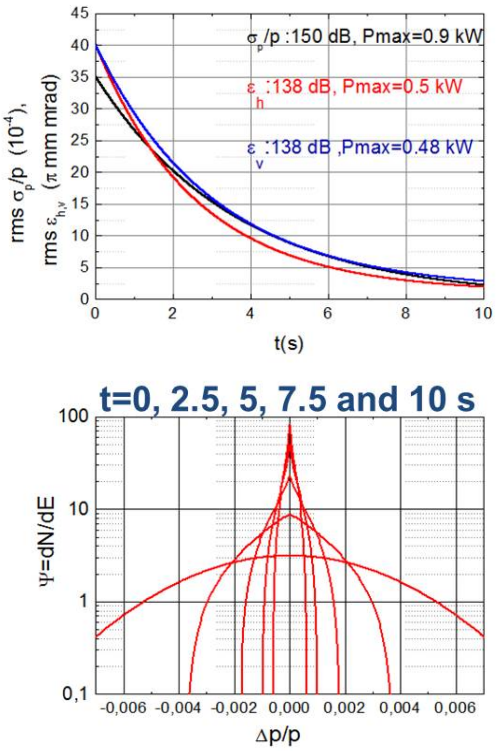

Figure 5: Reference case for stochastic cooling of 10^8 antiprotons at 3 GeV in the CR with the conservative assumption of no plunging. Four times (i.e. accounting for statistical beam signal fluctuations) the total maximum cw power is just within the installed microwave power of 8 kW.

DOI:10.15120/GR-2017-1

In-beam tests of the new secondary electron detector for FAIR*

P. Boutachkov[1], *C. Dorn*[1], *P. Forck*[1], *H. Graf*[1], *C. Müller*[1], *H. J. Reeg*[1], *A. Reiter*[1], *S. Schwarz*[1], *and B. Walasek-Höhne*[1]

[1]GSI, Darmstadt, Germany

The task of the Particle Detector Combination (PDC) detectors is to measure the beam intensity of slowly extracted ion beams. The complete range of possible beam intensities at FAIR cannot be covered by single detector type. At GSI this task is accomplished by a combination of three detectors, a plastic SCintillator (SC), an Ionization Chamber (IC) and a Secondary Electron Monitor (SEM).

The GSI-SEM detector has an active area of 80x80 mm^2, and is build from three 100 μm Al foils. For FAIR a larger and thinner detector is required. The new FAIR-PDC-SEM detector is shown in Fig. 1. The active area is a circle with a diameter of 107 mm. It is built from three 24 μm aluminum foils mounted 5 mm apart on ceramic isolators. The foils are shaped in order to remove mechanical vibrations. The outer foils were positively biased, collecting the secondary electrons knocked out by the ion beam. The central foil was connected via a short cable to the current-to-frequency converter described in Ref. [1]. The presented study investigates the response of the new FAIR-PDC-SEM detector.

Electrons are excited during the passage of charged particles through matter. Some of these electrons will have sufficient energy to migrate to the material surface and escape. The SEM detector measures the amount of these secondary electrons under controlled conditions. The beam current is calculated based on the measured secondary electron current and the experimentally determined secondary electron yield for a single beam ion. The yield for relativistic ions from thin foil is proportional to the energy lost in the material, for Al foil it is in the order of 30 electrons per $MeV/(mg/cm^2)$ [2]. It depends on the foil material and the surface condition. Assuming that the surface of the foil is saturated with defects created during manufacturing, shaping and cleaning, one expects similar yields for different foils from the same material.

The secondary electron yield is experimentally determined by first calibrating the IC detector relative to the SC. In a second measurement the SC detector is removed and the beam current is increased. The SEM secondary electron current is measured as a function of the beam intensity, determined by the IC.

A comparison between the data obtained in this work and the measurements by P. Forck et al. [2] is shown in Fig. 2. The derived secondary electron yields agree for the measurements performed with C, Xe and U beams.

In summary, secondary electron yields from different Al foils were compared. The data supports the idea that surfaces saturated with defects have similar secondary electron yields.

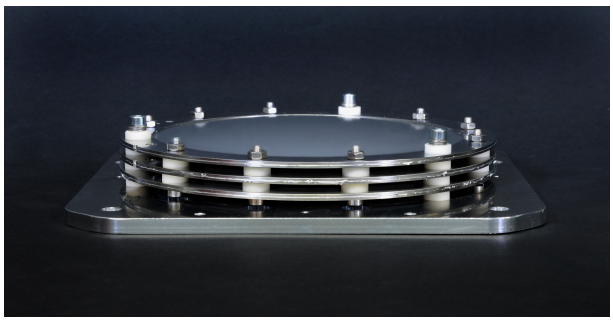

Figure 1: A photograph of the FAIR-PDC-SEM detector. The rings holding the Al foils have an inner diameter of 107 mm.

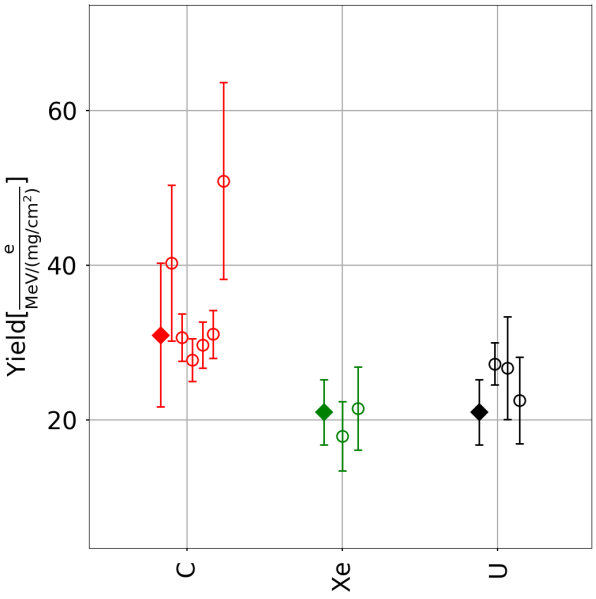

Figure 2: Secondary electron yields, measured with C, Xe and U. Filled-Rhombus: Data from the new FAIR-PDC-SEM, obtained at 300 MeV/u. Open-circles: Data from the GSI-SEM, Ref. [2], obtained at energies between 270 MeV/u and 1095 MeV/u.

References

[1] H. Reeg, DIPAC99, Chester, p. 147 (1999)

[2] P. Forck, P. Heeg, A. Peters, AIP Conf. Proc. 390, 422 (1997)

* It is pleasure to acknowledge the members of the GSI operating team for their support during the experiments.

Pressure profiles simulations of HEBT vacuum system for the FAIR project

P.M. Suherman, L. Urban, A. Kraemer, J. Cavaco, F. Hagenbuck
GSI, Darmstadt, Germany

Introduction

To achieve the aimed operating pressure (10^{-8} mbar), the pressure profiles of the HEBT (High Energy Beam Transport) beam lines for the FAIR project have been simulated. The simulation of pressure profiles are used to optimise the amount and specifications of the required pumps at specific locations along the beam lines. This report only presents the T1S beam line of the HEBT system. T1S beam line consists of 4 consecutive beam line sections, i.e. T1S1, T1S2, T1S3, and T1S4. T1S1 is the first incoming beam line to the HEBT system from existing synchrotron SIS18 (after TE1 section), whereas, T1S4 beam line section is an injection beam line from HEBT to a new built synchrotron SIS100.

Pressure Profile Simulations

The pressure profile reported in this work was calculated based on an analytical model [1]. Figure 1 shows a comparison of pressure profiles of T1S beam line calculated using different nominal pumping speeds (200, 400, and 800 l/s). As shown in Figure 1, there is no significant difference in pressure profiles for different nominal pumping speeds. This demonstrates that the constraint in the pump optimisation for the HEBT system is conductance limited. Since the chambers are conductance limited, adding more pumps with different pumping speed at more positions may be one of the alternatives to improve the pressure profile distribution. The addition of more pumps, however, is sometimes restrained by the available space. Some beam lines are mostly occupied by quadrupole, dipole, and steerer magnets.

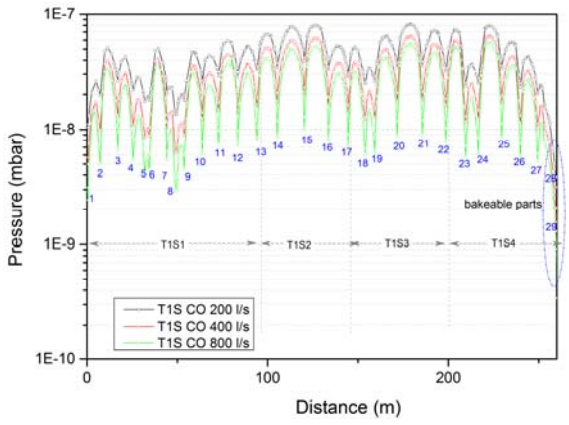

Figure 1: Pressure profiles for T1S beam line for CO based conductance. The numbers in sequence show positions for vacuum pumps.

Figure 2 shows pressure profiles for T1S beam line calculated based on CO conductance, with a combination of various pumping speeds and additional pumps at some locations at the beam line. The 200 l/s pumps were used as additional pumps, which were located in the middle of long straight chambers. The additional pumps of 400 l/s and 800 l/s were also introduced at the end of the T1S4 section that is connected to the synchrotron SIS100. As shown in Figure 2, the pressure profile distribution improved slightly with the use of additional pumps. The improvement was more pronounced at the end of T1S4 section, where the bakeable parts that are connected to the synchrotron SIS100 can now achieve the required pressure range of approximately 10^{-11} mbar.

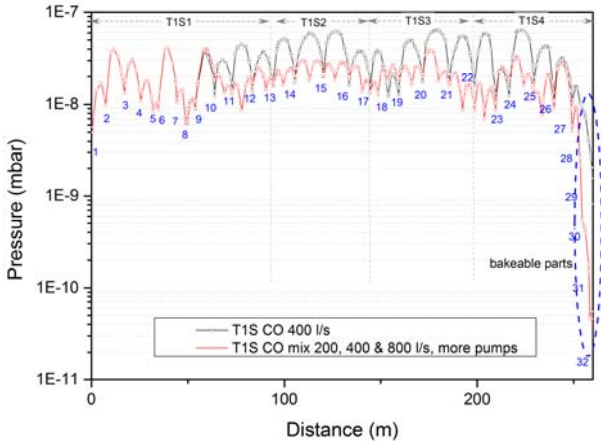

Figure 2: Pressure profiles for T1S beam line for CO based conductance with additional pumps. The numbers in sequence show positions for vacuum pumps. The positions of extra pumps are not all numbered.

The pressure profile presented in this work is only a guideline to estimate the specification and the amount of vacuum pumps needed for the HEBT vacuum system. There are many other factors that are not considered in the calculation, such as the use of partial pressure in the calculation, gas dependence for nominal pumping speed, dynamic gas loads in the system and the 'beam effect' on the chamber materials that may affect the desorption yield and conductance.

Note:

- The simulation in this work was based on the beam line from CATIA® drawing for HEBT in 2014. Based on this calculation, the pump distributions for some of the HEBT beam lines have been slightly changed, in order to reach a better operating pressure.
- Part of this work has been published in [2].

References

[1] V. Ziemann, http://ziemann.web.cern.ch/ziemann/
[2] P.M. Suherman, et. al, Vacuum, 2015, v. 122, p. 268

DOI:10.15120/GR-2017-1

Tests of ZnO, fast inorganic scintilators for Counting Applications at FAIR*

P. Boutachkov, C. Andre, A. Reiter, and B. Walasek-Höhne
GSI, Darmstadt, Germany

In the FAIR High Energy Beam Transport (HEBT) lines scintillation counting detectors will be used to measure the absolute beam intensity and spill structure as a function of time. The measurements will be performed with an organic plastic sintilator inserted into the path of the ion beam. The same type of detectors are used at GSI, see Reference [1] for further details. Due to radiation damage, the routinely used scitillators are exchanged yearly. The presented study was started in order to find a radiation hard scintillation material to be used in the HEBT particle counters. We investigated the response to heavy ions and the radiation hardness of ZnO:Ga and ZnO:In ceramic scintillators. The samples are described in Reference [2].

A photograph of the experimental setup is shown in Figure 1. The heavy ion beam from SIS-18 comes from the right. It is collimated to a spot with a diameter of 5 mm by the Aluminum collimator, indicated as COL in the picture. An ionization chamber (IC) is used to determine the dose deposited by the beam into the studied samples. The samples are inserted into the beam with a remotely controlled manipulator, indicated as SCI. A photo-multiplier (PMT) detected the scintillation light.

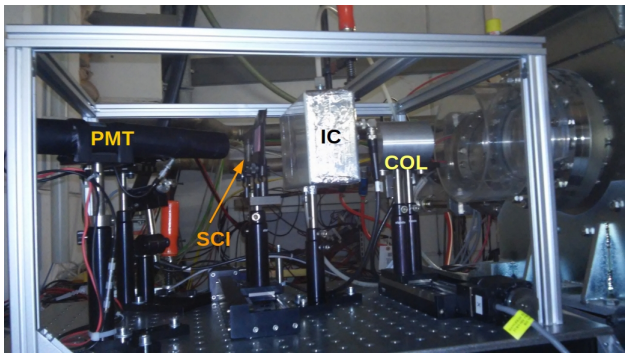

Figure 1: A photograph of the experimental setup. See the text for details.

The response to 300 MeV/u ^{238}U ions of 1 mm thick BC400 plastic scintillator and 0.4 mm thick ZnO:Ga and ZnO:In ceramics is shown in Figure 2. The measurement demonstrates that the fall times of the different scintillating materials is similar. In contrast, the light yield of the ZnO ceramics was about 2 times lower compared to the one of the BC400 scintilator. Hence, in terms of counting capability the ZnO ceramics can be used as a replacement of the plastic scintilators as the lower light yield can be compensated by a higher PMT gain.

The radiation hardness of the ZnO samples was studied with 300 MeV/u U, Xe beams. The ions punched through the material. The preliminary data analysis showed that the ZnO:In and ZnO:Ga generate usable signals for particle counting at 1000 higher integral particle number than the number of particles sufficient to damage a BC400 plastic scintillator.

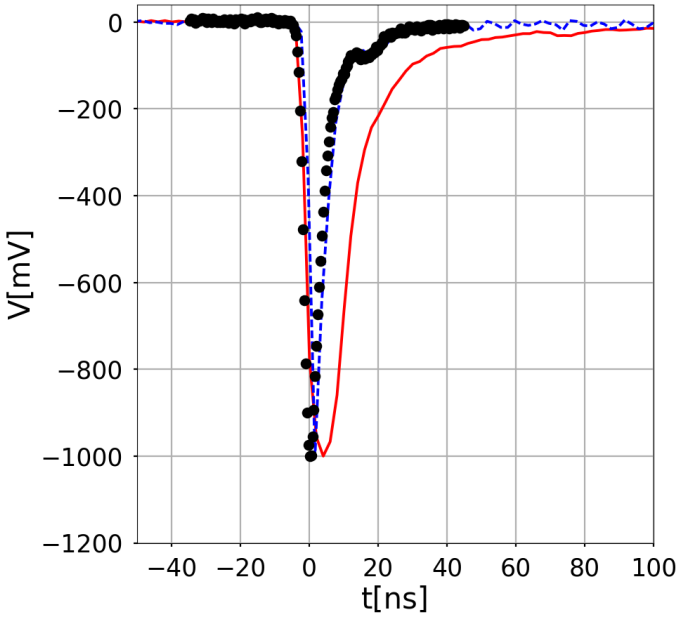

Figure 2: Comparison of the rise and fall times of the studied materials. The signals are scaled to 1V. Red line: BC400 signal. Blue-dotted: ZnO:Ga signal. Black-circles: ZnO:In signal.

In summary, ZnO:In and ZnO:Ga are promising substitutes of the plastic scintilators used in the HEBT particle counting detectors. Further investigations of these promising materials and the construction of large size detectors for heavy ions are planned.

References

[1] P. Forck, P. Heeg, A. Peters, AIP Conf. Proc. 390, 422 (1997)

[2] P. A. Rodnyi, K. A. Chernenko, E. I. Gorokhova, S. S. Kozlovskii, V. M. Khanin, IEEE Trans. Nucl. Sci. 59, 2152 (2012)

* It is pleasure to acknowledge the members of the GSI operating team for their support during the experiments.

DOI:10.15120/GR-2017-1

Publications and dissertations in 2016

Matter and universe – 610

200 publications listed in Web of Science or SCOPUS

Y. Abe and K. Fukushima.
Analytic studies of the complex Langevin equation with a Gaussian ansatz and multiple solutions in the unstable region.
Physical review / D, 94(9):094506.
doi: 10.1103/PhysRevD.94.094506.

M. Ablikim et al.
Improved measurement of the absolute branching fraction of $D^+ \to \bar{K}^0 \mu^+ \nu_\mu$ D + → K ¯ 0 μ + ν μ.
The European physical journal / C, 76(7):369.
doi: 10.1140/epjc/s10052-016-4198-2.

M. Ablikim et al.
Measurement of azimuthal asymmetries in inclusive charged dipion production in e^+e^- annihilations at $\sqrt{s}$ = 3.65 GeV.
Physical review letters, 116(4):042001.
doi: 10.1103/PhysRevLett.116.042001.

M. Ablikim et al.
Measurement of Singly Cabibbo Suppressed Decays Λ c + → p π + π − and Λ c + → p K + K −.
Physical review letters, 117(23):232002.
doi: 10.1103/PhysRevLett.117.232002.

M. Ablikim et al.
Measurement of the absolute branching fraction of D + → K 0 e + ν e via K 0 → π 0 π 0.
Chinese physics / C, 40(11):113001.
doi: 10.1088/1674-1137/40/11/113001.

M. Ablikim et al.
Measurement of the D s + → ℓ + ν ℓ branching fractions and the decay constant f D s +.
Physical review / D, 94(7):072004.
doi: 10.1103/PhysRevD.94.072004.

M. Ablikim et al.
Measurement of the $e^+e^- \to \pi^+\pi^-$ cross section between 600 and 900 MeV using initial state radiation.
Physics letters / B, 753:629.
doi: 10.1016/j.physletb.2015.11.043.

M. Ablikim et al.
Measurement of the leptonic decay width of J/ψ using initial state radiation.
Physics letters / B, 761:98.
doi: 10.1016/j.physletb.2016.08.011.

M. Ablikim et al.
Measurements of absolute hadronic branching fractions of Λ_c^+ baryon.
Physical review letters, 116(5):052001.
doi: 10.1103/PhysRevLett.116.052001.

M. Ablikim et al.
Measurements of the absolute branching fractions for D s + → η e + ν e and D s + → η ′ e + ν e.
Physical review / D, 94(11):112003.
doi: 10.1103/PhysRevD.94.112003.

M. Ablikim et al.
Observation of an Anomalous Line Shape of the η ′ π + π − Mass Spectrum near the p p ¯ Mass Threshold in J / ψ → γ η ′ π + π −.
Physical review letters, 117(4):042002.
doi: 10.1103/PhysRevLett.117.042002.

M. Ablikim et al.
Observation of e + e − → η ′ J / ψ at center-of-mass energies between 4.189 and 4.600 GeV.
Physical review / D, 94(3):032009.
doi: 10.1103/PhysRevD.94.032009.

M. Ablikim et al.
Observation of $e + e^- \to \omega\chi_{c1,2}$ near $\sqrt{s}$ = 4.42 and 4.6 GeV.
Physical review / D, 93(1):011102.
doi: 10.1103/PhysRevD.93.011102.

M. Ablikim et al.
Observation of h c Radiative Decay h c → γ η ′ and Evidence for h c → γ η.
Physical review letters, 116(25):251802.
doi: 10.1103/PhysRevLett.116.251802.

M. Ablikim et al.
Observation of J / ψ → γ η π 0.
Physical review / D, 94(7):072005.
doi: 10.1103/PhysRevD.94.072005.

M. Ablikim et al.
Observation of pseudoscalar and tensor resonances in J / ψ → γ .
Physical review / D, 93(11):112011.
doi: 10.1103/PhysRevD.93.112011.

M. Ablikim et al.
Observation of the Singly Cabibbo-Suppressed Decay D + → ω π + and Evidence for D 0 → ω π 0.
Physical review letters, 116(8):082001.
doi: 10.1103/PhysRevLett.116.082001.

M. Ablikim et al.
Search for a light C P -odd Higgs boson in radiative decays of J / ψ.
Physical review / D, 93(5):052005.
doi: 10.1103/PhysRevD.93.052005.

M. Ablikim et al.
Search for the weak decay η′ → K ± π and precise measurement of the branching fraction B (J / ψ → η′).
Physical review / D, 93(7):072008.
doi: 10.1103/PhysRevD.93.072008.

M. Ablikim et al.
Study of D + → K − π + e + ν e.
Physical review / D, 94(3):032001.
doi: 10.1103/PhysRevD.94.032001.

M. Ablikim et al.
Study of J / ψ → p p ¯ at BESIII.
Physical review / D, 93(5):052010.
doi: 10.1103/PhysRevD.93.052010.

M. Ablikim et al.
Study of ψ decays to the Ξ − Ξ ¯ + and Σ (1385) Σ ¯ (1385) ± final states.
Physical review / D, 93(7):072003.
doi: 10.1103/PhysRevD.93.072003.

A. Abuhoza* et al.
Building and commissioning of a setup to study ageing phenomena in gaseous detectors.
13th Pisa meeting on advanced detectors, La Biodola (Italy), 24 May 2015 - 30 May 2015.
North-Holland Publ. Co., Amsterdam, 24th May 2015.
doi: 10.1016/j.nima.2015.11.091.

B. Acharya, C. Ji and L. Platter.
Effective-field-theory analysis of Efimov physics in heteronuclear mixtures of ultracold atomic gases.
Physical review / A, 94(3):032702.
doi: 10.1103/PhysRevA.94.032702.

J. Adam et al.
Centrality dependence of the nuclear modification factor of charged pions, kaons, and protons in Pb-Pb collisions at $\sqrt{s_{\mathrm{NN}}} = 2.76$ TeV.
Physical review / C, C93(3):034913.
doi: 10.1103/PhysRevC.93.034913.

J. Adam et al.
Production of light nuclei and anti-nuclei in p p and Pb-Pb collisions at energies available at the CERN Large Hadron Collider.
Physical review / C, 93(2):024917.
doi: 10.1103/PhysRevC.93.024917.

J. Adamczewski-Musch* et al.
Λ p interaction studied via femtoscopy in p + Nb reactions at $\sqrt{s_{NN}}$ = 3.18 GeV.
Physical review / C, 94(2):025201.
doi: 10.1103/PhysRevC.94.025201.

G. Agakishiev et al.
Statistical hadronization model analysis of hadron yields in p + Nb and Ar + KCl at SIS18 energies.
The European physical journal / A, 52(6):178.
doi: 10.1140/epja/i2016-16178-x.

V. Akishina* and I. Kisel*.
Parallel 4-Dimensional Cellular Automaton Track Finder for the CBM Experiment.
17th International Workshop on Advanced Computing and Analysis Techniques in Physics Research, Valparaiso (Chile), 18 Jan 2016 - 22 Jan 2016.
IOP Publ., Bristol, 18th Jan. 2016.
doi: 10.1088/1742-6596/762/1/012047.

S. V. Akkelin and Y. M. Sinyukov*.
Quantum canonical ensemble and correlation femtoscopy at fixed multiplicities.
Physical review / C, 94(1):014908.
doi: 10.1103/PhysRevC.94.014908.

ALICE Collaboration.
$^{3}_{\Lambda}\mathrm{H}$ and $^{3}_{\bar{\Lambda}}\overline{\mathrm{H}}$ production in Pb-Pb collisions at $\sqrt{s_{\mathrm{NN}}} = 2.76$ TeV.
Physics letters / B, B754:360.
doi: 10.1016/j.physletb.2016.01.040.

ALICE Collaboration.
Anisotropic flow of charged particles in Pb-Pb collisions at $\sqrt{s_{\mathrm{NN}}} = 5.02$ TeV.
Physical review letters, 116(13):132302.
doi: 10.1103/PhysRevLett.116.132302.

ALICE Collaboration.
Azimuthal anisotropy of charged jet production in $\sqrt{s_{\mathrm{NN}}}$ = 2.76 TeV Pb-Pb collisions.
Physics letters / B, B753:511.
doi: 10.1016/j.physletb.2015.12.047.

ALICE Collaboration.
Centrality dependence of (2S) suppression in p-Pb collisions at $\sqrt{s_{\mathrm{NN}}}$ = 5.02 TeV.
Journal of high energy physics, 1606(6):50.
doi: 10.1007/JHEP06(2016)050.

ALICE Collaboration.
Centrality dependence of charged jet production in p–Pb collisions at $\sqrt{s_{\mathrm{NN}}}$ = 5.02 TeV.
The European physical journal / C, C76(5):271.
doi: 10.1140/epjc/s10052-016-4107-8.

ALICE Collaboration.
Centrality dependence of pion freeze-out radii in Pb-Pb collisions at $\sqrt{s_{NN}} = 2.76$ TeV.
Physical review / C, C93(2):024905.
doi: 10.1103/PhysRevC.93.024905.

ALICE Collaboration.
Centrality dependence of the charged-particle multiplicity density at midrapidity in Pb-Pb collisions at $\sqrt{s_{\mathrm{NN}}}$ = 5.02 TeV.
Physical review letters, 116(22):222302.
doi: 10.1103/PhysRevLett.116.222302.

ALICE Collaboration.
Centrality evolution of the charged-particle pseudorapidity density over a broad pseudorapidity range in Pb-Pb collisions at $\sqrt{s_{\mathrm{NN}}} = 2.76$ TeV.
Physics letters / B, B754:373.
doi: 10.1016/j.physletb.2015.12.082.

DOI:10.15120/GR-2017-1

ALICE Collaboration.
Charge-dependent flow and the search for the chiral magnetic wave in Pb-Pb collisions at $\sqrt{s_{\rm NN}} = 2.76$ TeV.
Physical review / C, C93(4):044903.
doi: 10.1103/PhysRevC.93.044903.

S. G. Weber.
Charmonium production at mid-rapidity in Pb-Pb and p-Pb collisions with ALICE.
1. Strangeness in Quark Matter 2015, Dubna (Russia), 6 Jul 2015 - 11 Jul 2015.
IOP Publ., Bristol, 6th July 2015.
doi: 10.1088/1742-6596/668/1/012096.

ALICE Collaboration.
Correlated event-by-event fluctuations of flow harmonics in Pb-Pb collisions at $\sqrt{s_{\rm NN}} = 2.76$ TeV.
Physical review letters, 117(18):182301.
doi: 10.1103/PhysRevLett.117.182301.

ALICE Collaboration.
Differential studies of inclusive J/ψ and ψ(2S) production at forward rapidity in Pb-Pb collisions at $\sqrt{s_{\rm NN}} = 2.76$ TeV.
Journal of high energy physics, 1605(5):179.
doi: 10.1007/JHEP05(2016)179.

ALICE Collaboration.
Direct photon production in Pb-Pb collisions at $\sqrt{s_{\rm NN}} = 2.76$ TeV.
Physics letters / B, B754:235.
doi: 10.1016/j.physletb.2016.01.020.

ALICE Collaboration.
D-meson production in p-Pb collisions at $\sqrt{s_{\rm NN}} = 5.02$ TeV and in pp collisions at $\sqrt{s} = 7$ TeVsu.
Physical review / C, C94(5):054908.
doi: 10.1103/PhysRevC.94.054908.

ALICE Collaboration.
Elliptic flow of electrons from heavy-flavour hadron decays at mid-rapidity in Pb-Pb collisions at $\sqrt{s_{\rm NN}} = 2.76$ TeV.
Journal of high energy physics, 1609(9):28.
doi: 10.1007/JHEP09(2016)028.

ALICE Collaboration.
Elliptic flow of muons from heavy-flavour hadron decays at forward rapidity in Pb–Pb collisions at $\sqrt{s_{\rm NN}} = 2.76$ TeV.
Physics letters / B, B753:41.
doi: 10.1016/j.physletb.2015.11.059.

ALICE Collaboration.
Event shape engineering for inclusive spectra and elliptic flow in Pb-Pb collisions at $\sqrt{s_{\rm NN} = 2.76}$ TeV.
Physical review / C, C93(3):034916.
doi: 10.1103/PhysRevC.93.034916.

ALICE Collaboration.
Forward-central two-particle correlations in p-Pb collisions at $\sqrt{s_{\rm NN}}$ = 5.02 TeV.
Physics letters / B, B753:126.
doi: 10.1016/j.physletb.2015.12.010.

ALICE Collaboration.
Higher harmonic flow coefficients of identified hadrons in Pb-Pb collisions at $\sqrt{s_{\rm NN}}$ = 2.76 TeVs.
Journal of high energy physics, 1609(9):164.
doi: 10.1007/JHEP09(2016)164.

ALICE Collaboration.
Inclusive quarkonium production at forward rapidity in pp collisions at $\sqrt{s} = 8$ TeV.
The European physical journal / C, C76(4):184.
doi: 10.1140/epjc/s10052-016-3987-y.

ALICE Collaboration.
Jet-like correlations with neutral pion triggers in pp and central Pb–Pb collisions at 2.76 TeV.
Physics letters / B, B763:238.
doi: 10.1016/j.physletb.2016.10.048.

ALICE Collaboration.
Measurement of an excess in the yield of J/ψ at very low $p_{\rm T}$ in Pb-Pb collisions at $\sqrt{s_{\rm NN}}$ = 2.76 TeV.
Physical review letters, 116(22):222301.
doi: 10.1103/PhysRevLett.116.222301.

ALICE Collaboration.
Measurement of D-meson production versus multiplicity in p-Pb collisions at $\sqrt{s_{\rm NN}} = 5.02$ TeVuc.
Journal of high energy physics, 1608(8):78.
doi: 10.1007/JHEP08(2016)078.

ALICE Collaboration.
Measurement of $\rm D_s^+$ production and nuclear modification factor in Pb-Pb collisions at $\sqrt{s_{\rm NN}} = 2.76$ TeV.
Journal of high energy physics, 1603(3):82.
doi: 10.1007/JHEP03(2016)082.

ALICE Collaboration.
Measurement of electrons from heavy-flavour hadron decays in p-Pb collisions at $\sqrt{s_{\rm NN}} = 5.02$ TeV.
Physics letters / B, B754:81.
doi: 10.1016/j.physletb.2015.12.067.

ALICE Collaboration.
Measurement of transverse energy at midrapidity in Pb-Pb collisions at $\sqrt{s_{\rm NN}} = 2.76$ TeV.
Physical review / C, C94(3):034903.
doi: 10.1103/PhysRevC.94.034903.

ALICE Collaboration.
Multipion Bose-Einstein correlations in pp,p -Pb, and Pb-Pb collisions at energies available at the CERN Large Hadron Collider.
Physical review / C, C93(5):054908.
doi: 10.1103/PhysRevC.93.054908.

ALICE Collaboration.
Multiplicity and transverse momentum evolution of charge-dependent correlations in pp, p–Pb, and Pb–Pb collisions at the LHC.
The European physical journal / C, C76(2):86.
doi: 10.1140/epjc/s10052-016-3915-1.

ALICE Collaboration.
Multiplicity dependence of charged pion, kaon, and (anti)proton production at large transverse momentum in p-Pb collisions at $\sqrt{s_{\rm NN}}$ = 5.02 TeVc.
Physics letters / B, B760:720.
doi: 10.1016/j.physletb.2016.07.050.

ALICE Collaboration.
Multi-strange baryon production in p-Pb collisions at $\sqrt{s_{\rm NN}} =$ 5.02 TeV.
Physics letters / B, 758:389.
doi: 10.1016/j.physletb.2016.05.027.

ALICE Collaboration.
Particle identification in ALICE: a Bayesian approach.
The European physical journal / Plus, 131(5):168.
doi: 10.1140/epjp/i2016-16168-5.

ALICE Collaboration.
Production of K^* $(892)^0$ and ϕ (1020) in p–Pb collisions at $\sqrt{s_{NN}}$ = 5.02 TeVc.
The European physical journal / C, C76(5):245.
doi: 10.1140/epjc/s10052-016-4088-7.

ALICE Collaboration.
Pseudorapidity and transverse-momentum distributions of charged particles in proton–proton collisions at $\sqrt{s} = 13$ TeV.
Physics letters / B, B753:319.
doi: 10.1016/j.physletb.2015.12.030.

ALICE Collaboration.
Pseudorapidity dependence of the anisotropic flow of charged particles in Pb-Pb collisions at $\sqrt{s_{\rm NN}} = 2.76$ TeV.
Physics letters / B, B762:376.
doi: 10.1016/j.physletb.2016.07.017.

ALICE Collaboration.
Search for weakly decaying $\bar{\Lambda}$n and $\Lambda\Lambda$ exotic bound states in central Pb-Pb collisions at $\sqrt{s_{\rm NN}}$ = 2.76 TeV.
Physics letters / B, B752:267.
doi: 10.1016/j.physletb.2015.11.048.

ALICE Collaboration.
Study of cosmic ray events with high muon multiplicity using the ALICE detector at the CERN Large Hadron Collider.
Journal of cosmology and astroparticle physics, 1601(01):032.
doi: 10.1088/1475-7516/2016/01/032.

ALICE Collaboration.
Transverse momentum dependence of D-meson production in Pb-Pb collisions at $\sqrt{s_{\rm NN}} = 2.76$ TeV.
Journal of high energy physics, 1603(3):81.
doi: 10.1007/JHEP03(2016)081.

G. A. Almási, B. Friman* and K. Redlich*.
Modeling chiral criticality and its consequences for heavy-ion collisions.
Quark Matter 2015, Kobe (Japan), 27 Sep 2015 - 3 Oct 2015.
North-Holland Publ. Co., Amsterdam, 27th Sept. 2015.
doi: 10.1016/j.nuclphysa.2016.01.073.

D. Alvarez-Castillo et al.
Neutron star mass limit at 2M supports the existence of a CEP.
The European physical journal / A, 52(8):232.
doi: 10.1140/epja/i2016-16232-9.

D. Alvarez-Castillo et al.
New class of hybrid EoS and Bayesian M - R data analysis.
The European physical journal / A, 52(3):69.
doi: 10.1140/epja/i2016-16069-2.

B. Andel et al.
Short-lived isomers in ^{192}Pa and ^{194}Po.
Physical review / C, 93(6):064316.
doi: 10.1103/PhysRevC.93.064316.

A. Andronic* et al.
Heavy-flavour and quarkonium production in the LHC era: from proton–proton to heavy-ion collisions.
The European physical journal / C, 76(3):107.
doi: 10.1140/epjc/s10052-015-3819-5.

N. Armesto et al.
Nuclear collisions at the Future Circular Collider.
Quark Matter 2015, Kobe (Japan), 27 Sep 2015 - 3 Oct 2015.
North-Holland Publ. Co., Amsterdam, 27th Sept. 2015.
doi: 10.1016/j.nuclphysa.2016.02.051.

O. Arnold and H. Collaboration*.
Medium effects in proton-induced strangeness production.
XITH CONFERENCE ON QUARK CONFINEMENT and HADRON SPECTRUM, Saint Petersburg (Russia), 8 Sep 2014 - 12 Sep 2014.
IOP Publ., Bristol, 8th Sept. 2014.
doi: 10.1088/1742-6596/668/1/012037.

A. Arzhanov*, T. R. Rodríguez and G. M. Pinedo*.
Systematic study of infrared energy corrections in truncated oscillator spaces with Gogny energy density functionals.
Physical review / C, 94(5):054319.
doi: 10.1103/PhysRevC.94.054319.

R. Averbeck*.
Open heavy-flavor measurements in ultra-relativistic nuclear collisions.
Nuclear physics / A, 956:112.
doi: 10.1016/j.nuclphysa.2016.03.037.

J. Äystö et al.
Experimental program of the Super-FRS Collaboration at FAIR and developments of related instrumentation.
Nuclear instruments & methods in physics research / B, 376:111.
doi: 10.1016/j.nimb.2016.02.042.

D. L. Balabanski et al.
Photofission experiments at ELI-NP.
Romanian reports in physics, 68:S621.

J. Barnes et al.
Radioactivity and thermalization in the ejecta of compact object mergers and theri impact on kilonova light curves.
The astrophysical journal / 1, 829(2):110.
doi: 10.3847/0004-637X/829/2/110.

DOI:10.15120/GR-2017-1

BESIII Collaboration.
Measurement of the branching fraction for $\psi(3770) \to \gamma\chi_{c0}$.
Physics letters / B, 753:103.
doi: 10.1016/j.physletb.2015.11.074.

S. Biswas et al.
Systematic measurements of the gain and the energy resolution of single and double mask GEM detectors.
13th Pisa meeting on advanced detectors, La Biodola (Italy), 24 May 2015 - 30 May 2015.
North-Holland Publ. Co., Amsterdam, 24th May 2015.
doi: 10.1016/j.nima.2015.11.086.

M. Block*.
Recent developments in Penning-trap mass spectrometry.
Nuclear instruments & methods in physics research / B, 376:265.
doi: 10.1016/j.nimb.2016.02.027.

A. S. Botvina et al.
Formation of hypernuclei in evaporation and fission processes.
Physical review / C, 94(5):054615.
doi: 10.1103/PhysRevC.94.054615.

A. S. Botvina et al.
Relativistic ion collisions as the source of hypernuclei.
The European physical journal / A, 52(8):242.
doi: 10.1140/epja/i2016-16242-7.

N. S. Brady et al.
Dynamical coupling of pygmy and giant resonances in relativistic Coulomb excitation.
Physics letters / B, 757:553.
doi: 10.1016/j.physletb.2016.04.038.

B. B. Brandt et al.
On the strength of the U A (1) anomaly at the chiral phase transition in N f = 2 QCD.
Journal of high energy physics, 2016(12):158.
doi: 10.1007/JHEP12(2016)158.

P. Braun-Munzinger* et al.
Confronting fluctuations of conserved charges in central nuclear collisions at the LHC with predictions from Lattice QCD.
Nuclear physics / A, A956:805.
doi: 10.1016/j.nuclphysa.2016.02.024.

P. Braun-Munzinger* et al.
Properties of hot and dense matter from relativistic heavy ion collisions.
Physics reports, 621:76.
doi: 10.1016/j.physrep.2015.12.003.

A. Bzdak, R. Holzmann* and V. Koch.
Multiplicity-dependent and nonbinomial efficiency corrections for particle number cumulants.
Physical review / C, 94(6):064907.
doi: 10.1103/PhysRevC.94.064907.

R. Caballero-Folch et al.
First Measurement of Several β -Delayed Neutron Emitting Isotopes Beyond N = 126.
Physical review letters, 117(1):012501.
doi: 10.1103/PhysRevLett.117.012501.

CBM Collaboration*.
Automated quality assurance for silicon microstrip sensors of the CBM Silicon Tracking System.
Journal of Instrumentation, 11(01):C01033.
doi: 10.1088/1748-0221/11/01/C01033.

V. Friese*.
Strangeness Prospects with the CBM Experiment.
Strangeness in Quark Matter 2015, Dubna (Russia), 6 Jul 2015 - 11 Jul 2015.
IOP Publ., Bristol, 6th July 2015.
doi: 10.1088/1742-6596/668/1/012014.

L. Chlad and HADES collaboration.
Exploring neutron detection with HADES.
4th FAIR NExt generation Scientists, Garmich-Partenkirchen (Germany), 14 Feb 2016 - 19 Feb 2016.
IOP Publ., Bristol, 14th Feb. 2016.
doi: 10.1088/1742-6596/742/1/012033.

U. Datta* et al.
Direct experimental evidence for a multiparticle-hole ground state configuration of deformed Mg 33.
Physical review / C, 94(3):034304.
doi: 10.1103/PhysRevC.94.034304.

V. Derya et al.
Decay of quadrupole-octupole 1^- states in ^{40}Ca and ^{140}Ce.
Physical review / C, 93(3):034311.
doi: 10.1103/PhysRevC.93.034311.

T. Dickel* et al.
Conceptional design of a novel next-generation cryogenic stopping cell for the Low-Energy Branch of the Super-FRS.
Nuclear instruments & methods in physics research / B, 376:216.
doi: 10.1016/j.nimb.2016.01.015.

C. Domingo-Pardo et al.
Approaching the precursor nuclei of the third r-process peak with RIBs.
6th Nuclear Physics in Astrophysics Conference (NPA), Lisbon (Portugal), 19 May 2013 - 24 May 2013.
IOP Publ., Bristol, 19th May 2013.
doi: 10.1088/1742-6596/665/1/012045.

A. A. Dzhioev et al.
Thermal quasiparticle random-phase approximation with Skyrme interactions and supernova neutral-current neutrino-nucleus reactions.
Physical review / C, 94(1):015805.
doi: 10.1103/PhysRevC.94.015805.

R. Dzhygadlo* et al.
The PANDA Barrel DIRC.
05. International Workshop on Fast Cherenkov Detectors - Photon detection, DIRC design and DAQ, Castle Rauischholzhausen (Germany), 11 Nov 2015 - 13 Nov 2015.
Inst. of Physics, London, 11th Nov. 2015.
doi: 10.1088/1748-0221/11/05/C05013.

M. Eichler et al.
The Impact of Fission on R-Process Calculations.
Journal of physics / Conference Series, 665:012054.
doi: 10.1088/1742-6596/665/1/012054.

T. Ertl et al.
Erratum: "Progenitor-explosion Connection and Remnant Birth Masses for Neutrino-driven Supernovae of Iron-core Progenitors".
The astrophysical journal / 1, 821(1):69.
doi: 10.3847/0004-637X/821/1/69.

E. Etzelmüller et al.
Tests and developments of the PANDA Endcap Disc DIRC.
04. International Workshop on Fast Cherenkov Detectors - Photon detection, DIRC design and DAQ, Castle Rauischholzhausen (Germany), 11 Nov 2015 - 13 Nov 2015.
Inst. of Physics, London, 11th Nov. 2015.
doi: 10.1088/1748-0221/11/04/C04014.

C. Ewerz* et al.
Helicity in proton–proton elastic scattering and the spin structure of the pomeron.
Physics letters / B, 763:382.
doi: 10.1016/j.physletb.2016.10.064.

A. L. Fèvre* et al.
Constraining the nuclear matter equation of state around twice saturation density.
Nuclear physics / A, 945:112.
doi: 10.1016/j.nuclphysa.2015.09.015.

P. Filianin et al.
The decay energy of the pure s-process nuclide ^{123}Te.
Physics letters / B, 758:407.
doi: 10.1016/j.physletb.2016.04.059.

R. Fiore, L. Jenkovszky and R. Schicker.
Resonance production in Pomeron–Pomeron collisions at the LHC.
The European physical journal / C, 76(1):38.
doi: 10.1140/epjc/s10052-015-3846-2.

First Collaboration.
Measurement of fragmentation cross sections of ^{12}C ions on a thin gold target with the FIRST apparatus.
Physical review / C, 93(6):064601.
doi: 10.1103/PhysRevC.93.064601.

U. Forsberg et al.
A new assessment of the alleged link between element 115 and element 117 decay chains.
Physics letters, 760:293.
doi: 10.1016/j.physletb.2016.07.008.

U. Forsberg et al.
Recoil-α-fission and recoil-α–α-fission events observed in the reaction ^{48}Ca + ^{243}Am.
Nuclear physics, 953:117.
doi: 10.1016/j.nuclphysa.2016.04.025.

P. Ghosh*.
Non-invasive characterization and quality assurance of silicon micro-strip detectors using pulsed infrared laser.
01. 17th International Workshop on Radiation Imaging Detectors, Hamburg (Germany), 28 Jun 2015 - 2 Jul 2015.
Inst. of Physics, London, 28th June 2015.
doi: 10.1088/1748-0221/11/01/C01019.

K. Göbel* et al.
Measurement of the ^{92,93,94,100}Mo(γ,n) reactions by Coulomb Dissociation.
6th Nuclear Physics in Astrophysics Conference (NPA), Lisbon (Portugal), 19 May 2013 - 24 May 2013.
IOP Publ., Bristol, 19th May 2013.
doi: 10.1088/1742-6596/665/1/012034.

T. A. Golubkova et al.
Transition from direct to sequential two-proton decay in s–d shell nuclei.
Physics letters / B, 762:263.
doi: 10.1016/j.physletb.2016.09.034.

J. Grund et al.
Implementation of an aerodynamic lens for TRIGA-SPEC.
Nuclear instruments & methods in physics research / B, 376:225.
doi: 10.1016/j.nimb.2015.12.017.

M. Heil* et al.
Stellar neutron capture cross sections of ^{41}K and ^{45}Sc.
Physical review / C, 93(5):055807.
doi: 10.1103/PhysRevC.93.055807.

F.-P. Hessberger* et al.
Alpha- and EC-decay measurements of ^{257}Rf.
The European physical journal / A, 52(7):192.
doi: 10.1140/epja/i2016-16192-0.

F.-P. Hessberger* et al.
Investigation of electron capture decay of ^{258}Db and alpha decay of ^{258}Rf.
The European physical journal / A, 52(11):328.
doi: 10.1140/epja/i2016-16328-2.

J. Heuser*.
Status of the Compressed Baryonic Matter Experiment at FAIR and Its Silicon Tracking System.
2. XI Workshop on Particle Correlations, Femtoscopy and NICA Days 2015, Warsaw (Poland), 3 Nov 2015 - 7 Nov 2015.
Inst. of Physics, Jagellonian Univ., Cracow, 3rd Nov. 2015.
doi: 10.5506/APhysPolBSupp.9.221.

S. Hofmann* et al.
Remarks on the fission barriers of super-heavy nuclei.
The European physical journal / A, 52(4):116.
doi: 10.1140/epja/i2016-16116-0.

S. Hofmann* et al.
Review of even element super-heavy nuclei and search for element 120.
The European physical journal / A, 52(6):180.
doi: 10.1140/epja/i2016-16180-4.

Y. Ilieva et al.
MCP-PMT studies at the High-B test facility at Jefferson Lab.
03. International Workshop on Fast Cherenkov Detectors - Photon detection, DIRC design and DAQ, Castle Rauischholzhausen (Germany), 11 Nov 2015 - 13 Nov 2015.
Inst. of Physics, London, 11th Nov. 2015.
doi: 10.1088/1748-0221/11/03/C03061.

DOI:10.15120/GR-2017-1

A. Jaiswal* and V. Roy.
Relativistic Hydrodynamics in Heavy-Ion Collisions: General Aspects and Recent Developments.
Advances in high energy physics, 2016:1.
doi: 10.1155/2016/9623034.

A. Jarmola et al.
Optically detected magnetic resonances of nitrogen-vacancy ensembles in C 13 -enriched diamond.
Physical review / B, 94(9):094108.
doi: 10.1103/PhysRevB.94.094108.

G. Kalicy et al.
High-performance DIRC detector for the future Electron Ion Collider experiment.
07. International Workshop on Fast Cherenkov Detectors - Photon detection, DIRC design and DAQ, Castle Rauischholzhausen (Germany), 11 Nov 2015 - 13 Nov 2015.
Inst. of Physics, London, 11th Nov. 2015.
doi: 10.1088/1748-0221/11/07/C07015.

R. Kanungo et al.
Proton Distribution Radii of $^{12-19}$C Illuminate Features of Neutron Halos.
Physical review letters, 117(10):102501.
doi: 10.1103/PhysRevLett.117.102501.

F. Karsch*, K. Morita and K. Redlich*.
Effects of kinematic cuts on net electric charge fluctuations.
Physical review / C, 93(3):034907.
doi: 10.1103/PhysRevC.93.034907.

D. F. J. Kimball et al.
Magnetic shielding and exotic spin-dependent interactions.
Physical review / D, 94(8):082005.
doi: 10.1103/PhysRevD.94.082005.

P. Klaus et al.
Prototyping the read-out chain of the CBM Microvertex Detector.
03. Topical Workshop on Electronics for Particle Physics, Lisbon (Portugal), 28 Sep 2015 - 2 Oct 2015.
Inst. of Physics, London, 28th Sept. 2015.
doi: 10.1088/1748-0221/11/03/C03046.

R. Knöbel* et al.
First direct mass measurements of stored neutron-rich ^{129,130,131}Cd isotopes with FRS-ESR.
Physics letters / B, 754:288.
doi: 10.1016/j.physletb.2016.01.039.

R. Knöbel* et al.
New results from isochronous mass measurements of neutron-rich uranium fission fragments with the FRS-ESR-facility at GSI.
The European physical journal / A, 52(5):138.
doi: 10.1140/epja/i2016-16138-6.

F. Köhler* et al.
Isotope dependence of the Zeeman effect in lithium-like calcium.
Nature Communications, 7:10246.
doi: 10.1038/ncomms10246.

A. Koloczek et al.
Sensitivity study for s process nucleosynthesis in AGB stars.
Atomic data and nuclear data tables, 108:1.
doi: 10.1016/j.adt.2015.12.001.

N. Kuzminchuk-Feuerstein* et al.
Efficiency and rate capability studies of the time-of-flight detector for isochronous mass measurements of stored short-lived nuclei with the FRS-ESR facility.
Nuclear instruments & methods in physics research / A, 821:160.
doi: 10.1016/j.nima.2016.03.036.

M. Laatiaoui* et al.
Atom-at-a-time laser resonance ionization spectroscopy of nobelium.
Nature, 538(7626):495.
doi: 10.1038/nature19345.

F. Lautenschläger* et al.
Developments for resonance ionization laser spectroscopy of the heaviest elements at SHIP.
Nuclear instruments & methods in physics research / B, 383:115.
doi: 10.1016/j.nimb.2016.06.001.

N. Leefer* et al.
Search for the Effect of Massive Bodies on Atomic Spectra and Constraints on Yukawa-Type Interactions of Scalar Particles.
Physical review letters, 117(27):271601.
doi: 10.1103/PhysRevLett.117.271601.

A. Lehmann et al.
Lifetime of MCP-PMTs.
05. International Workshop on Fast Cherenkov Detectors - Photon detection, DIRC design and DAQ, Castle Rauischholzhausen (Germany), 11 Nov 2015 - 13 Nov 2015.
Inst. of Physics, London, 11th Nov. 2015.
doi: 10.1088/1748-0221/11/05/C05009.

P. M. Lo et al.
Missing baryonic resonances in the Hagedorn spectrum.
The European physical journal / A, 52(8):235.
doi: 10.1140/epja/i2016-16235-6.

B. Löher et al.
The decay pattern of the Pygmy Dipole Resonance of ^{140}Ce.
Physics letters / B, 756:72.
doi: 10.1016/j.physletb.2016.02.042.

M. Lorenz* et al.
Strange hadron production at SIS energies: an update from HADES.
Quark Confinement and the Hadron Spectrum XI, Saint Petersburg (Russia), 8 Sep 2014 - 12 Sep 2014.
IOP Publ., Bristol, 8th Sept. 2014.
doi: 10.1088/1742-6596/668/1/012022.

M. Lutz* et al.
Resonances in QCD.
Nuclear physics / A, 948:93.
doi: 10.1016/j.nuclphysa.2016.01.070.

J. Marganiec* et al.
Coulomb and nuclear excitations of narrow resonances in ^{17}Ne.
Physics letters / B, 759:200.
doi: 10.1016/j.physletb.2016.05.073.

J. Marganiec* et al.
Coulomb dissociation of ^{27}P at 500 MeV/u.
Physical review / C, 93(4):045811.
doi: 10.1103/PhysRevC.93.045811.

J. Marganiec* et al.
Experimental study of the ^{15}O(2 p , γ)^{17}Ne cross section by Coulomb Dissociation for the rp process.
6th Nuclear Physics in Astrophysics Conference (NPA), Lisbon (Portugal), 19 May 2013 - 24 May 2013.
IOP Publ., Bristol, 19th May 2013.
doi: 10.1088/1742-6596/665/1/012046.

T. Marketin, L. Huther and G. M. Pinedo*.
Large-scale evaluation of β -decay rates of r -process nuclei with the inclusion of first-forbidden transitions.
Physical review / C, 93(2):025805.
doi: 10.1103/PhysRevC.93.025805.

D. Martin et al.
Impact of Nuclear Mass Uncertainties on the r Process.
Physical review letters, 116(12):121101.
doi: 10.1103/PhysRevLett.116.121101.

J. J. Mendoza-Temis et al.
On the robustness of the r-process in neutron-star mergers against variations of nuclear masses.
39th Symposium on Nuclear Physics, Cocoyoc (Mexico), 5 Jan 2016 - 8 Jan 2016.
IOP Publ., Bristol, 5th Jan. 2016.
doi: 10.1088/1742-6596/730/1/012018.

J. Menendez* et al.
Testing the importance of collective correlations in neutrinoless β β decay.
Physical review / C, 93(1):014305.
doi: 10.1103/PhysRevC.93.014305.

V. Mikhaylov et al.
Performance study of the anisotropic flow and reaction plane reconstruction in the CBM experiment.
4th FAIR NExt generation ScientistS, Garmisch-Partenkirchen (Germany), 14 Feb 2016 - 19 Feb 2016.
IOP Publ., Bristol, 14th Feb. 2016.
doi: 10.1088/1742-6596/742/1/012023.

I. Momot et al.
Radiation tolerance studies of silicon microstrip sensors for the CBM Silicon Tracking System.
Journal of physics / Conference Series, 668:012117.
doi: 10.1088/1742-6596/668/1/012117.

P. Moreau et al.
Examinations of the early degrees of freedom in ultrarelativistic nucleus-nucleus collisions.
Physical review / C, 93(4):044916.
doi: 10.1103/PhysRevC.93.044916.

M. Mrozek et al.
Coherent population oscillations with nitrogen-vacancy color centers in diamond.
Physical review / B, 94(3):035204.
doi: 10.1103/PhysRevB.94.035204.

H. Nagahama et al.
Highly sensitive superconducting circuits at 700 kHz with tunable quality factors for image-current detection of single trapped antiprotons.
Review of scientific instruments, 87(11):113305.
doi: 10.1063/1.4967493.

P. D. Group.
Review of Particle Physics.
Chinese physics / C, C40(10):100001.
doi: 10.1088/1674-1137/40/10/100001.

H. Pai et al.
Magnetic dipole excitations of ^{50}Cr.
Physical review / C, 93(1):014318.
doi: 10.1103/PhysRevC.93.014318.

I. Panasenko et al.
A Custom Probe Station for Microstrip Detector Quality Assurance of the CBM Experiment.
4th FAIR NExt generation ScientistS, Garmisch-Partenkirchen (Germany), 14 Feb 2016 - 19 Feb 2016.
IOP Publ., Bristol, 14th Feb. 2016.
doi: 10.1088/1742-6596/742/1/012037.

L.-G. Pang et al.
Longitudinal fluctuations and decorrelation of anisotropic flow.
Nuclear physics / A, 956:272.
doi: 10.1016/j.nuclphysa.2016.02.049.

V. Panin* et al.
Exclusive measurements of quasi-free proton scattering reactions in inverse and complete kinematics.
Physics letters / B, 753:204.
doi: 10.1016/j.physletb.2015.11.082.

V. Perschina-Nägele*.
A relativistic periodic DFT study on interaction of superheavy elements 112 (Cn) and 114 (Fl) and their homologs Hg and Pb, respectively, with a quartz surface.
Physical chemistry, chemical physics, 18(26):17750.
doi: 10.1039/C6CP02253G.

V. Perschina-Nägele*.
A Theoretical Study on the Adsorption Behavior of Element 113 and Its Homologue Tl on a Quartz Surface: Relativistic Periodic DFT Calculations.
The journal of physical chemistry / C, 120(36):20232.
doi: 10.1021/acs.jpcc.6b07834.

H. Petersen* et al.
Influence of kinematic cuts on the net charge distribution.
Nuclear physics / A, 956:336.
doi: 10.1016/j.nuclphysa.2016.01.059.

S. Pustelny et al.
Dichroic atomic vapor laser lock with multi-gigahertz stabilization range.
Review of scientific instruments, 87(6):063107.
doi: 10.1063/1.4952962.

DOI:10.15120/GR-2017-1

S. Raeder* et al.
Developments towards in-gas-jet laser spectroscopy studies of actinium isotopes at LISOL.
Nuclear instruments & methods in physics research / B, 376:382.
doi: 10.1016/j.nimb.2015.12.014.

A. Rahaman et al.
Coulomb breakup of neutron-rich ^{29,30}Na isotopes near the island of inversion.
Journal of physics / G.
doi: 10.1088/1361-6471/aa594d.

K. Redlich* and K. Zalewski.
Thermodynamics of the low-density excluded-volume hadron gas.
Physical review / C, 93(1):014910.
doi: 10.1103/PhysRevC.93.014910.

K. Redlich* and K. Zalewski.
Thermodynamics of van der Waals Fluids with Quantum Statistics.
Acta physica Polonica / B, 47(7):1943.
doi: 10.5506/APhysPolB.47.1943.

R. Reifarth* et al.
Nuclear astrophysics with radioactive ions at FAIR.
Nuclear Physics in Astrophysics VI, Lisbon (Portugal), 19 May 2013 - 24 May 2013.
IOP Publ., Bristol, 19th May 2013.
doi: 10.1088/1742-6596/665/1/012044.

M. P. Reiter et al.
Rate capability of a cryogenic stopping cell for uranium projectile fragments produced at 1000MeV/u.
Nuclear instruments & methods in physics research / B, 376:240.
doi: 10.1016/j.nimb.2015.12.016.

J. Rieke et al.
Resolution changes of MCP-PMTs in magnetic fields.
05. International Workshop on Fast Cherenkov Detectors - Photon detection, DIRC design and DAQ, Castle Rauischholzhausen (Germany), 11 Nov 2015 - 13 Nov 2015.
Inst. of Physics, London, 11th Nov. 2015.
doi: 10.1088/1748-0221/11/05/C05002.

D. B. Ríos et al.
Measurement of the parity violating asymmetry in the quasielastic electron-deuteron scattering and improved determination of the magnetic strange form factor and the isovector anapole radiative correction.
Physical review / D, 94(5):051101.
doi: 10.1103/PhysRevD.94.051101.

S. M. Rochester et al.
Efficient polarization of high-angular-momentum systems.
Physical review / A, 94(4):043416.
doi: 10.1103/PhysRevA.94.043416.

M. Röder et al.
Coulomb dissociation of ^{20,21}N.
Physical review / C, 93(6):065807.
doi: 10.1103/PhysRevC.93.065807.

P. Rodríguez-Ramos.
Pion induced reaction with carbon and polyethylene targets obtained by HADES-GSI in 2014.
4th FAIR NExt generation ScientistS, Garmich-Partenkirchen (Germany), 14 Feb 2016 - 19 Feb 2016.
IOP Publ., Bristol, 14th Feb. 2016.
doi: 10.1088/1742-6596/742/1/012029.

J. L. Rodríguez-Sánchez et al.
Light charged particles emitted in fission reactions induced by protons on ^{208}Pb.
Physical review / C, 94(3):034605.
doi: 10.1103/PhysRevC.94.034605.

J. L. Rodríguez-Sánchez et al.
Presaddle and postsaddle dissipative effects in fission using complete kinematics measurements.
Physical review / C, 94(6):061601.
doi: 10.1103/PhysRevC.94.061601.

P. Russotto et al.
Results of the ASY-EOS experiment at GSI: The symmetry energy at suprasaturation density.
Physical review / C, 94(3):034608.
doi: 10.1103/PhysRevC.94.034608.

T. Saito* et al.
Summary of the HypHI Phase 0 experiment and future plans with FRS at GSI (FAIR Phase 0).
Nuclear physics / A, 954:199.
doi: 10.1016/j.nuclphysa.2016.05.011.

C. Schmitt, K.-H. Schmidt* and A. Kelić-Heil*.
Erratum: SPACS: A semi-empirical parameterization for isotopic spallation cross sections [Phys. Rev. C 90, 064605 (2014)].
Physical review / C, 94(3):039901.
doi: 10.1103/PhysRevC.94.039901.

F. Schneider et al.
Resonance ionization of holmium for ion implantation in microcalorimeters.
Nuclear instruments & methods in physics research / B, 376:388.
doi: 10.1016/j.nimb.2015.12.012.

B. Seiferle et al.
A VUV detection system for the direct photonic identification of the first excited isomeric state of ^{229}Th.
The European physical journal / D, 70(3):58.
doi: 10.1140/epjd/e2016-60653-4.

B. Singh et al.
Study of doubly strange systems using stored antiprotons.
Nuclear physics / A, 954:323.
doi: 10.1016/j.nuclphysa.2016.05.014.

M. Singla* et al.
Radiation tolerance studies of neutron irradiated double sided silicon microstrip detectors.
Nuclear instruments & methods in physics research / A, 824:462.
doi: 10.1016/j.nima.2015.09.003.

T. F. Sjolander et al.
Transition-Selective Pulses in Zero-Field Nuclear Magnetic Resonance.
The journal of physical chemistry / A, 120(25):4343.
doi: 10.1021/acs.jpca.6b04017.

J. Stevens et al.
The GlueX DIRC project.
07. International Workshop on Fast Cherenkov Detectors - Photon detection, DIRC design and DAQ, Castle Rauischholzhausen (Germany), 11 Nov 2015 - 13 Nov 2015.
Inst. of Physics, London, 11th Nov. 2015.
doi: 10.1088/1748-0221/11/07/C07010.

H. Stoecker* et al.
Glueballs amass at the RHIC and LHC! The early quarkless first-order phase transition at T = 270 MeV—from pure Yang–Mills glue plasma to Hagedorn glueball states.
Journal of physics / G, 43(1):015105.
doi: 10.1088/0954-3899/43/1/015105.

Y. Suzuki et al.
Parameter-free calculation of charge-changing cross sections at high energy.
Physical review / C, 94(1):011602.
doi: 10.1103/PhysRevC.94.011602.

Y. K. Tanaka et al.
Measurement of Excitation Spectra in the ^{12}C(p , d) Reaction near the η′ Emission Threshold.
Physical review letters, 117(20):202501.
doi: 10.1103/PhysRevLett.117.202501.

I. Tanihata et al.
Observation of large enhancements of charge exchange cross sections with neutron-rich carbon isotopes.
Progress of theoretical and experimental physics, 2016(4):043D05.
doi: 10.1093/ptep/ptw034.

R. Thies et al.
Systematic investigation of projectile fragmentation using beams of unstable B and C isotopes.
Physical review / C, 93(5):054601.
doi: 10.1103/PhysRevC.93.054601.

O. Y. Tretiak et al.
Raman and nuclear magnetic resonance investigation of alkali metal vapor interaction with alkene-based anti-relaxation coating.
The journal of chemical physics, 144(9):094707.
doi: 10.1063/1.4943123.

V. L. Truesdale et al.
β -delayed fission and α decay of ^{196}At.
Physical review / C, 94(3):034308.
doi: 10.1103/PhysRevC.94.034308.

G. M. Tveten et al.
Completing the nuclear reaction puzzle of the nucleosynthesis of ^{92}Mo.
Physical review / C, 94(2):025804.
doi: 10.1103/PhysRevC.94.025804.

S. Typel*.
Reaction theory.
The European physical journal / Plus, 131(1):13.
doi: 10.1140/epjp/i2016-16013-y.

S. Typel*.
Variations on the excluded-volume mechanism.
The European physical journal / A, 52(1):16.
doi: 10.1140/epja/i2016-16016-3.

I. Usoltsev et al.
Decomposition studies of group 6 hexacarbonyl complexes. Part 1: Production and decomposition of $Mo(CO)_6$ and $W(CO)_6$.
Radiochimica acta, 104(3):141.
doi: 10.1515/ract-2015-2445.

L. v. d. Wense et al.
The extraction of $^{229}Th^{3+}$ from a buffer-gas stopping cell.
Nuclear instruments & methods in physics research / B, 376:260.
doi: 10.1016/j.nimb.2015.12.049.

L. von der Wense et al.
Direct detection of the ^{229}Th nuclear clock transition.
Nature, 533(7601):47.
doi: 10.1038/nature17669.

A. Wickenbrock et al.
Microwave-free magnetometry with nitrogen-vacancy centers in diamond.
Applied physics letters, 109(5):053505.
doi: 10.1063/1.4960171.

H. Witała et al.
Role of the Total Isospin 3/2 Component in Three-Nucleon Reactions.
Few-body systems, 57(12):1213.
doi: 10.1007/s00601-016-1156-3.

M.-R. Wu et al.
Production of the entire range of r -process nuclides by black hole accretion disc outflows from neutron star mergers.
Monthly notices of the Royal Astronomical Society, 463(3):2323.
doi: 10.1093/mnras/stw2156.

E. Zhivun et al.
Vector light shift averaging in paraffin-coated alkali vapor cells.
Optics express, 24(14):15383.
doi: 10.1364/OE.24.015383.

38 dissertations

B. Andel.
Study of neutron deficient polonium isotopes.
Comenius Universität Bratislava, 2016.

A. Bleile*.
Experimentelle Untersuchungen thermischer Eigenschaften schnell gepulster supraleitender Beschleunigermagnete.
Johannes Gutenberg-Universität Mainz, 2016.

DOI:10.15120/GR-2017-1

K. Boguslavski and J. Berges.
Universality classes far from equilibrium: From heavy-ion collisions to superfluid Bose systems.
Heidelberg, 2016.

M. Dhar.
Hyperon interaction in free space and nuclear matter within a SU(3) based meson exchange model.
Justus-Liebig-Universität Gießen, 2016.

S. Diehl.
Optimization of the Influence of Longitudinal and Lateral Non-Uniformity on the Performance of an Electromagnetic Calorimeter.
Justus-Liebig-Universität Gießen, 2016.

J. Ebert.
Mass measurements of ^{238}U-projectile fragments for the first time with a Multiple-Reflection Time-Of-Flight Mass Spectrometer.
Justus-Liebig-Universität Gießen, 2016.

D. Eschweiler.
Efficient Device Drivers for Supercomputers.
Johann Wolfgang Goethe-Universität Frankfurt, 2015.

A. Frassino.
Gauge-gravity duality, phase transition of nuclear matter, beyond the Einstein gravity limit.
Johann Wolfgang Goethe-Universität Frankfurt, 2016.

H. F. Fuhrmann.
Vector mesons in meson-baryon scatteringand large-N$_c$ Quantum Chromodynamics.
Technische Universität Darmstadt, 2016.

J. Gebelein.
FPGA fault tolerance in radiation environments.
Johann Wolfgang Goethe-Universität Frankfurt, 2016.

P. Ghosh*.
Characterization and qualilty assurance of silicon micro-strip sensors using infrared laser for the CBM experiment.
Johann Wolfgang Goethe-Universität Frankfurt, 2016.

K. Henninger.
Structure of isomultiplets in A=8 and A=9 nuclei in the framework of Fermionic Molecular Dynamics.
Technische Universität Darmstadt, 2016.

C. Jesch.
The Multiple-Reflection Time-of-Flight Isobar Separator for TITAN and Direct Mass Measurements at the FRS Ion Catcher.
Justus-Liebig-Universität Gießen, 2016.

E. Krebs.
Application of the CBM micro vertex detector for dielectron analysis.
Johann Wolfgang Goethe-Universität Frankfurt, 2016.

P. Larionov.
Systematic irradiation studies and Quality Assurance of silicon strip sensors for the CBM Silicon Tracking System.
Johann Wolfgang Goethe-Universität Frankfurt, 2016.

F. Lautenschläger.
Laserspektroskopie an Nobelium (Z=102) in einer Puffergaszelle.
Technische Universität Darmstadt, 2016.

W. Lippert.
Further Development and Application of a Mobile Multiple-Reflection Time-of-Flight Mass Spectrometer for Analytical High-Resolution Tandem Mass Spectrometry.
Justus-Liebig-Universität Gießen, 2016.

J. Onderwaater*.
Charge dependent correlations and collective dynamics in Pb-Pb collisions at $\sqrt{s_{\mathrm{NN}}}$ = 2.76 TeV.
Technische Universität Darmstadt, 2017.

S. Reinecke.
Characterisation of photon sensors for the CBM-RICH and its use for the reconstruction of neutral mesons via conversion.
Bergischen Universität Wuppertal, 2016.

D. Renisch.
Installation and operation of a high-temperature surface ion source for the online coupling of TRIGA-SPEC to the TRIGA Mainz research reactor and high-precision mass measurements of transuranium nuclides at TRIGA-TRAP.
Johannes Gutenberg-Universität Mainz, 2016.

C. Rosenbaum.
Optimization of the Front-End electronics of the PANDA Barrel EMC.
Justus-Liebig-Universität Gießen, 2016.

A. Samberg.
Applied String Theory, Hot and Cold: A Holographic View on Quark–Gluon Plasma and Superfluids.
Universität Heidelberg, 2016.

H. Schuldes.
Charged kaon and Φ reconstruction in Au+Au collisions at 1.23 AGeV.
Johann Wolfgang Goethe-Universität Frankfurt, 2016.

P. Scior.
Lattice Simulations of QCD-like Theories at Finite Baryon Density.
Technische Universität Darmstadt, 2016.

M. Stappel.
Eine vakuumultraviolette Laserquelle zur Rydberganregung von Calciumionen.
Johannes Gutenberg-Universität Mainz, 2016.

J. Stiller.
Full kinematic reconstruction of charged B mesons with the upgraded inner tracking system of the ALICE experiment.
Universität Heidelberg, 2016.

M. L. C. Sua.
Inelastic scattering of Ni and Zn isotopes off a proton target.
Technische Universität Darmstadt, 2016.

M. Völkl.
Electrons from beauty-hadron decays in central Pb–Pb collisions at $\sqrt{(s_{\mathrm{NN}})}$ = 2.76 TeV.
Universität Heidelberg, 2016.

DOI:10.15120/GR-2017-1

J. Wagner*.
Electrons from decays of open charm and beauty hadrons in p-Pb collisions at $\sqrt{s_{\mathrm{NN}}}$ = 5.02 TeV.
Technische Universität Darmstadt, 2016.

M. Wagner.
Studies towards the data acquisition of the PANDA experiment & measurement of a new upper limit of the production cross section of of $p\bar{p} \to h_c$.
Justus-Liebig-Universität Gießen, 2016.

C. Welzbacher.
Quarks and gluons in the phase diagram of quantum chromodynamics.
Justus-Liebig-Universität Gießen, 2016.

J. Wilkinson.
Analysis of D^0 and D^{*+}-meson production in pp and p-Pb collisions with ALICE at the LHC.
Universität Heidelberg, 2016.

M. Winn.
Inclusive J/psi production at mid-rapidity in p-Pb collisions at $\sqrt{s_{NN}}$ = 5.02 TeV.
Universität Heidelberg, 2016.

X. Xu.
Observation and investigation of the new proton-unbound nuclei ^{30}Ar and ^{29}Cl with in-flight decay spectroscopy.
Justus-Liebig-Universität Gießen, 2016.

A. Zimmermann.
Production of strange hadrons in charged jets in Pb-Pb collisions measured with ALICE at the LHC.
Universität Heidelberg, 2016.

V. Zinyuk.
Systematic study of strangeness production and dynamic behaviour with the FOPI experiment at SIS-18.
Universität Heidelberg, 2016.

M. Zühlsdorf*.
Alternative geometrical designs for quartz-based Cherenkov detectors for the PANDA barrel DIRC detector.
Johann Wolfgang Goethe-Universität Frankfurt, 2016.

M. Zyzak*.
Online selection of short-lived particles on many-core computer architectures in the CBM experiment at FAIR.
Johann Wolfgang Goethe-Universität Frankfurt, 2016.

From matter to materials and life – 620

178 publications listed in Web of Science or SCOPUS

A. Alejo et al.
High resolution Thomson Parabola Spectrometer for full spectral capture of multi-species ion beams.
Review of scientific instruments, 87(8):083304.
doi: 10.1063/1.4961028.

I. Alencar et al.
Irradiation effects in CaF_2 probed by Raman scattering.
Journal of Raman spectroscopy, 47(8):978.
doi: 10.1002/jrs.4927.

V. Alexeev et al.
Charge spectrum of heavy and superheavy componets of galactic cosmic rays: results of the OLIMPIYA experiment.
The astrophysical journal / 1, 829(2):120.
doi: 10.3847/0004-637X/829/2/120.

M. Ali*, S. Nasir and W. Ensinger.
Stereoselective detection of amino acids with protein-modified single asymmetric nanopores.
Electrochimica acta, 215:231.
doi: 10.1016/j.electacta.2016.08.067.

M. Ali* et al.
Label-Free Pyrophosphate Recognition with Functionalized Asymmetric Nanopores.
Small, 12(15):2014.
doi: 10.1002/smll.201600160.

P. Y. Apel et al.
Shedding light on the mechanism of asymmetric track etching: an interplay between latent track structure, etchant diffusion and osmotic flow.
Physical chemistry, chemical physics, 18(36):25421.
doi: 10.1039/C6CP05465J.

Asavei et al.
Materials in extreme environments for energy, accelerators and space applications at ELI-NP.
Romanian reports in physics, 68:S275.

C. Babcock et al.
Quadrupole moments of odd-A $^{53-63}$Mn: Onset of collectivity towards N = 40.
Physics letters / B, 760:387.
doi: 10.1016/j.physletb.2016.07.016.

B. Bergmann et al.
Angular correlation function of the hypersatellite-satellite x-ray cascade following K -shell electron capture of ^{55}Fe.
Physical review / C, 94(1):014611.
doi: 10.1103/PhysRevC.94.014611.

D. Bernhardt et al.
Absolute rate coefficients for photorecombination of beryllium-like and boron-like silicon ions.
Journal of physics / B, 49(7):074004.
doi: 10.1088/0953-4075/49/7/074004.

D. Bernhardt et al.
Erratum: Electron-ion collision spectroscopy: Lithium-like xenon ions [Phys. Rev. A 91, 012710 (2015)].
Physical review / A covering atomic, molecular, and optical physics and quantum information, 94(2):029903.
doi: 10.1103/PhysRevA.94.029903.

H. Bernhardt* et al.
High purity x-ray polarimetry with single-crystal diamonds.
Applied physics letters, 109(12):121106.
doi: 10.1063/1.4962806.

DOI:10.15120/GR-2017-1

M. L. Bissell et al.
Cu charge radii reveal a weak sub-shell effect at N = 40.
Physical review / C, 93(6):064318.
doi: 10.1103/PhysRevC.93.064318.

A. Blinne* and E. Strobel.
Comparison of semiclassical and Wigner function methods in pair production in rotating fields.
Physical review / D, 93(2):025014.
doi: 10.1103/PhysRevD.93.025014.

K.-H. Blumenhagen et al.
Erratum: Polarization transfer in Rayleigh scattering of hard x-rays (2016 New J. Phys. 18 103034).
New journal of physics, 18(11):119601.
doi: 10.1088/1367-2630/18/11/119601.

K.-H. Blumenhagen* et al.
Polarization transfer in Rayleigh scattering of hard x-rays.
New journal of physics, 18(10):103034.
doi: 10.1088/1367-2630/18/10/103034.

K.-J. Boehm et al.
Design and Engineering of a Target for X-Ray Thomson Scattering Measurements on Matter at Extreme Densities and Gigabar Pressures.
Fusion science and technology, 70(2):324.
doi: 10.13182/FST15-242.

A. V. Bogatskaya et al.
Polarization response in extreme nonlinear optics: when can the semiclassical approach be used?
Laser physics letters, 13(4):045301.
doi: 10.1088/1612-2011/13/4/045301.

J. Borchardt, H. Gies* and R. Sondenheimer.
Global flow of the Higgs potential in a Yukawa model.
The European physical journal / C, 76(8):472.
doi: 10.1140/epjc/s10052-016-4300-9.

B. Borm* et al.
Improvement of density resolution in short-pulse hard x-ray radiographic imaging using detector stacks.
Review of scientific instruments, 87(9):093104.
doi: 10.1063/1.4961666.

A. Borovik et al.
Electron-impact single ionization of W^{19+} ions.
Physical review / A, 93(1):012708.
doi: 10.1103/PhysRevA.93.012708.

J. Braun* et al.
Crystalline ground states in Polyakov-loop extended Nambu–Jona-Lasinio models.
Physical review / D, 93(1):014032.
doi: 10.1103/PhysRevD.93.014032.

S. Breitkopf et al.
Extraction of enhanced, ultrashort laser pulses from a passive 10-MHz stack-and-dump cavity.
Applied physics / B, 122(12):297.
doi: 10.1007/s00340-016-6574-x.

L. Breuer et al.
Secondary ion and neutral mass spectrometry with swift heavy ions: Organic molecules.
Journal of vacuum science & technology / B, 34(3):03H130.
doi: 10.1116/1.4943158.

P. A. Butler et al.
TSR: A storage and cooling ring for HIE-ISOLDE.
Nuclear instruments & methods in physics research / B, 376:270.
doi: 10.1016/j.nimb.2015.12.006.

P. A. Butler et al.
TSR: A Storage Ring for HIE-ISOLDE.
Acta physica Polonica / B, 47(3):627.
doi: 10.5506/APhysPolB.47.627.

M. Cassinelli* et al.
Low temperature annealing effects on the stability of Bi nanowires.
Physica status solidi / A, 213(3):603.
doi: 10.1002/pssa.201532613.

W. Cayzac* et al.
Simulations of the energy loss of ions at the stopping-power maximum in a laser-induced plasma.
Journal of physics / Conference Series, 688:012009.
doi: 10.1088/1742-6596/688/1/012009.

X. Chen* et al.
Intensity-sensitive and position-resolving cavity for heavy-ion storage rings.
Nuclear instruments & methods in physics research / A, 826:39.
doi: 10.1016/j.nima.2016.04.056.

M.-C. Clochard et al.
Large area fabrication of self-standing nanoporous graphene-on-PMMA substrate.
Materials letters, 184:47.
doi: 10.1016/j.matlet.2016.07.133.

S. Cousens et al.
Temporal Structure of Attosecond Pulses from Laser-Driven Coherent Synchrotron Emission.
Physical review letters, 116(8):083901.
doi: 10.1103/PhysRevLett.116.083901.

N. Dimitrov et al.
Pulse front tilt measurement of femtosecond laser pulses.
Optics communications, 371:51.
doi: 10.1016/j.optcom.2016.03.054.

T. Döppner et al.
Improving a high-efficiency, gated spectrometer for x-ray Thomson scattering experiments at the National Ignition Facility.
Review of scientific instruments, 87(11):11E515.
doi: 10.1063/1.4959874.

J. L. Duan et al.
Vertically-Aligned Single-Crystal Nanocone Arrays: Controlled Fabrication and Enhanced Field Emission.
ACS applied materials & interfaces, 8(1):472.
doi: 10.1021/acsami.5b09374.

J. Duan et al.
Surface plasmonic spectroscopy revealing the oxidation dynamics of copper nanowires embedded in polycarbonate ion-track templates.
Journal of materials chemistry / C, 4(18):3956.
doi: 10.1039/C5TC03897A.

M. S. Ebrahimi et al.
Superconducting radio-frequency resonator in magnetic fields up to 6 T.
Review of scientific instruments, 87(7):075110.
doi: 10.1063/1.4958647.

L. Filippin et al.
Multiconfiguration calculations of electronic isotope shift factors in Al i.
Physical review / A, 94(6):062508.
doi: 10.1103/PhysRevA.94.062508.

E. D. Filippov et al.
Parameters of supersonic astrophysically-relevant plasma jets collimating via poloidal magnetic field measured by x-ray spectroscopy method.
31st International Conference on Equations of State for Matter, Elbrus (Russia), 1 Mar 2016 - 6 Mar 2016.
IOP Publ., Bristol, 1st Mar. 2016.
doi: 10.1088/1742-6596/774/1/012114.

S. Fuchs* et al.
Nanometer resolution optical coherence tomography using broad bandwidth XUV and soft x-ray radiation.
Scientific reports, 6:20658.
doi: 10.1038/srep20658.

C. Gaida et al.
Thulium-doped fiber chirped-pulse amplification system with 2 GW of peak power.
Optics letters, 41(17):4130.
doi: 10.1364/OL.41.004130.

H. Gies*, F. Karbstein* and N. Seegert*.
Photon merging and splitting in electromagnetic field inhomogeneities.
Physical review / D, 93(8):085034.
doi: 10.1103/PhysRevD.93.085034.

H. Gies* and G. Torgrimsson.
Critical Schwinger Pair Production.
Physical review letters, 116(9):090406.
doi: 10.1103/PhysRevLett.116.090406.

A. Gopal* et al.
Smith–Purcell radiation in the terahertz regime using charged particle beams from laser–matter interactions.
Laser and particle beams, 34(01):187.
doi: 10.1017/S0263034615001093.

A. N. Grum-Grzhimailo et al.
Photoelectron angular distributions and correlations in sequential double and triple atomic ionization by free electron lasers.
Journal of modern optics, 63(4):334.
doi: 10.1080/09500340.2015.1047805.

S. Gupta et al.
Conducting ion tracks generated by charge-selected swift heavy ions.
Nuclear instruments & methods in physics research / B, 381:76.
doi: 10.1016/j.nimb.2016.05.010.

J. Haber et al.
Collective strong coupling of X-rays and nuclei in a nuclear optical lattice.
Nature photonics, 10(7):445.
doi: 10.1038/nphoton.2016.77.

S. Hädrich* et al.
Energetic sub-2-cycle laser with 216W average power.
Optics letters, 41(18):4332.
doi: 10.1364/OL.41.004332.

S. Hädrich et al.
Scalability of components for kW-level average power few-cycle lasers.
Applied optics, 55(7):1636.
doi: 10.1364/AO.55.001636.

S. Hädrich* et al.
Single-pass high harmonic generation at high repetition rate and photon flux.
Journal of physics / B, 49(17):172002.
doi: 10.1088/0953-4075/49/17/172002.

C. Hahn* et al.
CdTe Timepix detectors for single-photon spectroscopy and linear polarimetry of high-flux hard x-ray radiation.
Review of scientific instruments, 87(4):043106.
doi: 10.1063/1.4945362.

M. Hahn et al.
Storage ring cross section measurements for electron impact ionization of Fe^{8+}.
Journal of physics / B, 49(8):084006.
doi: 10.1088/0953-4075/49/8/084006.

P. Hansinger et al.
White light generated by femtosecond optical vortex beams.
Journal of the Optical Society of America / B, 33(4):681.
doi: 10.1364/JOSAB.33.000681.

A. G. Hayrapetyan et al.
Electromagnetic wave propagation in spatially homogeneous yet smoothly time-varying dielectric media.
Journal of quantitative spectroscopy & radiative transfer, 178:158.
doi: 10.1016/j.jqsrt.2015.12.007.

H. Heylen et al.
Changes in nuclear structure along the Mn isotopic chain studied via charge radii.
Physical review / C, 94(5):054321.
doi: 10.1103/PhysRevC.94.054321.

P.-M. Hillenbrand* et al.
Strong asymmetry of the electron-loss-to-continuum cusp of multielectron U^{28+} projectiles in near-relativistic collisions with gaseous targets.
Physical review / A, 93(4):042709.
doi: 10.1103/PhysRevA.93.042709.

DOI:10.15120/GR-2017-1

J. Hofbrucker*, A. V. Volotka* and S. Fritzsche*.
Relativistic calculations of the nonresonant two-photon ionization of neutral atoms.
Physical review / A, 94(6):063412.
doi: 10.1103/PhysRevA.94.063412.

S. Höfer* et al.
Communication: The formation of rarefaction waves in semiconductors after ultrashort excitation probed by grazing incidence ultrafast time-resolved x-ray diffraction.
Structural dynamics, 3(5):051101.
doi: 10.1063/1.4963011.

M. Hornung* et al.
54J pulses with 18nm bandwidth from a diode-pumped chirped-pulse amplification laser system.
Optics letters, 41(22):5413.
doi: 10.1364/OL.41.005413.

J.-G. Hwang, T.-K. Yang and P. Forck*.
High precision capacitive beam phase probe for KHIMA project.
Nuclear instruments & methods in physics research / A, 837:34.
doi: 10.1016/j.nima.2016.08.042.

I. P. Ivanov et al.
Double-slit experiment in momentum space.
epl, 115(4):41001.
doi: 10.1209/0295-5075/115/41001.

I. P. Ivanov et al.
Elastic scattering of vortex electrons provides direct access to the Coulomb phase.
Physical review / D, 94(7):076001.
doi: 10.1103/PhysRevD.94.076001.

C. Jauregui et al.
Optimizing high-power Yb-doped fiber amplifier systems in the presence of transverse mode instabilities.
Optics express, 24(8):7879.
doi: 10.1364/OE.24.007879.

C. Jean et al.
Spatiotemporal Imaging of the Acoustic Field Emitted by a Single Copper Nanowire.
Nano letters, 16(10):6592.
doi: 10.1021/acs.nanolett.6b03260.

T. Kämpfer* et al.
Linear polarization of the characteristic x-ray lines following inner-shell photoionization of tungsten.
Physical review / A, 93(3):033409.
doi: 10.1103/PhysRevA.93.033409.

A. V. Kantsyrev et al.
Quadrupole lenses on the basis of permanent magnets for a PRIOR proton microscope prototype.
Instruments and experimental techniques, 59(5):712.
doi: 10.1134/S0020441216040072.

S. Kar et al.
Guided post-acceleration of laser-driven ions by a miniature modular structure.
Nature Communications, 7:10792.
doi: 10.1038/ncomms10792.

F. Karbstein* and C. Sundqvist*.
Probing vacuum birefringence using x-ray free electron and optical high-intensity lasers.
Physical review / D, 94(1):013004.
doi: 10.1103/PhysRevD.94.013004.

I. Karpov, V. Kornilov* and O. Boine-Frankenheim*.
Early transverse decoherence of bunches with space charge.
Physical review accelerators and beams, 19(12):124201.
doi: 10.1103/PhysRevAccelBeams.19.124201.

S. Keppler et al.
The generation of amplified spontaneous emission in high-power CPA laser systems.
Laser & photonics reviews, 10(2):264.
doi: 10.1002/lpor.201500186.

S. Keppler et al.
Tunable filters for precise spectral gain control in ultra-short-pulse laser systems.
Optics letters, 41(20):4708.
doi: 10.1364/OL.41.004708.

V. Y. Kharin*, D. Seipt* and S. G. Rykovanov*.
Temporal laser-pulse-shape effects in nonlinear Thomson scattering.
Physical review / A, 93(6):063801.
doi: 10.1103/PhysRevA.93.063801.

M. Kienel* et al.
12mJkW-class ultrafast fiber laser system using multidimensional coherent pulse addition.
Optics letters, 41(14):3343.
doi: 10.1364/OL.41.003343.

R. Klas* et al.
Table-top milliwatt-class extreme ultraviolet high harmonic light source.
Optica, 3(11):1167.
doi: 10.1364/OPTICA.3.001167.

C. Kohlfürst* and R. Alkofer.
On the effect of time-dependent inhomogeneous magnetic fields in electron–positron pair production.
Physics letters / B, 756:371.
doi: 10.1016/j.physletb.2016.03.027.

J. Körner, J. Hein* and M. Kaluza*.
Compact Aberration-Free Relay-Imaging Multi-Pass Layouts for High-Energy Laser Amplifiers.
Applied Sciences, 6(11):353.
doi: 10.3390/app6110353.

J. Körner et al.
Spatially and temporally resolved temperature measurement in laser media.
Optics letters, 41(11):2525.
doi: 10.1364/OL.41.002525.

O. F. Kostenko et al.
On the hot electrons and K α x-rays generation in the intense laser interaction with silver targets.
31st International Conference on Equations of State for Matter (ELBRUS), Elbrus (Russia), 1 Mar 2016 - 6 Mar 2016.
IOP Publ., Bristol, 1st Mar. 2016.
doi: 10.1088/1742-6596/774/1/012112.

Y. E. Krasik et al.
Underwater Electrical Explosion of Wires and Wire Arrays and Generation of Converging Shock Waves.
IEEE transactions on plasma science, 44(4):412.
doi: 10.1109/TPS.2015.2513757.

D. Kraus et al.
Nanosecond formation of diamond and lonsdaleite by shock compression of graphite.
Nature Communications, 7:10970.
doi: 10.1038/ncomms10970.

D. Kraus et al.
Platform for spectrally resolved x-ray scattering from imploding capsules at the National Ignition Facility.
Journal of physics / Conference Series, 717:UNSP 012067.
doi: 10.1088/1742-6596/717/1/012067.

D. Kraus et al.
X-ray scattering measurements on imploding CH spheres at the National Ignition Facility.
Physical review / E, 94(1):011202.
doi: 10.1103/PhysRevE.94.011202.

J. Krey et al.
Effect of B_2O_3 and fluoride additions on the Yb^{3+} luminescence of an alumosilicate glass in the system $Li_2O/MgO/Al_2O_3/SiO_2$.
Optical materials express, 6(8):2662.
doi: 10.1364/OME.6.002662.

J. Krieg* et al.
Exploring the Electronic Structure and Chemical Homogeneity of Individual Bi_2Te_3 Nanowires by Nano-Angle-Resolved Photoemission Spectroscopy.
Nano letters, 16(7):4001.
doi: 10.1021/acs.nanolett.6b00400.

M. Kübel et al.
Complete characterization of single-cycle double ionization of argon from the nonsequential to the sequential ionization regime.
Physical review / A, 93(5):053422.
doi: 10.1103/PhysRevA.93.053422.

B. Landgraf* et al.
Broadband stimulated Raman backscattering.
New journal of physics, 18(7):073048.
doi: 10.1088/1367-2630/18/7/073048.

M. Lestinsky* et al.
Physics book: CRYRING@ESR.
European physical journal special topics, 225(5):797.
doi: 10.1140/epjst/e2016-02643-6.

H. Li et al.
Intensity dependence of the dissociative ionization of DCl in few-cycle laser fields.
Journal of physics / B, 49(1):015601.
doi: 10.1088/0953-4075/49/1/015601.

H. Liebetrau et al.
High contrast, 86fs, 35mJ pulses from a diode-pumped, Yb:glass, double-chirped-pulse amplification laser system.
Optics letters, 41(13):3006.
doi: 10.1364/OL.41.003006.

A. Lushchik et al.
Influence of complex impurity centres on radiation damage in wide-gap metal oxides.
Nuclear instruments & methods in physics research / B, 374:90.
doi: 10.1016/j.nimb.2015.07.004.

G. Ma et al.
Control of transmission of right circularly polarized laser light in overdense plasma by applied magnetic field pulses.
Physical review / E, 93(5):053209.
doi: 10.1103/PhysRevE.93.053209.

F. Maimone* et al.
Investigation of pulsed mode operation with the frequency tuned CAPRICE ECRIS.
Review of scientific instruments, 87(2):02A712.
doi: 10.1063/1.4933339.

A. Meftah et al.
Data consistencies of swift heavy ion induced damage creation in yttrium iron garnet analyzed by different techniques.
Nuclear instruments & methods in physics research / B, 366:155.
doi: 10.1016/j.nimb.2015.10.030.

B. Mei* et al.
Odd-even staggering in yields of neutron-deficient nuclei produced by projectile fragmentation.
Physical review / C, 94(4):044615.
doi: 10.1103/PhysRevC.94.044615.

F. Meinerzhagen et al.
A new setup for the investigation of swift heavy ion induced particle emission and surface modifications.
Review of scientific instruments, 87(1):013903.
doi: 10.1063/1.4939899.

K. Minamisono et al.
Charge Radii of Neutron Deficient ^{52,53}Fe Produced by Projectile Fragmentation.
Physical review letters, 117(25):252501.
doi: 10.1103/PhysRevLett.117.252501.

V. Mintsev et al.
Non-Ideal Plasma and Early Experiments at FAIR: HIHEX - Heavy Ion Heating and EXpansion.
Contributions to plasma physics, 56(3-4):281.
doi: 10.1002/ctpp.201500105.

L. Movsesyan* et al.
Influence of electrodeposition parameters on the structure and morphology of ZnO nanowire arrays and networks synthesized in etched ion-track membranes.
Semiconductor science and technology, 31(1):014006.
doi: 10.1088/0268-1242/31/1/014006.

M. Mueller et al.
Phase stabilization of spatiotemporally multiplexed ultrafast amplifiers.
Optics express, 24(8):7893.
doi: 10.1364/OE.24.007893.

DOI:10.15120/GR-2017-1

F. Muench et al.
Electrodeposition and electroless plating of hierarchical metal superstructures composed of 1D nano- and microscale building blocks.
Electrochimica acta, 202:47.
doi: 10.1016/j.electacta.2016.03.188.

M. Müller et al.
1 kW 1 mJ eight-channel ultrafast fiber laser.
Optics letters, 41(15):3439.
doi: 10.1364/OL.41.003439.

R. A. Müller* et al.
Photoionization of neutral atoms by X waves carrying orbital angular momentum.
Physical review / A, 94(4):041402.
doi: 10.1103/PhysRevA.94.041402.

T. Murböck et al.
A compact source for bunches of singly charged atomic ions.
Review of scientific instruments, 87(4):043302.
doi: 10.1063/1.4944946.

T. Murböck et al.
Rapid crystallization of externally produced ions in a Penning trap.
Physical review / A, 94(4):043410.
doi: 10.1103/PhysRevA.94.043410.

A. Nadzri et al.
Composition dependent thermal annealing behaviour of ion tracks in apatite.
Nuclear instruments & methods in physics research / B, 379:211.
doi: 10.1016/j.nimb.2016.04.050.

M. A. Najafi* et al.
CsI–Silicon Particle detector for Heavy ions Orbiting in Storage rings (CsISiPHOS).
Nuclear instruments & methods in physics research / A, 836:1.
doi: 10.1016/j.nima.2016.08.040.

T. Nousch et al.
Spectral caustics in laser assisted Breit–Wheeler process.
Physics letters / B, 755:162.
doi: 10.1016/j.physletb.2016.01.062.

A. Ortner* et al.
A novel experimental setup for energy loss and charge state measurements in dense moderately coupled plasma using laser-heated hohlraum targets.
Journal of physics / Conference Series, 688:012081.
doi: 10.1088/1742-6596/688/1/012081.

A. Otto et al.
Pair production by Schwinger and Breit–Wheeler processes in bi-frequent fields.
Journal of plasma physics, 82(03):655820301.
doi: 10.1017/S0022377816000428.

M. K. Pavićević et al.
Erosion rate study at the Allchar deposit (Macedonia) based on radioactive and stable cosmogenic nuclides (^{26}Al, ^{36}Cl, ^{3}He, and ^{21}Ne).
Geochemistry, geophysics, geosystems, 17(2):410.
doi: 10.1002/2015GC006054.

G. Pérez-Mitta et al.
Noncovalent functionalization of solid-state nanopores via self-assembly of amphipols.
Nanoscale, 8(3):1470.
doi: 10.1039/C5NR08190D.

G. Pérez-Mitta et al.
The Influence of Divalent Anions on the Rectification Properties of Nanofluidic Diodes: Insights from Experiments and Theoretical Simulations.
ChemPhysChem, 17(17):2718.
doi: 10.1002/cphc.201600370.

A. A. Peshkov* et al.
Absorption of twisted light by a mesoscopic atomic target.
Physica scripta, 91(6):064001.
doi: 10.1088/0031-8949/91/6/064001.

A. R. Piriz, Y. B. Sun and N. A. Tahir*.
Entropy shaping by shock decay.
Physics of plasmas, 23(11):112704.
doi: 10.1063/1.4967463.

A. R. Piriz, Y. B. Sun and N. A. Tahir*.
Hydrodynamic growth and decay of planar shock waves.
Physics of plasmas, 23(3):032704.
doi: 10.1063/1.4943198.

S. G. Podorov* and E. Förster*.
Direct inversion of digital 3D Fraunhofer holography maps.
Applied optics, 55(3):A150.
doi: 10.1364/AO.55.00A150.

R. H. Pratt, R. A. Müller and A. Surzhykov*.
Sum rules for the polarization correlations in photoionization and bremsstrahlung.
Physical review / A, 93(5):053421.
doi: 10.1103/PhysRevA.93.053421.

L. P. Pugachev et al.
Acceleration of electrons under the action of petawatt-class laser pulses onto foam targets.
Nuclear instruments & methods in physics research / A, 829:88.
doi: 10.1016/j.nima.2016.02.053.

Y. Qiu et al.
Role of Particle Focusing in Resistive-Pulse Technique: Direction-Dependent Velocity in Micropores.
ACS nano, 10(3):3509.
doi: 10.1021/acsnano.5b07709.

J. Rothhardt* et al.
100W average power femtosecond laser at 343nm.
Optics letters, 41(8):1885.
doi: 10.1364/OL.41.001885.

J. Rothhardt et al.
High-repetition-rate and high-photon-flux 70 eV high-harmonic source for coincidence ion imaging of gas-phase molecules.
Optics express, 24(16):18133.
doi: 10.1364/OE.24.018133.

S. G. Rykovanov* et al.
Reply to "Comment on 'Controlling the spectral shape of nonlinear Thomson scattering with proper laser chirping'".
Physical review accelerators and beams, 19(9):098002.
doi: 10.1103/PhysRevAccelBeams.19.098002.

R. Sachan et al.
Insights on dramatic radial fluctuations in track formation by energetic ions.
Scientific reports, 6:27196.
doi: 10.1038/srep27196.

A. S. El-Said et al.
Modifications of gallium phosphide single crystals using slow highly charged ions and swift heavy ions.
Nuclear instruments & methods in physics research / B, 382:86.
doi: 10.1016/j.nimb.2016.04.058.

M. Schäfer, I. Huet and H. Gies*.
Worldline numerics for energy-momentum tensors in Casimir geometries.
Journal of physics / A, 49(13):135402.
doi: 10.1088/1751-8113/49/13/135402.

S. Schippers et al.
Prominent role of multielectron processes in K -shell double and triple photodetachment of oxygen anions.
Physical review / A, 94(4):041401.
doi: 10.1103/PhysRevA.94.041401.

M. S. Schöffler et al.
Laser-subcycle control of sequential double-ionization dynamics of helium.
Physical review / A, 93(6):063421.
doi: 10.1103/PhysRevA.93.063421.

T. Scholtes et al.
Suppression of spin-exchange relaxation in tilted magnetic fields within the geophysical range.
Physical review / A, 94(1):013403.
doi: 10.1103/PhysRevA.94.013403.

A. Schönlein et al.
Generation and characterization of warm dense matter isochorically heated by laser-induced relativistic electrons in a wire target.
epl, 114(4):45002.
doi: 10.1209/0295-5075/114/45002.

I. Schubert* et al.
Porous Gold Nanowires: Plasmonic Response and Surface-Enhanced Infrared Absorption.
Advanced optical materials, 1:1.
doi: 10.1002/adom.201600430.

D. Seipt* et al.
Analytical results for nonlinear Compton scattering in short intense laser pulses.
Journal of plasma physics, 82(02):655820203.
doi: 10.1017/S002237781600026X.

D. Seipt* et al.
Caustic structures in x-ray Compton scattering off electrons driven by a short intense laser pulse.
New journal of physics, 18(2):023044.
doi: 10.1088/1367-2630/18/2/023044.

D. Seipt* et al.
Two-color above-threshold ionization of atoms and ions in XUV Bessel beams and intense laser light.
Physical review / A, 94(5):053420.
doi: 10.1103/PhysRevA.94.053420.

C. Serrat et al.
Avalanche of stimulated forward scattering in high harmonic generation.
Optics express, 24(8):8028.
doi: 10.1364/OE.24.008028.

C. Shah et al.
Strong higher-order resonant contributions to x-ray line polarization in hot plasmas.
Physical review / E, 93(6):061201.
doi: 10.1103/PhysRevE.93.061201.

J. Shamblin et al.
Structural response of titanate pyrochlores to swift heavy ion irradiation.
Acta materialia, 117:207.
doi: 10.1016/j.actamat.2016.07.017.

P. Shuai et al.
An improvement of isochronous mass spectrometry: Velocity measurements using two time-of-flight detectors.
Nuclear instruments & methods in physics research / B, 376:311.
doi: 10.1016/j.nimb.2016.02.006.

E. Siminos et al.
Modeling ultrafast shadowgraphy in laser-plasma interaction experiments.
Plasma physics and controlled fusion, 58(6):065004.
doi: 10.1088/0741-3335/58/6/065004.

A. Sokolov*, G. Fehrenbacher* and T. Radon*.
Design development of a passive neutron dodemeter for the use at high-energy accelerators.
Radiation protection dosimetry, 170(1-4):195.
doi: 10.1093/rpd/ncv489.

P. Spädtke* et al.
Ion beam emittance from an ECRIS.
Review of scientific instruments, 87(2):02A724.
doi: 10.1063/1.4934210.

A. Surzhykov, D. Seipt* and S. Fritzsche*.
Probing the energy flow in Bessel light beams using atomic photoionization.
Physical review / A, 94(3):033420.
doi: 10.1103/PhysRevA.94.033420.

DOI:10.15120/GR-2017-1

G. K. Tadesse et al.
High speed and high resolution table-top nanoscale imaging.
Optics letters, 41(22):5170.
doi: 10.1364/OL.41.005170.

N. A. Tahir* et al.
Beam Induced Hydrodynamic Tunneling in the Future Circular Collider Components.
Physical review accelerators and beams, 19(8):081002.
doi: 10.1103/PhysRevAccelBeams.19.081002.

N. A. Tahir* et al.
High energy density physics effects predicted in simulations of the CERN HiRadMat beam–target interaction experiments.
High energy density physics, 21:27.
doi: 10.1016/j.hedp.2016.09.002.

N. A. Tahir* et al.
High Energy Density Physics Research Using Intense Heavy Ion Beam at FAIR: The HEDgeHOB Program.
8th International Conference on Inertial Fusion Sciences and Applications, Bristol (UK), 8 Sep 2013 - 13 Sep 2013.
IOP Publ., Bristol, 8th Sept. 2013.
doi: 10.1088/1742-6596/688/1/012118.

A. I. Titov et al.
Determination of the carrier envelope phase for short, circularly polarized laser pulses.
Physical review / D, 93(4):045010.
doi: 10.1103/PhysRevD.93.045010.

M. Toulemonde, W. Assmann and C. Trautmann*.
Electronic sputtering of vitreous SiO_2: Experimental and modeling results.
Nuclear instruments & methods in physics research / B, 379:2.
doi: 10.1016/j.nimb.2016.03.023.

C. L. Tracy et al.
Anisotropic expansion and amorphization of Ga_2O_3 irradiated with 946MeV Au ions.
Nuclear instruments & methods in physics research / B, 374:40.
doi: 10.1016/j.nimb.2015.08.059.

C. L. Tracy et al.
Role of composition, bond covalency, and short-range order in the disordering of stannate pyrochlores by swift heavy ion irradiation.
Physical review / B, 94(6):064102.
doi: 10.1103/PhysRevB.94.064102.

X. L. Tu* et al.
Indirect mass determination for the neutron-deficient nuclides ^{44}V, ^{48}Mn, ^{52}Co and ^{56}Cu.
Nuclear physics / A, 945:89.
doi: 10.1016/j.nuclphysa.2015.09.016.

C. Ullmann* et al.
Investigation of ion beam space charge compensation with a 4-grid analyzer.
Review of scientific instruments, 87(2):02B938.
doi: 10.1063/1.4939782.

D. Varentsov et al.
Commissioning of the PRIOR proton microscope.
Review of scientific instruments, 87(2):023303.
doi: 10.1063/1.4941685.

M. Vogel*.
Dark energy, by Miao Li, Xiao-Dong Li, Shuang Wang and Yi Wang.
Contemporary physics, 57(3):455.
doi: 10.1080/00107514.2016.1205669.

M. Vogel*.
Handbook of accelerator physics and engineering, by A.W. Chao, K.H. Mess, M. Tigner and F. Zimmermann; 2. ed.
Contemporary physics, 57(2):263.
doi: 10.1080/00107514.2015.1133708.

M. Vogel*.
Laser physics: from principles to practical work in the lab, by Marc Eichhorn.
Contemporary physics, 57(4):617.
doi: 10.1080/00107514.2016.1221468.

M. Vogel*.
Masers and lasers, second edition: an historical approach, by Mario Bertolotti.
Contemporary physics, 57(2):255.
doi: 10.1080/00107514.2015.1117141.

M. Vogel*.
Plasma physics: an introduction, by Richard Fitzpatrick.
Contemporary physics, 57(4):606.
doi: 10.1080/00107514.2016.1217047.

M. Vogel*.
Properties of materials, by P.F. Kelly.
Contemporary physics, 57(3):449.
doi: 10.1080/00107514.2016.1173109.

M. Vogel*.
Superconductors, by A. V. Narlikar.
Contemporary physics, 57(2):255.
doi: 10.1080/00107514.2015.1111422.

M. Vogel*.
The Formation of the Solar System: Theories Old and New (2nd Edition), by Michael Woolfson.
Contemporary physics, 57(1):134.
doi: 10.1080/00107514.2015.1081623.

M. Vogel*.
Thermodynamics, kinetics, and microphysics of clouds, by V.I. Khvorostyanov and J.A. Curry.
Contemporary physics, 57(2):271.
doi: 10.1080/00107514.2016.1156753.

A. V. Volotka* et al.
Many-electron effects on x-ray Rayleigh scattering by highly charged He-like ions.
Physical review / A, 93(2):023418.
doi: 10.1103/PhysRevA.93.023418.

A. V. Volotka* et al.
Nuclear Excitation by Two-Photon Electron Transition.
Physical review letters, 117(24):243001.
doi: 10.1103/PhysRevLett.117.243001.

M. F. P. Wagner* et al.
Fabrication and thermoelectrical characterization of three-dimensional nanowire networks.
Physica status solidi / A, 213(3):610.
doi: 10.1002/pssa.201532616.

I. S. Wahyutama* et al.
Influence of detector noise in holographic imaging with limited photon flux.
Optics express, 24(19):22013.
doi: 10.1364/OE.24.022013.

Q. Wen et al.
Highly Selective Ionic Transport through Subnanometer Pores in Polymer Films.
Advanced functional materials, 26(32):5796.
doi: 10.1002/adfm.201601689.

Z. W. Wu* et al.
Level sequence and splitting identification of closely spaced energy levels by angle-resolved analysis of fluorescence light.
Physical review / A, 93(6):063413.
doi: 10.1103/PhysRevA.93.063413.

C. Xiao et al.
Measurement of the transverse four-dimensional beam rms-emittance of an intense uranium beam at 11.4MeV/u.
Nuclear instruments & methods in physics research / A, 820:14.
doi: 10.1016/j.nima.2016.02.090.

C. Xiao et al.
Rotating system for four-dimensional transverse rms-emittance measurements.
Physical review accelerators and beams, 19(7):072802.
doi: 10.1103/PhysRevAccelBeams.19.072802.

X. Xu et al.
Identification of the Lowest $T = 2$, $J^{\pi} = 0^{+}$ Isobaric Analog State in ^{52}Co and Its Impact on the Understanding of β -Decay Properties of ^{52}Ni.
Physical review letters, 117(18):182503.
doi: 10.1103/PhysRevLett.117.182503.

M. Yamamoto et al.
Vacuum tube operation analysis under multi-harmonic driving and heavy beam loading effect in J-PARC RCS.
Nuclear instruments & methods in physics research / A, 835:119.
doi: 10.1016/j.nima.2016.08.028.

X. Yan* et al.
Preface [Nuclear Physics in Astrophysics VI (NPA6)].
Journal of physics / Conference Series, 665:011001.
doi: 10.1088/1742-6596/665/1/011001.

X. Yan* et al.
Recent results on mass measurements of exotic nuclides in storage rings.
Journal of physics / Conference Series, 665:012053.
doi: 10.1088/1742-6596/665/1/012053.

X. F. Yang et al.
Isomer Shift and Magnetic Moment of the Long-Lived $1/2^{+}$ Isomer in $^{79}_{30}Zn_{49}$: Signature of Shape Coexistence near ^{78}Ni.
Physical review letters, 116(18):182502.
doi: 10.1103/PhysRevLett.116.182502.

V. A. Yerokhin et al.
Electric dipole polarizabilities of Rydberg states of alkali-metal atoms.
Physical review / A, 94(3):032503.
doi: 10.1103/PhysRevA.94.032503.

X. Yin, W. Bayer* and I. Hofmann*.
Linac code benchmarking of HALODYN and PARMILA based on beam experiments.
Nuclear instruments & methods in physics research / A, 806:92.
doi: 10.1016/j.nima.2015.10.012.

R. Zabels et al.
MeV-energy Xe ion-induced damage in LiF: The contribution of electronic and nuclear stopping mechanisms.
Physica status solidi / B, 253(8):1511.
doi: 10.1002/pssb.201552704.

Y. H. Zhang et al.
Storage ring mass spectrometry for nuclear structure and astrophysics research.
Physica scripta, 91(7):073002.
doi: 10.1088/0031-8949/91/7/073002.

N. A. Zubova et al.
Isotope shifts of the $2p_{3/2} - 2p_{1/2}$ transition in B-like ions.
Physical review / A, 93(5):052502.
doi: 10.1103/PhysRevA.93.052502.

17 dissertations

S. Alzubaidi.
Control system for the FRANZ facility.
Johann Wolfgang Goethe-Universität Frankfurt, Frankfurt, 2016.

D. Atanasov*.
Precision mass measurements for studies of nucleosynthesis via the rapid neutron-capture process.
Universität Heidelberg, 2016.

K.-H. Blumenhagen*.
Experimental studies on polarization correlations in hard x-ray Rayleigh scattering.
Friedrich-Schiller-Universität Jena, Jena, 2016.

L. Burr.
Ion-track technology based synthesis and characterization of gold and gold alloys nanowires and nanocones.
Technische Universität Darmstadt, 2016.

M. Cassinelli*.
Thermoelectric Properties of Bi1-xSbx Nanowires Electrodeposited in Etched Ion-Track Membranes.
Technische Universität Darmstadt, 2016.

DOI:10.15120/GR-2017-1

T. Gaßner*.
High precision x-ray spectroscopy of highly charged heavy ions.
Friedrich-Schiller-Universität Jena, 2017.

J. Helfrich*.
Röntgen-Thomson-Streuung an warmem dichten Kohlenstoff.
Technische Universität Darmstadt, 2016.

B. Höltkemeier.
Sympathetic Cooling of Ions in a Hybrid Atom Ion Trap.
Universität Heidelberg, 2016.

C. Hubert*.
Characterization of radiation damage induced by swift heavy ions in graphite.
Technische Universität Darmstadt, Darmstadt, 2016.

D. Khaghani*.
Investigation of laser interaction with nano-, micro-structures for ion acceleration, intense X-ray production & high energy density generation.
Johann Wolfgang Goethe-Universität Frankfurt, 2016.

A. Klenke.
Performance scaling of laser amplifiers via coherent combination of ultrashort pulses.
Friedrich-Schiller-Universität Jena, Berlin, 2016.

K. Kupka*.
Intense heavy ion beam-induced effects in carbon-based stripper foils.
Technische Universität Darmstadt, 2016.

L. Movsesyan*.
Template-assisted growth and characterization of ZnO-based nanowire arrays and 3D networks.
Technische Universität Darmstadt, Darmstadt, 2016.

A. Romanenko*.
Radiation damage produced by swift heavy ions in rare earth phosphates.
Technische Universität Darmstadt, Darmstadt, 2016.

S. M. W. Schmidt.
Untersuchung mesoskopischer Coulomb-Kristalle zum sympathischen Kühlen hochgeladener Ionen und direkte Bestimmung der Massendifferenz von ^{123}Te und ^{123}Sb.
Johannes Gutenberg-Universität Mainz, 2016.

A. Spende*.
Surface Modification of Etched Ion-Track Polymer Membranes by Atomic Layer Deposition.
Technische Universität Darmstadt, 2016.

J. Steinmann*.
Analytical and numerical investigations of resistive cooling of trapped ion clouds.
Friedrich-Alexander-Universität Erlangen-Nürnberg, 2016.

Matter and technologies – 630

16 publications listed in Web of Science or SCOPUS

A. Adonin* et al.
Production of high current proton beams using complex H-rich molecules at GSI.
Review of scientific instruments, 87(2):02B709.
doi: 10.1063/1.4934620.

O. Boine-Frankenheim*, I. Hofmann and J. Struckmeier*.
Parametric sum envelope instability of periodically focused intense beams.
Physics of plasmas, 23(9):090705.
doi: 10.1063/1.4963851.

M. Chung et al.
Generalized Kapchinskij-Vladimirskij Distribution and Beam Matrix for Phase-Space Manipulations of High-Intensity Beams.
Physical review letters, 117(22):224801.
doi: 10.1103/PhysRevLett.117.224801.

M. Ciobanu et al.
Simulations and Test Results of Large Area Continuous Position Sensitive Diamond Detectors.
Diamond and related materials, 65:115.
doi: 10.1016/j.diamond.2016.02.016.

M. Drągowski et al.
Monte Carlo study of the effective Sherman function for electron polarimetry.
Nuclear instruments & methods in physics research / B, 389-390:48.
doi: 10.1016/j.nimb.2016.11.018.

B. Dromey et al.
Picosecond metrology of laser-driven proton bursts.
Nature Communications, 7:10642.
doi: 10.1038/ncomms10642.

B. Faatz et al.
Simultaneous operation of two soft x-ray free-electron lasers driven by one linear accelerator.
New journal of physics, 18(6):062002.
doi: 10.1088/1367-2630/18/6/062002.

S. Kuschel* et al.
Demonstration of passive plasma lensing of a laser wakefield accelerated electron bunch.
Physical review accelerators and beams, 19(7):071301.
doi: 10.1103/PhysRevAccelBeams.19.071301.

E. Metral et al.
Beam Instabilities in Hadron Synchrotrons.
IEEE transactions on nuclear science, 63(2):1001.
doi: 10.1109/TNS.2015.2513752.

A. S. Novo et al.
Optimizing laser-driven proton acceleration from overdense targets.
Scientific reports, 6:29402.
doi: 10.1038/srep29402.

S. G. Rykovanov* et al.
Tunable polarization plasma channel undulator for narrow bandwidth photon emission.
Physical review accelerators and beams, 19(9):090703.
doi: 10.1103/PhysRevAccelBeams.19.090703.

P. Schmidt and O. Boine-Frankenheim*.
A gas-dynamical approach to radiation pressure acceleration.
Physics of plasmas, 23(6):063106.
doi: 10.1063/1.4952623.

T. Tanikawa et al.
First observation of SASE radiation using the compact wide-spectral-range XUV spectrometer at FLASH2.
Nuclear instruments & methods in physics research / A, 830:170.
doi: 10.1016/j.nima.2016.05.088.

F. Wagner* et al.
Maximum Proton Energy above 85 MeV from the Relativistic Interaction of Laser Pulses with Micrometer Thick CH_2 Targets.
Physical review letters, 116(20):205002.
doi: 10.1103/PhysRevLett.116.205002.

J. W. Wang* et al.
High-energy-density electron beam from interaction of two successive laser pulses with subcritical-density plasma.
Physical review accelerators and beams, 19(2):021301.
doi: 10.1103/PhysRevAccelBeams.19.021301.

M. Yeung et al.
Experimental observation of attosecond control over relativistic electron bunches with two-colour fields.
Nature photonics, 11(1):32.
doi: 10.1038/nphoton.2016.239.

3 dissertations

O. Köster.
Combining rotating-coil measurements of large-aperture accelerator magnets.
Technische Universität Darmstadt, 2016.

F. Kurian*.
Cryogenic Current Comparators for Precise Ion Beam Current Measurements.
Friedrich-Schiller-Universität Jena, 2015.

P. Schmidt*.
Radiation Pressure Acceleration and Laser Induced Focusing.
Technische Universität Darmstadt, 2016.

Cancer Research – 310

24 publications listed in Web of Science or SCOPUS

K. Anderle* et al.
In silico comparison of photons versus carbon ions in single fraction therapy of lung cancer.
Physica medica, 32(9):1118.
doi: 10.1016/j.ejmp.2016.08.014.

O. Arrizabalaga* et al.
Ionizing Radiation Alters Human Embryonic Stem Cell Properties and Differentiation Capacity by Diminishing the Expression of Activin Receptors.
Stem Cells and Development, -:scd.2016.0277.
doi: 10.1089/scd.2016.0277.

O. Arrizabalaga et al.
Ionizing Radiation Impacts on Cardiac Differentiation of Mouse Embryonic Stem Cells.
Stem Cells and Development, 25(2):178.
doi: 10.1089/scd.2015.0260.

N. B. Averbeck* et al.
Efficient Rejoining of DNA Double-Strand Breaks despite Increased Cell-Killing Effectiveness following Spread-Out Bragg Peak Carbon-Ion Irradiation.
Frontiers in oncology, 6:28.
doi: 10.3389/fonc.2016.00028.

A. Constantinescu* et al.
Treatment Planning Studies in Patient Data With Scanned Carbon Ion Beams for Catheter-Free Ablation of Atrial Fibrillation.
Journal of cardiovascular electrophysiology, 27(3):335.
doi: 10.1111/jce.12888.

J. G. Eley et al.
Comparative Risk Predictions of Second Cancers After Carbon-Ion Therapy Versus Proton Therapy.
International journal of radiation oncology, biology, physics, 95(1):279.
doi: 10.1016/j.ijrobp.2016.02.032.

A. Ewe et al.
Optimized polyethylenimine (PEI)-based nanoparticles for siRNA delivery, analyzed in vitro and in an ex vivo tumor tissue slice culture model.
Drug Delivery and Translational Research, -:1.
doi: 10.1007/s13346-016-0306-y.

T. Friedrich* et al.
Impact of fractionation and number of fields on dose homogeneity for intra-fractionally moving lung tumors using scanned carbon ion treatment.
Radiotherapy and oncology, 118(3):498.
doi: 10.1016/j.radonc.2015.12.011.

T. Friedrich* et al.
Response to the "Letter to the Editor" by K. H. Chadwick on our Article "A Comparison of Kinetic Photon Cell Survival Models".
Radiation research, 185(4):440.
doi: 10.1667/RR14387.S2.

C. Graeff* et al.
Feasibility Study on Cardiac Arrhythmia Ablation Using High-Energy Heavy Ion Beams.
Scientific reports, 6:38895.
doi: 10.1038/srep38895.

A. Helm* et al.
The Influence of C-Ions and X-rays on Human Umbilical Vein Endothelial Cells.
Frontiers in oncology, 6:5, 1.
doi: 10.3389/fonc.2016.00005.

DOI:10.15120/GR-2017-1

S. Hild* et al.
Scanned ion beam therapy for prostate carcinoma : Comparison of single plan treatment and daily plan-adapted treatment.
Strahlentherapie und Onkologie, 192(2):118.
doi: 10.1007/s00066-015-0925-0.

K.-J. Lee et al.
Phosphorylation of Ku dictates DNA double-strand break (DSB) repair pathway choice in S phase.
Nucleic acids symposium series, 44(4):1732.
doi: 10.1093/nar/gkv1499.

V. Manakov, A. Cucu* and C. Fournier*.
Inflammatory effects of TNFα are counteracted by X-ray irradiation and AChE inhibition in mouse micromass cultures.
Chemico-biological interactions, 259:S0009279716300953.
doi: 10.1016/j.cbi.2016.03.027.

A. Patel et al.
The Influence of the CTIP Polymorphism, Q418P, on Homologous Recombination and Predisposition to Radiation-Induced Tumorigenesis (mainly rAML) in Mice.
Radiation research, 186(6):RR14495.1.
doi: 10.1667/RR14495.1.

M. Prall* et al.
High-energy proton imaging for biomedical applications.
Scientific reports, 6:27651.
doi: 10.1038/srep27651.

T. P. Ringbæk et al.
Dosimetric comparisons of carbon ion treatment plans for 1D and 2D ripple filters with variable thicknesses.
Physics in medicine and biology, 61(11):4327.
doi: 10.1088/0031-9155/61/11/4327.

M. Saager et al.
The relative biological effectiveness of carbon ion irradiations of the rat spinal cord increases linearly with LET up to 99keV/µm.
Acta oncologica / Supplement, -:1.
doi: 10.1080/0284186X.2016.1250947.

E. Scifoni* et al.
Helium ions for radiotherapy? Physical and biological verifications of a novel treatment modality.
Medical physics, 43(4):1995.
doi: 10.1118/1.4944593.

S. Timm, B. Jakob* and G. Taucher-Scholz*.
Clustered double-strand breaks in heterochromatin perturb DNA repair after high linear energy transfer irradiation.
Radiotherapy and oncology, 121(1):154.
doi: 10.1016/j.radonc.2016.08.028.

F. Tommasino*.
Experimental and modelling studies for the validation of the mechanistic basis of the Local Effect Model.
Il nuovo cimento / C, 39:287.
doi: 10.1393/ncc/i2016-16287-8.

J. Wiedemann* et al.
Exposure to Carbon Ions Triggers Proinflammatory Signals and Changes in Homeostasis and Epidermal Tissue Organization to a Similar Extent as Photons.
Frontiers in oncology, 5:00294.
doi: 10.3389/fonc.2015.00294.

I. Yohannes et al.
Technical Note: Radiation properties of tissue- and water-equivalent materials formulated using the stoichiometric analysis method in charged particle therapy.
Medical physics, 43(1):308.
doi: 10.1118/1.4938587.

Z. Yu* et al.
The Effect of X-Ray and Heavy Ions Radiations on Chemotherapy Refractory Tumor Cells.
Frontiers in oncology, 6:64.
doi: 10.3389/fonc.2016.00064.

3 dissertations

K. Anderle*.
In silico comparison of photons versus carbon ions in single fraction therapy of lung cancer.
Technische Universität Darmstadt, 2016.

M. Rovituso*.
Fragmentation and lateral scattering of 120 and 200 MeV/u ^{4}He ions on water targets.
Technische Universität Darmstadt, Darmstadt, 2016.

J. Wiedemann*.
Untersuchung von entzündungrelevanter interzellulärer Kommunikation in einem 3D-Haut-Modell.
Technische Universität Darmstadt, 2016.

Ministerialdirigent Dr. Rolf Bernhardt,
Hessisches Ministerium für Wissenschaft und Kunst, Wiesbaden (Germany),
as representative of the State of Hesse in Germany

Dr. Bernd Ebersold,
Thüringer Ministerium für Wirtschaft, Wissenschaft und digitale Gesellschaft, Erfurt (Germany),
as representative of the State of Thuringia in Germany

Dr. Carola Zimmermann,
Ministerium für Bildung, Wissenschaft, Weiterbildung und Kultur, Mainz (Germany),
as representative of the State of Rhineland-Palatinate in Germany

Prof. Dr. Uschi Steigenberger,
ISIS Rutherford Appleton Laboratory, Oxfordshire (United Kingdom),
as representatives from the fields of science and economy

Prof. Dr. Thomas Glasmacher,
Facility for Rare Isotope Beams, East Lansing (USA)
as representatives from the fields of science and economy

Prof. Dr. Klaus Blaum,
Max-Planck-Institut für Kernphysik, Heidelberg (Germany),
Vice-Chair of the Joint Scientific Council GSI/FAIR

Dr. Bettina Lommel,
GSI Helmholtzzentrum für Schwerionenforschung,
as spokesperson of the Scientific-Technical Council of GSI

Directors' Board / Geschäftsführung (GF):

Ursula Weyrich, Prof. Dr. K. Langanke, Jörg Blaurock [since Feb. 2016]

Joint Scientific Council of GSI and FAIR (JSC):

https://www.gsi.de/work/organisation/wissenschaftliche_gremien/sc.htm
S. Raha [chair], Bose Institute, Kolkata (India);
K. Blaum [vice-chair and Head of GSI-SC], MPI-K, Heidelberg (Germany);
F. Azaiez, IPN-Orsay (France); *M. J. Borge*, Madrid University (Spain); *E. Lindroth*, Stockholm University (Sweden); *K. Redlich*, Wroclaw University (Poland); *P. Rossi*, Jefferson Laboratory, Newport News (USA); *Chr. Roy*, CNRS, Strasbourg (France); *N. Saito*, J-PARC Center, Ibaraki (Japan); *L. Sihver*, Vienna University of Technology & MedAustron GmbH, Vienna (Austria); *R. Tribble*, Brookhaven National Laboratory (USA); *G. V. Trubnikov*, Joint Institute for Nuclear Research, Dubna (Russia);
Secretary: D. Nicmorus

DOI:10.15120/GR-2017-1

Scientific and Technical Council / Wissenschaftlich-Technischer Rat (WTR):

https://www.gsi.de/work/organisation/wissenschaftliche_gremien/wtr.htm

B. Lommel (Spokesperson); *R. Bär; W. Barth; W. Bayer; P. Braun-Munzinger; A. Bräuning-Demian; R. Fuchs; M. Gorska; F. Herfurth; C. Kausch; O. Kester [until summer 2016]; Y. Leifels* (Vice-Spokesperson)*; V. Lindenstruth; Y. Litvinov; P. Malzacher; F. Maas; D. Ondreka; K. Peters; H. Reich-Sprenger; C. Scheidenberger; C.J. Schmidt; L. Schmitt; M. Schwickert; P. Senger; H. Simon; P. Spiller; J. Stadlmann; T. Stöhlker; J. Stroth; C. Trautmann; U. Weinrich;*

Scientific Programme Advisory Committees of GSI

https://www.gsi.de/work/organisation/wissenschaftliche_gremien.htm

PHELIX Committee:

www.gsi.de/phelix_committee

P. Thirolf [chair], LMU, München (Germany);
B. Cros, CNRS, LPGP, Université Paris-Sud, Orsay (France), *D. Gericke*, University of Warwick, Coventry (UK); *A. Golubev*, ITEP, Moscow (Russia); V. *Tikhonchuk*, University of Bordeaux 1, Talence (France).

DOI:10.15120/GR-2017-1

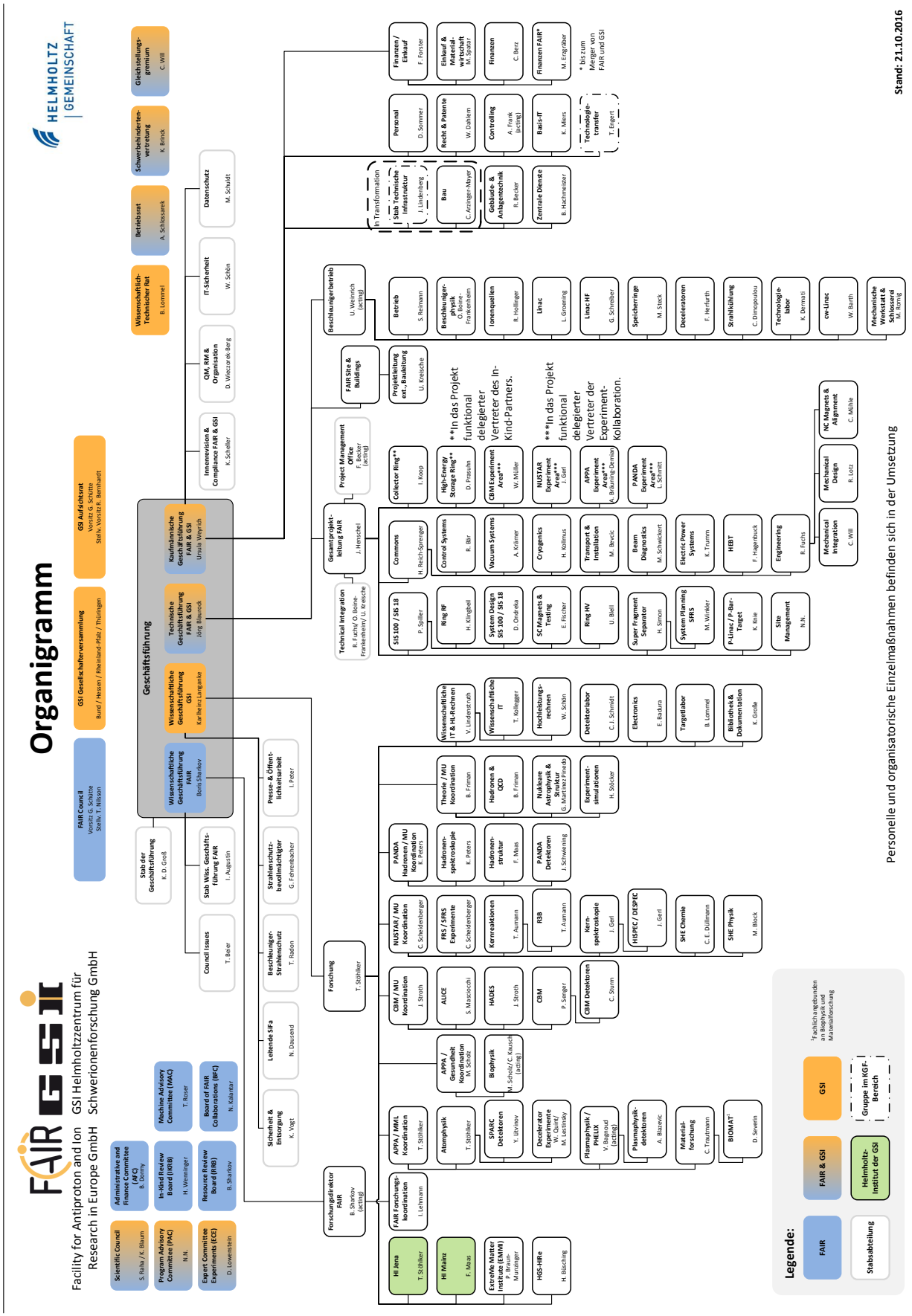

DOI:10.15120/GR-2017-1

Experiments performed at the GSI accelerators in 2016

Compiled by D. Severin[1], beam time coordinator 2016
[1]GSI, Darmstadt, Germany

In all tables 1 shift represents 8 hours of beam delivered to an experiment including necessary accelerator tuning time.

Exp.	Short title	Spokesperson	Area	Ion	Shifts (8h)	
					main	parasite
U293	Laser spectroscopy of nobelium and lawrencium	Laatiaoui, M.	Y7	Ca	47	57
U300	First chemical study of element 113 behind TASCA	Yakushev, A.	X8	Ca	58	26
U301	LIGHT: First application of ultra-intense proton bunches and investigation of the transport of heavy ions	Roth, M.	Z6	only rf	0	27
U303	Ion energy loss in plasma at the maximum of the stopping power".	Cayzac, W.	Z6	C	0	25
U305	High energy resolution spectroscopy of the target K-shell radiation induced under the action of U-ions	Rosmej, O.	Z6	Au	0	9
U306	Charge state and energy loss of heavy ions after interaction with inductively coupled plasma	Xu, G.	Z6	Au	0	18
U304	Large area continuous position sensitive diamond detectors	Ciobanu, M.	X0	C	0	7
UBIO	Biology Experiments at UNILAC	Friedrich, T.	X0, X6	He, C, O, Au	13	29
UMAT	Material Science Experiments at the UNILAC	Trautmann, C.	X0, M1, M2, M3	C, Ca, Au, U	54	124

DOI:10.15120/GR-2017-1